

STATE OF THE CLIMATE IN 2022



Special Supplement to the
Bulletin of the American Meteorological Society
Vol. 104, No. 9, September 2023

Cover Credit:

Climate Change - Skiing and snowboarding during Winter Holidays in the Bavarian Alps around Oberstdorf.

Oberstdorf, Germany

Matthias Manuel / Alamy Stock Photo

How to cite this document:

Special Supplement to the Bulletin of the American Meteorological Society, Vol. 104, No. 9, September 2023 <https://doi.org/10.1175/2023BAMSStateoftheClimate.1>. Compiled by NOAA's National Centers for Environmental Information, *State of the Climate in 2022* is based on contributions from scientists from around the world. It provides a detailed update on global climate indicators, notable weather events, and other data collected by environmental monitoring stations and instruments located on land, water, ice, and in space.

Citing the complete report:

Blunden, J., T. Boyer, and E. Bartow-Gillies, Eds., 2023: "State of the Climate in 2022". Bull. Amer. Meteor. Soc., 104 (9), Si–S501 <https://doi.org/10.1175/2023BAMSStateoftheClimate.1>.

Corresponding author: Full Report: Jessica Blunden / jessica.blunden@noaa.gov

©2023 American Meteorological Society

For information regarding reuse of this content and general copyright information, consult the [AMS Copyright Policy](#).

STATE OF THE CLIMATE IN 2022

Table of Contents

Abstract	Siii
1. Introduction	S1
2. Global Climate	S11
3. Global Oceans	S146
4. The Tropics	S207
5. The Arctic	S271
6. Antarctica and the Southern Ocean	S322
7. Regional Climates	S366
8. Relevant Datasets and Sources	S474

Abstract

—J. BLUNDEN, T. BOYER, AND E. BARTOW-GILLIES

Earth's global climate system is vast, complex, and intricately interrelated. Many areas are influenced by global-scale phenomena, including the "triple dip" La Niña conditions that prevailed in the eastern Pacific Ocean nearly continuously from mid-2020 through all of 2022; by regional phenomena such as the positive winter and summer North Atlantic Oscillation that impacted weather in parts the Northern Hemisphere and the negative Indian Ocean dipole that impacted weather in parts of the Southern Hemisphere; and by more localized systems such as high-pressure heat domes that caused extreme heat in different areas of the world. Underlying all these natural short-term variabilities are long-term climate trends due to continuous increases since the beginning of the Industrial Revolution in the atmospheric concentrations of Earth's major greenhouse gases.

In 2022, the annual global average carbon dioxide concentration in the atmosphere rose to 417.1 ± 0.1 ppm, which is 50% greater than the pre-industrial level. Global mean tropospheric methane abundance was 165% higher than its pre-industrial level, and nitrous oxide was 24% higher. All three gases set new record-high atmospheric concentration levels in 2022.

Sea-surface temperature patterns in the tropical Pacific characteristic of La Niña and attendant atmospheric patterns tend to mitigate atmospheric heat gain at the global scale, but the annual global surface temperature across land and oceans was still among the six highest in records dating as far back as the mid-1800s. It was the warmest La Niña year on record. Many areas observed record or near-record heat. Europe as a whole observed its second-warmest year on record, with sixteen individual countries observing record warmth at the national scale. Records were shattered across the continent during the summer months as heatwaves plagued the region. On 18 July, 104 stations in France broke their all-time records. One day later, England recorded a temperature of 40°C for the first time ever. China experienced its second-warmest year and warmest summer on record. In the Southern Hemisphere, the average temperature across New Zealand reached a record high for the second year in a row. While Australia's annual temperature was slightly below the 1991–2020 average, Onslow Airport in Western Australia reached 50.7°C on 13 January, equaling Australia's highest temperature on record.

While fewer in number and locations than record-high temperatures, record cold was also observed during the year. Southern Africa had its coldest August on record, with minimum temperatures as much as 5°C below normal over Angola, western Zambia, and northern Namibia. Cold outbreaks in the first half of December led to many record-low daily minimum temperature records in eastern Australia.

The effects of rising temperatures and extreme heat were apparent across the Northern Hemisphere, where snow-cover extent by June 2022 was the third smallest in the 56-year record, and the seasonal duration of lake ice cover was the fourth shortest since 1980. More frequent and intense heatwaves contributed to the second-greatest average mass balance loss for Alpine glaciers around the world since the start of the record in 1970. Glaciers in the Swiss Alps lost a record 6% of their volume. In South America, the combination of drought and heat left many central Andean glaciers snow free by mid-summer in early 2022; glacial ice has a much lower albedo than snow, leading to accelerated heating of the glacier. Across the global cryosphere, permafrost temperatures continued to reach record highs at many high-latitude and mountain locations.

In the high northern latitudes, the annual surface-air temperature across the Arctic was the fifth highest in the 123-year record. The seasonal Arctic minimum sea-ice extent, typically reached in September, was the 11th-smallest in the 43-year record; however, the amount of multiyear ice—ice that survives at least one summer melt season—remaining in the Arctic continued to decline. Since 2012, the Arctic has been nearly devoid of ice more than four years old.

In Antarctica, an unusually large amount of snow and ice fell over the continent in 2022 due to several landfalling atmospheric rivers, which contributed to the highest annual surface mass balance, 15% to 16% above the 1991–2020 normal, since the start of two reanalyses records dating to 1980. It was the second-warmest year on record for all five of the long-term staffed weather stations on the Antarctic Peninsula. In East Antarctica, a heatwave event led to a new all-time record-high temperature of -9.4°C — 44°C above the March average—on 18 March at Dome C. This was followed by the collapse of the critically unstable Conger Ice Shelf. More than 100 daily low sea-ice extent and sea-ice area records were set in 2022, including two new all-time annual record lows in net sea-ice extent and area in February.

Across the world's oceans, global mean sea level was record high for the 11th consecutive year, reaching 101.2 mm above the 1993 average when satellite altimetry measurements began, an increase of 3.3 ± 0.7 over 2021. Globally-averaged ocean heat content was also record high in 2022, while the global sea-surface temperature was the sixth highest on record, equal with 2018. Approximately 58% of the ocean surface experienced at least one marine heatwave in 2022. In the Bay of Plenty, New Zealand's longest continuous marine heatwave was recorded.

A total of 85 named tropical storms were observed during the Northern and Southern Hemisphere storm seasons, close

to the 1991–2020 average of 87. There were three Category 5 tropical cyclones across the globe—two in the western North Pacific and one in the North Atlantic. This was the fewest Category 5 storms globally since 2017. Globally, the accumulated cyclone energy was the lowest since reliable records began in 1981. Regardless, some storms caused massive damage. In the North Atlantic, Hurricane Fiona became the most intense and most destructive tropical or post-tropical cyclone in Atlantic Canada’s history, while major Hurricane Ian killed more than 100 people and became the third costliest disaster in the United States, causing damage estimated at \$113 billion U.S. dollars. In the South Indian Ocean, Tropical Cyclone Batsirai dropped 2044 mm of rain at Commerson Crater in Réunion. The storm also impacted Madagascar, where 121 fatalities were reported.

As is typical, some areas around the world were notably dry in 2022 and some were notably wet. In August, record high areas of land across the globe (6.2%) were experiencing extreme drought. Overall, 29% of land experienced moderate or worse categories of drought during the year. The largest drought footprint in the contiguous United States since 2012 (63%) was observed in late October. The record-breaking megadrought of central Chile continued in its 13th consecutive year, and 80-year record-low river levels in northern Argentina and Paraguay disrupted fluvial transport. In China, the Yangtze River reached record-low values. Much of equatorial eastern

Africa had five consecutive below-normal rainy seasons by the end of 2022, with some areas receiving record-low precipitation totals for the year. This ongoing 2.5-year drought is the most extensive and persistent drought event in decades, and led to crop failure, millions of livestock deaths, water scarcity, and inflated prices for staple food items.

In South Asia, Pakistan received around three times its normal volume of monsoon precipitation in August, with some regions receiving up to eight times their expected monthly totals. Resulting floods affected over 30 million people, caused over 1700 fatalities, led to major crop and property losses, and was recorded as one of the world’s costliest natural disasters of all time. Near Rio de Janeiro, Brazil, Petrópolis received 530 mm in 24 hours on 15 February, about 2.5 times the monthly February average, leading to the worst disaster in the city since 1931 with over 230 fatalities.

On 14–15 January, the Hunga Tonga-Hunga Ha'apai submarine volcano in the South Pacific erupted multiple times. The injection of water into the atmosphere was unprecedented in both magnitude—far exceeding any previous values in the 17-year satellite record—and altitude as it penetrated into the mesosphere. The amount of water injected into the stratosphere is estimated to be 146 ± 5 Terragrams, or ~10% of the total amount in the stratosphere. It may take several years for the water plume to dissipate, and it is currently unknown whether this eruption will have any long-term climate effect.

Editor and Author Affiliations (alphabetical by name)

- Abida, A.**, Agence Nationale de l'Aviation Civile et de la Météorologie, Moroni, Union of the Comoros
- Ades, Melanie**, European Centre for Medium-Range Weather Forecasts, Reading, United Kingdom
- Adler, Robert**, CMNS-Earth System Science Interdisciplinary Center, University of Maryland, College Park, Maryland
- Adusumilli, Susheel**, Scripps Institution of Oceanography, University of California, San Diego, La Jolla, California
- Agyakwah, W.**, NOAA/NWS National Centers for Environmental Prediction Climate Prediction Center, College Park, Maryland
- Ahmasuk, Brandon**, Kawerak Inc., Nome, Alaska
- Aldeco, Laura S.**, Servicio Meteorológico Nacional, Buenos Aires, Argentina
- Alexe, Mihai**, European Centre for Medium-Range Weather Forecasts, Bonn, Germany
- Alfaro, Eric J.**, Center for Geophysical Research and School of Physics, University of Costa Rica, San José, Costa Rica
- Allan, Richard P.**, Department of Meteorology and National Centre for Earth Observation, University of Reading, Reading, United Kingdom
- Allgood, Adam**, NOAA/NWS National Centers for Environmental Prediction Climate Prediction Center, College Park, Maryland
- Alves, Lincoln M.**, Centro Nacional de Monitoramento e Alertas de Desastres Naturais CEMADEN, São Paulo, Brazil
- Amador, Jorge A.**, Center for Geophysical Research and School of Physics, University of Costa Rica, San José, Costa Rica
- Anderson, John**, Hampton University, Hampton, Virginia
- Andrade, B.**, Seychelles Meteorological Authority, Mahe, Seychelles
- Anneville, Orlane**, National Research Institute for Agriculture, Food and Environment (INRAE), CARRTEL, Université Savoie Mont Blanc, Chambéry, France
- Aono, Yasuyuki**, Graduate School of Agriculture, Osaka Metropolitan University, Sakai, Japan
- Arguez, Anthony**, NOAA/NESDIS National Centers for Environmental Information, Asheville, North Carolina
- Arosio, Carlo**, University of Bremen, Bremen, Germany
- Atkinson, C.**, Met Office Hadley Center, Exeter, United Kingdom
- Augustine, John A.**, NOAA Global Monitoring Laboratory, Boulder, Colorado
- Avalos, Grinia**, Servicio Nacional de Meteorología e Hidrología del Perú, Lima, Perú
- Azorin-Molina, Cesar**, Centro de Investigaciones sobre Desertificación – Spanish National Research Council (CSIC-UV-GVA), Valencia, Spain
- Backensto, Stacia A.**, National Park Service, Fairbanks, Alaska
- Bader, Stephan**, Federal Office of Meteorology and Climatology MeteoSwiss, Switzerland
- Baez, Julian**, Universidad Católica Nuestra Señora de la Asunción, Asunción, Paraguay
- Baiman, Rebecca**, Department of Atmospheric and Oceanic Sciences, University of Colorado Boulder, Boulder, Colorado
- Ballinger, Thomas J.**, International Arctic Research Center, University of Alaska Fairbanks, Fairbanks, Alaska
- Banwell, Alison F.**, Earth Science Observation Center, Cooperative Institute for Research in Environmental Sciences (ESOC/CIRES), University of Colorado Boulder, Boulder, Colorado
- Bardin, M. Yu**, Yu. A. Izrael Institute of Global Climate and Ecology, Institute of Geography, Russian Academy of Sciences, Moscow, Russia
- Barichivich, Jonathan**, Instituto de Geografía, Pontificia Universidad Católica de Valparaíso, Valparaíso, Chile; Laboratoire des Sciences du Climat et de l'Environnement (LSCE), LSCE/IPSL, CEA-CNRS-UVSQ, Gif-sur-Yvette, France
- Barnes, John E.**, retired, NOAA Global Monitoring Laboratory, Boulder, Colorado
- Barreira, Sandra**, Argentine Naval Hydrographic Service, Buenos Aires, Argentina
- Bartow-Gillies, Ellen**, NOAA/NESDIS National Centers for Environmental Information, Asheville, North Carolina
- Beadling, Rebecca L.**, Department of Earth and Environmental Science, Temple University, Philadelphia, Pennsylvania
- Beck, Hylke E.**, Physical Science and Engineering Division, King Abdullah University of Science and Technology, Thuwal, Saudi Arabia
- Becker, Emily J.**, University of Miami Rosenstiel School of Marine and Atmospheric Science, Miami, Florida
- Bekele, E.**, NOAA/NWS National Centers for Environmental Prediction Climate Prediction Center, College Park, Maryland
- Bellido, Guillem Martín**, Govern d'Andorra, Andorra la Vella, Andorra
- Bellouin, Nicolas**, University of Reading, Reading, United Kingdom
- Benedetti, Angela**, European Centre for Medium-Range Weather Forecasts, Reading, United Kingdom
- Benestad, Rasmus**, Norwegian Meteorological Institute, Oslo, Norway
- Berne, Christine**, Météo France, Toulouse, France
- Berner, Logan T.**, Northern Arizona University, Flagstaff, Arizona
- Bernhard, Germar H.**, Biospherical Instruments Inc., San Diego, California
- Bhatt, Uma S.**, Geophysical Institute, University of Alaska Fairbanks, Fairbanks, Alaska
- Bhuiyan, MD A. E.**, NOAA/NWS Climate Prediction Center, Silver Spring, Maryland
- Bigalke, Siiri**, Plant, Soils and Climate Department, Utah State University, Logan, Utah
- Biló, Tiago**, Cooperative Institute for Marine and Atmospheric Studies, University of Miami, Miami, Florida; NOAA/OAR Atlantic Oceanographic and Meteorological Laboratory, Miami, Florida
- Bissolli, Peter**, Deutscher Wetterdienst, WMO RA VI Regional Climate Centre Network, Offenbach, Germany
- Bjerke Jarle, W.**, Department of Arctic Ecology, Norwegian Institute for Nature Research, Trondheim, Norway
- Blagrove, Kevin**, Department of Biology, York University, Toronto, Canada
- Blake, Eric S.**, NOAA/NWS National Hurricane Center, Miami, Florida
- Blenkinsop, Stephen**, School of Engineering, Newcastle University, Newcastle-upon-Tyne, United Kingdom
- Blunden, Jessica**, NOAA/NESDIS National Centers for Environmental Information, Asheville, North Carolina
- Bochníček, Oliver**, Slovak Hydrometeorological Institute, Bratislava, Slovakia
- Bock, Olivier**, Université Paris Cité, Institut de Physique du Globe de Paris, CNRS, IGN, F-75005 Paris, France; ENSG-Géomatique, IGN, F-77455 Marne-la-Vallée, France
- Bodin, Xavier**, Laboratoire EDYTEM, CNRS/Université Savoie Mont-Blanc, Chambéry, France
- Bosilovich, Michael**, Global Modeling and Assimilation Office, NASA Goddard Space Flight Center, Greenbelt, Maryland
- Boucher, Olivier**, Sorbonne Université, Paris, France
- Boyer, Tim**, NOAA/NESDIS National Centers for Environmental Information, Silver Spring, Maryland
- Bozkurt, Deniz**, Department of Meteorology, University of Valparaíso, Valparaíso, Chile; Center for Climate and Resilience Research (CR)2, Santiago, Chile
- Brettschneider, Brian**, NOAA/NWS Alaska Region, Anchorage, Alaska
- Bringas, Francis G.**, NOAA/OAR Atlantic Oceanographic and Meteorological Laboratory, Miami, Florida
- Bringas, Francis**, NOAA/OAR Atlantic Oceanographic and Meteorological Laboratory, Miami, Florida
- Buechler, Dennis**, University of Alabama in Huntsville, Huntsville, Alabama
- Buehler, Stefan A.**, Universität Hamburg, Hamburg, Germany
- Bukunt, Brandon**, NOAA/NWS Weather Forecast Office, Tiyan, Guam
- Calderón, Blanca**, Center for Geophysical Research, University of Costa Rica, San José, Costa Rica

Editor and Author Affiliations (continued)

- Camargo, Suzana J.**, Lamont-Doherty Earth Observatory, Columbia University, Palisades, New York
- Campbell, Jayaka**, Department of Physics, The University of the West Indies, Kingston, Jamaica
- Campos, Diego**, Dirección Meteorológica de Chile (DMC), Santiago, Chile
- Carrea, Laura**, Department of Meteorology, University of Reading, Reading, United Kingdom
- Carter, Brendan R.**, Cooperative Institute for Climate, Ocean, and Ecosystem Studies, University of Washington, Seattle, Washington; NOAA/OAR Pacific Marine Environmental Laboratory, Seattle, Washington
- Cetinić, Ivona**, NASA Goddard Space Flight Center, Greenbelt, Maryland; Morgan State University, Baltimore, Maryland
- Chambers, Don P.**, College of Marine Science, University of South Florida, St. Petersburg, Florida
- Chan, Duo**, Woods Hole Oceanographic Institution, Woods Hole, Massachusetts
- Chandler, Elise**, Bureau of Meteorology, Melbourne, Australia
- Chang, Kai-Lan**, Cooperative Institute for Research in Environmental Sciences, University of Colorado Boulder, Boulder, Colorado; NOAA Chemical Sciences Laboratory, Boulder, Colorado
- Chen, Hua**, Nanjing University of Information Science and Technology, Nanjing, China
- Chen, Lin**, Institute for Climate and Application Research (ICAR)/KLME/ILCEC/CIC-FEMD, Nanjing University of Information Science and Technology, Nanjing, China
- Cheng, Lijing**, International Center for Climate and Environment Sciences, Institute of Atmospheric Physics, Chinese Academy of Sciences, Beijing, China
- Cheng, Vincent Y. S.**, Environment and Climate Change Canada, Toronto, Ontario, Canada
- Chomiak, Leah**, Cooperative Institute for Marine and Atmospheric Studies, University of Miami; NOAA/OAR Atlantic Oceanographic and Meteorological Laboratory, Miami, Florida; Rosenstiel School of Marine, Atmospheric, and Earth Science, University of Miami, Miami, Florida
- Christiansen, Hanne H.**, Geology Department, University Centre in Svalbard, Longyearbyen, Norway
- Christy, John R.**, University of Alabama in Huntsville, Huntsville, Alabama
- Chung, Eui-Seok**, Korea Polar Research Institute, Incheon, South Korea
- Ciasto, Laura M.**, NOAA/NWS National Centers for Environmental Prediction Climate Prediction Center, College Park, Maryland
- Clarke, Leonardo**, Department of Physics, The University of the West Indies, Kingston, Jamaica
- Clem, Kyle R.**, School of Geography, Environment and Earth Sciences, Victoria University of Wellington, Wellington, New Zealand
- Clingan, Scott**, Cooperative Institute for Research in the Earth Sciences, NOAA Global Monitoring Laboratory, Boulder, Colorado
- Coelho, Caio A.S.**, Centro de Previsão do Tempo e Estudos Climáticos/National Institute for Space Research, Center for Weather Forecasts and Climate Studies, Cachoeira Paulista, Brazil
- Cohen, Judah L.**, Atmospheric and Environmental Research, Lexington, Massachusetts
- Coldewey-Egbers, Melanie**, DLR (German Aerospace Center) Oberpfaffenhofen, Germany
- Colwell, Steve**, British Antarctic Survey, Cambridge, United Kingdom
- Cooper, Owen R.**, Cooperative Institute for Research in Environmental Sciences, University of Colorado Boulder, Boulder, Colorado; NOAA Chemical Sciences Laboratory, Boulder, Colorado
- Cornes, Richard C.**, National Oceanography Centre, Southampton, United Kingdom
- Correa, Kris**, Servicio Nacional de Meteorología e Hidrología del Perú, Lima, Perú
- Costa, Felipe**, Centro Internacional para la Investigación del Fenómeno de El Niño (CIIFEN), Guayaquil, Ecuador
- Covey, Curt**, Lawrence Livermore National Laboratory, Livermore, California
- Coy, Lawrence**, Science Systems and Applications, Inc., Lanham, Maryland; NASA Goddard Space Flight Center, Greenbelt, Maryland
- Créatux, Jean-François**, LEGOS (CNES/CNRS/IRD/UPS), University of Toulouse, Toulouse, France
- Crhova, Lenka**, Czech Hydrometeorological Institute, Prague, Czech Republic
- Crimmins, Theresa**, USA National Phenology Network, School of Natural Resources and the Environment, University of Arizona, Tucson, Arizona
- Cronin, Meghan F.**, NOAA/OAR Pacific Marine Environmental Laboratory, Seattle, Washington
- Cropper, Thomas**, National Oceanography Centre, Southampton, United Kingdom
- Crotwell, Molly**, Cooperative Institute for Research in the Earth Sciences, NOAA Global Monitoring Laboratory, Boulder, Colorado
- Culpepper, Joshua**, Department of Biology, York University, Toronto, Canada
- Cunha, Ana P.**, Centro Nacional de Monitoramento e Alertas de Desastres Naturais CEMADEN, São Paulo, Brazil
- Cusicanqui, Diego**, Université Grenoble Alpes, Institut de Géosciences de l'Environnement (IGE), Grenoble, France
- Datta, Rajashree T.**, Department of Atmospheric and Oceanic Sciences, University of Colorado Boulder, Boulder, Colorado
- Davis, Sean M.**, NOAA Chemical Sciences Laboratory, Boulder, Colorado
- De Boek, Veerle**, Royal Meteorological Institute of Belgium (KMI), Brussels, Belgium
- de Jeu, Richard A. M.**, Planet Labs, Haarlem, The Netherlands
- De Laat, Jos**, Royal Netherlands Meteorological Institute (KNMI), DeBilt, The Netherlands
- Decharme, Bertrand**, Centre National de Recherches Météorologiques, Météo-France/CNRS, Toulouse, France
- Degenstein, Doug**, University of Saskatchewan, Saskatoon, Canada
- Delaloye, Reynald**, Department of Geosciences, University of Fribourg, Fribourg, Switzerland
- Demircan, Mesut**, Turkish State Meteorological Service, Igdir, Türkiye
- Derksen, Chris**, Climate Research Division, Environment and Climate Change Canada, Toronto, Canada
- Deus, Ricardo**, Portuguese Sea and Atmosphere Institute, Lisbon, Portugal
- Dhurmea, K. R.**, Mauritius Meteorological Service, Vacoas, Mauritius
- Diamond, Howard J.**, NOAA/OAR Air Resources Laboratory, College Park, Maryland
- Dirkse, S.**, Namibia Meteorological Service, Windhoek, Namibia
- Divine, Dmitry**, Norwegian Polar Institute, Fram Centre, Tromsø, Norway
- Dokulil, Martin T.**, Research Institute for Limnology, University of Innsbruck, Mondsee, Austria
- Donat, Markus G.**, Barcelona Supercomputing Centre, Barcelona, Spain; Catalan Institution for Research and Advanced Studies (ICREA), Barcelona, Spain
- Dong, Shenfu**, NOAA/OAR Atlantic Oceanographic and Meteorological Laboratory, Miami, Florida
- Dorigo, Wouter A.**, TU Wien, Department of Geodesy and Geoinformation, Vienna, Austria
- Drost Jensen, Caroline**, Danish Meteorological Institute, Copenhagen, Denmark
- Druckenmiller, Matthew L.**, National Snow and Ice Data Center, Cooperative Institute for Research in Environmental Sciences, University of Colorado, Boulder, Colorado
- Drumond, Paula**, Portuguese Sea and Atmosphere Institute, Lisbon, Portugal
- du Plessis, Marcel**, Department of Marine Sciences, University of Gothenburg, Gothenburg, Sweden
- Dugan, Hilary A.**, Center for Limnology, University of Wisconsin-Madison, Madison, Wisconsin
- Dulamsuren, Dashkhuu**, Institute of Meteorology, Hydrology and Environment, National Agency for Meteorology, Ulaanbaatar, Mongolia
- Dunmire, Devon**, Department of Atmospheric and Oceanic Sciences, University of Colorado Boulder, Boulder, Colorado
- Dunn, Robert J. H.**, Met Office Hadley Centre, Exeter, United Kingdom
- Durre, Imke**, NOAA/NESDIS National Centers for Environmental Information, Asheville, North Carolina

Editor and Author Affiliations (continued)

- Dutton, Geoff**, Cooperative Institute for Research in the Earth Sciences, NOAA Global Monitoring Laboratory, Boulder, Colorado
- Duveiller, Gregory**, Max Planck Institute for Biogeochemistry, Jena, Germany
- Ekici, Mithat**, Turkish State Meteorological Service, Ankara, Türkiye
- Elias Chereque, Alesksandra**, Department of Physics, University of Toronto, Toronto, Canada
- ElKharrim, M.**, Direction de la Météorologie Nationale Maroc, Rabat, Morocco
- Epstein, Howard E.**, University of Virginia, Charlottesville, Virginia
- Espinoza, Jhan-Carlo**, Université Grenoble Alpes, Institut des Géosciences de l'Environnement, IRD, CNRS, Grenoble INP, Grenoble, France
- Estilow, Thomas W.**, Rutgers University, Piscataway, New Jersey
- Estrella, Nicole**, Ecoclimatology, Department of Life Science Systems, TUM School of Life Sciences, Technical University of Munich, Freising, Germany
- Fauchereau, Nicolas**, National Institute of Water and Atmospheric Research, Ltd., Auckland, New Zealand
- Fausto, Robert S.**, Geological Survey of Denmark and Greenland (GEUS), Copenhagen, Denmark
- Feely, Richard A.**, NOAA/OAR Pacific Marine Environmental Laboratory, Seattle, Washington
- Fenimore, Chris**, NOAA/NESDIS National Centers for Environmental Information, Asheville, North Carolina
- Fereday, David**, Met Office Hadley Centre, Exeter, United Kingdom
- Fettweis, Xavier**, University of Liège, Belgium
- Fioletov, Vitali E.**, Environment and Climate Change Canada, Toronto, Canada
- Flemming, Johannes**, European Centre for Medium-Range Weather Forecasts, Reading, United Kingdom
- Fogarty, Chris**, Canadian Hurricane Centre, Environment and Climate Change Canada, Dartmouth, Nova Scotia, Canada
- Fogt, Ryan L.**, Department of Geography, Ohio University, Athens, Ohio
- Forbes, Bruce C.**, Arctic Centre, University of Lapland, Rovaniemi, Finland
- Foster, Michael J.**, Cooperative Institute for Meteorological Satellite Studies, Space Science and Engineering Center, University of Wisconsin-Madison, Madison, Wisconsin
- Franz, Bryan A.**, NASA Goddard Space Flight Center, Greenbelt, Maryland
- Freeman, Natalie M.**, Department of Atmospheric and Oceanic Sciences, University of Colorado Boulder, Boulder, Colorado
- Fricke, Helen A.**, Scripps Institution of Oceanography, University of California, San Diego, La Jolla, California
- Frith, Stacey M.**, Science Systems and Applications, Inc, Lanham, Maryland; NASA Goddard Space Flight Center, Greenbelt, Maryland
- Froidevaux, Lucien**, Jet Propulsion Laboratory, California Institute of Technology, Pasadena, California
- Frost, Gerald V. (JJ)**, ABR Inc., Fairbanks, Alaska
- Fuhrman, Steven**, NOAA/NWS NOAA/NWS National Centers for Environmental Prediction Climate Prediction Center, College Park, Maryland
- Füllekrug, Martin**, University of Bath, Bath, United Kingdom
- Ganter, Catherine**, Bureau of Meteorology, Melbourne, Australia
- Gao, Meng**, NASA Goddard Space Flight Center, Greenbelt, Maryland;
- Gardner, Alex S.**, NASA Jet Propulsion Laboratory, Pasadena, California
- Garforth, Judith**, Woodland Trust, Grantham, United Kingdom
- Garg, Jay**, Science Systems and Applications Inc., Hampton, Virginia
- Gerland, Sebastian**, Norwegian Polar Institute, Fram Centre, Tromsø, Norway
- Gibbes, Badin**, School of Civil Engineering, The University of Queensland, Brisbane, Australia
- Gille, Sarah T.**, Scripps Institution of Oceanography, University of California, San Diego, La Jolla, California
- Gilson, John**, Scripps Institution of Oceanography, University of California San Diego, La Jolla, California
- Gleason, Karin**, NOAA/NESDIS National Centers for Environmental Information, Asheville, North Carolina
- Gobron, Nadine**, European Commission Joint Research Centre, Ispra, Italy
- Goetz, Scott J.**, Northern Arizona University, Flagstaff, Arizona
- Goldenberg, Stanley B.**, NOAA/OAR Atlantic Oceanographic and Meteorological Laboratory, Miami, Florida
- Goni, Gustavo**, NOAA/OAR Atlantic Oceanographic and Meteorological Laboratory, Miami, Florida
- Goodman, Steven**, Thunderbolt Global Analytics, Huntsville, Alabama
- Goto, Atsushi**, World Meteorological Organization, Geneva, Switzerland
- Grooß, Jens-Uwe**, Forschungszentrum Jülich, Jülich, Germany
- Gruber, Alexander**, TU Wien, Department of Geodesy and Geoinformation, Vienna, Austria
- Gu, Guojun**, CMNS-Earth System Science Interdisciplinary Center, University of Maryland, College Park, Maryland
- Guard, Charles "Chip" P.**, Tropical Weather Sciences, Sinajana, Guam
- Hagos, S.**, Pacific Northwest National Lab, Department of Energy, Richland, Washington
- Hahn, Sebastian**, TU Wien, Department of Geodesy and Geoinformation, Vienna, Austria
- Haimberger, Leopold**, University of Vienna, Vienna, Austria
- Hall, Bradley D.**, NOAA Global Monitoring Laboratory, Boulder, Colorado
- Hamlington, Benjamin D.**, Center for Coastal Physical Oceanography, Old Dominion University, Norfolk, Virginia
- Hanna, Edward**, Department of Geography and Lincoln Climate Research Group, Lincoln, United Kingdom
- Hanssen-Bauer, Inger**, Norwegian Meteorological Institute, Oslo, Norway
- Harnos, Daniel S.**, NOAA/NWS National Centers for Environmental Prediction Climate Prediction Center, College Park, Maryland
- Harris, Ian**, National Centre for Atmospheric Science (NCAS), University of East Anglia, Norwich, United Kingdom; Climatic Research Unit, School of Environmental Sciences, University of East Anglia, Norwich, United Kingdom
- He, Qiong**, Earth System Modeling Center, Nanjing University of Information Science and Technology, Nanjing, China
- Heim, Richard R. Jr.**, NOAA/NESDIS National Centers for Environmental Information, Asheville, North Carolina
- Hellström, Sverker**, Swedish Meteorological and Hydrological Institute, Norrköping, Sweden
- Hemming, Deborah L.**, Met Office Hadley Centre, Exeter, United Kingdom; Birmingham Institute of Forest Research, Birmingham University, Birmingham, United Kingdom
- Hendricks, Stefan**, Alfred Wegener Institute, Helmholtz Centre for Polar and Marine Research, Bremerhaven, Germany
- Hicks, J.**, NOAA/NWS National Centers for Environmental Prediction Climate Prediction Center, College Park, Maryland
- Hidalgo, Hugo G.**, Center for Geophysical Research and School of Physics, University of Costa Rica, San José, Costa Rica
- Hirschi, Martin**, ETH Zurich, Department of Environmental Systems Science, Zürich, Switzerland
- Ho, Shu-peng (Ben)**, Center for Satellite Applications and Research, NOAA, College Park, Maryland; Remote Sensing Systems, Santa Rosa, California
- Hobbs, W.**, Australian Antarctic Program Partnership, Institute for Marine and Antarctic Studies; Australian Research Council Centre of Excellence for Climate Extremes, University of Tasmania, Hobart, Tasmania
- Holmes, Robert M.**, Woodwell Climate Research Center, Falmouth, Massachusetts
- Holzworth, Robert**, University of Washington, Seattle, Washington
- Hrbáček, Filip**, Department of Geography, Masaryk University, Brno, Czech Republic
- Hu, Guojie**, Cryosphere Research Station on Qinghai-Tibet Plateau, Northwestern Institute of Eco-Environment and Resources, CAS, Beijing, China
- Hu, Zeng-Zhen**, NOAA/NWS Climate Prediction Center, College Park, Maryland

Editor and Author Affiliations (continued)

- Huang, Boyin**, NOAA/NESDIS National Centers for Environmental Information, Asheville, North Carolina
- Huang, Hongjie**, Nanjing University of Information Science and Technology, Nanjing, China
- Hurst, Dale F.**, Cooperative Institute for Research in Environmental Sciences, University of Colorado Boulder, Boulder, Colorado; NOAA Global Monitoring Laboratory, Boulder, Colorado
- Ialongo, Iolanda**, Finnish Meteorological Institute, Helsinki, Finland
- Inness, Antje**, European Centre for Medium-Range Weather Forecasts, Reading, United Kingdom
- Isaksen, Ketil**, Norwegian Meteorological Institute, Oslo, Norway
- Ishii, Masayoshi**, Department of Atmosphere, Ocean and Earth System Modeling Research, Meteorological Research Institute, Japan Meteorological Agency, Tsukuba, Japan
- Jadra, Gerardo**, Instituto Uruguayo de Meteorología, Montevideo, Uruguay
- Jevrejeva, Svetlana**, National Oceanography Centre, Liverpool, United Kingdom
- John, Viju O.**, EUMETSAT, Darmstadt, Germany
- Johns, W.**, Rosenstiel School of Marine, Atmospheric, and Earth Science, University of Miami, Miami, Florida
- Johnsen, Bjørn**, Norwegian Radiation and Nuclear Safety, Østerås, Norway
- Johnson, Bryan**, NOAA/OAR Earth System Research Laboratory, Global Monitoring Division, Boulder, Colorado; University of Colorado Boulder, Boulder, Colorado
- Johnson, Gregory C.**, NOAA/OAR Pacific Marine Environmental Laboratory, Seattle, Washington
- Jones, Philip D.**, Climatic Research Unit, School of Environmental Sciences, University of East Anglia, Norwich, United Kingdom
- Jones, Timothy**, Coastal Observation and Seabird Survey Team, University of Washington, Seattle, Washington
- Josey, Simon A.**, National Oceanography Centre, Southampton, United Kingdom.
- Jumaux, G.**, Météo France, Direction Interregionale Pour L'Océan Indien, Reunion
- Junod, Robert**, Earth System Science Center (ESSC), University of Alabama in Huntsville, Huntsville, Alabama
- Kääb, Andreas**, Department of Geosciences, University of Oslo, Norway
- Kabidi, K.**, Direction de la Météorologie Nationale Maroc, Rabat, Morocco
- Kaiser, Johannes W.**, SatFire Kaiser, Hofheim am Taunus, Germany
- Kaler, Robb S.A.**, U.S. Fish and Wildlife Service, Alaska Region, Anchorage, Alaska
- Kaleschke, Lars**, Alfred Wegener Institute, Helmholtz Centre for Polar and Marine Research, Bremerhaven, Germany
- Kaufmann, Viktor**, Institute of Geodesy, Working Group Remote Sensing and Photogrammetry, Graz University of Technology, Graz, Austria
- Kazemi, Amin Fazl**, Iran National Climate and Drought Crisis Management, National Meteorology Organization, Tehran, Iran
- Keller, Linda M.**, Antarctic Meteorological Research and Data Center, Space Science and Engineering Center, University of Wisconsin-Madison, Madison, Wisconsin
- Kellerer-Pirklbauer, Andreas**, Institute of Geography and Regional Science, Cascade – The Mountain Processes and Mountain Hazards Group, University of Graz, Graz, Austria
- Kendon, Mike**, Met Office National Climate Information Centre, Exeter, United Kingdom
- Kennedy, John**, Met Office Hadley Centre, Exeter, United Kingdom
- Kent, Elizabeth C.**, National Oceanography Centre, Southampton, United Kingdom
- Kerr, Kenneth**, Trinidad and Tobago Meteorological Service, Piarcó, Trinidad
- Khan, Valentina**, Hydrometcenter of Russia, WMO North EurAsia Climate Center, Moscow, Russia
- Khiem, Mai Van**, Vietnam National Center for Hydro-Meteorological Forecasting, Vietnam Meteorological and Hydrological Administration, Hanoi, Vietnam
- Kidd, Richard**, EODC GmbH, Vienna, Austria
- Kim, Mi Ju**, Climate Change Monitoring Division, Korea Meteorological Administration, Seoul, South Korea
- Kim, Seong-Joong**, Korea Polar Research Institute, Incheon, South Korea
- Kipling, Zak**, European Centre for Medium-Range Weather Forecasts, Reading, United Kingdom
- Klotzbach, Philip J.**, Department of Atmospheric Science, Colorado State University, Fort Collins, Colorado
- Knaff, John A.**, NOAA/NESDIS Center for Satellite Applications and Research, Fort Collins, Colorado
- Koppa, Akash**, Hydro-Climate Extremes Lab (H-CEL), Ghent University, Ghent, Belgium
- Korshunova, Natalia N.**, All-Russian Research Institute of Hydrometeorological Information, World Data Center, Obninsk, Russia
- Kraemer, Benjamin M.**, University of Konstanz, Konstanz, Germany
- Kramarova, Natalya A.**, NASA Goddard Space Flight Center, Greenbelt, Maryland
- Kruger, A. C.**, Climate Service, South African Weather Service, Pretoria, South Africa
- Kruger, Andries**, Climate Service, South African Weather Service, Pretoria, South Africa
- Kumar, Arun**, NOAA/NWS National Centers for Environmental Prediction Climate Prediction Center, College Park, Maryland
- L'Heureux, Michelle**, NOAA/NWS National Centers for Environmental Prediction Climate Prediction Center, College Park, Maryland
- La Fuente, Sofia**, Dundalk Institute of Technology, Dundalk, Ireland
- Laas, Alo**, Estonian University of Life Sciences, Tartumaa, Estonia
- Labe, Zachary M.**, Princeton University, Princeton, New Jersey
- Lader, Rick**, International Arctic Research Center, University of Alaska Fairbanks, Fairbanks, Alaska
- Lakatos, Mónika**, Climatology Unit, Hungarian Meteorological Service, Budapest, Hungary
- Lakkala, Kaisa**, Finnish Meteorological Institute, Sodankylä, Finland
- Lam, Hoang Phuc**, Vietnam National Center for Hydro-Meteorological Forecasting, Vietnam Meteorological and Hydrological Administration, Hanoi, Vietnam
- Lan, Xin**, CIRES, University of Colorado Boulder & NOAA Global Monitoring Laboratory, Boulder, Colorado
- Landschützer, Peter**, Flanders Marine Institute, InnovOcean Campus, Ostend, Belgium
- Landsea, Chris W.**, NOAA/NWS National Hurricane Center, Miami, Florida
- Lang, Timothy**, NASA Marshall Space Flight Center, Huntsville, Alabama
- Lankhorst, Matthias**, Scripps Institution of Oceanography, University of California San Diego, La Jolla, California
- Lantz, Kathleen O.**, NOAA Global Monitoring Laboratory, Boulder, Colorado
- Lara, Mark J.**, University of Illinois at Urbana-Champaign, Urbana, Illinois
- Lavado-Casimiro, Waldo**, Servicio Nacional de Meteorología e Hidrología del Perú, Lima, Perú
- Lavers, David A.**, European Centre for Medium-Range Weather Forecasts, Reading, United Kingdom
- Lazzara, Matthew A.**, Department of Physical Sciences, School of Arts and Sciences, Madison Area Technical College, Madison, Wisconsin; Antarctic Meteorological Research and Data Center, Space Science and Engineering Center, University of Wisconsin-Madison, Madison, Wisconsin
- Leblanc, Thierry**, Jet Propulsion Laboratory, California Institute of Technology, Wrightwood, California
- Lee, Tsz-Cheung**, Hong Kong Observatory, Hong Kong, China
- Leibensperger, Eric M.**, Department of Physics and Astronomy, Ithaca College, Ithaca, New York
- Lennard, Chris**, Department of Environmental and Geographical Science, University of Cape Town, Cape Town, South Africa
- Leuliette, Eric**, NOAA/NWS NCWCP Laboratory for Satellite Altimetry, College Park, Maryland
- Leung, Kinson H. Y.**, Environment and Climate Change Canada, Toronto, Ontario, Canada
- Lieser, Jan L.**, Australian Bureau of Meteorology and Institute for Marine and Antarctic Studies (IMAS), University of Tasmania, Hobart, Australia

Editor and Author Affiliations (continued)

- Likso, Tanja**, Croatian Meteorological and Hydrological Service, Zagreb, Croatia
- Lin, I-I.**, National Taiwan University, Taipei, Taiwan
- Lindsey, Jackie**, Coastal Observation and Seabird Survey Team, University of Washington, Seattle, Washington
- Liu, Yakun**, Massachusetts Institute of Technology, Cambridge, Massachusetts
- Locarnini, Ricardo**, NOAA/NESDIS National Centers for Environmental Information, Silver Spring, Maryland
- Loeb, Norman G.**, NASA Langley Research Center, Hampton, Virginia
- Loomis, Bryant D.**, NASA Goddard Space Flight Center, Greenbelt, Maryland
- Lorrey, Andrew M.**, National Institute of Water and Atmospheric Research, Ltd., Auckland, New Zealand
- Loyola, Diego**, DLR (German Aerospace Center) Oberpfaffenhofen, Germany
- Lu, Rui**, Nanjing University of Information Science and Technology, Nanjing, China
- Lumpkin, Rick**, NOAA/OAR Atlantic Oceanographic and Meteorological Laboratory, Miami, Florida
- Luo, Jing-Jia**, Institute for Climate and Application Research, Nanjing University of Information Science and Technology, Nanjing, China
- Luojus, Kari**, Arctic Research Centre, Finnish Meteorological Institute, Helsinki, Finland
- Lyman, John M.**, Cooperative Institute for Marine and Atmospheric Research, University of Hawaii, Honolulu, Hawaii; NOAA/OAR Pacific Marine Environmental Laboratory, Seattle, Washington
- Maberly, Stephen C.**, UK Centre for Ecology & Hydrology, Lancaster, United Kingdom
- Macander, Matthew J.**, ABR Inc., Fairbanks, Alaska
- MacFerrin, Michael**, Earth Science and Observation Center, CIRES, University of Colorado, Boulder, Colorado
- MacGilchrist, Graeme A.**, University of St. Andrews, St Andrews, United Kingdom; Princeton University, Princeton, New Jersey
- MacLennan, Michelle L.**, Department of Atmospheric and Oceanic Sciences, University of Colorado Boulder, Boulder, Colorado
- Madelon, Remi**, CESBIO, Université de Toulouse, CNES/CNRS/INRAe/IRD/UPS, Toulouse, France
- Magee, Andrew D.**, Centre for Water, Climate and Land, School of Environmental and Life Sciences, University of Newcastle, Callaghan, Australia
- Magnin, Florence**, Laboratoire EDYTEM, CNRS/Université Savoie Mont-Blanc, Chambéry, France
- Mamen, Jostein**, Norwegian Meteorological Institute, Oslo, Norway
- Mankoff, Ken D.**, Business Integra, New York, New York; NASA Goddard Institute for Space Studies, New York, New York
- Manney, Gloria L.**, NorthWest Research Associates, Socorro, New Mexico
- Marcinonienė, Izolda**, Lithuanian Hydrometeorological Service, Vilnius, Lithuania
- Marengo, Jose A.**, Centro Nacional de Monitoramento e Alertas de Desastres Naturais CEMADEN, São Paulo, Brazil
- Marjan, Mohammadi**, Iran National Climate and Drought Crisis Management, National Meteorology Organization, Tehran, Iran
- Martínez, Ana E.**, National Meteorological Service of Mexico, Mexico City, Mexico
- Massom, Robert A.**, Australian Antarctic Division, Australian Antarctic Program Partnership (AAPP) and Australian Centre for Excellence in Antarctic Science (ACEAS), Tasmania, Australia
- Matsuzaki, Shin-Ichiro**, National Institute for Environmental Studies, Tsukuba, Japan
- May, Linda**, UK Centre for Ecology & Hydrology, Edinburgh, United Kingdom
- Mayer, Michael**, University of Vienna, Vienna, Austria; European Centre for Medium-Range Weather Forecasts, Reading, United Kingdom
- Mazloff, Matthew R.**, Scripps Institution of Oceanography, University of California, San Diego, La Jolla, California
- McAfee, Stephanie A.**, Department of Geography, University of Nevada Reno, Reno, Nevada
- McBride, C.**, Climate Service, South African Weather Service, Pretoria, South Africa
- McCabe, Matthew F.**, Climate and Livability Initiative, Division of Biological and Environmental Sciences and Engineering, King Abdullah University of Science and Technology, Thuwal, Saudi Arabia
- McClelland, James W.**, Marine Biological Laboratory, Woods Hole, Massachusetts
- McPhaden, Michael J.**, NOAA/OAR Pacific Marine Environmental Laboratory, Seattle, Washington
- McVicar, Tim R.**, CSIRO Environment, Canberra, Australia; Australian Research Council Centre of Excellence for Climate Extremes, Sydney, Australia
- Mears, Carl A.**, Remote Sensing Systems, Santa Rosa, California
- Meier, Walter N.**, National Snow and Ice Data Center, Cooperative Institute for Research in Environmental Sciences, University of Colorado, Boulder, Colorado
- Mekonnen, A.**, North Carolina A&T University, Greensboro, North Carolina
- Menzel, Annette**, Ecoclimatology, Department of Life Science Systems, TUM School of Life Sciences, Technical University of Munich, Freising, Germany; Institute for Advanced Study, Technical University of Munich, Garching, Germany
- Merchant, Christopher J.**, Department of Meteorology, University of Reading, Reading, United Kingdom
- Merrifield, Mark A.**, Cooperative Institute for Marine and Atmospheric Research, University of Hawaii, Honolulu, Hawaii
- Meyer, Michael F.**, United States Geological Survey, Madison, Wisconsin
- Meyers, Tristan**, National Institute of Water and Atmospheric Research, Ltd. (NIWA), Auckland, New Zealand
- Mikolajczyk, David E.**, Antarctic Meteorological Research and Data Center, Space Science and Engineering Center, University of Wisconsin-Madison, Madison, Wisconsin
- Miller, John B.**, NOAA Global Monitoring Laboratory, Boulder, Colorado
- Miralles, Diego G.**, Hydro-Climate Extremes Lab (H-CEL), Ghent University, Ghent, Belgium
- Misevicius, Noelia**, Instituto Uruguayo de Meteorología, Montevideo, Uruguay
- Mishonov, Alexey**, Earth System Science Interdisciplinary Center/Cooperative Institute for Satellite Earth System Studies Maryland, University of Maryland, College Park, Maryland; NOAA/NESDIS National Centers for Environmental Information, Silver Spring, Maryland
- Mitchum, Gary T.**, College of Marine Science, University of South Florida, St. Petersburg, Florida
- Moat, Ben I.**, National Oceanography Centre, Southampton, United Kingdom
- Moesinger, Leander**, TU Wien, Vienna, Austria
- Moise, Aurel**, Centre for Climate Research Singapore, Meteorological Service Singapore, Singapore
- Molina-Carpio, Jorge**, Universidad Mayor de San Andrés, La Paz, Bolivia
- Monet, Ghislaine**, Université Savoie Mont Blanc, INRAE, CARRTEL, Chambéry, France
- Montzka, Stephan A.**, NOAA Global Monitoring Laboratory, Boulder, Colorado
- Moon, Twila A.**, National Snow and Ice Data Center, Cooperative Institute for Research in Environmental Sciences, University of Colorado, Boulder, Colorado
- Moore, G. W. K.**, University of Toronto Mississauga, Mississauga, Canada
- Mora, Natali**, Center for Geophysical Research, University of Costa Rica, San José, Costa Rica
- Morán, Johnny**, Centro Internacional para la Investigación del Fenómeno de El Niño (CIIFEN), Guayaquil, Ecuador
- Morehen, Claire**, Environment and Climate Change Canada, Vancouver, British Columbia, Canada
- Morice, Colin**, Met Office Hadley Centre, Exeter, United Kingdom
- Mostafa, A. E.**, Department of Seasonal Forecast and Climate Research, Cairo Numerical Weather Prediction, Egyptian Meteorological Authority, Cairo, Egypt
- Mote, Thomas L.**, University of Georgia, Athens, Georgia
- Mrekaj, Ivan**, Technical University in Zvolen, Zvolen, Slovakia
- Mudryk, Lawrence**, Climate Research Division, Environment and Climate Change Canada, Toronto, Canada

Editor and Author Affiliations (continued)

- Mühle, Jens**, AGAGE, Scripps Institution of Oceanography, University of California, San Diego, La Jolla, California
- Müller, Rolf**, Forschungszentrum Jülich, Jülich, Germany
- Nance, David**, Cooperative Institute for Research in the Earth Sciences, NOAA Global Monitoring Laboratory, Boulder, Colorado
- Nash, Eric R.**, Science Systems and Applications, Inc., Lanham, Maryland; NASA Goddard Space Flight Center, Greenbelt, Maryland
- Nerem, R. Steven**, Colorado Center for Astrodynamics Research, Cooperative Institute for Research in Environmental Sciences, University of Colorado Boulder, Boulder, Colorado
- Newman, Paul A.**, NASA Goddard Space Flight Center, Greenbelt, Maryland
- Nicolas, Julien P.**, European Centre for Medium-Range Weather Forecasts, Bonn, Germany
- Nieto, Juan J.**, Centro Internacional para la Investigación del Fenómeno de El Niño (CIIFEN), Guayaquil, Ecuador
- Noetzi, Jeannette**, WSL Institute for Snow and Avalanche Research SLF, Davos-Dorf, Switzerland; Climate Change, Extremes and Natural Hazards in Alpine Regions Research Center CERC, Davos Dorf, Switzerland
- Noll, Ben**, National Institute of Water and Atmospheric Research, Auckland, New Zealand
- Norton, Taylor**, Antarctic Meteorological Research and Data Center, Space Science and Engineering Center, University of Wisconsin-Madison, Madison, Wisconsin
- Nyland, Kelsey E.**, Department of Geography, George Washington University, Washington, DC
- O'Keefe, John**, The Harvard Forest, Harvard University, Petersham, Massachusetts
- Ochwat, Naomi**, Earth Science Observation Center, Cooperative Institute for Research in Environmental Sciences (ESOC/CIRES), University of Colorado Boulder, Boulder Colorado
- Oikawa, Yoshinori**, Tokyo Climate Center, Japan Meteorological Agency, Tokyo, Japan
- Okunaka, Yuka**, Tokyo Climate Center, Japan Meteorological Agency, Tokyo, Japan
- Osborn, Timothy J.**, Climatic Research Unit, School of Environmental Sciences, University of East Anglia, Norwich, United Kingdom
- Overland, James E.**, NOAA Pacific Marine Environmental Laboratory, Seattle, Washington
- Park, Taejin**, NASA Ames Research Center, Mountain View, California; Bay Area Environmental Research Institute, Mountain View, California
- Parrington, Mark**, European Centre for Medium-Range Weather Forecasts, Bonn, Germany
- Parrish, Julia K.**, Coastal Observation and Seabird Survey Team, University of Washington, Seattle, Washington
- Pasch, Richard J.**, NOAA/NWS National Hurricane Center, Miami, Florida
- Pascual Ramírez, Reynaldo**, National Meteorological Service of Mexico, Mexico City, Mexico
- Pellet, Cécile**, Department of Geosciences, University of Fribourg, Fribourg, Switzerland
- Pelto, Mauri S.**, Nichols College, Dudley, Massachusetts
- Perčec Tadić, Melita**, Croatian Meteorological and Hydrological Service, Zagreb, Croatia
- Perovich, Donald K.**, University of Dartmouth, Hanover, New Hampshire
- Petersen, Guðrún Nína**, Icelandic Meteorological Office, Reykjavik, Iceland
- Petersen, Kyle**, Cooperative Institute for Research in the Earth Sciences, NOAA Global Monitoring Laboratory, Boulder, Colorado
- Petropavlovskikh, Irina**, NOAA/OAR Earth System Research Laboratory, Global Monitoring Division, Boulder, Colorado; University of Colorado Boulder, Boulder, Colorado
- Petty, Alek**, NASA Goddard Space Flight Center, Greenbelt, Maryland
- Pezza, Alexandre B.**, Greater Wellington Regional Council, Wellington, New Zealand
- Pezzi, Luciano P.**, Laboratory of Ocean and Atmosphere Studies (LOA), Earth Observation and Geoinformatics Division (DIOTG), National Institute for Space Research (INPE), São José dos Campos, Brazil
- Phillips, Coda**, Cooperative Institute for Meteorological Satellite Studies, Space Science and Engineering Center, University of Wisconsin-Madison, Madison, Wisconsin
- Phoenix, Gareth, K.**, University of Sheffield, Sheffield, United Kingdom
- Pierson, Don**, Department of Ecology and Genetics, Uppsala University, Uppsala, Sweden
- Pinto, Izidine**, Royal Netherlands Meteorological Institute (KNMI), De Bilt, The Netherlands
- Pires, Vanda**, Portuguese Sea and Atmosphere Institute, Lisbon, Portugal
- Pitts, Michael**, NASA Langley Research Center, Hampton, Virginia
- Po-Chedley, Stephen**, Lawrence Livermore National Laboratory, Livermore, California
- Pogliotti, Paolo**, Environmental Protection Agency of Valle d'Aosta, Saint-Christophe, Italy
- Poinar, Kristin**, University at Buffalo, Buffalo, New York
- Polvani, Lorenzo**, Columbia University, New York, New York
- Preimesberger, Wolfgang**, TU Wien, Department of Geodesy and Geoinformation, Vienna, Austria
- Price, Colin**, Tel Aviv University, Tel Aviv, Israel
- Pulkkanen, Merja**, Finnish Environment Institute (SYKE), Jyväskylä, Finland
- Purkey, Sarah G.**, Scripps Institution of Oceanography, University of California San Diego, La Jolla, California
- Qiu, Bo**, Department of Oceanography, University of Hawaii at Manoa, Honolulu, Hawaii
- Quisbert, Kenny**, Servicio Nacional de Meteorología e Hidrología de Bolivia, La Paz, Bolivia
- Quispe, Willy R.**, Servicio Nacional de Meteorología e Hidrología de Bolivia, La Paz, Bolivia
- Rajeevan, M.**, Ministry of Earth Sciences, New Delhi, India
- Ramos, Andrea M.**, Instituto Nacional de Meteorología, Brasília, Brazil
- Randel, William J.**, National Center for Atmospheric Research, Boulder, Colorado
- Rantanen, Mika**, Finnish Meteorological Institute, Helsinki, Finland
- Raphael, Marilyn N.**, Department of Geography, University of California, Los Angeles, Los Angeles, California
- Reagan, James**, NOAA/NESDIS National Centers for Environmental Information, Silver Spring, Maryland
- Recalde, Cristina**, NOAA/NWS National Centers for Environmental Prediction, Climate Prediction Center, College Park, Maryland
- Reid, Phillip**, Australian Bureau of Meteorology and Australian Antarctic Program Partnership (AAPP), Hobart, Australia
- Rémy, Samuel**, HYGEOS, Lille, France
- Reyes Kohler, Alejandra J.**, Dirección de Meteorológica de Chile, Santiago de Chile, Chile
- Ricciardulli, Lucrezia**, Remote Sensing Systems, Santa Rosa, California
- Richardson, Andrew D.**, School of Informatics, Computing, and Cyber Systems, Flagstaff, Arizona; Center for Ecosystem Science and Society, Northern Arizona University, Flagstaff, Arizona
- Ricker, Robert**, NORCE Norwegian Research Centre, Tromsø, Norway
- Robinson, David A.**, Rutgers University, Piscataway, New Jersey
- Robjhon, M.**, NOAA/NWS National Centers for Environmental Prediction Climate Prediction Center, College Park, Maryland
- Rocha, Willy**, Servicio Nacional de Meteorología e Hidrología, Bolivia
- Rodell, Matthew**, Earth Sciences Division, NASA Goddard Space Flight Center, Greenbelt, Maryland
- Rodriguez Guisado, Esteban**, Agencia Estatal de Meteorología, Madrid, Spain
- Rodriguez-Fernandez, Nemesio**, CESBIO, Université de Toulouse, CNES/CNRS/INRAe/IRD/UPS, Toulouse, France

Editor and Author Affiliations (continued)

- Romanovsky, Vladimir E.**, Geophysical Institute, University of Alaska Fairbanks, Fairbanks, Alaska; Earth Cryosphere Institute, Tyumen Science Center, Tyumen, Russia
- Ronchail, Josyane**, Laboratoire LOCEAN-IPSL, Paris, France
- Rosencrans, Matthew**, NOAA/NWS National Centers for Environmental Prediction Climate Prediction Center, College Park, Maryland
- Rosenlof, Karen H.**, NOAA Chemical Sciences Laboratory, Boulder, Colorado
- Rösner, Benjamin**, Laboratory for Climatology and Remote Sensing, Faculty of Geography, University of Marburg, Marburg, Germany
- Rösner, Henrieke**, Humboldt University, Berlin, Germany
- Rozanov, Alexei**, University of Bremen, Bremen, Germany
- Rozkošný, Jozef**, Slovak Hydrometeorological Institute, Bratislava, Slovakia
- Rubek, Frans**, Danish Meteorological Institute, Copenhagen, Denmark
- Rusanovskaya, Olga O.**, Irkutsk State University, Institute of Biology, Irkutsk, Russia
- Rutishauser, This**, Swiss Academy of Sciences (SCNAT), Bern, Switzerland
- Sabeerali, C. T.**, India Meteorological Department, Ministry of Earth Sciences, Pune, India
- Salinas, Roberto**, Dirección de Meteorología e Hidrología / Dirección Nacional de Aeronáutica Civil, Asunción, Paraguay
- Sánchez-Lugo, Ahira**, NOAA/NESDIS National Centers for Environmental Information, Asheville, North Carolina
- Santee, Michelle L.**, NASA Jet Propulsion Laboratory, Pasadena, California
- Santini, Marcelo**, Laboratory of Ocean and Atmosphere Studies (LOA), Earth Observation and Geoinformatics Division (DIOTG), National Institute for Space Research (INPE), São José dos Campos, Brazil
- Sato, Katsunari**, Japan Meteorological Agency, Tokyo, Japan
- Sawaengphokhai, Parnchai**, Science Systems and Applications, Inc. (SSAI), Hampton, Virginia
- Sayouri, A.**, Direction de la Météorologie Nationale Maroc, Rabat, Morocco
- Scambos, Theodore**, Earth Science Observation Center, Cooperative Institute for Research in Environmental Sciences (ESOC/CIRES), University of Colorado Boulder, Boulder, Colorado
- Schenzinger, Verena**, Medical University of Innsbruck, Innsbruck, Austria
- Schimanke, Semjon**, Swedish Meteorological and Hydrological Institute, Norrköping, Sweden
- Schlegel, Robert W.**, Laboratoire d'Océanographie de Villefranche, Sorbonne Université, CNRS, Villefranche-sur-mer, France
- Schmid, Claudia**, NOAA/OAR Atlantic Oceanographic and Meteorological Laboratory, Miami, Florida
- Schmid, Martin**, Eawag, Swiss Federal Institute of Aquatic Science and Technology, Surface Waters - Research and Management, Kastanienbaum, Switzerland
- Schneider, Udo**, Global Precipitation Climatology Centre, Deutscher Wetterdienst, Offenbach, Germany
- Schreck, Carl J.**, North Carolina State University, North Carolina Institute for Climate Studies, Cooperative Institute Satellite Earth System Studies, Asheville, North Carolina
- Schultz, Cristina**, Northeastern University, Boston, Massachusetts
- Science Systems and Applications Inc., Lanham**, Maryland
- Segele, Z. T.**, NOAA/NWS National Centers for Environmental Prediction Climate Prediction Center, College Park, Maryland
- Sensoy, Serhat**, Turkish State Meteorological Service, Ankara, Türkiye
- Serbin, Shawn P.**, Brookhaven National Laboratory, Upton, New York
- Serreze, Mark C.**, National Snow and Ice Data Center, University of Colorado, Boulder, Colorado
- Setiawan, Amsari Mudzakir**, Division for Climate Variability Analysis, BMKG, Jakarta, Indonesia
- Sezaki, Fumi**, Japan Meteorological Agency, Tokyo, Japan
- Sharma, Sapna**, Department of Biology, York University, Toronto, Canada
- Sharp, Jonathan D.**, Cooperative Institute for Climate, Ocean, and Ecosystem Studies, University of Washington, Seattle, Washington; NOAA/OAR Pacific Marine Environmental Laboratory, Seattle, Washington
- Sheffield, Gay**, Alaska Sea Grant, Marine Advisory Program, University of Alaska Fairbanks, Nome, Alaska
- Shi, Jia-Rui**, Woods Hole Oceanographic Institution, Woods Hole, Massachusetts
- Shi, Lei**, NOAA/NESDIS National Centers for Environmental Information, Asheville, North Carolina
- Shiklomanov, Alexander I.**, University of New Hampshire, Durham, New Hampshire; Arctic and Antarctic Research Institute, St. Petersburg, Russia
- Shiklomanov, Nikolay I.**, Department of Geography, George Washington University, Washington, DC
- Shimaraeva, Svetlana V.**, Irkutsk State University, Institute of Biology, Irkutsk, Russia
- Shukla, R.**, NOAA/NWS National Centers for Environmental Prediction Climate Prediction Center, College Park, Maryland
- Siegel, David A.**, University of California, Santa Barbara, Santa Barbara, California
- Silow, Eugene A.**, Irkutsk State University, Institute of Biology, Irkutsk, Russia
- Sima, F.**, Division of Meteorology, Department of Water Resources, Banjul, The Gambia
- Simmons, Adrian J.**, European Centre for Medium-Range Weather Forecasts, Reading, United Kingdom
- Smeed, David A.**, National Oceanography Centre, Southampton, United Kingdom
- Smith, Adam**, NOAA/NESDIS National Centers for Environmental Information, Asheville, North Carolina
- Smith, Sharon L.**, Geological Survey of Canada, Natural Resources Canada, Ottawa, Canada
- Soden, Brian J.**, University of Miami, Miami, Florida
- Sofieva, Viktoria**, FMI (Finnish Meteorological Institute), Helsinki, Finland
- Souza, Everaldo**, Federal University of Pará (UFPA), Belém, Brazil
- Sparks, Tim H.**, Poznań University of Life Sciences, Poznań, Poland
- Spence-Hemmings, Jacqueline**, Meteorological Service, Jamaica, Kingston, Jamaica
- Spencer, Robert G. M.**, Florida State University, Tallahassee, Florida
- Spillane, Sandra**, Climate Services Division, Met Éireann, The Irish Meteorological Service, Dublin, Ireland
- Spillane, Sandra**, Met Éireann, Dublin, Ireland
- Sreejith, O. P.**, India Meteorological Department, Ministry of Earth Sciences, Pune, India
- Srivastava, A. K.**, India Meteorological Department, Pune, India
- Stackhouse Jr., Paul W.**, NASA Langley Research Center, Hampton, Virginia
- Stammerjohn, Sharon**, Institute of Arctic and Alpine Research, University of Colorado Boulder, Boulder, Colorado
- Stauffer, Ryan**, NASA Goddard Space Flight Center, Greenbelt, Maryland
- Steinbrecht, Wolfgang**, DWD (German Weather Service), Hohenpeissenberg, Germany
- Steiner, Andrea K.**, Wegener Center for Climate and Global Change, University of Graz, Graz, Austria
- Stella, Jose L.**, Servicio Meteorológico Nacional, Buenos Aires, Argentina
- Stephenson, Tannecia S.**, Department of Physics, The University of the West Indies, Kingston, Jamaica
- Stradiotti, Pietro**, TU Wien, Department of Geodesy and Geoinformation, Vienna, Austria
- Strahan, Susan E.**, University of Maryland, Baltimore County, Baltimore, Maryland; NASA Goddard Space Flight Center, Greenbelt, Maryland
- Streletskiy, Dmitry A.**, George Washington University, Washington DC
- Surendran, Divya E.**, India Meteorological Department, Ministry of Earth Sciences, Pune, India

Editor and Author Affiliations (continued)

- Suslova, Anya**, Woodwell Climate Research Center, Falmouth, Massachusetts
- Svendby, Tove**, Norwegian Institute for Air Research, Kjeller, Norway
- Sweet, William**, NOAA/NOS Center for Operational Oceanographic Products and Services, Silver Spring, Maryland
- Takahashi, Kiyotoshi**, Tokyo Climate Center, Japan Meteorological Agency, Tokyo, Japan
- Takemura, Kazuto**, Tokyo Climate Center, Japan Meteorological Agency, Tokyo, Japan
- Tank, Suzanne E.**, University of Alberta, Edmonton, Canada
- Taylor, Michael A.**, Department of Physics, The University of the West Indies, Kingston, Jamaica
- Tedesco, Marco**, Lamont-Doherty Earth Observatory, Columbia University, Palisades, New York; NASA Goddard Institute of Space Studies, New York, New York
- Thackeray, Stephen J.**, UK Centre for Ecology and Hydrology, Lancaster, United Kingdom
- Thiaw, W. M.**, NOAA/NWS National Centers for Environmental Prediction Climate Prediction Center, College Park, Maryland
- Thibert, Emmanuel**, Université Grenoble Alpes, INRAE, CNRS, IRD, Grenoble INP, IGE, Grenoble, France.
- Thoman, Richard L.**, International Arctic Research Center, University of Alaska Fairbanks, Fairbanks, Alaska
- Thompson, Andrew F.**, California Institute of Technology, Pasadena, California
- Thompson, Philip R.**, Cooperative Institute for Marine and Atmospheric Research, University of Hawaii, Honolulu, Hawaii
- Tian-Kunze, Xiangshan**, Alfred Wegener Institute, Helmholtz Centre for Polar and Marine Research, Bremerhaven, Germany
- Timmermans, Mary-Louise**, Yale University, New Haven, Connecticut
- Timofeyev, Maxim A.**, Irkutsk State University, Institute of Biology, Irkutsk, Russia
- Tobin, Skie**, Bureau of Meteorology, Melbourne, Australia
- Tømmervik, Hans**, Arctic Department, Norwegian Institute for Nature Research, Tromsø, Norway
- Tourpali, Kleareti**, Aristotle University, Thessaloniki, Greece
- Trescilo, Lidia**, State Hydrometeorological Service, Chisinau, Republic of Moldova
- Tretiakov, Mikhail**, Arctic and Antarctic Research Institute, St. Petersburg, Russia
- Trewin, Blair C.**, Australian Bureau of Meteorology, Melbourne, Australia
- Triñanes, Joaquin A.**, Laboratory of Systems, Technological Research Institute, Universidad de Santiago de Compostela, Campus Universitario Sur, Santiago de Compostela, Spain; Cooperative Institute for Marine and Atmospheric Studies, Rosenstiel School of Marine and Atmospheric Science, University of Miami, Miami, Florida; NOAA/OAR Atlantic Oceanographic and Meteorological Laboratory, Miami, Florida
- Trotman, Adrian**, Caribbean Institute for Meteorology and Hydrology, Bridgetown, Barbados
- Truchelut, Ryan E.**, WeatherTiger, Tallahassee, Florida
- Trusel, Luke D.**, Pennsylvania State University, University Park, Pennsylvania
- Tye, Mari R.**, National Center for Atmospheric Research, Boulder, Colorado
- van der A, Ronald**, Royal Netherlands Meteorological Institute (KNMI), De Bilt, The Netherlands
- van der Schalie, Robin**, Planet Labs, Haarlem, The Netherlands
- van der Schrier, Gerard**, Royal Netherlands Meteorological Institute (KNMI), De Bilt, The Netherlands
- Van Meerbeek, Cedric J.**, Caribbean Institute for Meteorology and Hydrology, Bridgetown, Barbados
- van Vliet, Arnold J.H.**, Environmental Systems Analysis Group, Wageningen University and Research, The Netherlands
- Vazife, Ahad**, Iran National Climate and Drought Crisis Management, National Meteorology Organization, Tehran, Iran
- Verburg, Piet**, National Institute of Water and Atmospheric Research, Wellington, New Zealand
- Vernier, Jean-Paul**, NASA Langley Research Center, Hampton, Virginia
- Vimont, Isaac J.**, NOAA Global Monitoring Laboratory, Boulder, Colorado
- Virts, Katrina**, University of Alabama in Huntsville, Huntsville, Alabama
- Vivero, Sebastián**, Department of Geosciences, University of Fribourg, Fribourg, Switzerland
- Volkov, Denis L.**, Cooperative Institute for Marine and Atmospheric Studies, University of Miami; NOAA/OAR Atlantic Oceanographic and Meteorological Laboratory, Miami, Florida
- Vömel, Holger**, Earth Observing Laboratory, National Center for Atmospheric Research, Boulder, Colorado
- Vose, Russell S.**, NOAA/NESDIS National Centers for Environmental Information, Asheville, North Carolina
- Walker, Donald (Skip) A.**, Institute of Arctic Biology, University of Alaska Fairbanks, Fairbanks, Alaska
- Walsh, John E.**, International Arctic Research Center, University of Alaska Fairbanks, Fairbanks, Alaska
- Wang, Bin**, School of Ocean and Earth Science and Technology, Department of Meteorology, University of Hawaii; International Pacific Research Center, Honolulu, Hawaii
- Wang, Hui**, NOAA/NWS National Centers for Environmental Prediction Climate Prediction Center, College Park, Maryland
- Wang, Muyin**, NOAA Pacific Marine Environmental Laboratory, Seattle, Washington; Cooperative Institute for Climate, Ocean, and Ecosystem Studies, University of Washington, Seattle, Washington
- Wang, Ray H. J.**, Georgia Institute of Technology, Atlanta, Georgia
- Wang, Xinyue**, National Center for Atmospheric Research, Boulder, Colorado
- Wanninkhof, Rik**, NOAA/OAR Atlantic Oceanographic and Meteorological Laboratory, Miami, Florida
- Warnock, Taran**, University of Saskatchewan, Saskatoon, Canada
- Weber, Mark**, University of Bremen, Bremen, Germany
- Webster, Melinda**, University of Washington, Seattle, Washington
- Wehrlé, Adrian**, University of Zürich, Zürich, Switzerland
- Wen, Caihong**, NOAA/NWS National Centers for Environmental Prediction Climate Prediction Center, College Park, Maryland
- Westberry, Toby K.**, Oregon State University, Corvallis, Oregon
- Widlansky, Matthew J.**, Cooperative Institute for Marine and Atmospheric Research, University of Hawaii, Honolulu, Hawaii
- Wiese, David N.**, Jet Propulsion Laboratory, California Institute of Technology, Pasadena, California
- Wild, Jeannette D.**, ESSIC/University of Maryland, College Park, Maryland; NOAA NESDIS/STAR, College Park, Maryland
- Wille, Jonathan D.**, Institute for Atmospheric and Climate Science, ETH Zürich, Zürich, Switzerland; Institut des Géosciences de l'Environnement, CNRS/UGA/IRD/G-INP, Saint Martin d'Hères, France
- Willems, An**, Royal Meteorological Institute of Belgium (KMI), Brussels, Belgium
- Willett, Kate M.**, Met Office Hadley Centre, Exeter, United Kingdom
- Williams, Earle**, Massachusetts Institute of Technology, Cambridge, Massachusetts
- Willis, J.**, Jet Propulsion Laboratory, California Institute of Technology, Pasadena, California
- Wong, Takmeng**, NASA Langley Research Center, Hampton, Virginia
- Wood, Kimberly M.**, Department of Geosciences, Mississippi State University, Mississippi State, Mississippi
- Woolway, Richard Iestyn**, School of Ocean Sciences, Bangor University, Menai Bridge, Anglesey, Wales
- Xie, Ping-Ping**, NOAA/NWS National Centers for Environmental Prediction Climate Prediction Center, College Park, Maryland
- Yang, Daqing**, National Hydrology Research Centre, Environment Canada, Saskatoon, Canada

Editor and Author Affiliations (continued)

Yin, Xungang, NOAA/NESDIS National Centers for Environmental Information, Asheville, North Carolina

Yin, Ziqi, Department of Atmospheric and Oceanic Sciences, University of Colorado Boulder, Boulder, Colorado

Zeng, Zhenzhong, School of Environmental Science and Engineering, Southern University of Science and Technology, Shenzhen, China

Zhang, Huai-min, NOAA/NESDIS National Centers for Environmental Information, Asheville, North Carolina

Zhang, Li, NOAA/NWS National Centers for Environmental Prediction Climate Prediction Center, College Park, Maryland; ERT, Laurel, Maryland

Zhang, Peiqun, Beijing Climate Center, Beijing, China

Zhao, Lin, School of Geographical Sciences, Nanjing University of Information Science and Technology, Nanjing, China

Zhou, Xinjia, Center for Satellite Applications and Research, NOAA, College Park, Maryland

Zhu, Zhiwei, Nanjing University of Information Science and Technology, Nanjing, China

Ziemke, Jerry R., Goddard Earth Sciences Technology and Research, Morgan State University, Baltimore, Maryland; NASA Goddard Space Flight Center, Greenbelt, Maryland

Ziese, Markus, Global Precipitation Climatology Centre, Deutscher Wetterdienst, Offenbach, Germany

Zolkos, Scott, Woodwell Climate Research Center, Falmouth, Massachusetts

Zotta, Ruxandra M., TU Wien, Vienna, Austria

Zou, Cheng-Zhi, NOAA/NESDIS Center for Satellite Applications and Research, College Park, Maryland

Editorial and Production Team

Allen, Jessica, Graphics Support, Cooperative Institute for Satellite Earth System Studies, North Carolina State University, Asheville, North Carolina

Camper, Amy V., Graphics Support, Innovative Consulting and Management Services, LLC, NOAA/NESDIS National Centers for Environmental Information, Asheville, North Carolina

Haley, Bridgette O., Graphics Support, NOAA/NESDIS National Centers for Environmental Information, Asheville, North Carolina

Hammer, Gregory, Content Team Lead, Communications and Outreach, NOAA/NESDIS National Centers for Environmental Information, Asheville, North Carolina

Love-Brotak, S. Elizabeth, Lead Graphics Production, NOAA/NESDIS National Centers for Environmental Information, Asheville, North Carolina

Ohlmann, Laura, Technical Editor, Innovative Consulting and Management Services, LLC, NOAA/NESDIS National Centers for Environmental Information, Asheville, North Carolina

Noguchi, Lukas, Technical Editor, Innovative Consulting and Management Services, LLC, NOAA/NESDIS National Centers for Environmental Information, Asheville, North Carolina

Riddle, Deborah B., Graphics Support, NOAA/NESDIS National Centers for Environmental Information, Asheville, North Carolina

Veasey, Sara W., Visual Communications Team Lead, Communications and Outreach, NOAA/NESDIS National Centers for Environmental Information, Asheville, North Carolina

STATE OF THE CLIMATE IN 2022

INTRODUCTION

T. Boyer, E. Bartow-Gillies, J. Blunden, and R. J. H. Dunn



Special Online Supplement to the *Bulletin of the American Meteorological Society* Vol. 104, No. 9, September, 2023

https://doi.org/10.1175/2023BAMSSStateoftheClimate_Intro.1

Corresponding author: Jessica Blunden / jessica.blunden@noaa.gov

©2023 American Meteorological Society

For information regarding reuse of this content and general copyright information, consult the [AMS Copyright Policy](#).

STATE OF THE CLIMATE IN 2022

Introduction

Editors

Ellen Bartow-Gillies
Jessica Blunden
Tim Boyer

Chapter Editors

Peter Bissolli
Kyle R. Clem
Howard J. Diamond
Matthew L. Druckenmiller
Robert J. H. Dunn
Catherine Ganter
Nadine Gobron
Gregory C. Johnson
Rick Lumpkin
Ademe Mekonnen
John B. Miller
Twila A. Moon
Marilyn N. Raphael
Ahira Sánchez-Lugo
Carl J. Schreck III
Richard L. Thoman
Kate M. Willett
Zhiwei Zhu

Technical Editor

Lukas Noguchi

BAMS Special Editor for Climate

Michael A. Alexander

American Meteorological Society

Cover Credit:

panaramka/Wild peaks of the Carpathians in a thunderstorm/Getty.

Self portrait: Traveling of a lone tourist in the snowy Carpathians among wild forests and fields, during a strong storm with a winter thunderstorm against the backdrop of mountains.

How to cite this document:

Introduction is one chapter from the *State of the Climate in 2022* annual report and is available from https://doi.org/10.1175/2023BAMSStateoftheClimate_Intro.1. Compiled by NOAA's National Centers for Environmental Information, *State of the Climate in 2022* is based on contributions from scientists from around the world. It provides a detailed update on global climate indicators, notable weather events, and other data collected by environmental monitoring stations and instruments located on land, water, ice, and in space. The full report is available from <https://doi.org/10.1175/2023BAMSStateoftheClimate.1>.

Citing the complete report:

Blunden, J., T. Boyer, and E. Bartow-Gillies, Eds., 2023: "State of the Climate in 2022". Bull. Amer. Meteor. Soc., 104 (9), Si–S501 <https://doi.org/10.1175/2023BAMSStateoftheClimate.1>.

Citing this chapter:

Boyer, T., E. Bartow-Gillies, J. Blunden, and R J. H. Dunn, 2023: Introduction [in "State of the Climate in 2022"]. Bull. Amer. Meteor. Soc., 104 (9), S1–S10, https://doi.org/10.1175/2023BAMSStateoftheClimate_Intro.1.

Editor and Author Affiliations (alphabetical by name)

Bartow-Gillies, Ellen, NOAA/NESDIS National Centers for Environmental Information, Asheville, North Carolina

Blunden, Jessica, NOAA/NESDIS National Centers for Environmental Information, Asheville, North Carolina

Boyer, Tim, NOAA/NESDIS National Centers for Environmental Information, Silver Spring, Maryland

Dunn, Robert J. H., Met Office Hadley Centre, Exeter, United Kingdom

Editorial and Production Team

Allen, Jessica, Graphics Support, Cooperative Institute for Satellite Earth System Studies, North Carolina State University, Asheville, North Carolina

Camper, Amy V., Graphics Support, Innovative Consulting and Management Services, LLC, NOAA/NESDIS National Centers for Environmental Information, Asheville, North Carolina

Haley, Bridgette O., Graphics Support, NOAA/NESDIS National Centers for Environmental Information, Asheville, North Carolina

Hammer, Gregory, Content Team Lead, Communications and Outreach, NOAA/NESDIS National Centers for Environmental Information, Asheville, North Carolina

Love-Brotak, S. Elizabeth, Lead Graphics Production, NOAA/NESDIS National Centers for Environmental Information, Asheville, North Carolina

Ohlmann, Laura, Technical Editor, Innovative Consulting and Management Services, LLC, NOAA/NESDIS National Centers for Environmental Information, Asheville, North Carolina

Noguchi, Lukas, Technical Editor, Innovative Consulting and Management Services, LLC, NOAA/NESDIS National Centers for Environmental Information, Asheville, North Carolina

Riddle, Deborah B., Graphics Support, NOAA/NESDIS National Centers for Environmental Information, Asheville, North Carolina

Veasey, Sara W., Visual Communications Team Lead, Communications and Outreach, NOAA/NESDIS National Centers for Environmental Information, Asheville, North Carolina

1. INTRODUCTION

T. Boyer, E. Bartow-Gillies, J. Blunden, and R. J. H. Dunn

The year 2022 was marked by unusual (though not unprecedented) disruptions in the climate system. The first was the third successive year of below-average temperatures in the tropical Pacific. A “triple-dip” La Niña nearly continuous from August 2020 through the end of 2022 marked the first such occurrence in the twenty-first century. Note that the triple-dip La Niña should not be confused with the double-dip La Niña described in the *State of the Climate 2021*, as the double-dip referred to the short interruption between two La Niña events in 2021 which was the only break in the triple-dip period. Descriptions of the large-scale characteristics of the triple-dip La Niña are found in Chapters 2 (Global Climate) and 3 (Global Ocean). The El Niño–Southern Oscillation phenomena, of which the triple-dip La Niña is an anomalous manifestation, has major short-term influence on the climate system. The specific details of the effects of the triple-dip La Niña on other aspects of the climate system are found throughout the report. A perspective of the triple-dip La Niña and its implications for long-term climate are discussed in a sidebar of Chapter 3.

The second unusual event was the extraordinary amount of precipitation over Antarctica in 2022, which led to a record-high annual surface mass balance (since 1980) and the first net positive annual ice-sheet mass balance on the continent since satellite measurements began in 1993. The heavy precipitation was closely tied to an unusually high number of atmospheric rivers over the continent, which carry moisture over Antarctica that mainly falls as snow. March precipitation totals in the Wilkes and Adelie regions were particularly high, estimated to exceed 300% of the 1991–2020 climatological mean. While an increase in ice-sheet mass in Antarctica has positive implications for global continental water storage and hence lessening sea-level increase, atmospheric rivers also have a large impact on surface melt and ice-sheet stability. Surface melt in turn has an impact on ‘firn’, the underlying layer of recrystallized snow from previous years. Firn density is an important factor in determining how surface melt water flows on and within ice shelves, which can reduce glacial stability and lead to their breakup and collapse. There was also record-low sea ice surrounding Antarctica in 2022, and on the eastern Antarctic Peninsula which allowed large swells to reach the coast and caused a breakout of fast ice that contributed to an acceleration of upstream glaciers. The complex interactions of climate factors on the Antarctic continent are discussed in Chapter 6, with particulars in the two sidebars: 1) The Antarctic heatwave of March 2022 and 2) Larsen-B fast ice breakout and glacier response.

A third event in 2022 was the eruption of the Hunga Tonga–Hunga Ha’apai underwater volcano (HTHH) in January. This eruption propelled immense amounts of water vapor (50 Tg to 150 Tg, upwards of 10% of the total stratospheric water vapor burden) and other gases into the stratosphere, with a plume higher than any previous eruption in the satellite era. Implications of the eruption, detailed in a sidebar and elsewhere in Chapter 2, include increased stratospheric aerosols and observations of cool stratospheric temperatures outside normal ranges with correspondingly anomalous winds. Long-term effects on tropospheric temperatures and the Antarctic ozone hole remain to be seen. The HTHH eruption also had an effect on our ability to make observations. For example, as detailed in Chapter 3, the calculation of ocean carbon biomass from satellite measurements has been greatly affected by the amount of sulfate aerosols injected by the HTHH eruption.

Another instance of volcanic activity, though not of the scale of HTHH, but with significant effects on the climate observing system, was the eruption of Mauna Loa in late November 2022. This eruption and subsequent lava flow shut down access and power to the NOAA Mauna Loa Observatory (featured on the cover of Chapter 8, Datasets), interrupting one of the longest time series for a variety of atmospheric variables, including atmospheric carbon dioxide (CO₂) levels. After a 10-day interruption, NOAA's CO₂ measurements were transferred to the University of Hawaii's Maunakea Observatories. The Mauna Loa CO₂ time series is an invaluable monitor of the changes in our climate system (as detailed in Chapter 2). This serves as a reminder of the importance of long-term continuous time series in our understanding of Earth's climate system and the importance of continuing such time series.

All the above singular events, along with the status of essential climate variables (ECVs) and their implications for Earth's climate system are detailed in the *State of the Climate 2022* due to the persistent dedication of the chapter editors and section authors—this year 576 authors from 66 different countries, including Andorra and Namibia for the first time. A distillation of the state of the climate for 2022 in the context of long-term trends and variability of selected essential climate variables is found in the 36 panels of Plate 1.1. The *State of the Climate* report continues to advance toward a more comprehensive survey of essential climate variables (ECVs). A new section on lightning (Chapter 2, Global Climate) documents global distributions in this ECV. A new section on Arctic Precipitation (Chapter 5, the Arctic) adds regional insight into the precipitation ECV.

The layout of this Supplement is similar to previous years. Following this introduction (Chapter 1), Chapter 2 catalogs global climate, Chapter 3 the oceans, Chapter 4 the tropics, Chapters 5 and 6 the high latitudes (Arctic and Antarctic, respectively), and Chapter 7 other specific regions of the globe (North America, Central America/Caribbean, South America, Africa, Europe, Asia, and Oceania). Finally, Chapter 8 is a listing of many (though not all) datasets used in the various sections of the *State of the Climate in 2022* and a link to dataset access and further information. Datasets are listed by chapter. Most of the datasets are readily downloadable by the reader who would like to reproduce the results found in the *State of the Climate* report or investigate further.

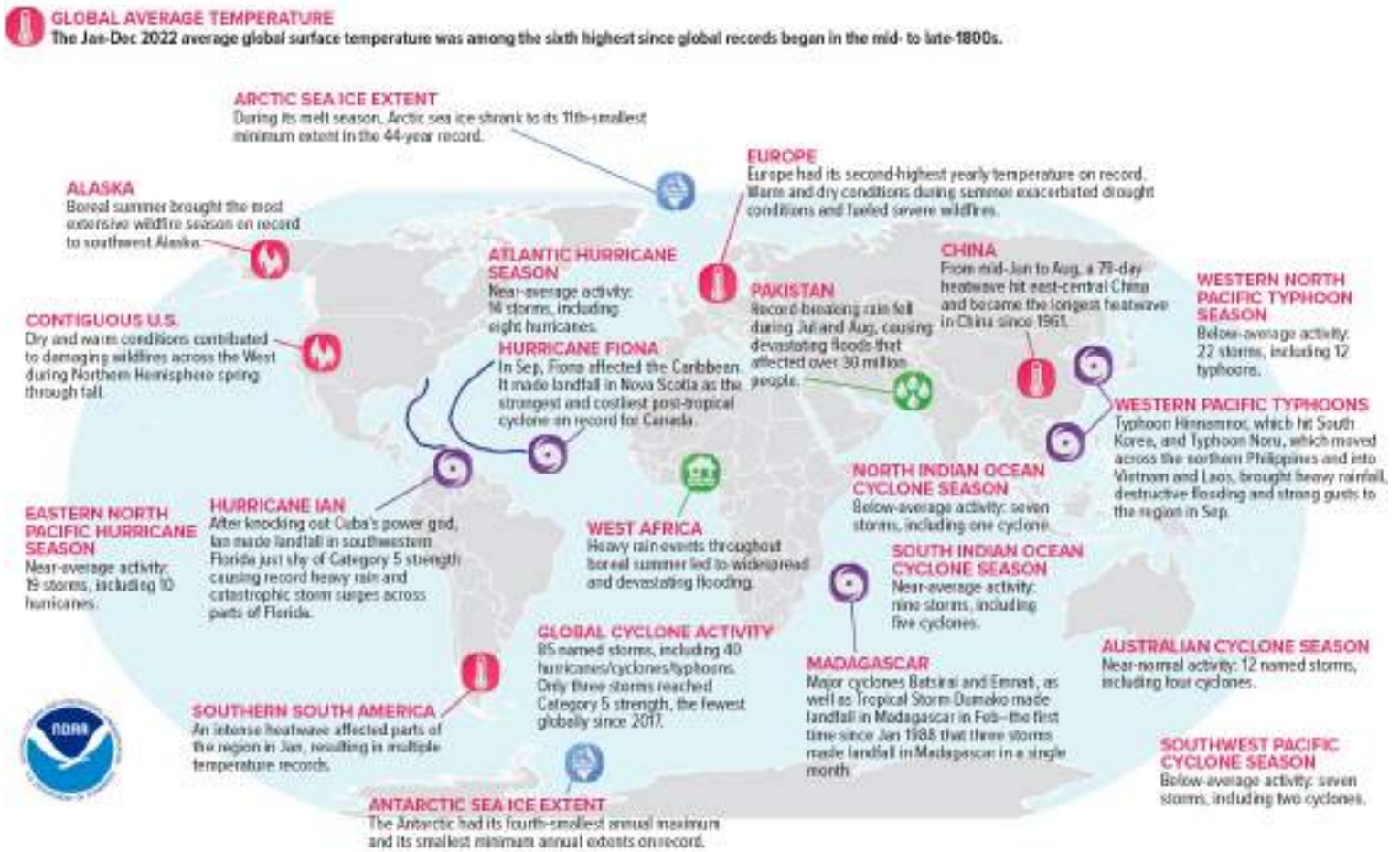
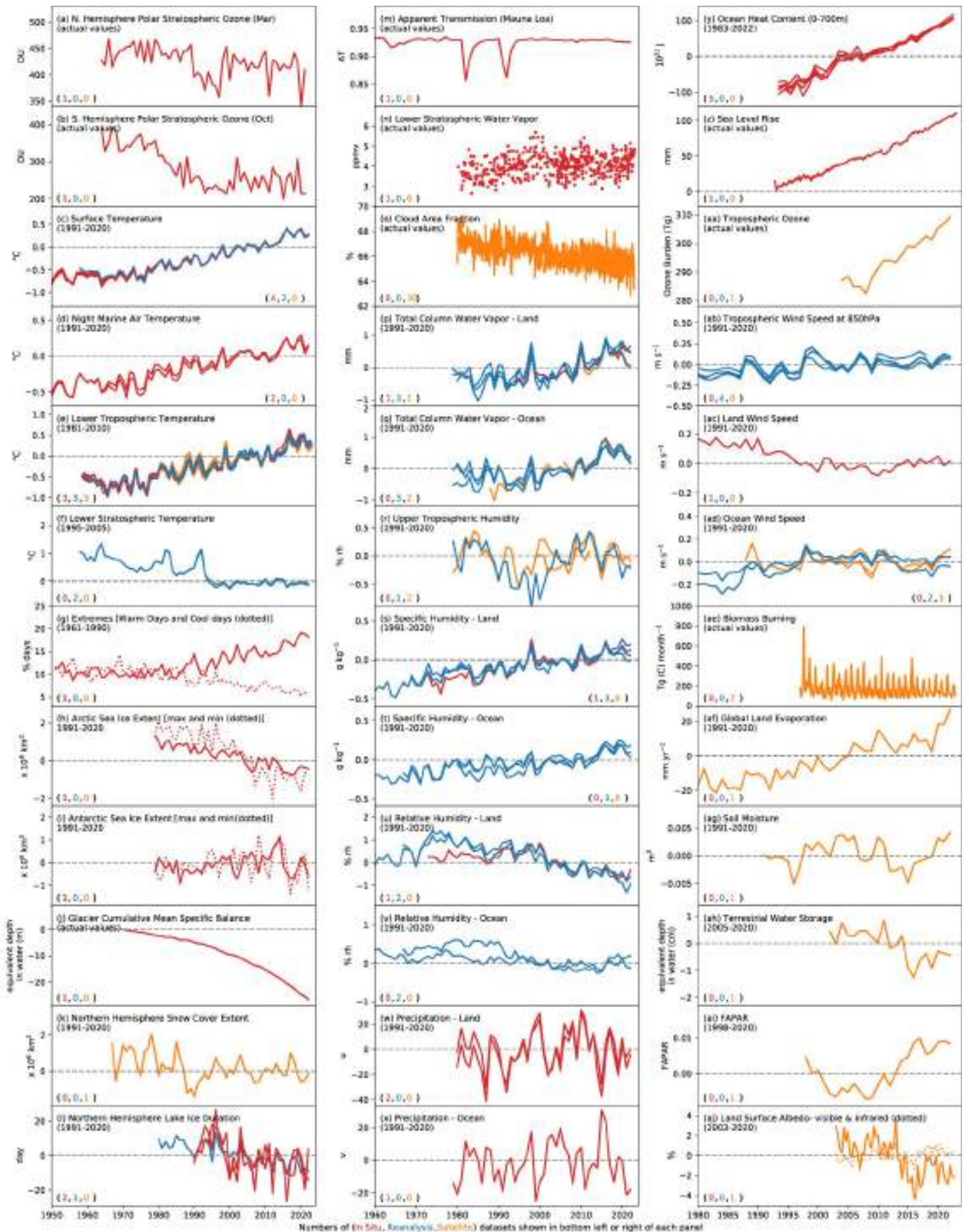


Fig. 1.1. Geographical distribution of selected notable climate anomalies and events in 2022.

Plate 1.1. (Next page) Global (or representative) average time series for essential climate variables through 2019. Anomalies are shown relative to the base period in parentheses although base periods used in other sections of the report may differ. The numbers in the parentheses in the lower left or right side of each panel indicate how many in situ (red), reanalysis (blue), and satellite (orange) datasets are used to create each time series in that order. (a) NH polar stratospheric ozone (Mar); (b) SH polar stratospheric ozone (Oct); (c) surface temperature; (d) night marine air temperature; (e) lower-tropospheric temperature; (f) lower-stratospheric temperature; (g) extremes (warm days [solid] and cool days [dotted]); (h) Arctic sea-ice extent (max [solid]) and min [dotted]); (i) Antarctic sea-ice extent (max [solid] and min [dotted]); (j) glacier cumulative mean specific balance; (k) NH snow-cover extent; (l) NH lake ice duration; (m) Mauna Loa apparent transmission; (n) lower-stratospheric water vapor; (o) cloud area fraction; (p) total column water vapor – land; (q) total column water vapor – ocean; (r) upper-tropospheric humidity; (s) specific humidity – land; (t) specific humidity – ocean; (u) relative humidity – land; (v) relative humidity – ocean; (v) precipitation – land; (x) precipitation – ocean; (y) ocean heat content (0 m–700 m); (z) sea-level rise; (aa) tropospheric ozone; (ab) tropospheric wind speed at 850 hPa; (ac) land wind speed; (ad) ocean wind speed; (ae) biomass burning; (ae) global land evaporation; (af) soil moisture; (ag) terrestrial groundwater storage; (ah) fraction of absorbed photosynthetically active radiation (FAPAR); (ai) land surface albedo – visible (solid) and infrared (dotted).



Essential Climate Variables

—T. BOYER, E. BARTOW-GILLIES, J. BLUNDEN, AND R.H. DUNN

The following variables are considered fully monitored in this report, in that there are sufficient spatial and temporal data, with peer-reviewed documentation to characterize them on a global scale:

- Surface atmosphere: air pressure, precipitation, temperature, water vapor, wind speed and direction
- Upper atmosphere: Earth radiation budget, temperature, water vapor, wind speed and direction, lightning
- Atmospheric composition: carbon dioxide, methane and other greenhouse gases, ozone
- Ocean physics: ocean surface heat flux, sea ice, sea level, surface salinity, sea-surface temperature, subsurface salinity, subsurface temperature, surface currents, surface stress
- Ocean biogeochemistry: ocean color
- Ocean biogeosystems: plankton
- Land: albedo, river discharge, snow

The following variables are considered partially monitored, in that there is systematic, rigorous measurement found in this report, but some coverage of the variable in time and space is

lacking due to observing limitations or availability of data or authors:

- Atmospheric composition: aerosols properties, cloud properties, precursors of aerosol and ozone
- Ocean physics: subsurface currents
- Ocean biogeochemistry: inorganic carbon
- Land: above-ground biomass, anthropogenic greenhouse gas fluxes, fire, fraction of absorbed photosynthetically active radiation, glaciers, groundwater, ice sheets and ice shelves, lakes, permafrost, soil moisture
- Surface atmosphere: surface radiation budget

The following variables are not yet covered in this report, or are outside the scope of it.

- Ocean physics: sea state
- Ocean biogeochemistry: nitrous oxide, nutrients, oxygen, transient tracers
- Ocean biogeosystems: marine habitat properties
- Land: anthropogenic water use, land cover, land surface temperature, latent and sensible heat fluxes, leaf area index, soil carbon

Acknowledgments

The editors thank the BAMS editorial staff, in particular Bryan Hanssen, who provided technical guidance, oversaw publication of the report, and continues to help us shepherd the report into a digital publishing era; Andrea Herbst, who provided peer review support; Nicole Rietmann, who oversaw the hundreds of citations and references this year; and the NCEI Graphics team for facilitating the construction of the report and executing the countless number of technical edits needed. We thank our technical editor, Lukas Noguchi, for his dedication and attention to detail. We also express our gratitude to Dr. Michael Alexander, who served for the third year as the AMS special editor for this report. Finally, we thank all of the authors and chapter editors who provide these valuable contributions each year, always with an aim to improve and expand their analyses for the readers.

STATE OF THE CLIMATE IN 2022

GLOBAL CLIMATE

R. J. H. Dunn, J. B. Miller, K. M. Willett, and N. Gobron, Eds.



Special Online Supplement to the *Bulletin of the American Meteorological Society* Vol. 104, No. 9, September, 2023

<https://doi.org/10.1175/BAMS-D-23-0090.1>

Corresponding author: Robert Dunn / robert.dunn@metoffice.gov.uk

©2023 American Meteorological Society

For information regarding reuse of this content and general copyright information, consult the [AMS Copyright Policy](#).

STATE OF THE CLIMATE IN 2022

Global Climate

Editors

Ellen Bartow-Gillies
Jessica Blunden
Tim Boyer

Chapter Editors

Peter Bissolli
Kyle R. Clem
Howard J. Diamond
Matthew L. Druckenmiller
Robert J. H. Dunn
Catherine Ganter
Nadine Gobron
Gregory C. Johnson
Rick Lumpkin
Ademe Mekonnen
John B. Miller
Twila A. Moon
Marilyn N. Raphael
Ahira Sánchez-Lugo
Carl J. Schreck III
Richard L. Thoman
Kate M. Willett
Zhiwei Zhu

Technical Editor

Lukas Noguchi

BAMS Special Editor for Climate

Michael A. Alexander

American Meteorological Society

Cover Credit:

Photo by Taaniela Kula, Tongan Geological Services (TGS).

Eruption at Hunga Tonga–Hunga Ha‘apai, witnessed by TGS observer team, a 5-kilometer wide plume rises over 18 kilometers above sea level, 14 January 2022, 5:14 pm local time.

How to cite this document:

Global Climate is one chapter from the *State of the Climate in 2022* annual report and is available from <https://doi.org/10.1175/BAMS-D-23-0090.1>. Compiled by NOAA’s National Centers for Environmental Information, *State of the Climate in 2022* is based on contributions from scientists from around the world. It provides a detailed update on global climate indicators, notable weather events, and other data collected by environmental monitoring stations and instruments located on land, water, ice, and in space. The full report is available from <https://doi.org/10.1175/2023BAMSStateoftheClimate.1>.

Citing the complete report:

Blunden, J., T. Boyer, and E. Bartow-Gillies, Eds., 2023: “State of the Climate in 2022”. *Bull. Amer. Meteor. Soc.*, 104 (9), S1–S501 <https://doi.org/10.1175/2023BAMSStateoftheClimate.1>.

Citing this chapter:

Dunn, R. J. H., J. B. Miller, K. M. Willett, and N. Gobron, Eds., 2023: Global Climate [in “State of the Climate in 2022”]. *Bull. Amer. Meteor. Soc.*, 104 (9), S11–S145, <https://doi.org/10.1175/BAMS-D-23-0090.1>.

Citing a section (example):

Füllekrug, M., E. Williams, C. Price, S. Goodman, R. Holzworth, K. Virts, D. Buechler, T. Lang, and Y. Liu, 2023: Lightning [in “State of the Climate in 2022”]. *Bull. Amer. Meteor. Soc.*, 104 (9), S76–S78, <https://doi.org/10.1175/BAMS-D-23-0090.1>.

Editor and Author Affiliations (alphabetical by name)

- Ades, Melanie**, European Centre for Medium-Range Weather Forecasts, Reading, United Kingdom
- Adler, Robert**, CMNS-Earth System Science Interdisciplinary Center, University of Maryland, College Park, Maryland
- Alexe, Mihai**, European Centre for Medium-Range Weather Forecasts, Bonn, Germany
- Allan, Richard P.**, Department of Meteorology and National Centre for Earth Observation, University of Reading, Reading, United Kingdom
- Anderson, John**, Hampton University, Hampton, Virginia
- Anneville, Orlane**, National Research Institute for Agriculture, Food and Environment (INRAE), CARRTEL, Université Savoie Mont Blanc, Chambéry, France
- Aono, Yasuyuki**, Graduate School of Agriculture, Osaka Metropolitan University, Sakai, Japan
- Arguez, Anthony**, NOAA/NESDIS National Centers for Environmental Information, Asheville, North Carolina
- Arosio, Carlo**, University of Bremen, Bremen, Germany
- Augustine, John A.**, NOAA Global Monitoring Laboratory, Boulder, Colorado
- Azorin-Molina, Cesar**, Centro de Investigaciones sobre Desertificación – Spanish National Research Council (CSIC-UV-GVA), Valencia, Spain
- Barichivich, Jonathan**, Instituto de Geografía, Pontificia Universidad Católica de Valparaíso, Valparaíso, Chile; Laboratoire des Sciences du Climat et de l'Environnement (LSCE), LSCE/IPSL, CEA-CNRS-UVSQ, Gif-sur-Yvette, France
- Barnes, John E.**, retired, NOAA Global Monitoring Laboratory, Boulder, Colorado
- Beck, Hylke E.**, Physical Science and Engineering Division, King Abdullah University of Science and Technology, Thuwal, Saudi Arabia
- Bellouin, Nicolas**, University of Reading, Reading, United Kingdom
- Benedetti, Angela**, European Centre for Medium-Range Weather Forecasts, Reading, United Kingdom
- Blagrove, Kevin**, Department of Biology, York University, Toronto, Canada
- Blenkinsop, Stephen**, School of Engineering, Newcastle University, Newcastle-upon-Tyne, United Kingdom
- Bock, Olivier**, Université Paris Cité, Institut de Physique du Globe de Paris, CNRS, IGN, F-75005 Paris, France; ENSG-Géomatique, IGN, F-77455 Marne-la-Vallée, France
- Bodin, Xavier**, Laboratoire EDYTEM, CNRS/Université Savoie Mont-Blanc, Chambéry, France
- Bosilovich, Michael**, Global Modeling and Assimilation Office, NASA Goddard Space Flight Center, Greenbelt, Maryland
- Boucher, Olivier**, Sorbonne Université, Paris, France
- Buechler, Dennis**, University of Alabama in Huntsville, Huntsville, Alabama
- Buehler, Stefan A.**, Universität Hamburg, Hamburg, Germany
- Campos, Diego**, Dirección Meteorológica de Chile (DMC), Santiago, Chile
- Carrea, Laura**, Department of Meteorology, University of Reading, Reading, United Kingdom
- Chang, Kai-Lan**, Cooperative Institute for Research in Environmental Sciences, University of Colorado Boulder, Boulder, Colorado; NOAA Chemical Sciences Laboratory, Boulder, Colorado
- Christiansen, Hanne H.**, Geophysics Department, University Centre in Svalbard, Longyearbyen, Norway
- Christy, John R.**, University of Alabama in Huntsville, Huntsville, Alabama
- Chung, Eui-Seok**, Korea Polar Research Institute, Incheon, South Korea
- Ciasto, Laura M.**, NOAA/NWS National Centers for Environmental Prediction Climate Prediction Center, College Park, Maryland
- Clingan, Scott**, Cooperative Institute for Research in the Earth Sciences, NOAA Global Monitoring Laboratory, Boulder, Colorado
- Coldewey-Egbers, Melanie**, DLR (German Aerospace Center) Oberpfaffenhofen, Germany
- Cooper, Owen R.**, Cooperative Institute for Research in Environmental Sciences, University of Colorado Boulder, Boulder, Colorado; NOAA Chemical Sciences Laboratory, Boulder, Colorado
- Cornes, Richard C.**, National Oceanography Centre, Southampton, United Kingdom
- Covey, Curt**, Lawrence Livermore National Laboratory, Livermore, California
- Créatux, Jean-François**, LEGOS (CNES/CNRS/IRD/UPS), University of Toulouse, Toulouse, France
- Crimmins, Theresa**, USA National Phenology Network, School of Natural Resources and the Environment, University of Arizona, Tucson, Arizona
- Cropper, Thomas**, National Oceanography Centre, Southampton, United Kingdom
- Crotwell, Molly**, Cooperative Institute for Research in the Earth Sciences, NOAA Global Monitoring Laboratory, Boulder, Colorado
- Culpepper, Joshua**, Department of Biology, York University, Toronto, Canada
- Cusicanqui, Diego**, Université Grenoble Alpes, Institut de Géosciences de l'Environnement (IGE), Grenoble, France
- Davis, Sean M.**, NOAA Chemical Sciences Laboratory, Boulder, Colorado
- de Jeu, Richard A. M.**, Planet Labs, Haarlem, The Netherlands
- Degenstein, Doug**, University of Saskatchewan, Saskatoon, Canada
- Delaloye, Reynald**, Department of Geosciences, University of Fribourg, Fribourg, Switzerland
- Dokulil, Martin T.**, Research Institute for Limnology, University of Innsbruck, Mondsee, Austria
- Donat, Markus G.**, Barcelona Supercomputing Centre, Barcelona, Spain; Catalan Institution for Research and Advanced Studies (ICREA), Barcelona, Spain
- Dorigo, Wouter A.**, TU Wien, Department of Geodesy and Geoinformation, Vienna, Austria
- Dugan, Hilary A.**, Center for Limnology, University of Wisconsin-Madison, Madison, Wisconsin
- Dunn, Robert J. H.**, Met Office Hadley Centre, Exeter, United Kingdom
- Durre, Imke**, NOAA/NESDIS National Centers for Environmental Information, Asheville, North Carolina
- Dutton, Geoff**, Cooperative Institute for Research in the Earth Sciences, NOAA Global Monitoring Laboratory, Boulder, Colorado
- Duveiller, Gregory**, Max Planck Institute for Biogeochemistry, Jena, Germany
- Estilow, Thomas W.**, Rutgers University, Piscataway, New Jersey
- Estrella, Nicole**, Ecoclimatology, Department of Life Science Systems, TUM School of Life Sciences, Technical University of Munich, Freising, Germany
- Fereday, David**, Met Office Hadley Centre, Exeter, United Kingdom
- Fioletov, Vitali E.**, Environment and Climate Change Canada, Toronto, Canada
- Flemming, Johannes**, European Centre for Medium-Range Weather Forecasts, Reading, United Kingdom
- Foster, Michael J.**, Cooperative Institute for Meteorological Satellite Studies, Space Science and Engineering Center, University of Wisconsin-Madison, Madison, Wisconsin
- Franz, Bryan**, NASA Goddard Space Flight Center, Greenbelt, Maryland
- Frith, Stacey M.**, Science Systems and Applications, Inc, Lanham, Maryland; NASA Goddard Space Flight Center, Greenbelt, Maryland
- Froidevaux, Lucien**, Jet Propulsion Laboratory, California Institute of Technology, Pasadena, California
- Füllekrug, Martin**, University of Bath, Bath, United Kingdom
- Garforth, Judith**, Woodland Trust, Grantham, United Kingdom
- Garg, Jay**, Science Systems and Applications, Inc. (SSAI), Hampton, Virginia
- Gibbes, Badin**, School of Civil Engineering, The University of Queensland, Brisbane, Australia
- Gobron, Nadine**, European Commission Joint Research Centre, Ispra, Italy
- Goodman, Steven**, Thunderbolt Global Analytics, Huntsville, Alabama
- Goto, Atsushi**, World Meteorological Organization, Geneva, Switzerland

Editor and Author Affiliations (continued)

- Gruber, Alexander**, TU Wien, Department of Geodesy and Geoinformation, Vienna, Austria
- Gu, Guojun**, CMNS-Earth System Science Interdisciplinary Center, University of Maryland, College Park, Maryland
- Hahn, Sebastian**, TU Wien, Department of Geodesy and Geoinformation, Vienna, Austria
- Haimberger, Leopold**, University of Vienna, Vienna, Austria
- Hall, Bradley D.**, NOAA Global Monitoring Laboratory, Boulder, Colorado
- Harris, Ian**, National Centre for Atmospheric Science (NCAS), University of East Anglia, Norwich, United Kingdom; Climatic Research Unit, School of Environmental Sciences, University of East Anglia, Norwich, United Kingdom
- Hemming, Deborah L.**, Met Office Hadley Centre, Exeter, United Kingdom; Birmingham Institute of Forest Research, Birmingham University, Birmingham, United Kingdom
- Hirschi, Martin**, ETH Zurich, Department of Environmental Systems Science, Zürich, Switzerland
- Ho, Shu-peng (Ben)**, Center for Satellite Applications and Research, NOAA, College Park, Maryland; Remote Sensing Systems, Santa Rosa, California
- Holzworth, Robert**, University of Washington, Seattle, Washington
- Hrbáček, Filip**, Department of Geography, Masaryk University, Brno, Czech Republic
- Hu, Guojie**, Cryosphere Research Station on Qinghai-Tibet Plateau, Northwestern Institute of Eco-Environment and Resources, CAS, Beijing, China
- Hurst, Dale F.**, Cooperative Institute for Research in Environmental Sciences, University of Colorado Boulder, Boulder, Colorado; NOAA Global Monitoring Laboratory, Boulder, Colorado
- Inness, Antje**, European Centre for Medium-Range Weather Forecasts, Reading, United Kingdom
- Isaksen, Ketil**, Norwegian Meteorological Institute, Oslo, Norway
- John, Viju O.**, EUMETSAT, Darmstadt, Germany
- Jones, Philip D.**, Climatic Research Unit, School of Environmental Sciences, University of East Anglia, Norwich, United Kingdom
- Junod, Robert**, Earth System Science Center (ESSC), University of Alabama in Huntsville, Huntsville, Alabama
- Kääb, Andreas**, Department of Geosciences, University of Oslo, Norway
- Kaiser, Johannes W.**, SatFire Kaiser, Hofheim am Taunus, Germany
- Kaufmann, Viktor**, Institute of Geodesy, Working Group Remote Sensing and Photogrammetry, Graz University of Technology, Graz, Austria
- Kellerer-Pirklbauer, Andreas**, Institute of Geography and Regional Science, Cascade – The Mountain Processes and Mountain Hazards Group, University of Graz, Graz, Austria
- Kent, Elizabeth C.**, National Oceanography Centre, Southampton, United Kingdom
- Kidd, Richard**, EODC GmbH, Vienna, Austria
- Kipling, Zak**, European Centre for Medium-Range Weather Forecasts, Reading, United Kingdom
- Koppa, Akash**, Hydro-Climate Extremes Lab (H-CEL), Ghent University, Ghent, Belgium
- Kraemer, Benjamin M.**, University of Konstanz, Konstanz, Germany
- Kramarova, Natalya**, NASA Goddard Space Flight Center, Greenbelt, Maryland
- Kruger, Andries**, Climate Service, South African Weather Service, Pretoria, South Africa
- La Fuente, Sofia**, Dundalk Institute of Technology, Dundalk, Ireland
- Laas, Alo**, Estonian University of Life Sciences, Tartumaa, Estonia
- Lan, Xin**, CIRES, University of Colorado Boulder & NOAA Global Monitoring Laboratory, Boulder, Colorado
- Lang, Timothy**, NASA Marshall Space Flight Center, Huntsville, Alabama
- Lantz, Kathleen O.**, NOAA Global Monitoring Laboratory, Boulder, Colorado
- Lavers, David A.**, European Centre for Medium-Range Weather Forecasts, Reading, United Kingdom
- Leblanc, Thierry**, Jet Propulsion Laboratory, California Institute of Technology, Wrightwood, California
- Leibensperger, Eric M.**, Department of Physics and Astronomy, Ithaca College, Ithaca, New York
- Lennard, Chris**, Department of Environmental and Geographical Science, University of Cape Town, Cape Town, South Africa
- Liu, Yakun**, Massachusetts Institute of Technology, Cambridge, Massachusetts
- Loeb, Norman G.**, NASA Langley Research Center, Hampton, Virginia
- Loyola, Diego**, DLR (German Aerospace Center) Oberpfaffenhofen, Germany
- Maberly, Stephen C.**, UK Centre for Ecology & Hydrology, Lancaster, United Kingdom
- Madelon, Remi**, CESBIO, Université de Toulouse, CNES/CNRS/INRAe/IRD/UPS, Toulouse, France
- Magnin, Florence**, Laboratoire EDYTEM, CNRS/Université Savoie Mont-Blanc, Chambéry, France
- Matsuzaki, Shin-Ichiro**, National Institute for Environmental Studies, Tsukuba, Japan
- May, Linda**, UK Centre for Ecology & Hydrology, Edinburgh, United Kingdom
- Mayer, Michael**, University of Vienna, Vienna, Austria; European Centre for Medium-Range Weather Forecasts, Reading, United Kingdom
- McCabe, Matthew F.**, Climate and Livability Initiative, Division of Biological and Environmental Sciences and Engineering, King Abdullah University of Science and Technology, Thuwal, Saudi Arabia
- McVicar, Tim R.**, CSIRO Environment, Canberra, Australia; Australian Research Council Centre of Excellence for Climate Extremes, Sydney, Australia
- Mears, Carl A.**, Remote Sensing Systems, Santa Rosa, California
- Menzel, Annette**, Ecoclimatology, Department of Life Science Systems, TUM School of Life Sciences, Technical University of Munich, Freising, Germany; Institute for Advanced Study, Technical University of Munich, Garching, Germany
- Merchant, Christopher J.**, Department of Meteorology, University of Reading, Reading, United Kingdom
- Meyer, Michael F.**, United States Geological Survey, Madison, Wisconsin
- Miller, John B.**, NOAA Global Monitoring Laboratory, Boulder, Colorado
- Miralles, Diego G.**, Hydro-Climate Extremes Lab (H-CEL), Ghent University, Ghent, Belgium
- Moesinger, Leander**, TU Wien, Vienna, Austria
- Monet, Ghislaine**, Université Savoie Mont Blanc, INRAE, CARRTEL, Chambéry, France
- Montzka, Stephan A.**, NOAA Global Monitoring Laboratory, Boulder, Colorado
- Morice, Colin**, Met Office Hadley Centre, Exeter, United Kingdom
- Mrekaj, Ivan**, Technical University in Zvolen, Zvolen, Slovakia
- Mühle, Jens**, AGAGE, Scripps Institution of Oceanography, University of California, San Diego, La Jolla, California
- Nance, David**, Cooperative Institute for Research in the Earth Sciences, NOAA Global Monitoring Laboratory, Boulder, Colorado
- Nicolas, Julien P.**, European Centre for Medium-Range Weather Forecasts, Bonn, Germany
- Noetzli, Jeannette**, WSL Institute for Snow and Avalanche Research SLF, Davos-Dorf, Switzerland; Climate Change, Extremes and Natural Hazards in Alpine Regions Research Center CERC, Davos Dorf, Switzerland
- Noll, Ben**, National Institute of Water and Atmospheric Research, Auckland, New Zealand
- O'Keefe, John**, The Harvard Forest, Harvard University, Petersham, Massachusetts
- Osborn, Timothy J.**, Climatic Research Unit, School of Environmental Sciences, University of East Anglia, Norwich, United Kingdom
- Park, Taejin**, NASA Ames Research Center, Mountain View, California; Bay Area Environmental Research Institute, Mountain View, California

Editor and Author Affiliations (continued)

- Parrington, Mark**, European Centre for Medium-Range Weather Forecasts, Bonn, Germany
- Pellet, Cécile**, Department of Geosciences, University of Fribourg, Fribourg, Switzerland
- Pelto, Mauri S.**, Nichols College, Dudley, Massachusetts
- Petersen, Kyle**, Cooperative Institute for Research in the Earth Sciences, NOAA Global Monitoring Laboratory, Boulder, Colorado
- Phillips, Coda**, Cooperative Institute for Meteorological Satellite Studies, Space Science and Engineering Center, University of Wisconsin-Madison, Madison, Wisconsin
- Pierson, Don**, Department of Ecology and Genetics, Uppsala University, Uppsala, Sweden
- Pinto, Izidine**, Royal Netherlands Meteorological Institute (KNMI), De Bilt, The Netherlands
- Po-Chedley, Stephen**, Lawrence Livermore National Laboratory, Livermore, California
- Pogliotti, Paolo**, Environmental Protection Agency of Valle d'Aosta, Saint-Christophe, Italy
- Polvani, Lorenzo**, Columbia University, New York, New York
- Preimesberger, Wolfgang**, TU Wien, Department of Geodesy and Geoinformation, Vienna, Austria
- Price, Colin**, Tel Aviv University, Tel Aviv, Israel
- Pulkkanen, Merja**, Finnish Environment Institute (SYKE), Jyväskylä, Finland
- Randel, William J.**, National Center for Atmospheric Research, Boulder, Colorado
- Rémy, Samuel**, HYGEOS, Lille, France
- Ricciardulli, Lucrezia**, Remote Sensing Systems, Santa Rosa, California
- Richardson, Andrew D.**, School of Informatics, Computing, and Cyber Systems, Flagstaff, Arizona; Center for Ecosystem Science and Society, Northern Arizona University, Flagstaff, Arizona
- Robinson, David A.**, Rutgers University, Piscataway, New Jersey
- Rocha, Willy**, Servicio Nacional de Meteorología e Hidrología, Bolivia
- Rodell, Matthew**, Earth Sciences Division, NASA Goddard Space Flight Center, Greenbelt, Maryland
- Rodriguez-Fernandez, Nemesio**, CESBIO, Université de Toulouse, CNES/CNRS/INRAe/IRD/UPS, Toulouse, France
- Rosenlof, Karen H.**, NOAA Chemical Sciences Laboratory, Boulder, Colorado
- Rozanov, Alexei**, University of Bremen, Bremen, Germany
- Rozkošný, Jozef**, Slovak Hydrometeorological Institute, Bratislava, Slovakia
- Rusanovskaya, Olga O.**, Irkutsk State University, Institute of Biology, Irkutsk, Russia
- Rutishauser, This**, Swiss Academy of Sciences (SCNAT), Bern, Switzerland
- Sabeerali, C. T.**, India Meteorological Department, Ministry of Earth Sciences, Pune, India
- Sánchez-Lugo, Ahira**, NOAA/NESDIS National Centers for Environmental Information, Asheville, North Carolina
- Sawaengphokhai, Parnchai**, Science Systems and Applications, Inc. (SSAI), Hampton, Virginia
- Schenzinger, Verena**, Medical University of Innsbruck, Innsbruck, Austria
- Schlegel, Robert W.**, Laboratoire d'Océanographie de Villefranche, Sorbonne Université, CNRS, Villefranche-sur-mer, France
- Schmid, Martin**, Eawag, Swiss Federal Institute of Aquatic Science and Technology, Surface Waters - Research and Management, Kastanienbaum, Switzerland
- Schneider, Udo**, Global Precipitation Climatology Centre, Deutscher Wetterdienst, Offenbach, Germany
- Sezaki, Fumi**, Japan Meteorological Agency, Tokyo, Japan
- Sharma, Sapna**, Department of Biology, York University, Toronto, Canada
- Shi, Lei**, NOAA/NESDIS National Centers for Environmental Information, Asheville, North Carolina
- Shimaraeva, Svetlana V.**, Irkutsk State University, Institute of Biology, Irkutsk, Russia
- Silow, Eugene A.**, Irkutsk State University, Institute of Biology, Irkutsk, Russia
- Simmons, Adrian J.**, European Centre for Medium-Range Weather Forecasts, Reading, United Kingdom
- Smith, Sharon L.**, Geological Survey of Canada, Natural Resources Canada, Ottawa, Canada
- Soden, Brian J.**, University of Miami, Miami, Florida
- Sofieva, Viktoria**, FMI (Finnish Meteorological Institute), Helsinki, Finland
- Sparks, Tim H.**, Poznań University of Life Sciences, Poznań, Poland
- Sreejith, O.P.**, India Meteorological Department, Ministry of Earth Sciences, Pune, India
- Stackhouse, Jr., Paul W.**, NASA Langley Research Center, Hampton, Virginia
- Stauffer, Ryan**, NASA Goddard Space Flight Center, Greenbelt, Maryland
- Steinbrecht, Wolfgang**, DWD (German Weather Service), Hohenpeissenberg, Germany
- Steiner, Andrea K.**, Wegener Center for Climate and Global Change, University of Graz, Graz, Austria
- Stradiotti, Pietro**, TU Wien, Department of Geodesy and Geoinformation, Vienna, Austria
- Streletskiy, Dmitry A.**, George Washington University, Washington DC
- Surendran, Divya E.**, India Meteorological Department, Ministry of Earth Sciences, Pune, India
- Thackeray, Stephen J.**, UK Centre for Ecology and Hydrology, Lancaster, United Kingdom
- Thibert, Emmanuel**, Université Grenoble Alpes, INRAE, CNRS, IRD, Grenoble INP, IGE, Grenoble, France.
- Timofeyev, Maxim A.**, Irkutsk State University, Institute of Biology, Irkutsk, Russia
- Tourpali, Kleareti**, Aristotle University, Thessaloniki, Greece
- Tye, Mari R.**, National Center for Atmospheric Research, Boulder, Colorado
- van der A, Ronald**, Royal Netherlands Meteorological Institute (KNMI), De Bilt, The Netherlands
- van der Schalie, Robin**, Planet Labs, Haarlem, The Netherlands
- van der Schrier, Gerard**, Royal Netherlands Meteorological Institute (KNMI), De Bilt, The Netherlands
- van Vliet, Arnold J.H.**, Environmental Systems Analysis Group, Wageningen University and Research, The Netherlands
- Verborg, Piet**, National Institute of Water and Atmospheric Research, Wellington, New Zealand
- Vernier, Jean-Paul**, NASA Langley Research Center, Hampton, Virginia
- Vimont, Isaac J.**, NOAA Global Monitoring Laboratory, Boulder, Colorado
- Virts, Katrina**, University of Alabama in Huntsville, Huntsville, Alabama
- Vivero, Sebastián**, Department of Geosciences, University of Fribourg, Fribourg, Switzerland
- Vömel, Holger**, Earth Observing Laboratory, National Center for Atmospheric Research, Boulder, Colorado
- Vose, Russell S.**, NOAA/NESDIS National Centers for Environmental Information, Asheville, North Carolina
- Wang, Ray H. J.**, Georgia Institute of Technology, Atlanta, Georgia
- Wang, Xinyue**, National Center for Atmospheric Research, Boulder, Colorado
- Warnock, Taran**, University of Saskatchewan, Saskatoon, Canada
- Weber, Mark**, University of Bremen, Bremen, Germany
- Wiese, David N.**, Jet Propulsion Laboratory, California Institute of Technology, Pasadena, California
- Wild, Jeannette D.**, ESSIC/University of Maryland, College Park, Maryland; NOAA NESDIS/STAR, College Park, Maryland
- Willett, Kate M.**, Met Office Hadley Centre, Exeter, United Kingdom

Editor and Author Affiliations (continued)

Williams, Earle, Massachusetts Institute of Technology, Cambridge, Massachusetts

Wong, Takmeng, NASA Langley Research Center, Hampton, Virginia

Woolway, Richard Iestyn, School of Ocean Sciences, Bangor University, Menai Bridge, Anglesey, Wales

Yin, Xungang, NOAA/NESDIS National Centers for Environmental Information, Asheville, North Carolina

Zeng, Zhenzhong, School of Environmental Science and Engineering, Southern University of Science and Technology, Shenzhen, China

Zhao, Lin, School of Geographical Sciences, Nanjing University of Information Science and Technology, Nanjing, China

Zhou, Xinjia, Center for Satellite Applications and Research, NOAA, College Park, Maryland

Ziemke, Jerry R., Goddard Earth Sciences Technology and Research, Morgan State University, Baltimore, Maryland; NASA Goddard Space Flight Center, Greenbelt, Maryland

Ziese, Markus, Global Precipitation Climatology Centre, Deutscher Wetterdienst, Offenbach, Germany

Zotta, Ruxandra M., TU Wien, Vienna, Austria

Zou, Cheng-Zhi, NOAA/NESDIS Center for Satellite Applications and Research, College Park, Maryland

Editorial and Production Team

Allen, Jessica, Graphics Support, Cooperative Institute for Satellite Earth System Studies, North Carolina State University, Asheville, North Carolina

Camper, Amy V., Graphics Support, Innovative Consulting and Management Services, LLC, NOAA/NESDIS National Centers for Environmental Information, Asheville, North Carolina

Haley, Bridgette O., Graphics Support, NOAA/NESDIS National Centers for Environmental Information, Asheville, North Carolina

Hammer, Gregory, Content Team Lead, Communications and Outreach, NOAA/NESDIS National Centers for Environmental Information, Asheville, North Carolina

Love-Brotak, S. Elizabeth, Lead Graphics Production, NOAA/NESDIS National Centers for Environmental Information, Asheville, North Carolina

Ohlmann, Laura, Technical Editor, Innovative Consulting and Management Services, LLC, NOAA/NESDIS National Centers for Environmental Information, Asheville, North Carolina

Noguchi, Lukas, Technical Editor, Innovative Consulting and Management Services, LLC, NOAA/NESDIS National Centers for Environmental Information, Asheville, North Carolina

Riddle, Deborah B., Graphics Support, NOAA/NESDIS National Centers for Environmental Information, Asheville, North Carolina

Veasey, Sara W., Visual Communications Team Lead, Communications and Outreach, NOAA/NESDIS National Centers for Environmental Information, Asheville, North Carolina

2. Table of Contents

List of authors and affiliations	S14
a. Overview	S20
b. Temperature	S27
1. Global surface temperature.....	S27
2. Lake surface water temperature.....	S28
3. Night marine air temperature.....	S31
4. Surface temperature extremes.....	S33
5. Tropospheric temperature.....	S36
6. Stratospheric temperature.....	S38
c. Cryosphere	S39
1. Permafrost temperature and active layer thickness.....	S39
2. Rock glacier velocity.....	S41
3. Alpine glaciers.....	S43
4. Lake ice.....	S45
5. Northern Hemisphere continental snow-cover extent.....	S47
d. Hydrological cycle	S49
1. Surface humidity.....	S49
Sidebar 2.1: Assessing humid heat extremes over land.....	S51
2. Total column water vapor.....	S54
3. Upper-tropospheric humidity.....	S55
4. Precipitation.....	S57
5. Land surface precipitation extremes.....	S58
6. Cloudiness.....	S60
7. Lake water levels.....	S61
8. Groundwater and terrestrial water storage.....	S63
9. Soil moisture.....	S65
10. Monitoring global drought using the self-calibrating Palmer Drought Severity Index.....	S66
11. Land evaporation.....	S68
e. Atmospheric circulation	S69
1. Mean sea-level pressure and related modes of variability.....	S69
2. Land and ocean surface winds.....	S72
3. Upper air winds.....	S74
4. Lightning.....	S76
f. Earth radiation budget	S79
1. Earth radiation budget at top-of-atmosphere.....	S79
2. Mauna Loa apparent transmission record.....	S81

2. Table of Contents

Sidebar 2.2: Hunga Tonga–Hunga Ha’apai eruption.....	S82
g. Atmospheric composition.....	S85
1. Long-lived greenhouse gases.....	S85
2. Ozone-depleting substances and their substitutes.....	S87
3. Aerosols.....	S91
4. Stratospheric ozone.....	S94
5. Stratospheric water vapor.....	S96
6. Tropospheric ozone.....	S98
7. Carbon monoxide.....	S101
h. Land surface properties.....	S102
1. Terrestrial surface albedo dynamics.....	S102
2. Terrestrial vegetation dynamics.....	S103
3. Biomass burning.....	S105
4. Phenology of primary producers.....	S107
5. Vegetation optical depth.....	S110
Acknowledgments.....	S113
Appendix 1: Chapter 2 – Acronyms.....	S118
Appendix 2: Chapter 2 – Supplemental Material.....	S122
References.....	S130

Please refer to Chapter 8 (Relevant Datasets and Sources) for a list of all climate variables and datasets used in this chapter for analyses, along with their websites for more information and access to the data.

2. GLOBAL CLIMATE

R. J. H. Dunn, J. B. Miller, K. M. Willett, and N. Gobron, Eds.

a. Overview

—R. J. H. Dunn, J. B. Miller, K. M. Willett, and N. Gobron

Throughout 2022, the “triple-dip” La Niña (three consecutive years) showed its hand in a large number of the essential climate variables and metrics that are covered in this chapter. La Niña conditions tend to have a cooling effect on global temperatures in comparison to neutral or El Niño years and impact precipitation patterns around the globe. Upper-level wind patterns at 200 hPa across the globe for 2020–22 showed a striking similarity with the last triple-dip La Niña that occurred in 1998–2000.

Yet, despite the cooling effect of the ongoing La Niña, 2022 was still among the six warmest years since global records began in the mid-to-late 1880s, according to six datasets of global surface temperatures. It was also the warmest La Niña year on record, surpassing 2021.

Exceptional heatwaves occurred across the globe in 2022, boosted by above-average temperatures that continue their relentless long-term rise. In Europe, the “unweather”—an Old English term for weather so severe that it appears to come from a different climate or world—shattered records across the continent during the summer months, while rivers and reservoirs fell to critically low levels. Meanwhile China experienced its hottest summer on record and at Wuhan, the Yangtze River reached record-low values.

The extreme high summer temperatures over Europe resulted in unprecedented melting of glaciers in the Alps, with over 6% of their volume lost in Switzerland this year alone, a record loss. Globally, 2022 was the 35th consecutive year of glacier mass loss and the 14th consecutive year of exceptional loss (more than 500 mm water equivalent). Ice cover on lakes was almost nine days shorter than average, the fourth shortest since 1980; the five shortest ice seasons have all occurred since 2016. The average temperature anomaly for more than 1950 lakes across the Northern Hemisphere was the second highest since the beginning of the record in 1995.

Drought conditions were pervasive, occurring across Europe (linked to the extreme summer temperatures), as well as the American West, China, and most of Southern Hemisphere South America. Globally, record-high areas of land experiencing extreme drought (6.2%) were reached in August 2022; overall, 29% of land experienced moderate or worse categories of drought. Low values of terrestrial water storage also occurred in Europe and parts of China (linked to the heatwaves), but La Niña influenced high values in southeastern Australia. Extreme rainfall was observed in southeastern and eastern Australia as well as in Pakistan, which received around three times its normal August monsoon rainfall. However, precipitation amounts for the globe as a whole and over the ocean was much lower than normal, but close to normal over land. Total column water vapor and surface humidity were close to normal over the ocean. Despite ‘normal’ rainfall amounts over land and lower terrestrial water storage, 2022 saw continued above-average soil moisture values, which are approaching the level of the previous global record in 2011. Lake water levels were higher than normal overall, but cloudiness was below normal. Overall, 2022 was a mixed year for the hydrological variables presented in this chapter.

In addition to the ongoing La Niña, other climate modes of variability in 2022 included a negative Indian Ocean dipole, a positive winter North Atlantic Oscillation (NAO), and the second highest summer NAO on record. The Southern Annular Mode was positive for a record-equaling

76% of days in 2022; it was the sixth time 60% of days has been exceeded since 2015, compared to only 10 years between 1979 and 2014 where high positive rates of >60% of days occurred.

The most significant long-term changes in atmospheric composition continue to be record levels of long-lived greenhouse gases (LLGHGs). Globally averaged carbon dioxide, methane, and nitrous oxide levels in 2022 continued to increase rapidly by 2.2 ppm, 14.4 ppb, and 1.3 ppb to 417.1 ppm, 1911.8 ppb, and 335.7 ppb, respectively. Collectively, all LLGHGs contributed 3.4 W m^{-2} of all radiative forcing, with the main three LLGHGs accounting for 98% of the increase in the last five years. As measured by equivalent effective stratospheric chlorine, the gases that destroy stratospheric ozone continue to decline nearly linearly. Since the 2018 discovery of post-2011 renewed trichlorofluoromethane (CFC-11) emissions, in violation of the Montreal Protocol, illegal emissions have mostly disappeared.

Considering short-lived atmospheric components, global mean aerosol optical depth in 2022 was the lowest on record, as was carbon monoxide, reflecting fewer fires in 2022 on top of a long-term decreasing trend likely reflecting global improvements in fossil fuel combustion efficiency. Tropospheric ozone has continued to trend upwards with an 8% increase since 2004. The most remarkable impact on short-lived species in 2022 resulted from the Hunga Tonga–Hunga Haʻapai underwater volcanic eruption (HTHH) in January 2022, discussed in Sidebar 2.2. Stratospheric aerosols registered their largest perturbation since the Mt. Pinatubo eruption of 1991. The HTHH eruption injected ~50 Tg–150 Tg of water vapor into the stratosphere, an amount unprecedented in the satellite record which represents more than 10% of the entire stratospheric water vapor burden, an anomaly that will persist for several years.

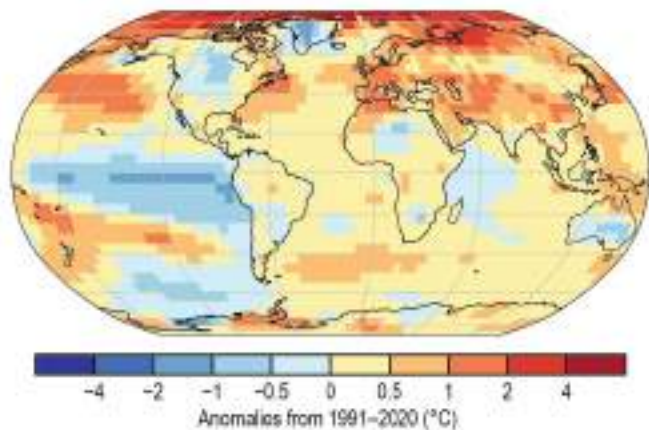
Low amounts of early summer snow cover in the Northern Hemisphere, along with increased plant growth and associated greening resulting from La Niña-induced rainfall decreased the global albedo in 2022. Carbon emissions from biomass burning during 2022 were 22% below the long-term average, making it the lowest fire year on record. However, considerable fire activity was still observed in boreal North America, parts of Europe, and central South America.

This year, a new measure of humid heat events is introduced in Sidebar 2.1, using equivalent heat indices based on the wet bulb temperature rather than air temperature. Humid heat extremes have increased in both magnitude and frequency since 1973, and 2022 was above average for both.

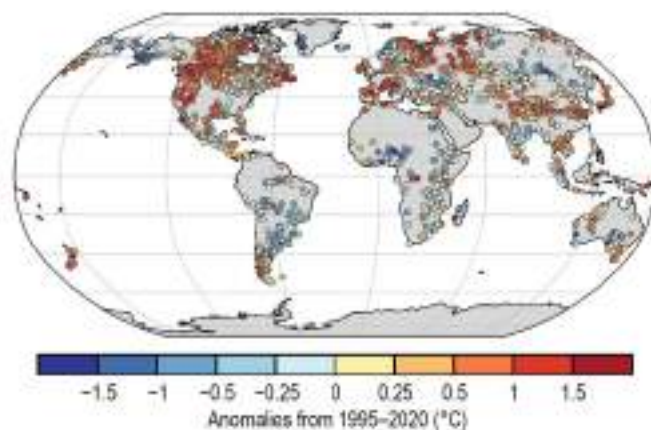
Time series and anomaly maps for 2022 from many of the variables described in this chapter can be found in Plates 1.1 (Chapter 1) and 2.1. Most sections now use the 1991–2020 climatological reference period, in line with World Meteorological Organization recommendations. This was not possible for all datasets depending on their length of record or legacy processing methods at the time of writing and is noted accordingly.

Finally, already looking towards the next reports, we welcome expressions of interest from those who wish to propose new sections for this chapter or wish to bring their expertise to existing author teams.

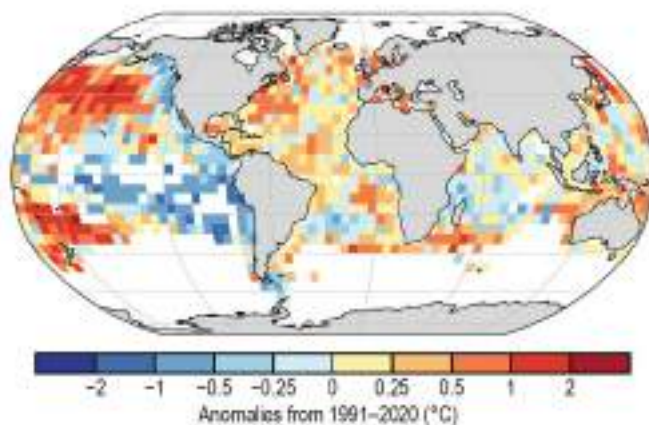
(a) Surface Temperature



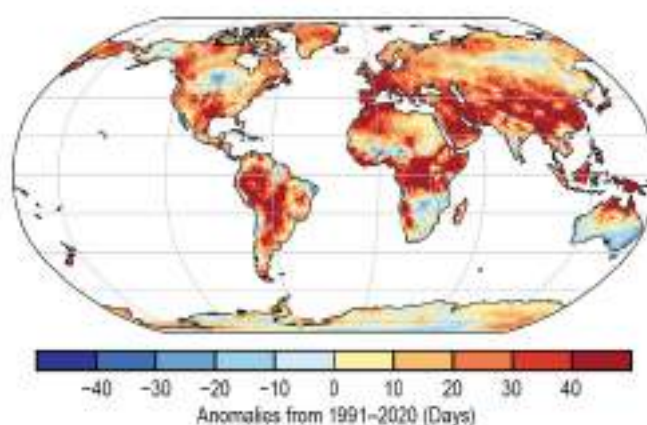
(b) Lake Temperature



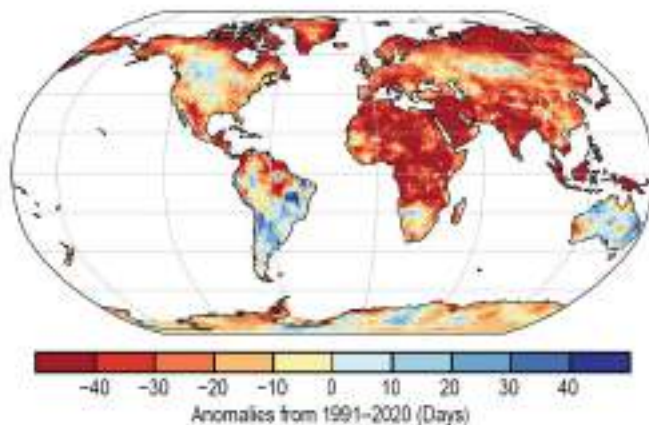
(c) Night Marine Air Temperature



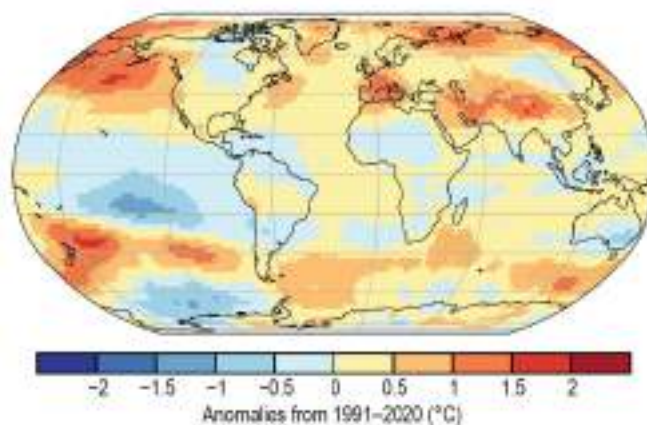
(d) Warm Days



(e) Cool Nights



(f) Lower Tropospheric Temperature



(g) Surface Specific Humidity

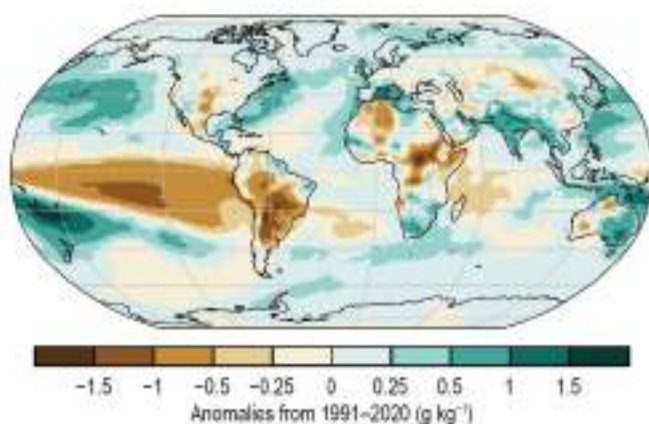
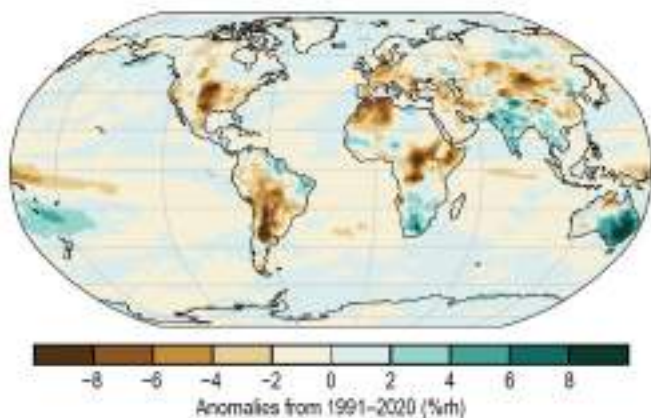
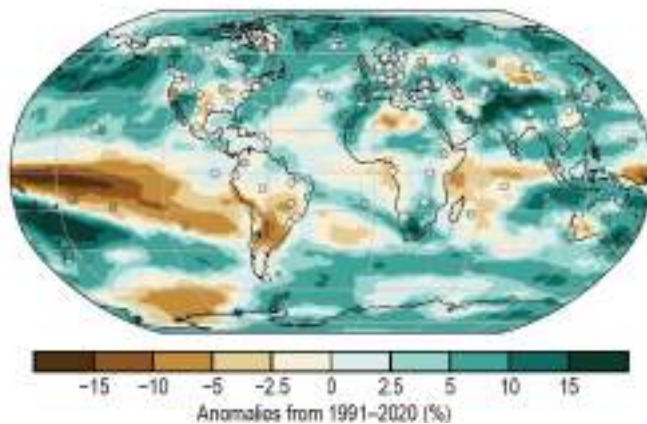


Plate 2.1. (a) NOAA NCEI Global land and ocean surface annual temperature anomalies (°C); (b) Satellite-derived lake surface water temperature anomalies, from ESA CCI LAKES/Copernicus C3S (°C); (c) CLASSmat night marine air temperature annual average anomalies (°C); (d) ERA5 warm day threshold exceedance (TX90p); (e) ERA5 cool night threshold exceedance (TN10p); (f) Average of RSS and UAH lower-tropospheric temperature anomalies (°C). Hatching denotes regions in which 2022 was the warmest year on record; (g) ERA5 surface specific humidity anomalies (g kg⁻¹);

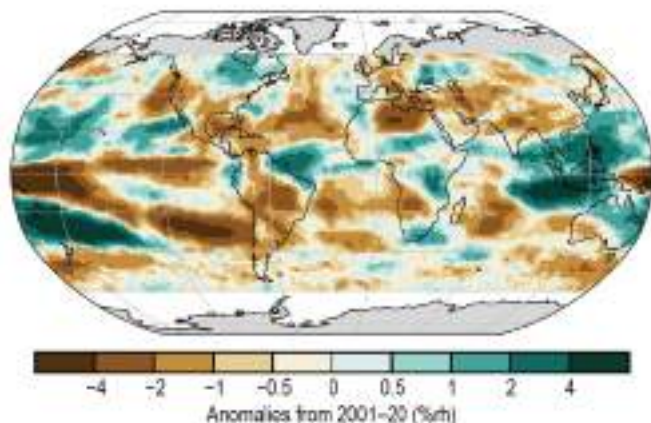
(h) Surface Relative Humidity



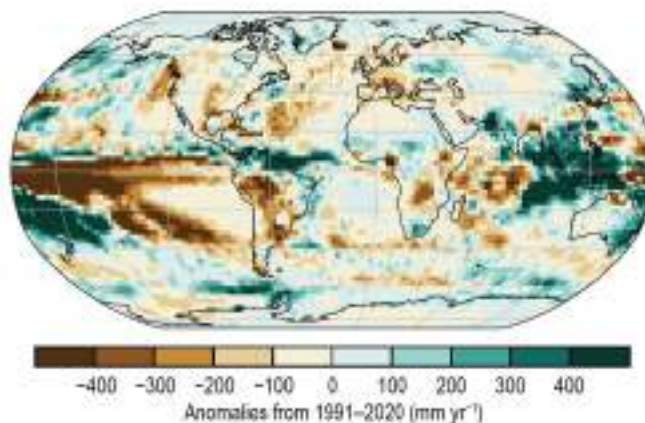
(i) Total Column Water Vapor



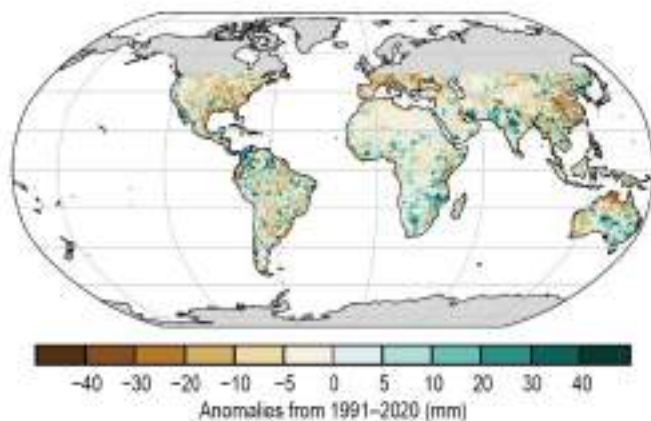
(j) Upper Tropospheric Humidity



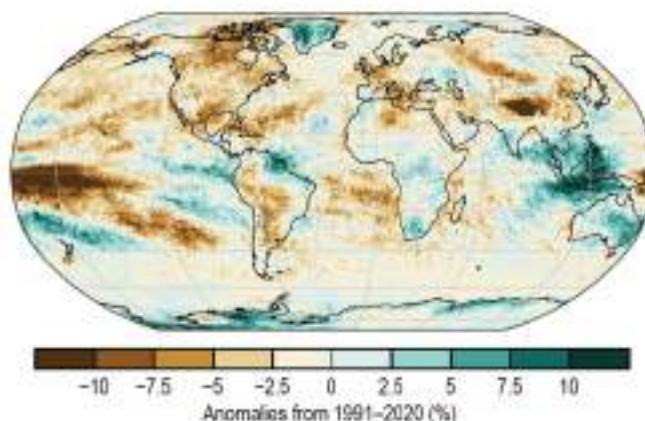
(k) Precipitation



(l) Maximum 1 Day Precipitation Amount



(m) Cloudiness



(n) Lake Water Level

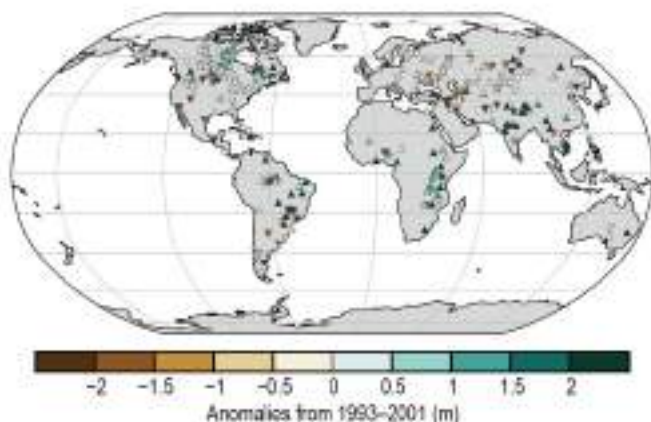
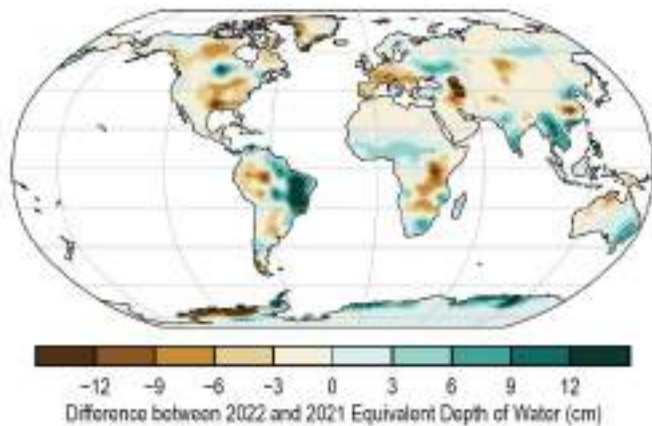
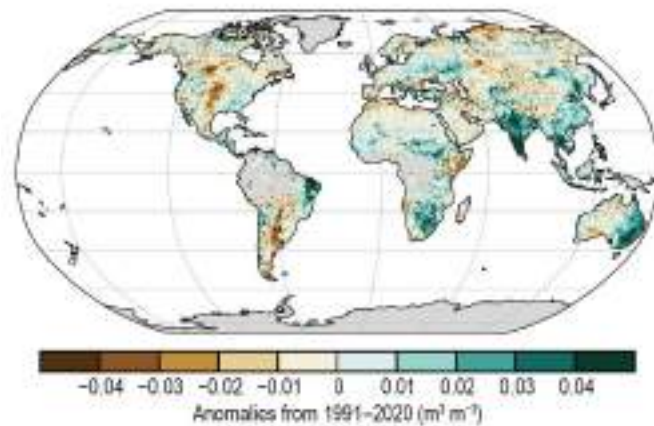


Plate 2.1 (cont.) (h) ERA5 surface relative humidity anomalies (%rh); (i) ERA5 TCWV anomalies (%). Data from GNSS stations are plotted as filled circles; (j) Annual microwave-based UTH anomalies (%rh); (k) GPCP v2.3 annual mean precipitation anomalies (mm yr⁻¹); (l) CHIRPS maximum 1-day (Rx1day) annual precipitation anomalies (mm); (m) PATMOS-x 6.0 cloud fraction annual anomalies (%); (n) G_REALM lake water level anomalies. Triangles pointing upward indicate positive anomalies, and triangles pointing down indicate negative anomalies;

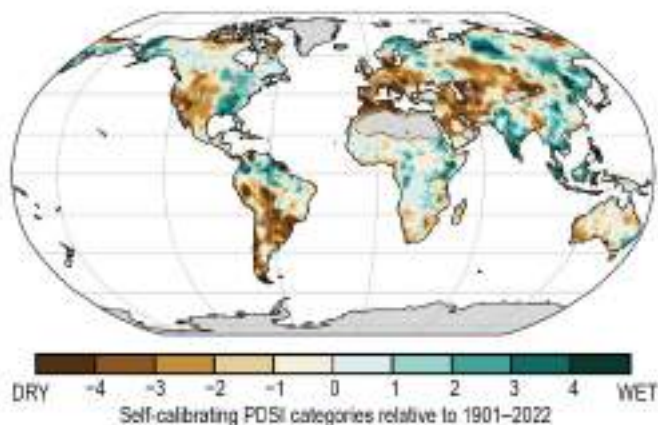
(o) Terrestrial Water Storage



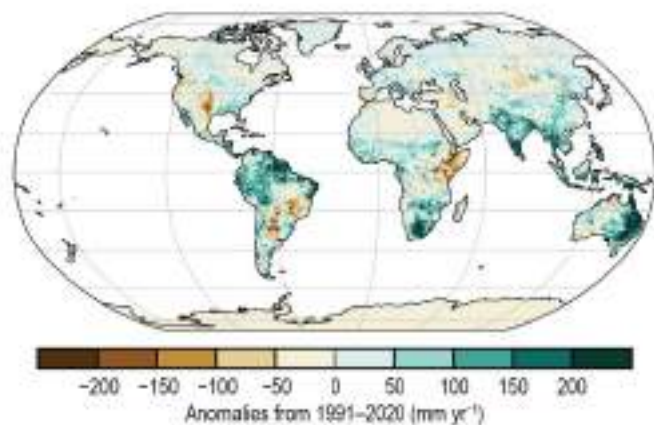
(p) Soil Moisture



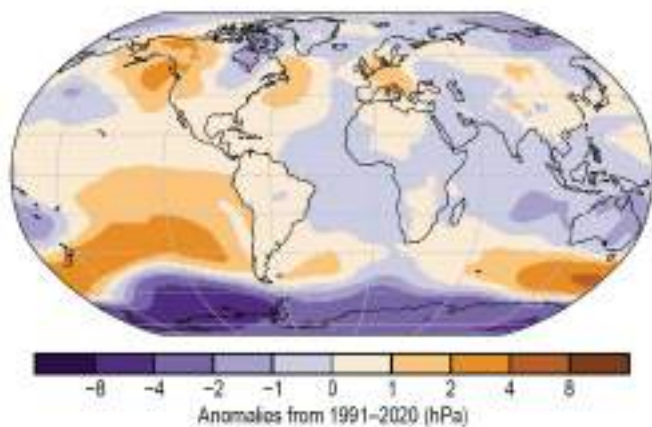
(q) Drought



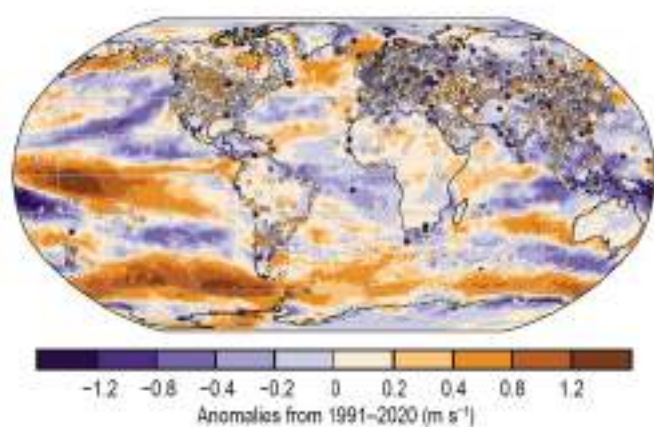
(r) Land Evaporation



(s) Sea Level Pressure



(t) Surface Winds



(u) Upper Air (850-hPa) Eastward Winds

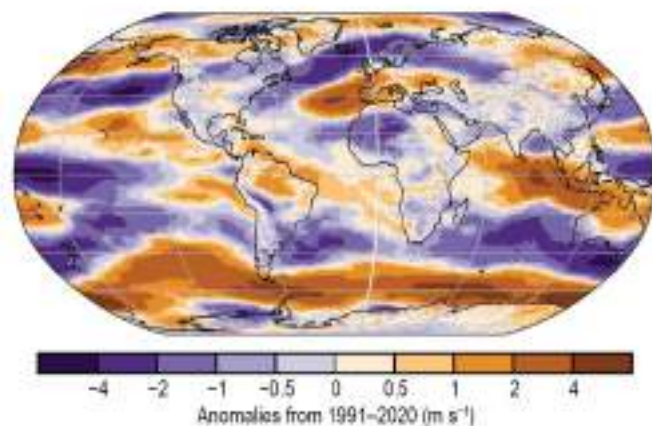
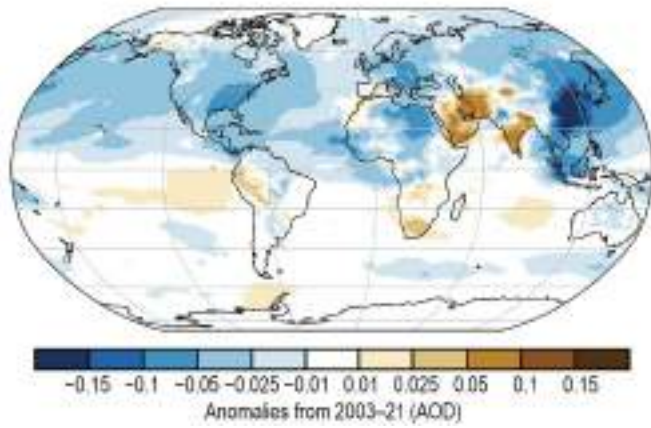
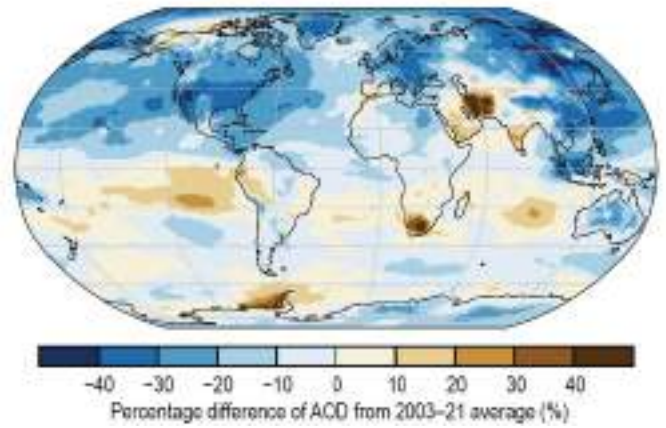


Plate 2.1 (cont.) (o) GRACE and GRACE-FO difference in annual-mean terrestrial water storage between 2020 and 2021 (cm); (p) C3S average surface soil moisture anomalies ($m^3 m^{-3}$). Data are masked where no retrieval is possible or where the quality is not assured and flagged, for example due to dense vegetation, frozen soil, or radio frequency interference; (q) Mean scPDSI for 2021. Droughts are indicated by negative values (brown), wet episodes by positive values (green); (r) GLEAM land evaporation anomalies ($mm yr^{-1}$); (s) ERA5 mean sea-level pressure anomalies (hPa); (t) Surface wind speed anomalies ($m s^{-1}$) from the observational HadISD3 dataset (land, circles), the ERA5 reanalysis output (land, shaded areas), and RSS satellite observations (ocean, shaded areas); (u) ERA5 850-hPa eastward wind speed anomalies ($m s^{-1}$);

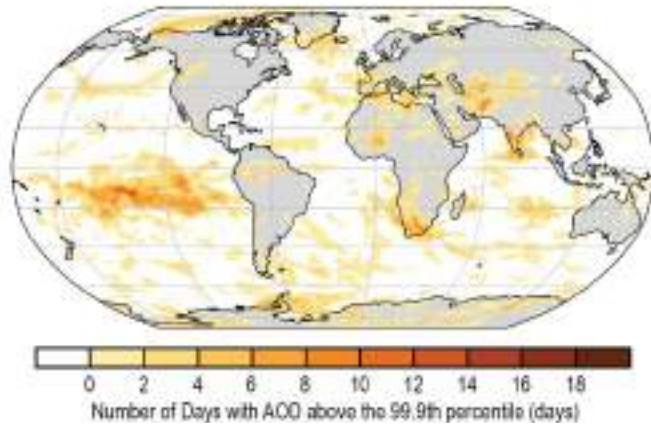
(v) Total Aerosol



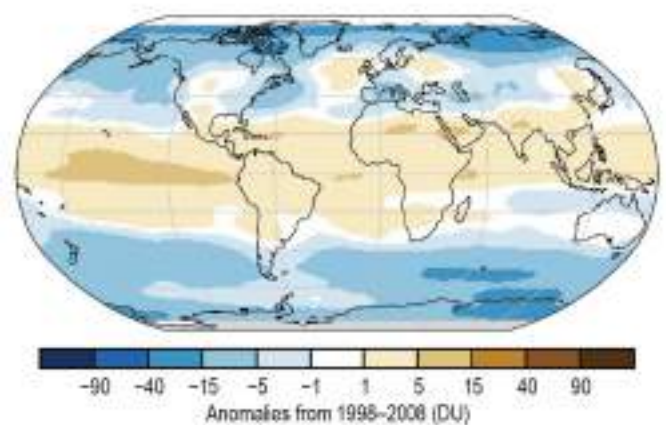
(w) AOD Percentage Anomaly



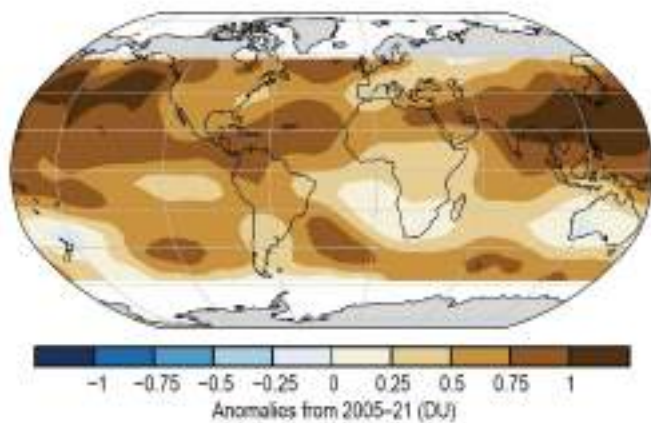
(x) Extreme Aerosol Days



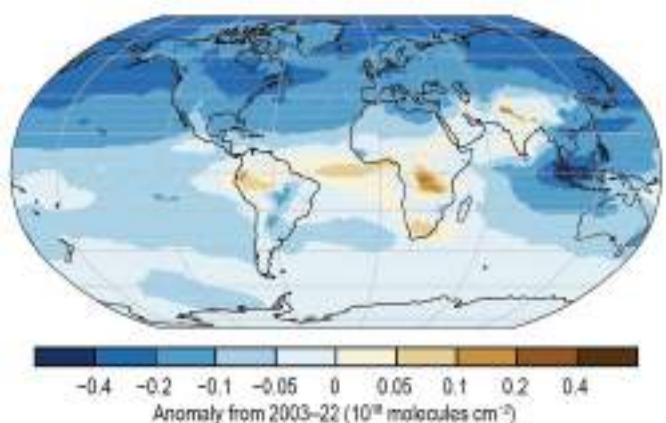
(y) Stratospheric (Total Column) Ozone



(z) OMI/MLS Tropospheric Column Ozone



(aa) Carbon Monoxide



(ab) Land Surface Albedo in the Visible

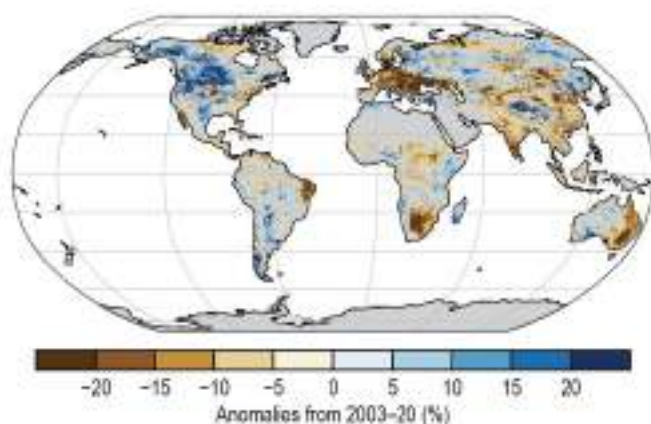
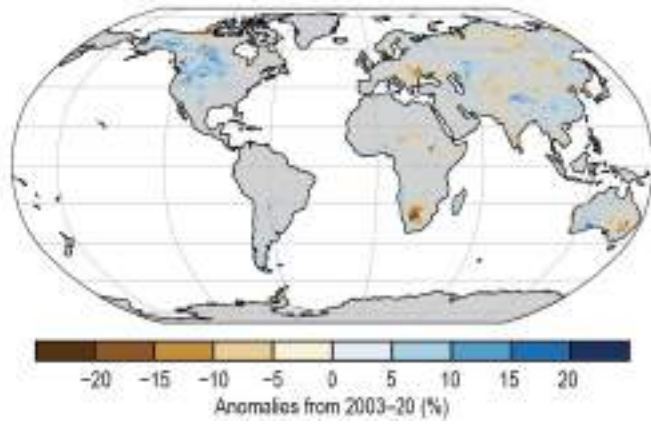
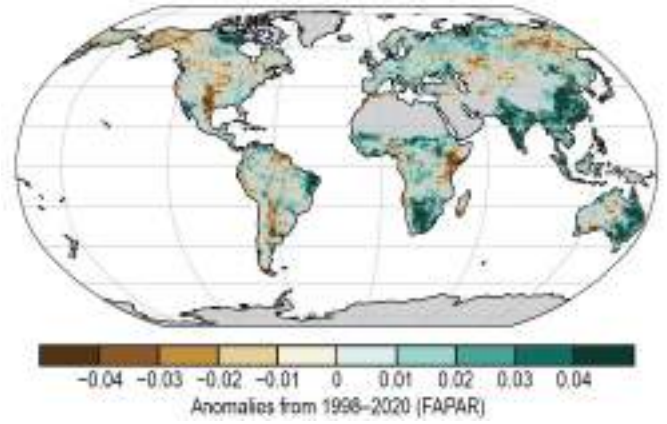


Plate 2.1 (cont.) (v) Total aerosol optical depth (AOD) anomalies at 550 nm; (w) Percent difference of total AOD at 550 nm in 2022 relative to 2003-21; (x) Number of days with AOD above the 99.9th percentile. Areas with zero days appear as the white/gray background; (y) TROPOMI aboard Sentinel-5 Precursor (S5P) measurements of total column ozone anomalies relative to the 1998-2008 mean from GSG merged dataset (DU); (z) OMI /MLS tropospheric ozone column anomalies for 60°S-60°N (DU); (aa) CAMS reanalysis total column CO anomalies ($\times 10^{18}$ molecules cm^{-2}); (ab) Land surface visible broadband albedo anomalies (%);

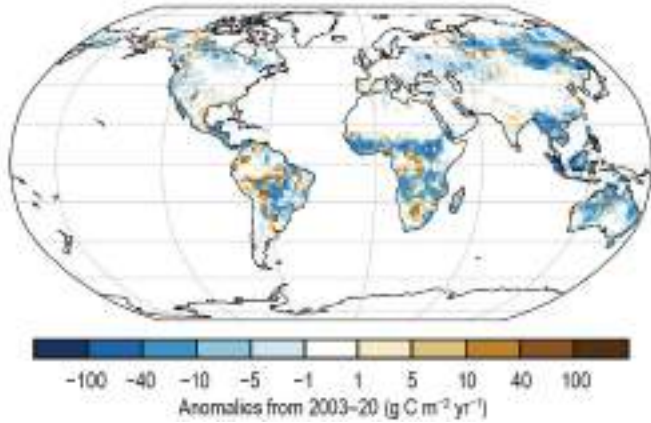
(ac) Land Surface Albedo in the Near-Infrared



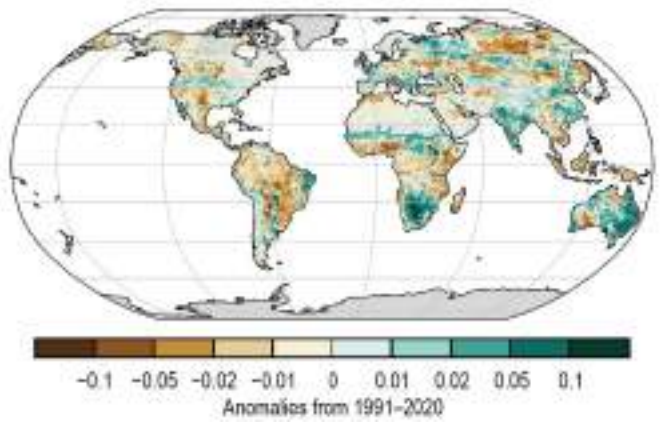
(ad) Fraction of Absorbed Photosynthetically Active Radiation



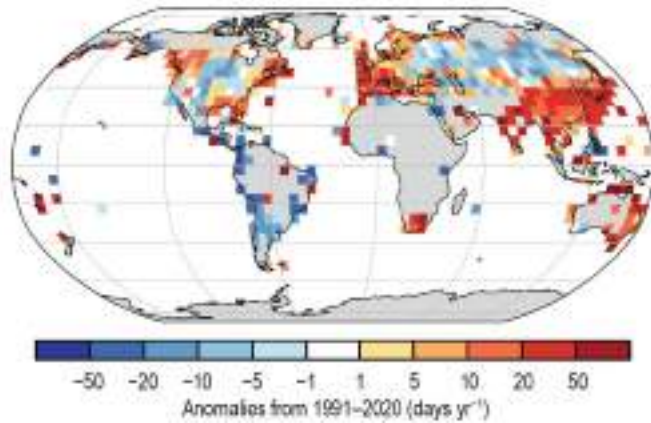
(ae) Carbon Emissions from Biomass Burning



(af) Vegetation Optical Depth



(ag) Humid-heat days (T_{wX90p})



(ah) Maximum T_{wet}

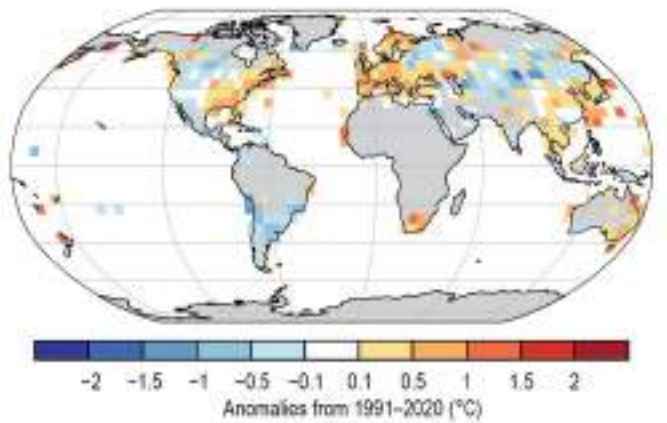


Plate 2.1 (cont.) (ac) Land surface near-infrared albedo anomalies (%); (ad) FAPAR anomalies; (ae) GFASv1.4 carbonaceous emission anomalies ($\text{g C m}^{-2} \text{ yr}^{-1}$) from biomass burning; (af) VODCA Ku-band VOD anomalies; (ag) HadISDH extremes daily maximum wet bulb temperature 90th percentile exceedances (days yr^{-1}); (ah) HadISDH extremes annual mean anomaly in daily maximum wet bulb of the month ($^{\circ}\text{C}$).

b. Temperature

1. GLOBAL SURFACE TEMPERATURE

—A. Sánchez-Lugo, C. Morice, J. P. Nicolas, A. Arguez, F. Sezaki, A. Goto, and W. Rocha

The year 2022 secured its place as one of the 10 warmest years since global records began (in the mid-1800s to mid-1900s, with the length of record depending on the dataset), with a global surface temperature between 0.25° and 0.30°C above the 1991–2020 average, according to six global temperature datasets (Table 2.1). Depending on the dataset, 2022 was either the fifth-warmest (equal with 2015 in some datasets) or sixth-warmest year on record. Despite these minor differences in anomalies and ranks between datasets, all six datasets agree that the last eight years (2015–22) were the eight warmest years on record (Fig. 2.1), and the global trends at the short- (1980–2022) and long-term (1880–2022) periods for each dataset are consistent with each other. The annual global average surface temperature has increased at an average rate of 0.08°C decade⁻¹ to 0.09°C decade⁻¹ since 1880 and at a rate more than twice that since 1980 (0.19°C decade⁻¹ to 0.20°C decade⁻¹). The datasets consist of four global in situ surface temperature analyses (NASA GISS Surface Temperature Analysis version 4 [NASA-GISSTEMP v4], Lenssen et al. 2019; Hadley Centre/Climatic Research Unit Temperature version 5 [HadCRUT5], Morice et al. 2021; NOAA Merged Land Ocean Global Surface Temperature Analysis version 5.1.0 [NOAAGlobalTemp v5.1.0], Vose et al. 2021; Berkeley Earth, Rhode and Hausfather 2020) and two global atmospheric reanalyses (European Centre for Medium-Range Weather Forecasts Reanalysis version 5 [ERA5], Hersbach et al. 2020, Bell et al. 2021; Japanese 55-year Reanalysis [JRA-55], Kobayashi et al. 2015).

Even though 2022 ranked as one of the six warmest years on record, the presence of

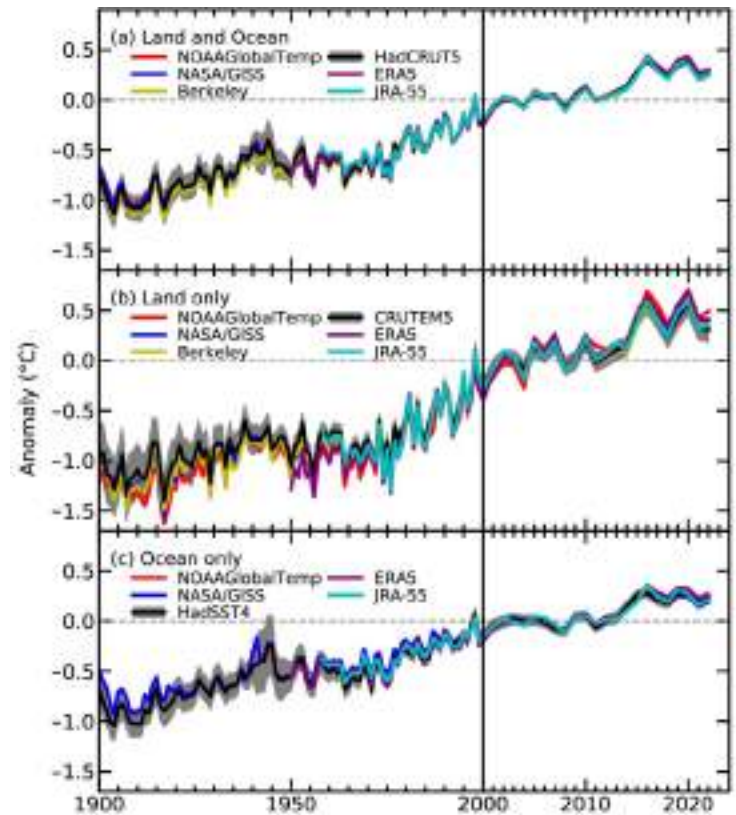


Fig. 2.1. Global average surface air temperature anomalies (°C; 1991–2020 base period) for (a) land and ocean, (b) land only, and (c) ocean only. In situ estimates are shown from the datasets NOAA GlobalTemp (Vose et al. 2021), NASA-GISS (Lenssen et al. 2019), HadCRUT5 (Morice et al. 2021), CRUTEM5 (Osborn et al. 2021), HadSST4 (Kennedy et al. 2019), and Berkeley (Rhode and Hausfather 2020). The 95% confidence ranges are also shown for HadCRUT5, CRUTEM5, and HadSST4. Reanalyses estimates are shown from the datasets ERA5 (Hersbach et al. 2020) and JRA-55 (Kobayashi et al. 2015).

Table 2.1. Temperature anomalies (°C; 1991–2020 base period) for 2022. Note that for the HadCRUT5 column, land values were computed using the CRUTEM.5.0.1.0 dataset (Osborn et al. 2021), ocean values were computed using the HadSST.4.0.1.0 dataset (Kennedy et al. 2019), and global land and ocean values used the HadCRUT.5.0.1.0 dataset (Morice et al. 2021).

	Global	NASA-GISS	HadCRUT5	NOAA GlobalTemp	Berkeley Earth	ERA5	JRA-55
Land		+0.40	+0.30	+0.49	+0.34	+0.41	+0.34
Ocean		+0.19	+0.23	+0.19	–	+0.26	+0.22
Land and Ocean		+0.28	+0.26	+0.28	+0.27	+0.30	+0.25

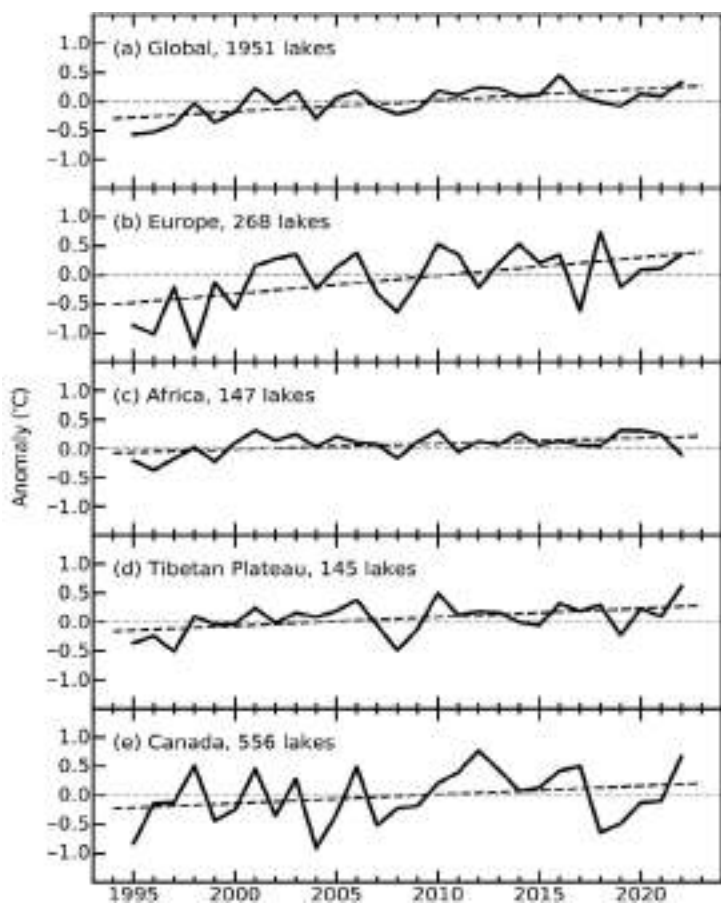
La Niña—the cool phase of the El Niño–Southern Oscillation (ENSO)—in the Pacific Ocean had a dampening effect on the global temperatures, in comparison to years characterized by El Niño or ENSO-neutral conditions. The year began with La Niña conditions, which first developed in August 2020 and persisted throughout most of 2021 and all of 2022 (see section 4b for details). 2022 was also the warmest La Niña year on record, surpassing the previous record set in 2021.

While it is common, and arguably expected, for each newly completed year to rank as a top 10 warmest year (see Arguez et al. 2020), the global annual temperature for 2022 was lower than we would expect due to the secular warming trend alone, with trend-adjusted anomalies registering between the 20th and 40th percentiles (depending on the dataset) following the Arguez et al. (2020) approach. Trend-adjusted anomalies for 2022 are consistent with the typical slight cooling influence of La Niña and similar to the trend-adjusted anomalies recorded over the relatively cool years from 2011 to 2014, as well as 2021, years that also predominantly exhibited cooler-than-normal ENSO index values.

Above-normal temperatures were observed across much of the world’s land and ocean surfaces during 2022 (Plate 2.1a; Appendix Figs. A2.1–A2.4). Notably, record-high annual temperatures were present across Europe, northern Africa, and parts of the Middle East, central Asia, and China, as well as the northern and southwestern Pacific, Atlantic, and Southern Oceans. Below-normal annual temperatures were present across parts of northern North America, South America, Africa, Australia, and the southeastern, central, and eastern tropical Pacific Ocean. The global land-only surface temperature was 0.30°C–0.49°C above normal, the fifth to seventh highest on record, depending on the dataset. The annual global sea-surface temperature was also fifth or sixth highest on record, at 0.19°C–0.26°C above normal.

2. LAKE SURFACE WATER TEMPERATURE

—L. Carrea, C. J. Merchant, J.-F. Creatux, T. M. Dokulil, H. A. Dugan, B. Gibbes, A. Laas, E. M. Leibensperger, S. Maberly, L. May, S.-I. Matsuzaki, G. Monet, D. Pierson, M. Pulkkanen, O. O. Rusanovskaya, S. V. Shimaraeva, E. A. Silow, M. Schmid, M. A. Timofeyev, P. Verburg, and R. I. Woolway



In 2022, the worldwide averaged satellite-derived lake surface water temperature (LSWT) warm-season anomaly was +0.33°C with respect to the 1995–2020 baseline, the second highest since the record began in 1995. The mean LSWT trend between 1995 and 2022 was $0.20 \pm 0.01^\circ\text{C decade}^{-1}$, broadly consistent with previous analyses (e.g., Carrea et al. 2020, 2021, 2022a; Fig. 2.2a). Warm-season anomalies for each lake are shown in Plate 2.1b. The lake-mean temperature anomalies were positive for 70% and negative for 30% of the 1951 globally distributed lakes. For about 30 other lakes, no anomalies could be computed since no water was found in 2022.

Large regions of coherently high LSWT anomalies were identified in 2022, with 40% of the observed lakes experiencing LSWT

Fig. 2.2. Annual time series of satellite-derived warm-season lake surface water temperature anomalies (°C; 1995–2020 base period) from 1995 to 2022 for lakes distributed (a) globally, and regionally in (b) Europe, (c) Africa, (d) the Tibetan Plateau, and (e) Canada.

anomalies in excess of +0.5°C (Plate 2.1b). The highest anomalies were for lakes situated in the northwestern contiguous United States and Canada. Negative LSWT anomalies were consistently observed throughout most of South America (except Patagonia), parts of Africa, and in Alaska and Greenland.

Four regions of interest were studied in more detail: Canada (number of lakes, $n = 556$, Figs. 2.2e, 2.3c), Europe ($n = 268$, Figs. 2.2b, 2.3a), Tibet ($n = 145$, Figs. 2.2d, 2.3d), and Africa ($n = 147$, Figs. 2.2c, 2.3b). In these regions, the warm season LSWT anomalies are consistent with the corresponding 2-m air temperature anomalies, as measured by NASA GISS (Hansen et al. 2010; GISS Surface Temperature Analysis [GISTEMP] Team 2022) and show an average warming trend of $+0.31 \pm 0.03^\circ\text{C decade}^{-1}$ in Europe (Fig. 2.2b) and $+0.15 \pm 0.03^\circ\text{C decade}^{-1}$ in Canada (Fig. 2.2e). In Africa, long-term change in LSWT is comparatively smaller at $+0.10 \pm 0.01^\circ\text{C decade}^{-1}$ (Fig. 2.2c), while in Tibet the warming tendency has increased relative to previous reports with the largest positive anomaly in 2022. The warming rate of LSWT in Tibet from 1995 to 2022 was $+0.15 \pm 0.02^\circ\text{C decade}^{-1}$ (Fig. 2.2d). Moreover, in Tibet, all the observed lakes, except one, experienced positive LSWT anomalies in 2022 with an average of $+0.6^\circ\text{C}$, which is more than double the standard deviation of mean anomalies from 1995 to 2022 and confirmed by high anomalies for the air temperature (Fig. 2.3d). In Europe, below-normal LSWT in northern Europe (80 lakes) was less prevalent than above-normal LSWT (188 lakes), resulting in an average of $+0.35^\circ\text{C}$. In Africa, 60% of the 147 lakes experienced negative LSWT anomalies, and the average anomaly in 2022 was -0.11°C . In Canada, 91% of the observed lakes experienced positive anomalies, with only 9% experiencing negative anomalies for an average of $+0.67^\circ\text{C}$ in 2022.

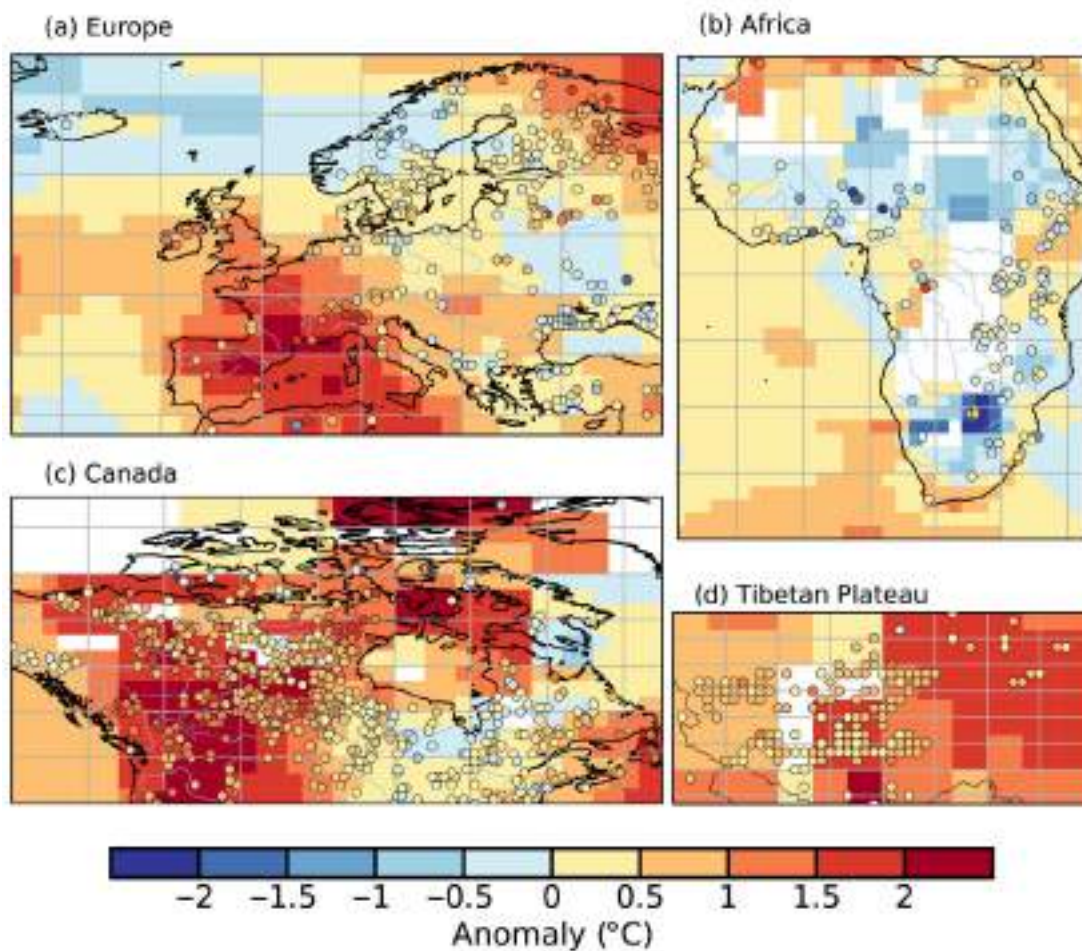


Fig. 2.3. Lake temperature anomalies ($^\circ\text{C}$, colored dots) and 2-m air temperature anomalies ($^\circ\text{C}$) in 2022 for lakes in (a) Europe, (b) Africa, (c) Canada, and (d) the Tibetan Plateau. These values were calculated for the warm season (Jul–Sep in the extratropical Northern Hemisphere; Jan–Mar in the extratropical Southern Hemisphere; Jan–Dec in the tropics) with reference to the 1995–2020 base period.

In situ observations of warm season LSWT anomalies from the 1995–2020 mean for 40 lakes, 18 of which have measurements for the year 2022, are shown in Fig. 2.4 with an average anomaly of -0.03°C . Fourteen lakes experienced positive anomalies (average: $+0.70^{\circ}\text{C}$) and four lakes negative anomalies (average: -2.60°C) in 2022. At the in situ measurement site on Lake Baikal in Siberia, a temperature anomaly of -6.9°C was recorded, which is very different from the satellite lake-mean anomaly of -0.47°C , suggesting a within-lake variation of the LSWT anomalies (see Carrea et al. 2022a; Toffolon et al. 2020) on Lake Baikal. At the in situ site, such a large negative anomaly suggests a potential intrusion of colder water resembling upwellings in ocean waters; this has been recorded on the lake for more than 20 years at different depths. Overall, the time series of the 18 lakes show clearly that lakes are warming, especially after the year 2000.

In North America, the anomalies recorded from the in situ data for Lakes Superior, Erie, Michigan, and Huron are -2.98°C , $+0.67^{\circ}\text{C}$, $+0.69^{\circ}\text{C}$, and $+0.55^{\circ}\text{C}$, respectively, which are noticeably larger (in absolute terms) than those estimated from satellite measurements (-0.61°C , $+0.20^{\circ}\text{C}$, $+0.28^{\circ}\text{C}$, and $+0.18^{\circ}\text{C}$, respectively). The difference is largely because in situ data are point measurements whereas satellite data represent lake-wide averages, suggesting spatial patterns of the LSWT anomalies (see Carrea et al. 2022a; Toffolon et al. 2020). In Europe, all the lakes with in situ data had positive anomalies, except Lake Balaton (Hungary) which was 0.36°C below its 1995–2020 average (-0.01°C with satellite). Mondsee (Austria) was 1.51°C warmer than average in 2022 and the highest recorded value for the in situ data. In New Zealand, Lake Taupō had a slight negative anomaly of -0.15°C ($+0.98^{\circ}\text{C}$ from satellites) while Rotorua had a positive anomaly of $+0.51^{\circ}\text{C}$ (with reference period 2011–2020) compared to the anomaly from satellite of $+0.6^{\circ}\text{C}$ (with reference period 1995–2020).

The LSWT warm-season averages for midlatitude lakes are computed for summers (July–September in the Northern Hemisphere and January–March in the Southern Hemisphere), and whole-year averages are presented for tropical lakes (within 23.5° of the equator).

LSWT time series were derived from the European Space Agency Climate Change Initiative LAKES/Copernicus C3S climate data record (Carrea et al. 2022b, 2023). For 2022, satellite observation from the Sea and Land Surface Temperature Radiometer on Sentinel3B and MODIS on *Terra* were used. The retrieval method of MacCallum and Merchant (2012) was applied on image pixels filled with water according to both the inland water dataset of Carrea et al. (2015) and a reflectance-based water detection scheme (Carrea et al. 2023).

The satellite-derived LSWT data are spatial averages for each of a total of 1951 lakes. The satellite-derived LSWT data were validated with in situ measurements with an average satellite-minus-in situ temperature difference of less than 0.5°C (Carrea et al. 2023). Lake-wide average surface temperatures have been shown to give a more representative picture of LSWT responses to climate change than single-point measurements (Woolway and Merchant 2018).

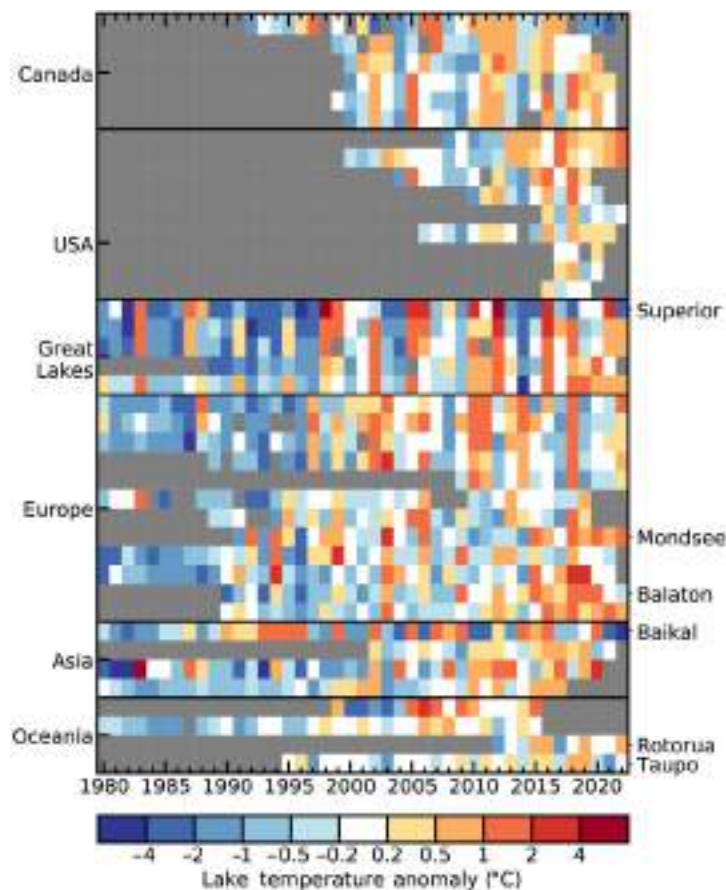


Fig. 2.4. In situ lake surface water temperature (LSWT) observations from 40 globally distributed lakes (the name is reported for the lakes mentioned in the text), showing the annually averaged warm season (Jul–Sep in the Northern Hemisphere; Jan–Mar in the Southern Hemisphere) anomalies ($^{\circ}\text{C}$; 1995–2020 base period).

3. NIGHT MARINE AIR TEMPERATURE

—R. C. Cornes, T. Cropper, R. Junod, and E. C. Kent

Air temperature measurements have been made onboard ships for centuries and continue to be collected today thanks to the Voluntary Observing Ship initiative (<https://www.ocean-ops.org/reportcard2022/>). Gridded datasets of marine air temperature (MAT) are constructed from the individual measurements, and two such datasets that are routinely updated are used in this section: University of Alabama in Huntsville night-time MAT (UAHNMAT; Junod and Christy 2020) and Climate Linked Atlantic Sector Science night MAT (CLASSnmat; Cornes et al. 2020). Since daytime MAT observations are biased warm due to heating from the ship superstructure, only night-time values are currently used in these datasets and, hence, they are referred to as night marine air temperature (NMAT). These NMAT datasets provide comparison against the more widely used sea-surface temperature (SST) datasets. In keeping with this theme, we also include SST statistics from The Met Office Hadley Centre's sea-surface temperature dataset (HadSST4; Kennedy et al. 2019) in this section. Note, however, that the large-scale average values from HadSST4 presented in this section (Fig. 2.5 and Table 2.2) may differ slightly from other estimates from the dataset presented in this report because the data have been masked such that the spatial coverage is the same across the three datasets in order to ensure a fair comparison.

Evidence from the NMAT datasets and HadSST4 indicates that across global ocean regions, 2022 was the fifth-warmest year since 1900 (Table 2.2). As with the global estimates of temperature discussed in section 2b1, the “triple-dip” La Niña conditions (see Sidebar 3.1 for details) suppressed

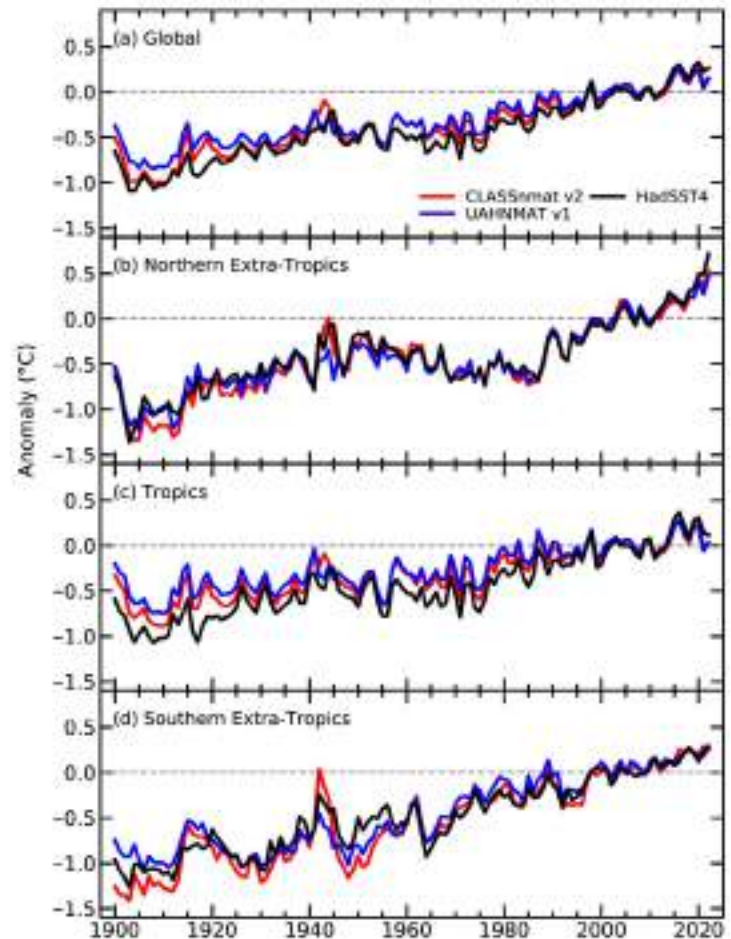


Fig. 2.5. Annual mean night marine air and sea-surface temperature anomalies (°C; 1991–2020 base period) calculated from the CLASSnmat, UAHNMAT, and HadSST4 datasets averaged over the (a) globe, (b) northern extra-tropics, (c) tropics, and (d) southern extra-tropics. The tropics is defined as the latitude range 30°S–30°N and the northern (southern) extra-tropics as >30°N (<30°S). The averages only include values that are common to all three datasets for a given year and since UAHNMAT starts in 1900, only values for the period 1900–2022 are plotted.

Table 2.2. Average anomalies (°C; 1991–2020 base period) for 2022 calculated from two NMAT datasets (CLASSnmat and UAHNMAT) and HadSST4. The regions are defined as in Fig. 2.5. The values in parentheses indicate the ranking of 2022 values within the period 1900–2022.

Dataset	Global	Northern Extra-Tropics	Tropics	Southern Extra-Tropics
CLASSnmat	0.16 (5)	0.52 (1)	0.03 (16)	0.25 (3)
UAHNMAT	0.15 (5)	0.47 (1)	0.03 (20)	0.28 (1)
HadSST4	0.26 (5)	0.71 (1)	0.12 (8)	0.29 (1)

the global average NMAT values during the year. This feature is apparent in the maps of temperature anomalies (Fig. 2.6) and is reflected in the average anomalies for the tropics, where 2022 ranked as only the 16th- or 20th-warmest year on record (Table 2.2).

Across the northern extra-tropics (north of 30°N), 2022 was the warmest year in the 123-year record according to all three datasets. Monthly anomalies were more than 0.3°C above the 1991–2020 average throughout all months of the year, with particularly large anomalies greater than +0.7°C recorded from August to November. The annual average anomaly was greatest in HadSST4 (+0.7°C) compared to the NMAT datasets where it was approximately +0.5°C. The highest positive temperature anomalies in this region were recorded across the northern Pacific Ocean (Fig. 2.6). Across all datasets, relatively high anomalies were also recorded in the north-east Atlantic Ocean, particularly in the seas around western Europe and the Mediterranean, and across the western boundary current region of the North Atlantic.

Across the southern extra-tropics, NMAT anomalies were also high in 2022, with relatively high anomalies recorded in the western South Pacific/Coral Sea region. For CLASSnmat, the year ranked as third warmest for the region whereas both UAHNMAT and HadSST4 ranked 2022 as the warmest year in the series. Due to the incorporation of drifting buoy data in HadSST4, the spatial coverage is generally better than for the NMAT datasets, which only use ship-based measurements of air temperature, and this is most apparent across the Southern Ocean. This sparser coverage results in a greater uncertainty in the NMAT datasets in this region.

In previous *State of the Climate* reports (e.g., Cornes et al. 2022), the discrepancy in trends between the NMAT and SST datasets has been discussed. While the global average trend between 1900 and 2022 is slightly higher in HadSST4 compared to the NMAT datasets (c.f. 0.09°C decade⁻¹ in UAHNMAT and 0.11°C decade⁻¹ in CLASSnmat compared to 0.16°C decade⁻¹ in HadSST4) there is a much larger discrepancy in temperature trends between SST and NMAT after around 1990. This is particularly the case in the tropics where temperature increased at a rate of 0.05°C decade⁻¹ or 0.07°C decade⁻¹ in NMAT compared to 0.13°C decade⁻¹ in HadSST4. The reason for this discrepancy remains unclear and a wider discussion of this feature of the data, which also considers trends in Coupled Model Intercomparison Project (CMIP) simulations, is provided by Cross-chapter box 2.3 in Gulev et al. (2021).

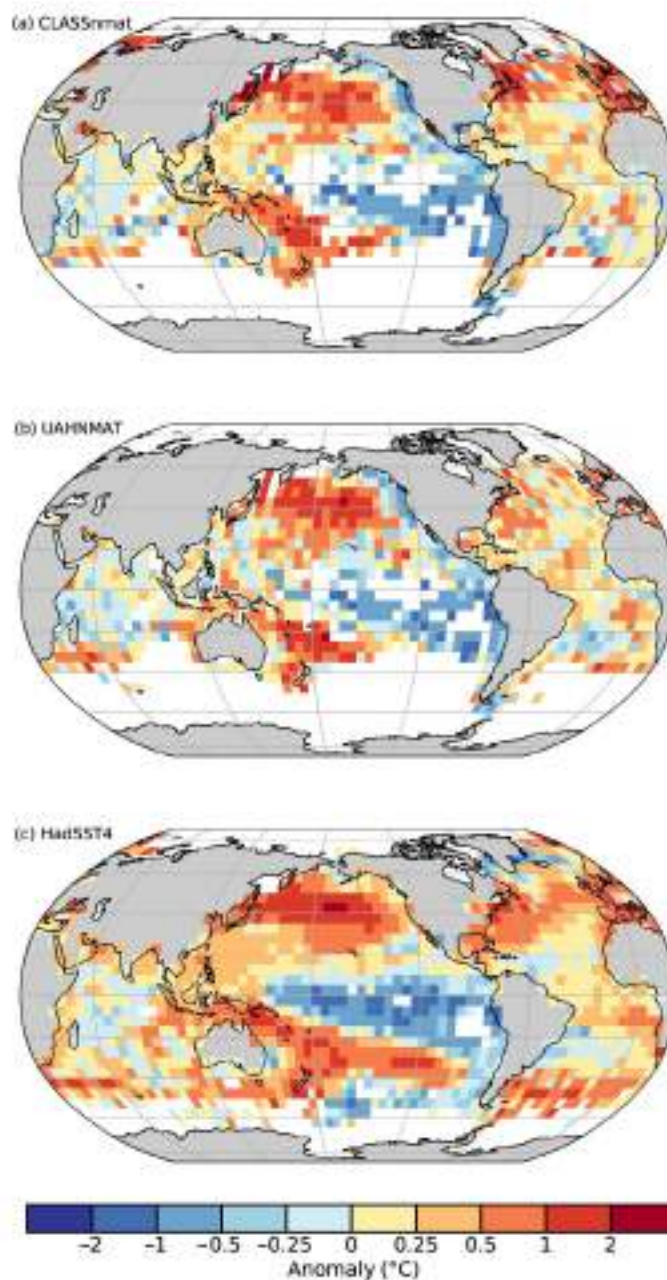


Fig. 2.6. Average annual night marine air and sea-surface anomalies (°C; 1991–2020 base period) for 2022 in the (a) CLASSnmat, (b) UAHNMAT, and (c) HadSST4 datasets. Averages were calculated for a grid-cell where more than six months of data are present. This calculation has been done separately for each dataset and results in a different spatial coverage in the three datasets.

4. SURFACE TEMPERATURE EXTREMES

—M. G. Donat, R. J. H. Dunn, R. W. Schlegel, and A. Kruger

In 2022, the globally averaged frequency of warm days (TX90p; see Table 2.3 for the definition) in reanalyses products was about 49 (ERA5, Hersbach et al. 2020), 40 (MERRA-2, Gelaro et al. 2017) and 44 (JRA-55, Kobayashi et al. 2015), and 66 based on observational data from the Global Historical Climatology Network Index (GHCNDEX; which has more limited spatial coverage and uses a different reference period; Donat et al. 2013), slightly lower than in the previous year (Fig. 2.7). While the global average warm-day frequency in 2022 cannot be regarded as extraordinary compared to previous years, the frequencies are substantially above the average value of 36 days per year (Fig 2.7).

Large areas of the globe were affected by strong, and in some places record-breaking hot extremes in 2022. In particular, large parts of Europe, Asia, and South America were affected by anomalously frequent warm days (in many areas, more than double the average frequency; Plate 2.1d). The frequency of warm days was highest on record in large parts of China and Western and southwestern Europe (and northwestern Africa, for ERA5; Fig. 2.8; Supp. Fig. A2.5b). This high frequency of warm days was accompanied by heat events of record-breaking intensity. Large parts of China, Central Asia, and Central and Western Europe show the highest TXx values (annual maximum of daily maximum temperatures) in the GHCNDEX record (Supp. Fig. A2.5a). These extreme

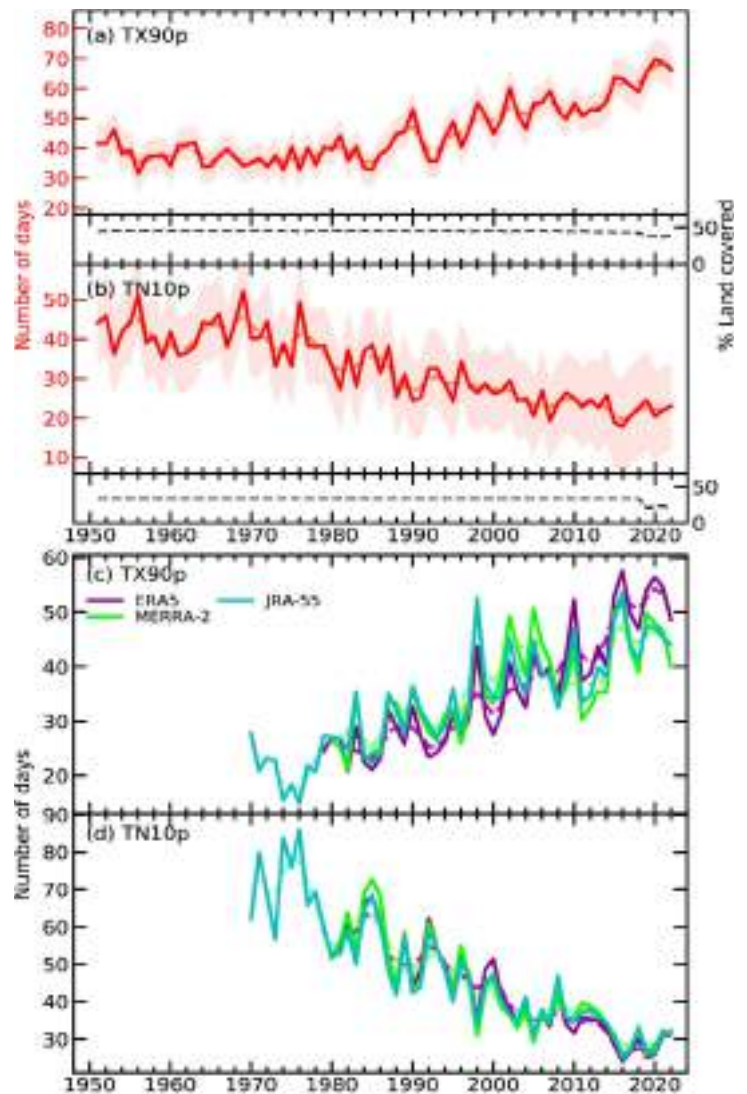


Fig. 2.7. Time series of the annual number of (a),(c) warm days and (b),(d) cool nights averaged over global land regions based on gridded station data from the GHCNDEX dataset (a),(b) and three atmospheric reanalyses (ERA5, MERRA-2, JRA-55; (c),(d)). The spatial coverage in GHCNDEX is limited; the black dotted lines show the percentage of land area covered (right y-axis in (a),(b)), and the coverage uncertainty ($2\text{-}\sigma$, following Brohan et al. 2006, Dunn et al. 2020) is shown as the light red bands in (a),(b).

Table 2.3. Definitions of temperature extremes indices, along with 2022 value and ranks from the four datasets. Reference period for GHCNDEX (1961–90) is different to that used for the reanalyses products (1991–2020).

Index	Name	Definition	GHCNDEX (1951–2022) Value, Rank	ERA5 (1979–2022) Value, Rank	MERRA-2 (1980–2022) Value, Rank	JRA-55 (1970–2022) Value, Rank
TX90p	Warm days	The annual count of days when the daily maximum temperature exceeds the 90th percentile	66.2 days, 3rd highest	48.6 days, 8th highest	40.0 days, 14th highest	44.0 days, 10th highest
TN10p	Cool nights	The annual count of nights when the daily minimum temperature falls below the 10th percentile	23.0 days, 11th lowest	31.1 days, 8th lowest	32.3 days, 9th lowest	31.2 days, 6th lowest
TXx	Hottest Day	Annual highest value of daily maximum temperature	–	–	–	–

temperature values include the first-ever occurrence of temperatures exceeding 40°C in the United Kingdom and other parts of northwestern Europe (see section 7f for more details). In contrast, likely due to the persisting La Niña conditions, southeastern Australia recorded its lowest TXx values in 2022 in the ERA5 and GHCNDEX records (Fig. 2.8a and Supp. Fig. A2.6a, respectively).

The frequency of cool nights (TN10p; see definition in Table 2.3) was the eighth lowest on record for ERA5 and 16th lowest based on the GHCNDEX global average. Regions affected by an above-average frequency of cool nights, reflecting relatively low temperatures in general, include parts of Australia, South America, and northwestern North America (Plate 2.1e). Parts of South America had minimum night-time temperatures that were among the lowest on record based on ERA5 (Fig. 2.8c). In contrast, most other land regions showed below-average frequency of cold extremes (Plate 2.1e).

Analysis of NOAA Optimum Interpolation Sea Surface Temperature (NOAA OISST v2.1; Huang et al. 2021) showed that, in 2022, 58% of the ocean surface experienced at least one marine heatwave (MHW; Hobday et al. 2016; Figs. 2.9a,b), and 25% experienced at least one marine cold spell (MCS; Figs. 2.9c,d). Category 2 Strong MHWs (Hobday et al. 2018) were the most common (26%) warm events for the ninth consecutive year, whereas Category 1 Moderate MCSs have remained the most common (20%) cool events in all years since 1985. The ocean experienced a global average of 57 MHW days (18 MCS days) in 2022, which is greater than the 2021 average of 48 days (13 days), but less than the 2016 record of 61 days (1982 record of 27 days; Figs. 2.9a,c). This daily average equates to 16% (5%) of the surface of the ocean experiencing a MHW (MCS) on any given day (Figs. 2.9a,c).

Land surface temperature extremes are characterized by indices developed by the former World Meteorological Organization Expert Team in Climate Change Detection and Indices (Zhang et al. 2011). The observations-based GHCNDEX (Donat et al. 2013) uses daily maximum and minimum temperatures from the GHCND dataset (Menne et al. 2012) to calculate these indices for each station, which are then interpolated onto a regular 2.5° grid. Spatial coverage for 2022 is, as in previous years, limited to primarily the Northern

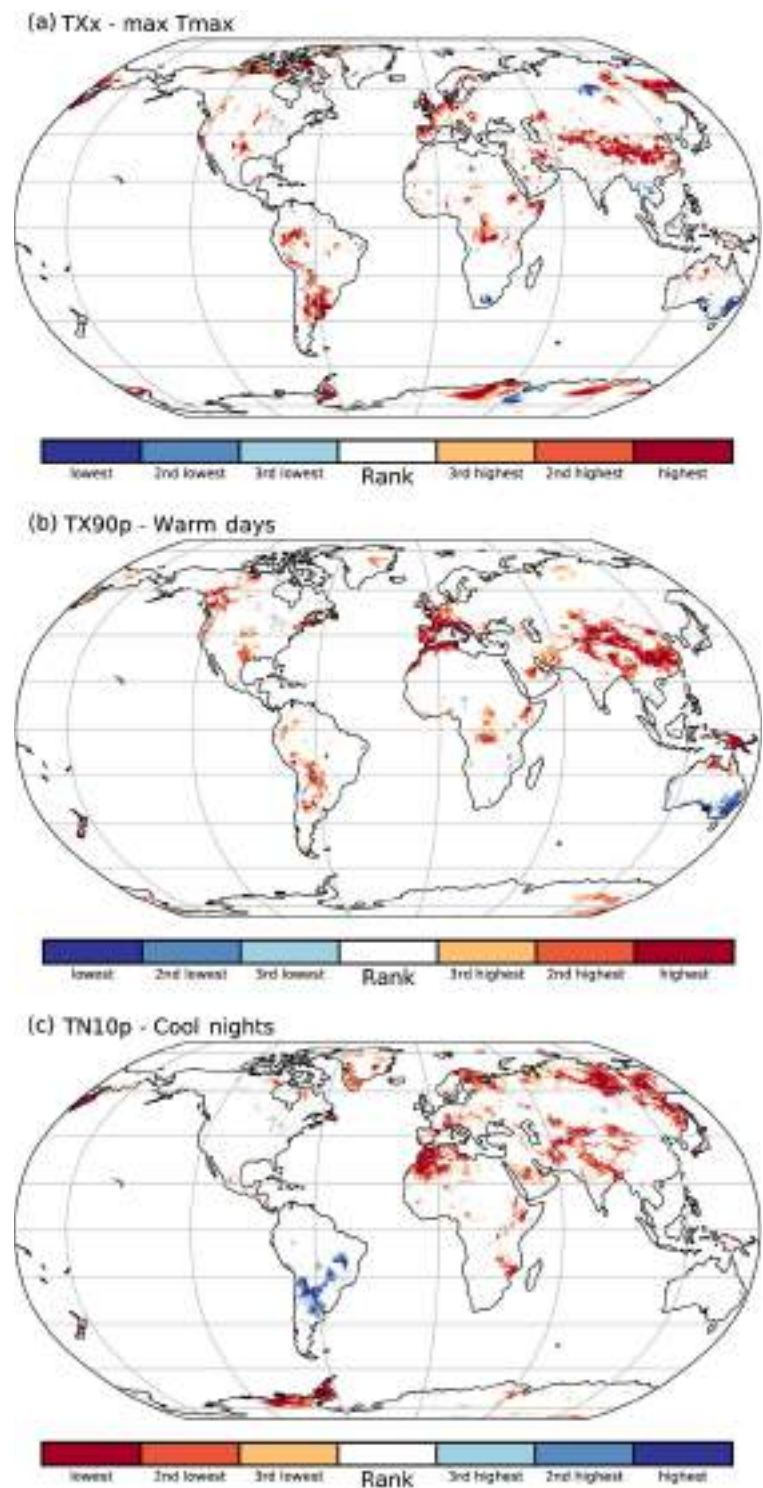


Fig. 2.8. Maps indicating grid cells where the temperature indices for 2022 ranked in the three highest or three lowest values based on ERA5 since 1979: (a) hottest day of the year (TXx), (b) annual number of warm days (TX90p), and (c) annual number of cool nights (TN10p).

Hemisphere extra-tropics and Australia, with very little coverage in Africa and South America (Fig. A2.5). We use the ERA5 reanalysis (Hersbach et al. 2020) to provide globally complete fields of these indices covering 1979–2022, which performed well in a recent intercomparison between observation and reanalyses datasets (Dunn et al. 2022). The indices quantifying exceedances of percentile-based thresholds use a fixed reference period, and intercomparison between these is complex in a strongly warming climate (Dunn et al. 2020; Yosef et al. 2021; Dunn and Morice 2022). The percentile period in GHCNDEX is 1961–90, whereas for the index calculations with ERA5 the percentiles are calculated for the 1991–2020 period.

An MHW is detected when five or more consecutive days of temperature are above a 90th percentile daily climatology (Hobday et al. 2016). MHWs are categorized as moderate when the greatest temperature anomaly during the event is less than double the 90th percentile for the seasonal anomaly. When this value is more than double, triple, or quadruple the distance, the MHW is categorized as strong, severe, or extreme, respectively (Hobday et al. 2018). The direct inverse is used to detect and categorize MCSs (i.e., days below the 10th percentile). The baseline period used to detect events in this report is 1982–2011, because 1982 is the first full year of the NOAA OISST product.

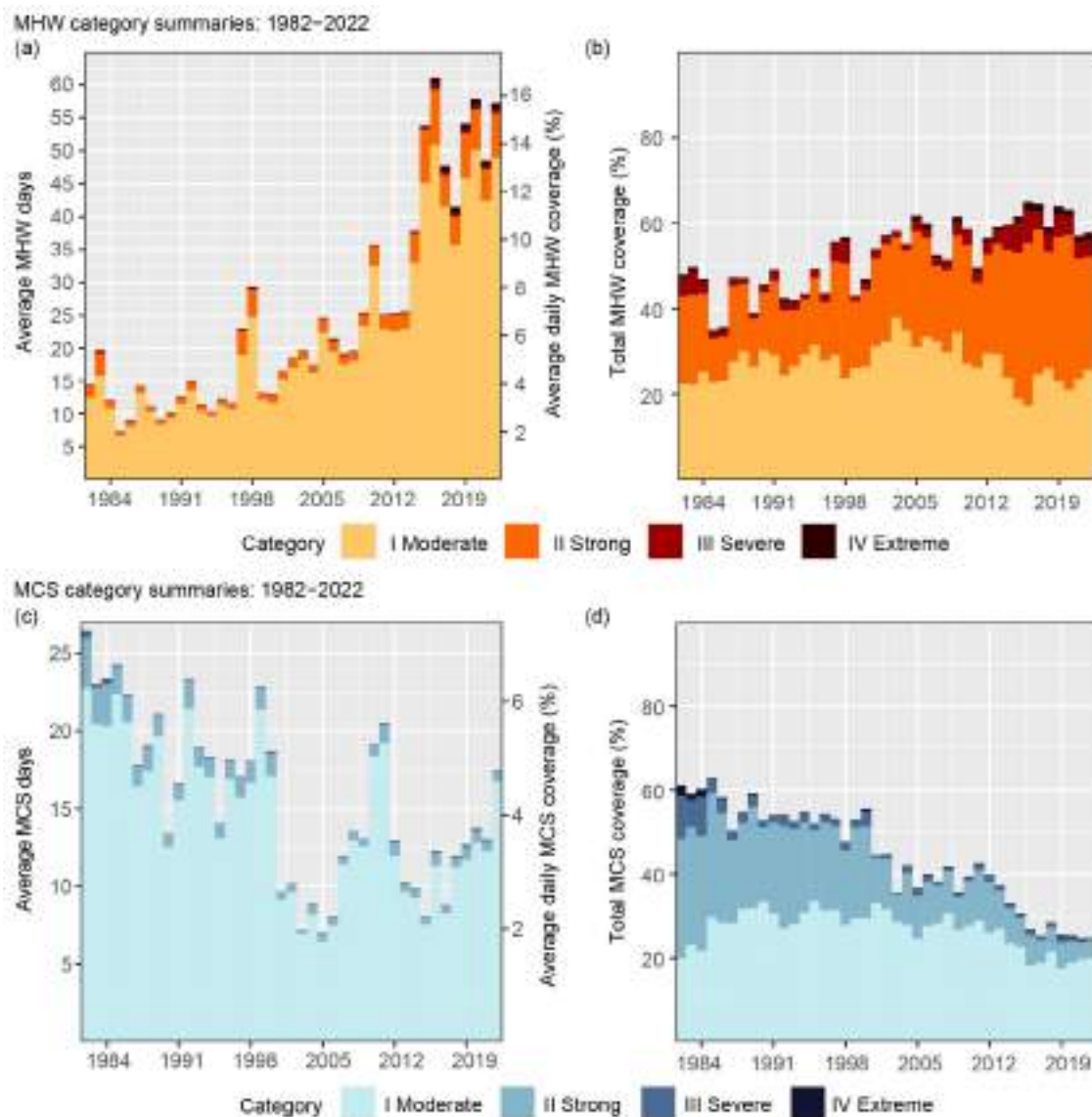


Fig. 2.9. (a),(c) Average annual number of global marine heatwave (MHW) and marine cold-spell (MCS) days experienced over the surface of the ocean each year (left y-axis), also expressed as the percent of the surface of the ocean experiencing an MHW/MCS on any given day (right y-axis) of that year. (b),(d) Total percent of the surface area of the ocean that experienced an MHW/MCS at some point during the year. The values shown are for the highest category of MHW/MCS experienced at any point. The base period is 1982–2011. (Source: NOAA OISST v2.1.)

5. TROPOSPHERIC TEMPERATURE

—S. Po-Chedley, J. R. Christy, C.-Z. Zou, C. A. Mears, and L. Haimberger

The 2022 globally averaged lower-tropospheric temperature (LTT) anomaly was 0.26°C (0.17°C to 0.37°C) above the 1991–2020 average, ranking among the nine warmest years on record (fourth to ninth warmest, depending on the dataset). Long-term warming of the troposphere is consistent with our understanding of greenhouse warming. Other factors, such as volcanic eruptions, decadal variability, and solar activity also modulate the long-term warming trend (Christy and McNider 2017; Po-Chedley et al. 2022). Interannual variations in global LTT are dominated by the El Niño–Southern Oscillation, which has largely been in a La Niña state since August 2020 (see section 4b and Sidebar 3.1 for details; Figs. 2.10a,b). As with the year 2021, the depression of atmospheric temperature due to La Niña combined with the background warming trend (Table 2.4) produced a year that was warmer than average, but not record breaking.

La Niña events are accompanied by a distinct pattern of tropospheric temperature anomalies, which are evident in the annual average departures in both 2022 (Plate 2.1f) and 2021 (see Plate 2.1f

Table 2.4. Temperature trends (units of °C decade⁻¹) for global lower-tropospheric temperature (LTT) and tropical tropospheric temperature (TTT) over the periods 1958–2022 and 1979–2022. NASA MERRA-2 data begins in 1980 and NOAA STAR v5.0 TLT begins in 1981. UW does not produce an LTT product.

Method	Source	LTT (90°S–90°N) 1958–2022	LTT (90°S–90°N) 1979–2022	TTT (20°S–20°N) 1958–2022	TTT (20°S–20°N) 1979–2022
Radiosonde	NOAA RATPAC vA2 (Free et al. 2005)	0.18	0.22	0.17	0.18
Radiosonde	RAOBCORE v1.9 (Haimberger et al. 2012)	0.16	0.17	0.13	0.15
Radiosonde	RICH v1.9 (Haimberger et al. 2012)	0.18	0.20	0.18	0.19
Satellite	UAH v6.0 (Spencer et al. 2017)	–	0.13 ^[1]	–	0.12
Satellite	RSS v4.0 (Mears and Wentz, 2016)	–	0.21	–	0.16
Satellite	UW v1.0 (Po-Chedley et al. 2015)	–	–	–	0.16
Satellite	NOAA STAR v5.0 (Zou et al. 2023)	–	0.13 ^[1]	–	0.10
Reanalysis	ERA5 (Hersbach et al. 2020)	–	0.18	–	0.15
Reanalysis	JRA-55 (Kobayashi et al. 2015)	0.17	0.18	0.16	0.14
Reanalysis	NASA MERRA-2 (Gelaro et al. 2017)	–	0.19	–	0.17
Median	Calculated from previous values	0.17	0.18	0.16	0.15

^[1]The vertical sampling in UAH and NOAA STAR LTT is slightly different from other datasets and results in temperature trends that are approximately 0.01°C decade⁻¹ smaller than other datasets.

in Blunden and Boyer 2022). La Niña conditions over late 2021 through 2022 contributed to record-breaking LTT values over the North and South Pacific Ocean, China, and parts of South Asia. Persistent summertime heatwaves during June to August contributed to record-breaking tropospheric temperatures over Europe in 2022. Large positive total column water vapor anomalies were collocated with the anomalous tropospheric warmth (Plate 2.1i; section 2d2). Overall, the global LTT was above average across 70% of the globe, with 6% of Earth experiencing the highest temperatures since the start of the record in 1979 (Plate 2.1f; Fig. 2.10c). In contrast, 1% of Earth experienced its coldest year on record.

Atmospheric temperature data are derived from balloon-borne radiosonde measurements, satellite-based microwave soundings, and atmospheric reanalyses (Table 2.4). Each dataset employs different strategies to remove biases and drifts from sources of atmospheric temperature data. Across datasets and measurement techniques, there is good agreement on interannual timescales (Fig. 2.10a; Supp. Fig. A2.7), but structural uncertainty leads to non-negligible difference in long-term warming trends (Table 2.4).

One issue in the construction of tropospheric temperature microwave records is that short-term trends from overlapping satellites do not always agree after estimated biases are removed. For example, tropospheric warming inferred from the Microwave Sounding Unit (MSU) onboard the NOAA-14 satellite exceeds that from Advanced MSU (AMSU) data from NOAA-15. Reliance on data from NOAA-14 (NOAA-15) results in larger (smaller) estimates of tropospheric warming (Mears and Wentz 2016; Santer et al. 2021). A new version of the NOAA STAR dataset treats data from the latest microwave sounding instruments (AMSU and the Advanced Technology Microwave Sounder) as a reference with which to calibrate earlier data from earlier MSU instruments (Zou et al. 2021, 2023). This decision has the effect of substantially reducing global tropical tropospheric temperature (TTT) warming over 1979 to 2021 (from $0.23^{\circ}\text{C decade}^{-1}$ to $0.14^{\circ}\text{C decade}^{-1}$; Zou et al. 2023). Changes in the estimated rate of warming of a few hundredths of a degree per decade are common when tropospheric temperature datasets are updated. These changes illustrate the challenges and pronounced structural uncertainty in constructing records of tropospheric warming.

General circulation models (GCMs) tend to simulate greater tropospheric warming than satellite observations over 1979 to present, particularly in the tropics (McKittrick and Christy 2020; Po-Chedley et al. 2021; Zou et al. 2023). Observed tropical sea-surface warming, which is closely coupled to tropospheric warming, is also smaller than the average warming in GCMs (Eyring et al. 2021). Two factors likely contribute to faster-than-observed model warming: biases in

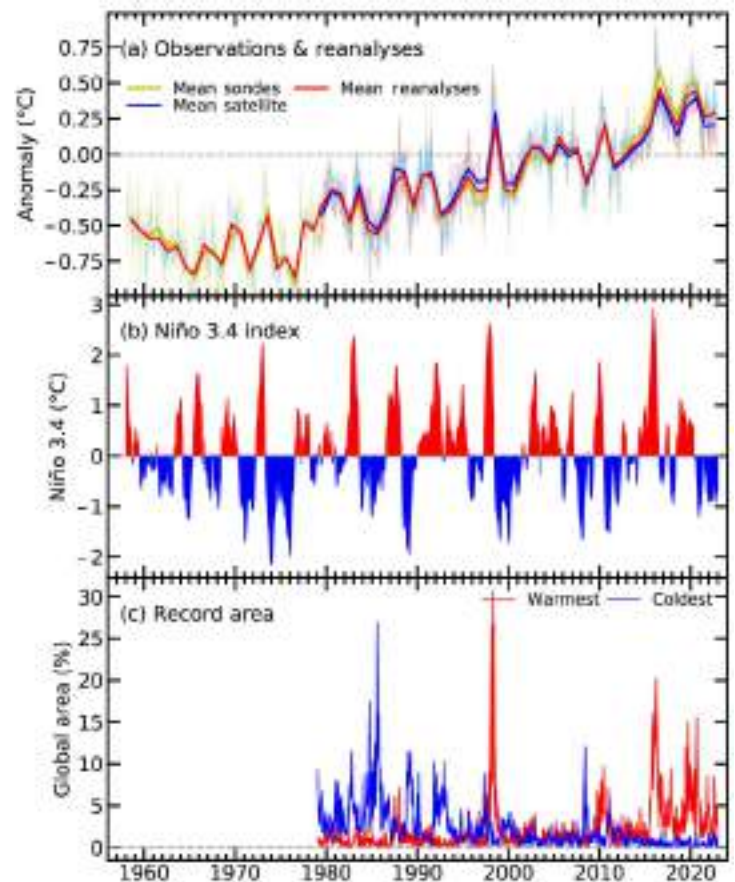


Fig. 2.10. Time series of (a) global average lower-tropospheric temperature (LTT; $^{\circ}\text{C}$) anomalies, (b) central Pacific (Niño-3.4 region) sea-surface temperature anomalies ($^{\circ}\text{C}$), and (c) percentage of Earth experiencing record-high (red) and low (blue) LTT values, according to RSS and UAH LTT datasets for the period 1979–2022. Bold lines in (a) represent the annual average values (across datasets) for sondes (yellow), reanalysis (red), and satellite (blue) data. Monthly values for individual datasets are also plotted with thinner and lighter lines for context. The climatological base period for (a) and (b) is 1991–2020. Niño-3.4 anomalies are calculated using the HadISST1 dataset (Rayner et al. 2003). STAR data are not included in the satellite LTT time series because the time series begins in 1981 (versus 1979 for RSS and UAH data).

the prescribed model forcing and biases in the GCM response to greenhouse gas forcing. For example, Fasullo et al. (2022) shows that a discontinuity in the biomass-burning aerosol forcing prescribed to models in Phase 6 of the Coupled Model Intercomparison Project (CMIP6) results in inflated warming in version 2 of the Community Earth System Model—an issue that may affect other CMIP6 GCMs. Several GCMs also exceed the likely range of estimates of climate sensitivity (Forster et al. 2021)—the global surface warming response to a doubling of atmospheric carbon dioxide—which in turn contributes to overestimates of historical warming (Scafetta 2023). Multidecadal internal variability has also reduced observed warming since 1979 (Po-Chedley et al. 2022), which contributes to the difference between observed and simulated warming. Aside from these factors, it is also possible that observational biases may affect observed tropospheric warming (Santer et al. 2021).

6. STRATOSPHERIC TEMPERATURE

—W. J. Randel, C. Covey, L. Polvani, and A. K. Steiner

Global mean temperatures in the lower, middle, and upper stratosphere were anomalously low during 2022, a result of the large volcanic eruption of Hunga Tonga–Hunga Ha‘apai (HTHH) in January 2022 (Sidebar 2.2). These cold anomalies were primarily observed in the Southern Hemisphere (SH), and these volcanic effects accentuated the multi-decadal global-scale cooling of the stratosphere due to increases of anthropogenic carbon dioxide concentrations in the atmosphere. The Antarctic polar vortex was strong and persistent in 2022, while the Arctic polar vortex was disturbed by a major stratospheric warming in March. The stratospheric quasi-biennial oscillation (QBO) progressed normally, with equatorial westerly winds and positive temperature anomalies descending from the middle stratosphere to the lower stratosphere during the year.

The HTHH eruption (~20°S, 175°W) on 15 January 2022 injected extreme amounts of water vapor (H₂O) and a moderate amount of the aerosol precursor sulfur dioxide into the stratosphere. The amount of stratospheric H₂O injected from HTHH is unprecedented in the continuous satellite record beginning in the middle 1980s (Davis et al. 2016; Milan et al. 2022; Vömel et al. 2022). The H₂O and aerosol perturbations persisted throughout 2022 (e.g., Schoeberl et al. 2022; Mishra et al. 2022), and the radiative effects of enhanced H₂O resulted in large-scale cooling of the SH stratosphere, in contrast to aerosol-induced warming of the stratosphere observed from past large volcanic eruptions (e.g., Labitzke and McCormick 1992). Additional H₂O cools the stratosphere because of enhanced longwave emission to space (e.g., Forster and Shine 1999). Observations show low temperatures in 2022 that are well outside the range of previous variability (Fig. 2.11a), with corresponding anomalies in stratospheric winds and circulation in balance

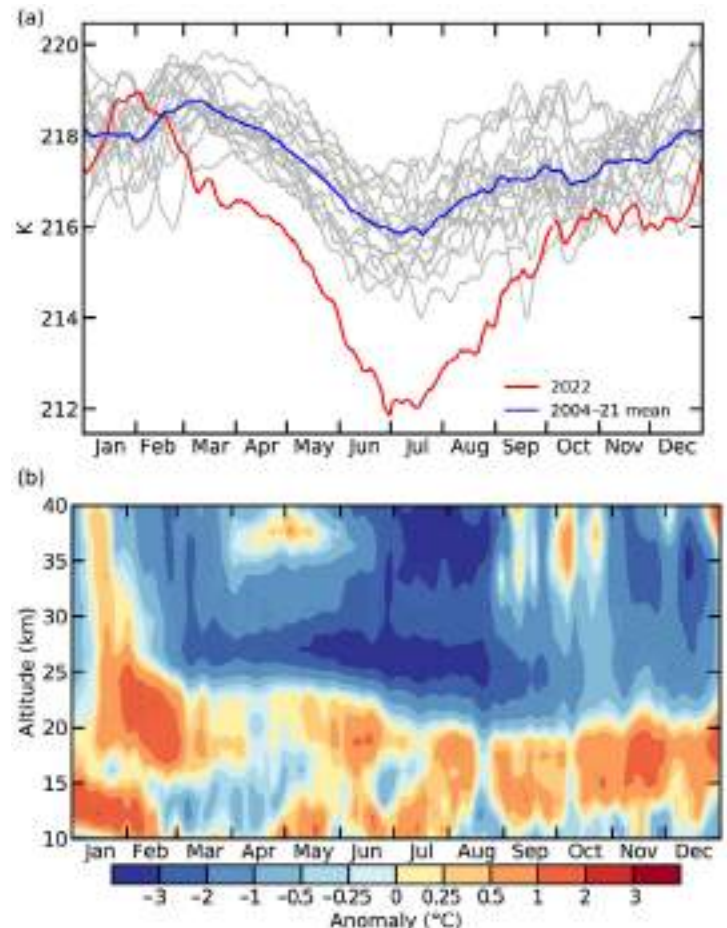


Fig. 2.11. Evolution of Southern Hemisphere midlatitude (10°S–50°S) stratospheric temperature anomalies (°C) in 2022 from Aura MLS measurements (<https://aura.gsfc.nasa.gov/>). (a) Time series of temperatures at 25 km for each individual year, highlighting anomalously cold temperatures in 2022 (red) compared to previous years 2004–21. (b) Height–time evolution of temperature anomalies in 2022 (2022 minus 2004–21 average). Hatching denotes 2022 anomalies that are outside of all previous variability during 2004–21.

with the anomalous temperatures (Coy et al. 2022; Wang et al. 2022). Low anomalies were largest during SH winter (Fig. 2.11b), with a corresponding equatorward shift of the Antarctic polar vortex and circulation-induced midlatitude ozone losses (Wang et al. 2022). While the HTHH H₂O plume is slowly dispersing throughout the global stratosphere, it is expected to persist for a number of years as H₂O is chemically inert, and the main loss processes are due to transport in the slow overturning stratospheric circulation. Hence the HTHH H₂O anomalies will continue to influence stratospheric temperatures beyond 2022.

The Antarctic polar vortex was strong and characterized by anomalously low temperatures during spring 2022, persisting through December (see section 6b for details). Springtime polar temperatures and vortex persistence are closely linked with springtime polar ozone amounts, due to ozone radiative forcing after the sun returns in October. Springtime polar ozone was also relatively low in 2022 (section 2g4), likely contributing to the observed low temperatures.

The Arctic polar vortex was stable and relatively cold during winter but was disturbed by a major stratospheric warming event in March (Vargin et al. 2022), with polar temperature increases over a few days of about 30K. The vortex did not recover, and this event thus corresponded to the ‘final warming’ for that winter. The stratospheric QBO in 2022 continued its usual regular progression (as observed since the 1950s) in contrast to the anomalous disruption events of 2016 and 2020 (section 2e3).

c. Cryosphere

1. PERMAFROST TEMPERATURE AND ACTIVE LAYER THICKNESS

—J. Noetzli, H. H. Christiansen, F. Hrbáček, G. Hu, K. Isaksen, F. Magnin, P. Pogliotti, S. L. Smith, L. Zhao, and D. A. Streletskiy

Permafrost is a subsurface phenomenon in polar and high mountain regions and defined as ground with a maximum temperature of 0°C throughout the year. Permafrost temperatures close to the depth where annual fluctuations become minimal (the depth of zero annual amplitude) increased across all permafrost regions in the past decades with rates ranging from below 0.3°C decade⁻¹ in warm permafrost (with temperatures close to 0 °C) to above 0.8°C decade⁻¹ in cold permafrost (Biskaborn et al. 2019; Smith et al. 2022; Etzelmüller et al. 2020; Zhao et al. 2020; Fig. 2.12; see also section 5i). The thickness of the active layer (ALT), the layer above the permafrost that thaws during summer, increased in the Arctic by a few centimeters per decade in cold continuous permafrost and by more than 10 cm decade⁻¹ in discontinuous permafrost. ALT increased by 19.6 cm decade⁻¹ over the past 40 years in the Qinghai-Tibet Plateau (Fig. 2.13) and has increased by a few meters in the past 20 years at several sites in the European Alps.

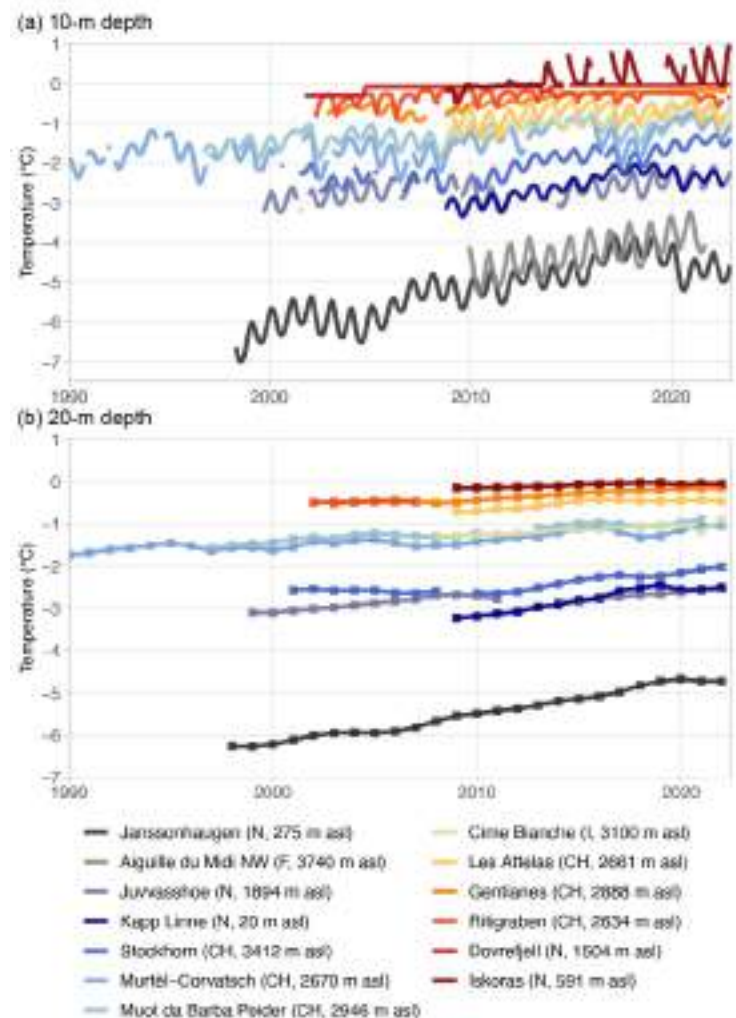


Fig. 2.12. Permafrost temperatures (°C) measured in boreholes in the European Alps and the Nordic countries at a depth of (a) ~10 m (monthly means) and (b) 20 m (annual means). (Sources: Switzerland: Swiss Permafrost Monitoring Network; Norway: Norwegian Meteorological Institute and the Norwegian Permafrost Database; France: updated from Magnin et al. 2015; Italy: updated from Pogliotti et al. 2015.)

Permafrost temperatures in 2022 were the highest on record at 11 of the 25 sites monitored in the Arctic (section 5i), while they were lower than in 2021 in northern Alaska, the northern Mackenzie region in northwestern Canada, and the Canadian high Arctic. This is partly associated with lower air temperatures in those regions over the past two to three years. ALT in Arctic Alaska was one of the lowest since 1995 where most of the sites were established. ALT was lower than 2021 but above the long-term averages in Interior Alaska, northwestern Canada, Greenland, and northern European Russia. ALT in West Siberia was on average 5 cm higher in 2022 than in 2021, while in Central Siberia it was 6 cm lower, but 13 cm higher than average. In East Siberia and Chukotka, ALT was 2 cm–3 cm higher than in 2021, but close to the long-term mean. In high-Arctic Svalbard, permafrost temperatures were the fourth highest on record. ALT was not at maximum due to lower air temperatures in April and early May, and despite record air temperatures in summer 2022 in western and northern Svalbard.

Several countries in Europe recorded extremely dry and warm conditions in summer 2022 (see section 7f; sections 2b4, 2d11; Copernicus 2023). In northern Norway, the permafrost degradation continued, with permafrost thaw down to 20-m depth at Iskoras, and in southern Norway the permafrost temperature was the highest on record at Juvvasshøe (Fig. 2.12). Nearby, on Dovrefjell, since 2021 the active layer has not completely frozen down to the underlying permafrost during winter, resulting in a talik (unfrozen zone; Isaksen et al. 2022). In the European Alps, mean annual ground surface temperature increased in 2022 by more than 1°C compared to 2021 at the majority of the 30 Swiss sites due to higher air temperatures and early snow melt (section 2c5; MeteoSwiss 2023; Pielmeier et al. 2023). The active layer was the thickest on record at most monitoring sites in the Swiss, French, and Italian Alps. In contrast, permafrost temperatures at 10-m depth decreased in 2022 at many sites (update from the Swiss Permafrost Monitoring Network [PERMOS] 2022; Pogliotti et al. 2015; Magnin et al. 2015; Fig. 2.12) reflecting the colder conditions of 2021 (Noetzli et al. 2022). Permafrost temperatures at 20-m depth—where they react to longer-term trends—continued to increase in 2022 at most sites and were close to record levels.

Permafrost temperatures in the Qinghai-Tibet Plateau continued to increase from 2005 to 2021 at 10- and 20-m depth at six sites, with stronger warming in colder permafrost. At the 10 ALT sites along the Qinghai-Tibet Highway (Kunlun mountain pass), ALT increased from the start of the measurements in 1981 to a new maximum of 250 cm in 2021 (the latest value available; Fig. 2.12).

On James Ross Island in the northern Antarctic Peninsula, 2022 was the warmest of the instrumental records since 2004. The mean annual near-surface temperature (−3.2°C) was 2.2°C above the 2011–20 mean (reference site AWS-JGM), leading to a mean annual temperature at the permafrost table (i.e., the top of permafrost) 1.6°C above average. The ALT was 71 cm in 2022 and 22 cm above the mean during 2011–20 (Kaplan-Pastirikova et al. 2023). ALT has been increasing at all Antarctic Peninsula monitoring sites since 2015, whereas it has remained stable in the other regions of Antarctica.

International field data of ALT, permafrost temperatures, and rock glacier velocity (Streletskiy et al. 2021; section 2c2) are collected by the Global Terrestrial Network for Permafrost (GTN-P). Permafrost temperatures are manually recorded or continuously logged in boreholes with a

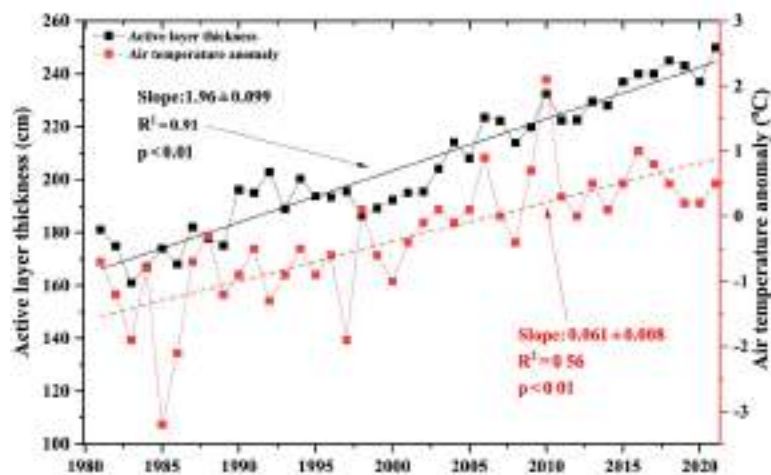


Fig. 2.13. Active layer thickness (cm) and air temperature anomaly (°C; 1991–2020 base period) in the permafrost zone along the Qinghai-Tibet Highway for the period 1981–2021. (Source: Cryosphere Research Station on Qinghai-Xizang Plateau, CAS.)

measurement accuracy of $\sim 0.1^{\circ}\text{C}$ (Biskaborn et al. 2019; Noetzi et al. 2021; Streletskiy et al. 2021). ALT is either determined by mechanical probing (with an accuracy of ~ 1 cm) or interpolated from borehole temperature measurements. The global coverage of permafrost monitoring sites is sparse and biased to the Northern Hemisphere. Permafrost data are particularly limited in regions such as Siberia, central Canada, Antarctica, and the Himalayan and Andes Mountains.

2. ROCK GLACIER VELOCITY

—C. Pellet, X. Bodin, D. Cusicanqui, R. Delaloye, A. Kääh, V. Kaufmann, J. Noetzi, E. Thibert, S. Vivero, and A. Kellerer-Pirklbauer

Rock glaciers are debris landforms generated by the creep of frozen ground (permafrost) whose velocity changes are indicative of changes in the thermal state of permafrost (RGIK 2022a,b). Rock glacier velocities (RGV) observed in different mountain ranges worldwide have been increasing since the 1950s, with large regional and inter-annual variability. In 2022, RGVs in the European Alps decreased at all monitoring sites. For some rock glaciers this was the second consecutive year of decreasing velocities. These changes are consistent with the evolution of permafrost temperatures (section 2c1) to which rock glacier surface velocities respond synchronously (e.g., Kenner et al. 2017; Staub et al. 2016).

Although summer was marked by exceptionally high air temperatures (Fig. 2.14a; section 2b4), RGVs in the European Alps decreased at all sites in 2022, which contrasts with the general

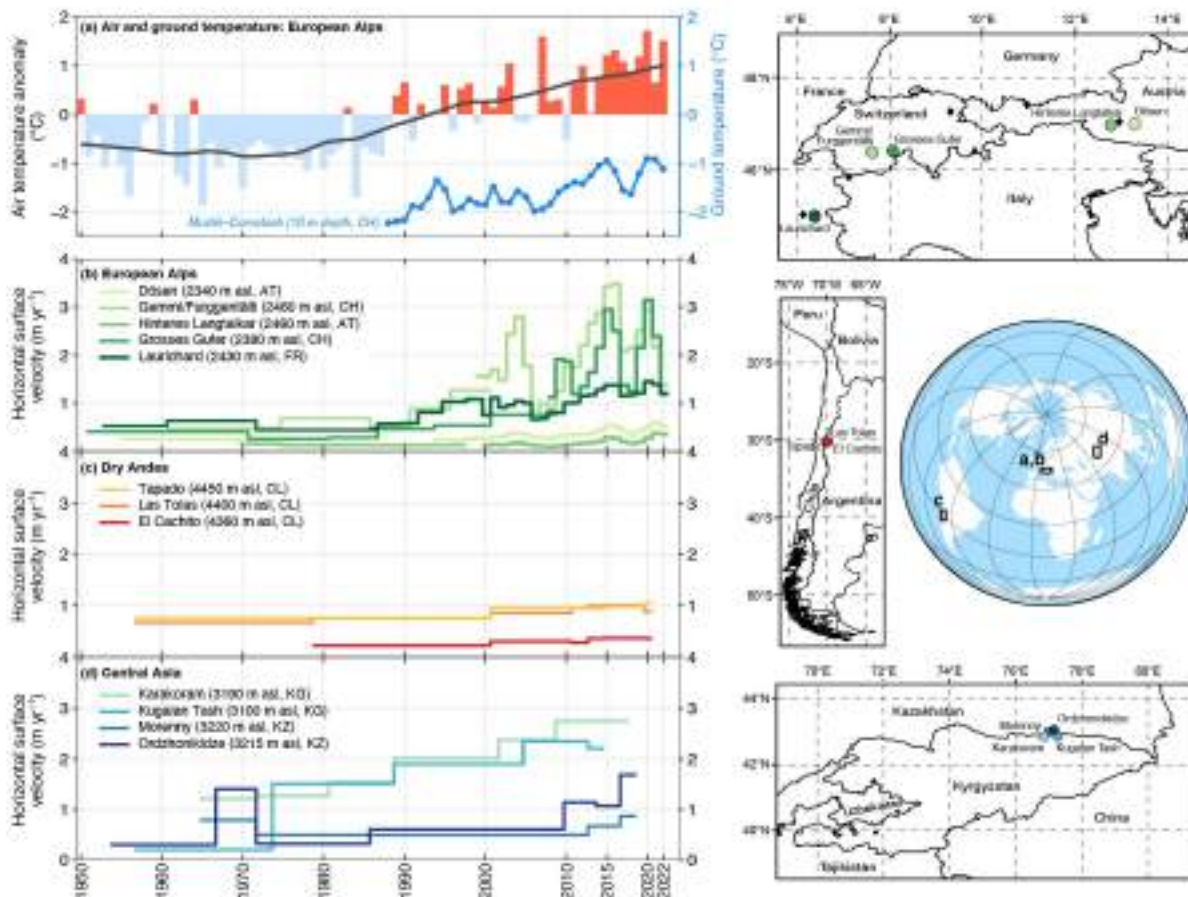


Fig. 2.14. (a) Air and ground temperatures ($^{\circ}\text{C}$) in the European Alps, (b) rock glacier velocities (m yr^{-1}) at selected sites in the European Alps, (c) the Dry Andes (adapted from Vivero et al. 2021), and (d) Central Asia (adapted from Kääh et al. 2021). Rock glacier velocities are based on in situ geodetic surveys or photogrammetry in the context of long-term monitoring. In situ hydrological mean annual permafrost temperature measured at 10-m depth (blue line) at Murtèl Corvatsch (black triangle on Europe map) and air temperature: composite anomaly to the 1981–2010 average (bars) and composite 20-yr running mean (solid line) at Besse (FR), Grand Saint-Bernard (CH), Saentis (CH), Sonnblick (AT), and Zugspitze (D, black diamonds on Europe map). (Sources: Météo France, Deutscher Wetterdienst, MeteoSwiss, GeoSphere Austria, Swiss Permafrost Monitoring Network, University of Fribourg, University of Graz, Graz University of Technology, Université Grenoble Alpes, University of Oslo.)

acceleration trend observed since the 1950s (Pellet et al. 2022; PERMOS 2022). Maximum velocity decrease compared to 2021 was observed in the Swiss Alps (e.g., Grosses Gufer: -49% and Gemmi/Furggentälti: -37%), whereas a smaller decrease was reported in the French (e.g., Laurichard: -14%) and Austrian (e.g., Dösen: -15% and Hinteres Langtalkar: -5%) Alps (Fig. 2.14b). The velocity decrease is consistent with a decrease in permafrost temperatures observed at 10-m depth (section 2c1), which reflects the comparatively cold year of 2021. The relatively dry winter of 2021/22 and dry and warm spring and summer of 2022 affected the geohydrological conditions at all sites (i.e., reduced the amount of water available in the terrain) and also contributed to velocity decrease (i.e., reduced shearing due to reduced pore water pressure; see Cicoira et al. 2019)

There are only a few long-term in situ RGV measurements outside of the European Alps. However, RGVs have been increasingly observed and reconstructed using (archival) aerial photographs and high-resolution satellite data (e.g., Cusicanqui et al. 2021; Eriksen et al. 2018). In the Dry Andes, RGVs reconstructed on three rock glaciers show low velocities from 1950 to 2000, followed by a steady acceleration since the 2000s (Fig. 2.14c), consistent with the climatic conditions in the region (Vivero et al. 2021).

RGVs observed in Central Asia have increased overall since the first available measurements in the 1950s, although their inter-annual evolution differs (Fig. 2.14d; Kääb et al. 2021). This general trend is consistent with increasing air temperatures in the region and with the acceleration reported in the European Alps and Dry Andes.

RGVs are mostly related to the evolution of ground temperature and liquid water content between the upper surface of permafrost (i.e., permafrost table) and the layer at depth where most of the deformation occurs (the so-called shear horizon; Cicoira et al. 2019; Frauenfelder et al. 2003; Kenner et al. 2017; Staub et al. 2016). Despite variable size, morphology, topographical and geological settings, and velocity ranges, consistent regional RGV evolutions have been highlighted in several studies (e.g., Delaloye et al. 2010; Kääb et al. 2021; Kellerer-Pirklbauer et al. 2018). Given the global occurrence of rock glaciers and the sensitivity of their surface velocity to ground temperatures and, by extension, to climate change, RGV was adopted in 2021 as a new associated product to the essential climate variable permafrost by the Global Climate Observing System (GCOS 2022a,b) and the GTN-P (Streletskiy et al. 2021). Multi-annual long-term RGV time series are reconstructed using repeated aerial or optical satellite images. Horizontal displacements are computed based on cross-correlation feature tracking on multi-temporal ortho-images or digital elevation model matching (Kääb et al. 2021; Vivero et al. 2021). The resulting accuracy strongly depends on the spatial resolution of the images and on the image quality (i.e., snow-free and shadows). Surface displacements are averaged for a cluster of points/pixels selected within areas representative of the downslope movement of the rock glacier (RGIK 2022a). Annual rock glacier velocities are measured using terrestrial geodetic surveys performed each year at the same time (usually at the end of summer). The positions of selected boulders (10–100 per landform) are measured with an average accuracy in the range of mm to cm (Delaloye et al. 2008; Kellerer-Pirklbauer and Kaufmann. 2012; PERMOS 2022; Thibert and Bodin 2022).

3. ALPINE GLACIERS

—M. S. Pelto

In 2022 heat events in the European Alps, Svalbard, High Mountain Asia, and the central Andes of Argentina and Chile resulted in a global mean annual mass balance of -1433 mm w.e. (water equivalent) for all 108 reporting alpine (mountain-region) glaciers, with data reported from 20 nations on five continents. In the hydrological year 2021/22, the preliminary regionally averaged annual mass balance based on the World Glacier Monitoring Service (WGMS 2021) reference glaciers was -1179 mm w.e. compared to the 1970–2020 average of -490 mm w.e. This makes 2022 the 35th consecutive year with a global alpine mass balance loss and the 14th consecutive year with a mean global mass balance below -500 mm w.e. (Fig. 2.15). This acceleration in mass loss from global alpine glaciers in the twenty-first century matches the findings of Huguenot et al. (2021). Since the start of the record in 1970, 9 of the 10 most negative mass balances have occurred since 2013.

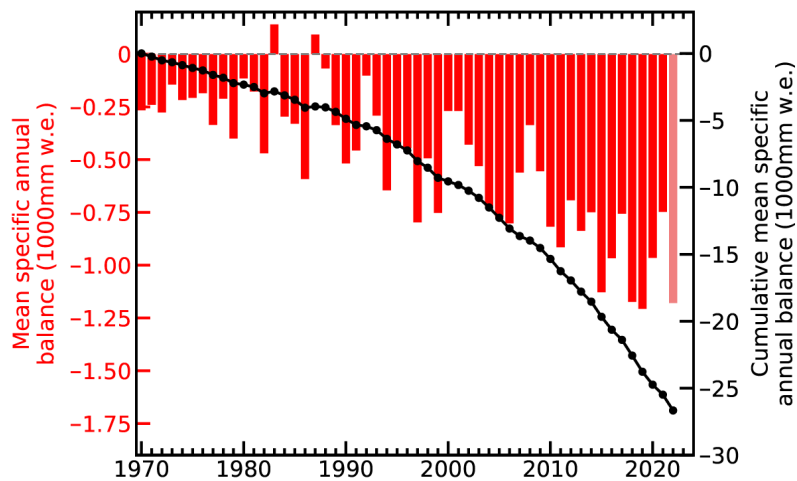


Fig. 2.15. Global average annual (left axis, red bars) and cumulative (right axis, black line) mass balance (1000 mm w.e.) of alpine glaciers for the period 1970–2022. (Source: WGMS regionally averaged reference glacier network.)

In 2022, a negative annual mass balance was reported from 34 of the 37 reference glaciers reported to WGMS. The mean annual mass balance of the 37 reference glaciers was -1547 mm w.e. Reference glaciers each with at least 30 continuous years of observation are used to generate regional averages. Global values are calculated using a single value (averaged) for each of 19 mountain regions in order to avoid a bias toward well-observed regions.

More frequent and intense heatwaves impacting glaciated ranges continued to take a toll on alpine glaciers in 2022. Heatwaves reduce snow cover extent earlier in the melt season, exposing ice surfaces earlier and enhancing surface darkening, both of which cause higher melt rates on alpine glaciers (Shaw et al. 2021; Pelto et al. 2022; Cremona et al. 2023).

All 32 reporting glaciers in the Alps, Pyrenees, and Caucasus Mountains had a negative mass balance averaging -3100 mm w.e. in 2022. In the European Alps, the combination of low winter snowpack and several summer heatwaves generated unprecedented mass loss (sections 2b4, 7f3). In Switzerland, the 25 days of heatwaves in 2022 are estimated to have melted 1.27 ± 0.10 km³ w.e., equivalent to 35% of the overall glacier mass loss that occurred during the summer, a period that led to a 6.2% overall glacier volume loss (Cremona et al. 2023).

In Norway and Sweden, the average balance of 11 reporting glaciers was -443 mm w.e., with three glaciers in Norway having a positive balance. Iceland completed surveys of nine glaciers; five had a positive balance and four a negative balance, with a mean mass balance of -7 mm w.e., close to equilibrium.

On Svalbard, the mean loss of the four reporting glaciers was -1102 mm w.e. The negative mass balances were due to several summer heat events (see section 5b, Sidebar 5.1), which led to many glaciers and ice caps losing all or most of their snow cover, further accelerating mass loss (Fig. 2.16).

In Alberta and British Columbia, Canada, and in Alaska and Washington, United States, 19 glaciers had a negative mass balance, averaging -965 mm w.e. The Alberta, British Columbia, and Washington regions experienced several prolonged heatwaves as they did in 2021. Daily glacier ablation in this region was noted as increasing by 30%–40% during heatwave periods (Pelto et al. 2022).

In South America, mass balance data, reported from five Andean glaciers in Ecuador, Argentina, and Chile were negative, with a mean of -1465 mm w.e. The combination of drought and heat events left many central Andean glaciers snow free by mid-summer in early 2022. Shaw et al. (2021) noted a significant decline in surface albedo (section 2h1) due to decreased fractional snow cover that further enhances melt.

In High Mountain Asia, mass balance measurements were completed on glaciers in China, Kazakhstan, Kyrgyzstan, Russia, and Tajikistan. All 20 glaciers reported negative balances, with an average of -1040 mm w.e. The negative balances were driven by above-average melting during the May–July period.

In New Zealand, the mass balance assessed on Brewster and Rolleston Glaciers were strongly negative at -1125 mm and -1065 mm w.e., respectively. The end of year snowline observations on 50 glaciers was one of the five highest of the last 45 years.

Annual mass balance is reported in mm water equivalent (w.e.). A value of -1000 m w.e. per year represents a mass loss of 1000 kg m^{-2} of ice, or an annual glacier-wide thickness loss of about 1100 mm yr^{-1} .

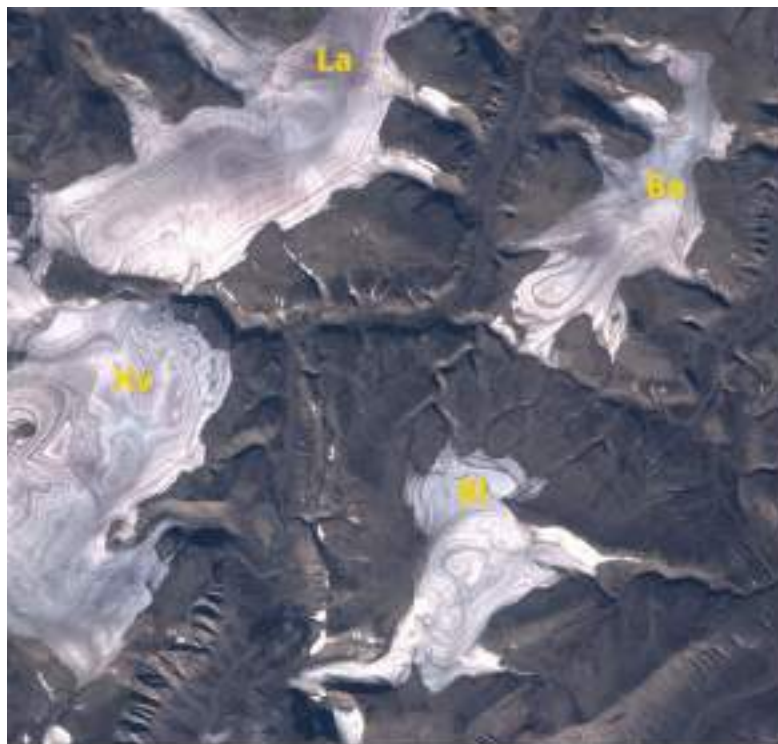


Fig. 2.16. Langjokulen (La), Kvitisen (Kv), Bergfonna (Be), and Blaisen (Bl) ice caps on the northeastern island of Edgeøya, Svalbard, in Copernicus Sentinel-2 MSI image (RGB) on 20 Aug 2022 illustrating the lack of snow cover, limited firn areas, and numerous annual layers. This pattern of annual layers due to glaciers being stripped of snow cover is becoming increasingly frequent.

4. LAKE ICE

—S. Sharma, R. I. Woolway, J. Culpepper, and K. Blagrave

In winter 2021/22, many, but not all lakes across the Northern Hemisphere (NH) had later ice-on dates, earlier ice-off dates, and shorter seasonal ice cover, thus continuing the pattern observed in recent decades (Sharma and Woolway 2021; Sharma et al. 2022).

NH lakes froze on average 5.6 days later and thawed 3.2 days earlier, with 8.9 days shorter ice duration relative to the 1991–2020 base period based on ERA5 reanalysis data (Figs. 2.17, 2.18). The duration of lake ice cover was the fourth shortest since the start of the record in 1980 (Fig. 2.18c). The regional variations in ice duration were consistent with NH winter air temperature anomalies. Some regions in North America, such as western Canada and Alaska, experienced below-average air temperatures, which resulted in longer-than-average ice duration. Conversely, many regions in Eurasia, in particular Siberia, experienced warmer-than-average conditions that resulted in shorter-than-average ice duration (Fig. 2.17).

In situ ice records from 118 lakes distributed across North America, Europe, and Asia revealed mixed patterns for the 2021/22 winter relative to 1991–2020. On average, across this set of 118 lakes,

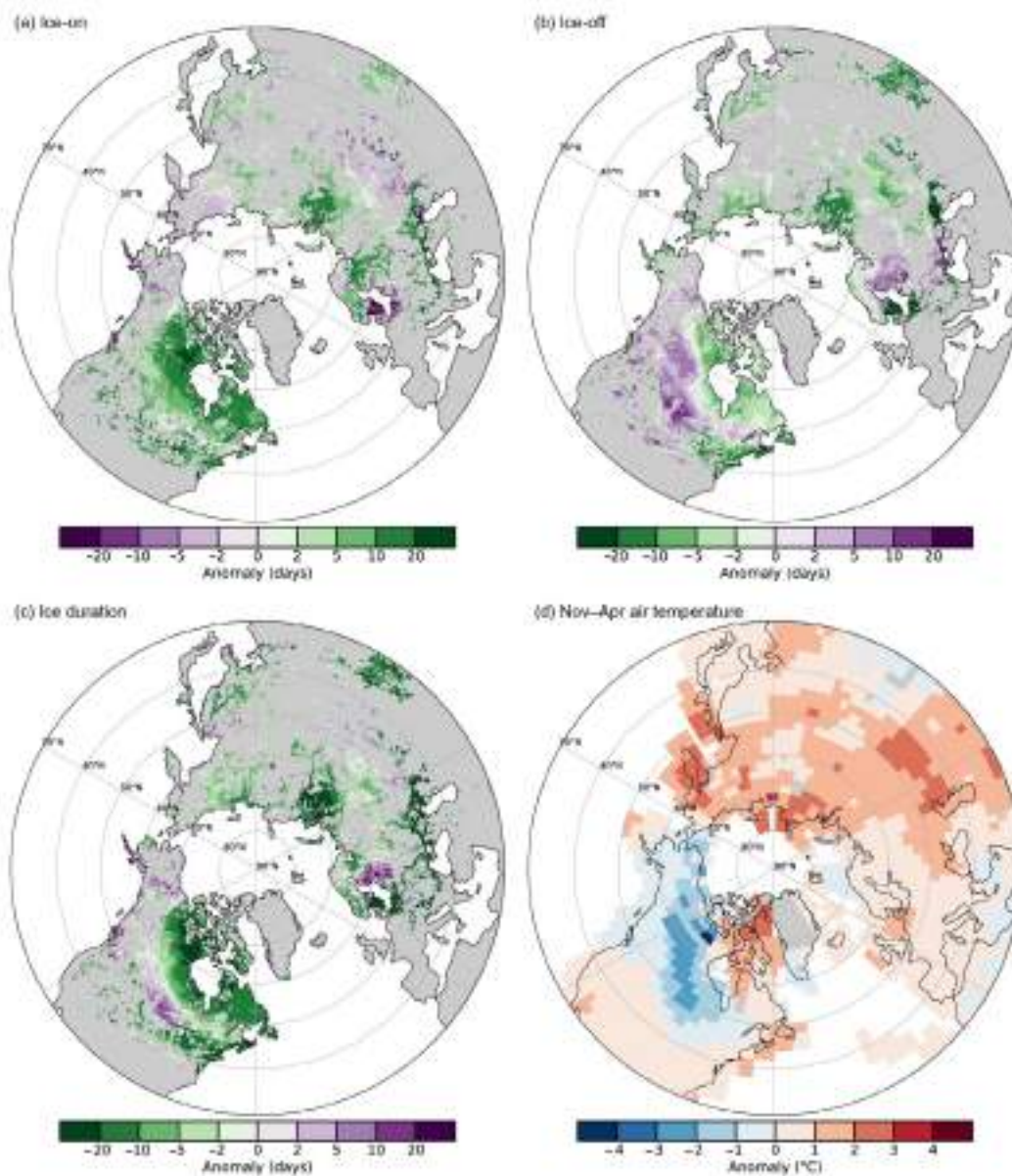


Fig. 2.17. Anomalies (days) in 2022 for (a) ice-on, (b) ice-off, and (c) ice duration for lakes across the Northern Hemisphere (NH), and (d) surface air temperature anomalies (°C) for the NH cold season (Nov–Apr average), the time of year in which lakes typically freeze. The base period is 1991–2020. In (a)–(c), green colors represent higher ice loss (i.e., later ice-on, earlier ice-off, and shorter ice duration), and purple colors represent higher ice coverage (i.e., earlier ice-on, later ice-off, and shorter ice duration). (Sources: ERA5, GISTEMP.)

ice-on was 0.5 days later, ice-off was 3.5 days later, and ice duration was 3.7 days longer (Fig. 2.18). For North American lakes on average, ice duration was 1 day longer, whereas for European lakes, ice-on was 7.1 days longer in 2021/22 relative to 1991–2020. In Asia, Lake Suwa in Japan froze on 7 January 2022. This lake has frozen two years in a row, an event that has not occurred in a decade, though historically the lake froze most years (Sharma et al. 2016, 2021).

We further collated in situ records from 18 mountain lakes (>1000 m a.s.l.) as Pepin et al. (2015) suggests that high-elevation regions will experience more rapid warming than lower elevations.

On average, these mountain lakes froze 11 days later and thawed 5.3 days earlier than the 1991–2020 baseline period (Fig. 2.18). Lake Lunz in Austria showed particularly strong reductions in ice cover as it only froze for 1 day in January and 2 days in February, freezing 41.3 days later, thawing 21.1 days earlier, and losing 58.2 days of duration. This lake also showed multiple freeze and breakup events during the last two years, which had not occurred previously in its continuous 102-year record (Kainz et al. 2017).

The Laurentian Great Lakes had 10.9% more maximal ice coverage, relative to the winters of 1991–2020. Lake Superior was the most anomalous with 25% more ice coverage in 2022, followed by Lake Ontario which had 17.8% more ice coverage (Fig. 2.19). Ice formation was quite late in the Great Lakes owing to warmer autumn water temperatures in late 2021.

We used ice simulations from the European Centre for Medium-Range Weather Forecasts (ECMWF) Reanalysis version 5 (ERA5) reanalysis product (Hersbach et al. 2020) to calculate ice-on and ice-off dates, in addition to ice duration dates across NH lakes following the methodology of Grant et al. (2021). We obtained in situ data for 118 lakes: Canada (4), United States (74), Estonia (1), Finland (27), Norway (10), Sweden (1), and Japan (1). We also obtained in situ data for mountain lakes for the United States (8) and Europe (10; Benson et al. 2000, updated 2022). Furthermore, we acquired annual maximum ice cover (%) data for each of the Laurentian Great Lakes from 1973–2022 (<https://www.glerl.noaa.gov/data/ice/>). Surface air temperature data for the NH cold season (November–April average) were downloaded from the NASA GISS surface temperature analysis (GISTEMP Team 2023). Anomalies for each of our ice metrics were calculated for the 2021/22 winter relative to the 1991–2020 normal base period.

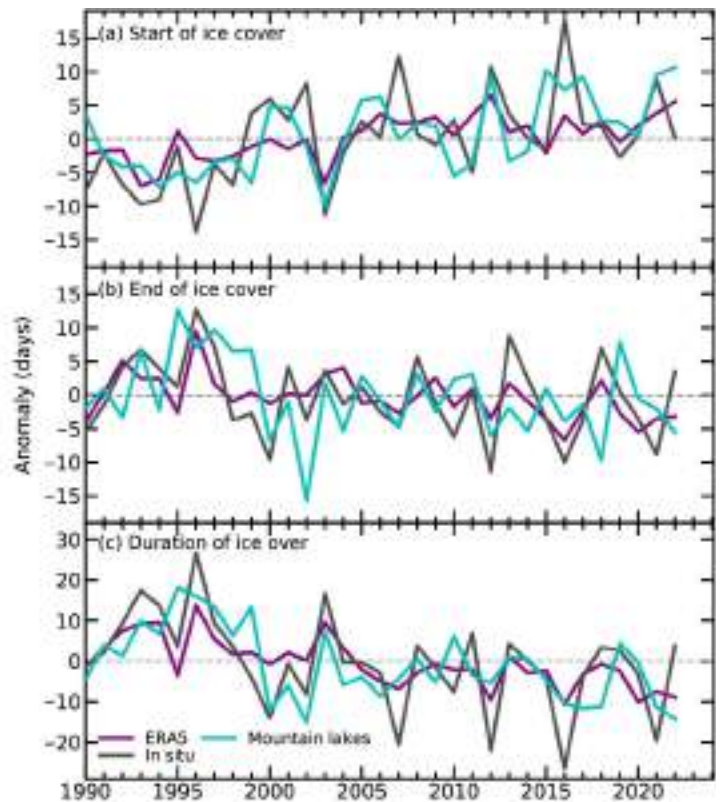


Fig. 2.18. Lake (a) ice-on, (b) ice-off, and (c) ice duration anomalies (days) from 1980 to 2022, relative to the 1991–2020 base period, derived from ERA5 reanalysis, in situ observations, and mountain lakes. Positive values for ice-on suggest later freezing, whereas negative values for ice-off and ice-duration indicate earlier ice-thaw and shorter ice duration.

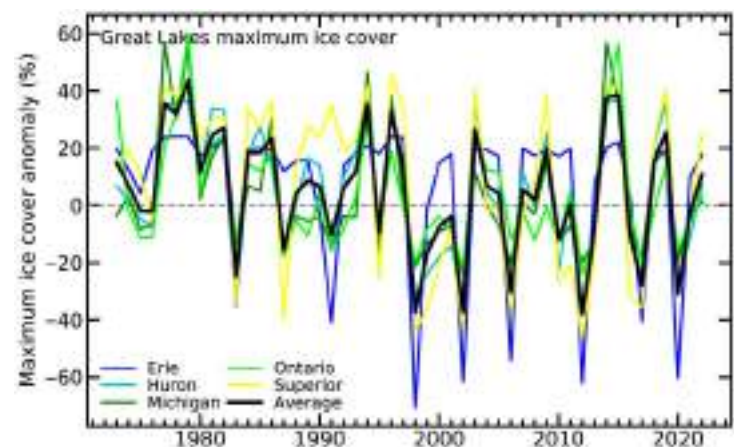


Fig. 2.19. Anomalies in Great Lakes maximum ice cover extent (%) for the period 1973–2022, relative to the 1991–2020 base period. The black line shows the average anomaly for all of the Great Lakes, whereas the lines in color show individual lakes (Erie, Michigan, Superior, Ontario, and Huron).

5. NORTHERN HEMISPHERE CONTINENTAL SNOW-COVER EXTENT

—D. A. Robinson and T.W. Estilow

Annual snow-cover extent (SCE) over NH lands averaged 24.9 million km² in 2022. This is 0.04 million km² less than the 1991–2020 mean and 0.23 million km² below the full period of record (1967–2022) mean (Fig.2.20; Table 2.5). This ranks 2022 as having the 24th least-extensive cover (33rd most) on record. Monthly SCE in 2022 ranged from 47.3 million km² in January to 2.4 million km² in August (Fig. 2.21).

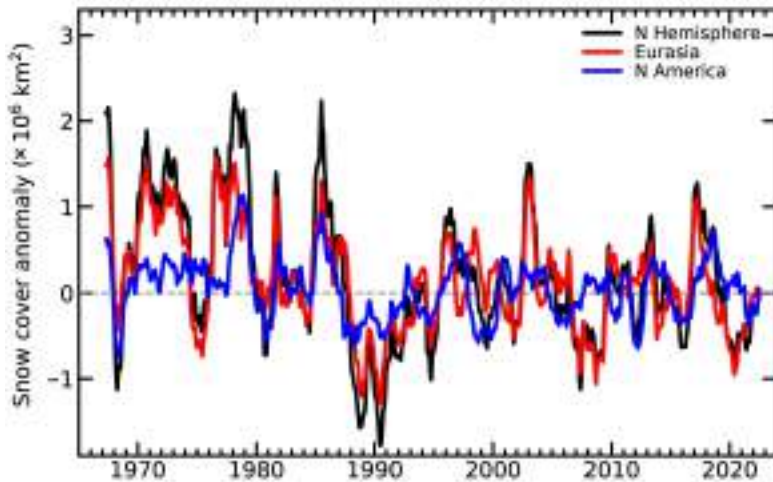


Fig. 2.20. Twelve-month running anomalies of monthly snow-cover extent (SCE; $\times 10^6$ km²) over Northern Hemisphere (NH) lands as a whole and Europe (EUR) and North America (NA) separately plotted on the seventh month using values from Nov 1966 to Dec 2022. Anomalies from the 1991-2020 mean are calculated from NOAA snow maps. Mean NH SCE is 25.1×10^6 km² for the full period of record. Monthly means for the period of record are used for nine missing months during 1968, 1969, and 1971 to create a continuous series of running means. The missing months fall between Jun and Oct.

Table 2.5. Monthly and annual climatological information on Northern Hemisphere (NH), Eurasian (EUR), and North American (NA) snow cover extent (SCE) between Nov 1966 and Dec 2022. Included are the numbers of years with data used in the calculations, NH means, standard deviations (std. dev.), 2022 values, and rankings. Areas are in millions of square kilometers (km²). The years 1968, 1969, and 1971 have 1, 5, and 3 missing months respectively, thus are not included in the annual (Ann) calculations. NA includes Greenland. Ranks are from most (1) to least extensive.

Month	Yrs	NH Mean	Std. Dev.	2022	2022 NH rank	2022 EUR rank	2022 NA rank
Jan	56	47.1	1.5	47.3	26	24	32
Feb	56	46.0	1.8	45.8	27	22	37
Mar	56	40.4	1.8	40.0	31	33	32
Apr	56	30.5	1.7	30.9	23	32	13
May	56	19.1	2.0	18.0	40	44	23
Jun	55	9.3	2.5	5.5	53	54	51
Jul	53	3.9	1.2	2.7	45	51	43
Aug	54	3.0	0.7	2.4	43	45	38
Sep	54	5.4	0.9	5.9	14	6	45
Oct	55	18.6	2.6	18.7	25	22	34
Nov	57	34.3	2.1	37.7	4	11	3
Dec	57	43.7	1.8	43.6	37	48	13
Annual Calculations	53	25.1	0.8	24.9	33	34	30

The first four months of 2022 saw NH SCE rank in the middle tercile of the 56-year record. This dropped to the lower tercile in May, and June was the third least extensive on record (Fig. 2.22a). When snowfall resumed in September the SCE over Eurasia (EUR) quickly climbed to sixth most extensive, while North America (NA) SCE grew more slowly. NH October SCE was in the middle tercile before both continents experienced above-normal November SCE (NA ranking third most extensive and EUR 11th; Fig. 2.22b). However, the pace of seasonally advancing SCE slowed considerably across EUR in December (10th least extensive on record), while NA continued to see above-normal SCE (13th most extensive).

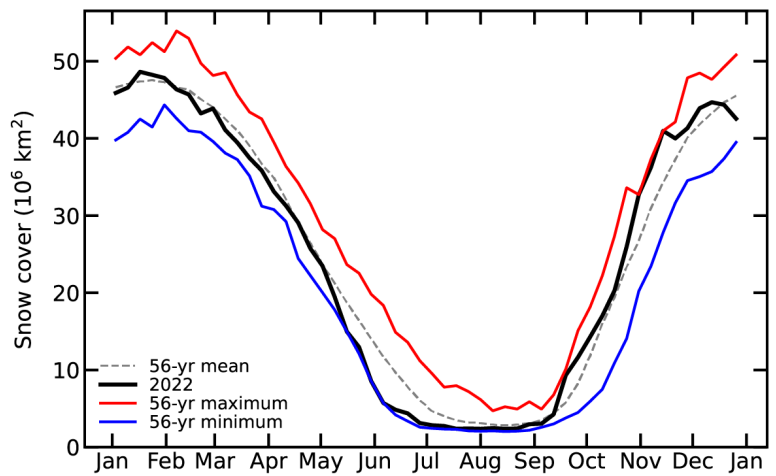


Fig. 2.21. Weekly Northern Hemisphere snow-cover extent (SCE; $\times 10^6 \text{ km}^2$) for 2022 (black) plotted with the mean (gray dashed line), maximum (red), and minimum (blue) SCE for each week. Mean weekly SCE and extremes are calculated using the 56-yr record from Jan 1967 to Dec 2022. Weekly data granules represent SCE for each seven-day period ending on Monday.

Compared to normal, monthly SCE over the contiguous United States varied considerably in 2022. Rankings were in the middle tercile in January, the lowest tercile in February, and was the seventh least extensive on record in March. Melt slowed considerably in April, with the 19th most extensive cover occurring, followed by a middle tercile ranking in May. End-of-year SCE for the United States was above normal, ranking 11th, 6th, and 14th most extensive in October, November, and December, respectively.

SCE is calculated at the Rutgers Global Snow Lab (GSL) from daily SCE maps produced by meteorologists at the U.S. National Ice Center, who rely primarily on visible satellite imagery to construct the maps (Estilow et al. 2015). Maps depicting daily, weekly, and monthly conditions, anomalies, and climatologies may be viewed at the GSL website (<https://snowcover.org>).

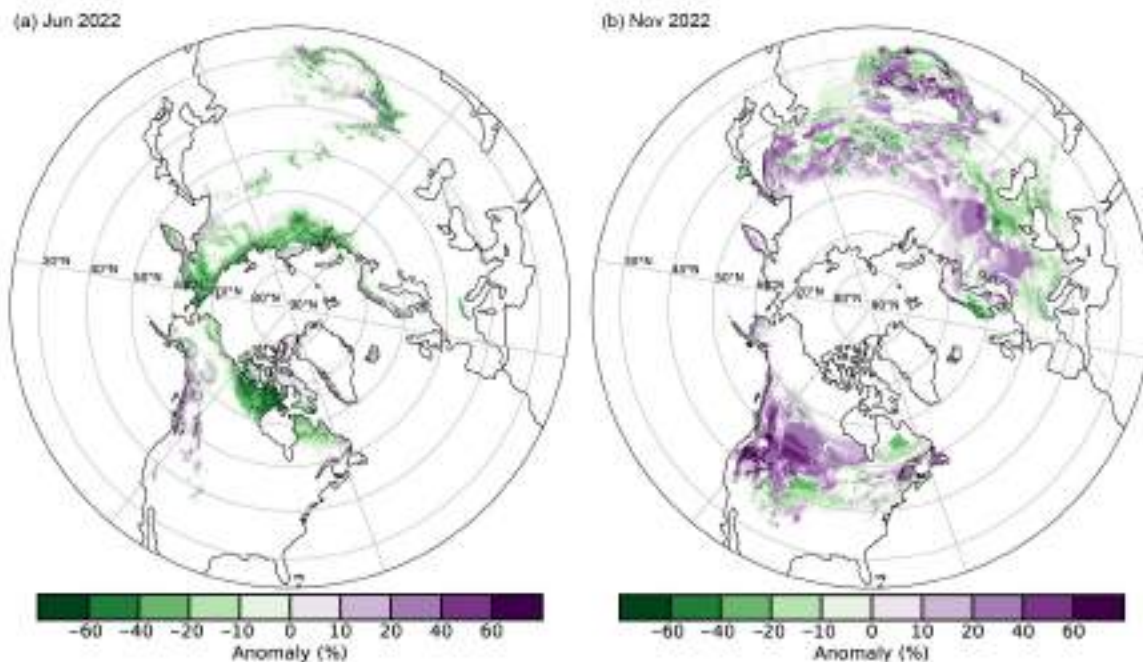


Fig. 2.22. Monthly snow-cover extent (SCE) departure (%; 1991–2020 base period) maps showing (a) Jun 2022 and (b) Nov 2022. The monthly percent anomaly for a grid cell is based on the percent of days that cell was snow covered in that month compared to the long-term climatological average of snow cover days. Jun exhibited the lowest SCE anomaly (-3.91 million km^2) during 2022, while Nov was the highest above normal ($+3.79$ million km^2). Negative departures indicate less SCE than normal (green) with positive departures (purple) showing areas of SCE above the 30-year mean.

d. Hydrological cycle

1. SURFACE HUMIDITY

—K. M. Willett, A. J. Simmons, M. Bosilovich, and D. A. Lavers

In 2022, surface humidity exhibited similar levels of water vapor to 2021, as measured by specific humidity (q). Saturation levels, as measured by relative humidity (RH), were slightly higher than in 2021 over land, yet remained drier than the 1991–2020 average (Figs. 2.23e,f). This finding is common to all products shown here, which comprise the in situ Hadley Centre Integrated Surface Database Humidity (HadISDH [v4.5.1.2022f]) and the European Centre for Medium-Range Weather Forecasts (ECMWF) Reanalysis version 5 (ERA5), Modern-Era Retrospective Analysis for Research and Applications version 2 (MERRA-2), and Japanese 55-year Reanalysis (JRA-55) reanalysis products. It is consistent with the similarity of global near-surface temperatures to those in 2021 and the continuing La Niña conditions that were mostly present throughout both years. Relative humidity over oceans remained highly uncertain, as represented by the spread across the two reanalysis estimates (ERA5 and JRA-55; Figs. 2.23h). Note that this year HadISDH.marine is not included while a discrepancy linked to reduced data coverage in the updated version is investigated.

Despite overall agreement between products for much of the more-than-40-year record, 2022 saw a continued widening of the divergence in anomaly estimates apparent from around 2019. HadISDH showed 2022 as having a slightly higher water vapor content compared to 2021 with the specific humidity anomaly over land (q_{land}) remaining wetter than the 1991–2020 average at 0.13 (0.09 to 0.17 2-sigma uncertainty range) g kg^{-1} . ERA5 placed q_{land} much lower at -0.01 g kg^{-1} , identical to its estimate in 2021. ERA5 q_{ocean} was slightly drier than 2021 at 0.03 g kg^{-1} . MERRA-2 and

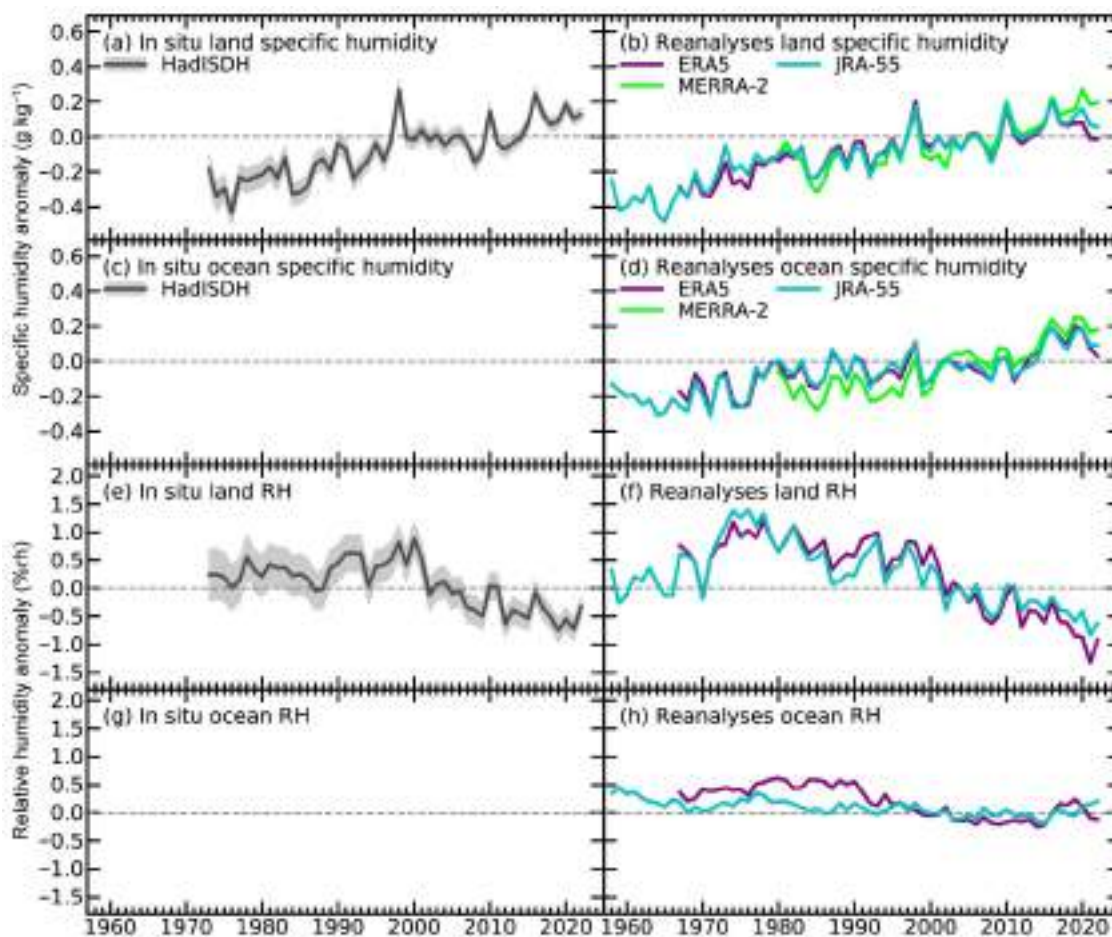


Fig. 2.23. Global average surface humidity annual anomalies (1991–2020 base period). For the in situ datasets 2-m surface humidity is used over land and ~10 m over the oceans. For the reanalysis, 2-m humidity is used over the whole globe. For ERA5 ocean series-only points over open sea are selected. 2- σ uncertainty is shown for the HadISDH dataset capturing the observation, gridbox sampling, and spatial coverage uncertainty. (Sources: HadISDH [Willett et al. 2013, 2014]; ERA5 [Hersbach et al. 2020]; JRA-55 [Kobayashi et al. 2015]; MERRA-2 [Gelaro et al. 2017].)

JRA-55 remained wetter-than-average over land and ocean, with MERRA-2 anomalies reaching the highest at 0.19 g kg^{-1} and 0.18 g kg^{-1} for q_{land} and q_{ocean} , respectively.

In terms of saturation, all products show that RH_{land} remained drier-than-average but was more humid than in 2021. Anomalies ranged from -0.93 \%rh for ERA5 to -0.33 (-0.53 to -0.13 2-sigma uncertainty range) \%rh for HadISDH. ERA5 has consistently presented drier RH_{land} anomalies than HadISDH since 2019. Over ocean, ERA5 and JRA-55 had RH_{ocean} anomalies drier than average at -0.12 \%rh and more humid than average at 0.21 \%rh , respectively.

Interestingly, the divergence in products is also apparent in the global land average for total column water vapor (TCWV; section 2d2; Fig. 2.23c). ERA5 and GPS radio occultation (GPS-RO) estimates show TCWV close to average for 2022 whereas MERRA-2, JRA-55, and the more spatially limited ground-based global navigation satellite system (GNSS) record place 2022 much wetter at levels comparable with the previous five years.

At least part of the reason behind the ERA5-HadISDH land divergence is driven by spatial coverage differences. Plates 2.1g,h and Fig. 2.24 show that central South America and western and central Africa are regions of dry anomalies in ERA5 but mostly missing gridboxes in HadISDH. Over Africa, MERRA-2 shows mostly wet anomalies, contributing to its wetter q_{land} anomaly for 2022 which appears more comparable with HadISDH. This is similar to 2021, where La Niña was also present, with near-identical spatial patterns of anomalies. Plate 2.1g (using ERA5) shows expansive dry q anomalies spreading across the central Pacific, surrounded by expansive strong wet anomalies. These are characteristic of La Niña and are respectively drier and wetter in 2022 compared to 2021. Over land, wet anomalies over India extended farther west over Pakistan in 2022 (when Pakistan had severe flooding, section 2d5) compared to 2021, and they were also more expansive over eastern Australia and southern Africa in 2022. Dry anomalies over the northern midlatitudes were similar but located farther east compared to 2021. The

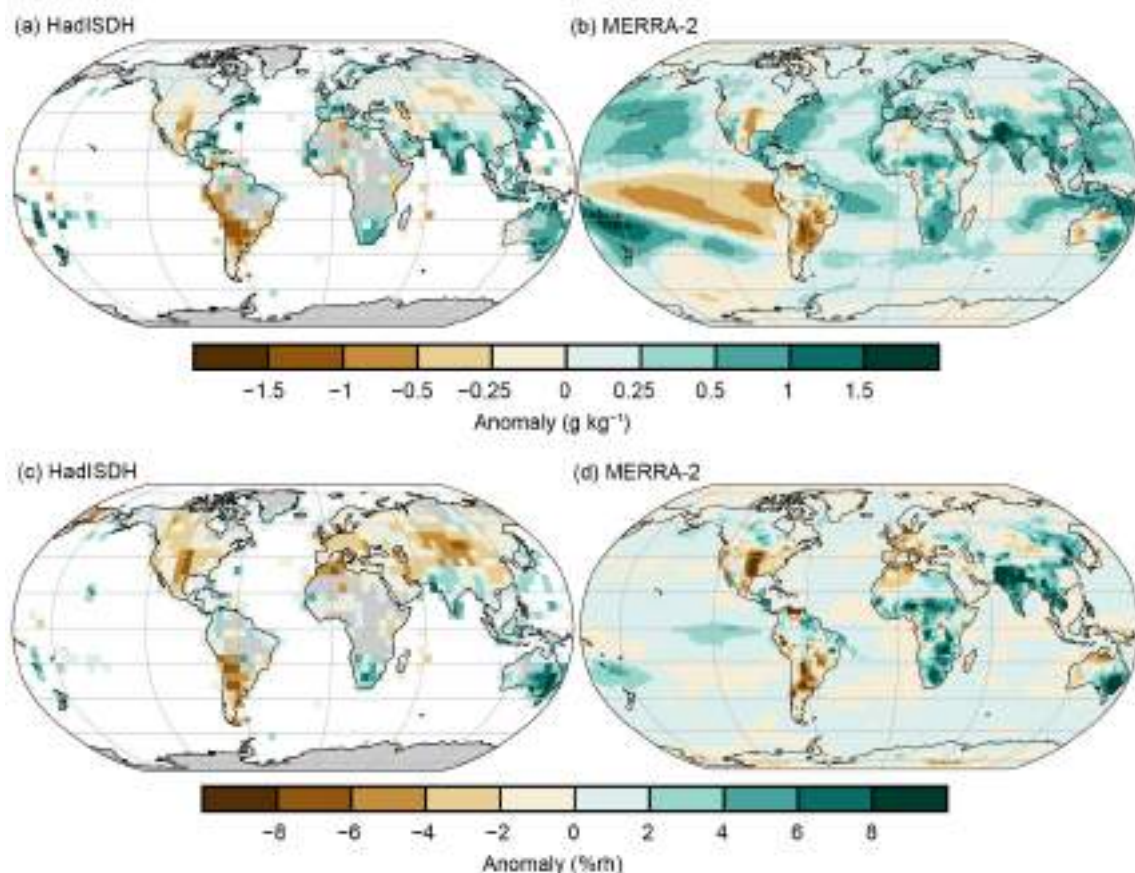


Fig. 2.24. Annual average surface humidity anomalies from the 1991–2020 average for (a),(b) specific humidity (g kg^{-1}) and (c),(d) relative humidity (\%rh). Maps for (a) and (c) are from the HadISDH in situ product that uses weather station observations. Maps for (b) and (d) are from the MERRA-2 reanalysis product.

south-central United States and subtropical South America experienced very dry anomalies in 2022. These were also regions suffering from drought.

Li et al. (2020) and Freychet et al. (2020) demonstrate a possible dry bias in ERA5 (and HadISDH.land [Willett 2023a,b]) over China from the early 2000s onward when manual wet bulb thermometers were replaced with automated RH sensors nationwide. All products contain some degree of uncertainty. For HadISDH, this is dominated by incomplete coverage and remaining inhomogeneity from changes to the observing system over time, despite considerable efforts to homogenize the data (Willett et al. 2013, 2014). For reanalyses, observation sparseness and quality and the drop in/out of data platforms over time are all sources of uncertainty. These do not undermine the conclusion of generally increasing water vapor alongside decreasing saturation levels.

Sidebar 2.1: Assessing humid heat extremes over land

— K. M. WILLETT

Extremes of heat based solely on temperature have been routinely monitored for some time using a wide range of Climpact indices (which includes those from the World Meteorological Organization Expert Team on Climate Change Detection and Indices; section 2b4; <https://climpact-sci.org/>). Although temperature is likely the dominant factor for heat-related mortality (Armstrong et al. 2019; Lo et al. 2023), humidity can also play an important role. In fact, even at more moderate temperatures, high humidity increases the overall ‘heat’ loading on the body and can therefore lead to negative impacts on health. Physical and even mental tasks can become more difficult to complete, slowing the rate at which people function and increasing the amount of rest required. The resulting decreased productivity can have a negative economic impact in addition to health and wellbeing impacts (Parsons et al. 2022).

Relative humidity is the level of water vapor saturation in the atmosphere. As this depends both on the water vapor content and the temperature of the air, knowing the relative humidity alone is not a useful measure in terms of heat stress. The wet bulb temperature, T_w , was until recently a commonly observed meteorological variable and can be relatively easily calculated from standard meteorological variables in most conditions. The lower the level of saturation, the lower the T_w will be compared to the air temperature. If the air is completely saturated (relative humidity [RH]=100%rh), then the T_w will

equal the air temperature. This becomes important for human health when the T_w approaches skin temperature, which is on average about 35°C. At this point the air closest to the skin is then saturated, meaning that sweat can no longer evaporate from the body and therefore it is no longer an effective cooling mechanism. This is then a theoretical critical threshold above which humans cannot survive, as we have no other biophysical cooling mechanisms available and so would overheat rapidly even if inactive. In practice, the critical level of T_w for the human body to function is below 32°C (Vecellio et al. 2022).

With this in mind, quantifying the current exposure to high T_w and monitoring change over time is important, as is looking at future potential changes given further warming. Building on the existing surface-humidity monitoring product HadISDH.land (Willett et al. 2013, 2014), a new dataset of gridded, monthly, wet bulb and air temperature extremes indices from 1973 to present has been developed: HadISDH.extremes (v1.0.0.2022f, Willett 2023a,b). By utilizing the existing framework of the Climpact indices we can assess the different exposures to dry versus humid heat, exploring the concept of ‘stealth heat events’, where the temperature may not be considered extreme but the humidity is high. Such events may not be sufficient to cause fatalities but could still impact productivity and health. Table SB2.1 describes the core indices used here; more indices are available from the HadISDH.extremes.

Table SB2.1. Heat extreme indices for wet bulb temperature (T_w). A bigger range of indices are available at HadISDH.extremes dataset pages on HadOBS and CEDA (HadOBSID: www.metoffice.gov.uk/hadobs/hadisdh CEDA: <https://catalogue.ceda.ac.uk/uuid/2d1613955e1b4cd1b156e5f3edbd7e66>).

Index	Long name	Description
T_wX	Maximum wet bulb temperature	Gridbox mean of station month maxima of daily maximum T_w
T_wX90p	90th percentile maximum wet bulb temperature exceedance	Gridbox mean of station percentages of days where the daily maximum T_w exceeds the climatological 90th percentile of daily maxima for the month
T_wX29	29°C maximum wet bulb temperature exceedance	Gridbox mean of station percentages of days where the daily maximum $T_w \geq 29^\circ\text{C}$

HadISDH.extremes uses hourly weather station observations of wet bulb temperature that have been quality controlled from the HadISD dataset (Dunn et al. 2012, 2014, 2016; Dunn 2019; Smith et al. 2011). Wet bulb temperature is calculated from dew point temperature and air temperature using the Stull (2011) formula. To ensure a high-quality final product, only stations with sufficient data completeness are included and the final grid boxes are filtered to remove those stations where large inhomogeneities are present (see Willett 2023a,b for more details). Importantly, the high-variability nature of extremes and dependence on a single daily observation ultimately means that uncertainty is larger than for monthly mean

quantities such as those provided by HadISDH.land (section 2d1).

There are many regions of the globe for which high T_w is rare or non-existent. Fig. SB.2.1 shows the percentage of days where the T_w exceeded 25, 29, and 31°C over the 1973–2022 record (panels a,c,e), and the number of days for 2022 as an anomaly compared to the 1991–2020 baseline (panels b,d,f). Even the lower midlatitudes experience ‘moderate’ T_w (T_w X25, Figs. SB.2.2a,b), but ‘high’ T_w (T_w X29 and T_w X31, Figs. SB.2.1c–f) are so far mostly limited to the lower latitudes. In the Middle East, the Persian Gulf and Red Sea regions typically experience the most frequent ‘high’ T_w but

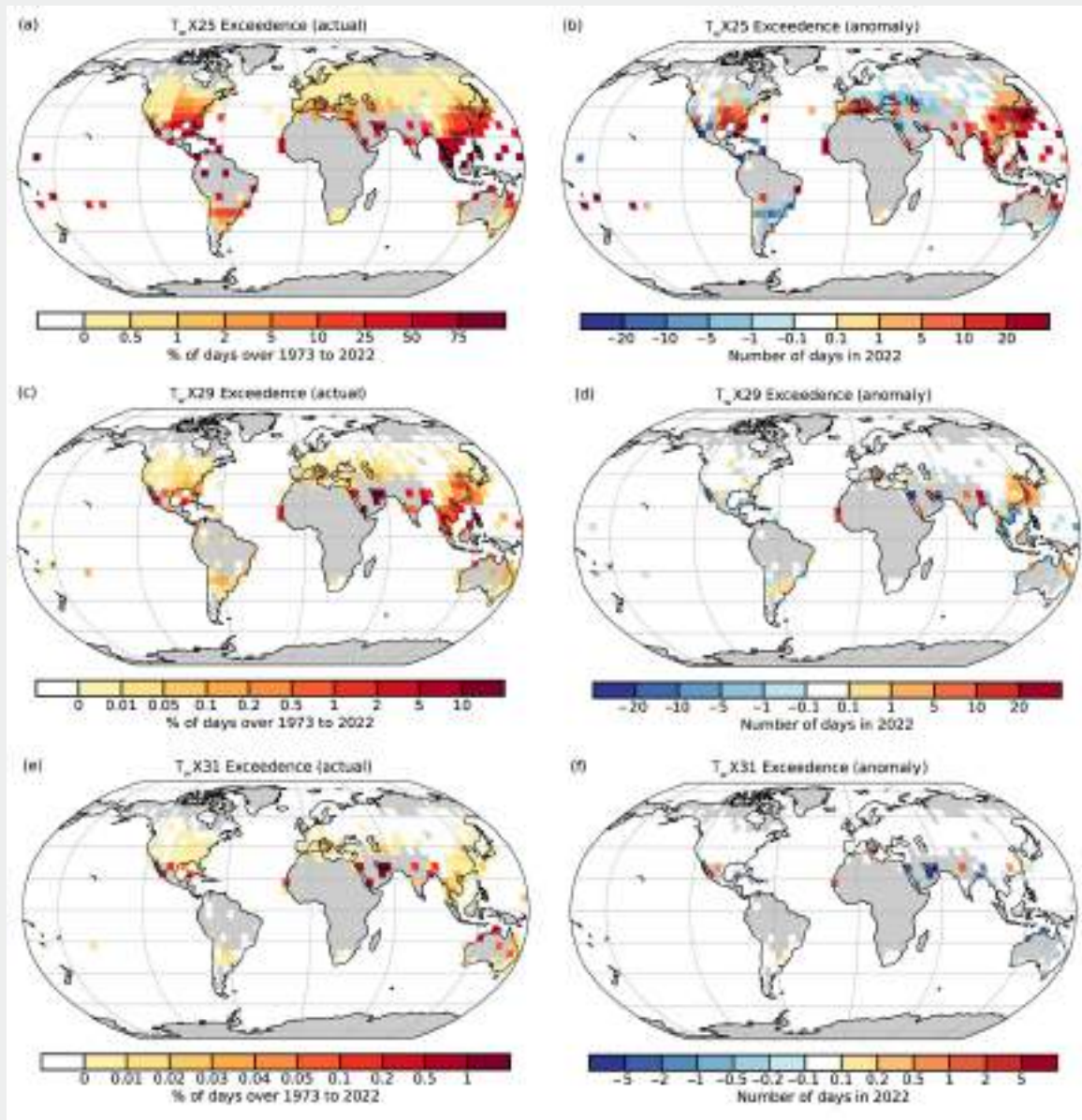


Fig. SB2.1. Number of days where the daily maximum wet bulb temperature is equal to or exceeds set thresholds from HadISDH.extremes. Data have been screened to remove grid boxes where temporal completeness is less than 70% (<35 of 50 yrs). (a),(c),(e) show the percentage of days over the 1973–2022 period and (b),(d),(f) show 2022 annual anomalies compared to the 1991–2020 base period as number of days per year. Panels (a), (c), and (e) identify land regions where there are no exceedances specifically as white grid boxes. This is different from the gray “missing data” regions.

did not during 2022. Interestingly, the 2022 heatwave in the United Kingdom (UK; sections 2b4, 7f2), despite record-breaking dry bulb temperatures, remained below the T_{wX25} threshold and relatively dry in terms of humidity. When averaged globally (Fig. SB2.2a), the T_{wX25} and T_{wX29} indices show significant trends in days at 0.13 ± 0.03 days yr^{-1} decade $^{-1}$ and 0.02 ± 0.01 days yr^{-1} decade $^{-1}$, respectively.

The T_{wX90p} index is more globally applicable, though the current (1991–2020) 90th percentiles for higher latitude grid boxes are less likely to be at levels sufficient to cause significant health impacts. Plate 2.1ag shows eastern North America, the UK/Europe, India, China, Japan, much of Southeast Asia, and eastern Australia with widespread higher-than-average exceedances in 2022. When averaged globally (Fig. SB2.2b) it is clear that the frequency of these ‘moderate’ humid heat extremes are increasing, and 2022 saw a near-record-high number of day counts, surpassed only by 1998, 2016, 2020, and 2021. The long-term trend is 4.6 ± 1.08 days yr^{-1} decade $^{-1}$. This time series also shows clearly that while high-humidity heat events are more common in El Niño years, with peaks occurring in 1998, 2010, and 2016, the more neutral and La Niña years of 2020 and 2021, respectively, were actually comparable.

The T_{wX} index shows that humid heat extremes are also becoming more severe. The global average T_{wX} has significantly increased since the 1970s at 0.13 ± 0.04 °C decade $^{-1}$ and was higher than average for 2022 (Fig. SB2.2c). The spatial anomalies (Plate 2.1ah) for 2022 follow the pattern of T_{wX90p} generally, demonstrating that many regions are experiencing both more frequent and more extreme humid heat events.

This new dataset, HadISDH.extremes, will be updated annually and so can be used to track changes in the frequency and severity of humid heat events. HadISDH.extremes also provides equivalent dry bulb temperature indices that have been identically processed, therefore uniquely enabling analysis of the varying contributions of dry and humid heat to a range of societal impacts.

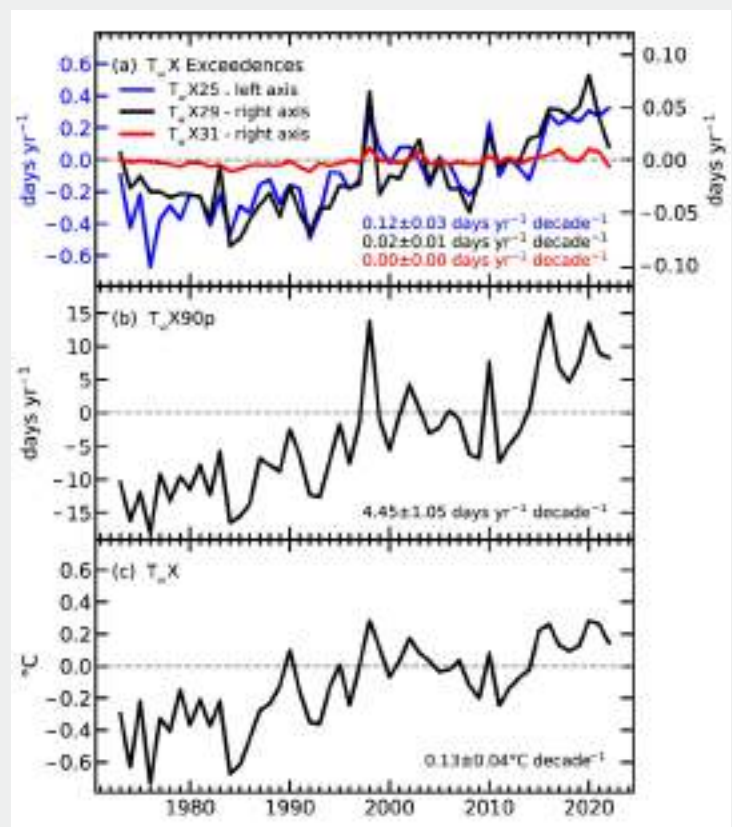


Fig. SB2.2. Global mean annual anomaly time series of various daily maximum wet bulb temperature indices from HadISDH.extremes relative to a 1991–2020 base period. Decadal trends are also shown. These were fitted using an ordinary least squares regression with AR(1) correction following Santer et al. (2008). (a) Annual sums of the daily maximum wet bulb temperature (T_{wX}) $\geq 25^\circ\text{C}$, $\geq 29^\circ\text{C}$, and $\geq 31^\circ\text{C}$ thresholds. (b) Annual sum of the daily maximum wet bulb temperature exceedances of the 90th percentile (T_{wX90p}). (c) Annual mean of the daily maximum wet bulb temperature (T_{wX}) of the month.

2. TOTAL COLUMN WATER VAPOR

—C. A. Mears, J. P. Nicolas, O. Bock, S. P. Ho, and X. Zhou

In 2022, the global land and ocean averages of total column water vapor (TCWV) were near or slightly above the 1991–2020 climatological averages, despite the ongoing presence of La Niña conditions in the tropical Pacific Ocean, which usually reduces the TCWV due to lower tropospheric temperatures. In reanalysis output, 2022 was the 8th (MERRA-2), 10th (JRA-55), and 14th (ERA5) highest/wettest vapor year since 1980. Time series of annual vapor anomalies from different products (Fig. 2.25) agree well for combined land and ocean averages and ocean-only averages. Over land, there is a considerable discrepancy between ERA5 and GPS-RO observations, which show a substantial decrease over land for the last two years, and ground-based GNSS observations and JRA-55 and MERRA-2, which do not show such a drop. The differences arise mainly over Africa and South America (not shown). Similar discrepancies are observed between ERA5 and surface-specific humidity and relative humidity for the last two to three years, where ERA5 is very dry compared to MERRA-2 and HadISDH (section 2d1).

The global map of TCWV anomalies (presented as percent of annual mean values to more clearly show extratropical changes) for 2022 (Plate 2.1i) shows a strong low vapor (or dry) anomaly in the central equatorial Pacific, with a strong high vapor (or wet) anomaly directly to the south and west, including much of Australia and the eastern Indian Ocean south of the equator. Much of the extratropical Northern Hemisphere shows high (wet) anomalies, which are most pronounced in the North Pacific, northern India, and the Tibetan Plateau.

Several regions had record-high or record-low vapor in the annual mean during 2022. Figure 2.26 shows a global map of the number of the three reanalysis products that indicated high or low records by evaluating annual means for the years 1980–2022. All three products agree that the central and eastern equatorial Pacific Ocean experienced a record-low anomaly; the general pattern

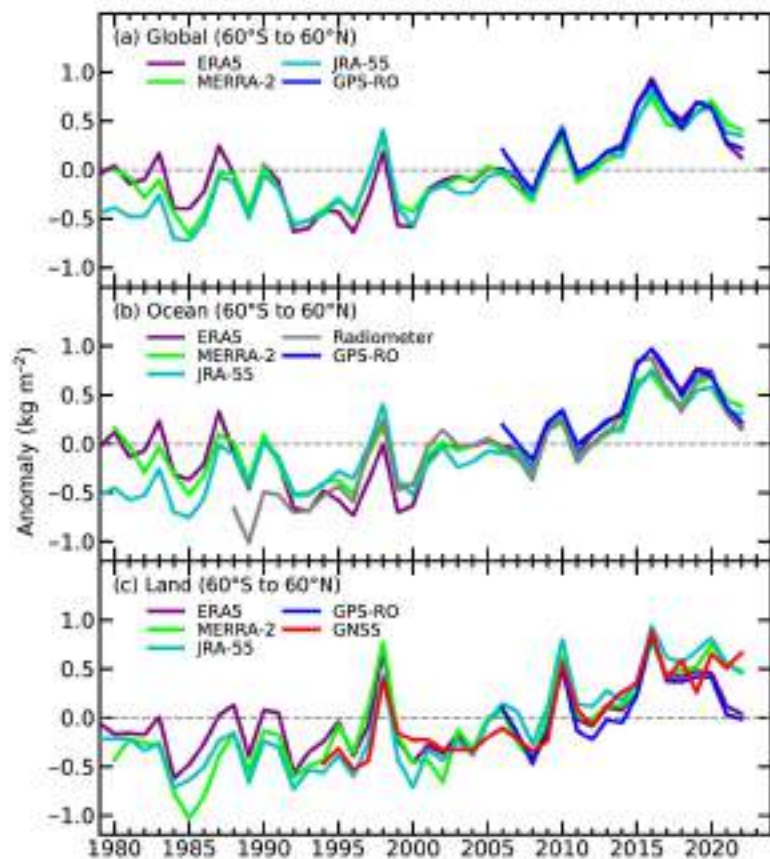


Fig. 2.25. Global mean total column water vapor annual anomalies (kg m^{-2}) over (a) land and ocean, (b) ocean only, and (c) land only from observations and reanalyses (ERA5, MERRA-2, JRA-55). The shorter time series from the observations have been adjusted so that there is zero mean difference relative to the ERA5 results during their respective periods of record.

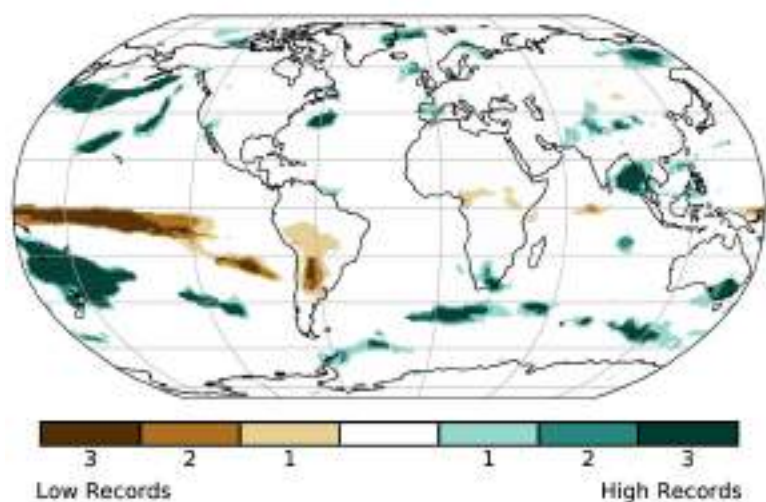


Fig. 2.26. Global map of the number of reanalysis products (out of three) that indicated a record-low or record-high annual mean total column water vapor (TCWV) anomaly during 2022 relative to the 1980–2022 period.

is consistent with typical La Niña behavior (Mears et al. 2022), but the reasons for the strength of the signal in 2022 are not yet understood. The dry anomaly extends into southern South America with slightly less agreement, where it is associated with a multiyear drought in Chile and Argentina (Heath 2022). Several regions of record-high vapor occurred over the midlatitude oceans in both hemispheres, as well as southeast Australia, which also experienced anomalously high rainfall (section 2d4), the north of New Zealand, the Bay of Bengal, and eastern Siberia.

This assessment used three global reanalysis products: ERA5 (Hersbach et al. 2020), MERRA-2 (Gelaro et al. 2017), and JRA-55 (Kobayashi et al. 2015). Measurements made over the oceans by satellite-borne microwave radiometers were used (Remote Sensing Systems Satellite; Mears et al. 2018). GPS-RO observations from the Constellation Observing System for Meteorology, Ionosphere, and Climate (COSMIC), Metop-A, -B, and -C, COSMIC2 (Ho et al. 2020a, b, 2010; Teng et al. 2013; Huang et al. 2013) and Spire satellite missions were used over both land and ocean. The approach to merge the RO data products from multiple RO missions into consistent climate data records is detailed in Shao et al. (2023). The ground-based GNSS dataset (Bock 2022) used in this analysis counts 240 stations, located mainly on continental land and a few islands, with more than 10 years of measurements (Plate 2.1i) among which 207 are located within 60°S–60°N (Fig. 2.25). All three reanalyses assimilate satellite microwave radiometer and GPS-RO data and are, therefore, not entirely independent from these two datasets. Ground-based GNSS measurements are not assimilated and serve as a completely independent dataset.

3. UPPER-TROPOSPHERIC HUMIDITY

—V. O. John, L. Shi, E.-S. Chung, R. P. Allan, S. A. Buehler, and B. J. Soden

Upper-tropospheric humidity (UTH) in 2022 was close to, or slightly below, the 2001–20 average (Fig. 2.27a). The mean and standard deviation of 2022 anomalies was -0.25 ± 0.28 %rh for the satellite microwave humidity sounder dataset (Chung et al. 2013), -0.15 ± 0.60 %rh for the satellite High Resolution Infrared Sounder (HIRS) dataset (Shi and Bates 2011), and -0.17 ± 0.33 %rh for the ERA5 reanalysis (Hersbach et al. 2020). Over the 44-year record, the HIRS and ERA5 time series have statistically insignificant trends of 0.007 ± 0.023 %rh decade⁻¹ and 0.008 ± 0.020 %rh decade⁻¹, respectively. This is consistent with the theoretical consideration that the large-scale relative humidity in the upper troposphere remains approximately constant (Ingram 2010) and implies that the absolute amount of water vapor in the upper troposphere has increased over time.

Increased upper-tropospheric water vapor is also depicted in Fig. 2.27b by a significant positive trend ($+0.105 \pm 0.008$ K decade⁻¹) in the difference between mid- to upper-tropospheric brightness temperature data from satellite microwave sounding unit (MSU) and advanced microwave sounding unit (AMSU) instruments (Zou et al. 2023) and the HIRS upper-tropospheric (UT) water vapor brightness temperatures. MSU instruments measure the radiation emitted by oxygen molecules in the atmosphere. As the concentration of oxygen is not changing, the emission level of the

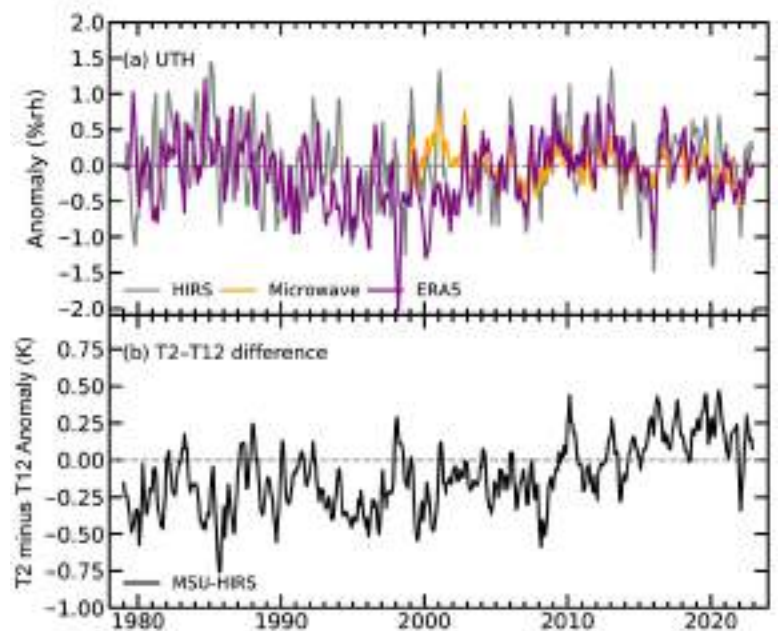


Fig. 2.27. Time series of 60°S–60°N monthly mean anomaly of (a) upper-tropospheric relative humidity (%rh) for the three datasets (see text for details) and (b) the difference between mid to upper-tropospheric temperature (MSU T2) and water vapor channel (HIRS T12) brightness temperatures (K). Anomalies are with respect to the 2001–20 base period.

oxygen channel (measuring UT temperature) is not changing, but as the temperature of the UT increases with time, there is a positive trend in the measurement of this channel (not shown). If there were no increase in water vapor, the emission level of the HIRS water vapor channel would also stay constant in time, which, due to the UT temperature increase, would result in a positive trend in the measurement of this channel and no trend in the difference between the two time series. However, as the water vapor in the UT increases, the water vapor emission level of the HIRS channel shifts higher in the troposphere and measures water vapor emissions from a colder temperature, diverging from the oxygen emission level of MSU. Differencing the time series removes the effect of the temperature increase and shows only the impact of the water vapor changes (e.g., see Soden et al. 2005; Chung et al. 2014).

Monitoring of upper-tropospheric water vapor is crucial to determining one of the strongest positive (amplifying) feedbacks contributing to anthropogenic warming due to its powerful greenhouse effect (see Coleman and Soden 2021 for a detailed description of water vapor feedback).

The agreement among the three UTH datasets is reasonable; the correlations of HIRS and ERA5 with the microwave series during their common period (1999–2022) are 0.6 and 0.5, respectively, despite their structural differences. For example, satellites represent a layer-average UTH with one satellite sampling the same location over Earth only twice a day while ERA5 represents the 400-hPa level RH with hourly sampling. The microwave data have almost all-sky sampling while the HIRS data sample only clear-sky conditions; this sampling difference is one reason for the higher interannual variability in the HIRS data as illustrated in John et al. (2011). Water vapor increases in the upper and lower troposphere since 1979 are captured by climate models when observed sea-surface temperatures are prescribed but smaller than those simulated by coupled climate simulations (Allan et al. 2022). This can be explained by the unusual spatial pattern and resulting magnitude of observed warming compared to that simulated by coupled climate models in the recent period, which included a number of strong La Niña events (Andrews et al. 2022) such as the extended event that affected 2022.

The spatial anomaly patterns (Plate 2.1j for microwave UTH; Fig. 2.28 for HIRS) relate to large-scale weather conditions, with positive (negative) anomalies associated with wetter (drier) conditions at the surface. This is because one of the main drivers of UTH is convection; therefore, UTH is useful for monitoring changes in large-scale dynamics in the atmosphere. Clear La Niña patterns are visible, with positive anomalies over the Maritime Continent and a strong dry signal in the western equatorial Pacific (centered near the date line). Prevailing drought conditions over the western United States, central Europe, and southern China are also reflected in lower-than-average UTH. Drought conditions affecting parts of South America and Angola/Namibia in Africa in 2021 may be associated with low UTH in these regions during 2022, yet severe drought affecting East Africa in 2022 is not, implying that the link between UTH and dry conditions is complex. Higher-than-average UTH over Pakistan, Nigeria, eastern Australia, and northern Brazil are associated with a series of substantial rainfall events with associated flooding in 2022.

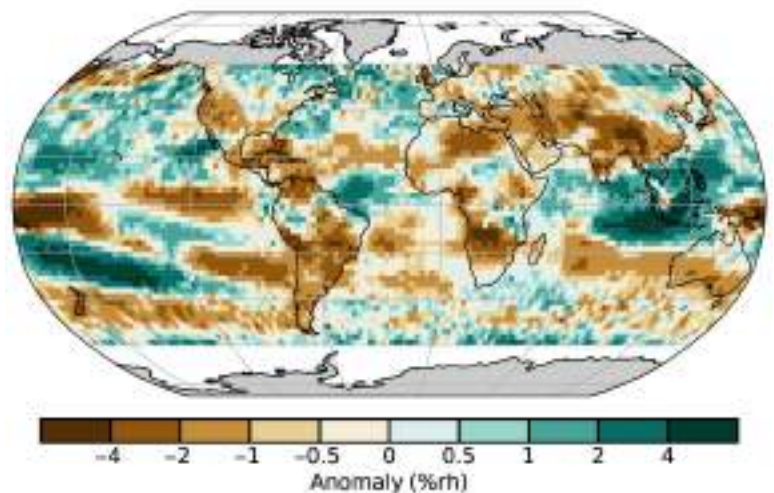


Fig. 2.28. Upper-tropospheric humidity anomaly map (%rh) for 2022 for the HIRS data record with respect to the 2001–20 base period.

4. PRECIPITATION

—R. S. Vose, R. Adler, G. Gu, U. Schneider, and X. Yin

Precipitation over global land areas in 2022, as estimated from two different monitoring products, was near or slightly below the 1991–2020 long-term average (Fig. 2.29a). In particular, the gauge-based product from the Global Precipitation Climatology Centre (GPCC; Becker et al. 2013) had an anomaly of -4.34 mm for 2022, and the blended gauge–satellite product from the Global Precipitation Climatology Project (GPCP; Adler et al. 2018) had an anomaly of -0.11 mm. Both products indicate that mean global land precipitation in 2022 was less negative than in 2021.

According to the GPCP product, the precipitation anomaly over the global ocean (Fig. 2.29b) was -18.03 mm, and the overall global (i.e., land plus ocean) anomaly (Fig. 2.29c) was -13.02 mm. Both anomalies are less negative than the previous year. The negative ocean and global anomalies are typical of La Niña, wherein below-normal sea-surface temperatures in the eastern tropical Pacific Ocean are associated with suppressed convection and rainfall. Overall, the GPCP product ranks 2022 as the fourth-driest year in the global record (Fig. 2.29c), which begins in 1979.

Over global land areas, the highest positive precipitation anomalies in 2022 were across northern South America and the Maritime Continent, and the greatest negative precipitation anomalies were over western and central North America, central South America, western Europe, and parts of southern and eastern Africa (Plate 2.1k). Over the global oceans, high positive precipitation anomalies extended from the eastern Indian Ocean southeastward to the tropical western Pacific Ocean. Parts of the equatorial Atlantic Ocean and the Southern Ocean near South America were also much wetter than average. In contrast, large negative precipitation anomalies were apparent over much of the central Pacific Ocean and the western Indian Ocean and, to a somewhat lesser extent, over parts of the north Atlantic Ocean.

La Niña, along with the Indian Ocean dipole, influenced precipitation patterns across the globe again in 2022, particularly in the tropics. The current La Niña began in 2020, and while it has varied in intensity since that time, there is a notable resemblance between the annual precipitation anomaly patterns of the past two years. For example, wetter-than-normal conditions once again extended from the Maritime Continent into the South Pacific Ocean and from northern South America into the equatorial Atlantic Ocean. Likewise, much of the central Pacific Ocean near and south of the equator were drier than normal again in 2022, as was much of the North Atlantic Ocean. The largest anomalies at the core of these wet and dry features exceeded 500 mm per year. These tropical La Niña features in 2022 helped to fuel frequent flood and landslide conditions (section 2d5), for example, in Indonesia and Malaysia, Indochina, southern India, Pakistan, and the southeast quadrant of Australia. Floods and landslides were also more prevalent across northern South America and eastern Brazil.

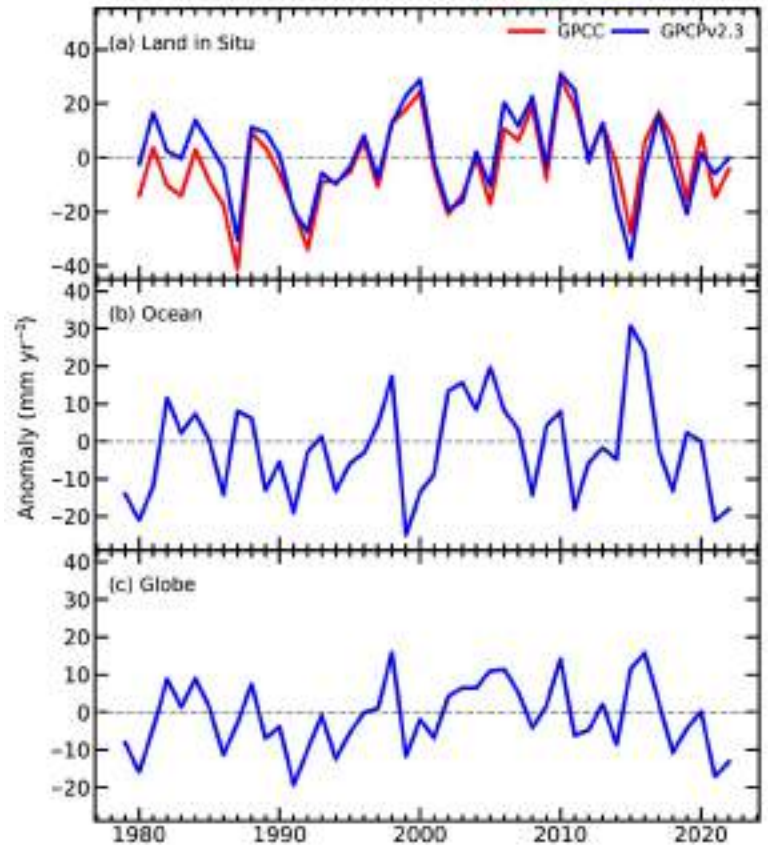


Fig. 2.29. Globally averaged precipitation anomalies (mm yr^{-1} ; 1991–2020 base period) over (a) land, (b) ocean, and (c) the globe (land and ocean). Land and ocean time series were created using a proportional land/sea mask at the $1^\circ \times 1^\circ$ scale.

5. LAND SURFACE PRECIPITATION EXTREMES

—M. R. Tye, S. Blenkinsop, M. G. Bosilovich, M. G. Donat, I. Durre, C. Lennard, I. Pinto, A. J. Simmons, and M. Ziese

Continuing La Niña conditions (see Sidebar 3.1 and section 4b for details) contributed to lower maximum-intensity rainfall than the 1991–2020 mean in South America and southern Africa and higher maximum-intensity rainfall in eastern Australia (Plate 2.11; Figs. 2.30, 2.31), continuing the pattern from recent years. Some regions with less intense rainfall extremes than average, such as Bangladesh, China, southern Europe, and the central and southwestern United States, also experienced wide-spread drought, exacerbating the resultant floods and landslides when extreme precipitation occurred over dry land.

Here, we focus on rainfall intensity indices: Rx1day (maximum rainfall in 24 hours) and Rx5day (maximum accumulated rainfall over five consecutive days). These metrics reflect strong potential for societal impacts from flooding. We use a combination of gauge-based (Global Historical Climatology Network daily [GHCND], Menne et al. 2012; GPCC, Ziese et al. 2022), reanalysis (ERA5, Hersbach et al. 2020; MERRA-2, Gelaro et al. 2017) and satellite (Climate Hazards Group InfraRed Precipitation with Station data [CHIRPS], Funk et al. 2015) data. Records demonstrate that a proportion of the globe experiences extreme precipitation in any given year. The reported events were exceptional in terms of Rx1Day and Rx5Day but are not a comprehensive list. Details on extreme flooding events can also be found in Chapter 7.

Pakistan received around three times its normal volume of monsoon precipitation in August (ECMWF 2022), with some regions receiving up to eight times their expected monthly totals (PMDNWFC 2022). It was the wettest August since Pakistan records began in 1961. Figures 2.30 and 2.31 (and Plate 2.11) show widespread strong positive Rx5day anomalies over the region. The monsoon axis was farther south than normal and was accompanied by a strong land/sea heat contrast (PMDCDPC 2022). Approximately 15% of the South Asia region (as defined in Iturbide et al. 2020) received Rx1day and Rx5day precipitation totals up to 2.5 times greater than their previous records. Recent analysis indicates that Rx5day over the Sindh and Balochistan provinces is now about 75% more intense than it would have been without climate change (Otto et al. 2022). Similar to

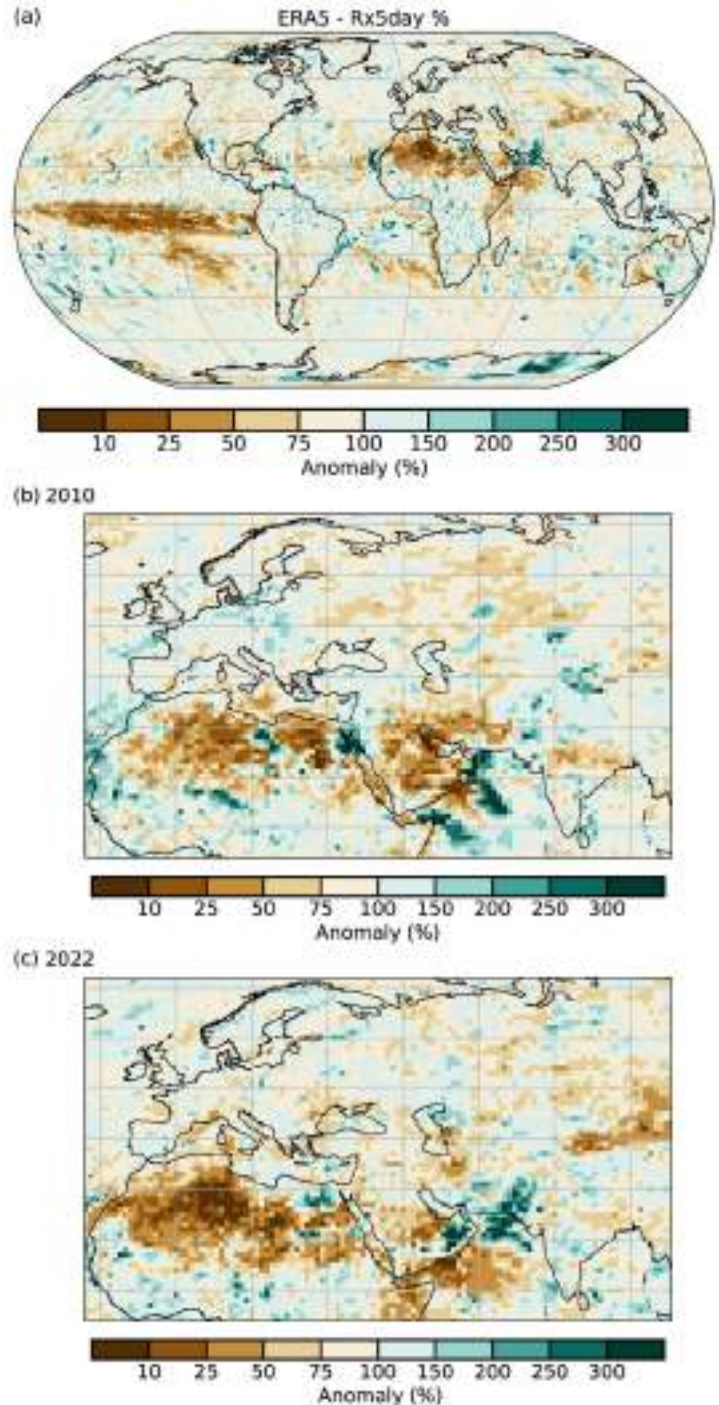


Fig. 2.30. Annual maximum five-day precipitation (Rx5day) as a percentage of the 1991–2020 average for (a) the globe and over Europe and South Asia in (b) 2010 and (c) 2022. (Source: ERA5.)

the 2010 La Niña, the duration and intensity of the most extreme rains over Pakistan in 2022 were abnormally high, while net monsoon rains over Bangladesh were below average (Rajeevan et al. 2011; Figs. 2.39b,c). Heavy rains in south and east China in June exceeded decades-old records (NCEI 2023; Fig. 2.30a), continuing a pattern of above-average Rx1day observed in this region in 2020 and 2021.

Australian floods in Queensland and eastern New South Wales between February and March caused 22 fatalities and were the costliest on record for the insurance sector (Aon 2023). Several locations had Rx5day >1000 mm during February, with Brisbane receiving 677 mm over three days and some locations doubling their previous five-day annual record (Fig. 2.31). Further flooding occurred in eastern Australia during October and November, with around 11% of Victoria gauges and 13% of New South Wales gauges reporting record Rx1day totals over the two months and around 67% of the area in the top 1% of recorded daily totals (Bureau of Meteorology [BOM] 2023; Plate 2.11; Fig. 2.30a).

Floods and landslides occurred following heavy rainfall between 11 and 13 April over southeastern South Africa (OCHA 2022a). Rx1day at Pennington South (307.2 mm) and at King Shaka Airport (221.2 mm) were more than three and four times their previous daily records, respectively (SAWS 2022). This resulted in more than \$3.6 billion in economic loss and 455 fatalities (Aon 2023).

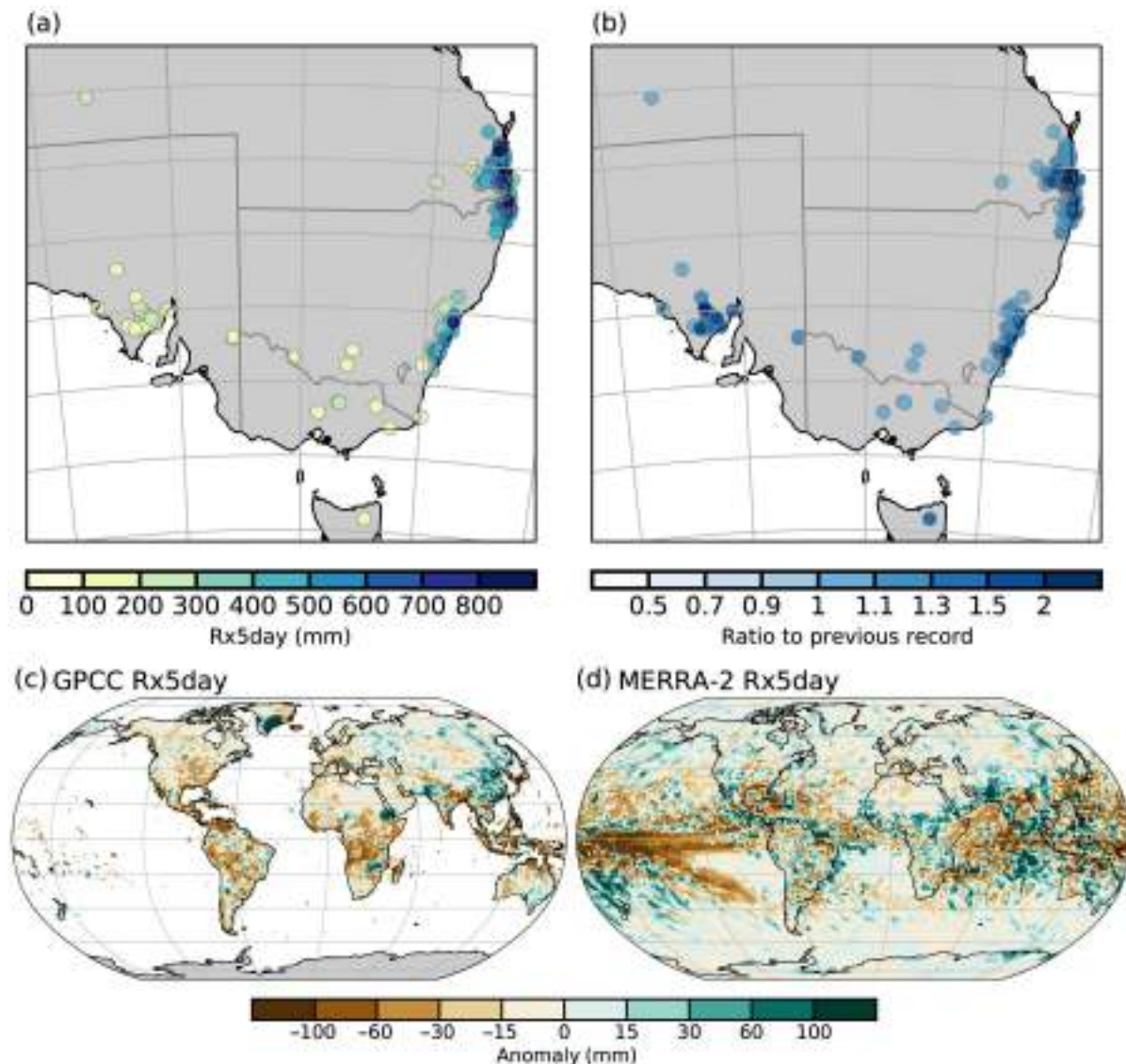


Fig. 2.31. Annual maximum five-day precipitation record-breaking totals from GHCN over southeastern Australia in Feb 2022 for (a) absolute values (mm) and (b) ratios to the previous record; (c) GPCP global Rx5day anomalies from 1981–2022 mean (mm); and (d) MERRA-2 global Rx5day anomalies from 1991–2020 mean (mm).

Heavy rainfall associated with a succession of four tropical cyclones between January and February 2022 over Madagascar, Mozambique, and Malawi caused severe humanitarian impacts and infrastructure destruction (see sections 4g6 and 7e5 for details).

Despite a wetter-than-average autumn over some parts of western and northern Europe, drier-than-average conditions persisted over most of Europe (section 7f) and were accompanied by ~67% of the Mediterranean and southern Europe region experiencing Rx1day up to 70% lower than normal (Plate 2.1l; Fig.2.30a). Exceptions to this pattern were Spain and Portugal during December. NOAA’s Climate Extremes Index component 4 (CEI4; Gleason et al. 2008) reported a slightly above-average year (12% compared to the long-term mean of 10.4%) for the percentage of the contiguous United States experiencing extreme one-day precipitation. While some regions had record-breaking values of CEI4 in summer and autumn, they do not include those affected by Hurricanes Fiona and Ian. Hurricane Ian was the second-costliest disaster on record (see Sidebar 4.1), bringing exceptional Rx1day and Rx5day to Florida as evidenced in Fig. 2.30a and Plate 2.1l.

6. CLOUDINESS

—C. Phillips and M. J. Foster

Cloudiness in 2022 was at its lowest coverage since the Pathfinder Atmospheres – Extended (PATMOS-x v6.0; Foster et al. 2023) satellite record began in 1980, with a mean global cloud area fraction of 65% (Figure 2.32). Dataset reliability is lower this year (see below), but the Clouds and the Earth’s Radiant Energy System Energy Balance and Filled (CERES EBAF) record, beginning in 2000 supports this by showing 2022 as having the second-lowest amount of solar radiation reflected by clouds relative to clear-sky. The eruption of the large Hunga Tonga–Hunga Ha’apai volcano in the South Pacific, which ended on 15 January, had the potential to impact the global or regional cloud amount, and a sharp decrease in global cloudiness was observed afterwards. However, Plate 2.1m and closer spatial analysis did not indicate any definitive connection to the eruption.

During 2022, there were several important satellite transitions, launches, and changes affecting cloud observation from space. Most relevant here, the *Aqua* satellite used previously (Platnick et al. 2015; Phillips and Foster 2022) started to drift significantly in orbit. The effective sampling time-of-day is no longer stable, and systematic diurnal variation of cloudiness must be accounted for. The PATMOS-x v6.0 cloud climate dataset (Foster et al. 2023) is used instead. Its constituent satellites also suffer from severe orbital drift and intersatellite differences, but the record starts in 1980 and is thus much longer than *Aqua* Moderate Resolution Imaging Spectroradiometer (MODIS), which begins in 2002.

Differences in sensors can make comparison difficult, as the errors in cloud area fraction are likely to be systematic and conditional on the cloud type, time of day, scan angle, surface type, etc. This is exemplified by the differing trends between the PATMOS-x cloudiness (Fig. 2.32) and the *Aqua* MODIS-C6.1 cloudiness. PATMOS-x shows a long-term decline in cloud area fraction, whereas *Aqua* MODIS-C6.1 previously showed an increase (Phillips and Foster 2022), and the drifting *Aqua* MODIS-C6.1 recorded the most cloud coverage on record for 2022 (not shown). For context, Fig. 2.33 shows the cloud radiative effects from CERES EBAF-top-of-atmosphere

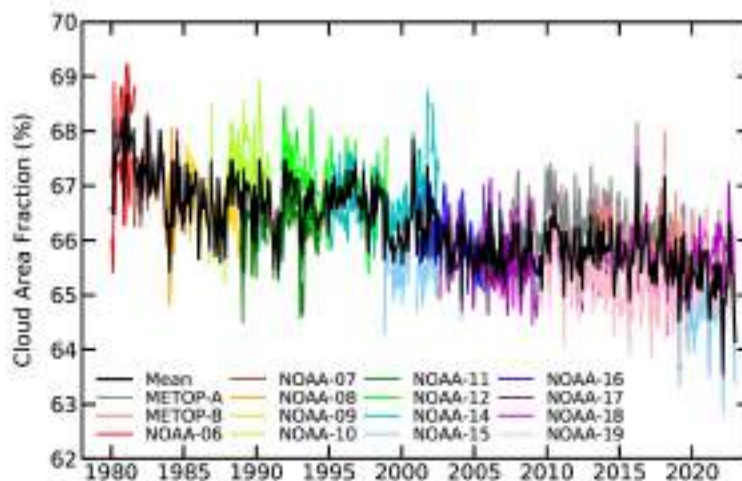


Fig. 2.32. Global mean cloud area fraction (%). (Source: PATMOS-x v6.0 [Foster et al. 2023].)

Ed4.2 through December 2022 (Loeb et al. 2018). Cloud radiative effect in this case is defined as the difference between average clear-sky observed radiative flux and average all-sky observed radiative flux. Shortwave cloud radiative effect (SWCRE) in 2022 was the second highest since the record began in 2000. This means that clouds had an anomalously large warming effect (less cooling) in the shortwave as a result of reflecting less radiation back out to space and permitting more to reach the surface. Conversely, the longwave cloud radiative effect (LWCRE) in 2022 was the second lowest. This corresponds to clouds having a stronger cooling effect (less warming) in the longwave as a result of permitting more radiation out into space and trapping less close to the surface. Added together, the shortwave and longwave cancel out such that the cloud radiative effect in 2022 was close to the mean value ($+0.05 \text{ W m}^{-2}$). More details on radiative flux and energy budget can be found in section 2f1.

Note that the cloud radiative effect can vary as the surface warms and/or changes albedo (section 2h1) without any change in cloud properties at all. However, if the cloud area fraction is indeed decreasing (as measured by PATMOS-x), this is consistent with the observed positive shortwave and negative longwave cloud radiative effect. Fewer clouds mean more absorbed solar radiation as opposed to reflected and also more longwave emission to space from the warm surface. Cloudiness has long been a difficult essential climate variable to quantify, and we conclude that uncertainty remains large.

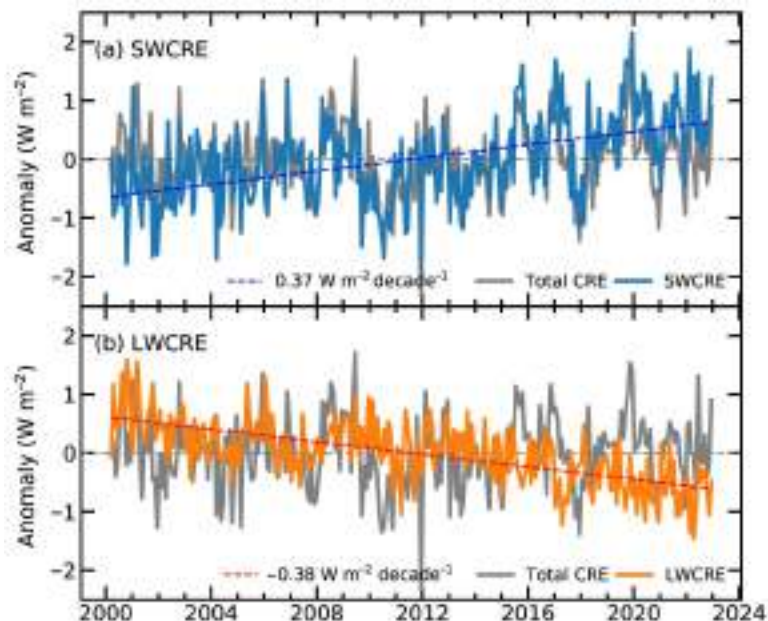


Fig. 2.33. Cloud radiative effect (CRE) anomaly (W m^{-2}) from the dataset CERES EBAF Ed4.2 (Loeb et al. 2018) representing the changes in top-of-atmosphere radiative forcing that are attributable to clouds (which could include both changes to clouds themselves and surface changes masked by clouds). Positive values indicate (a) cloudiness-related warming through more radiation reaching the surface and less being reflected back out to space (SWCRE, blue line) or (b) more being trapped close to the surface rather than escaping out to space (LWCRE, orange line). Gray line is total CRE. Negative values indicate cloudiness-related cooling.

7. LAKE WATER LEVELS

—B. M. Kraemer, H. A. Dugan, S. La Fuente, and M. F. Meyer

For 264 of the world's largest lakes, the 2022 mean water-level anomaly was 1.59 m above the 1992–2002 baseline, with 67% having higher-than-average levels (data from Birkett et al. [2022]; Birkett and Beckley [2010]; Crétaux et al. [2011]). Water-level anomalies ranged widely from -65.75 m to $+157.02 \text{ m}$, with the most extreme anomalies due to reservoir filling and drainage. The median water-level anomaly was $+0.28 \text{ m}$ with an interquartile range of -0.14 m to $+1.12 \text{ m}$. These measurements support understanding of global hydrological changes, water availability, drought, and the impact of human water diversions on lake water levels. Climate change affects these water levels by altering global precipitation patterns (Konapala et al. 2020) and increasing atmospheric water loss from inland waters due to higher evaporation rates (Zhao et al. 2022; Sharma et al. 2019).

Water-level anomalies in lakes varied greatly but with some regional consistency (Plate 2.1n). Lakes in the western United States, southern South America, the Middle East, and the Caucasus in eastern Europe had consistently below-normal water levels, due to a combination of a surface-vapor pressure deficit (as seen in Plate 2.1 and section 2d1), enhanced water evaporative loss, reduced precipitation, increasing human water use, and other factors (Friedrich et al. 2018;

Khazaei et al. 2019; Pisano et al. 2020). The largest negative volumetric anomalies (water-level anomalies multiplied by static lake surface area from HydroLAKES; Messenger et al. 2016) were all in the Middle East, including the Caspian Sea, Aral Sea, and Lake Urmia (Fig. 2.34). Lakes in Canada, the tropics, and southern Asia tended to have positive water-level anomalies. The six largest positive volumetric anomalies were all found in tropical Africa: Lakes Victoria, Tanganyika, Malawi/Nyasa, Turkana, Volta, and Nasser (Fig. 2.34) due to years of above-average precipitation (although the tropical African precipitation anomaly for 2022 was not above average, as seen in Plate 2.1k). Positive water-level anomalies can be explained in general by climate variability and change through increasing heavy precipitation, as well as by dam management and reductions in human water demand (Vanderkelen et al. 2018). Snowmelt may also contribute to higher water levels in northern and high-altitude regions (Zhang et al. 2019; Woolway et al. 2020; Kraemer et al. 2019). In general, the global patterns in water-level anomalies with radar altimetry match those observed using data from the Gravity Recovery and Climate Experiment (GRACE) satellite mission (as seen in Fig. 2.34 and section 2d8; Landerer and Swenson 2012) with exceptions in East Africa and northern North America where local lake conditions may cause water levels to diverge from terrestrial water storage patterns.

To detect water-level anomalies for 2022, we used radar altimeter measurements obtained from the NASA/CNES Topex/Poseidon and Jason satellite missions through the Global Reservoir and Lake Monitoring (G-REALM; https://ipad.fas.usda.gov/cropexplorer/global_reservoir/) project

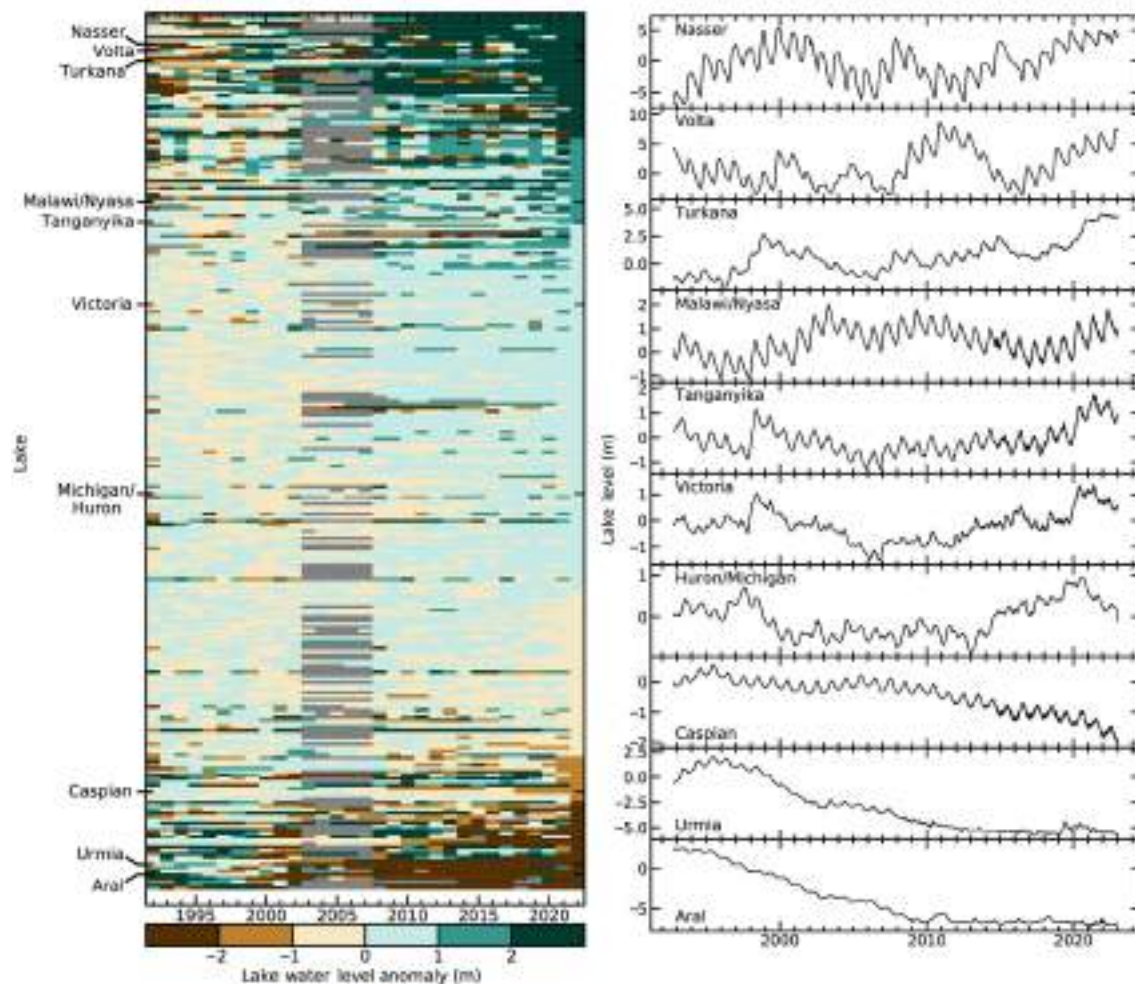


Fig. 2.34. Lake water-level anomaly (m) time series for 264 globally distributed lakes ranked by their 2022 anomaly relative to the 1992–2002 mean (based on data from Birkett et al. 2022; Birkett and Beckley 2010; Crétaux et al. 2011). Of the 264 water level time series, 106 had substantial data gaps from 2003 to 2008 due to changes in the orbital pathways of the satellite altimeters during that time period. The subset of lakes that are named on the y-axis of (a) and plotted in (b) are those with the 10 largest anomalies (either positive or negative) when water levels anomalies were weighted by the surface area of each lake. The time series plots (b) are sorted by volumetric anomalies with the largest positive anomaly on the top and the largest negative anomaly on the bottom.

version 2.5 (Birkett et al. 2022; Birkett and Beckley 2010) and Theia's Hydroweb database (downloaded 16 January 2022; <https://hydroweb.theia-land.fr/>; Crétaux et al. 2011). Lake surface areas are from the HydroLAKES database (Messenger et al. 2016). The 264 lakes in this analysis contain more than 90% of Earth's liquid surface freshwater (Messenger et al. 2016), have the longest (31+ years) and highest resolution time series, and are updated in near real-time. Water levels are usually measured every 10 days, but with some lake-to-lake variation. To ensure consistency, the lake time series were linearly interpolated to daily timescales. Due to changes in orbital pathways of the satellite altimeters, 103 of the 264 lakes had substantial data gaps from 2003 to 2008, thus a period before these gaps (1992–2002) was used as the baseline for calculating anomalies. Monitoring lake water levels on-site is important for verifying and adjusting satellite estimates of long-term water level changes. However, the lack of readily available, machine readable, and near-real-time data limits our ability to monitor global-scale changes using only on-site data. Comparisons between satellite altimeter and on-site measurements have a root mean square error of ~5 cm for large lakes (Birkett and Beckley 2010).

Satellite radar altimeters are an effective tool for monitoring volumetric change in inland waters, as they provide frequent coverage regardless of cloudiness. However, most satellite altimeters were designed for mapping ocean heights and are best used to monitor the largest lakes (Crétaux et al. 2011; >1000 km²). By chance, 155 smaller lakes (10 km²–1000 km²) are also included here because they had enough overpasses. Multispectral satellites like LandSat-8/9 and Sentinel-2 can detect changes in lake area (Khandelwal et al. 2022; Pekel et al. 2016; Meyer et al. 2020) at high-resolution (30 m) and frequent coverage (10 days–16 days), but require cloud-free conditions. The December 2022 launch of the Surface Water and Ocean Topography (SWOT) satellite is anticipated to revolutionize lake water-level monitoring due to its high spatial resolution (50 m) and frequent coverage (≤ 21 days) (Biancamaria et al. 2016). Meanwhile, efforts to harmonize existing lake water-level data sources and develop tools to improve accessibility will enhance our understanding of water cycle variations.

8. GROUNDWATER AND TERRESTRIAL WATER STORAGE

—M. Rodell and D. N. Wiese

Terrestrial Water Storage (TWS; the sum of groundwater, soil moisture, surface water, snow, and ice) reached 20-year highs or lows in several regions in 2022. Changes in mean annual TWS between 2022 and 2021 are plotted in Plate 2.10 as equivalent heights of water (cm). Drought and heat continued to affect southern Europe in 2022, with TWS reaching 20-year lows in the Danube River basin and in the Alps. Drought in western Iran also worsened with another year of large TWS losses (some >9 cm). Above-normal precipitation provided some relief to western Russia, but TWS remained below average. Large increases in TWS (some >12 cm) were seen in Southeast Asia, due in part to the heaviest rain in 60 years falling in southern China in June and Typhoon Noru causing flooding in Vietnam and Laos in September (see section 7g for details). TWS in central and southern India approached 20-year highs as well. Extreme drought struck the Yangtze River basin in the summer of 2022, causing the river to reach record-low levels and severely depressing TWS in the region. Southeastern Australia had a very wet year, with multiple episodes of extreme rain and flooding contributing to 20-year high TWS in the Murray-Darling River basin by the end of the year. Conversely, north-central Australia became notably drier (section 7h4). Wet weather caused TWS increases in the northern portion of sub-Saharan Africa and in South Africa, with the latter experiencing record-breaking rainfall in April. Drought affected a large area of south-central Africa centered on Lake Tanganyika, diminishing TWS, yet TWS remained above normal in almost all of sub-Saharan Africa. In North America, dry weather caused TWS declines up and down the U.S. Central Plains, while previously elevated TWS dropped closer to normal levels in the eastern United States. As a result, TWS in the Mississippi River basin dropped to a 20-year low, as water levels in October in the lower Mississippi River itself were the lowest since at least 1988. TWS in the southwestern United States was nearly unchanged from the low levels in that region in 2021. TWS increased in south-central Canada

and decreased in north-central Canada. In South America, eastern Brazil gained a huge amount of water, exceeding 12 cm over a large area, while northern Brazil added to already elevated TWS levels. Much of the western half of the continent's TWS experienced declines due to subpar rainfall.

Figures 2.35 and 2.36 depict zonal-mean and global-mean TWS anomalies, respectively, since April 2002 after removing the seasonal cycle. Data gaps occur during the interim between the GRACE and GRACE-FO missions and when onboard instruments were shut down for various reasons. In addition to excluding from these averages TWS declines associated with ice sheet and glacier losses in Antarctica, Greenland, the Gulf Coast of Alaska, and polar islands (as per Rodell and Wiese 2022), more areas where glacier ablation caused long-term trends in High Mountain Asia, western Canada, and in the southern Andes were also excluded this year. Most notably, 2022 witnessed intensification of both a dry zone between about 25°N and 45°N and a wet zone between about 8°S and 15°N (Fig. 2.35). The former is attributable to TWS declines in the central and eastern United States, southern Europe, the Caspian Sea and adjacent lands, and eastern China. The latter was caused by TWS gains in eastern Brazil, northern sub-Saharan Africa, southern India, and southeastern Asia. South of that zone of wetness, dryness that began in 2019 or earlier appears to be abating, also owing to TWS gains in eastern Brazil. At the global scale (Fig. 2.36), TWS, excluding ice sheets and glaciers, fluctuated by about 1 cm throughout the year, remaining stable with respect to 2021 and somewhat low overall.

TWS is a useful indicator of hydroclimatic variability because it reflects the integrated effects of weather over months to years. Groundwater and terrestrial water storage are not well monitored at regional and larger scales using conventional approaches, but the GRACE and GRACE Follow-On satellite missions have provided global, monthly time series of TWS anomalies (departures from the long-term mean) since 2002 (Tapley et al. 2004; Landerer et al. 2020). On a monthly scale, uncertainties are typically around 1 cm to 2 cm equivalent height of water over a 500,000 km² region at midlatitudes (Wiese et al. 2016). Groundwater typically dominates the interannual variations in TWS except in the wet tropics (dominated by surface water) and high latitude and alpine regions (dominated by ice and snow; Getirana et al. 2017).

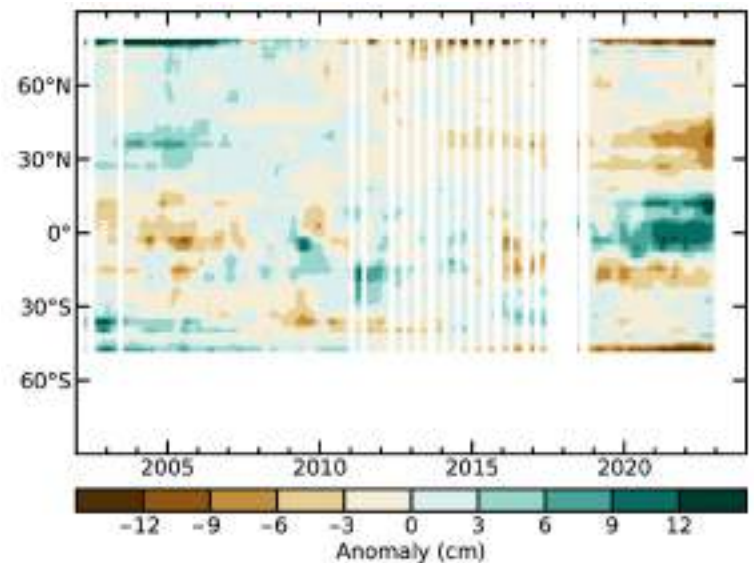


Fig. 2.35. Zonal means of monthly terrestrial water storage anomalies, excluding those in Antarctica, Greenland, the Gulf Coast of Alaska, polar islands, and major glacier systems, in cm equivalent height of water (cm), based on gravity observations from GRACE and GRACE-FO. Anomalies are relative to a 2003–20 base period.

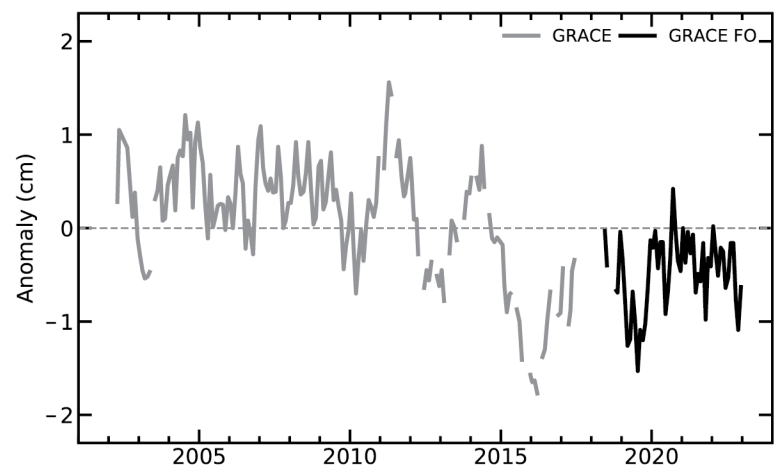


Fig. 2.36. Global average terrestrial water storage anomalies from GRACE (gray) and GRACE-FO (black), in cm equivalent height of water (cm), relative to a 2003–20 base period.

9. SOIL MOISTURE

—P. Stradiotti, W. Preimesberger, R. van der Schalie, R. Madelon, N. Rodriguez-Fernandez, M. Hirschi, A. Gruber, S. Hahn, W. A. Dorigo, R. A. M. de Jeu, and R. Kidd

The year 2022 saw a global increase in average soil moisture for the fourth consecutive year, with conditions close to the previous wet record of 2011 and of similar magnitude in both the Southern and Northern Hemisphere (SH and NH; Fig. 2.37). The year was generally a continuation of 2021 (van der Schalie et al. 2022), the largest difference between the two consisting of a transition from below- to above-average soil moisture (compared with the 1991–2020 base period) in parts of the SH (Fig. 2.38).

The third consecutive La Niña year (2020–22; see Sidebar 3.1 for details) brought about distinct patterns of precipitation (section 2d4) resulting regionally in above-average soil moisture. This was the case for eastern Australia, where wetter-than-normal conditions persisted throughout the year and turned into localized strong positive anomalies (above $0.1 \text{ m}^3 \text{ m}^{-3}$; Supp. Fig. A2.8). Widespread strong positive anomalies of similar magnitude also characterized most of South and mainland Southeast Asia since the start of the year, linked to the effect of La Niña on rainfall in the wet season (Hrudya et al. 2021). With the onset of the Indian summer monsoon, these conditions shifted from central and southern India to northwestern India and Pakistan, coinciding with severe floods (Smiljanic et al. 2022). Consistent with 2021, southeastern Africa (including southern Mozambique and South Africa) experienced a wetter-than-usual phase starting in April and characterizing the whole dry season until November. Northeast Brazil started the year with strong wet anomalies that dried to average conditions by April, only to strengthen again in November and December. Areas of above-average soil moisture were also noticeable in eastern Europe and in the coastal regions surrounding the Yellow Sea for most of 2022.

While on average 2022 recorded wetter-than-normal soil moisture conditions, dry conditions were dominant in several regions. The Great Plains of central North America experienced notable below-average conditions (consistent with the deeper layers; section 2d8) that worsened during the year. These likely intensified the summer heatwaves affecting the region through local land–atmosphere interactions (Benson and Dirmeyer 2021). The strong (below $-0.1 \text{ m}^3 \text{ m}^{-3}$) dry anomalies developed in the southern Great Plains and moved northward, reaching Montana and the Canadian Prairies

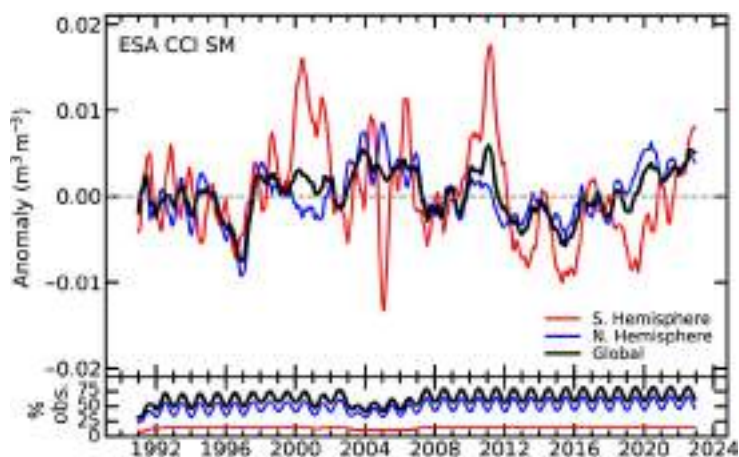


Fig. 2.37. Time series of global (black), Northern Hemisphere (blue), and Southern Hemisphere (red) monthly surface soil moisture anomalies for the period 1991–2022 (upper, $\text{m}^3 \text{ m}^{-3}$; 1991–2020 base period) and the valid observations as a percentage of total global land surface (lower, %). Data are masked where no retrieval is possible or where the quality is not assured and flagged, for example due to dense vegetation, frozen soil, or radio frequency interference. (Source: C3S Soil Moisture.)

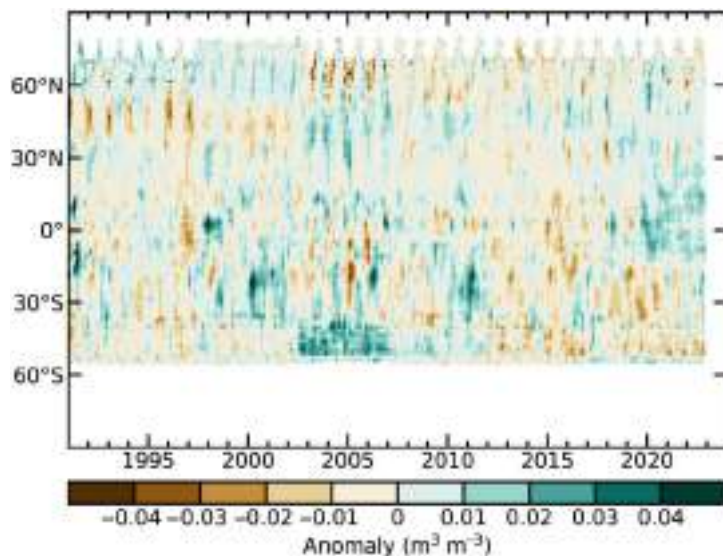


Fig. 2.38. Time–latitude diagram of monthly surface soil moisture anomalies ($\text{m}^3 \text{ m}^{-3}$; 1991–2020 base period) for the period 1991–2022. Data are masked where no retrieval is possible or where the quality is not assured and flagged, for example due to dense vegetation, frozen soil, or radio frequency interference. (Source: C3S Soil Moisture.)

in autumn. This aggravated the water deficit of the region for the second consecutive year (van der Schalie et al. 2022). Persistent dry conditions also continued in southern South America and were especially pronounced in the Rio Paraná basin and Patagonia, now in a four-year-long drought spell (Naumann et al. 2021). In eastern Africa, the Indian Ocean dipole (IOD) is one of the main drivers of intra-annual climatic variability along with the El Niño–Southern Oscillation (Nicholson 2017; Marchant et al. 2007; Anderson et al. 2022). The negative IOD mode, which lasted until October 2022 (see section 4f for details), is consistent with the below-average soil moisture observed for most of the Horn of Africa, northern Mozambique, and Madagascar, developing into very dry conditions toward the end of the year. Negative anomalies for the region are a continuation of the severe droughts in recent years (Anderson et al. 2022). Mild negative anomalies remained steady throughout 2022 around the Mediterranean Sea regions (Spain, northern Morocco, Libya, and Tunisia). In large parts of China and northern Asia, widespread negative anomalies persisted and intensified in the eastern Siberian tundra region at the end of the boreal autumn. However, the strong negative water deficit in the Yangtze River basin (section 2d8) is not as visible in the surface layer.

A strong intra-annual variation was observed in western and northern Australia, with average to very dry conditions (below $-0.1 \text{ m}^3 \text{ m}^{-3}$) in the first part of the year giving way to slightly positive anomalies from mid-year. A similar progression was observed for the Arabian Peninsula and the Persian plateau, northern Europe (Scandinavian peninsula), and the southern Sahel regions. In contrast, the Pacific Northwest region started 2022 with above-average conditions, which subsided toward the boreal summer, turning to below-average soil moisture by the end of the year.

Soil moisture was observed by microwave satellite remote sensing of the upper few centimeters of the soil layer, as provided by the COMBINED product of the Copernicus Climate Change Service (C3S) v202012 (Dorigo et al. 2017). C3S combines multi-sensor data in the 1978–2022 period through statistical merging (Gruber et al. 2017, 2019). Wet and dry anomalies here refer to the positive and negative deviations respectively from the 1991–2020 climatological average.

10. MONITORING GLOBAL DROUGHT USING THE SELF-CALIBRATING PALMER DROUGHT SEVERITY INDEX

—J. Barichivich, T. J. Osborn, I. Harris, G. van der Schrier, and P. D. Jones

The self-calibrating Palmer Drought Severity Index (scPDSI) over the period 1950–2022 shows that the ongoing increase in global drought since mid-2019 (Barichivich et al. 2020, 2021) reached a new historical peak in October 2022 (Fig. 2.39), surpassing the peak in August 2021 (Barichivich et al. 2022). A historical maximum of 6.2% of the global land area experienced extreme drought conditions ($\text{scPDSI} \leq -4$) in August 2022, slightly greater than the previous maximum in October 1984 (6.1%). The extent of severe plus extreme drought conditions ($\text{scPDSI} \leq -3$) in 2022 exceeded 15% of the global land area between July and November, reaching a historical maximum of 15.8% in August. Similarly, moderate or worse drought conditions ($\text{scPDSI} \leq -2$) peaked in October at a historical maximum of 29% of the global land area.

The global pattern of regional droughts in 2021 largely persisted through 2022 (Plate 2.1q). Drought severity through western

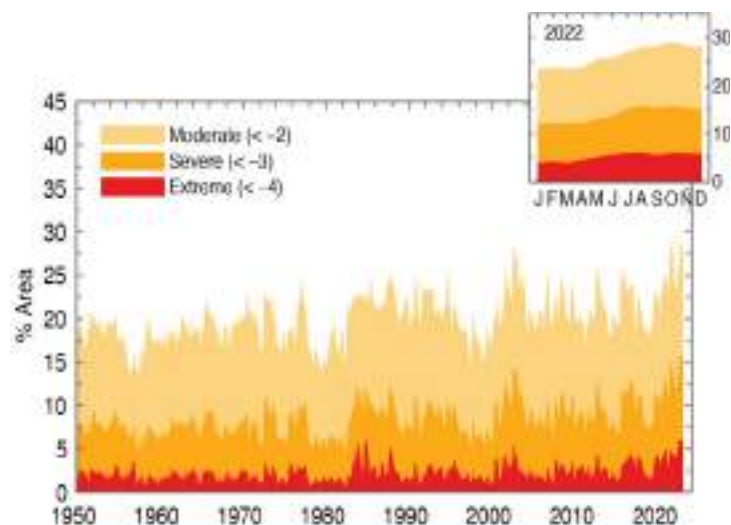


Fig. 2.39. Percentage of global land area (excluding ice sheets and deserts) with the self-calibrating Palmer Drought Severity Index (scPDSI) indicating moderate (<-2), severe (<-3), and extreme (<-4) drought for each month during 1950–2022. Inset: each month of 2022.

North America remained mostly unchanged from 2021 to 2022, but worsened in Europe, parts of South America, and the midlatitudes of Asia (Fig. 2.40). Despite persistent drought conditions in western North America, California experienced a milder fire season than in 2021 (section 2h3) but the west–east moisture contrast observed across the United States since 2017 persisted (Plate 2.1q). In South America, earlier drought hot spots through most of Chile and around the El Gran Chaco region in northern Argentina intensified (Barichivich et al. 2022). The record-breaking megadrought of central Chile reached its 13th consecutive year in 2022, and 80-year record-low river levels in northern Argentina and Paraguay (e.g., Bermejo and Paraná) disrupted fluvial transport.

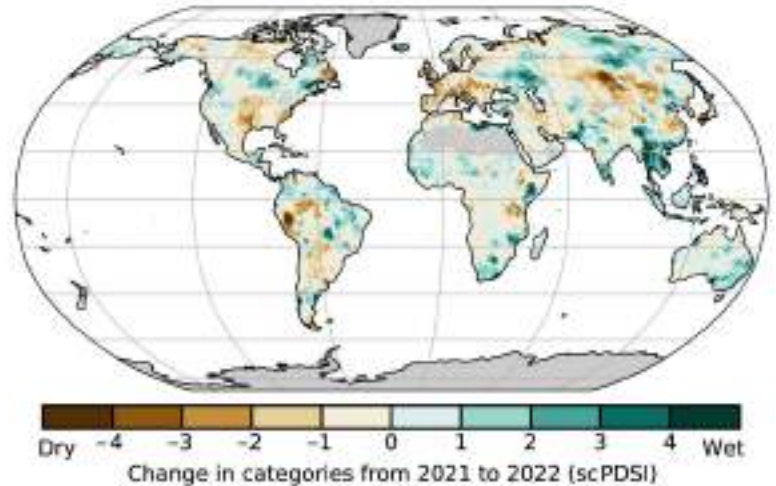


Fig. 2.40. Change in drought (self-calibrating Palmer Drought Severity Index [scPDSI]) from 2021 to 2022 (mean scPDSI for 2022 minus mean scPDSI for 2021). Increases in drought severity are indicated by negative values (brown), decreases by positive values (green). No calculation is made where a drought index is not physically meaningful (gray areas: ice sheets or deserts with approximately zero mean precipitation).

A persistent lack of precipitation in large areas of Europe from winter to summer, together with warmer-than-usual conditions and a sequence of heatwaves (sections 2b4, 7f) triggered a severe-to-extreme drought (Plate 2.1q). At its peak, the drought affected more than two-thirds of Europe, becoming one of the worst historical droughts in France, Spain, Germany, and Italy. In northern Italy, the Po River and canals in Venice reached record-low levels. The drought did not extend into northern Europe, where wet conditions across Fennoscandia continued through 2022. In northern Africa, previous moderate drought intensified to extreme drought along the Mediterranean coast from Morocco to Tunisia (Plate 2.1q). Most of the Middle East from eastern Turkey to Pakistan also saw an intensification of drought to severe or extreme conditions.

Although changes in moisture anomalies through tropical Africa are uncertain due to the sparse coverage of meteorological station data, this region largely saw a continuation of the wet conditions that began in 2019 (Plate 2.1q). In southern Africa, drought conditions seen since 2018 continued through 2022 but eased slightly compared to 2021 (Fig. 2.40). In Australia, previous drought eased in the east but most of the country continued under moderate drought during 2022 (Plate 2.1q). In contrast, India and Southeast Asia experienced predominantly wet conditions. The Yangtze River basin in central-eastern China saw severe drought as a result of precipitation deficit combined with an extreme heatwave, though most of northern China saw wet conditions (see section 7g and Sidebar 7.2 for details). Previous moderate-to-severe drought in parts of northeastern Siberia and the Russian Far East continued in 2022 (Plate 2.1q).

The update of the scPDSI (Wells et al. 2004; van der Schrier et al. 2013) for this year uses global precipitation and Penman-Monteith Potential Evapotranspiration (ET) from an early update of the Climatic Research Unit gridded Time Series (CRU TS) 4.07 dataset (Harris et al. 2020). It incorporates new estimates of some variables in CRU TS4.07 compared with CRU TS4.06 used last year, affecting potential ET via an improved baseline climatology for cloud cover. These revisions modify the scPDSI drought index values throughout, notably a small reduction in the global areas of moderate and severe drought that is consistent throughout the time series.

11. LAND EVAPORATION

—D. G. Miralles, A. Koppa, H. E. Beck, and M. F. McCabe

Around two-thirds of the precipitation that falls over land is returned to the atmosphere through evaporation (Dorigo et al. 2021). Understanding the spatial and temporal dynamics of evaporation is of key importance for agriculture and water management, as well as for diagnosing the influence of short-term climate variability and long-term climate changes on water resources (Miralles et al. 2014). In 2022, most land regions experienced positive (more than normal) evaporation anomalies relative to the 1991–2020 reference period (Plate 2.1r). Abnormally high values were observed in Amazonia, Southeast Asia and India, southern Africa, and eastern Australia. Most of these anomalies were linked to high precipitation (section 2d4) and coincided with reports of extreme-intensity events and floods (section 2d5). In the Amazon, precipitation enhances evaporation mainly through its influence on interception loss—the vaporization of rain stored on tree canopies and understory vegetation. For drier regions, such as eastern Australia or southern Africa, positive soil evaporation and transpiration anomalies occurred mostly in response to increased soil moisture availability (section 2d9). Conversely, anomalously low evaporation was observed across the Horn of Africa, the U.S. Central Plains, and parts of Brazil and Argentina. In water-limited regions, negative anomalies in evaporation are mainly caused by below-average precipitation (Orimoloye et al. 2022). In the Horn of Africa, the abnormally low evaporation can be linked to a prolonged meteorological drought that has already persisted for five consecutive rainfall seasons (section 7e; Anderson et al. 2023). Interestingly, despite the summer drought and heatwave events striking western Europe (sections 2d10, 7f2), no anomalously low evaporation was recorded in the region.

The global mean land evaporation in 2022 was above the 1991–2020 mean, and even above the expectation based on the positive 1980–2021 trend. This 28 mm yr⁻¹ global mean anomaly is in fact the largest on record (Fig. 2.41). The geographical patterns shown in Plate 2.1r are typical of La Niña conditions (Miralles et al. 2014; Martens et al. 2018), which tend to cause an increase in global mean evaporation (see Southern Oscillation Index [SOI] in Fig. 2.41). This El Niño–Southern Oscillation-induced variability in evaporation is superimposed on a long-term trend of 0.78 mm yr⁻¹, which falls towards the high-end of trend estimates reported in the recent literature (Zhang et al. 2016; Brutsaert et al. 2017; Anabalón and Sharma 2017). This positive trend has been attributed to increasing global temperatures (Miralles et al. 2014) and terrestrial greening (Cheng et al. 2017). Both hemispheres experienced positive evaporation anomalies

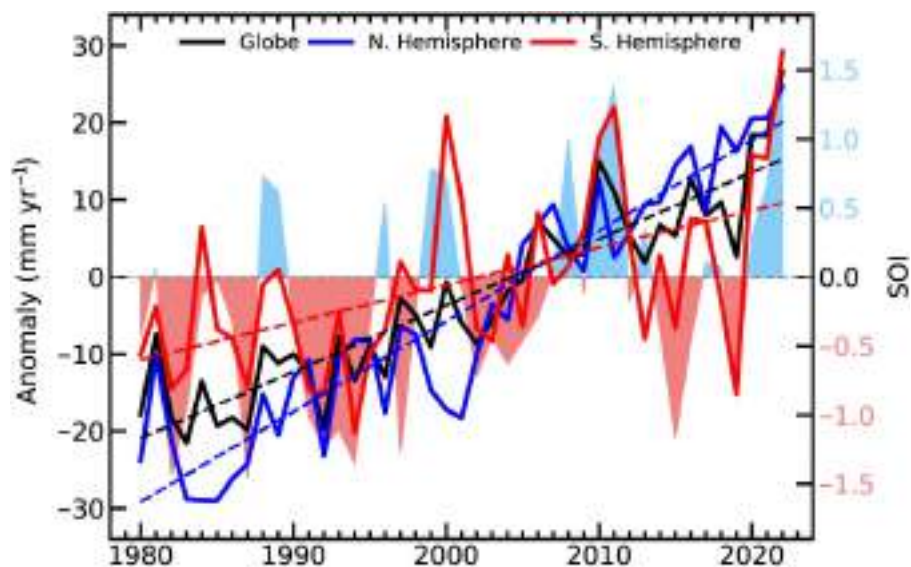


Fig. 2.41. Land evaporation anomalies (mm yr⁻¹; 1991–2020 base period) for the Northern Hemisphere, Southern Hemisphere, and the entire globe (blue, red, and black solid lines, respectively). Linear trends in evaporation (dashed lines) and the Southern Oscillation Index (SOI) from CRU (right axis, shaded area) are also shown. (Sources: GLEAM; <https://crudata.uea.ac.uk/cru/data/soi/>.)

throughout the year, with the Southern Hemisphere in particular (Fig. 2.42) reflecting behavior consistent with La Niña conditions.

The evaporation results are based on version 3.7 of the Global Land Evaporation Assessment Model (GLEAM; Miralles et al. 2011). This version is driven by satellite observations of soil and vegetation water content (Dorigo et al. 2017; Moesinger et al. 2019), a blend of gauge, satellite, and reanalysis data for precipitation (Beck et al. 2019), and reanalysis data for radiation and air temperature (Beck et al. 2022). The reported long-term trends are affected by the indirect representation of the influence of carbon dioxide and atmospheric aridity on vegetation stress in GLEAM v3 (Martens et al. 2017). The unbiased root-mean square error is approximately 0.7 mm day^{-1} and the temporal correlation against in situ eddy-covariance measurements is around 0.8 on average (Martens et al. 2017).

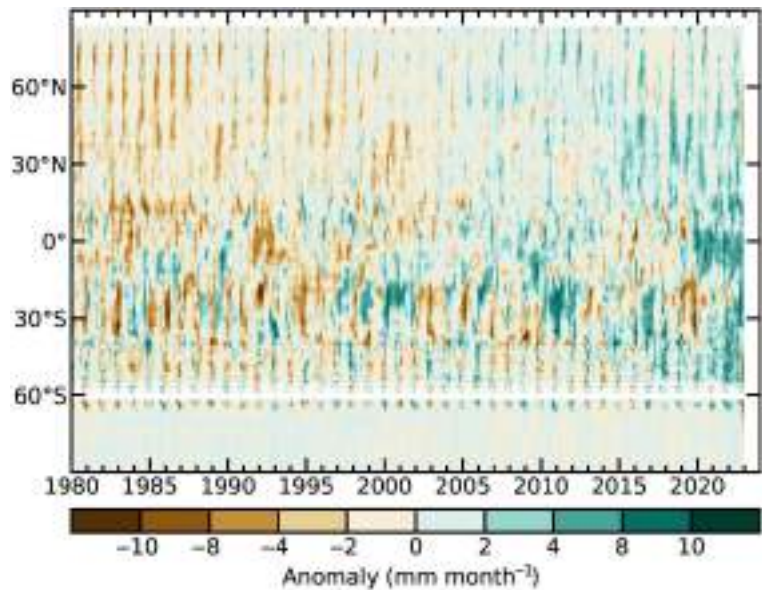


Fig. 2.42. Zonal mean terrestrial evaporation anomalies (mm month^{-1} ; 1991–2020 base period). (Source: GLEAM.)

e. Atmospheric circulation

1. MEAN SEA-LEVEL PRESSURE AND RELATED MODES OF VARIABILITY

—B. Noll, D. Fereday, and D. Campos

Mean sea-level pressure (MSLP) can be used to derive indices that describe globally important modes of atmospheric variability, which provide context to weather and climate anomalies and extremes. One of the most globally impactful modes is the El Niño–Southern Oscillation (ENSO), not only owing to its direct effects in the Indo-Pacific region but also to its teleconnections across the mid and high latitudes of both hemispheres (Capotondi et al. 2015). ENSO can be described by the Southern Oscillation Index (SOI), the normalized MSLP difference between Tahiti and Darwin (Allan et al. 1996; Kaplan 2011). The SOI was mostly positive from late 2020 through 2022, coinciding with an impactful, protracted La Niña event (following Allan and D’Arrigo 1999), which has been associated with heavy rainfall and floods in Australia and New Zealand (see sections 7h4 and 7h5, respectfully, for details), a wet summer and dry winter in south-central Chile (section 7d4), and a persistence of drought in the western United States (section 7b2).

In the tropical Indian Ocean, the Indian Ocean dipole (IOD) also influences MSLP patterns (Saji et al. 1999). The negative phase of the IOD, which developed during austral winter 2022, is associated with above-normal ocean temperatures in the tropical eastern Indian Ocean and below-normal ocean temperatures in the west (see section 4f for details). The development of an IOD event is correlated with ENSO by way of variations in the Walker Circulation (Behera et al. 2006). The combined effect of La Niña and a negative IOD contributed to a stronger-than-normal rising branch of the Walker Circulation in the eastern Indian Ocean, western Pacific, and across Australasia, which influenced regional moisture availability and global atmospheric circulation patterns during the year.

Variability in MSLP is also expressed at the regional scale by modes including the Arctic Oscillation (AO), the North Atlantic Oscillation (NAO), and the Pacific/North American (PNA) in the Northern Hemisphere (NH) as well as the Southern Annular Mode (SAM)/Antarctic Oscillation (AAO) in the Southern Hemisphere (SH; Kaplan 2011).

In the NH, the winter NAO is the leading winter mode of variability in the North Atlantic/European (NAE) region, comprising an MSLP dipole with centers over Iceland and the Azores. The NAO was positive in January and February (Fig. 2.43a), consistent with the strong

stratospheric polar vortex, while (as in 2021) the PNA index was mostly negative throughout the year, in line with the persistent La Niña event (Yeh et al. 2018). The winter NAO and PNA are generally independent (Soulard and Lin 2017). A prolonged high-pressure anomaly occurred over Europe in spring and summer (Figs. 2.43b,c) driving extreme dry and hot conditions (see section 7f for details). The summer NAO (the leading NAE-region mode of variability in July and August; Folland et al. 2009) is an MSLP dipole with centers over Greenland and northern Europe. The 2022 summer NAO index was the second highest in the series dating to 1959, underlining the strength of the MSLP anomaly (Fig. 2.43e). In December, the winter NAO was once again negative, as is weakly favored by La Niña in early winter (e.g., Moron and Plaut 2003).

The SAM, which contributes to up to 34% of the variability in the extratropical SH atmospheric circulation (Fogt and Marshall 2020), was positive for a record-tying 76% of days during 2022 (Fig. 2.44e). This matched the record set in 1998 and was the sixth time since 2015 that the SAM was positive for more than 60% of days. Positive SAM events often occur during La Niña, and the SOI and SAM show a positive correlation starting around 1990 (Clem and Fogt 2013). The upward SAM trend in recent decades, particularly during austral summer, has been associated with a poleward shift of the westerly wind belt in the SH (Fogt and Marshall 2020), which also

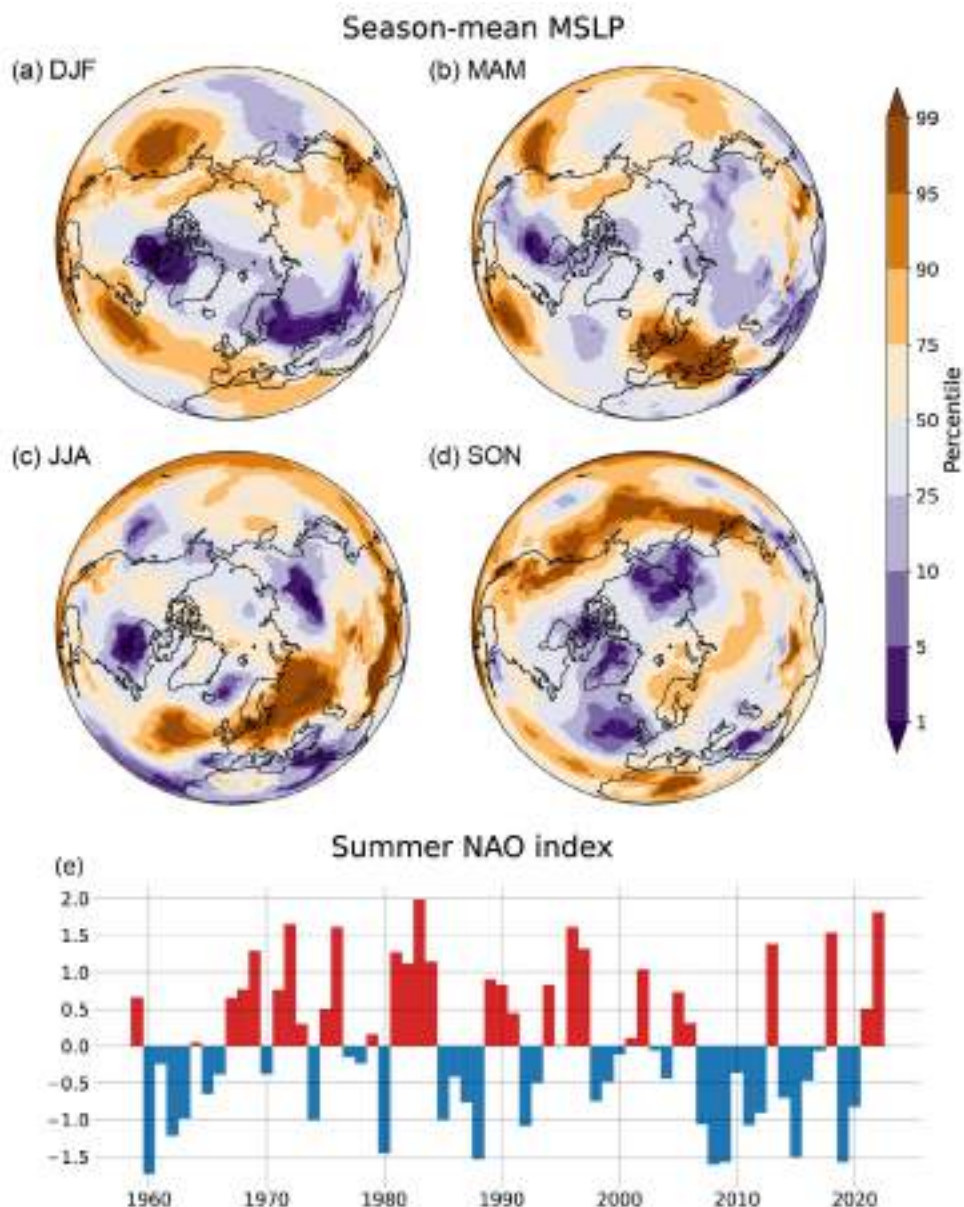


Fig. 2.43. Northern Hemisphere circulation in 2022. (a)–(d) seasonal mean sea-level pressure (MSLP) anomalies with respect to the 1991–2020 base period, shown as percentiles based on the 1959–2022 period. (e) Jul/Aug summer North Atlantic Oscillation (NAO) index for the period 1959–2022. (Source: ERA5 [Hersbach et al. 2020].)

occurred in 2022. This was associated with a prominent belt of higher-than-normal MSLP from the sub-Antarctic Indian Ocean, across New Zealand, and into southern South America (Fig. 2.44; Plate 2.1s), contributing to New Zealand’s warmest year on record (section 7h5). The combined effect of the SAM, ENSO, and IOD teleconnections contributed to lower-than-normal MSLP across Australia and the Maritime Continent. 2022 was Australia’s ninth-wettest year on record, with parts of New South Wales experiencing its wettest year on record (section 7h4). In association with higher-than-normal sea-surface temperatures (SSTs), annual precipitable water values were above normal in the tropical eastern Indian Ocean, across northern and eastern Australia, and into the southwestern Pacific, contributing to greater moisture availability for low-pressure systems in the region and culminating in some impactful atmospheric river events, such as New Zealand’s strongest August atmospheric river on record (see section 7h5; NIWA 2022b). In the South Pacific, a prominent pressure dipole was observed, especially during the winter, in response to La Niña, a positive SAM, and the presence of above-normal SST anomalies in the southwestern Pacific (Garreaud et al. 2021).

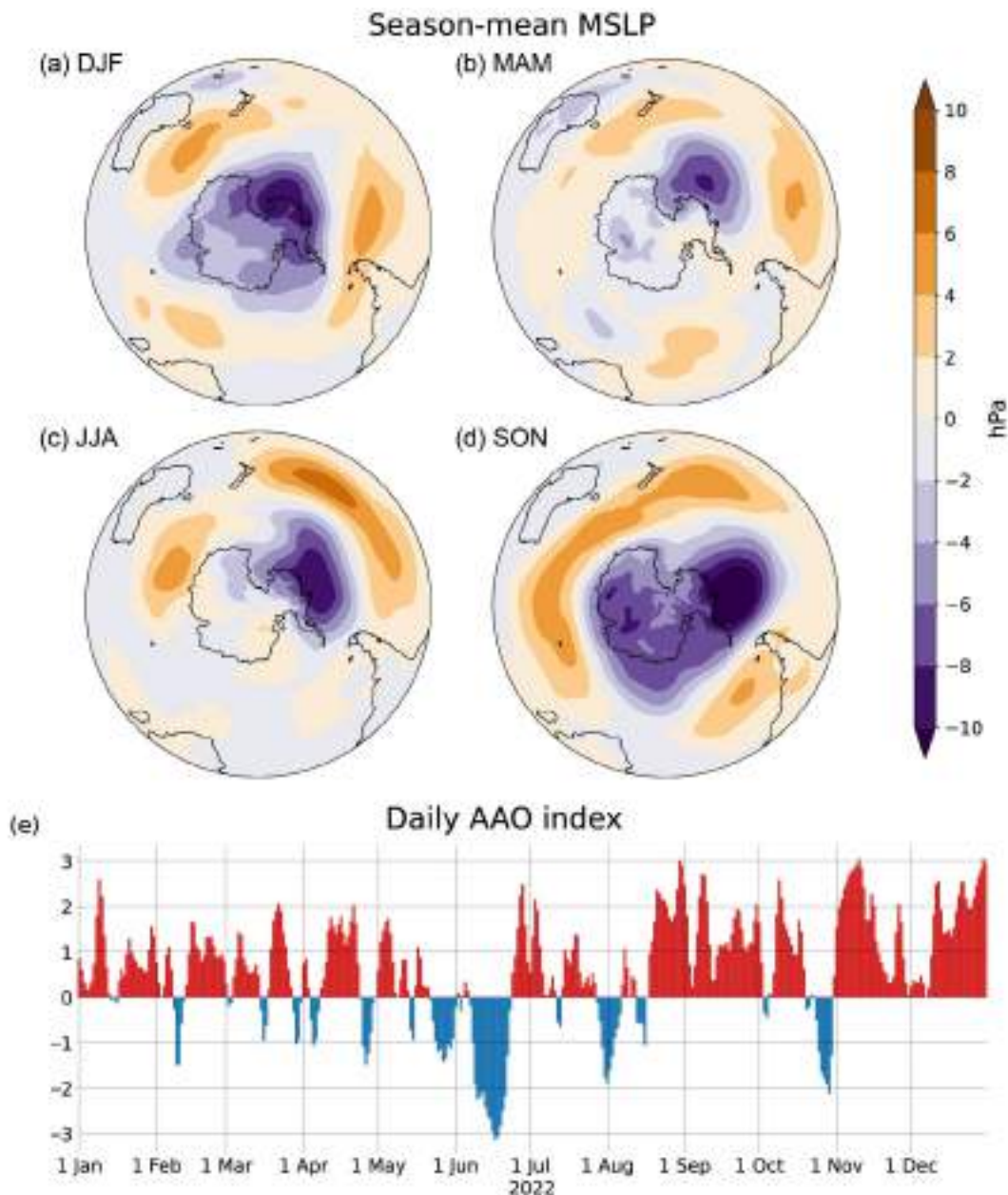


Fig. 2.44. Southern Hemisphere circulation in 2022. Seasonal mean sea-level pressure (MSLP) anomalies (hPa; 1991–2020 base period) for (a) DJF 2021/22, (b) MAM 2022, (c) JJA 2022, and (d) SON 2022. (Source: ERA5 reanalysis.) (e) Daily Antarctic Oscillation (AAO) index time series. (Source: NOAA Climate Prediction Center.)

2. LAND AND OCEAN SURFACE WINDS

—C. Azorin-Molina, R. J. H. Dunn, L. Ricciardulli, C.A. Mears, J. P. Nicolas, T. R. McVicar, Z. Zeng, and M. G. Bosilovich

Relative to the 1991–2020 climatology, land surface wind-speed anomalies at ~10 m above the ground in 2022 were dominated by positive values (Table 2.6). North and South America showed the highest positive anomalies relative to the climatology ($+0.070 \text{ m s}^{-1}$ and $+0.112 \text{ m s}^{-1}$, respectively), followed by East and Central Asia ($+0.012 \text{ m s}^{-1}$ and $+0.007 \text{ m s}^{-1}$, respectively). One exception was Europe, where annual mean wind speeds below the climatology persisted in 2022 (-0.072 m s^{-1} ; Plate 2.1t). The positive anomalies in 2022 agree with the recent reversal or stabilization of surface winds observed since the 2010s (Zeng et al. 2019) after decades of decrease, denoted as “stilling” (Roderick et al. 2007; McVicar et al. 2012; Fig. 2.45a). The changes in the frequency of wind intensities still show long-term trends since the 1970s, with no trends or weak declines for moderate winds ($>3 \text{ m s}^{-1}$; Fig. 2.45c) and clear slowdowns for the strongest winds ($>10 \text{ m s}^{-1}$; Fig. 2.45d).

Changes and variability of land surface winds were assessed using: 1) anemometer observations from the Hadley Centre Integrated Surface Database version 3 (HadISD3) dataset (1973–2022; Dunn et al. 2012, 2016; Dunn 2019) and 2) two reanalyses: European Centre for Medium-Range Weather Forecasts Reanalysis version 5

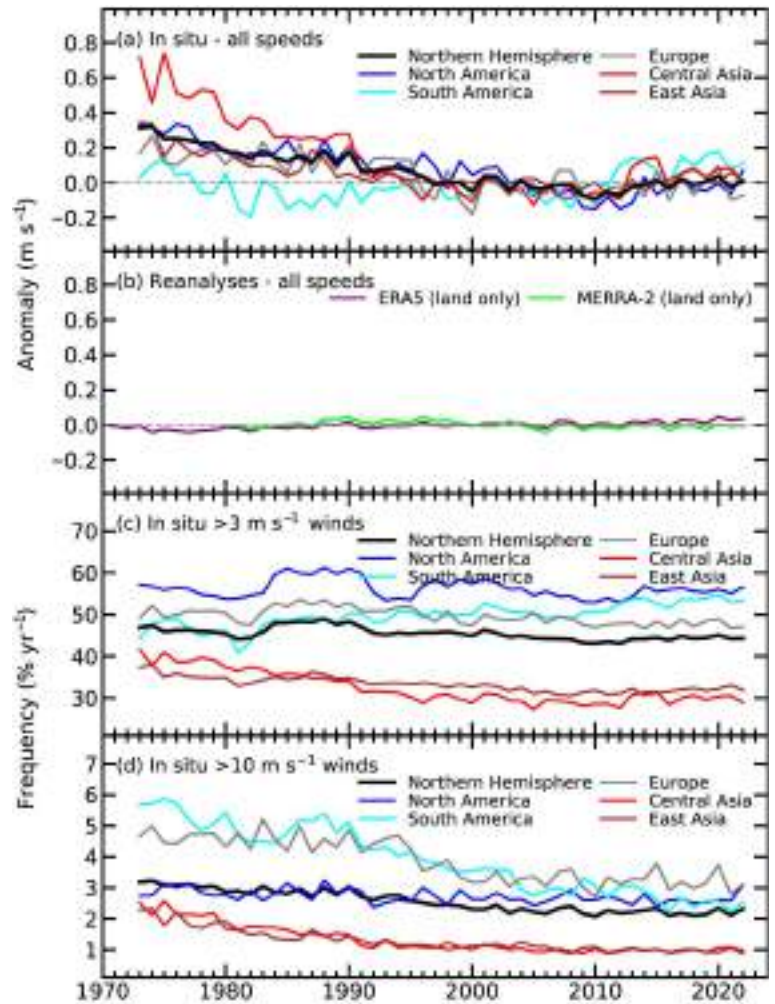


Fig. 2.45. Land surface Northern Hemisphere (20°N – 70°N) and regional surface wind-speed anomaly time series (m s^{-1} ; 1991–2020 base period). Panel (a) shows the HadISD3 observational dataset (1973–2022) and (b) ERA5 (1979–2022) and MERRA-2 (1980–2022) reanalyses. HadISD3 occurrence frequencies ($\% \text{ yr}^{-1}$) are shown for wind speeds (c) $>3 \text{ m s}^{-1}$, and (d) $>10 \text{ m s}^{-1}$.

Table 2.6. Northern Hemisphere (20°N – 70°N) and regional statistics for land surface wind speed (m s^{-1}) using the observational HadISD3 dataset for the period 1979–2022.

Region	Mean 1991–2020 (m s^{-1})	Anomaly 2022 (m s^{-1})	Trend 1979–2022 ($\text{m s}^{-1} \text{ decade}^{-1}$), and 5th to 95th percentile confidence range	Number of stations
Northern Hemisphere	3.308	+0.009	-0.055 ($-0.070 \rightarrow -0.041$)	2877
North America	3.643	+0.070	-0.068 ($-0.085 \rightarrow -0.051$)	842
Europe	3.648	-0.072	-0.050 ($-0.071 \rightarrow -0.035$)	934
Central Asia	2.738	+0.007	-0.072 ($-0.012 \rightarrow -0.046$)	304
East Asia	2.715	+0.012	-0.028 ($-0.044 \rightarrow -0.015$)	537
South America	3.452	+0.112	$+0.051$ ($+0.033 \rightarrow +0.069$)	101

(ERA5; 1979–2022, Hersbach et al. 2020; Bell et al. 2021) and Modern-Era Retrospective Analysis for Research and Applications version 2 (MERRA-2; 1980–2022, Gelaro et al. 2017). Note that surface wind-speed anomalies and trends differ between observations and reanalyses due to the difficulty that reanalysis systems have in reproducing long-term variability (Fig. 2.45b; e.g., Torralba et al. 2017; Ramon et al. 2019; Wohland et al. 2019).

Overall, observed trends of land surface winds for the past 44 years (i.e., since 1979) show a dominance of negative values (Fig. 2.46). In situ wind speeds declined by $0.055 \text{ m s}^{-1} \text{ decade}^{-1}$ across the NH over that time (Table 2.6). Over the last decade there has been a stabilization or reversal of wind speed trends globally (e.g. Zeng et al. 2019), which has also been observed regionally (e.g., Utrabo-Carazo et al. 2022). The exception is South America, where both the few observations and ERA5 reanalysis (Fig. 2.46) show positive trends, which support inter-hemispheric asymmetry of surface wind changes (Deng et al. 2022; Yu et al. 2022).

The recent reversal of the long-term surface wind speed decline over land has resulted in an increase in wind energy production over the last decade (e.g., over China; Liu et al. 2022). Observed surface wind speed changes are likely to be associated with internal decadal ocean–atmosphere oscillations (Zeng et al. 2019) along with temperature gradient variations arising from global warming (Zhang et al. 2021) but local-to-regional land use changes (Minola et al. 2022), instrumentation (Azorin-Molina et al. 2018), and encoding issues (Dunn et al. 2022) are also factors.

Compared to a 1991–2020 climatology, 2022 had positive anomalies over oceans recorded by satellite radiometers (Remote Sensing Systems [RSS]: $+0.11 \text{ m s}^{-1}$), slightly larger than satellite scatterometers (Advanced Scatterometer [ASCAT]: $+0.037 \text{ m s}^{-1}$) and reanalysis (ERA5: $+0.036 \text{ m s}^{-1}$; Fig. 2.47). The most prominent anomalies were recorded in the Pacific Ocean, with strong positive anomalies ($>+1.2 \text{ m s}^{-1}$) in the central tropical Pacific and negative ($<-1.2 \text{ m s}^{-1}$) in the western tropical Pacific and Maritime Continent, extending well into the eastern equatorial Indian Ocean—a strong signature of a persistent La Niña phase.

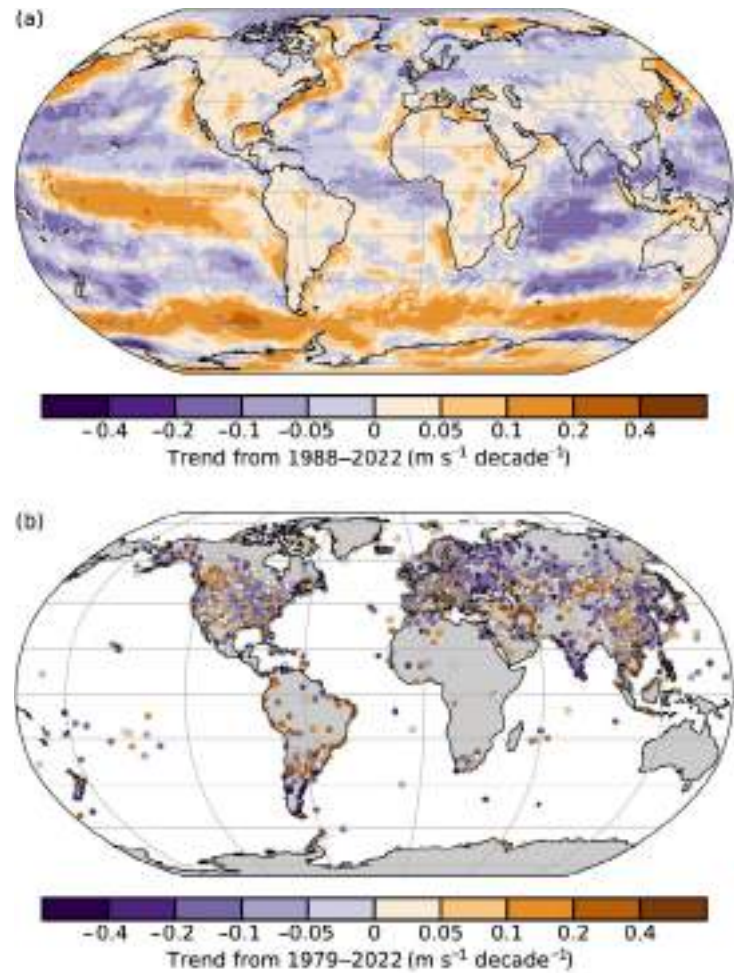


Fig. 2.46. Wind speed trends ($\text{m s}^{-1} \text{ decade}^{-1}$) from the (a) ERA5 reanalysis output over land/ice and Remote Sensing Systems (RSS) satellite radiometers (SSM/I, SSMIS, TMI, AMSR2, ASMR-E, and WindSat) over ocean for the period 1988–2022 (shaded areas) and (b) observational HadISD3 dataset over land (circles) for the period 1979–2022.

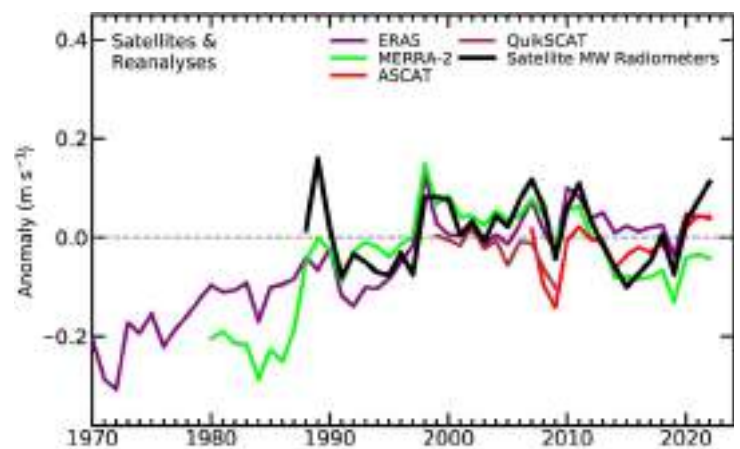


Fig. 2.47. Annual global mean wind speed anomalies (m s^{-1} ; 1991–2020 base period) over the ocean from satellite radiometers and scatterometers.

Similar to 2021, the mid-to-high latitude South Pacific Ocean experienced a strong positive anomaly ($>+1.2 \text{ m s}^{-1}$), consistent with the observed strengthening of the Southern Hemisphere westerlies (e.g., Deng et al. 2022; section 2e1). Strong positive anomalies were also seen in the Northern Hemisphere high-latitude regions (e.g., the Gulf of Alaska and the Greenland Sea).

Changes in ocean surface winds show widespread midlatitude negative trends for the period 1988–2022 and a strong negative trend in the Indian Ocean (Fig. 2.46). In contrast, positive trends prevail in the Pacific trade winds, the Southern Ocean, the Bering Sea, and near the coastlines (e.g., North America). The overall global ocean wind trend for 1988–2022 over 60°S – 60°N is close to zero (RSS Radiometers: $<+0.01 \text{ m s}^{-1} \text{ decade}^{-1}$; ERA5: $+0.036 \text{ m s}^{-1} \text{ decade}^{-1}$).

Over the ocean, surface winds were evaluated over the period 1988–2022 by 1) ERA5; and 2) satellite-based products: merged radiometer winds (including Special Sensor Microwave/Imager [SSM/I], the Special Sensor Microwave Imager/Sounder [SSMIS], the Advanced Microwave Scanning Radiometer-Earth Observing System [AMSRE], and the Advanced Microwave Scanning Radiometer 2 [AMSR2], Tropical Rainfall Measuring Mission [TRMM], Microwave Imager [TMI], and WindSat), and scatterometer winds Quick Scatterometer [QuikSCAT] and ASCAT (Wentz 1997, 2015; Wentz et al. 2007; Ricciardulli and Wentz 2015; Ricciardulli and Manaster 2021).

3. UPPER AIR WINDS

—M. Mayer, L. Haimberger, C. T. Sabeerali, V. Schenzinger, D. E. Surendran, and O. P. Sreejith

The 2022 global mean wind-speed anomaly at 850 hPa was about 0.1 m s^{-1} above the 1991–2020 climatology (Fig. 2.48a). The linear trend for the period 1991–2022 of $0.05 \text{ m s}^{-1} \text{ decade}^{-1}$ in the case of ERA5 and $0.04 \text{ m s}^{-1} \text{ decade}^{-1}$ for the Japanese 55-year Reanalysis (JRA55) is significant (p -value <0.01) but not statistically significant in MERRA-2. It is worth noting that the time series has been extended to the 1940s due to a recent backward extension of ERA5 (Hersbach et al. 2023).

Figure 2.48b together with Plate 2.1u indicate the mostly strongly positive zonal 850-hPa wind-speed anomalies at 50°S – 70°S in 2022. The increase in wind speed in this latitude belt

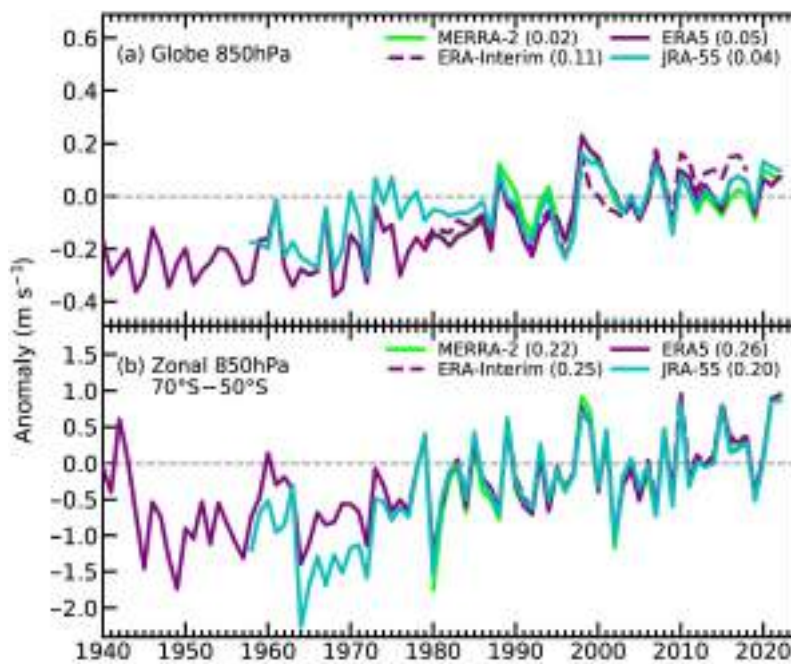


Fig. 2.48. Annual anomalies of (a) global mean and (b) 70°S – 50°S belt mean eastward wind speed (m s^{-1} ; 1991–2020 base period) at 850 hPa from four reanalyses (ERA5 [Hersbach et al. 2020], ERA-Interim [Dee et al. 2011], MERRA-2 [Gelaro et al. 2017], and JRA-55 [Kobayashi et al. 2015]). The numbers in parentheses are linear trends in $\text{m s}^{-1} \text{ decade}^{-1}$ for the period 1991–2020. The ERA-Interim time series ends in 2019.

has therefore continued, with 2022 close to the absolute maxima of the shown time series. The linear trends of the annual means are highly significant (p -value <0.002) for the period 1991–2022, between 0.20 and $0.26 \text{ m s}^{-1} \text{ decade}^{-1}$. This result is consistent with the high positive SAM (Marshall 2003) that continued to increase from the already high annual value of 1.2 in 2021 to 1.5 in 2022 (see also section 2e1). The AAO index, which is closely related to the SAM, was also strongly positive (0.79 in 2021 and 0.71 in 2022).

Plate 2.1u shows the annual zonal wind anomaly speed map at 850 hPa, averaged over September–December (SOND) 2022. The high (3 m s^{-1} near 60°S) wind speed anomaly in the Southern Ocean is the most prominent feature there. It is consistent with higher-than-average baroclinicity that was caused by record-high lower-tropospheric temperatures just north of the 50°S – 70°S belt (section 2b5).

2022 was the third La Niña year in a row (see Sidebar 3.1 and section 4b for details), the first time such an event has formed in the twenty-first century and only the third time in the last 50 years. The last “triple La Niña” occurred after the intense 1997/98 El Niño. Figures 2.49a,b show how similar the 200-hPa velocity potential patterns are for these events, indicating persistent and widespread circulation anomalies in the tropics during the three consecutive peak La Niña phases. Negative velocity potential anomalies over the Indo-Pacific Warm Pool are consistent with enhanced convective activity in this region, and the positive anomalies to the west and east are consistent with the expected changes to the Walker Circulation. The latter describes tropospheric circulation in the zonal-vertical plane in the equatorial regions in association with zonally varying sea-surface temperatures and convective activity (Bjerknes 1969). Figures 2.49c,d show the composite anomalies of pressure vertical velocity and zonal/vertical velocities averaged over 10°S–10°N, which complements the picture of the Walker circulation. The similarity is striking in this view, particularly for the main centers of activity over Indonesia and near the date line. Even the weaker maxima and minima over eastern Africa and northeastern Brazil look qualitatively similar.

In terms of equatorial stratospheric winds, the quasi-biennial oscillation (QBO) of 2022 was quite regular in terms of wind speeds and evolution of the easterly and westerly zones, comparable to 1982, 1992, or 2015. Despite the 2021 westerly lingering around 70 hPa until mid-April,

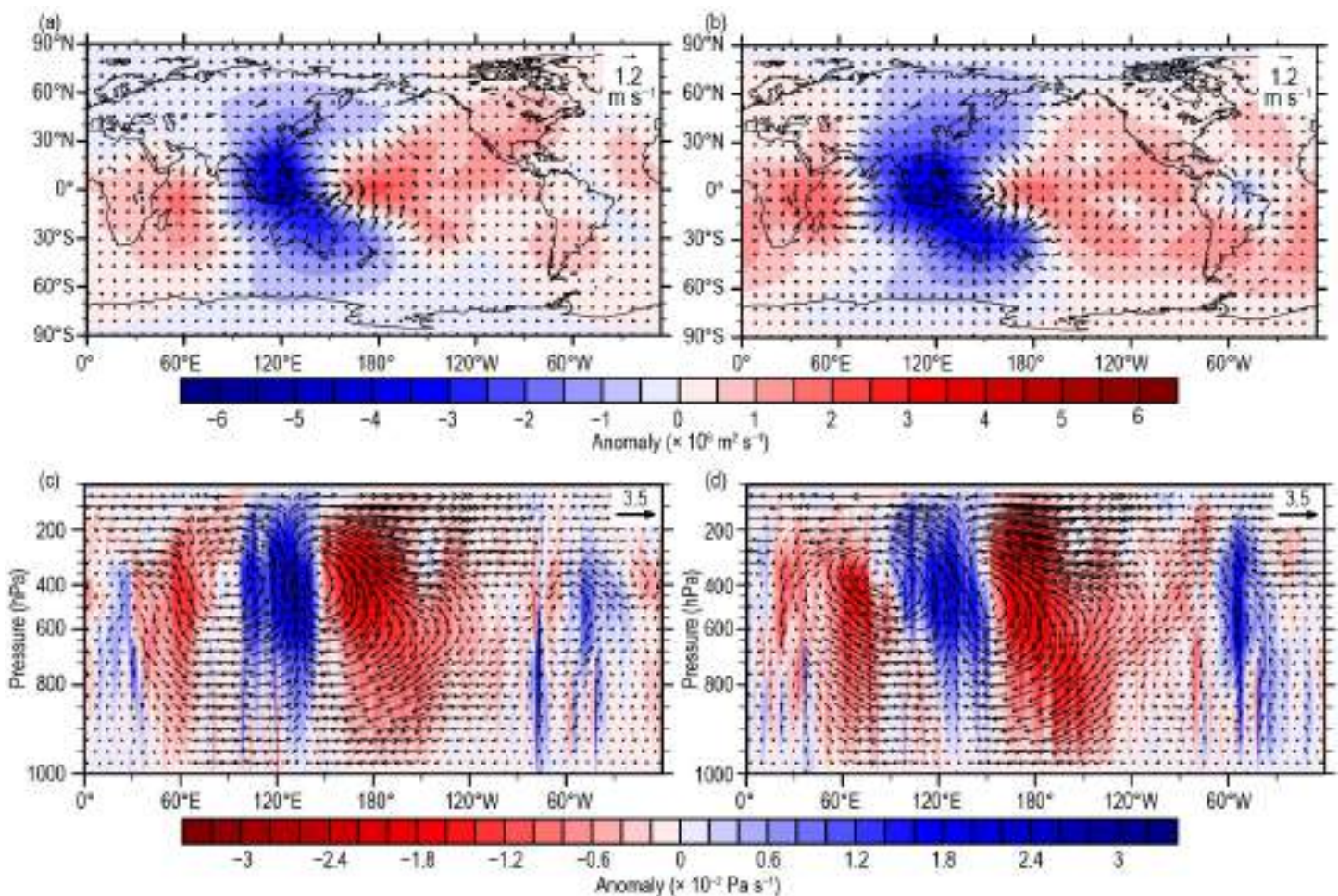


Fig. 2.49. Composites of 200-hPa velocity potential (colors; $\times 10^6 \text{ m}^2 \text{ s}^{-1}$) and divergent wind anomalies (arrows; 1991–2020 base period) for three consecutive OND seasons: (a) 1998–2000 and (b) 2020–22. Composite of 10°S–10°N averaged pressure vertical velocity anomalies (colors; $\times 10^{-2} \text{ Pa s}^{-1}$) and u/ω anomalies (arrows; zonal wind anomaly u : m s^{-1}) for three consecutive OND seasons: (c) 1998–2000 and (d) 2020–22. (Source: ERA5.)

thus stalling the easterly zone for this period of time, the already-formed westerly at 10 hPa descended with a normal speed of 1.13 km yr^{-1} . Its amplitude reached a maximum at the 10-hPa level in February, with a speed of 19.2 m s^{-1} , which is also within its usual range. A plot of zonal wind as a function of height and season over Singapore, which serves as a proxy for the global state of the QBO due to its zonal symmetry, is shown in Fig. 2.50a. The stratospheric state at the end of the year with one westerly shear zone present from 10 hPa to 80 hPa resembles that of 2015 (see Fig. 2.50b for a comparison of recent years), when the first major disruption of the QBO took place (Osprey et al. 2016).

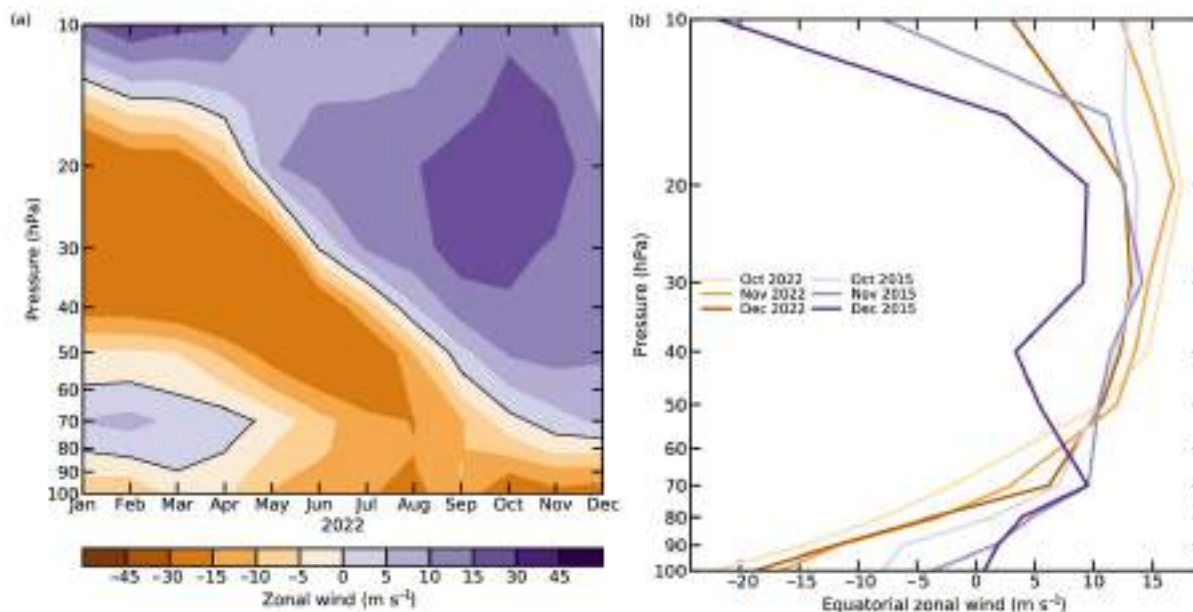


Fig. 2.50. (a) Stratospheric monthly mean zonal-wind values (m s^{-1}) based on daily measurements in Singapore. Easterlies (negative values) are shown in brown, westerlies (positive) in purple. (b) Monthly profiles of Singapore zonal wind averaged for Oct, Nov, and Dec in 2015 and 2022. Westerly winds are prominent above 70 hPa for both years, though the weakening of the westerlies at 40 hPa in 2015, which lead up to the first observed quasi-biennial oscillation disruption, is already visible in Dec.

4. LIGHTNING

—M. Füllekrug, E. Williams, C. Price, S. Goodman, R. Holzworth, K. Virts, D. Buechler, T. Lang, and Y. Liu

The Geostationary Lightning Mapper (GLM) on Geostationary Operational Environmental Satellites 16 and 17 reported the first lightning anomaly map covering the Western Hemisphere Americas and adjacent oceans, while the Lightning Imaging Sensor (LIS) on board the International Space Station (ISS LIS) has recorded lightning from February 2017 to present and thereby extends over 25 years of global lightning observations with previous satellites in low-Earth orbit (Blakeslee et al. 2020).

Figure 2.51a displays the average lightning density over the Americas and the Pacific Ocean calculated over 2019–22 from the GLMs. Coastlines and some topographic features, such as the Cordilleras in Central America and the Andes in South America, can act as meteorological divides for lightning densities to change on relatively small spatial scales. Over the oceans, lightning flashes indicate the tracks of thunderstorms that follow the trade winds, the westerlies at midlatitudes, and the easterlies at low latitudes. The Intertropical Convergence Zone over the Pacific Ocean is located slightly north of the equator.

The spatial distribution of anomalies in lightning density for 2022 is shown in Fig. 2.51b. Given the relatively short period of the record, it is currently expected that these anomalies exhibit an annual variability caused primarily by the long-term varying state of the climate (Williams 2020); in the case of the period 2020–22, the ongoing La Niña conditions following the El Niño event in 2018/19.

During El Niño, the three-dimensional structure of deep convection is taller and stronger (Hamid et al. 2001) than it is during La Niña. In South America, deeper storms during El Niño relate to increased convective available potential energy, a strengthening of the South American low-level jet, and a stronger upper-level jet stream (Bruick et al. 2019). Velasco and Fritsch (1987) report that large mesoscale convective systems (MCS), the most extreme lightning-producing weather systems on Earth (Zipser et al. 2006), are concentrated downwind of major mountain ranges in both North and South America. In North America, latitudinal shifts of storm tracks occur in association with El Niño and jet stream steering winds (Goodman et al. 2000). El Niño may contribute to extreme lightning climatology anomalies relative to the mean, as ~25% of the annual lightning at a single location has been shown to occur during the passage of a single MCS at midlatitudes during the strong El Niño years of 1982/83 (Goodman and MacGorman 1986).

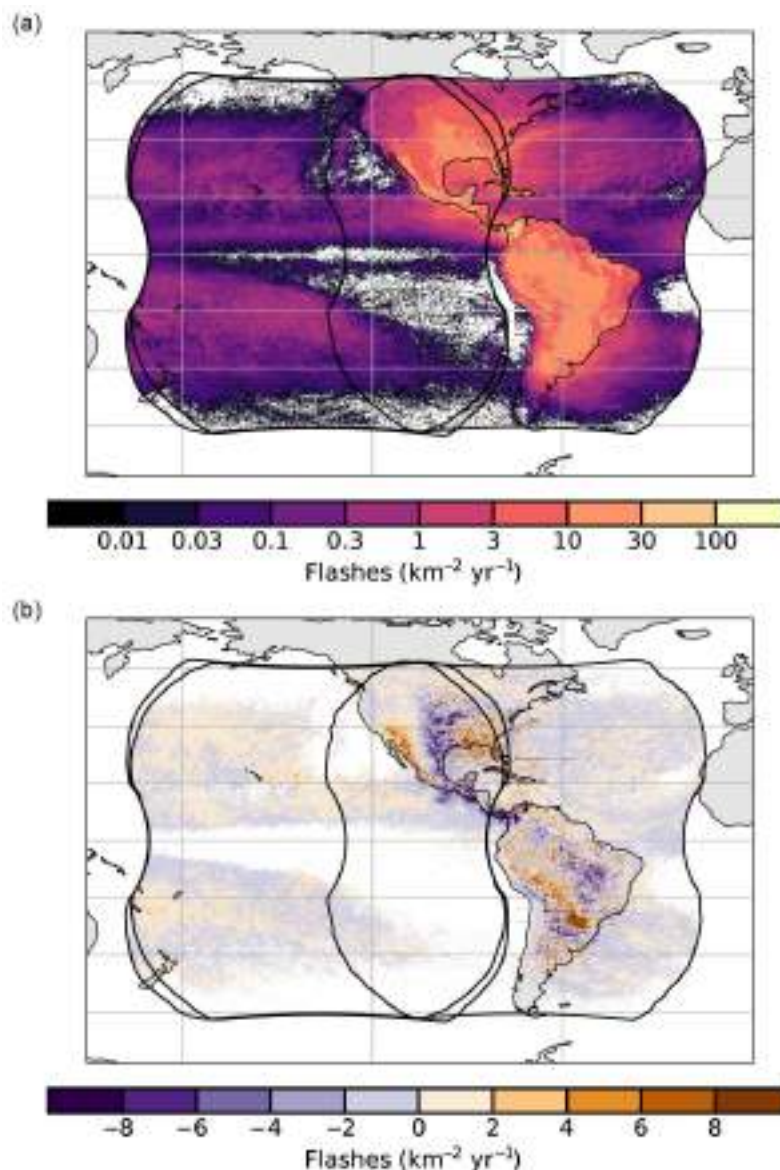


Fig. 2.51. (a) Lightning flash rate density for the period 2019–22 from NOAA’s Geostationary Lightning Mapper (GLM) on GOES 16 & 17. The black outline indicates the nominal GLM field of view for each satellite. (b) Western Hemisphere anomalies in lightning density for 2022 that are calculated relative to the 2019–21 mean. Units are $\text{fl km}^{-2} \text{yr}^{-1}$.

In Füllekrug et al. (2022), a distinct downturn in the reference year 2020 was apparent in the longest available uniform record of global lightning (LIS on TRMM), in a matched detector on the ISS, and in the GLM record for lightning over the Western Hemisphere (Virts et al. 2023). In contrast, the LIS record for the period 1998–2014 (Williams et al. 2019) was statistically flat. Two sustained events beginning in early 2020 could have caused the 2020 downturn: the transition from El Niño to La Niña and the aerosol reduction during the first COVID lockdown in many countries. Evidence for tropical lightning reductions in La Niña relative to El Niño is abundant (Williams 1992; Hamid et al. 2001; Yoshida et al. 2007; Satori et al. 2009; Goodman et al. 2000; Williams et al. 2021). Lightning reductions with reduced aerosol (Altaratz et al. 2017; Thornton et al. 2017; Fan et al. 2018; Wang et al. 2018; Liu et al. 2020) have a microphysical basis (Rosenfeld and Woodley 2003; Rosenfeld et al. 2008), and a global reduction in aerosol optical depth in satellite observations in 2020 (Sanap 2021) arises from reduced fossil fuel consumption and associated aerosol emissions during the COVID lockdowns (e.g., Rémy et al. 2021).

The 2019–21 reference period might therefore be slightly biased during the main COVID lockdown that occurred between March and May 2020 (Fig. 2.52). During this three-month period, the lightning densities over the Gulf of Mexico exhibit larger densities than during the 2019–21 reference period, while the central regions of North America and South America exhibit lower lightning densities, as reported by GLM16 (Fig. 2.52a). This is consistent with lightning densities measured by ISS LIS, which offers a global view of lightning density changes (Fig. 2.52b). As a result, the two main confounding variables affecting lightning density (ENSO and aerosol loading) need to be disentangled and require some in-depth discussion in the future.

La Niña kept 2022 globally cooler than years with El Niño or ENSO-neutral conditions (section 2b1). Both the ISS LIS and the GLM records are consistent in showing that global lightning totals during the present La Niña phase have not returned to the levels of the previous El Niño in 2019. Despite the identification of consistent physical connections and a La Niña that is behaving similarly to earlier La Niñas (Williams et al. 2020), the global reductions in lightning in 2020 and thereafter are not yet fully understood.

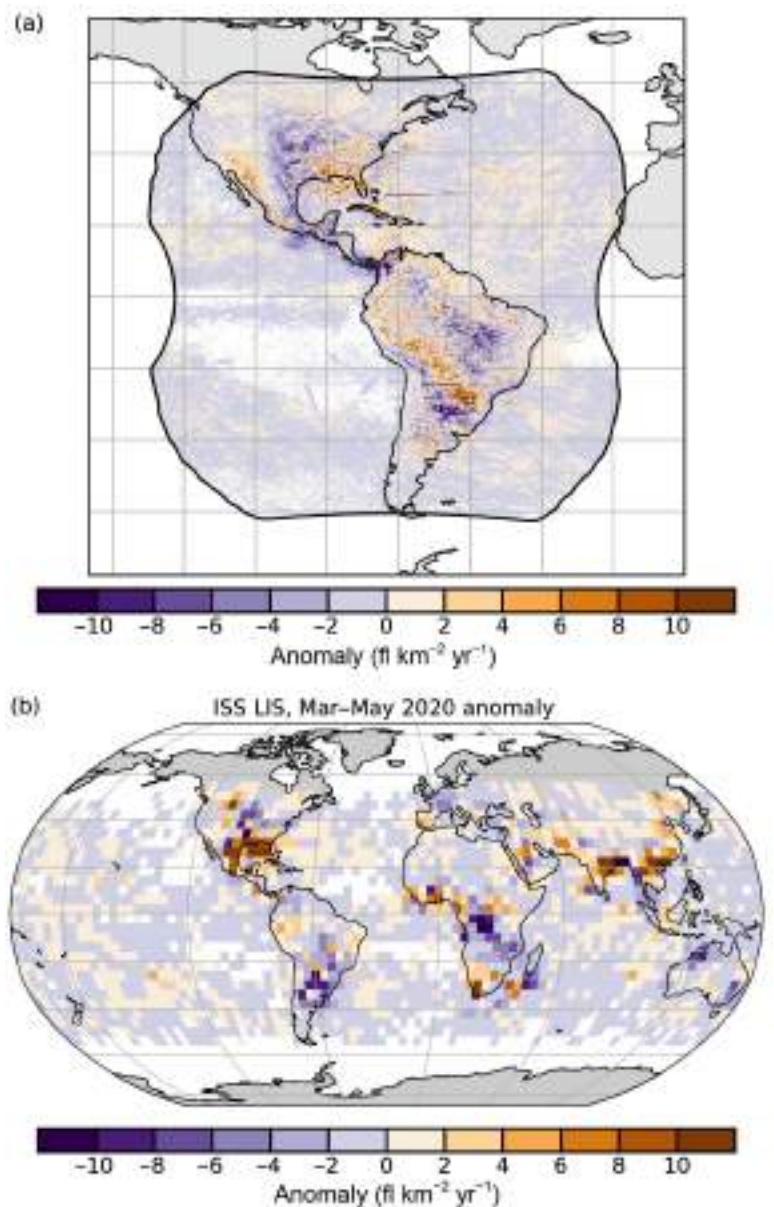


Fig. 2.52. Seasonal lightning density anomalies ($\text{fl km}^{-2} \text{yr}^{-1}$) for Mar–May 2020, potentially associated with the reduction of aerosol during the first COVID lockdown in many countries. (a) Spatial distribution of anomalies in seasonal lightning density from GLM16. (b) Global distribution of anomalies (relative to MAM 2017–19) in seasonal lightning density observed from the Lightning Imaging Sensor on board the International Space Station.

f. Earth radiation budget

1. EARTH RADIATION BUDGET AT TOP-OF-ATMOSPHERE

—T. Wong, P. W. Stackhouse Jr., P. Sawaengphokhai, J. Garg, and N. G. Loeb

The top-of-atmosphere (TOA) Earth radiation budget (ERB) is defined as the difference between incoming total solar irradiance (TSI) and outgoing radiation from Earth given by the sum of reflected shortwave (RSW) and outgoing longwave radiation (OLR). Regional imbalances in TOA ERB drive atmospheric and oceanic circulations. Thus, monitoring the variability in TOA ERB is essential for understanding the changes in the climate system.

An analysis of Clouds and the Earth's Radiant Energy System (CERES) TOA ERB measurements (Table 2.7) shows that the global annual mean OLR and TSI increased by 0.30 W m^{-2} and 0.15 W m^{-2} , respectively, in 2022 relative to 2021 (rounded to the nearest 0.05 W m^{-2}). In contrast, the global annual-mean RSW and net radiation decreased by 0.10 W m^{-2} and 0.05 W m^{-2} , respectively, over the same period. Fig. 2.53 shows regional annual-mean maps of the difference between 2022 and 2021 in TOA OLR and TOA RSW. The largest increases in OLR and decreases in RSW are observed over a large extent of the equatorial Pacific Ocean between New Guinea and 120°W longitude. Reductions in OLR and increases in RSW are observed over Southeast Asia, the northeastern Indian Ocean, the Philippines, Indonesia, Australia, and the tropical southwestern Pacific Ocean. These regional changes are associated with La Niña conditions that

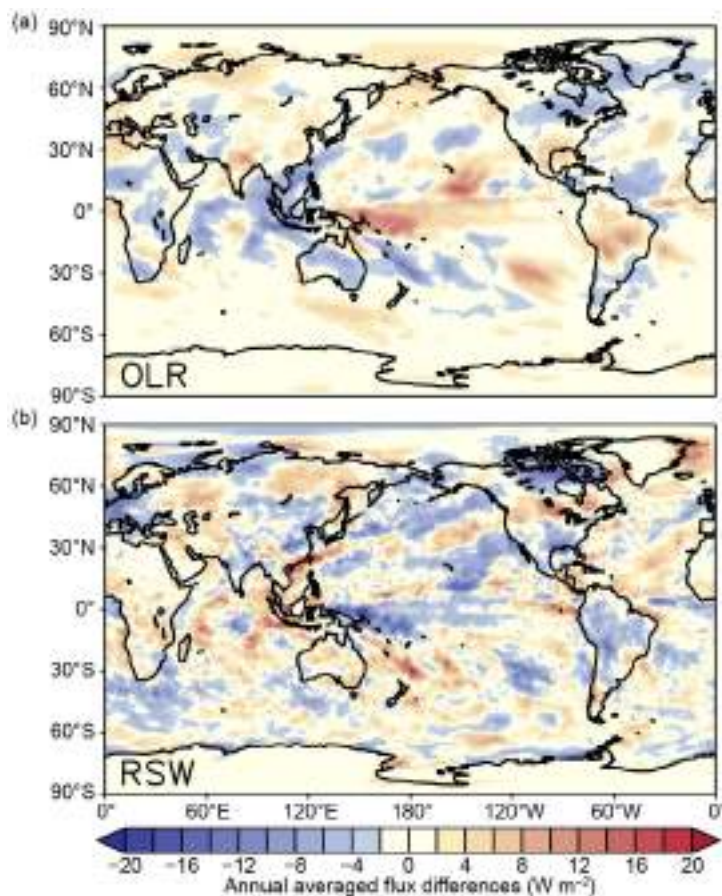


Fig. 2.53. Annual average top-of-atmosphere (TOA) flux differences (W m^{-2}) between 2022 and 2021 for (a) outgoing longwave radiation (OLR) and (b) reflected shortwave radiation (RSW). The annual-mean maps for 2022 were derived after adjusting Dec 2022 FLASHFlux version 4A data using the difference between CERES EBAF Ed4.2 and CERES FLASHFlux version 4A data in 2021.

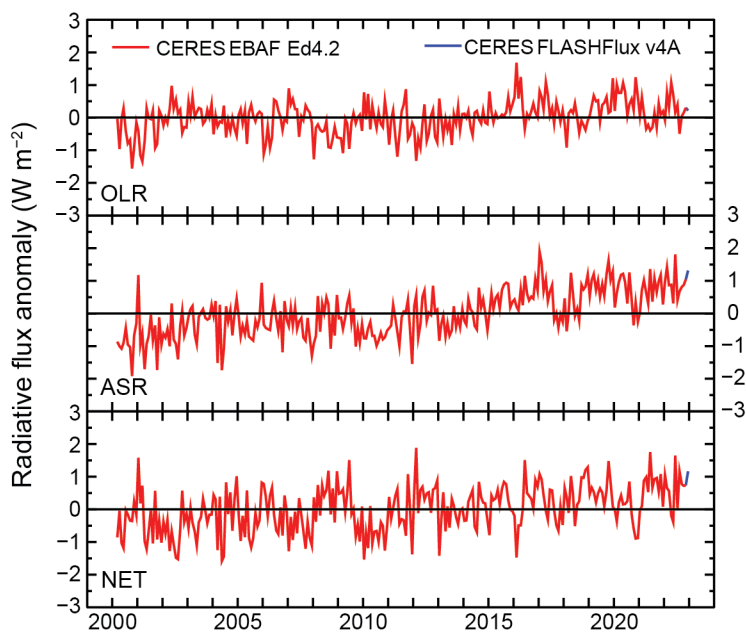
Table 2.7. Global annual mean top-of-atmosphere (TOA) radiative flux changes between 2021 and 2022, the 2022 global annual mean radiative flux anomalies relative to their corresponding 2001–21 mean climatological values, and the $2\text{-}\sigma$ interannual variabilities of the 2001–21 global annual mean fluxes (all units in W m^{-2}) for the outgoing longwave radiation (OLR), total solar irradiance (TSI), reflected shortwave (RSW), absorbed solar radiation (ASR, determined from $\text{TSI}-\text{RSW}$), and total net fluxes. All flux values have been rounded to the nearest 0.05 W m^{-2} and only balance to that level of significance.

Global	One Year Change (2022 minus 2021) (W m^{-2})	2022 Anomaly (Relative to 2001–21) (W m^{-2})	Climatological Mean (2001–21) (W m^{-2})	Interannual Variability (2001–21) (W m^{-2})
OLR	+0.30	+0.30	240.35	± 0.60
TSI	+0.15	+0.20	340.20	± 0.15
RSW	-0.10	-0.75	99.00	± 1.00
ASR	+0.25	+0.95	241.15	± 0.95
Net	-0.05	+0.65	0.80	± 0.80

persisted and intensified between 2020 and 2022, according to the Multivariate El Niño–Southern Oscillation (ENSO) index (Wolter and Timlin 1998; section 2e1). Relative to the multiyear average from 2001 to 2021, the 2022 global annual mean TOA flux anomalies are +0.30 for OLR, +0.20 for TSI, −0.75 for RSW, and +0.65 $W m^{-2}$ for total net flux (Table 2.7). These anomalies are near or within their respective 2- σ interannual variability (Table 2.7) for this period.

Throughout 2022, the global monthly mean TOA OLR anomaly remained largely positive (Fig. 2.54). The OLR anomaly dipped to a value of −0.50 $W m^{-2}$ for one month in August but recovered quickly back to positive values in the following months. These results are generally consistent with NOAA High Resolution Infrared Sounder (HIRS; Lee and NOAA CDR Program 2018) and NASA Atmospheric Infrared Sounder (AIRS; Susskind et al. 2012) OLR datasets (not shown). For the year as a whole, the 2022 global mean TOA OLR anomaly was +0.30 $W m^{-2}$. The global monthly mean TOA absorbed solar radiation (ASR; determined from TSI minus RSW) anomaly remained positive throughout 2022, peaking at +1.80 $W m^{-2}$ in June. For the year as a whole, the 2022 global mean TOA ASR anomaly was +0.95 $W m^{-2}$. The global monthly mean TOA total net anomaly, which is calculated from ASR anomaly minus OLR anomaly, also stayed mostly positive throughout 2022, reaching a maximum of +1.65 $W m^{-2}$ in June. For the year as a whole, the 2022 global mean TOA total net anomaly was +0.65 $W m^{-2}$. In terms of the global annual mean TOA ERB, the positive 2022 ASR anomaly was much larger than the negative effect of the 2022 OLR anomaly to produce the observed positive 2022 total net anomaly. Further analyses are needed to understand the significances and impacts of these observed global changes.

The TSI data were obtained from the Total Irradiance Monitor aboard the Solar Radiation and Climate Experiment (SORCE) mission (Kopp and Lean 2011), the Royal Meteorological Institute of Belgium composite dataset (Dewitte et al. 2004), and the Total Solar and Spectral Irradiance Sensor-1 (Coddington 2017) mission, all renormalized to the SORCE Version 15. The TOA RSW and TOA OLR data come from two different CERES datasets. The data for March 2000–November 2022 are based on the CERES Energy Balance and Filled (EBAF) Ed4.2 product (Loeb et al. 2009,



2012, 2018), which are constructed with measurements from the CERES instruments (Wielicki et al. 1996, 1998) aboard *Terra*, *Aqua*, and NOAA-20 spacecraft. The data for December 2022 comes from the CERES Fast Longwave and Shortwave Radiative Fluxes (FLASHFlux) version 4A product (Kratz et al. 2014), which are created using CERES measurements from *Terra* and *Aqua* spacecraft. The FLASHFlux to EBAF data normalization procedure (Stackhouse et al. 2016) results in 2- σ monthly uncertainties of ± 0.35 , ± 0.05 , ± 0.15 , and ± 0.50 $W m^{-2}$ for the OLR, TSI, RSW, and total net radiation, respectively (rounded to nearest 0.05 $W m^{-2}$).

Fig. 2.54. Time series of global monthly mean deseasonalized anomalies ($W m^{-2}$) of top-of-atmosphere (TOA) Earth radiation budget for outgoing longwave radiation (OLR; upper), absorbed solar radiation (ASR, determined from total solar irradiance (TSI) minus RSW; middle), and total net (TSI-RSW-OLR; lower) from Mar 2000 to Dec 2022. Anomalies are relative to their calendar month climatology (2001–21). The time series show the CERES EBAF Ed4.2 1-Deg data (Mar 2000–Nov 2022) in red and the CERES FLASHFlux version 4A data (Dec 2022) in blue; see text for merging procedure. (Sources: <https://ceres-tool.larc.nasa.gov/ord-tool/jsp/EBAFTOA42Selection.jsp> and https://ceres-tool.larc.nasa.gov/ord-tool/jsp/FLASH_TISASelection.jsp.)

2. MAUNA LOA APPARENT TRANSMISSION RECORD

—J. A. Augustine, K. O. Lantz, J.-P. Vernier, and J. E. Barnes

The Mauna Loa Observatory (MLO) on Hawaii (19.536°N, 155.576°W) at 3397 m a.s.l. has made pyrhelimeter measurements since 1958. Because of its high elevation, morning apparent atmospheric transmission computed from those measurements is a good proxy for stratospheric extinction.

The apparent transmission time series from 1958 through 2022 is shown in Fig. 2.55; the inset highlights new data for 2022. January and February 2022 transmissions continue at relatively stable levels of ~0.928 observed at the end of 2021. This relatively low transmission has been maintained since 2019 by a series of volcanic eruptions and wildfires (Augustine et al. 2020, 2021). A broad reduction in transmission began in March 2022 and reached a minimum of 0.919 in May. A sharp recovery in June to values observed earlier was followed by relatively stable transmissions through November (Mauna Loa erupted on 27 November, ending data collection for 2022). The springtime reduction in transmission coincided with the violent underwater eruption in January of Hunga Tonga–Hunga Ha‘apai (HTHH; 20.536°S, 175.382°W; Sidebar 2.2) and the seasonal passage of dust from Asia.

Most of the 70+ volcanic eruptions in 2022 had Volcanic Explosivity Indexes (VEI) less than 2, limiting their effect on the stratosphere. HTHH’s initial eruption on 13 January sent material as high as 20 km. A second more powerful eruption on 15 January (VEI 5) reached the lower mesosphere (~58 km) but within the day settled to between 25 km and 35 km (Proud et al. 2022). The westerly phase of the quasi-biennial oscillation of stratospheric winds (QBO) propagated the HTHH plume westward. The plume was concentrated at ~10°S but Cloud-Aerosol LIDAR and Infrared Pathfinder Satellite Observations (CALIPSO) imagery shows lateral transport branches in the 19 km–27 km layer reaching 30°S and 20°N in March (see supplemental material), in agreement with the Ozone Mapping and Profiler Suite (OMPS) and the Stratospheric Aerosol and Gas Experiment (SAGE) limb sounder (Taha et al. 2022). Discrete CALIPSO images at 19-day intervals in Legras et al. (2022) show the northern extent of Tonga’s stratospheric plume near 20°N at least through 3 May, but by 22 May it retreated south and remained there at least through 18 July (no published data thereafter). Lidar observations at MLO first sensed the HTHH plume on 1 March at an altitude of 24.5 km. A much larger signal was observed near 24 km on 14 March, in agreement with CALIPSO, which shows the northern periphery of the plume over MLO from 14 to 16 March (see supplemental material). Distinguishing HTHH from other large volcanic stratospheric events is its relatively small sulfur dioxide injection, ~50 times less than Mt. Pinatubo (Taha et al. 2022), and stratospheric aerosol optical depth (AOD) six times less than Pinatubo at 0.015, which represents a 4–5 factor increase from background (Khaykin et al. 2022). Those discrepancies are likely due to wet deposition (Proud et al. 2022) as HTHH increased stratospheric water by 10%–13% (Millan et al. 2022; Khaykin et al. 2022). Zhu et al. (2022) suggests the added water promoted faster sulfate aerosol formation and greater extinction but shortened its long-term effect on surface radiation.

While there were several springtime dust storms in Asia in 2022, none were as severe as those in 2021. Monthly average

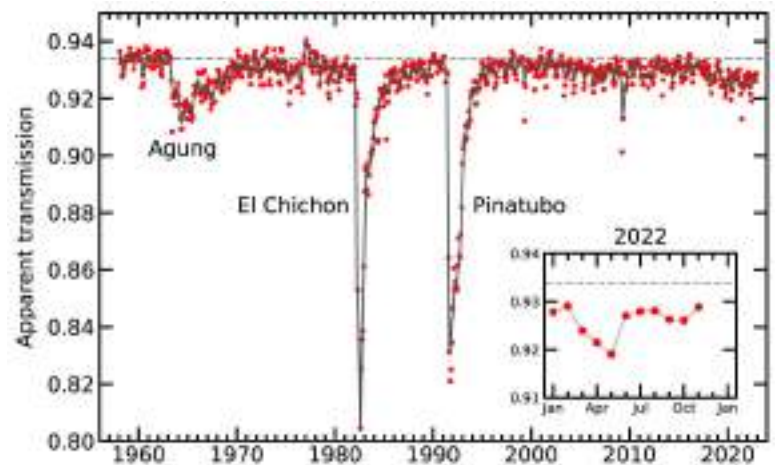


Fig. 2.55. Apparent transmission at Mauna Loa, Hawaii, from 1958 through 2022. Red dots are monthly averages of morning apparent transmission, and the gray curve is a locally weighted scatterplot smoothing (LOWESS) fit with a six-month smoother applied. The insert is an enlargement of the newest data for 2022. The horizontal dashed gray lines represent the average transmission of the clean period before the eruption of Agung. The Dec 2022 transmission is not available because the eruption of Mauna Loa in late Nov cut power to the station.

global AOD images for 2022 from the Moderate Resolution Imaging Spectroradiometer (MODIS [Barnes et al. 1998]; https://earthobservatory.nasa.gov/global-maps/MODAL2_M_AER_OD) show slightly elevated AOD over Hawaii in March, peak AOD in April, a reduction in May, and gone by June.

In summary, HTHH’s plume and Asian dust were primary contributors to the reduction of apparent transmission over MLO from March through May 2022. Both sources of enhanced extinction vanished by June, returning transmission to levels observed in January and February for the remainder of the 2022 record, which ended in November.

Atmospheric transmission is calculated from the ratio of direct-normal pyrheliometer measurements at two integer solar elevations (Ellis and Pueschel 1971). Three ratios from clear-morning measurements at 2, 3, 4, and 5 atmospheric pathlengths are averaged to get representative daily value. Daily transmissions are then averaged over monthly periods. Our calculation is referred to as an “apparent” transmission because atmospheric variability at longer pathlengths adds to the uncertainty.

Sidebar 2.2: Hunga Tonga–Hunga Ha’apai eruption

— S. DAVIS, W. RANDEL, J. AUGUSTINE, B. FRANZ, N. KRAMAROVA, T. LEBLANC, J.-P. VERNIER, X. WANG, AND M. WEBER

On 14–15 January 2022, the Hunga Tonga–Hunga Ha’apai (HTHH) submarine volcano (20.54°S, 175.4°W) erupted multiple times, injecting ash, water vapor, and sulfur dioxide (SO₂, an aerosol precursor) into the atmosphere. The underwater eruption on 15 January was among the strongest in the modern geophysical record, with an estimated Volcanic Explosivity Index (VEI) similar to that of Mt. Pinatubo in 1991 (VEI=6; Poli and Shapiro, 2022). The eruption produced a number of impacts, including audible sound heard ~10,000 km away, perturbations to the ionosphere, global tsunamis, as well as a Lamb wave and seismic activity similar in magnitude

to the 1883 eruption of Krakatau (Kubota et al. 2022; Matoza et al. 2022).

The plume from the HTHH eruption was observed to reach as high as ~55 km, a record in the geostationary satellite era that exceeded the ~40 km height reported for Mt. Pinatubo (Fig. SB.2.3; Carr et al. 2022). Following this transient peak in the plume height reaching the mesosphere, an umbrella of gas and ash spread out in the stratosphere between approximately 26 km and 34 km. The trace gases and aerosols injected into the stratosphere by the HTHH eruptions quickly spread as far north as 20°N in the month following the eruption, before

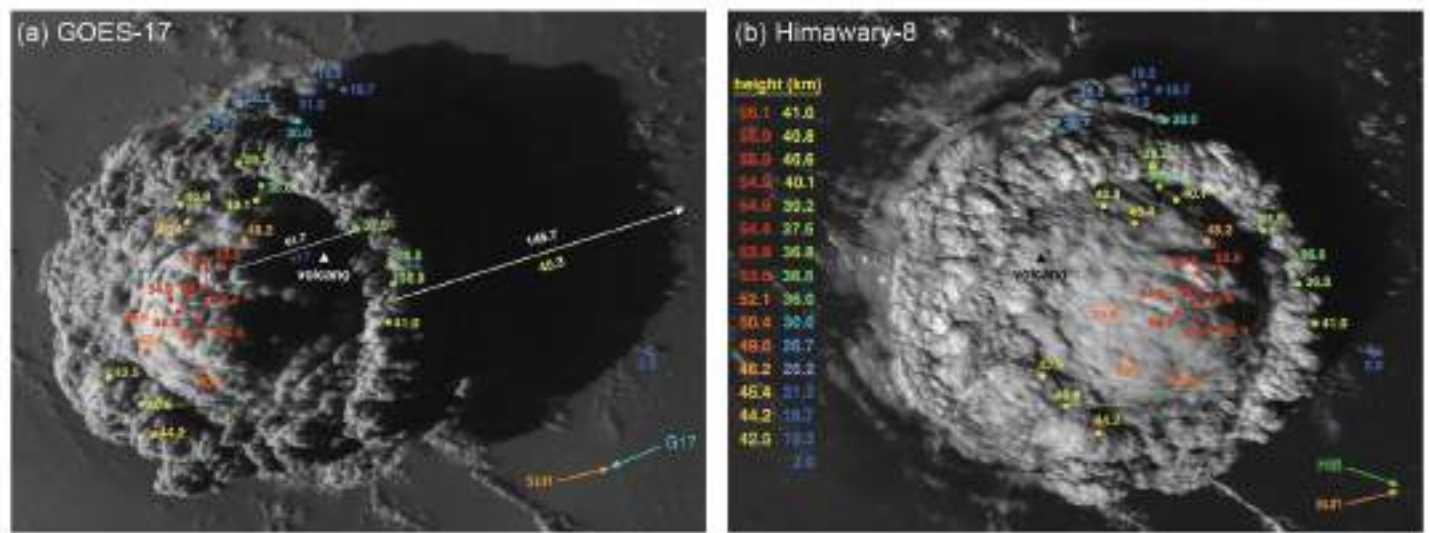


Fig. SB2.3. (From Carr et al. 2022, their caption. Figure used under **CC BY 4.0**): Image of the plume on 15 Jan 2022 at 0430 UTC from (a) GOES-17 and (b) Himawari-8. Colored dots mark manual stereo height estimates (in km), and the white/black triangles show the volcano’s location. The white arrows in panel (a) depict the shadow of a plume edge feature and a dome feature, with the shadow length and the derived height given above/below the arrow. Arrows in the lower right of each panel indicate the sun-to-pixel and satellite-to-pixel azimuths.

being transported to higher Southern Hemisphere (SH) latitudes in subsequent months and into the northern midlatitudes by the end of 2022. Here, we elaborate on some of the notable perturbations to the atmosphere, as well as some of the possible chemical and climate effects that are likely to occur in the coming years.

As the HTHH eruption occurred underwater, a vast amount of water vapor (WV) was present in the eruption plume, and this water vapor-enriched plume has had a dramatic impact on the stratosphere. By injecting water vapor and ice directly into the stratosphere, the HTHH eruption bypassed the typical tropical tropopause layer “cold trap” that normally limits the amount of water vapor entering the stratosphere (section 2g5). While previous volcanic eruptions and pyrocumulonimbus events have also injected water vapor into the stratosphere,

HTHH injected ~ 50 Tg H_2O to ~ 150 Tg H_2O , which is unprecedented in the satellite record and represents upwards of 10% of the entire stratospheric burden of WV (Khaykin et al. 2022; Millán et al. 2022; Randel et al. 2023; Vömel et al. 2022). Measurements from within the HTHH plume in the week immediately after the eruption showed water vapor mixing ratios exceeding 1000 ppmv between 25 km and 30 km (Khaykin et al. 2022; Randel et al. 2023; Vömel et al. 2022), in contrast to typical background stratospheric values of ~ 5 ppmv and enhancements on the order of 10 ppmv from other recent volcanoes and the early 2020 Australian wildfires (e.g., Sioris et al. 2016; Kablick et al. 2020; Schwartz et al. 2020). Enhanced water vapor amounts persisted in the stratosphere throughout 2022 (Fig. SB.2.4a). As an example, the quasi-global monthly anomaly (averaged over $\sim 80^\circ S$ – $80^\circ N$, relative to the

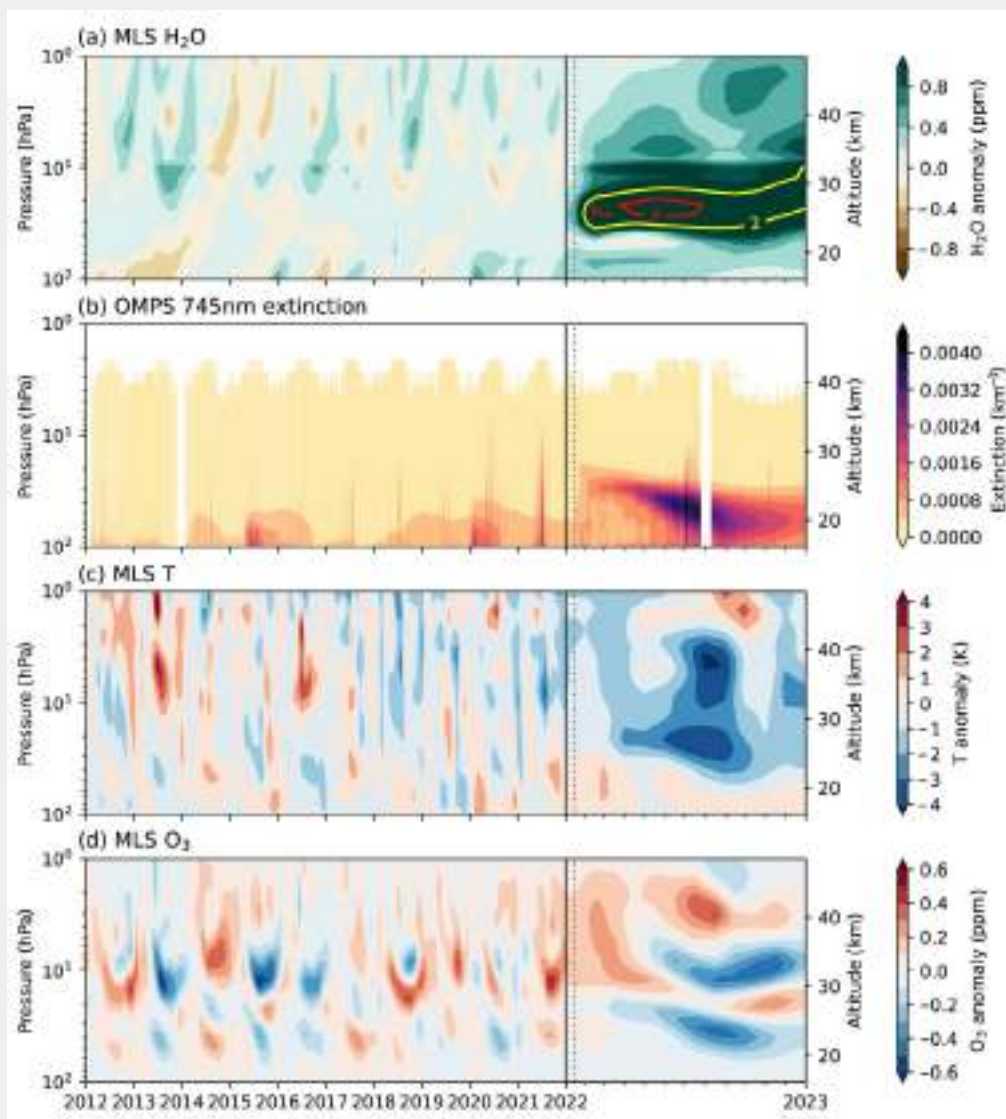


Fig. SB2.4. Southern Hemisphere ($10^\circ S$ – $50^\circ S$) average (a) stratospheric water vapor (H_2O) anomaly (ppm), (b) aerosol extinction (km^{-1}), (c) temperature anomaly (K), and (d) ozone (O_3) anomaly (ppm) for the period 2012–22. The start of 2022 is indicated by the vertical solid line, and the HTHH eruption is indicated by the vertical dotted line. Water vapor, ozone, and temperature anomaly data are from the Aura MLS and calculated as departures from the 2004–21 mean. Aerosol extinction at 745 nm is based on Suomi National Polar-Orbiting Partnership OMPs Limb Profiler data.

2004–21 average) in December 2022 at 26 hPa (~25 km) from the Aura Microwave Limb Sounder (MLS) satellite was +1.1 ppmv, which corresponds to a 12-sigma and 24% deviation from the mean for that month. Because the main WV removal process is due to the slow stratospheric overturning circulation, it is expected that anomalous stratospheric water vapor will persist for a number of years.

It is estimated that HTHH emitted ~0.5 Tg SO₂ (Carn et al. 2022), which is relatively small compared to the ~20 Tg SO₂ emitted by the similarly sized Mt. Pinatubo eruption (Guo et al. 2004). Stratospheric sulfate aerosols formed anomalously quickly in the HTHH plume, likely influenced by rapid oxidation of SO₂ in the extreme water vapor plume (Carn et al. 2022; Zhu et al. 2022). The sulfate aerosol layer gradually separated from the water vapor plume and descended into the SH lower stratosphere due to gravitational settling (Fig. SB.2.4b; see also Legras et al. 2022; Wang et al. 2022), dispersing over latitudes from the tropics to the Antarctic after several months. This resulted in a five-fold increase in the stratospheric aerosol load, which is the highest in the last three decades (Khaykin et al. 2022; see also section 2g3). This stratospheric perturbation had a visible impact on SH aerosol optical depth at 550-nm anomalies in 2022 (section 2g3).

As water vapor and aerosols are radiatively active and persisted in the stratosphere throughout 2022, there are expected impacts on stratospheric temperatures (section 2b6). Enhanced stratospheric water vapor is expected to lead to local (stratospheric) cooling, while elevated stratospheric sulfate aerosol concentrations lead to local warming. Observations show cold stratospheric temperatures in 2022 that were well outside the range of previous variability (Figs. SB.2.4c, 2.11a), with corresponding anomalies in stratospheric winds and circulation that are in balance with the anomalous temperatures (Coy et al. 2022; Wang et al. 2022).

Elevated stratospheric water vapor and aerosol concentrations are expected to affect surface climate and tropospheric temperatures in a manner opposite to their stratospheric impacts (e.g., enhanced stratospheric water vapor leads to surface warming). Although unambiguous detection of a tropospheric/surface temperature signal may be nearly impossible given the potentially small magnitude of any perturbation relative to natural variability, it is estimated that the HTHH eruption increases the likelihood of exceeding an annual mean global surface temperature anomaly of 1.5°C by 7% in the five years following the eruption (Jenkins et al. 2023).

The HTHH eruption is also likely to have effects on stratospheric ozone (Fig. SB.2.4d; sections 2g4, 6h). Impacts from HTHH on stratospheric aerosols and water vapor (and other species) may be perturbing stratospheric ozone chemistry in both midlatitudes and in the polar regions, in addition to the ozone changes from forced circulation changes (Wang et al. 2022). Since the HTHH plume was primarily confined to the SH during 2022, the greatest potential effects are on SH midlatitude ozone (as already evident in Fig. SB.2.4d) and the Antarctic ozone hole. Ozone profile data and total column ozone data in 2022 reveal anomalously low ozone in the SH midlatitude lower stratosphere during 2022, in general agreement with these expectations (section 2g4). However, MLS observations inside the Antarctic vortex showed near-average water vapor (Fig. 6.15h), and other stratospheric perturbations in recent years (e.g., Australian wildfires in early 2020 and earlier volcanic eruptions such as that of La Soufrière in April 2021) as well as anomalously weak planetary wave activity in austral spring have also likely impacted the 2022 Antarctic ozone hole. Further studies are needed to quantify the role of HTHH in perturbing stratospheric ozone.

g. Atmospheric composition

1. LONG-LIVED GREENHOUSE GASES

—X. Lan, B. D. Hall, G. Dutton, and I. Vimont

Increases in atmospheric greenhouse gas burdens, especially the long-lived greenhouse gases (LLGHGs) carbon dioxide (CO₂), methane (CH₄), and nitrous oxide (N₂O), are largely responsible for increasing global temperature (Foster et al. 2021).

Carbon dioxide is the most important and prevalent anthropogenic GHG. The atmospheric pre-industrial abundance of CO₂ is estimated to be ~278 ppm (parts per million by moles in dry air), based on air extracted from ice in Greenland and Antarctica (Etheridge et al. 1996). Globally averaged CO₂ derived from remote marine boundary layer measurements made by NOAA's Global Monitoring Laboratory was 417.1±0.1 ppm in 2022 (Fig. 2.56a), 50% higher than the pre-industrial level. Annual growth in global mean CO₂ has risen steadily from 0.6±0.1 ppm yr⁻¹ in the early 1960s to an average of 2.4 ppm yr⁻¹ during 2013–22 with the 2022 annual growth rate at 2.2 ppm yr⁻¹ (Fig. 2.56a; the global trend is updated monthly on www.gml.noaa.gov/ccgg/trends, and uncertainties are reported as one sigma in this section).

The main driver of increasing atmospheric CO₂ is fossil fuel (FF) burning, with total fossil emissions (including ~5% from cement production) increasing from 3.0±0.2 Pg C yr⁻¹ in the 1960s to 9.6±0.5 Pg C yr⁻¹ in the past decade (2012–21; Friedlingstein et al. 2022). Comparing fossil emissions to the atmospheric increase, we can conclude that only about half of the fossil CO₂ emitted since 1958 has remained in the atmosphere, with the other half taken up by the oceans and terrestrial biosphere. While emissions of CO₂ from FF combustion drive its increasing atmospheric burden, the interannual variability in the CO₂ growth rate is mostly driven by terrestrial biosphere exchange of CO₂ driven by climate variability such as El Niño–Southern Oscillation (ENSO), which is confirmed by measurements of stable (¹³C:¹²C) carbon isotope ratios (e.g., Keeling and Revelle 1985; Alden et al. 2010).

Fossil CO₂ emissions are estimated to have declined by 5.4% in 2020 relative to 2019 due to the COVID-19 pandemic but returned to pre-COVID levels in 2021

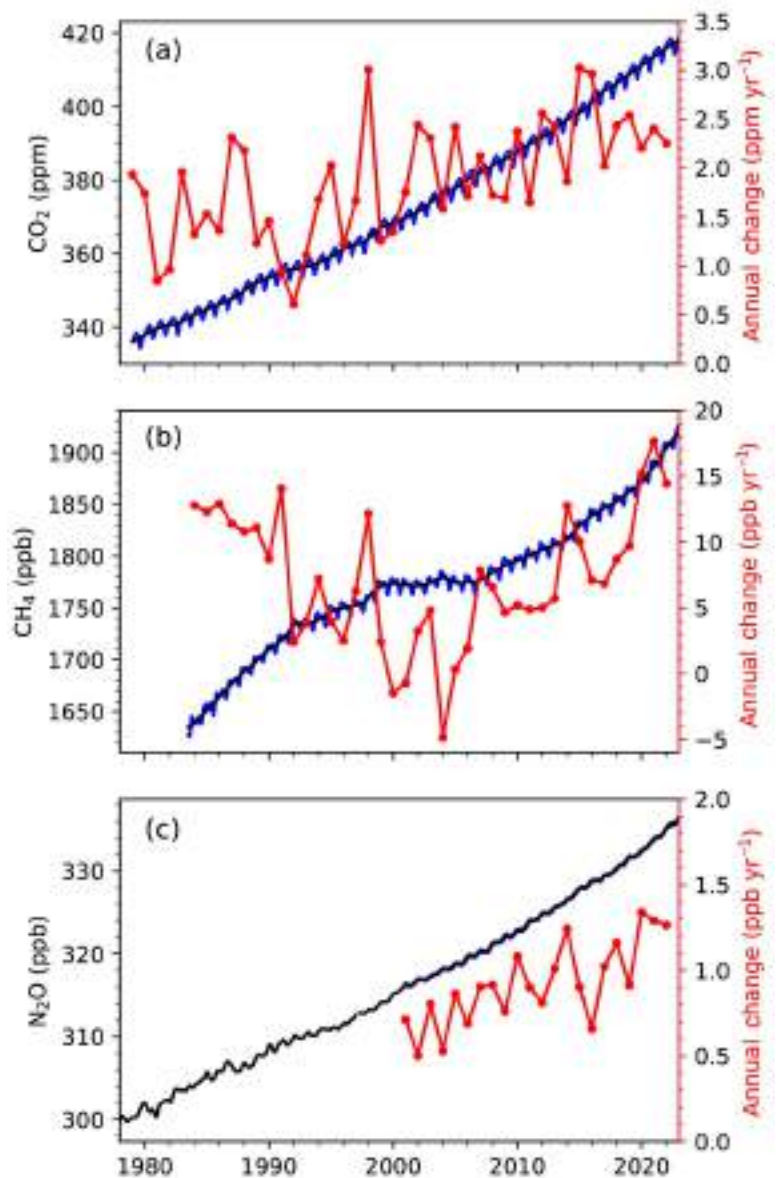


Fig. 2.56. Global mean dry-air remote surface mole fractions (approximately weekly data in blue and deseasonalized trend in black [see Dlugokencky et al. 1994b for methods], left axis) and annual change (red, right axis) of (a) carbon dioxide (CO₂, ppm), (b) methane (CH₄, ppb), and (c) nitrous oxide (N₂O, ppb) derived from the NOAA Global Greenhouse Gases Reference Network. N₂O data prior to 2000 are insufficient and noisy and thus hinder the calculation of a growth rate.

(Friedlingstein et al. 2022). However, these emission changes are not reflected in observed global atmospheric CO₂ signals, because it is a relatively small signal compared to the natural variability that is driven by the large fluxes from photosynthesis and respiration of ecosystems on land.

The impacts of LLGHGs on global climate are estimated using the effective radiative forcings (ERFs) of LLGHGs, following the Intergovernmental Panel on Climate Change Sixth Assessment Report (Forster et al. 2021). Increasing atmospheric CO₂ has accounted for 66% increase in ERF by LLGHGs, by 2.26 W m⁻² in 2022 compared with preindustrial times (before 1750). The rate of increase in CO₂ ERF during 2018–22 accounted for 78% of the total increase by LLGHGs. A pulse of CO₂ will remain in the atmosphere for thousands of years (Archer and Brovkin 2008) and cause long-lasting warming (Pierrehumbert 2014).

Atmospheric CH₄ has a lifetime of ~9 years, meaning that its atmospheric abundance and ERF can be reduced much more quickly by reducing emissions compared to CO₂ (United Nations Global Methane Assessment 2021). Global mean tropospheric CH₄ abundance increased to 1911.8±0.6 ppb (parts per billion by moles in dry air) in 2022, a 165% increase compared to its pre-industrial level of 729±9 ppb (Mitchell et al. 2013). Global CH₄ increased by an average of 12±1 ppb yr⁻¹ between 1984 and 1991, followed by a smaller increase of 4±2 ppb yr⁻¹ between 1992 and 1998, and further reduced to near zero (1±3 ppb yr⁻¹) during 1999–2006. Atmospheric CH₄ growth restarted in 2007 and has significantly accelerated since 2014 (Fig. 2.56b). The highest annual CH₄ growth rates were recorded in 2020 and 2021 at 15.2±0.4 ppb and 17.7±0.4 ppb, respectively, since the beginning of NOAA's systematic CH₄ measurements in 1983. Preliminary results also reveal large growth in 2022 of 14.4±0.4 ppb. The increase in CH₄ contributed to a 0.56 W m⁻² increase in ERF in 2022 from preindustrial times while the CH₄-related production of tropospheric ozone (O₃) and stratospheric H₂O also contributes to ~0.30 W m⁻² indirect radiative forcing (Myhre et al. 2014).

Atmospheric measurements of ¹³C:¹²C of CH₄ (denoted δ¹³C-CH₄) are sensitive to different CH₄ emission and sink processes (Lan et al. 2021). The ongoing reduction in δ¹³C-CH₄ since 2008 (Michel et al. 2022) indicates increased emissions from microbial sources (Basu et al. 2022), including both anthropogenic emissions from livestock and waste/landfills and natural wetland and lakes, which have more negative δ¹³C-CH₄ signatures. A decrease in biomass burning (Worden et al. 2017) and a small increase in FF emissions (leakage, not combustion) may also play a smaller role in 2007–16 global CH₄ change (Lan et al. 2019, 2021; Oh et al. 2022; Basu et al. 2022).

Recent studies suggest a dominant role of increased tropical wetland emissions in the 2020 CH₄ surge (Feng et al. 2021; Peng et al. 2022). An increased contribution from wetland emissions also agrees with the acceleration of atmospheric δ¹³C-CH₄ reductions in 2020 and 2021 (Michel et al. 2022). Rapid increases in wetland CH₄ emissions can be an indication of ongoing climate feedback. A reduction in the hydroxyl radical (OH, the main sink for CH₄) may have contributed to the growth in 2020 due to the COVID-19 pandemic impact on major OH precursors, NO_x, and CO (Laughner et al. 2021; Peng et al. 2022). However, COVID-19-related processes are unlikely to explain the continued rapid increase in 2021 and 2022. Additionally, Lan et al. (2021) showed that the reduction in the OH sink portion would push atmospheric δ¹³C-CH₄ upward when the atmospheric CH₄ mass balance is satisfied.

Nitrous oxide is an ozone-depleting LLGHG (Ravishankara et al. 2009) produced by microbes that rely on nitrogen substrates from natural and agricultural soils, animal manure, and the oceans (Davidson 2009). Atmospheric N₂O has been increasing steadily throughout the industrial era, except for a brief period in the 1940s (MacFarling Meure et al. 2006; Thompson et al. 2019). The mean global atmospheric N₂O abundance in 2022 was 335.7±0.1 ppb, a 24% increase over its preindustrial level of 270 ppb. The annual increase of 1.3±0.1 ppb in 2020 was the largest in NOAA's measurement record since 2000, while similarly large growth rates were observed in 2021 and 2022 at 1.3±0.1 ppb and 1.3±0.1 ppb (Fig. 2.56c). Recent growth rates are larger than the average increase during 2010–19 (1.0 ± 0.2 ppb), suggesting increased emissions. The increase in atmospheric N₂O abundance contributed to a 0.22 W m⁻² increase in ERF in 2022. The rate of increase in N₂O contributed to 9% of the rate of increase in radiative forcing by all LLGHGs

in the past five years (2018–22), comparable to the 11% contribution from CH₄ increase.

The combined radiative forcing in 2022 from all LLGHGs was 3.44 W m⁻² (Fig. 2.57), which is 3.6 times larger than in 1950. The post-industrial increases in atmospheric CO₂, CH₄, and N₂O abundances have contributed to 88% of ERF increase (Fig. 2.57a), while the mean rate of ERF increase for CO₂, CH₄, and N₂O in the past five years (2018–22) accounts for 98% of the mean rate of ERF increase resulting from growth of all LLGHGs (Fig. 2.57b).

2. OZONE-DEPLETING SUBSTANCES AND THEIR SUBSTITUTES

—I. J. Vimont, B. D. Hall, G. Dutton, S. A. Montzka, J. Mühle, M. Crotnell, K. Petersen, S. Clingan, and D. Nance

Ozone-depleting substances (ODSs) include chlorofluorocarbons (CFCs), methyl bromide, various chlorinated hydrocarbons, halons, and the CFC replacements hydrochlorofluorocarbons (HCFCs). These compounds influence global climate both through direct absorption of infrared energy and via their ability to deplete stratospheric ozone, a strong greenhouse gas (Karpechko and Maycock 2018). Hydrofluorocarbons (HFCs) are increasingly used as ODS replacements that do not destroy ozone, but they are highly efficient infrared absorbers.

The consumption and production of these classes of halogenated compounds is controlled by the 1987 Montreal Protocol (hereafter referred to as The Protocol), and its subsequent amendments, both of which aim to limit damage to the stratospheric ozone layer and the climate. The Protocol first specified the phase-out of production and consumption for dispersive uses of ODSs starting with the CFCs, followed by halons and then HCFCs. More recently, a phase down of select HFCs with high global warming potentials (GWPs) used as ODS substitutes has been mandated through the Kigali Amendment to The Protocol. Importantly, the Kigali Amendment was signed by China in 2021 and by the United States in 2022, further strengthening the ability of The Protocol and the global community to reduce the impacts of these gases on the climate.

Even as production of these controlled substances ends, other factors affect their atmospheric abundance. Their atmospheric lifetimes vary considerably, such that long-lived chlorofluorocarbons like CFC-11 and CFC-12 have only declined 18% and 10% from their peak atmospheric abundances (in 1994 and 2003, respectively), while the shorter-lived solvent methyl chloroform has declined by 99% (Fig. 2.58). Production of CFC-11 and CFC-12 was reported to have been globally phased out in 2010, while methyl chloroform (CH₃CCl₃) was reported to have been globally phased out by 2015. Additionally, the slow long-term release or sudden leakage of chemicals from some applications (e.g., insulating foams and refrigeration units) plays an important role in maintaining emissions even after production has been phased out.

It is important to note that for compounds controlled by The Protocol, the scheduled phase-down or phase-out of production of these compounds is agreed upon, and efforts to accomplish this are self-reported by individual countries to the United Nation’s Ozone Secretariat. Recent studies of CFC-11 exemplify the critical need for continued monitoring of these compounds in the atmosphere to ensure the success of The Protocol. The unexpected slowdown in the reduction of the atmospheric abundance of CFC-11 after 2012 led to the discovery of renewed, unreported emissions through to 2018 in an apparent violation of The Protocol (Montzka et al.

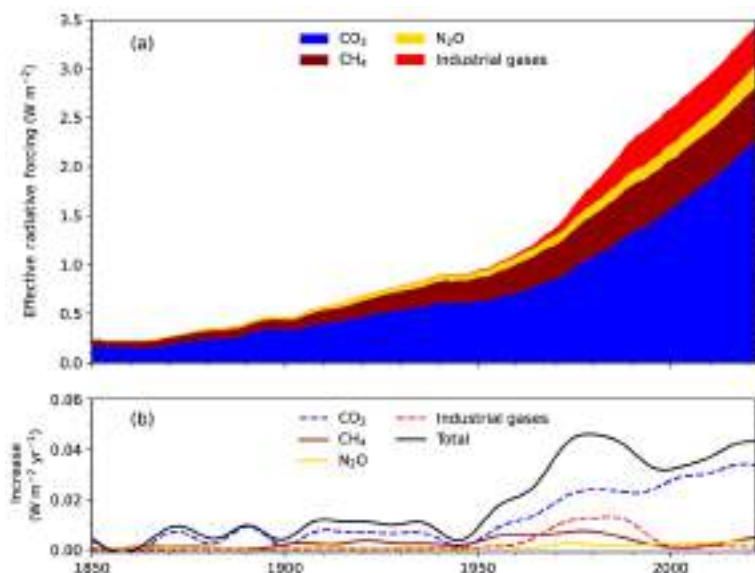


Fig. 2.57. (a) Effective radiative forcing (W m⁻²) due to long-lived greenhouse gases (LLGHGs; see Table 2.8 for details on industrial gases). (b) Annual increase in direct radiative forcing (W m⁻²).

2018; Rigby et al. 2019). Since then, an accelerated decline in abundance has been measured, suggesting that the problem may be mostly resolved (Montzka et al. 2021; Park et al. 2021).

Tangentially, signatories to the Kigali Amendment pledged to begin controlling select HFCs under The Protocol, including HFC-23 and HFC-134a. Reported abatement of HFC-23 independent of the Kigali Amendment suggests that emissions of this high-GWP compound should have been decreasing in recent years (e.g., Stanley et al. 2020 and references therein). However, measurements show its global abundance increasing by about 1.0 ppt (parts per trillion by moles in dry air) per year (since 2013), reaching 35.9 ppt in 2022 (Table 2.8 and Fig. 2.58), indicating that emissions are instead increasing (Stanley et al. 2020; Park et al. 2023). Likewise, the most abundant

Table 2.8. Summary table of long-lived greenhouse gases for 2022 (CO₂ mixing ratios are in ppm, N₂O and CH₄ in ppb, and all others in ppt).

Compound Class	Industrial Designation or Common Name	Chemical Formula	ERF ^a	Rad. Efficiency (W m ⁻² ppb ⁻¹) ^b	Rad. Forcing ^a (ERF/SARF) (W m ⁻²)	Mean surface mole fraction, 2022 [change from prior year] ^c	Lifetime (yrs) ^b
Acidic oxide	Carbon Dioxide	CO ₂	Y	1.33 × 10 ⁻⁵	2.3	417.1 [2.4]	
Alkane	Methane	CH ₄	Y	3.88 × 10 ⁻⁴	0.56	1911.9 [13.0]	9.1
Nitride	Nitrous Oxide	N ₂ O	Y	3.2 × 10 ⁻³	0.22	335.7 [1.3] ^d	123
Chlorofluorocarbon	CFC-11	CCl ₃ F	N(Y) ^e	0.26	0.057(0.064)	219.6 [−2.1] ^d	52
Chlorofluorocarbon	CFC-12	CCl ₂ F ₂	N(Y) ^e	0.32	0.157(0.176)	489.7 [−3.5] ^d	102
Chlorofluorocarbon	CFC-113	CCl ₂ FCClF ₂	N	0.30	0.020	67.8 [−0.5] ^d	93
Hydrochlorofluorocarbon	HCFC-22	CHClF ₂	N	0.21	0.052	248.8 [−0.1]	11.9
Hydrochlorofluorocarbon	HCFC-141b	CH ₃ CCl ₂ F	N	0.16	0.004	24.6 [0.0]	9.4
Hydrochlorofluorocarbon	HCFC-142b	CH ₃ CClF ₂	N	0.19	0.004	21.2 [−0.3]	18
Hydrofluorocarbon	HFC-134a	CH ₂ FCF ₃	N	0.17	0.021	124.5 [5.6]	14
Hydrofluorocarbon	HFC-152a	CH ₃ CHF ₂	N	0.10	<0.001	7.4 [0.2]	1.6
Hydrofluorocarbon	HFC-143a	CH ₃ CF ₃	N	0.17	0.005	27.5 [1.8]	51

^a Effective Radiative Forcing (ERF) calculated by multiplying the stratospheric-temperature adjusted radiative efficiency (SARF) by the global mole fraction (in ppb) and then applying a tropospheric adjustment factor for the species indicated based on recommended values from chapters 6 and 7 in the IPCC AR6 WGI Report. The Radiative Forcing column is either ERF (where indicated) or SARF. The adjustments to the SARF are CO₂: 5% ± 5%, CH₄: −14% ± 15%, N₂O: 7% ± 13–16%.

^b Radiative efficiencies and lifetimes were taken from Appendix A in WMO (2018) and Hodnebrog et al. (2020a), except for SF₆ lifetime from Ray et al. (2017), CH₄ lifetime from Prather et al. (2012). For CO₂, numerous removal processes complicate the derivation of a global lifetime. AGGI = Annual Greenhouse Gas Index. For radiative forcing, see <https://www.esrl.noaa.gov/gmd/aggi/aggi.html>.

^c Mole fractions are global, annual, midyear surface means determined from the NOAA cooperative global air sampling network (Hofmann et al. 2006), except for PFC-14, PFC-116, PFC-218, PFC-318, and HFC-23, which were measured by AGAGE (Mühle et al. 2010; Miller et al. 2010). Changes indicated in brackets are the differences between the 2022 and 2021 means, the relevant quantities for calculating radiative forcing. These changes are somewhat different from the 2022 annual increases reported in (LLGHG SECTION), which are determined as the difference between 1 Jan 2022 and 1 Jan 2021. All values are preliminary and subject to minor updates.

^d Global mean estimates derived from multiple NOAA measurement programs (“Combined Dataset”).

^e ERF calculated values for CFC-11 and CFC-12 are highly uncertain but recommended by the IPCC AR6 WGI Report. Thus, they are included in parentheses here as the lower confidence value. The adjustment to the SARF for these values is 12% ± 13% (Hodnebrog et al. (2020b).

Compound Class	Industrial Designation or Common Name	Chemical Formula	ERF ^a	Rad. Efficiency (W m ⁻² ppb ⁻¹) ^b	Rad. Forcing ^a (ERF/SARF) (W m ⁻²)	Mean surface mole fraction, 2022 [change from prior year] ^c	Lifetime (yrs) ^b
Hydrofluorocarbon	HFC-125	CHF ₂ CF ₃	N	0.23	0.007	37.0 [3.7]	30
Hydrofluorocarbon	HFC-32	CH ₂ F ₂	N	0.11	0.002	26.3 [3.5]	5.4
Hydrofluorocarbon	HFC-23	CHF ₃	N	0.18	0.006	35.9 [0.9]	228
Hydrofluorocarbon	HFC-365mfc	CH ₃ CF ₂ CH ₂ CF ₃	N	0.22	<0.001	1.07 [0.02]	8.9
Hydrofluorocarbon	HFC-227ea	CF ₃ CHFCF ₃	N	0.26	<0.001	2.04 [0.17]	36
Chlorocarbon	Methyl Chloroform	CH ₃ CCl ₃	N	0.07	<0.001	1.1 [-0.1]	5.0
Chlorocarbon	Carbon Tetrachloride	CCl ₄	N	0.17	0.013	75.5 [-1.2] ^d	32
Chlorocarbon	Methyl Chloride	CH ₃ Cl	N	0.01	<0.001	547.5 [0.2]	0.9
Chlorocarbon	Methyl Bromide	CH ₃ Br	N	0.004	<<0.001	6.61 [-0.06]	0.8
Chlorocarbon	Halon 1211	CBrClF ₂	N	0.29	0.001	2.93 [-0.1]	16
Chlorocarbon	Halon 1301	CBrF ₃	N	0.30	0.001	3.31 [0.0]	72
Chlorocarbon	Halon 2402	CBrF ₂ CBrF ₂	N	0.31	<0.001	0.397 [0.001]	28
Fully fluorinated species	Sulfur Hexafluoride	SF ₆	N	0.57	0.006	11.02 [0.37]	>600
Fully fluorinated species	PFC-14	CF ₄	N	0.09	0.005	88.5 [1.0]	~50,000
Fully fluorinated species	PFC-116	C ₂ F ₆	N	0.25	0.001	5.15 [0.12]	~10,000
Fully fluorinated species	PFC-218	C ₃ F ₈	N	0.28	<0.001	0.74 [0.02]	~2600
Fully fluorinated species	PFC-318	c-C ₄ F ₈	N	0.32	<0.001	1.99 [0.09]	~3200

^a Effective Radiative Forcing (ERF) calculated by multiplying the stratospheric-temperature adjusted radiative efficiency (SARF) by the global mole fraction (in ppb) and then applying a tropospheric adjustment factor for the species indicated based on recommended values from chapters 6 and 7 in the IPCC AR6 WGI Report. The Radiative Forcing column is either ERF (where indicated) or SARF. The adjustments to the SARF are CO₂: 5% ± 5%, CH₄: -14% ± 15%, N₂O: 7% ± 13–16%.

^b Radiative efficiencies and lifetimes were taken from Appendix A in WMO (2018) and Hodnebrog et al. (2020a), except for SF₆ lifetime from Ray et al. (2017), CH₄ lifetime from Prather et al. (2012). For CO₂, numerous removal processes complicate the derivation of a global lifetime. AGGI = Annual Greenhouse Gas Index. For radiative forcing, see <https://www.esrl.noaa.gov/gmd/aggi/aggi.html>.

^c Mole fractions are global, annual, midyear surface means determined from the NOAA cooperative global air sampling network (Hofmann et al. 2006), except for PFC-14, PFC-116, PFC-218, PFC-318, and HFC-23, which were measured by AGAGE (Mühle et al. 2010; Miller et al. 2010). Changes indicated in brackets are the differences between the 2022 and 2021 means, the relevant quantities for calculating radiative forcing. These changes are somewhat different from the 2022 annual increases reported in {LLGHG SECTION}, which are determined as the difference between 1 Jan 2022 and 1 Jan 2021. All values are preliminary and subject to minor updates.

^d Global mean estimates derived from multiple NOAA measurement programs (“Combined Dataset”).

^e ERF calculated values for CFC-11 and CFC-12 are highly uncertain but recommended by the IPCC AR6 WGI Report. Thus, they are included in parentheses here as the lower confidence value. The adjustment to the SARF for these values is 12% ± 13% (Hodnebrog et al. (2020b).

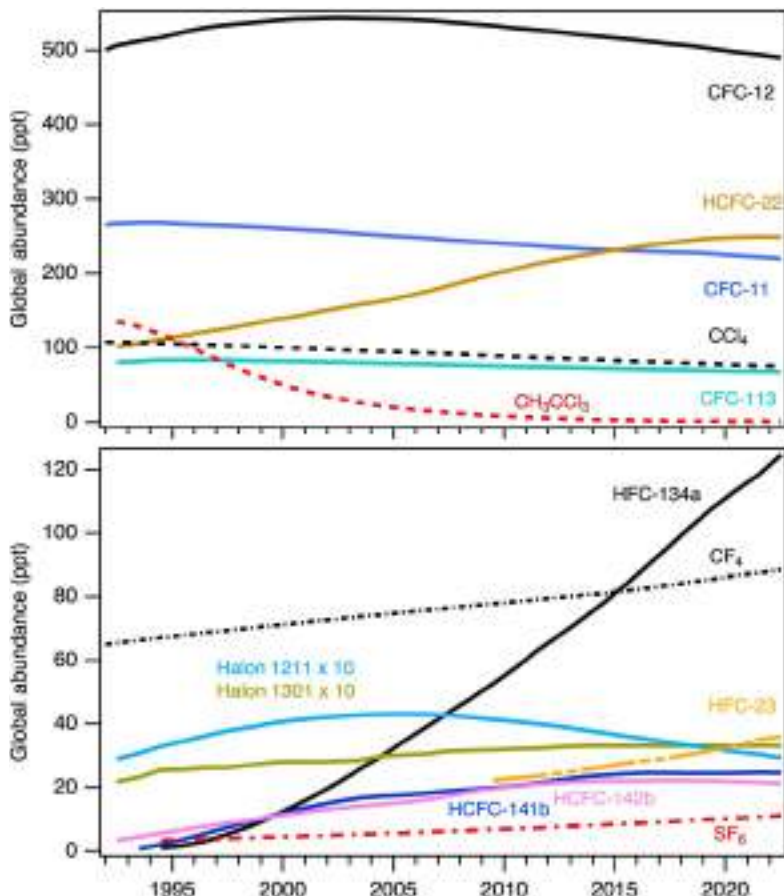


Fig. 2.58. Global mean abundances (mole fractions) at Earth's surface (ppt = nmol mol⁻¹ in dry air) for a suite of halogenated gases, most of which deplete stratospheric ozone. See Table 2.8 for the 2022 global mean mole fractions of these and other gases. All compounds, except hydrofluorocarbon (HFC)-23, are mid-year global means taken from <https://gml.noaa.gov/aftp/data/hats/>. HFC-23 data derived from AGAGE mid-year global means taken from https://age2.eas.gatech.edu/data_archive/global_mean/global_mean_ms.txt.

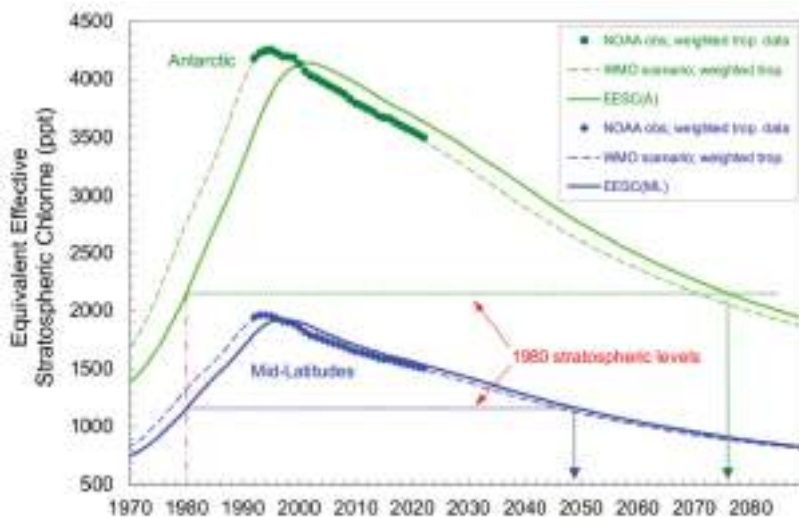


Fig. 2.59. The equivalent effective stratospheric chlorine in the Antarctic and midlatitudes (EESC(A) and EESC(ML), respectively) values represent EESC on 1 Jan of each year since 1970. Dashed lines represent tropospheric measurement-derived scenarios, based on past measurements and, for the future, full adherence to all controls from The Protocol based on the WMO/UNEP 2018 Ozone Assessment. Solid lines depict inferred stratospheric changes based on the measured tropospheric curves. In 2022, midlatitude and Antarctic EESC were at 1537 ppt and 3635 ppt, which represent reductions of 21% and 12.5% in stratospheric reactive halogen loading from their peaks. Translating this to the Ozone Depleting Gas Index (ODGI), the midlatitude ODGI is 48.6 and the Antarctic ODGI is 74.1, meaning the stratospheric reactive halogen loading has declined 52.4% and 25.9% relative to the 1980 benchmark reactive halogen abundance.

HFC, HFC-134a, a common mobile air-conditioning fluid, has increased by an average of 5.8 ppt yr⁻¹ since 2012, reaching 124.5 ppt in 2022 (Table 2.8; Fig. 2.58).

One measure of the reactive halogen loading at a given time and place in the stratosphere is the equivalent effective stratospheric chlorine (EESC; Daniel et al. 1995; Montzka et al. 1996; Newman et al. 2007). The presence of reactive halogen radicals in the stratosphere is mostly due to the breakdown of CFCs, which still have high abundances in the atmosphere and contribute strongly to EESC. While EESC provides a measure of reactive stratospheric halogen (Fig. 2.59), it is useful to scale the EESC to provide context relative to stratospheric ozone recovery, and thus the Ozone Depleting Gas Index (ODGI) was developed (Hoffmann and Montzka 2009). For a full description of both EESC and ODGI, see <https://gml.noaa.gov/odgi/>. Briefly, EESC and the ODGI are separated

into two categories, midlatitude and Antarctic, because transport processes cause widely different reactive halogen abundances in these stratospheric regions. ODGI is derived from a simple scaling of EESC such that an ODGI of 100 represents the peak EESC value, and an ODGI of 0 represents the value of EESC in 1980 (Hoffmann and Montzka 2009). Using the ODGI, recovery of the stratospheric ozone layer is expected to reach 1980 levels in 2049 for the midlatitudes and 2076 in the Antarctic (Fig. 2.59).

3. AEROSOLS

—S. Rémy, N. Bellouin, M. Ades, M. Alexe, A. Benedetti, O. Boucher, and Z. Kipling

Atmospheric aerosols play an important role in the climate system by scattering and absorbing radiation and by affecting the life cycle, optical properties, and precipitation activity of clouds (IPCC AR6, chapter 6; Szopa et al. 2021). Aerosols also represent a serious public health issue in many countries, and hence are subject to monitoring and forecasting as part of air quality policies. There is also growing evidence that aerosols influence ecosystems through changes in the quality and quantity of light and deposition flux of nutrients over land and ocean (Mahowald et al. 2017).

The Copernicus Atmosphere Monitoring Service (CAMS; <http://atmosphere.copernicus.eu>) runs a near-real-time global analysis of aerosols and trace gases. It also produces a reanalysis of global aerosols and trace gases covering the years 2003–22 (CAMS Reanalysis [CAMRA]; Inness et al. 2019), by combining state-of-the-art numerical modeling and in the case of aerosols, remote sensing retrievals from the Moderate Resolution Imaging Spectroradiometer (MODIS; Levy et al. 2013) and the Advanced Along Track Scanning Radiometer (AATSR; Popp et al. 2016).

Aerosol optical depth (AOD) at 550 nm and particulate matter $\leq 2.5\mu\text{m}$ (PM_{2.5}) concentrations ($\mu\text{g m}^{-3}$) in 2022 (Figs. 2.60a,b) show maxima over India and China, mostly from anthropogenic sources, as well as from dust over the Sahara and the Middle East. High values from seasonal or occasional extreme fires are noted over equatorial Africa, Siberia, parts of North America, and the Amazon basin. There is strong seasonality in AOD (Fig. 2.60c), driven mainly by dust episodes

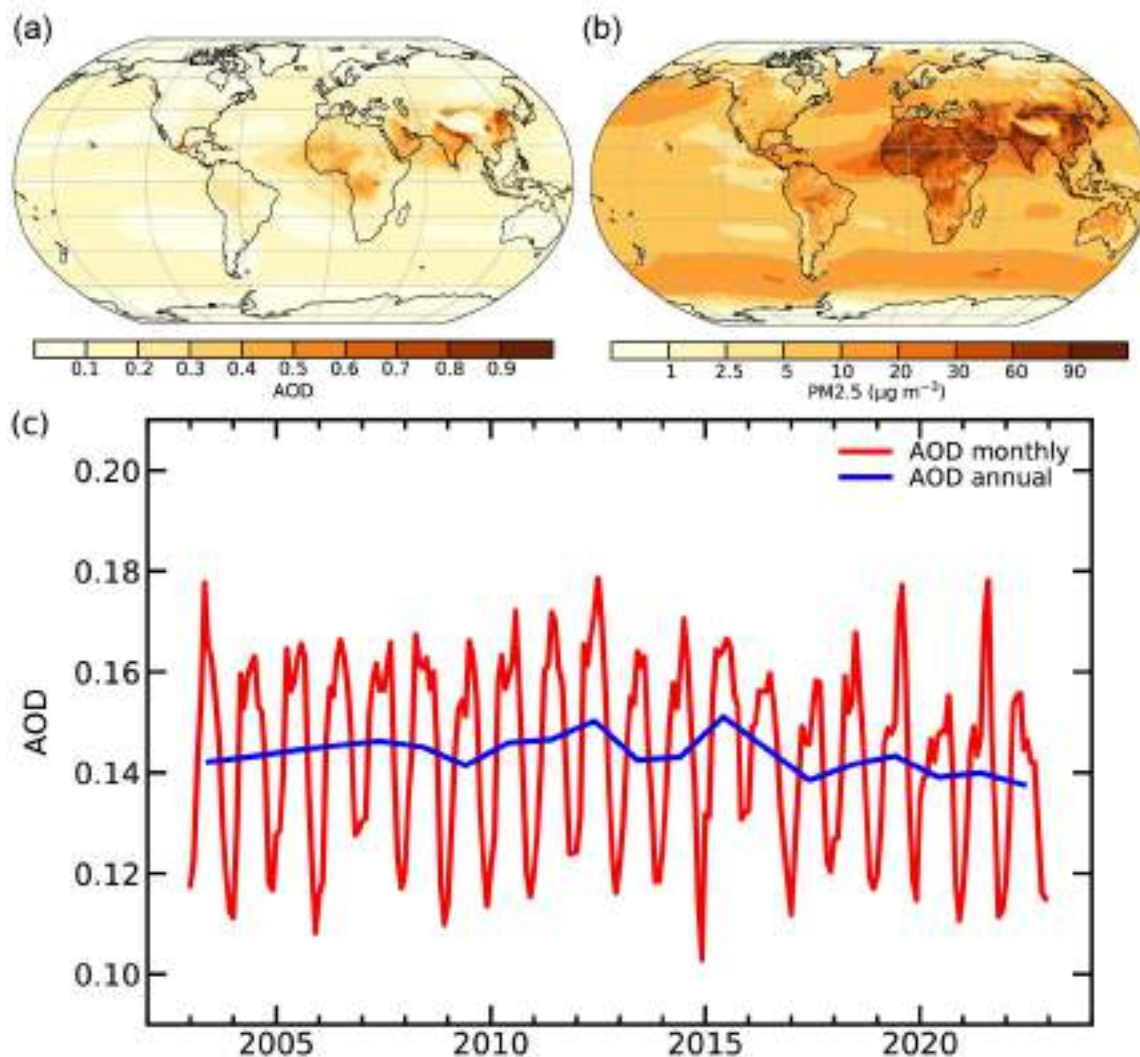


Fig. 2.60. (a) Global aerosol optical depth (AOD) at 550 nm in 2022; (b) global surface PM_{2.5} concentrations ($\mu\text{g m}^{-3}$) in 2022; and (c) global average of total AOD at 550 nm averaged over monthly (red) and annual (blue) periods for 2003–22.

between March and July in the Sahara, Middle East, and Taklimakan/Gobi desert and seasonal biomass burning in Africa, South America, and Indonesia. Globally averaged AOD in 2022 was the lowest on record, slightly lower than in 2021 and 2020. The summer maximum was much less pronounced than in 2021, as there were fewer fire emissions in 2022.

The 2022 AOD (Plates 2.1v,w) was much less impacted by large fire events than in 2021. Positive anomalies due to fires are found above parts of the Amazon basin, following an active fire season in July and August 2022, and parts of Alaska. South Africa also experienced exceptional fires from the end of July to early October, which led to a large positive AOD anomaly and a number of exceptional AOD days (Plate 2.1x). Dust storm activity was in general lower than usual over most of the Sahara except over its northwest fringe, while the Taklimakan and most of the Arabian Peninsula experienced a higher-than-usual amount of dust. Most of the Southern Hemisphere witnessed a small positive AOD anomaly (see Plates 2.1v,w) between January and March 2022 associated with the Hunga Tonga–Hunga Ha’apai (HTHH) eruption of 13–15 January. This eruption led to the largest stratospheric aerosol disturbance since the June 1991 Mt. Pinatubo eruption (Legras et al. 2022), although HTHH mostly impacted the Southern Hemisphere (see Sidebar 2.2). Monthly stratospheric AOD increased by 0.05 to 0.1 AOD units over the most affected areas (west of Australia, eastern equatorial Pacific Ocean), where there were also signals in terms of number of extreme AOD days. The negative anomalies of AOD over East Asia, Europe, and the Amazon basin (positive anomalies over India and Iran) are associated with ongoing decreasing (increasing) trends in these regions.

The AOD and PM_{2.5} 2003–22 and 2012–22 trends are shown in Figs. 2.61a–d and are generally consistent. Between 2003 and 2022, there is a strong negative trend over most of United States, Europe, East Asia, and parts of the Amazon basin, the latter from reduced deforestation activity. Positive trends are noted over parts of Siberia, driven by biomass burning events, as well as over India and Iran, driven by an increase in anthropogenic emissions of aerosol constituents (e.g., Wang et al. 2021). Between 2012 and 2022, the picture is slightly different: there is no decreasing

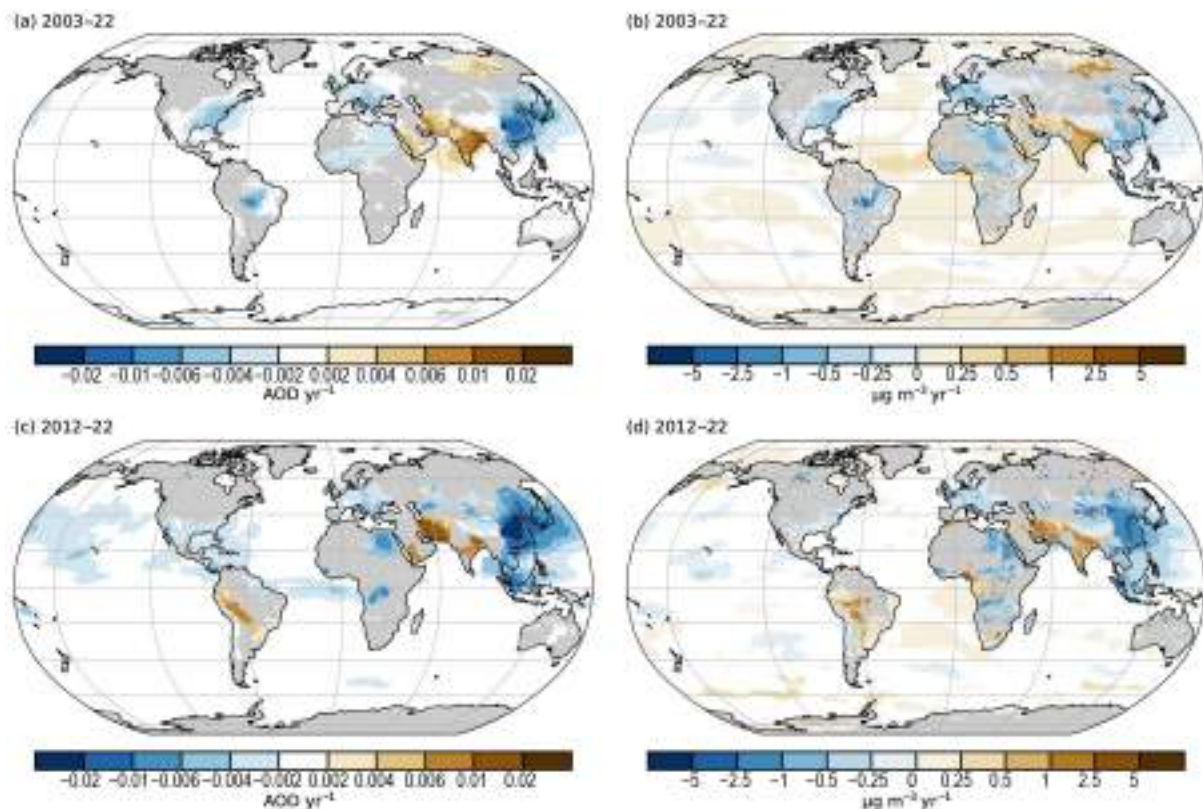


Fig. 2.61. (a),(b) linear trends of total aerosol optical depth (AOD unit yr⁻¹) and PM_{2.5} (µg m⁻³ yr⁻¹) for 2003–22; and (c),(d) linear trends of total AOD (AOD unit yr⁻¹) and PM_{2.5} (µg m⁻³ yr⁻¹) for 2012–22. Only trends that are statistically significant (95% confidence level) are shown. Regions with decreasing trends include the eastern United States, most of Europe, parts of Brazil and China, as well as the Korean Peninsula and Japan.

trend over the Amazon basin, showing that most of the 2003–22 reduction can be explained by the evolution from 2003 to 2012. The 2012–22 negative trend over Europe and the eastern United States is weaker than the 2003–22 trend, while over East Asia it is stronger, which is consistent with the observed decrease of anthropogenic emissions predominantly occurring since 2012 (Li et al. 2017; Wang et al. 2021). A stronger positive trend between 2012 and 2022 is noted over most of Iran, while over the same period the positive trend over India is smaller than the 2003–22 trend.

Anthropogenic AOD and radiative forcing resulting from aerosol-radiation (RFari) and aerosol-cloud interactions (RFaci; see Bellouin et al. 2020 for details) are shown in Fig. 2.62 for 2022 and the period 2003–22. 2022 is the fifth consecutive year showing a decrease in the average anthropogenic AOD and of the absolute magnitude of RFari and RFaci. This is qualitatively consistent with a reduction in anthropogenic aerosol load (Quaas et al. 2022).

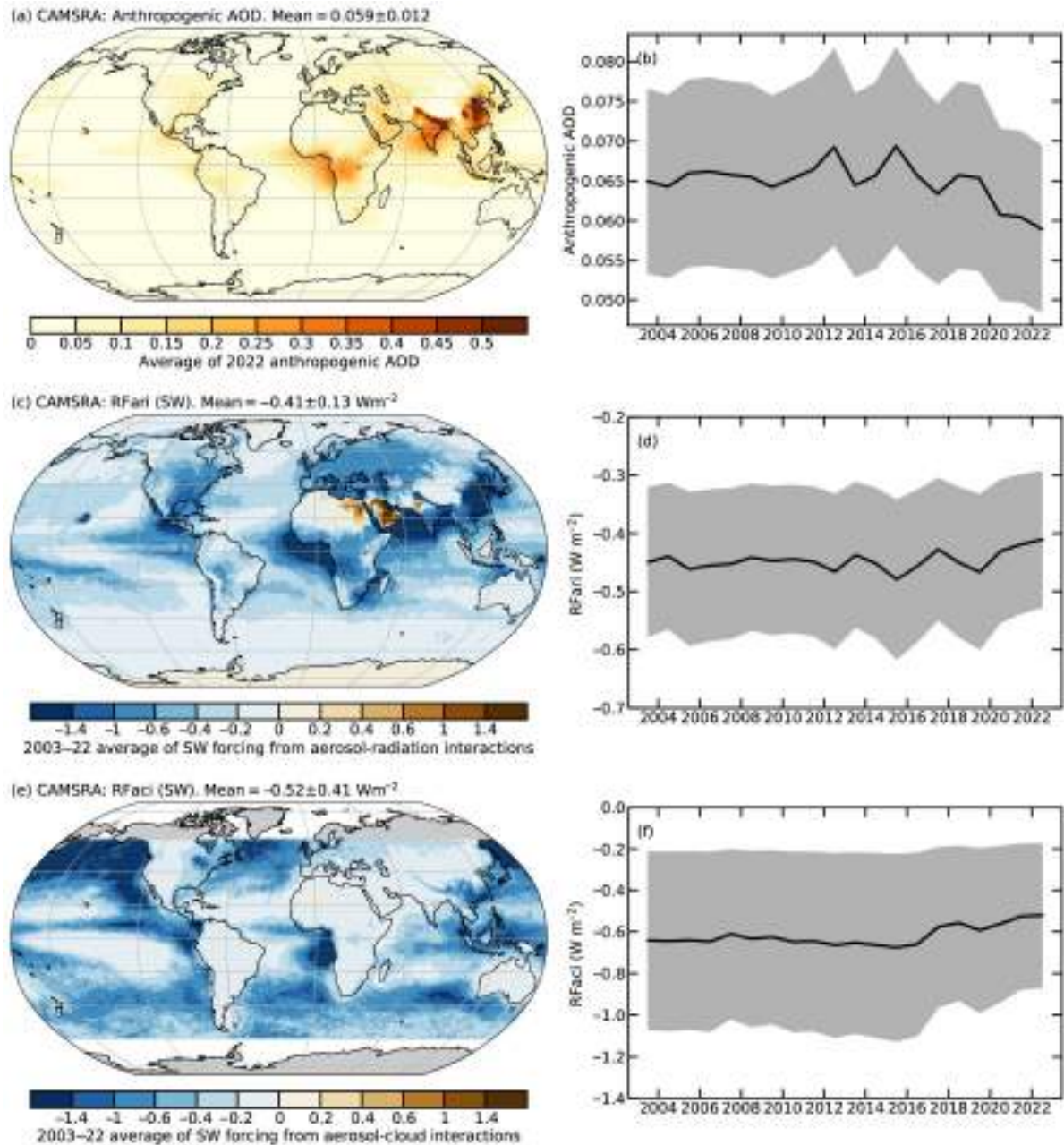


Fig. 2.62. CAMSRA (a) 2022 average of anthropogenic aerosol optical depth (AOD); (b) global annual average of anthropogenic AOD from 2003 to 2022. Radiative forcing in the shortwave (SW) spectrum due to (c),(d) aerosol-radiation (RFari) and (e),(f) aerosol-cloud interactions (RFaci). The left column shows the distributions for the year 2022. The right column shows time series of global averages for the period 2003–22, with the 1- σ uncertainties of these estimates shown in gray.

4. STRATOSPHERIC OZONE

—M. Weber, W. Steinbrecht, C. Arosio, R. van der A, S. M. Frith, J. Anderson, L. M. Ciasto, M. Coldewey-Egbers, S. Davis, D. Degenstein, V. E. Fioletov, L. Froidevaux, D. Loyola, A. Rozanov, V. Sofieva, K. Tourpali, R. Wang, T. Warnock, and J. D. Wild

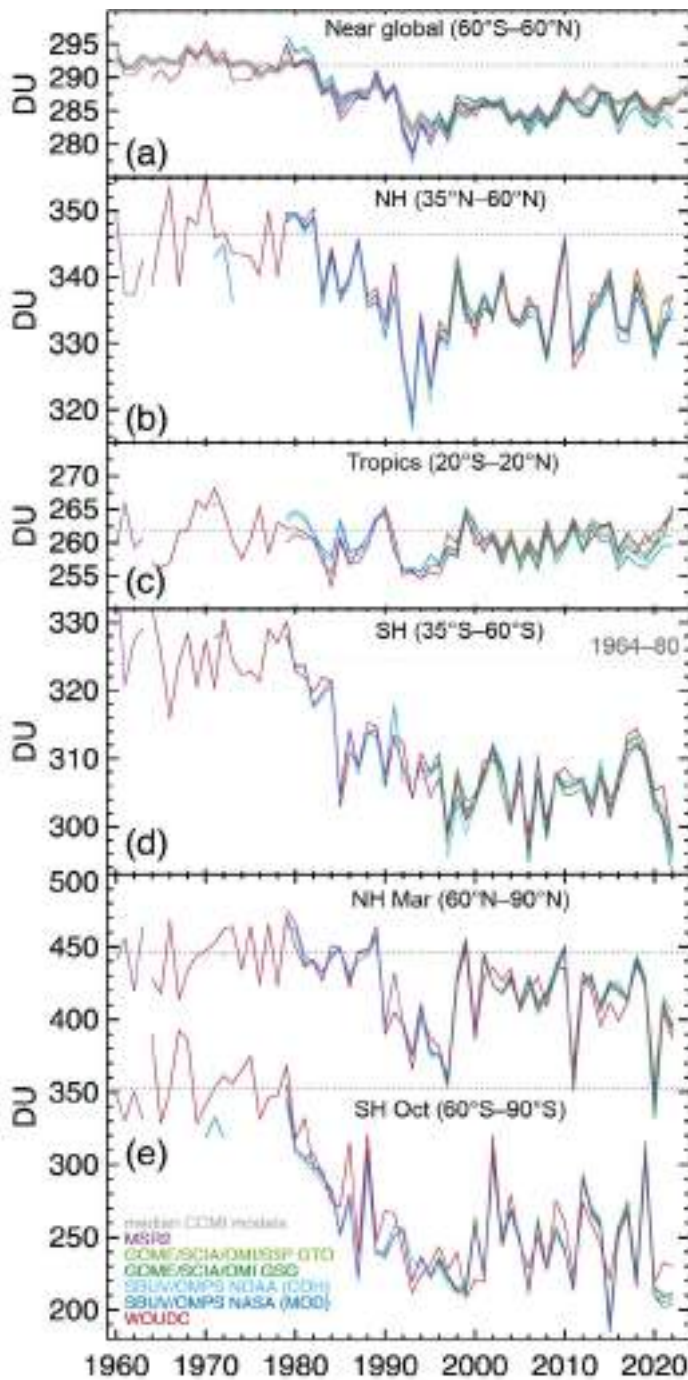


Fig. 2.63. Time series of annual mean total column ozone (DU) in (a)–(d) four zonal bands and (e) polar (60°–90°) total column ozone in Mar (Northern Hemisphere, NH) and Oct (Southern Hemisphere, SH), the months when polar ozone losses usually are largest. Data are from World Ozone and Ultraviolet Radiation Data Centre (WOUDC) ground-based measurements combining Brewer, Dobson, Système D’Analyse par Observations Zénithales (SAOZ), and filter spectrometer data (red; Fioletov et al. 2002, 2008); the BUV/SBUV/SBUV2/OMPS merged products from NASA (V8.7; dark blue; Frith et al. 2014, 2017), and NOAA (SBUV V8.6, OMPS V4r1; light blue; Wild and Long pers. comm., 2019); the GOME/SCIAMACHY/GOME-2/OMPS/(TROPOMI) products GSG from University of Bremen (dark green; Weber et al. 2022), and GTO from the ESA/DLR dataset (light green; Coldewey-Egbers et al. 2015; Garane et al. 2018). MSR2 (purple) assimilates nearly all ozone datasets after corrections based on the ground-based data (van der A et al. 2015). All datasets have been bias-corrected by subtracting averages for the reference period 1998–2008 and adding back the mean of these averages. The dotted gray lines in each panel show the average ozone level for 1964–80 calculated from the WOUDC data. The thick gray lines in (a) show the median ozone level from CCM1-1 ref C2 model runs (SPARC/IO3C/GAW 2019). Most of the observational data for 2022 are preliminary.

Stratospheric ozone protects Earth’s biosphere from harmful ultraviolet (UV) radiation. The phase-out of ozone-depleting substances (ODSs) mandated by the Montreal Protocol and its Amendments (section 2g2) stopped the continuous decline of stratospheric ozone observed before the mid-1990s (Fig. 2.63). Some regions indicate a slow recovery attributed to the ODS decline, most notably the upper stratosphere (Figs. 2.64a–c; WMO 2022; Arosio et al. 2019; Sofieva, et al. 2021; Coldewey-Egbers et al. 2022; Godin-Beekmann et al. 2022; Weber et al. 2022). The rate and the sign of long-term ozone changes depend on changes in chemical composition (e.g., ODSs) and stratospheric circulation, which vary by region and altitude and are partly due to increasing long-lived greenhouse gases (LLGHGs). Both stratospheric cooling due to LLGHG and ODS decline are expected to reduce stratospheric ozone loss outside the polar region (Stolarski et al. 2015).

Relative to a base period of 1998–2008, 2022 annual mean total ozone anomalies poleward of 30° latitude in each hemisphere were mostly negative, while positive anomalies were observed at lower latitudes and in the tropics (Plate 2.1y). These anomalies are related to the La Niña (<https://psl.noaa.gov/enso/mei/>) and the mostly westerly shear phase of the quasi-biennial oscillation (above 30 hPa) in 2022. The associated weakening of the tropical upwelling and Brewer-Dobson circulation (BDC) leads to higher ozone in the tropics and reduced ozone transport into high latitudes and, at the same time, decreases polar stratospheric temperatures in winter/spring, thereby enhancing spring polar ozone losses (Domeisen et al. 2019).

The variability in lower stratospheric ozone is largest in winter/spring in both hemispheres, which drives the annual mean variations, as seen in Figs. 2.63 and 2.64.

The various annual mean time series of total ozone (Fig. 2.63) convey the same picture as observed in Plate 2.1y. At midlatitudes (35° – 60°) in both hemispheres (Figs. 2.63b,d), the annual mean total ozone in 2022 was close to the long-term mean (1998–2008) in the Northern Hemisphere and at the lower end of values during the last decade in the Southern Hemisphere (SH). Particularly striking are the very low 2022 values in the SH, which are close to the all-time low of the previous sixty years. Very low stratospheric ozone is also evident at the 50-hPa level (Fig. 2.64f). Contrastingly, 50-hPa ozone and total columns from selected datasets (WOUDC,

GSG, GTO) are close to the maximum observed during the last two decades (Figs. 2.63c, 2.64e).

In addition to the effect of La Niña, the underwater volcanic eruption from Hunga Tonga–Hunga Ha’pai (HTHH) in January 2022 may have contributed to this low annual mean SH ozone in 2022. HTHH injected large quantities of aerosols and water vapor into the stratosphere that reduced stratospheric temperatures and modified chemical reaction cycles (sections 2g5, 2g3; Sidebar 2.2; Bourassa et al. 2022; Millán et al. 2022; Vömel et al. 2022). The weakening of the residual BDC in the SH caused by HTHH contributed to the drop in SH middle lower stratospheric and column ozone in 2022 (Coy et al. 2022; Wang et al. 2022). The transport of enhanced aerosol levels into the polar region, and circulation-driven lower polar temperatures may have caused additional Antarctic ozone losses (Wang et al. 2022). While the anomalously weak planetary wave activity in austral spring was the main cause of the deeper Antarctic ozone holes during the last three years (section 6i), recent studies suggest that Australian wildfires in December 2019, volcanic events of La Soufrière in April 2021, and HTHH in early 2022 contributed to the low ozone levels in the lower stratosphere at southern midlatitudes

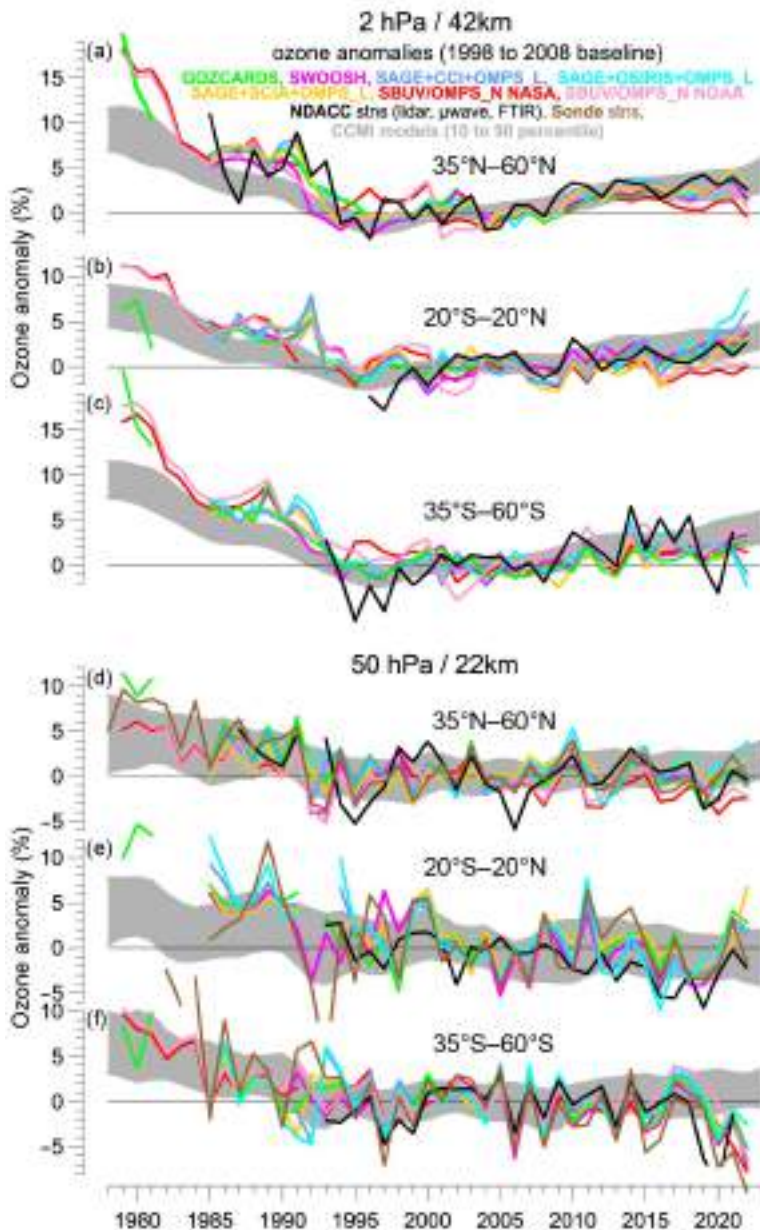


Fig. 2.64. Annual mean anomalies of ozone in (a)–(c) the upper stratosphere near 42-km altitude or 2-hPa pressure, and (d)–(f) in the lower stratosphere near 22 km or 50-hPa pressure for three zonal bands: (a),(d) 35° N– 60° N, (b),(e) 20° S– 20° N (tropics), and (c),(f) 35° S– 60° S. Anomalies are with respect to the 1998–2008 base period. Colored lines are long-term records obtained by merging different limb (GOZCARDS, SWOOSH, SAGE+CCI+OMPS-L, SAGE+SCIAMACHY+OMPS-L) or nadir-viewing (SBUV, OMPS-N) satellite instruments. The nadir-viewing instruments have much coarser altitude resolution than the limb-viewing instruments. This can cause differences in some years, especially at 50 hPa. The black line is from merging ground-based ozone records at seven Network for the Detection of Atmospheric Composition Changes (NDACC) stations employing differential absorption lidars and microwave radiometers. See Steinbrecht et al. (2017), WMO (2018), and Arosio et al. (2018) for details on the various datasets. Gray shaded area shows the range of chemistry-climate model simulations from CCM1 refC2 (SPARC/IO3C/GAW 2019). Ozone data for 2022 are not yet complete for all instruments and are still preliminary.

(Figs. 2.63d, 2.64f) and deeper Antarctic ozone holes (Figs. 2.64f; Rieger et al. 2021; Ansmann et al. 2022; Yook et al. 2022; Strahan et al. 2022; Wang et al. 2022, Solomon et al. 2023).

Ozone profile data (Fig. 2.64f) confirm the low total ozone at southern midlatitudes. Apart from this, Fig. 2.64 shows ozone values in 2022 that are generally consistent with expectations from model simulations of the Phase 1 Chemistry Climate Model Initiative (CCMI) based on current scenarios of ODS and greenhouse gas changes (thick gray line in Fig. 2.63a; shaded area in Fig. 2.64; SPARC/IO3C/GAW 2019): 1) slow but noticeable recovery of ozone in the upper stratosphere over the last 20 years (WMO 2022; Godin-Beekmann et al. 2022), with observations in recent years closer to the lower end of the model simulations; and 2) little or no recovery of ozone in the lower stratosphere, with recent midlatitude observations at the lower end of the simulations (Ball et al. 2020; Thompson et al. 2021; Godin-Beekmann et al. 2022; WMO 2022).

5. STRATOSPHERIC WATER VAPOR

—S. M. Davis, K. H. Rosenlof, D. F. Hurst, H. Vömel, and R. Stauffer

Normally, water vapor (WV) entering the stratosphere is regulated by temperatures in the tropical tropopause layer (TTL; ~14 km–19 km), with higher WV concentrations occurring when TTL temperatures are higher. However, the 14–15 January 2022 eruptions of the Hunga Tonga–Hunga Ha’apai (HTHH) submarine volcano (20.54°S, 175.4°W) injected an amount of

water vapor (~50 Tg–150 Tg) into the stratosphere that is unprecedented in the satellite record and represents upwards of 10% of the entire stratospheric burden of WV (Carr et al. 2022; Khaykin et al. 2022; Legras et al. 2022; Millán et al. 2022; Proud et al. 2022; Vömel et al. 2022; see also Sidebar 2.2). By being injected at between approximately 26 km and 34 km, WV associated with the HTHH eruption bypassed the TTL “cold trap” and resulted in a dramatic perturbation to WV and other stratospheric species (e.g., ozone, section 2g4) that will likely persist for years.

This direct injection of WV into the stratosphere by HTHH is evident in the so-called “tropical tape recorder” (Mote et al. 1996) plot (Fig. 2.65a). The WV anomaly appears suddenly in early 2022 between roughly 40 hPa and 10 hPa and then ascends through the stratosphere as part of the meridional overturning circulation. Within the tropical latitude band (15°S–15°N), this unprecedented zonal-mean monthly-mean anomaly (relative to the 2004–21 mean) peaked at 6.4 ppm (parts per million, i.e., $\mu\text{mol mol}^{-1}$) above the climatological normal of 4.1 ppm

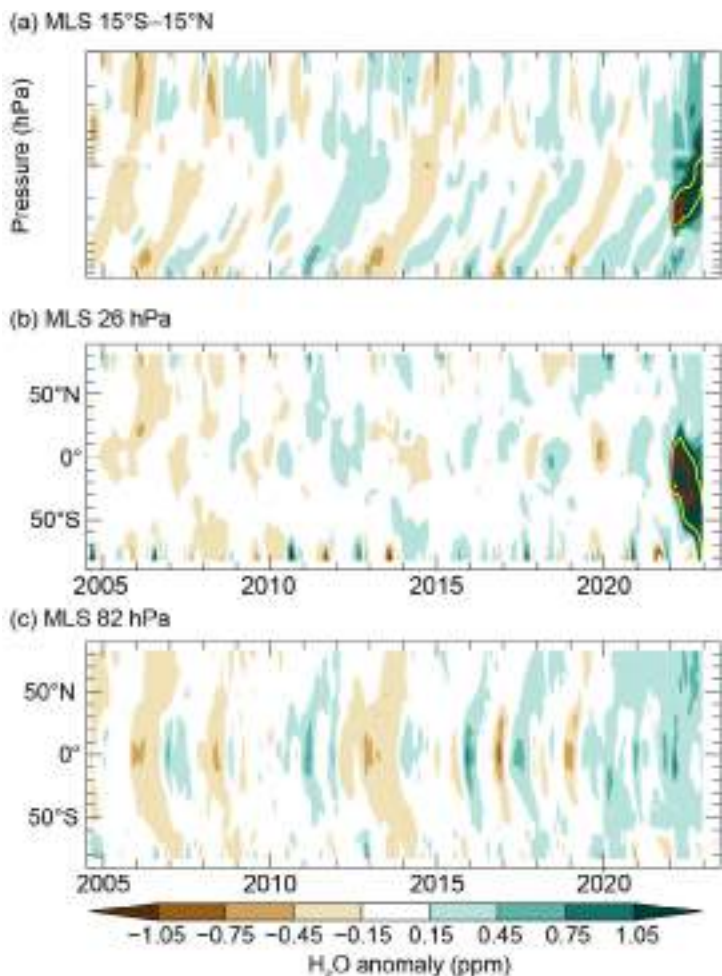


Fig. 2.65. (a) Latitude–time contour of tropical (15°S–15°N) lower-stratospheric water vapor (WV) anomalies, with the +2 ppm and +4 ppm values shown as yellow and red contour lines, respectively. (b),(c) Latitude–time contour of WV anomalies at (b) 26 hPa and (c) 82 hPa, respectively. All panels are based on version 5.01 Aura MLS data, which has collected near-global (82°S–82°N) measurements since Aug 2004. Anomalies are differences from the mean 2004–21 WV mixing ratios (ppm) for each month. (a) shows the unprecedented injection of water vapor directly into the stratosphere by the Hunga Tonga–Hunga Ha’apai eruption. (b) shows the southward propagation of the plume at 26 hPa, while (c) shows a more general propagation of tropical lower-stratospheric WV anomalies to higher latitudes in both hemispheres as well as the influences of dehydrated air masses from the Antarctic polar vortex as they are transported toward the Southern Hemisphere midlatitudes at the end of each year. Tick marks denote the beginning of each year.

at 26 hPa (~25 km) in March after the enhancement spread northward to fill this band, corresponding to a deviation from the climatological monthly zonal mean of 160% (31 standard deviations). A latitude–time cross-section of WV anomalies at 26 hPa (Fig. 2.65b) shows that the HTHH plume quickly spread as far north as 20°N immediately following the eruption, before being transported into the Southern Hemisphere in subsequent months. Maps of WV anomalies at 82 hPa (~17 km) and 26 hPa reveal the impact on lower- and mid-stratospheric WV, respectively, from the quiescent period in December 2021 through to the aftermath of the eruption in February (Fig. 2.66).

Even though they pale in comparison to the mid-stratospheric impacts, tropical lower stratospheric WV anomalies were positive (wet) for all months in 2022 (Figs. 2.65a,c). These anomalies were greatest in February (the first full month post-eruption of HTHH), with values of +1.1 ppm, corresponding to deviations from the climatological monthly mean of 40%. Over the tropical latitude band, anomalies were either the most positive on record or second-most positive between February and July. In addition to propagating upwards, the 82-hPa WV anomalies also propagated poleward in each hemisphere (Fig. 2.65c).

Lower stratospheric WV observed by Aura Microwave Limb Sounder (MLS) is consistent with balloon-borne frost point hygrometer soundings (Fig. 2.67). As is well known, at the tropical stations the WV anomalies are highly correlated with the tropical cold-point tropopause (CPT) temperature anomalies (Figs. 2.67c,d).

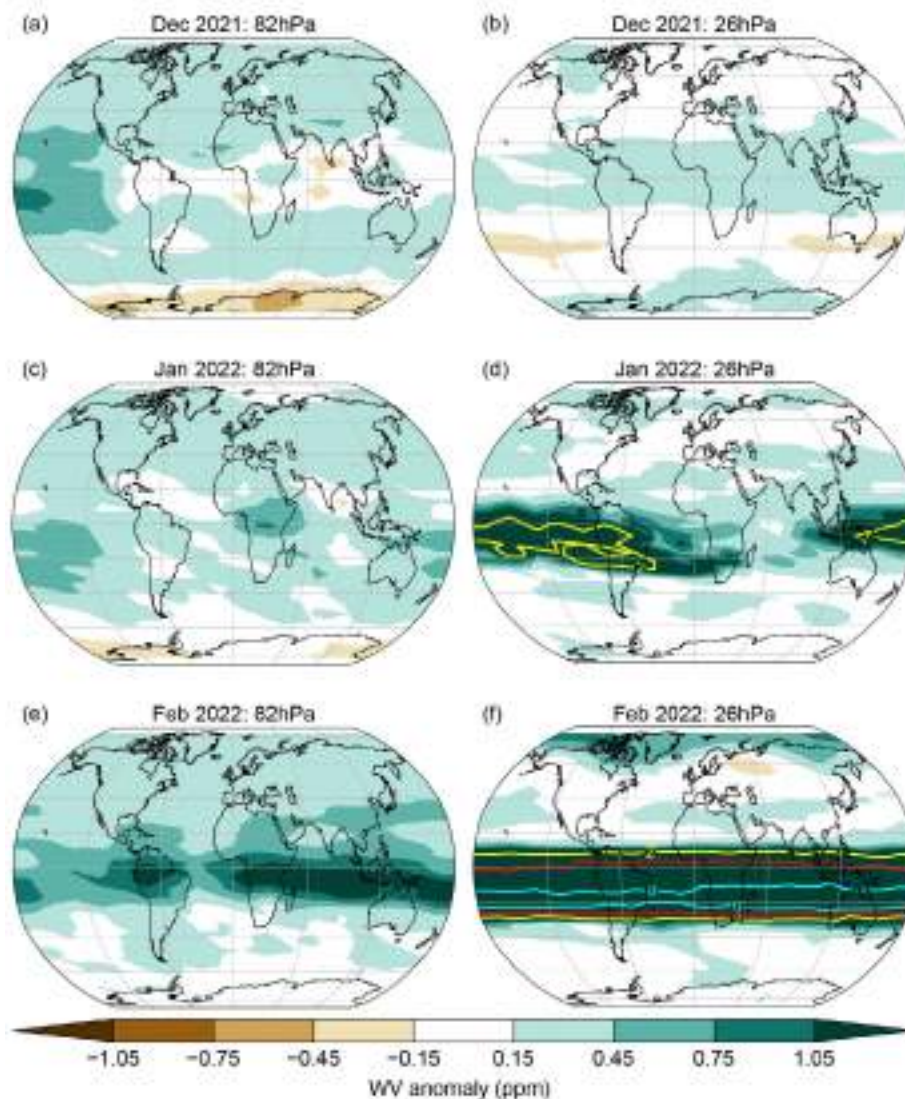


Fig. 2.66. Deseasonalized monthly lower stratospheric Aura MLS vapor (WV) anomalies (ppm; 2004–21 base period) at (a),(c),(e) 82 hPa and (b),(d),(f) 26 hPa for (a),(b) Dec 2021, (c),(d) Jan 2022, and (e),(f) Feb 2022. Contours of WV anomalies of +2, +4, and +8 ppm are shown in yellow, red, and cyan, respectively.

In 2022, the tropical CPT temperatures were anomalously high throughout the entire year except for July (deseasonalized monthly anomaly of -0.04 K), with an annual mean anomaly of $+0.73$ K. Interannual variations in CPT temperatures are correlated with interannual variability in climate modes, such as ENSO and the quasi-biennial oscillation (QBO) in equatorial stratospheric winds (e.g., Randel et al. 2004), so these are briefly discussed below.

The criteria for La Niña was met throughout 2022 (see section 4b for details). La Niña conditions in boreal winter

are typified by weaker tropical lower stratospheric upwelling, anomalously warmer CPTs, and enhanced WV in the tropical lower stratosphere (e.g., Garfinkel et al. 2021). The observed positive anomalies in tropical lower-stratospheric WV at the beginning and end of 2022 are thus consistent with the expected behavior associated with a La Niña.

The QBO phase was easterly through to September until switching to westerly for the remainder of 2022. The QBO westerly phase is associated with anomalously weak tropical upwelling and warm temperatures. Thus, the La Niña and QBO easterlies had offsetting effects on CPTs (and hence WV) at the beginning of 2022, whereas the QBO westerlies and La Niña at the end of 2022 likely contributed to the anomalously warm CPTs and enhanced lower-stratospheric WV at that time.

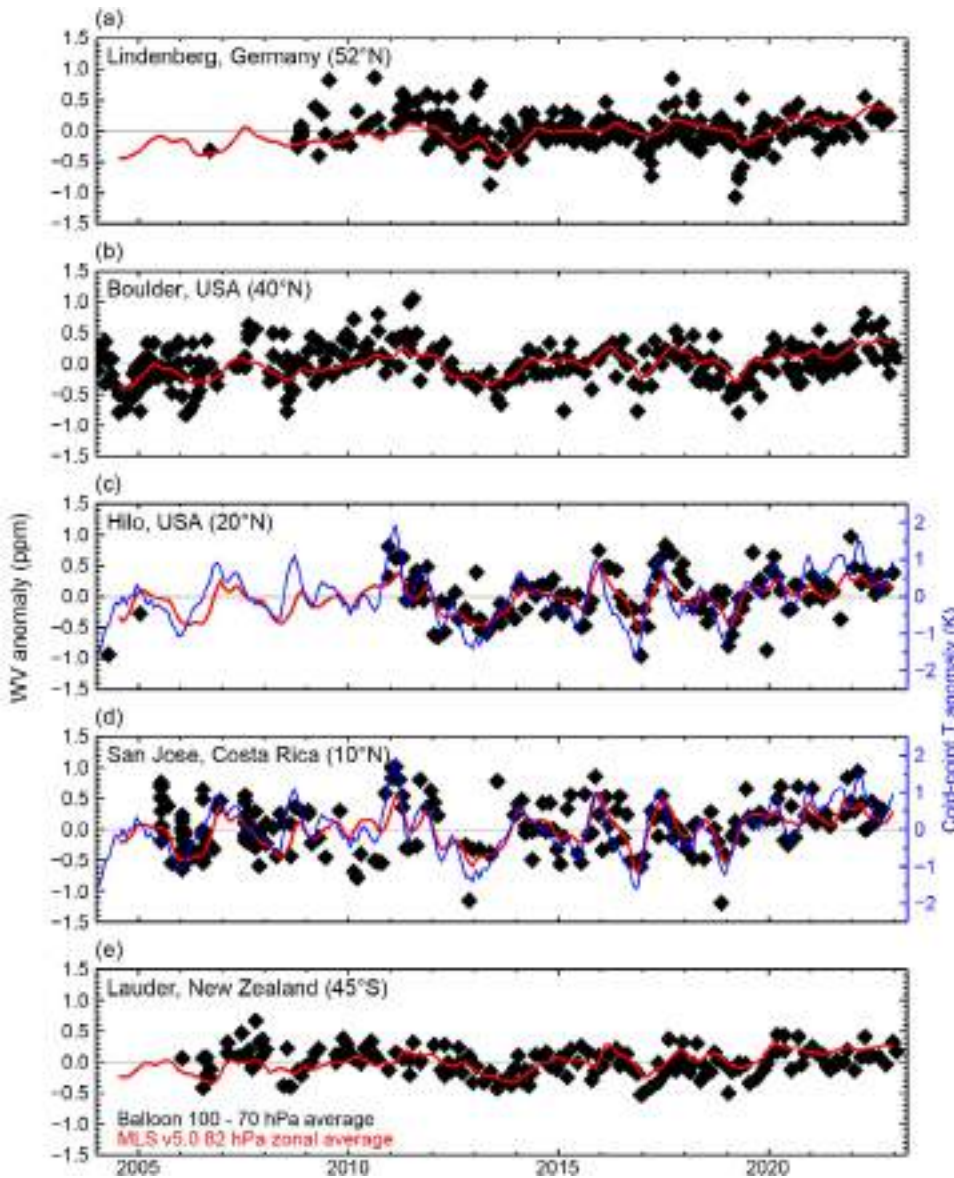


Fig. 2.67. Lower-stratospheric water vapor (WV) anomalies (ppm) over five balloon-borne frost point (FP) hygrometer stations. Each panel shows the lower stratospheric anomalies of individual FP soundings (black) and of monthly zonal averages from MLS data at 82 hPa in the 5° latitude band containing the FP station (red). High-resolution FP vertical profile data were averaged between 70 hPa and 100 hPa to emulate the MLS averaging kernel for 82 hPa. Each MLS monthly zonal mean was determined from 2000–3000 profiles. Anomalies for MLS and FP data are calculated relative to the 2004–21 period for all sites except for Lindenber (2009–21) and Hilo (2011–21). Tropical cold-point tropopause temperature (CPT) anomalies based on the MERRA-2 reanalysis (c,d, blue curve) are generally well correlated with the tropical lower stratospheric WV.

6. TROPOSPHERIC OZONE

—O. R. Cooper, J. R. Ziemke, and K.-L. Chang

Tropospheric ozone is the third most important greenhouse gas, after carbon dioxide and methane. It contributes to almost all of the effective radiative forcing due to ozone (tropospheric and stratospheric), estimated by the IPCC Sixth Assessment Report to be 0.47 (0.24 to 0.70) $W m^{-2}$ (Forster et al. 2021). A short-lived climate forcer, its lifetime is on the order of three to

four weeks (Archibald et al. 2020) and, therefore, its global distribution is highly variable (Gaudel et al. 2018). In situ observations are too sparse and infrequent to provide an accurate quantification of the global distribution and trends in tropospheric ozone, although in some areas they are abundant enough to provide reliable regional-scale trends (Tarasick et al. 2019; Cooper et al. 2020; Gaudel et al. 2020; Gulev et al. 2021; Chang et al. 2022).

While the current generation of atmospheric chemistry models is showing reasonable skill in quantifying the global tropospheric ozone burden (TOB) and reproducing long-term trends (Skeie et al. 2020; Szopa et al. 2021; Christiansen et al. 2022; Fiore et al. 2022; Wang et al. 2022), their estimates vary, and further development is required before they can provide reliable near-real time estimates of the global ozone distribution. Instruments on polar-orbiting satellites are our best means for monitoring tropospheric ozone on the global scale. While currently available satellite products have limited vertical resolution, they can report tropospheric column ozone values, which can be summed to provide near-global estimates of the tropospheric ozone burden.

Since 2012, *State of the Climate* reports have relied on the combined Aura Ozone Monitoring Instrument and Microwave Limb Sounder satellite ozone measurements (OMI/MLS) to quantify the near-global tropospheric ozone burden and trends (Ziemke et al. 2019). Vertical resolution of OMI/MLS monthly tropospheric column ozone (TCO) is ~ 3 km near the tropopause with ~ 2 Dobson units (DU; 7%) precision regionally; trend uncertainties are about 0.5 DU decade $^{-1}$ (1.5% decade $^{-1}$). In 2022, the strongest positive TCO anomalies (relative to 2005–21) occurred from East Asia to the northeastern North Pacific (~ 1.2 DU; 3%), while the negative anomalies were weak and were limited to Australia and New Zealand (Plate 2.1z). Hemispheric and global TOB were 160 ± 6 Tg (0° – 60° N), 149 ± 6 Tg (0° – 60° S), and 309 ± 8 Tg (60° S– 60° N) for 2022 (95% confidence ranges). Globally (60° S– 60° N), the 2004–22 TOB increase was approximately 1.50 ± 0.37 Tg yr $^{-1}$, equal to a total increase of $\sim 8\%$ since 2004 (Fig. 2.68). Spatially, the trends are overwhelmingly positive (Fig. 2.69), with the strongest trends occurring in the tropics, consistent with the conclusions of the IPCC AR6, which assessed

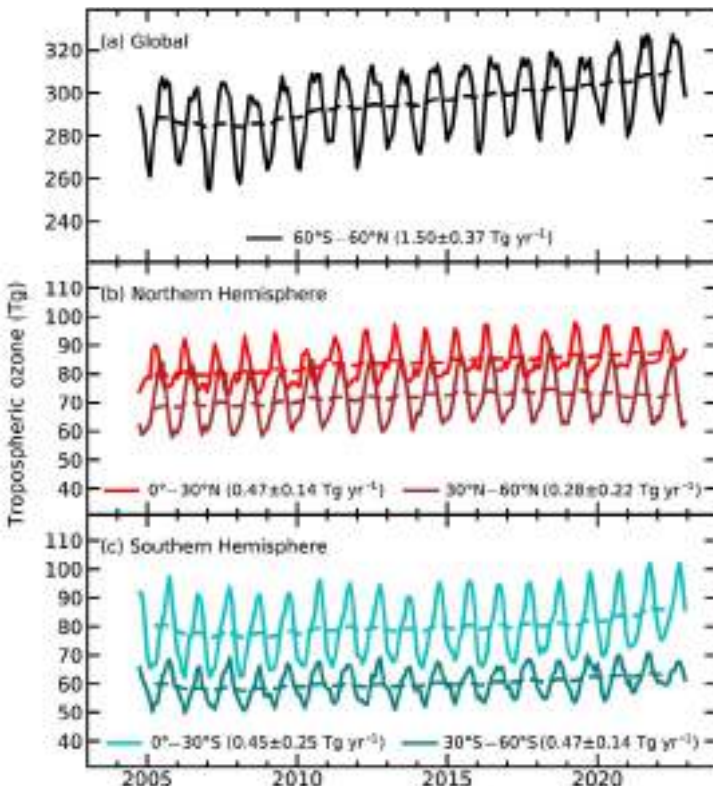


Fig. 2.68. Monthly averages (solid lines) and 12-month running means (dashed lines) of OMI/MLS tropospheric ozone burdens (Tg) from Oct 2004 through Dec 2022 for (a) 60°S – 60°N (black), (b) the Northern Hemisphere tropics (red) and midlatitudes (dark red), and (c) the Southern Hemisphere tropics (light blue) and midlatitudes (dark green). Slopes of linear fits to the data are presented with their 95% confidence-level uncertainties.

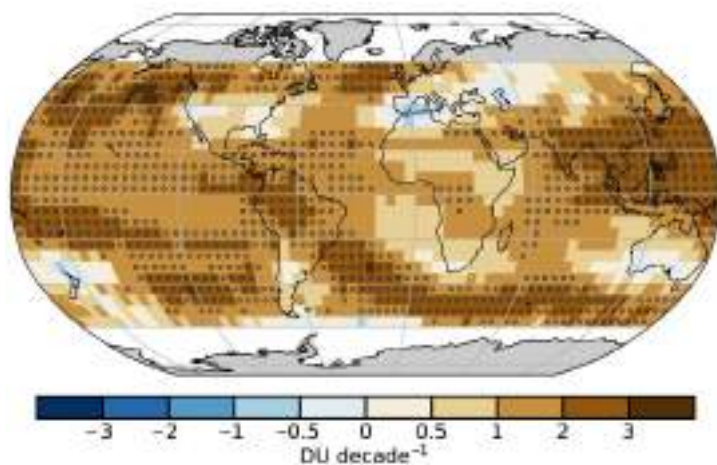


Fig. 2.69. Linear trends in OMI/MLS tropospheric column ozone (DU decade $^{-1}$) on a $5^\circ \times 5^\circ$ grid from Oct 2004 through Dec 2022. Circles denote trends with p -values < 0.05 . Trends were calculated using a multivariate linear regression model (e.g., Randel and Cobb 1994 and references therein) that included a seasonal cycle fit and the Niño-3.4 index as an El Niño–Southern Oscillation proxy; trend uncertainties included autoregressive adjustment via Weatherhead et al. (1998).

observed tropospheric ozone trends from the late twentieth century to 2016–18 (Gulev et al. 2021).

At the surface, six baseline sites are available for quantifying multi-decadal ozone trends through the end of 2022 (Fig. 2.70; Table 2.9). Trends are estimated by the generalized least squares method, based on monthly anomalies referenced to the monthly climatological values over 2000–20 (Chang et al. 2021). At northern high latitudes, ozone has increased at the rate of 0.50 ± 0.32 ppbv decade⁻¹ ($p < 0.01$) since 1973 at Barrow Observatory, Alaska, while ozone at Summit, Greenland, has decreased by 2.25 ± 0.92 ppbv decade⁻¹ ($p < 0.01$) since 2000. At northern midlatitudes, ozone has decreased by 0.97 ± 1.15 ppbv decade⁻¹ ($p = 0.09$) since 1988 at Tudor Hill, Bermuda, but with large fluctuations. Nighttime observations at Mauna Loa Observatory (MLO), Hawaii, are representative of the lower free troposphere of the central North Pacific Ocean and show a positive trend of 0.92 ± 0.40 ppbv decade⁻¹ ($p < 0.01$) since 1973. In the southern high latitudes, ozone at Arrival Heights, Antarctica, changed little since 1996, with a weak increase of 0.27 ± 0.56 ppbv decade⁻¹ ($p = 0.33$). Ozone at South Pole, the most remote location on Earth, increased by 0.35 ± 0.35 ppbv decade⁻¹ ($p = 0.05$) since 1975. While these data provide a range of trends at remote locations, they are too sparse to provide a global mean surface trend, and surface trends do not necessarily reflect trends in the free troposphere, which have been overwhelmingly positive since the 1990s (Gulev et al. 2021; Fiore et al. 2022), in agreement with OMI/MLS tropospheric column product.

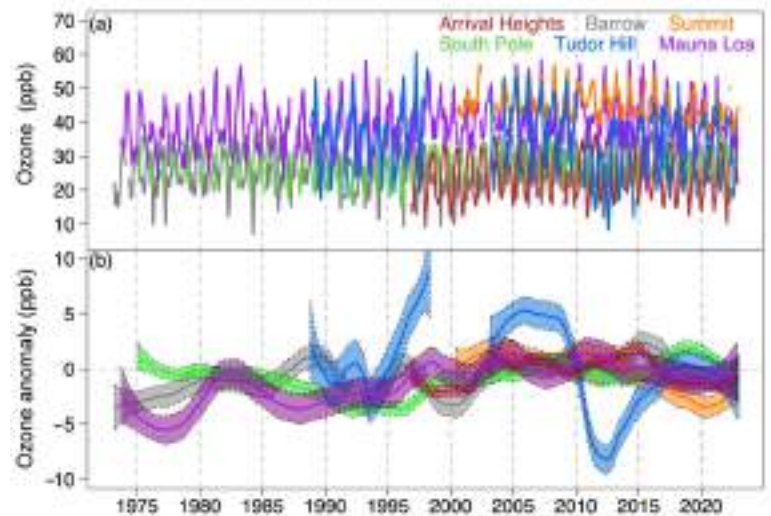


Fig. 2.70. (a) Monthly mean surface ozone (ppb) at Barrow Observatory, Alaska (gray), Summit, Greenland (orange), Tudor Hill, Bermuda (blue), Mauna Loa, Hawaii (purple), Arrival Heights, Antarctica (red), and South Pole (green). Monthly means are produced for months with at least 50% data availability using observations from all 24 hours of the day. The locations of each site are listed in Table 2.9. (b) The same time series after conversion to monthly anomalies referenced to the monthly climatological values over 2000–20 and smoothed variability based on the locally weighted scatterplot smoothing (LOWESS) regression.

Table 2.9. Ozone trends at the six baseline monitoring sites shown in Fig. 2.70. Trends are estimated by the generalized least squares method, based on monthly anomalies referenced to the monthly 2000–20 base period (Chang et al. 2021), and reported with 95% confidence intervals and p-values.

Site name — latitude, longitude, elevation (m)	Yrs with data	Trend, ppbv decade ⁻¹	p-value
Summit, Greenland — 72.6°N, 38.5°W, 3238 m	2000–present	-2.25 ± 0.92	$p < 0.01$
Barrow, Alaska — 71.3°N, 156.6°W, 11 m	1973–present	0.50 ± 0.32	$p < 0.01$
Tudor Hill, Bermuda — 32.3°N, 64.9°W, 30 m	1988–1998, 2003–present	-0.97 ± 1.15	$p = 0.09$
Mauna Loa Observatory (MLO), Hawaii — 19.5°N, 155.6°W, 3397 m	1973–present	0.92 ± 0.40	$p < 0.01$
Arrival Heights, Antarctica — 77.8°S, 166.8°W, 50 m	1996–present	0.27 ± 0.56	$p = 0.33$
South Pole, Antarctica — 90.0°S, 59.0°E, 2840 m	1975–present	0.35 ± 0.35	$p = 0.05$

7. CARBON MONOXIDE

—J. Flemming and A. Inness

Carbon monoxide (CO) is an indirect climate forcing agent because of its chemical feedbacks with the hydroxyl radical (OH), which controls the atmospheric lifetime of methane (CH₄), and because of its role as a precursor for tropospheric ozone (Szopa et al. 2021, section 6.3.3.2). Both methane and tropospheric ozone are also short-lived climate pollutants. CO is emitted into the atmosphere by combustion processes originating from anthropogenic sources, such as road transport and energy generation, as well as from natural sources, such as wildfires and biogenic emissions. Of similar or larger size than these emissions is the chemical production of CO in the atmosphere from formaldehyde as part of the oxidation chains of CH₄, isoprene, and other volatile organic trace gases (Zheng et al. 2019). Oxidation of CO by reaction with OH is the main loss process for CO, resulting in an atmospheric lifetime of one to two months. The greater abundance of OH in the summer of each hemisphere is a main reason for the typical CO seasonal cycle that peaks in winter.

Monthly and annual global mean total columns of CO together with combined annual anthropogenic and wildfire emissions for the period 2003–22 are shown in Fig. 2.71. The year 2022 has the lowest overall global CO burden and the lowest total CO emissions in the period. The low emissions in 2022 were a consequence of less intense wildfire activity and a general decrease in anthropogenic CO emissions. Figure 2.71 suggests a good qualitative agreement between the variability and trends of global CO burden (lines) and global CO emissions (points) for the study period. However, the CO emissions and the CO burden are not perfectly correlated, which is an indication of the additional influence of the varied chemical production and destruction of CO on its global burden. Furthermore, while the CO wildfire emissions and CO burden were inferred from satellite observations, the anthropogenic emissions are only projections based on inventories and the biogenic emissions are from a modeled multi-year climatology, both with considerable uncertainties for the details for 2022.

The spatial distribution of the annual anomalies of 2022 with respect to the period 2003–22 is shown in Plate 2.1aa. The mid and high latitudes show large-scale negative anomalies throughout the year. These were most pronounced in the summer seasons when the wildfire activity was lower than in some previous years (e.g., 2021, 2019) that saw strong wildfires. The positive CO anomalies in northern India can be attributed to anthropogenic sources, such as agricultural fires. The continuation of La Niña conditions in the tropical Pacific resulted in a pronounced negative anomaly over Maritime Southeast Asia during September–November. Stronger-than-usual wildfire activity in tropical and southern Africa and tropical South America led to positive CO anomalies, particularly in the second half of 2022.

The Copernicus Atmosphere Monitoring Service (CAMS; <https://atmosphere.copernicus.eu/>) has produced a retrospective analysis of CO, aerosols, and ozone since 2003 by assimilating satellite retrievals of atmospheric composition with the European Centre for Medium-Range Weather Forecasts (ECMWF) model (Inness et al. 2019). This CAMS reanalysis assimilated global Thermal Infra-Red total column CO retrievals (V6 from 2003 to 2016; Near Real Time [NRT] V7 from January 2017 to June 2019; NRT V8 from July 2019 to present) of the Measurement of Pollution in the Troposphere instrument (Deeter et al. 2014, 2017, 2019), excluding observations poleward of 65° N/S, using the ECMWF 4D-VAR data assimilation system. The anthropogenic emissions were taken from the Monitoring Atmospheric Composition and Climate megacity (MACCity) inventory

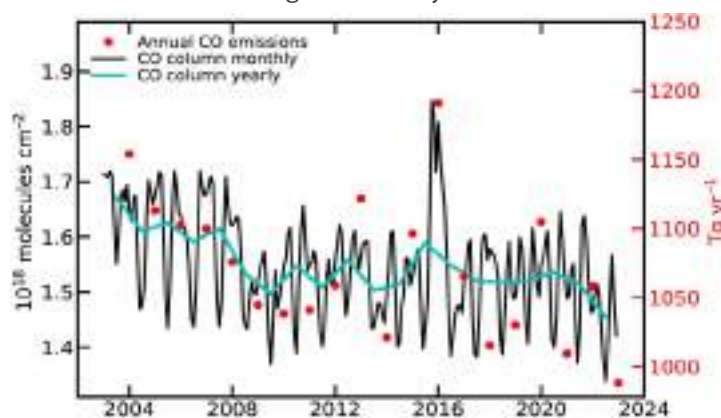


Fig. 2.71. Time series of the area-averaged global total column of carbon monoxide (CO) from the CAMS reanalysis ($\times 10^{18}$ molecules cm^{-2} , left axis, black: monthly mean values; cyan: annual mean values) and annual total global CO emissions (Tg yr^{-1} , right axis, red circles) for the period 2003–22.

(Granier et al. 2011) that accounts for projected emission trends according to the Representative Concentration Pathway (RCP) 8.5 scenario, but COVID-19-related emissions modifications were not applied. Biomass burning emissions were taken from the Global Fire Assimilation System (v1.2; Kaiser et al. 2012; section 2h3) that is based on MODIS fire radiative power retrievals (Giglio et al. 2016). Monthly mean biogenic CO emissions simulated by the Model of Emissions of Gases and Aerosols from Nature version 2.1 (MEGAN2.1) model following Sindelarova et al. (2014) were used for the period 2003–17, after a monthly-mean climatology derived from the 2003–17 simulations was applied.

h. Land surface properties

1. TERRESTRIAL SURFACE ALBEDO DYNAMICS

—G. Duveiller and N. Gobron

The changes in brightness of the land’s surface, referred to as its albedo, emerge from the combined effect of multiple land processes, notably a darkening in the visible part of the spectrum caused by increased vegetation growth, a brightening due to dry conditions, and a strong effect depending on the presence of snow. In 2022, the land surface was overall darker compared to the reference period of 2003–20. This darkening can be attributed to a combination of greener-than-usual regions along with considerable snow cover deficits in the Northern Hemisphere (section 2c5), which were not offset by the brightening that could have been expected following the multiple heatwaves that occurred in 2022 (section 2b4).

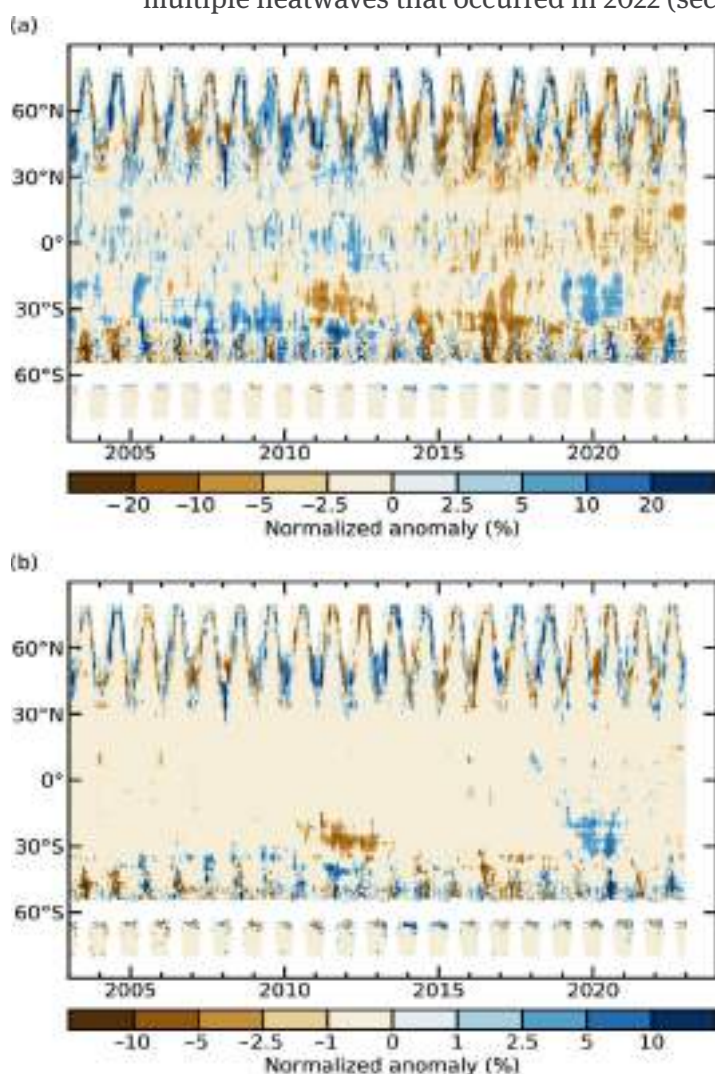


Fig. 2.72. Zonally averaged (a) white sky visible (%) and (b) near infrared (%) albedo anomalies for the period 2003–22 using a 2003–20 base period.

La Niña was responsible for increased precipitation in several areas during 2022, leading to greening (and thus darkening), generating distinct features in the global anomaly maps (see Plate 2.1ab for anomalies in visible albedo and compare to anomalies in precipitation), notably in southern Africa, eastern Australia, and northeastern Brazil. Snow deficits in the Arctic, in Eastern Europe, and in a small area of the midwestern United States further characterize the darkening patterns in 2022, while larger and longer extents of snow cover in North America and Tibet brightened these latter areas. Drier conditions following heatwaves did not offset the darkening effects, with localized exceptions in eastern Africa, Paraguay and Argentina, Mexico and the central United States, and Turkey.

The patterns of surface albedo anomalies consolidate the darkening trend over the years, specifically for visible albedo (Figs. 2.72, 2.73). Surface albedo is generally known to be decreasing considerably in the Arctic due to reductions of terrestrial snow cover, snow cover fraction over sea ice, and sea-ice extent, driven mostly by increasing surface air temperature and declining snowfall (Zhang et al. 2019; see Chapter 5). Negative trends of albedo have also been reported over the vegetated surfaces in various regions, even though land-cover change and other effects can

brighten the land as well (Chrysoulakis et al. 2019). The non-snow-related albedo reductions are in line with increasing trends in the fraction of absorbed photosynthetically active radiation (FAPAR; section 2h2), that could possibly be associated with increasing trends in greening across some areas, while browning occurs in others (Cortés et al. 2021).

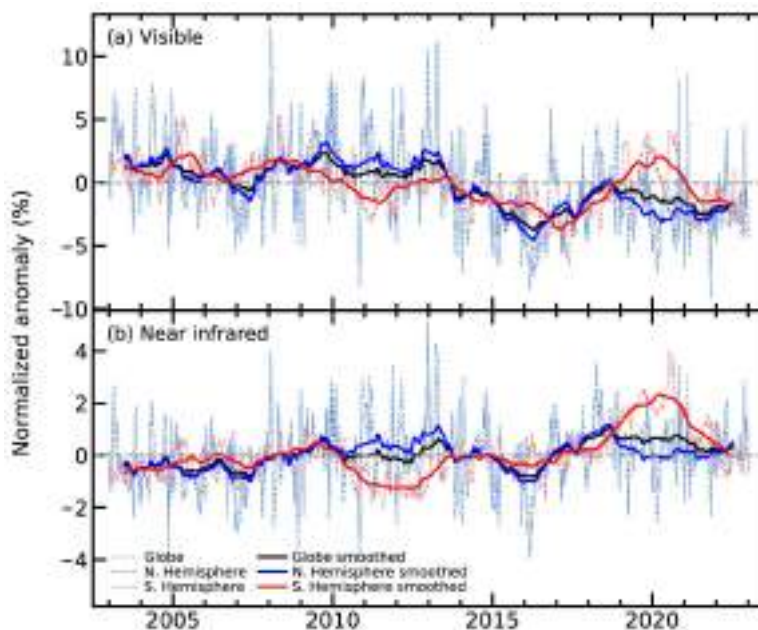


Fig. 2.73. Global (black lines), Northern Hemisphere (blue), and Southern Hemisphere (red) land surface (a) visible and (b) near infrared albedo anomalies (%; 2003–20 base period) for the period 2003–22. Dotted lines denote each monthly period; solid lines indicate the six-month running averaged mean.

This analysis is based on satellite records of visible and near-infrared white-sky albedo estimated from the Moderate Resolution Imaging Spectroradiometer (MODIS) instrument onboard the *Aqua* and *Terra* satellite platforms (Schaaf et al. 2002). Also known as bi-hemispherical reflectance, it is defined as the fraction of radiation that is reflected by the surface in the absence of a direct radiation component and when the diffuse radiation component is isotropic. This situation would correspond to a hypothetical overcast or foggy day, in which the sky would be white (and hence the name: white-sky albedo). Various studies have shown that these products represent ground properties well, whether it be ice sheets (Stroeve et al. 2013) or vegetation (Cescatti et al. 2012). The baseline reference period used here is 2003–20, covering the extent of the MODIS record where data from both satellite platforms (*Terra* and *Aqua*) are available.

2. TERRESTRIAL VEGETATION DYNAMICS

—N. Gobron

The fraction of absorbed photosynthetically active radiation (FAPAR) provides evidence on the amount of vegetation and its health status, and is, therefore, important in assessing the primary productivity of the vegetative cover, the associated fixing of atmospheric carbon dioxide and the energy balance at the surface. FAPAR anomalies in 2022 compared to the 1998–2020 average show wide variations in terms of value and geographic coverage of vegetation productivity worldwide (Plate 2.1ad).

The largest negative anomalies (decreased plant photosynthesis) occurred in North America, across Alaska and the Yukon territory, Kansas, and Texas through to northeast Mexico and in East Africa (Somalia, Ethiopia, Kenya, Uganda, and Tanzania). Negative anomalies also occurred in South America (Argentina, Paraguay, and Bolivia). To a lesser extent, negative anomalies appeared on the Pacific zones of Colombia and Ecuador, southern zone of Chile, and Atlantic coast of Angola and Namibia. Madagascar, Morocco, and northern Algeria were also affected. Several negative hotspots concerned southwest and northern Australia, western Russia, and central Europe.

The most noticeable positive anomalies (increased vegetated photosynthesis) appeared over northern Canada, northeastern Brazil, Botswana, southern Africa, southern and eastern Asia, and eastern Australia. Smaller anomalies were noticeable over the Sahel region and over northern Russia.

The negative anomalies over the boreal forest in Alaska and the Yukon were due to spring wildfires associated with earlier snowmelt. Summer rainfall was lower and later than normal, with higher temperatures than usual (see section 7b). There were precipitation deficits from Kansas in the United States to the northeast of Mexico throughout the year, which affected shrubland growth. Heatwaves occurred in January and July over northern Argentina and Paraguay,

respectively, and temperatures were the highest on record at both the start and the end of 2022 with a strong deficit of precipitation over these regions, as well as Bolivia (see section 7d). East African vegetation health declined in the spring as the temperature was higher than normal with a rainy season ending with cumulatively low rainfall. Strong seasonal negative anomalies occurred over Europe in spring and summer and over the northern United States in autumn;

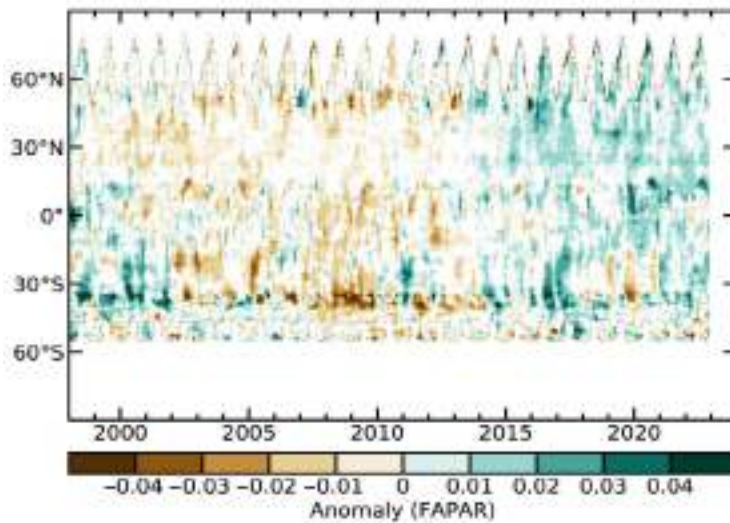


Fig. 2.74. Zonally averaged fraction of absorbed photosynthetically active radiation (FAPAR) anomalies for 1998–2022 (1998–2020 base period).

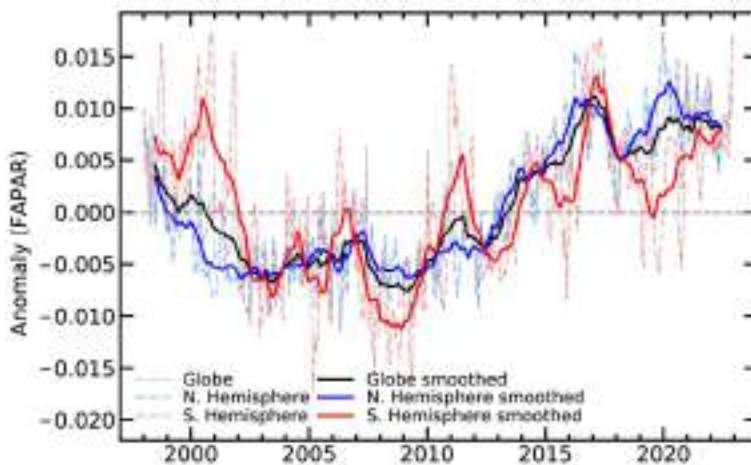


Fig. 2.75. Global (black lines), Northern Hemisphere (blue), and Southern Hemisphere (red) fraction of absorbed photosynthetically active radiation (FAPAR) anomalies for 1998–2022 (1998–2020 base period). Dotted lines denote each monthly period; solid lines indicate the six-month running averaged mean.

negative until 2010/11 and during the summer periods in 2015/16, 2018/19, and 2019/20, but were positive for all of 2022. The NH experienced fewer negative events compared to the SH. Since 2021/22, both the SH and NH recorded only positive FAPAR anomalies.

Space-based earth observations are crucial for monitoring terrestrial photosynthetic activity worldwide. Optical sensors are used to infer FAPAR, an essential climate variable (as defined by GCOS [2016, 2022]). The 2022 analysis merges 25 years of global FAPAR monthly products based on three optical sensors from 1998 to 2022 (Gobron et al. 2010; Pinty et al. 2011; Gobron and Robustelli 2013). Uncertainties of each dataset were derived through error propagation techniques and comparisons against multiple proxies using ground-based measurements and radiative transfer simulations that all provide an estimate of the uncertainties and biases. This long-term FAPAR dataset has an estimated uncertainty close to 5%–10%.

however, these seasonal events were not detectable in the annual anomaly as positive anomalies occurred in other seasons.

The Arctic ecosystem, characterized by low tundra vegetation over northern Canada (Nunavut) and northern Russia (Kara Sea) shows a greening trend due to higher temperatures during the summer. Terrestrial photosynthesis was enhanced over eastern China and India, with vegetation growth increasing since 2015 due to land use changes, along with an intensification of the production of multiple crops (Gobron 2019; Chen et al. 2019). Northeastern Brazil, with tropical forests along the coast and savanna, had a positive FAPAR annual anomaly of above +0.4, as both precipitation and temperature were above normal. Similar conditions occurred over Botswana, South Africa, and eastern Australia, which correspond to the typical impact of La Niña.

Figure 2.74 shows the average latitudinal anomalies from 1998 to 2022 compared to the reference period 1998–2020. In 2022, the anomaly was positive at nearly all latitudes, apart from a few places such as above the equator and south of 30°S, highlighting the greening of land surfaces. The Southern Hemisphere (SH) was affected by negative anomalies (i.e., less than -0.04), from 2002 to 2014, except in 2010–12, and in 2019/20.

Figure 2.75 shows the global and hemispheric anomalies, with more seasonal variability in the SH than in the Northern Hemisphere (NH). FAPAR anomalies over the SH were positive before 2002, started to be

3. BIOMASS BURNING

—J. W. Kaiser and M. Parrington

The year 2022 continued to illustrate the two distinct trends that have emerged in global biomass burning over the last decade that are shaping current pyrogeography: a declining trend in many savanna regions related to agricultural expansion and an increasing trend in many forested regions where climate change with severe drought periods increases the flammability of the landscape (Plate 2.1ae). Here we characterize the amount of biomass burning, also referred to here as “fire activity” and more widely as wildfires, with the amount of carbon that is consumed by fire; 80%–95% of this is emitted as carbon dioxide, depending on fire type (smoldering vs. flaming), 1%–2% is emitted as particulate matter and subject to deposition within a few days, and the remainder (CO, CH₄, and others) is further oxidized to carbon dioxide in the atmosphere. In a stable ecosystem, virtually all of this carbon dioxide is assimilated again on time scales of years by re-growth of vegetation. In the current situation however, 20% is estimated to contribute to the long-term buildup of atmospheric carbon dioxide (Zheng et al. 2023).

On one hand, 2022 had the lowest fire activity in the Global Fire Assimilation System (GFAS) record (1603 Tg C, 22% below the 2003–20 average; Table 2.10; Plate 1.1), with fire activity in tropical Asia at its lowest since at least 2003. On the other hand, there was significant regional fire activity in boreal North America, southwestern and Central Europe, and central South

Table 2.10. Annual continental-scale biomass burning budgets in terms of carbon emission (Tg C yr⁻¹) from GFASv1.4. The Arctic and western United States are listed as subregions of frequent interest; their values are contained in those for North America plus Northern Asia.

Name of Region	Location	2003–20 Mean value ^a (min–max)	2022 Value ^a	2022 Anomaly ^a (%)
Global	–	2062 (1781–2421)	1603	–460 (–22%)
North America	30°N–75°N, 190°E–330°E	85 (57–114)	77	–8 (–10%)
Central America	13°N–30°N, 190°E–330°E	52 (38–72)	45	–7 (–14%)
South America	60°S–13°N, 190°E–330°E	368 (242–537)	376	+9 (+2%)
Europe and Mediterranean	30°N–75°N, 330°E–60°E	42 (28–72)	37	–5 (–12%)
N. Hem. Africa	0°–30°N, 330°E–60°E	421 (308–494)	333	–88 (–21%)
S. Hem. Africa	0°–35°S, 330°E–60°E	477 (429–532)	450	–27 (–6%)
Northern Asia	30°N–75°N, 60°E–190°E	199 (116–436)	110	–89 (–45%)
Southeast Asia	10°N–30°N, 60°E–190°E	122 (86–162)	69	–53 (–44%)
Tropical Asia	10°N°–10°S, 60°E–190°E	166 (27–475)	22	–144 (–87%)
Australia	10°S–50°S, 60°E–190°E	129 (60–232)	83	–46 (–36%)
Arctic (sub-region)	67°N–90°N, 0°–360°	8 (1–37)	7	–1 (–17%)
Western United States (sub-region)	30°N–49°N, 230°E–260°E	19 (8–42)	16	–2 (–12%)

^a Quantity given in Tg C yr⁻¹

America (Plate 2.1ae; Fig. 2.76). After the extreme fires of 2019 and 2020, fire activity in the Arctic Circle and southeast Australia was again near and below average, respectively.

Global fire emissions are dominated by savanna burning except for rare episodes of extreme tropical peat burning during El Niño conditions. African fire emissions account for roughly half of the total fire carbon emissions in the Global Fire Emissions Database (GFED) and GFAS time series, and fires over savanna regions have decreased over the past decade (Andela et al. 2017). This trend continued in 2022 over Northern Hemisphere Africa with emissions 21% below the 2003–20 average, marking the third successive year with lower fire activity than any years in the record before 2019 (Fig. 2.77a). Southern Hemisphere Africa also contributed to the trend, albeit to a lesser degree. Fire activity in tropical Asia—including Indonesia—was the lowest on record (Fig. 2.77c); here, wet La Niña-related conditions continued as the dominant physical driver. While the long-term global trend is partly driven by agricultural expansion into savanna ecosystems and its associated fragmentation of the landscape, unusual patterns of high or low rainfall and more or less environmental protection also influence interannual variability on top of the declining trend.

South America was the only continental region to experience above-average activity (+2%; Fig. 2.77b) in 2022, due to the increased numbers of fires across northern Argentina, Paraguay, Bolivia, and some parts of the Amazon. In this region, 2020 and 2022 saw the highest fire activity of the last 12 years, which is consistent with the significant droughts in much of this region (section 2d10) as well as increased deforestation in the Amazon since 2019 for Brazil (<http://www.obt.inpe.br/OBT/assuntos/programas/amazonia/prodes>). At higher northern latitudes, North America and northern Asia experienced negative anomalies (−10% and −45%, respectively) overall, although there was regionally increased fire activity during the summer months for Alaska, the Yukon and Northwest Territories, and Khabarovsk Krai.

GFAS is operated to produce global fire emission estimates in near real-time by the Copernicus Atmosphere Monitoring Service (CAMS; Kaiser et al. 2012). It is based on the MODIS

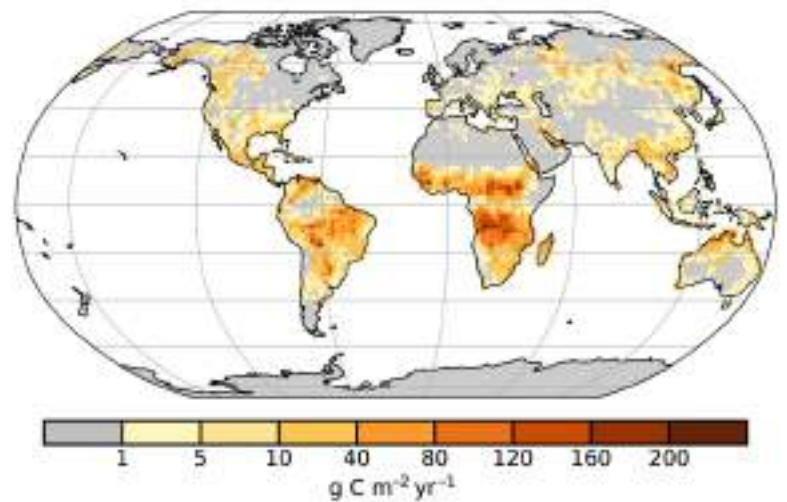


Fig. 2.76. Global map of fire activity in 2022 in terms of carbon consumption ($\text{g C m}^{-2} \text{yr}^{-1}$). (Source: GFASv1.4.)

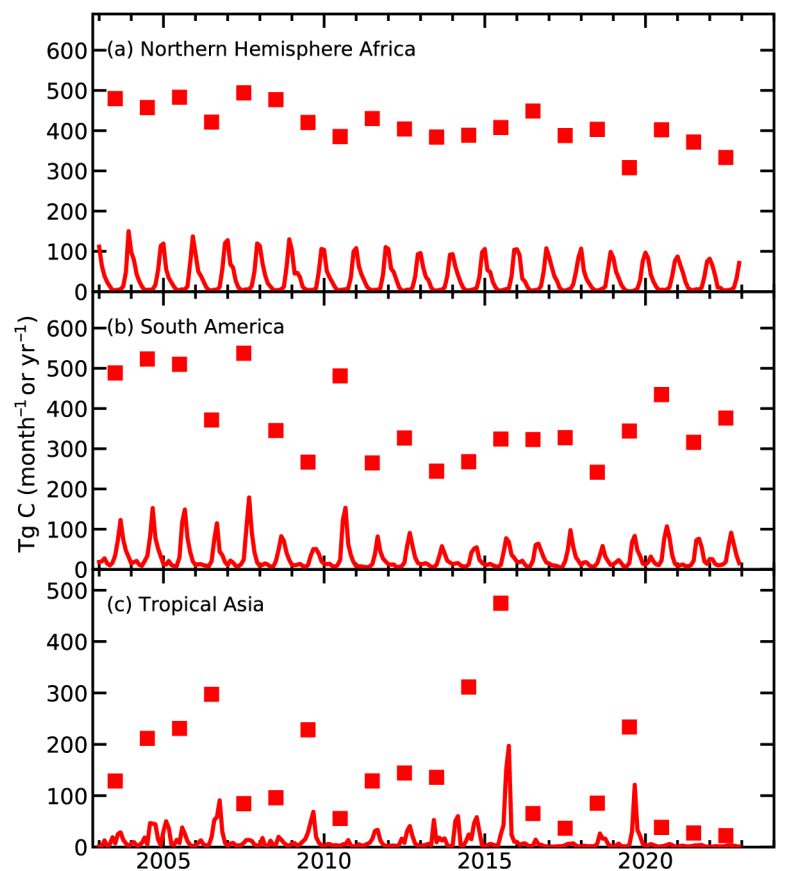


Fig. 2.77. Regional time series of monthly (lines in Tg C month^{-1}) and annual (squares in Tg C yr^{-1}) biomass burning activity in (a) Northern Hemisphere Africa, (b) South America, and (c) tropical Asia.

Fire Radiative Power products (Giglio et al. 2016). Here, we use consistent reprocessing with input from MODIS Collection 6 for the entire period of 2003–22. The 14% bias with respect to Collection 5 has been corrected, and the satellite- and observation time-specific bias correction factors from Hüser et al. (2018) have been applied in order to compensate for several outages of observations from the MODIS instruments during 2022. The *Aqua* and *Terra* satellites carrying MODIS have been in drifting orbits during 2022 with an overall shift of the local equator crossing times of <15 minutes (<https://aqua.nasa.gov/sites/default/files/AquaStatus.pdf>; <https://terra.nasa.gov/wp-content/uploads/2022/09/Orbit-Changes-Terra.pdf>); we consider this to be negligible for GFAS. The time series in Plate 1.1 also puts GFAS in the context of GFED4s, which is mostly based on burnt area observation and dates back to 1997 (van der Werf et al. 2017).

4. PHENOLOGY OF PRIMARY PRODUCERS

—D. L. Hemming, O. Anneville, Y. Aono, T. Crimmins, N. Estrella, A. Menzel, I. Mrekaj, J. O’Keefe, T. Park, A. D. Richardson, J. Rozkošný, T. Rutishauser, T. H. Sparks, S. J. Thackeray, A. J. H. van Vliet, and F. West.

During 2022, land surface phenology derived from the MODIS Normalized Difference Vegetation Index (NDVI, a dimensionless index of the difference between visible and near-infrared reflectance of vegetation cover, where higher values indicate denser, green vegetation) over the Northern Hemisphere (>30°N; Park et al. 2016), was compared to NDVI over the 2000–20 baseline period (Fig. 2.78). The hemispheric mean Start and End of Season (SOS_M and EOS_M) for the

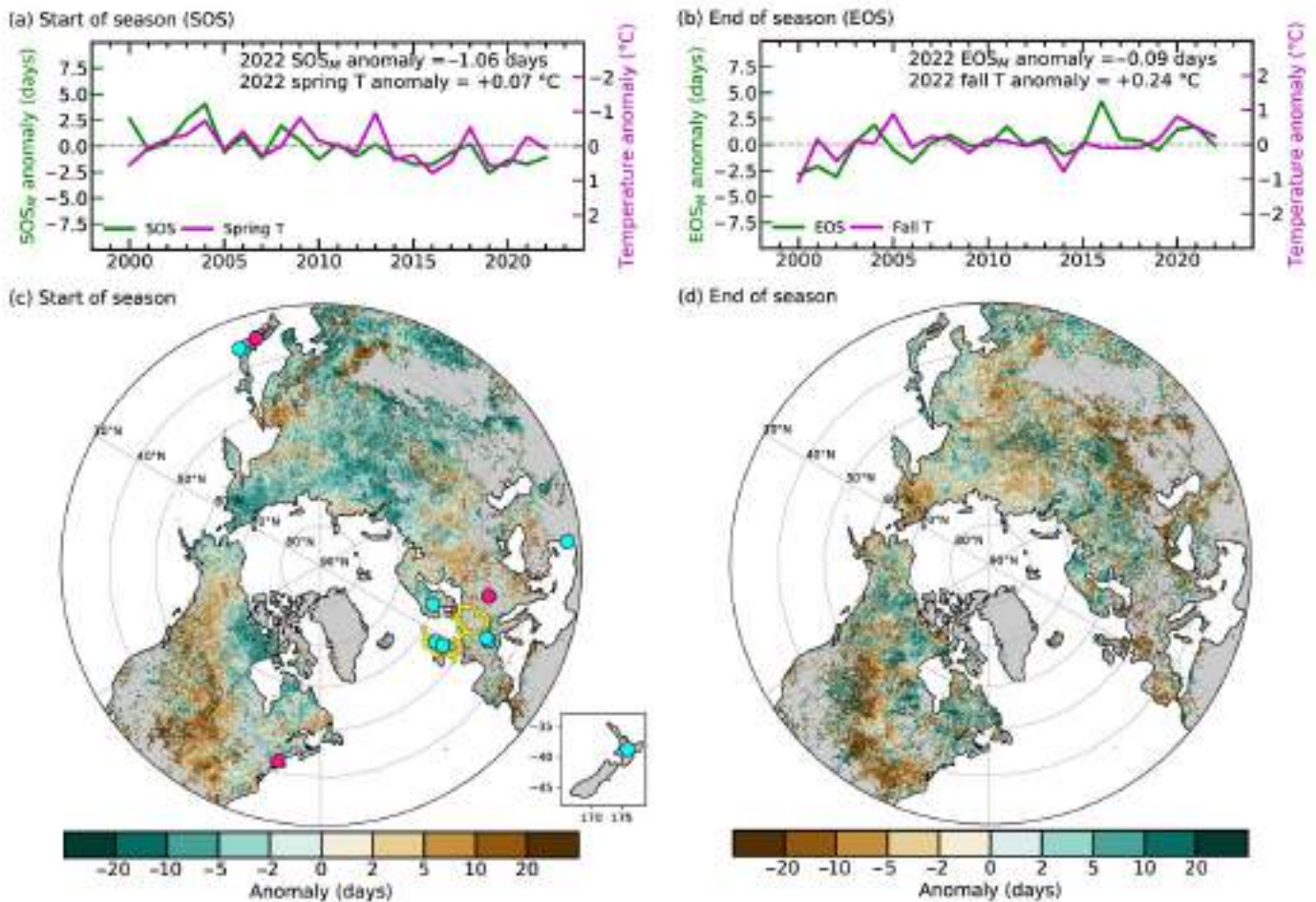


Fig. 2.78. (a) Time series of area-mean anomalies (days relative to 2000–20 baseline) in MODIS Normalized Difference Vegetation Index (NDVI)-based vegetation-growing-season onset (start of season, SOS_M , green) and satellite-derived (MERRA-2) spring (Mar–May, pink) temperature for the Northern Hemisphere. (b) Same as (a) but for growing season end (end of season, EOS_M , green) and autumn (Sep–Nov, pink) temperature. Note the temperature scale reversal for (a). (c),(d) Spatial pattern of (c) SOS_M and (d) EOS_M anomalies in 2022 with respect to the baseline. Highlights identify the location of sites shown in Figs. 2.79 and 2.80 and discussed in the text (country mean phenology data, yellow; site PhenoCam and phenology observations, magenta; lake phytoplankton, blue).

baseline period is 16 May and 11 October, respectively, and in 2022, SOS_M was 1.1 days earlier and EOS_M was similar to the baseline (Figs. 2.78a,b; Table 2.11). Regionally, earlier SOS_M occurred across central and northeastern Eurasia (EA), Alaska, and northern Canada. The warmer spring ($+0.23^\circ\text{C}$) led to 2.5 days earlier SOS_M in EA. Most of North America (NA) experienced later SOS_M ($+1.7$ days) in 2022 (Fig. 2.78c) due to the colder (-0.18°C) and wetter ($+0.05$ mm day $^{-1}$) spring, particularly over U.S. croplands. Northern NA and western EA showed later EOS_M ($+0.8$ days) whereas earlier EOS_M (-0.4 days) was observed in southern NA and eastern EA (Fig. 2.78d). Time series of the two decades of the MODIS record show continuous advancement and delay trends in SOS_M and EOS_M (SOS_M : -1.6 ± 0.4 days decade $^{-1}$, $p < 0.001$; EOS_M : $+1.2 \pm 0.5$ days decade $^{-1}$, $p = 0.07$).

PhenoCam data (Seyednasrollah et al. 2019) helped link the coarse resolution of satellite-derived phenology with fine-resolution visual observations on organisms and ecosystems (Richardson 2019). PhenoCam estimates (2008–22) of SOS (SOS_{PC}) and EOS (EOS_{PC}) at Harvard Forest, a deciduous forest in Massachusetts (United States) were compared with ground observations of red oak (*Quercus rubra*; SOS_{RO} and EOS_{RO} ; Richardson and O’Keefe 2009; O’Keefe

Table 2.11. Start of season (SOS), end of season (EOS), and full bloom dates (FBD; for native cherry tree observations only) for MODIS mean across the Northern Hemisphere (NH MODIS, $>30^\circ\text{N}$), land phenology records in USA (Harvard: PhenoCam, red oak, and MODIS mean across Harvard Forest; USA National Phenology Network, USA-NPN, mean covering northeastern United States), Europe oak records (Germany, Netherlands, Slovakia, UK, and MODIS mean across UK) and Japan (native cherry tree observations and MODIS mean across Japan). The baseline period is 2000–20 for all records except PhenoCam and NPN, which have baseline periods of 2008–22 and 2011–22, respectively, spanning the available observations. Negative/positive values represent earlier/later dates.

Location/Record	SOS/FBD 2022 (date)	SOS/FBD Baseline (date)	SOS/FBD Difference 2022-Baseline (days)	EOS 2022 (date)	EOS Baseline (date)	EOS Difference 2022-Baseline (days)
NH MODIS	15 May	16 May	-1	11 Oct	11 Oct	0
Harvard MODIS	26 Apr	24 Apr	-2	1 Dec	5 Dec	+3
Harvard PhenoCam	9 May	7 May	-2	16 Oct	22 Oct	+5
Harvard red oak	13 May	6 May	-7	18 Oct	19 Oct	0
USA-NPN	7 May	6 May	-1	27 Sep	3 Oct	+6
UK MODIS	6 Apr	30 Mar	-7	23 Dec	12 Dec	-10
Germany	29 Apr	28 Apr	+1	12 Nov	6 Nov	+6
Netherlands	17 Apr	20 Apr	-3	19 Dec	27 Nov	+22
Slovakia	1 May	26 Apr	+6	14 Oct	18 Oct	-4
UK	19 Apr	24 Apr	-5	10 Dec	1 Dec	+9
Japan MODIS	9 Apr	21 Apr	-12	-	-	-
Japan	1 Apr	6 Apr	-5	-	-	-

2021) and MODIS (SOS_M and EOS_M) for the associated pixel (Figs. 2.79a,b). These were also compared with red oak observations contributed to *Nature's Notebook*, the United States National Phenology Network's (NPN) monitoring across the northeastern United States (Rosemartin et al. 2014; Crimmins et al. 2022). In 2022, SOS_{PC} , SOS_{RO} , and SOS_M were zero, three, and two days later, respectively, compared to 2021. EOS_{PC} , EOS_{RO} , and EOS_M were 17, 7, and 13 days earlier compared to 2021 (Figs. 2.79a,b). Interannual variability of start and end of season for Harvard Forest are broadly consistent with those from the NPN, which underscore the value of volunteer-contributed data for tracking phenology at local to continental scales. The earlier EOS_{PC} in 2022 yielded a growing season of 160 days, more than two weeks shorter compared to 2021 and a full week shorter compared to the 2011–20 average (167 ± 7 days; Table 2.11).

'First leaf'/'start of leaf unfolding' (SOS_0) and 'leaf falling'/'bare tree' (EOS_0) dates for oak (*Quercus robur* and/or *Q. petraea*) from Germany (D), the United Kingdom (UK), Netherlands (NL), and Slovakia (SK) are presented (Figs. 2.79c,d). In 2022, SOS_0 dates varied across Europe from 5 and 3 days earlier than the baseline (in UK and NL) to 1 and 6 days later (in D and SK), while EOS_0 dates were earlier by 4 days (SK) and later by 6, 9, and 22 days (D, UK, and NL; Table 2.11).

Start- and end-of-season events across Europe are strongly influenced by temperature (Menzel et al. 2020); SOS_0 advances by four to six days per 1°C increase in the mean February–April temperature, and EOS_0 is delayed by two to four days per 1°C increase in the mean September–October temperature. In 2022, the later EOS_0 dates in D, UK, and NL were, in part, associated with unusually high autumn temperatures, encouraging leaf activity and resulting in a longer 2022 'oak season' at these locations (for UK, see Kendon et al. 2022). In SK, high spring, summer, and autumn air temperatures and soil moisture deficits in 2022 encouraged later leaf out and early leaf fall and led to the shortest oak season since 2000.

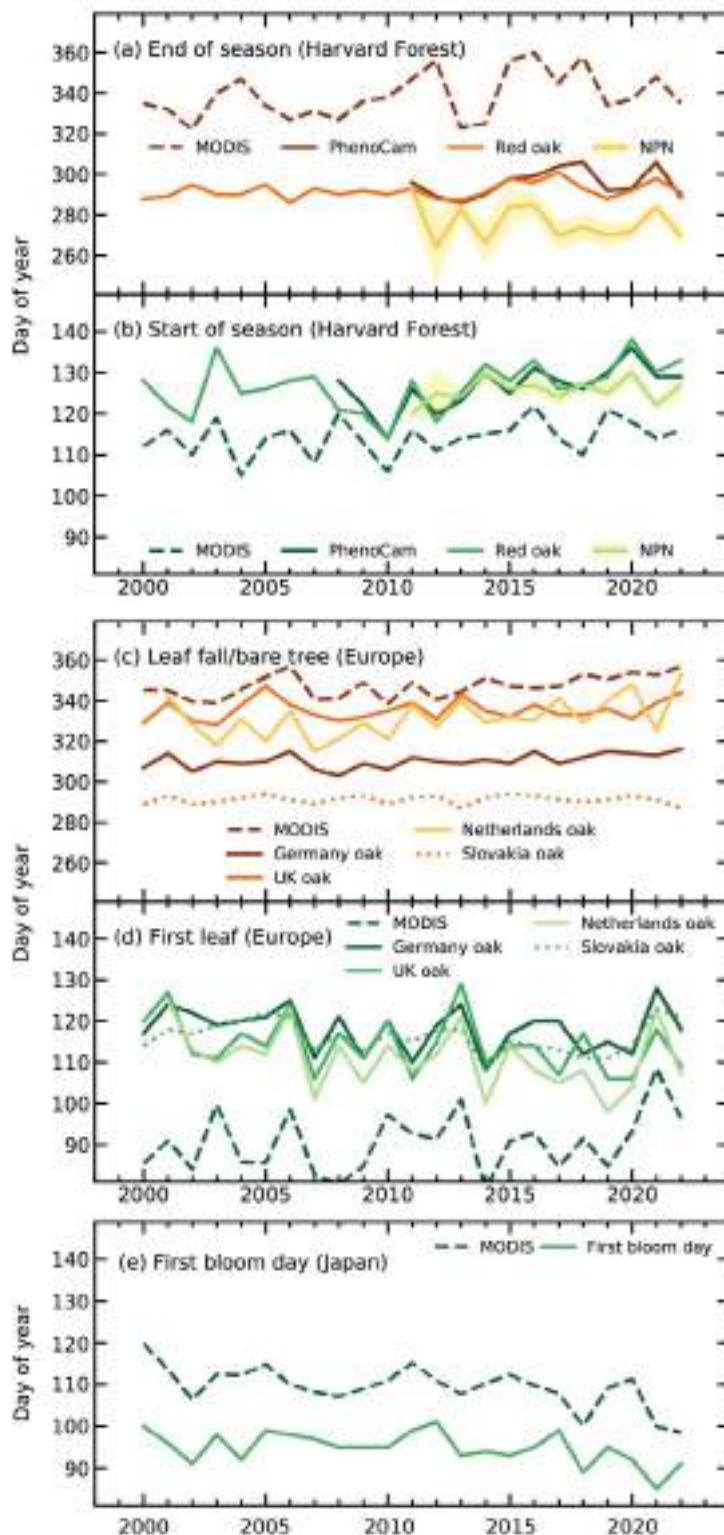


Fig. 2.79. Day of year of spring (green shades) and autumn (orange and brown) vegetation phenology indicators for (a),(b) Harvard Forest, Massachusetts, derived from PhenoCam, red oak ground observations, MODIS remote sensing (dashed), and USA-National Phenology Network (NPN) regional-scale means for red oak (calculated across the northeastern states of Pennsylvania, New Jersey, New York, Connecticut, Rhode Island, Massachusetts, Vermont, New Hampshire, and Maine, ± 1 std. error shaded), (c),(d), Germany, UK, Netherlands, and Slovakia mean oak and MODIS Europe mean, and (e) Kyoto, Japan, full bloom day observations for cherry trees and MODIS Japan mean start of season.

In Kyoto, Japan, full bloom dates (FBD) for a native cherry tree species, *Prunus jamasakura*, were acquired from historical documents dating back to 812 AD (Aono and Kazui 2008) and updated with current observations at Arashiyama, which are compiled from daily observations made by railway passengers at train stations and recorded in newspapers and on web sites (Fig. 2.79e). In 2022, FBD was five days earlier than the 2000–20 mean (Table. 2.11).

Monitoring data on lake water concentrations of the photosynthetic pigment chlorophyll-*a* were available to estimate spring phytoplankton phenology in 1 Southern Hemisphere and 10 Northern Hemisphere lakes (Fig. 2.80). Seasonal timing was quantified for start of season (SOS_L ; Park et al. 2016), day of maximum concentration (DOM_L), and center of gravity (COG_L , an estimate of the mid-point of the plankton bloom; Edwards and Richardson 2004). Lake basins showed great interannual variation and mixed phenological behavior in 2022 relative to the 2000–20 baseline. The Norway lake, Mjøsa, and the Southern Hemisphere lake in New Zealand, Taupo, showed different seasonal changes to other lakes related to snow melt and southern season, respectively. SOS_L occurred earlier than the baseline median for most (8 of 11) lakes, and DOM_L occurred later in most lakes (8 of 11). For COG_L , no consistent pattern was observed.

5. VEGETATION OPTICAL DEPTH

—R. M. Zotta, R. van der Schalie,
W. Preimesberger, L. Moesinger,
R. A. M. de Jeu, and W. Dorigo

Microwave radiation emitted or reflected by Earth's surface is strongly affected by available surface water, including that which is stored in living biomass. The portion of the radiance attenuated by the canopy is expressed by vegetation optical depth (VOD), a parameter used in radiative transfer models to describe radiance interaction with vegetation. VOD is closely related to canopy water content (Konings et al. 2017), leaf area index (Vreugdenhil et al. 2017), and gross primary production (Teubner et al. 2019; Wild et al. 2022) and is a good indicator of vegetation response to climate variability. Positive

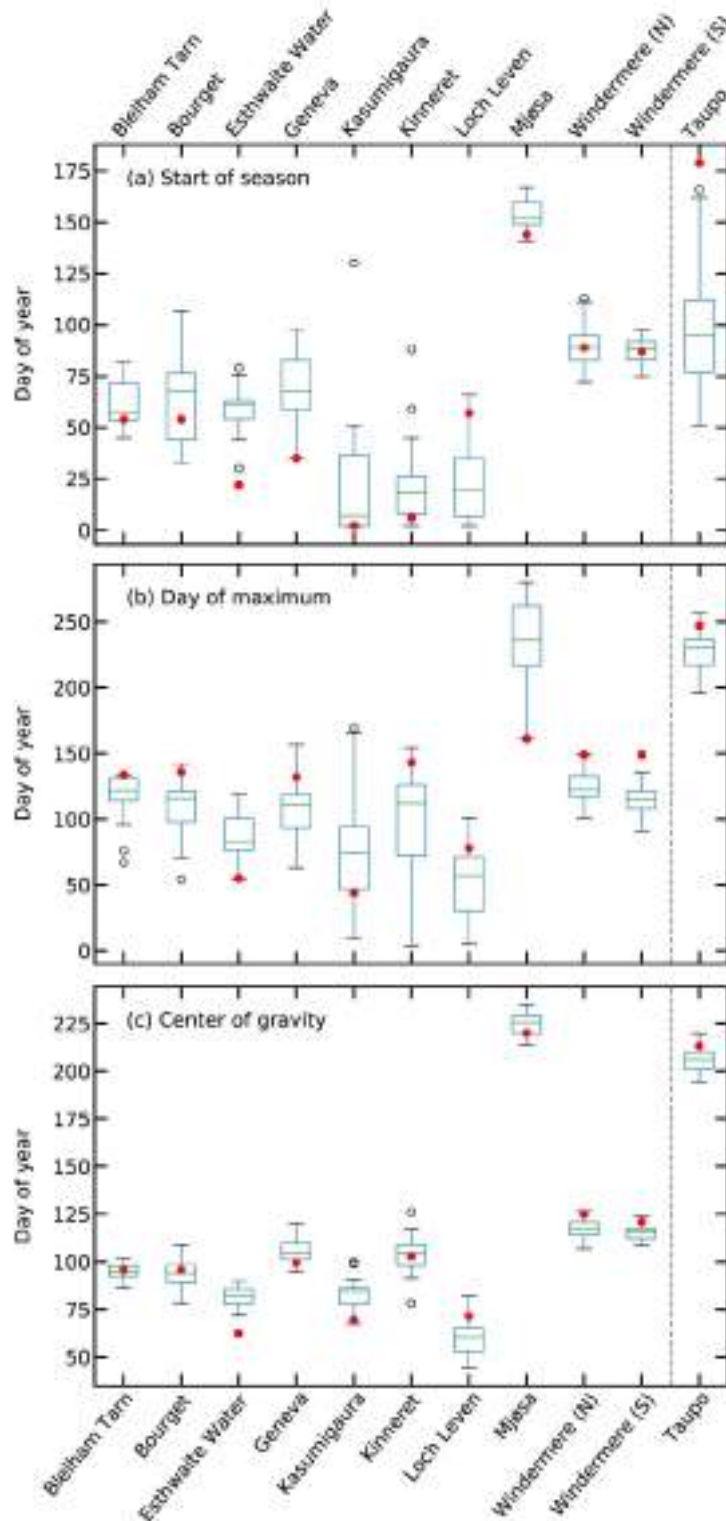


Fig. 2.80. Phenological metrics based on lake chlorophyll-*a* concentrations, as a proxy of phytoplankton biomass: (a) start of season, (b) day of maximum, and (c) center of gravity. Boxplots show variation during the 2000–20 baseline period, and red dots show 2022 values. Dashed line identifies Northern Hemisphere (Blelham Tarn in UK, Bourget in France, Esthwaite Water in UK, Geneva in France/Switzerland, Kasumigaura in Japan, Kinneret in Israel, Loch Leven in UK, Mjøsa in Norway, north and south basins of Windermere in UK) and Southern Hemisphere (Taupo in New Zealand) lakes.

VOD anomalies correspond to above-average vegetation development, while negative VOD anomalies indicate stressed or underdeveloped vegetation.

Globally, the year 2022 saw similar annual VOD anomaly patterns to 2021 and 2020 (Dorigo et al. 2022, 2021). In the Southern Hemisphere, where there is a clear connection between vegetation activity and variations in the El Niño–Southern Oscillation (Miralles et al. 2014; Martens et al. 2017), anomalies became positive (Figs. 2.81, 2.82). The relationship with climate modes is not straightforward, however, as VOD is also affected by drivers such as moisture availability, temperature, radiation, carbon dioxide fertilization, and land management (Gonsamo et al. 2021; Reichstein et al. 2013).

Widespread positive anomalies are seen in southern Africa and Australia (Plate 2.1af). In these regions, the patterns became more positive compared to 2021 (Supp. Fig. A2.9), coinciding with the persistence of La Niña throughout 2022, which brought above-average rainfall (see sections 7e5, 7h4). Other regions where positive patterns have prevailed include the Sahel, India, and northeastern China. Negative VOD anomalies occurred in the Great Plains in North America, the Parana River Basin in South America, and eastern Africa (Plate 2.1af). Most of these negative patterns coincided with precipitation deficits associated with La Niña and/or the negative Indian Ocean dipole mode (section 2e1; Mo et al. 2009; Santos et al. 2021; Anderson et al. 2022; Barlow et al. 2002). The negative VOD anomalies in the Great Plains (Plate 2.1af) coincide with reports of poor vegetation health issued by the NOAA National Centers for Environmental Information (NOAA 2023) for the American West, central and southern Plains, through the Mississippi Valley, and into the northeast. The negative patterns in the Parana River basin occurred in a region with intense wildfire activity (section 2h3), facilitated by dry conditions that persisted for a fourth consecutive year (Neumann et al. 2021). Below-average precipitation trends continued in East Africa (Anderson et al. 2022) and intensified towards the end of the year, leading to strong negative VOD anomalies (Plate 2.1af). Other remarkable negative VOD anomalies were observed in Europe from July to September (Supp. Fig. A2.10). Notably, in Spain, France, central and northern Italy, central Germany, Hungary, Romania, Slovenia,

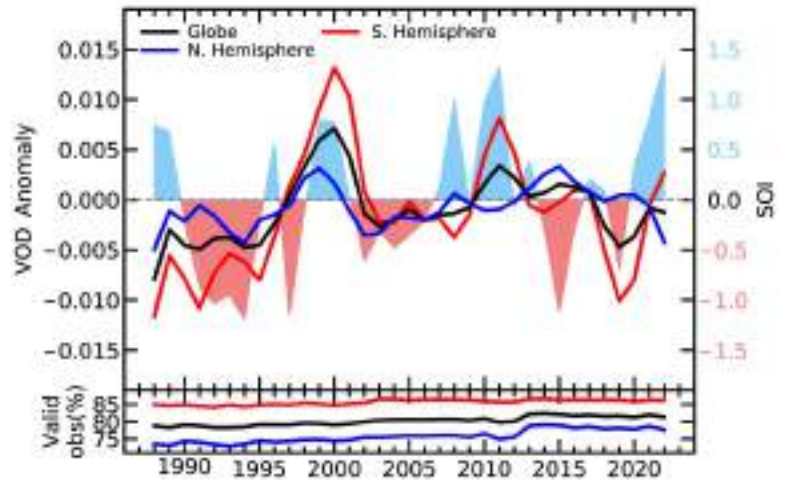


Fig. 2.81. Yearly CXKu vegetation optical depth (VOD) anomalies computed from the 1991–2020 climatology and their agreement with the Southern Oscillation Index (SOI). SOI tracks the state of the El Niño–Southern Oscillation. The SOI has been divided by 10, so that values >0.7 indicate La Niña and values <-0.7 indicate El Niño episodes. (Source: VODCA; <http://www.bom.gov.au/climate/enso/soi/>.)

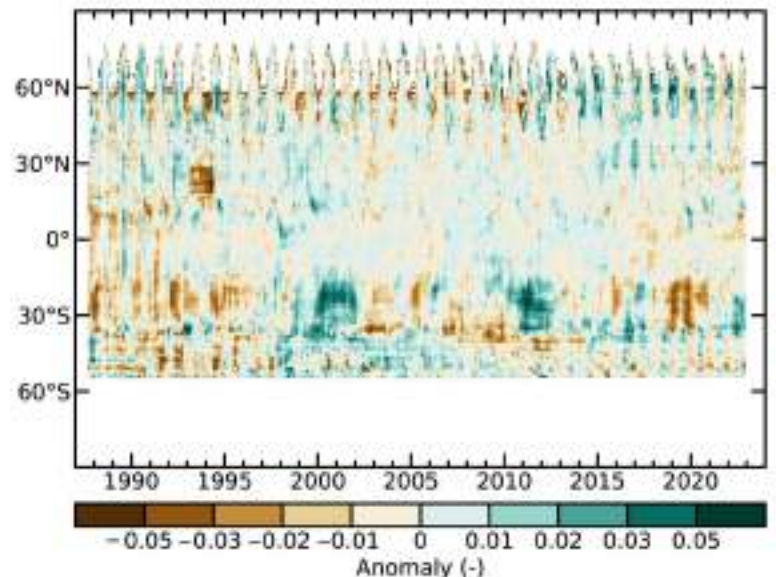


Fig. 2.82. Time–latitude diagram of vegetation optical depth (VOD) anomalies (1991–2020 base period). Data are masked where no retrievals is possible, where no vegetation is present (bare soil), or where the quality is not assured and flagged due to frozen soil, radio frequency interference, etc. (Source: VODCA.)

and Croatia, the main summer crops were severely affected due to exceptionally hot and dry weather conditions (Baruth et al. 2022). Negative VOD prevailed in Algeria and Morocco (Plate 2.1af) as well, with the Food and Agriculture Organization (FAO) reporting below-average cereal production due to widespread drought (FAO 2022). In China, vegetation conditions were affected by a precipitation deficit and heatwave in August (Toreti et al. 2022), which appear as negative VOD anomalies in central China, especially during July, August, and September (Supp. Fig. A2.10).

Several long-term patterns resulting from land-use change also prevailed in 2022 (Plate 2.1af; Dorigo et al. 2021). Due to deforestation and land degradation, below-average VOD occurred in Mongolia, Bolivia, Paraguay, and Brazil (Song et al. 2018). The intensification of agricultural production and reforestation led to above-average VOD in India and northeastern China, respectively (Song et al. 2018).

The VOD anomalies were computed from the VOD Climate Archive (VODCA; Moesinger et al. 2020). VODCA fuses VOD observations derived from several space-borne radiometers (Special Sensor Microwave/Imager [SSM/I], Tropical Rainfall Measuring Mission [TRMM], WindSat, Advanced Microwave Scanning Radiometer-Earth Observing System [AMSR-E] and Advanced Microwave Scanning Radiometer 2 [AMSR2]) through the Land Parameter Retrieval Model (Meesters et al. 2005; van der Schalie et al. 2017) into a harmonized, long-term (1987–2022) dataset. VODCA version 2 contains individual products for Ku-band (covering 1987–2022), X-band (1997–2022), C-band (2002–22), and L-band (2010–22), as well as a multi-frequency product called VODCA CXXu (1987–2022) which blends the highly correlated Ku-, X-, and C-band observations. All VODCA products are at 0.25° spatial and daily temporal resolutions. Here, we used VODCA CXXu to compute anomalies from the long-term (1991–2020) climatology. VODCA CXXu is indicative of upper canopy dynamics.

Acknowledgments

2.a.1 Overview

The editors thank the BAMS special editor, Mike Alexander, the five anonymous reviewers, as well as David Parker, John Kennedy, Katrina MacNeill, and Josh Blannin for their insight, thoughts, and suggestions when developing this chapter. We also thank Fumi Sezaki (JMA), Julien Nicolas (ECMWF), and Mike Bosilovich (NASA) for their help in providing the reanalysis data used in this chapter. R. J. H. Dunn and K. M. Willett were supported by the Met Office Hadley Centre Climate Programme funded by BEIS. R. J. H. Dunn also thanks Bill Little for his assistance with the plots.

2.b.2 Lake surface water temperature

Lake surface water temperatures from satellite data have been generated within the Climate Change Initiative Lakes project funded by the European Space Agency (4000125030/18/I-NB) with adaptation and extensions funded by the EU Copernicus Climate Change Service (C3S) programme. Part of the in situ data used for the validation of the satellite data and for this report have kindly been made publicly available by the Fisheries and Oceans Canada (FOC), the National Data Buoy Center from NOAA, the Hungarian Meteorological Office, the Upper Great Lakes Observing System (UGLOS), the North Temperate Lakes Long-Term Ecological Research (NTL-LTER), and the Swedish Infrastructure for Ecosystem Science (SITES), and the King County Water and Land Resources Division, Washington. The authors gratefully acknowledge the late Alon Rimmer for always supplying data for Lake Kinneret. The in situ temperature measurements for Lake Baikal were supported by Foundation for support of applied ecological studies “Lake Baikal” (<https://baikalfoundation.ru/project/tochka-1/>). Temperature data for the UK lakes were supported by the Natural Environment Research Council award number NE/R016429/1 as part of the UK-SCaPE program delivering National Capability.

2.b.3 Night marine air temperature

R. C. Cornes, T. Cropper and E. C. Kent were supported by the NERC NC CLASS programme (NE/R015953/1) and the NERC GloSAT project (NE/S015647/2). R. Junod was supported by funding from the U.S. Department of Energy (DE-SC0023332).

2.b.4 Surface temperature extremes

R. J. H. Dunn was supported by the Met Office Hadley Centre Climate Programme funded by BEIS.

2.b.5 Tropospheric temperature

Work performed by Stephen Po-Chedley at Lawrence Livermore National Laboratory (LLNL) was supported by LDRD 23-FS-009 and performed under the auspices of the DOE under Contract DE-AC52-07NA27344.

2.c.1 Permafrost temperatures and active layer thickness

The Circumpolar Active Layer Monitoring (CALM) program is funded by the US NSF Project OPP-1836377. The Swiss Permafrost Monitoring Network (PERMOS) is financially supported by MeteoSwiss (in the framework of GCOS Switzerland), the Federal Office for the Environment, and the Swiss Academy of Sciences and acknowledges the important contribution of its partner institutions and principal investigators. The French Network PermaFRANCE is financially supported by the Observatoire des Sciences de l'Univers Grenoble and the French Research Infrastructure OZCAR. Research on James Ross Island was supported by the Czech Antarctic Research Programme and the Czech Science Foundation project (GM22-28659M). The Chinese Permafrost Monitoring Network is financially supported by the Chinese National Science Foundation (41931180) and the Cryosphere Research Station on Qinghai-Xizang Plateau, CAS.

2.c.2 Rock glacier velocity

Rock glacier monitoring at Hinteres Langtalkar and Dösen rock glaciers (AT) is supported by the Hohe Tauern National Park Carinthia through its long-term permafrost monitoring program. The Laurichard (FR) survey is supported by CryobsClim “Long-term Observation and Experimentation System for Environmental Research” (SOERE/All’envi-OZCAR Research Infrastructure) and the PermaFrance observatory “monitoring the mountain permafrost in the French Alps” as well as French National Research Agency in the framework of the Investissements d’Avenir programs: Risk@UGA (ANR-15-IDEX-02) and LabEx OSUG@2020 (ANR10 LABX56). The Ecrins National Park helps field surveys since the early 2000s. The Swiss Permafrost Monitoring Network (PERMOS) is financially supported by MeteoSwiss in the framework of GCOS Switzerland, the Federal Office for the Environment and the Swiss Academy of Sciences. PERMOS acknowledges the important contribution of the partner institutions and principal investigators. The time series for Central Asian rock glaciers was compiled with the ESA Permafrost_CCI project (4000123681/18/I-NB). The time series for the Dry Andes was supported by the Centro de Estudios Avanzados en Zonas Áridas (CEAZA) and the Leading House for the Latin American Region (University of St. Gallen), grant number MOB1829.

2.c.3 Alpine glaciers

The World Glacier Monitoring Service data collection system is the basis for nearly all data used in this section.

2.c.4 Lake ice

We thank Alexander Mills, Huaxia Yao, Merja Pulkkanen, Shin-Ichiro Matsuzaki, Jan Henning L’Abée-Lund, Don Pierson, Lars Rudstam, Beth Kohlman, BJ Bauer, Douglas Pierzina, Bonny Pederson, Brendan Wiltse, Carol Wendorf, Cheryl and Dorothy Zingler, Craig Hillman, Calvin Maurer, Dale Robertson, David Kahan, Doug Fitzgerald, Earl Cook, Gay Alberts Ruby, Greg Sass, John Maier, James and Sharon Fenner, Susan Reineking, Jerry Evans, Jerry Sondreal, Tom Stangl, Jim and Judy Daugherty, Joel Rasmussen, John and Catherine Bart, Joy Krubsack, Kay and Rich Rezanka, Kay Wepfer, Ken Blumenfeld, Pete Boulay, Holly Waterfield, Larry Peterson, Lolita Olson, Lowell Dague, Marge Kellor, Mark Biller, Michael Kolecheck, Michael Bradley, Michael Allen, Michael Traufler, Mike, Jeff, and Thomm Backus, Mickey and Dennis Chick, Ann LaLiberte, Nancy Steenport, Patricia Bebak, Patrick Collins, Peter Bearup, Joe Jenkins, Bob Katzenberger, Ronald Jones, Sandra Anderson, Scott Schoepp, Travis Campbell, Susan Verhaalen, Thomas Sommerfeldt, Water Dahlke III, Rachel Dahlke, William Hanson, and Clare and Dan Shirley for their dedication and efforts in collecting and sharing *in situ* ice phenological records over the past 32+ years with us.

2.c.5 Northern Hemisphere snow cover extent

This work is funded in part by NOAA’s Climate Data Record (CDR) Program at the National Centers for Environmental Information.

2.d.1 Surface humidity

Kate Willett was supported by the Met Office Hadley Centre Climate Programme funded by BEIS. Adrian Simmons and David Lavers were supported by the Copernicus Climate Change Service implemented by ECMWF on behalf of the European Commission.

2.d.5 Precipitation extremes

The National Center for Atmospheric Research is sponsored by the National Science Foundation under Cooperative Agreement No. 1852977.

2.d.6 Cloudiness

CERES EBAF data were obtained from the NASA Langley Research Center CERES ordering tool at <https://ceres.larc.nasa.gov/data/>.

2.d.7 Lake water level

B. M. Kraemer recognizes support from the grant “SeeWandel: Life in Lake Constance - the Past, Present and Future” within the framework of the Interreg V programme “Alpenrhein-Bodensee-Hochrhein (Germany/Austria/Switzerland/Liechtenstein)” whose funds are provided by the European Regional Development Fund as well as the Swiss Confederation and cantons. M.F. Meyer was supported by a USGS Mendenhall Fellowship from the Water Mission Area. The funders had no role in study design, data collection and analysis, decision to publish, or preparation of the manuscript. Any use of trade, firm, or product names is for descriptive purposes only and does not imply endorsement by the U.S. Government.

2.d.8 Groundwater and terrestrial water storage

Work on the Groundwater and Terrestrial Water Storage section was funded by NASA’s GRACE-FO Science Team.

2.d.9 Soil moisture

This study uses satellite soil moisture observations from the Copernicus Climate Change Service (C3S) Climate Data Store (CDS): Soil moisture gridded data from 1978 to present. (Accessed on 19-01-2023), 10.24381/cds.d7782f18

2.d.10 Drought

Jonathan Barichivich was supported by the European Research Council (ERC) under the Horizon Europe research and innovation programme (ERC-starting grant CATES, grant agreement No. 101043214). Tim Osborn received funding from UK NERC (NE/S015582/1). Ian Harris received funding from UK National Centre for Atmospheric Science (NCAS). The research presented in the drought section was carried out on the High-Performance Computing Cluster supported by the Research and Specialist Computing Support service at the University of East Anglia.

2.d.11 Land evaporation

D. G. Miralles acknowledges support from the European Research Council (ERC) under grant agreement no. 101088405 (HEAT). M.F. McCabe and H.E. Beck are supported by the King Abdullah University of Science and Technology.

2.e.2 Surface winds

C. Azorin-Molina was supported by CSIC-UV-GVA and funded by AICO/2021/023, LINGGLOBAL-CSIC ref. INCGLO0023, INTRAMURAL-CSIC ref. 202230I068, and PTI-CLIMA.R. J. H. Dunn was supported by the Met Office Hadley Centre Climate Programme funded by BEIS. L. Ricciardulli was supported by NASA Ocean Vector Wind Science Team grant 80HQTR19C0003. Z. Zeng was supported by the National Natural Science Foundation of China grant 42071022.

2.e.4 Lightning

The work of M. Füllekrug was sponsored by the Royal Society (UK) grant NMG/R1/180252 and the Natural Environment Research Council (UK) under grants NE/L012669/1 and NE/H024921/1.

E. Williams is supported for studies on global circuit response to climate change from the Physical and Dynamic Meteorology Program at the National Science Foundation on grant no. 6942679.

C. Price was supported in his lightning research by the Israel Science Foundation (ISF) grant 2701/17, and the Ministry of Energy grant no. 220-17-002. S. Goodman was supported by NASA Grant 80NSSC21K0923 and NASA Contract 80GSFC20C044. K.Virts is supported in part by the GOES-R Series Science, Demonstration, and Cal/Val Program at Marshall Space Flight Center. D. Buechler is supported by the NASA MSFC/UAH Cooperative Agreement NNM11AA01A. The authors wish to thank Peter Thorne at Maynooth University in Ireland and at the European Centre for Medium Range Weather Forecast (ECMWF) for suggesting and initiating this work and for recommending that lightning be made an essential climate variable. ISS LIS acknowledges support from the NASA Science Mission Directorate.

2.f.1 Earth radiation budget at top of atmosphere

This research has been supported by the NASA CERES project. The NASA Langley Atmospheric Sciences Data Center processed the instantaneous Single Scanner Footprint (SSF) data used as input to EBAF Ed4.2 and processes the FLASHFlux TISA version 4A.

2.g.3 Aerosols

Samuel Rémy, Melanie Ades, and Mihai Alexe are grateful to the EU Copernicus Atmosphere Monitoring Service (CAMS), which supports the CAMS reanalysis used in the aerosols section.

2.g.4 Stratospheric ozone

Carlo Arosio, Melanie Coldewey-Egbers, Diego Loyola, Viktoria Sofieva, Alexei Rozanov, and Mark Weber are grateful to the EU Copernicus Climate Change Service, 312b Lot4 Ozone and to ESA's Climate Change Initiative Ozone (CCI+) projects for supporting the generation and extension of the GTO-ECV total ozone and SAGE-CCI-OMPS data records. Mark Weber, Carlo Arosio, Kleareti Tourpali, and Alexei Rozanov are grateful for the support by the ESA project "Ozone Recovery from Merged Observational Data and Model Analysis (OREGANO)". Stacey M. Frith is supported by the NASA Long Term Measurement of Ozone program WBS 479717. Lucien Froidevaux's contribution, with the assistance of Ryan Fuller, was performed at the Jet Propulsion Laboratory, California Institute of Technology, under contract with NASA. Jeannette Wild was supported by NOAA grant NA19NES4320002 (Cooperative Institute for Satellite Earth System Studies - CISESS) at the University of Maryland/ESSIC. Melanie Coldewey-Egbers and Diego Loyola acknowledge the partial support by the DLR projects MABAK and INPULS.

2.g.6 Tropospheric ozone

O. R. Cooper and K.-L. Chang were supported by NOAA cooperative agreement NA22OAR4320151.

2.g.7 Carbon monoxide

The Copernicus Atmosphere Monitoring Service is funded by the European Union.

2.h.2 Terrestrial vegetation dynamics

N. Gobron thanks Mirko Marioni for his technical support and the providers of the remote sensing dataset needed to perform this research, i.e. the SeaWiFS Project (Code 970.2) and the Goddard Earth Sciences Data and Information Services Center/Distributed Active Archive Center (Code 902) at the Goddard Space Flight Center, Greenbelt, MD 20771. MERIS products were processed at the Grid On Demand facility of the European Space Agency (ESA/ESRIN) using JRC software code.

2.h.1 Albedo

The authors thank Mirko Marioni for his technical support and NASA's Land Processes Distributed Active Archive Center (LP DAAC) for providing access to the remote sensing data.

2.h.3 Biomass burning

J. W Kaiser and M. Parrington were supported by the Copernicus Atmosphere Monitoring Service implemented by ECMWF on behalf of the European Commission. Data processing facilities were provided by the Max Planck Institute for Chemistry, Mainz, Germany.

2.h.4 Phenology of primary producers

Debbie Hemming acknowledges support from the Met Office Hadley Centre Climate Programme funded by BEIS, and thanks all co-authors for their interesting and helpful contributions. Taejin Park acknowledges support from the NASA Earth Science Directorate (grants NNX16AO34H and 80NSSC18K0173-CMS). Andrew Richardson acknowledges support from the National Science Foundation through the Macrosystems Biology (award 1702697) and LTER (award 1832210) programs. John O'Keefe also acknowledges support from the National Science Foundation through the LTER (award 1832210) program. Nature's Calendar (Woodland Trust) in the UK thanks all its volunteer recorders and support from players of People's Postcode

Lottery. Theresa Crimmins and the USA-NPN acknowledge support from the National Science Foundation through the Division of Biological Infrastructure (award 2031660), the US Fish and Wildlife Service (agreements F16AC01075 and F19AC00168), and the US Geological Survey (G14AC00405 and G18AC00135). The USA National Phenology Network thanks the many participants contributing phenology observations to *Nature's Notebook*. De Natuurkalender (Nature's Calendar) program in the Netherlands thanks all the volunteers and school children in the GLOBE program for their many observations. Annette Menzel and Nicole Estrella acknowledge support from the Bavarian State Ministry of Science and the Arts in the context of the Bavarian Climate Research Network (BayKlif) (Bavarian Citizen Science Portal for Climate Research and Science Communication [BAYSICS project]). The Slovak Hydrometeorological Institute thanks all its volunteer observers for participating in the phenological observation program. Orlane Anneville acknowledges support from INRAE. Stephen Thackeray thanks Werner Eckert, Heidrun Feuchtmayr, Shin-Ichiro Matsuzaki, Linda May, Ryuichiro Shinohara, Jan-Erik Thrane, Piet Verburg, Tamar Zohary and all field and lab workers associated with the provision of the lake chlorophyll-a data. We acknowledge funding from Vassdragsforbundet for Mjøsa med tilløpselver (<https://www.vassdragsforbundet.no/om-oss/>) and Natural Environment Research Council award number NE/R016429/1 as part of the UK-SCAPE programme delivering National Capability. Data for Lakes Geneva and Bourget were contributed by the Observatory of alpine LAKes (OLA), © SOERE OLA-IS, AnaEE-France, INRAE of Thonon-les-Bains, CIPEL, CISALB.

2.h.5 Vegetation optical depth

R. M. Zotta and W. Dorigo acknowledge the TU Wien Wissenschaftspreis 2015, a personal grant awarded to W. Dorigo.

We also acknowledge support from the ESA Climate Change Initiative and the Copernicus Climate Change Service (C3S).

Sidebar 2.1 Humid heat extremes

Kate Willett was supported by the Met Office Hadley Centre Climate Programme funded by BEIS.

Appendix 1: Chapter 2 – Acronyms

4D-VAR	four-dimensional variational data assimilation
AAO	Antarctic Oscillation
AATSR	Advanced Along Track Scanning Radiometer
AGAGE	Advanced Global Atmospheric Gases Experiment
AIRS	Atmospheric Infrared Sounder
ALT	active layer thickness
AMSR2	Advanced Microwave Scanning Radiometer 2
AMSR-E	Advanced Microwave Scanning Radiometer-Earth Observing System
AMSU	Advanced Microwave Sounding Unit
AO	Arctic Oscillation
AOD	aerosol optical depth
ASCAT	Advanced Scatterometer
ASR	absorbed solar radiation
BDC	Brewer-Dobson circulation
BOM	Bureau of Meteorology
BUV	backscattering ultraviolet
C3S	Copernicus Climate Change Service
CALIPSO	Cloud-Aerosol LIDAR and Infrared Pathfinder Satellite Observations
CAMS	Copernicus Atmosphere Monitoring Service
CAMSRA	Copernicus Atmosphere Monitoring Service Reanalysis
CCI	Climate Change Initiative
CCMI	Chemistry Climate Model Initiative
CDR	climate data record
CEI4	Climate Extremes Index component 4
CERES EBAF	Clouds and the Earth’s Radiant Energy System Energy Balance and Filled
CFC-11	trichlorofluoromethane
CFC	chlorofluorocarbon
CH ₃ CCl ₃	methyl chloroform
CH ₄	methane
CHIRPS	Climate Hazards Group Infrared Precipitation with Station data
CLASSmat	Climate Linked Atlantic Sector Science night marine air temperature
CMIP	Coupled Model Intercomparison Project
CMIP6	Phase 6 of the Coupled Model Intercomparison Project
CO	carbon monoxide
CO ₂	carbon dioxide
COG _L	center of gravity
COSMIC	Constellation Observing System for Meteorology, Ionosphere, and Climate
CPT	cold-point tropopause
CRU TS	Climatic Research Unit Gridded Time Series
DOM _L	day of maximum concentration
DU	Dobson units
EBAF	Energy Balance and Filled
ECMWF	European Centre for Medium-Range Weather Forecasts
ECV	essential climate variable
EESC	equivalent effective stratospheric chlorine
ENSO	El Niño–Southern Oscillation
EOS	end of season
ERA5	European Centre for Medium-Range Weather Forecasts Reanalysis version 5
ERB	Earth radiation budget

ERFs	effective radiative forcings
ESA	European Space Agency
ET	Penman-Monteith Potential Evapotranspiration
ETCCDI	Expert Team in Climate Change Detection and Indices
EUR	Eurasia
EUR	Europe
FAO	Food and Agriculture Organization
FAPAR	fraction of absorbed photosynthetically active radiation
FBD	full bloom dates
FF	fossil fuel
FLASHFlux	Fast Longwave and Shortwave Radiative Fluxes
FP	frost point
GAW	Global Atmosphere Watch
GCM	general circulation model
GCOS	Global Climate Observing System
GFAS	Global Fire Assimilation System
GFED	Global Fire Emissions Database
GHCND	Global Historical Climatology Network Daily
GHCNDEX	Global Historical Climatology Network Index
GISTEMP	GISS Surface Temperature Analysis
GLEAM	Global Land Evaporation Assessment Model
GLM	Geostationary Lightning Mapper
GNSS	global navigation satellite system
GOES	Geostationary Operational Environmental Satellite
GOME	Global Ozone Monitoring Experiment
GOZCARDS	Global Ozone Chemistry and Related Trace Gas Data Records for the Stratosphere
GPCC	Global Precipitation Climatology Centre
GPCP	Global Precipitation Climatology Project
GPS-RO	GPS radio occultation
GRACE	Gravity Recovery and Climate Experiment
GRACE-FO	Gravity Recovery and Climate Experiment Follow-On
G-REALM	Global Reservoir and Lake Monitoring
GSL	Global Snow Lab
GTN-P	Global Terrestrial Network for Permafrost
GWP	global warming potential
H ₂ O	water vapor
HadCRUT5	Hadley Centre/Climatic Research Unit Temperature version 5
HadISD3	Hadley Centre Integrated Surface Database version 3
HadISDH	Hadley Centre Integrated Surface Database Humidity
HadSST	The Met Office Hadley Centre's sea surface temperature dataset
HCFC	hydrochlorofluorocarbon
HFC	hydrofluorocarbon
HIRS	High-Resolution Infrared Sounder
HTHH	Hunga Tonga–Hunga Ha'apai
IOD	Indian Ocean dipole
IPCC AR6	Intergovernmental Panel on Climate Change Sixth Assessment Report
ISS	International Space Station
ITCZ	Intertropical Convergence Zone
JRA-55	Japanese 55-year Reanalysis
LIS	Lightning Imaging Sensor
LLGHG	long-lived greenhouse gases
LOWESS	locally weighted scatterplot smoothing

LSWT	lake-surface water temperature
LTT	lower-tropospheric temperature
LWCRE	longwave cloud radiative effect
MACCity	Monitoring Atmospheric Composition and Climate megacity
MAT	marine air temperature
MCS	marine cold-spell
MCS	mesoscale convective systems
MEGAN2.1	Model of Emissions of Gases and Aerosols from Nature version 2.1
MERRA-2	Modern-Era Retrospective Analysis for Research and Applications version 2
MHW	marine heatwave
MLO	Mauna Loa Observatory
MLS	Microwave Limb Sounder
MODIS	Moderate Resolution Imaging Spectroradiometer
MOPITT	Measurement of Pollution in the Troposphere
MSLP	mean sea-level pressure
MSU	Microwave Sounding Unit
N ₂ O	nitrous oxide
NA	North America
NAE	North Atlantic/European
NAO	North Atlantic Oscillation
NDACC	Network for the Detection of Atmospheric Composition Changes
NDVI	Normalized Difference Vegetation Index
NH	Northern Hemisphere
NIWA	National Institute of Water and Atmospheric Research
NMAT	night marine air temperature
NOAAGlobalTemp	NOAA Merged Land Ocean Global Surface Temperature Analysis
NPN	National Phenology Network
NRT	near real time
O ₃	tropospheric ozone
ODGI	Ozone Depleting Gas Index
ODS	Ozone-depleting substance
OH	hydroxyl radical
OISST	Optimum Interpolation Sea Surface Temperature
OLR	outgoing longwave radiation
OMI	Ozone Monitoring Instrument
OMPS	Ozone Mapping and Profiler Suite
OMPS-L	Ozone Mapping and Profiler Suite-Limb
OMPS-N	Ozone Mapping and Profiler Suite-Nadir
PATMOS-X	Pathfinder Atmospheres – Extended
PERMOS	Swiss Permafrost Monitoring Network
PNA	Pacific/North American
q	specific humidity
QBO	quasi-biennial oscillation
QuikSCAT	Quick Scatterometer
RCP	Representative Concentration Pathway
RFaci	aerosol-cloud interactions
RFari	aerosol-radiation
RGIK	rock glacier inventories and kinematics
RGV	rock glacier velocities
RH	relative humidity
RSS	Remote Sensing Systems
RSW	reflected shortwave

SAGE	Stratospheric Aerosol and Gas Experiment
SAM	Southern Annular Mode
SAOZ	Système D'Analyse par Observations Zénithales
SAWS	South African Weather Service
SBUV	Solar Backscatter Ultraviolet Radiometer
SCE	snow-cover extent
SCIAMACHY	Scanning Imaging Absorption Spectrometer for Atmospheric Cartography
scPDSI	self-calibrating Palmer Drought Severity Index
SH	Southern Hemisphere
SLSTR	Sea and Land Surface Temperature Radiometer
SO ₂	sulfur dioxide
SOI	Southern Oscillation Index
SORCE	Solar Radiation and Climate Experiment
SOS	start of season
SPARC	Spatial Analysis and Resource Characterization
SSM/I	Special Sensor Microwave/Imager
SSMIS	Special Sensor Microwave Imager/Sounder
SST	sea-surface temperature
SW	shortwave
SWCRE	shortwave cloud radiative effect
SWOT	Surface Water and Ocean Topography
TCO	tropospheric column ozone
TCWV	total column water vapor
TMI	TRMM Microwave Imager
TOA	top-of-atmosphere
TOB	tropospheric ozone burden
TRMM	Tropical Rainfall Measuring Mission
TSI	total solar irradiance
TSIS-1	Total Solar and Spectral Irradiance Sensor-1
TTL	tropical tropopause layer
TTT	tropical tropospheric temperature
T _w	wet bulb temperature
TWS	terrestrial water storage
UAHNMAT	University of Alabama in Huntsville night-time marine air temperature
UT	upper tropospheric
UTH	upper-tropospheric humidity
UV	ultraviolet
VEI	Volcanic Explosivity Index
VOD	vegetation optical depth
VODCA	Vegetation Optical Depth Climate Archive
w.e.	water equivalent
WGMS	World Glacier Monitoring Service
WMO	World Meteorological Organization
WOUDC	World Ozone and Ultraviolet Radiation Data Centre
WV	water vapor

Appendix 2: Chapter 2 – Supplemental Material

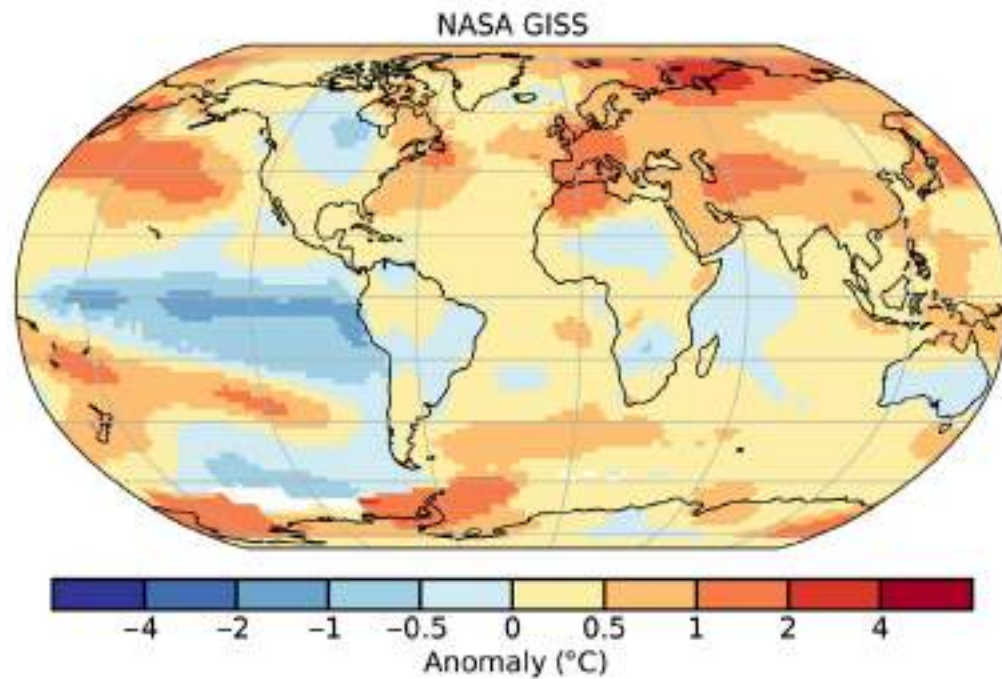


Fig. A2.1. NASA GISS 2-m surface temperature anomalies (°C; 1991–2020 base period).

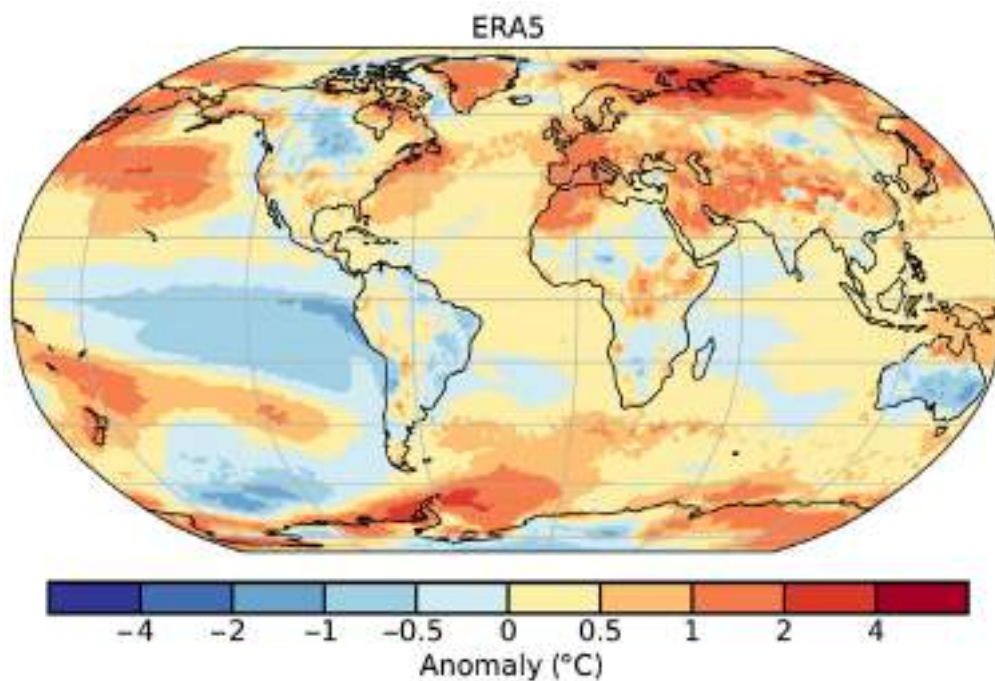


Fig. A2.2. ERA5 2-m surface temperature anomalies (°C; 1991–2020 base period).

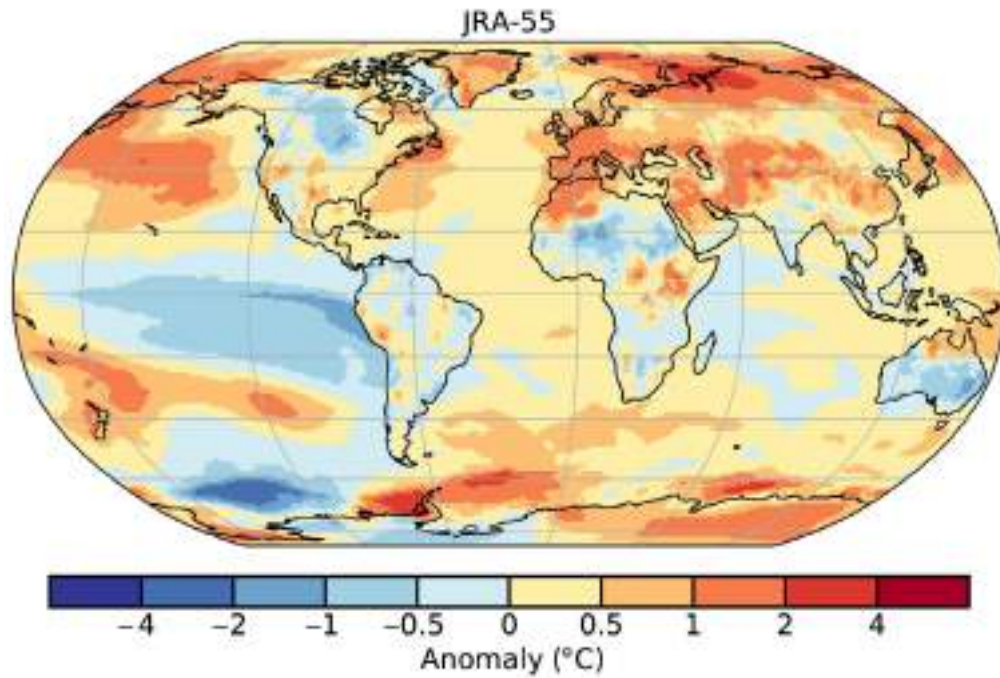


Fig. A2.3. JRA-55 2-m surface temperature anomalies (°C; 1991–2020 base period).

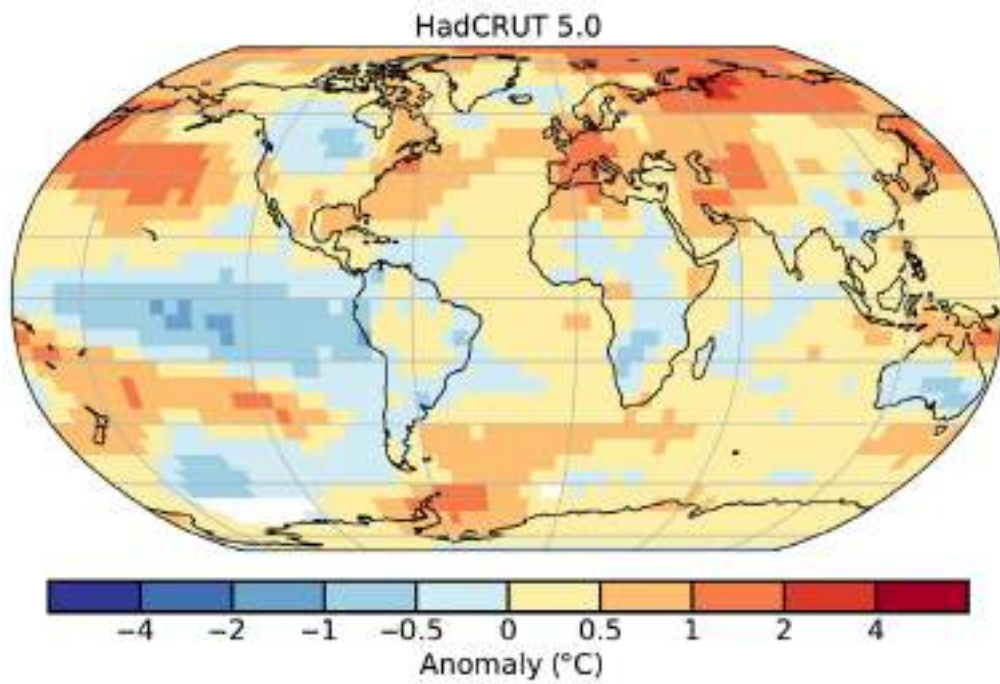


Fig. A2.4. HadCRUT5 2-m surface temperature anomalies (°C; 1991–2020 base period).

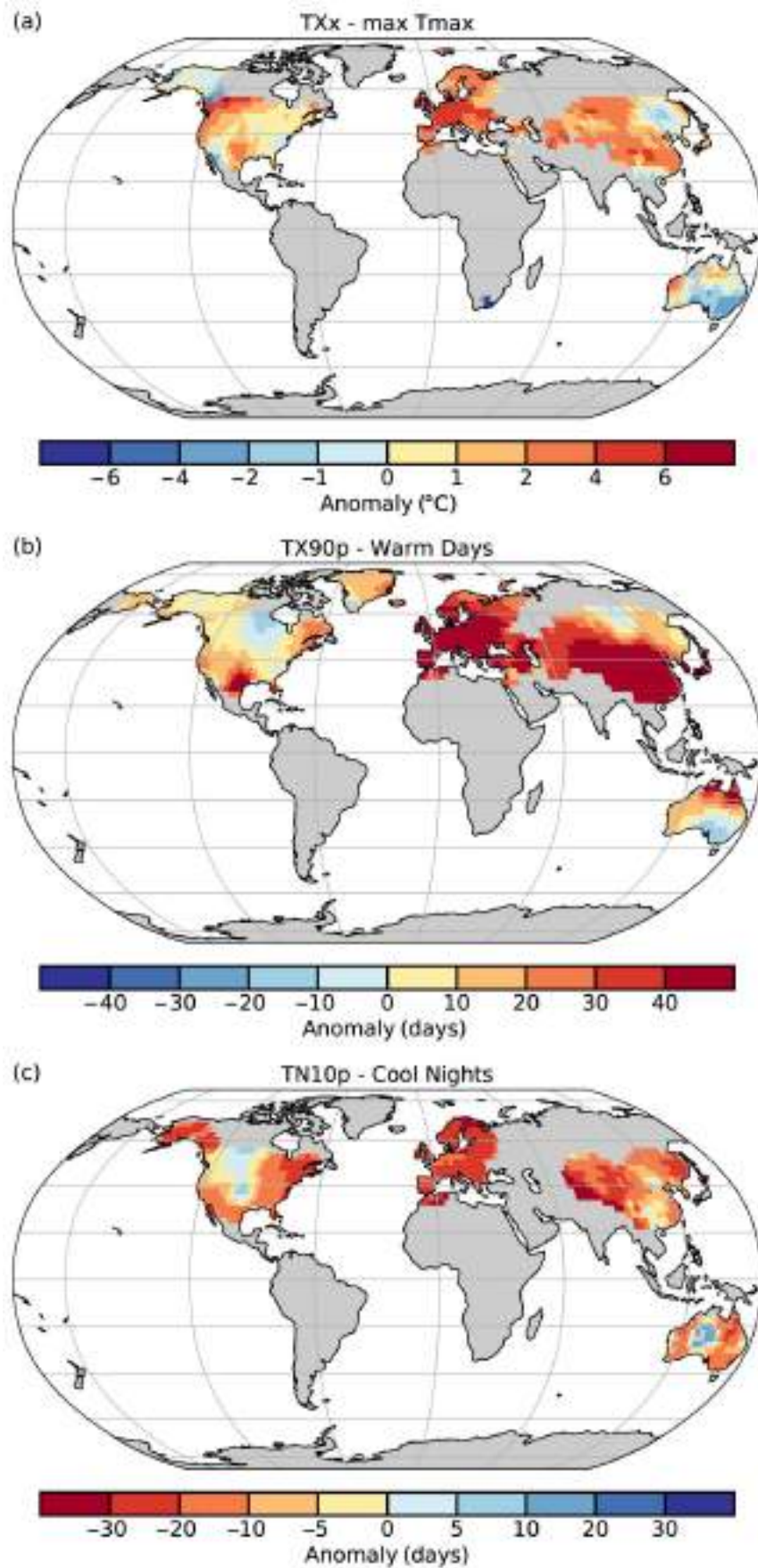


Fig. A2.5. (a) Extreme temperature anomalies in 2022 based on GHCNDEX for (a) hottest day of the year (°C; TXx), (b) annual number of warm days (TX90p), and (c) annual number of cool nights (TN10p). Base period is 1961–90.

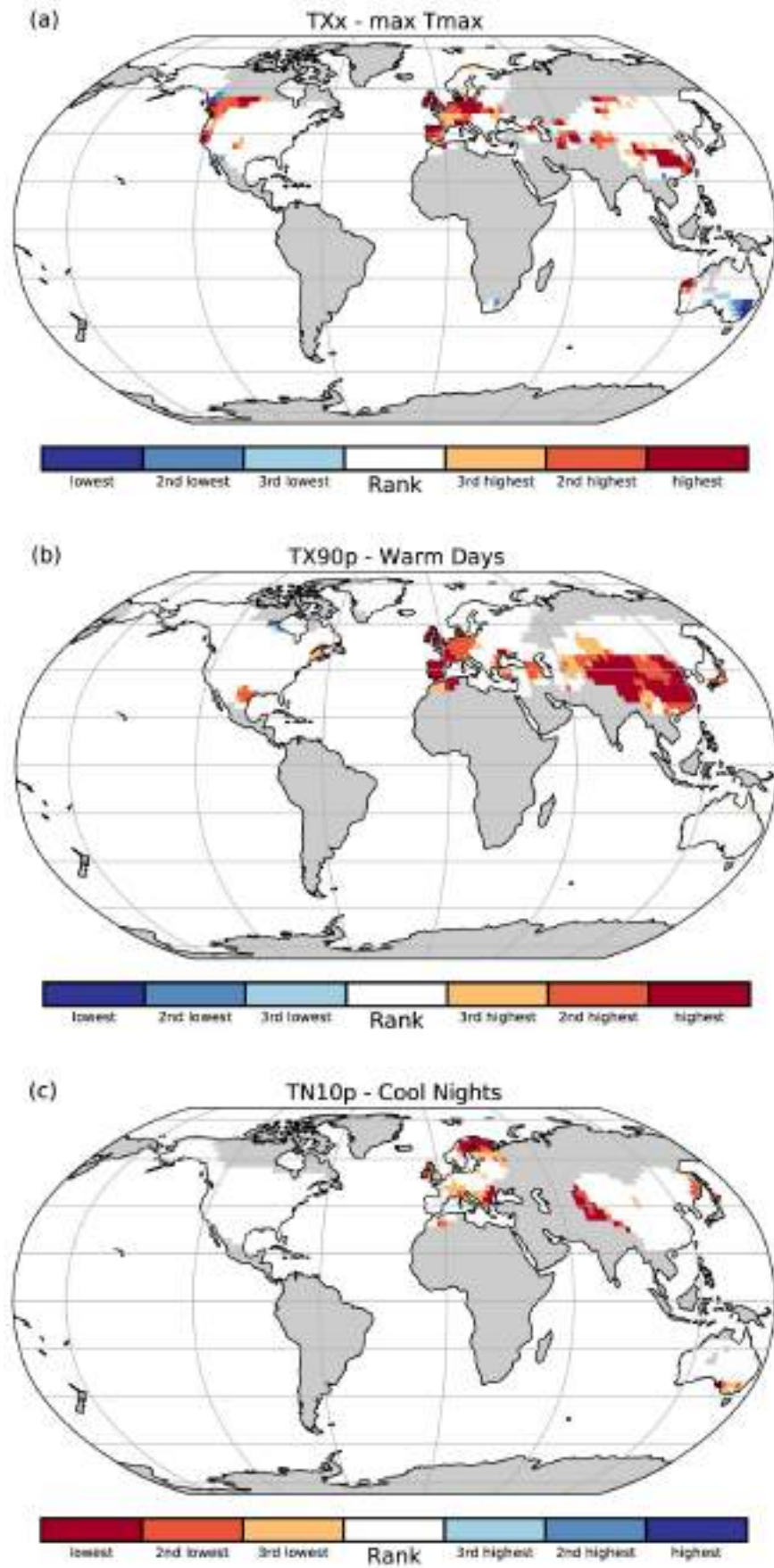


Fig. A2.6. Maps indicating grid cells where the temperature indices for 2022 ranked in the three highest or three lowest values based on GHCNDEX since 1951 for (a) hottest day of the year (TXx), (b) annual number of warm days (TX90p), and (c) annual number of cool nights (TN10p).

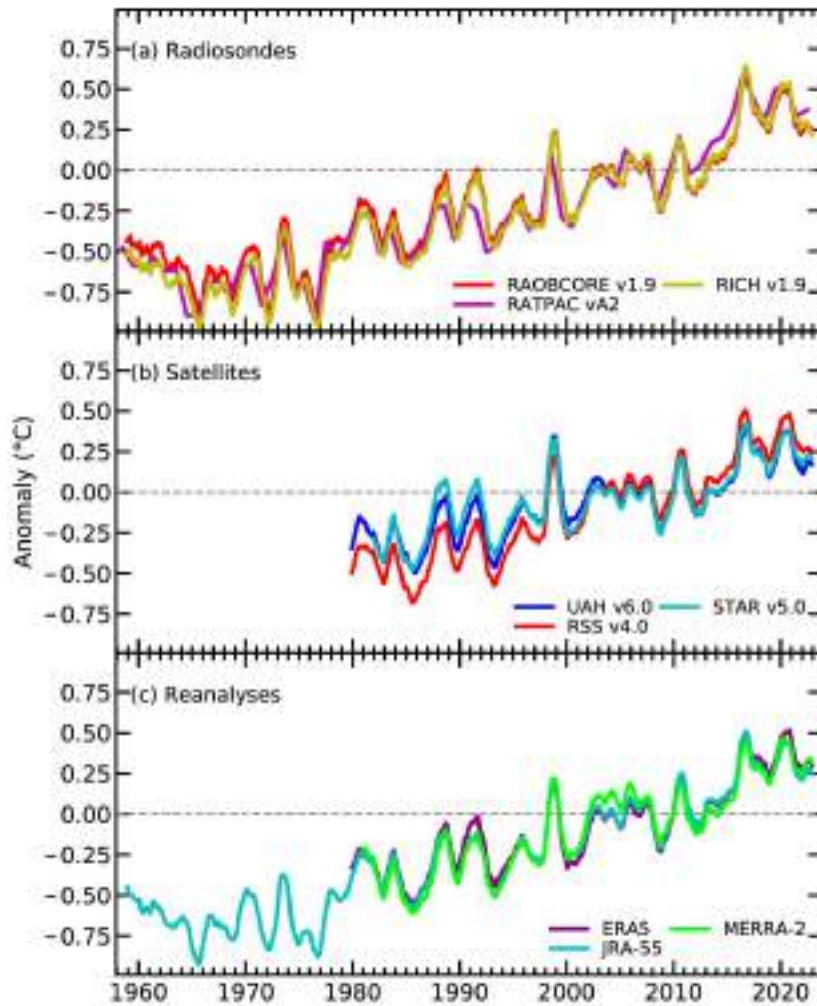


Fig. A2.7. Monthly average global lower-tropospheric temperature (LTT) anomalies (°C; 1991–2020 base period) for (a) radiosonde, (b) satellite, and (c) reanalysis datasets. Time series are smoothed using a 12-month running average. Annual averages are displayed for the RATPAC dataset.

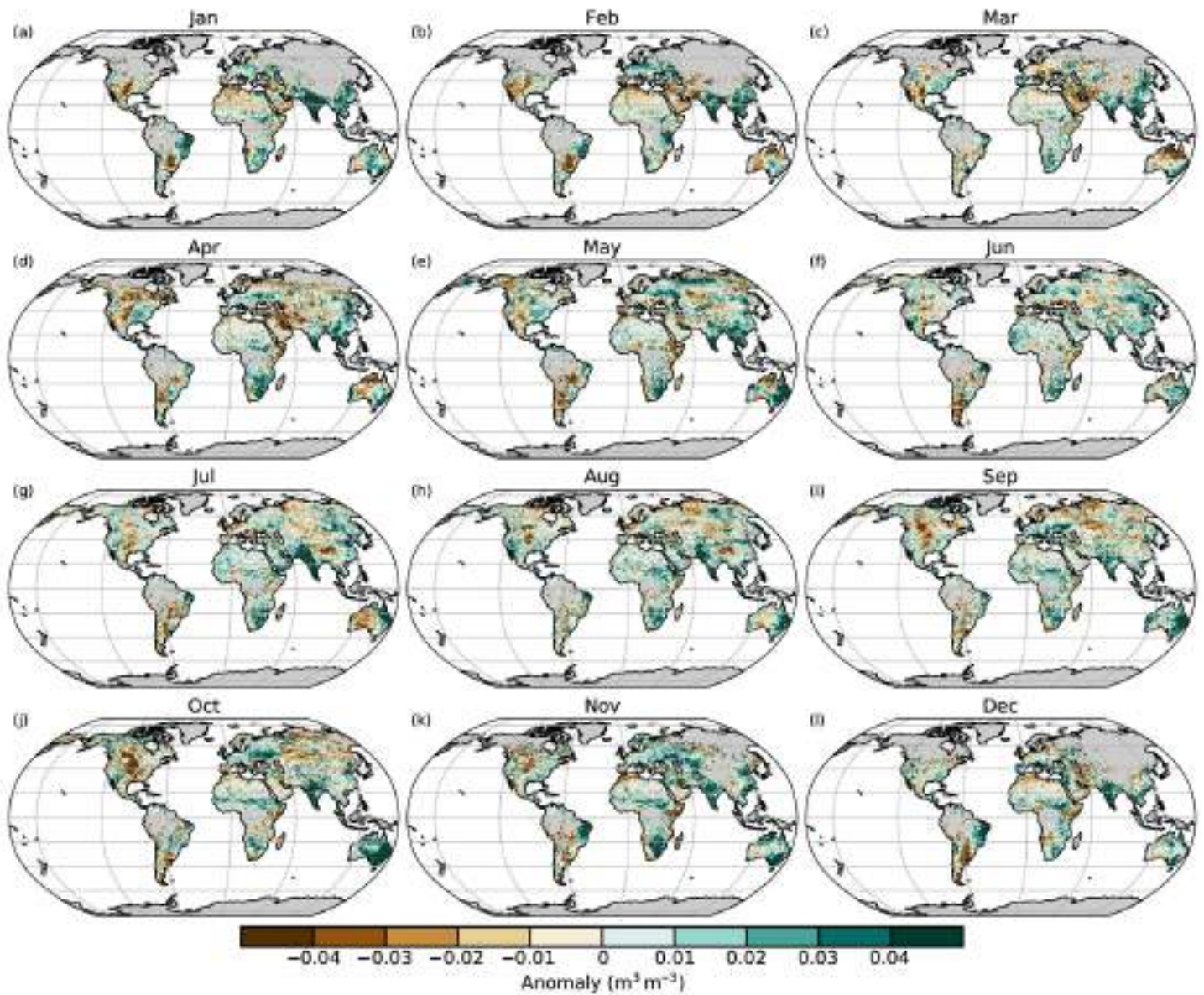


Fig. A2.8. Monthly average soil moisture anomalies for 2022 ($\text{m}^3 \text{m}^{-3}$; 1991–2020 base period). Data are masked where no retrieval is possible or where the quality is not assured and flagged, for example due to dense vegetation, frozen soil, or radio frequency interference. (Source: C3S Soil Moisture.)

2.f.2 Mauna Loa Apparent Transmission

Simulation of Tonga aerosol dispersion in the layer 19–27 km for 8–18 Mar 2022, derived from Cloud-Aerosol Lidar and Infrared Pathfinder Satellite Observations (CALIPSO) data.

https://figshare.com/articles/media/CALIOP_Latm-GMAO-19_27km_v2-10_20MAR-22_mp4/22704607/1

2.h.5 Vegetation Optical Depth

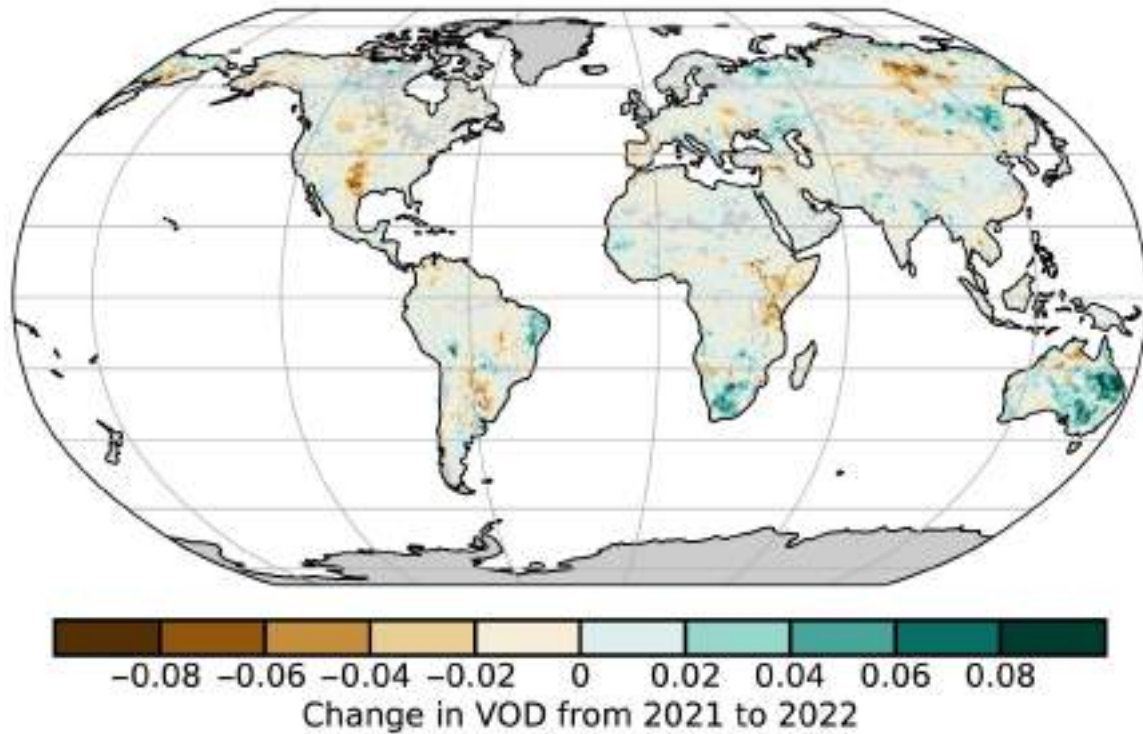


Fig. A2.9. Difference in average CXKu vegetation optical depth (VOD) between the years 2022 and 2021. Brown/green colors indicate areas where VOD in 2022 was lower/higher than in 2021. (Source: VODCA.)

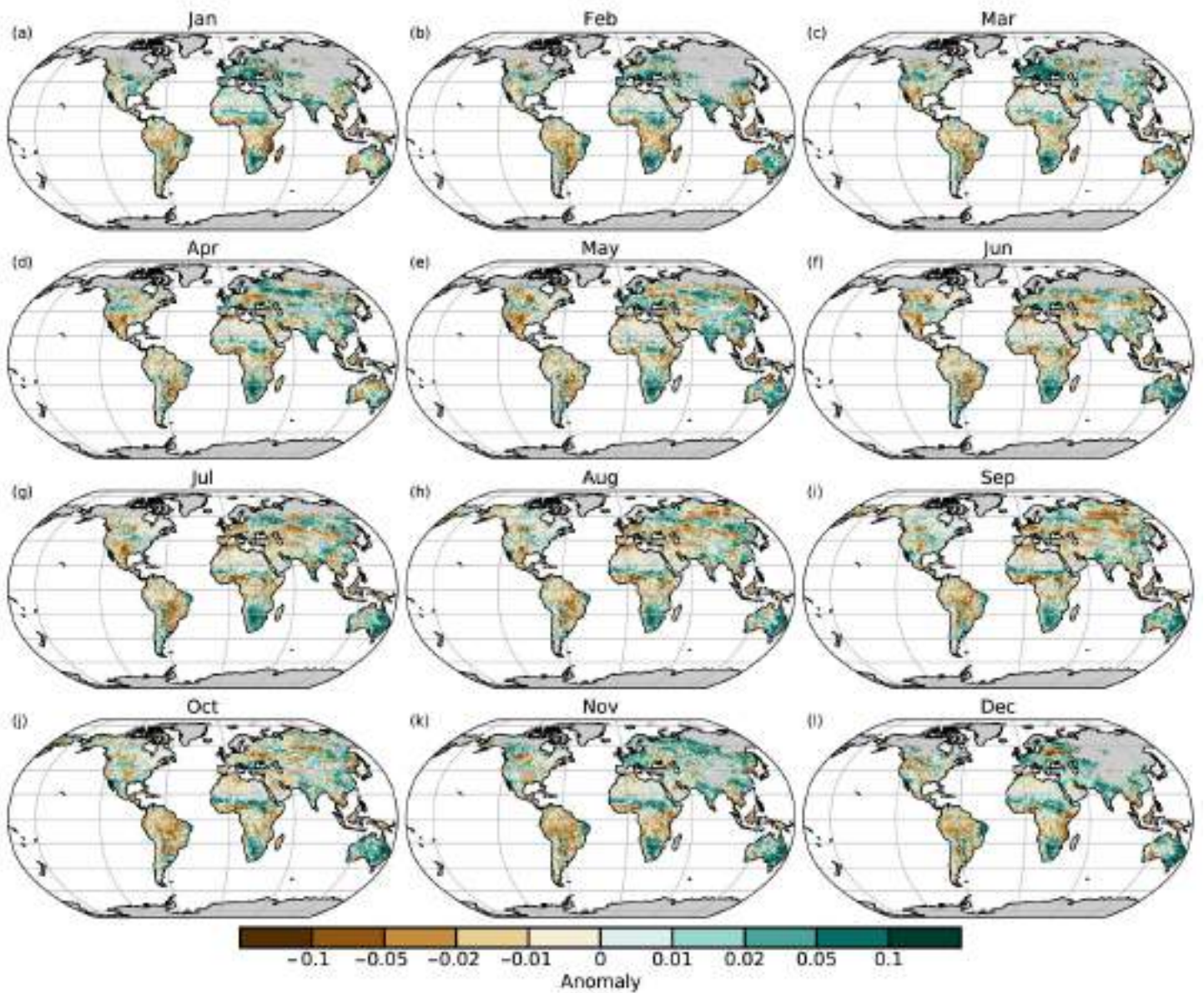


Fig. A2.10. VODCA monthly CXXu vegetation optical depth (VOD) anomalies for 2022 (1991–2020 base period). VOD cannot be retrieved over frozen or snow-covered areas, which is why they are masked in winter.

References

- Adler, R., and Coauthors, 2018: The Global Precipitation Climatology Project (GPCP) monthly analysis (new version 2.3) and a review of 2017 global precipitation. *Atmosphere*, **9**, 138, <https://doi.org/10.3390/atmos9040138>.
- Alden, C. B., J. B. Miller, and J. W. C. White, 2010: Can bottom-ocean CO₂ fluxes be reconciled with atmospheric ¹³C observations?. *Tellus*, **62B**, 369–388, <https://doi.org/10.1111/j.1600-0889.2010.00481.x>.
- Allan, R. J., and R. D. D'Arrigo, 1999: 'Persistent' ENSO sequences: How unusual was the 1990–1995 El Niño? *Holocene*, **9**, 101–118, <https://doi.org/10.1191/095968399669125102>.
- , J. A. Lindesay, and D. E. Parker, 1996: *El Niño Southern Oscillation and Climatic Variability*. CSIRO Publishing, 405 pp.
- Allan, R. P., K. M. Willett, V. O. John, and T. Trent, 2022: Global changes in water vapor 1979–2020. *J. Geophys. Res. Atmos.*, **127**, e2022JD036728, <https://doi.org/10.1029/2022JD036728>.
- Altaratz, O., B. Kucienska, A. Kostinski, G. B. Raga, and I. Koren, 2017: Global association of aerosol with flash density of intense lightning. *Environ. Res. Lett.*, **12**, 114037, <https://doi.org/10.1088/1748-9326/aa922b>.
- Anabalón, A., and A. Sharma, 2017: On the divergence of potential and actual evapotranspiration trends: An assessment across alternate global datasets. *Earth's Future*, **5**, 905–917, <https://doi.org/10.1002/2016EF000499>.
- Andela, N., and Coauthors, 2017: A human-driven decline in global burned area. *Science*, **356**, 1356–1362, <https://doi.org/10.1126/science.aal4108>.
- Anderson, W., B. I. Cook, K. Slinski, K. Schwarzwald, A. McNally, and C. Funk, 2023: Multiyear La Niña events and multiseason drought in the Horn of Africa. *J. Hydrometeorol.*, **24**, 119–131, <https://doi.org/10.1175/JHM-D-22-0043.1>.
- Andrews, T., and Coauthors, 2022: On the effect of historical SST patterns on radiative feedback. *J. Geophys. Res. Atmos.*, **127**, e2022JD036675, <https://doi.org/10.1029/2022JD036675>.
- Ansmann, A., and Coauthors, 2022: Ozone depletion in the Arctic and Antarctic stratosphere induced by wildfire smoke. *Atmos. Chem. Phys.*, **22**, 11 701–11 726, <https://doi.org/10.5194/acp-22-11701-2022>.
- Aon, 2023: Weather, climate and catastrophe insight. Aon plc, 115 pp., <https://www.aon.com/getmedia/f34ec133-3175-406c-9e0b-25cea768c5cf/20230125-weather-climate-catastrophe-insight.pdf>.
- Aono, Y., and K. Kazui, 2008: Phenological data series of cherry tree flowering in Kyoto, Japan, and its application to reconstruction of springtime temperatures since the 9th century. *Int. J. Climatol.*, **28**, 905–914, <https://doi.org/10.1002/joc.1594>.
- Archer, D., and V. Brovkin, 2008: The millennial atmospheric lifetime of anthropogenic CO₂. *Climatic Change*, **90**, 283–297, <https://doi.org/10.1007/s10584-008-9413-1>.
- Archibald, A. T., and Coauthors, 2020: Tropospheric Ozone Assessment Report: A critical review of changes in the tropospheric ozone burden and budget from 1850 to 2100. *Elementa*, **8**, 034, <https://doi.org/10.1525/elementa.2020.034>.
- Arguez, A., S. Hurley, A. Inamdar, L. Mahoney, A. Sanchez-Lugo, and L. Yang, 2020: Should we expect each year in the next decade (2019–28) to be ranked among the top 10 warmest years globally? *Bull. Amer. Meteor. Soc.*, **101**, E655–E663, <https://doi.org/10.1175/BAMS-D-19-0215.1>.
- Armstrong, B., and Coauthors, 2019: The role of humidity in associations of high temperature with mortality: A multicountry, multicity study. *Environ. Health Perspect.*, **127**, 097007, <https://doi.org/10.1289/EHP5430>.
- Arosio, C., A. Rozanov, E. Malinina, K.-U. Eichmann, T. von Clarman, and J. P. Burrows, 2018: Retrieval of ozone profiles from OMPS limb scattering observations. *Atmos. Meas. Tech.*, **11**, 2135–2149, <https://doi.org/10.5194/amt-11-2135-2018>.
- , —, —, M. Weber, and J. P. Burrows, 2019: Merging of ozone profiles from SCIAMACHY, OMPS and SAGE II observations to study stratospheric ozone changes. *Atmos. Meas. Tech.*, **12**, 2423–2444, <https://doi.org/10.5194/amt-12-2423-2019>.
- Augustine, J. A., K. O. Lantz, J.-P. Vernier, and H. Telg, 2020: Mauna Loa clear-sky "apparent" solar transmission [in "State of the Climate in 2019"]. *Bull. Amer. Meteor. Soc.*, **101** (8), S61–S62, <https://doi.org/10.1175/BAMS-D-20-0104.1>.
- , —, and —, 2021: Mauna Loa apparent transmission [in "State of the Climate in 2020"]. *Bull. Amer. Meteor. Soc.*, **102** (8), S82–S83, <https://doi.org/10.1175/BAMS-D-21-0098.1>.
- Azorin-Molina, C., J. Asin, T. R. McVicar, L. Minola, J. I. Lopez-Moreno, S. M. Vicente-Serrano, and D. Chen, 2018: Evaluating anemometer drift: A statistical approach to correct biases in wind speed measurement. *Atmos. Res.*, **203**, 175–188, <https://doi.org/10.1016/j.atmosres.2017.12.010>.
- Ball, W. T., G. Chiodo, M. Abalos, J. Alsing, and A. Stenke, 2020: Inconsistencies between chemistry–climate models and observed lower stratospheric ozone trends since 1998. *Atmos. Chem. Phys.*, **20**, 9737–9752, <https://doi.org/10.5194/acp-20-9737-2020>.
- Barichivich, J., T. J. Osborn, I. Harris, G. van der Schrier, and P. D. Jones, 2020: Monitoring global drought using the self-calibrating Palmer Drought Severity Index [in "State of the Climate in 2019"]. *Bull. Amer. Meteor. Soc.*, **101** (8), S59–S60, <https://doi.org/10.1175/BAMS-D-20-0104.1>.
- , —, —, —, and —, 2021: Monitoring global drought using the self-calibrating Palmer Drought Severity Index [in "State of the Climate in 2020"]. *Bull. Amer. Meteor. Soc.*, **102** (8), S68–S70, <https://doi.org/10.1175/BAMS-D-21-0098.1>.
- , —, —, —, and —, 2022: Monitoring global drought using the self-calibrating Palmer Drought Severity Index [in "State of the Climate in 2021"]. *Bull. Amer. Meteor. Soc.*, **103** (8), S66–S67, <https://doi.org/10.1175/BAMS-D-22-0092.1>.
- Barlow, M., H. Cullen, and B. Lyon, 2002: Drought in central and southwest Asia: La Niña, the warm pool, and Indian Ocean precipitation. *J. Climate*, **15**, 697–700, [https://doi.org/10.1175/1520-0442\(2002\)0152.0.CO;2](https://doi.org/10.1175/1520-0442(2002)0152.0.CO;2).
- Barnes, W. L., T. S. Pagano, and V. V. Salomonson, 1998: Prelaunch characteristics of the Moderate Resolution Imaging Spectroradiometer (MODIS) on EOS-AM1. *IEEE Trans. Geosci. Remote Sens.*, **36**, 1088–1100, <https://doi.org/10.1109/36.700993>.
- Baruth, B., and Coauthors, 2022: Crop monitoring in Europe. *JRC MARS Bulletin*, Vol. 30, No 8, European Commission, Luxembourg, <https://doi.org/10.2760/31930>.
- Basu, S., and Coauthors, 2022: Estimating emissions of methane consistent with atmospheric measurements of methane and δ¹³C of methane. *Atmos. Chem. Phys.*, **22**, 15 351–15 377, <https://doi.org/10.5194/acp-22-15351-2022>.

- Beck, H. E., E. F. Wood, M. Pazn, C. K. Fisher, D. G. Miralles, A. I. J. M. van Dijk, T. R. McVicar, and R. F. Adler, 2019: MSWEP V2 global 3-hourly 0.1° precipitation: Methodology and quantitative assessment. *Bull. Amer. Meteor. Soc.*, **100**, 473–500, <https://doi.org/10.1175/BAMS-D-17-0138.1>.
- , A. I. J. M. van Dijk, P. R. Larraondo, T. R. McVicar, M. Pan, E. Dutra, and D. G. Miralles, 2022: MSWX: Global 3-hourly 0.1° bias-corrected meteorological data including near real-time updates and forecast ensembles. *Bull. Amer. Meteor. Soc.*, **103**, E710–E732, <https://doi.org/10.1175/BAMS-D-21-0145.1>.
- Becker, A., P. Finger, A. Meyer-Christoffer, B. Rudolf, K. Schamm, U. Schneider, and M. Ziese, 2013: A description of the global land-surface precipitation data products of the Global Precipitation Climatology Centre with sample applications including centennial (trend) analysis from 1901–present. *Earth Syst. Sci. Data*, **5**, 71–99, <https://doi.org/10.5194/essd-5-71-2013>.
- Behera, S. K., J. J. Luo, S. Masson, S. A. Rao, H. Sakuma, and T. Yamagata, 2006: A CGCM study on the interaction between IOD and ENSO. *J. Climate*, **19**, 1688–1705, <https://doi.org/10.1175/JCLI3797.1>.
- Bell, B., and Coauthors, 2021: The ERA5 global reanalysis: Preliminary extension to 1950. *Quart. J. Roy. Meteor. Soc.*, **147**, 4186–4227, <https://doi.org/10.1002/qj.4174>.
- Bellouin, N., and Coauthors, 2020: Radiative forcing of climate change from the Copernicus reanalysis of atmospheric composition. *Earth Syst. Sci. Data*, **12**, 1649–1677, <https://doi.org/10.5194/essd-12-1649-2020>.
- Benson, B., J. Magnuson, and S. Sharma, 2000: Global Lake and River Ice Phenology Database, version 1. National Snow and Ice Data Center, accessed 1 February 2023, <https://doi.org/10.7265/N5W66HP8>.
- Benson, D. O., and P. A. Dirmeyer, 2021: Characterizing the relationship between temperature and soil moisture extremes and their role in the exacerbation of heat waves over the contiguous United States. *J. Climate*, **34**, 2175–2187, <https://doi.org/10.1175/JCLI-D-20-0440.1>.
- Biancamaria, S., D. P. Lettenmaier, and T. M. Pavelsky, 2016: The SWOT mission and its capabilities for land hydrology. *Remote Sensing and Water Resources*, A. Cazenave et al., Eds., Springer, 117–147, https://doi.org/10.1007/978-3-319-32449-4_6.
- Birkett, C. M., and B. Beckley, 2010: Investigating the performance of the Jason-2/OSTM radar altimeter over lakes and reservoirs. *Mar. Geod.*, **33**, 204–238, <https://doi.org/10.1080/01490419.2010.488983>.
- , K. O'Brien, S. Kinsey, M. Ricko, and Y. Li, 2022: Enhancement of a global lake and reservoir database to aid climate studies and resource monitoring utilizing satellite radar altimetry. *J. Great Lakes Res.*, **48**, 37–51, <https://doi.org/10.1016/j.jglr.2021.11.013>.
- Biskaborn, B. K., and Coauthors, 2019: Permafrost is warming at a global scale. *Nat. Commun.*, **10**, 264, <https://doi.org/10.1038/s41467-018-08240-4>.
- Bjerknes, J., 1969: Atmospheric teleconnections from the equatorial Pacific. *Mon. Wea. Rev.*, **97**, 163–172, [https://doi.org/10.1175/1520-0493\(1969\)0972.3.CO;2](https://doi.org/10.1175/1520-0493(1969)0972.3.CO;2).
- Blakeslee, R. J., and Coauthors, 2020: Three years of the Lightning Imaging Sensor onboard the International Space Station: Expanded global coverage and enhanced applications. *J. Geophys. Res. Atmos.*, **125**, e2020JD032918, <https://doi.org/10.1029/2020JD032918>.
- Blunden, J., and T. Boyer, Eds., 2022: "State of the Climate in 2021." *Bull. Amer. Meteor. Soc.*, **103** (8) Si–S465, <https://doi.org/10.1175/2022BAMSStateoftheClimate.1>.
- Bock, O., 2022: Global GNSS integrated water vapour data, 1994–2022. AERIS, accessed 24 July 2023, <https://doi.org/10.25326/68>.
- Bourassa, A. E., D. J. Zawada, L. A. Rieger, T. W. Warnock, M. Toohey, and D. A. Degenstein, 2023: Tomographic retrievals of Hunga Tonga-Hunga Ha'apai volcanic aerosol. *Geophys. Res. Lett.*, **50**, e2022GL101978, <https://doi.org/10.1029/2022GL101978>.
- Brohan, P., J. J. Kennedy, I. Harris, S. F. Tett, and P. D. Jones, 2006: Uncertainty estimates in regional and global observed temperature changes: A new data set from 1850. *J. Geophys. Res.*, **111**, D12106, <https://doi.org/10.1029/2005JD006548>.
- Bruick, Z. S., K. L. Rasmussen, A. K. Rowe, and L. A. McMurdie, 2019: Characteristics of intense convection in subtropical South America as influenced by El Niño–Southern Oscillation. *Mon. Wea. Rev.*, **147**, 1947–1966, <https://doi.org/10.1175/MWR-D-18-0342.1>.
- Brutsaert, W., 2017: Global land surface evaporation trend during the past half century: Corroboration by Clausius-Clapeyron scaling. *Adv. Water Resour.*, **106**, 3–5, <https://doi.org/10.1016/j.advwatres.2016.08.014>.
- Bureau of Meteorology, 2023: Daily rainfall extremes graph(s) for Australia. Accessed 7 February 2023, http://www.bom.gov.au/cgi-bin/climate/extremes/extreme_graphs_annual.cgi?graph=rain&year=2022&area=qld&percent=99.
- Capotondi, A., and Coauthors, 2015: Understanding ENSO diversity. *Bull. Amer. Meteor. Soc.*, **96**, 921–938, <https://doi.org/10.1175/BAMS-D-13-00117.1>.
- Carn, S. A., N. A. Krotkov, B. L. Fisher, and C. Li, 2022: Out of the blue: Volcanic SO₂ emissions during the 2021–2022 eruptions of Hunga Tonga—Hunga Ha'apai (Tonga). *Front. Earth Sci.*, **10**, 976962, <https://doi.org/10.3389/feart.2022.976962>.
- Carr, J. L., Á. Horváth, D. L. Wu, and M. D. Friberg, 2022: Stereo plume height and motion retrievals for the record-setting Hunga Tonga-Hunga Ha'apai eruption of 15 January 2022. *Geophys. Res. Lett.*, **49**, e2022GL098131, <https://doi.org/10.1029/2022GL098131>.
- Carrea, L., O. Embury, and C. J. Merchant, 2015: Datasets related to in-land water for limnology and remote sensing applications: Distance-to-land, distance-to-water, water-body identifier and lake-centre co-ordinates. *Geosci. Data J.*, **2**, 83–97, <https://doi.org/10.1002/gdj3.32>.
- , and Coauthors, 2020: Lake surface temperature [in "State of the Climate in 2019"]. *Bull. Amer. Meteor. Soc.*, **101** (8), S26–S28, <https://doi.org/10.1175/BAMS-D-20-0104.1>.
- , C. Merchant, B. Calmettes, and J.-F. Cretaux, 2021: Lake surface water temperature [in "State of the Climate in 2020"]. *Bull. Amer. Meteor. Soc.*, **102** (8), S28–S31, <https://doi.org/10.1175/BAMS-D-21-0098.1>.
- , —, and R. I. Woolway, 2022a: Lake surface water temperature [in "State of the Climate in 2021"]. *Bull. Amer. Meteor. Soc.*, **103** (8), S28–S30, <https://doi.org/10.1175/BAMS-D-22-0092.1>.
- , and Coauthors, 2022b: ESA Lakes Climate Change Initiative (Lakes_cci): Lake products, version 2.0.2. NERC EDS Centre for Environmental Data Analysis, accessed 24 July 2023, <https://doi.org/10.5285/a07deacaffb8453e93d57ee214676304>.
- , and Coauthors, 2023: Satellite-derived multivariate worldwide lake physical variable timeseries for climate studies. *Sci. Data*, **10**, 30, <https://doi.org/10.1038/s41597-022-01889-z>.
- Cescatti, A., and Coauthors, 2012: Intercomparison of MODIS albedo retrievals and in situ measurements across the global FLUXNET network. *Remote Sens. Environ.*, **121**, 323–334, <https://doi.org/10.1016/j.rse.2012.02.019>.

- Chang, K.-L., M. G. Schultz, X. Lan, A. McClure-Begley, I. Petropavlovskikh, X. Xu, and J. R. Ziemke, 2021: Trend detection of atmospheric time series: Incorporating appropriate uncertainty estimates and handling extreme events. *Elementa*, **9**, 00035, <https://doi.org/10.1525/elementa.2021.00035>.
- , and Coauthors, 2022: Impact of the COVID-19 economic downturn on tropospheric ozone trends: An uncertainty weighted data synthesis for quantifying regional anomalies above western North America and Europe. *AGU Adv.*, **3**, e2021AV000542, <https://doi.org/10.1029/2021AV000542>.
- Chen, C., and Coauthors, 2019: China and India lead in greening of the world through land-use management. *Nat. Sustainability*, **2**, 122–129, <https://doi.org/10.1038/s41893-019-0220-7>.
- Cheng, L., and Coauthors, 2017: Recent increases in terrestrial carbon uptake at little cost to the water cycle. *Nat. Commun.*, **8**, 110, <https://doi.org/10.1038/s41467-017-00114-5>.
- Christiansen, A., L. J. Mickley, J. Liu, L. D. Oman, and L. Hu, 2022: Multidecadal increases in global tropospheric ozone derived from ozonesonde and surface site observations: Can models reproduce ozone trends? *Atmos. Chem. Phys.*, **22**, 14751–14782, <https://doi.org/10.5194/acp-22-14751-2022>.
- Christy, J. R., and R. T. McNider, 2017: Satellite bulk tropospheric temperatures as a metric for climate sensitivity. *Asia-Pac. J. Atmos. Sci.*, **53**, 511–518, <https://doi.org/10.1007/s13143-017-0070-z>.
- Chrysoulakis, N., Z. Mitraka, and N. Gorelick, 2019: Exploiting satellite observations for global surface albedo trends monitoring. *Theor. Appl. Climatol.*, **137**, 1171–1179, <https://doi.org/10.1007/s00704-018-2663-6>.
- Chung, E.-S., B. Soden, and V. O. John, 2013: Intercalibrating microwave satellite observations for monitoring long-term variations in upper- and midtropospheric water vapor. *J. Atmos. Oceanic Technol.*, **30**, 2303–2319, <https://doi.org/10.1175/JTECH-D-13-00001.1>.
- , —, B. J. Sohn, and L. Shi, 2014: Upper-tropospheric moistening in response to anthropogenic warming. *Proc. Natl. Acad. Sci. USA*, **111**, 11636–11641, <https://doi.org/10.1073/pnas.1409659111>.
- Cicoira, A., J. Beutel, J. Faillettaz, and A. Vieli, 2019: Water controls the seasonal rhythm of rock glacier flow. *Earth Planet. Sci. Lett.*, **528**, 115844, <https://doi.org/10.1016/j.epsl.2019.115844>.
- Clem, K. R., and R. L. Fogt, 2013: Varying roles of ENSO and SAM on the Antarctic Peninsula climate in austral spring. *J. Geophys. Res. Atmos.*, **118**, 11481–11492, <https://doi.org/10.1002/jgrd.50860>.
- Coddington, O. M., 2017: TSIS Algorithm Theoretical Basis Document. Laboratory for Atmospheres and Space Physics (LASP) Document 151430 RevA, 108 pp., https://docserver.gesdisc.eosdis.nasa.gov/public/project/TSIS/TSIS_Algorithm_Theoretical_Basis_Document_151430RevA.pdf.
- Coldewey-Egbers, M., and Coauthors, 2015: The GOME-type Total Ozone Essential Climate Variable (GTO-ECV) data record from the ESA Climate Change Initiative. *Atmos. Meas. Tech.*, **8**, 3923–3940, <https://doi.org/10.5194/amt-8-3923-2015>.
- , D. G. Loyola, C. Lerot, and M. Van Roozendaal, 2022: Global, regional and seasonal analysis of total ozone trends derived from the 1995–2020 GTO-ECV climate data record. *Atmos. Chem. Phys.*, **22**, 6861–6878, <https://doi.org/10.5194/acp-22-6861-2022>.
- Coleman, R., and B. J. Soden, 2021: Water vapor and lapse rate feedbacks in the climate system. *Rev. Mod. Phys.*, **93**, 045002, <https://doi.org/10.1103/RevModPhys.93.045002>.
- Cooper, O. R., and Coauthors, 2020: Multi-decadal surface ozone trends at globally distributed remote locations. *Elementa*, **8**, 23, <https://doi.org/10.1525/elementa.420>.
- Copernicus, 2023a: 2022 Global Climate Highlights of the Copernicus Climate Change Service (C3S). Accessed 6 February 2023, <https://climate.copernicus.eu/global-climate-highlights-2022>.
- Cornes, R. C., E. C. Kent, D. I. Berry, and J. J. Kennedy, 2020: CLASSnmat: A global night marine air temperature data set, 1880–2019. *Geosci. Data J.*, **7**, 170–184, <https://doi.org/10.1002/gdj3.100>.
- , T. Cropper, R. Junod, and E. C. Kent, 2022: Night marine air temperature [in “State of the Climate in 2021”]. *Bull. Amer. Meteor. Soc.*, **103** (8), S31–S33, <https://doi.org/10.1175/BAMS-D-22-0092.1>.
- Cortés, J., M. D. Mahecha, M. Reichstein, R. B. Myneni, C. Chen, and A. Brenning, 2021: Where are global vegetation greening and browning trends significant? *Geophys. Res. Lett.*, **48**, e2020GL091496, <https://doi.org/10.1029/2020GL091496>.
- Coy, L., P. A. Newman, K. Wargan, G. Partyka, S. E. Strahan, and S. Pawson, 2022: Stratospheric circulation changes associated with the Hunga Tonga-Hunga Ha’apai eruption. *Geophys. Res. Lett.*, **49**, e2022GL100982, <https://doi.org/10.1029/2022GL100982>.
- Cremona, A., M. Huss, J. Landmann, J. Borner, and D. Farinotti, 2023: European heat waves 2022: Contribution to extreme glacier melt in Switzerland inferred from automated ablation readings. *Cryosphere*, **17**, 1895–1912, <https://doi.org/10.5194/tc-17-1895-2023>.
- Crétaux, J. F., and Coauthors, 2011: SOLS: A lake database to monitor in the near real time water level and storage variations from remote sensing data. *Adv. Space Res.*, **47**, 1497–1507, <https://doi.org/10.1016/j.asr.2011.01.004>.
- Crimmins, T. M., E. G. Denny, E. E. Posthumus, A. H. Rosemartin, R. Croll, M. Montano, and H. Panci, 2022: Science and management advancements made possible by the USA National Phenology Network’s Nature’s Notebook platform. *BioScience*, **72**, 908–920, <https://doi.org/10.1093/biosci/biac061>.
- Cusicanqui, D., A. Rabatel, C. Vincent, X. Bodin, E. Thibert, and B. Francou, 2021: Interpretation of volume and flux changes of the Laurichard rock glacier between 1952 and 2019, French Alps. *J. Geophys. Res. Earth Surf.*, **126**, e2021JF006161, <https://doi.org/10.1029/2021JF006161>.
- Daniel, J. S., S. Solomon, and D. L. Albritton, 1995: On the evaluation of halocarbon radiative forcing and global warming potentials. *J. Geophys. Res.*, **100**, 1271–1285, <https://doi.org/10.1029/94JD02516>.
- Davidson, E. A., 2009: The contribution of manure and fertilizer nitrogen to atmospheric nitrous oxide since 1860. *Nat. Geosci.*, **2**, 659–662, <https://doi.org/10.1038/ngeo608>.
- Davis, S. M., and Coauthors, 2016: The Stratospheric Water and Ozone Satellite Homogenized (SWOOSH) database: A long-term database for climate studies. *Earth Syst. Sci. Data*, **8**, 461–490, <https://doi.org/10.5194/essd-8-461-2016>.
- Dee, D. P., and Coauthors, 2011: The ERA-Interim reanalysis: Configuration and performance of the data assimilation system. *Quart. J. Roy. Meteor. Soc.*, **137**, 553–597, <https://doi.org/10.1002/qj.828>.
- Deeter, M. N., and Coauthors, 2014: The MOPITT version 6 product: Algorithm enhancements and validation. *Atmos. Meas. Tech.*, **7**, 3623–3632, <https://doi.org/10.5194/amt-7-3623-2014>.

- , D. P. Edwards, G. L. Francis, J. C. Gille, S. Martínez-Alonso, H. M. Worden, and C. Sweeney, 2017: A climate-scale satellite record for carbon monoxide: The MOPITT version 7 product. *Atmos. Meas. Tech.*, **10**, 2533–2555, <https://doi.org/10.5194/amt-10-2533-2017>.
- , and Coauthors, 2019: Radiance-based retrieval bias mitigation for the MOPITT instrument: The version 8 product. *Atmos. Meas. Tech.*, **12**, 4561–4580, <https://doi.org/10.5194/amt-12-4561-2019>.
- Delaloye, R., and Coauthors, 2008: Recent interannual variations of rock glacier creep in the European Alps. *Proc. Ninth Int. Conf. on Permafrost*, Fairbanks, AK, University of Alaska Fairbanks, 343–348.
- , C. Lambiel, and I. Gärtner-Roer, 2010: Overview of rock glacier kinematics research in the Swiss Alps. *Geogr. Helv.*, **65**, 135–145, <https://doi.org/10.5194/gh-65-135-2010>.
- Deng, K., C. Azorin-Molina, S. Yang, C. Hu, G. Zhang, L. Minola, and D. Chen, 2022: Changes of Southern Hemisphere westerlies in the future warming climate. *Atmos. Res.*, **270**, 106040, <https://doi.org/10.1016/j.atmosres.2022.106040>.
- Dewitte, S., D. Crommelynck, and A. Joukof, 2004: Total solar irradiance observations from DIARAD/VIRGO. *J. Geophys. Res.*, **109**, A02102, <https://doi.org/10.1029/2002JA009694>.
- Dlugokencky, E. J., L. P. Steele, P. M. Lang, and K. A. Masarie, 1994: The growth rate and distribution of atmospheric methane. *J. Geophys. Res. Atmos.*, **99**(D8), 17 021–17 043, <https://doi.org/10.1029/94JD01245>.
- Domeisen, D. I. V., C. I. Garfinkel, and A. H. Butler, 2019: The teleconnection of El Niño Southern Oscillation to the stratosphere. *Rev. Geophys.*, **57**, 5–47, <https://doi.org/10.1029/2018RG000596>.
- Donat, M. G., L. V. Alexander, H. Yang, I. Durre, R. Vose, and J. Caesar, 2013: Global land-based datasets for monitoring climatic extremes. *Bull. Amer. Meteor. Soc.*, **94**, 997–1006, <https://doi.org/10.1175/BAMS-D-12-00109.1>.
- Dorigo, W., and Coauthors, 2017: ESA CCI soil moisture for improved Earth system understanding: State-of-the art and future directions. *Remote Sens. Environ.*, **203**, 185–215, <https://doi.org/10.1016/j.rse.2017.07.001>.
- , and Coauthors, 2021a: Closing the water cycle from observations across scales: Where do we stand? *Bull. Amer. Meteor. Soc.*, **102**, E1897–E1935, <https://doi.org/10.1175/BAMS-D-19-0316.1>.
- , L. Moesinger, R. van der Schalie, R. M. Zotta, T. Scanlon, and R. A. M. de Jeu, 2021b: Long-term monitoring of vegetation state through passive microwave satellites [in “State of the Climate in 2020”]. *Bull. Amer. Meteor. Soc.*, **102** (8), S110–S112, <https://doi.org/10.1175/BAMS-D-21-0098.1>.
- , R. Zotta, R. van der Schalie, W. Preimesberger, L. Moesinger, and R. A. M. de Jeu, 2022: Vegetation optical depth [in “State of the Climate in 2021”]. *Bull. Amer. Meteor. Soc.*, **103** (8), S108–S109, <https://doi.org/10.1175/BAMS-D-22-0092.1>.
- Dunn, R. J. H., 2019: HadISD version 3: Monthly updates. Hadley Centre Tech. Note 103, 10 pp., <http://www.metoffice.gov.uk/research/library-and-archive/publications/science/climate-science-technical-notes>.
- , and C. P. Morice, 2022: On the effect of reference periods on trends in percentile-based extreme temperature indices. *Environ. Res. Lett.*, **17**, 034026, <https://doi.org/10.1088/1748-9326/ac52c8>.
- , K. M. Willett, P. W. Thorne, E. V. Woolley, I. Durre, A. Dai, D. E. Parker, and R. S. Vose, 2012: HadISD: A quality-controlled global synoptic report database for selected variables at long-term stations from 1973–2011. *Climate Past*, **8**, 1649–1679, <https://doi.org/10.5194/cp-8-1649-2012>.
- , —, C. P. Morice, and D. E. Parker, 2014: Pairwise homogeneity assessment of HadISD. *Climate Past*, **10**, 1501–1522, <https://doi.org/10.5194/cp-10-1501-2014>.
- , —, D. E. Parker, and L. Mitchell, 2016: Expanding HadISD: Quality-controlled, sub-daily station data from 1931. *Geosci. Instrum. Methods Data Syst.*, **5**, 473–491, <https://doi.org/10.5194/gi-5-473-2016>.
- , and Coauthors, 2020: Development of an updated global land in situ-based data set of temperature and precipitation extremes: HadEX3. *J. Geophys. Res. Atmos.*, **125**, e2019JD032263, <https://doi.org/10.1029/2019JD032263>.
- , M. G. Donat, and L. V. Alexander, 2022a: Comparing extremes indices in recent observational and reanalysis products. *Front. Climate*, **4**, 989505, <https://doi.org/10.3389/fclim.2022.989505>.
- , C. Azorin-Molina, M. J. Menne, Z. Zeng, N. W. Casey, and C. Shen, 2022b: Reduction in reversal of global stilling arising from correction to encoding of calm periods. *Environ. Res. Commun.*, **4**, 061003, <https://doi.org/10.1088/2515-7620/ac770a>.
- ECMWF, 2022: Pakistan devastated by August floods. Copernicus Climate Change Service, accessed 24 January 2023, <https://climate.copernicus.eu/pakistan-devastated-august-floods>.
- Edwards, M., and A. Richardson, 2004: Impact of climate change on marine pelagic phenology and trophic mismatch. *Nature*, **430**, 881–884, <https://doi.org/10.1038/nature02808>.
- Ellis, H. T., and R. F. Pueschel, 1971: Solar radiation: Absence of air pollution trends at Mauna Loa. *Science*, **172**, 845–846, <https://doi.org/10.1126/science.172.3985.845>.
- Eriksen, H. Ø., L. Rouyet, T. R. Lauknes, I. Berthling, K. Isaksen, H. Hindberg, Y. Larsen, and G. D. Corner, 2018: Recent acceleration of a rock glacier complex, Ådjet, Norway, documented by 62 years of remote sensing observations. *Geophys. Res. Lett.*, **45**, 8314–8323, <https://doi.org/10.1029/2018GL077605>.
- Estilow, T. W., A. H. Young, and D. A. Robinson, 2015: A long-term Northern Hemisphere snow cover extent data record for climate studies and monitoring. *Earth Syst. Sci. Data*, **7**, 137–142, <https://doi.org/10.5194/essd-7-137-2015>.
- Etheridge, D. M., L. P. Steele, R. L. Langenfelds, R. J. Francey, J. M. Barnola, and V. I. Morgan, 1996: Natural and anthropogenic changes in atmospheric CO₂ over the last 1000 years from air in Antarctic ice and firn. *J. Geophys. Res.*, **101**, 4115–4128, <https://doi.org/10.1029/95JD03410>.
- Etzelmüller, B., and Coauthors, 2020: Twenty years of European mountain permafrost dynamics—The PACE legacy. *Environ. Res. Lett.*, **15**, 104070, <https://doi.org/10.1088/1748-9326/abae9d>.
- Eyring, V., and Coauthors, 2021: Human influence on the climate system. *Climate Change 2021: The Physical Science Basis*, V. Masson-Delmotte et al., Eds., Cambridge University Press, 423–552, <https://doi.org/10.1017/9781009157896.005>.
- Fan, J., and Coauthors, 2018: Substantial convection and precipitation enhancements by ultrafine aerosol particles. *Science*, **359**, 411–418, <https://doi.org/10.1126/science.aan8461>.
- FAO, 2022: Crop prospects and food situation. Quarterly Global Rep. 4, 46 pp., <https://www.fao.org/3/cc3233en/cc3233en.pdf>.

- Fasullo, J. T., J.-F. Lamarque, C. Hannay, N. Rosenbloom, S. Tilmes, P. DeRepentigny, A. Jahn, and C. Deser, 2022: Spurious late historical-era warming in CESM2 driven by prescribed biomass burning emissions. *Geophys. Res. Lett.*, **49**, e2021GL097420, <https://doi.org/10.1029/2021GL097420>.
- Feng, L., P. I. Palmer, S. Zhu, R. J. Parker, and Y. Liu, 2022: Tropical methane emissions explain large fraction of recent changes in global atmospheric methane growth rate. *Nat. Commun.*, **13**, 1378, <https://doi.org/10.1038/s41467-022-28989-z>.
- Fioletov, V. E., G. E. Bodeker, A. J. Miller, R. D. McPeters, and R. Stolarski, 2002: Global and zonal total ozone variations estimated from ground-based and satellite measurements: 1964–2000. *J. Geophys. Res.*, **107**, 4647, <https://doi.org/10.1029/2001JD001350>.
- , and Coauthors, 2008: The performance of the ground-based total ozone network assessed using satellite data. *J. Geophys. Res.*, **113**, D14313, <https://doi.org/10.1029/2008JD009809>.
- Fiore, A. M., and Coauthors, 2022: Understanding recent tropospheric ozone trends in the context of large internal variability: A new perspective from chemistry-climate model ensembles. *Environ. Res. Climate*, **1**, 025008, <https://doi.org/10.1088/2752-5295/ac9cc2>.
- Fogt, R. L., and G. J. Marshall, 2020: The Southern Annular Mode: Variability, trends, and climate impacts across the Southern Hemisphere. *Wiley Interdiscip. Rev.: Climate Change*, **11**, e652, <https://doi.org/10.1002/wcc.652>.
- Folland, C. K., J. Knight, H. W. Linderholm, D. Fereday, S. Ineson, and J. W. Hurrell, 2009: The summer North Atlantic Oscillation: Past, present and future. *J. Climate*, **22**, 1082–1103, <https://doi.org/10.1175/2008JCLI2459.1>.
- Foster, M. J., C. Phillips, A. K. Heidinger, E. E. Borbas, Y. Li, W. P. Menzel, A. Walther, and E. Weisz, 2023: PATMOS-x version 6.0: 40 years of merged AVHRR and HIRS global cloud data. *J. Climate*, **36**, 1143–1160, <https://doi.org/10.1175/JCLI-D-22-0147.1>.
- Forster, P. M. F., and K. P. Shine, 1999: Stratospheric water vapour changes as a possible contributor to observed stratospheric cooling. *Geophys. Res. Lett.*, **26**, 3309–3312, <https://doi.org/10.1029/1999GL010487>.
- , and Coauthors, 2021: The Earth's energy budget, climate feedbacks, and climate sensitivity. *Climate Change 2021: The Physical Science Basis*, V. Masson-Delmotte et al., Eds., Cambridge University Press, 923–1054, <https://doi.org/10.1017/9781009157896.009>.
- Frauenfelder, R., W. Haeberli, and M. Hoelzle, 2003: Rock glacier occurrence and related terrain parameters in a study area of the Eastern Swiss Alps. *Permafrost: Proceedings of the 8th International Conference on Permafrost*, M. Phillips, S. M. Springman, and L. U. Arenson, Eds., A. A. Balkema, 253–258.
- Free, M., D. J. Seidel, J. K. Angel, J. Lanzante, I. Durre, and T. C. Peterson, 2005: Radiosonde Atmospheric Temperature Products for Assessing Climate (RATPAC): A new dataset of large-area anomaly time series. *J. Geophys. Res.*, **110**, D22101, <https://doi.org/10.1029/2005JD006169>.
- Freychet, N., S. F. B. Tett, Z. Yan, and Z. Li, 2020: Underestimated change of wet-bulb temperatures over East and South China. *Geophys. Res. Lett.*, **47**, e2019GL086140, <https://doi.org/10.1029/2019GL086140>.
- Friedlingstein, P., and Coauthors, 2022: Global carbon budget 2022. *Earth Syst. Sci. Data*, **14**, 4811–4900, <https://doi.org/10.5194/essd-14-4811-2022>.
- Friedrich, K., and Coauthors, 2018: Reservoir evaporation in the western United States: Current science, challenges, and future needs. *Bull. Amer. Meteor. Soc.*, **99**, 167–187, <https://doi.org/10.1175/BAMS-D-15-00224.1>.
- Frith, S. M., N. A. Kramarova, R. S. Stolarski, R. D. McPeters, P. K. Bhartia, and G. J. Labow, 2014: Recent changes in total column ozone based on the SBUV version 8.6 Merged Ozone Data Set. *J. Geophys. Res. Atmos.*, **119**, 9735–9751, <https://doi.org/10.1002/2014JD021889>.
- , R. S. Stolarski, N. A. Kramarova, and R. D. McPeters, 2017: Estimating uncertainties in the SBUV version 8.6 merged profile ozone data set. *Atmos. Chem. Phys.*, **17**, 14695–14707, <https://doi.org/10.5194/acp-17-14695-2017>.
- Füllekrug, M., E. Williams, C. Price, S. Goodman, R. Holzworth, K. Virts, and D. Buechler, 2022: Sidebar 2.1 lightning [in “State of the Climate in 2021”]. *Bull. Amer. Meteor. Soc.*, **103** (8), S79–S81, <https://doi.org/10.1175/BAMS-D-22-0092.1>.
- Funk, C., and Coauthors, 2015: The climate hazards infrared precipitation with stations—A new environmental record for monitoring extremes. *Sci. Data*, **2**, 150066, <https://doi.org/10.1038/sdata.2015.66>.
- Garane, K., and Coauthors, 2018: Quality assessment of the Ozone_cci Climate Research Data Package (release 2017) – Part 1: Ground-based validation of total ozone column data products. *Atmos. Meas. Tech.*, **11**, 1385–1402, <https://doi.org/10.5194/amt-11-1385-2018>.
- Garfinkel, C. I., and Coauthors, 2021: Influence of the El Niño–Southern Oscillation on entry stratospheric water vapor in coupled chemistry–ocean CCM1 and CMIP6 models. *Atmos. Chem. Phys.*, **21**, 3725–3740, <https://doi.org/10.5194/acp-21-3725-2021>.
- Garreaud, R. D., K. Clem, and J. V. Veloso, 2021: The South Pacific pressure trend dipole and the Southern Blob. *J. Climate*, **34**, 7661–7676, <https://doi.org/10.1175/JCLI-D-20-0886.1>.
- Gaudel, A., and Coauthors, 2018: Tropospheric Ozone Assessment Report: Present-day distribution and trends of tropospheric ozone relevant to climate and global atmospheric chemistry model evaluation. *Elem. Sci. Anthropocene*, **6**, 39, <https://doi.org/10.1525/elementa.291>.
- , and Coauthors, 2020: Aircraft observations since the 1990s reveal increases of tropospheric ozone at multiple locations across the Northern Hemisphere. *Sci. Adv.*, **6**, eaba8272, <https://doi.org/10.1126/sciadv.aba8272>.
- GCOS, 2016: The Global Observing System for Climate: Implementation needs. Tech. Rep. GCOS-200, World Meteorological Organization, 315 pp., https://library.wmo.int/doc_num.php?explnum_id=3417.
- , 2022a: The 2022 Global Climate Observing System (GCOS) implementation plan. GCOS-244, WMO, 98 pp., <https://gcos.wmo.int/en/publications/gcos-implementation-plan2022>.
- , 2022b: The 2022 GCOS ECVs requirements. GCOS-245, WMO, 244 pp., https://library.wmo.int/doc_num.php?explnum_id=11318.
- Gelaro, R., and Coauthors, 2017: The Modern-Era Retrospective Analysis for Research and Applications, version 2 (MERRA-2). *J. Climate*, **30**, 5419–5454, <https://doi.org/10.1175/JCLI-D-16-0758.1>.
- Getirana, A., S. Kumar, M. Giroto, and M. Rodell, 2017: Rivers and floodplains as key components of global terrestrial water storage variability. *Geophys. Res. Lett.*, **44**, 10359–10368, <https://doi.org/10.1002/2017GL074684>.

- Giglio, L., W. Schroeder, and C. O. Justice, 2016: The Collection 6 MODIS active fire detection algorithm and fire products. *Remote Sens. Environ.*, **178**, 31–41, <https://doi.org/10.1016/j.rse.2016.02.054>.
- GISTEMP Team, 2022: GISS Surface Temperature Analysis (GIS-TEMP), v4. NASA Goddard Institute for Space Studies, accessed 15 February 2022, <https://data.giss.nasa.gov/gistemp/>.
- , 2023: GISS Surface Temperature Analysis (GISTEMP), v4. NASA Goddard Institute for Space Studies, accessed 1 March 2023, <https://data.giss.nasa.gov/gistemp/>.
- Gleason, K. L., J. H. Lawrimore, D. H. Levinson, T. R. Karl, and D. J. Karoly, 2008: A revised U.S. Climate Extremes Index. *J. Climate*, **21**, 2124–2137, <https://doi.org/10.1175/2007JCLI1883.1>.
- Gobron, N., 2019: Terrestrial vegetation dynamics [in “State of the Climate in 2018”]. *Bull. Amer. Meteor. Soc.*, **100** (9), S63–S64, <https://doi.org/10.1175/2019BAMSStateoftheClimate.1>.
- , and M. Robustelli, 2013: Monitoring the state of the global terrestrial surfaces. *Proc. 2013 ESA Living Planet Symp.*, Edinburgh, United Kingdom, European Space Agency, JRC84937, <https://publications.jrc.ec.europa.eu/repository/handle/JRC84937>.
- , A. S. Belward, B. Pinty, and W. Knorr, 2010: Monitoring biosphere vegetation 1998–2009. *Geophys. Res. Lett.*, **37**, L15402, <https://doi.org/10.1029/2010GL043870>.
- Godin-Beekmann, S., and Coauthors, 2022: Updated trends of the stratospheric ozone vertical distribution in the 60°S–60°N latitude range based on the LOTUS regression model. *Atmos. Chem. Phys.*, **22**, 11 657–11 673, <https://doi.org/10.5194/acp-22-11657-2022>.
- Gonsamo, A., and Coauthors, 2021: Greening drylands despite warming consistent with carbon dioxide fertilization effect. *Global Change Biol.*, **27**, 3336–3349, <https://doi.org/10.1111/gcb.15658>.
- Goodman, S. J., and D. R. MacGorman, 1986: Cloud-to-ground lightning activity in mesoscale convective complexes. *Mon. Wea. Rev.*, **114**, 2320–2328, [https://doi.org/10.1175/1520-0493\(1986\)114<2320.CO;2](https://doi.org/10.1175/1520-0493(1986)114<2320.CO;2).
- , D. E. Buechler, K. Knupp, D. Driscoll, and E. E. McCaul Jr., 2000: The 1997–98 El Niño event and related wintertime lightning variations in the southeastern United States. *Geophys. Res. Lett.*, **27**, 541–544, <https://doi.org/10.1029/1999GL010808>.
- Granier, C., and Coauthors, 2011: Evolution of anthropogenic and biomass burning emissions of air pollutants at global and regional scales during the 1980–2010 period. *Climatic Change*, **109**, 163–190, <https://doi.org/10.1007/s10584-011-0154-1>.
- Grant, L., and Coauthors, 2021: Attribution of global lake systems change to anthropogenic forcing. *Nat. Geosci.*, **14**, 849–854, <https://doi.org/10.1038/s41561-021-00833-x>.
- Gruber, A., W. A. Dorigo, W. Crow, and W. Wagner, 2017: Triple collocation-based merging of satellite soil moisture retrievals. *IEEE Trans. Geosci. Remote Sens.*, **55**, 6780–6792, <https://doi.org/10.1109/TGRS.2017.2734070>.
- , T. Scanlon, R. van der Schalie, W. Wagner, and W. Dorigo, 2019: Evolution of the ESA CCI Soil Moisture climate data records and their underlying merging methodology. *Earth Syst. Sci. Data*, **11**, 717–739, <https://doi.org/10.5194/essd-11-717-2019>.
- Gulev, S. K., and Coauthors, 2021: Changing state of the climate system. *Climate Change 2021: The Physical Science Basis*, V. Masson-Delmotte et al., Eds., Cambridge University Press, 287–422, <https://doi.org/10.1017/9781009157896.004>.
- Guo, S., G. J. S. Bluth, W. I. Rose, I. M. Watson, and A. J. Prata, 2004: Re-evaluation of SO₂ release of the 15 June 1991 Pinatubo eruption using ultraviolet and infrared satellite sensors. *Geochem. Geophys. Geosyst.*, **5**, Q04001, <https://doi.org/10.1029/2003GC000654>.
- Haimberger, L., C. Tavalato, and S. Sperka, 2012: Homogenization of the global radiosonde temperature dataset through combined comparison with reanalysis background series and neighboring stations. *J. Climate*, **25**, 8108–8131, <https://doi.org/10.1175/JCLI-D-11-00668.1>.
- Hamid, E. Y., Z.-I. Kawasaki, and R. Mardiana, 2001: Impact of the 1997–98 El Niño events on lightning activity over Indonesia. *Geophys. Res. Lett.*, **28**, 147–150, <https://doi.org/10.1029/2000GL011374>.
- Hansen, J., R. Ruedy, M. Sato, and K. Lo, 2010: Global surface temperature change. *Rev. Geophys.*, **48**, RG4004, <https://doi.org/10.1029/2010RG000345>.
- Harris, I., T. J. Osborn, P. D. Jones, and D. H. Lister, 2020: Version 4 of the CRU TS monthly high-resolution gridded multivariate climate dataset. *Sci. Data*, **7**, 109, <https://doi.org/10.1038/s41597-020-0453-3>.
- Heath, M., 2022: Arid wheat fields and dead cows: A snapshot of Argentina’s worst drought in decades. Reuters, 9 December, www.reuters.com/business/environment/arid-wheat-fields-dead-cows-snapshot-argentinas-worst-drought-decades-2022-12-09/.
- Hersbach, H., and Coauthors, 2020: The ERA5 global reanalysis. *Quart. J. Roy. Meteor. Soc.*, **146**, 1999–2049, <https://doi.org/10.1002/qj.3803>.
- , and Coauthors, 2023: ERA5 monthly averaged data on pressure levels from 1940 to present. Copernicus Climate Change Service Climate Data Store, accessed 14 June 2023, <https://doi.org/10.24381/cds.6860a573>.
- Ho, S.-P., X. Zhou, Y.-H. Kuo, D. Hunt, and J.-H. Wang, 2010: Global evaluation of radiosonde water vapor systematic biases using GPS radio occultation from COSMIC and ECMWF analysis. *Remote Sens.*, **2**, 1320–1330, <https://doi.org/10.3390/rs2051320>.
- , and Coauthors, 2020a: The COSMIC/FORMOSAT-3 radio occultation mission after 12 years: Accomplishments, remaining challenges, and potential impacts of COSMIC-2. *Bull. Amer. Meteor. Sci.*, **101**, E1107–E1136, <https://doi.org/10.1175/BAMS-D-18-0290.1>.
- , and Coauthors, 2020b: Initial assessment of the COSMIC-2/FORMOSAT-7 neutral atmosphere data quality in NESDIS/STAR using in situ and satellite data. *Remote Sens.*, **12**, 4099, <https://doi.org/10.3390/rs12244099>.
- Hobday, A. J., and Coauthors, 2016: A hierarchical approach to defining marine heatwaves. *Prog. Oceanogr.*, **141**, 227–238, <https://doi.org/10.1016/j.pocean.2015.12.014>.
- , and Coauthors, 2018: Categorizing and naming marine heatwaves. *Oceanography*, **31**, 162–173, <https://doi.org/10.5670/oceanog.2018.205>.
- Hodnebrog, O., and Coauthors, 2020a: Updated global warming potentials and radiative efficiencies of halocarbons and other weak atmospheric absorbers. *Rev. Geophys.*, **58**, e2019RG000691, <https://doi.org/10.1029/2019RG000691>.
- , and Coauthors, 2020b: The effect of rapid adjustments to halocarbons and N₂O on radiative forcing. *npj Climate Atmos. Sci.*, **3**, 43, <https://doi.org/10.1038/s41612-020-00150-x>.
- Hofmann, D. J., and S. A. Montzka, 2009: Recovery of the ozone layer: The ozone depleting gas index. *Eos, Trans. Amer. Geophys. Union*, **90**, 1–2, <https://doi.org/10.1029/2009EO010001>.

- , J. H. Butler, E. J. Dlugokencky, J. W. Elkins, K. Masarie, S. A. Montzka, and P. Tans, 2006: The role of carbon dioxide in climate forcing from 1979 to 2004: Introduction of the annual greenhouse gas index. *Tellus*, **58B**, 614–619, <https://doi.org/10.1111/j.1600-0889.2006.00201.x>.
- Hrudya, P. H., H. Varikoden, and R. Vishnu, 2021: A review on the Indian summer monsoon rainfall, variability and its association with ENSO and IOD. *Meteor. Atmos. Phys.*, **133**, 1–14, <https://doi.org/10.1007/s00703-020-00734-5>.
- Huang, B., C. Liu, V. Banzon, E. Freeman, G. Graham, B. Hankins, T. Smith, and H.-M. Zhang, 2021: Improvements of the Daily Optimum Interpolation Sea Surface Temperature (DOISST) version 2.1. *J. Climate*, **34**, 2923–2939, <https://doi.org/10.1175/JCLI-D-20-0166.1>.
- Huang, C.-Y., W.-H. Teng, S.-P. Ho, and Y. H. Kuo, 2013: Global variation of COSMIC precipitable water over land: Comparisons with ground-based GPS measurements and NCEP reanalyses. *Geophys. Res. Lett.*, **40**, 5327–5331, <https://doi.org/10.1002/grl.50885>.
- Hugonnet, R., and Coauthors, 2021: Accelerated global glacier mass loss in the early twenty-first century. *Nature*, **592**, 726–731, <https://doi.org/10.1038/s41586-021-03436-z>.
- Hüser, I., B. Gehrke, and J. W. Kaiser, 2018: Methodology to correct biases in individual satellite FRP products. CAMS Rep. CAMS44-2016SC3-D44.3.3.1-2018-20187, ECMWF, <https://atmosphere.copernicus.eu/node/1029t>.
- Ingram, W., 2010: A very simple model for the water vapour feedback on climate change. *Quart. J. Roy. Meteor. Soc.*, **136**, 30–40, <https://doi.org/10.1002/qj.546>.
- Inness, A., and Coauthors, 2019: The CAMS reanalysis of atmospheric composition. *Atmos. Chem. Phys.*, **19**, 3515–3556, <https://doi.org/10.5194/acp-19-3515-2019>.
- Isaksen, K., J. Lutz, A. M. Sørensen, Ø. Godøy, L. Ferrighi, S. Eastwood, and S. Aaboe, 2022: Advances in operational permafrost monitoring on Svalbard and in Norway. *Environ. Res. Lett.*, **17**, 095012, <https://doi.org/10.1088/1748-9326/ac8e1c>.
- Ilturbide, M., and Coauthors, 2020: An update of IPCC climate reference regions for subcontinental analysis of climate model data: Definition and aggregated datasets. *Earth Syst. Sci. Data*, **12**, 2959–2970, <https://doi.org/10.5194/essd-12-2959-2020>.
- Jenkins, S., C. Smith, M. Allen, and R. Grainger, 2023: Tonga eruption increases chance of temporary surface temperature anomaly above 1.5°C. *Nat. Climate Change*, **13**, 127–129, <https://doi.org/10.1038/s41558-022-01568-2>.
- John, V. O., G. Holl, R. P. Allan, S. A. Buehler, D. E. Parker, and B. J. Soden, 2011: Clear-sky biases in satellite infra-red estimates of upper tropospheric humidity and its trends. *J. Geophys. Res.*, **116**, D14108, <https://doi.org/10.1029/2010JD015355>.
- Junod, R. A., and J. R. Christy, 2020: A new compilation of globally gridded night-time marine air temperatures: The UAHN-MATV1 dataset. *Int. J. Climatol.*, **40**, 2609–2623, <https://doi.org/10.1002/joc.6354>.
- Kääb, A., T. Strozzi, T. Bolch, R. Caduff, H. Trefall, M. Stoffel, and A. Kokarev, 2021: Inventory and changes of rock glacier creep speeds in Ile Alatau and Kungöy Ala-Too, northern Tien Shan, since the 1950s. *Cryosphere*, **15**, 927–949, <https://doi.org/10.5194/tc-15-927-2021>.
- Kablick, G. P., D. R. Allen, M. D. Fromm, and G. E. Nedoluha, 2020: Australian pyroCb smoke generates synoptic-scale stratospheric anticyclones. *Geophys. Res. Lett.*, **47**, e2020GL088101, <https://doi.org/10.1029/2020GL088101>.
- Kainz, M. J., R. Ptacnik, S. Rasconi, and H. H. Hager, 2017: Irregular changes in lake surface water temperature and ice cover in subalpine Lake Lunz, Austria. *Inland Waters*, **7**, 27–33, <https://doi.org/10.1080/20442041.2017.1294332>.
- Kaiser, J. W., and Coauthors, 2012: Biomass burning emissions estimated with a global fire assimilation system based on observed fire radiative power. *Biogeosciences*, **9**, 527–554, <https://doi.org/10.5194/bg-9-527-2012>.
- Kaplan, A., 2011: Patterns and indices of climate variability [in “State of the Climate in 2010”]. *Bull. Amer. Meteor. Soc.*, **92** (6), S20–S25, <https://doi.org/10.1175/1520-0477-92.6.S1>.
- Kaplan Pastíriková, L., F. Hrbacek, T. Uxa, and K. Laska, 2023: Permafrost table temperature and active layer thickness variability on James Ross Island, Antarctic Peninsula, in 2004–2021. *Sci. Total Environ.*, **869**, 161690, <https://doi.org/10.1016/j.scitotenv.2023.161690>.
- Karpechko, A. Y., and A. C. Maycock, 2018: Stratospheric ozone changes and climate. Scientific Assessment of Ozone Depletion: 2018. Global Ozone Research and Monitoring Project Rep. 58, 5.1–5.50, <https://ozone.unep.org/sites/default/files/2019-05/SAP-2018-Assessment-report.pdf>.
- Keeling, C. D., and R. Revelle, 1985: Effects of El-Nino Southern Oscillation on the atmospheric content of carbon-dioxide. *Meteoritics*, **20**, 437–450.
- Kellerer-Pirklbauer, A., and V. Kaufmann, 2012: About the relationship between rock glacier velocity and climate parameters in central Austria. *Aust. J. Earth Sci.*, **105**, 94–112.
- , and Coauthors, 2018: Interannual variability of rock glacier flow velocities in the European Alps. *Fifth European Conf. on Permafrost*, Chamonix, France, Laboratoire EDYTEM, 615–616, <https://hal.archives-ouvertes.fr/hal-01816115/>.
- Kendon, M., M. McCarthy, S. Jevrejeva, A. Matthews, T. Sparks, and J. Garforth, 2022: State of the UK climate 2021. *Int. J. Climatol.*, **42** (S1), 1–80, <https://doi.org/10.1002/joc.7787>.
- Kennedy, J. J., N. A. Rayner, C. P. Atkinson, and R. E. Killick, 2019: An ensemble data set of sea surface temperature change from 1850: The Met Office Hadley Centre HadSST.4.0.0.0 data set. *J. Geophys. Res. Atmos.*, **124**, 7719–7763, <https://doi.org/10.1029/2018JD029867>.
- Kenner, R., M. Phillips, J. Beutel, M. Hiller, P. Limpach, E. Pointner, and M. Volken, 2017: Factors controlling velocity variations at short-term, seasonal and multiyear time scales, Ritigraben rock glacier, western Swiss Alps. *Permafrost Periglacial Processes*, **28**, 675–684, <https://doi.org/10.1002/ppp.1953>.
- Khandelwal, A., A. Karpatne, P. Ravirathinam, R. Ghosh, Z. Wei, H. A. Dugan, P. C. Hanson, and V. Kumar, 2022: RealSAT, a global dataset of reservoir and lake surface area variations. *Sci. Data*, **9**, 356, <https://doi.org/10.1038/s41597-022-01449-5>.
- Khaykin, S., and Coauthors, 2022: Global perturbation of stratospheric water and aerosol burden by Hunga eruption. *Commun. Earth Environ.*, **3**, 316, <https://doi.org/10.1038/s43247-022-00652-x>.
- Khazaei, B., and Coauthors, 2019: Climatic or regionally induced by humans? Tracing hydro-climatic and land-use changes to better understand the Lake Urmia tragedy. *J. Hydrol.*, **569**, 203–217, <https://doi.org/10.1016/j.jhydrol.2018.12.004>.
- Kobayashi, S., and Coauthors, 2015: The JRA-55 reanalysis: General specifications and basic characteristics. *J. Meteor. Soc. Japan*, **93**, 5–48, <https://doi.org/10.2151/jmsj.2015-001>.

- Konapala, G., A. K. Mishra, Y. Wada, and M. E. Mann, 2020: Climate change will affect global water availability through compounding changes in seasonal precipitation and evaporation. *Nat. Commun.*, **11**, 3044, <https://doi.org/10.1038/s41467-020-16757-w>.
- Konings, A. G., Y. Yu, L. Xu, Y. Yang, D. S. Schimel, and S. S. Saatchi, 2017: Active microwave observations of diurnal and seasonal variations of canopy water content across the humid African tropical forests. *Geophys. Res. Lett.*, **44**, 2290–2299, <https://doi.org/10.1002/2016GL072388>.
- Kopp, G., and J. L. Lean, 2011: A new, lower value of total solar irradiance: Evidence and climate significance. *Geophys. Res. Lett.*, **38**, L01706, <https://doi.org/10.1029/2010GL045777>.
- Kraemer, B. M., A. Seimon, R. Adrian, and P. B. McIntyre, 2020: Worldwide lake level trends and responses to background climate variation. *Hydrol. Earth Syst. Sci.*, **24**, 2593–2608, <https://doi.org/10.5194/hess-2019-470>.
- Kratz, D. P., P. W. Stackhouse Jr., S. K. Gupta, A. C. Wilber, P. Sawaengphokhai, and G. R. McGarragh, 2014: The Fast Longwave and Shortwave Flux (FLASHFlux) data product: Single-scanner footprint fluxes. *J. Appl. Meteor. Climatol.*, **53**, 1059–1079, <https://doi.org/10.1175/JAMC-D-13-061.1>.
- Kubota, T., T. Saito, and K. Nishida, 2022: Global fast-traveling tsunamis driven by atmospheric Lamb waves on the 2022 Tonga eruption. *Science*, **377**, 91–94, <https://doi.org/10.1126/science.abo4364>.
- Labitzke, K., and M. P. McCormick, 1992: Stratospheric temperature increases due to Pinatubo aerosols. *Geophys. Res. Lett.*, **19**, 207–210, <https://doi.org/10.1029/91GL02940>.
- Lan, X., and Coauthors, 2019: Long-term measurements show little evidence for large increases in total US methane emissions over the past decade. *Geophys. Res. Lett.*, **46**, 4991–4999, <https://doi.org/10.1029/2018GL081731>.
- , and Coauthors, 2021: Improved constraints on global methane emissions and sinks using $\delta^{13}\text{C}-\text{CH}_4$. *Global Biogeochem. Cycles*, **35**, e2021GB007000, <https://doi.org/10.1029/2021GB007000>.
- Landerer, F. W., and S. C. Swenson, 2012: Accuracy of scaled GRACE terrestrial water storage estimates. *Water Resour. Res.*, **48**, W04531, <https://doi.org/10.1029/2011WR011453>.
- , and Coauthors, 2020: Extending the global mass change data record: GRACE Follow-On instrument and science data performance. *Geophys. Res. Lett.*, **47**, e2020GL088306, <https://doi.org/10.1029/2020GL088306>.
- Laughner, J. L., and Coauthors, 2021: Societal shifts due to COVID-19 reveal large-scale complexities and feedbacks between atmospheric chemistry and climate change. *Proc. Natl. Acad. Sci. USA*, **118**, e2109481118, <https://doi.org/10.1073/pnas.2109481118>.
- Lee, H.-T., and NOAA CDR Program, 2018: NOAA Climate Data Record (CDR) of Monthly Outgoing Longwave Radiation (OLR), version 2.7. NOAA National Centers for Environmental Information, accessed 5 January 2023, <https://doi.org/10.7289/V5W37TKD>.
- Legras, B., and Coauthors, 2022: The evolution and dynamics of the Hunga Tonga–Hunga Ha’apai sulfate aerosol plume in the stratosphere. *Atmos. Chem. Phys.*, **22**, 14957–14970, <https://doi.org/10.5194/acp-22-14957-2022>.
- Lenssen, N. J. L., G. A. Schmidt, J. E. Hansen, M. J. Menne, A. Persin, R. Ruedy, and D. Zyss, 2019: Improvements in the GISTEMP uncertainty model. *J. Geophys. Res. Atmos.*, **124**, 6307–6326, <https://doi.org/10.1029/2018JD029522>.
- Levy, R. C., S. Mattoo, L. A. Munchak, L. A. Remer, A. M. Sayer, F. Patadia, and N. C. Hsu, 2013: The Collection 6 MODIS aerosol products over land and ocean. *Atmos. Meas. Tech.*, **6**, 2989–3034, <https://doi.org/10.5194/amt-6-2989-2013>.
- Li, M., and Coauthors, 2017: Anthropogenic emission inventories in China: A review. *Natl. Sci. Rev.*, **4**, 834–866, <https://doi.org/10.1093/nsr/nwx150>.
- Li, Z., Z. W. Yan, Y. N. Zhu, N. Freychet, and S. Tett, 2020: Homogenized daily relative humidity series in China during 1960–2017. *Adv. Atmos. Sci.*, **37**, 318–327, <https://doi.org/10.1007/s00376-020-9180-0>.
- Liu, Ya., A. Guha, R. Said, E. Williams, J. Lapierre, M. Stock, and S. Heckman, 2020: Aerosol effects on lightning characteristics: A comparison of polluted and clean regimes. *Geophys. Res. Lett.*, **47**, e2019GL086825, <https://doi.org/10.1029/2019GL086825>.
- Liu, Y., and Coauthors, 2022: Increases in China’s wind energy production from the recovery of winds since 2012. *Environ. Res. Lett.*, **17**, 114035, <https://doi.org/10.1088/1748-9326/ac9cf4>.
- Lo, Y. T. E., and Coauthors, 2023: Optimal heat stress metric for modelling heat-related mortality varies from country to country. *Int. J. Climatol.*, **43**, 1–16, <https://doi.org/10.1002/joc.8160>.
- Loeb, N. G., B. A. Wielicki, D. R. Doelling, G. L. Smith, D. F. Keyes, S. Kato, N. Manalo-Smith, and T. Wong, 2009: Toward optimal closure of the Earth’s top-of-atmosphere radiation budget. *J. Climate*, **22**, 748–766, <https://doi.org/10.1175/2008JCLI2637.1>.
- , S. Kato, W. Su, T. Wong, F. Rose, D. R. Doelling, and J. Norris, 2012: Advances in understanding top-of-atmosphere radiation variability from satellite observations. *Surv. Geophys.*, **33**, 359–385, <https://doi.org/10.1007/s10712-012-9175-1>.
- , and Coauthors, 2018: Clouds and the Earth’s Radiant Energy System (CERES) Energy Balanced and Filled (EBAF) Top-of-Atmosphere (TOA) edition-4.0 data product. *J. Climate*, **31**, 895–918, <https://doi.org/10.1175/JCLI-D-17-0208.1>.
- MacCallum, S. N., and C. J. Merchant, 2012: Surface water temperature observations of large lakes by optimal estimation. *Can. J. Remote Sens.*, **38**, 25–45, <https://doi.org/10.5589/m12-010>.
- MacFarling Meure, C., D. Etheridge, C. Trudinger, P. Steele, R. Langenfelds, T. van Ommen, A. Smith, and J. Elkins, 2006: Law Dome CO₂, CH₄ and N₂O ice core records extended to 2000 years BP. *Geophys. Res. Lett.*, **33**, L14810, <https://doi.org/10.1029/2006GL026152>.
- Magnin, F., P. Deline, L. Ravelin, J. Noetzi, and P. Pogliotti, 2015: Thermal characteristics of permafrost in the steep alpine rock walls of the Aiguille du Midi (Mont Blanc Massif, 3842 m a.s.l.). *Cryosphere*, **9**, 109–121, <https://doi.org/10.5194/tc-9-109-2015>.
- Mahowald, N. M., R. Scanza, J. Brahney, C. L. Goodale, P. G. Hess, J. K. Moore, and J. Neff, 2017: Aerosol deposition impacts on land and ocean carbon cycles. *Curr. Climate Change Rep.*, **3**, 16–31, <https://doi.org/10.1007/s40641-017-0056-z>.
- Marchant, R., C. Mumbi, S. Behera, and T. Yamagata, 2007: The Indian Ocean dipole – The unsung driver of climatic variability in East Africa. *Afr. J. Ecol.*, **45**, 4–16, <https://doi.org/10.1111/j.1365-2028.2006.00707.x>.
- Marshall, G. J., 2003: Trends in the Southern Annular Mode from observations and reanalyses. *J. Climate*, **16**, 4134–4143, [https://doi.org/10.1175/1520-0442\(2003\)0162.0.CO;2](https://doi.org/10.1175/1520-0442(2003)0162.0.CO;2).
- Martens, B., and Coauthors, 2017: GLEAM v3: Satellite-based land evaporation and root-zone soil moisture. *Geosci. Model Dev.*, **10**, 1903–1925, <https://doi.org/10.5194/gmd-10-1903-2017>.

- , W. Waegeman, W. A. Dorigo, N. E. C. Verhoest, and D. G. Miralles, 2018: Terrestrial evaporation response to modes of climate variability. *npj Climate Atmos. Sci.*, **1**, 43, <https://doi.org/10.1038/s41612-018-0053-5>.
- Matoza, R. S., and Coauthors, 2022: Atmospheric waves and global seismoacoustic observations of the January 2022 Hunga eruption, Tonga. *Science*, **377**, 95–100, <https://doi.org/10.1126/science.abo7063>.
- McKittrick, R., and J. Christy, 2020: Pervasive warming bias in CMIP6 tropospheric layers. *Earth Space Sci.*, **7**, e2020EA001281, <https://doi.org/10.1029/2020EA001281>.
- McVicar, T. R., and Coauthors, 2012: Global review and synthesis of trends in observed terrestrial near-surface wind speeds: Implications for evaporation. *J. Hydrol.*, **416–417**, 182–205, <https://doi.org/10.1016/j.jhydrol.2011.10.024>.
- Mears, C. A., and F. J. Wentz, 2016: Sensitivity of satellite-derived tropospheric temperature trends to the diurnal cycle adjustment. *J. Climate*, **29**, 3629–3646, <https://doi.org/10.1175/JCLI-D-15-0744.1>.
- , D. K. Smith, L. Ricciardulli, J. Wang, H. Huelsing, and F. J. Wentz, 2018: Construction and uncertainty estimation of a satellite-derived total precipitable water data record over the world's oceans. *Earth Space Sci.*, **5**, 197–210, <https://doi.org/10.1002/2018EA000363>.
- , J. P. Nicolas, O. Bock, S. P. Ho, and X. Zhou, 2022: Total column water vapor [in “State of the Climate in 2021”]. *Bull. Amer. Meteor. Soc.*, **103** (8), 552–554, <https://doi.org/10.1175/BAMS-D-22-0092.1>.
- Meesters, A. G. C. A., R. A. M. De Jeu, and M. Owe, 2005: Analytical derivation of the vegetation optical depth from the microwave polarization difference index. *IEEE Trans. Geosci. Remote Sens.*, **2**, 121–123, <https://doi.org/10.1109/LGRS.2005.843983>.
- Menne, M. J., I. Durre, R. S. Vose, B. E. Gleason, and T. G. Houston, 2012a: An overview of the Global Historical Climatology Network-Daily database. *J. Atmos. Oceanic Technol.*, **29**, 897–910, <https://doi.org/10.1175/JTECH-D-11-00103.1>.
- , and Coauthors, 2012b: Global Historical Climatology Network—Daily (GHCN-Daily), version 3.24. NOAA National Climatic Data Center, accessed 24 July 2023, <https://doi.org/10.7289/V5D21VHZ>.
- Menzel, A., Y. Yuan, M. Matiu, T. H. Sparks, H. Scheifinger, R. Gehrig, and N. Estrella, 2020: Climate change fingerprints in recent European plant phenology. *Global Change Biol.*, **26**, 2599–2612, <https://doi.org/10.1111/gcb.15000>.
- Messenger, M. L., B. Lehner, G. Grill, I. Nedeva, and O. Schmitt, 2016: Estimating the volume and age of water stored in global lakes using a geo-statistical approach. *Nat. Commun.*, **7**, 13603, <https://doi.org/10.1038/ncomms13603>.
- MeteoSwiss, 2023: Klimabulletin Jahr 2022. MeteoSwiss, 13 pp., www.meteoschweiz.admin.ch/service-und-publikationen/publikationen/berichte-und-bulletins/2022/klimabulletin-jahr-2022.html.
- Meyer, M. F., S. G. Labou, A. N. Cramer, M. R. Brousil, and B. T. Luff, 2020: The global lake area, climate, and population dataset. *Sci. Data*, **7**, 174, <https://doi.org/10.1038/s41597-020-0517-4>.
- Michel, S. E., J. R. Clark, B. H. Vaughn, M. Crotwell, M. Madronich, E. Moglia, D. Neff, and J. Mund, 2022: Stable isotopic composition of atmospheric methane (^{13}C) from the NOAA GML Carbon Cycle Cooperative Global Air Sampling Network, 1998–2021. University of Colorado, Institute of Arctic and Alpine Research (INSTAAR), accessed 15 December 2022, <https://doi.org/10.15138/9p89-1x02>.
- Millán, L., and Coauthors, 2022: The Hunga Tonga-Hunga Ha’apai hydration of the stratosphere. *Geophys. Res. Lett.*, **49**, e2022GL099381, <https://doi.org/10.1029/2022GL099381>.
- Miller, B. R., and Coauthors, 2010: HFC-23 (CHF_3) emission trend response to HCFC-22 (CHClF_2) production and recent HFC-23 emission abatement measures. *Atmos. Chem. Phys.*, **10**, 7875–7890, <https://doi.org/10.5194/acp-10-7875-2010>.
- Minola, L., H. Reese, H. W. Lai, C. Azorin-Molina, J. A. Guijarro, S. W. Son, and D. Chen, 2022: Wind stilling-reversal across Sweden: The impact of land-use and large-scale atmospheric circulation changes. *Int. J. Climatol.*, **42**, 1049–1071, <https://doi.org/10.1002/joc.7289>.
- Miralles, D. G., T. R. H. Holmes, R. A. M. De Jeu, J. H. Gash, A. G. C. A. Meesters, and A. J. Dolman, 2011: Global land-surface evaporation estimated from satellite-based observations. *Hydrol. Earth Syst. Sci.*, **15**, 453–469, <https://doi.org/10.5194/hess-15-453-2011>.
- , and Coauthors, 2014: El Niño–La Niña cycle and recent trends in continental evaporation. *Nat. Climate Change*, **4**, 122–126, <https://doi.org/10.1038/nclimate2068>.
- Mishra, M. K., L. Hoffmann, and P. K. Thapliyal, 2022: Investigations on the global spread of the Hunga Tonga-Hunga Ha’apai volcanic eruption using space-based observations and Lagrangian transport simulations. *Atmosphere*, **13**, 2055, <https://doi.org/10.3390/atmos13122055>.
- Mitchell, L., E. Brook, J. E. Lee, C. Buizert, and T. Sowers, 2013: Constraints on the late Holocene anthropogenic contribution to the atmospheric methane budget. *Science*, **342**, 964–966, <https://doi.org/10.1126/science.1238920>.
- Mo, K. C., J. K. E. Schemm, and S. H. Yoo, 2009: Influence of ENSO and the Atlantic multidecadal oscillation on drought over the United States. *J. Climate*, **22**, 5962–5982, <https://doi.org/10.1175/2009JCLI2966.1>.
- Moesinger, L., W. Dorigo, R. de Jeu, R. van der Schalie, T. Scanlon, I. Teubner, and M. Forkel, 2020: The global long-term microwave Vegetation Optical Depth Climate Archive (VODCA). *Earth Syst. Sci. Data*, **12**, 177–196, <https://doi.org/10.5194/essd-12-177-2020>.
- Montzka, S. A., J. H. Butler, R. C. Myers, T. M. Thompson, T. H. Swanson, A. D. Clarke, L. T. Lock, and J. W. Elkins, 1996: Decline in the tropospheric abundance of halogen from halocarbons: Implications for stratospheric ozone depletion. *Science*, **272**, 1318–1322, <https://doi.org/10.1126/science.272.5266.1318>.
- , and Coauthors, 2018: An unexpected and persistent increase in global emissions of ozone-depleting CFC-11. *Nature*, **557**, 413–417, <https://doi.org/10.1038/s41586-018-0106-2>.
- , and Coauthors, 2021: A decline in global CFC-11 emissions during 2018–2019. *Nature*, **590**, 428–432, <https://doi.org/10.1038/s41586-021-03260-5>.
- Morice, C. P., and Coauthors, 2021: An updated assessment of near-surface temperature change from 1850: The HadCRUT5 data set. *J. Geophys. Res. Atmos.*, **126**, e2019JD032361, <https://doi.org/10.1029/2019JD032361>.
- Moron, V., and G. Plaut, 2003: The impact of El Niño–Southern Oscillation upon weather regimes over Europe and the North Atlantic during boreal winter. *Int. J. Climatol.*, **23**, 363–379, <https://doi.org/10.1002/joc.890>.
- Mote, P. W., and Coauthors, 1996: An atmospheric tape recorder: The imprint of tropical tropopause temperatures on stratospheric water vapor. *J. Geophys. Res.*, **101**, 3989–4006, <https://doi.org/10.1029/95JD03422>.

- Mühle, J., and Coauthors, 2010: Perfluorocarbons in the global atmosphere: Tetrafluoromethane, hexafluoroethane, and octafluoropropane. *Atmos. Chem. Phys.*, **10**, 5145–5164, <https://doi.org/10.5194/acp-10-5145-2010>.
- , and Coauthors, 2019: Perfluorocyclobutane (PFC-318, $c\text{-C}_4\text{F}_8$) in the global atmosphere. *Atmos. Chem. Phys.*, **19**, 10335–10359, <https://doi.org/10.5194/acp-19-10335-2019>.
- Myhre, G., and Coauthors, 2013: Anthropogenic and natural radiative forcing. *Climate Change 2013: The Physical Science Basis*, T. F. Stocker et al., Eds., Cambridge University Press, 659–740.
- Naumann, G., and Coauthors, 2021: The 2019–2021 extreme drought episode in La Plata Basin. EUR 30833 EN, Publications Office of the European Union, 44 pp., <https://doi.org/10.2760/773>.
- NCEI, 2023: Annual 2022 Global Climate Report. Accessed 8 February 2023, <https://www.ncei.noaa.gov/access/monitoring/monthly-report/global/202213>.
- Newman, P. A., J. S. Daniel, D. W. Waugh, and E. R. Nash, 2007: A new formulation of equivalent effective stratospheric chlorine (EESC). *Atmos. Chem. Phys.*, **7**, 4537–4552, <https://doi.org/10.5194/acp-7-4537-2007>.
- Nicholson, S. E., 2017: Climate and climatic variability of rainfall over eastern Africa. *Rev. Geophys.*, **55**, 590–635, <https://doi.org/10.1002/2016RG000544>.
- NIWA, 2022: “Exceptional” August atmospheric river sets record. NIWA, <https://niwa.co.nz/news/exceptional-august-atmospheric-river-sets-record>.
- NOAA/NCEI, 2023: Monthly global climate report for annual 2022. Accessed 24 January 2023, <https://www.ncei.noaa.gov/access/monitoring/monthly-report/global/202213>.
- Noetzli, J., and Coauthors, 2021: Best practice for measuring permafrost temperature in boreholes based on the experience in the Swiss Alps. *Front. Earth Sci.*, **9**, 607875, <https://doi.org/10.3389/feart.2021.607875>.
- , H. H. Christiansen, P. Deline, M. Gugliemin, K. Isaksen, S. Smith, L. Zhao, and D. A. Streletskiy, 2022: Permafrost temperature and active layer thickness [in “State of the Climate in 2021”]. *Bull. Amer. Meteor. Soc.*, **103** (8), 541–543, <https://doi.org/10.1175/BAMS-D-22-0092.1>.
- OCHA, 2022: South Africa: Floods and landslides – Apr 2022. ReliefWeb, accessed 9 February 2023, <https://reliefweb.int/disaster/fl-2022-000201-zaf>.
- Oh, Y., and Coauthors, 2022: Improved global wetland carbon isotopic signatures support post-2006 microbial methane emission increase. *Commun. Earth Environ.*, **3**, 159, <https://doi.org/10.1038/s43247-022-00488-5>.
- O’Keefe, J., 2021: Phenology of woody species at Harvard Forest since 1990. Harvard Forest Data Archive: HF003, accessed 25 July 2023, <https://harvardforest1.fas.harvard.edu/exist/apps/datasets/showData.html?id=HF003>.
- Orimoloye, I. R., J. A. Belle, Y. M. Orimoloye, A. O. Olusola, and O. O. Ololade, 2022: Drought: A common environmental disaster. *Atmosphere*, **13**, 111, <https://doi.org/10.3390/atmos13010111>.
- Osborn, T. J., P. D. Jones, D. H. Lister, C. P. Morice, I. R. Simpson, J. P. Winn, E. Hogan, and I. C. Harris, 2021: Land surface air temperature variations across the globe updated to 2019: The CRUTEM5 dataset. *J. Geophys. Res. Atmos.*, **126**, e2019JD032352, <https://doi.org/10.1029/2019JD032352>.
- Osprey, S. M., N. Butchart, J. R. Knight, A. A. Scaife, K. Hamilton, J. A. Anstey, V. Schenzinger, and C. Zhang, 2016: An unexpected disruption of the atmospheric quasi-biennial oscillation. *Science*, **353**, 1424–1427, <https://doi.org/10.1126/science.aah4156>.
- Otto, F. E. L., and Coauthors, 2022: Climate change likely increased extreme monsoon rainfall, flooding highly vulnerable communities in Pakistan. World Weather Attribution, 36 pp., <https://www.worldweatherattribution.org/wp-content/uploads/Pakistan-floods-scientific-report.pdf>.
- Park, H., and Coauthors, 2023: Continuous increase in East Asia HFC-23 emissions inferred from high-frequency atmospheric observations from 2008 to 2019. *EGU Sphere*, <https://doi.org/10.5194/egusphere-2023-6>.
- Park, S., and Coauthors, 2021: A decline in emissions of CFC-11 and related chemicals from eastern China. *Nature*, **590**, 433–437, <https://doi.org/10.1038/s41586-021-03277-w>.
- Park, T., and Coauthors, 2016: Changes in growing season duration and productivity of northern vegetation inferred from long-term remote sensing data. *Environ. Res. Lett.*, **11**, 084001, <https://doi.org/10.1088/1748-9326/11/8/084001>.
- Parsons, L. A., Y. J. Masuda, T. Kroeger, D. Shindell, N. H. Wolff, and J. T. Spector, 2022: Global labor loss due to humid heat exposure underestimated for outdoor workers. *Environ. Res. Lett.*, **17**, 014050, <https://doi.org/10.1088/1748-9326/ac3dae>.
- Pekel, J.-F., A. Cottam, N. Gorelick, and A. S. Belward, 2016: High-resolution mapping of global surface water and its long-term changes. *Nature*, **540**, 418–422, <https://doi.org/10.1038/nature20584>.
- Pellet, C., and Coauthors, 2022: Rock glacier velocity [in “State of the Climate in 2021”]. *Bull. Amer. Meteor. Soc.*, **103** (8), 543–545, <https://doi.org/10.1175/BAMS-D-22-0092.1>.
- Pelto, M., M. Dryak, J. Pelto, T. Matthews, and L. B. Perry, 2022: Contribution of glacier runoff during heat waves in the Nooksack River Basin USA. *Water*, **14**, 1145, <https://doi.org/10.3390/w14071145>.
- Peng, S., and Coauthors, 2022: Wetland emission and atmospheric sink changes explain methane growth in 2020. *Nature*, **612**, 477–482, <https://doi.org/10.1038/s41586-022-05447-w>.
- Pepin, N., and Coauthors, 2015: Elevation-dependent warming in mountain regions of the world. *Nat. Climate Change*, **5**, 424–430, <https://doi.org/10.1038/nclimate2563>.
- PERMOS, 2022: Swiss Permafrost Bulletin 2021. J. Noetzli and C. Pellet, Eds., Swiss Permafrost Monitoring Network, 22 pp., <https://doi.org/10.13093/permos-bull-2022>.
- Phillips, C., and M. J. Foster, 2022: Cloudiness [in “State of the Climate in 2021”]. *Bull. Amer. Meteor. Soc.*, **103** (8), 531–533, <https://doi.org/10.1175/BAMS-D-22-0092.1>.
- Pielmeier, C., B. Zweifel, F. Techel, C. Marty, and T. Stucki, 2023: *Schnee und Lawinen in den Schweizer Alpen. Hydrologisches Jahr 2021/22*. WSL Berichte, Vol. 128, WSL-Institut für Schnee- und Lawinenforschung SLF, 72 pp., <https://doi.org/10.55419/wsl:32462>.
- Pierrehumbert, R. T., 2014: Short-lived climate pollution. *Annu. Rev. Earth Planet. Sci.*, **42**, 341–379, <https://doi.org/10.1146/annurev-earth-060313-054843>.
- Pinty, B., and Coauthors, 2011: Exploiting the MODIS albedos with the Two-stream Inversion Package (JRC-TIP): 2. Fractions of transmitted and absorbed fluxes in the vegetation and soil layers. *J. Geophys. Res.*, **116**, D09106, <https://doi.org/10.1029/2010JD015373>.
- Pisano, M. F., G. D’Amico, N. Ramos, N. Pommarés, and E. Fucks, 2020: Factors that control the seasonal dynamics of the shallow lakes in the Pampean region, Buenos Aires, Argentina. *J. South Amer. Earth Sci.*, **98**, 102468, <https://doi.org/10.1016/j.jsames.2019.102468>.

- Platnick, S., and Coauthors, 2015: MODIS atmosphere L3 monthly product. NASA MODIS Adaptive Processing System, Goddard Space Flight Center, accessed 11 February 2022, https://doi.org/10.5067/MODIS/MYD08_M3.061.
- PMDCDPC, 2022: Pakistan monsoon 2022 rainfall report. Pakistan Meteorological Department-CDPC, 3 pp., https://www.pmd.gov.pk/cdpc/Monsoon_2022_update/Pakistan_Monsoon_2022_Rainfall_Update.pdf.
- PMDNWFC, 2022: Monthly weather report August 2022. National Weather Forecasting Center Islamabad, Pakistan Meteorological Department, 23 pp., <https://nwfc.pmd.gov.pk/new/assets/monthly-weather-reports/1664253472.pdf>.
- Po-Chedley, S., T. J. Thorsen, and Q. Fu, 2015: Removing diurnal cycle contamination in satellite-derived tropospheric temperatures: Understanding tropical tropospheric trend discrepancies. *J. Climate*, **28**, 2274–2290, <https://doi.org/10.1175/JCLI-D-13-00767.1>.
- , B. D. Santer, S. Fueglistaler, M. D. Zelinka, P. J. Cameron-Smith, J. Painter, and Q. Fu, 2021: Natural variability contributes to model-satellite differences in tropical tropospheric warming. *Proc. Natl. Acad. Sci. USA*, **118**, e2020962118, <https://doi.org/10.1073/pnas.2020962118>.
- , J. T. Fasullo, N. Siler, E. A. Barnes, Z. M. Labe, C. J. W. Bonfils, and B. D. Santer, 2022: Internal variability and forcing influence model-satellite differences in the rate of tropical tropospheric warming. *Proc. Natl. Acad. Sci. USA*, **119**, e2209431119, <https://doi.org/10.1073/pnas.2209431119>.
- Pogliotti, P., M. Guglielmin, E. Cremonese, U. M. di Cella, G. Filippa, C. Pellet, and C. Hauck, 2015: Warming permafrost and active layer variability at Cime Bianche, western European Alps. *Cryosphere*, **9**, 647–661, <https://doi.org/10.5194/tc-9-647-2015>.
- Poli, P., and N. M. Shapiro, 2022: Rapid characterization of large volcanic eruptions: Measuring the impulse of the Hunga Tonga Ha'apai explosion from teleseismic waves. *Geophys. Res. Lett.*, **49**, e2022GL098123, <https://doi.org/10.1029/2022GL098123>.
- Popp, T., and Coauthors, 2016: Development, production and evaluation of aerosol climate data records from European satellite observations (Aerosol_cci). *Remote Sens.*, **8**, 421, <https://doi.org/10.3390/rs8050421>.
- Prather, M. J., C. D. Holmes, and J. Hsu, 2012: Reactive greenhouse gas scenarios: Systematic exploration of uncertainties and the role of atmospheric chemistry. *Geophys. Res. Lett.*, **39**, L09803, <https://doi.org/10.1029/2012GL051440>.
- Proud, S. R., A. T. Prata, and S. Schmauß, 2022: The January 2022 eruption of Hunga Tonga-Hunga Ha'apai volcano reached the mesosphere. *Science*, **378**, 554–557, <https://doi.org/10.1126/science.abo4076>.
- Quaas, J., and Coauthors, 2022: Robust evidence for reversal of the trend in aerosol effective climate forcing. *Atmos. Chem. Phys.*, **22**, 12 221–12 239, <https://doi.org/10.5194/acp-22-12221-2022>.
- Rajeevan, M., K. L. Srivastava, Z. Lareef, and J. Revadekar, 2011: South Asia [in "State of the Climate in 2010"]. *Bull. Amer. Meteor. Soc.*, **92** (6), S217–S219, <https://doi.org/10.1175/1520-0477-92.6.S1>.
- Ramon, J., L. Lledó, V. Torralba, A. Soret, and F. J. Doblas-Reyes, 2019: What global reanalysis best represents near-surface winds? *Quart. J. Roy. Meteor. Soc.*, **145**, 3236–3251, <https://doi.org/10.1002/qj.3616>.
- Randel, W. J., and J. B. Cobb, 1994: Coherent variations of monthly mean total ozone and lower stratospheric temperature. *J. Geophys. Res.*, **99**, 5433–5447, <https://doi.org/10.1029/93JD03454>.
- , F. Wu, S. J. Oltmans, K. Rosenlof, and G. E. Nedoluha, 2004: Interannual changes of stratospheric water vapor and correlations with tropical tropopause temperatures. *J. Atmos. Sci.*, **61**, 2133–2148, [https://doi.org/10.1175/1520-0469\(2004\)0612.0.CO;2](https://doi.org/10.1175/1520-0469(2004)0612.0.CO;2).
- Randel, W. J., B. R. Johnston, J. J. Braun, S. Sokolovskiy, H. Vömel, A. Podglajen, and B. Legras, 2023: Stratospheric water vapor from the Hunga Tonga–Hunga Ha'apai volcanic eruption deduced from COSMIC-2 radio occultation. *Remote Sens.*, **15**, 2167, <https://doi.org/10.3390/rs15082167>.
- Ravishankara, A. R., J. S. Daniel, and R. W. Portmann, 2009: Nitrous oxide (N₂O): The dominant ozone-depleting substance emitted in the 21st century. *Science*, **326**, 123–125, <https://doi.org/10.1126/science.1176985>.
- Ray, E. A., F. L. Moore, J. W. Elkins, K. H. Rosenlof, J. C. Laube, T. Röckmann, D. R. Marsh, and A. E. Andrews, 2017: Quantification of the SF₆ lifetime based on mesospheric loss measured in the stratospheric polar vortex. *J. Geophys. Res. Atmos.*, **122**, 4626–4638, <https://doi.org/10.1002/2016JD026198>.
- Rayner, N. A., D. E. Parker, E. B. Horton, C. K. Folland, L. V. Alexander, D. P. Rowell, E. C. Kent, and A. Kaplan, 2003: Global analyses of sea surface temperature, sea ice, and night marine air temperature since the late nineteenth century. *J. Geophys. Res.*, **108**, 4407, <https://doi.org/10.1029/2002JD002670>.
- Reichstein, M., and Coauthors, 2013: Climate extremes and the carbon cycle. *Nature*, **500**, 287–295, <https://doi.org/10.1038/nature12350>.
- Rémy, S., N. Bellouin, Z. Kipling, M. Ades, A. Benedetti, and O. Boucher, 2021: Aerosols [in "State of the Climate in 2021"]. *Soc.*, **102** (8), S11–S42, <https://doi.org/10.1175/BAMS-D-22-0092.1>.
- RGIK, 2022a: Rock glacier velocity as an associated parameter of ECV permafrost: Baseline concepts (version 3.1). IPA Action Group Rock Glacier Inventories and Kinematics, 12 pp., https://bigweb.unifr.ch/Science/Geosciences/Geomorphology/Pub/Website/IPA/CurrentVersion/Current_RockGlacierVelocity.pdf.
- , 2022b: Towards standard guidelines for inventorying rock glaciers: Baseline concepts (version 4.2.2). IPA Action Group Rock Glacier Inventories and Kinematics, 13 pp., https://bigweb.unifr.ch/Science/Geosciences/Geomorphology/Pub/Website/IPA/CurrentVersion/Current_Baseline_Concepts_Inventorying_Rock_Glaciers.pdf.
- Ricciardulli, L., and F. J. Wentz, 2015: A scatterometer geophysical model function for climate-quality winds: QuikSCAT Ku-2011. *J. Atmos. Oceanic Technol.*, **32**, 1829–1846, <https://doi.org/10.1175/JTECH-D-15-0008.1>.
- , and A. Manaster, 2021: Intercalibration of ASCAT scatterometer winds from MetOp-A, -B, and -C, for a stable climate data record. *Remote Sens.*, **13**, 3678, <https://doi.org/10.3390/rs13183678>.
- Richardson, A. D., 2019: Tracking seasonal rhythms of plants in diverse ecosystems with digital camera imagery. *New Phytol.*, **222**, 1742–1750, <https://doi.org/10.1111/nph.15591>.
- , and J. O'Keefe, 2009: Phenological differences between understory and overstory. *Phenology of Ecosystem Processes*, A. Noormets, Ed., Springer, 87–117.
- Rieger, L. A., W. J. Randel, A. E. Bourassa, and S. Solomon, 2021: Stratospheric temperature and ozone anomalies associated with the 2020 Australian New Year fires. *Geophys. Res. Lett.*, **48**, e2021GL095898, <https://doi.org/10.1029/2021GL095898>.

- Rigby, M., and Coauthors, 2019: Increase in CFC-11 emissions from eastern China based on atmospheric observations. *Nature*, **569**, 546–550, <https://doi.org/10.1038/s41586-019-1193-4>.
- Rodell, M., and D. Wiese, 2022: Groundwater and terrestrial water storage [in “State of the Climate in 2021”]. *Bull. Amer. Meteor. Soc.*, **103** (8), 563–564, <https://doi.org/10.1175/BAMS-D-22-0092.1>.
- Roderick, M. L., L. D. Rotstayn, G. D. Farquhar, and M. T. Hobbins, 2007: On the attribution of changing pan evaporation. *Geophys. Res. Lett.*, **34**, L17403, <https://doi.org/10.1029/2007GL031166>.
- Rohde, R. A., and Z. Hausfather, 2020: The Berkeley Earth land/ocean temperature record. *Earth Syst. Sci. Data*, **12**, 3469–3479, <https://doi.org/10.5194/essd-12-3469-2020>.
- Rosemartin, A. H., and Coauthors, 2014: Organizing phenological data resources to inform natural resource conservation. *Biol. Conserv.*, **173**, 90–97, <https://doi.org/10.1016/j.biocon.2013.07.003>.
- Rosenfeld, D., and W. L. Woodley, 2003: Closing the 50-year circle: From cloud seeding to space and back to climate change through precipitation physics. *Cloud Systems, Hurricanes, and the Tropical Rainfall Measuring Mission (TRMM)*, Meteor. Monogr., No. 51, Amer. Meteor. Soc., 59–80.
- , U. Lohmann, G. B. Raga, C. D. O’Dowd, M. Kulmala, S. Fuzzi, A. Reissell, and M. O. Andreae, 2008: Flood or drought: How do aerosols affect precipitation? *Science*, **321**, 1309–1313, <https://doi.org/10.1126/science.1160606>.
- Saji, N. H., B. N. Goswami, P. N. Vinayachandran, and T. Yamagata, 1999: A dipole mode in the tropical Indian Ocean. *Nature*, **401**, 360–363, <https://doi.org/10.1038/43854>.
- Sanap, S. D., 2021: Global and regional variations in aerosol loading during COVID-19 imposed lockdown. *Atmos. Environ.*, **246**, 118132, <https://doi.org/10.1016/j.atmosenv.2020.118132>.
- Santer, B. D., and Coauthors, 2008: Consistency of modelled and observed temperature trends in the tropical troposphere. *Int. J. Climatol.*, **28**, 1703–1722, <https://doi.org/10.1002/joc.1756>.
- , and Coauthors, 2021: Using climate model simulations to constrain observations. *J. Climate*, **34**, 6281–6301, <https://doi.org/10.1175/JCLI-D-20-0768.1>.
- Santos, E. B., E. D. de Freitas, S. A. A. Raífe, T. Fujita, A. P. Rudke, L. D. Martins, R. A. F. de Souza, and J. A. Martin, 2021: Spatio-temporal variability of wet and drought events in the Paraná River basin—Brazil and its association with the El Niño–Southern Oscillation phenomenon. *Int. J. Climatol.*, **41**, 4879–4897, <https://doi.org/10.1002/joc.7104>.
- Sátori, G., E. Williams, and I. Lempferger, 2009b: Variability of global lightning activity on the ENSO time scale. *Atmos. Res.*, **91**, 500–507, <https://doi.org/10.1016/j.atmosres.2008.06.014>.
- SAWS, 2022: Media release: Extreme rainfall and widespread flooding overnight: KwaZulu-Natal and parts of Eastern Cape. South African Weather Service, 12 April, accessed 14 February 2023, https://www.weathersa.co.za/Documents/Corporate/Medrel12April2022_12042022142120.pdf.
- Scafetta, N., 2023: CMIP6 GCM ensemble members versus global surface temperatures. *Climate Dyn.*, **60**, 3091–3120, <https://doi.org/10.1007/s00382-022-06493-w>.
- Schaaf, C. B., and Coauthors, 2002: First operational BRDF, albedo nadir reflectance products from MODIS. *Remote Sens. Environ.*, **83**, 135–148, [https://doi.org/10.1016/S0034-4257\(02\)00091-3](https://doi.org/10.1016/S0034-4257(02)00091-3).
- Schoeberl, M. R., Y. Wang, R. Ueyama, G. Taha, E. Jensen, and W. Yu, 2022: Analysis and impact of the Hunga Tonga-Hunga Ha’apai stratospheric water vapor plume. *Geophys. Res. Lett.*, **49**, e2022GL100248, <https://doi.org/10.1029/2022GL100248>.
- Schwartz, M. J., and Coauthors, 2020: Australian New Year’s PyroCb impact on stratospheric composition. *Geophys. Res. Lett.*, **47**, e2020GL090831, <https://doi.org/10.1029/2020GL090831>.
- Seyednasrollah, B., A. M. Young, K. Hufkens, T. Milliman, M. A. Friedl, S. Frolking, and A. D. Richardson, 2019: Publisher correction: Tracking vegetation phenology across diverse biomes using version 2.0 of the PhenoCam Dataset. *Sci. Data*, **6**, 261, <https://doi.org/10.1038/s41597-019-0270-8>.
- Shao, X., S.-P. Ho, X. Jing, X. Zhou, Y. Chen, T.-C. Liu, B. Zhang, and J. Dong, 2023: Characterizing the tropospheric water vapor variation using COSMIC radio occultation and ECMWF reanalysis data. *Atmos. Chem. Phys. Discuss.*, <https://doi.org/10.5194/acp-2022-660>.
- Sharma, S., and R. I. Woolway, 2021: Lake ice [in “State of the Climate in 2020”]. *Bull. Amer. Meteor. Soc.*, **102** (8), S48–S51, <https://doi.org/10.1175/BAMS-D-21-0098.1>.
- , J. J. Magnuson, R. D. Batt, L. Winslow, J. Korhonen, and Y. Aono, 2016: Direct observations of ice seasonality reveal changes in climate over the past 5–7 centuries. *Sci. Rep.*, **6**, 25061, <https://doi.org/10.1038/srep25061>.
- , and Coauthors, 2019: Widespread loss of lake ice around the Northern Hemisphere in a warming world. *Nat. Climate Change*, **9**, 3, <https://doi.org/10.1038/s41558-018-0393-5>.
- , K. Blagrove, A. Filazzola, M. A. Imrit, and H.-J. Hendricks Franssen, 2021: Forecasting the permanent loss of lake ice within the 21st century. *Geophys. Res. Lett.*, **48**, e2020GL091108, <https://doi.org/10.1029/2020GL091108>.
- , and Coauthors, 2022: Lake ice [in “State of the Climate in 2021”]. *Bull. Amer. Meteor. Soc.*, **103** (8), S47–S49, <https://doi.org/10.1175/BAMS-D-22-0092.1>.
- Shaw, T., G. Ulloa, D. Fariás-Barahona, R. Fernandez, J. Lattus, and J. McPhee, 2021: Glacier albedo reduction and drought effects in the extratropical Andes, 1986–2020. *J. Glaciol.*, **67**, 158–169, <https://doi.org/10.1017/jog.2020.102>.
- Shi, L., and J. J. Bates, 2011: Three decades of intersatellite-calibrated high-resolution infrared radiation sounder upper tropospheric water vapor. *J. Geophys. Res.*, **116**, D04108, <https://doi.org/10.1029/2010JD014847>.
- Sindelarova, K., and Coauthors, 2014: Global data set of biogenic VOC emissions calculated by the MEGAN model over the last 30 years. *Atmos. Chem. Phys.*, **14**, 9317–9341, <https://doi.org/10.5194/acp-14-9317-2014>.
- Sioris, C. E., A. Malo, C. A. McLinden, and R. D’Amours, 2016: Direct injection of water vapor into the stratosphere by volcanic eruptions. *Geophys. Res. Lett.*, **43**, 7694–7700, <https://doi.org/10.1002/2016GL069918>.
- Skeie, R., and Coauthors, 2020: Historical total ozone radiative forcing derived from CMIP6 simulations. *npj Climate Atmos. Sci.*, **3**, 32, <https://doi.org/10.1038/s41612-020-00131-0>.
- Smiljanic, I., M. Higgins, D. Melfi, and I. A. Abdulsalam, 2022: Monsoon floods in Pakistan. EUMETSAT, 13 September, accessed 23 January 2023, <https://www.eumetsat.int/monsoon-floods-pakistan>.
- Smith, A., N. Lott, and R. Vose, 2011: The integrated surface database: Recent developments and partnerships. *Bull. Amer. Meteor. Soc.*, **92**, 704–708, <https://doi.org/10.1175/2011BAMS3015.1>.

- Smith, S. L., H. B. O'Neill, K. Isaksen, J. Noetzi, and V. E. Romanovsky, 2022: The changing thermal state of permafrost. *Nat. Rev. Earth Environ.*, **3**, 14, <https://doi.org/10.1038/s43017-021-00240-1>.
- Soden, B. J., D. L. Jackson, V. Ramaswamy, M. D. Schwarzkopf, and X. Huang, 2005: The radiative signature of upper tropospheric moistening. *Science*, **310**, 841–844, <https://doi.org/10.1126/science.1115602>.
- Sofieva, V. F., and Coauthors, 2021: Measurement report: Regional trends of stratospheric ozone evaluated using the Merged GRidded Dataset of Ozone Profiles (MEGRIDOP). *Atmos. Chem. Phys.*, **21**, 6707–6720, <https://doi.org/10.5194/acp-21-6707-2021>.
- Solomon, S., K. Stone, P. Yu, D. M. Murphy, D. Kinnison, A. R. Ravishankara, and P. Wang, 2023: Chlorine activation and enhanced ozone depletion induced by wildfire aerosol. *Nature*, **615**, 259–264, <https://doi.org/10.1038/s41586-022-05683-0>.
- Song, X.-P., M. C. Hansen, S. V. Stehman, P. V. Potapov, A. Tyukavina, E. F. Vermote, and J. R. Townshend, 2018: Global land change from 1982 to 2016. *Nature*, **560**, 639–643, <https://doi.org/10.1038/s41586-018-0411-9>.
- Soulard, N., and H. Lin, 2017: The spring relationship between the Pacific-North American pattern and the North Atlantic Oscillation. *Climate Dyn.*, **48**, 619–629, <https://doi.org/10.1007/s00382-016-3098-3>.
- SPARC/IO3C/GAW, 2019: SPARC/IO3C/GAW report on long-term ozone trends and uncertainties in the stratosphere. I. Petropavlovskikh et al., Eds., SPARC Rep. 9, WCRP-17/2018, GAW Rep. 241, 99 pp., <https://doi.org/10.17874/f899e57a20b>.
- Spencer, R. W., J. R. Christy, and W. D. Braswell, 2017: UAH version 6 global satellite temperature products: Methodology and results. *Asia-Pac. J. Atmos. Sci.*, **53**, 121–130, <https://doi.org/10.1007/s13143-017-0010-y>.
- Stackhouse, P. W., T. Wong, D. P. Kratz, P. Sawaengphokhai, A. C. Wiber, S. K. Gupta, and N. G. Loeb, 2016: Earth radiation budget at top-of-atmosphere [in "State of the Climate in 2015"]. *Bull. Amer. Meteor. Soc.*, **97** (8), 541–543, <https://doi.org/10.1175/2016BAMSStateoftheClimate.1>.
- Stanley, K. M., and Coauthors, 2020: Increase in global emissions of HFC-23 despite near-total expected reductions. *Nat. Commun.*, **11**, 397, <https://doi.org/10.1038/s41467-019-13899-4>.
- Staub, B., C. Lambiel, and R. Delaloye, 2016: Rock glacier creep as a thermally-driven phenomenon: A decade of inter-annual observation from the Swiss Alps. *XI Int. Conf. on Permafrost*, Potsdam, Germany, Alfred Wegener Institute Helmholtz Center for Polar and Marine Research, 96–97, <https://doi.org/10.2312/GFZ.LIS.2016.001>.
- Steinbrecht, W., and Coauthors, 2017: An update on ozone profile trends for the period 2000 to 2016. *Atmos. Chem. Phys.*, **17**, 10675–10690, <https://doi.org/10.5194/acp-17-10675-2017>.
- Stolarski, R. S., A. R. Douglass, L. D. Oman, and D. W. Waugh, 2015: Impact of future nitrous oxide and carbon dioxide emissions on the stratospheric ozone layer. *Environ. Res. Lett.*, **10**, 034011, <https://doi.org/10.1088/1748-9326/10/3/034011>.
- Strahan, S. E., and Coauthors, 2022: Unexpected repartitioning of stratospheric inorganic chlorine after the 2020 Australian wildfires. *Geophys. Res. Lett.*, **49**, e2022GL098290, <https://doi.org/10.1029/2022GL098290>.
- Streletskiy, D., J. Noetzi, S. L. Smith, G. Vieira, P. Schoeneich, F. Hrbacek, and A. M. Irrgang, 2021: Strategy and implementation plan for the Global Terrestrial Network for Permafrost (GTN-P) 2021–2024. International Permafrost Association, 44 pp., <https://doi.org/10.5281/ZENODO.6075468>.
- Stroeve, J., J. E. Box, Z. Wang, C. Schaaf, and A. Barrett, 2013: Re-evaluation of MODIS MCD43 Greenland albedo accuracy and trends. *Remote Sens. Environ.*, **138**, 199–214, <https://doi.org/10.1016/j.rse.2013.07.023>.
- Stull, R., 2011: Wet-bulb temperature from relative humidity and air temperature. *J. Appl. Meteor. Climatol.*, **50**, 2267–2269, <https://doi.org/10.1175/JAMC-D-11-0143.1>.
- Susskind, J., G. Molnar, L. Iredell, and N. G. Loeb, 2012: Interannual variability of outgoing longwave radiation as observed by AIRS and CERES. *J. Geophys. Res.*, **117**, D23107, <https://doi.org/10.1029/2012JD017997>.
- Szopa, S., and Coauthors, 2021: Short-lived climate forcers. *Climate Change 2021: The Physical Science Basis*, V. Masson-Delmotte et al., Eds., Cambridge University Press, 817–922, <https://doi.org/10.1017/9781009157896.008>.
- Taha, G., R. Loughman, P. R. Colarco, T. Zhu, L. W. Thomason, and G. Jaross, 2022: Tracking the 2022 Hunga Tonga-Hunga Ha'apai aerosol cloud in the upper and middle stratosphere using space-based observations. *Geophys. Res. Lett.*, **49**, e2022GL100091, <https://doi.org/10.1029/2022GL100091>.
- Tapley, B. D., S. Bettadpur, J. C. Ries, P. F. Thompson, and M. M. Watkins, 2004: GRACE measurements of mass variability in the Earth system. *Science*, **305**, 503–505, <https://doi.org/10.1126/science.1099192>.
- Tarasick, D. W., and Coauthors, 2019: Tropospheric ozone assessment report: Tropospheric ozone from 1877 to 2016, observed levels, trends and uncertainties. *Elementa*, **7**, 39, <https://doi.org/10.1525/elementa.376>.
- Teng, W.-H., C.-Y. Huang, S.-P. Ho, Y.-H. Kuo, and X.-J. Zhou, 2013: Characteristics of global precipitable water in ENSO events revealed by COSMIC measurements. *J. Geophys. Res. Atmos.*, **118**, 8411–8425, <https://doi.org/10.1002/jgrd.50371>.
- Teubner, I. E., and Coauthors, 2019: A carbon sink-driven approach to estimate gross primary production from microwave satellite observations. *Remote Sens. Environ.*, **229**, 100–113, <https://doi.org/10.1016/j.rse.2019.04.022>.
- Thibert, E., and X. Bodin, 2022: Changes in surface velocities over four decades on the Laurichard rock glacier (French Alps). *Permafrost Periglacial Processes*, **33**, 323–335, <https://doi.org/10.1002/ppp.2159>.
- Thompson, A. M., R. M. Stauffer, K. Wargan, J. C. Witte, D. E. Kolonig, and J. R. Ziemke, 2021: Regional and seasonal trends in tropical ozone from SHADOZ profiles: Reference for models and satellite products. , **126**, e2021JD034691, <https://doi.org/10.1029/2021JD034691>.
- Thompson, R. L., and Coauthors, 2019: Acceleration of global N₂O emissions seen from two decades of atmospheric inversion. *Nat. Climate Change*, **9**, 993–998, <https://doi.org/10.1038/s41558-019-0613-7>.
- Thornton, J. A., K. S. Virts, R. H. Holzworth, and T. P. Mitchell, 2017: Lightning enhancement over major shipping lanes. *Geophys. Res. Lett.*, **44**, 9102–9111, <https://doi.org/10.1002/2017GL074982>.
- Toffolon, M., S. Piccolroaz, and E. Calamita, 2020: On the use of averaged indicators to assess lakes' thermal response to changes in climatic conditions. *Environ. Res. Lett.*, **15**, 034060, <https://doi.org/10.1088/1748-9326/ab763e>.
- Toreti, A., and Coauthors, 2022: Drought in China September 2022. GDO Analytical Rep. EUR 31245 EN, JRC130850, 33 pp., <https://doi.org/10.2760/377056>.

- Torralla, V., F. J. Doblas-Reyes, and N. Gonzalez-Reviriegol, 2017: Uncertainty in recent near-surface wind speed trends: A global reanalysis intercomparison. *Environ. Res. Lett.*, **12**, 114019, <https://doi.org/10.1088/1748-9326/aa8a58>.
- United Nations Environment Programme, 2021: Global methane assessment: Benefits and costs of mitigating methane emissions. United Nations Environment Programme and Climate and Clean Air Coalition Rep., 172 pp., <https://www.unep.org/resources/report/global-methane-assessment-benefits-and-costs-mitigating-methane-emissions>.
- Utrabo-Carazo, E., C. Azorin-Molina, E. Serrano-Navarro, E. Aguilar, M. Brunet, and J. A. Guijarro, 2022: Wind stilling ceased in the Iberian Peninsula since the 2000s, 1961–2019. *Atmos. Res.*, **272**, 106153, <https://doi.org/10.1016/j.atmosres.2022.106153>.
- van der A, R. J., Allaart, M. A. F., and Eskes, H. J., 2015: Extended and refined multi sensor reanalysis of total ozone for the period 1970–2012. *J. Geophys. Res.*, **120**, 3021–3035, <https://doi.org/10.5194/amt-8-3021-2015>.
- Vanderkelen, I., N. P. M. Van Lipzig, and W. Thiery, 2018: Modelling the water balance of Lake Victoria (East Africa)-Part 2: Future projections. *Hydrol. Earth Syst. Sci.*, **22**, 5527–5549, <https://doi.org/10.5194/hess-22-5527-2018>.
- van der Schalie, R., and Coauthors, 2017: The merging of radiative transfer-based surface soil moisture data from SMOS and AMSR-E. *Remote Sens. Environ.*, **189**, 180–193, <https://doi.org/10.1016/j.rse.2016.11.026>.
- , and Coauthors, 2022: Soil moisture [in “State of the Climate in 2021”]. *Bull. Amer. Meteor. Soc.*, **103** (8), 564–566, <https://doi.org/10.1175/BAMS-D-22-0092.1>.
- van der Schrier, G., J. Barichivich, K. R. Briffa, and P. D. Jones, 2013: A scPDSI-based global dataset of dry and wet spells for 1901–2009. *J. Geophys. Res. Atmos.*, **118**, 4025–4048, <https://doi.org/10.1002/jgrd.50355>.
- van der Werf, G. R., and Coauthors, 2017: Global fire emissions estimates during 1997–2016. *Earth Syst. Sci. Data*, **9**, 697–720, <https://doi.org/10.5194/essd-9-697-2017>.
- Vargin, P. N., A. V. Koval, and V. V. Guryanov, 2022: Arctic stratosphere dynamical processes in the winter 2021–2022. *Atmosphere*, **13**, 1550, <https://doi.org/10.3390/atmos13101550>.
- Veccilio, D. J., S. T. Wolf, R. M. Cottle, and W. M. Kenney, 2022: Evaluating the 35°C wet-bulb temperature adaptability threshold for young, healthy subjects (PSU HEAT Project). *J. Appl. Physiol.*, **132**, 340–345, <https://doi.org/10.1152/jappphysiol.00738.2021>.
- Velasco, I., and J. M. Fritsch, 1987: Mesoscale convective complexes in the Americas. *J. Geophys. Res.*, **92**, 9591–9613, <https://doi.org/10.1029/JD092iD08p09591>.
- Virts, K., T. Lang, D. Buechler, and P. Bitzer, 2023: Bayesian analysis of the detection performance of the lightning imaging sensors. *11th Conf. on the Meteorological Application of Lightning Data*, Denver, CO, Amer. Meteor. Soc., 12 pp., https://ntrs.nasa.gov/api/citations/20220019219/downloads/2023_AMS_LIS_absde_final.pdf.
- Vivero, S., X. Bodin, D. Farías-Barahona, S. MacDonell, N. Schaffer, B. A. Robson, and C. Lambiel, 2021: Combination of aerial, satellite, and UAV photogrammetry for quantifying rock glacier kinematics in the dry Andes of Chile (30°S) since the 1950s. *Front. Remote Sens.*, **2**, 784015, <https://doi.org/10.3389/frsen.2021.784015>.
- Vömel, H., S. Evan, and M. Tully, 2022: Water vapor injection into the stratosphere by Hunga Tonga-Hunga Ha’apai. *Science*, **377**, 1444–1447, <https://doi.org/10.1126/science.abq2299>.
- Vose, R. S., and Coauthors, 2021: Implementing full spatial coverage in NOAA’s global temperature analysis. *Geophys. Res. Lett.*, **48**, e2020GL090873, <https://doi.org/10.1029/2020GL090873>.
- Vreugdenhil, M., S. Hahn, T. Melzer, B. Bauer-Marschallinger, C. Reimer, W. Dorigo, and W. Wagner, 2017: Assessing vegetation dynamics over mainland Australia with Metop ASCAT. *IEEE J. Sel. Top. Appl. Earth Obs. Remote Sens.*, **10**, 2240–2248, <https://doi.org/10.1109/JSTARS.2016.2618838>.
- Wang, H., and Coauthors, 2022: Global tropospheric ozone trends, attributions, and radiative impacts in 1995–2017: An integrated analysis using aircraft (IAGOS) observations, ozonesonde, and multi-decadal chemical model simulations. *Atmos. Chem. Phys.*, **22**, 13 753–13 782, <https://doi.org/10.5194/acp-22-13753-2022>.
- Wang, Q., Z. Li, J. Guo, C. Zhao, and M. Cribb, 2018: The climate impact of aerosols on lightning: Is it detectable from long-term aerosol and meteorological data? *Atmos. Chem. Phys.*, **18**, 12 797–12 816, <https://doi.org/10.5194/acp-18-12797-2018>.
- Wang, X., and Coauthors, 2022: Stratospheric climate anomalies and ozone loss caused by the Hunga Tonga volcanic eruption. ESS Open Archive, <https://essopenarchive.org/doi/full/10.1002/essoar.10512922.1>.
- Wang, Z., and Coauthors, 2021: Incorrect Asian aerosols affecting the attribution and projection of regional climate change in CMIP6 models. *npj Climate Atmos. Sci.*, **4**, 2, <https://doi.org/10.1038/s41612-020-00159-2>.
- Weatherhead, E. C., and Coauthors, 1998: Factors affecting the detection of trends: Statistical considerations and applications to environmental data. *J. Geophys. Res.*, **103**, 17 149–17 161, <https://doi.org/10.1029/98JD00995>.
- Weber, M., and Coauthors, 2022: Global total ozone recovery trends attributed to ozone-depleting substance (ODS) changes derived from five merged ozone datasets. *Atmos. Chem. Phys.*, **22**, 6843–6859, <https://doi.org/10.5194/acp-22-6843-2022>.
- Wells, N., S. Goddard, and M. J. Hayes, 2004: A self-calibrating Palmer drought severity index. *J. Climate*, **17**, 2335–2351, [https://doi.org/10.1175/1520-0442\(2004\)0172.0.CO;2](https://doi.org/10.1175/1520-0442(2004)0172.0.CO;2).
- Wentz, F. J., 1997: A well calibrated ocean algorithm for Special Sensor Microwave/Imager. *J. Geophys. Res.*, **102**, 8703–8718, <https://doi.org/10.1029/96JC01751>.
- , 2015: A 17-year climate record of environmental parameters derived from the Tropical Rainfall Measuring Mission (TRMM) microwave imager. *J. Climate*, **28**, 6882–6902, <https://doi.org/10.1175/JCLI-D-15-0155.1>.
- , L. Ricciardulli, K. Hilburn, and C. Mears, 2007: How much more rain will global warming bring? *Science*, **317**, 233–235, <https://doi.org/10.1126/science.1140746>.
- WGMS, 2021: Global Glacier Change Bulletin No. 4 (2018-2019). M. Zemp et al., Eds., ISC(WDS)/IUGG(IACS)/UNEP/UNESCO/WMO, World Glacier Monitoring Service, 278 pp., <https://doi.org/10.5904/wgms-fog-2021-05>.
- Wielicki, B. A., B. R. Barkstrom, E. F. Harrison, R. B. Lee III, G. L. Smith, and J. E. Cooper, 1996: Clouds and the Earth’s Radiant Energy System (CERES): An Earth observing system experiment. *Bull. Amer. Meteor. Soc.*, **77**, 853–868, [https://doi.org/10.1175/1520-0477\(1996\)0772.0.CO;2](https://doi.org/10.1175/1520-0477(1996)0772.0.CO;2).
- , and Coauthors, 1998: Clouds and the Earth’s Radiant Energy System (CERES): Algorithm overview. *IEEE Trans. Geosci. Remote Sens.*, **36**, 1127–1141, <https://doi.org/10.1109/36.701020>.
- Wiese, D. N., F. W. Landerer, and M. M. Watkins, 2016: Quantifying and reducing leakage errors in the JPL RL05M GRACE mascon solution. *Water Resour. Res.*, **52**, 7490–7502, <https://doi.org/10.1002/2016WR019344>.

- Wild, B., I. Teubner, L. Moesinger, R.-M. Zotta, M. Forkel, R. van der Schalie, S. Sitch, and W. Dorigo, 2022: VODCA2GPP—A new, global, long-term (1988–2020) gross primary production dataset from microwave remote sensing. *Earth Syst. Sci. Data*, **14**, 1063–1085, <https://doi.org/10.5194/essd-14-1063-2022>.
- Willett, K., 2023a: HadISDH.extremes Part 1: A gridded wet bulb temperature extremes index product for climate monitoring. *Adv. Atmos. Sci.*, <http://www.iapjournals.ac.cn/aas/en/article/doi/10.1007/s00376-023-2347-8>, in press.
- , 2023b: HadISDH.extremes Part 2: Exploring humid heat extremes using wet bulb temperature indices. *Adv. Atmos. Sci.*, <http://www.iapjournals.ac.cn/aas/en/article/doi/10.1007/s00376-023-2348-7>, in press..
- , C. N. Williams Jr., R. J. H. Dunn, P. W. Thorne, S. Bell, M. de Podesta, P. D. Jones, and D. E. Parker, 2013: HadISDH: An updated land surface specific humidity product for climate monitoring. *Climate Past*, **9**, 657–677, <https://doi.org/10.5194/cp-9-657-2013>.
- , R. J. H. Dunn, P. W. Thorne, S. Bell, M. de Podesta, D. E. Parker, P. D. Jones, and C. N. Williams Jr., 2014: HadISDH land surface multi-variable humidity and temperature record for climate monitoring. *Climate Past*, **10**, 1983–2006, <https://doi.org/10.5194/cp-10-1983-2014>.
- Williams, E. R., 1992: The Schumann resonance: A global tropical thermometer. *Science*, **256**, 1184–1187, <https://doi.org/10.1126/science.256.5060.1184>.
- , 2020: Lightning and climate change. *Fundamentals and Modelling*, Vol. 1, *Lightning Interaction with Power Systems*, A. Piantini, Ed., CRC Press, 1–46, https://doi.org/10.1049/PB-P0172F_ch1.
- , A. Guha, R. Boldi, H. Christian, and D. Buechler, 2019: Global lightning activity and the hiatus in global warming. *J. Atmos. Sol.-Terr. Phys.*, **189**, 27–34, <https://doi.org/10.1016/j.jastp.2019.03.011>.
- , and Coauthors, 2020: Evolution of global lightning in the transition from cold to warm phase preceding two super El Niño events. *J. Geophys. Res. Atmos.*, **126**, e2020JD033526, <https://doi.org/10.1029/2020JD033526>.
- WMO, 2018: Scientific assessment of ozone depletion, 2018. Global Ozone Research and Monitoring Project Rep. 58, 588 pp., <https://csl.noaa.gov/assessments/ozone/2018>.
- , 2022: Scientific assessment of ozone depletion: 2022. GAW Rep. 278, 509 pp., <https://ozone.unep.org/sites/default/files/2023-02/Scientific-Assessment-of-Ozone-Depletion-2022.pdf>.
- Wohland, J., N.-E. Omrani, D. Witthaut, and N.-S. Keenlyside, 2019: Inconsistent wind speed trends in current twentieth century reanalyses. *J. Geophys. Res. Atmos.*, **124**, 1931–1940, <https://doi.org/10.1029/2018JD030083>.
- Wolter, K., and M. S. Timlin, 1998: Measuring the strength of ENSO events – How does 1997/98 rank? *Weather*, **53**, 315–324, <https://doi.org/10.1002/j.1477-8696.1998.tb06408.x>.
- Woolway, R. I., and C. J. Merchant, 2018: Intralake heterogeneity of thermal responses to climate change: A study of large Northern Hemisphere lakes. *J. Geophys. Res. Atmos.*, **123**, 3087–3098, <https://doi.org/10.1002/2017JD027661>.
- , B. M. Kraemer, J. D. Lenters, C. J. Merchant, C. M. O'Reilly, and S. Sharma, 2020: Global lake responses to climate change. *Nat. Rev. Earth Environ.*, **1**, 388–403, <https://doi.org/10.1038/s43017-020-0067-5>.
- Worden, J. R., A. A. Bloom, S. Pandey, Z. Jiang, H. M. Worden, T. W. Walker, S. Houweling, and T. Röckmann, 2017: Reduced biomass burning emissions reconcile conflicting estimates of the post-2006 atmospheric methane budget. *Nat. Commun.*, **8**, 2227, <https://doi.org/10.1038/s41467-017-02246-0>.
- Yeh, and Coauthors, 2018: ENSO atmospheric teleconnections and their response to greenhouse gas forcing. *Rev. Geophys.*, **56**, 185–206, <https://doi.org/10.1002/2017RG000568>.
- Yook, S., D. W. J. Thompson, and S. Solomon, 2022: Climate impacts and potential drivers of the unprecedented Antarctic ozone holes of 2020 and 2021. *Geophys. Res. Lett.*, **49**, e2022GL098064, <https://doi.org/10.1029/2022GL098064>.
- Yosef, Y., E. Aguilar, and P. Alpert, 2021: Is it possible to fit extreme climate change indices together seamlessly in the era of accelerated warming? *Int. J. Climatol.*, **41**, E952–E963, <https://doi.org/10.1002/joc.6740>.
- Yoshida, S., T. Morimoto, T. Ushio, and Z. Kawasaki, 2007: ENSO and convective activities in Southeast Asia and western Pacific. *Geophys. Res. Lett.*, **34**, L21806, <https://doi.org/10.1029/2007GL030758>.
- Yu, B., X. Zhang, G. Li, and W. Yu, 2022: Interhemispheric asymmetry of climate change projections of boreal winter surface winds in CanESM5 large ensemble simulations. *Climatic Change*, **170**, 23, <https://doi.org/10.1007/s10584-022-03313-2>.
- Zeng, Z., and Coauthors, 2019: A reversal in global terrestrial stilling and its implications for wind energy production. *Nat. Climate Change*, **9**, 979–985, <https://doi.org/10.1038/s41558-019-0622-6>.
- Zhang, G., W. Luo, W. Chen, and G. Zheng, 2019: A robust but variable lake expansion on the Tibetan Plateau. *Sci. Bull.*, **64**, 1306–1309, <https://doi.org/10.1016/j.scib.2019.07.018>.
- Zhang, G. F., and Coauthors 2021: Uneven warming likely contributed to declining near-surface wind speeds in northern China between 1961 and 2016. *J. Geophys. Res. Atmos.*, **126**, e2020JD033637, <https://doi.org/10.1029/2020JD033637>.
- Zhang, R., H. Wang, Q. Fu, P. J. Rasch, and X. Wang, 2019: Unraveling driving forces explaining significant reduction in satellite-inferred Arctic surface albedo since the 1980s. *Proc. Natl. Acad. Sci. USA*, **116**, 23 947–23 953, <https://doi.org/10.1073/pnas.1915258116>.
- Zhang, X., L. Alexander, G. C. Hegerl, P. Jones, A. K. Tank, T. C. Peterson, B. Trewin, and F. W. Zwiers, 2011: Indices for monitoring changes in extremes based on daily temperature and precipitation data. *Wiley Interdiscip. Rev.: Climate Change*, **2**, 851–870, <https://doi.org/10.1002/wcc.147>.
- Zhang, Y., and Coauthors, 2016: Multi-decadal trends in global terrestrial evapotranspiration and its components. *Sci. Rep.*, **5**, 19124, <https://doi.org/10.1038/srep19124>.
- Zhao, G., Y. Li, L. Zhou, and H. Gao, 2022: Evaporative water loss of 1.42 million global lakes. *Nat. Commun.*, **13**, 3686, <https://doi.org/10.1038/s41467-022-31125-6>.
- Zhao, L., and Coauthors, 2020: Changing climate and the permafrost environment on the Qinghai–Tibet (Xizang) Plateau. *Permafrost Periglacial Processes*, **31**, 396–405, <https://doi.org/10.1002/ppp.2056>.
- Zheng, B., and Coauthors, 2019: Global atmospheric carbon monoxide budget 2000–2017 inferred from multi-species atmospheric inversions. *Earth Syst. Sci. Data*, **11**, 1411–1436, <https://doi.org/10.5194/essd-11-1411-2019>.
- , and Coauthors, 2023: Record-high CO₂ emissions from boreal fires in 2021. *Science*, **379**, 912–917, <https://doi.org/10.1126/science.ade0805>.

- Zhu, Y., and Coauthors, 2022: Perturbations in stratospheric aerosol evolution due to the water rich plume of the 2022 Hunga-Tonga eruption. *Commun. Earth Environ*, **3**, 248, <https://doi.org/10.1038/s43247-022-00580-w>.
- Ziemke, J. R., and Coauthors, 2019: Trends in global tropospheric ozone inferred from a composite record of TOMS/OMI/MLS/OMPS satellite measurements and the MERRA-2 GMI simulation. *Atmos. Chem. Phys.*, **19**, 3257–3269, <https://doi.org/10.5194/acp-19-3257-2019>.
- Ziese, M., A. Rauthe-Schöch, A. Becker, P. Finger, E. Rustemeier, S. Hänsel, U. Schneider, 2022: GPCP full data daily version 2022 at 1.0°: Daily land-surface precipitation from rain-gauges built on GTS-based and historic data. DWD, accessed 24 July 2023, https://doi.org/10.5676/DWD_GPCC/FD_D_V2022_100.
- Zipser, E. J., C. Liu, D. J. Cecil, S. W. Nesbitt, and D. P. Yorty, 2006: Where are the most intense thunderstorms on Earth? *Bull. Amer. Meteor. Soc.*, **87**, 1057–1071, <https://doi.org/10.1175/BAMS-87-8-1057>.
- Zou, C.-Z., H. Xu, X. Hao, and Q. Fu, 2021: Post-millennium atmospheric temperature trends observed from satellites in stable orbits. , **48**, e2021GL093291, <https://doi.org/10.1029/2021GL093291>.
- , —, —, and Q. Liu, 2023: Mid-tropospheric layer temperature record derived from satellite microwave sounder observations with backward merging approach. *J. Geophys. Res. Atmos.*, **128**, e2022JD037472, <https://doi.org/10.1029/2022JD037472>.

STATE OF THE CLIMATE IN 2022

GLOBAL OCEANS

G. C. Johnson and R. Lumpkin, Eds.



Special Online Supplement to the *Bulletin of the American Meteorological Society* Vol. 104, No. 9, September, 2023

<https://doi.org/10.1175/BAMS-D-23-0076.2>

Corresponding author: Greg C. Johnson / Gregory.C.Johnson@noaa.gov

©2023 American Meteorological Society

For information regarding reuse of this content and general copyright information, consult the [AMS Copyright Policy](#).

STATE OF THE CLIMATE IN 2022

Global Oceans

Editors

Ellen Bartow-Gillies
Jessica Blunden
Tim Boyer

Chapter Editors

Peter Bissolli
Kyle R. Clem
Howard J. Diamond
Matthew L. Druckenmiller
Robert J. H. Dunn
Catherine Ganter
Nadine Gobron
Gregory C. Johnson
Rick Lumpkin
Ademe Mekonnen
John B. Miller
Twila A. Moon
Marilyn N. Raphael
Ahira Sánchez-Lugo
Carl J. Schreck III
Richard L. Thoman
Kate M. Willett
Zhiwei Zhu

Technical Editor

Lukas Noguchi

BAMS Special Editor for Climate

Michael A. Alexander

American Meteorological Society

Cover Credit:

Surf's Up by Gregory C. Johnson. Livestock Marker on Oil Paper

How to cite this document:

Global Oceans is one chapter from the *State of the Climate in 2022* annual report and is available from <https://doi.org/10.1175/BAMS-D-23-0076.2>. Compiled by NOAA's National Centers for Environmental Information, *State of the Climate in 2022* is based on contributions from scientists from around the world. It provides a detailed update on global climate indicators, notable weather events, and other data collected by environmental monitoring stations and instruments located on land, water, ice, and in space. The full report is available from <https://doi.org/10.1175/2023BAMSStateoftheClimate.1>.

Citing the complete report:

Blunden, J., T. Boyer, and E. Bartow-Gillies, Eds., 2023: "State of the Climate in 2022". Bull. Amer. Meteor. Soc., 104 (9), Si–S501 <https://doi.org/10.1175/2023BAMSStateoftheClimate.1>.

Citing this chapter:

Johnson, G. C. and R. Lumpkin, Eds., 2023: Global Oceans [in "State of the Climate in 2022"]. Bull. Amer. Meteor. Soc., 104 (9), S146–S206, <https://doi.org/10.1175/BAMS-D-23-0076.2>.

Citing a section (example):

Thompson, P. R., M. J. Widlansky, E. Leuliette, D. P. Chambers, W. Sweet, B. D. Hamlington, S. Jevrejeva, M. A. Merrifield, G. T. Mitchum, and R. S. Nerem, 2023: Sea-level variability and change [in "State of the Climate in 2022"]. Bull. Amer. Meteor. Soc., 104 (9), S173–S176, <https://doi.org/10.1175/BAMS-D-23-0076.2>.

Editor and Author Affiliations (alphabetical by name)

- Atkinson, C.**, Met Office Hadley Center, Exeter, United Kingdom
- Biló, Tiago**, Cooperative Institute for Marine and Atmospheric Studies, University of Miami, Miami, Florida; NOAA/OAR Atlantic Oceanographic and Meteorological Laboratory, Miami, Florida
- Boyer, Tim**, NOAA/NESDIS National Centers for Environmental Information, Silver Spring, Maryland
- Bringas, Francis**, NOAA/OAR Atlantic Oceanographic and Meteorological Laboratory, Miami, Florida
- Carter, Brendan R.**, Cooperative Institute for Climate, Ocean, and Ecosystem Studies, University of Washington, Seattle, Washington; NOAA/OAR Pacific Marine Environmental Laboratory, Seattle, Washington
- Cetinić, Ivona**, NASA Goddard Space Flight Center, Greenbelt, Maryland; Morgan State University, Baltimore, Maryland
- Chambers, Don P.**, College of Marine Science, University of South Florida, St. Petersburg, Florida
- Chan, Duo**, Woods Hole Oceanographic Institution, Woods Hole, Massachusetts
- Cheng, Lijing**, International Center for Climate and Environment Sciences, Institute of Atmospheric Physics, Chinese Academy of Sciences, Beijing, China
- Chomiak, Leah**, Cooperative Institute for Marine and Atmospheric Studies, University of Miami; NOAA/OAR Atlantic Oceanographic and Meteorological Laboratory, Miami, Florida; Rosenstiel School of Marine, Atmospheric, and Earth Science, University of Miami, Miami, Florida
- Cronin, Meghan F.**, NOAA/OAR Pacific Marine Environmental Laboratory, Seattle, Washington
- Dong, Shenfu**, NOAA/OAR Atlantic Oceanographic and Meteorological Laboratory, Miami, Florida
- Feely, Richard A.**, NOAA/OAR Pacific Marine Environmental Laboratory, Seattle, Washington
- Franz, Bryan A.**, NASA Goddard Space Flight Center, Greenbelt, Maryland
- Gao, Meng**, NASA Goddard Space Flight Center, Greenbelt, Maryland; Science Systems and Applications Inc., Lanham, Maryland
- Garg, Jay**, Science Systems and Applications Inc., Hampton, Virginia
- Gilson, John**, Scripps Institution of Oceanography, University of California San Diego, La Jolla, California
- Goni, Gustavo**, NOAA/OAR Atlantic Oceanographic and Meteorological Laboratory, Miami, Florida
- Hamlington, Benjamin D.**, Center for Coastal Physical Oceanography, Old Dominion University, Norfolk, Virginia
- Hobbs, W.**, Australian Antarctic Program Partnership, Institute for Marine and Antarctic Studies; Australian Research Council Centre of Excellence for Climate Extremes, University of Tasmania, Hobart, Tasmania
- Hu, Zeng-Zhen**, NOAA/NWS National Centers for Environmental Prediction Climate Prediction Center, College Park, Maryland
- Huang, Boyin**, NOAA/NESDIS National Centers for Environmental Information, Asheville, North Carolina
- Ishii, Masayoshi**, Department of Atmosphere, Ocean and Earth System Modeling Research, Meteorological Research Institute, Japan Meteorological Agency, Tsukuba, Japan
- Jevrejeva, Svetlana**, National Oceanography Centre, Liverpool, United Kingdom
- Johns, W.**, Rosenstiel School of Marine, Atmospheric, and Earth Science, University of Miami, Miami, Florida
- Johnson, Gregory C.**, NOAA/OAR Pacific Marine Environmental Laboratory, Seattle, Washington
- Landschützer, Peter**, Flanders Marine Institute, InnovOcean Campus, Ostend, Belgium
- Lankhorst, Matthias**, Scripps Institution of Oceanography, University of California San Diego, La Jolla, California
- Leuliette, Eric**, NOAA/NWS NCWCP Laboratory for Satellite Altimetry, College Park, Maryland
- Locarnini, Ricardo**, NOAA/NESDIS National Centers for Environmental Information, Silver Spring, Maryland
- Lumpkin, Rick**, NOAA/OAR Atlantic Oceanographic and Meteorological Laboratory, Miami, Florida
- Lyman, John M.**, Cooperative Institute for Marine and Atmospheric Research, University of Hawaii, Honolulu, Hawaii; NOAA/OAR Pacific Marine Environmental Laboratory, Seattle, Washington
- McPhaden, Michael J.**, NOAA/OAR Pacific Marine Environmental Laboratory, Seattle, Washington
- Merrifield, Mark A.**, Cooperative Institute for Marine and Atmospheric Research, University of Hawaii, Honolulu, Hawaii
- Mishonov, Alexey**, Earth System Science Interdisciplinary Center/Cooperative Institute for Satellite Earth System Studies Maryland, University of Maryland, College Park, Maryland; NOAA/NESDIS National Centers for Environmental Information, Silver Spring, Maryland
- Mitchum, Gary T.**, College of Marine Science, University of South Florida, St. Petersburg, Florida
- Moat, Ben I.**, National Oceanography Centre, Southampton, United Kingdom
- Mrekaj, Ivan**, Technical University in Zvolen, Zvolen, Slovakia
- Nerem, R. Steven**, Colorado Center for Astrodynamic Research, Cooperative Institute for Research in Environmental Sciences, University of Colorado Boulder, Boulder, Colorado
- Purkey, Sarah G.**, Scripps Institution of Oceanography, University of California San Diego, La Jolla, California
- Qiu, Bo**, Department of Oceanography, University of Hawaii at Manoa, Honolulu, Hawaii
- Reagan, James**, NOAA/NESDIS National Centers for Environmental Information, Silver Spring, Maryland
- Sato, Katsunari**, Japan Meteorological Agency, Tokyo, Japan
- Schmid, Claudia**, NOAA/OAR Atlantic Oceanographic and Meteorological Laboratory, Miami, Florida
- Sharp, Jonathan D.**, Cooperative Institute for Climate, Ocean, and Ecosystem Studies, University of Washington, Seattle, Washington; NOAA/OAR Pacific Marine Environmental Laboratory, Seattle, Washington
- Siegel, David A.**, University of California, Santa Barbara, Santa Barbara, California
- Smeed, David A.**, National Oceanography Centre, Southampton, United Kingdom
- Stackhouse Jr., Paul W.**, NASA Langley Research Center, Hampton, Virginia
- Sweet, William**, NOAA/NOS Center for Operational Oceanographic Products and Services, Silver Spring, Maryland
- Thompson, Philip R.**, Cooperative Institute for Marine and Atmospheric Research, University of Hawaii, Honolulu, Hawaii
- Triñanes, Joaquin A.**, Laboratory of Systems, Technological Research Institute, Universidad de Santiago de Compostela, Campus Universitario Sur, Santiago de Compostela, Spain; Cooperative Institute for Marine and Atmospheric Studies, Rosenstiel School of Marine and Atmospheric Science, University of Miami, Miami, Florida; NOAA/OAR Atlantic Oceanographic and Meteorological Laboratory, Miami, Florida
- Volkov, Denis L.**, Cooperative Institute for Marine and Atmospheric Studies, University of Miami; NOAA/OAR Atlantic Oceanographic and Meteorological Laboratory, Miami, Florida
- Wanninkhof, Rik**, NOAA/OAR Atlantic Oceanographic and Meteorological Laboratory, Miami, Florida
- Wen, Caihong**, NOAA/NWS National Centers for Environmental Prediction Climate Prediction Center, College Park, Maryland
- Westberry, Toby K.**, Oregon State University, Corvallis, Oregon
- Widlansky, Matthew J.**, Cooperative Institute for Marine and Atmospheric Research, University of Hawaii, Honolulu, Hawaii

Editor and Author Affiliations (continued)

Willis, J., Jet Propulsion Laboratory, California Institute of Technology, Pasadena, California
Xie, Ping-Ping, NOAA/NWS National Centers for Environmental Prediction Climate Prediction Center, College Park, Maryland
Yin, Xungang, NOAA/NESDIS National Centers for Environmental Information, Asheville, North Carolina

Zhang, Huai-min, NOAA/NESDIS National Centers for Environmental Information, Asheville, North Carolina
Zhang, Li, NOAA/NWS National Centers for Environmental Prediction Climate Prediction Center, College Park, Maryland; ERT, Laurel, Maryland

Editorial and Production Team

Allen, Jessica, Graphics Support, Cooperative Institute for Satellite Earth System Studies, North Carolina State University, Asheville, North Carolina
Camper, Amy V., Graphics Support, Innovative Consulting and Management Services, LLC, NOAA/NESDIS National Centers for Environmental Information, Asheville, North Carolina
Haley, Bridgette O., Graphics Support, NOAA/NESDIS National Centers for Environmental Information, Asheville, North Carolina
Hammer, Gregory, Content Team Lead, Communications and Outreach, NOAA/NESDIS National Centers for Environmental Information, Asheville, North Carolina
Love-Brotak, S. Elizabeth, Lead Graphics Production, NOAA/NESDIS National Centers for Environmental Information, Asheville, North Carolina

Ohlmann, Laura, Technical Editor, Innovative Consulting and Management Services, LLC, NOAA/NESDIS National Centers for Environmental Information, Asheville, North Carolina
Noguchi, Lukas, Technical Editor, Innovative Consulting and Management Services, LLC, NOAA/NESDIS National Centers for Environmental Information, Asheville, North Carolina
Riddle, Deborah B., Graphics Support, NOAA/NESDIS National Centers for Environmental Information, Asheville, North Carolina
Veasey, Sara W., Visual Communications Team Lead, Communications and Outreach, NOAA/NESDIS National Centers for Environmental Information, Asheville, North Carolina

3. Table of Contents

List of authors and affiliations	S149
a. Overview	S152
b. Sea-surface temperatures	S153
Sidebar 3.1: The 2020–22 triple-dip La Niña.....	S157
c. Ocean heat content	S159
d. Salinity	S163
1. Introduction.....	S163
2. Sea-surface salinity.....	S163
3. Subsurface salinity.....	S165
e. Global ocean heat, freshwater, and momentum fluxes	S168
1. Surface heat fluxes.....	S168
2. Surface freshwater fluxes.....	S170
3. Wind stress.....	S171
4. Long-term perspective.....	S172
f. Sea-level variability and change	S173
g. Surface currents	S177
1. Pacific Ocean.....	S177
2. Indian Ocean.....	S179
3. Atlantic Ocean.....	S179
h. Meridional overturning circulation and heat transport in the Atlantic Ocean	S181
i. Global ocean phytoplankton	S184
Sidebar 3.2: Tracking global ocean oxygen content.....	S189
j. Global ocean carbon cycle	S191
1. Introduction.....	S191
2. Air–sea carbon dioxide fluxes.....	S191
3. Ocean interior developments: Utilization of Argo.....	S194
Acknowledgments	S196
Appendix 1: Chapter 3 – Acronyms	S197
References	S199

Please refer to Chapter 8 (Relevant Datasets and Sources) for a list of all climate variables and datasets used in this chapter for analyses, along with their websites for more information and access to the data.

3. GLOBAL OCEANS

G. C. Johnson and R. Lumpkin, Eds.

a. Overview

—G. C. Johnson and R. Lumpkin

An unusual “triple-dip” La Niña, described in Sidebar 3.1, had continuing, wide-spread ramifications for the state of ocean and climate in 2022. Triple-dip La Niñas are not unprecedented, but until now have always followed an extreme El Niño. Anomalously low sea-surface temperatures (SSTs) in the eastern tropical Pacific persisted from August 2020 through December 2022, with only a brief intermission in May–July 2021. Strengthened easterly trade winds drove anomalously strong westward surface currents and brought cold waters to the surface in the eastern equatorial Pacific while also accumulating anomalously salty and warm waters in the western equatorial Pacific, raising sea level there. These cold upwelled waters resulted in anomalously large fluxes of carbon dioxide from the ocean to the atmosphere and heat from the atmosphere to the ocean, with anomalously high chlorophyll concentrations found around its edges. Fresh sea-surface salinity (SSS) anomalies strengthened off the equator in the Pacific as the Intertropical Convergence Zone (ITCZ) and South Pacific Convergence Zone and associated rainfall shifted poleward.

A negative phase of the Pacific Decadal Oscillation continued in 2022, with warm SST and high ocean heat content values in the center of the North Pacific basin, and colder and lower values around the edges. However, the North Pacific marginal seas, except the eastern Bering Sea, were anomalously warm. A persistent 2020–22 poleward shift in the Kuroshio extension was evident in both ocean heat content and zonal surface current anomalies.

The Indian Ocean dipole (IOD) was negative in 2022, with positive SST anomalies in the east and negative anomalies in the west. As expected with a negative IOD, upper-ocean heat content and sea-surface height were anomalously high in the east and lower (although still above the climatological means) in the west. With warm water in the east came an eastward shift in precipitation, yielding anomalously low SSS there and anomalously high SSS in the west.

In the Atlantic, SST, upper-ocean heat content, and sea level were all above average over much of the basin in 2022, with especially high values off the east coast of North America. The only location with both cold SST and low ocean heat content anomalies was southeast of Greenland, potentially a fingerprint of slowing meridional overturning circulation. Sea-surface salinity values were anomalously high in salty regions and anomalously low around the ITCZ, off the Amazon, and in the subpolar North Atlantic. All of this was similar to 2021 conditions in that basin.

As discussed in Sidebar 3.1, continued La Niña conditions through 2022 kept global annual average SST anomalies below record-high territory, but the last decade of SST is higher than any other in the observation period. In addition, from 2021 to 2022, annual average ocean heat content from 0 to 2000 dbar increased at a rate equivalent to $\sim 1.1 \text{ W m}^{-2}$ of energy applied over the ocean surface, and global sea level increased by $\sim 3.3 \text{ mm}$. Both set new record highs. In haiku form:

*Surface cooling from,
triple-dip La Niña but,
seas rise, absorb heat.*

In addition, the oceans absorbed anthropogenic carbon at a rate of $\sim 3.3 \text{ Pg C yr}^{-1}$ in 2022, 23% above the 1990–2020 average. The continued ocean uptake of heat and carbon dioxide delay and reduce atmospheric warming, respectively, but at the cost of sea-level rise, ocean warming and marine heatwaves, ocean acidification, and reduced ocean-dissolved oxygen concentrations, as discussed in Sidebar 3.2.

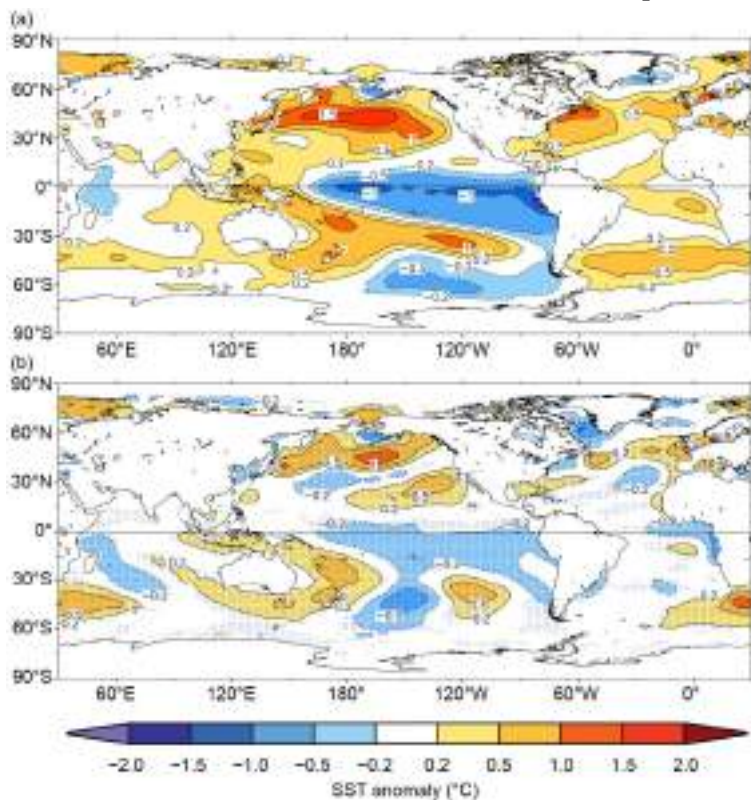
b. Sea-surface temperatures

—X. Yin, B. Huang, Z.-Z. Hu, D. Chan, and H.-M. Zhang

Sea-surface temperature (SST) changes and their uncertainties in 2022 are assessed over the global and individual ocean basins using three updated SST products: Extended Reconstruction SST version 5 (ERSSTv5; Huang et al. 2017, 2020), U.K. Met Office Hadley Centre SST (HadSST.4.0.1.0; Kennedy et al. 2019), and Daily Optimum Interpolation SST (DOISST v2.1; Huang et al. 2021a). SST anomalies (SSTAs) are calculated relative to their 1991–2020 baseline period climatologies. The magnitudes of SSTAs are compared against SST standard deviations (SD) over 1991–2020.

The year ended with the third La Niña winter in a row (see Sidebar 3.1). This prolonged La Niña resulted in a slowdown in the global ocean warming trend during 2020–22. Specifically, the 2022 global mean ERSSTv5 SSTA relative to a 1991–2020 baseline was $0.18 \pm 0.01^\circ\text{C}$, slightly higher than that of 2021 ($0.14 \pm 0.01^\circ\text{C}$), but lower than those of 2019 ($0.25 \pm 0.02^\circ\text{C}$) and 2020 ($0.23 \pm 0.01^\circ\text{C}$), the years prior to and at the beginning of the triple-dip La Niña. Despite the influence of La Niña, 2022 still ranked as the sixth-hottest year on record since 1854 in terms of global-mean SST, equal with 2018. Here, uncertainty, reported as 95% confidence intervals, is estimated by a Student's t-test using a 500-member ERSSTv5 ensemble with randomly drawn parameter values within reasonable ranges during SST reconstructions (Huang et al. 2015, 2020).

Annually averaged SSTAs in 2022 (Fig. 3.1a) exhibited a pattern typical of La Niña in the Pacific. In the central and eastern tropical Pacific, SSTAs were mostly lower than -0.5°C and



between -1.0°C and -1.5°C along the equator, extending from South America westward to the central Pacific. In the South Pacific, east of 170°W between 65°S and 45°S , SSTAs were between -0.2°C and -1.0°C . Between the two colder-than-normal regions and in the western Pacific, SSTs were mostly above normal by over 0.5°C . Except for the areas along the western North American coast, the North Pacific was dominated by positive SSTAs, particularly over the northwest region between 30°N and 50°N , where high SSTAs were observed between $+1.0^\circ\text{C}$ and $+2.0^\circ\text{C}$. The Atlantic Ocean was marked by positive SSTAs of between $+0.2^\circ\text{C}$ and $+1.0^\circ\text{C}$ in the North Atlantic and between $+0.2^\circ\text{C}$ and $+0.5^\circ\text{C}$ in the tropical and South Atlantic. In the tropical Indian Ocean, an Indian Ocean dipole (IOD; Saji et al. 1999) was formed with SSTAs between -0.2°C and -0.5°C in the west and between $+0.2^\circ\text{C}$ and $+0.5^\circ\text{C}$ in the east (see section 4f for details). The IOD index has been negative since May 2021 and was the strongest (-1.2°C in July 2022) since the 1920s. SSTAs above $+0.5^\circ\text{C}$ were observed in parts of the Arctic Ocean, particularly in the Barents Sea.

Fig. 3.1. (a) Annually averaged sea-surface temperature anomalies (SSTAs) in 2022 ($^\circ\text{C}$) and (b) difference of annually averaged SSTAs from the previous year (2022 minus 2021; $^\circ\text{C}$). Values are relative to 1991–2020 climatology and the SSTA difference is significant at 95% confidence in stippled areas.

The 2022-minus-2021 SSTAs show mixed localized patterns of increases and decreases (Fig. 3.1b). The lower cold-tongue SSTs and higher SSTs in the western Pacific around Australia indicate the strengthening of La Niña in 2022. Except for the western Pacific between 20°N and 40°N and in the Bering Sea, the North Pacific was mostly warmer in 2022 than 2021. The pronounced warming in the central and western North Pacific, more than +1.5°C around 45°N and 165°W, is consistent with a persistent negative phase of the Pacific Decadal Oscillation (Mantua and Hare 2002). In the Indian Ocean, there was no obvious SST change north of the equator (<0.2°C). Areas north and south of Australia and southeast of southern Africa showed warming of between +0.2°C and +1.0°C. Cooling of up to -0.5°C was seen in the area from the middle of the tropical southern Indian Ocean northwestward across Madagascar to the coast of equatorial East Africa. As a result, a negative IOD event lasting from May to October was observed in 2022.

Overall patterns of seasonal mean SSTAs (Fig. 3.2) are similar to the annual mean pattern (Fig. 3.1) due to the sustained La Niña event. The negative SSTAs in the central-eastern tropical Pacific persisted (-1.0°C to -1.5°C; 1 to 2 SDs below average) in all seasons, particularly in December–February (DJF) and September–November (SON). In the North Pacific, positive SSTAs were first seen in the central-western region across 45°N in DJF and continued getting stronger while expanding rapidly with nearly full coverage of the North Pacific during June–August (JJA) and SON. In the Indian Ocean, the negative IOD pattern peaked in JJA. The seasonal variability of SSTAs in the North Atlantic Ocean was high, with negative anomalies in the subarctic surrounding Greenland during March–May (MAM), but became overall positive during SON, with a center in the western midlatitude North Atlantic Ocean. The midlatitude Atlantic Ocean was warmer than normal throughout the year, with SSTAs largest during SON 2022 in the North Atlantic and DJF 2021/22 in the South Atlantic. SSTAs in the tropical Atlantic were only weakly

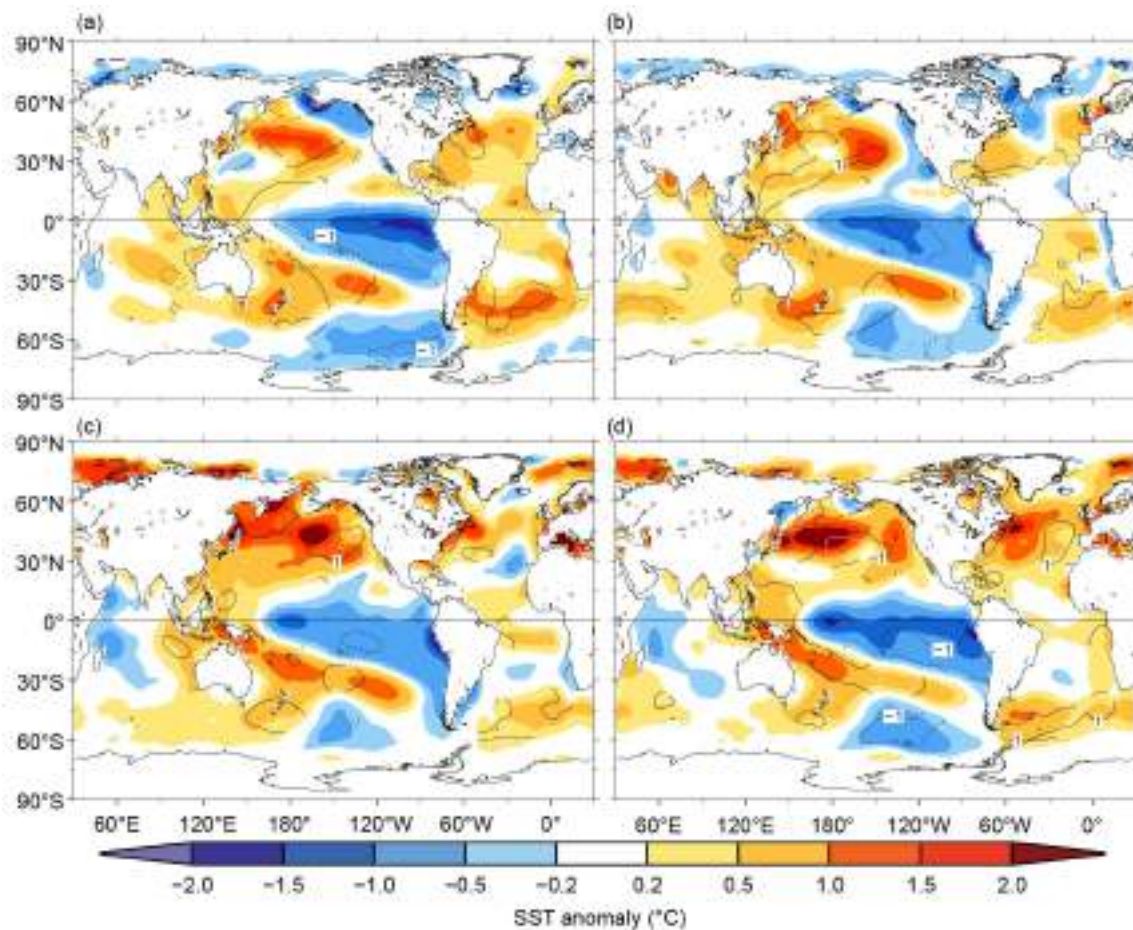


Fig. 3.2. Seasonally averaged sea-surface temperature anomalies (SSTAs) of ERSSTv5 (°C; shading) for (a) Dec 2021–Feb 2022, (b) Mar–May 2022, (c) Jun–Aug 2022, and (d) Sep–Nov 2022. The normalized seasonal mean SSTAs based on the seasonal mean standard deviation (1 SD) over 1991–2020 are indicated by contours of -2 (dashed white), -1 (dashed black), 1 (solid black), and 2 (solid white).

positive, and the Atlantic Niño index (ATL3; Zebiak 1993), which was greater than 0.5°C during May–December 2021, was below 0.5°C except in January and March 2022. SSTAs in the Arctic Ocean were slightly negative (−0.5°C to −0.2°C) in DJF and MAM but mostly positive (+0.5°C to +2.0°C) in JJA and SON.

In 2022, large positive SSTAs resulted in a series of marine heatwaves (Oliver et al. 2017; Perkins-Kirkpatrick et al. 2019; Babcock et al. 2019; Huang et al. 2021b) in various parts of the world. For example, in the Bay of Plenty, New Zealand, the country’s longest continuous marine heatwave was recorded (Moana Project 2022; Figs. 3.2a,b). Also, in the summer of 2022, the Mediterranean Sea observed record-setting marine heatwave events, increasing from the previous summer in duration, total surface area impacted, and intensity as per the Mercator Ocean International organization (Fig. 3.2c; see section 2b4 for more details on marine heatwaves).

Global-mean SSTs manifest the acceleration in global warming (Figs. 3.3a,b), with 9 years in the last decade included in the top 10 hottest years on record. Based on ERSSTv5 (Table 3.1; Fig. 3.3), from 1950 to 2022, the linear trend in global-mean SSTA was $0.10 \pm 0.01^\circ\text{C decade}^{-1}$. Regionally, warming was largest in the tropical Indian Ocean ($0.14 \pm 0.02^\circ\text{C decade}^{-1}$) and smallest in the North Pacific ($0.09 \pm 0.04^\circ\text{C decade}^{-1}$). In recent decades, trends in all areas have increased, and in some areas substantially. From 2000 to 2022, the global mean trend was $0.15 \pm 0.06^\circ\text{C decade}^{-1}$. In the North Pacific, the regional 1950–2022 trend was the smallest but became the largest ($0.40 \pm 0.12^\circ\text{C decade}^{-1}$) considering only the recent period from 2000 onward (Fig. 3.3d).

Large variations of North Atlantic annual mean SSTAs are evident at interannual to interdecadal time scales (Li et al. 2020; Fig. 3.3f). The interdecadal component is mainly associated with the Atlantic Multidecadal Variability (AMV; Schlesinger and Ramankutty 1994), also known as the Atlantic Multidecadal Oscillation. Some possible contributors to the AMV include aerosol emissions and variations in the strength of the Atlantic meridional overturning circulation (AMOC; Zhang et al. 2019; Wang and Yang 2017; section 3h). The North Atlantic experienced warm periods from the 1930s to the 1950s and from the late 1990s to the 2010s, and cold periods before 1930 and from the 1960s to the early 1990s (Li et al. 2020). SSTAs in the North Pacific (Fig. 3.3d) decreased from the 1960s to the late 1980s, followed by an increase from the later 1980s to the 2010s.

Table 3.1. Linear trends ($^\circ\text{C decade}^{-1}$) of annually and regionally averaged sea-surface temperature anomalies (SSTAs) from ERSSTv5, HadSST4.0.1.0, and DOISST. The uncertainties at a 95% confidence level are estimated while accounting for the effective degrees of freedom (sampling number) quantified using lag-1 autocorrelation of annual-mean SST time series.

Product	Region	2000–22	1950–2022
HadSST4.0.1.0	Global	0.17 ± 0.06	0.12 ± 0.02
DOISST	Global	0.19 ± 0.05	N/A
ERSSTv5	Global	0.15 ± 0.06	0.10 ± 0.01
ERSSTv5	Tropical Pacific (30°S–30°N)	0.11 ± 0.16	0.10 ± 0.02
ERSSTv5	North Pacific (30°N–60°N)	0.40 ± 0.12	0.09 ± 0.04
ERSSTv5	Tropical Indian (30°S–30°N)	0.17 ± 0.08	0.14 ± 0.02
ERSSTv5	North Atlantic (30°N–60°N)	0.18 ± 0.09	0.12 ± 0.04
ERSSTv5	Tropical Atlantic (30°S–30°N)	0.14 ± 0.08	0.11 ± 0.02
ERSSTv5	southern oceans (30°S–60°S)	0.13 ± 0.05	0.10 ± 0.02

ERSSTv5 was compared with HadSST.4.0.1.0 and DOISST v2.1. SSTA departures of DOISST and HadSST.4.0.1.0 from ERSSTv5 are largely within 2 SDs (gray shading in Fig. 3.3) except in the 1960s–1970s and before the 1910s. The 2-SD was derived from a 500-member ensemble analysis based on ERSSTv5 (Huang et al. 2020) and centered on SSTAs of ERSSTv5. During both the longer and shorter trend periods (Table 3.1), the warming trend of global SST in HadSST4.0.1.0 was consistent with those of ERSSTv5 but at a higher rate. In the 2000s–2010s, SSTAs were slightly higher in DOISST than in ERSSTv5 in the Southern Ocean, tropical Atlantic, tropical Indian Ocean, and tropical Pacific. As a result, SST trends were slightly larger in DOISST over 2000–22 than in ERSSTv5.

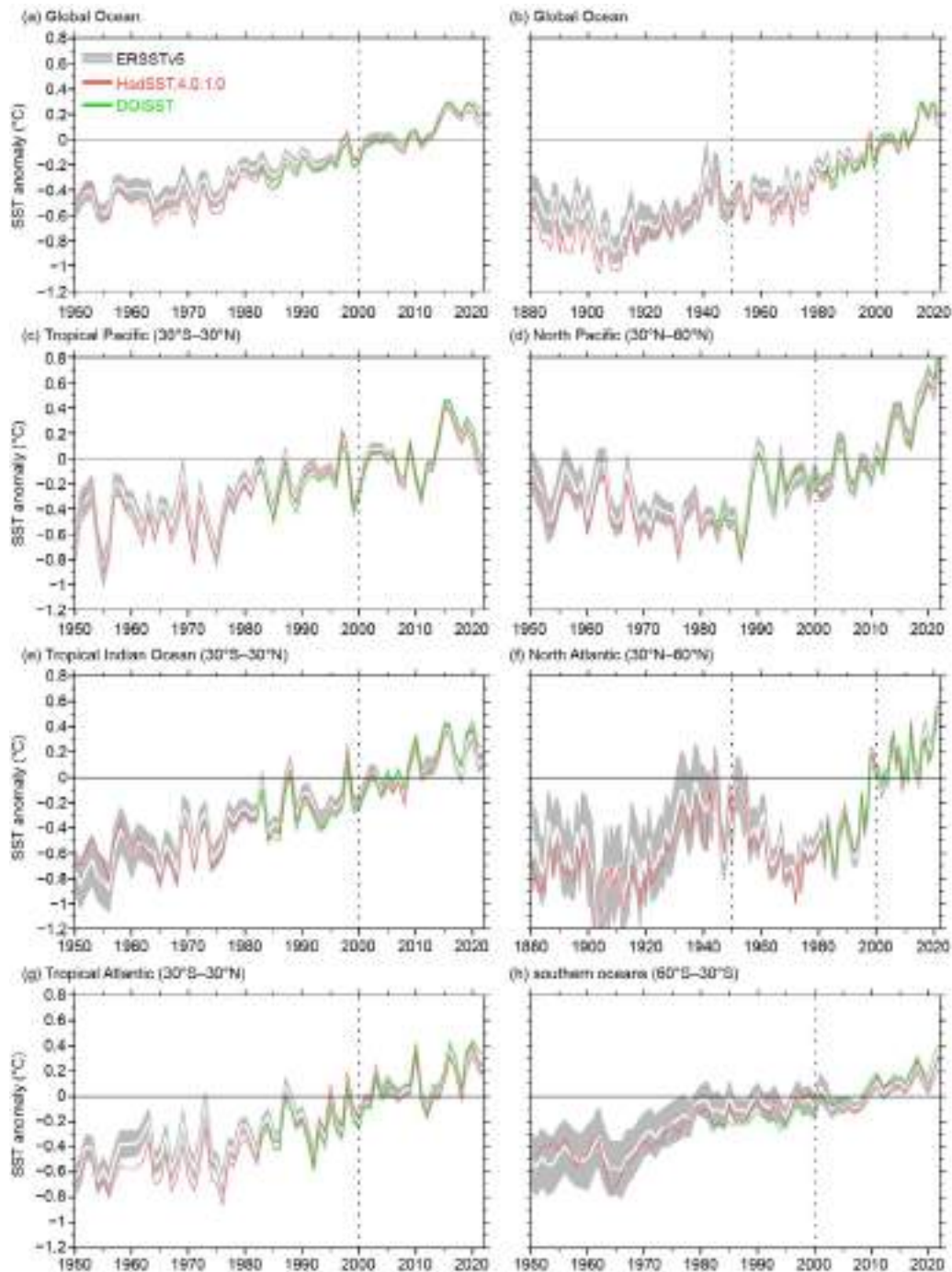


Fig. 3.3. Annually averaged sea-surface temperature anomalies (SSTAs; °C) of ERSSTv5, (solid white) and 2 standard deviations (SDs, gray shading) of ERSSTv5, SSTAs of HadSST.4.0.1.0 (solid red), and SSTAs of DOISST (solid green) in 1950–2022 except for (b) and (f). (a) Global, (b) global in 1880–2022, (c) tropical Pacific, (d) North Pacific, (e) tropical Indian, (f) North Atlantic in 1880–2022, (g) tropical Atlantic, and (h) southern oceans (30°S–60°S). The 2-SD envelope was derived from a 500-member ensemble analysis based on ERSSTv5 and centered to SSTAs of ERSSTv5. The years 2000 and 1950 are indicated by dotted vertical black lines.

Sidebar 3.1: The 2020–22 triple-dip La Niña

—M. J. MCPHADEN

The tropical Pacific experienced a third successive year of unusually cold sea-surface temperatures (SSTs) in 2022, making 2020–22 the first "triple-dip" La Niña of the twenty-first century (Fig. SB3.1a). Three-year La Niña events are rare but not unprecedented; similar events occurred in 1998–2001 and in 1973–76. Compared to single-year El Niño–Southern Oscillation (ENSO) events, such extended periods of anomalous SSTs in the tropical Pacific result in elevated risks from natural hazards because of the prolonged impacts these multi-year events have on patterns of weather variability world-wide. Back-to-back years of excessive rains in Australia, one of the most severe and extended droughts on record for the Horn of Africa, and exceptional drought in portions of the western United States during 2020–22 are just a few examples of how this multi-year La Niña affected the climate system. Moreover, these protracted La Niña conditions have occurred in the context of a warming world, so impacts have not only been felt over consecutive years but have also been compounded by human-caused climate change.

Below-normal SST anomalies first appeared in the eastern and central equatorial Pacific in August 2020 and, except for a brief period in May–July 2021, equatorial SSTs remained below the -0.5°C threshold considered to be an indicator of La Niña (Fig. SB3.1a). As illustrated for October–December 2022 (Figs. SB3.1b,c), associated with these below-normal SSTs is an intensified and westward-shifted Pacific Walker circulation characterized by stronger-than-normal surface trade winds (see Fig. 3.13a), unusually strong westerly winds in the upper troposphere, a westward shift in atmospheric deep convection, and a drying of the central equatorial Pacific. In addition, rain bands of both the Intertropical Convergence Zone in the Northern Hemisphere and the South Pacific Convergence Zone in the Southern Hemisphere were shifted poleward away from the unusually cold equatorial SSTs that favor suppressed convection. Heavy rains and flooding in Australia, Indonesia, and the Philippines and drought conditions in the island states of the central Pacific (see Fig. 3.12a) we direct consequences of these shifts in precipitation, prevalent not just in October–December 2022, but over much of the past three years. Anomalous atmospheric heating that accompanied this large-scale rearrangement in rainfall also drove far-field teleconnections to other parts of the globe (e.g., Taschetto et al. 2020), affecting many of the extreme weather events that were observed outside the tropical Pacific since late 2020.

A leading hypothesis for multi-year La Niñas is that they occur on the rebound from preceding strong El Niños (DiNezio et al. 2017) which, through recharge oscillator dynamics (Jin 1997), drain the equatorial band of upper-ocean heat content leaving a large heat deficit that takes multiple years to recover.

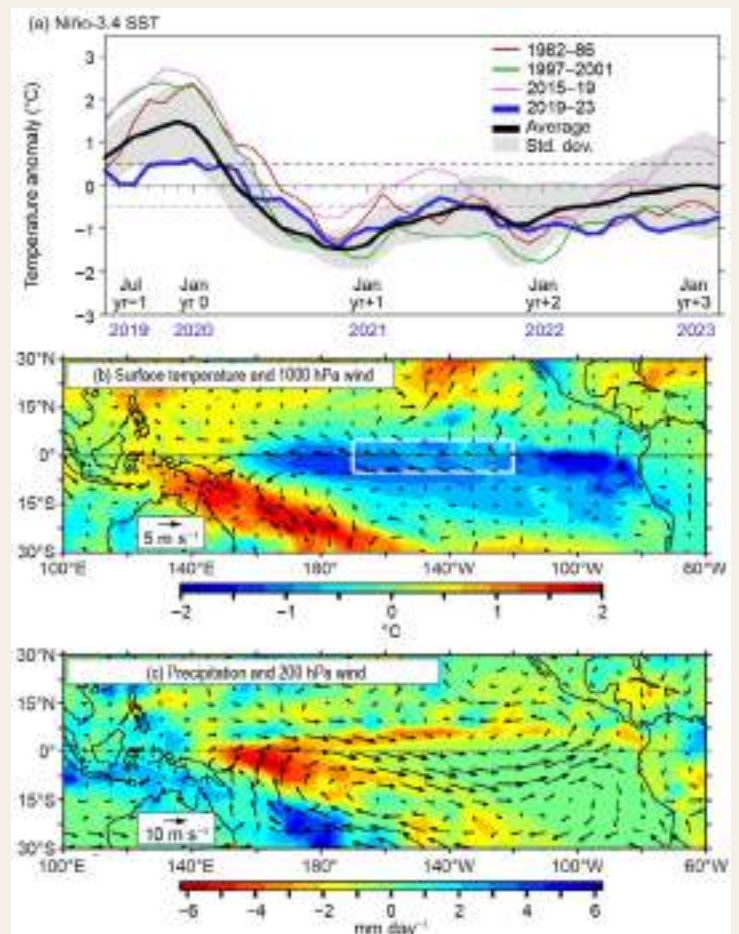


Fig. SB3.1. (a) Monthly mean sea-surface temperature (SST) anomalies from Jul 2019 to Jan 2023 (blue line) in the Niño-3.4 index region (5°S – 5°N , 120°W – 170°W). Also plotted is the monthly mean Niño-3.4 SST averaged over 10 La Niña events since the 1950s beginning in Jul the year before (Yr -1) the first SST minimum (in Yr 0), extending to the beginning of the third year (Yr +3) following the La Niña onset (black line). Shading indicates ± 1 std. dev. The evolution of La Niña following the three strongest El Niños of the last 40 years, namely 1982/83, 1997/98, and 2015/16, is also shown. Dashed horizontal lines indicate the threshold for El Niño ($> 0.5^{\circ}\text{C}$) and La Niña ($< -0.5^{\circ}\text{C}$). Niño-3.4 SSTs are from ERSSTv5 (Huang et al. 2017). (b) Surface (1000 hPa) wind (m s^{-1}) and temperature ($^{\circ}\text{C}$) anomalies for Oct–Dec 2022 with the Niño-3.4 region outlined in white. (c) Precipitation and upper level (200-hPa) wind anomalies for Oct–Dec 2022. Winds are from the NCEP/DOE Reanalysis (Kanamitsu et al. 2002), precipitation is from the Global Precipitation Climatology Project (Huffman et al. 2009), and surface air and sea temperatures are from HadISST (Rayner et al. 2003). All anomalies are relative to a 1991–2020 climatology.

The three strongest El Niños of the past 40 years illustrate this pattern (Fig. SB3.1a). The 1982/83 and 2015/16 El Niños were both followed by La Niñas extending over two years and the 1997/98 event was followed by three successive years of unusually cold tropical Pacific SSTs. Each of these El Niños was associated with a significant discharge of upper-ocean heat content from the equatorial band (McPhaden et al. 2021). However, the current multi-year La Niña does not conform to this scenario. Antecedent conditions in the tropical Pacific in 2019 were characterized by a borderline El Niño (Fig. SB3.1a) that did not lead to a large upper-ocean heat content discharge. What caused this latest three-year La Niña is thus a topic of considerable interest. One hypothesis is that the onset was triggered by a record positive Indian Ocean dipole in late 2019, then boosted in 2021 by unusually warm conditions in the tropical Atlantic involving the strongest Atlantic Niño since the 1970s (Hasan et al. 2022). Other possible explanations include influences from higher latitudes of the North Pacific (Park et al. 2021) or the impact of atmospheric aerosols from the 2019–20 Australian wildfires (Fasullo et al. 2023). Quantifying the relative contributions of these and other possible factors is a priority given the extraordinary socio-economics consequences of this multi-year La Niña.

Global mean surface air temperature (GMST) over the last eight years (2015–22) have been the warmest on record (see section 2b), attesting to the reality of climate change. However, the highest annual temperature in this record occurred in 2016 during a strong El Niño event rather than in 2022 (Fig. SB3.2), even though carbon dioxide concentrations in the

atmosphere have risen over 2 parts per million per year during this time. The reason is that year-to-year variations in GMST are strongly influenced by the state of ENSO (Trenberth et al. 2002). During El Niño, unusually high SSTs in the tropical Pacific lead to increased evaporative cooling of the ocean. At the same time, increased cloudiness over the large expanse of usually warm water reduces the amount of sunlight entering the ocean, while cloud condensation in convective regions heats the atmosphere. During La Niña, the opposite happens. Thus, ENSO redistributes heat on a planetary scale, with an anomalously high heat flux from the ocean to the atmosphere during El Niño and an anomalously high heat flux from the atmosphere to the ocean during La Niña. For every 1°C of El Niño warming in the Niño-3.4 region, GMST rises by $0.073 \pm 0.024^\circ\text{C}$ (with 95% confidence) with a delay of three months. A 1°C cooling in the Niño-3.4 region during La Niña results in a comparable drop in GMST (Fig. SB3.2). As a consequence, the predominance of unusually cold La Niña conditions since the end of the 2015/16 El Niño temporarily arrested the rise in GMST despite rising greenhouse gas concentrations.

The present situation is analogous to the previous hiatus in global warming in the first decade of the twenty-first century (Fig. SB3.2), which coincided with a period dominated by strong multi-year La Niñas (Fyfe et al. 2016; Hu and Fedorov 2017). That hiatus ended with the 2015/16 El Niño. The triple-dip La Niña dissipated in early 2023, and warm El Niño conditions will eventually return. When that happens, GMST will rise again with the likelihood of new record highs at some point in the near future.

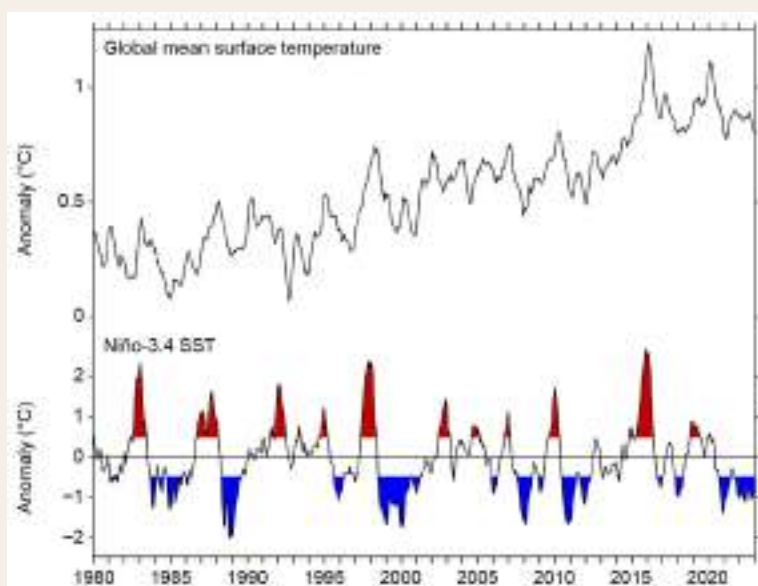


Fig. SB3.2. (top) Monthly averaged global mean surface temperature (GMST; °C) over 1980–2022 relative to the twentieth-century average. (bottom) Monthly sea-surface temperature (SST) anomalies (°C) in the Niño-3.4 region relative to a 1991–2020 climatology. El Niño periods are colored red and La Niña periods blue. Niño-3.4 SSTs are based on ERSSTv5 (Huang et al. 2017) and GMST is based on NOAA/NCEI global surface temperature anomalies (<https://www.ncei.noaa.gov/access/monitoring/global-temperature-anomalies/anomalies>). Dates shown along the x-axis are centered on tick marks, which are placed at the beginning of calendar years.

c. Ocean heat content

—G. C. Johnson, J. M. Lyman, C. Atkinson, T. Boyer, L. Cheng, J. Gilson, M. Ishii, R. Locarnini, A. Mishonov, S. G. Purkey, J. Reagan, and K. Sato

As a result of increasing atmospheric greenhouse gas concentrations, Earth's climate system has been absorbing more energy than it re-radiates back into space. The ocean stored ~91% of that excess energy from 1971 to 2018 (IPCC 2021). As seawater warms, it expands, and that expansion accounted for ~50% of the global average sea-level rise during that period (IPCC 2021). This warming is surface intensified, but can be seen down to the 2000-dbar sampling limit of core Argo (Wijffels et al. 2016), as well as in the coldest, densest ocean bottom waters that sink around Antarctica (Purkey and Johnson 2010). A warming ocean increases the atmosphere's temperature and capacity to carry moisture, affecting the frequency, intensity, perhaps duration, and rain amounts of atmospheric rivers (e.g., Payne et al. 2020) and cyclones (e.g., Walsh et al. 2016). Despite variations in ocean heat content from variations in ocean currents driven primarily by the wind, statistically significant regional warming trends are emerging over time (Johnson and Lyman 2020). Marine heatwaves have increased in intensity and duration as a result of these warming trends (Oliver et al. 2021). Ocean warming also increases undercutting of glaciers around Greenland (Wood et al. 2021) and melting around Antarctica (Schmidtko et al. 2014).

Maps of annual upper (0-m–700-m) ocean heat content anomaly (OHCA) relative to a 1993–2022 baseline mean (Fig. 3.4) were generated from a combination of in situ ocean temperature data and satellite altimetry data following Willis et al. (2004), but using Argo (Riser et al. 2016) data downloaded from an Argo Global Data Assembly Centre in January 2023 (<http://doi.org/10.17882/42182#98916>). Near-global average seasonal temperature anomalies versus pressure from Argo data (Roemmich and Gilson 2009, updated) since 2004 (Fig. 3.5) and in situ

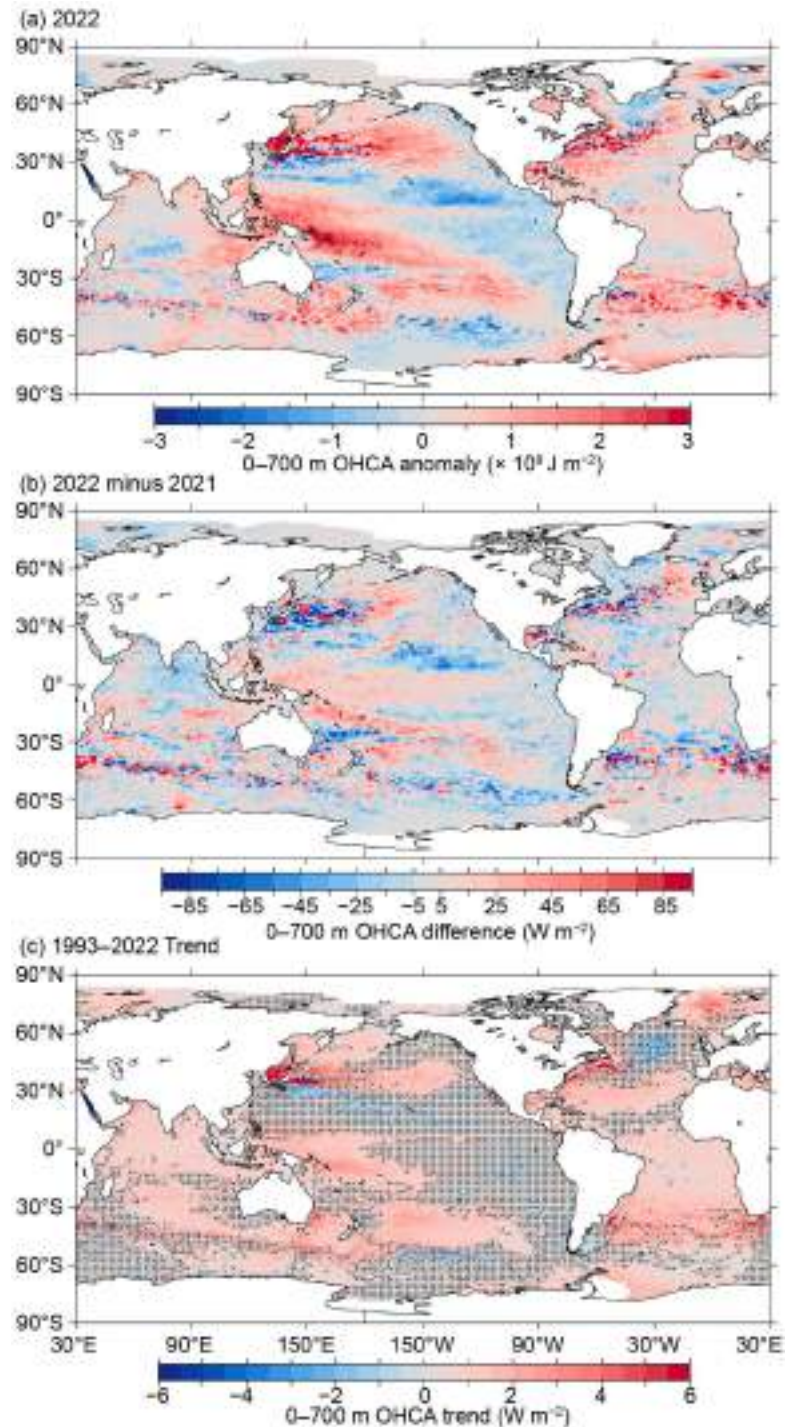


Fig. 3.4. (a) Combined satellite altimeter and in situ ocean temperature data estimate of upper (0 m–700 m) ocean heat content anomaly (OHCA; $\times 10^9 \text{ J m}^{-2}$) for 2022 analyzed following Willis et al. (2004) but using an Argo monthly climatology and displayed relative to the 1993–2022 baseline. (b) 2022-minus-2021 combined estimates of OHCA expressed as a local surface heat flux equivalent (W m^{-2}). For (a) and (b) comparisons, note that 95 W m^{-2} applied over one year results in a $3 \times 10^9 \text{ J m}^{-2}$ change of OHCA. (c) Linear trend from 1993 to 2022 of the combined estimates of upper (0 m–700 m) annual OHCA (W m^{-2}). Areas with statistically insignificant trends are stippled.

global estimates of OHCA for three pressure layers (0-m–700-m, 700-m–2000-m, and 2000-m–6000-m) from five different research groups (Fig. 3.6) are also discussed.

La Niña conditions were present for a third year in row, in a rare “triple-dip” event (see Sidebar 3.1 and section 4b for details). They resumed most recently in August 2021 and continued throughout 2022. However, the 2022-minus-2021 difference of upper OHCA (Fig. 3.4b) in the tropical Pacific shows an increase everywhere but in its northeast quadrant, in contrast with the 2021-minus-2020 and 2020-minus-2019 differences, both of which showed more increases in the western tropical Pacific and decreases in the central to eastern equatorial Pacific, more typical of La Niña years. As in the two previous years, 2022 upper-ocean heat content anomalies (Fig. 3.4a) in the equatorial Pacific were negative in the east and positive in the west, associated with anomalously westward currents on the equator (see Fig. 3.18a) driven by strong easterly trade winds (see Fig. 3.13a). Equatorward of the subtropical western boundary current extensions, 2022-minus-2021 differences exhibit zonally elongated low values in both hemispheres. The centers of the North and South Pacific were both anomalously warm in 2022, with colder conditions around the edges, consistent with a continued negative Pacific Decadal Oscillation index in the Northern Hemisphere (section 3b). The cold anomalies just south of the Kuroshio Extension and warm anomalies within that current are associated with a northward shift of that current (see Fig. 3.20), visible as a similarly zonally elongated anomaly dipole in surface current anomalies (see Fig. 3.18a). The Sea of Japan/East Sea, the Sea of Okhotsk, and the Bering Sea were all warmer than their long-term means in 2022.

In the Indian Ocean, the 2022-minus-2021 difference of upper OHCA (Fig. 3.4b) mostly decreased north of about 5°S and mostly increased south of that latitude. The 2022 OHCA anomalies (Fig. 3.4a) were negative in the center of the tropical South Indian Ocean and especially positive in the east between Australia and Indonesia. This pattern is broadly consistent with a negative phase of the Indian Ocean dipole index during 2022, with warm sea-surface temperature anomalies in the east Indian Ocean, and cold ones in the west (Fig. 3.1a).

The 2022-minus-2021 differences of upper OHCA (Fig. 3.4b) in the Atlantic Ocean were weakly negative in the Labrador Sea and the Irminger Sea, whereas much of the Gulf of Mexico exhibited an increase. Overall, the year-to-year differences in the Atlantic were small or not regionally coherent. Hence the broad pattern of upper OHCA in 2022 (Fig. 3.4a) is similar to that in 2021, with much of the Atlantic Ocean exhibiting upper OHCA above the 1993–2022 average (Fig. 3.4a) with the main exception, as in recent years, being cooler-than-average conditions southeast of Greenland. Anomalies were again especially high in the western North Atlantic and the subtropical South Atlantic in 2022.

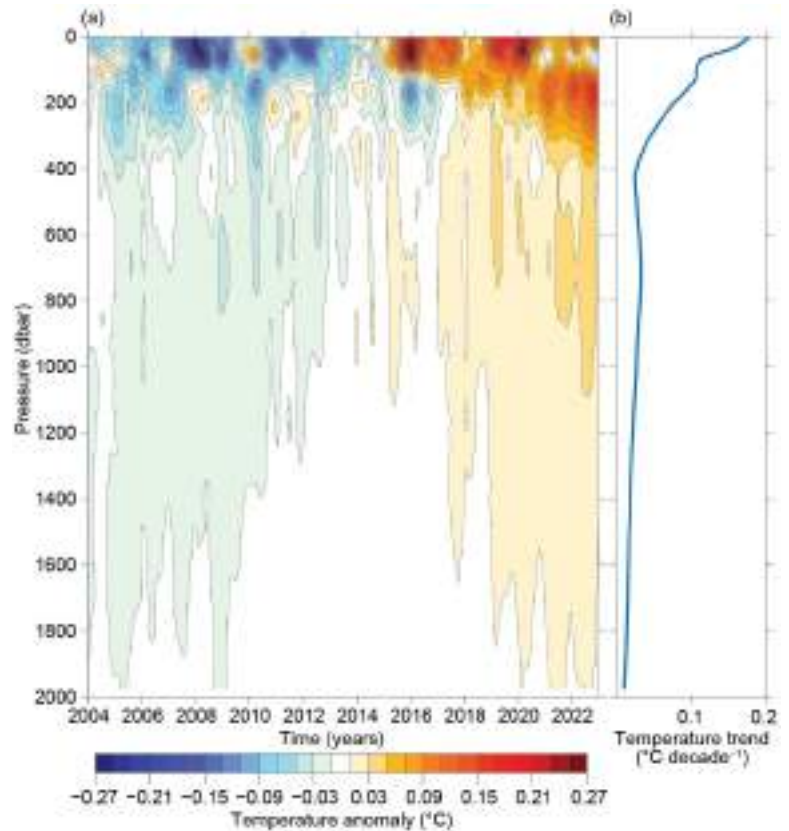


Fig. 3.5. (a) Near-global (65°S–80°N, excluding continental shelves, the Indonesian seas, and the Sea of Okhotsk) average monthly ocean temperature anomalies (°C; updated from Roemmich and Gilson [2009]) relative to record-length average monthly values, smoothed with a five-month Hanning filter and contoured at odd 0.02°C intervals (see color bar) vs. pressure and time. (b) Linear trend of temperature anomalies over time for the length of the record in (a) plotted vs. pressure in °C decade⁻¹ (blue line).

As expected, the large-scale statistically significant regional patterns in the 1993–2022 local linear trends of upper OHCA (Fig. 3.4c) were similar to those from 1993 to 2021 (Johnson et al. 2022) and earlier reports. In general, the longer the period over which these trends are estimated, the more of the ocean surface area warms and the less of it cools at statistically significant rates (Johnson and Lyman 2020). In 2022 that tendency stands out in the Bering Sea and the northwest Pacific, where the coverage of statistically significant warming trends noticeably expanded relative to the 2021 results. Warming trends that were statistically significant occupied 55% of the global ocean surface area as of 2022, up from 49% for 1993–2021. Statistically significant cooling trends occupied only 2% of the ocean area, down from 3% for 1993–2021, most prominently southeast of Greenland.

Near-global average seasonal temperature anomalies (Fig. 3.5a) show the signature of La Niña (see Sidebar 3.1), which results in a reduction of warm anomalies from the surface to 100 dbar and an increase in warm anomalies from 100 dbar to 400 dbar and were most pronounced in the boreal winter. This pattern arises as strong easterly trade winds bring the cold waters below the equatorial thermocline to the surface in the eastern equatorial Pacific and create a large deep pool of warm waters in the western equatorial Pacific. A similar pattern can be seen in the 2007/08, 2010/11, and 2011/12 boreal winters. El Niño years (e.g., 2009/10, 2015/16, and 2018/19) have warmer near-surface and colder sub-surface waters, as expected given the deepening of the equatorial thermocline in the east, its shoaling in the west, and the spread of warm waters across much of the near-surface equatorial Pacific. Overlaid on this global signature of the El Niño–Southern Oscillation is an overall warming trend (Fig. 3.5b), strongest near the surface but evident all the way to the 2000-dbar sampling limit of Core Argo.

As noted in previous reports, the analysis is extended back in time from the Argo period to 1993 and expanded to examine greater depths, using sparser, more heterogeneous historical data collected mostly from ships (e.g., Abraham et al. 2013). Shallow expendable bathythermograph coverage may allow reasonable estimates of globally integrated OHCA in the upper 0-m–300-m or even 0-m–450-m back to the late 1960s, but it may be prudent to limit global 0-m–700-m estimates to the early 1990s and later (Lyman and Johnson 2014), as is done here.

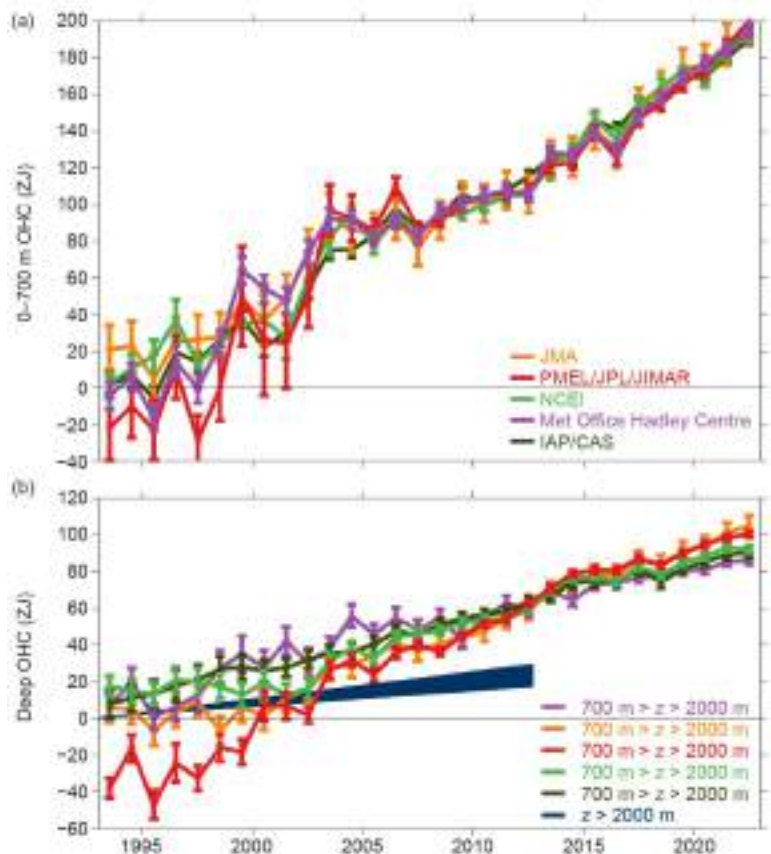


Fig. 3.6. (a) Annual average global integrals of in situ estimates of upper (0 m–700 m) ocean heat content anomaly (OHCA; ZJ; $1 \text{ ZJ} = 10^{21} \text{ J}$) for 1993–2022 with standard errors of the mean. The MRI/JMA estimate is an update of Ishii et al. (2017). The PMEL/JPL/JIMAR estimate is an update and refinement of Lyman and Johnson (2014). The Met Office Hadley Centre estimate is computed from gridded monthly temperature anomalies following Palmer et al. (2007) and Good et al. (2013). Both the PMEL and Met Office estimates use Cheng et al. (2014) XBT corrections and Gouretski and Cheng (2020) MBT corrections. The NCEI estimate follows Levitus et al. (2012). The IAP/CAS estimate is reported in Cheng et al. (2023). See Johnson et al. (2014) for details on uncertainties, methods, and datasets. For comparison, all estimates have been individually offset (vertically on the plot), first to their individual 2005–22 means (the best sampled time period), and then to their collective 1993 mean. (b) Annual average global integrals of in situ estimates of intermediate (700 m–2000 m) OHCA for 1993–2022 (ZJ) with standard errors of the mean, and a long-term trend with one standard error uncertainty shown from Sep 1992 to Jan 2013 for deep and abyssal ($z > 2000 \text{ m}$) OHCA following Purkey and Johnson (2010) but updated using all repeat hydrographic section data available from <https://cchdo.ucsd.edu/> as of Jan 2023.

The results for the 700-m–2000-m layer, which is quite sparsely sampled prior to the start of the Argo era (circa 2005–06), should be interpreted with caution before those years.

The different estimates of annual globally integrated upper OHCA (Fig. 3.6a) all reveal a large increase since 1993, with all of the five analyses reporting 2022 as a record high. Four out of five of the globally integrated 700-m–2000-m OHCA annual analyses (Fig. 3.6b) also report 2022 as a record high, and the long-term warming trend in this layer is also clear. The water column from 0 m to 700 m and 700 m to 2000 m gained 11.0 (± 1.7) ZJ and 1.4 (± 1.7) ZJ, respectively (means and standard deviations given) from 2021 to 2022. Causes of differences among estimates are discussed in Johnson et al. (2015).

The estimated linear rates of heat gain for each of the five global integral estimates of upper OHCA from 1993 through 2022 (Fig. 3.6a) range from 0.38 (± 0.05) $W m^{-2}$ to 0.44 (± 0.10) $W m^{-2}$ applied over the surface area of Earth (Table 3.2) rather than the surface area of the ocean, to better compare to the top-of-the-atmosphere energy imbalance (e.g., Loeb et al. 2021). These results are not much different from those in previous reports, although with an increasing record length, trend uncertainties tend to decrease and differences among analyses tend to diminish. Linear trends from the 700-m–2000-m layer over the same time period range from 0.17 (± 0.03) $W m^{-2}$ to 0.32 (± 0.04) $W m^{-2}$. Trends in the upper 0-m–700-m layer all agree within their 5%–95% confidence intervals. However, as noted in previous reports, the trends in the 700-m–2000-m layer, which is quite sparsely sampled prior to the start of the Argo era, do not all overlap within their uncertainties. Different methods for dealing with under-sampled regions likely cause this disagreement. Using repeat hydrographic section data collected from 1981 through 2022 to update the estimate of Purkey and Johnson (2010) for 2000 m–6000 m, the linear trend is 0.07 (± 0.03) $W m^{-2}$ from September 1992 to January 2013 (these dates are global average times of first and last sampling of the sections). Summing the three layers (despite their slightly different time periods as given above), the full-depth ocean heat gain rate applied to Earth’s entire surface ranges from 0.64 $W m^{-2}$ to 0.83 $W m^{-2}$.

Table 3.2. Trends of ocean heat content increase (in $W m^{-2}$ applied over the $5.1 \times 10^{14} m^2$ surface area of Earth) from six different research groups over three depth ranges (see Fig. 3.6 for details). For the upper (0 m–700 m) and intermediate (700 m–2000 m) depth ranges, estimates cover 1993–2022, with 5%–95% uncertainties based on the residuals taking their temporal correlation into account when estimating degrees of freedom (Von Storch and Zwiers 1999). The 2000 m–6000 m depth range estimate, an update of Purkey and Johnson (2010), uses data from 1981 to 2022, having a global average start and end date of Sep 1992 to Jan 2013, also with 5%–95% uncertainty.

Research Group	0 m–700 m Global ocean heat content trends ($W m^{-2}$)	700 m–2000 m Global ocean heat content trends ($W m^{-2}$)	2000 m–6000 m Global ocean heat content trends ($W m^{-2}$)
MRI/JMA	0.38 \pm 0.05	0.24 \pm 0.04	—
PMEL/JPL/JIMAR	0.44 \pm 0.10	0.32 \pm 0.04	—
NCEI	0.39 \pm 0.05	0.19 \pm 0.04	—
Met Office Hadley Centre	0.40 \pm 0.07	0.17 \pm 0.03	—
IAP/CAS	0.41 \pm 0.03	0.18 \pm 0.01	—
Purkey and Johnson	—	—	0.07 \pm 0.03

d. Salinity

—G. C. Johnson, J. Reagan, J. M. Lyman, T. Boyer, C. Schmid, and R. Locarnini

1. INTRODUCTION

Variations in ocean salinity and temperature set the density of the ocean, and thus the vertical stratification which impacts the depth to which the ocean communicates directly with the atmosphere. Lateral density variations are linked to ocean currents via the thermal wind relation. At high latitudes, where temperatures are cold and often have a small range, salinity is often the dominant factor in setting the vertical density structure. Salinity variations, created by advection, precipitation/evaporation, river runoff, and ice melt or freezing (Ren et al. 2011; Yu 2011) can influence ocean–atmosphere exchanges of heat and dissolved gases (including influencing marine heatwaves, ocean carbon dioxide uptake, tropical cyclones, and deep or bottom water formation), the exchange of nutrients or oxygen between the surface mixed layer and denser waters below, and so on.

Global average practical salinity is about 34.7. Surface values are below 28.0 or above 37.4 for only 1% of the ocean surface area each. In general, regions where evaporation dominates (such as the subtropics) have higher salinity values and where precipitation is dominant (the Intertropical Convergence Zone [ITCZ] and high latitudes), it is fresher (e.g., Wüst 1936; Schmitt 1995). Multi-decadal trends in ocean salinity have been used to show increases in the hydrological cycle (e.g., Durack et al. 2012; Skliris et al. 2014; Skliris 2016). Springtime sea-surface salinity values in the subtropical North Atlantic Ocean have even shown skill in predicting summer-monsoon rainfall in the African Sahel (Li et al. 2016).

To investigate interannual changes of subsurface salinity, all available salinity profile data are quality controlled following Boyer et al. (2018) and then used to derive 1° monthly mean gridded salinity anomalies relative to a long-term monthly mean for the years 1955–2017 (World Ocean Atlas 2018; Zweng et al. 2018) at standard depths from the surface to 2000 m. In recent years, the largest source of salinity profiles is the profiling floats of the Argo program (Riser et al. 2016). These data are a mix of real-time (preliminary) and delayed-mode (scientific quality controlled) observations. Hence, the estimates presented here may be subject to instrument biases such as a positive salinity drift identified in a subset of Argo Conductivity-Temperature-Depth, and will change after all data are subjected to scientific quality control. The sea-surface salinity (SSS) analysis relies on Argo data downloaded in January 2023, with annual anomaly maps relative to a seasonal climatology generated following Johnson and Lyman (2012) as well as monthly maps of bulk (as opposed to skin) SSS data from the Blended Analysis of Surface Salinity (BASS; Xie et al. 2014). BASS blends in situ SSS data with data from the *Aquarius* (Le Vine et al. 2014; mission ended in June 2015), Soil Moisture and Ocean Salinity (SMOS; Font et al. 2013), and the Soil Moisture Active Passive (SMAP; Fore et al. 2016) satellite missions. Despite the larger uncertainties of satellite data relative to Argo data, their higher spatial and temporal sampling allows higher spatial and temporal resolution maps than are possible using in situ data alone at present. All salinity values used in this section are reported as observed, on the dimensionless Practical Salinity Scale-78 (Fofonoff and Lewis 1979).

2. SEA-SURFACE SALINITY

G. C. Johnson and J. M. Lyman

As noted in previous reports (e.g., Johnson et al. 2020), since salinity has no direct feedback to the atmosphere, large-scale SSS anomalies can be quite persistent. (In contrast, sea-surface temperature anomalies are often damped by air–sea heat exchange.) Salty anomalies along and just south of the equator in the western and central Pacific, respectively, strengthened in 2022 (Figs. 3.7ab), for the third consecutive year. This pattern, owing to anomalous westward surface currents advecting relatively salty water westward along with shifts in precipitation, has built up over the past three years during the triple-dip La Niña (Sidebar 3.1). The relatively fresh feature in the western South Pacific near 20°S also built in strength from 2021 to 2022, at least partially owing to a poleward shift in the South Pacific ITCZ with La Niña. In the North Pacific, the center

of the basin was mostly anomalously salty in 2022, and the periphery was generally anomalously fresh. South of 30°S, the Pacific was primarily salty in 2022.

SSS in the Atlantic freshened from 2021 to 2022 off most of the east coast of North, Central, and South America (Fig. 3.7b). As a result, in 2022, SSS was anomalously fresh around the Caribbean, possibly owing to a record flood of the Amazon River in 2021 (e.g., Espinoza et al. 2022), but remained anomalously salty off the east coast of North America from the Gulf of Mexico to Labrador. Other fresh regions in the Atlantic in 2022 include the Irminger Sea, the ITCZ, and portions of the Atlantic Southern Ocean sector. The regions around the subtropical salinity maximum were anomalously salty in both the North and South Atlantic, as for many other recent years.

Freshening in the southeastern tropical Indian Ocean and salinification in much of the north and west continued from 2021 to 2022 (Fig. 3.7b), as it did from 2020 to 2021, again consistent with a negative Indian Ocean dipole (IOD) index for much of 2022, associated with a drying in the west and increased precipitation in the east (see Figs. 3.12a,b), as discussed in last year’s report. The ocean offshore of much of India was also anomalously fresh in 2022, with the western freshening persisting from 2021 and the eastern freshening building from 2021 (Figs. 3.7a,b).

As the atmosphere warms, it can hold more moisture, enabling an increased hydrological cycle over the ocean (Held and Soden 2006; Durack and Wijffels 2010). Since upper-ocean salinity values can function as a sort of evaporation pan and rain gauge wrapped into one, the expected pattern from this change is “salty gets saltier and fresh gets fresher,” and has been evident in *State of the Climate* reports since 2006, the first year of the salinity section. In 2022 this pattern held (Fig. 3.7a), with salty SSS anomalies in at least a portion of all of the subtropical salinity maxima and fresh SSS anomalies in the subpolar North Pacific and part of the subpolar North Atlantic, as well as the ITCZs of the Pacific and Atlantic. The 2005–22 SSS trends (Fig. 3.7c) reflect this pattern to some extent as well, with statistically significant (unstippled areas) freshening trends evident in the eastern subpolar North Pacific and

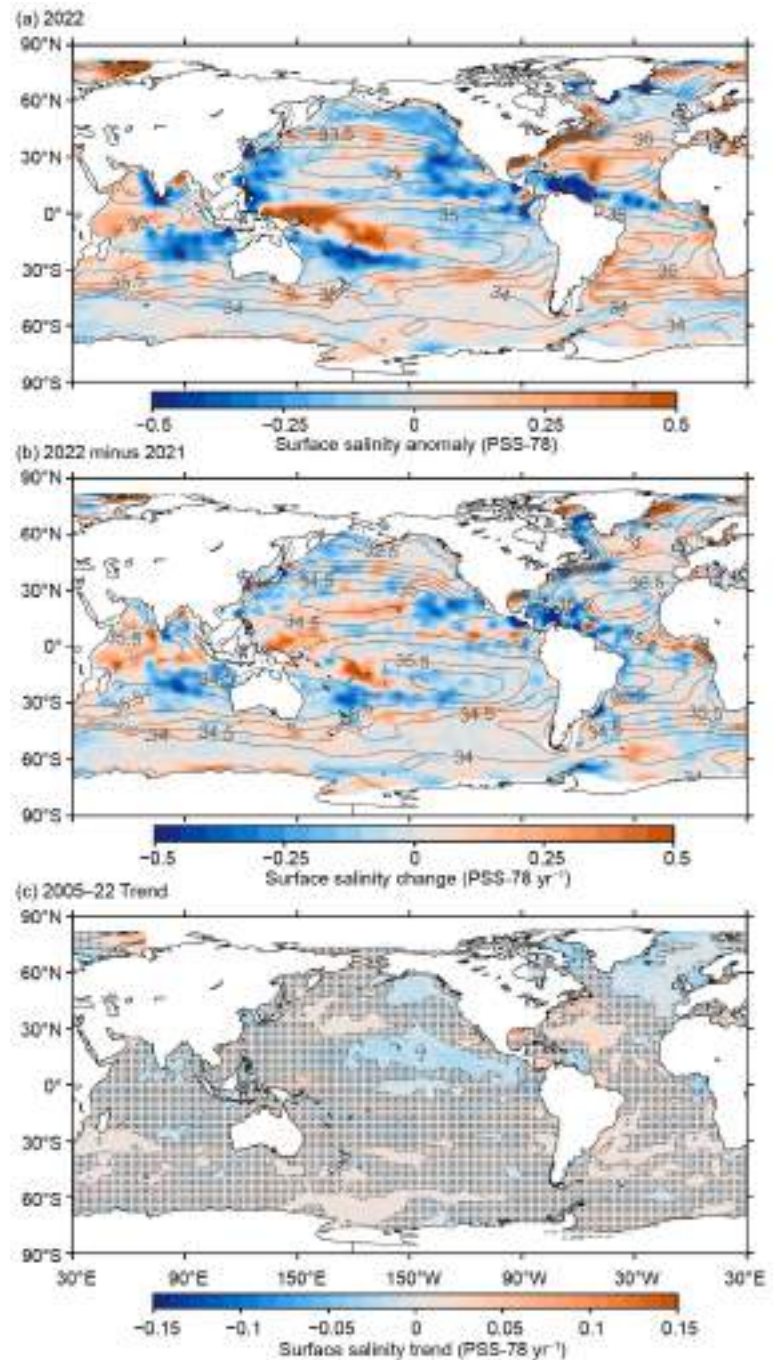


Fig. 3.7. (a) Map of the 2022 annual sea-surface salinity anomaly (colors, Practical Salinity Scale-78 [PSS-78]) with respect to monthly climatological 1955–2012 salinity fields from WOA13v2 (yearly average; gray contours at 0.5 intervals, PSS-78). (b) Difference of 2022 and 2021 sea-surface salinity maps (colors, PSS-78 yr⁻¹). White ocean areas are too data-poor (retaining <80% of a large-scale signal) to map. (c) Map of local linear trends estimated from annual sea-surface salinity anomalies for 2005–22 (colors, PSS-78 yr⁻¹). Areas with statistically insignificant trends at 5%–95% confidence are stippled. All maps are made using Argo data.

North Atlantic, the Pacific ITCZ, and the Gulf of Guinea, as well as statistically significant salty trends in parts of the subtropics in all basins.

In 2022, the seasonal BASS (Xie et al. 2014) SSS anomalies (Fig. 3.8) show the progressions of many of the features in the annual anomaly map using Argo data alone (Fig. 3.7a), and with higher spatial resolution, albeit with less accuracy. The anomalously fresh conditions in the Caribbean Seas build between December–February and March–May. The build-up of anomalously salty water in the western equatorial Pacific over the year is also clear in these maps, as is the development of the fresh anomaly discussed above just to the south of it. A zonally elongated anomalously salty band just south of an anomalously fresh band, with the transition at around 9°N, extends across much of the Pacific, and is especially apparent in September–November 2022. These are associated with a poleward shift of the ITCZ owing to the La Niña (see Sidebar 3.1 and Fig. 3.12a) and/or an intensified and northward-shifted North Equatorial Countercurrent indicated by eastward surface current anomalies of 8 cm s⁻¹ to 10 cm s⁻¹ at 6°N–8.5°N, 90°W–175°W (see Fig. 3.18a).

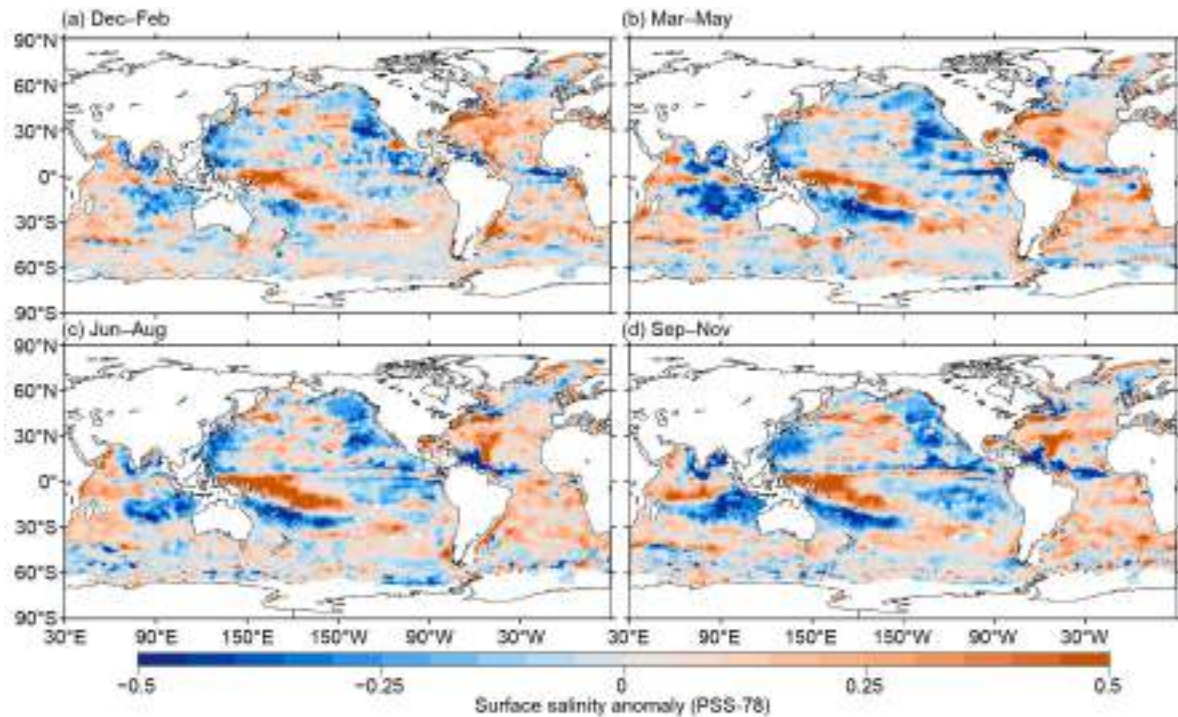


Fig. 3.8. Seasonal maps of sea-surface salinity anomalies (colors) from monthly blended maps of satellite and in situ salinity data (BASS; Xie et al. 2014) relative to monthly climatological 1955–2012 salinity fields from WOA13v2 for (a) Dec 2021–Feb 2022, (b) Mar–May 2022, (c) Jun–Aug 2022, and (d) Sep–Nov 2022.

3. SUBSURFACE SALINITY

J. Reagan, T. Boyer, C. Schmid, and R. Locarnini

Salinity is a conservative tracer and therefore is expected to retain much of its surface signature as it flows into the ocean’s interior. Sinking into the ocean’s interior primarily occurs through subduction (downward flow along constant density surfaces) and convection (deep vertical mixing; Talley 2002). Thus, in the absence of mixing, subsurface salinity anomalies will retain their surface footprint as they flow deeper into the ocean, which can ultimately impact ocean dynamics through changes in density.

The year 2022 was the third consecutive year the Atlantic basin exhibited only positive salinity anomalies from 0 m to 1000 m (Fig. 3.9a). The largest (>0.07) basin-averaged salinity anomalies in 2022 were constrained to depths between 75 m and 100 m with slightly smaller positive anomalies (~0.05) at the surface. Similar to 2020 and 2021, the 2022 monthly salinity anomalies below 100 m weakened with depth, reaching ~0.01 near 700 m. However, unlike in previous years back to 2016, there was no clear deepening of the Atlantic salinity anomalies in 2022 (Fig. 3.9a). This pattern is even more evident when examining the 2021 to 2022 Atlantic basin salinity changes

(Fig. 3.9b) and the 2021 to 2022 changes in zonally averaged salinity (Fig. 3.9c). Between 2021 and 2022, the upper 100 m freshened (maximum ~ -0.015 at 50 m; Fig. 3.9b) which is primarily associated with 0-m to 100-m freshening centered at 10°N , 40°N , and 60°N (Figs. 3.9c and 3.7b). This near-surface freshening is consistent with the freshening from 2020 to 2021 (Fig. 3.9b in Reagan et al. 2022); however, unlike the salinification that had occurred from 100 m to 1000 m between 2020 and 2021, there was slight freshening from 100 m to 600 m (maximum of ~ -0.002 at 300 m) between 2021 and 2022 (Fig. 3.9b).

In 2022, the structure of the 0-m to 1000-m Pacific basin-averaged salinity anomaly continued resembling the pattern that has existed since mid-2014, with near-surface fresh anomalies (upper 100 m) followed by a 100-m to 200-m thick salty subsurface anomaly layer followed by weak ($<|0.01|$) anomalies below (Fig. 3.9d). Fresh near-surface anomalies (<-0.03) that were common during the latter half of the 2010s have been absent since early 2020. The 2021 to 2022 salinification in the upper 30 m marked the fourth straight year in which salinity increased in this layer of the Pacific (Fig. 3.9e; Fig. 3.9e in Reagan et al. 2020, 2021, 2022). There is also salinification from 150 m to 250 m (maximum of ~ 0.005 at 200 m) and weak freshening from 300 m to 700 m (maximum of ~ -0.002 at 400 m) from 2021 to 2022 in the Pacific (Fig. 3.9e). The upper 150 m significant zonally averaged salinity changes from 2021 to 2022 from 30°S to 30°N reflect the changes in precipitation patterns (Fig. 3.12b) and zonal geostrophic flow anomalies (Figs. 3.18a,b) as the Pacific reentered a La Niña in August of 2021 and remained there throughout 2022 (Fig. 3.9f; see Sidebar 3.1).

The 2022 0-m to 1000-m monthly Indian basin-averaged salinity anomalies were a continuation of the anomaly structure exhibited in both 2020 and 2021 (Fig. 3.9g; Reagan et al. 2021, 2022). The salinification that took place from 2020 to 2021 in the upper ~ 100 m (Fig. 3.9h in

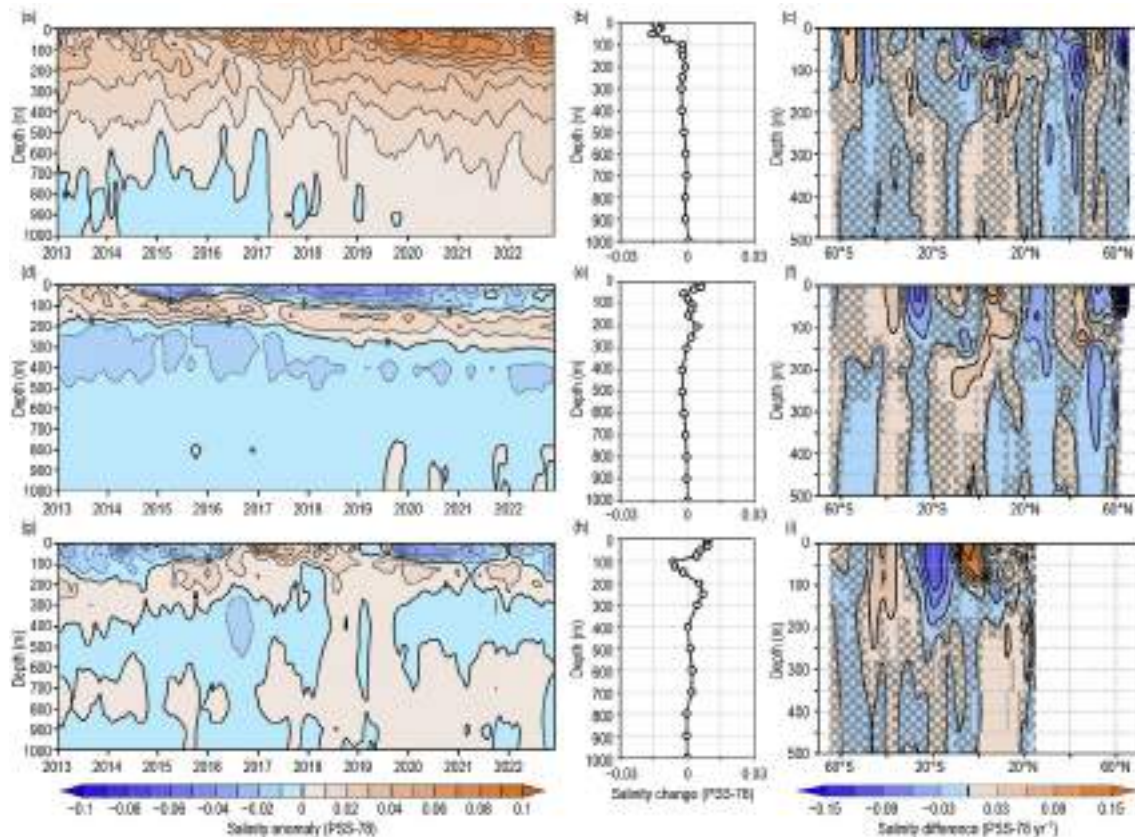


Fig. 3.9. Average monthly salinity anomalies from 0 m to 1000 m for 2013–22 for the (a) Atlantic, (d) Pacific, and (g) Indian basins. Change in salinity from 2021 to 2022 for the (b) Atlantic, (e) Pacific, and (h) Indian basins. Change in the 0 m to 500 m zonal-average salinity from 2021 to 2022 in the (c) Atlantic, (f) Pacific, and (i) Indian basins with areas of statistically insignificant change, defined as $< \pm 1$ std. dev. and calculated from all year-to-year changes between 2005 and 2022, stippled in dark gray. Data were smoothed using a three-month running mean. Anomalies are relative to the long-term (1955–2017) WOA18 monthly salinity climatology (Zweng et al. 2018).

Reagan et al. 2022) continued in 2022 (Fig. 3.9h) in the form of weakening fresh anomalies in the near-surface (upper 100 m, maximum of ~ 0.01 at 10 m). While the fresh anomalies weakened from 2021 to 2022, they also deepened, leading to freshening between 80 m and 160 m (maximum of ~ -0.0075 at 100 m). The 2021 to 2022 significant zonally averaged salinity anomaly changes were primarily confined to the upper 200 m (Fig. 3.9i), with freshening centered at 20°S (maximum ~ -0.09 at 50 m) and the salinification centered at 5°S (maximum ~ 0.15 at 10 m), a reflection of the persistent La Niña and the 2022 negative Indian Ocean dipole precipitation patterns (Fig. 3.12b). There was also significant salinification (~ 0.03) from 2021 to 2022 centered at 40°S and extending from the surface to 250 m (Fig. 3.9i).

Despite the Atlantic experiencing near-surface freshening for the past two years (Fig. 3.9b; Fig. 3.9b in Reagan et al. 2022) and slight subsurface freshening from 2021 to 2022 (Fig. 3.9b), the 2005–22 significant zonally averaged salinity trends (Fig. 3.10a) remained similar to the 2005–21 trends (Fig. 3.10a in Reagan et al. 2022) with salinification south of 45°N and freshening toward the Arctic. The 2005–22 Pacific significant zonally averaged salinity trends (Fig. 3.10b) remained largely unchanged when compared to 2005–21 (Fig. 3.10b in Reagan et al. 2022). However, the La Niña-related near-equatorial near-surface salinification from 2021 to 2022 (Fig. 3.9f) reduced the significance of the 2005–22 freshening in this region. Finally, the 2005–22 Indian basin significant zonally averaged trends (Fig. 3.10c) strongly resemble those from 2005–21 (Fig. 3.10c in Reagan et al. 2022), despite the strong changes observed in the upper 200 m between 2021 and 2022 (Fig. 3.9i) associated with precipitation patterns from La Niña and negative IOD phases.

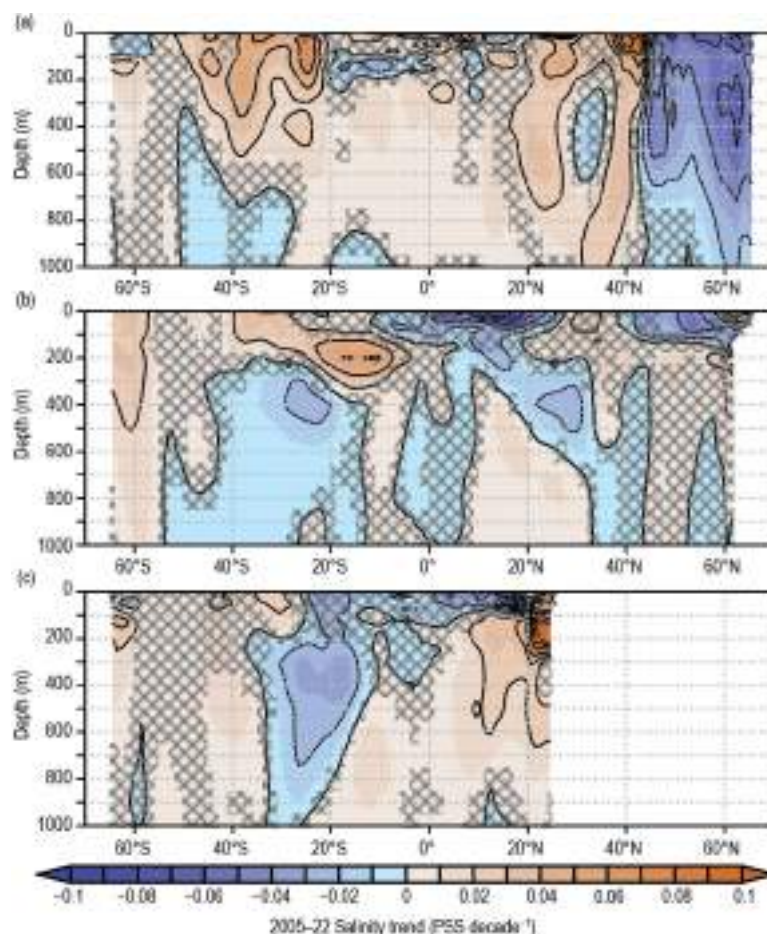


Fig. 3.10. The linear trend of zonally averaged salinity from 2005 to 2022 over the upper 1000 m for the (a) Atlantic, (b) Pacific, and (c) Indian basins. The salinity trend is per decade and computed using least squares regression. Areas that are stippled in dark gray are not significant at the 95% confidence interval.

e. Global ocean heat, freshwater, and momentum fluxes

—C. Wen, P. W. Stackhouse, Jr., J. Garg, P.-P. Xie, L. Zhang, and M. F. Cronin

Surface fluxes (i.e., heat, freshwater, and momentum fluxes) play a crucial role in keeping the energy and water cycles of the atmosphere–ocean coupled system in balance against external forcing from the Sun. Most of the shortwave radiation (SW) absorbed by the ocean’s surface is vented into the atmosphere via net longwave radiation (LW) emitted by the ocean surface, turbulent heat loss by evaporation (latent heat flux, or LH), and by conduction (sensible heat flux, or SH) associated with air–sea temperature differences. The remaining heat acts to change the temperature of the near-surface water column and/or is transported away by the ocean’s wind-driven circulation and mixed into the deeper ocean. Evaporation, which is associated with both a turbulent LH and moisture flux, connects the energy and water cycles. Evaporation minus precipitation (and in some regions runoff and ice melt or freezing) determines the local surface freshwater flux. Air–sea fluxes act as forces on both the ocean and atmosphere. Identifying air–sea flux anomalies is essential for understanding observed changes in surface water masses and in ocean circulation and its transport of heat and freshwater.

Here we examine surface heat fluxes, freshwater fluxes, and wind stress anomalies in 2022 and their differences from the previous year. The net surface heat flux, Q_{net} , is the sum of four terms: SW + LW + LH + SH. Monthly surface net SW and LW fluxes are from Clouds and the Earth’s Radiant Energy Systems (CERES) Surface Energy Balanced and Filled (EBAF) Edition 4.2 (Kato et al. 2018) and the Fast Longwave And Shortwave Radiative Fluxes (FLASHFlux) version 4A product (Stackhouse et al. 2006; FLASHFlux fluxes from 2022 are radiometrically scaled to Surface EBAF Ed4.2). LH and SH are from European Centre for Medium-Range Weather Forecasts Reanalysis version 5 (ERA5; Hersbach et al. 2020). The net surface freshwater flux into the ocean (neglecting runoff from land and ice melting or formation) is simplified as Precipitation (P) minus Evaporation (E), or the $P-E$ flux. Monthly precipitation is from the Global Precipitation Climatology Project (GPCP) version 2.3 products (Adler et al. 2018). Monthly evaporation is from ERA5. Wind stress τ is also from ERA5. Ekman velocity is derived from τ following the equation $W_{\text{EK}} = 1/\rho \nabla \times (\tau/f)$, where ρ is the water density and f the Coriolis parameter.

1. SURFACE HEAT FLUXES

Global surface net heat-flux annual mean anomalies for 2022 relative to a 2001–15 climatology (Fig. 3.11a) showed strongest positive net heat fluxes (indicating a warming effect on the ocean surface) in the far western tropical South Pacific, the cold tongue in the tropical southeastern Pacific, and in the northeastern Pacific. In the eastern Pacific just north of the equator, a narrow band of negative net heat flux (dominated by turbulent heat fluxes cooling the ocean and warming the atmosphere) was associated with the northward movement of the Intertropical Convergence Zone (ITCZ), which can be seen in a northward shift of 2022 $P-E$ anomalies (Fig. 3.12a). The magnitudes of maximum positive and negative net heat-flux anomalies exceed 25 W m^{-2} . The distribution of net heat-flux anomalies is associated with the ongoing La Niña in 2022. In the far western tropical Pacific, over the Maritime Continent, enhanced convection/precipitation caused less SW into the ocean, giving rise to the negative 2022 net heat-flux anomaly in this region. For the area near the Coral Sea and central Pacific, SH+LH anomalies (not shown) were the primary factor contributing to the net heat-flux anomalies. The locations with positive net heat-flux anomalies coincided with locations with reduced wind anomalies, and those with negative heat-flux anomalies were associated with increased wind anomalies (Fig. 3.13), consistent with the larger turbulent flux anomalies relative to the radiative flux anomalies in these regions. In regions where winds were moderate and less variable, LH+SH heat release into the atmosphere decreased with decreasing sea-surface temperature (SST) and vice versa. During the 2022 La Niña, SST anomalies (see Fig. 3.1a) in the southeastern Pacific were below -1°C , giving rise to less LH+SH release compared to normal years. In the tropical Indian Ocean, the negative IOD pattern in 2022 was associated with negative net heat-flux anomalies in the southeastern Indian Ocean and positive net heat-flux anomalies in the northwestern Indian Ocean.

In the North Pacific, the 2022 net heat flux anomaly distribution displayed a positive phase Pacific Decadal Oscillation-like pattern (Mantua and Hare 2002), with negative net heat-flux anomalies dominating the western-central Pacific between 25°N and 50°N, surrounded by positive anomalies. In the North Pacific, 2022 SST anomalies (see Fig. 3.1) in regions with positive net heat-flux anomalies were below average and vice versa. The anti-phase relationship between Q_{net} and SST anomalies suggests that surface heat flux acted as a damping of the local SST anomalies there. This anti-phase relationship did not apply to the North Atlantic Ocean in 2022. Negative Q_{net} anomalies were present near the Labrador Sea, with positive Q_{net} anomalies found south of 40°N. The negative ocean net heat-flux anomalies were associated with marked enhanced surface wind anomalies and vice versa (Figs. 3.11a and 3.13a). A similar dipole pattern of SST anomaly, albeit centered on ~50°N, was also observed in the North Atlantic (see Fig. 3.1).

The 2022-minus-2021 Q_{net} difference map (Fig 3.11b) has a similar spatial structure to the 2022 anomaly map in most regions. 2022 was the third year of a triple-dip La Niña event (see Sidebar 3.1), and La Niña intensity slightly strengthened in 2022 relative to 2021, with stronger SST cooling (~0.2°C cooler; see Fig. 3.1a) and trade winds in the central-eastern tropical Pacific (Fig. 3.13b). The magnitude and pattern of LH+SH 2022-minus-2021 differences were close to those of Q_{net} differences. A pronounced dipole pattern in the subpolar North Atlantic (40°N–70°N) suggests that the LH+SH change was the primary factor contributing to Q_{net} 2022-minus-2021 differences. The SW+LW differences had similar sign to LH+SH differences in most regions although the amplitude of the former was smaller.

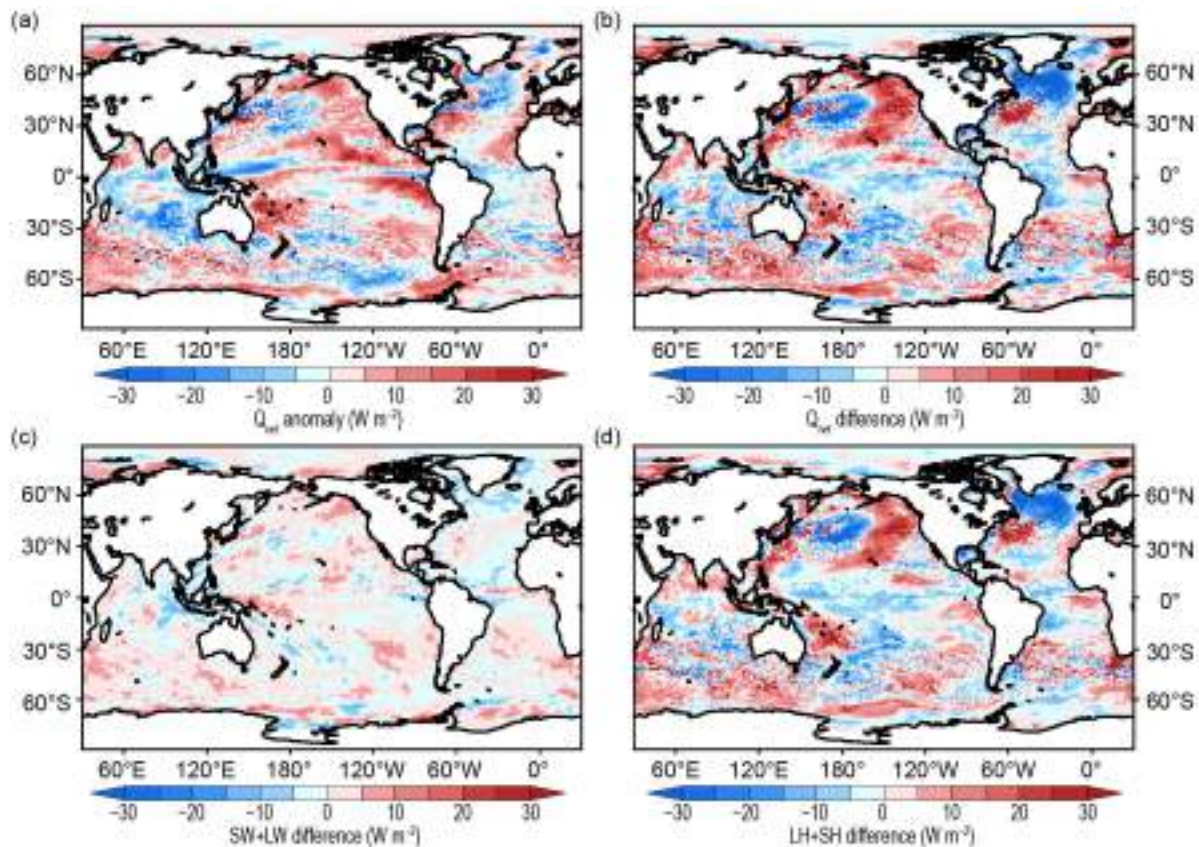


Fig. 3.11. (a) Surface heat flux (Q_{net}) anomalies for 2022 relative to the 2001–15 climatology. Positive values denote ocean heat gain. (b) 2022-minus-2021 difference for Q_{net} , (c) net surface radiation shortwave + longwave (SW+LW), and (d) turbulent heat fluxes latent heat + sensible heat (LH+SH), respectively. Positive tendencies denote more ocean heat gain in 2022 than in 2021. All units are in W m^{-2} . LH+SH is from ERA5, and SW+LW is from the NASA FLASHFlux version 4A adjusted to CERES Surface EBAF Ed4.2. Net radiative fluxes defined as the difference between the incoming and outgoing radiation (positive indicates radiative flux into the ocean).

2. SURFACE FRESHWATER FLUXES

As expected, $P-E$ anomalies in 2022 (Fig. 3.12a) exhibit a large-scale distribution generally reminiscent of sea-surface salinity anomalies (see Fig. 3.7a). The largest $P-E$ anomalies in 2022 were found in the tropics. Strong positive ($>60 \text{ cm yr}^{-1}$) $P-E$ anomalies (a freshening effect on the ocean surface) were located west of the Maritime Continent that acts as a border between the Pacific and Indian Oceans and over the Coral Sea, while large negative $P-E$ anomalies (indicating a salinification effect on the ocean surface) spread over much of the equatorial Pacific and southern tropical Pacific regions. The largest $P-E$ anomaly exceeded 60 cm yr^{-1} . The pattern is consistent with the La Niña-associated SST anomaly distribution (see Fig. 3.2), where above-normal SST in the western Pacific and below-normal SST in the central-eastern Pacific cause the centers of east–west-oriented Walker circulation to shift westward (see Sidebar 3.1). For the Indian Ocean, in addition to the La Niña impact, the negative Indian dipole mode event enhanced the dipole pattern with a positive 2022 $P-E$ anomaly over the eastern Indian Ocean and a negative anomaly over the western Indian Ocean. In the tropical Atlantic Ocean, a positive $P-E$ anomaly dominated the Atlantic ITCZ, which is often observed during La Niña years.

The 2022-minus-2021 $P-E$ difference (Fig. 3.12b) is similar to the 2022 anomaly (Fig. 3.12a) in the Pacific and Indian Oceans. This is consistent with SST differences (see Fig. 3.1b) and surface-wind stress differences (Fig. 3.13b), where stronger east–west SST gradients led to a stronger Walker circulation and stronger convection in the western Pacific. For the Atlantic Ocean, negative $P-E$ differences are observed north of the equator and are not found in the $P-E$ anomaly map for 2022. This is because an extremely strong Atlantic Niño occurred in 2021 (Crespo et al. 2022) while 2022 was a normal year. Similar to its counterpart in the Pacific, strong warming in the eastern Atlantic Ocean tends to enhance precipitation near the Gulf of Guinea (Vallès-Casanova et al. 2020). Overall, the $P-E$ differences are determined primarily by P changes (Fig. 3.12d) and secondarily by E (Fig. 3.12c). Note the centers of SW+LW differences (Fig. 3.11c) have a high negative correlation with P differences, where areas with increased SW+LW coincide with areas of reduced precipitation.

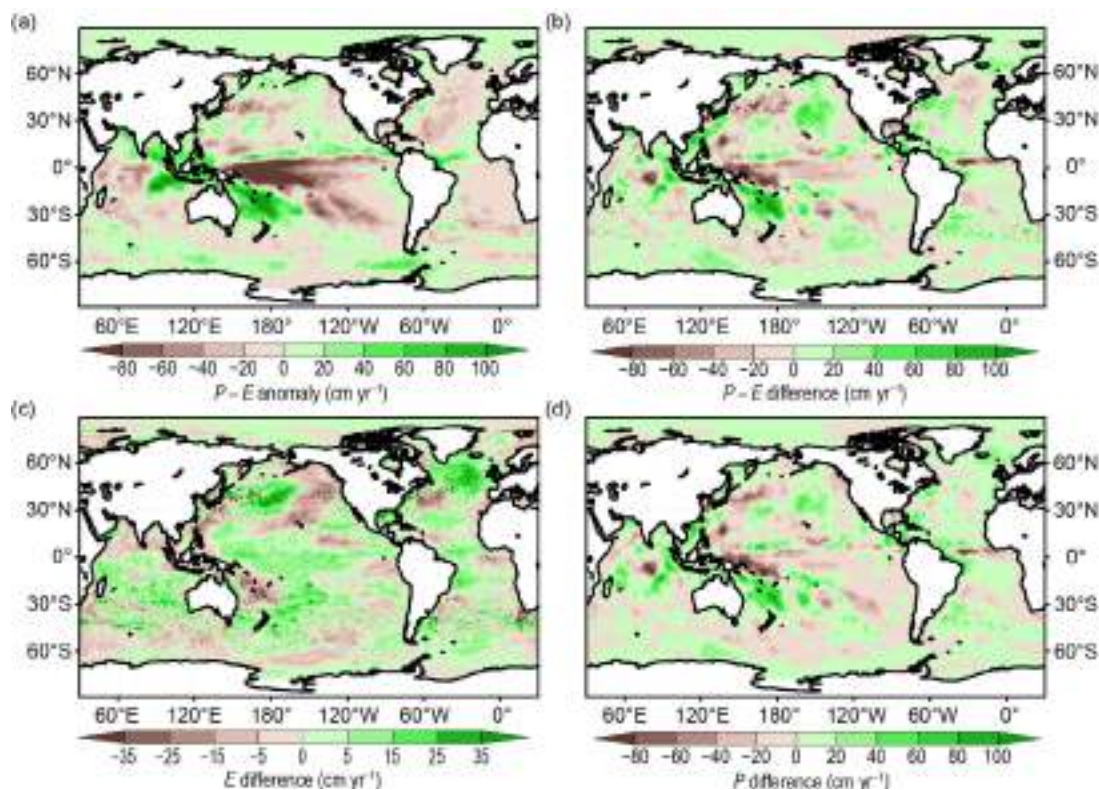


Fig. 3.12. (a) Surface freshwater precipitation minus evaporation ($P-E$) flux anomalies (cm yr^{-1}) for 2022 relative to the 1988–2015 climatology. Positive values denote ocean freshwater gain. (b)–(d) 2022-minus-2021 differences for (b) $P-E$, (c) evaporation (E), and (d) precipitation (P). Positive values denote ocean freshwater gain, and negative values denote ocean freshwater loss. P is from the GPCP version 2.3 product, and E is from ERA5.

3. WIND STRESS

The 2022 wind-stress anomalies (Fig. 3.13a) exceeded 0.02 N m^{-2} in the mid-high latitudes and over the central tropical Pacific Ocean. In the Southern Hemisphere, strong positive anomalies exceeding 0.04 N m^{-2} were observed over the Antarctic Circumpolar Current (ACC) region between 50°N and 60°N , where the westerly winds were strengthened. Enhanced easterly trade winds were present over the central equatorial Pacific, a canonical La Niña signature. Wind enhancement was also observed in the north subpolar Atlantic (50°N – 70°N). Significant wind changes from 2021 to 2022 ($>0.02 \text{ N m}^{-2}$; Fig. 3.13b) were mainly in the mid-high latitudes. Anticyclone-like changes were present in the North Pacific, with westerly winds strengthened near the Kuroshio and weakened northwesterly winds along the west coast of North America. In the North Atlantic, easterly winds strengthened substantially south of Greenland, with wind stress changes exceeding 0.04 N m^{-2} .

Surface winds not only influence the ocean by modulating heat fluxes, but also by redistributing water masses via wind-driven currents. The spatial variations of winds and meridional gradient of the Coriolis parameter lead to divergence and convergence of the Ekman transport, which results in a vertical velocity W_{EK} at the base of Ekman layer, denoted as Ekman pumping (downwelling, downward direction) and Ekman suction (upwelling, upward direction). The 2022 W_{EK} anomalies (Fig. 3.13c) were large and negative ($<-12 \text{ cm day}^{-1}$) in the western Pacific and in a narrow band north of the equator. A narrow band of positive anomalies (upwelling) was present near the central and eastern equatorial region of the Pacific, a typical La Niña pattern. Strong positive anomalies ($>12 \text{ cm day}^{-1}$) were also present in the northeastern Indian Ocean. The 2022-minus-2021 W_{EK} differences suggest enhanced downwelling in the western equatorial Pacific, consistent with the strengthening warming in the western Pacific.

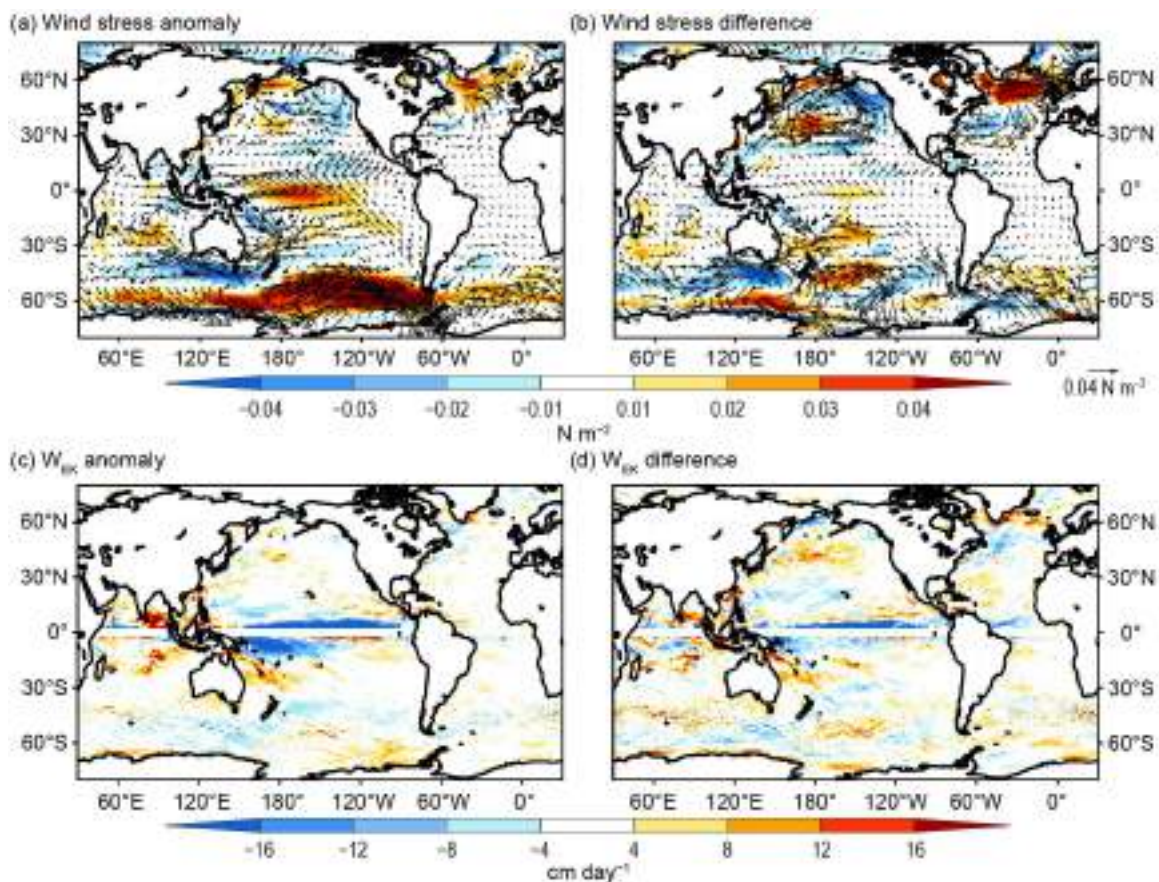


Fig. 3.13. (a) Wind stress magnitude (shaded) and vector anomalies (N m^{-2}) for 2022 relative to a 1988–2015 climatology. (b) 2022-minus-2021 differences in wind stress (N m^{-2}). (c) Ekman vertical velocity (W_{EK} ; cm day^{-1}) anomalies for 2022 relative to a 1988–2015 climatology. Positive (negative) values denote upwelling (downwelling). (d) 2022-minus-2021 differences of W_{EK} (cm day^{-1}). Wind stress fields are from ERA5.

4. LONG-TERM PERSPECTIVE

A long-term perspective on the change of ocean surface fluxes is examined in the context of annual-mean series of Q_{net} , $P-E$, and wind-stress magnitude anomalies averaged over the global ocean (Figs. 3.14a–c). The Q_{net} time series commenced in 2001, when CERES EBAF4.2 surface radiation products became available. Q_{net} anomalies are relative to the 2001–15 climatology. Both $P-E$ and wind-stress time series start from 1988 when Special Sensor Microwave/Imager satellite retrievals are available. Annual mean anomalies are relative to 1988–2015 climatology.

While accurately determining the order 1 W m^{-2} net energy flux entering the ocean from global ocean average Q_{net} would be very challenging, the time series does exhibit decadal fluctuations. The Q_{net} anomaly decreased from $+1.5 \text{ W m}^{-2}$ in 2001 to -2 W m^{-2} in 2010 and then gradually increased to the peak value of $+2.8 \text{ W m}^{-2}$ in 2019. Q_{net} displayed a decreasing trend during the 2020–22 triple-dip La Niña event. The $P-E$ time series displayed a clear downward trend during 1988–2022. The global average $P-E$ anomaly was above normal prior to 1998 and generally below normal thereafter. During 2015–22, $P-E$ variations were closely related to El Niño–Southern Oscillation conditions. The global $P-E$ anomaly was close to zero during 2015 and then decreased during the double-dip 2016/17 La Niña. After the $P-E$ rebounded to zero in the 2019 El Niño year, $P-E$ continued to decrease during the triple-dip La Niña and reached the historical low in 2022 ($\sim 5.4 \text{ cm yr}^{-1}$). Wind stress was strongest during the 1998 La Niña. Wind stress anomalies remained above average after 2010, consistent with more frequent La Niñas in the last decade.

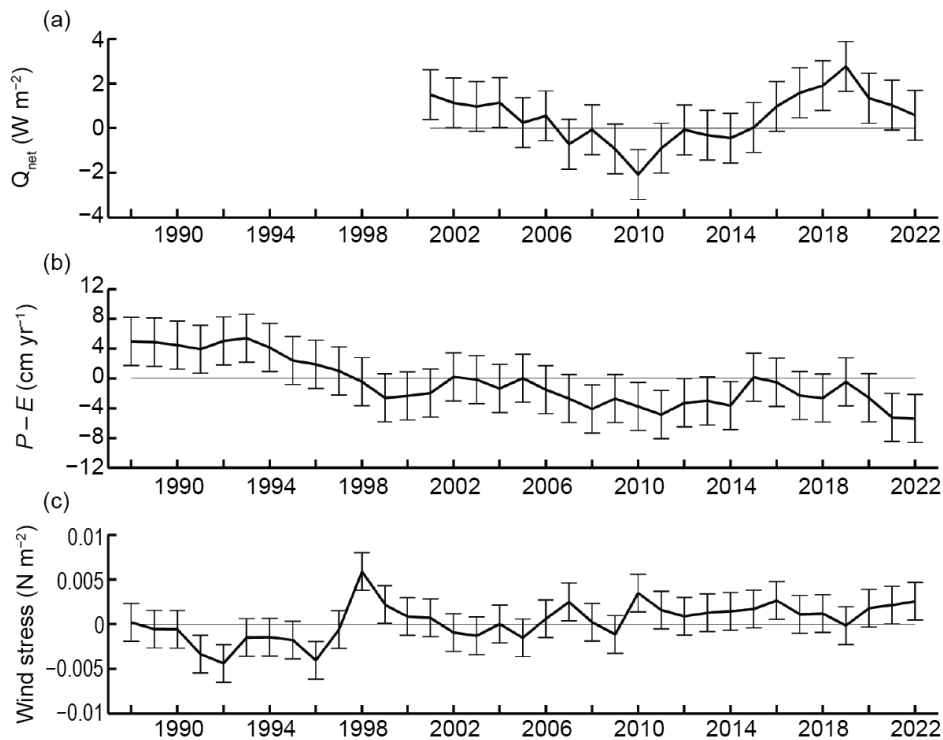


Fig. 3.14. Annual-mean time series of global average of ocean-only (a) net surface heat flux (Q_{net} ; W m^{-2}) from a combination of CERES EBAF4.2 shortwave radiation + longwave radiation (SW + LW) and ERA5 latent heat flux + sensible heat flux (LH+SH). The 2022 Q_{net} is based on FLASHFlux SW+LW as adjusted to EBAF and ERA5 LH+SH. (b) Net freshwater flux anomaly precipitation minus evaporation ($P-E$; cm yr^{-1}) from a combination of P and ERA5 E . (c) Wind stress magnitude anomalies (N m^{-2}) from ERA5. Error bars denote 1 std. dev. of annual-mean variability.

f. Sea-level variability and change

—P. R. Thompson, M. J. Widlansky, E. Leuliette, D. P. Chambers, W. Sweet, B. D. Hamlington, S. Jevrejeva, M. A. Merrifield, G. T. Mitchum, and R. S. Nerem

Annual average global mean sea level (GMSL) from satellite altimetry (1993–present) reached a new high in 2022, rising to 101.2 mm above 1993 (Fig. 3.15a). This marks the 11th consecutive year (and 27th out of the last 29) that GMSL increased relative to the previous year, reflecting an ongoing multi-decadal trend of 3.4 ± 0.4 mm yr⁻¹ in GMSL during the satellite altimetry era (Fig. 3.15a). A quadratic fit with corrections for the eruption of Mount Pinatubo (Fasullo et al. 2016) and El Niño–Southern Oscillation effects (Hamlington et al. 2020) yields a climate-driven trend of 3.0 ± 0.4 mm yr⁻¹ and acceleration of 0.081 ± 0.025 mm yr⁻² (updated from Nerem et al. 2018).

Independent observing systems measure the contributions to GMSL rise from increasing ocean mass, primarily due to melting of glaciers and ice sheets (see sections 5f, 6d, 6e), and decreasing ocean density, primarily due to ocean warming (section 3c). Data from Argo profiling floats analyzed by Scripps Institution of Oceanography (SIO; Roemmich and Gilson 2009) show a global mean steric (i.e., density-related) sea-level trend of 1.3 ± 0.2 mm yr⁻¹ during 2005–22 (Fig. 3.15a). Global ocean mass (excluding regions within 300 km of land) produced by the NASA Jet Propulsion Laboratory using mass concentration anomalies from the Gravity Recovery and Climate Experiment (GRACE) and GRACE Follow-On (GRACE-FO) missions show a global mean ocean-mass trend of 2.1 ± 0.4 mm yr⁻¹ during 2005–22 (Fig. 3.15a). The sum of these trend contributions, 3.4 ± 0.4 mm yr⁻¹, agrees within uncertainties with the GMSL trend of 3.9 ± 0.4 mm yr⁻¹ measured by satellite altimetry since 2005 (Leuliette and Willis 2011; Chambers et al. 2017). Consistency among trends from these independent observing systems is a significant achievement and increases confidence in estimates of Earth’s energy imbalance (e.g., Hakuba et al. 2021; Marti et al. 2022).

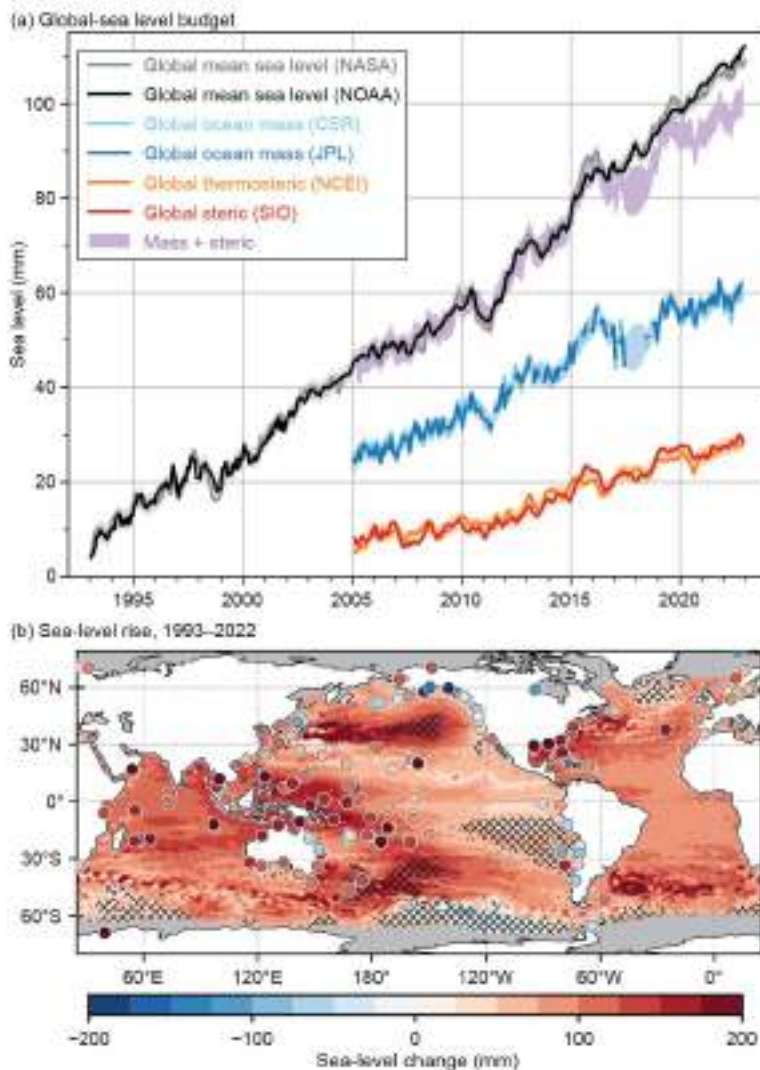


Fig. 3.15. (a) Global mean sea level (GMSL; mm) observed by satellite altimeters (1993–2022) from the NOAA Laboratory for Satellite Altimetry (black) and NASA Sea Level Change Program (gray). Monthly global ocean mass (2005–22) from GRACE and GRACE-FO calculated from mass concentrations produced by NASA JPL (blue) and University of Texas Center for Space Research (CSR, cyan). GRACE and GRACE-FO data within 300 km of land were excluded in both ocean mass time series. Monthly global mean steric sea level (2004–22) from SIO Argo data (red). Monthly global mean thermosteric sea level from NCEI Argo and hydrographic data (orange). Monthly global ocean mass plus steric (purple). Shading around all data sources represents a 95% confidence range based on Gaussian process regressions onto each pair of time series. (b) Total local sea-level change (mm) during 1993–2022 as measured by satellite altimetry (contours) and tide gauges (circles). Hatching indicates local changes that differ from the change in GMSL by more than 1 std. dev. Altimetry data used to generate the trend map were obtained from the NASA MEaSUREs Gridded Sea Surface Height Anomalies Version 2205. Tide-gauge observations were obtained from the University of Hawaii Sea Level Center Fast Delivery database.

Annually averaged GMSL from satellite altimetry increased 3.3 ± 0.7 mm from 2021 to 2022, exceeding the sum of year-over-year increases in global mean steric sea level from Argo, 1.9 ± 0.4 mm, and global mean ocean mass from GRACE-FO, 0.2 ± 0.7 mm. The sum of global steric and mass increases, 2.1 ± 1.0 mm, is less than the observed increase in GMSL from altimetry, but the two do agree within standard error uncertainties. A portion of the discrepancy may be due to incomplete annual updates to the global steric and mass time series, which at the time of writing were updated through November and October 2022, respectively. The increase in GMSL from satellite altimetry through October 2022 was 2.73 ± 0.6 mm, which reduces the discrepancy between year-over-year increases in the budget terms by almost half.

Sea-level budget misclosure is larger since 2016 (Fig. 3.15a; Chen et al. 2020). This misclosure does not seem likely to be owing to one cause. Uncertainties in the global mass budget (e.g., leakage near land, geocenter, and glacial isostatic adjustment) do warrant investigation (Chen et al. 2020). Error sources in the altimeter measurements, such as the wet tropospheric correction, may also contribute (Barnoud et al. 2021). Drift in Argo salinity measurements (Roemmich et al. 2019) can artificially suppress increasing global mean steric sea level, but quality-control procedures applied in the SIO data product used here mitigate that impact (Barnoud et al. 2021). The SIO time series of steric sea level compares favorably with a time series of global mean thermosteric sea level from the NOAA National Centers for Environmental Information (Fig. 3.15a). Undersampling of the ocean by Argo, especially around the Malay Archipelago between Asia and Australia (von Schuckmann et al. 2014), could also lead to underestimates of global mean steric rise.

Spatial structure in sea-level changes over the 30-year altimeter record (Fig. 3.15b) is due to a combination of natural fluctuations in coupled modes of atmosphere–ocean variability (Han et al. 2017) and the oceanic response to anthropogenic radiative forcing (Fasullo and Nerem 2018). As the altimetry record grows in length, the impact of natural fluctuations on regional sea-level trends decreases. Presently, only a small fraction of the global ocean has experienced sea-level trends that differ from the global mean trend by more than one standard deviation (hatched areas, Fig. 3.15b). Reduced sea-level trends in the tropical eastern Pacific reflect the impact of multidecadal variability in the strength of Pacific trade winds (e.g., Merrifield 2011), while enhanced sea-level change in the high latitude South Pacific can be attributed to regional warming (Llovel and Terray 2016; Volkov et al. 2017). Sea-level change relative to land (i.e., the quantity measured by tide gauges; circles, Fig. 3.15b) is most relevant for societal impacts and can differ substantially from satellite-derived changes in tectonically active regions (e.g., Japan) and areas strongly affected by glacial isostatic adjustment (e.g., Alaska; Fig. 3.15b).

Annual sea-level anomalies during 2022 were positive nearly everywhere (Fig. 3.16a), mostly because of the long-term trend of rising sea levels (Fig. 3.15b). In the tropics, the highest sea-level anomalies were in the western Pacific and the eastern Indian Ocean (exceeding 15 cm above normal in some locations), whereas the lowest anomalies were in the northeastern Pacific (about 5 cm below normal). In the midlatitudes of both hemispheres (i.e., between the 30° – 60° latitudes), sea-level anomalies also exceeded 15 cm in places, especially in the extension regions of the Kuroshio and Gulf Stream Currents. Upwelling mesoscale eddy activity in the midlatitudes contributed to small-scale areas of negative sea-level anomalies (e.g., east of Japan and in the North Atlantic).

Prolonged La Niña conditions that developed during mid-2020 re-intensified during 2021, and continued throughout all of 2022 (see Sidebar 3.1 and section 4b) explain the mostly consistent sea-level pattern in the equatorial Pacific during the past three years (Fig. 3.16b). In 2022, a noticeable change from 2021 was in the tropical southwestern Pacific where sea-level anomalies increased by about 10 cm (a similar change also occurred in the southeastern part of the tropical Indian Ocean). In this so-called South Pacific Convergence Zone region (Brown et al. 2020), the largest expanse of sea-level anomalies exceeded 15 cm above normal. The largest regions of

decreasing sea levels during 2022 compared to 2021 were in the tropical North Pacific and the North Indian Oceans. Sea levels around Hawaii decreased about 5 cm and were near normal for the year (i.e., locally, the year-to-year change mostly cancelled the long-term sea-level rise trend). In the Atlantic, 2022-minus-2021 differences were mostly positive along the U.S. East Coast, in the Gulf of Mexico, throughout the Caribbean Sea, and just north of the equator (most of these changes were less than 10 cm). In the midlatitudes, year-to-year sea-level changes were typically larger, especially in the regions most affected by mesoscale oceanic eddies.

In 2022, the triple-dip La Niña (see Sidebar 3.1) is associated with the continuation of above-normal sea levels in the western half of the equatorial Pacific. Long-term sea-level rise partially masks a negative sea-level anomaly in the eastern Pacific otherwise expected during La Niña. During 2022, only minor inter-seasonal changes are evident in the comparison of December 2021–February 2022 (DJF) and September–November 2022 (SON) anomalies (Figs. 3.16c,d). In the Indian Ocean, the sea-level pattern showed evidence of the Dipole Mode Index becoming more negative during 2022 (i.e., sea-level anomalies decreasing in the west and increasing in the east; see section 4f). Some of the highest regional sea-level anomalies during 2022 occurred in the Bay of Bengal as well as near western Australia, where in both places satellite-observed seasonal anomalies exceeded 15 cm above normal during SON. In the north-western Atlantic Ocean, seasonal sea-level anomalies were consistently above normal during 2022, with only minor differences comparing DJF and SON near the U.S. East Coast.

Ongoing trends, year-to-year variability, and seasonal changes in sea level impact coastal communities by increasing the magnitude and frequency of positive sea-level extremes that contribute to flooding and erosion. Minor impacts tend to emerge when local water levels exceed the 99th percentile of daily sea-level maxima (Sweet et al. 2014). Using 1993–2022 as the analysis epoch (consistent with the altimetry baseline), daily sea-level maxima that exceed the 99th percentile—hereafter extreme sea-level events—occurred more frequently in recent years compared to previous decades. Across 119 tide-gauge locations with sufficient data volume and quality for analysis, the median number of extreme sea-level events per year and location

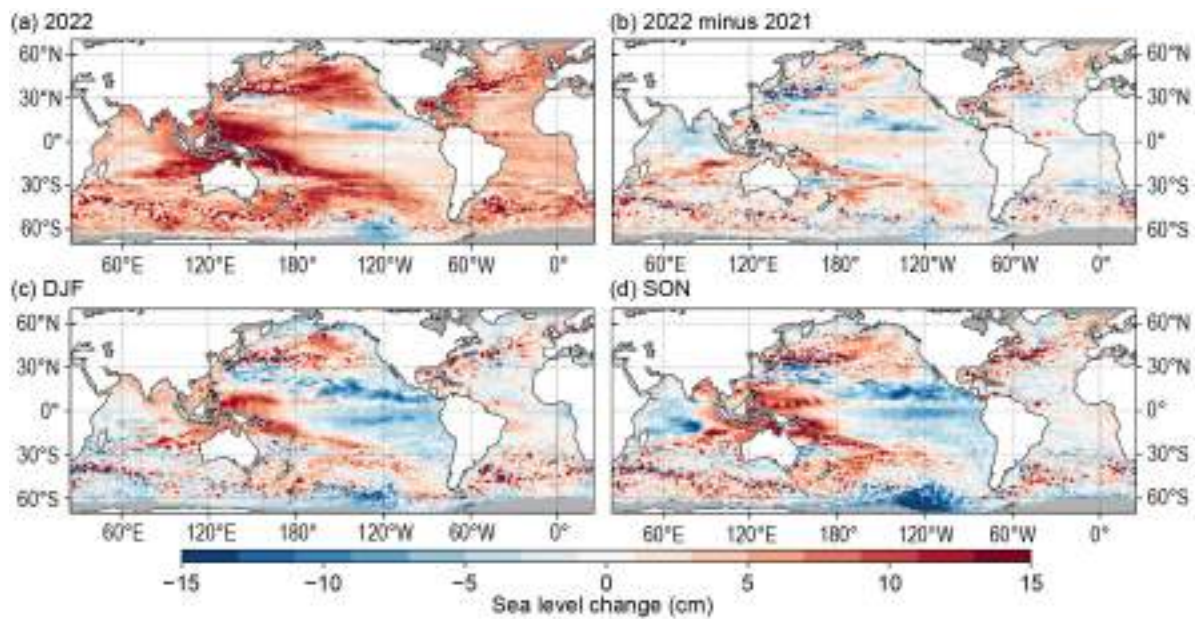


Fig. 3.16. (a) Annual average sea-level anomaly during 2022 relative to average sea level at each location during 1993–2022. (b) Average 2022-minus-2021 sea-level anomaly. (c) Average sea-level anomaly during DJF 2021/22 relative to the 1993–2022 DJF average. (d) Same as (c), but for SON. Units are given in cm. Global mean sea level was subtracted from panels (c),(d) to emphasize regional, non-secular change. Altimetry data were obtained from the NASA MEaSUREs Gridded Sea Surface Height Anomalies Version 2205.

increased from one during 1993–97 to six during 2018–22 (not shown). The 90th percentile of events per year and location increased from 6 during 1993–97 to 15 during 2018–22 (not shown).

Twenty-nine of the 119 locations experienced more than 10 extreme sea-level events during 2022, concentrated in the southwestern Pacific and along western boundary currents in the Northern Hemisphere (Fig. 3.17a) where annual sea-level anomalies were largest (Figs. 3.16a, 3.17b). The greatest numbers of events occurred in the Solomon Islands (51) and Papua New Guinea (37), which experienced high sea-level anomalies related to ongoing La Niña conditions (Fig. 3.16a). The elevated numbers of events in the North Atlantic western boundary current system reflect elevated coastal sea levels due to the combined effects of warm ocean heat content anomalies (see Fig. 3.4a) and weaker-than-average geostrophic currents during the latter third of the year (see Fig. 3.22b) when the seasonal cycles in ocean temperature and tidal amplitude peak. Just 8 locations experienced increases of more than 10 extreme events from 2021 to 2022 (Fig. 3.17c), reflecting the generally moderate year-over-year differences in annual mean sea level across the global ocean (Figs. 3.16b, 3.17d). Ten locations experienced at least 10 fewer extreme events per year in 2022 compared to 2021, concentrated in the Pacific and Indian Oceans (Fig. 3.17c) in areas where annual mean sea level during 2022 was either mostly unchanged or lower compared to the prior year (Figs. 3.16b, 3.17d).

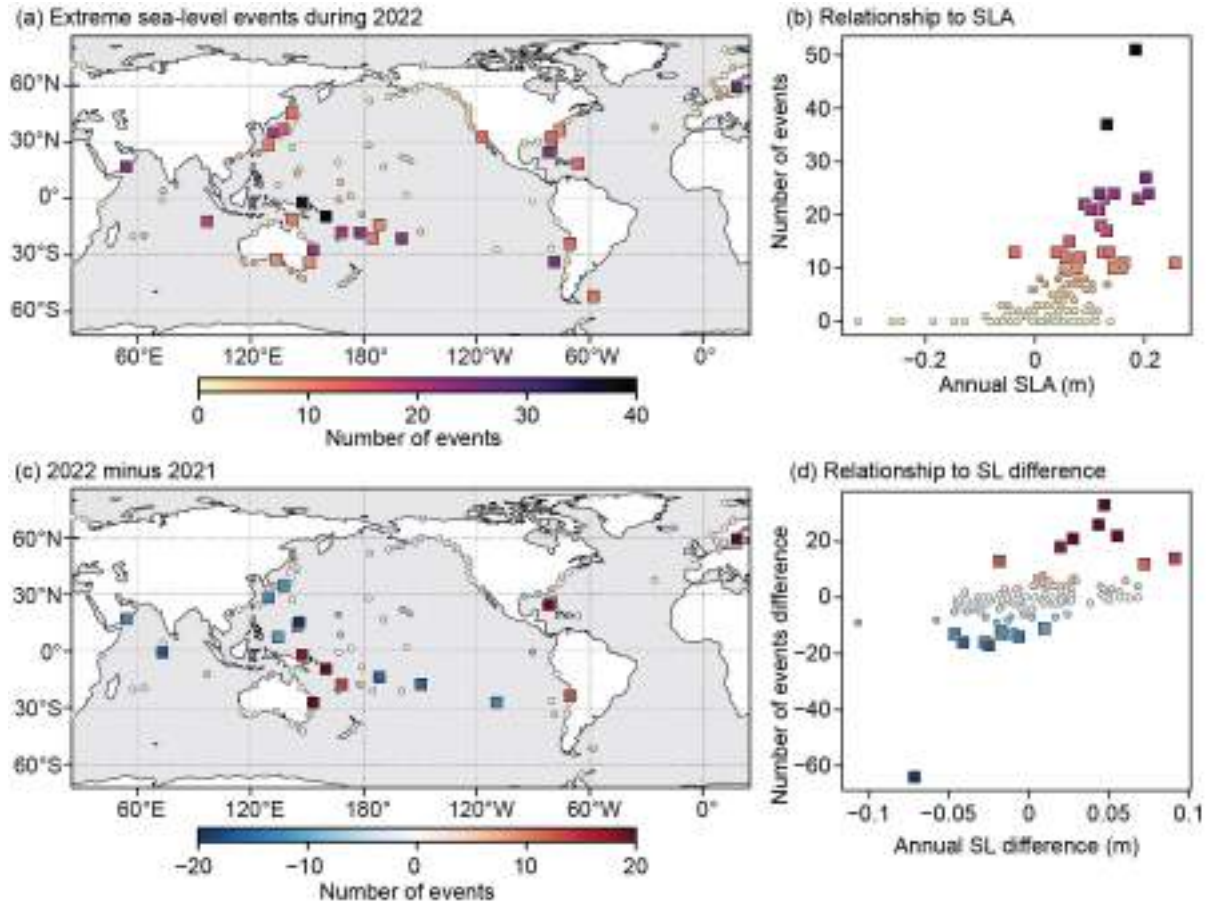


Fig. 3.17. (a) Number of extreme sea-level (SL) events from tide gauges during 2022. (b) Counts in (a) as a function of annual sea-level anomaly (SLA) during 2022. Square markers in (a) and (b) highlight locations with more than 10 extreme events. (c) Change in number of extreme SL events from 2021 to 2022. (d) Counts in (c) as a function of the change in annual SL from 2021 to 2022. Square markers in (c) and (d) highlight locations where the magnitudes of changes in counts of extreme events were greater than 10. Counts of extreme SL events were calculated from hourly tide gauge observations obtained from the University of Hawaii Sea Level Center Fast Delivery database. Only records with at least 80% completeness during 1993–2022 and 80% completeness during both 2021 and 2022, individually, were analyzed.

g. Surface currents

—R. Lumpkin, F. Bringas, G. Goni, and B. Qiu

This section describes variations of ocean surface currents, transports, and associated features, such as rings. Surface currents are obtained from in situ and satellite observations. Transports are derived from a combination of sea-surface height anomaly (from altimetry) and climatological hydrography. See Lumpkin et al. (2012) for details of these calculations. Zonal surface-current anomalies are calculated with respect to a 1993–2020 climatology and are discussed below for individual ocean basins.

1. PACIFIC OCEAN

In 2022, zonal currents in the equatorial Pacific (Fig. 3.18a) exhibited annual mean westward current anomalies of 10 cm s^{-1} on the equator from 140°E – 115°W , with the strongest anomalies of 20 cm s^{-1} at 150°E – 170°E , associated with the persistent La Niña conditions throughout the year (see Sidebar 3.1 and Fig. 4 of Lumpkin and Johnson 2013) and strengthened trade winds in the western half of the basin (Fig. 3.13a). Eastward anomalies of 8 cm s^{-1} to 10 cm s^{-1} were present at 6°N – 8.5°N , 90°W – 175°W , consistent with an intensification and slight northward shift of the eastward North Equatorial Countercurrent (NECC) from its climatological peak of 30 cm s^{-1} at 6.5°N to 40 cm s^{-1} at 7°N and with eastward wind anomalies in this region (Fig. 3.18a).

In 2021/22, the annual-average latitude of the Kuroshio Extension in the region 141°E – 153°E , 32°N – 38°N was shifted north of its long-term (1993–2022) location of 35.4°N , to 36.8°N (2021) and 36.6°N (2022), as seen by alternating eastward/westward anomalies in Fig. 3.18a that persisted

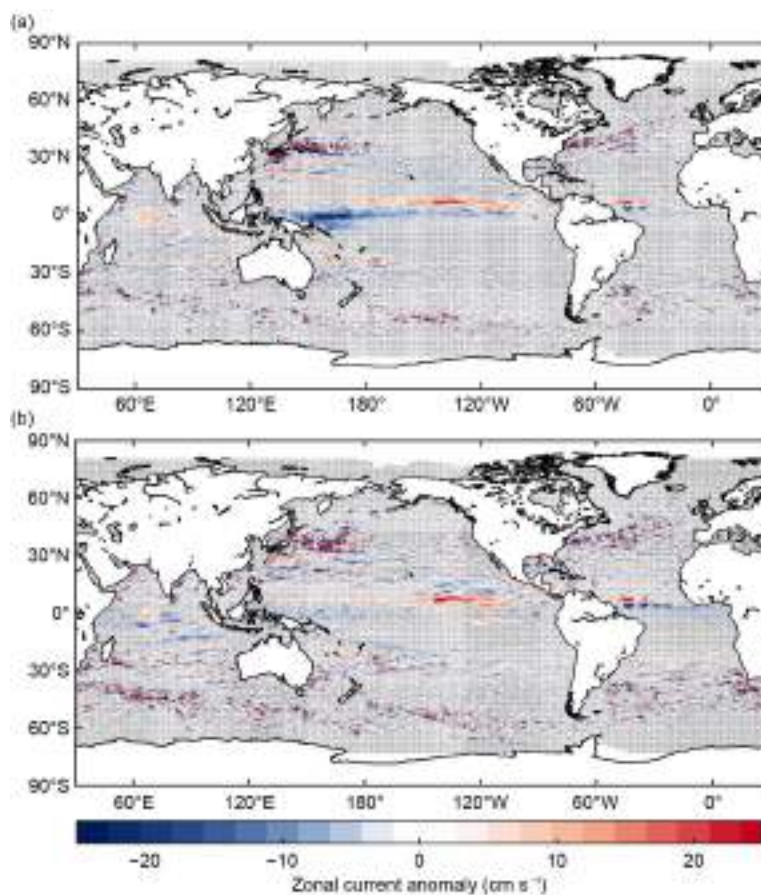


Fig. 3.18. Annually averaged geostrophic zonal current anomalies (cm s^{-1}) for (a) 2022 and (b) 2022 minus 2021 derived from a synthesis of drifters, altimetry, and winds. Values are stippled where they are not significantly different from zero.

through the year (Fig. 3.19) and also in a band of increased ocean heat content anomaly (see Fig. 3.4a). This 2021/22 shift was the largest northward shift in the 1993–2022 record (Fig. 3.20c) and corresponded with a two-year increase in averaged eddy kinetic energy (EKE) of $0.03 \text{ m}^2 \text{ s}^{-2}$ above the long-term average of $0.12 \text{ m}^2 \text{ s}^{-2}$ (Fig 3.20d); this pattern is inconsistent with

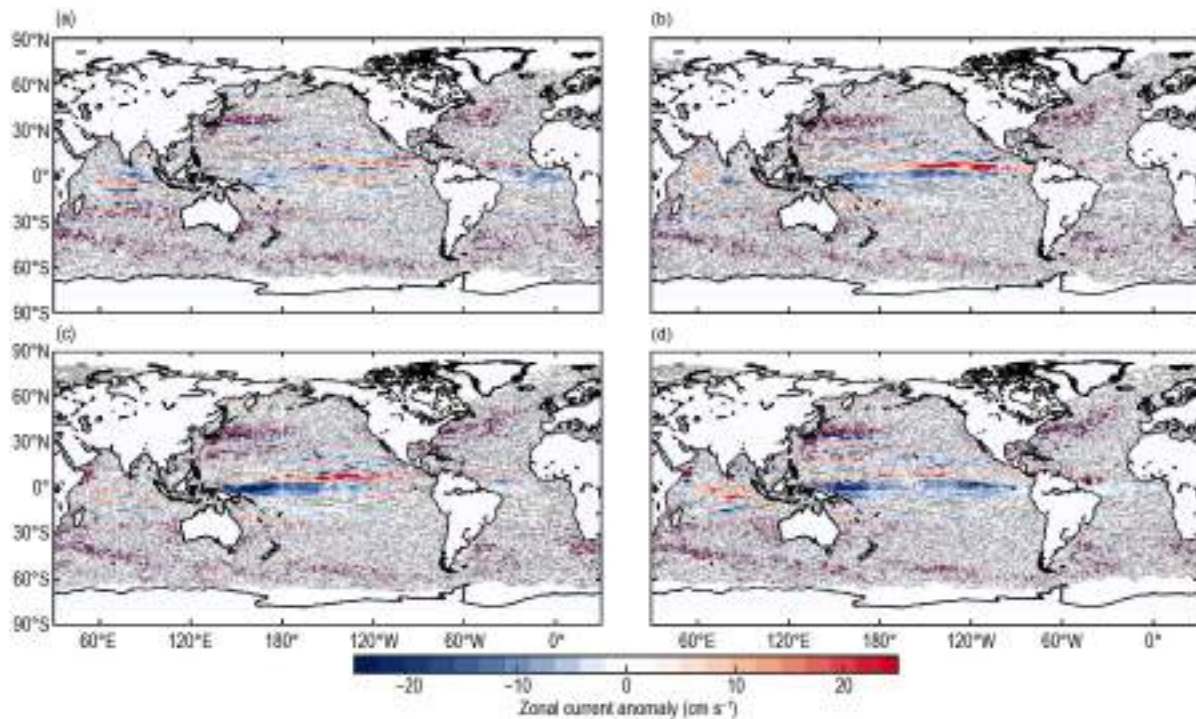


Fig. 3.19. Seasonally averaged zonal geostrophic anomalies (cm s^{-1}) with respect to seasonal climatology for (a) Dec 2021–Feb 2022, (b) Mar–May 2022, (c) Jun–Aug 2022, and (d) Sep–Nov 2022. Values are stippled where they are not significantly different from zero.

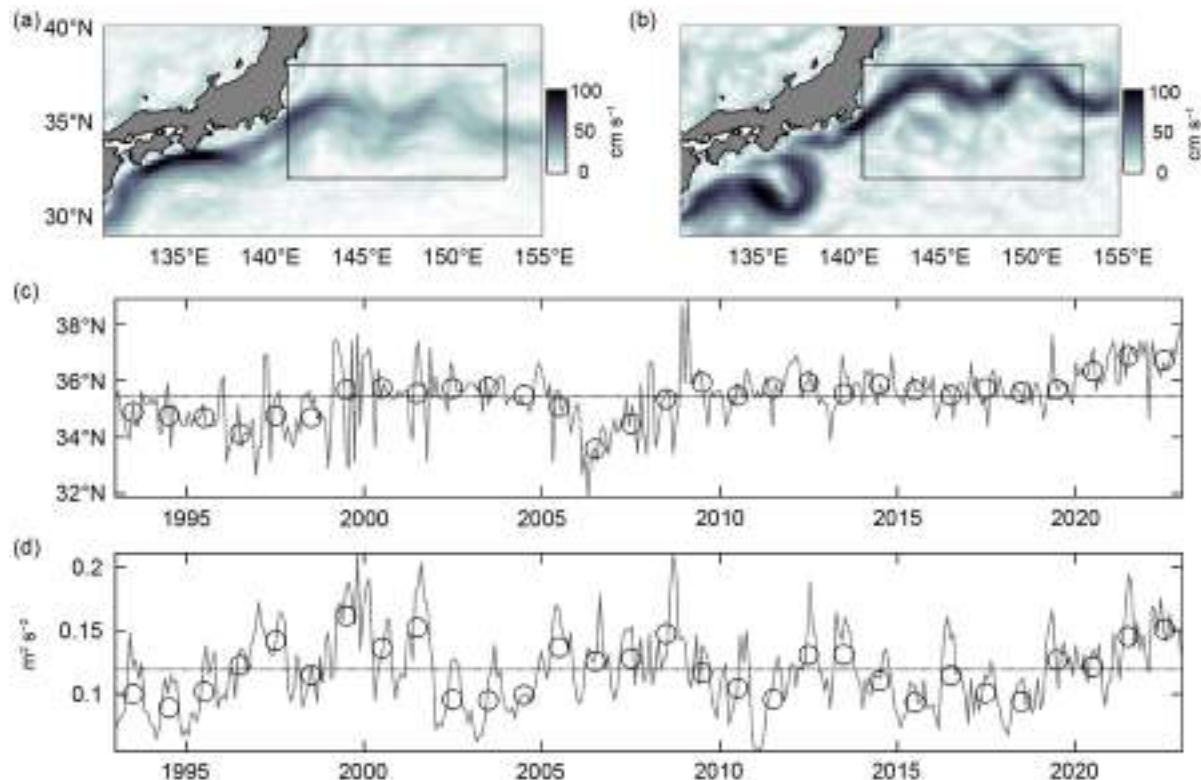


Fig. 3.20. (a) Climatological geostrophic surface current speed (cm s^{-1}) from Mulet et al. (2021) in the Kuroshio Current region (box) and surrounding regions. (b) 2022 mean geostrophic currents (cm s^{-1}) after Mulet et al. (2021) and Copernicus near-real-time altimetry. (c) Latitude of maximum zonal currents (U) averaged in the Kuroshio Current region. (d) Mean eddy kinetic energy (EKE; $\text{m}^2 \text{ s}^{-2}$) in the Kuroshio Current region. Annual means are indicated by circles and overall time means by the dashed lines in (c) and (d).

decadal shifts between increased/decreased EKE and a southward/northward shift of the Kuroshio Extension because of the influence of a Kuroshio meander off the southern coast of Japan (Qiu et al. 2020). This meander is clearly seen in the 2022 altimetry data (Fig. 3.20b) and has been present since 2017, the longest known persistence of a Kuroshio large meander, consistent with wind anomalies associated with positive Pacific Decadal Oscillation forcing in the subtropical western North Pacific (Qiu and Chen 2021). A long-term northward trend in the Kuroshio extension is consistent with the poleward expansion of the Hadley cell seen in coupled climate models (Yang et al. 2020).

Because the equatorial westward anomalies have persisted since 2021, the 2022-minus-2021 difference map (Fig. 3.18b) does not exhibit these anomalies, but highlights the intensification of the eastward Pacific NECC that appeared in 2022.

Equatorial zonal current anomalies were close to zero in December–February (Fig. 3.19a), with weak (5 cm s^{-1} – 6 cm s^{-1}) eastward anomalies at 1°S – 3°S in the central and eastern basin consistent with a weakening of the westward South Equatorial Current (SEC). Eastward anomalies of $\sim 10 \text{ cm s}^{-1}$ at 8°N – 9°N indicated a strengthening and northward shift of the NECC at the beginning of the year. By March–May (Fig. 3.19b) the NECC intensified, with eastward anomalies of 15 cm s^{-1} – 20 cm s^{-1} at 5°N – 7°N in the eastern half of the basin. Westward anomalies of 10 cm s^{-1} also developed at 0° – 2°N across the Pacific and strengthened to $\sim 25 \text{ cm s}^{-1}$ in June–August at 140°E – 175°W (Fig. 3.19c), where climatological equatorial currents are eastward at 4 cm s^{-1} to 5 cm s^{-1} . The NECC intensification persisted through these months. In September–November (Fig. 3.19d), both anomaly patterns weakened, with equatorial anomalies near zero in the central basin and exceeding 20 cm s^{-1} only in the eastern basin ($\sim 150^{\circ}\text{E}$ – 175°E) and a narrow band of 10 cm s^{-1} – 18 cm s^{-1} eastward anomalies at 0° – 4°N , 105°W – 130°W .

2. INDIAN OCEAN

Annually averaged zonal currents in the Indian Ocean were close to their 1993–2020 climatological averages, with weak (1 cm s^{-1} – 3 cm s^{-1}) eastward anomalies at 1°S – 9°S across most of the basin (Fig. 3.18a). Because eastward anomalies in this latitude range were slightly stronger in 2021, the 2022-minus-2021 difference map (Fig. 3.18b) exhibits weak negative (westward) anomalies of $\sim -5 \text{ cm s}^{-1}$ across the basin. Relatively strong (15 cm s^{-1} – 20 cm s^{-1}) negative/positive anomalies immediately offshore Somalia indicate an anomalous southward contraction of the Great Whirl, a circulation feature most prominent in June–August during the Southwest Monsoon (Beal et al. 2013). The eastward currents at the northern edge of the Whirl have a climatological annual mean of $\sim 42 \text{ cm s}^{-1}$ at 10°N , but shifted to 8.5°N – 9°N and weakened to 33 cm s^{-1} in 2022. These anomalies were not present in December–May (Figs. 3.19a,b); they appeared in June–August (Fig. 3.19c) and strengthened to $\pm 30 \text{ cm s}^{-1}$ – 40 cm s^{-1} in September–November (Fig. 3.19d).

3. ATLANTIC OCEAN

Annual mean zonal currents in the western tropical Atlantic Ocean in 2022 exhibited eastward anomalies of 10 cm s^{-1} at 7°N – 8°N and westward anomalies of 5 cm s^{-1} – 10 cm s^{-1} at 2°N – 5°N , consistent with a 5 cm s^{-1} strengthening and $\sim 0.75^{\circ}$ northward shift of the eastward Atlantic NECC and an $\sim 8 \text{ cm s}^{-1}$ strengthening of the westward northern core of the SEC (see Lumpkin and Garzoli 2005). These changes are consistent with the change in wind stress from 2021 to 2022 associated with the end of the 2021 Atlantic Niño (see Fig. 3.13b) and may have played a role in the evolution of strong fresh anomalies in the western tropical Atlantic seen in Fig. 3.8. The 2022-minus-2021 map (Fig. 3.18b) contains stronger (-10 cm s^{-1} to -20 cm s^{-1}) differences along the equator, reflecting the strong eastward currents in 2021 associated with the exceptionally strong 2021 Atlantic Niño (Crespo et al. 2022). The 2022 NECC anomalies were present at $\sim 10 \text{ cm s}^{-1}$ in December–February (Fig. 3.19a) and weakened significantly (to $\sim 5 \text{ cm s}^{-1}$) in March–August (Figs. 3.19b,c). In September–November the eastward NECC anomalies reappeared, reaching 20 cm

s^{-1} at 7°N , along with the first appearance of the westward SEC anomalies of $>10 \text{ cm s}^{-1}$, peaking at 4°N off the east coast of Brazil.

The variability of key Atlantic Ocean currents is continuously monitored in near realtime using a combination of in situ and satellite altimetry (<https://www.aoml.noaa.gov/phod/altimetry/cvar>). In the South Atlantic, the number of rings shed by the Agulhas Current remained similar to the average annual number of shedding events during the 1993–2021 record. The annual transport of the Agulhas Current, an indicator of Indian-Atlantic Ocean interbasin water exchange, was 50.8 Sv ($1 \text{ Sv}=10^6 \text{ m}^3 \text{ s}^{-1}$) in a cross section at $\sim 28^{\circ}\text{E}$ and between 34°S and 40°S , and during the last five years has remained within 1 standard deviation of the long-term mean of $50.9\pm 2.8 \text{ Sv}$. In the southwestern Atlantic, the location of the Brazil-Malvinas Confluence has demonstrated a southward trend since 1993 at decadal time scales (Lumpkin and Garzoli 2011; Goni et al. 2011). During 2022, the Confluence was located at 37.4°S , slightly to the north of the long-term mean of $37.76\pm 0.61^{\circ}\text{S}$ and a northward shift of 1.2°S compared to 2021 (see https://www.aoml.noaa.gov/phod/altimetry/cvar/mal/BM_ts.php). In the North Atlantic, the North Brazil Current (NBC) and associated rings serve as interhemispheric conduits for water masses and heat from the South Atlantic into the North Atlantic (Goni and Johns 2003). A portion of these waters enter the Caribbean Sea carrying low-salinity Amazon River waters (Field 2007), known for creating barrier layer conditions that are often associated with hurricane intensification (e.g., Balaguru et al. 2012; Domingues et al. 2015).

During 2022, freshwater contributions from the Amazon and Orinoco River systems covered most of the eastern and central Caribbean Sea for most of the year, creating negative sea-surface salinity anomalies (Fig. 3.7a) perhaps related to the record Amazon basin flood of mid-2021 (Espinoza et al. 2022). The northwestward flow of the NBC in 2022 was 7.8 Sv , similar to its long-term mean of $7.10\pm 0.76 \text{ Sv}$. However, the retroflected flow increased by more than 2 standard deviations from the long-term mean of $14.9\pm 1.8 \text{ Sv}$, the largest observed annual mean retroflected transport. This is consistent with the increased 2022 NECC strength as the NECC is fed by this retroflexion. To the north, the Yucatan Current (YC) and Florida Current (FC) exhibited anomalies of $+0.29 \text{ Sv}$ and -1.6 Sv , respectively, compared to their 1993–2021 means of $27.76\pm 0.90 \text{ Sv}$ and $31.0\pm 1.2 \text{ Sv}$. The YC transport was 1.43 Sv above its 2021 annual average while the FC transport decreased 1.1 Sv , with 2022 exhibiting the lowest FC annual average transport since 2000 (Fig. 3.22b). The lower-than-usual FC transport is tied to higher coastal sea level and “sunny day” flooding events along the southeast coast of the United States (Ezer and Atkinson 2014; Domingues et al. 2016; Volkov et al. 2020). Further studies addressing the delayed NBC to FC connection may help develop early warnings for such flooding events.

h. Meridional overturning circulation and heat transport in the Atlantic Ocean

—D. L. Volkov, D. A. Smeed, M. Lankhorst, S. Dong, B. I. Moat, J. Willis, W. Hobbs, T. Biló, W. Johns, and L. Chomiak

The Atlantic meridional overturning circulation (MOC) and heat transport (MHT) have been observed (Fig. 3.21) at several trans-basin and western boundary moored arrays (e.g., Frajka-Williams et al. 2019; Berx et al. 2021; Hummels et al. 2022), as well as by synthesizing in situ and satellite altimetry measurements at several latitudes (Hobbs and Willis 2012; Sanchez-Franks et al. 2021; Dong et al. 2021; Kersalé et al. 2021). Here we provide updates on the MOC and MHT estimates from the Rapid Climate Change/MOC and Heatflux Array/Western Boundary Time Series (RAPID-MOCHA-WBTS) moored array at 26.5°N and from the synthetic approach at 41°N and at several latitudes in the South Atlantic. While updates for the Overturning in the Subpolar North Atlantic Program and the South Atlantic MOC Basin-wide Array at 34.5°S are pending, we report on recent advances in observing the variability of flows comprising the lower limb of the North Atlantic MOC, including the Meridional Overturning Variability Experiment (MOVE, 16°N).

The RAPID moored array has provided MOC and MHT estimates at 26.5°N since April 2004 (Moat et al. 2020; Johns et al. 2011). The upper-limb (northward) MOC transport at 26.5°N is represented as the sum of 1) the Florida Current transport obtained by submarine cable measurements between Florida and the Bahamas, 2) the upper-midocean transport east of the Bahamas and above the streamfunction maximum at 1100 m, and 3) the near-surface meridional Ekman transport estimated using European Centre for Medium-Range Weather Forecasts Reanalysis version 5 zonal wind stress (e.g., McCarthy et al. 2015). The MOC and MHT time series for RAPID were recently extended to 20 December 2020 (Moat et al. 2022; Fig. 3.22). The annual mean MOC in 2020 was 17.0 Sv, close to the 2004–20 mean value of 16.9 Sv, but significantly stronger than 15.2 Sv in 2019, given the ± 0.9 Sv uncertainty of annual transport estimates (McCarthy et al. 2015). The 2019 annual mean MOC was as low as in 2012; only 2009 and 2010 had lower annual means (14.6 and 14.9 Sv). The low 2019 value was mainly due to a reduction of the transport through the Florida Strait (Fig. 3.22b). This is in contrast with the previous lows, which were caused by changes in the Ekman and upper midocean transports (Figs. 3.22c,d). It has been reported that interannual variability of the MOC transport at 26.5°N is primarily due to isopycnal displacements on the western boundary, reflected in the upper-midocean transport changes (Frajka-Williams et al. 2016). However, since

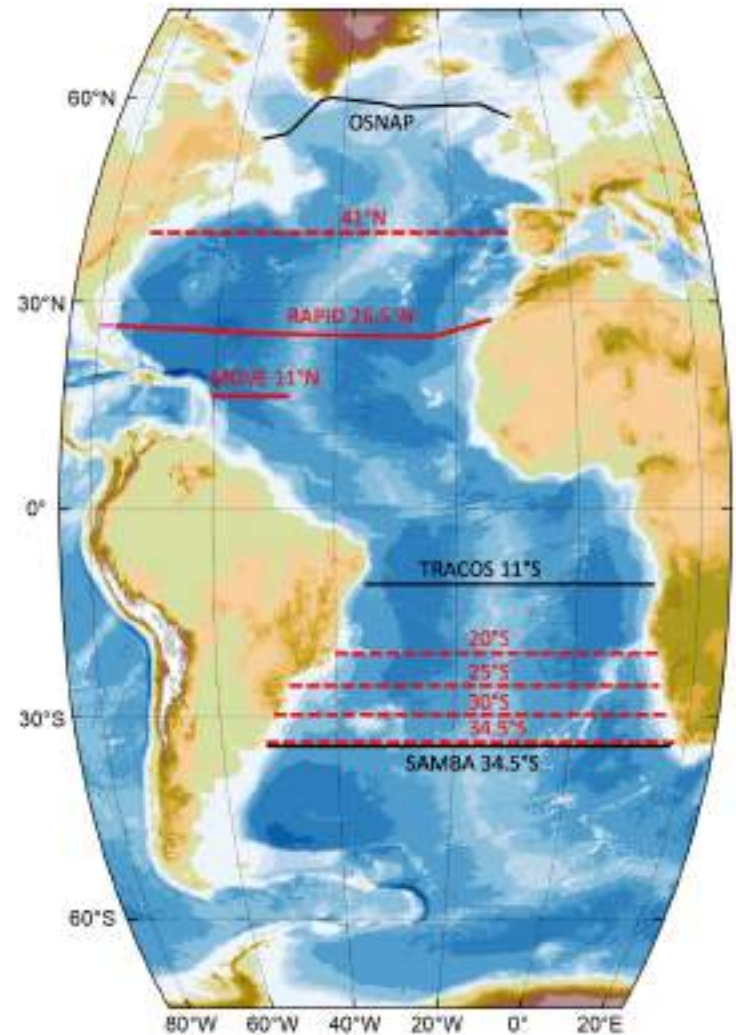


Fig. 3.21. (a) The Atlantic meridional overturning circulation (AMOC) observing system: moored arrays (solid red and black lines) and sections across which the MOC and meridional heat transport are estimated by synthesizing in situ measurements (Argo, XBT) with satellite altimetry data (dashed red lines). The red lines show the sections that have updates covered in this report, while the black lines show the sections for which updates are pending.

about 2014, interannual variability of the MOC has been dominated by variations of the Florida Current transport (Figs. 3.22a,b; Dong et al. 2022). The reasons for this change are still unknown.

Synthetic MOC and MHT time series are evaluated at several latitudes in both the North and the South Atlantic (Fig. 3.23). Monthly estimates at 41°N (Fig. 3.23a), based on satellite altimetry and Argo measurements, were reproduced from Willis (2010) and Hobbs and Willis (2012) and extended through October 2022. Each individual estimate represents a three-month average with an uncertainty of ± 2.3 Sv for the MOC and ± 0.23 PW for the MHT. The mean MOC and MHT are 12.0 Sv and 0.44 PW, respectively. The MOC transport at 41°N was 13.2 Sv in January–October 2022 and 10.6 Sv in 2021, with both values not statistically different from the mean within uncertainty. The MHT in 2022 was 0.57 PW, statistically significantly greater than the time mean and the MHT of 0.39 PW in 2021. As the quality control of Argo and altimeter data is always ongoing, improvements in the estimate implemented since the *State of the Climate in 2021* report (Volkov et al. 2022) resulted in a small increase in the MOC transport equivalent to about 1 Sv from about 2019. While this change is smaller than the year-to-year uncertainty in the estimate at 41°N, it does reduce the small negative trend in the MOC since the record began in 2002, as reported last year (Volkov et al. 2022). Hence no significant trend exists in the MOC and MHT at 41°N over the past two decades.

In the South Atlantic, synthetic MOC and MHT estimates are routinely produced for 20°S, 25°S, 30°S, and 35°S (Figs. 3.23b–e) using a suite of hydrographic data (Argo, Expendable

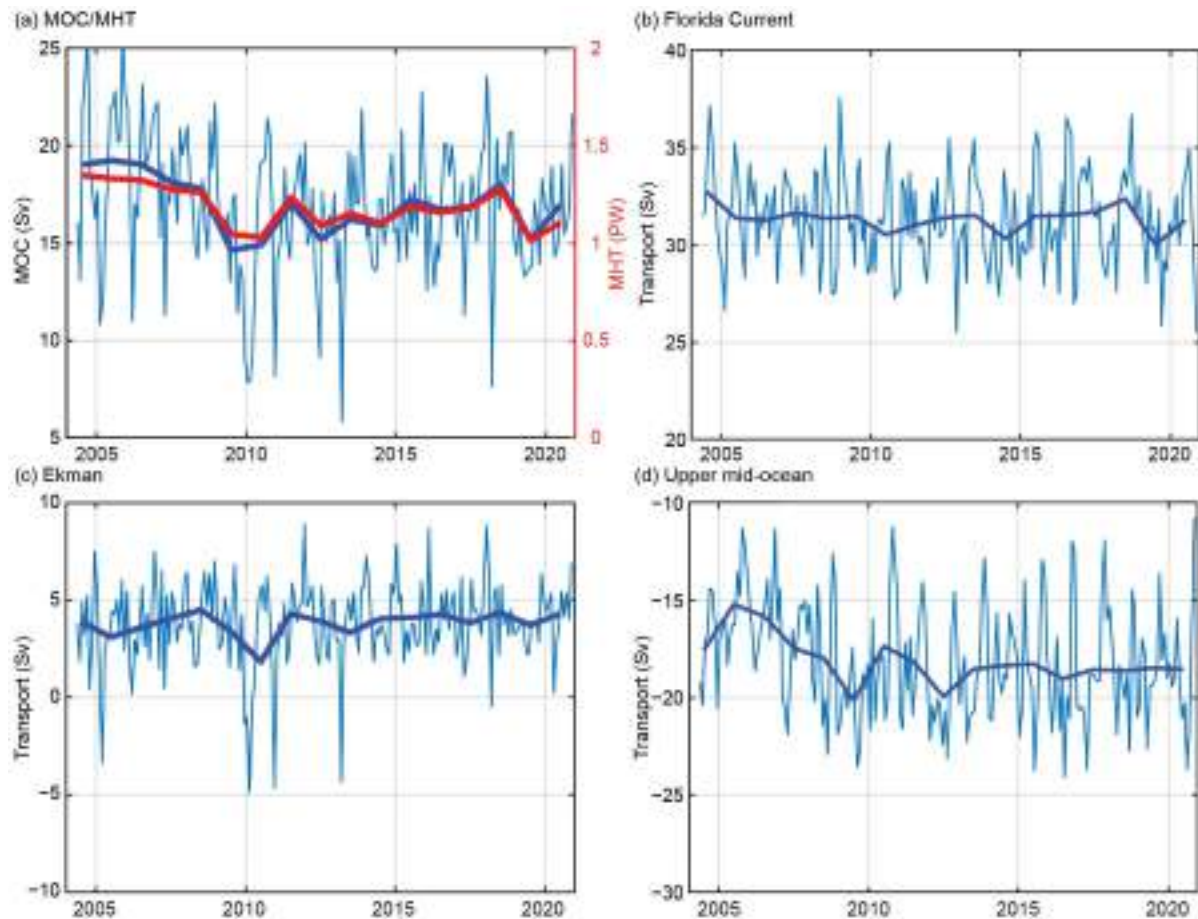


Fig. 3.22. The monthly (thin blue lines) and annual (thick lines) averages of the Atlantic meridional overturning circulation (MOC; Sv) and its components at 26.5°N: (a) the upper-limb (blue) MOC and (red) meridional heat transport (MHT; PW), (b) the Florida Current transport (Sv), (c) the near-surface Ekman transport (Sv), (d) the upper mid-ocean transport (between the Bahamas and Africa and above 1100 m; Sv). Positive/negative values mean northward/southward transports.

Bathythermographs [XBT], and Conductivity-Temperature-Depth [CTD]) and satellite altimetry (Dong et al. 2021). In 2022, the MOC and MHT estimates at 20°S, 25°S, and 30°S (16.2, 19.8, and 18.3 Sv) were nearly the same as those in 2021 (16.1, 19.5, and 18.8 Sv). At 34.5°S, both the MOC and MHT in 2022 (18.7 Sv and 0.62 PW) were lower than in 2021 by 1.1 Sv and 0.10 PW, respectively, but these differences are not statistically significant. The long-term trends in the MOC and MHT remain the same as those reported in Volkov et al. (2022). Meaningful positive trends in both the MOC and the MHT are observed at 25°S and 34.5°S only. While the MOC shows significant negative trends at 20°S and 30°S (both -0.03 ± 0.02 Sv yr⁻¹), the corresponding trends in the MHT are statistically insignificant. These trends in the MOC and MHT are mostly dominated by the geostrophic component.

In the North Atlantic, the MOC lower limb is dominated by southward flow of North Atlantic Deep Water (NADW) formed in the subpolar North Atlantic. The sum of the upper (1100 m–3000 m) and lower (3000 m–5000 m) NADW transports at 26.5°N (Fig. 3.24a), with a time-mean of -17.8 Sv, compensates for the northward transport in the MOC upper limb (Fig. 3.22a) and about 1 Sv of northward flowing Antarctic Bottom Water. The majority of the southward NADW transport is carried within the Deep Western Boundary Current (DWBC) along the eastern continental margins of the Americas. The DWBC transport measured by current meter-equipped moorings at the western end of the RAPID array since 2004 shows a time mean of -31.0 ± 1.0 Sv, a standard deviation of about 19 Sv (for 12-hourly data), and a statistically insignificant weakening trend of 0.27 Sv yr⁻¹ (Fig. 3.24a; adapted from Biló and Johns 2020). Because the moorings observe the fixed region where the DWBC's velocity core is typically found, the strong oscillations of the transport and the absence of correlation between the DWBC transport and the zonally integrated NADW flow are mainly due to the DWBC's vigorous meandering activity at time scales ranging from several weeks to a few years. Because of this strong variability, a longer time series is required to determine if the weakening trend in the DWBC transport is robust.

Farther south, the MOVE array in the western tropical North Atlantic (Fig. 3.21) has been observing the NADW flow at 16°N since 2000 (Kanzow et al. 2006). Salinity data were reprocessed in 2022, which somewhat altered the MOVE time series (Fig. 3.24b). The time series shows a relatively strong southward flow of 17 Sv–18 Sv in the early 2000s, which weakened to about 15 Sv in 2005 and 2012 and increased again to near 18 Sv in 2019. The observed MOVE transport tendencies are consistent with those obtained from satellite gravimetry (Koelling et al. 2020). There is some consistency between the decadal changes of the southward flow at 16°N and

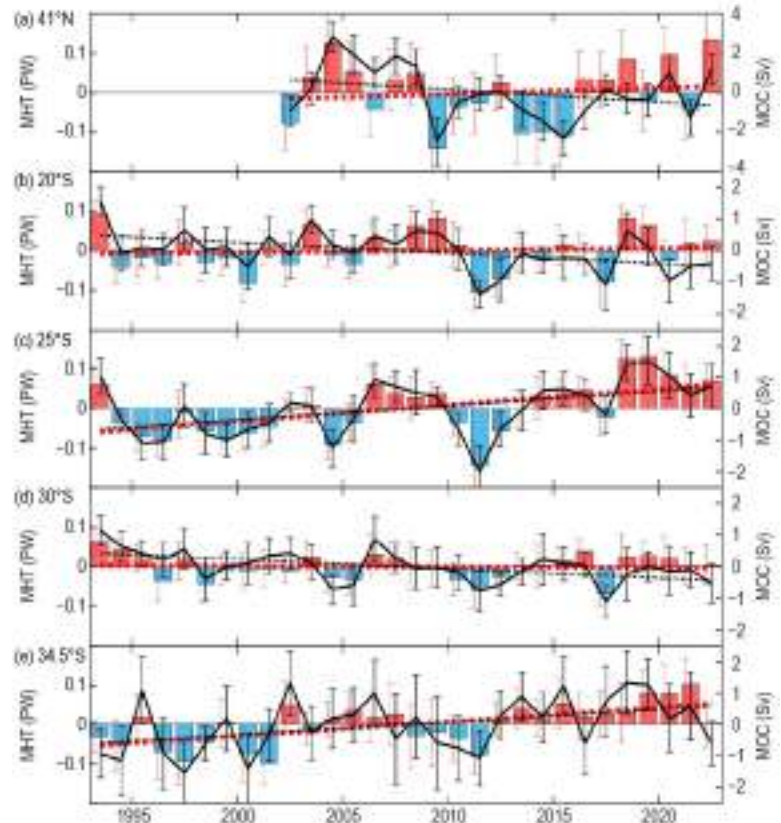


Fig. 3.23. Meridional heat transport (MHT; PW, colored bars) and the meridional overturning circulation (MOC; Sv, black curves) anomalies with respect to the record means obtained by combining satellite altimetry and in situ data at (a) 41°N, (b) 20°S, (c) 25°S, (d) 30°S, and (e) 34.5°S. The vertical error bars show standard errors (red) for MHT and (black) for MOC. The record-mean MHT and MOC values are: 0.44 PW and 12.0 Sv at 41°N, 0.62 PW and 16.6 Sv at 20°S, 0.66 PW and 19.1 Sv at 25°S, 0.62 PW and 18.9 Sv at 30°S, 0.62 PW and 19.3 Sv at 34.5°S.

26.5°N, namely the overall weakening in the 2000s and strengthening in the 2010s (Figs. 3.24a,b). Recent model results have also demonstrated agreement between the centennial trends at the RAPID and MOVE sites (Danabasoglu et al. 2021), which suggest that the consistency between the two observational estimates may improve as the time series become longer.

Meridional coherence of NADW is expected due to the export of subpolar-originated deep waters to lower latitudes. Although a proper assessment of the lower NADW southward spreading patterns is still lacking, several studies have traced the advection of the upper NADW's primary component—Labrador Sea Water (LSW; e.g., van Sebille et al. 2011; Le Bras et al. 2017; Chomiak et al. 2022). Chomiak et al. (2022) investigated the advective spread of two unique LSW classes formed in 1987–94 ($LSW_{1987-94}$) and in 2000–03 ($LSW_{2000-03}$), from the Labrador Sea to 26.5°N via hydrographic arrays transecting the DWBC. The deeper and denser $LSW_{1987-94}$ class took approximately 10 years to reach the subtropics, while the lighter and shallower $LSW_{2000-03}$ class took 10–15 years. Both LSW classes were also observed to arrive within the Atlantic interior prior to or at the same time as observed farther south along the DWBC. This result, along with other recent studies (e.g., Bower et al. 2019; Biló and Johns 2019; Koelling et al. 2020; Lozier et al. 2022), suggests the importance of interior advective pathways, which have the potential to delay the communication of subpolar water masses to the subtropics.

In conclusion, multi-year monitoring of the MOC has greatly advanced our knowledge of large-scale ocean circulation variability at various timescales. With the existing MOC observing system, we are just starting to detect decadal-scale signals relevant for climate variability. While some climate models project a decline in the MOC toward the end of the twenty-first century in response to anthropogenic forcing (e.g., Cheng et al. 2013; Schleussner et al. 2014), it cannot yet be supported by the relatively short observational records. Continued MOC observations are thus necessary for detecting and mechanistic understanding of climate-related changes.

i. Global ocean phytoplankton

—B. A. Franz, I. Cetinić, M. Gao, D. A. Siegel, and T. K. Westberry

Marine phytoplankton contribute ~50% of global net primary production, serving the energy needs of oceanic ecosystems and providing a critical pathway for carbon sequestration to the deep oceans (Field et al. 1998; Siegel et al. 2023). The diversity, abundance, and spatio-temporal distribution of phytoplankton are controlled by biotic factors such as zooplankton grazing and viruses, as well as abiotic factors such as nutrient and light availability that are highly dependent on physical properties and processes, including ocean temperature, stratification, and circulation (e.g., Behrenfeld et al. 2006). Spaceborne ocean color radiometers such as the Sea-Viewing Wide Field-of-View Sensor (SeaWiFS; McClain 2009) and Moderate Resolution Imaging Spectroradiometer (MODIS; Esaias et al. 1998) provide a synoptic view of spatial and temporal changes in phytoplankton through measurements of near-surface concentrations of phytoplankton pigment chlorophyll-*a* ($Chla$; $mg\ m^{-3}$) and phytoplankton carbon (C_{phy} ; $mg\ m^{-3}$).

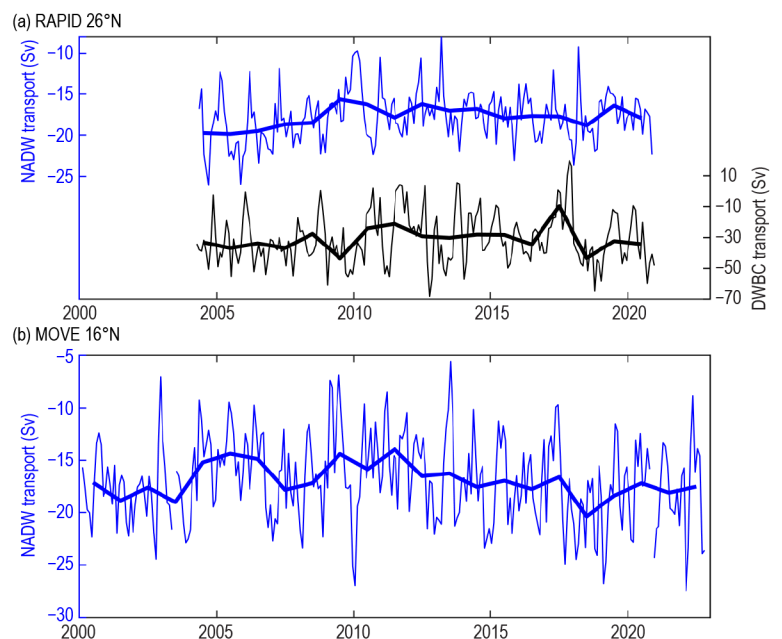


Fig. 3.24. Monthly (thin lines) and yearly (thick lines) transports (Sv) of (a) North Atlantic Deep Water (NADW) between 1100 m and 5000 m (blue) and Deep Western Boundary Current (DWBC) at 26.5°N (black; RAPID array), and (b) NADW at 16°N (MOVE array).

Measurements of *Chl a* contain information pertaining to both biomass and phytoplankton physiology, while C_{phy} measures phytoplankton carbon biomass. C_{phy} and *Chl a* often covary, but discrepancies in their distributions are indicative of changes in the physiological or compositional characteristics of phytoplankton communities (Dierssen 2010; Geider et al. 1997; Siegel et al. 2013; Westberry et al. 2016).

In this report, we evaluate the global distribution of phytoplankton over the period October 2021–September 2022 (the analysis year) using remotely sensed *Chl a* and C_{phy} measurements from the continuous 25-year record that combine observations of SeaWiFS (1997–2010) and MODIS on *Aqua* (MODIS-A, 2002–present). The MODIS-A daytime sea-surface temperature (SST; °C) is also assessed over a consistent time period to provide context on the physical state of the oceans. A key difference in the data sources between this report and previous reports (e.g., Franz et al. 2022) is that the ocean color data from MODIS-A and SeaWiFS were reprocessed by NASA from version R2018.0 to version R2022.0. This reprocessing had only minor impact to the observed trends in the two missions, as temporal calibration updates were minimal, but it did introduce small bias changes in the derived phytoplankton indices. As in R2018.0, the *Chl a* product was derived using the Ocean Color Index algorithm of Hu et al. (2012) but with updated algorithm coefficients applied in R2022.0 (Hu et al. 2019; O’Reilly and Werdell 2019). C_{phy} was derived from the particle backscattering coefficient, b_{bp} , at 443 nm (Generalized Inherent Optical Properties [GIOP] algorithm; Werdell et al. 2013) and a linear relationship between b_{bp} and C_{phy} (Graff et al. 2015). The GIOP algorithm was also updated for the R2022.0 reprocessing to include correction for Raman scattering (McKinna et al. 2016). In merging the time series of SeaWiFS and MODIS-A, differences between the sensors were assessed over the overlapping period from 2003 through 2008, and a bias correction ($-0.0021 \text{ mg m}^{-3}$ in *Chl a* and $-6.7 \times 10^{-5} \text{ m}^{-1}$ in b_{bp} or -0.78 mg m^{-3} of C_{phy}) was derived and applied to the SeaWiFS time series.

A major event likely influencing the quality of *Chl a* and C_{phy} measurements in 2022 was the eruption of Hunga Tonga–Hunga Ha’apai in January 2022 (see Sidebar 2.2). This eruption injected water vapor and sulfur dioxide into the stratosphere and resulted in a substantial increase in stratospheric sulfate aerosols that remained aloft through 2022 (Taha et al. 2022; Schoeberl et al. 2022; Zhu et al. 2022; Sellitto et al. 2022). The atmospheric correction algorithm as applied in NASA’s R2022.0 reprocessing does not properly correct for the effect of light scattering and absorption by these high-altitude aerosols, and thus increased error can be expected in the retrieved spectral water-leaving reflectances from which C_{phy} and *Chl a* are derived. The *Chl a* measurements, however, are less sensitive to atmospheric correction errors due to the nature of the algorithm (Hu et al. 2012), and thus we have higher confidence in the distribution of changes observed in *Chl a*. While further research is underway to fully assess the impact and mitigation of this eruption on satellite ocean-color retrievals, the quality of phytoplankton measurements is likely impacted by this eruption, and thus our ability to interpret the results is compromised.

Given that caveat, changes in the two phytoplankton distribution metrics were evaluated by subtracting monthly climatological means for MODIS-A *Chl a* and C_{phy} (October 2002–September 2021) from their monthly mean values for the 2022 analysis year. These monthly anomalies were then averaged to produce the global *Chl a* and C_{phy} annual mean anomaly maps (Figs. 3.25a,b). Similar calculations were performed on MODIS-A SST data to produce an equivalent SST annual mean anomaly for the same time period (Fig. 3.25c). The permanently stratified ocean (PSO), used for the analysis depicted in Figs. 3.26 and 3.27, is defined as the region, spanning the tropical and subtropical oceans, where annual average SST is greater than 15°C and surface mixed layers are typically low in nutrients and shallower than the nutricline (black lines near 40°N and 40°S in Fig. 3.25; Behrenfeld et al. 2006).

For the 2022 analysis year, the distribution of SST anomalies (Fig. 3.25c) replicated patterns observed in 2021, including a pronounced tongue of anomalously cold waters across the equatorial Pacific. This feature is indicative of the prevailing La Niña conditions during 2022 (see Sidebar 3.1 and section 4b for details), as is the highly elevated (+50%) *Chl a* concentrations that follow the edges of the cold-water tongue and extend into the equatorial Pacific (Fig. 3.25a).

Patches of higher-than-usual Chl a were also observed along equatorial regions of the Indian Ocean (up to +50%) and throughout the North and South Atlantic. Regions with elevated Chl a are typically associated with negative SST anomalies. Within the PSO away from strong upwelling regions, these cooler regions generally correspond to deeper-surface mixed layers (Deser et al. 2010), resulting in reduced phytoplankton light exposure rates and thus increased cellular Chl a and a decoupling between Chl a and C_{phy} variability (Behrenfeld et al. 2015). A key feature in the C_{phy} anomalies for this year (Fig. 3.25b) is a general reduction (5%–10%) over much of the PSO in the Southern Hemisphere that is largely anticorrelated with the changes in Chl a , but this is likely associated in part with error in the C_{phy} measurements due to the Hunga Tonga eruption. Patches of elevated Chl a are visible throughout the subpolar and polar regions poleward of the PSO (Fig. 3.25a) and largely covary with C_{phy} anomalies in these well-mixed regions (Fig. 3.25b). Observed heterogeneity in biomass indicators outside of the PSO is consistent with previous reports (e.g., Franz et al. 2022) and is a result of the ephemeral nature of blooms in these regions, as well as poor spatial and temporal sampling at higher latitudes due to clouds and low-light conditions.

To provide greater insight into inter-annual temporal variability in phytoplankton distributions, Figs. 3.26a,b show the climatological mean seasonal cycle for Chl a and C_{phy} in the PSO. Superimposed on this climatology is the corresponding mean for each month of the 2022 analysis year (red circles in Fig. 3.26). Annual variability of Chl a and C_{phy} in the PSO typically displays two distinct peaks (Figs. 3.26a,b), reflecting the springtime increases of biomass in Northern (Figs. 3.26c,d) and Southern Hemispheres (Figs. 3.26g,h). Peaks in C_{phy} lag 2–3 months behind those of Chl a , reflecting a reduction in phytoplankton chlorophyll-to-carbon ratios as the seasonal bloom progresses (e.g., Westberry et al. 2016). While patterns observed this year are similar to previous years (e.g., Franz et al. 2022), observed changes over the PSO region are dominated by changes in the equatorial and Southern Hemisphere regions (Figs. 3.26e–h). The Chl a was elevated over nearly the entire analysis year, with the February peak exceeding all previous observations, before returning to climatological norms in September 2022. In contrast, C_{phy} showed elevated values in the last quarter of 2021 relative to climatology, but transitioned to depressed values by March of 2022 and remained below all previous measurements

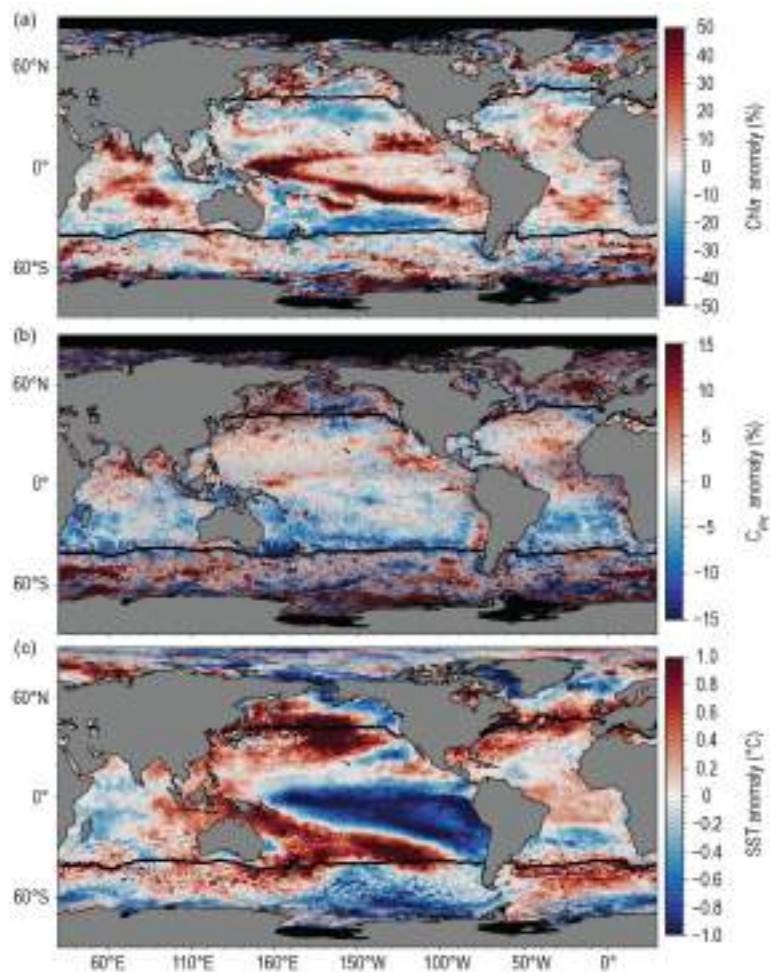


Fig. 3.25. Spatial distribution of average monthly (a) MODIS-A chlorophyll-a (Chl a) anomalies (%), (b) MODIS-A phytoplankton carbon (C_{phy}) anomalies (%), and (c) MODIS-A sea-surface temperature (SST) anomalies ($^{\circ}$ C) for Oct 2021–Sep 2022, where monthly differences were derived relative to the MODIS-A 19-year climatological record (Oct 2002–Sep 2021). Chl a and C_{phy} are stated as % difference from climatology, while SST is shown as an absolute difference. Also shown in each panel is the location of the mean 15 $^{\circ}$ C SST isotherm (black lines) delineating the permanently stratified ocean. Differences in the SST anomalies here versus in Fig. 3.1 are owing to differences in climatological periods, smoothing, and data sources.

through September. The geographic distribution and timing of this progression in C_{phy} from elevated to depressed is consistent with the progression of stratospheric aerosols over the tropics and Southern Hemisphere from the Hunga Tonga eruption (Taha et al. 2022).

Over the 25-year time series of spatially-averaged monthly-mean Chla within the PSO (Fig. 3.27a), concentrations vary by 5.8% (0.008 mg m^{-3} , standard deviation) around a long-term average of 0.136 mg m^{-3} (Fig. 3.27a). C_{phy} over the same 25-year period varies by 3.4% (0.75 mg m^{-3}) around an average of 21.8 mg m^{-3} (Fig. 3.27c). Chla monthly anomalies within the PSO (Fig. 3.27b) vary by 4.7% (0.006 mg m^{-3}) over the multi-mission time series, with the largest deviations generally associated with the El Niño–Southern Oscillation (ENSO) events ($r = -0.38$), as demonstrated by the correspondence of Chla anomaly variations with the Multivariate ENSO Index (MEI; Wolter and Timlin 1998; presented in the inverse to illustrate the covariation). C_{phy} anomalies (Fig. 3.27d), which vary by 2.2% (0.47 mg m^{-3}), are less correlated with the MEI ($r = -0.16$) due to the inherent lag between environmental change and growth. A major observation for

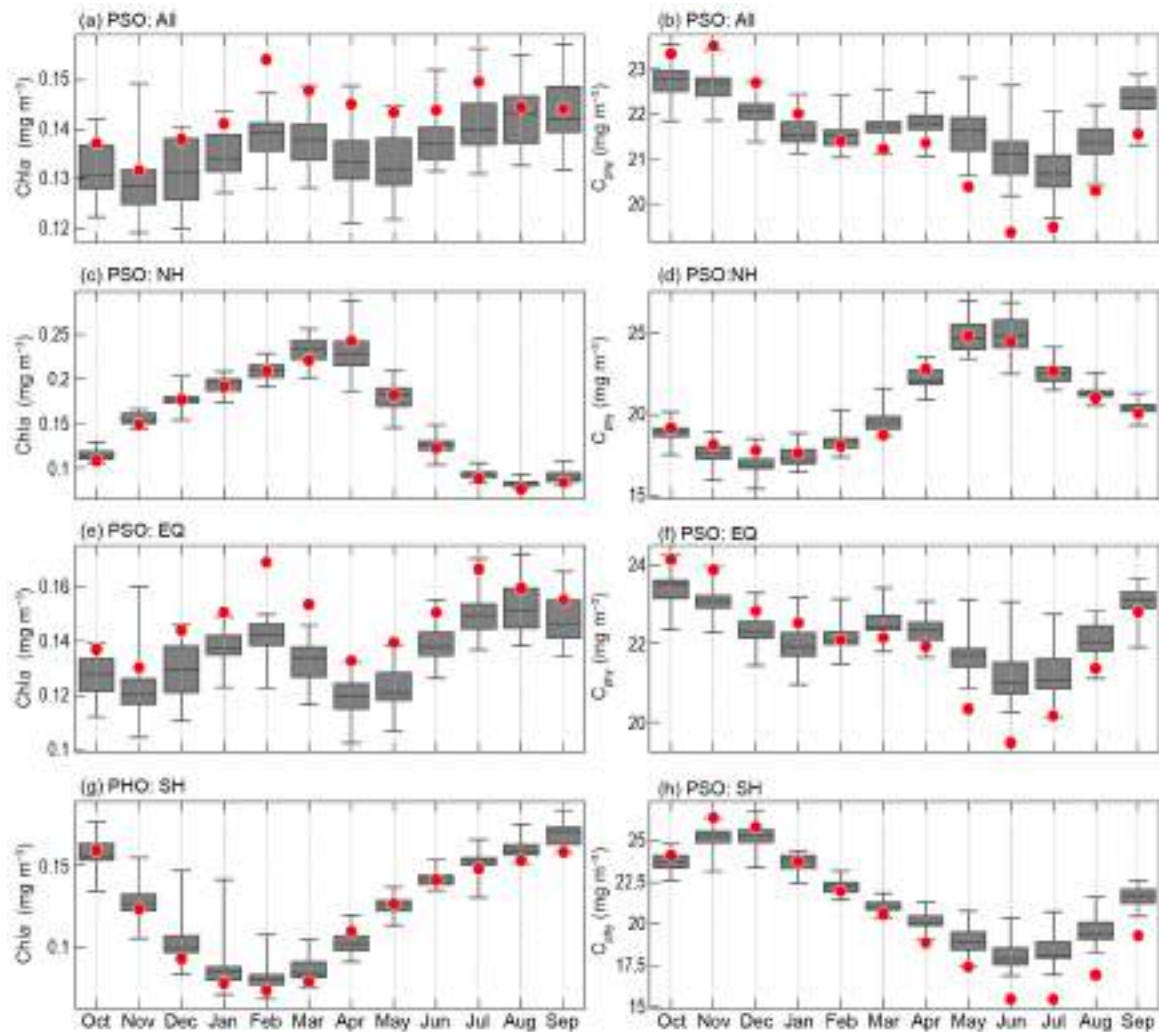


Fig. 3.26. Distribution of Oct 2021–Sep 2022 monthly means (red circles) for (a) MODIS-A chlorophyll-a (Chla) and (b) MODIS-A phytoplankton carbon (C_{phy}) for the permanently stratified ocean (PSO) region (see Fig. 3.25), superimposed on the climatological values as derived from the combined time series of SeaWiFS and MODIS-A over the 24-year period of Oct 1998–Sep 2021. Gray boxes show the interquartile range of the climatology, with a black line for the median value and whiskers extending to minimum and maximum values. Subsequent panels show latitudinally segregated subsets of the (c),(d) PSO for the Northern Hemisphere (NH, north of tropics), (e),(f) tropical $\pm 23.5^\circ$ -latitude subregion (EQ), and (g),(h) Southern Hemisphere (SH, south of tropics). Units for (a), (c), (e), and (g) are Chla (mg m^{-3}) and (b), (d), (f), and (h) are C_{phy} (mg m^{-3}).

2022 is that, while the Chl_a anomaly remains elevated and consistent with expectation under prevailing La Niña conditions, the C_{phy} anomaly is depressed, with values nearly 1 mg m⁻³ below the lowest value previously observed. While this suggests a significant shift in chlorophyll-to-carbon ratios and thus a notable change in phytoplankton physiology or community composition, we cannot yet rule out the likely possibility that the changes we see in C_{phy} (and Chl_a to a lesser extent) reflect error in the time series due to the Hunga Tonga eruption. Hence, we emphasize caution in interpretation of these observed trends until a more detailed assessment can be completed.

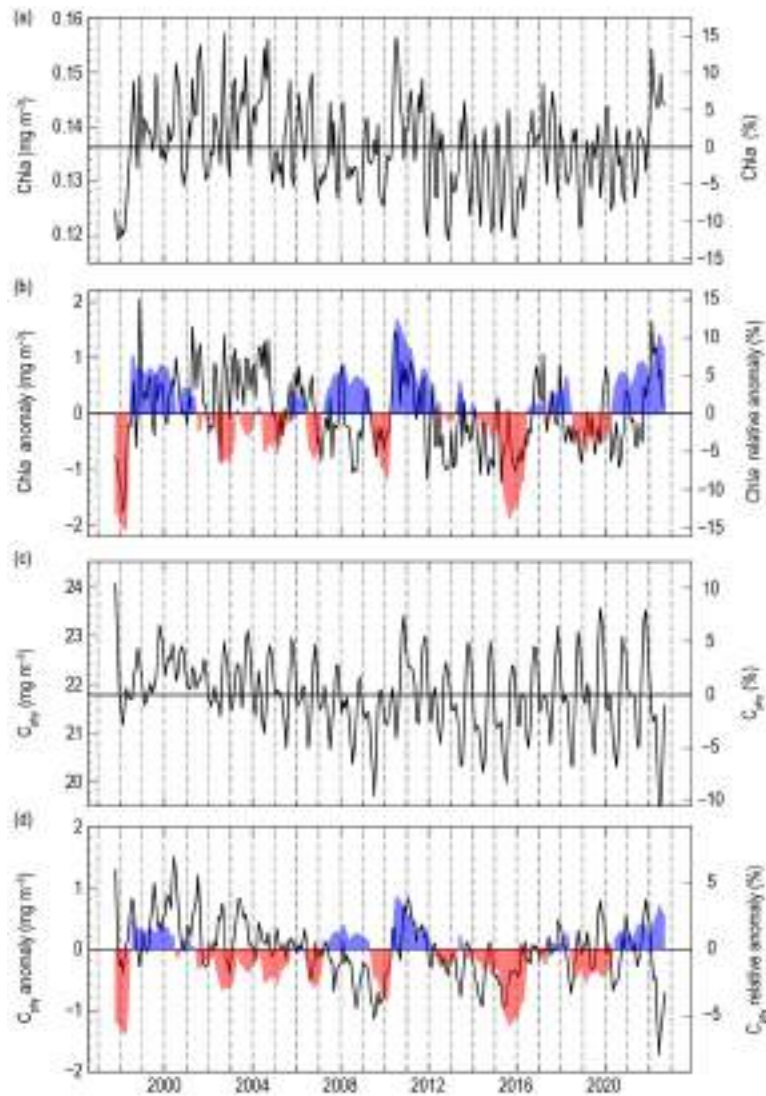


Fig. 3.27. Twenty-five-year, multi-mission record of chlorophyll-a (Chl_a; mg m⁻³) and phytoplankton carbon (C_{phy}; mg m⁻³) averaged over the permanently stratified ocean (PSO) region. (a) Monthly Chl_a, with the horizontal line indicating the multi-mission mean Chl_a concentration for the entire PSO region. (b) Monthly Chl_a anomalies after subtraction of the 24-year multi-mission monthly climatological mean (Fig. 3.26a). (c) Monthly C_{phy}, with the horizontal line indicating the multi-mission mean C_{phy} concentration for the entire PSO region. (d) Monthly C_{phy} anomalies after subtraction of the 24-year multi-mission monthly climatological mean (Fig. 3.26b). Shaded blue and red colors (b) and (d) show the Multivariate El Niño–Southern Oscillation Index, inverted and scaled to match the range of the Chl_a and C_{phy} anomalies, where blue indicates La Niña conditions and red indicates El Niño conditions.

Sidebar 3.2: Tracking global ocean oxygen content —J. SHARP

Dissolved oxygen is fundamental for meeting the physiological demands of marine organisms and for controlling elemental cycles in seawater. Multicellular aerobic marine organisms use oxygen to extract energy from organic material (Koch and Britton 2008). Consequently, the geographic distributions of suitable habitats for aerobic marine taxa are set by temperature-dependent oxygen availability (Pörtner and Knust 2007; Deutsch et al. 2015). Whereas lethal thresholds of dissolved oxygen vary between species, many marine taxa cannot tolerate an oxygen content ($[O_2]$) below about $60 \mu\text{mol kg}^{-1}$ (an approximate threshold for hypoxia) for an extended period of time (Vaquer-Sunyer and Duarte 2008; Levin et al. 2009). On an ecosystem scale, oxygen availability influences the rates and prevalence of biologically mediated processes that transform dissolved elements in seawater. For example, below dissolved $[O_2]$ concentrations of about $5 \mu\text{mol kg}^{-1}$, denitrification becomes favored over aerobic respiration, meaning a critically important nutrient (nitrate) is removed from seawater (Gruber 2008). Further, nitrous oxide produced by incomplete denitrification in low-oxygen conditions (Babbin et al. 2015; Bourbonnais et al. 2017) can escape to the atmosphere where it acts as a potent greenhouse gas (Forster et al. 2021).

Oxygen enters the ocean via dissolution at the air–sea interface, is generated near the ocean surface by photosynthesis, is transported throughout the ocean interior by advection and diffusion, and is depleted by respiration at depth as water masses age. This interplay between physics and biology sets the general distribution of dissolved oxygen throughout the global ocean (Keeling et al. 2010; Fig. SB3.3). Since at least the middle of the twentieth century, however, the oceans have been losing oxygen on a global scale (Oschlies et al. 2017; Breitburg et al. 2018; Bindoff et al. 2019; Canadell et al. 2021). This deoxygenation is primarily caused by: 1) anthropogenic ocean warming that directly decreases the capacity of seawater for dissolved oxygen (Garcia and Gordon 1992) and 2) ocean stratification, which is caused by ocean warming and decreases the degree to which subsurface waters exchange with the atmosphere (Levin 2018; Oschlies et al. 2018). Other potential contributions to deoxygenation include changes in subsurface respiration (e.g., Oschlies et al. 2008), large-scale overturning (e.g., Talley et al. 2016), and ocean circulation (e.g., Brandt et al. 2015).

Oxygen content has historically been measured on discrete seawater samples by a chemical titration (Carpenter 1965;

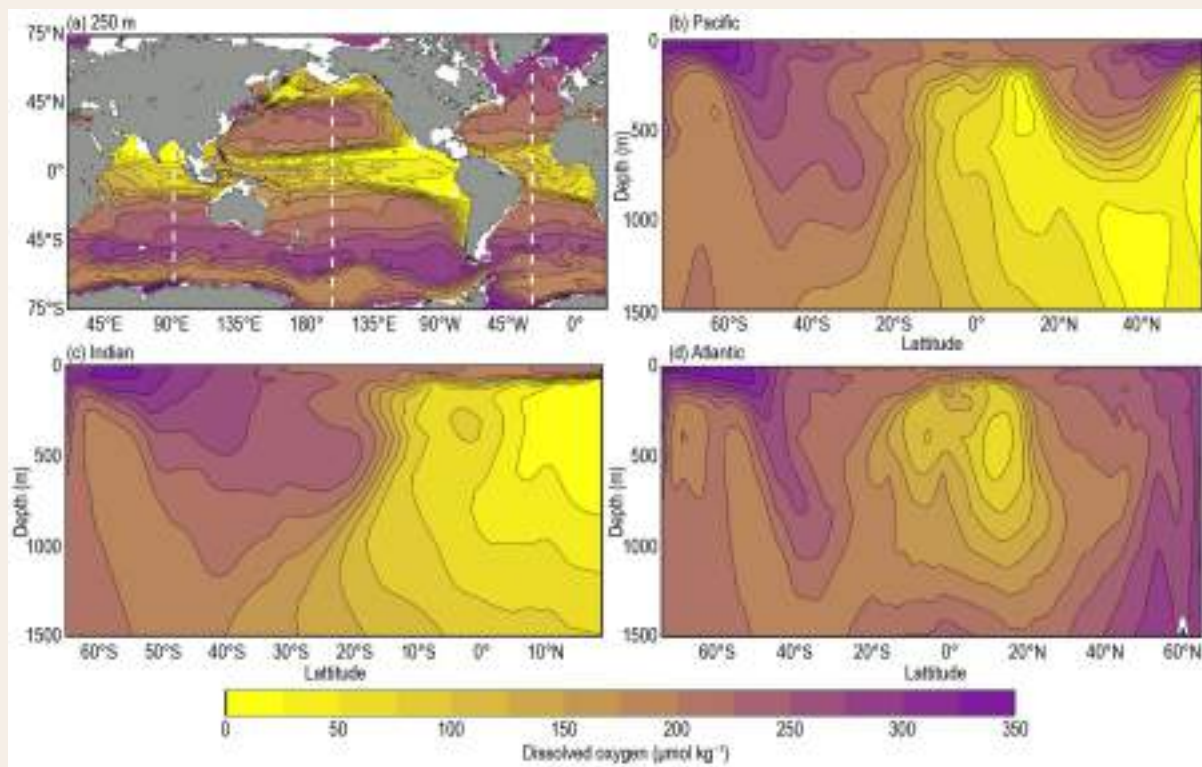


Fig. SB3.3. (a) Global distribution of dissolved oxygen content ($\mu\text{mol kg}^{-1}$) at 250-m depth, along with meridional sections in the (b) Pacific, (c) Indian, and (d) Atlantic Oceans from the surface to 1500 m. Dissolved oxygen content is from the GLODAPv2 mapped product (Lauvset et al. 2016).

Langdon 2010) first introduced by Winkler (1888). The collection of Winkler titrations performed on repeat hydrography cruises over multiple decades (Talley et al. 2016) have built up a large dataset of $[O_2]$ measured via a consistent method, which has been quality controlled and curated into databases and visual atlases. A significant portion of the global observational $[O_2]$ dataset is also composed of measurements from sensors on Conductivity-Temperature-Depth profilers, although some of these are less rigorously quality controlled than Winkler titration data (Boyer et al. 2018).

Over the past two decades, autonomous platforms carrying oxygen sensors have been distributed throughout the global ocean, primarily associated with the scaling up of the biogeochemical Argo program (BGC Argo; Claustre et al. 2020). BGC Argo floats carry chemical and bio-optical sensors, in addition to the temperature and salinity sensors that are implemented on all Argo floats (Roemmich et al. 2009). One of those chemical sensors is for dissolved oxygen (Gruber et al. 2010); most common are optodes that measure $[O_2]$ by quantification of luminescence quenching by oxygen (Bittig et al. 2018). Extensive research over the past two decades has been directed toward ensuring high-quality optode-based $[O_2]$ measurements on BGC Argo floats, including the implementation of drift corrections, establishment of calibration procedures, and recommendation of delayed-mode quality control practices (e.g., D'Asaro and McNeil 2013; Bittig and Körtzinger 2015; Bushinsky et al. 2016; Maurer et al. 2021).

Compilations of $[O_2]$ measured by Winkler titrations have indicated that oxygen content in the upper 1000 m of the global ocean has decreased by about 2% from 1970 to 2010 (Fig. SB3.4; Helm et al. 2011; Ito et al. 2017; Schmidtko et al. 2017), with a very likely (90% confidence) range of 0.5% to 3.3% (Bindoff et al. 2019). These studies have sought to interpolate between scattered observations, average measurements across time intervals, and otherwise scale up the available observational coverage to estimate long-term oxygen trends at the global scale. Earth system models (ESMs) have also been used to evaluate global ocean deoxygenation, with estimated decreases of closer to 1% in the upper 1000 m of the ocean from 1970 to 2010 (Fig. SB3.4; Bopp et al. 2013; Kwiatkowski et al. 2020). Global and regional discrepancies between observational products and ESMs have been attributed to inadequate simulation of ocean circulation and wind-driven ventilation, poorly constrained biogeochemical processes, and the roles of equatorial jets and mixing processes in oxygen transport (Oschlies et al. 2017, 2018; Buchanan and Tagliabue 2021). Existing discrepancies, however, do appear to be getting

smaller as representations of physical and biogeochemical processes in ocean models are improved (Canadell et al. 2021).

Newly emerging observational estimates of global ocean oxygen content are incorporating measurements from BGC Argo floats and other autonomous platforms. One such data product (Gridded Ocean Biogeochemistry from Artificial Intelligence- O_2 [GOBAI- O_2]; Sharp et al. 2022a) uses machine learning to fill gaps in observations, relying on relationships between $[O_2]$ and ocean temperature, salinity, and spatio-temporal coordinates. GOBAI- O_2 shows an oxygen decline of $\sim 0.7\%$ decade $^{-1}$ in the upper 1000 m of the ocean from 2004 to 2022 ($-1.12 \mu\text{mol kg}^{-1}$ decade $^{-1}$; Sharp et al. 2022b). This is somewhat higher than the other observation-based estimates shown in Fig. SB3.4, albeit for a distinctly different time period, indicating a potential acceleration in global deoxygenation. Emerging data products like GOBAI- O_2 will offer the opportunity for researchers to investigate sub-decadal variability in global and regional oxygen content, which has not previously been feasible outside of dedicated time-series locations.

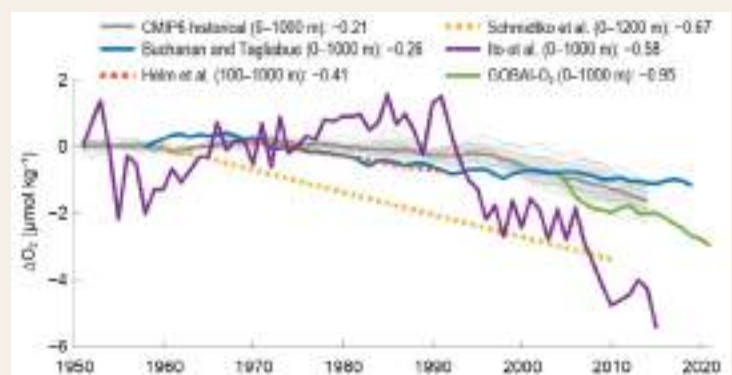


Fig. SB3.4. Estimates of global ocean deoxygenation over recent decades. Initial $\Delta[O_2]$ for each line is adjusted to the average CMIP6 value. Trends in the legend are in $\mu\text{mol kg}^{-1}$ decade $^{-1}$ over the period of time each line spans. Data for individual CMIP6 models (thin gray lines with the average given as a thick gray line), Buchanan and Tagliabue (2021), and Ito et al. (2017) are taken from the supplemental material of Buchanan and Tagliabue (2021). Straight dotted lines represent estimates taken only from reported slopes and converted to $\mu\text{mol kg}^{-1}$ decade $^{-1}$: $-0.93 \mu\text{mol L}^{-1}$ from 1970 to 1992 from Helm et al. (2011) and $-257.5 \text{ Tmol decade}^{-1}$ in a volume of $376.14 \times 10^6 \text{ km}^3$ from Schmidtko et al. (2017). The GOBAI- O_2 estimate was calculated from the gridded product of Sharp et al. (2022a). Gray shading represents the standard deviation among individual CMIP6 models, and green shading represents uncertainty in the GOBAI- O_2 estimate, determined via a model simulation experiment described in Sharp et al. (2022b).

j. Global ocean carbon cycle

—R. Wanninkhof, J. A. Triñanes, P. Landschützer, R. A. Feely, and B. R. Carter

1. INTRODUCTION

The oceans play a major role in the global carbon cycle by taking up a significant fraction of the excess carbon dioxide that humans release into the atmosphere. As a consequence of humankind's collective carbon dioxide (CO₂) emissions into the atmosphere, referred to as anthropogenic CO₂ (C_{ant}) emissions, the atmospheric CO₂ concentration has risen from pre-industrial levels of about 278 ppm (parts per million) to 417 ppm in 2022. Marine C_{ant} is the major cause of anthropogenic ocean acidification. Over the last decade the global ocean has continued to take up C_{ant} emissions and therefore is a major mediator of global climate change. Of the 10.8 (±0.8) Pg C yr⁻¹ C_{ant} released during the period 2012–21, 2.9 (±0.4) Pg C yr⁻¹ (26%) accumulated in the ocean, 3.1 (±0.6) Pg C yr⁻¹ (28%) accumulated on land, and 5.2 (±0.02) Pg C yr⁻¹ (46%) remained in the atmosphere with an imbalance of -0.3 Pg C yr⁻¹ (-3%; Table 6 in Friedlingstein et al. 2022). This decadal ocean carbon uptake estimate is a consensus view from a combination of measured decadal CO₂ inventory changes, models, and global air–sea CO₂ flux estimates based on surface ocean fugacity of CO₂ (fCO_{2w})¹ measurements from ships, uncrewed surface vehicles (USV), and moorings.

Independent decadal estimates of uptake based on interior measurements by Müller et al. (2023) show that the global ocean storage of anthropogenic carbon grew by 29±3 and 27±3 Pg C decade⁻¹ from 1994 to 2004 and 2004 to 2014, respectively. The fraction of anthropogenic emissions taken up by the ocean decreased from 36±4 to 27±3 % from the first to the second decade. This reduction is attributed to a decrease of the ocean buffer capacity (i.e., the consumption of carbonate and other basic chemical species with continued ocean uptake of CO₂) and changes in ocean circulation. From models and observations, Friedlingstein et al. (2022) showed that the oceanic anthropogenic carbon sink has grown from 1.1 (±0.4) Pg C yr⁻¹ in the decade of the 1960s to 2.9 (±0.4) Pg C yr⁻¹ in 2022.

2. AIR–SEA CARBON DIOXIDE FLUXES

Ocean uptake of CO₂ is estimated from the net air–sea CO₂ flux derived from the bulk flux formula with differences in air (a) and surface-seawater (w) CO₂ fugacity ($\Delta f\text{CO}_2 = f\text{CO}_{2w} - f\text{CO}_{2a}$) and gas transfer coefficients as input. Gas transfer is parameterized with wind as described in Wanninkhof (2014). This provides a net flux estimate. A steady contribution of carbon from riverine runoff, with estimates ranging from 0.45 to 0.78 Pg C yr⁻¹ (Resplandy et al. 2018) needs to be included to obtain the C_{ant} estimate. Here, 0.65 Pg C yr⁻¹ is used as the river adjustment as recommended in the Global Carbon Budget 2022 (Friedlingstein et al. 2022). The data sources for fCO_{2w} are annual updates of observations from the Surface Ocean CO₂ Atlas (SOCAT) composed of moorings, USV, and ship-based observations (Bakker et al. 2016), with SOCAT version 2022 containing 33.7 million datapoints through 2021 (https://www.socat.info/wp-content/uploads/2022/06/2022_Poster_SOCATv2022_release.pdf). The increased observations and improved mapping techniques, including machine learning methods summarized in Rödenbeck et al. (2015), now provide annual global fCO_{2w} fields on a 1° latitude × 1° longitude grid at monthly time scales. This allows investigation of variability on sub-annual to decadal time scales.

The monthly 2022 $\Delta f\text{CO}_2$ maps are based on a self-organizing maps feed-forward neural network (SOM-FNN) approach of Landschützer et al. (2013, 2014). The 2022 maps use sea-surface temperature (SST), Chlorophyll-*a*, atmospheric CO₂, mixed-layer depth, and salinity (NOAA IOSSTv2 [Huang et al. 2021a]; Globcolour Chlorophyll-*a* [Maritorena et al. 2010]; NOAA MBL atmospheric CO₂ [Dlugokencky et al. 2021]; DeBoyer Mixed layer depth climatology [de Boyer Montégut et al. 2004] and Hadley center EN4 salinity [Good et al, 2013]) as predictor variables. The fluxes are determined using European Centre for Medium-Range Weather Forecasts

¹ The fugacity is the partial pressure of CO₂ (pCO₂) corrected for non-ideality. They are numerically similar for surface waters with fCO₂≈0.994 pCO₂.

Reanalysis version 5 (ERA5) winds (Hersbach et al. 2018). For 2022 flux calculations, the final ERA5 winds from January through August and their early release (ERA5T) winds from September through December are used.

The SOM FNN results (Fig. 3.28) show a slightly increasing ocean sink from 1982 to 1994, followed by a period of rapidly decreasing uptake from 1995 to 2002. There is a strong increase in the ocean sink from 2002 onward that continues through 2016. The amplitude of seasonal variability is ≈ 1.2 Pg C with a minimum uptake in the June–September timeframe. Variability in seasonal amplitudes does not correlate with annual uptake or its variability. The C_{ant} flux of 3.3 Pg C yr^{-1} for 2022 (green line in Fig. 3.28) was 23% above the 1990–2020 average of $2.68 (\pm 0.52) \text{ Pg C yr}^{-1}$.

The annual average flux map for 2022 (Fig. 3.29a) shows the characteristic pattern of effluxes (ocean-to-air CO_2 fluxes) in tropical, coastal upwelling, and open-ocean upwelling regions. Coastal upwelling regions include those in the Arabian Sea and off the west coasts of North and South America. The western Bering Sea in the northwest Pacific was a strong CO_2 source as well in 2022; a clear juxtaposition to the strong sink in the surrounding regions. The region with the largest efflux was the upwelling region of the eastern and central equatorial Pacific. Cumulatively, the regions of effluxes are significant CO_2 sources to the atmosphere ($\approx 1 \text{ Pg C}$). The primary CO_2 uptake regions are in the subtropical and subpolar regions. The largest sinks are poleward of the sub-tropical fronts. In the Southern Ocean, the area near the polar front ($\sim 60^\circ\text{S}$) is nearly neutral with the polar frontal region in the eastern South Pacific being a source in 2022.

In the Northern Hemisphere, the entire North Atlantic is a large sink while in the North Pacific the sink region is punctuated by a significant source of CO_2 in the western to central Bering Sea. This pattern is, in part, due to the position of the western boundary currents whose cooling waters contribute to CO_2 sinks at high latitudes. In particular, the Gulf Stream/North Atlantic Drift in the Atlantic extends farther north than the Kuroshio in the Pacific.

The ocean carbon uptake anomalies (Fig. 3.29c) in 2022 relative to the 1990–2020 average are attributed to the increasing ocean CO_2 uptake with time due to atmospheric CO_2 increases yielding a 0.6 Pg C greater annual uptake than the 30-year average (Fig. 3.28). Therefore, the anomalies are largely negative. However, large regions show positive anomalies due to variations in large-scale climate modes, particularly the El Niño–Southern Oscillation. Large positive anomalies are seen in the central equatorial Pacific, particularly in large areas in the sub-tropical regions from 20°N to 40°N in the eastern North Pacific and North Atlantic, and 20°S to 40°S in the western Pacific. The increased effluxes in the central equatorial Pacific are related to La Niña conditions that have persisted almost uninterrupted since August 2020 (see Sidebar 3.1 and section 4b for details). The negative sea-surface temperature anomaly (SSTA) there (see Fig. 3.1a) indicates that increased upwelling of cold waters with high CO_2 content in the central Pacific returned after a period of lower-than-normal upwelling prior

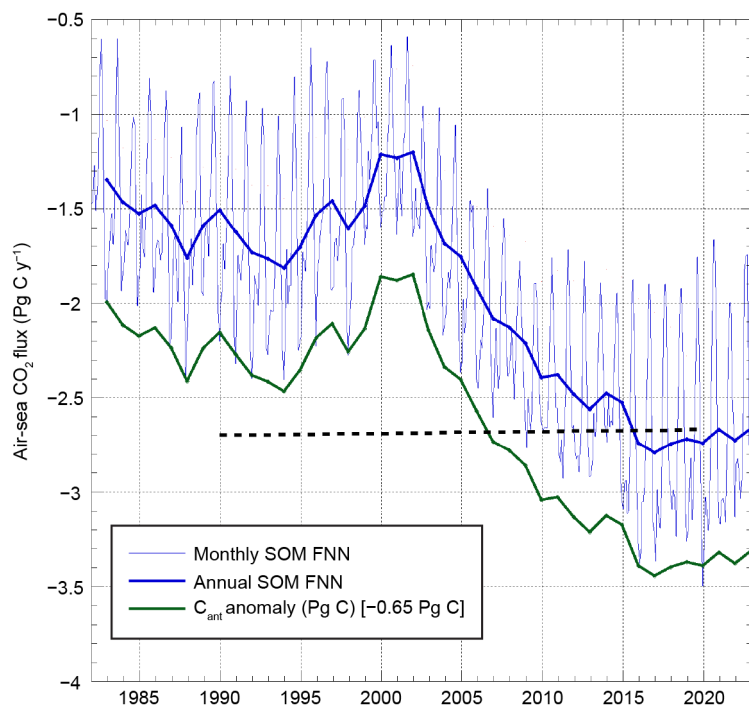


Fig. 3.28. Global annual (thick blue line) and monthly (thin blue line) net carbon dioxide (CO_2) fluxes (Pg C yr^{-1}) for 1982–2022 using a self-organizing maps feed-forward neural network (SOM-FNN) approach. The annual anthropogenic CO_2 (C_{ant}) flux (thick green line) includes a riverine adjustment of -0.65 Pg C . The black dashed line is the 1990–2020 mean C_{ant} flux. Negative values indicate CO_2 uptake by the ocean.

to 2020. However, the eastern equatorial Pacific, southeast of the Galapagos, shows a negative CO_2 flux anomaly. The positive anomalies in fluxes (more efflux/less influx in 2022 compared to the long-term mean) in the subtropics closely correspond to positive temperature anomalies (see Fig. 3.1a), suggesting that the flux anomalies in these regions are temperature driven.

The difference in fluxes between 2022 and 2021 (Fig. 3.29b) are quite muted, with broad regions in the northern Pacific subtropics showing positive anomalies (less strong sinks) closely corresponding with the SSTA changes observed between 2022 and 2021 (see Fig. 3.1b). The South Atlantic sector of the Southern Ocean ($\sim 60^\circ\text{S}$) shows a significant decrease in sink strength between 2022 and 2021 that does not correspond to a SST change but appears to be associated with a sea-surface salinity increase from 2021 to 2022 (see Fig. 3.7b). Most prevalent in Fig. 3.29b are the large regions of slight negative anomalies (greater uptake in 2022 compared to 2021), which in the South Pacific corresponds to negative SSTA.

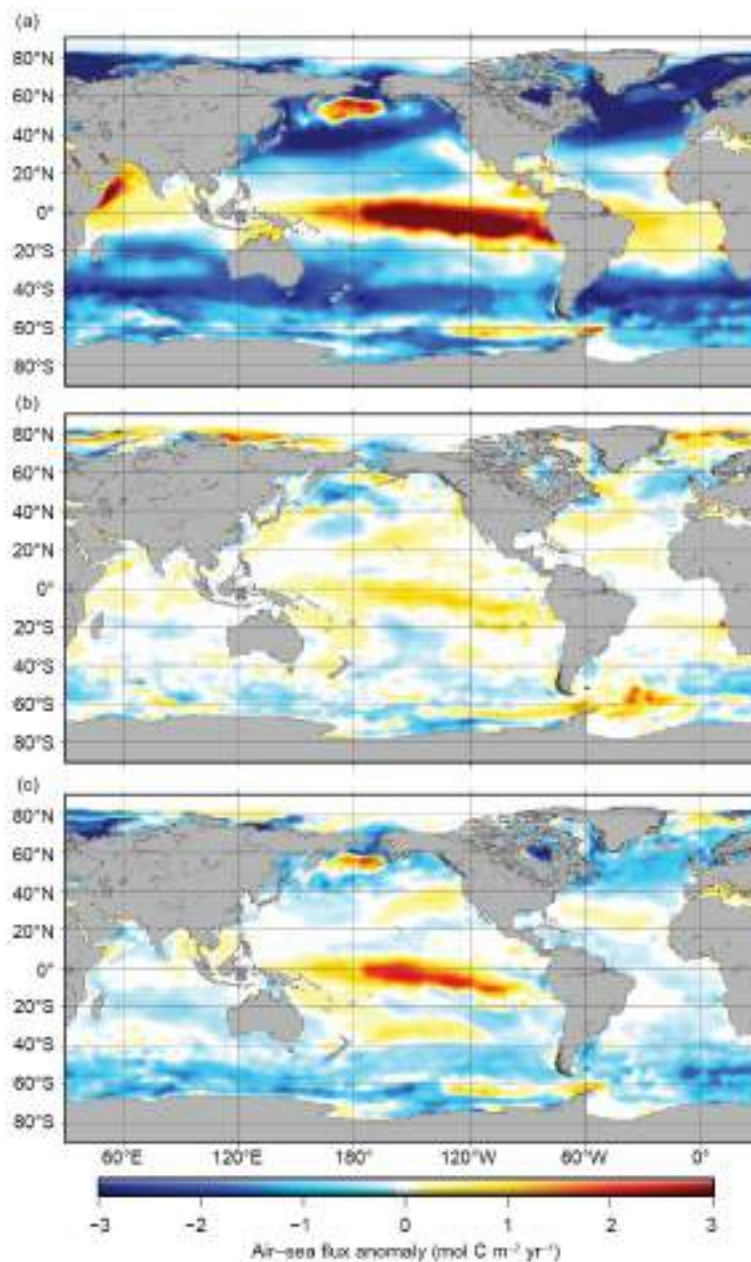


Fig. 3.29. Global map of (a) net air–sea carbon dioxide (CO_2) fluxes for 2022, (b) net air–sea CO_2 flux anomalies for 2022 minus 2021, and (c) net air–sea CO_2 flux anomalies for 2022 relative to 1990–2020 average values using the SOM-FNN approach of Landschützer et al. (2013). Units are all $\text{mol C m}^{-2} \text{yr}^{-1}$. Ocean CO_2 uptake regions shown in the blue colors.

3. OCEAN INTERIOR DEVELOPMENTS: UTILIZATION OF ARGO

Global-scale CO₂ emissions from human activities and associated CO₂ uptake are causing ocean interior C_{ant} increases and acidification. Delineating how the biogeochemical processes in the ocean interior will be affected by the changing heat content and C_{ant} uptake is essential for developing future mitigation and adaptation responses to climate change. Interior ocean carbon distributions have historically been quantified from observations from ship-based chemical surveys, many of which are currently being repeated decadal under the auspices of the international Global Ocean Ship-based Hydrographic Investigations Program. The measured distributions are analyzed to characterize both the natural and anthropogenic carbon components of the variability observed between reoccupations, and there are several such synthesis efforts underway including a decadal update to the first Regional Carbon Cycle Assessment and Processes (Khatiwala et al. 2013) study, and an update to decadal anthropogenic carbon accumulation estimates appropriate to the period 1994–2007 (Gruber et al. 2019) by Müller et al. (2023).

In recent years, oceanographers have developed algorithms that enable predictions of total dissolved inorganic carbon (DIC) and other carbonate chemistry parameters in the interior ocean from a variety of predictors (Alin et al. 2012; Williams et al. 2016; Carter et al. 2016, 2018, 2021; Bittig et al. 2018; Sauzède et al. 2017). Notably, there now exist algorithms (e.g., Carter et al. 2021; Keppler et al. 2022) that allow estimation of DIC from combinations of predictors (e.g., temperature and salinity) that are available at high resolution from Argo measurements throughout the top 2000 m of the ocean (Roemmich and Gilson 2009, and updates thereof). These algorithms can be used with the predictor data products to generate gap-filled monthly DIC distributions, e.g., for December 2022 (Fig. 3.30). However, seasonally resolved training data are needed for the algorithms to resolve seasonality with high fidelity (Carter et al. 2021; Gloege et al. 2021), and, while there are regions such as the northwest Pacific where this temporal coverage already exists from ship-based measurements thanks to regular cruises led by researchers based in Japan, these regions are few. Thus, the utility of these fully resolved carbon budgets remains limited at present.

The nascent and growing biogeochemical Argo program is poised to change this status quo by providing total scale seawater pH (pH_T) measurements over the top 2000 m at 10-day resolution throughout the various ocean basins, co-located with temperature, salinity, oxygen, and nitrate measurements. This information can be combined with estimates of seawater total alkalinity (TA), which has strong predictability from salinity due to the large role played by freshwater cycling in controlling the TA distribution, and macronutrients to allow calculations of DIC in the top 2000 m of the ocean at significantly greater temporal resolution than is achievable from discrete shipboard TA measurements. This information can then be used as additional training data to produce much more skillful DIC algorithms, similar to recent work using Argo O₂ sensor data (Sharp et al. 2022b; also see Sidebar 3.2), with a goal of annual updates of interior global ocean biogeochemistry.

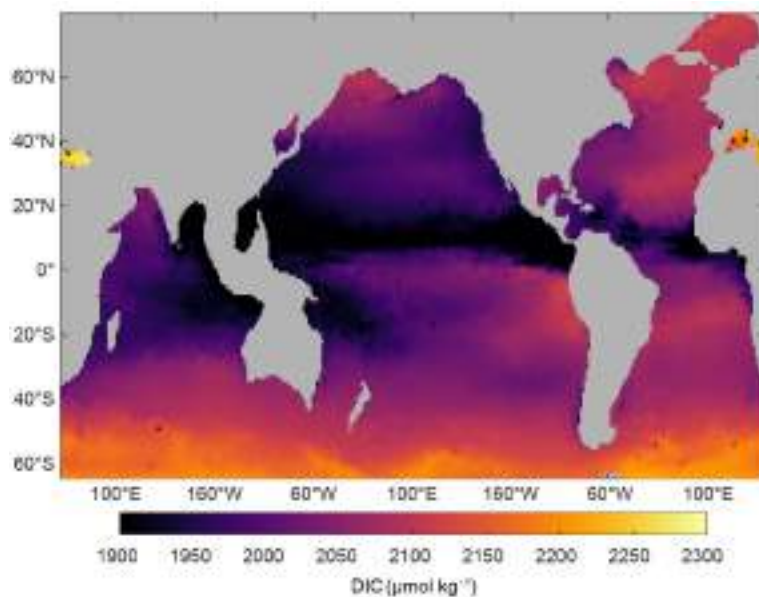


Fig. 3.30. Map of monthly average surface dissolved inorganic carbon (DIC; $\mu\text{mol kg}^{-1}$) for December 2022 estimated using the empirical seawater DIC estimation routine of Carter et al. (2021) and the monthly temperature and salinity record from Roemmich and Gilson (2009, updated).

A global surface ocean (top 2000 m) DIC inventory serves as an example of the information that can be obtained from this approach, albeit with large and yet-unconstrained uncertainties (Fig. 3.31a). These estimates were produced using the algorithms from Carter et al. (2021), which combine a large number of regionally specific linear regressions with machine learning approaches and the temperature and salinity climatology from Roemmich and Gilson (2009, with updates). There is an adjustment to the predictions to account for anthropogenic contributions to DIC, and this adjustment can be set to be appropriate for a fixed reference year (e.g., 2002 in Fig. 3.31) to isolate the variability in the DIC inventory estimates that is not attributable to estimated long-term secular change in the inventory. These estimates imply a strong anti-correlation between monthly ($R^2=0.94$) and annual ($R^2=0.97$) upper-ocean DIC inventory and temperature, which is not surprising given that the temperature is the main predictor used to generate the DIC estimates. Also, DIC and temperature tend to be anti-correlated due to the tendency for seawater to lose DIC to gas exchange when temperature increases. These early results point to a new frontier for interior ocean carbon cycle science that will likely see significant advances in the coming years with the advent of new data streams and continued iteration on machine learning mapping strategies.

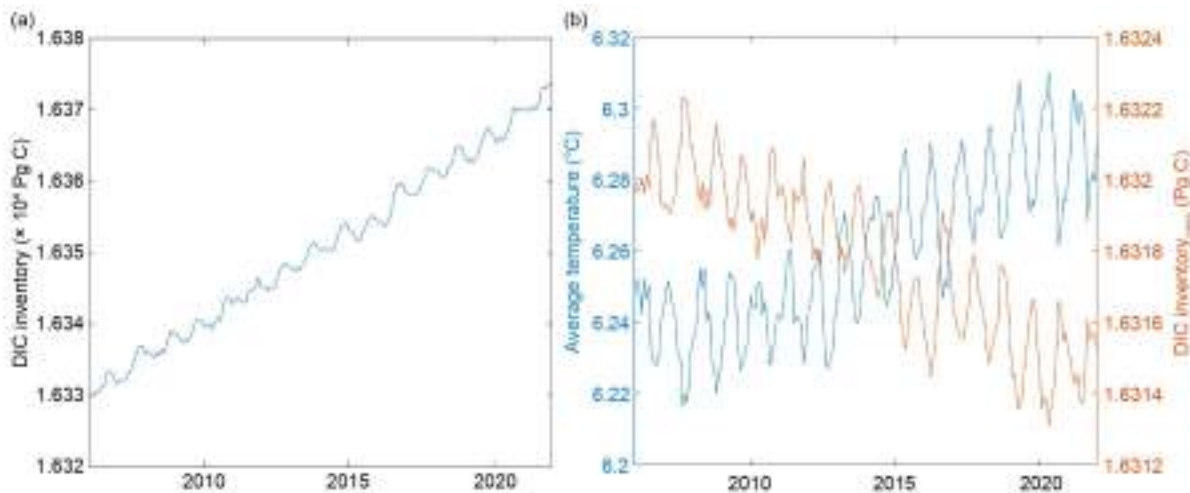


Fig. 3.31. (a) Estimated total dissolved inorganic carbon (DIC) inventory (Pg C) across the top 2000 m of the region covered by the Roemmich and Gilson (2009) product (see Fig. 3.30) and (b) estimated total DIC inventory (Pg C) over this same region that would be expected if anthropogenic carbon distributions were held at levels found in a reference year (2002) to reveal how patterns of estimated inventory change covary with the mass-weighted mean temperature product values used to produce the DIC estimates.

Acknowledgments

- Sidebar 3.1. This is NOAA's Pacific Marine Environmental Laboratory contribution no. 5470.
- Atlantic meridional overturning circulation. This work was carried out in part under the auspices of the Cooperative Institute for Marine and Atmospheric Studies, a Cooperative Institute of the University of Miami and the National Oceanic and Atmospheric Administration (NOAA), cooperative agreement #NA200AR4320472. The MOC observations at 26.5°N have been jointly funded by the U.K. Natural Environment Research Council, the National Science Foundation, and NOAA's Global Ocean Monitoring and Observing (GOMO) program. The MOC estimates at 41°N were obtained at the Jet Propulsion Laboratory under a contract with NASA.
- D. L. Volkov was supported by NOAA's Climate Variability and Predictability program (Grant NA200AR4310407) and Atlantic Oceanographic and Meteorological Laboratory (AOML).
- Shenfu Dong was supported via NOAA's GOMO program with additional support from NOAA's Atlantic Oceanographic & Meteorological Laboratory.
- W. Hobbs received grant funding from the Australian Government as part of the Antarctic Science Collaboration Initiative program.

Appendix 1: Chapter 3 – Acronyms

ACC	Antarctic Circumpolar Current
AMOC	Atlantic meridional overturning circulation
AMV	Atlantic Multidecadal Variability
AOML	Atlantic Oceanographic and Meteorological Laboratory
BASS	Blended Analysis of Surface Salinity
b_{bp}	particle backscattering coefficient
BGC	biogeochemical
C_{ant}	anthropogenic CO ₂
CERES	Clouds and the Earth's Radiant Energy Systems
Chla	chlorophyll-a
C_{phy}	phytoplankton carbon
CMIP	Coupled Model Intercomparison Project
CO ₂	carbon dioxide
CSR	Center for Space Research
CTD	Conductivity-Temperature-Depth
DIC	dissolved inorganic carbon
DJF	December–February
DOISST	Daily Optimum Interpolation SST
DWBC	Deep Western Boundary Current
E	evaporation
EBAF	Energy Balanced and Filled
ECMWF	European Centre for Medium-Range Weather Forecasts
EKE	eddy kinetic energy
ENSO	El Niño–Southern Oscillation
ERA5	European Centre for Medium-Range Weather Forecasts Reanalysis version 5
ERSSTv5	Extended Reconstruction SST version 5
ESM	Earth system models
FC	Florida Current
fCO_{2w}	surface ocean fugacity of CO ₂
FLASHFlux	Fast Longwave And Shortwave Radiative Fluxes
GIOP	Generalized Inherent Optical Properties
GMSL	global mean sea level
GMST	global mean surface air temperature
GO-SHIP	Global Ocean Ship-based Hydrographic Investigations Program
GOBAI-O2	Gridded Ocean Biogeochemistry from Artificial Intelligence-O ₂
GOMO	Global Ocean Monitoring and Observing
GPCP	Global Precipitation Climatology Project
GRACE	Gravity Recovery and Climate Experiment
GRACE-FO	GRACE Follow-On
HadSST	U.K. Met Office Hadley Centre SST
IOD	Indian Ocean dipole
ITCZ	Intertropical Convergence Zone
JJA	June–August
JPL	Jet Propulsion Laboratory
LH	latent heat flux
LSW	Labrador Sea Water
LW	longwave radiation
MAM	March–May
MEI	Multivariate ENSO Index

MHT	meridional heat transport
MOC	meridional overturning circulation
MODIS	Moderate Resolution Imaging Spectroradiometer
MODIS-A	MODIS on <i>Aqua</i>
MOVE	Meridional Overturning Variability Experiment
NADW	North Atlantic Deep Water
NASA	National Aeronautics and Space Administration
NBC	North Brazil Current
NCEI	National Centers for Environmental Information
NECC	North Equatorial Countercurrent
NH	Northern Hemisphere
NOAA	National Oceanic and Atmospheric Administration
O ₂	oxygen
OHCA	ocean heat content anomaly
P	Precipitation
pH _T	total scale seawater pH
PSO	permanently stratified ocean
PSS-78	Practical Salinity Scale-78
Q _{net}	net surface heat flux
RAPID/MOCHA/WBTS	Rapid Climate Change/MOC and Heatflux Array/Western Boundary Time Series
SD	standard deviation
SEC	South Equatorial Current
SH	Southern Hemisphere
SIO	Scripps Institution of Oceanography
SL	sea level
SLA	sea-level anomaly
SMAP	Soil Moisture Active Passive
SMOS	Soil Moisture and Ocean Salinity
SOCAT	Surface Ocean CO ₂ Atlas
SOM-FNN	self-organizing maps feed-forward neural network
SON	September–November
SPCZ	South Pacific Convergence Zone
SSM/I	Special Sensor Microwave/Imager
SSS	sea-surface salinity
SST	sea-surface temperature
SSTA	sea-surface temperature anomaly
SW	shortwave radiation
TA	total alkalinity
U	maximum zonal currents
USV	uncrewed surface vehicles
W _{EK}	Ekman velocity
XBT	Expendable Bathythermographs
YC	Yucatan Current

References

- Abraham, J. P., and Coauthors, 2013: A review of global ocean temperature observations: Implications for ocean heat content estimates and climate change. *Rev. Geophys.*, **51**, 450–483, <https://doi.org/10.1002/rog.20022>.
- Adler, R. F., and Coauthors, 2018: The Global Precipitation Climatology Project (GPCP) Monthly analysis (new version 2.3) and a review of 2017 global precipitation. *Atmosphere*, **9**, 138, <https://doi.org/10.3390/atmos9040138>.
- Alin, S. R., R. A. Feely, A. G. Dickson, J. M. Hernández-Ayón, L. W. Juraneck, M. D. Ohman, and R. Goericke, 2012: Robust empirical relationships for estimating the carbonate system in the southern California Current System and application to CalCOFI hydrographic cruise data (2005–2011). *J. Geophys. Res.*, **117**, C05033, <https://doi.org/10.1029/2011JC007511>.
- Babbin, A. R., D. Bianchi, A. Jayakumar, and B. B. Ward, 2015: Rapid nitrous oxide cycling in the suboxic ocean. *Science*, **348**, 1127–1129, <https://doi.org/10.1126/science.aaa8380>.
- Babcock, R. C., and Coauthors, 2019: Severe continental-scale impacts of climate change are happening now: Extreme climate events impact marine habitat forming communities along 45% of Australia's coast. *Front. Mar. Sci.*, **6**, 411, <https://doi.org/10.3389/fmars.2019.00411>.
- Bakker, D. C. E., and Coauthors, 2016: A multi-decade record of high-quality fCO_2 data in version 3 of the Surface Ocean CO_2 Atlas (SOCAT). *Earth Syst. Sci. Data*, **8**, 383–413, <https://doi.org/10.5194/essd-8-383-2016>.
- Balaguru, K., P. Chang, R. Saravanan, L. R. Leung, Z. Xu, M. Li, and J. S. Hsieh, 2012: Ocean barrier layers' effect on tropical cyclone intensification. *Proc. Natl. Acad. Sci. USA*, **109**, 14 343–14 347, <https://doi.org/10.1073/pnas.1201364109>.
- Barnoud, A., and Coauthors, 2021: Contributions of altimetry and Argo to non-closure of the global mean sea level budget since 2016. *Geophys. Res. Lett.*, **48**, e2021GL092824, <https://doi.org/10.1029/2021GL092824>.
- Beal, L. M., V. Hormann, R. Lumpkin, and G. R. Foltz, 2013: The response of the surface circulation of the Arabian Sea to monsoonal forcing. *J. Phys. Oceanogr.*, **43**, 2008–2022, <https://doi.org/10.1175/JPO-D-13-033.1>.
- Behrenfeld, M. J., and Coauthors, 2006: Climate-driven trends in contemporary ocean productivity. *Nature*, **444**, 752–755, <https://doi.org/10.1038/nature05317>.
- , and Coauthors, 2015: Reevaluating ocean warming impacts on global phytoplankton. *Nat. Climate Change*, **6**, 323–330, <https://doi.org/10.1038/nclimate2838>.
- Berx, B., and Coauthors, 2021: Climate-relevant ocean transport measurements in the Atlantic and Arctic Oceans. *Oceanography*, **34**, 10–11, <https://doi.org/10.5670/oceanog.2021.supplement.02-04>.
- Biló, T. C., and W. E. Johns, 2019: Interior pathways of Labrador Sea Water in the North Atlantic from the Argo perspective. *Geophys. Res. Lett.*, **46**, 3340–3348, <https://doi.org/10.1029/2018GL081439>.
- , and —, 2020: The deep western boundary current and adjacent interior circulation at 24°–30°N: Mean structure and mesoscale variability. *J. Phys. Oceanogr.*, **50**, 2735–2758, <https://doi.org/10.1175/JPO-D-20-0094.1>.
- Bindoff, N. L., and Coauthors, 2019: Changing ocean, marine ecosystems, and dependent communities. *The Ocean and Cryosphere in a Changing Climate*, H.-O. Pörtner et al., Eds., Cambridge University Press, 447–588, <https://doi.org/10.1017/9781009157964>.
- Bittig, H. C., and A. Körtzinger, 2015: Tackling oxygen optode drift: Near-surface and in-air oxygen optode measurements on a float provide an accurate in situ reference. *J. Atmos. Oceanic Technol.*, **32**, 1536–1543, <https://doi.org/10.1175/JTECH-D-14-00162.1>.
- , and Coauthors, 2018: Oxygen optode sensors: Principle, characterization, calibration, and application in the ocean. *Front. Mar. Sci.*, **4**, 429, <https://doi.org/10.3389/fmars.2017.00429>.
- Bopp, L., and Coauthors, 2013: Multiple stressors of ocean ecosystems in the 21st century: Projections with CMIP5 models. *Biogeosciences*, **10**, 6225–6245, <https://doi.org/10.5194/bg-10-6225-2013>.
- Bourbonnais, A., R. T. Letscher, H. W. Bange, V. Echevin, J. Larkum, J. Mohn, N. Yoshida, and M. A. Altabet, 2017: N_2O production and consumption from stable isotopic and concentration data in the Peruvian coastal upwelling system. *Global Biogeochem. Cycles*, **31**, 678–698, <https://doi.org/10.1002/2016GB005567>.
- Bower, A., and Coauthors, 2019: Lagrangian views of the pathways of the Atlantic meridional overturning circulation. *J. Geophys. Res. Oceans*, **124**, 5313–5335, <https://doi.org/10.1029/2019JC015014>.
- Boyer, T. P., and Coauthors, 2018: World Ocean Database 2018. A.V. Mishonov, Ed., NOAA Atlas NESDIS 87, 207 pp., www.ncei.noaa.gov/sites/default/files/2020-04/wod_intro_0.pdf.
- Brandt, P., and Coauthors, 2015: On the role of circulation and mixing in the ventilation of oxygen minimum zones with a focus on the eastern tropical North Atlantic. *Biogeosciences*, **12**, 489–512, <https://doi.org/10.5194/bg-12-489-2015>.
- Breitburg, D., and Coauthors, 2018: Declining oxygen in the global ocean and coastal waters. *Science*, **359**, eaam7240, <https://doi.org/10.1126/science.aam7240>.
- Brown, J. R., and Coauthors, 2020: South Pacific Convergence Zone dynamics, variability and impacts in a changing climate. *Nat. Rev. Earth Environ.*, **1**, 530–543, <https://doi.org/10.1038/s43017-020-0078-2>.
- Buchanan, P. J., and A. Tagliabue, 2021: The regional importance of oxygen demand and supply for historical ocean oxygen trends. *Geophys. Res. Lett.*, **48**, e2021GL094797, <https://doi.org/10.1029/2021GL094797>.
- Bushinsky, S. M., S. R. Emerson, S. C. Riser, and D. D. Swift, 2016: Accurate oxygen measurements on modified Argo floats using in situ air calibrations. *Limnol. Oceanogr.: Methods*, **14**, 491–505, <https://doi.org/10.1002/lom3.10107>.
- Canadell, J. G., and Coauthors, 2021: Global carbon and other biogeochemical cycles and feedbacks. *Climate Change 2021: The Physical Science Basis*, V. Masson-Delmotte et al., Eds., Cambridge University Press, 673–816, <https://doi.org/10.1017/9781009157896.007>.
- Carpenter, J. H., 1965: The Chesapeake Bay Institute technique for the Winkler dissolved oxygen method. *Limnol. Oceanogr.*, **10**, 141–143, <https://doi.org/10.4319/lo.1965.10.1.0141>.
- Carter, B. R., N. L. Williams, A. R. Gray, and R. A. Feely, 2016: Locally interpolated alkalinity regression for global alkalinity estimation. *Limnol. Oceanogr.: Methods*, **14**, 268–277, <https://doi.org/10.1002/lom3.10087>.
- , R. A. Feely, N. L. Williams, A. G. Dickson, M. B. Fong, and Y. Takeshita, 2018: Updated methods for global locally interpolated estimation of alkalinity, pH, and nitrate. *Limnol. Oceanogr.: Methods*, **16**, 119–131, <https://doi.org/10.1002/lom3.10232>.

- , and Coauthors, 2021: New and updated global empirical seawater property estimation routines. *Limnol. Oceanogr.: Methods*, **19**, 785–809, <https://doi.org/10.1002/lom3.10461>.
- Chambers, D. P., A. Cazenave, N. Champollion, H. Dieng, W. Llovel, R. Forsberg, K. von Schuckmann, and Y. Wada, 2017: Evaluation of the global mean sea level budget between 1993 and 2014. *Surv. Geophys.*, **38**, 309–327, <https://doi.org/10.1007/s10712-016-9381-3>.
- Chen, J., B. Tapley, C. Wilson, A. Cazenave, K. W. Seo, and J. S. Kim, 2020: Global ocean mass change from GRACE and GRACE Follow-On and altimeter and Argo measurements. *Geophys. Res. Lett.*, **47**, e2020GL090656, <https://doi.org/10.1029/2020GL090656>.
- Cheng, L., J. Zhu, R. Cowley, T. Boyer, and S. Wijffels, 2014: Time, probe type, and temperature variable bias corrections to historical expendable bathythermograph observations. *J. Atmos. Oceanic Technol.*, **31**, 1793–1825, <https://doi.org/10.1175/JTECH-D-13-00197.1>.
- , and Coauthors, 2023: Another year of record heat for the oceans. *Adv. Atmos. Sci.*, **40**, 963–974, <https://doi.org/10.1007/s00376-023-2385-2>.
- Cheng, W., J. C. Chiang, and D. Zhang, 2013: Atlantic meridional overturning circulation (AMOC) in CMIP5 models: RCP and historical simulations. *J. Climate*, **26**, 7187–7197, <https://doi.org/10.1175/JCLI-D-12-00496.1>.
- Chomiak, L. N., I. Yashayaev, D. L. Volkov, C. Schmid, and J. A. Hooper, 2022: Inferring advective timescales and overturning pathways of the Deep Western Boundary Current in the North Atlantic through Labrador Sea Water advection. *J. Geophys. Res. Oceans*, **127**, e2022JC018892, <https://doi.org/10.1029/2022JC018892>.
- Claustre, H., K. S. Johnson, and Y. Takeshita, 2020: Observing the global ocean with biogeochemical-Argo. *Annu. Rev. Mar. Sci.*, **12**, 23–48, <https://doi.org/10.1146/annurev-marine-010419-010956>.
- Crespo, L. R., A. Prigent, N. Keenlyside, S. Koseki, L. Svendsen, I. Richter, and E. Sánchez-Gómez, 2022: Weakening of the Atlantic Niño variability under global warming. *Nat. Climate Change*, **12**, 822–827, <https://doi.org/10.1038/s41558-022-01453-y>.
- Danabasoglu, G., F. S. Castruccio, R. J. Small, R. Tomas, E. Frajka-Williams, and M. Lankhorst, 2021: Revisiting AMOC transport estimates from observations and models. *Geophys. Res. Lett.*, **48**, e2021GL093045, <https://doi.org/10.1029/2021GL093045>.
- D'Asaro, E. A., and C. McNeil, 2013: Calibration and stability of oxygen sensors on autonomous floats. *J. Atmos. Oceanic Technol.*, **30**, 1896–1906, <https://doi.org/10.1175/JTECH-D-12-00222.1>.
- de Boyer Montégut, C., G. Madec, A. S. Fischer, A. Lazar, and D. Ludicone, 2004: Mixed layer depth over the global ocean: An examination of profile data and a profile-based climatology. *J. Geophys. Res.*, **109**, C12003, <https://doi.org/10.1029/2004JC002378>.
- Deser, C., M. A. Alexander, S. P. Xie, and A. S. Phillips, 2010: Sea surface temperature variability: Patterns and mechanisms. *Annu. Rev. Mar. Sci.*, **2**, 115–143, <https://doi.org/10.1146/annurev-marine-120408-151453>.
- Deutsch, C., A. Ferrel, B. Seibel, H. O. Pörtner, and R. B. Huey, 2015: Climate change tightens a metabolic constraint on marine habitats. *Science*, **348**, 1132–1135, <https://doi.org/10.1126/science.aaa1605>.
- Dierssen, H. M., 2010: Perspectives on empirical approaches for ocean color remote sensing of chlorophyll in a changing climate. *Proc. Natl. Acad. Sci. USA*, **107**, 17073–17078, <https://doi.org/10.1073/pnas.0913800107>.
- DiNezio, P. N., C. Deser, Y. M. Okumura, and A. Karspeck, 2017: Predictability of 2-year La Niña events in a coupled general circulation model. *Climate Dyn.*, **49**, 4237–4261, <https://doi.org/10.1007/s00382-017-3575-3>.
- Dlugokencky, E. J., K. W. Thoning, X. Lan, and P. P. Tans, 2021: NOAA greenhouse gas reference from atmospheric carbon dioxide dry air mole fractions from the NOAA GML Carbon Cycle Cooperative Global Air Sampling Network. NOAA, ftp://aftp.cmdl.noaa.gov/data/trace_gases/co2/flask/surface/.
- Domingues, R., and Coauthors, 2015: Upper ocean response to Hurricane Gonzalo (2014): Salinity effects revealed by targeted and sustained underwater glider observations. *Geophys. Res. Lett.*, **42**, 7131–7138, <https://doi.org/10.1002/2015GL065378>.
- , M. Baringer, and G. Goni, 2016: Remote sources for year-to-year changes in the seasonality of the Florida Current transport. *J. Geophys. Res. Oceans*, **121**, 7547–7559, <https://doi.org/10.1002/2016JC012070>.
- Dong, S., G. Goni, R. Domingues, F. Bringas, M. Goes, J. Christophersen, and M. Baringer, 2021: Synergy of in-situ and satellite ocean observations in determining meridional heat transport in the Atlantic Ocean. *J. Geophys. Res. Oceans*, **126**, e2020JC017073, <https://doi.org/10.1029/2020JC017073>.
- , D. L. Volkov, G. Goni, K. Pujiana, F. Tagklis, and M. Baringer, 2022: Remote impact of the equatorial Pacific on Florida Current transport. *Geophys. Res. Lett.*, **49**, e2021GL096944, <https://doi.org/10.1029/2021GL096944>.
- Durack, P. J., and S. E. Wijffels, 2010: Fifty-year trends in global ocean salinities and their relationship to broad-scale warming. *J. Climate*, **23**, 4342–4362, <https://doi.org/10.1175/2010JCLI3377.1>.
- , —, and R. J. Matear, 2012: Ocean salinities reveal strong global water cycle intensification during 1950 to 2000. *Science*, **336**, 455–458, <https://doi.org/10.1126/science.1212222>.
- Esaías, W. E., and Coauthors, 1998: An overview of MODIS capabilities for ocean science observations. *IEEE Trans. Geosci. Remote Sens.*, **36**, 1250–1265, <https://doi.org/10.1109/36.701076>.
- Espinoza, J.-C., J. A. Marengo, J. Schongart, and J. C. Jimenez, 2022: The new historical flood of 2021 in the Amazon River compared to major floods of the 21st century: Atmospheric features in the context of the intensification of floods. *Wea. Climate Extremes*, **35**, 100406, <https://doi.org/10.1016/j.wace.2021.100406>.
- Ezer, T., and L. P. Atkinson, 2014: Accelerated flooding along the U.S. East Coast: On the impact of sea-level rise, tides, storms, the Gulf Stream, and the North Atlantic Oscillations. *Earth's Future*, **2**, 362–382, <https://doi.org/10.1002/2014EF000252>.
- Fasullo, J. T., and R. S. Nerem, 2018: Altimeter-era emergence of the patterns of forced sea-level rise in climate models and implications for the future. *Proc. Natl. Acad. Sci. USA*, **115**, 12944–12949, <https://doi.org/10.1073/pnas.1813233115>.
- , —, and B. Hamlington, 2016: Is the detection of accelerated sea-level rise imminent? *Sci. Rep.*, **6**, 31245, <https://doi.org/10.1038/srep31245>.
- , N. Rosenbloom, and R. Buchholz, 2023: A multiyear tropical Pacific cooling response to recent Australian wildfires in CESM2. *Sci. Adv.*, **9**, eadg1213, <https://doi.org/10.1126/sciadv.adg1213>.
- Field, A., 2007: Amazon and Orinoco River plumes and NBC rings: Bystanders or participants in hurricane events? *J. Climate*, **20**, 316–333, <https://doi.org/10.1175/JCLI3985.1>.

- Field, C. B., M. J. Behrenfeld, J. T. Randerson, and P. Falkowski, 1998: Primary production of the biosphere: Integrating terrestrial and oceanic components. *Science*, **281**, 237–240, <https://doi.org/10.1126/science.281.5374.237>.
- Fofonoff, N. P., and E. L. Lewis, 1979: A practical salinity scale. *J. Oceanogr. Soc. Japan*, **35**, 63–64, <https://doi.org/10.1007/BF02108283>.
- Font, J., and Coauthors, 2013: SMOS first data analysis for sea surface salinity determination. *Int. J. Remote Sens.*, **34**, 3654–3670, <https://doi.org/10.1080/01431161.2012.716541>.
- Fore, A. G., S. H. Yueh, W. Q. Tang, B. W. Stiles, and A. K. Hayashi, 2016: Combined active/passive retrievals of ocean vector wind and sea surface salinity with SMAP. *IEEE Trans. Geosci. Remote Sens.*, **54**, 7396–7404, <https://doi.org/10.1109/TGRS.2016.2601486>.
- Forster, P., and Coauthors, 2021: The Earth's energy budget, climate feedbacks, and climate sensitivity. *Climate Change 2021: The Physical Science Basis*, V. Masson-Delmotte et al., Eds., Cambridge University Press, 923–1054, <https://doi.org/10.1017/9781009157896.009>.
- Frajka-Williams, E., and Coauthors, 2016: Compensation between meridional flow components of the Atlantic MOC at 26°N. *Ocean Sci.*, **12**, 481–493, <https://doi.org/10.5194/os-12-481-2016>.
- , and Coauthors, 2019: Atlantic meridional overturning circulation: Observed transports and variability. *Front. Mar. Sci.*, **6**, 260, <https://doi.org/10.3389/fmars.2019.00260>.
- Franz, B. A., I. Cetinić, M. Gao, A. Siegel, and T. K. Westberry, 2022: Global ocean phytoplankton [in “State of the Climate in 2021”]. *Bull. Amer. Meteor. Soc.*, **103** (8), S180–S183, <https://doi.org/10.1175/BAMS-D-22-0072.1>.
- Friedlingstein, P., and Coauthors, 2022: Global carbon budget 2022. *Earth Syst. Sci. Data*, **14**, 4811–4900, <https://doi.org/10.5194/essd-14-4811-2022>.
- Fyfe, J. C., and Coauthors, 2016: Making sense of the early-2000s warming slowdown. *Nat. Climate Change*, **6**, 224–228, <https://doi.org/10.1038/nclimate2938>.
- Garcia, H. E., and L. I. Gordon, 1992: Oxygen solubility in seawater: Better fitting equations. *Limnol. Oceanogr.*, **37**, 1307–1312, <https://doi.org/10.4319/lo.1992.37.6.1307>.
- Geider, R. J., H. L. MacIntyre, and T. M. Kana, 1997: Dynamic model of phytoplankton growth and acclimation: Responses of the balanced growth rate and the chlorophyll *a*: Carbon ratio to light, nutrient limitation and temperature. *Mar. Ecol.: Prog. Ser.*, **148**, 187–200, <https://doi.org/10.3354/meps148187>.
- Gloege, L., and Coauthors, 2021: Quantifying errors in observationally based estimates of ocean carbon sink variability. *Global Biogeochem. Cycles*, **35**, e2020GB006788, <https://doi.org/10.1029/2020GB006788>.
- Goni, G. J., and W. E. Johns, 2003: Synoptic study of warm rings in the North Brazil Current retroflexion region using satellite altimetry. *Interhemispheric Water Exchange in the Atlantic Ocean*, G. J. Goni and P. Malanotte-Rizzoli, Eds., Elsevier Oceanography Series, Vol. 68, Elsevier, 335–356, [https://doi.org/10.1016/S0422-9894\(03\)80153-8](https://doi.org/10.1016/S0422-9894(03)80153-8).
- , F. Bringas, and P. N. Di Nezio, 2011: Observed low frequency variability of the Brazil Current front. *J. Geophys. Res.*, **116**, C10037, <https://doi.org/10.1029/2011JC007198>.
- Good, S. A., M. J. Martin, and N. A. Rayner, 2013: EN4: Quality controlled ocean temperature and salinity profiles and monthly objective analyses with uncertainty estimates. *J. Geophys. Res. Oceans*, **118**, 6704–6716, <https://doi.org/10.1002/2013JC009067>.
- Gouretski, V., and L. Cheng, 2020: Correction for systematic errors in the global dataset of temperature profiles from mechanical bathythermographs. *J. Atmos. Oceanic Technol.*, **37**, 841–855, <https://doi.org/10.1175/JTECH-D-19-0205.1>.
- Graff, J. R., and Coauthors, 2015: Analytical phytoplankton carbon measurements spanning diverse ecosystems. *Deep-Sea Res. I*, **102**, 16–25, <https://doi.org/10.1016/j.dsr.2015.04.006>.
- Gruber, N., 2008: The marine nitrogen cycle: Overview and challenges. *Nitrogen in the Marine Environment*, 2nd ed. D. G. Capone et al., Eds., Academic Press, 1–50.
- , and Coauthors, 2010: Adding oxygen to Argo: Developing a global in-situ observatory for ocean deoxygenation and biogeochemistry. *Proc. OceanObs'09: Sustained Ocean Observations and Information for Society*, Venice, Italy, European Space Agency, 12 pp., <https://doi.org/10.5270/OceanObs09.cwp.39>.
- , and Coauthors, 2019: The oceanic sink for anthropogenic CO₂ from 1994 to 2007. *Science*, **363**, 1193–1199, <https://doi.org/10.1126/science.aau5153>.
- Hakuba, M. Z., T. Frederikse, and F. W. Landerer, 2021: Earth's energy imbalance from the ocean perspective (2005–2019). *Geophys. Res. Lett.*, **48**, e2021GL093624, <https://doi.org/10.1029/2021GL093624>.
- Hamlington, B. D., C. G. Piecuch, J. T. Reager, H. Chandanpurkar, T. Frederikse, R. S. Nerem, J. T. Fasullo, and S.-H. Cheon, 2020: Origin of interannual variability in global mean sea level. *Proc. Natl. Acad. Sci. USA*, **117**, 13983–13990, <https://doi.org/10.1073/pnas.1922190117>.
- Han, W., G. A. Meehl, D. Stammer, A. Hu, B. Hamlington, J. Kenigson, H. Palanisamy, and P. Thompson, 2017: Spatial patterns of sea level variability associated with natural internal climate modes. *Surv. Geophys.*, **38**, 217–250, <https://doi.org/10.1007/s10712-016-9386-y>.
- Hasan, N. A., Y. Chikamoto, and M. J. McPhaden, 2022: The influence of tropical basin interactions on the 2020–22 double-dip La Niña. *Front. Climate*, **4**, 1001174, <https://doi.org/10.3389/fclim.2022.1001174>.
- Held, I. M., and B. J. Soden, 2006: Robust responses of the hydrological cycle to global warming. *J. Climate*, **19**, 5686–5699, <https://doi.org/10.1175/JCLI3990.1>.
- Helm, K. P., N. L. Bindoff, and J. A. Church, 2011: Observed decreases in oxygen content of the global ocean. *Geophys. Res. Lett.*, **38**, L23602, <https://doi.org/10.1029/2011GL049513>.
- Hersbach, H., and Coauthors, 2018: ERA5 hourly data on single levels from 1940 to present. Copernicus Climate Change Service (C3S) Climate Data Store (CDS), accessed 4 January 2023, <https://doi.org/10.24381/cds.adbb2d47>.
- , and Coauthors, 2020: The ERA5 global reanalysis. *Quart. J. Roy. Meteor. Soc.*, **146**, 1999–2049, <https://doi.org/10.1002/qj.3803>.
- Hobbs, W. R., and J. K. Willis, 2012: Midlatitude North Atlantic heat transport: A time series based on satellite and drifter data. *J. Geophys. Res.*, **117**, C01008, <https://doi.org/10.1029/2011JC007039>.
- Hu, C., Z. Lee, and B. A. Franz, 2012: Chlorophyll *a* algorithms for oligotrophic oceans: A novel approach based on three-band reflectance difference. *J. Geophys. Res.*, **117**, C01011, <https://doi.org/10.1029/2011JC007395>.
- , L. Feng, Z. Lee, B. A. Franz, S. W. Bailey, P. J. Werdell, and C. W. Proctor, 2019: Improving satellite global chlorophyll *a* data products through algorithm refinement and data recovery. *J. Geophys. Res. Oceans*, **124**, 1524–1543, <https://doi.org/10.1029/2019JC014941>.

- Hu, S., and A. V. Fedorov, 2017: The extreme El Niño of 2015–2016 and the end of global warming hiatus. *Geophys. Res. Lett.*, **44**, 3816–3824, <https://doi.org/10.1002/2017GL072908>.
- Huang, B., and Coauthors, 2015: Extended Reconstructed Sea Surface Temperature version 4 (ERSST.v4). Part I: Upgrades and intercomparisons. *J. Climate*, **28**, 911–930, <https://doi.org/10.1175/JCLI-D-14-00006.1>.
- , and Coauthors, 2017: Extended Reconstructed Sea Surface Temperature version 5 (ERSSTv5): Upgrades, validations, and intercomparisons. *J. Climate*, **30**, 8179–8205, <https://doi.org/10.1175/JCLI-D-16-0836.1>.
- , and Coauthors, 2020: Uncertainty estimates for sea surface temperature and land surface air temperature in NOAA-GlobalTemp version 5. *J. Climate*, **33**, 1351–1379, <https://doi.org/10.1175/JCLI-D-19-0395.1>.
- , C. Liu, V. Banzon, E. Freeman, G. Graham, B. Hankins, T. Smith, and H.-M. Zhang, 2021a: Improvements of the Daily Optimum Interpolation Sea Surface Temperature (DOISST) version 2.1. *J. Climate*, **34**, 2923–2939, <https://doi.org/10.1175/JCLI-D-20-0166.1>.
- , Z. Wang, X. Yin, A. Arguez, G. Graham, C. Liu, T. Smith, H.-M. Zhang, 2021b: Prolonged marine heatwaves in the Arctic: 1982–2020. *Geophys. Res. Lett.*, **48**, e2021GL095590, <https://doi.org/10.1029/2021GL095590>.
- Huffman, G. J., R. F. Adler, D. T. Bolvin, and G. Gu, 2009: Improving the global precipitation record. GPCP version 2.1. *Geophys. Res. Lett.*, **36**, L17808, <https://doi.org/10.1029/2009GL040000>.
- Hummels, R., B. Johns, S. Speich, R. Perez, P. Brandt, M. Lankhorst, and U. Send, 2022: Theme 3: The AMOC in the Tropical Atlantic. *CLIVAR Exchanges*, No. 82, International CLIVAR Project Office, Southampton, United Kingdom, 22–28, <http://doi.org/10.36071/clivar.82.2022>.
- IPCC, 2021: *Climate Change 2021: The Physical Science Basis*. V. Masson-Delmotte et al., Eds., Cambridge University Press, 2391 pp.
- Ishii, M., Y. Fukuda, S. Hirahara, S. Yasui, T. Suzuki, and K. Sato, 2017: Accuracy of global upper ocean heat content estimation expected from present observational datasets. *SOLA*, **13**, 163–167, <https://doi.org/10.2151/sola.2017-030>.
- Ito, T., S. Minobe, M. C. Long, and C. Deutsch, 2017: Upper ocean O₂ trends: 1958–2015. *Geophys. Res. Lett.*, **44**, 4214–4223, <https://doi.org/10.1002/2017GL073613>.
- Jin, F.-F., 1997: An equatorial ocean recharge paradigm for ENSO. Part I: Conceptual model. *J. Atmos. Sci.*, **54**, 811–829, [https://doi.org/10.1175/1520-0469\(1997\)054<0811:CO;2](https://doi.org/10.1175/1520-0469(1997)054<0811:CO;2).
- Johns, W. E., and Coauthors, 2011: Continuous, array-based estimates of Atlantic Ocean heat transport at 26.5°N. *J. Climate*, **24**, 2429–2449, <https://doi.org/10.1175/2010JCLI3997.1>.
- Johnson, G. C., and J. M. Lyman, 2012: Sea surface salinity [in “State of the Climate in 2011”]. *Bull. Amer. Meteor. Soc.*, **93** (7), S68–S69, <https://doi.org/10.1175/2012BAMSStateoftheClimate.1>.
- , and —, 2020: Warming trends increasingly dominate Global Ocean. *Nat. Climate Change*, **10**, 757–761, <https://doi.org/10.1038/s41558-020-0822-0>.
- , —, J. K. Willis, T. Boyer, J. Antonov, S. A. Good, C. M. Domingues, and N. Bindoff, 2014: Ocean heat content [in “State of the Climate in 2013”]. *Bull. Amer. Meteor. Soc.*, **95** (7), S54–S57, <https://doi.org/10.1175/2014BAMSStateoftheClimate.1>.
- , —, J. Antonov, N. Bindoff, T. Boyer, C. M. Domingues, S. A. Good, M. Ishii, and J. K. Willis, 2015: Ocean heat content [in “State of the Climate in 2014”]. *Bull. Amer. Meteor. Soc.*, **96** (7), S64–S66, <https://doi.org/10.1175/2015BAMSStateoftheClimate.1>.
- , J. Reagan, J. M. Lyman, T. Boyer, C. Schmid, and R. Locarnini, 2020: Salinity [in “State of the Climate in 2019”]. *Bull. Amer. Meteor. Soc.*, **101** (8), S129–S183, <https://doi.org/10.1175/BAMS-D-20-0105.1>.
- , and Coauthors, 2022: Ocean heat content [in “State of the Climate in 2021”]. *Bull. Amer. Meteor. Soc.*, **103** (8), S153–S157, <https://doi.org/10.1175/>.
- Kanamitsu, M., W. Ebisuzaki, J. Woollen, S.-K. Yang, J. J. Hnilo, M. Fiorino, and G. L. Potter, 2002: NCEP–DOE AMIP-II Reanalysis (R-2). *Bull. Amer. Meteor. Soc.*, **83**, 1631–1644, <https://doi.org/10.1175/BAMS-83-11-1631>.
- Kanzow, T., U. Send, W. Zenk, A. D. Chave, and M. Rhein, 2006: Monitoring the integrated deep meridional flow in the tropical North Atlantic: Long-term performance of a geostrophic array. *Deep-Sea Res. I*, **53**, 528–546, <https://doi.org/10.1016/j.dsr.2005.12.007>.
- Kato, S., and Coauthors, 2018: Surface irradiances of Edition 4.0 Clouds and the Earth’s Radiant Energy System (CERES) Energy Balanced and Filled (EBAF) data product. *J. Climate*, **31**, 4501–4527, <https://doi.org/10.1175/JCLI-D-17-0523.1>.
- Keeling, R. F., A. Körtzinger, and N. Gruber, 2010: Ocean deoxygenation in a warming world. *Annu. Rev. Mar. Sci.*, **2**, 199–229, <https://doi.org/10.1146/annurev.marine.010908.163855>.
- Kennedy, J. J., N. A. Rayner, C. P. Atkinson, and R. E. Killick, 2019: An ensemble data set of sea surface temperature change from 1850: The Met Office Hadley Centre HadSST.4.0.0.0 data set. *J. Geophys. Res. Atmos.*, **124**, 7719–7763, <https://doi.org/10.1029/2018JD029867>.
- Keppeler, L., P. Landschützer, S. K. Lauvset, and N. Gruber, 2023: Recent trends and variability in the oceanic storage of dissolved inorganic carbon. *Global Biogeochem. Cycles*, **37**, e2022GB007677, <https://doi.org/10.1029/2022GB007677>.
- Kersalé, M., and Coauthors, 2021: Multi-year estimates of daily heat transport by the Atlantic meridional overturning circulation at 34.5°S. *J. Geophys. Res. Oceans*, **126**, e2020JC016947, <https://doi.org/10.1029/2020JC016947>.
- Khatiwal, S., and Coauthors, 2013: Global ocean storage of anthropogenic carbon. *Biogeosciences*, **10**, 2169–2191, <https://doi.org/10.5194/bg-10-2169-2013>.
- Koch, L. G., and S. L. Britton, 2008: Aerobic metabolism underlies complexity and capacity. *J. Physiol.*, **586**, 83–95, <https://doi.org/10.1113/jphysiol.2007.144709>.
- Koelling, J., U. Send, and M. Lankhorst, 2020: Decadal strengthening of interior flow of North Atlantic Deep Water observed by GRACE satellites. *J. Geophys. Res. Oceans*, **125**, e2020JC016217, <https://doi.org/10.1029/2020JC016217>.
- Kwiatkowski, L., and Coauthors, 2020: Twenty-first century ocean warming, acidification, deoxygenation, and upper-ocean nutrient and primary production decline from CMIP6 model projections. *Biogeosciences*, **17**, 3439–3470, <https://doi.org/10.5194/bg-17-3439-2020>.
- Landschützer, P., N. Gruber, D. C. E. Bakker, U. Schuster, S. Nakaoka, M. R. Payne, T. P. Sasse, and J. Zeng, 2013: A neural network-based estimate of the seasonal to inter-annual variability of the Atlantic Ocean carbon sink. *Biogeosciences*, **10**, 7793–7815, <https://doi.org/10.5194/bg-10-7793-2013>.
- , —, —, and —, 2014: Recent variability of the global ocean carbon sink. *Global Biogeochem. Cycles*, **28**, 927–949, <https://doi.org/10.1002/2014GB004853>.

- Langdon, C., 2010: Determination of dissolved oxygen in seawater by Winkler titration using Amperometric Technique. The GO-SHIP Repeat Hydrography Manual: A Collection of Expert Reports and Guidelines, Version 1, E. M. Hood, C. L. Sabine, and B. M. Sloyan, Eds., IOCCP Rep. 14, ICPO Publ. Series 134, 18 pp., <https://doi.org/10.25607/OBP-1350>.
- Lauvset, S. K., and Coauthors, 2016: A new global interior ocean mapped climatology: The 1 ° 1 GLODAP version 2. *Earth Syst. Sci. Data*, **8**, 325–340, <https://doi.org/10.5194/essd-8-325-2016>.
- Le Bras, I. A., I. Yashayaev, and J. M. Toole, 2017: Tracking Labrador Sea Water property signals along the Deep Western Boundary Current. *J. Geophys. Res. Oceans*, **122**, 5348–5366, <https://doi.org/10.1002/2017JC012921>.
- Leuliette, E. W., and J. K. Willis, 2011: Balancing the sea level budget. *Oceanography*, **24**, 122–129, <https://doi.org/10.5670/oceanog.2011.32>.
- Levin, L. A., 2018: Manifestation, drivers, and emergence of open ocean deoxygenation. *Annu. Rev. Mar. Sci.*, **10**, 229–260, <https://doi.org/10.1146/annurev-marine-121916-063359>.
- , and Coauthors, 2009: Effects of natural and human-induced hypoxia on coastal benthos. *Biogeosciences*, **6**, 2063–2098, <https://doi.org/10.5194/bg-6-2063-2009>.
- Le Vine, D. M., E. P. Dinnat, G. S. E. Lagerloef, P. de Matthaëis, S. Abraham, C. Utku, and H. Kao, 2014: Aquarius: Status and recent results. *Radio Sci.*, **49**, 709–720, <https://doi.org/10.1002/2014RS005505>.
- Levitus, S., and Coauthors, 2012: World ocean heat content and thermosteric sea level change (0–2000 m), 1955–2010. *Geophys. Res. Lett.*, **39**, L10603, <https://doi.org/10.1029/2012GL051106>.
- Li, L., R. W. Schmitt, C. C. Ummenhofer, and K. B. Karnauskas, 2016: North Atlantic salinity as a predictor of Sahel rainfall. *Sci. Adv.*, **2**, e1501588, <https://doi.org/10.1126/sciadv.1501588>.
- Li, X., Z.-Z. Hu, and B. Huang, 2020: Subannual to interannual variabilities of SST in the North Atlantic Ocean. *J. Climate*, **33**, 5547–5564, <https://doi.org/10.1175/JCLI-D-19-0556.1>.
- Llovel, W., and L. Terray, 2016: Observed southern upper-ocean warming over 2005–2014 and associated mechanisms. *Environ. Res. Lett.*, **11**, 124023, <https://doi.org/10.1088/1748-9326/11/12/124023>.
- Loeb, N. G., G. C. Johnson, T. J. Thorsen, J. M. Lyman, F. G. Rose, and S. Kato, 2021: Satellite and ocean data reveal marked increase in Earth's heating rate. *Geophys. Res. Lett.*, **48**, e2021GL093047, <https://doi.org/10.1029/2021GL093047>.
- Lozier, M. S., A. S. Bower, H. H. Furey, K. L. Drouin, X. Xu, and S. Zou, 2022: Overflow water pathways in the North Atlantic. *Prog. Oceanogr.*, **208**, 102874, <https://doi.org/10.1016/j.pocean.2022.102874>.
- Lumpkin, R., and S. L. Garzoli, 2005: Near-surface circulation in the tropical Atlantic Ocean. *Deep-Sea Res. I*, **52**, 495–518, <https://doi.org/10.1016/j.dsr.2004.09.001>.
- , and —: Interannual to decadal changes in the western South Atlantic's surface circulation. *J. Geophys. Res.*, **116**, C01014, <https://doi.org/10.1029/2010JC006285>.
- , and G. Johnson, 2013: Global ocean surface velocities from drifters: Mean, variance, El Niño–Southern Oscillation response, and seasonal cycle. *J. Geophys. Res. Oceans*, **118**, 2992–3006, <https://doi.org/10.1002/jgrc.20210>.
- , G. Goni, and K. Dohan, 2012: Surface currents [in "State of the Climate in 2011"]. *Bull. Amer. Meteor. Soc.*, **93** (7), S75–S78, <https://doi.org/10.1175/2012BAMSStateoftheClimate.1>.
- Lyman, J. M., and G. C. Johnson, 2014: Estimating global ocean heat content changes in the upper 1800 m since 1950 and the influence of climatology choice. *J. Climate*, **27**, 1945–1957, <https://doi.org/10.1175/JCLI-D-12-00752.1>.
- Mantua, N. J., and S. R. Hare, 2002: The Pacific decadal oscillation. *J. Oceanogr.*, **58**, 35–44, <https://doi.org/10.1023/A:1015820616384>.
- Maritorena, S., O. Hembise Fanton d'Andon, A. Mangin, and D. A. Siegel, 2010: Merged satellite ocean color data products using a bio-optical model: Characteristics, benefits and issues. *Remote Sens. Environ.*, **114**, 1791–1804, <https://doi.org/10.1016/j.rse.2010.04.002>.
- Marti, F., and Coauthors, 2022: Monitoring the ocean heat content change and the Earth energy imbalance from space altimetry and space gravimetry. *Earth Syst. Sci. Data*, **14**, 229–249, <https://doi.org/10.5194/essd-14-229-2022>.
- Maurer, T. L., J. N. Plant, and K. S. Johnson, 2021: Delayed-mode quality control of oxygen, nitrate, and pH data on SOCCOM biogeochemical profiling floats. *Front. Mar. Sci.*, **8**, 683207, <https://doi.org/10.3389/fmars.2021.683207>.
- McCarthy, G. D., and Coauthors, 2015: Measuring the Atlantic Meridional Overturning Circulation at 26°N. *Prog. Oceanogr.*, **130**, 91–111, <https://doi.org/10.1016/j.pocean.2014.10.006>.
- McClain, C. R., 2009: A decade of satellite ocean color observations. *Annu. Rev. Mar. Sci.*, **1**, 19–42, <https://doi.org/10.1146/annurev.marine.010908.163650>.
- McKinna, L. I. W., P. J. Werdell, and C. W. Proctor, 2016: Implementation of an analytical Raman scattering correction for satellite ocean-color processing. *Opt. Express*, **24**, A1123–A1137, <https://doi.org/10.1364/OE.24.0A1123>.
- McPhaden, M. J., T. Lee, S. Fournier, and M. A. Balmaseda, 2021: ENSO observations. *El Niño Southern Oscillation in a Changing Climate, Geophys. Monogr.*, Vol. 253, Amer. Geophys. Union, 39–63, <https://doi.org/10.1002/9781119548164.ch3>.
- Merrifield, M., 2011: A shift in western tropical Pacific sea level trends during the 1990s. *J. Climate*, **24**, 4126–4138, <https://doi.org/10.1175/2011JCLI3932.1>.
- Moana Project, 2022: It's been a hot year – Moana Project marine heatwave research. 2 pp., www.moanaproject.org/s/Marine-heatwaves.pdf.
- Moat, B. I., and Coauthors, 2020: Pending recovery in the strength of the meridional overturning circulation at 26°N. *Ocean Sci.*, **16**, 863–874, <https://doi.org/10.5194/os-16-863-2020>.
- , E. Frajka-Williams, D. A. Smeed, D. Rayner, W. E. Johns, M. O. Baringer, D. Volkov, and J. Collins, 2022: Atlantic meridional overturning circulation observed by the RAPID-MOCHA-WBTS (RAPID-Meridional Overturning Circulation and Heatflux Array-Western Boundary Time Series) array at 26N from 2004 to 2020 (v2020.2). NERC EDS British Oceanographic Data Centre NOC, accessed 24 January 2023, <https://doi.org/10.5285/e91b10af-6f0a-7fa7-e053-6c86abc05a09>.
- Mulet, S., and Coauthors, 2021: The new CNES-CLS18 global mean dynamic topography. *Ocean Sci.*, **17**, 789–808, <https://doi.org/10.5194/os-17-789-2021>.
- Müller, J. D., and Coauthors, 2023: Decadal trends in the oceanic storage of anthropogenic carbon from 1994 to 2014. ESS Open Archive, accessed 1 February 2023, <https://doi.org/10.22541/essoar.167525217.76035050/v1>.
- Nerem, R. S., B. D. Beckley, J. T. Fasullo, B. D. Hamlington, D. Masters, and G. T. Mitchum, 2018: Climate-change-driven accelerated sea-level rise detected in the altimeter era. *Proc. Natl. Acad. Sci. USA*, **115**, 2022–2025, <https://doi.org/10.1073/pnas.1717312115>.

- Oliver, E. C., J. A. Benthuisen, N. L. Bindoff, A. J. Hobday, N. J. Holbrook, C. N. Mundy, and S. E. Perkins-Kirkpatrick, 2017: The unprecedented 2015/16 Tasman Sea marine heatwave. *Nat. Commun.*, **8**, 16101, <https://doi.org/10.1038/ncomms16101>.
- , —, S. Darmaraki, M. G. Donat, A. J. Hobday, N. J. Holbrook, R. W. Schlegel, and A. Sen Gupta, 2021: Marine heatwaves. *Annu. Rev. Mar. Sci.*, **13**, 313–342, <https://doi.org/10.1146/annurev-marine-032720-095144>.
- O'Reilly, J. E., and P. J. Werdell, 2019: Chlorophyll algorithms for ocean color sensors – OC4, OC5 & OC6. *Remote Sens. Environ.*, **229**, 32–47, <https://doi.org/10.1016/j.rse.2019.04.021>.
- Oschlies, A., K. G. Schulz, U. Riebesell, and A. Schmittner, 2008: Simulated 21st century's increase in oceanic suboxia by CO₂-enhanced biotic carbon export. *Global Biogeochem. Cycles*, **22**, GB4008, <https://doi.org/10.1029/2007GB003147>.
- , O. Duteil, J. Getzlaff, W. Koeve, A. Landolfi, and S. Schmidtko, 2017: Patterns of deoxygenation: Sensitivity to natural and anthropogenic drivers. *Philos. Trans. Roy. Soc.*, **A375**, 20160325, <https://doi.org/10.1098/rsta.2016.0325>.
- , P. Brandt, L. Stramma, and S. Schmidtko, 2018: Drivers and mechanisms of ocean deoxygenation. *Nat. Geosci.*, **11**, 467–473, <https://doi.org/10.1038/s41561-018-0152-2>.
- Palmer, M. D., K. Haines, S. F. B. Tett, and T. J. Ansell, 2007: Isolating the signal of ocean global warming. *Geophys. Res. Lett.*, **34**, L23610, <https://doi.org/10.1029/2007GL031712>.
- Park, J.-H., J.-S. Kug, Y.-M. Yang, T. Li, and H.-S. Jo, 2021: Mid-latitude leading double-dip La Niña. *Int. J. Climatol.*, **41**, E1353–E1370, <https://doi.org/10.1002/joc.6772>.
- Payne, A. E., and Coauthors, 2020: Responses and impacts of atmospheric rivers to climate change. *Nat. Rev. Earth Environ.*, **1**, 143–157, <https://doi.org/10.1038/s43017-020-0030-5>.
- Perkins-Kirkpatrick, S. E., A. D. King, E. A. Cougnon, N. J. Holbrook, M. R. Grose, E. C. J. Oliver, S. C. Lewis, and F. Poursagar, 2019: The role of natural variability and anthropogenic climate change in the 2017/18 Tasman Sea marine heatwave [in "Explaining Extremes of 2017 from a Climate Perspective"]. *Bull. Amer. Meteor. Soc.*, **100** (1), S105–S110, <https://doi.org/10.1175/BAMS-D-18-0116.1>.
- Pörtner, H. O., and R. Knust, 2007: Climate change affects marine fishes through the oxygen limitation of thermal tolerance. *Science*, **315**, 95–97, <https://doi.org/10.1126/science.1135471>.
- Purkey, S. G., and G. C. Johnson, 2010: Warming of global abyssal and deep Southern Ocean waters between the 1990s and 2000s: Contributions to global heat and sea-level rise budgets. *J. Climate*, **23**, 6336–6351, <https://doi.org/10.1175/2010JCLI3682.1>.
- Qiu, B., and S. Chen, 2021: Revisit of the occurrence of the Kuroshio large meander south of Japan. *J. Phys. Oceanogr.*, **51**, 3679–3694, <https://doi.org/10.1175/JPO-D-21-0167.1>.
- , —, N. Schneider, E. Oka, and S. Sugimoto, 2020: On the reset of the wind-forced decadal Kuroshio Extension variability in late 2017. *J. Climate*, **33**, 10813–10828, <https://doi.org/10.1175/JCLI-D-20-0237.1>.
- Rayner, N. A., D. E. Parker, E. B. Horton, C. K. Folland, L. V. Alexander, D. P. Rowell, E. C. Kent, and A. Kaplan, 2003: Global analyses of sea surface temperature, sea ice, and night marine air temperature since the late nineteenth century. *J. Geophys. Res.*, **108**, 4407, <https://doi.org/10.1029/2002JD002670>.
- Reagan, J., T. Boyer, C. Schmid, and R. Locarnini, 2020: Subsurface salinity [in "State of the Climate in 2019"]. *Bull. Amer. Meteor. Soc.*, **101** (8), S144–S148, <https://doi.org/10.1175/BAMS-D-20-0105.1>.
- , —, —, and —, 2021: Subsurface salinity [in "State of the Climate in 2020"]. *Bull. Amer. Meteor. Soc.*, **102** (8), S162–S164, <https://doi.org/10.1175/BAMS-D-21-0083.1>.
- , —, —, and —, 2022: Subsurface salinity [in "State of the Climate in 2021"]. *Bull. Amer. Meteor. Soc.*, **103** (8), S160–S162, <https://doi.org/10.1175/BAMS-D-22-0072.1>.
- Ren, L., K. Speer, and E. P. Chassignet, 2011: The mixed layer salinity budget and sea ice in the Southern Ocean. *J. Geophys. Res.*, **116**, C08031, <https://doi.org/10.1029/2010JC006634>.
- Resplandy, L., and Coauthors, 2018: Revision of global carbon fluxes based on a reassessment of oceanic and riverine carbon transport. *Nat. Geosci.*, **11**, 504–509, <https://doi.org/10.1038/s41561-018-0151-3>.
- Riser, S. C., and Coauthors, 2016: Fifteen years of ocean observations with the global Argo array. *Nat. Climate Change*, **6**, 145–153, <https://doi.org/10.1038/nclimate2872>.
- Rödenbeck, C., and Coauthors, 2015: Data-based estimates of the ocean carbon sink variability – First results of the Surface Ocean pCO₂ Mapping intercomparison (SOCOM). *Biogeosciences*, **12**, 7251–7278, <https://doi.org/10.5194/bg-12-7251-2015>.
- Roemmich, D., and J. Gilson, 2009: The 2004–2008 mean and annual cycle of temperature, salinity, and steric height in the global ocean from the Argo Program. *Prog. Oceanogr.*, **82**, 81–100, <https://doi.org/10.1016/j.pocean.2009.03.004>.
- , and Coauthors, 2009: The Argo Program: Observing the global ocean with profiling floats. *Oceanography*, **22**, 34–43, <https://doi.org/10.5670/oceanog.2009.36>.
- , and Coauthors, 2019: On the future of Argo: A global, full-depth, multi-disciplinary array. *Front. Mar. Sci.*, **6**, 439, <https://doi.org/10.3389/fmars.2019.00439>.
- Saji, N. H., B. N. Goswami, P. N. Vinayachandran, and T. Yamagata, 1999: A dipole mode in the tropical Indian Ocean. *Nature*, **401**, 360–363, <https://doi.org/10.1038/43854>.
- Sanchez-Franks, A., E. Frajka-Williams, B. I. Moat, and D. A. Smeed, 2021: A dynamically based method for estimating the Atlantic meridional overturning circulation at 26°N from satellite altimetry. *Ocean Sci.*, **17**, 1321–1340, <https://doi.org/10.5194/os-17-1321-2021>.
- Sauzède, R., H. C. Bittig, H. Claustre, O. Pasqueron de Fommervault, J.-P. Gattuso, L. Legendre, and K. S. Johnson, 2017: Estimates of water-column nutrient concentrations and carbonate system parameters in the global ocean: A novel approach based on neural networks. *Front. Mar. Sci.*, **4**, 128, <https://doi.org/10.3389/fmars.2017.00128>.
- Schlesinger, M. E., and N. Ramankutty, 1994: An oscillation in the global climate system of period 65–70 years. *Nature*, **367**, 723–726, <https://doi.org/10.1038/367723a0>.
- Schleussner, C. F., A. Levermann, and M. Meinshausen, 2014: Probabilistic projections of the Atlantic overturning. *Climatic Change*, **127**, 579–586, <https://doi.org/10.1007/s10584-014-1265-2>.
- Schmidtko, S., K. J. Heywood, A. F. Thompson, and S. Aoki, 2014: Multidecadal warming of Antarctic waters. *Science*, **346**, 1227–1231, <https://doi.org/10.1126/science.1256117>.
- , L. Stramma, and M. Visbeck, 2017: Decline in global oceanic oxygen content during the past five decades. *Nature*, **542**, 335–339, <https://doi.org/10.1038/nature21399>.
- Schmitt, R. W., 1995: The ocean component of the global water cycle. *Rev. Geophys.*, **33**, 1395–1409, <https://doi.org/10.1029/95RG00184>.

- Schoeberl, M. R., Y. Wang, R. Ueyama, G. Taha, E. Jensen, and W. Yu, 2022: Analysis and impact of the Hunga Tonga-Hunga Ha'apai stratospheric water vapor plume. *Geophys. Res. Lett.*, **49**, e2022GL100248, <https://doi.org/10.1029/2022GL100248>.
- Sellitto, P., and Coauthors, 2022: The unexpected radiative impact of the Hunga Tonga eruption of 15th January 2022. *Nat. Commun. Earth Environ.*, **3**, 288, <https://doi.org/10.1038/s43247-022-00618-z>.
- Sharp, J. D., A. J. Fassbender, B. R. Carter, G. C. Johnson, C. Schultz, and J. P. Dunne, 2022a. GOBAI-O2: A global gridded monthly dataset of ocean interior dissolved oxygen concentrations based on shipboard and autonomous observations (NCEI Accession 0259304), V2.0. NOAA National Centers for Environmental Information, accessed 23 March 2023, <https://doi.org/10.25921/z72m-yz67>.
- , —, —, —, —, and —, 2022b: GOBAI-O2: Temporally and spatially resolved fields of ocean interior dissolved oxygen over nearly two decades. *Earth Syst. Sci. Data Discuss.*, <https://doi.org/10.5194/essd-2022-308>.
- Siegel, D. A., and Coauthors, 2013: Regional to global assessments of phytoplankton dynamics from the SeaWiFS mission. *Remote Sens. Environ.*, **135**, 77–91, <https://doi.org/10.1016/j.rse.2013.03.025>.
- , T. DeVries, I. Cetinić, and K. M. Bisson, 2023: Quantifying the ocean's biological pump and its carbon cycle impacts on global scales. *Annu. Rev. Mar. Sci.*, **15**, 329–356, <https://doi.org/10.1146/annurev-marine-040722-115226>.
- Skliris, N., R. Marsh, S. A. Josey, S. A. Good, C. Liu, and R. P. Allan, 2014: Salinity changes in the World Ocean since 1950 in relation to changing surface freshwater flux. *Climate Dyn.*, **43**, 709–736, <https://doi.org/10.1007/s00382-014-2131-7>.
- , J. D. Zika, G. Nurser, S. A. Josey, and R. Marsh, 2016: Global water cycle amplifying at less than the Clausius-Clapeyron rate. *Sci. Rep.*, **6**, 38752, <https://doi.org/10.1038/srep38752>.
- Stackhouse, P. W., D. P. Kratz, G. R. McGarragh, S. K. Gupta, and E. B. Geier, 2006: Fast Longwave and Shortwave Radiative Flux (FLASHFlux) products from CERES and MODIS measurements. *12th Conf. on Atmospheric Radiation*, Madison, WI, Amer. Meteor. Soc., P1.10, https://ams.confex.com/ams/Madison2006/techprogram/paper_113479.htm.
- Sweet, W. V., J. Park, J. J. Marra, C. Zervas, and S. Gill, 2014: Sea-level rise and nuisance flood frequency changes around the United States. NOAA Tech. Rep. NOS CO-OPS 73, 66 pp., https://tidesandcurrents.noaa.gov/publications/NOAA_Technical_Report_NOS_COOPS_073.pdf.
- Taha, G., R. Loughman, P. R. Colarco, T. Zhu, L. W. Thomason, and G. Jaross, 2022: Tracking the 2022 Hunga Tonga-Hunga Ha'apai aerosol cloud in the upper and middle stratosphere using space-based observations. *Geophys. Res. Lett.*, **49**, e2022GL100091, <https://doi.org/10.1029/2022GL100091>.
- Talley, L. D., 2002: Salinity patterns in the ocean. *The Earth System: Physical and Chemical Dimensions of Global Environmental Change*, Vol. 1, *Encyclopedia of Global Environmental Change*, M. C. MacCracken and J. S. Perry, Eds., John Wiley and Sons, 629–640.
- , and Coauthors, 2016: Changes in ocean heat, carbon content, and ventilation: A review of the first decade of GO-SHIP global repeat hydrography. *Annu. Rev. Mar. Sci.*, **8**, 185–215, <https://doi.org/10.1146/annurev-marine-052915-100829>.
- Taschetto, A., C. C. Ummenhofer, M. F. Stuecker, D. Dommenges, K. Ashok, R. R. Rodrigues, and S.-W. Yeh, 2020: ENSO atmospheric teleconnections. *El Niño Southern Oscillation in a Changing Climate*, *Geophys. Monogr.*, Vol. 253, Amer. Geophys. Union, 309–335, <https://doi.org/10.1002/9781119548164.ch14>.
- Trenberth, K. E., J. M. Caron, D. P. Stepaniak, and S. Worley, 2002: Evolution of El Niño Southern Oscillation and global atmospheric surface temperatures. *J. Geophys. Res.*, **107**, 4065, <https://doi.org/10.1029/2000JD000298>.
- Vallès-Casanova, I., S.-K. Lee, G. R. Foltz, and J. L. Pelegri, 2020: On the spatiotemporal diversity of Atlantic Niño and associated rainfall variability over West Africa and South America. *Geophys. Res. Lett.*, **47**, e2020GL087108, <https://doi.org/10.1029/2020GL087108>.
- van Sebille, E., M. O. Baringer, W. E. Johns, C. S. Meinen, L. M. Beal, M. F. de Jong, and H. M. Aken, 2011: Propagation pathways of classical Labrador Sea water from its source region to 26°N. *J. Geophys. Res.*, **116**, C12027, <https://doi.org/10.1029/2011JC007171>.
- Vaquer-Sunyer, R., and C. M. Duarte, 2008: Thresholds of hypoxia for marine biodiversity. *Proc. Natl. Acad. Sci. USA*, **105**, 15452–15457, <https://doi.org/10.1073/pnas.0803833105>.
- Volkov, D. L., S.-K. Lee, F. W. Landerer, and R. Lumpkin, 2017: Decade-long deep-ocean warming detected in the subtropical South Pacific. *Geophys. Res. Lett.*, **44**, 927–936, <https://doi.org/10.1002/2016GL071661>.
- , R. Domingues, C. S. Meinen, R. Garcia, M. Baringer, G. Goni, and R. H. Smith, 2020: Inferring Florida Current volume transport from satellite altimetry. *J. Geophys. Res. Oceans*, **125**, e2020JC016763, <https://doi.org/10.1029/2020JC016763>.
- , and Coauthors, 2022: Meridional overturning circulation and heat transport in the Atlantic Ocean [in "State of the Climate in 2021"]. *Bull. Amer. Meteor. Soc.*, **103** (8), S175–S178, <https://doi.org/10.1175/BAMS-D-22-0072.1>.
- von Schuckmann, K., J.-B. Sallée, D. Chambers, P.-Y. Le Traon, C. Cabanes, F. Gaillard, S. Speich, and M. Hamon, 2014: Consistency of the current global ocean observing systems from an Argo perspective. *Ocean Sci.*, **10**, 547–557, <https://doi.org/10.5194/os-10-547-2014>.
- Von Storch, H., and F. W. Zwiers, 1999: *Statistical Analysis in Climate Research*. Cambridge University Press, 484 pp.
- Walsh, K. J. E., and Coauthors, 2016: Tropical cyclones and climate change. *Wiley Interdiscip. Rev.: Climate Change*, **7**, 65–89, <https://doi.org/10.1002/wcc.371>.
- Wang, J., and B. Yang, 2017: Internal and external forcing of multidecadal Atlantic climate variability over the past 1,200 years. *Nat. Geosci.*, **10**, 512–517, <https://doi.org/10.1038/ngeo2962>.
- Wanninkhof, R., 2014: Relationship between wind speed and gas exchange over the ocean revisited. *Limnol. Oceanogr.: Methods*, **12**, 351–362, <https://doi.org/10.4319/lom.2014.12.351>.
- Werdell, P. J., and Coauthors, 2013: Generalized ocean color inversion model for retrieving marine inherent optical properties. *Appl. Opt.*, **52**, 2019–2037, <https://doi.org/10.1364/AO.52.002019>.
- Westberry, T. K., P. Schultz, M. J. Behrenfeld, J. P. Dunne, M. R. Hiscock, S. Maritorea, J. L. Sarmiento, and D. A. Siegel, 2016: Annual cycles of phytoplankton biomass in the subarctic Atlantic and Pacific Ocean. *Global Biogeochem. Cycles*, **30**, 175–190, <https://doi.org/10.1002/2015GB005276>.

- Wijffels, S., D. Roemmich, D. Monselesan, J. Church, and J. Gilson, 2016: Ocean temperatures chronicle the ongoing warming of Earth. *Nat. Climate Change*, **6**, 116–118, <https://doi.org/10.1038/nclimate2924>.
- Williams, N. L., and Coauthors, 2016: Empirical algorithms to estimate water column pH in the Southern Ocean. *Geophys. Res. Lett.*, **43**, 3415–3422, <https://doi.org/10.1002/2016GL068539>.
- Willis, J. K., 2010: Can in situ floats and satellite altimeters detect long-term changes in Atlantic Ocean overturning? *Geophys. Res. Lett.*, **37**, L06602, <https://doi.org/10.1029/2010GL042372>.
- , D. Roemmich, and B. Cornuelle, 2004: Interannual variability in upper ocean heat content, temperature, and thermocline expansion on global scales. *J. Geophys. Res.*, **109**, C12036, <https://doi.org/10.1029/2003JC002260>.
- Winkler, L. W., 1888: Die Bestimmung des im Wasser gelösten Sauerstoffes. *Ber. Dtsch. Chem. Ges.*, **21**, 2843–2854, <https://doi.org/10.1002/cber.188802102122>.
- Wolter, K., and M. S. Timlin, 1998: Measuring the strength of ENSO events: How does 1997/98 rank? *Weather*, **53**, 315–324, <https://doi.org/10.1002/j.1477-8696.1998.tb06408.x>.
- Wood, M., and Coauthors, 2021: Ocean forcing drives glacier retreat in Greenland. *Sci. Adv.*, **7**, eaba7282, <https://doi.org/10.1126/sciadv.aba7282>.
- Wüst, G., 1936: Oberflächensalzgehalt, Verdunstung und Niederschlag auf dem Weltmeere. *Länderkundliche Forschung: Festschrift zur Vollendung des sechzigsten Lebensjahres Norbert Krebs*, J. Engelhorn's Nachfahren, 347–359.
- Xie, P., and Coauthors, 2014: An in situ-satellite blended analysis of global sea surface salinity. *J. Geophys. Res. Oceans*, **119**, 6140–6160, <https://doi.org/10.1002/2014JC010046>.
- Yang, H., and Coauthors, 2020: Poleward shift of the major ocean gyres detected in a warming climate. *Geophys. Res. Lett.*, **47**, e2019GL085868, <https://doi.org/10.1029/2019GL085868>.
- Yu, L., 2011: A global relationship between the ocean water cycle and near-surface salinity. *J. Geophys. Res.*, **116**, C10025, <https://doi.org/10.1029/2010JC006937>.
- Zebiak, S. E., 1993: Air–sea interaction in the equatorial Atlantic region. *J. Climate*, **6**, 1567–1586, [https://doi.org/10.1175/1520-0442\(1993\)0062.0.CO;2](https://doi.org/10.1175/1520-0442(1993)0062.0.CO;2).
- Zhang, R., R. Sutton, G. Danabasoglu, Y.-O. Kwon, R. Marsh, S. G. Yeager, D. E. Amrhein, and C. M. Little, 2019: A review of the role of the Atlantic meridional overturning circulation in Atlantic multidecadal variability and associated climate impacts. *Rev. Geophys.*, **57**, 316–375, <https://doi.org/10.1029/2019RG000644>.
- Zhu, Y., and Coauthors, 2022: Perturbations in stratospheric aerosol evolution due to the water-rich plume of the 2022 Hunga-Tonga eruption. *Nat. Commun. Earth Environ.*, **3**, 248, <https://doi.org/10.1038/s43247-022-00580-w>.
- Zweng, M. M., and Coauthors, 2018: *Salinity*. Vol. 2, *World Ocean Atlas 2018*, NOAA Atlas NESDIS 82, 50 pp., https://data.nodc.noaa.gov/woa/WOA18/DOC/woa18_vol2.pdf.

STATE OF THE CLIMATE IN 2022

THE TROPICS

H. J. Diamond and C. J. Schreck, Eds.



Special Online Supplement to the *Bulletin of the American Meteorological Society* Vol. 104, No. 8, August, 2023

<https://doi.org/10.1175/BAMS-D-23-0078.1>

Corresponding author: Howard J. Diamond / howard.diamond@noaa.gov

©2023 American Meteorological Society

For information regarding reuse of this content and general copyright information, consult the [AMS Copyright Policy](#).

STATE OF THE CLIMATE IN 2022

The Tropics

Editors

Ellen Bartow-Gillies
Jessica Blunden
Tim Boyer

Chapter Editors

Peter Bissolli
Kyle R. Clem
Howard J. Diamond
Matthew L. Druckenmiller
Robert J. H. Dunn
Catherine Ganter
Nadine Gobron
Gregory C. Johnson
Rick Lumpkin
Ademe Mekonnen
John B. Miller
Twila A. Moon
Marilyn N. Raphael
Ahira Sánchez-Lugo
Carl J. Schreck III
Richard L. Thoman
Kate M. Willett
Zhiwei Zhu

Technical Editor

Lukas Noguchi

BAMS Special Editor for Climate

Michael A. Alexander

American Meteorological Society

Cover Credit:

Hurricane Ian as seen from NOAA's GOES-East satellite on 27 September 2022 at 0826 UTC in the Gulf of Mexico.

(Image credit: NOAA/NESDIS)

How to cite this document:

The Tropics is one chapter from the *State of the Climate in 2022* annual report and is available from <https://doi.org/10.1175/BAMS-D-23-0078.1>. Compiled by NOAA's National Centers for Environmental Information, *State of the Climate in 2022* is based on contributions from scientists from around the world. It provides a detailed update on global climate indicators, notable weather events, and other data collected by environmental monitoring stations and instruments located on land, water, ice, and in space. The full report is available from <https://doi.org/10.1175/2023BAMSStateoftheClimate.1>.

Citing the complete report:

Blunden, J., T. Boyer, and E. Bartow-Gillies, Eds., 2023: "State of the Climate in 2022". Bull. Amer. Meteor. Soc., 104 (8), S1–S501 <https://doi.org/10.1175/2023BAMSStateoftheClimate.1>.

Citing this chapter:

Diamond, H.J. and C. J. Schreck, Eds., 2023: The Tropics [in "State of the Climate in 2022"]. Bull. Amer. Meteor. Soc., 104 (8), S207–S270, <https://doi.org/10.1175/BAMS-D-23-0078.1>.

Citing a section (example):

Allgood, A. and C. J. Schreck, 2023: Tropical intraseasonal activity [in "State of the Climate in 2022"]. Bull. Amer. Meteor. Soc., 104 (8), S218–S220, <https://doi.org/10.1175/BAMS-D-23-0078.1>.

Editor and Author Affiliations (alphabetical by name)

Allgood, Adam, NOAA/NWS National Centers for Environmental Prediction Climate Prediction Center, College Park, Maryland

Becker, Emily J., University of Miami Rosenstiel School of Marine and Atmospheric Science, Miami, Florida

Blake, Eric S., NOAA/NWS National Hurricane Center, Miami, Florida

Bringas, Francis G., NOAA/OAR Atlantic Oceanographic and Meteorological Laboratory, Miami, Florida

Camargo, Suzana J., Lamont-Doherty Earth Observatory, Columbia University, Palisades, New York

Chen, Lin, Institute for Climate and Application Research (ICAR)/KLME/ILCEC/CIC-FEMD, Nanjing University of Information Science and Technology, Nanjing, China

Coelho, Caio A.S., Centro de Previsão do Tempo e Estudos Climáticos/National Institute for Space Research, Center for Weather Forecasts and Climate Studies, Cachoeira Paulista, Brazil

Diamond, Howard J., NOAA/OAR Air Resources Laboratory, College Park, Maryland

Fauchereau, Nicolas, National Institute of Water and Atmospheric Research, Ltd., Auckland, New Zealand

Fogarty, Chris, Canadian Hurricane Centre, Dartmouth, Canada

Goldenberg, Stanley B., NOAA/OAR Atlantic Oceanographic and Meteorological Laboratory, Miami, Florida

Goni, Gustavo, NOAA/OAR Atlantic Oceanographic and Meteorological Laboratory, Miami, Florida

Harnos, Daniel S., NOAA/NWS National Centers for Environmental Prediction Climate Prediction Center, College Park, Maryland

He, Qiong, Earth System Modeling Center, Nanjing University of Information Science and Technology, Nanjing, China

Hu, Zeng-Zhen, NOAA/NWS Climate Prediction Center, College Park, Maryland

Klotzbach, Philip J., Department of Atmospheric Science, Colorado State University, Fort Collins, Colorado

Knaff, John A., NOAA/NESDIS Center for Satellite Applications and Research, Fort Collins, Colorado

Kumar, Arun, NOAA/NWS National Centers for Environmental Prediction Climate Prediction Center, College Park, Maryland

L'Heureux, Michelle, NOAA/NWS National Centers for Environmental Prediction Climate Prediction Center, College Park, Maryland

Landsea, Chris W., NOAA/NWS National Hurricane Center, Miami, Florida

Lin, I-I., National Taiwan University, Taipei, Taiwan

Lorrey, Andrew M., National Institute of Water and Atmospheric Research, Ltd., Auckland, New Zealand

Luo, Jing-Jia, Institute for Climate and Application Research, Nanjing University of Information Science and Technology, Nanjing, China

Magee, Andrew D., Centre for Water, Climate and Land, School of Environmental and Life Sciences, University of Newcastle, Callaghan, Australia

Pasch, Richard J., NOAA/NWS National Hurricane Center, Miami, Florida

Pezza, Alexandre B., Greater Wellington Regional Council, Wellington, New Zealand

Rosencrans, Matthew, NOAA/NWS National Centers for Environmental Prediction Climate Prediction Center, College Park, Maryland

Rozkošný, Jozef, Slovak Hydrometeorological Institute, Bratislava, Slovakia

Schreck, Carl J., North Carolina State University, North Carolina Institute for Climate Studies, Cooperative Institute Satellite Earth System Studies, Asheville, North Carolina

Trewin, Blair C., Australian Bureau of Meteorology, Melbourne, Australia

Truchelut, Ryan E., WeatherTiger, Tallahassee, Florida

Wang, Bin, School of Ocean and Earth Science and Technology, Department of Meteorology, University of Hawaii; International Pacific Research Center, Honolulu, Hawaii

Wang, Hui, NOAA/NWS National Centers for Environmental Prediction Climate Prediction Center, College Park, Maryland

Wood, Kimberly M., Department of Geosciences, Mississippi State University, Mississippi State, Mississippi

Editorial and Production Team

Allen, Jessica, Graphics Support, Cooperative Institute for Satellite Earth System Studies, North Carolina State University, Asheville, North Carolina

Camper, Amy V., Graphics Support, Innovative Consulting and Management Services, LLC, NOAA/NESDIS National Centers for Environmental Information, Asheville, North Carolina

Haley, Bridgette O., Graphics Support, NOAA/NESDIS National Centers for Environmental Information, Asheville, North Carolina

Hammer, Gregory, Content Team Lead, Communications and Outreach, NOAA/NESDIS National Centers for Environmental Information, Asheville, North Carolina

Love-Brotak, S. Elizabeth, Lead Graphics Production, NOAA/NESDIS National Centers for Environmental Information, Asheville, North Carolina

Ohlmann, Laura, Technical Editor, Innovative Consulting and Management Services, LLC, NOAA/NESDIS National Centers for Environmental Information, Asheville, North Carolina

Noguchi, Lukas, Technical Editor, Innovative Consulting and Management Services, LLC, NOAA/NESDIS National Centers for Environmental Information, Asheville, North Carolina

Riddle, Deborah B., Graphics Support, NOAA/NESDIS National Centers for Environmental Information, Asheville, North Carolina

Veasey, Sara W., Visual Communications Team Lead, Communications and Outreach, NOAA/NESDIS National Centers for Environmental Information, Asheville, North Carolina

4. Table of Contents

List of authors and affiliations	S210
a. Overview	S212
b. ENSO and the tropical Pacific	S213
c. Tropical intraseasonal activity	S218
d. Intertropical convergence zones	S221
1. Pacific.....	S221
2. Atlantic.....	S222
e. Global monsoon summary	S224
f. Indian Ocean dipole	S228
g. Tropical cyclones	S230
1. Overview.....	S230
2. Atlantic Basin.....	S232
3. Eastern North Pacific and central North Pacific basins.....	S239
4. Western North Pacific basin.....	S243
5. North Indian Ocean.....	S248
6. South Indian Ocean.....	S250
7. Australian basin.....	S253
8. Southwest Pacific basin.....	S255
h. Tropical cyclone heat potential	S256
Sidebar 4.1: Hurricanes Fiona and Ian: A pair of impactful North Atlantic major hurricanes ...	S259
Sidebar 4.2: Tropical cyclone contributions during the 2022 North American monsoon.....	S262
Appendix 1: Chapter 4 – Acronyms	S263
Appendix 2: Chapter 4 – Supplemental Materials	S265
References	S266

Please refer to Chapter 8 (Relevant Datasets and Sources) for a list of all climate variables and datasets used in this chapter for analyses, along with their websites for more information and access to the data.

4. THE TROPICS

H. J. Diamond and C. J. Schreck, Eds.

a. Overview

—H. J. Diamond and C. J. Schreck

In 2022, the El Niño–Southern Oscillation (ENSO) continued a multi-year La Niña event spanning the period from 2020 to 2022. La Niña conditions started in July–September 2020 and have lasted nearly continuously for over two years, with a brief period of ENSO-neutral conditions between May–July and June–August 2021. In 2022, La Niña fluctuated between weak and moderate strength, with an Oceanic Niño Index (ONI) value of -1.1°C in March–May (peak ONI values between -1.0° and -1.4°C are defined to be moderate strength) and weakening to -0.8°C in June–August. Following the Northern Hemisphere summer, La Niña strengthened again with a peak intensity of -1.0°C in August–October and September–November 2022.

For the global tropics, the NOAA Merged Land Ocean Global Surface Temperature analysis (NOAA GlobalTemp; Vose et al. 2021) indicates that the combined average land and ocean surface temperature (measured 20°S – 20°N) was 0.01°C above the 1991–2020 average, tying with 2004 and 2006 as the 17th-warmest year for the tropics in the 173-year data record. The five warmest years in the tropics since 1850 have all occurred since 2015. Data from the Global Precipitation Climatology Project indicate a mean annual total precipitation value of 1413 mm across the 20°S – 20°N latitude band over land. This is 9 mm above the 1991–2020 average and ranks 20th wettest for the 1979–2022 period of record.

Globally, 85 named tropical cyclones (TCs; ≥ 34 kt; or ≥ 17 m s⁻¹) were observed during the 2022 Northern Hemisphere season (January–December 2022) and the 2021/22 Southern Hemisphere season (July–June 2021/22; see Table 4.2), as documented in the International Best Track Archive for Climate Stewardship version 4 (Knapp et al. 2010). Overall, this number was near the 1991–2020 global average of 87 TCs but below the 96 TCs reported during the 2021 season (Diamond and Schreck 2022) and the all-time record 104 named storms in 1992.

Of the 85 named storms, 40 reached tropical-cyclone strength and 16 reached major tropical-cyclone strength. Both of these counts were below their 1991–2020 averages. The accumulated cyclone energy (ACE; an integrated metric of the strength, frequency, and duration of tropical storms and hurricanes) was the lowest on record since reliable data began in 1981. No basin was more active than normal in terms of ACE. The North Atlantic, eastern North Pacific, and South Indian Ocean basins had near-normal activity. The other basins were all less active than normal, including the western North Pacific, which had its third consecutive season with below-normal activity. Three storms reached Category 5 on the Saffir-Simpson Hurricane Wind Scale during 2022. Two were from the western North Pacific: Super Typhoons Hinnamnor and Noru. The third was Hurricane Ian in the North Atlantic, which was upgraded to Category 5 during post-season analysis (Bucci et al. 2023). This was the fewest Category 5 storms globally since 2017.

The 14 named storms in the North Atlantic during 2022 were the fewest observed since 2015 when 11 named storms developed and well below the 21 named storms in 2021. Eight hurricanes developed in 2022, one more than occurred in 2021 and near the 1991–2020 average of seven. Two major hurricanes occurred, which was slightly below the 1991–2020 average of three and half as many as occurred in 2021. The 2022 North Atlantic hurricane season was classified by NOAA’s National Hurricane Center as a near-normal season based on ACE, ending the streak

of six consecutive above-normal seasons (2016–21). Even during near-normal seasons, a single hurricane can bring devastation to an area. Hurricane Ian caused over 100 deaths and more than \$100 billion (U.S. dollars) in damage, making it the third-costliest hurricane in U.S. history. Hurricane Fiona caused extreme flooding in Puerto Rico before making landfall in Canada as the country’s strongest storm on record in terms of pressure. Both storms are featured in Sidebar 4.1 as well as in section 4g2.

While we do not normally report on volcanic eruptions, given the climatic impact that a large volcanic eruption can have, we would be remiss in not mentioning the eruption of the Hunga Tonga-Hunga Ha’apai (HTHH) in the southwest island nation of Tonga on 15 January 2022. HTHH ranked a 5.7 on the Volcanic Explosivity Index, alongside other history makers like Vesuvius in 79 CE and Mount St. Helens in 1980 (Besl 2023). The injection of water into the atmosphere was unprecedented in both magnitude (far exceeding any previous values in the 17-year *Aura* Microwave Limb Sounder record) and altitude (penetrating into the mesosphere). Millán et al (2022) estimates that the mass of water injected into the stratosphere to be $146 \pm 5 \text{ Tg}$, or ~10% of the stratospheric burden.

It may take several years for the water plume to dissipate, and it is thought that this eruption could impact climate, not through surface cooling due to sulfate aerosols, but rather through possible surface warming due to the radiative forcing from the excess stratospheric water vapor. Similar to the climate effects (albeit cooling) of Mount Pinatubo in the Philippines in 1991, but unlike other eruptions its size, HTHH had a relatively low sulfur dioxide content. While it has been theorized that it may have added only 0.004°C of global cooling in 2022 (Zuo et al. 2022), it may take a few more years to fully determine if this eruption had any possible long-term climate effects.

b. ENSO and the tropical Pacific

—Z.-Z. Hu, M. L’Heureux, A. Kumar, and E. Becker

The El Niño–Southern Oscillation (ENSO) is an ocean and atmosphere-coupled climate phenomenon that occurs across the tropical Pacific Ocean. Its warm and cold phases are called El Niño and La Niña, respectively. For historical purposes, NOAA’s Climate Prediction Center classifies and assesses the strength and duration of El Niño and La Niña events using the Oceanic Niño Index (ONI; shown for mid-2020 through 2022 in Fig. 4.1). The ONI is the three-month (seasonal) running average of sea-surface temperature (SST) anomalies in the Niño-3.4 region (5°S – 5°N , 170°W – 120°W), currently calculated as the departure from the 1991–2020 base period mean¹. El Niño is classified when the ONI is at or greater than $+0.5^\circ\text{C}$ for at least five consecutive, overlapping seasons, while La Niña is classified when the ONI is at or less than -0.5°C for at least five consecutive, overlapping seasons.

The time series of the ONI (Fig. 4.1) shows a multi-year La Niña event spanning 2020–22 (Fang et al. 2023). La Niña conditions started in July–September

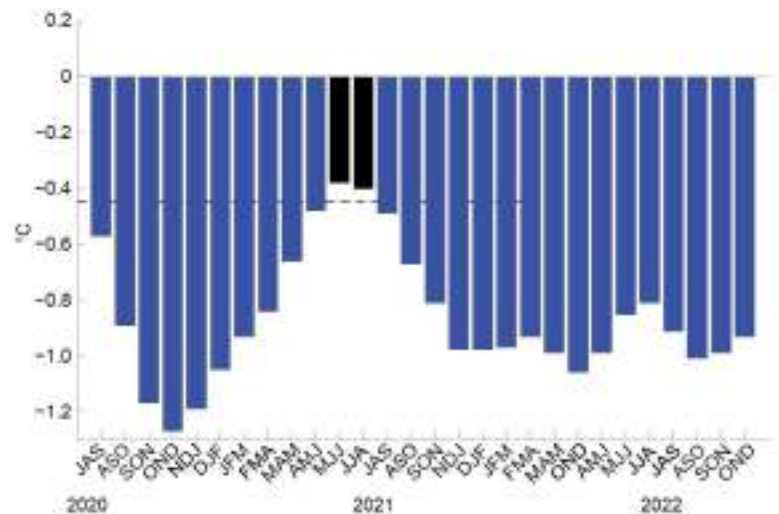


Fig. 4.1. Time series of the Oceanic Niño Index (ONI, °C) from mid-2020 through 2022. Overlapping three-month seasons are labeled on the x-axis, with initials indicating the first letter of each month in the season. Blue bars indicate negative values that are less than -0.5°C . ONI values are derived from the ERSSTv5 dataset and are based on departures from the 1991–2020 period monthly means (Huang et al. 2017).

¹ The ONI is an index measuring ENSO, and to highlight its seasonal-to-interannual component, the base period is updated every five years with a rolling 30-year climatology. SSTs in the Niño-3.4 region have multi-decadal and longer trends going back to 1950 or earlier, and the rolling climatology reduces the influence of trend on the state of ENSO.

2020 and have lasted nearly continuously for over two years, with a brief period of ENSO-neutral conditions between May–July and June–August (JJA) 2021 (Fig. 4.1). In 2022, La Niña fluctuated between moderate and weak strength with an ONI value of -1.1°C in March–May (MAM; peak ONI value between -1.0° and -1.4°C is defined to be moderate strength) and weakening to -0.8°C in June–August. Following the Northern Hemisphere summer, La Niña strengthened again with a peak intensity of -1.0°C in August–October and September–November (SON). Sidebar 3.1 in Chapter 3 describes the triple La Niña event.

(i) Oceanic conditions

Figure 4.2 displays the three-monthly mean SST (left column) and SST anomalies (right column) during December–February (DJF) 2021/22 through September–November (SON) 2022. Consistent with La Niña, below-average SSTs persisted across most of the equatorial Pacific Ocean during the year. During DJF (Fig. 4.2b), the strongest SST anomalies on the equator exceeded -2.0°C in a small portion of the eastern equatorial Pacific (between 120°E and 80°W), implying a strengthening of the cold tongue (Fig. 4.2a). During MAM, the negative SST anomalies strengthened in the central equatorial Pacific and expanded westward (Fig. 4.2d). Below-average SSTs were weakest across the equatorial Pacific in JJA, but remained in excess of -1.0°C in small regions of the central and far eastern Pacific (Fig. 4.2f). The western Pacific warm pool remained contracted to the west during most of the year, with the 30°C isotherm nearly vanishing during JJA (Fig. 4.2e). During SON, below-average SSTs re-strengthened in the central and eastern equatorial Pacific (Fig. 4.2h). A horseshoe-like pattern of above-average SSTs stretched from the western tropical Pacific to the extratropical North and South Pacific Oceans during all seasons.

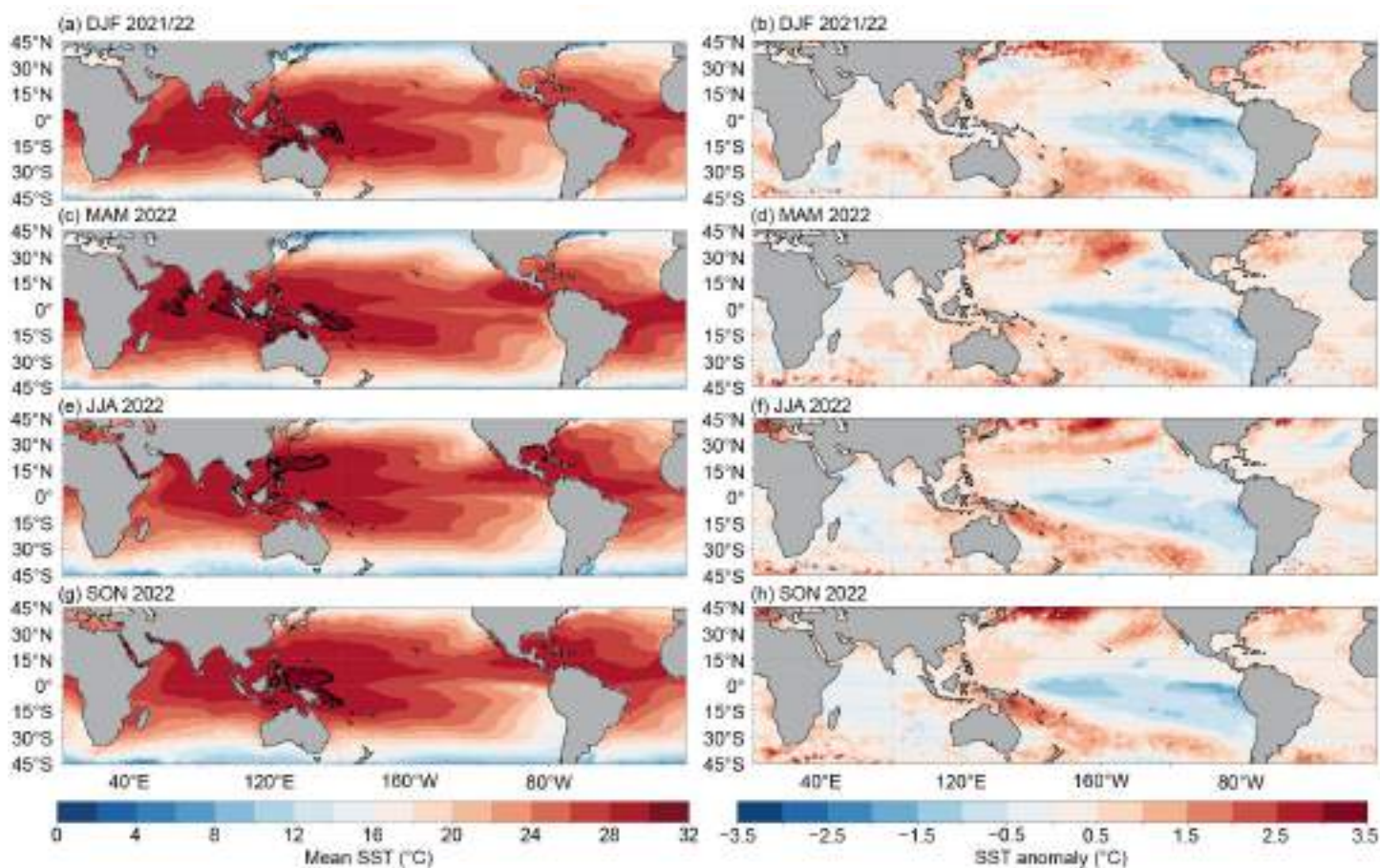


Fig 4.2. Mean sea-surface temperature (SST; left) and SST anomaly (right) for (a),(b) DJF 2021/22, (c),(d) MAM 2022, (e),(f) JJA 2022, and (g),(h) SON 2022. Units are in $^{\circ}\text{C}$. The bold contour for SST is located at 30°C . Anomalies are departures from the 1991–2020 seasonal adjusted Olv2.1 climatology (Huang et al. 2020).

Consistent with the evolution of SST anomalies and La Niña, the subsurface temperature anomalies were a dipole-like pattern centered along the thermocline in the western and eastern Pacific Ocean (Kumar and Hu 2014). The positive temperature anomalies were centered in the western and central equatorial Pacific, while negative temperature anomalies were strongest in the eastern Pacific throughout the year. These anomalies reflect a steeper-than-average thermocline slope (solid line) with shallow anomalies in the eastern Pacific and deep anomalies in the western Pacific (Fig. 4.3). Negative subsurface temperature anomalies also persisted within the mixed layer near the date line. The slope of the thermocline was steepest in SON, which was also when the anomalous subsurface temperature gradient was strongest (Fig. 4.3d). These subsurface features were relatively weaker in MAM and JJA (Figs. 4.3b,c).

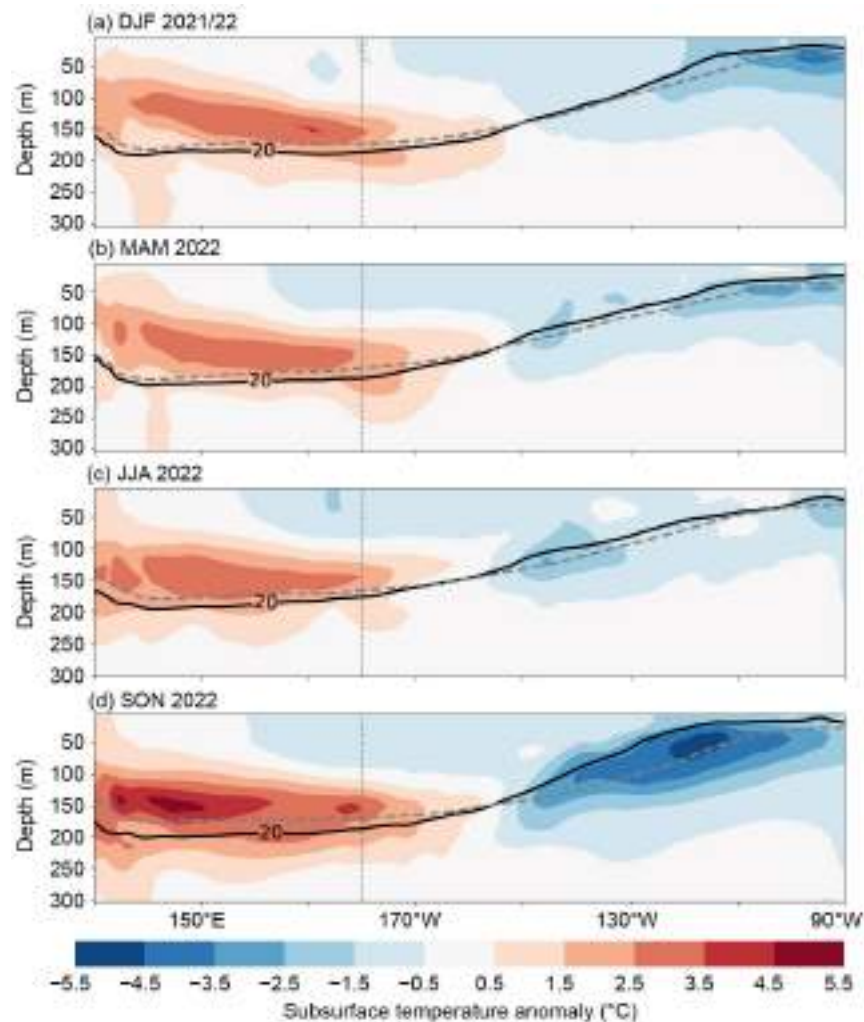


Fig 4.3. Equatorial depth–longitude section of Pacific Ocean temperature anomalies (°C) averaged between 5°S and 5°N during (a) DJF 2021/22, (b) MAM 2022, (c) JJA 2022, and (d) SON 2022. The 20°C isotherm (thick solid line) approximates the center of the oceanic thermocline. The gray dashed line shows the climatology of the 20°C isotherm based on 1991–2020. Anomalies are departures from the 1991–2020 period monthly means. Data are from GODAS; Behringer 2007.

(ii) Atmospheric circulation

In 2022, the large-scale tropical atmospheric circulation anomalies were also consistent with La Niña and persisted through the year. Figure 4.4 shows outgoing longwave radiation (OLR) anomalies, which is a proxy for tropical convection and rainfall. Typically, during La Niña, convection is suppressed (positive OLR, brown shading) over the western and central tropical Pacific and enhanced (negative OLR, green shading) over the Maritime Continent. Relative to the other seasons in the year, the dipole-like pattern in precipitation anomalies was shifted eastward

during DJF 2021/22, with suppressed convection located just to the east of the date line and enhanced convection over the western tropical Pacific (Fig. 4.4a). The anomalies then shifted westward after DJF with suppressed convection expanding into the western tropical Pacific and enhanced convection shifting over western Indonesia (Fig. 4.4b). During MAM 2022, convection over the date line was further suppressed, which occurred at the same time the ONI value reached its peak. Corresponding to the seasonal cycle, the region of enhanced precipitation over the Maritime Continent extended farther northwards toward the Philippines during DJF 2021/22 and MAM 2022. Following boreal spring, enhanced rainfall anomalies became mainly confined to the equator and south of the equator during JJA and SON, with anomalies also increasing in intensity (Figs. 4.4c,d).

Similar to convection, the lower- and upper-level wind anomalies were reflective of La Niña throughout the year. Stretching across most of the equatorial Pacific Ocean (Fig. 4.5), the tropical low-level 850-hPa easterly trade winds were enhanced. The low-level easterly wind anomalies were strongest over the eastern Pacific during DJF 2021/22 (Fig. 4.5a). During the other seasons (MAM through SON), the low-level easterly wind anomalies strengthened and expanded over the western tropical Pacific Ocean (Figs. 4.5b–d). The upper-level 200-hPa westerly wind anomalies prevailed throughout the year over most of the equatorial Pacific Ocean (Fig. 4.6). Like the low-level winds, upper-level westerly wind anomalies also expanded farther to the west after DJF (Figs. 4.6b–d). During all seasons, an anomalous cyclonic circulation couplet straddled the equator in both hemispheres (Fig. 4.6). At times, two pairs of cyclonic anomalies were evident, such as in MAM 2022, with centers around 160°E and 120°W, respectively. Overall, the lower- and

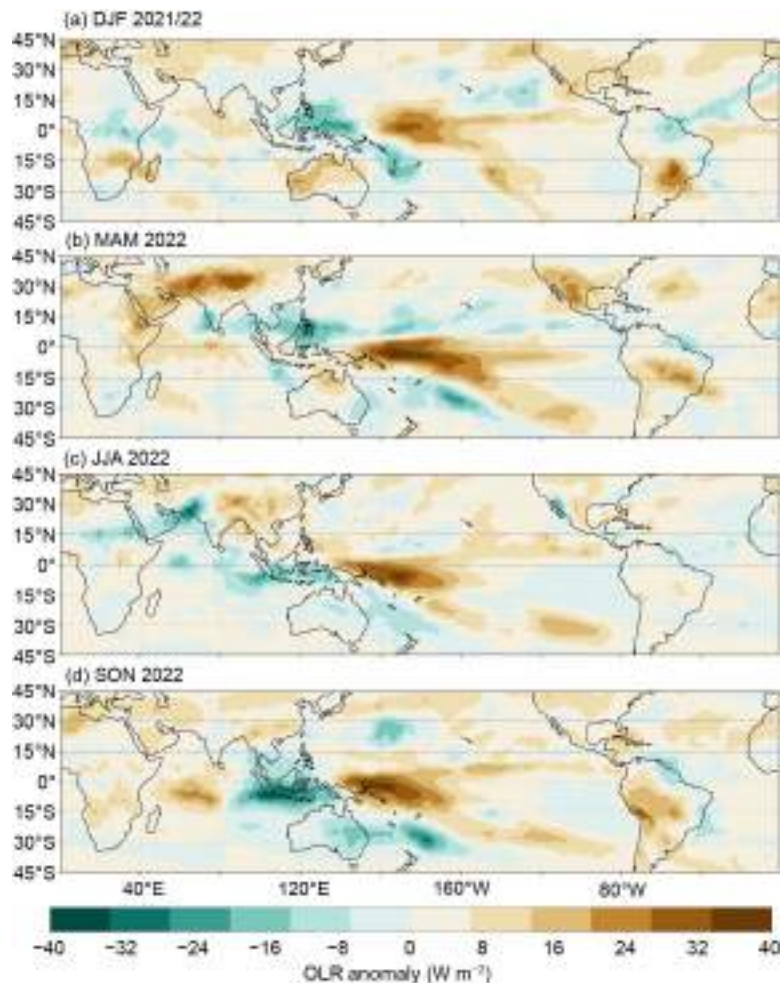


Fig. 4.4. Outgoing longwave radiation (OLR) anomalies ($W m^{-2}$) during (a) DJF 2021/22, (b) MAM 2022, (c) JJA 2022, and (d) SON 2022. Anomalies are departures from the 1991–2020 period monthly means. Data are from Liebmann and Smith (1996).

upper-level wind anomalies (Figs. 4.5, 4.6) and rainfall anomalies across the tropical Pacific (Fig. 4.4) were indicative of an enhanced equatorial Walker circulation over the tropical Pacific. Collectively, these oceanic and atmospheric anomalies reflected the well-known, basin-wide atmospheric and oceanic coupling of the La Niña phenomenon (Bjerknes 1969).

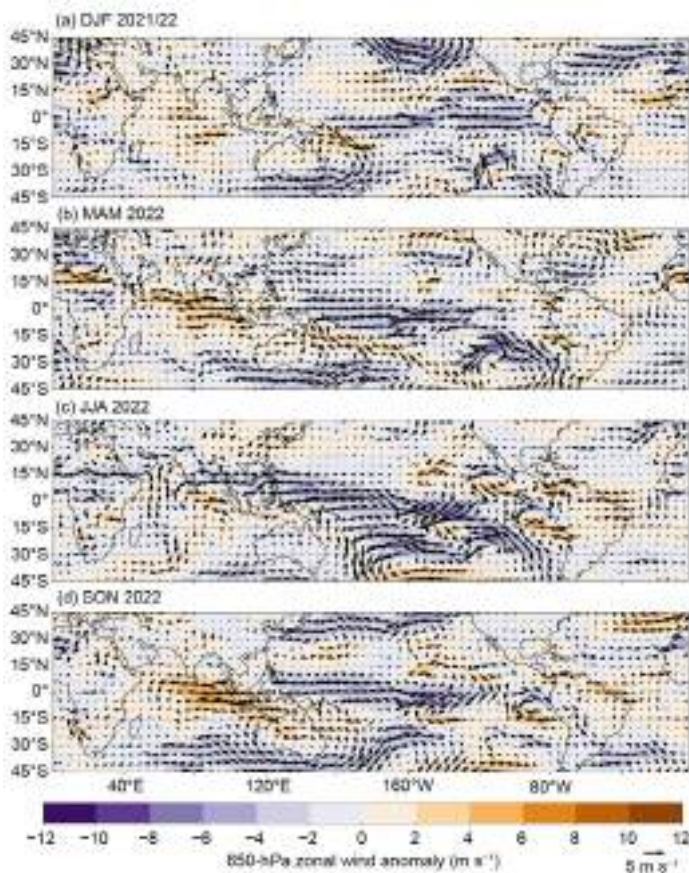


Fig. 4.5. Anomalous 850-hPa wind vectors and zonal wind speed (shading) during (a) DJF 2021/22, (b) MAM 2022, (c) JJA 2022, and (d) SON 2022. The reference wind vector is located at the bottom right. Anomalies are departures from the 1991–2020 period monthly means. Data are from the NCEP/NCAR reanalysis (Kalnay et al. 1996).

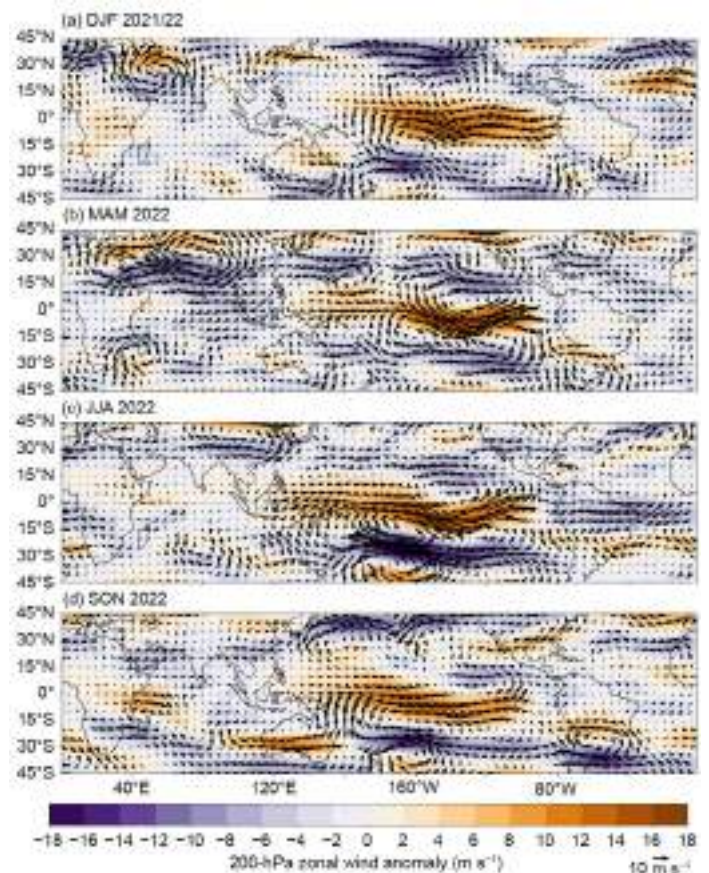


Fig. 4.6. Anomalous 200-hPa wind vectors and zonal wind speed (shading) during (a) DJF 2021/22, (b) MAM 2022, (c) JJA 2022, and (d) SON 2022. The reference wind vector is located at the bottom right. Anomalies are departures from the 1991–2020 period monthly means. Data are from the NCEP/NCAR reanalysis (Kalnay et al. 1996).

(iii) Global precipitation

ENSO-driven teleconnections can affect extratropical precipitation anomalies globally (Bjerknes 1969; Ropelewski and Halpert 1989). During JJA 2022, impacts were weaker and more confined to the immediate tropics and to the Southern Hemisphere, as is typical for this season (Appendix Fig. A4.1a). Enhanced precipitation was evident across some stations in Indonesia and eastern Australia. Drier-than-normal conditions were found over the southernmost parts of South America, while wetter conditions were observed over much of northern South America. During SON 2022, wetter-than-normal conditions remained over Indonesia and spread to northern Australia (Appendix Fig. A4.1b). Over southeastern China, drier-than-normal conditions were evident. Drier-than-normal conditions also remained over southern Brazil and Uruguay, while increased precipitation expanded to eastern Brazil and continued to influence parts of northern South America. Enhanced rainfall was present over central India, along with below-average rainfall over southern India and Sri Lanka, as is typical for La Niña.

c. Tropical intraseasonal activity

—A. Allgood and C. J. Schreck

Organized tropical intraseasonal activity is modulated by several different modes of coherent atmospheric variability, most notably the Madden-Julian Oscillation (MJO; Madden and Julian 1971, 1972, 1994; Zhang 2005). The MJO is characterized by eastward-propagating envelopes of large-scale anomalous enhanced and suppressed convection that typically circumnavigate the globe in a 30–60-day period. MJO-related convective anomalies are similar in spatial extent to those generated by the atmospheric response to the El Niño–Southern Oscillation (ENSO), but the latter signal remains largely stationary and lasts for at least several months. Other impactful modes of variability include convectively coupled atmospheric waves, such as Kelvin waves, which exhibit a faster phase speed than the MJO, and westward-propagating equatorial Rossby waves (Wheeler and Kiladis 1999; Kiladis et al. 2009). These waves are typically narrower zonally than the MJO and may not couple as well to the broader convective regime. Therefore, the MJO typically generates the strongest extratropical responses (Kiladis and Weickmann 1992; Riddle et al. 2012; Baxter et al. 2014) and plays a role in modulating both monsoonal activity (Krishnamurti and Subrahmanyam 1982; Lau and Waliser 2012) and tropical cyclone activity (Mo 2000; Frank and Roundy 2006; Camargo et al. 2009; Schreck et al. 2012; Diamond and Renwick 2015).

The MJO can exhibit sustained periods of robust activity as well as periods of weak or indiscernible activity (Matthews 2008). Active periods can be diagnosed through time–longitude analyses of various atmospheric fields, including anomalous outgoing longwave radiation (OLR; Fig. 4.7a), anomalous 200-hPa velocity potential (Fig. 4.7b), and anomalous zonal winds at 200-hPa and 850-hPa (Fig. 4.8a). OLR can be used as a proxy for convective anomalies due to the

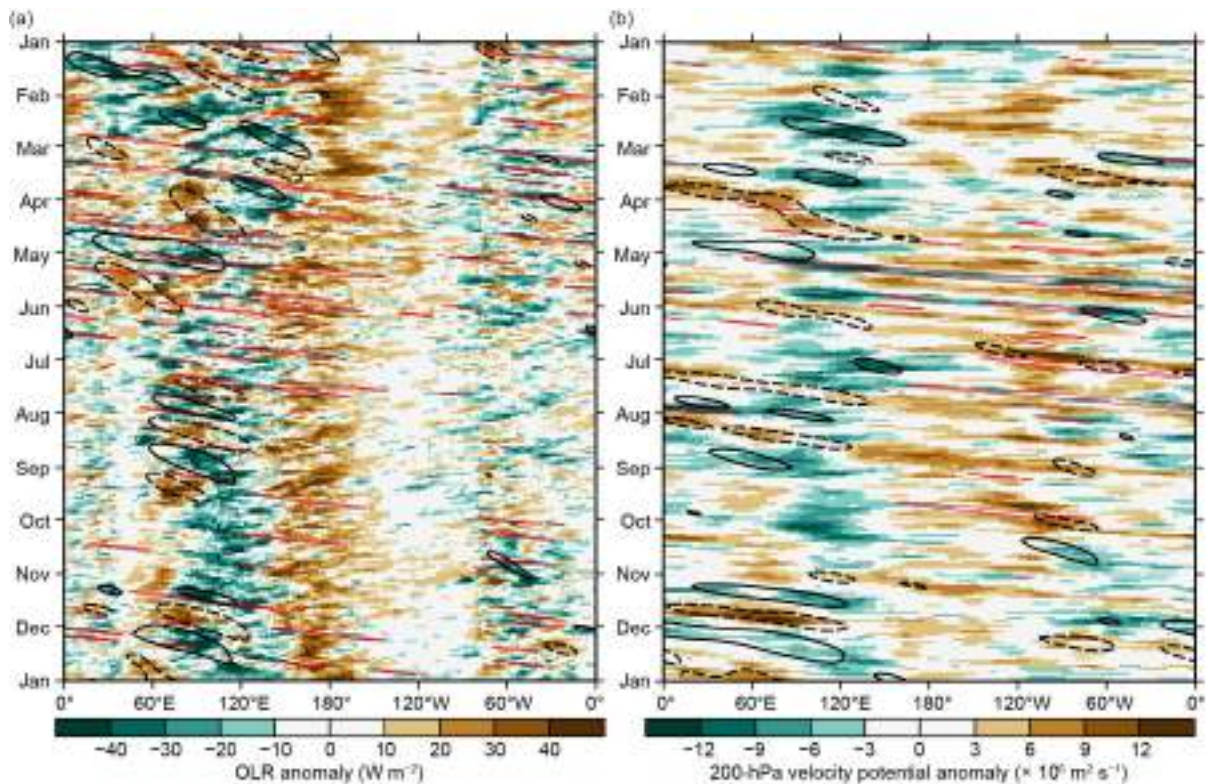


Fig. 4.7. (a) Time–longitude section with (a) outgoing longwave radiation (OLR) anomalies (W m^{-2} ; Schreck et al. 2018) and (b) 200-hPa velocity potential anomalies ($\times 10^6 \text{ m}^2 \text{ s}^{-1}$) from the CFSR (Saha et al. 2014). Both variables are averaged over 10°S – 10°N . Time increases downward on this graph, beginning with Jan 2022 at the top and ending with Jan 2023 at the bottom. Negative anomalies indicate enhanced convection, and positive anomalies indicate suppressed convection. Contours identify anomalies filtered for the Madden-Julian Oscillation (MJO; black) and atmospheric Kelvin waves (red). Contours are drawn at $\pm 12 \text{ W m}^{-2}$ and $\pm 4 \times 10^6 \text{ m}^2 \text{ s}^{-1}$ with the enhanced (suppressed) convective phase of these phenomena indicated by solid (dashed, MJO only) contours. Anomalies are departures from the 1991–2020 base period daily means.

strong connection between OLR and high cloud cover typically generated by thunderstorm activity in the tropics. MJO activity appears on Figs. 4.7 and 4.8a as coherent opposite-signed anomaly couplets that propagate eastward with time. Filtering these analyses for the wavelengths and periods associated with the MJO diagnoses its activity. Another diagnostic tool frequently used to identify MJO activity is the Wheeler-Hendon (2004) Real-time Multivariate MJO (RMM) index, which identifies the MJO from a combined signal in OLR and zonal winds at 850 hPa and 200 hPa. In RMM plots, robust atmospheric anomalies on a spatial scale resembling the MJO appear as a signal outside of the unit circle, and eastward propagation is represented by counterclockwise looping of the index about the origin (Fig. 4.9).

La Niña conditions persisted throughout 2022, which had a weakening effect on MJO activity due to destructive interference between the MJO-enhanced convective envelope and negative sea-surface temperature anomalies and enhanced trade winds across the equatorial Pacific, which in turn served to suppress widespread organized convection (Hendon et al. 1999; Zhang and Gottschalck 2002; Zhang 2005). Therefore, it is typical when La Niña conditions are present for MJO events that initiate over the Indian Ocean to strengthen as the enhanced convection reaches the Maritime Continent but weaken as they propagate to the Pacific. MJO activity was incoherent at the start of the year, although an active MJO signal that crossed the Pacific in late 2022 helped initiate a downwelling oceanic Kelvin wave that brought warm water from the West Pacific Warm Pool eastward across much of the basin (Fig. 4.8b).

The first period of somewhat sustained MJO activity during 2022 began in February and lasted through April, with most of the events initiating over the Indian Ocean and weakening as the enhanced convective envelopes reached the West Pacific. During May and June, eastward propagating signals continued to circumnavigate the globe, but the phase speeds of these signals were more consistent with unusually strong and convectively-coupled atmospheric Kelvin waves (Fig. 4.7, red contours). Despite the poor depiction on the MJO filtering of the time–longitude

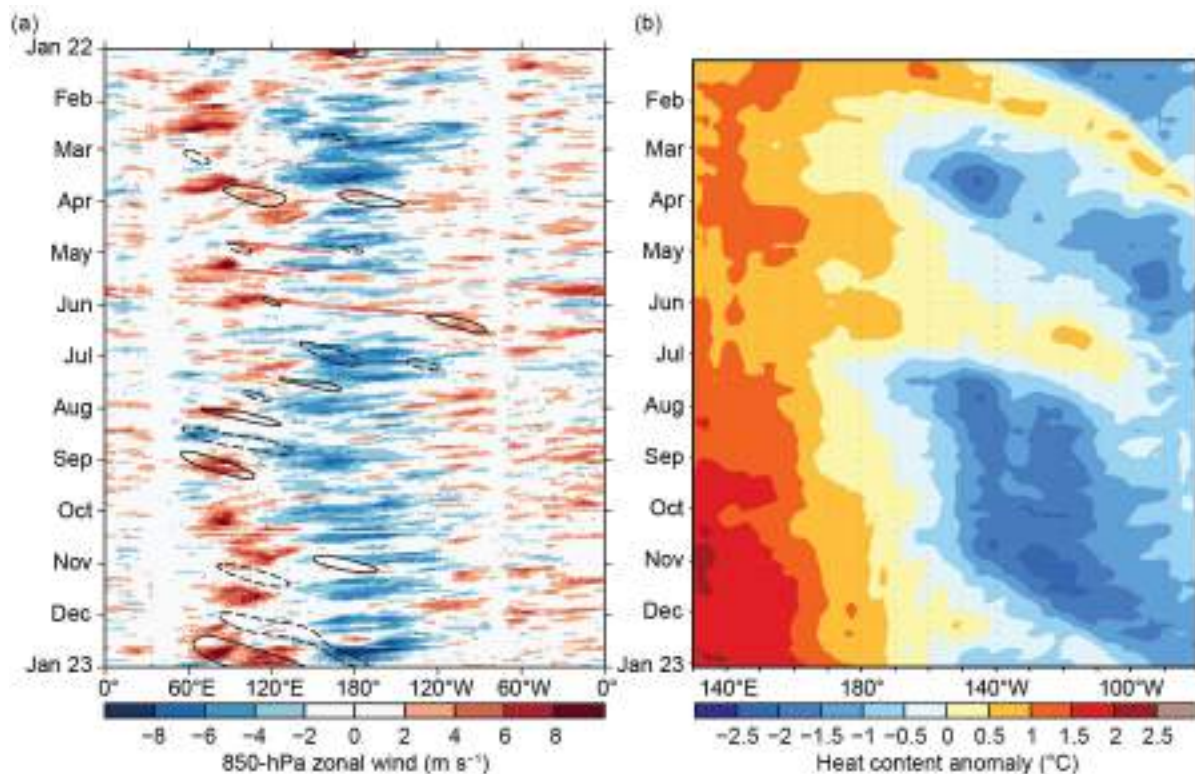


Fig. 4.8. (a) Time–longitude section for 2022 of anomalous 850-hPa zonal wind (m s^{-1}) averaged between 10°S and 10°N . Contours identify anomalies filtered for the Madden-Julian Oscillation (MJO; black) and atmospheric Kelvin waves (red). (b) Time–longitude section for 2022 of the anomalous equatorial Pacific Ocean heat content, calculated as the mean temperature anomaly ($^{\circ}\text{C}$) between 0-m and 300-m depth. Yellow/red (blue) shading indicates above- (below-) average heat content. Relative warming (dashed lines) and cooling (dotted lines) due to downwelling and upwelling equatorial oceanic Kelvin waves are indicated. Anomalies are departures from the 1991–2020 base period pentad means. Data in (b) are derived from GODAS (Behringer et al. 1998).

diagrams due to the faster phase speeds, this strong Kelvin wave activity projected strongly on the RMM-index diagrams (Fig. 4.9). Additionally, two subsequent Kelvin wave passages over the Pacific succeeded in generating brief westerly wind bursts near the equator (Fig. 4.8a), which helped generate a second downwelling oceanic Kelvin wave that propagated across the Pacific basin during June and July (Fig. 4.8b). The MJO produced an even stronger trade-wind surge in late June and July, which brought back significant upwelling and cooler water across the central and eastern Pacific. The MJO's enhanced convective phases failed to overcome the strong boreal summer La Niña conditions during July and August.

The MJO became weaker during September and October as the atmospheric response to the ongoing La Niña dominated the global tropical convective pattern. Coherent eastward propagating intraseasonal activity resumed in November and lasted through the end of 2022. During November, this activity was again on the fast side of the 30–60-day MJO circumnavigational period, but the signal began to slow down during December. Towards the end of 2022, the MJO reached the Pacific, though convection associated with the intraseasonal signal was observed primarily off of the equator (not shown) due to destructive interference from the ENSO base state.

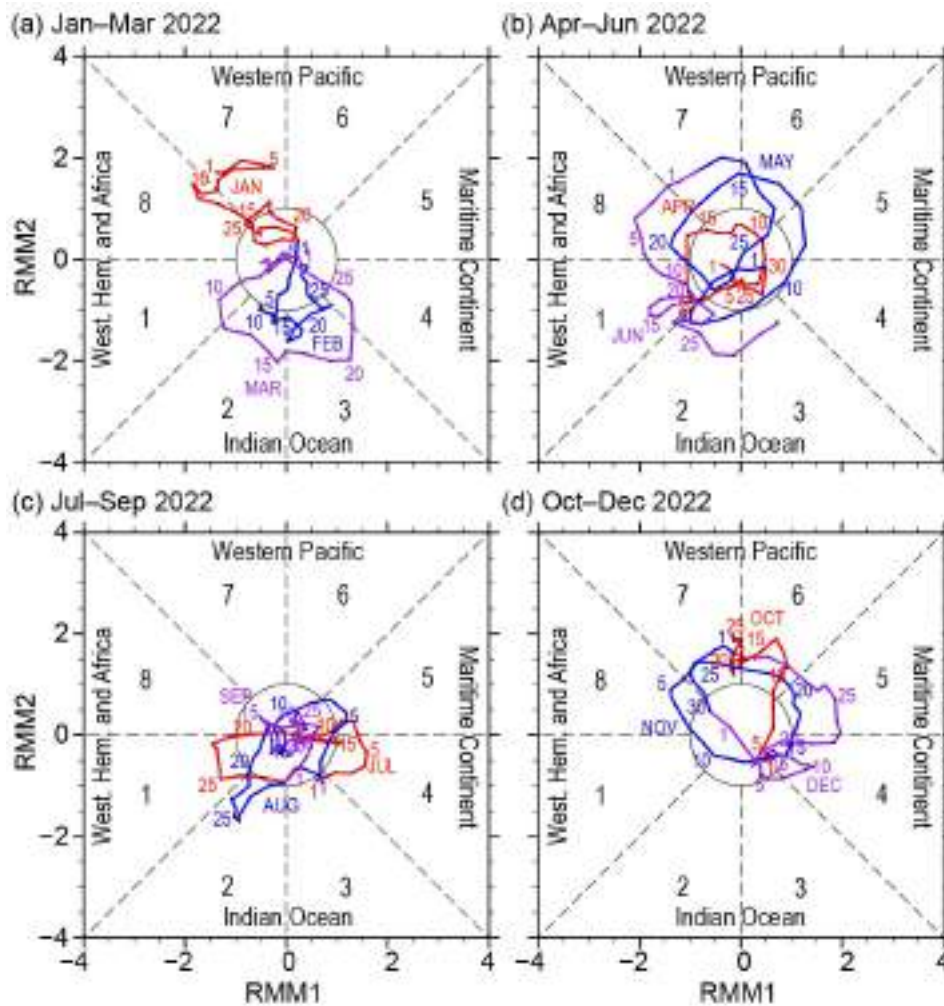


Fig. 4.9. Wheeler and Hendon (2004) Real-time Multivariate Madden-Julian Oscillation (RMM) index for (a) Jan–Mar, (b) Apr–Jun, (c) Jul–Sep, and (d) Oct–Dec 2022. Each point represents the Madden-Julian Oscillation (MJO) amplitude and location on a given day, and the connecting lines illustrate its propagation. Amplitude is indicated by distance from the origin, with points inside the circle representing weak or no MJO. The eight phases around the origin identify the region experiencing enhanced convection, and counter-clockwise movement is consistent with eastward propagation.

d. Intertropical convergence zones

1. PACIFIC

—N. Fauchereau

Tropical Pacific rainfall patterns are dominated by two convergence zones: the Intertropical Convergence Zone (ITCZ; Schneider et al. 2014) north of the equator and the South Pacific Convergence Zone (SPCZ; Vincent 1994) in the southwest Pacific. The position and intensity of these convergence zones throughout the year are highly sensitive to sea-surface temperature anomalies and, therefore, are also highly sensitive to the El Niño–Southern Oscillation (ENSO; Trenberth 1984).

As a whole, the tropical Pacific exhibited precipitation anomalies throughout 2022 that were consistent with the ongoing La Niña conditions. Figure 4.10 summarizes the behavior for both convergence zones during 2022 using rainfall from the Multi-Source Weighted-Ensemble Precipitation (MSWEP) 2.8.0 dataset (Beck et al. 2019). Rainfall transects over 30°S–20°N are presented for each quarter of the year, averaged across successive 30-degree longitude bands, starting in the western Pacific at 150°E–180°. The 2022 seasonal variation is compared against the longer-term 1991–2020 climatology. The transects for January–March (Fig. 4.10a) for the western and central Pacific (150°E–150°W, especially 150°E to the date line) show that the SPCZ was shifted south and west of its climatological position, while rainfall rates within the ITCZ were reduced compared to climatology. This is a signature consistent with typical anomalies recorded in the Southern Hemisphere summer during La Niña.

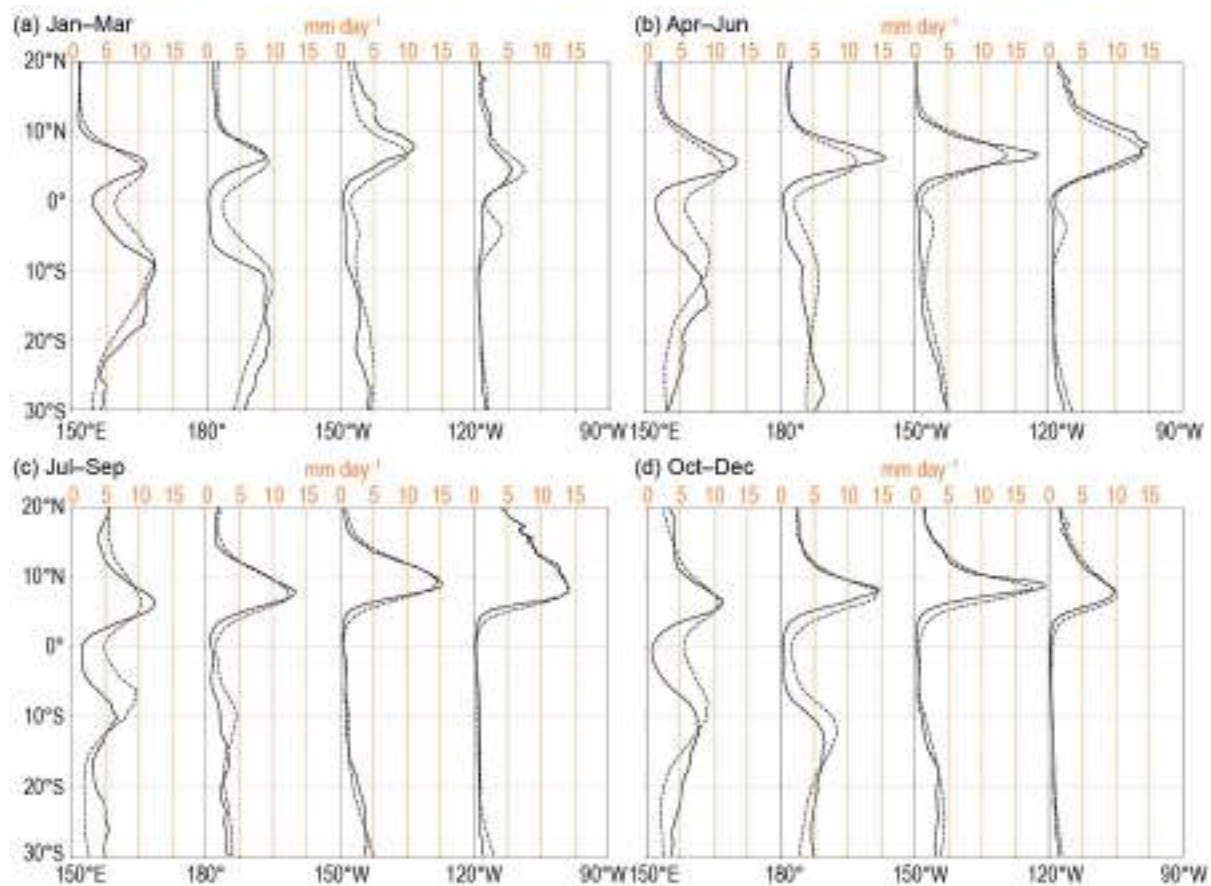


Fig. 4.10. Rainfall rate (mm day^{-1}) for (a) Jan–Mar, (b) Apr–Jun, (c) Jul–Sep, and (d) Oct–Dec 2022. The separate panels for each quarter show the rainfall cross-section between 30°S and 20°N (solid line) and the 1991–2020 climatology (dotted line), separately for four 30° sectors from 150°E–180° to 120°W–90°W. (Source: MSWEP v2.8.0.)

The precipitation anomaly patterns that persisted throughout 2022 in the tropical Pacific are shown in Fig. 4.11, which presents the precipitation anomalies for the period April–June with respect to the 1991–2020 climatological period. As was the case for most of the year, the tropical Pacific rainfall anomalies reflected a northward shift in the ITCZ and a southwestward shift in the SPCZ (Fig. 4.10b). Both of these are typical for La Niña and are reflected by anomalously dry conditions near the equatorial Pacific, with wetter-than-normal conditions to the north and the southwest.

Figure 4.12 shows a more detailed comparison of the western Pacific (150°E–180°) rainfall transect during January–March 2022, corresponding to well-established La Niña conditions, relative to all other years in this dataset. During this three-month period, the recorded rainfall, averaged over all longitudes (black line), closely corresponds to the rainfall rates recorded on average for all La Niña years (thick blue line).

In summary, precipitation anomaly patterns throughout 2022 as a whole indicated that the ITCZ was shifted north of its climatological position, while the SPCZ was shifted southwest of its climatological position. These variations in intensity and position of the Pacific convergence zones were consistent with typical anomalies recorded over the historical period during La Niña events.

2. ATLANTIC

—A. B. Pezza and C. A. S. Coelho

The Atlantic ITCZ is a well-organized convective band that oscillates between approximately 5°N–12°N during July–November and 5°S–5°N during January–May (Waliser and Gautier 1993; Nobre and Shukla 1996). Equatorial atmospheric Kelvin waves can modulate ITCZ intraseasonal variability (Guo et al. 2014). ENSO and the Southern Annular Mode (SAM) can also influence the ITCZ on interannual time scales (Münnich and Neelin 2005). The SAM, also known as the Antarctic Oscillation, describes the north–south movement of the westerly wind belt that circles Antarctica. A positive SAM event reflects a contraction of the westerly wind belt away from the equator, with stronger subtropical ridges and less precipitation in the midlatitudes (Ding et al. 2012; Liu et al. 2021; Moreno et al. 2018).

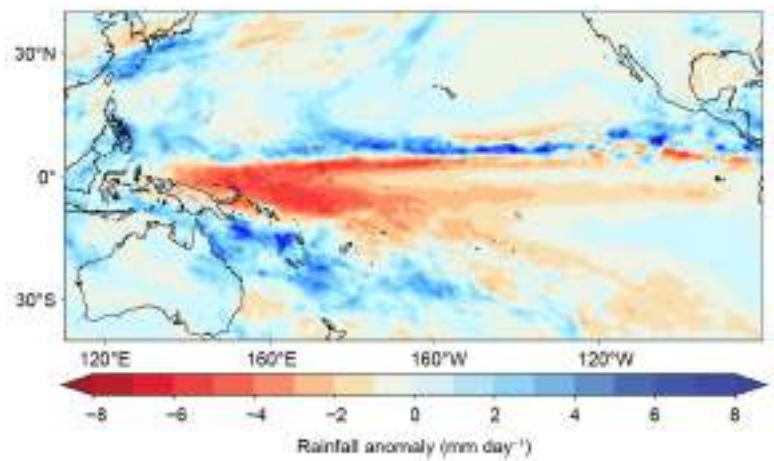


Fig. 4.11. Rainfall anomalies (mm day^{-1}) for Apr–Jun 2022. The anomalies are calculated with respect to the 1991–2020 climatology. (Source: MSWEP v2.8.0.)

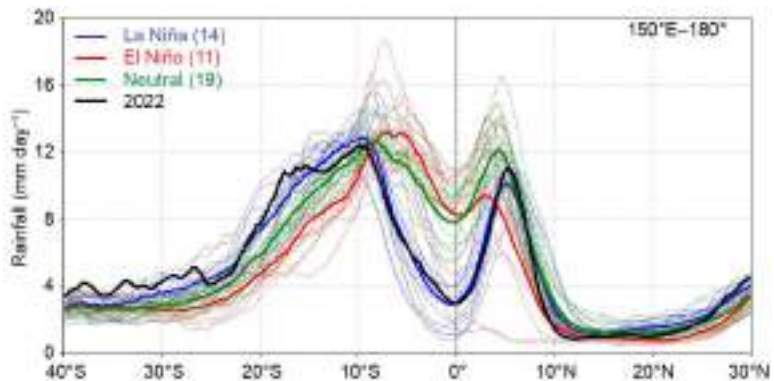


Fig. 4.12. Rainfall rate (mm day^{-1}) for the Jan–Mar 2022 quarter, for each year from 1979 to 2022, averaged over the longitude sector 150°W–180°E. The cross-sections are color-coded according to NOAA’s Oceanic Niño Index (with a threshold of $\pm 0.5^\circ\text{C}$), except 2022 which is shown in black. Dotted lines are individual years, and solid lines are the average overall years in each ENSO phase. The inset legend indicates how many years went into each composite. (Source: MSWEP v2.8.0.)

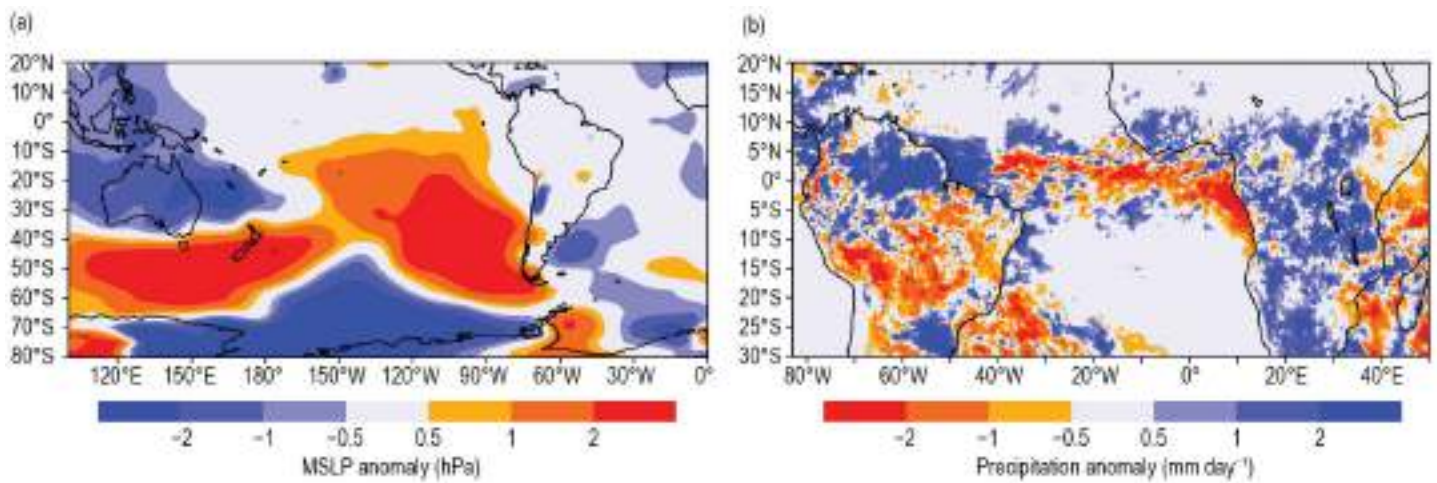


Fig. 4.13. Jan–May (a) South American and high-latitude mean sea-level pressure (MSLP) anomalies (hPa; Kalnay et al. 1996), and (b) precipitation anomalies (mm day^{-1}) over the Atlantic sector. MSLP anomalies are calculated with respect to the 1991–2020 climatology and are derived from NCEP/NCAR reanalysis (Kalnay et al. 1996). Precipitation anomalies are calculated with respect to the 2001–2021 climatology and are derived from IMERG (Huffman et al. 2014).

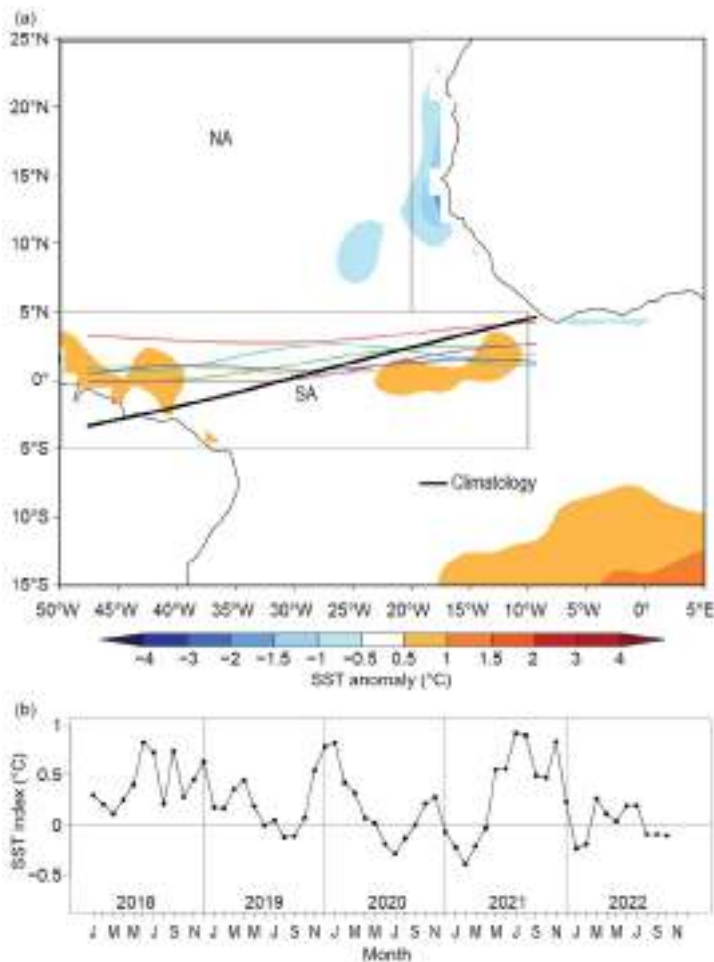


Fig. 4.14. (a) Atlantic Intertropical Convergence Zone (ITCZ) position inferred from outgoing longwave radiation (Liebmann and Smith 1996) during Mar 2022. The colored thin lines indicate the approximate position for the six pentads of the month. The black thick line indicates the Atlantic ITCZ climatological position for Mar. The sea-surface temperature (SST) anomalies ($^{\circ}\text{C}$) for Mar 2022 calculated with respect to the 1982–2020 climatology are shaded. The two boxes indicate the areas used for the calculation of the Atlantic index in panel (b), which shows the monthly OISST (Reynolds et al. 2002) anomaly time series averaged over the South Atlantic sector (SA region: 5°S – 5°N , 10°W – 50°W) minus the SST anomaly time series averaged over the North Atlantic sector (NA region: 5°N – 25°N , 20°W – 50°W) for the period 2017–22, forming the Atlantic index. The positive phase of the index indicates favorable conditions for enhanced Atlantic ITCZ activity south of the equator.

The Atlantic responded to the ongoing La Niña in a way that was similar to what was observed in 2021. Higher-than-normal pressure prevailed over the South Pacific and Patagonia during the key ITCZ period of influence (i.e., January–May; Fig. 4.13a). The Atlantic featured a weakened subtropical anticyclone with above-average precipitation over coastal northeastern and southern Brazil (Figs. 4.13a,b). Over other areas of inland Brazil, a precipitation deficit was observed during the ITCZ active period, highlighting a pronounced lack of balance in response to the irregularity of the dynamic flow. This pattern was accompanied by a largely positive SAM, as seen by the negative pressure anomalies at subpolar latitudes over the Pacific (Fig. 4.13a). The movement of the ITCZ and the Atlantic Index (see Fig. 4.14 for definition) were near normal (i.e., close to climatology) over the central Atlantic, while the ITCZ was north of its climatological position near the north coast of Brazil. This pattern was associated with low-level wind convergence slightly north of the equator at the start of the year (not shown).

e. Global monsoon summary

—B. Wang and Q. He

Globally, monsoon activity is the dominant mode of annual precipitation and circulation variability and one of the defining features of Earth's climate system (Wang and Ding 2008). Here, we summarize the global and regional monsoon precipitation anomalies in the 2022 monsoon year, which includes the Southern Hemisphere (SH) summer (November 2021–April 2022) and Northern Hemisphere (NH) summer (May–October 2022) monsoons. Figure 4.15 presents the monsoon domain (red lines) defined by rainfall characteristics (rainy summer versus dry winter; Wang 1994) rather than the traditional definition by winds (Ramage 1971). The NH monsoon includes five regional monsoons: northern Africa, India, East Asia, the western North Pacific, and North America. The SH monsoon consists of three monsoons: southern Africa, Australia, and South America.

We use regional monsoon precipitation and circulation indices to measure the integrated regional monsoon intensity. The precipitation indices represent the anomalous precipitation rate averaged over the blue rectangular box regions shown in Fig. 4.15. The precipitation averaged in each blue box well represents the precipitation averaged over the entire corresponding regional monsoon domain ($r > 0.90$; Yim et al. 2014). The definitions of the circulation indices for each monsoon region are provided in Table 4.1. Circulation indices are defined by the meridional shear of the zonal winds at 850 hPa, which measures the intensity (relative vorticity) of the monsoon troughs, except for the northern African and East Asian monsoons. The northern African monsoon circulation index is defined by the westerly monsoon strength, reflecting the

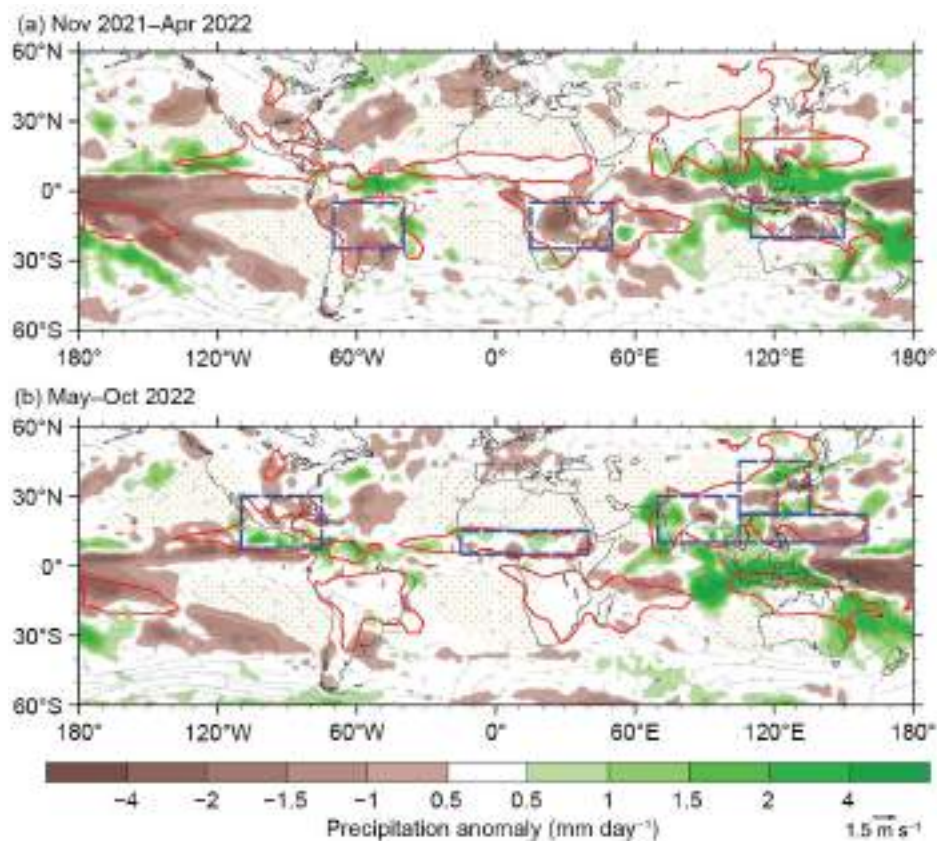


Fig. 4.15. Seasonal mean precipitation anomalies (mm day^{-1}) and 850-hPa wind anomalies (m s^{-1}) for (a) the Southern Hemisphere (SH) summer monsoon season: Nov 2021–Apr 2022 and (b) the Northern Hemisphere (NH) summer monsoon season: May–Oct 2022. The anomalies are departures from the 1991–2020 climatology. Red lines outline the global monsoon precipitation domain. Two criteria define the monsoon domains: 1) the annual precipitation range (summer-minus-winter mean) exceeds 300 mm, and 2) the summer precipitation is $>55\%$ of the total annual precipitation amount, where summer here means May–Sep for the NH and Nov–Mar for the SH (Wang and Ding 2008). The blue rectangular boxes denote the regions where the regional monsoon precipitation indices are measured. The dotted area represents the dry region where the local summer precipitation rate is below 1 mm day^{-1} . (Source: GPCP; Huffman et al. 2009.)

north–south thermal contrast between the South and North Atlantic. The East Asian summer monsoon (EASM) circulation index is determined by the meridional wind strength, reflecting the east–west thermal contrast between the Asian continent and the western North Pacific. The precipitation and circulation indices are well correlated for most regional monsoons, with correlation coefficients ranging from 0.70 to 0.88 (Table 4.1). Thus, the precipitation and circulation indices generally provide consistent measurements of the strength of each regional monsoon system except over the southern African monsoon region.

Table 4.1. Definition of the regional summer monsoon circulation indices and their correlation coefficients with the corresponding regional summer monsoon precipitation indices for 1979/80–2021/22. The precipitation indices are defined by the areal mean precipitation anomalies over the blue box regions shown in Fig. 4.15. R (r) represents the correlation coefficient between the total (land) monsoon precipitation and the corresponding circulation index. The correlation coefficients were computed using monthly time series (172 summer months; Jun–Sep in NH [1980–2022] and Dec–Mar in SH [1979/80–2021/22]). Bolded numbers represent significance at the 99% confidence level.

Regional monsoon	Definition of the circulation index	R (r)
Indian (ISM)	U850 (5°N–15°N, 40°E–80°E) minus U850 (25°N–35°N, 70°E–90°E)	0.72 (0.60)
Western North Pacific (WNPSM)	U850 (5°N–15°N, 100°E–130°E) minus U850 (20°N–35°N, 110°E–140°E)	0.87 (0.72)
East Asian (EASM)	V850 (20°N–35°N, 120°E–140°E) plus V850 (10°N–25°N, 105°E–115°E)	0.73 (0.72)
North American (NASM)	U850 (5°N–15°N, 130°W–100°W) minus U850 (20°N–30°N, 110°W–80°W)	0.85 (0.78)
Northern African (NAFSM)	U850 (0°–10°N, 40°W–10°E)	0.70 (0.70)
South American (SASM)	U850 (20°S–5°S, 70°W–40°W) minus U850 (35°S–20°S, 70°W–40°W)	0.81 (0.81)
Southern African (SAFSM)	U850 (12°S–2°S, 10°W–30°E) minus V850 (30°S–10°S, 40°E–60°E)	0.58 (0.47)
Australian (AUSM)	U850 (15°S–0°, 90°E–130°E) minus U850 (30°S–20°S, 100°E–140°E)	0.88 (0.80)

During the 2021/22 SH summer, the La Niña-enhanced Walker circulation contributed to suppressed rainfall over the central-eastern Pacific and to increased rainfall over the northern Maritime Continent and southeast Asia and the adjacent seas (Fig. 4.15a). Precipitation was significantly reduced over the South American and southern African monsoon regions, as well as northern Australia (Fig. 4.15a). Figure 4.16 shows areal-averaged monsoon intensities. The Australian summer monsoon precipitation showed average precipitation intensity and slightly above-normal circulation intensity (Fig. 4.16g). The South American monsoon precipitation was 1 standard deviation (std. dev.) below normal, but the related circulation’s strength was 0.5 std. dev. above normal (Fig. 4.16h). The southern African summer monsoon precipitation was 2 std. dev. below normal, with the circulation intensity 1 std. dev. below normal (Fig. 4.16f). Overall, the South American and southern African monsoons, as well as the northern Australian monsoon, responded uncharacteristically to the 2021/22 La Niña because La Niña conditions normally increase SH monsoon rainfall. The reasons for these uncharacteristic responses remain to be explored.

During the 2022 NH summer monsoon season (May–October), La Niña continued with the Niño-3.4 SST anomaly around -0.8°C to -1.0°C . Different from the SH monsoon, the NH summer monsoon responds to La Niña and follows a traditional pattern. Precipitation over the Maritime Continent was significantly above normal, but a noticeable reduction of precipitation occurred in the equatorial western Pacific and the Philippine Sea (Fig. 4.15b). Notably, the Indian summer monsoon was abundant and Pakistan experienced record flooding. The Indian summer monsoon precipitation and circulation indices were about 1 std. dev. above normal (Fig. 4.16b). Over East

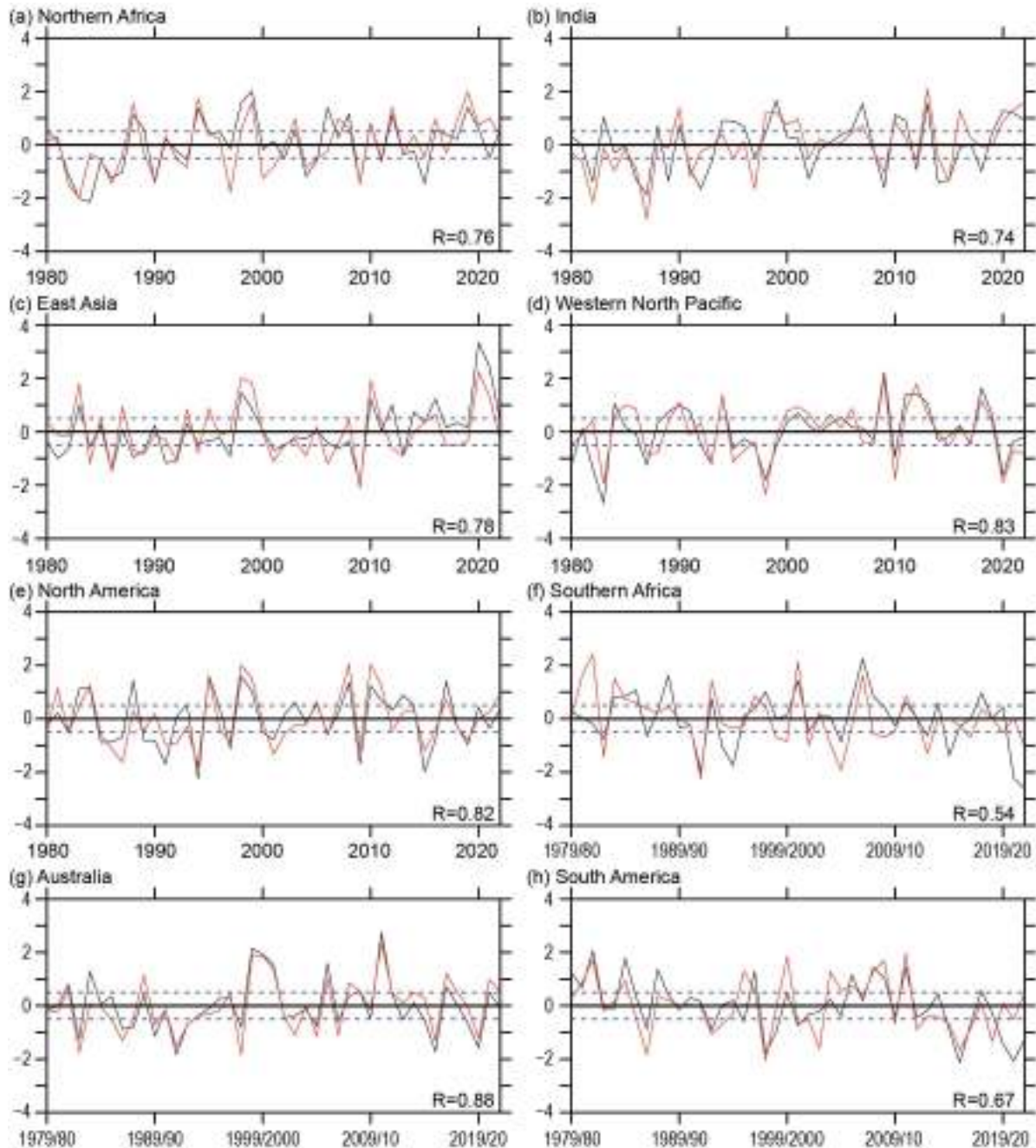


Fig. 4.16. (a)–(h). Temporal variations of summer monsoon precipitation (black lines) and low-level circulation (red lines) indices for eight regional monsoons. The precipitation indices represent the anomalous precipitation rate averaged over the blue rectangular box regions shown in Fig. 4.15. The corresponding circulation indices are defined in Table 4.1. All indices were normalized by their corresponding standard deviation (ordinate) derived for the period of 1979/80–2021/22. Numbers shown in the bottom right of each panel denote the correlation coefficient between the seasonal mean precipitation and circulation indices (sample size: 43). Dashed lines indicate ± 0.5 std. dev. The summer monsoon seasons are May–Oct for the Northern Hemisphere and Nov–Apr for the Southern Hemisphere. (Data source: GPCP for precipitation; ERA5 [Hersbach et al. 2020] for circulation).

Asia, drought conditions dominated the East Asian subtropical front zone (Meiyu/Baiu/Changma), whereas northern China experienced abundant rainfall (Fig. 4.15b). Northern African and North American monsoons had near-normal conditions (Figs. 4.16a,e). The western North Pacific oceanic monsoon circulation index was below normal (Fig. 4.16d).

Monsoon rainfall over land has more important socioeconomic impacts than oceanic monsoon rainfall. Therefore, we specifically examine land monsoon rainfall (LMR). The NH and SH LMR indices were computed by averaging precipitation over the corresponding land areas within the monsoon domain. The LMR on a global scale is significantly influenced by the El Niño–Southern Oscillation (Wang et al. 2012). Figure 4.17 shows that the NH and SH land summer monsoon precipitation are anti-correlated with the simultaneous Niño-3.4 index. The NH land monsoon rainfall has a simultaneous correlation of -0.75 from 1980 to 2022 (Fig. 4.17a). The SH land monsoon rainfall and Niño-3.4 index also had a negative correlation of -0.75 during 1979/80–2019/20. However, in the past two years the SH land monsoon and Niño-3.4 indices have both been negative (Fig. 4.17b) such that the correlation coefficient for 1979/80–2021/22 is only -0.58 . Further investigation is required to determine why the relationship has reversed in the past two years.

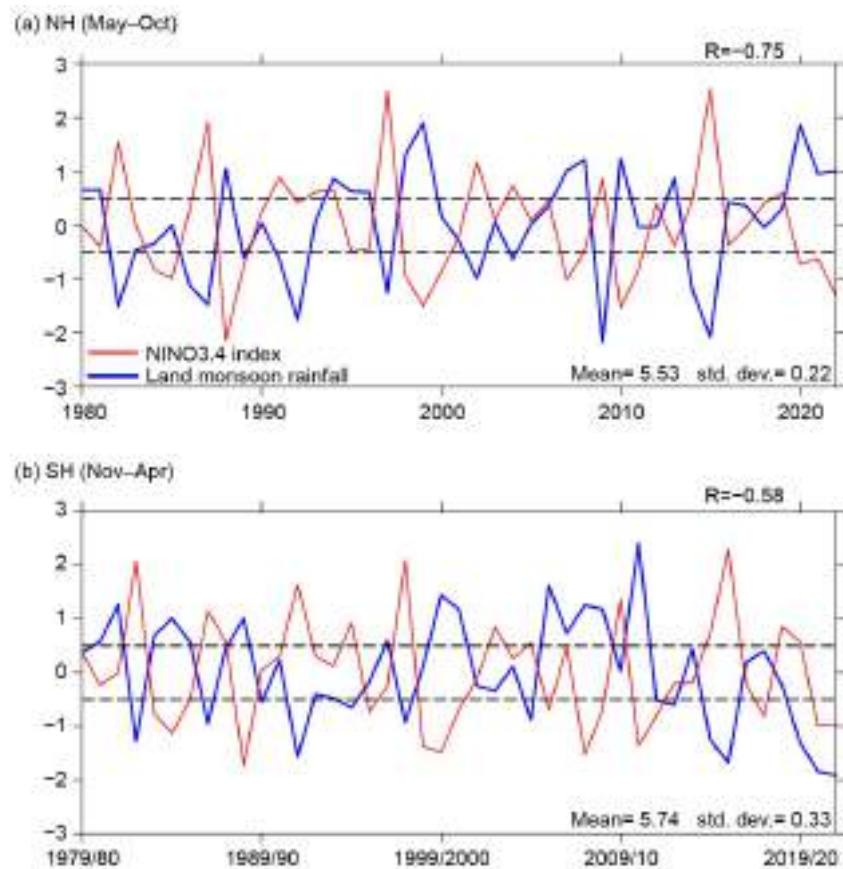


Fig. 4.17. (a) Northern Hemisphere (NH) summer (May–Oct) land monsoon precipitation anomaly (blue) normalized by its standard deviation (std. dev.). The climatological mean NH summer land monsoon precipitation (mean) and std. dev. are shown in the lower right panel (mm day^{-1}). Numbers shown in each panel’s top right denote the correlation coefficient (R) between the seasonal mean precipitation anomaly and the simultaneous Niño-3.4 index (red). Dashed lines indicate ± 0.5 . (b) As in (a) except for the Southern Hemisphere (SH) summer (Nov–Apr). Note that the land monsoon precipitation excludes the monsoon rainfall over the oceanic monsoon domain. (Source: GPCP for precipitation; HadISST and ERSSTv5 for SST.)

f. Indian Ocean dipole

—L. Chen and J.-J. Luo

The Indian Ocean dipole (IOD) is the dominant interannual mode in the tropical Indian Ocean (IO), characterized by a zonal dipole of sea-surface temperature (SST) anomalies in the equatorial IO (Saji et al. 1999; Luo et al. 2010, 2012). The IOD originates from local air–sea interaction processes in the tropical IO and/or the tropical El Niño–Southern Oscillation (ENSO) forcing (Luo et al. 2007, 2010). The dipole usually develops in austral autumn and winter, matures in spring, and terminates rapidly in early austral summer. A negative IOD event is characterized by anomalously high SSTs in the eastern IO and below-average SSTs in the western IO and vice versa for a positive IOD. The IOD phenomenon shows a strong nonlinear feature; that is, a positive IOD is usually stronger than a negative IOD due to the asymmetric air–sea feedback strength between the two phases (Luo et al. 2007; Hong et al. 2008).

In 2022, the tropical IO exhibited a strong negative IOD event with significant positive SST anomalies in the eastern pole and negative SST anomalies in the western pole (Fig. 4.18a). The IOD index of this event reached a seasonal average of -0.9°C in September–November 2022 based on the Optimum Interpolation Sea Surface Temperature (OISST) dataset (Fig. 4.18b, green line). The negative IOD event in 2022 was one of the strongest such events of the past 41 years (since 1982; Fig. 4.19).

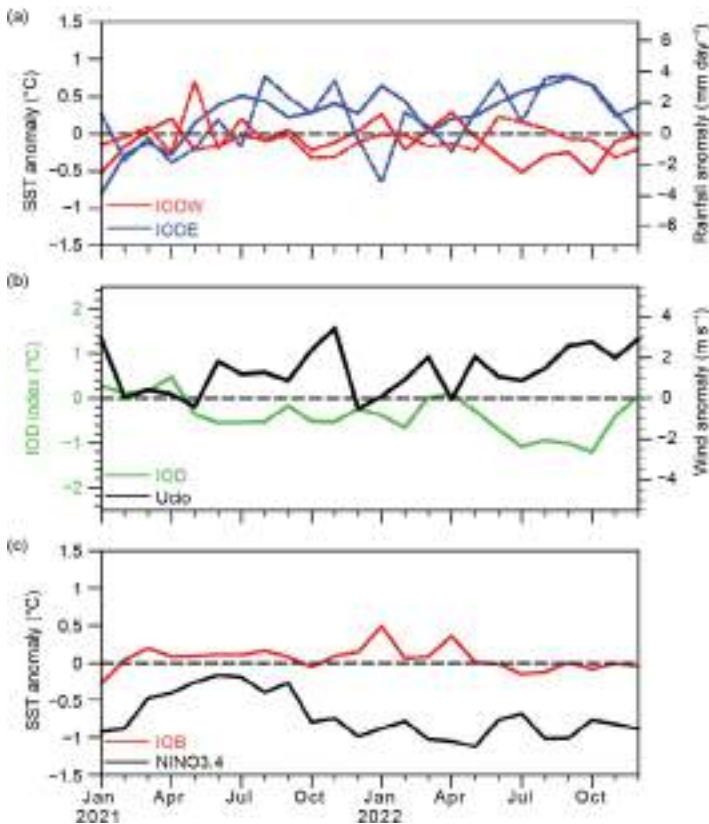


Fig. 4.18. (a) Monthly anomalies of sea-surface temperature (SST; $^{\circ}\text{C}$; solid lines) and precipitation (mm day^{-1} ; dashed lines) of the Indian Ocean dipole (IOD) in the eastern pole (IODE; 10°S – 0° , 90°E – 110°E ; blue lines) and the western pole (IODW; 10°S – 10°N , 50°E – 70°E ; red lines). (b) As in (a), but for the IOD index (measured by the SST difference between IODW and IODE, green line) and surface zonal wind anomaly (m s^{-1}) in the central equatorial IO (Ucio; 5°S – 5°N , 70°E – 90°E ; black line). (c) As in (a), but for the SST anomalies in the Niño-3.4 region (5°S – 5°N , 170°W – 120°W ; black line) and the tropical IO (IOB; 20°S – 10°N , 40°E – 120°E ; red line). Anomalies are relative to the 1982–2022 base period. (Sources: NOAA OISST [Reynolds et al. 2002]; monthly CMAP precipitation analysis [<http://ftp.prdd.ncep.noaa.gov/pub/precip/cmap/>]; and JRA-55 atmospheric reanalysis [Ebita et al. 2011].)

1982; Fig. 4.19).

The strong negative IOD started to develop in boreal spring 2022 and peaked in boreal summer and autumn (Fig. 4.18b). Following a weak negative IOD event in 2021, the tropical IO exhibited a weak positive Indian Ocean basin (IOB) mode from December 2021 to April 2022 (Figs. 4.18a,b). Beginning in April–May 2022, the anomalous warmth across the basin transitioned into an anomalous dipole, with warm SST anomalies over the eastern IO and cold SST anomalies over the western IO that then began to grow (Fig. 4.18a). Meanwhile,

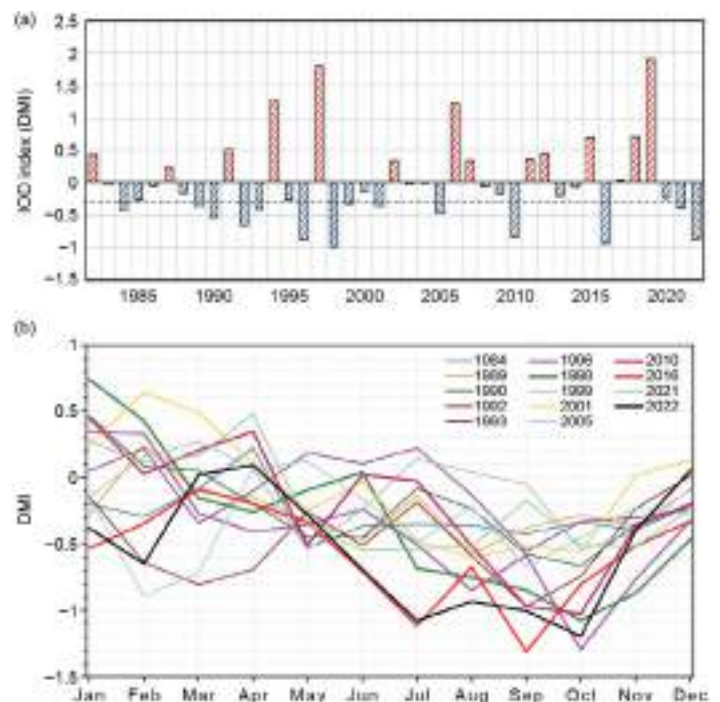


Fig. 4.19. (a) Sep–Nov IOD index (DMI) based on sea-surface temperature (SST) data from OISSTv2. (b) Annual DMI time series for all negative IOD events.

westerly surface wind anomalies occurred over the central IO region during that same period (Fig. 4.18b; see also Fig. 4.5). From the perspective of the tropical Indo-Pacific Ocean, these westerly wind anomalies over the central IO region can be associated with La Niña in the tropical Pacific (Fig. 4.18c). In response to La Niña, the Walker circulation across the equatorial sector of the Indo-Pacific Ocean increases in intensity. As indicated by the anomalous precipitation and surface winds (Figs. 4.4, 4.5) and the anomalous velocity potential field at 200 hPa (contours in Fig. 4.20), stronger descending motion and less rainfall occurred over the central equatorial Pacific, while stronger ascending motion and more rainfall occurred over the western equatorial Pacific and the Maritime Continent. Accordingly, an anomalous descending branch of the Walker circulation occurred for the majority of the year over eastern equatorial Africa and the western equatorial IO. After the dissipation of the positive IOB mode in early 2022, anomalous westerly winds over the equatorial IO began to increase in April–May 2022.

Owing to the positive feedback between the westerly wind anomalies and the dipole of SST anomalies over the equatorial sector of the IO, the negative IOD event quickly grew from its onset stage (i.e., April–May) to boreal summer 2022, as shown in Figs. 4.18b and 4.20b,c. Along with the increase of SST anomalies, some damping processes (e.g., negative cloud–radiation–SST feedback) may have played a role, leading to a relatively slow development of the negative IOD from boreal summer to boreal autumn. As would be expected given the negative IOD, the eastern part of the basin was characterized by anomalous warmth and increased precipitation, while the western part of the basin was characterized by anomalous coolness and decreased precipitation (Figs. 4.4, 4.5, 4.20).

The tropical Pacific was broadly characterized by La Niña for most of 2020–22 (Fig. 4.18c). During boreal summer/autumn, the IOD was generally neutral in 2020 (Chen and Luo 2021), weakly negative in 2021 (Chen and Luo 2022), and strongly negative in 2022. Although the two consecutive negative IOD events in 2021 and 2022 coincided with La Niña conditions in the Pacific, they appear to have had significantly different formation mechanisms. The weak negative IOD event in 2021 may have not only been triggered by La Niña, but may also have been influenced by other regions, such as wind and SST anomalies originating from the subtropical IO (Chen and Luo 2022). The strong negative IOD in 2022 seems to have been primarily driven by the La Niña, especially during its onset stage. This indicates the complexity of IOD formation mechanisms, which may be due to both local air–sea processes in the IO and/or remote impacts from the tropical Pacific.

In summary, a strong negative IOD event occurred in 2022, with the IOD index reaching a seasonal average of -0.9°C during boreal autumn. As noted in the previous paragraph, the development of this negative IOD event was largely driven by the La Niña. In response to La Niña, an anomalously strong

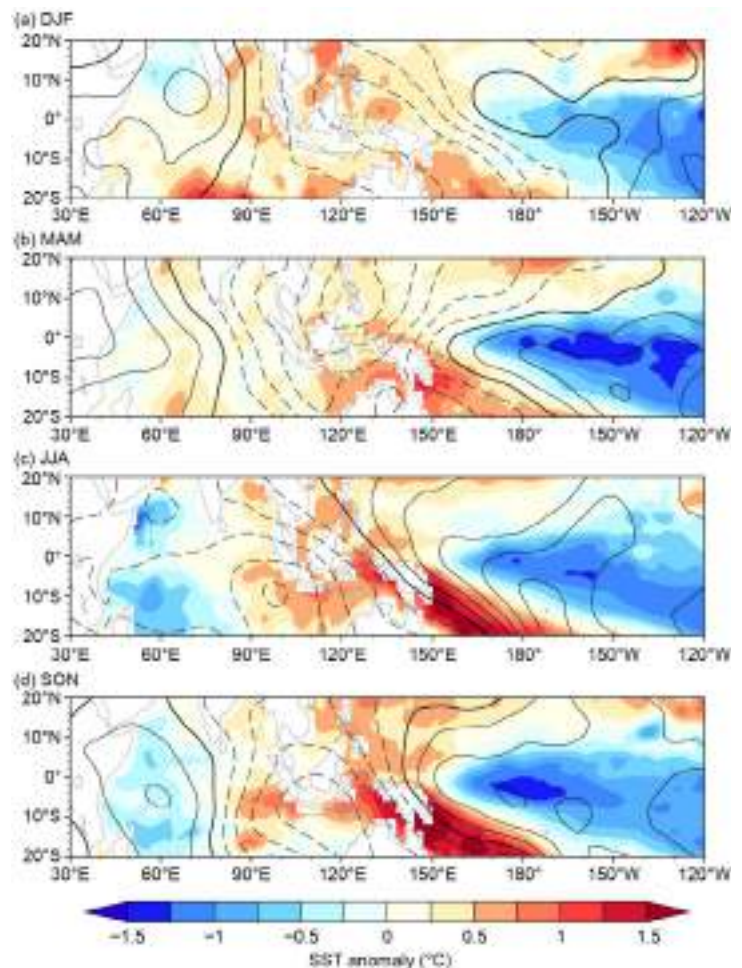


Fig. 4.20. Sea-surface temperature (SST) anomalies ($^{\circ}\text{C}$, colored scale) and 200-hPa velocity potential ($\times 10^6 \text{ m}^2 \text{ s}^{-1}$, contoured with an interval of 1; solid/dashed/bold curves denote positive/negative/zero values) during (a) Dec 2021–Feb 2022, (b) Mar–May 2022, (c) Jun–Aug 2022, and (d) Sep–Nov 2022. Anomalies were calculated relative to the climatology over the period 1982–2022. (Sources: NOAA OISST [Reynolds et al. 2002] and JRA-55 atmospheric reanalysis [Ebita et al. 2011].)

Walker circulation occurs over the tropical Indo-Pacific sector, with a stronger ascending of the Walker circulation branch over the western equatorial Pacific and the Maritime Continent and a stronger descending branching over the western equatorial IO. Consequently, anomalous westerly winds emerged in April–May 2022, and an anomalous SST dipole developed. A strong zonal dipole of SST and precipitation anomalies occurred in the equatorial IO during boreal summer and autumn, with anomalous warmth and increased precipitation in the eastern part of the basin and anomalous coolness and decreased precipitation in the western part of the basin. As is typical, the negative IOD began to decay in November–December. It is worth mentioning that such a strong negative IOD is conducive to the transition from a third-year (“triple”) La Niña into El Niño in 2023, based on the potential impacts of IOD on the succeeding ENSO (Izumo et al. 2010).

g. Tropical cyclones

1. OVERVIEW

—H. J. Diamond and C. J. Schreck

The International Best Track Archive for Climate Stewardship (IBTrACS) dataset comprises historical tropical cyclone (TC) best-track data from numerous sources around the globe, including

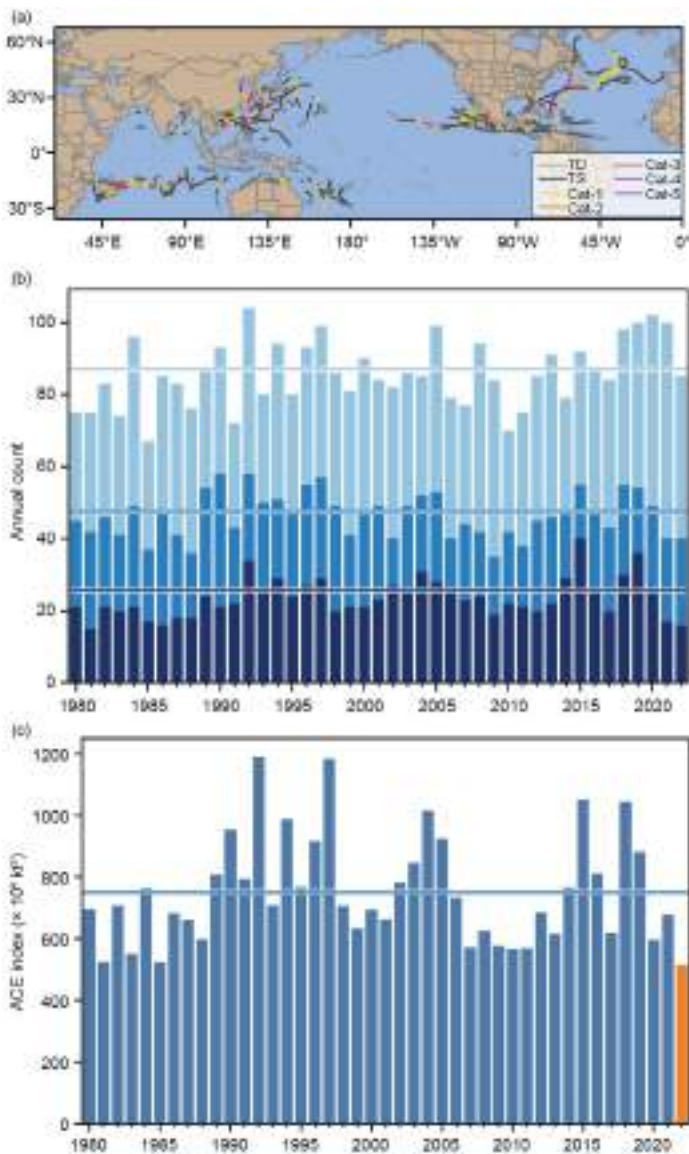


Fig. 4.21. (a) Global summary of tropical cyclone (TC) tracks; (b) global TC counts; and (c) global accumulated cyclone energy (ACE) values ($\times 10^4 \text{ kt}^2$). Horizontal lines on (b) and (c) are the 1991–2020 normals.

all of the World Meteorological Organization (WMO) Regional Specialized Meteorological Centers (RSMCs; Knapp et al. 2010). This dataset represents the most complete compilation of global TC data. From these data, 1991–2020 climatological values of TC activity for each basin using statistics from both the WMO RSMCs and the Joint Typhoon Warning Center (JTWC) are calculated following Schreck et al. (2014). These values are referenced in each subsection. Tallying the global TC numbers is challenging and involves more than simply adding up basin totals, as some storms cross TC basin boundaries, some TC basins overlap, and multiple agencies track and categorize TCs. The Northern Hemisphere (NH) basins are typically measured from January to December while Southern Hemisphere (SH) basins are typically measured from July to June. Global values here are the sum of NH for 2022 and SH for 2021/22.

Based on preliminary data from NOAA’s National Hurricane Center (NHC) and the JTWC as archived in IBTrACS (Fig. 4.21), the combined 2022 season had 85 named storms (sustained wind speeds $\geq 34 \text{ kt}$ or 17 m s^{-1}), which is 12 fewer than the previous season (2021; Diamond and Schreck 2022) but on par with the 1991–2020 average of 87. There were 40 hurricanes/typhoons/cyclones (HTCs; sustained wind speeds $\geq 64 \text{ kt}$ or 33 m s^{-1}), with only 16 of those reaching major HTC status (sustained wind speeds $\geq 96 \text{ kt}$ or 49 m s^{-1}), which equals 1986 for the fewest since 1982. The accumulated cyclone energy (ACE) for the season was $517 \times 10^4 \text{ kt}^2$, which is 22% lower than last year (Diamond and Schreck 2022) and the lowest on record since reliable global data began in 1981.

In sections 4g2–4g8, 2021/22 (SH) and 2022 (NH) seasonal TC activity are described and compared to the historical record for each of the seven WMO-defined TC basins. For simplicity, all counts are broken down by the U.S. Saffir-Simpson Hurricane Wind Scale (SSHWS)². The overall picture of global TCs during 2022 is shown in Fig. 4.21, and counts by category and intensity are documented in Table 4.2.

The eastern North Pacific, North Indian Ocean, and Australian basins each had an above-normal number of named storms. The eastern North Pacific was the only basin that had more HTCs than normal. However, all five HTCs in the South Indian Ocean reached major HTC strength, which was also more than normal. In terms of ACE, the Atlantic, eastern North Pacific, and South Indian Ocean basins were all near-normal while all other basins were below normal.

The western North Pacific was quieter than normal by most metrics for the third year in a row. However, the western North Pacific produced two of the three SSHWS Category 5 storms globally in 2022. This is five fewer than last year’s global count (Diamond and Schreck 2022) and below the 1991–2020 mean of 5.3. It was the fewest since 2008, when only one storm (Jangmi) reached SSHWS Category 5 status.

While not reaching Category 5 status, Major Hurricanes Fiona and Ian in the Atlantic caused tremendous damage and loss of life. Sidebar 4.1 and the following section, 4g2, describe their meteorological history and their impacts. Both parts of the chapter highlight the considerable damage that Fiona caused in the Atlantic Provinces of Canada and that Ian caused in Florida. Fiona also caused massive flooding damage in Puerto Rico, while Ian caused significant wind and storm surge damage in Cuba as well.

Table 4.2. Global counts of TC activity by basin for 2022. “+” denotes top tercile; “++” is top 10%; “–” is bottom tercile; “--” is bottom 10% (all relative to 1991–2020). “+++” denotes record values for the entire IBTrACS period of record. (Note that some inconsistencies between Table 4.2 and the text of the various basin write-ups in section g exist and are unavoidable, as tallying global TC numbers is challenging and involves more than simply adding up basin totals, because some storms cross TC basin boundaries, some TC basins overlap, and multiple agencies are involved in tracking and categorizing TCs.)

Region	TCs	HTCs	Major HTCs	SS Cat 5	ACE
North Atlantic	14	8	2	1	95
Eastern Pacific	19 +	10 +	4	0	117
Western Pacific	22 –	12 –	5 –	2	161 –
North Indian	7 +	1	0	0	11 –
South Indian	9 –	5	5 +	0	89
Australia	12 +	4	1 –	0	27 --
Southwest Pacific	6	2	0	0	19 –
Global	85	40 –	16 --	3 --	517 --

² SSHWS is based on 1-minute averaged winds, and the categories are defined at: <https://www.weather.gov/mfl/saffirsimpson>; the Australian category scale is based on 10-minute averaged winds, and those categories are defined at https://australiasevereweather.com/cyclones/tropical_cyclone_intensity_scale.htm

2. ATLANTIC BASIN

—M. Rosencrans, E. S. Blake, C. W. Landsea, H. Wang, S. B. Goldenberg, R. J. Pasch, and D. S. Harnos

(i) 2022 seasonal activity

The 2022 Atlantic hurricane season produced 14 named storms, of which 8 became hurricanes and 2 of those became major hurricanes (Fig. 4.22a). These are all near the 1991–2020 seasonal averages of 14.4 named storms, 7.2 hurricanes, and 3.2 major hurricanes based on the Hurricane Database (HURDAT2) historical archive (Landsea and Franklin 2013). HURDAT2 is also included in IBTrACS (Knapp et al. 2010). The 14 named storms were the least observed since 2015 when only 11 named storms developed. The 2022 hurricane season was classified by NOAA as a near-normal season, ending the consecutive streak of six above-normal seasons (2016–21).

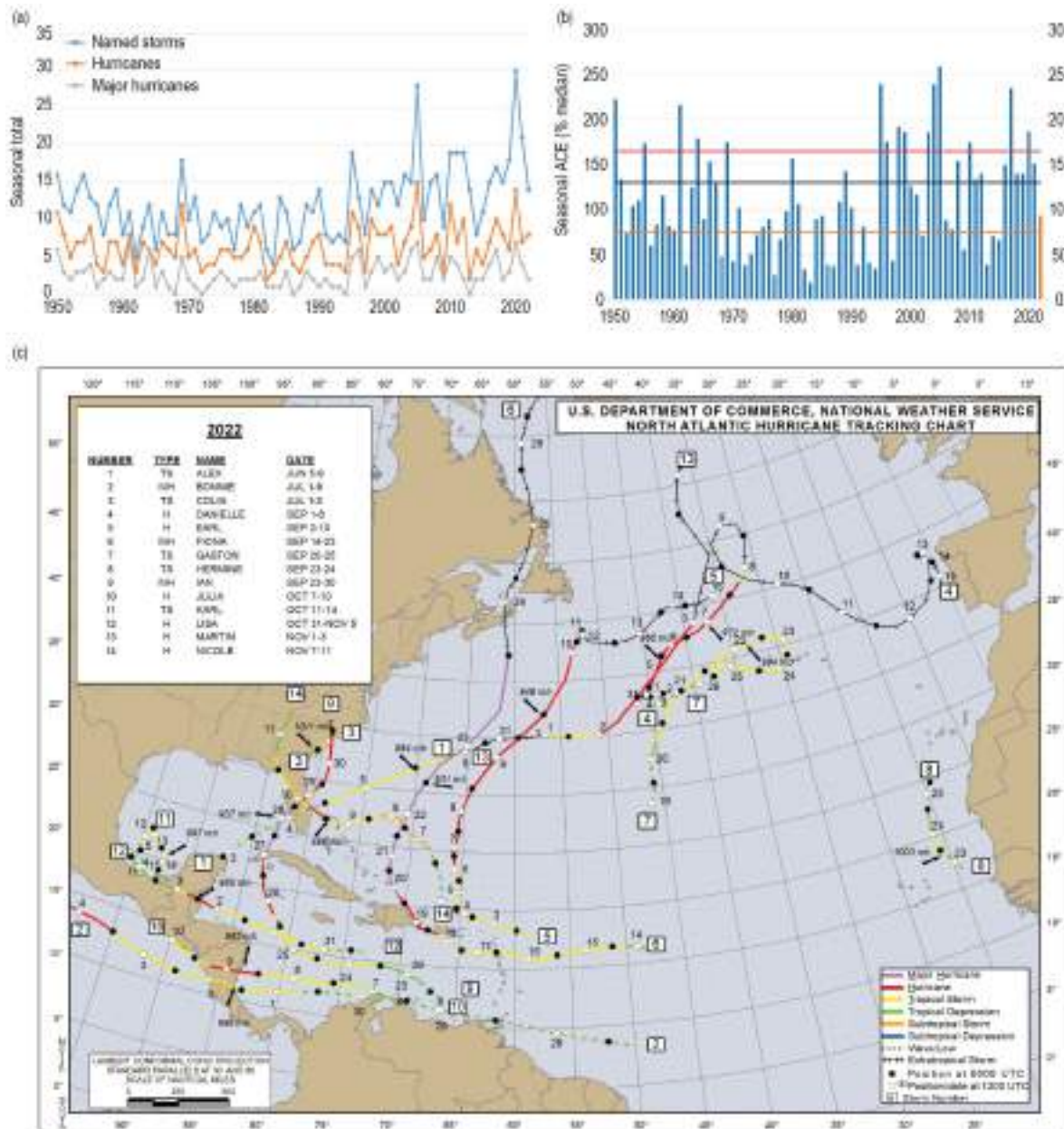


Fig. 4.22. (a) Seasonal Atlantic hurricane activity during 1950–2022 for named storms (blue), hurricanes (orange), and major hurricanes (gray). (b) The annual accumulated cyclone energy (ACE) index for 1950–2022 expressed as percent of the 1951–2020 median value. ACE is calculated by summing the squares of the six-hourly maximum sustained surface wind speed (kt) for all periods while the storm is at least tropical-storm strength. Black and orange lines correspond to NOAA’s classifications for above-normal and below-normal seasons, respectively (<https://www.cpc.ncep.noaa.gov/products/outlooks/Background.html>). The thick red horizontal line at 165% denotes the threshold for an extremely active season. Note that there is a low-bias in activity during the 1950s through early 1970s due to the lack of satellite imagery and technique (Dvorak) to interpret tropical-cyclone intensity for systems over the open ocean. (c) 2022 Atlantic basin storm tracks. (Source: HURDAT2 [Landsea and Franklin 2013].)

Even during near-normal seasons, a single hurricane can bring devastation to an area. In 2022, Hurricane Fiona brought devastating flooding to Puerto Rico. It later set a new record for minimum sea-level pressure over land in Canada and contributed the most ACE, ~27% of the annual total, of any individual storm. Fiona was the third-costliest storm to impact Puerto Rico and the costliest weather disaster in the Canadian Maritime Provinces' history. Hurricane Ian was a major hurricane for only two days but brought extensive damage to Cuba, Florida, and portions of the southeastern United States. It caused over 100 deaths and more than \$100 billion (U.S. dollars) in damage, making it the third-costliest U.S. hurricane on record. Please see Sidebar 4.1 for more discussion of Hurricanes Fiona and Ian.

Four of the 14 named storms during 2022 were short-lived (≤ 2 days). There has been a large increase (approximately five per year) in these “shorties” since 2000 (Landsea et al. 2010). These increased counts primarily reflect new observational capabilities such as scatterometers, Advanced Microwave Sounding Units, and the Advanced Dvorak Technique, and have no association with any known natural or anthropogenic climate variability (Villarini et al. 2011).

The 2022 seasonal ACE value was 97.8% of the 1951–2020 median (which is 96.7×10^4 kt²; Fig. 4.22b). This value is close to the median, falling in the near-normal category (between 73 and 126×10^4 kt²). Since the current Atlantic high-activity era began in 1995 (Goldenberg et al. 2001; Bell et al. 2019, 2020), there have been 19 above-normal seasons, with 10 of these being hyper-active. By comparison, the preceding 24-year low-activity era of 1971–94 had only two above-normal seasons, with none being extremely active.

(ii) Storm formation times, regions, and landfalls

Distinct active and inactive periods of TC activity occurred throughout the 2022 hurricane season. For the first time since 2014, no tropical storms formed before the official start of the hurricane season on 1 June. Activity in 2022 started with Tropical Storm Alex developing on 5 June. The first few days of July featured two tropical cyclones (Tropical Storms Bonnie and Colin). For the first time since 1997 and only the third time since 1950, there were no tropical storms during August. However, activity ramped up after that with six named storms developing during September, of which four became hurricanes. During the second half of September, two of the hurricanes (Fiona and Ian) attained major hurricane status and were the most destructive storms of the season. This was slightly above normal for September, which typically sees five named storms and three hurricanes. One depression, one tropical storm, and one hurricane formed during October, including the only named storm (Karl) to develop during the season in the Gulf of Mexico (The average year sees 2.2 named storms developing in the Gulf of Mexico). Three hurricanes developed in November, the last official month of the hurricane season. This ties with 2001 for the most observed on record. Historically, a hurricane only forms about every two years during November. Two of these November hurricanes made landfall, including Hurricane Nicole, which was the first November hurricane to make landfall in Florida since Kate in 1985. The majority of hurricane activity typically takes place during August–October, the climatological peak three months of the hurricane season, however, during 2022, the most active months were September–November.

Of the 14 named storms that developed in 2022, half of them formed in the Main Development Region (MDR; Fig. 4.23a, green box). The MDR spans the tropical Atlantic Ocean and Caribbean Sea between 9.5°N and 21.5°N (Goldenberg and Shapiro 1996; Goldenberg et al. 2001). That percentage of MDR formations (50%) is more typical of seasons with above-normal activity (average 52%) rather than near-normal seasons, which typically have about 38% of formations in the MDR. The MDR-related ACE value was 66% of its median and far exceeds the ACE associated with storms first named over the Gulf of Mexico (2% of the 2022 total) or in the extratropics (28%).

The storm tracks during 2022 (Fig. 4.22c) had two distinct clusters of tracks: one over the Caribbean and another over the western North Atlantic. Three storms formed at low latitudes,

with two crossing northern South America during their developing stages. Tropical Storm Bonnie moved across Central America intact, the first named storm to do so since Tropical Storm Otto in 2016, and intensified into a major hurricane over the eastern North Pacific. Hurricane Julia also crossed over from the Atlantic to the eastern North Pacific while maintaining at least tropical storm-force winds. No prior year on record has observed two systems that crossed over Central America while maintaining at least tropical-storm intensity.

(iii) Sea-surface temperatures

Sea-surface temperature (SST) anomalies ranged from just below 0°C to +0.5°C, and the area-averaged SST anomaly was +0.20°C (Figs. 4.23a,b). The area-averaged SST anomaly in the MDR was higher (by 0.28°C) than that of the global tropics (Fig. 4.23c). This signal typifies the warm phase of the Atlantic Multi-decadal Oscillation (AMO; Enfield and Mestas-Nuñez 1999; Bell and Chelliah 2006) and is a ubiquitous characteristic of Atlantic high-activity eras such as 1950–70 and 1995–present (Goldenberg et al. 2001; Vecchi and Soden 2007; Bell et al. 2018).

During August–October (ASO) 2022, above-average temperatures were also present across most of the North Atlantic Ocean. Outside of the MDR, the largest anomalies (exceeding +1.5°C) occupied portions of the central North Atlantic (Fig. 4.23a), areas where numerous tropical storms and hurricanes tracked. Extended Reconstructed Sea Surface Temperature version 5 (ERSST)-based anomalies over the entire North Atlantic for ASO were +0.47°C, consistent with a positive AMO. The continuing La Niña event typically reduces wind shear and increases mid-level moisture across the tropical Atlantic Ocean, both of which enhance tropical cyclone development.

(iv) Atmospheric conditions

Climatologically, the ASO peak in Atlantic hurricane activity largely reflects the June–September peak in the West African monsoon. The inter-related circulation features of an enhanced monsoon act to further increase hurricane activity, while those of an anomalously weak monsoon act to suppress it (Gray 1990; Hastenrath 1990; Landsea et al. 1992; Bell and Chelliah 2006; Bell et al. 2018, 2020). The association on multi-decadal time scales between the AMO and Atlantic hurricane activity largely exists because of their common relationship to the West African monsoon (Bell and Chelliah 2006) and reduced vertical shear due to weaker easterly trade winds in the MDR (Goldenberg et al. 2001). The West African

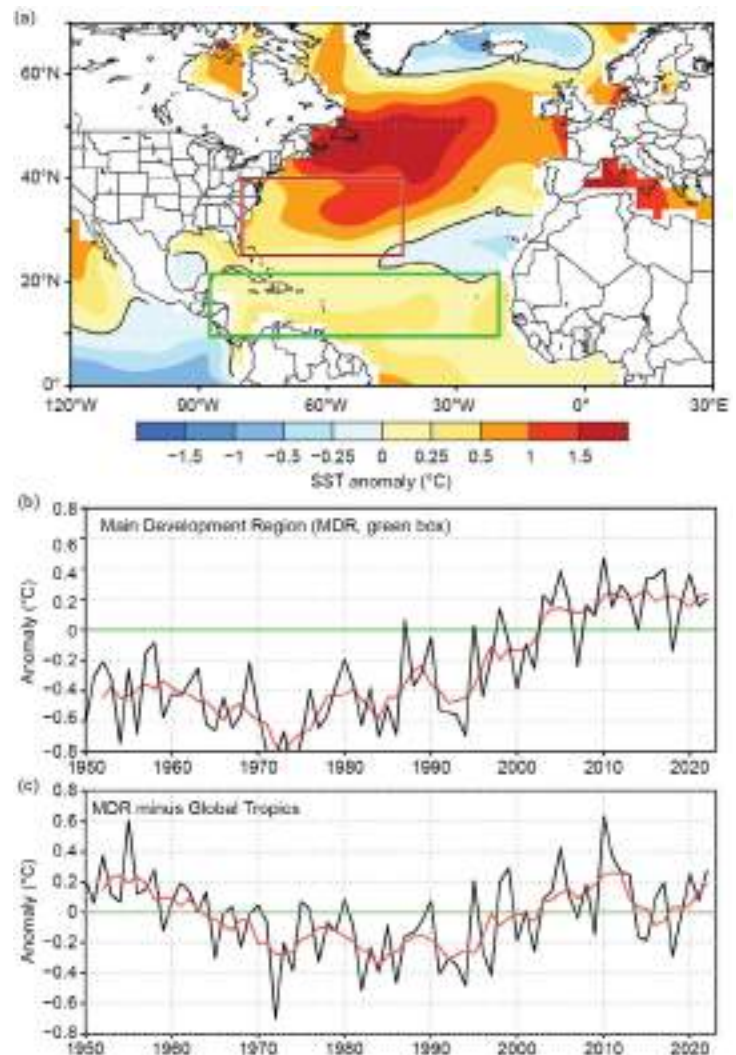


Fig. 4.23. (a) Aug–Oct 2022 sea-surface temperature (SST) anomalies (°C). (b),(c) Time series of Aug–Oct area-averaged SST anomalies (black) and 5-pt running mean of the time series (red): (b) In the Main Development Region (MDR, green box in (a) spanning 20°W–87.5°W and 9.5°N–21.5°N), and (c) difference between the MDR and the global tropics (20°S–20°N). Anomalies are departures from the 1991–2020 period means. The green horizontal line in (b) and (c) highlights the zero value, a critical reference value. (Source: ERSST-v5 [Huang et al. 2017].)

monsoon was enhanced during July–September (JAS) 2022, as indicated by negative outgoing longwave radiation (OLR) anomalies across the African Sahel (Fig. 4.24a, red box). Total OLR values in this region averaged 235 W m^{-2} (Fig. 4.24b), with values less than 240 W m^{-2} indicating deep tropical convection. The OLR time series shows that an enhanced monsoon has largely prevailed throughout the current Atlantic high-activity era and warm AMO of 1995–present (Fig. 4.24b). In contrast, a much weaker monsoon with OLR values well above 240 W m^{-2} in the Sahel region was typical of the low-activity era during the cool AMO period of the 1980s and early 1990s.

Consistent with a slightly above-normal monsoon, the large-scale divergent circulation at 200 hPa featured an extensive area of anomalous divergence over western Africa (Fig. 4.24c). The signal was not as robust as measured in 2021, with the core of negative velocity potential

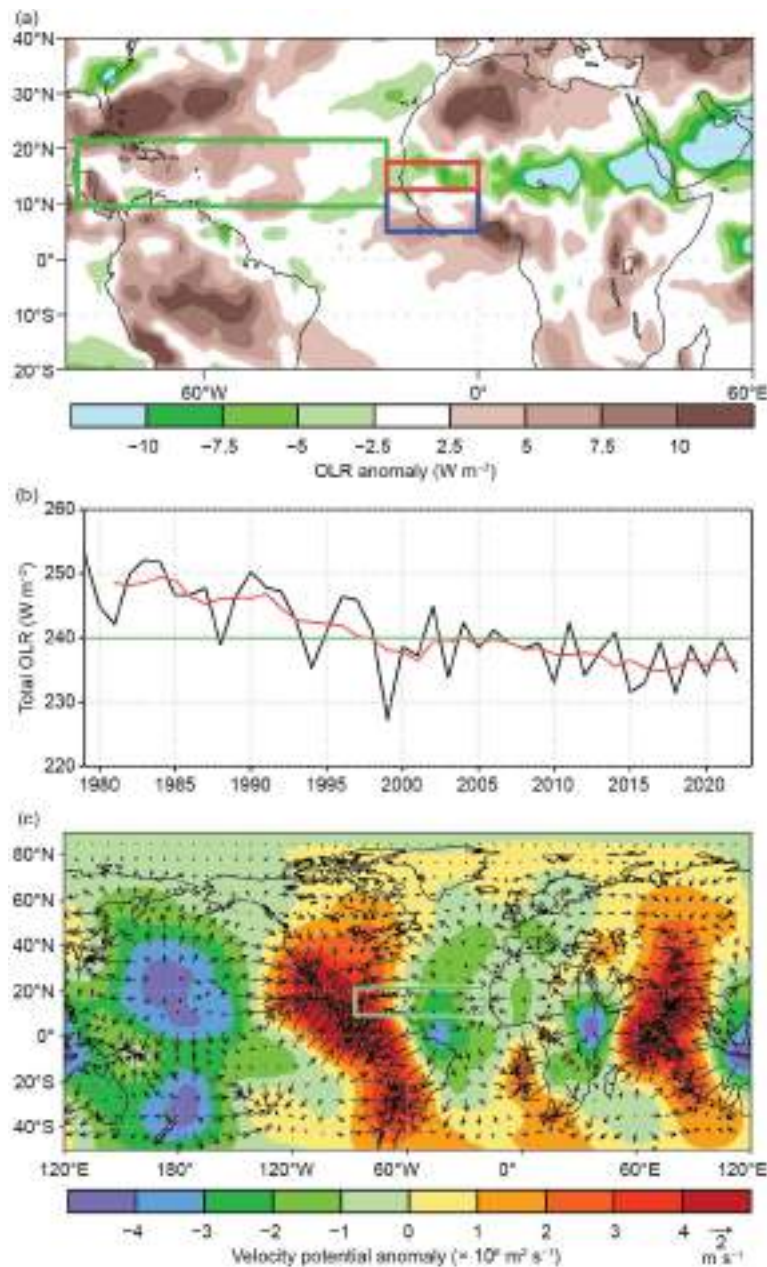


Fig. 4.24. (a) Jul–Sep 2022 anomalous outgoing longwave radiation (OLR; W m^{-2}), with negative (positive) values indicating enhanced (suppressed) convection. (b) Time series of Jul–Sep total OLR (black) and 5-yr running mean of the time series (red) averaged over the African Sahel region (red box in (a) spanning 20°W – 0° and 12.5°N – 17.5°N). (c) Jul–Sep 2022 anomalous 200-hPa velocity potential ($\times 10^6 \text{ m}^2 \text{ s}^{-1}$) and divergent wind vectors (m s^{-1}). In (a), (c), the green box denotes the Atlantic Main Development Region. Anomalies are departures from the 1991–2020 means. The green horizontal line in (b) highlights the 240 value, a critical reference value for relating OLR to convection. (Sources: Liebmann and Smith [1996] for OLR; NCEP/NCAR Reanalysis [Kalnay et al. 1996].)

anomalies split by an area of near-zero anomalies and anomalous convergence. Analysis of streamfunction at 200 hPa (Fig. 4.25a) shows anomalous anticyclones over the Caribbean and over the eastern Atlantic, with cyclonic anomalies over portions of the MDR and western Africa. Farther north, a large anticyclonic anomaly is evident over central Canada with a cyclonic anomaly over the western Atlantic. This ASO 2022 streamfunction pattern over the eastern MDR does not resemble those associated with La Niña and the positive phase of the multi-decadal mode that is associated with higher activity (Bell and Chelliah 2006). Over the eastern MDR, ASO 2022 featured a large cyclonic anomaly. The ASO 2022 200-hPa streamfunction pattern more closely resembles the 200-hPa streamfunction anomaly pattern that Bell and Chelliah (2006)

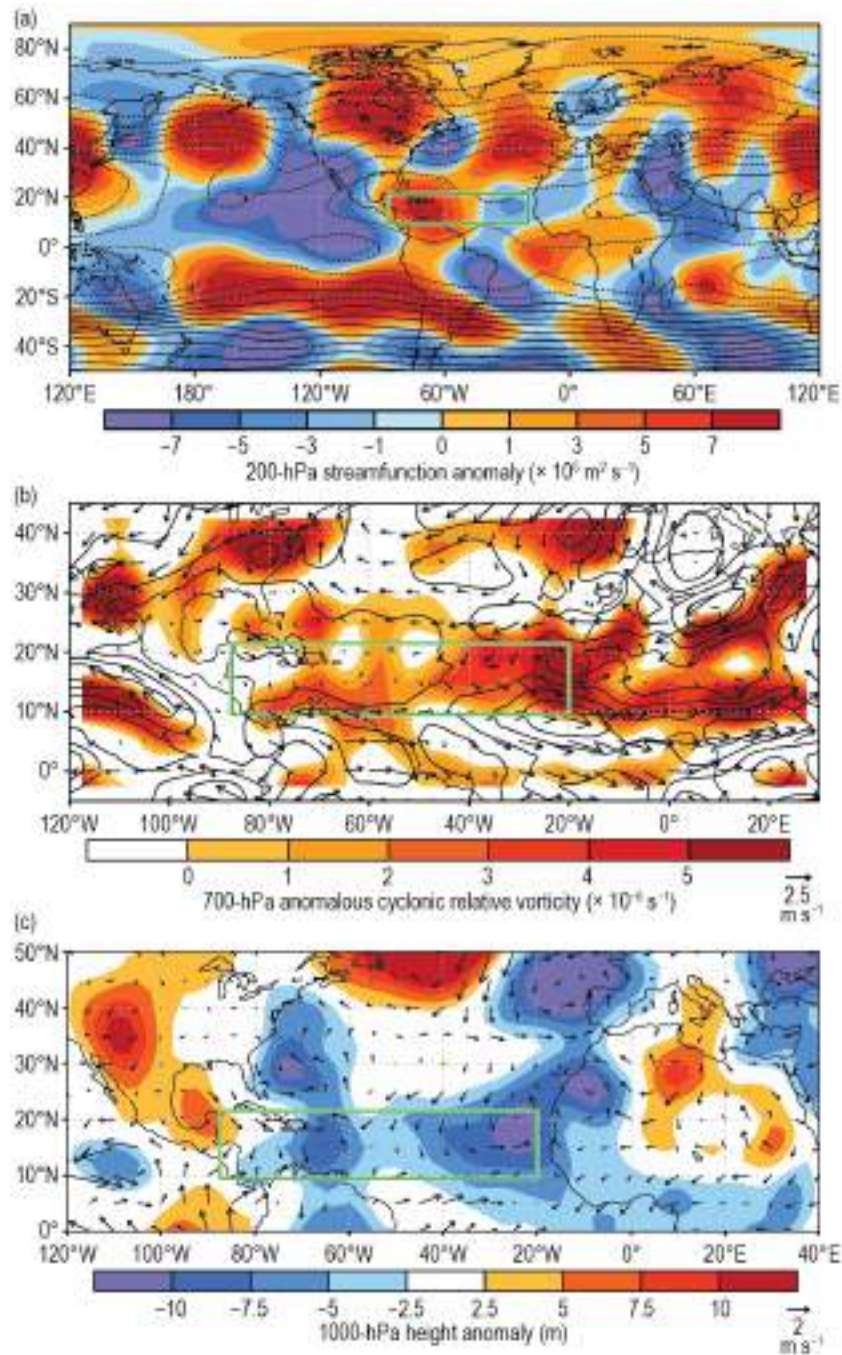


Fig. 4.25. Aug–Oct 2022: (a) 200-hPa streamfunction (contours, interval is $5 \times 10^6 \text{ m}^2 \text{ s}^{-1}$) and anomalies (shaded); (b) anomalous 700-hPa cyclonic relative vorticity (shaded, $\times 10^6 \text{ s}^{-1}$), wind speed (contours), and vector winds (m s^{-1}); (c) anomalous 1000-hPa heights (shaded, m) and vector winds. Vector scales differ for each panel and are below right of the color bar. Green box denotes the Main Development Region. Anomalies are departures from the 1991–2020 means. (Source: NCEP/NCAR reanalysis [Kalnay et al. 1996].)

found for La Niña episodes during 1975–1994 during a low-activity era rather than those during active eras. This discrepancy points to activity being mitigated by factors other than La Niña.

The 700-hPa anomalous wind and vorticity fields (Fig. 4.25b) indicate enhanced vorticity across the MDR. The 1000-hPa anomalous height and wind field (Fig. 4.25c) shows that the near-surface winds were largely aligned with the 700-hPa wind fields, with below-average heights and cyclonic turning of the winds across much of the MDR.

The ASO 2022 200-hPa–850-hPa wind shear was slightly above average for much of the MDR, with the highest positive anomalies located in the western MDR/Caribbean (Fig. 4.26a). The area-averaged magnitude of the vertical wind shear for the entire MDR was 9.1 m s^{-1} (Fig. 4.26b) and 11.2 m s^{-1} for the Gulf of Mexico (Fig. 4.26c). Shear values less than 10 m s^{-1} are generally considered conducive to hurricane formation (Gray 1968; DeMaria et al. 2005; Tippett et al. 2011). The lack of tropical storm activity over the Gulf of Mexico is likely related to the high shear, the highest value for that region since 2011.

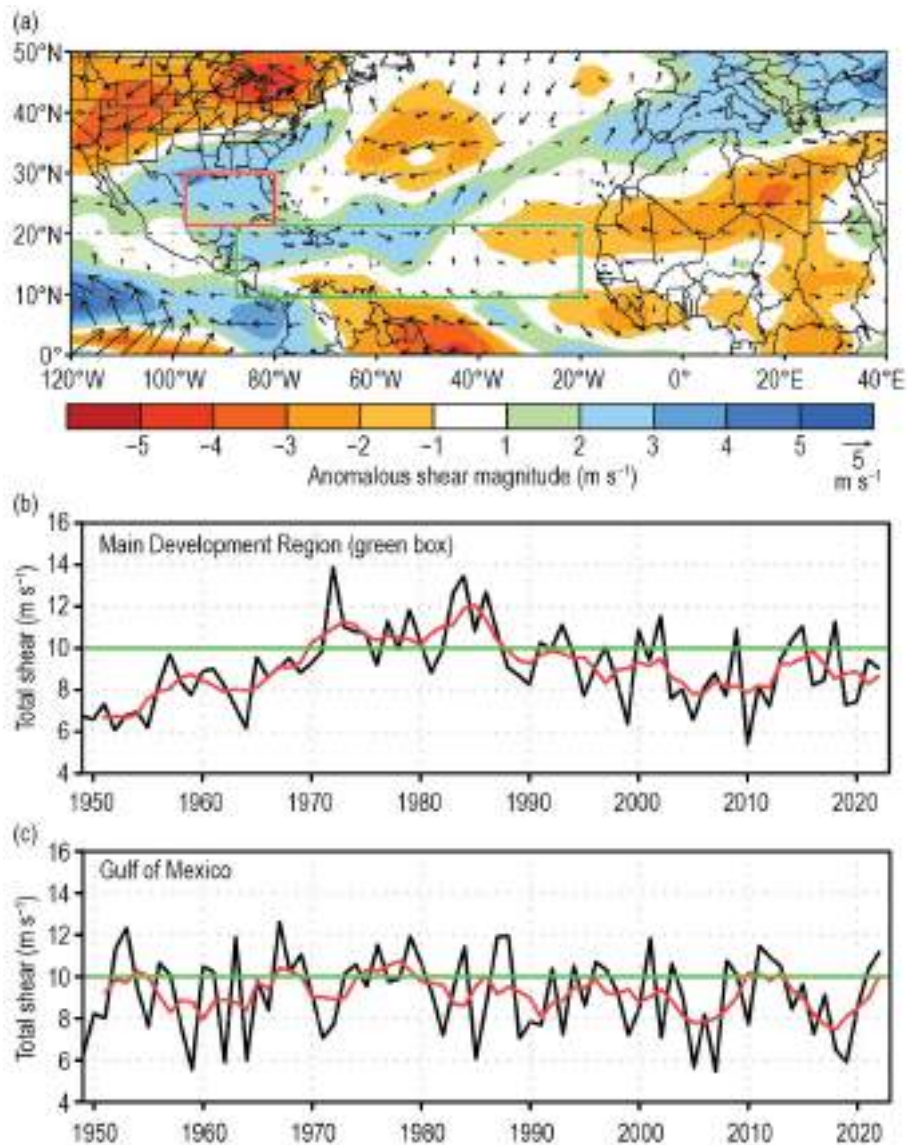


Fig. 4.26. Aug–Oct magnitude of the 200-hPa–850-hPa vertical wind shear (m s^{-1}): (a) 2022 anomalous magnitude and vector. (b), (c) Time series of Aug–Oct vertical shear magnitude (black) and 5-yr running mean of the time series (red) averaged over (b) the Main Development Region (green box in (a), spanning 87.5°W – 20°W and 9.5°N – 21.5°N) and (c) the Gulf of Mexico (21.5°N – 30°N and 97.5°W – 80°W). The green horizontal lines in (b) and (c) highlight the value 10, a critical reference value where shear is thought to inhibit tropical cyclone development on monthly and seasonal time scales. Anomalies are departures from the 1991–2020 means. (Source: NCEP/NCAR reanalysis [Kalnay et al. 1996].)

Further analysis shows that the largest anomalous 200-hPa–850-hPa wind-shear values were over the Caribbean, with anomaly values in excess of 5.0 m s^{-1} (Fig. 4.27a). The 200-hPa–850-hPa total wind shear over the MDR in August was 9.3 m s^{-1} (Fig. 4.27b), barely meeting the $<10 \text{ m s}^{-1}$ threshold conducive for tropical cyclogenesis. Additionally, specific humidity over the MDR (Fig. 4.27c) reflected anomalously dry conditions from about 30°W to 70°W . Furthermore, upper-level cyclonic flow was present over much of the MDR (Fig. 4.27d). Those factors likely

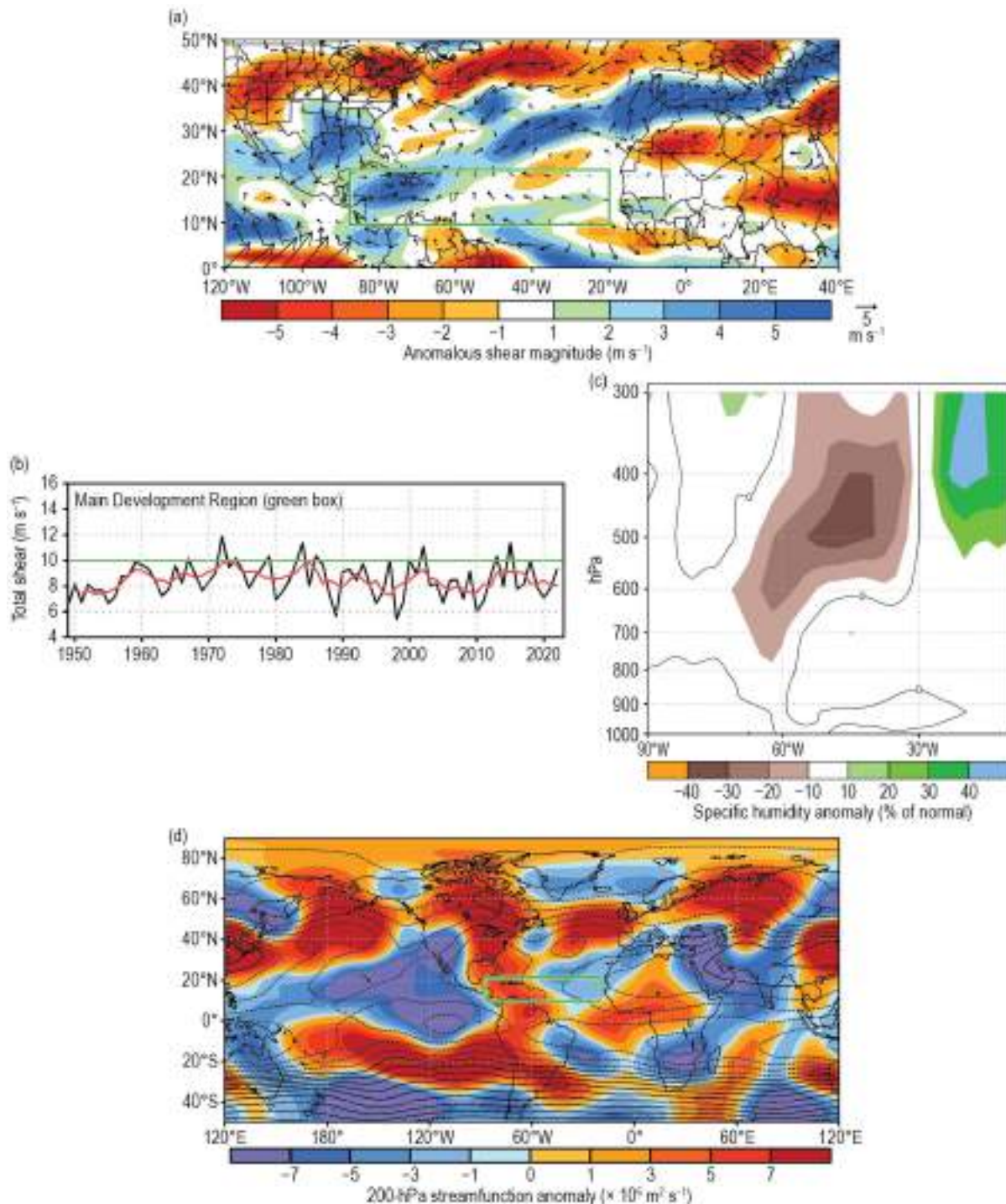


Fig. 4.27. (a) Aug 2022 magnitude of the 200-hPa–850-hPa vertical wind shear (m s^{-1}) showing anomalous magnitude and vector; (b) time series of vertical shear magnitude (black) and 5-yr running mean of the time series (red) averaged over the Main Development Region (MDR; green box in (a)), with the green horizontal line at 10, a critical reference value where shear is thought to inhibit tropical cyclone development on a monthly and seasonal time scales; (c) Aug 2022 MDR specific humidity deviations from normal (percent). Brown (green) shading represents below- (above-) normal values, with the thin black line representing no deviation; (d) Aug 2022 200-hPa streamfunction (contours, interval is $5 \times 10^6 \text{ m}^2 \text{ s}^{-1}$) and anomalies (shaded). (Source: NCEP/NCAR reanalysis [Kalnay et al. 1996].)

inhibited the development of tropical cyclones during August. In September, wind shear in the MDR dropped to 6.7 m s^{-1} (Fig. 4.28b), and specific humidity values returned closer to normal for much of the MDR (Fig. 4.28a).

The higher wind shear during August is not a typical response to La Niña conditions in the Pacific, and is also at odds with the Madden-Julian Oscillation (MJO) activity during late August. The anomalously low upper-level moisture and upper-level streamflow patterns being dissimilar from other low-activity years, where the low levels of activity were linked to tropical-based drivers, points to the likely driver of the high shear and low-upper level moisture being midlatitude influenced. An anomalously strong tropical upper tropospheric trough may correspond to relatively larger contributions from midlatitude influences on the tropical circulation (Klotzbach 2022). Therefore, additional research is required to determine if there was any predictable sub-seasonal forcing for this midlatitude influence.

As is typical during October, wind-shear values and specific humidity values increased significantly over the MDR. Near-normal shear was present near the Bay of Campeche, in the vicinity of where Tropical Storm Karl formed, and over portions of the Caribbean, near where Hurricanes Lisa and Julia developed. Hurricane Nicole developed in an area of extremely low 200-hPa–850-hPa wind shear, 4 m s^{-1} to 5 m s^{-1} below normal, a relatively moist environment, and anticyclonic flow to the north. Those factors likely aided in Nicole's development and westward turn toward the east coast of Florida. Other than the unusually quiet August, September, October, and November behaved more like a typical above-average season.

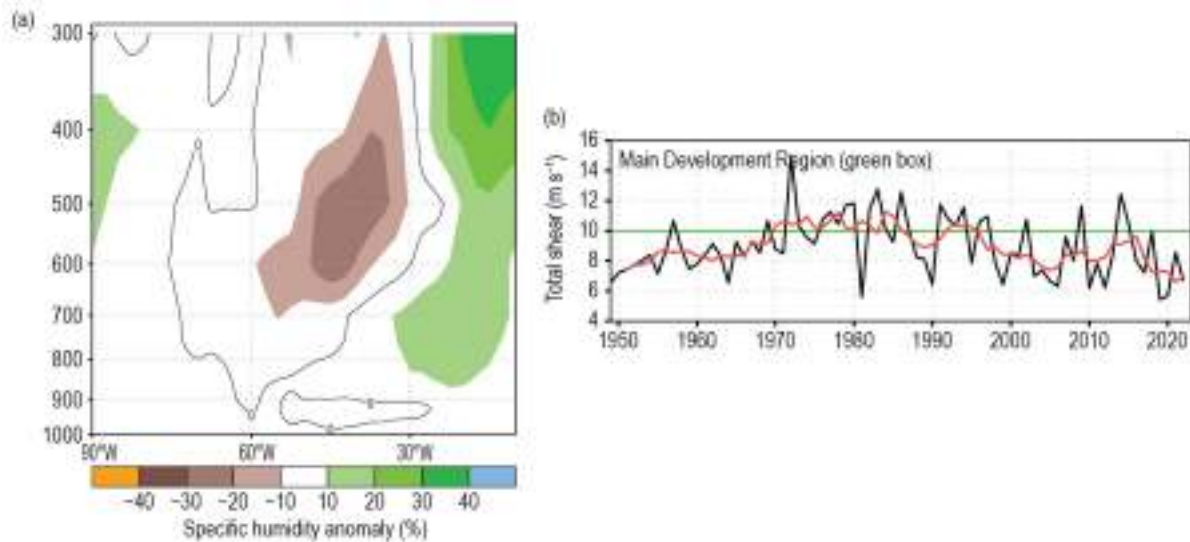


Fig 4.28. Sep 2022 conditions: (a) Main Development Region specific humidity deviations from normal (%). Brown (green) shading represents below- (above-) normal values, with the thin black line representing no deviation; (b) time series of vertical shear magnitude (black) and five-year running mean of the time series (red) averaged over the MDR (green box in Fig. 4.23a). The green horizontal line is at 10, a critical reference value where shear is thought to inhibit tropical cyclone development on a monthly and seasonal time scales.

3. EASTERN NORTH PACIFIC AND CENTRAL NORTH PACIFIC BASINS

—K. M. Wood and C. J. Schreck

(i) Seasonal activity

Numbers in this section are combined from the two agencies responsible for issuing advisories and warnings in the eastern North Pacific (ENP) basin: NOAA's National Hurricane Center in Miami, Florida (for the region from the Pacific coast of North America to 140°W), and NOAA's Central Pacific Hurricane Center in Honolulu, Hawaii (for the region between 140°W and the date line; the Central North Pacific [CNP]).

A total of 19 named storms formed within or crossed into the combined ENP/CNP basin in 2022, 10 of which became hurricanes and 4 became major hurricanes (Fig. 4.29a). This activity is above normal for named storms and hurricanes and near normal for major hurricanes compared

with the 1991–2020 averages of 16.9 named storms, 8.8 hurricanes, and 4.6 major hurricanes. All 2022 storms occurred between the official ENP hurricane season start date of 15 May and end date of 30 November. The first named storm of the season, Hurricane Agatha, developed on 28 May, and the final named storm, Hurricane Roslyn, dissipated on 24 October after making landfall in Mexico as a hurricane. Unusually, 2 of the 19 ENP named storms crossed Central America from the North Atlantic (Bonnie and Julia). No named storms formed within the CNP, but one dissipated about two and a half days after crossing 140°W (Darby), which is well below the 1991–2020 average of 3.4 named storms for the CNP.

Although TC counts were above normal, the 2022 seasonal ACE index was 116.9×10^4 kt², or 88% of the 1991–2020 mean of 132.8×10^4 kt² (Fig. 4.29b; Bell et al. 2000), continuing the streak of below-normal ACE activity that has persisted since 2019 (Fig. 4.29b; Wood and Schreck 2020, 2021, 2022). July TC activity was more than double the usual ACE for the month, contributing 45% of the season’s ACE from five named storms, including two hurricanes (Estelle, Frank) and two major hurricanes (Bonnie, Darby). In contrast, August produced only 6% of the season’s ACE, compared to the climatological average of 29% (Fig. 4.29c). October (16% of ACE) was slightly more active than September (15% of ACE). The four 2022 ENP TCs that reached major hurricane intensity (≥ 96 kt; 49 m s^{-1}) on the SSHWS contributed about 46% of the season’s total ACE: Bonnie, Darby, Orlene, and Roslyn.

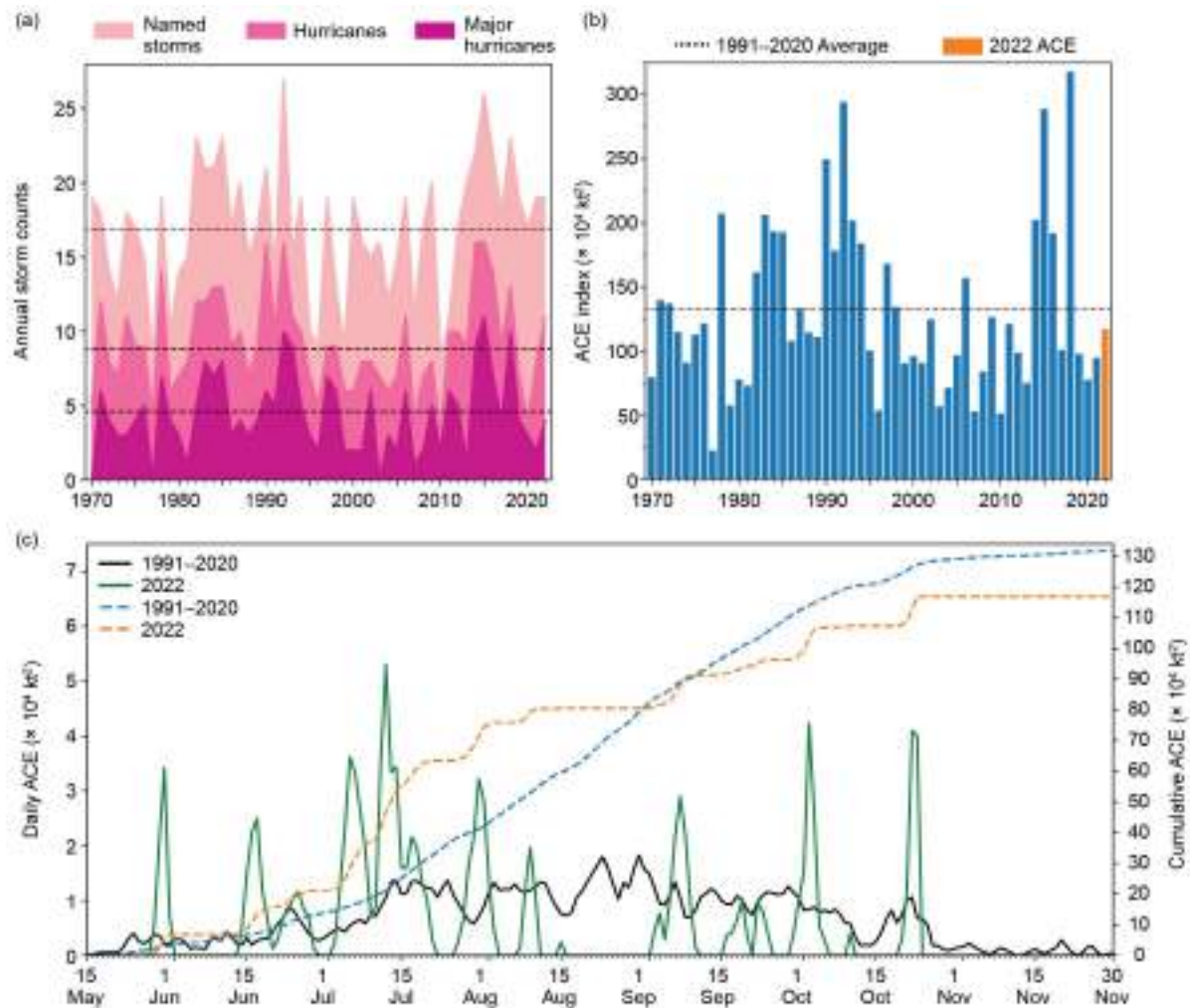


Fig. 4.29. Annual eastern North Pacific (a) storm counts by category during 1970–2022, with the 1991–2020 average by category denoted by each dashed line, and (b) accumulated cyclone energy (ACE) during 1970–2022, with 2022 highlighted in orange and the 1991–2020 average denoted by the dashed line. (c) Daily eastern North Pacific ACE for the 1991–2020 average (solid black) and during 2022 (solid green); accumulated daily ACE for the 1991–2020 average (dashed blue) and during 2022 (dashed orange).

(ii) Environmental influences on the 2022 season

Negative SST anomalies reminiscent of a typical La Niña pattern characterized the equatorial eastern Pacific during the 2022 ENP hurricane season, with co-located easterly 850-hPa wind anomalies between 180°W and 140°W (Figs. 4.30a,d). Storm formations were largely co-located with regions of seasonally near-normal OLR, near-to-above normal SSTs, and below-average vertical wind shear. Despite a broad region of below-average wind shear, TC activity was generally confined to the eastern half of the combined ENP/CNP basin, with only Darby crossing 140°W (Fig. 4.30c). As in 2021, enhanced 850-hPa westerly flow occurred near Central America, potentially supporting the observed clustering of TC activity via enhanced low-level cyclonic vorticity (Fig. 4.30d).

The development and intensity evolution of ENP TCs can be affected by the MJO as well as convectively-coupled Kelvin waves (e.g., Maloney and Hartmann 2001; Aiyyer and Molinari 2008; Schreck and Molinari 2011; Ventrice et al. 2012a,b; Schreck 2015, 2016). A relatively robust MJO signal coincident with a passing Kelvin wave may have contributed favorable conditions for Agatha's development in late May. In addition, the MJO may have supported Lester in

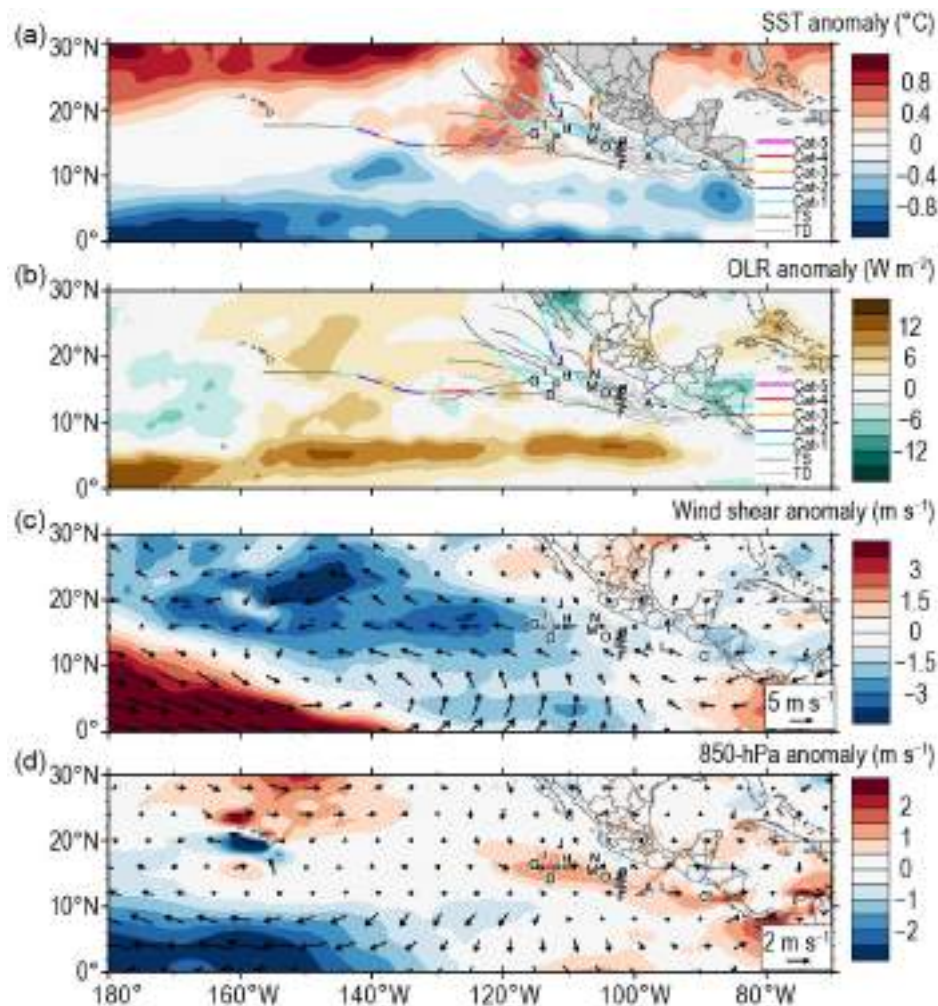
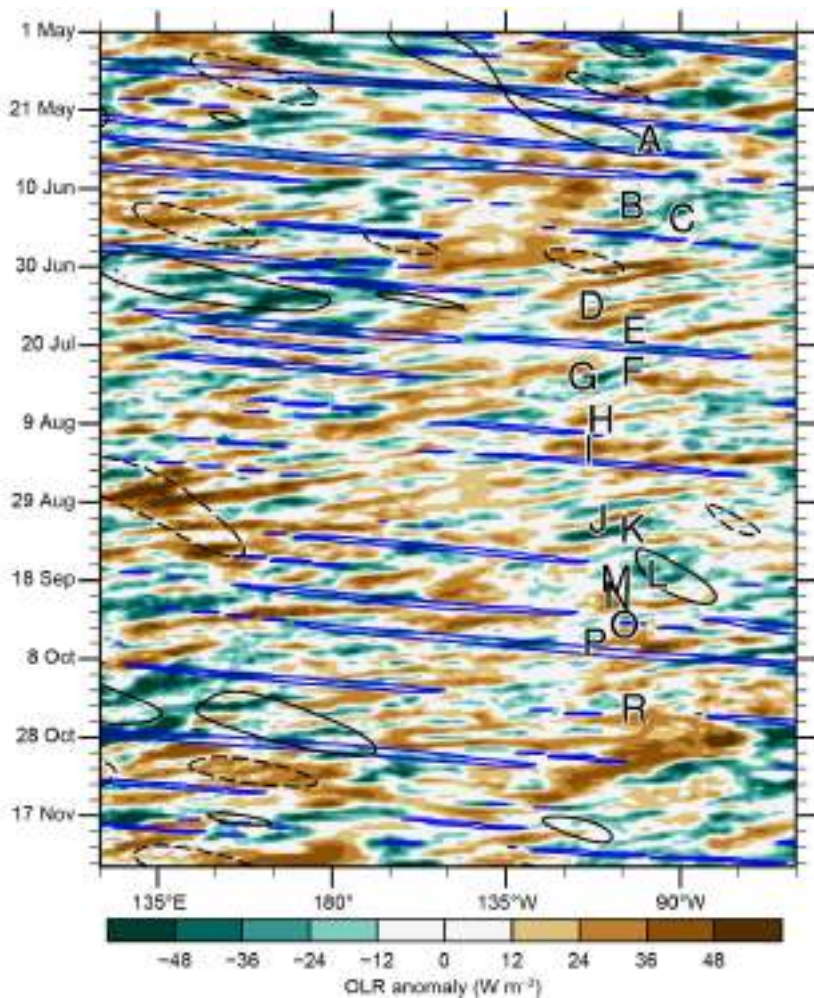


Fig. 4.30. 15 May–30 Nov 2022 anomaly maps of (a) sea-surface temperature (SST; °C; Banzon and Reynolds 2013), (b) outgoing longwave radiation (OLR; $W m^{-2}$; Schreck et al. 2018), (c) 200-hPa–850-hPa vertical wind shear ($m s^{-1}$) vector (arrows) and scalar (shading) anomalies, and (d) 850-hPa wind ($m s^{-1}$, arrows) and zonal wind (shading) anomalies. Anomalies are relative to the annual cycle from 1991 to 2020. Letters denote where each tropical cyclone attained tropical-storm intensity. Wind data are obtained from CFSR (Saha et al. 2014).



September, but otherwise MJO influences appeared relatively weak throughout the season (Fig. 4.31). Kelvin waves traversed the basin on a fairly regular basis, and cyclogenesis is generally favored within three days after a Kelvin wave passage. However, this pattern was not commonly observed in 2022. The formations of Agatha, Frank, and Paine were the most likely to have been influenced by Kelvin waves. Finally, easterly wave activity—which can be inferred from Fig. 4.31 as westward-moving negative (green) OLR anomalies—likely supported many ENP genesis events.

Fig. 4.31. Longitude–time Hovmöller diagram of 5°N–15°N average outgoing longwave radiation (OLR; $W m^{-2}$; Schreck et al. 2018). Unfiltered anomalies from a daily climatology are shaded. Negative anomalies (green) indicate enhanced convection. Anomalies filtered for Kelvin waves are contoured in blue at $-10 W m^{-2}$ and Madden-Julian Oscillation (MJO)-filtered anomalies in black at $\pm 10 W m^{-2}$ (dashed for positive, solid for negative). Letters are centered on the longitude and time when each tropical cyclone attained tropical-storm intensity.

(iii) Notable ENP TCs and impacts in 2022

Hurricane Bonnie, which was first named in the North Atlantic, fell short of the canonical rapid intensification threshold of ≥ 30 kt ($15.4 m s^{-1}$) in 24 hours as it approached its peak intensity of 100 kt but later rapidly weakened while over open ocean (≤ -30 kt or $-15.4 m s^{-1}$ in 24 hours; Wood and Ritchie 2015). Hurricane Darby rapidly intensified with a peak 24-hour intensity increase of 60 kt ($31 m s^{-1}$) prior to reaching its maximum intensity of 120 kt ($62 m s^{-1}$) and then underwent two periods of over-ocean rapid weakening. Hurricane Orlene reached a peak 24-hour intensity increase of 55 kt ($28 m s^{-1}$) before becoming a 115-kt major hurricane; the TC began weakening prior to landfall in southwestern Mexico with an estimated 75-kt intensity. Hurricane Roslyn followed a similar track to Orlene and also reached a peak 24-hour intensity increase of 55 kt ($28 m s^{-1}$) before becoming a 115-kt major hurricane. Compared to Orlene, however, Roslyn maintained more of its strength prior to its estimated 105-kt landfall in the same part of west-central Mexico as Orlene three weeks earlier. Bonnie, Darby, and Roslyn maintained peak intensity for only 12 hours and Orlene just 6 hours. In addition, Orlene and Roslyn were relatively short-lived TCs, factors that contributed to the four strongest TCs contributing less than half of the season's ACE, in contrast to recent seasons (e.g., 2021; Wood and Schreck 2022).

Four ENP TCs in 2022 made landfall along Mexico's west coast: Kay as a tropical storm, Agatha and Orlene as hurricanes, and Roslyn as a major hurricane. A fifth TC, Lester, impacted Mexico but as a tropical depression (Reinhart 2022). In addition, Julia hit Nicaragua from the North Atlantic as a hurricane, crossed Central America, and then made another landfall in El Salvador from the ENP as a tropical storm. Bonnie made landfall near the Nicaragua–Costa Rica border from the North Atlantic as a tropical storm, crossed Central America, and then grew to major hurricane status in the ENP but did not make any additional landfalls. Landfalling ENP TC

activity was higher than normal for Mexico, possibly as a consequence of many TCs forming near land in 2022. On average, 1.8 TCs make landfall per year (Raga et al. 2013).

Hurricane Agatha caused nine deaths attributed to mudslides and freshwater flooding in Mexico, plus six missing people and at least \$50 million (U.S. dollars) in economic losses (Beven 2022; Aon 2023). Hurricane Kay followed an unusual track (see Fig. SB4.3a), maintaining a warm core at relatively high latitudes for the ENP while moving parallel to and eventually making landfall in Baja California, where it delivered heavy rain and strong winds to portions of northwest Mexico and the southwestern United States. The rain and wind associated with Kay resulted in power outages in California as well as relief to fire danger conditions. Tropical Storm Lester caused one death due to large waves, as rainfall from the storm flooded over 400 homes, caused multiple injuries, and required water rescues (Reinhart 2022). Hurricane Orlene rapidly weakened from its peak intensity of 115 kt prior to a 75-kt landfall in western Mexico, causing power outages and some wind damage. Hurricane Roslyn was the strongest landfalling ENP TC since Patricia in 2015 when it made landfall as a Category 3 (105-kt) hurricane. Roslyn resulted in an estimated four deaths and widespread power outages. Hurricane Julia crossed Central America from the Atlantic and then made a second landfall from the Pacific in El Salvador. Overall, Julia caused 89 deaths and hundreds of millions of U.S. dollars in economic damage (Aon 2023; Cangialosi 2023).

4. WESTERN NORTH PACIFIC BASIN

—S. J. Camargo

(i) Overview

The 2022 tropical cyclone (TC) season in the western North Pacific was below normal by most measures of TC activity. The data used here are primarily from JTWC best-track data for 1945–2021, with preliminary operational data for 2022. All statistics are based on the 1991–2020 climatological period unless otherwise noted.

According to the JTWC, a total of 22 TCs (bottom quartile: 23) reached tropical-storm intensity in 2022. Of these, 12 reached typhoon intensity (bottom quartile: 13), with 3 reaching super typhoon status (≥ 130 kt; bottom quartile: 3). There were also 7 tropical depressions (upper quartile: 7). A total of 48% of the tropical storms intensified into typhoons (bottom quartile: 56%), while only 25% of the typhoons reached super typhoon intensity (median: 29%). Figure 4.32a shows the number of storms in each category for the period 1945–2022.

The Japan Meteorological Agency (JMA) total for 2022 was 25 named storms (median: 25.5). As is typically the case, there were differences between the JTWC and JMA counts³. Songda and Trases were considered tropical depressions by JTWC and tropical storms (TSs) by JMA. Kulap and Nalgae were considered typhoons by JTWC but only reached the severe tropical storm category per JMA. JMA included Mulan (8–11 October) as a TS, but this storm was not included by JTWC. The number of all TCs (1951–76) and TSs, severe tropical storms, and typhoons (1977–2022) according to the JMA are shown in Fig. 4.32b. The Philippine Atmospheric, Geophysical and Astronomical Services Administration (PAGASA) named 18 TCs that entered its area of responsibility, including Storms 13W and 25W, which were named Gardo and Obet locally by PAGASA, but were not named by JMA, and Tropical Depression Maymay (8–11 August), which was not numbered or named by either the JMA or JTWC.

(ii) Seasonal activity

The 2022 season started with Tropical Depression 01W at the end of March, followed by Typhoon Malakas and Tropical Storm Megi in April (top quartile: 1). No storms occurred in May. Typhoon Chaba and Tropical Storm Aere formed at the end of June (median: 1). The early season

³ It is well known that there are systematic differences between the JMA and the JTWC and the datasets, which have been extensively documented in the literature (e.g., Knapp et al. 2013; Schreck et al. 2014).

(January to June) had a total of four named storms (median: 4). The cumulative monthly number of named storms and typhoons for 2022 are shown in Figs. 4.32c,e, respectively, with the number of typhoons and super typhoons (>130 kt) per month displayed in Figs. 4.32d,f. In Figs. 4.32c–f, the 2022 values are compared with the climatological values, as well as the historical maxima and minima.

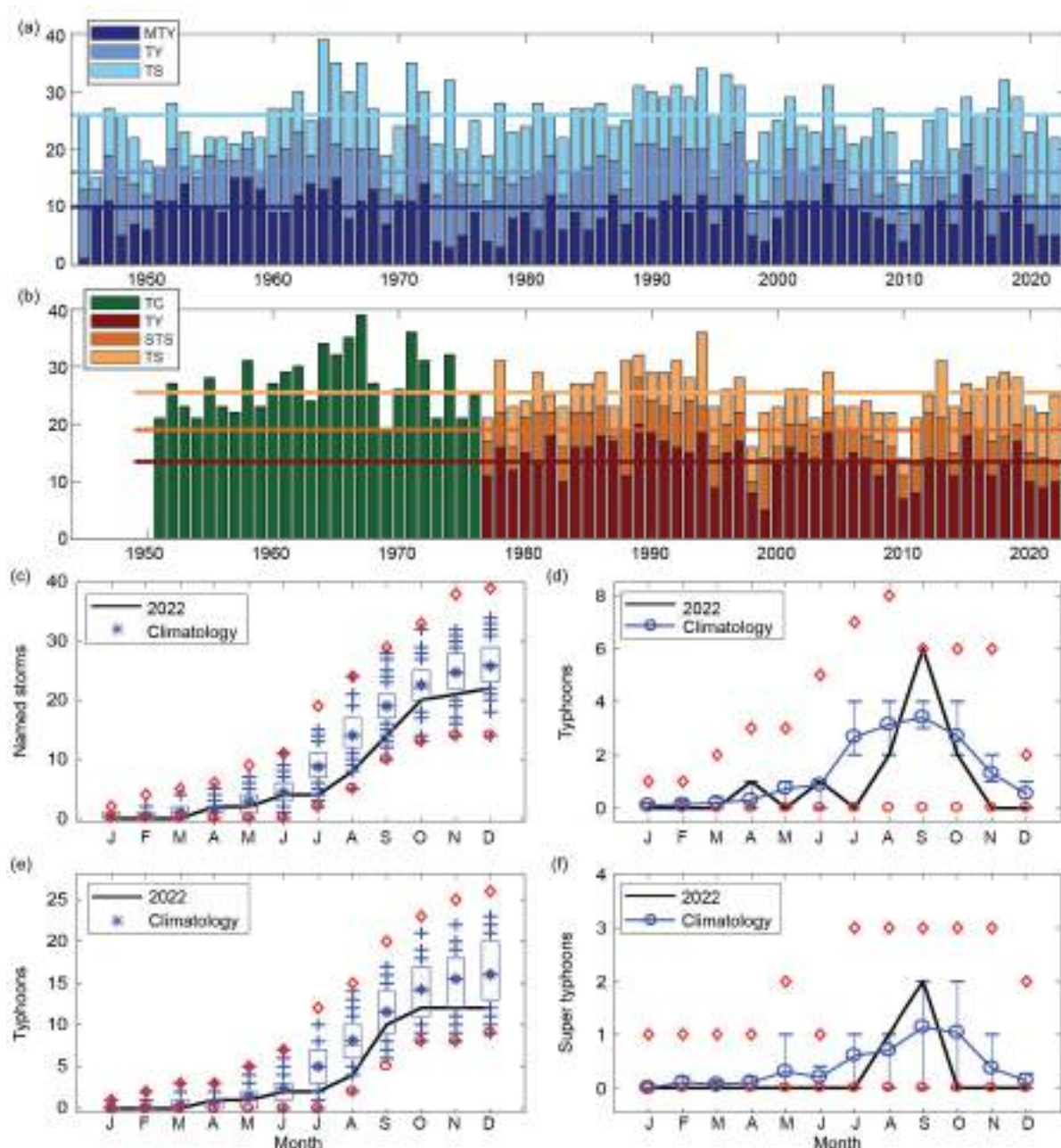


Fig. 4.32. (a) Number of tropical storms (TS), typhoons (TY), and major typhoons (MTY ≥ 96 kt) per year in the western North Pacific (WNP) for the period 1945–2022 based on JTWC. (b) Number of tropical cyclones (TCs; all storms which reach TS intensity or higher) from 1951 to 1976; number of TS, severe tropical storms (STS) and TY from 1977 to 2022 based on JMA. (c) Cumulative number of tropical cyclones with TS intensity or higher (named storms) per month in the WNP in 2022 (black line), and climatology (1991–2020) as box plots (interquartile range: box, median: red line, mean: blue asterisk, values in the top or bottom quartile: blue crosses, high [low] records in the 1945–2021 period: red diamonds [circles]). (e) As in (c) but for the number of typhoons. (d),(f) Number of typhoons and super typhoons (≥ 130 kt) per month in 2022 (black line) and the climatological mean (blue line). The red diamonds and circles denote the maximum and minimum monthly historical records, and the blue error bars show the climatological interquartile range for each month (in the case of no error bars, the upper and/or lower percentiles coincide with the median). (Sources: 1945–2021 JTWC best-track dataset; 2022 JTWC preliminary operational track data for panels (a) and (c)–(f); 1951–2022 Regional Specialized Meteorological Center-Tokyo, Japan Meteorological Agency [JMA] best-track dataset for (b).)

Chaba and Aere, both of which formed in June, were the only active storms in July. TC activity increased in August and was notable for having only four named storms (bottom quartile: 5): Tropical Storms Meari and Ma-On, Typhoon Tokage, and Super Typhoon Hinnamnor. September was the most active month of the season and the only month in 2022 with an above-average level of TC activity, with the occurrence of six typhoons (upper quartile: 4): Muifa, Merbok, Kulap, and Roke, with Nanmadol and Noru reaching super-typhoon intensity (upper quartile: 2). Seven storms formed in October, including four tropical storms, 21W, Sonca, Haitang, and Banyan, and two typhoons, Nesat and Nalgae (named storms, upper quartile: 5; typhoons, bottom quartile: 2).

Similar to the early part of the season, the late season (November and December) was quiet with only two tropical storms, Yamaneko and Pakhar (bottom quartile: 2), neither of which reached typhoon status. Despite the high level of activity in September, the rest of the season had a low number of storms. Overall, the 2022 season was characterized by below-normal levels of activity in the western North Pacific.

The total seasonal ACE in 2022 (Fig. 4.33a) was in the bottom quartile—the seventh lowest in the historical record. The ACE value was in the bottom quartile in the months of January–March, May, July, August, October, and November with zero ACE values in the months of January, February, March, and May, while July, October, and November ACE values were each the seventh or eighth lowest in the historical record. April and September ACE values were in the top quartiles for those months. ACE values in the peak and late season were in the bottom quartile and below the median in the early season. Climatologically, the months of July, August, September, and October contribute 11%, 19%, 23%, and 21% of the total ACE; in 2022, the highest ACE percentage occurred in September (56%), with July, August, and October contributions being low (3%, 18%, and 11%). Low seasonal ACE values are typical during La Niña events in the western North Pacific (Camargo and Sobel 2005), which was the case in 2022. Weaker and short-lived typhoons are characteristic of La Niña, which leads to low ACE values.

Four storms in 2022 had ACE values in the upper range for the climatological distribution of individual storms: Typhoon Noru and Super Typhoons Nanmadol, Muifa, and Hinnamnor. The ACE for Super Typhoon Hinnamnor was in the 99th percentile and contributed 24% of the total seasonal ACE for the basin, with the other three storms jointly contributing 35% of the total.

As is typical of La Niña events, the typhoon activity was shifted to the north-west part of the western North Pacific basin (Chia and Ropelewski 2002; Camargo and Sobel 2005; Camargo et al. 2007a), as seen in the storms' track and

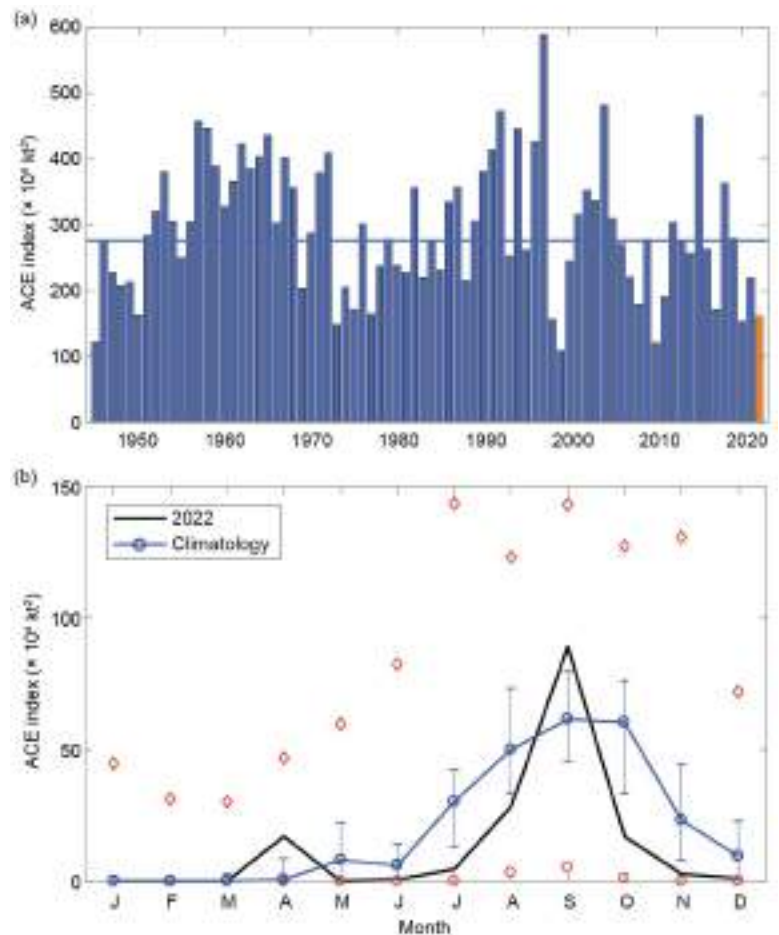


Fig. 4.33. (a) Accumulated cyclone energy (ACE) per year in the western North Pacific for 1945–2022. The solid blue line indicates the median for the 1991–2020 climatology. (b) ACE per month in 2022 (black line) and the median during 1991–2020 (blue line), where the blue error bars indicate the climatological interquartile range. In cases of no error bars, the upper and/or lower percentiles coincide with the median. The red diamonds and circles denote the maximum and minimum values, respectively, per month during the 1945–2021 period. (Source: 1945–2021 JTWC best-track dataset, 2022 JTWC preliminary operational track data.)

genesis locations (Figs. 4.34a,d) and in association with short tracks, weak storms, and low ACE values. The mean genesis position in 2022 was 19.5°N and 135.2°E, northwest of the climatological mean of 13.3°N and 140.5°E. These values are closer to the La Niña mean genesis positions 15.6°N and 136.3°E. Similarly, the mean track position in 2022 (21.5°N, 134.2°E) was northwest of the mean climatological track position (17.8°N, 135.9°E, with standard deviations of 1.6° and 5.2°, respectively).

In 2022, there were only 66.25 days with active named storms (bottom quartile: 86 days), the fifth-lowest number of active days in the historical record. From these active days, 33.25 had typhoons (bottom quartile: 42.7) and 12 days had major (including super) typhoons (SSHWS Categories 3–5; bottom quartile: 15.75). The percentage of active days with typhoons and major typhoons was 38% (median: 37%) and 14% (median: 15%), respectively. The median lifetime for TCs reaching tropical-storm intensity was 3.5 days (bottom quartile: 7 days) and for those reaching typhoon intensity was 6.25 days (bottom quartile: 7.75 days).

The longest-lived storm in 2022 was Typhoon Muifa (9.5 days), followed by Super Typhoon Hinnamnor (9.25 days), Tropical Storm Aere (8.5 days), and Typhoons Malakas (8.25 days) and Nalgae (7.75 days). None of the 2022 storms reached the top quartile of lifetime (10 days), and only the five named storms listed above had a duration above the median (7.25 days). During 13–14 September, three storms were active simultaneously in the basin: Typhoons Muifa, Merbok, and Nanmandol. This was the maximum number of simultaneous western North Pacific named storms in 2022. The record was set on 14–15 August 1996, with a total of six simultaneous named storms.

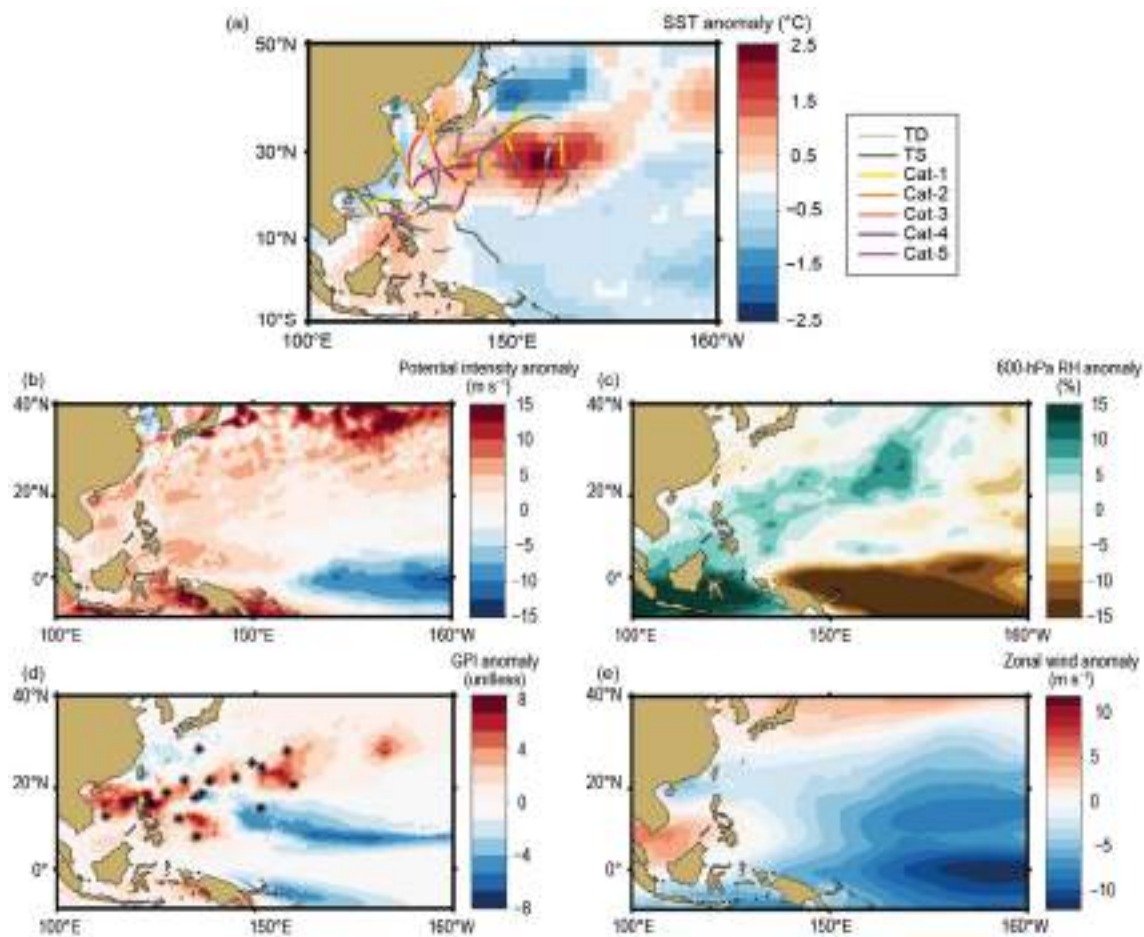


Fig. 4.34. Jul–Oct (JASO) 2022: (a) sea-surface temperature (SST) anomalies (°C) and the tracks of all 2022 storms with colors denoting their intensity; (b) potential intensity anomalies (m s⁻¹); (c) relative humidity 600-hPa anomalies (%); (d) genesis potential index anomalies and first position of JASO 2022 storms marked with an asterisk; and (e) zonal winds at 850 hPa (m s⁻¹). (Data sources: SST: ERSSTv5 [Huang et al. 2017]; other environmental fields: ECMWF ERA5 reanalysis [Hersbach et al. 2020], tracks and first position: JTWC preliminary operational track data.)

(iii) Environmental conditions

Figure 4.34 shows the tracks and environmental conditions associated with the 2022 typhoon season. The persistent La Niña strongly influenced the characteristics of the typhoon season. The SST anomalies (Fig. 4.34a) during the peak typhoon season of July–October (JASO) show a typical La Niña pattern, with below-normal SSTs in the eastern Pacific surrounded by above-normal SSTs. The typhoon tracks occurred in regions with warm SSTs (Fig. 4.34a). The potential intensity anomalies (Emanuel 1988; Fig. 4.34b) had similar characteristics, but with strong negative anomalies more concentrated in the equatorial region, surrounded by weak anomalies. Potential intensity anomalies were positive in the regions of warm SST anomalies.

In the equatorial region, there was a zonal dipole of mid-level relative humidity anomalies (Fig. 4.34c), with drier regions to the east and wetter to the west over the Maritime Continent. This equatorial band of wet anomalies extended poleward from southwest to the northeast, over the regions of positive SST anomalies. The genesis potential index (GPI; Fig. 4.34d; Emanuel and Nolan 2004; Camargo et al. 2007b) expresses the enhanced or reduced probability of TC formation through a nonlinear empirical combination of environmental factors known to affect TC genesis. In 2022, the JASO GPI showed positive anomalies in a southwest-to-northeast-oriented band starting in the South China Sea. These positive GPI anomalies were broadly co-located with areas of positive SST and moist relative humidity anomalies.

The genesis position of most typhoons in JASO 2022 occurred over or near this positive anomaly band. During La Niña events, the monsoon trough (defined by 850-hPa zonal wind anomalies) tends to be restricted to the western part of the basin. In 2022, this was clearly the case, with positive zonal winds anomalies (Fig. 4.34e) restricted to the region from the South China Sea to the Philippines. Many TCs tend to form along the edge of the monsoon trough, as was the case again in 2022. These environmental conditions help explain the low levels of activity in 2022, as only a small area in the western North Pacific had environmental conditions conducive to genesis formation, i.e., high SST, high potential intensity, and anomalously moist mid-level relative humidity during the peak typhoon season.

(iv) Tropical cyclone impacts

Including tropical depressions, 14 storms made landfall in 2022 (median: 17.5, 1961–2020 climatology). Landfall here is defined as when the storm track is over land and its previous location was over the ocean. In order to include landfall over small islands, tracks were interpolated from 6-hour to 15-minute intervals, and a high-resolution land mask was used. In the case of multiple landfalls, we considered the landfall with the highest intensity for each storm. Five storms made landfall as tropical depressions (top quartile: 5) and five as tropical storms (bottom quartile: 8). Four made landfall as typhoons (median: 4): Hinnamnor, Muifa, Nanmadol, and Noru. Noru made landfall as a major typhoon (bottom quartile: 1).

The largest economic impacts in terms of damage in 2022 were caused by Typhoons Hinnamnor (\$1.5 billion U.S. dollars) and Nanmandol (\$3.5 billion U.S. dollars; Gallagher Re 2023). Typhoon Hinnamnor hit Japan, Korea, and the Philippines. It was one of the strongest storms on record for South Korea. Nanmandol primarily affected Japan and Korea, with high rainfall rates that led to flooding. The most fatalities were caused by Tropical Storm Megi (or Agaton, 214 fatalities) and Typhoon Nalgae (or Paeng, 164 fatalities) in the Philippines, according to reports from the National Disaster Risk Reduction and Management Council and ReliefWeb.

5. NORTH INDIAN OCEAN

—C. J. Schreck

(i) Seasonal activity

The North Indian Ocean (NIO) TC season typically occurs between April and December, with two peaks of activity: May–June and October–December, due to the presence of the monsoon trough over tropical waters of the NIO during these periods. Tropical cyclone genesis typically occurs in the Arabian Sea and the Bay of Bengal between 8°N and 15°N. The Bay of Bengal, on average, experiences four times more TCs than the Arabian Sea (Dube et al. 1997).

The 2022 NIO TC season had seven named storms according to JTWC, which was above the IBTrACS–JTWC 1991–2020 climatology of 5.5. Two storms were in the Arabian Sea with the rest in the Bay of Bengal. Only one, Sitrang, became a cyclone, and none became major cyclones. These values were below the climatological averages of 2.2 cyclones and 1.1 major cyclones (Fig. 4.35). The 2022 seasonal ACE index (January–December) of 10.6×10^4 kt² was less than half of the 1991–2020 mean of 24.7×10^4 kt².

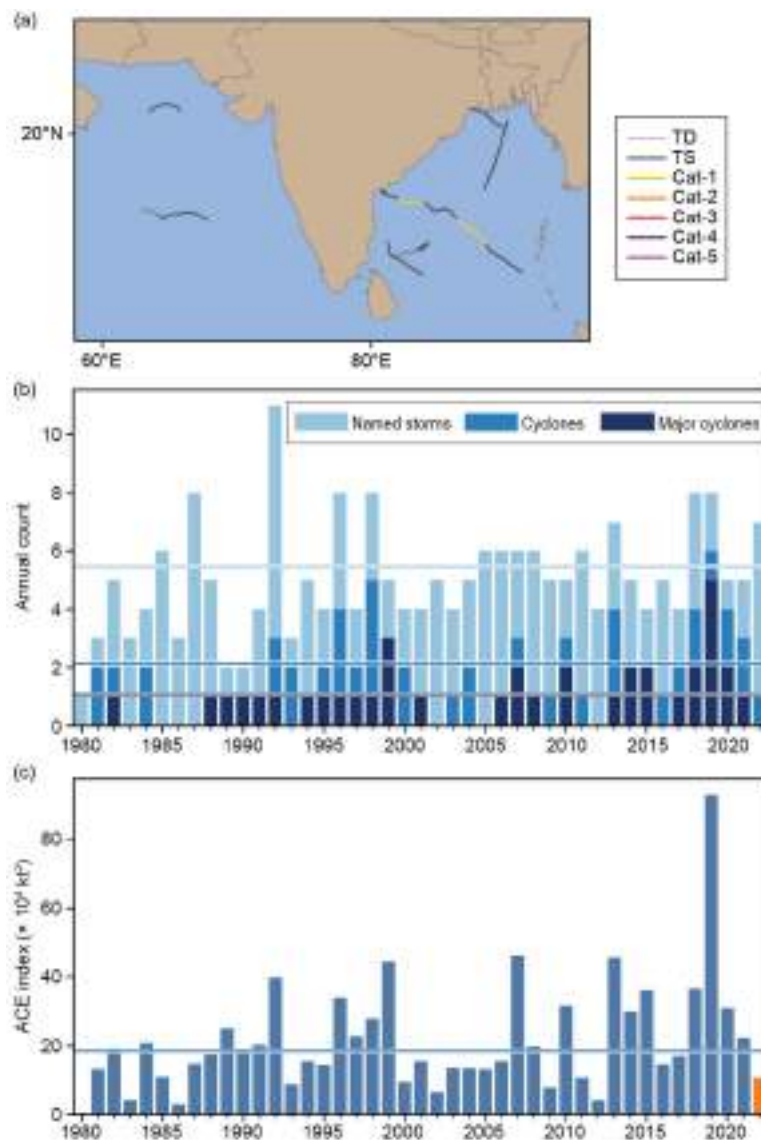


Fig. 4.35. Annual tropical cyclone statistics for the North Indian Ocean basin for 1990–2022: (a) storm tracks for 2022; (b) number of named storms, cyclones, and major cyclones; and (c) accumulated cyclone energy (ACE; $\times 10^4$ kt²). Horizontal lines, representing the 1991–2020 climatology, are included in both (b) and (c).

Indian Ocean dipole conditions, as measured by the Dipole Mode Index, were generally negative during 2022 (section 4f). During the post-monsoon period when three of the named storms occurred, SSTs were cooler in the western Arabian Sea and warmer in the Bay of Bengal (Fig. 4.36a). Convection was enhanced in the Bay of Bengal, where two tropical storms formed (Fig. 4.36b). Vertical wind shear was also below normal northward of 10°N (Fig. 4.36c), and low-level equatorial westerlies enhanced cyclonic vorticity in the basin (Fig. 4.36d). Overall, it was surprising that no storms reached tropical-cyclone strength amid these favorable environmental conditions.

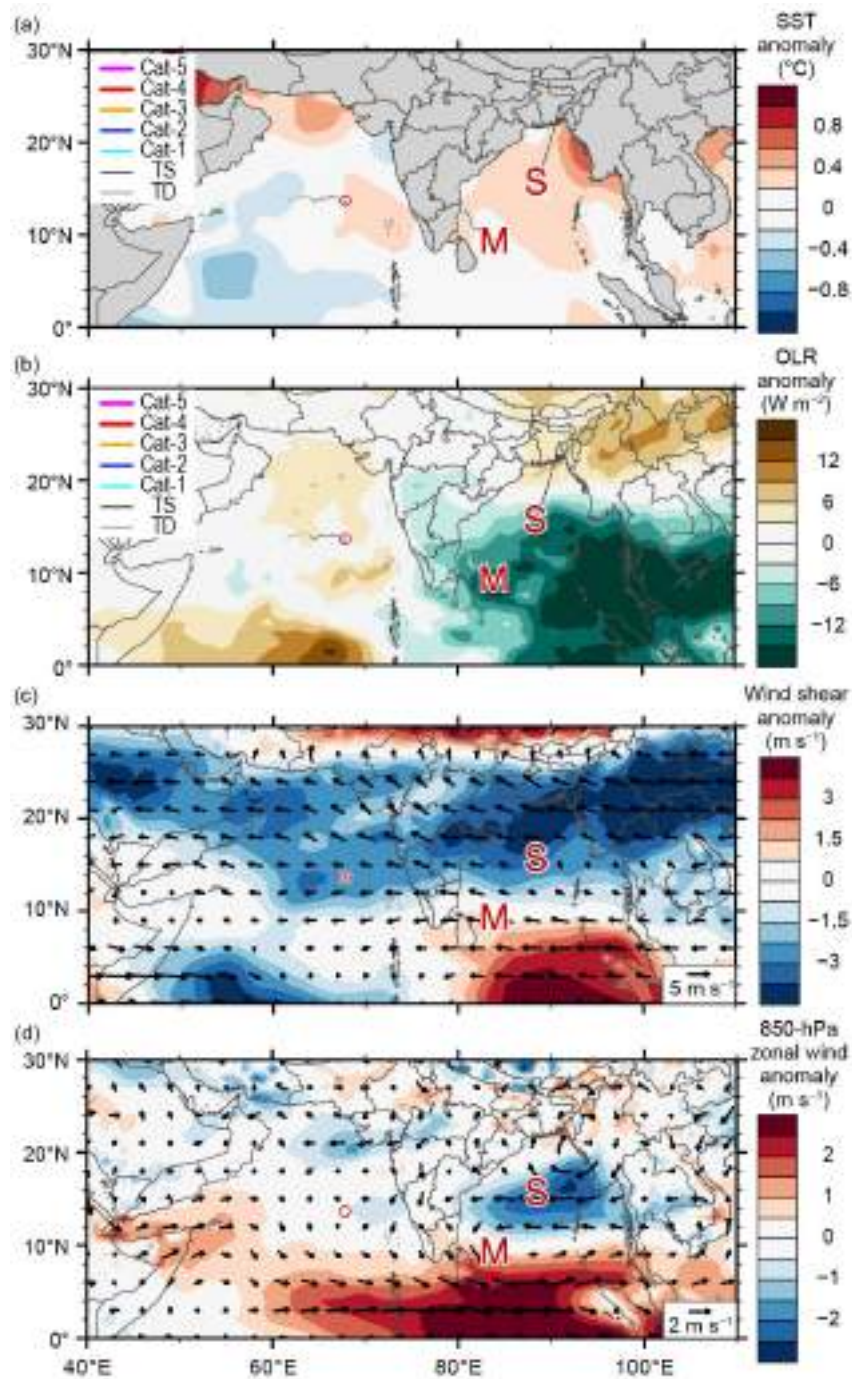


Fig. 4.36. Oct–Dec 2022 North Indian Ocean (NIO) anomaly maps of (a) SST (°C; Banzon and Reynolds 2013), (b) outgoing longwave radiation (OLR; W m⁻²; Schreck et al. 2018); (c) 200-hPa–850-hPa vertical wind shear (m s⁻¹) vector (arrows) and scalar anomalies (shading), and (d) 850-hPa winds (m s⁻¹, arrows) and zonal wind anomalies (shading). Anomalies are relative to the annual cycle from 1991 to 2020. Letter symbols denote where each NIO tropical cyclone attained its initial tropical-storm intensity, and the red circle represents an unnamed tropical storm. (Source: wind data from CFSR [Saha et al. 2014].)

(ii) Individual tropical cyclones and impacts

The North Indian Ocean cyclone season had an early start with an unnamed tropical storm on 4 March. The strongest storm of the season was Severe Cyclone Asani in May. Asani's winds briefly reached Category 1 strength on the SSHWS on two occasions over the Bay of Bengal. However, Asani weakened to a tropical depression before making landfall in eastern India, which limited its impacts.

Tropical cyclones are uncommon during the Indian summer monsoon season, but two tropical storms formed in August: one in the Bay of Bengal and one in the Arabian Sea. Each only lasted for about 24 hours. Only two other years (1979 and 1982) have observed a North Indian Ocean storm during August. This was the first time on record there were multiple storms in August. In the India Meteorological Department best track data, the Bay of Bengal storm persisted as a depression for three days after landfall as it traversed northern India. Its remnants also contributed to severe flooding in Pakistan that inundated nearly 600,000 homes (Aon 2023).

Tropical Storm Sitrang formed in the Bay of Bengal in October. After initially moving westward, the storm made a sharp northward turn that led to landfall in Bangladesh. Its heavy rainfall and flooding damaged or destroyed about 10,000 homes and caused economic damage totaling in the tens of millions of U.S. dollars (Aon 2023).

6. SOUTH INDIAN OCEAN

—A. D. Magee and C. J. Schreck

(i) Seasonal activity

The South Indian Ocean (SIO) TC basin extends south of the equator and from the east African coastline to 90°E. While tropical cyclone activity can occur year-round, the peak season is typically between November and April when the Intertropical Convergence Zone is situated in the Southern Hemisphere. The 2021/22 season includes TCs that occurred from July 2021 to June 2022. Landfalling TCs typically impact Madagascar, Mozambique, and the Mascarene Islands, including Mauritius and La Réunion; however, impacts can be felt in other locations within the region. Below-average storm activity was observed in the SIO basin, with nine named storms according to JTWC, compared to the IBTrACS-JTWC 1991–2020 mean of 10.5 (Fig. 4.37). The five cyclones in 2021/22 were near average (6.1). All five also became major cyclones, which is above the average of 3.5. The 2021/22 season had an unusually late start, with Tropical Storm Ana forming on 23 January: the latest-starting SIO TC since 1998. A record number of named storms (six) made landfall in Madagascar during the season.

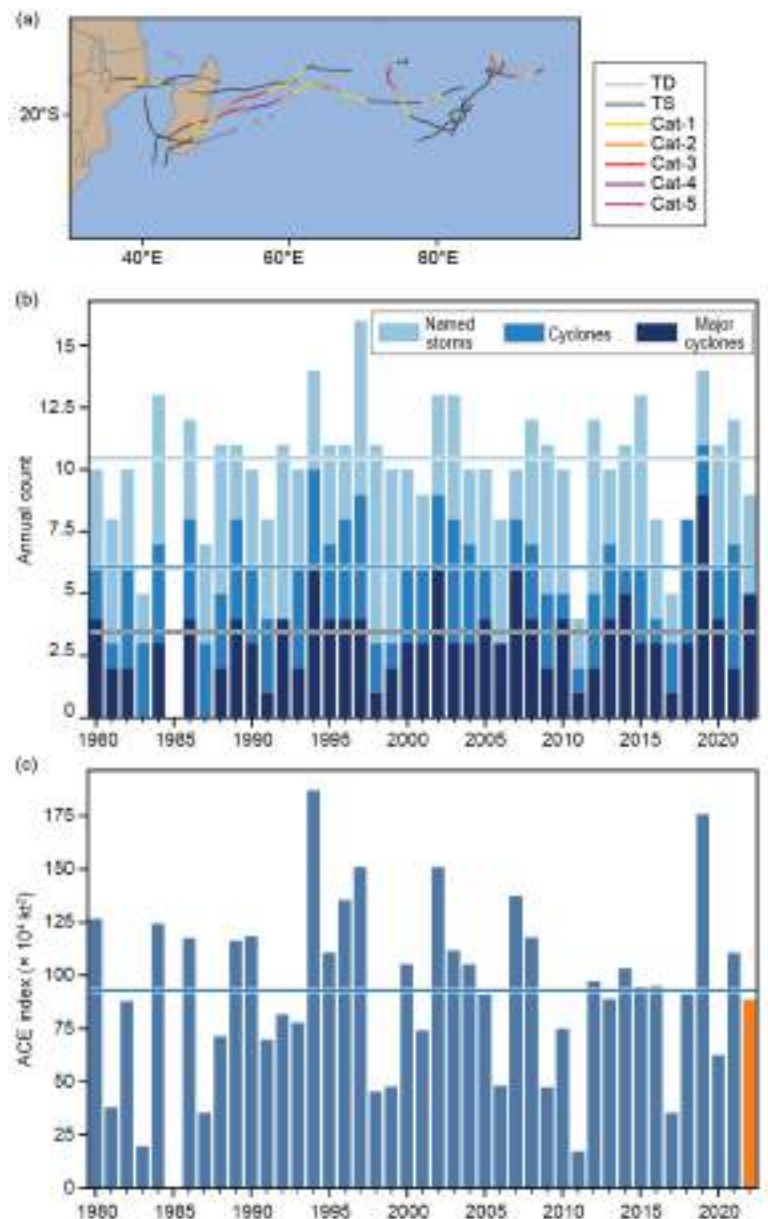


Fig. 4.37. Annual tropical cyclone statistics for the South Indian Ocean basin for 1980–2022: (a) storm tracks for the basin, (b) number of named storms, cyclones, and major cyclones, and (c) accumulated cyclone energy (ACE; $\times 10^4 \text{ kt}^2$). Horizontal lines represent the 1991–2020 climatology.

The 2021/22 seasonal ACE index was $88.8 \times 10^4 \text{ kt}^2$, which is near the 1991–2020 climatology of $94.3 \times 10^4 \text{ kt}^2$. Cyclone-favorable conditions, including anomalously high SSTs towards the east of the basin (Fig. 4.38a) and anomalously weak wind shear across the entire SIO (south of 15°S ; Fig. 4.38c), were present.

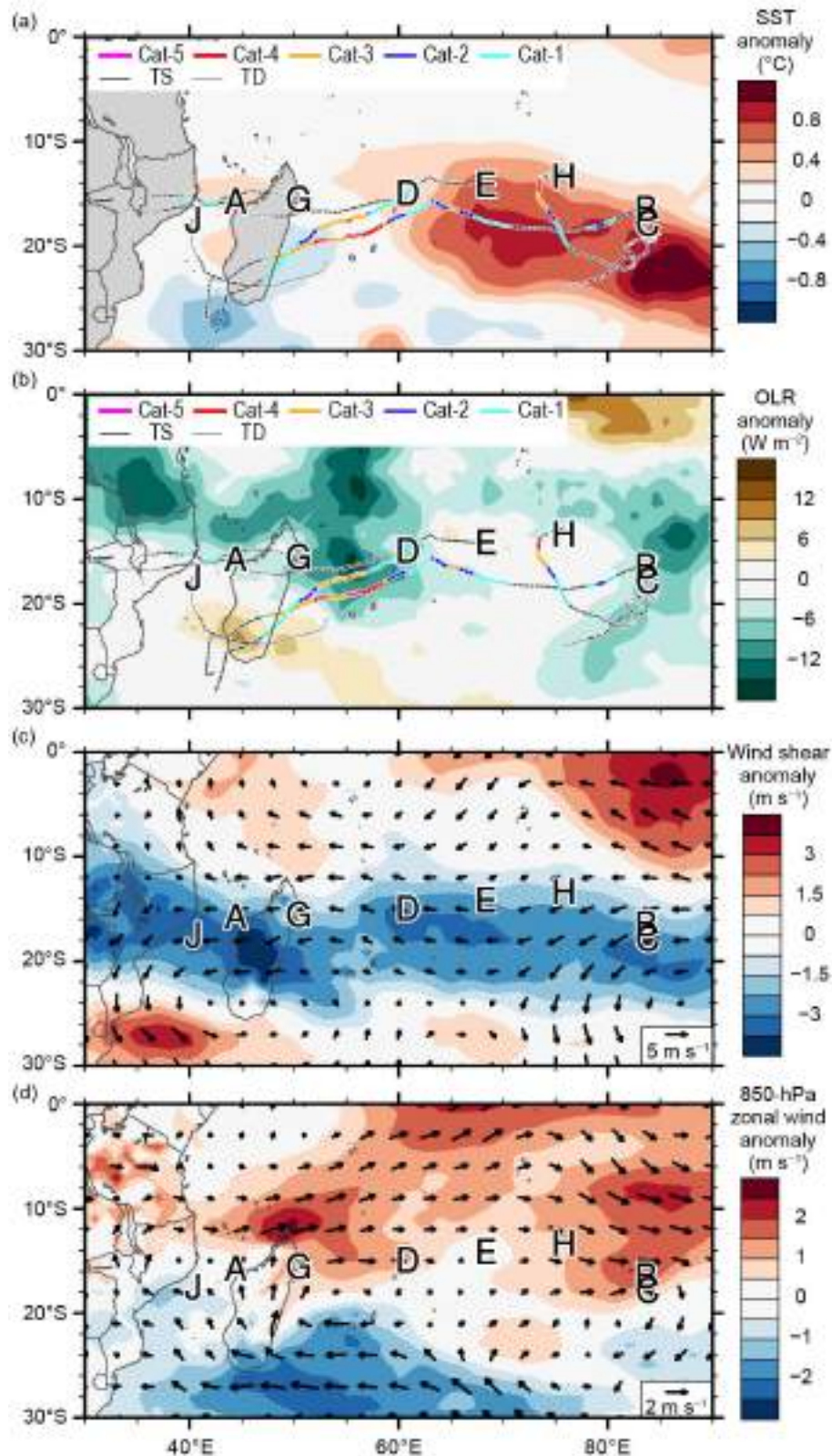


Fig. 4.38. Jan–Apr 2022 South Indian Ocean (SIO) anomaly maps of (a) sea-surface temperature (SST; $^\circ\text{C}$; Banzon and Reynolds 2013), (b) outgoing longwave radiation (OLR; W m^{-2} ; Schreck et al. 2018); (c) 200-hPa–850-hPa vertical wind shear (m s^{-1}) vector (arrows) and scalar anomalies (shading), and (d) 850-hPa winds (m s^{-1} , arrows) and zonal wind anomalies (shading). Anomalies are relative to the annual cycle from 1991 to 2020. Letter symbols denote where each SIO tropical cyclone attained its initial tropical-storm intensity (Source: wind data from CFSR [Saha et al. 2014].)

(ii) Noteworthy TCs and impacts

Tropical Storm Ana formed from an area of convection ~1200 km northeast of Madagascar. The system generally tracked to the southwest and made landfall between Toamasina and Île Sainte-Marie in Madagascar as a tropical depression. Upon entering the Mozambique Channel (24 January), favorable environmental conditions resulted in a peak intensity with maximum sustained winds of 50 kt (26 m s^{-1}) and a minimum central pressure of 993 hPa, which registered as a tropical storm event on the SSHWS. Shortly after, Ana made landfall in Mozambique. Ana reportedly resulted in over 140 fatalities, particularly impacting Madagascar, Mozambique, and Malawi. In Malawi, over 100,000 people were reportedly displaced, and most of the nation lost electricity. In Mozambique, approximately 10,000 houses were destroyed due to impacts associated with Ana.

Severe Tropical Cyclone Batsirai, the second and most intense tropical cyclone of the season, originated from a tropical disturbance in the central Indian Ocean. The compact system underwent periods of intensification and weakening, ultimately intensifying to an intense Category 4 cyclone on 2 February with maximum sustained winds of 125 kt (64 m s^{-1}) and a minimum central pressure of 932 hPa. The system continued to track westward toward Madagascar and made landfall as a Category 3 storm on 5 February near Nosy Varika, becoming the strongest cyclone to make landfall in Madagascar since Severe Tropical Cyclone Enawo in 2017. Batsirai particularly impacted La Reunion, where extreme wind and rainfall resulted in around \$53 million (U.S. dollars) of agricultural losses and widespread power outages across the island. The majority of the impacts were observed in Madagascar, particularly in Nosy Varika. In total, 121 deaths were reported, over 100,000 people were displaced, and 120,000 homes were affected, with damage estimated at \$190 million (U.S. dollars).

Tropical Storm Dumako (13–15 February) and Severe Tropical Cyclone Emnati (16–24 February) also made landfall in Madagascar within 18 days of Batsirai, marking the first time since January 1988 that three storms made landfall in Madagascar in a single month. Emnati initially formed from a tropical disturbance, favorable oceanic (SSTs $\sim 28^\circ\text{C}$) and environmental conditions (low vertical wind shear), which promoted intensification while initially tracking westward and then southwestward towards southern Madagascar. Cyclone Emnati achieved peak intensity as a Category 4 system on the SSHWS, with maximum sustained winds of 115 kt (59 m s^{-1}) and a minimum central pressure of 941 hPa on 20 February. A total of 15 fatalities were reported, and extreme wind, rainfall, and associated flooding caused considerable damage to houses and road infrastructure.

Severe Tropical Cyclone Gombe originated from an area of disturbed weather approximately 500 km from Mauritius and tracked toward the west, where it made landfall across Nampula Province in northern Madagascar as a tropical storm. Upon entering the Mozambique Channel, Gombe intensified to reach a peak intensity of 100 kt (51 m s^{-1}) and a minimum central pressure of 959 hPa, a Category 3 system, on 11 March. Impacts from Gombe resulted in 72 deaths and substantial damage to tens of thousands of homes across Madagascar, Mozambique, and Malawi. Across Mozambique, approximately 500,000 people were impacted and nearly 50,000 homes were destroyed. Thousands of hectares of crops were affected, and widespread power outages were reported across the Nampula province.

Tropical Storm Jasmine (24–27 April) formed from a tropical depression near Comoros and initially tracked towards the southwest, making landfall near Nampula, Mozambique. The system then tracked along the coastline and re-entered the Mozambique Channel, where it intensified, reaching a peak intensity of 55 kt (28 m s^{-1}) and a minimum central pressure of 984 hPa. Jasmine tracked on towards the southeast, making a second landfall across Toliara in Madagascar on 26 April, resulting in three deaths. The storm dissipated on 27 April after re-entering the southern Indian Ocean.

7. AUSTRALIAN BASIN

—B. C. Trewin

(i) Seasonal activity

The 2021/22 TC season was near normal in the broader Australian basin (areas south of the equator and between 90°E and 160°E⁴, which includes Australian, Papua New Guinean, and Indonesian areas of responsibility). The season produced 12 TCs in a season with weak to moderate La Niña conditions. The 1991–2020 IBTrACS-JTWC seasonal averages for the basin are 10.2 named storms, 5.0 TCs, and 2.5 major TCs, which compares with the 2021/22 IBTrACS-based counts of 12, 4, and 1, respectively (Fig. 4.39; Table 4.2), and is consistent with La Niña conditions. There were seven TCs in the western sector⁵ of the broader Australian region during 2021/22, two in the northern sector, and three in the eastern sector. Two TCs (Tiffany and Seth) made landfalls in Australia as tropical cyclones.

(ii) Landfalling and other significant TCs

The major impacts of tropical cyclones in Australia in the 2021/22 season resulted from flooding, most of which occurred from remnant lows well after the systems dropped below tropical-cyclone intensity. Tropical Cyclone Tiffany formed east of Cape York Peninsula and reached tropical-cyclone intensity on 9 January. Maximum sustained 10-minute winds reached 55 kt (28.3 m s⁻¹) early on 10 January, shortly before landfall on the east coast near Cape Melville. The system weakened below cyclone intensity as it crossed Cape York Peninsula but re-intensified after reaching the Gulf of Carpentaria. It made a second landfall on 12 January with 10-minute winds of 50 kt (25.7 m s⁻¹) near Port Roper, on the Gulf's southwest coast. Both landfalls brought limited wind damage, mostly to vegetation. The remnant low initially tracked west across the Northern Territory into the Kimberley region of Western Australia, before turning south on 15 January and moving southeast before dissipating in the far northwest of South Australia on 17 January. Flooding occurred along much of Tiffany's track but was especially significant in the normally arid inland areas of South Australia, with weekly rainfall totals for the 17–23 January period widely exceeding 50 mm and locally exceeding 200 mm. Cortlinye (33.0°S, 136.3°E), near Kimba, had a daily rainfall total of 206.0 mm, a January

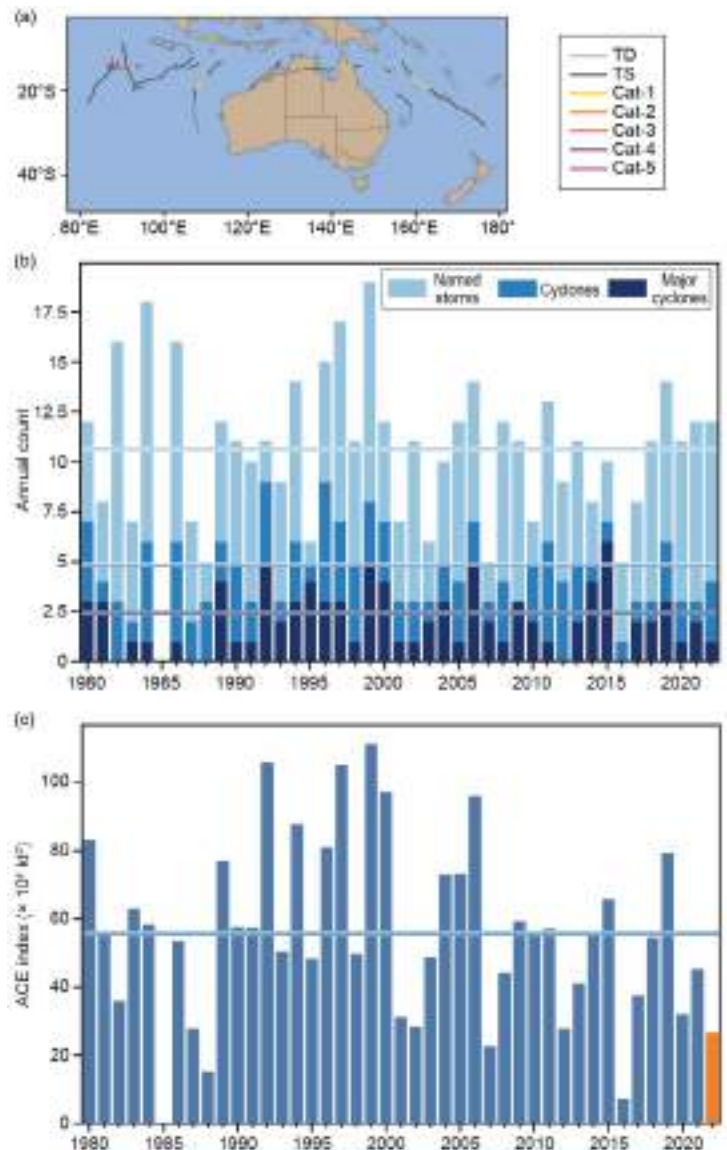


Fig. 4.39. Annual tropical cyclone statistics for the Australian basin for the period 1980–2022: (a) storm tracks for the basin, (b) number of named storms, cyclones, and major cyclones, and (c) accumulated cyclone energy (ACE; × 10⁴ kt²). Horizontal lines represent the 1991–2020 climatology.

⁴ The Australian Bureau of Meteorology's warning area overlaps both the southern Indian Ocean and southwest Pacific.

⁵ The western sector covers areas between 90°E and 125°E. The eastern sector covers areas east of the eastern Australian coast to 160°E, as well as the eastern half of the Gulf of Carpentaria. The northern sector covers areas from 125°E east to the western half of the Gulf of Carpentaria. The western sector incorporates the Indonesian area of responsibility, while the Papua New Guinea area of responsibility is incorporated in the eastern sector. Some cyclones crossed two or more sectors.

record for South Australia. There was severe flooding in places, and the main road and rail links between South Australia and the Northern Territory along with the railway to Western Australia were closed for extended periods.

Tropical Cyclone Seth was a long-lived system, although it only reached tropical-cyclone intensity briefly in the Coral Sea. The precursor low formed north of Darwin on 24 December and tracked east across northern Australia, emerging over the Coral Sea near Cairns on 30 December and reaching tropical-cyclone intensity near 19°S, 15°E on 31 December. After peaking later that day with maximum sustained 10-minute winds of 55 kt (28.3 m s⁻¹), with a maximum gust of 82 kt (42.2 m s⁻¹) at Frederick Reef (20.9°S, 154.4°E), Seth weakened quickly and fell below cyclone intensity by the evening of 1 January. The remnant low turned and moved slowly towards the east coast, reaching the coast near Hervey Bay on 7 January. Extreme rainfall totals occurred to the south of the landfall point, with a number of sites receiving more than 400 mm in 24 hours, the highest total being 674 mm at Marodian (25.9°S, 152.3°E). Major flooding occurred in the Mary and Burnett Rivers, with 30 homes and 50 businesses damaged by floodwaters in Maryborough and two confirmed deaths in the region.

The season's other landfalling system was Anika, which formed in the Timor Sea on 24 February. It reached tropical-cyclone intensity on 25 February and moved south towards the far north of Western Australia, reaching maximum sustained 10-minute winds of 50 kt (25.7 m s⁻¹) before making landfall near Kalumburu late on 26 February. Anika weakened quickly below cyclone intensity over land and tracked generally southwest parallel to the West Kimberley coast, re-emerging over water north of Broome on 1 March and intensifying to regain cyclone intensity on 2 March. It made a second landfall late that day at Wallal Downs, east of Port Hedland, having regained its earlier peak intensity of 10-minute sustained winds of 50 kt. Peak 24-hour rainfall totals included 333 mm at Truscott and 250 mm at Kalumburu on 27 February. Only minor damage was reported along Anika's path, along with some localized flooding.

The two most intense systems of the season were Vernon in late February and Charlotte in late March. Both cyclones were well to the west of Western Australia and did not affect any land areas. Vernon reached 10-minute sustained winds of 100 kt (51.4 m s⁻¹) near 15°S, 91°E on 26 February just before leaving the Australian region, while Charlotte had 10-minute sustained winds of 90 kt (46.3 m s⁻¹) near 17°S, 109°E on 22 March. Neither cyclone had any significant impacts.

Historically, La Niña years have had more TCs in the Australian region (and El Niño years fewer), both in the Pacific and Indian Ocean sectors (Nicholls 1979). However, recent La Niña events have failed to produce high numbers of TCs (although recent El Niños have produced low numbers). Even the strong 2010/11 La Niña was associated with only a near-average number of TCs, although there were also a large number of tropical lows that failed to reach TC intensity. It is unclear whether this is the same El Niño–Southern Oscillation variability superimposed on an overall downward trend or whether other factors are contributing to the La Niña-TC relationship. ACE values for this basin are summarized in Table 4.2.

8. SOUTHWEST PACIFIC BASIN

—A.D. Magee, A. M. Lorrey, and H. J. Diamond

(i) Seasonal activity

The 2021/22 Southwest Pacific tropical cyclone season officially began in November 2021 and ended in April 2022. Data for the season were gathered from the Fiji Meteorological Service, Australian Bureau of Meteorology, and New Zealand MetService, Ltd. The Southwest Pacific basin, defined by Diamond et al. (2012) as 135°E–120°W, experienced a total of seven tropical cyclones, including two severe storms. In addition, there was one out-of-season tropical cyclone that occurred in May.

Figure 4.40 (and Table 4.2) illustrates and documents the tropical cyclone activity in the basin, which spans the area 160°E–120°W to avoid overlap with the Australian basin and double counting of storms. It is important to note that the climatological definition of the Southwest Pacific basin (Diamond et al. 2012) is used for this seasonal description and does not align with WMO-designated boundaries for RSMC or Tropical Cyclone Warning Centre areas of responsibility.

In comparison to the 1991–2020 seasonal average of 9.8 named tropical cyclones, including 4.3 severe storms, as reported by the Southwest Pacific Enhanced Archive for Tropical Cyclones (SPEARTC), the 2021/22 Southwest Pacific tropical cyclone season was considered to be below normal. All winds reported are 10-minute averaged winds as noted in Diamond et al (2012).

(ii) Storm tracks, landfalls, and impacts

Tropical Cyclone Ruby, the first TC of the 2021/22 Southwest Pacific tropical cyclone season, initially formed as a tropical low in the Solomon Sea on 9 December. The low tracked towards the southeast and continued to intensify, eventually achieving peak intensity on 13 December, with maximum winds of 60 kt (31 m s^{-1}) and a minimum central pressure of 975 hPa. Ruby made landfall in New Caledonia, impacting electricity and transportation services across northern Grande Terre. This storm brought 303 mm of rainfall to Riviere Blanche on the southeastern side of the island, with maximum wind gusts of nearly 100 kt (51 m s^{-1}) reported at Poingam.

Severe Tropical Cyclone Cody, the first severe TC for the season, initially formed as a tropical depression to the northwest of Fiji. Strong wind shear in the region briefly inhibited intensification; however, the system organized and achieved Category 1 intensity to the southwest of Viti Levu, Fiji. Cody reached peak intensity of 70 kt (36 m s^{-1}) and a minimum central pressure of 980 hPa on 1 December. Cody resulted in one fatality, while flooding and other storm impacts

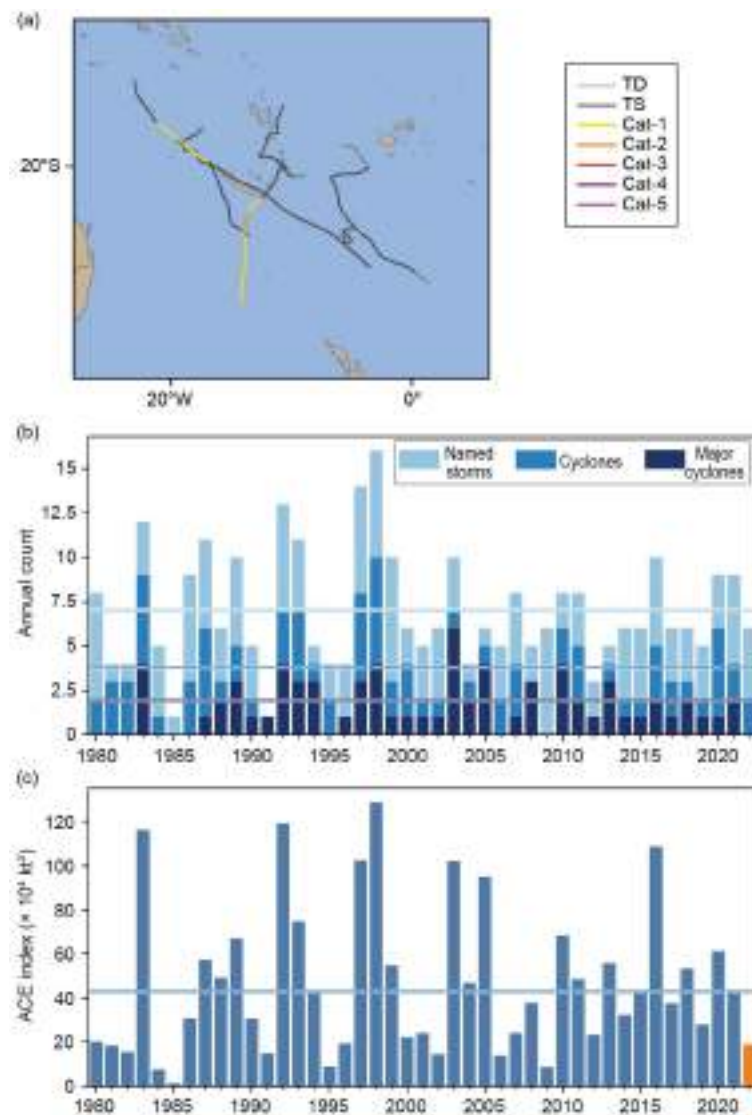


Fig. 4.40. Annual tropical cyclone statistics for the Southwest Pacific basin for the period 1990–2022: (a) storm tracks, (b) number of named storms, cyclones, and major cyclones, and (c) accumulated cyclone energy (ACE; $\times 10^4 \text{ kt}^2$). Horizontal lines represent the 1991–2020 climatology.

displaced approximately 5000 people, who took shelter at numerous evacuation centers across Fiji's Western, Central, and Northern Divisions. Damage in Fiji from Cody was estimated at \$25 million (U.S. dollars).

The season's second severe tropical cyclone, Dovi, originated as a tropical low in the eastern Coral Sea. The system initially tracked eastward towards Vanuatu, slowed, and began to intensify near Southern Vanuatu. On 9 February, the tropical low was named Tropical Cyclone Dovi and tracked to the south as a Category 1 system. As Dovi continued to intensify, it passed off the east coast of New Caledonia as a Category 3 system on 10 February. Dovi reached its peak intensity as an Australian Category 4 storm with sustained winds of 95 kt (49 m s^{-1}) and a minimum central pressure of 940 hPa on 11 February. Dovi then passed west of Norfolk Island and continued to track south, transitioning to a subtropical system as it approached New Zealand. The severe tropical cyclone caused significant flooding and power outages in Vanuatu and New Caledonia. The North Island of New Zealand was severely impacted by Dovi after it became an ex-tropical cyclone, particularly in the Bay of Plenty and Hawke's Bay regions where a significant number of homes were damaged. The strong winds from this decaying system caused power and communication lines to be disrupted, leaving many residents without electricity or phone services. High winds also closed the Auckland Harbour Bridge, which is a main thoroughfare. In addition, the water supply was compromised in the town of Featherston during this storm, and uprooted trees and broken tree limbs resulted in damage to water and road infrastructure. Approximately \$35 million (U.S. dollars) in damage was attributed to Dovi in New Zealand alone.

One out-of-season TC occurred in May: Tropical Cyclone Gina. Forming approximately 400 km northeast of Port Vila, Vanuatu, in an area of favorable oceanic (SSTs around 30°C) and environmental (low-to-moderate vertical wind shear) conditions, the tropical depression continued to intensify as it tracked westward towards Vanuatu. On 18 May, Gina reached maximum intensity of 35 kt (18 m s^{-1}) and a minimum central pressure of 998 hPa and maintained Category 1 intensity for approximately 48 hours, continuing to track towards the southeast. Prolonged and intense rainfall from Gina caused flooding in parts of Vanuatu and resulted in the temporary closure of Port Vila's Bauerfield Airport.

h. Tropical cyclone heat potential

—F. Bringas, G. J. Goni, I-I Lin, and J. A. Knaff

Tropical cyclone heat potential (TCHP; e.g., Goni et al. 2009, 2017) is an indicator of the available heat stored in the upper ocean that can potentially induce tropical cyclone (TC) intensification and regulate ocean-atmosphere enthalpy fluxes and TC-induced sea-surface temperature (SST) cooling (e.g., Lin et al. 2013). TCHP is calculated as the integrated heat content between the sea surface and the 26°C isotherm (D26), which is generally taken to be the minimum temperature required for TC genesis and intensification (Leipper and Volgenau 1972; Dare and McBride 2011).

Provided that atmospheric conditions are favorable, TC intensification, including rapid intensification, has been associated with areas in the ocean that have TCHP values above 50 kJ cm^{-2} (e.g., Shay et al. 2000; Mainelli et al. 2008; Lin et al. 2014, 2021; Knaff et al. 2018, 2020). High SSTs prior to TC formation usually lead to less SST cooling during the lifetime of the TC, and hence higher enthalpy fluxes from the ocean into the storm, which favors intensification (e.g., Lin et al. 2013). Similarly, upper-ocean salinity is another condition of relevance for TC intensification because fresh water-induced barrier layers may also modulate the upper-ocean mixing and cooling during a TC and thus the air-sea fluxes (e.g., Balaguru 2012; Domingues et al. 2015). Upper-ocean thermal conditions observed during 2022 are presented here in terms of two parameters: 1) TCHP anomaly values with respect to their long-term mean (1993–2020) and 2) TCHP anomaly values compared to conditions observed in 2021. TCHP anomalies during 2022 (Fig. 4.41) are computed for June–November in the Northern Hemisphere and November 2021–April 2022 in the Southern Hemisphere. In Fig. 4.41, the seven regions where TCs are known to form, travel, and intensify are highlighted. In all of these regions, TCHP values exhibit large

temporal and spatial variability due to mesoscale features, trends, and short- to long-term modes of variability, such as the North Atlantic Oscillation, El Niño–Southern Oscillation (ENSO), and the Pacific Decadal Oscillation. The differences in TCHP anomalies between 2021 and 2022 are also computed for the primary months of TC activity in each hemisphere (Fig. 4.42).

During 2022, TCHP anomaly conditions were above average for most TC regions and basins, with the exception of the eastern North Pacific, the southern portion of the South Indian, and near the center of the North Atlantic Gyre (Fig. 4.41). In particular, some areas in the North Indian Ocean, western North Pacific Ocean, east and west of Australia, and portions of the North Atlantic Ocean exhibited TCHP anomaly values above 30 kJ cm^{-2} , which are indicative of favorable oceanic conditions for the development and intensification of TCs.

Compared to 2021, TCHP anomalies during 2022 were larger in some regions of the western North Pacific and North Atlantic, most of the Gulf of Mexico, and much of the Southern Hemisphere. They were notably smaller in the central and eastern Pacific. These lower TCHP anomalies during 2022 were associated with the ongoing and stronger negative phase of ENSO (La Niña), prevalent in this region since mid-2021 (Fig. 4.42). In the Southern Hemisphere, TCHP anomalies during 2022 were average or above average, with values above 30 kJ cm^{-2} in small areas in the South Indian Ocean and more extended areas in the southwestern Pacific (Fig. 4.41). TCHP anomalies in 2022 were on average similar to those observed in 2021 in most of the Southern Hemisphere, with most areas showing differences between $\pm 10 \text{ kJ cm}^{-2}$, except for the southwestern Pacific (Fig. 4.42).

In the South Indian Ocean basin, the most intense storm of the season was Batsirai, which after being named on 28 January, underwent several periods of intensification and weakening until experiencing rapid intensification from Category 2 to Category 4 on 2 February, when it reached its peak intensity of 125 kt (64 m s^{-1}) and a minimum central barometric pressure of 932 hPa, while traveling over a region with SST $>27^\circ\text{C}$ and TCHP $>50 \text{ kJ cm}^{-2}$. Similar to Batsirai, Cyclone Gombe underwent rapid intensification on 9 March over a period of 18 hours while traveling over the Mozambique Channel with SST $>30^\circ\text{C}$ and TCHP $>80 \text{ kJ cm}^{-2}$, reaching peak intensity of 110 kt (57 m s^{-1}) and a minimum central barometric pressure of 959 hPa.

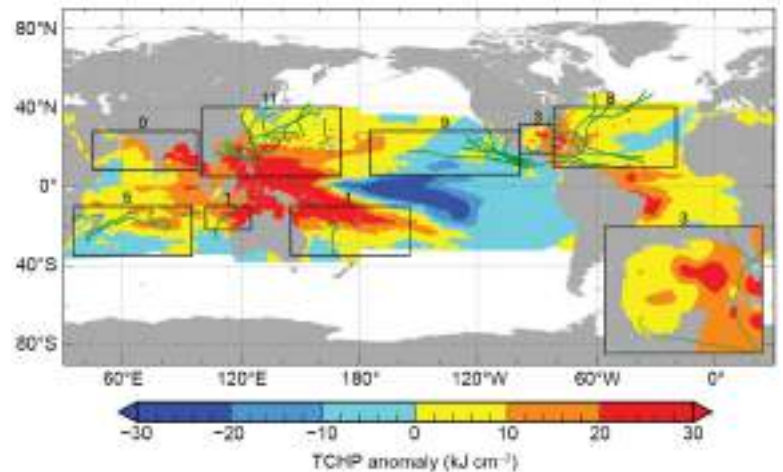


Fig. 4.41. Global anomalies of tropical cyclone heat potential (TCHP; kJ cm^{-2}) during 2022. The boxes indicate the seven regions where TCs occur: from left to right, southwest Indian, North Indian, west North Pacific, southeast Indian, South Pacific, east Pacific, and North Atlantic (shown as Gulf of Mexico and tropical Atlantic separately). The green lines indicate the trajectories of all tropical cyclones reaching at least Category 1 intensity (one-minute average wind $\geq 64 \text{ kt}$, 34 m s^{-1}) and above during Nov 2021–Apr 2022 in the Southern Hemisphere and Jun–Nov 2022 in the Northern Hemisphere. The numbers above each box correspond to the number of Category 1 and above cyclones that traveled within that box. The Gulf of Mexico conditions are shown in the inset in the lower right corner.

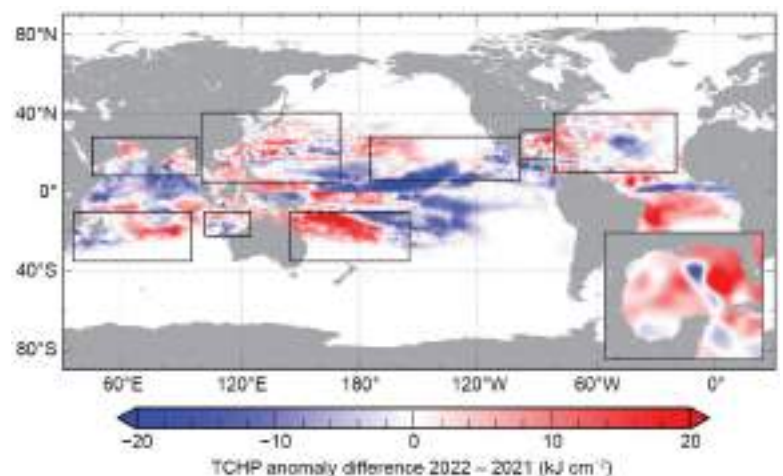


Fig. 4.42. Tropical cyclone heat potential (TCHP) anomaly difference between the 2022 and 2021 tropical cyclone seasons (kJ cm^{-2} ; Jun–Nov in the Northern Hemisphere and Nov–Apr in the Southern Hemisphere). The Gulf of Mexico conditions are shown in the inset in the lower right corner.

Large positive areas of high TCHP anomaly values were observed in the regions east and west of Australia where TCs typically translate. However, in 2021/22, below-average TC activity was observed in these two regions with a total of 10 TCs, of which only 2 reached Category 1 intensity or above.

Similar to the eastern and western Australia regions, the North Indian Ocean experienced above-average TCHP anomalies in excess of 30 kJ cm^{-2} during 2022 in the Bay of Bengal and northern Arabian Sea. No Category 1 or above storms were recorded during June–November (Fig. 4.41), which made for a below-average season in terms of TC intensity. One caveat associated with this result is that almost all TCs forming in this region do so during the pre- and post-monsoon seasons (May–June and October–December).

In the western North Pacific basin, the upper-ocean thermal conditions are largely modulated by the state of ENSO (e.g., Lin et al. 2014, 2020; Zheng et al. 2015). During all of 2022, La Niña was observed in this region with TCHP anomalies that were positive in the western North Pacific, with values well above 30 kJ cm^{-2} closer to the equator and a regional average of approximately 20 kJ cm^{-2} when compared to the long-term mean (Fig. 4.41), as is typical in a La Niña year (Lin et al. 2014; 2020). TCHP anomalies in the western North Pacific were fairly similar in 2021 and 2022, likely due to the predominance of La Niña conditions in both years (Fig. 4.42). Due to the influence of La Niña, TC activity during 2022 was below average for the western North Pacific. Nevertheless, there were two notable super typhoons: Hinnamnor and Nanmadol. Hinnamnor originated and intensified to Category 5 (140 kt; 72 m s^{-1}) over a region of high TCHP ($>60 \text{ kJ cm}^{-2}$), though at relatively high latitudes ($\sim 22^\circ\text{N}$ – 26°N). The storm reached its lifetime maximum intensity (LMI) of 140 kt (72 m s^{-1}) on 30 August. After a short period of intensity fluctuation to ~ 125 kt (64 m s^{-1}), Hinnamnor intensified back to 140 kt on 1 September. The most noteworthy feature in Hinnamnor was its sharp 90° turn in its track that was accompanied by dramatic reduction of its forward motion to near-stationary (i.e., $\sim 1 \text{ m s}^{-1}$ to 2 m s^{-1}) on 1–2 September. As a result of this slowing, a large cold pool was induced and contributed to Hinnamnor's weakening to ~ 75 kt (39 m s^{-1}). Super Typhoon Nanmadol also originated and intensified over areas with TCHP $>50 \text{ kJ cm}^{-2}$, and similarly at a relatively high latitude of $\sim 21^\circ\text{N}$ – 26°N . It reached its LMI of 135 kt (69 m s^{-1}) on 16 September. After LMI, Nanmadol maintained a northwest track while steadily weakening before it made landfall in Japan and affected both Japan and South Korea.

In the North Atlantic basin, upper-ocean thermal conditions during the 2022 hurricane season were characterized by TCHP anomalies larger than the long-term average except in areas of the eastern portion of this region, west of Africa, with values on the western part of the basin of around 20 kJ cm^{-2} on average for most of the region and up to 30 kJ cm^{-2} in smaller areas around Cuba (Fig. 4.41). TCHP anomalies were also positive during 2022 in areas associated with the location of the Loop Current's northern extension in the Gulf of Mexico, where these anomalies were greater than 25 kJ cm^{-2} during 2022 compared to the long-term mean. Differences of $\pm 20 \text{ kJ cm}^{-2}$ between 2022 and 2021 were observed, likely as a result of the variability of ocean currents in the region.

Hurricane Fiona formed during 12–14 September, despite environmental conditions considered to be only marginally favorable. The system became a named storm on 15 September while moving towards the Caribbean Sea region. After becoming a Category 3 hurricane, Fiona traveled over Puerto Rico and the Dominican Republic, where it weakened slightly, but emerged in the tropical North Atlantic and intensified into a Category 4 TC on 21 September. Fiona reached peak intensity of one-minute sustained wind speeds of 115 kt (58 m s^{-1}) and a minimum central barometric pressure of 932 hPa while traveling over a region with SST $>30^\circ\text{C}$ and TCHP $>80 \text{ kJ cm}^{-2}$, which is well above the 50-kJ cm^{-2} threshold required to support Atlantic hurricane intensification (Mainelli et al. 2008).

Major Hurricane Ian, the most intense Atlantic storm in 2022, reached Category 1 intensity on 26 September, and intensified to a Category 3 system while approaching the southwestern tip of Cuba. Ian continued traveling north into the Gulf of Mexico, where on 28 September it

strengthened into a Category 5 hurricane with peak intensity of one-minute sustained wind speeds of 140 kt (72 m s^{-1}) and minimum central barometric pressure of 936 hPa, while traveling over a region with SST $>31^\circ\text{C}$ and TCHP $> 115 \text{ kJ cm}^{-2}$. Ian then made landfall as a Category 4 hurricane in Florida.

In summary, favorable upper-ocean thermal conditions were observed in all TCHP basins during the 2022 season, except in the eastern North Pacific, where conditions were slightly below average compared to the long-term mean. Additionally, TCHP anomaly values during 2022 exhibited generally similar values in most regions compared to the previous year in most basins, with higher values reported in the western North Atlantic and the eastern Australia regions. This translated into above-average hurricane activity in the South Indian region, average activity in the North Atlantic and eastern North Pacific, and below-average activity in the northwest Pacific and North Indian Oceans. Several significant storms, including Intense Cyclones Batsirai and Gombe in the southwestern Indian Ocean, Super Typhoons Hinnamnor and Nanmadol in the western North Pacific, and Major Hurricanes Fiona and Ian in the North Atlantic, Caribbean Sea, and Gulf of Mexico, underwent rapid intensification while traveling over areas with favorable ocean conditions including high TCHP values.

Sidebar 4.1: **Hurricanes Fiona and Ian: A pair of impactful North Atlantic major hurricanes**

—C. FOGARTY, R. TRUCHELUT, AND P. KLOTZBACH

Both major hurricanes that formed during the 2022 Atlantic hurricane season (Fiona and Ian) caused tremendous damage and loss of life. This sidebar details the meteorology and briefly summarizes the impacts that these storms caused. Here we highlight the damage that Fiona caused in the Atlantic Provinces of Canada and that Ian caused in Florida. We also note that Fiona also caused massive flooding damage in Puerto Rico, and Ian caused significant wind and storm surge damage in Cuba. Observed statistics are taken from the National Hurricane Center (NHC)'s Tropical Cyclone Reports on Fiona (Pasch et al. 2023) and Ian (Bucci et al. 2023).

Hurricane Fiona developed from a tropical wave off the coast of Africa, reaching tropical depression status $\sim 8000 \text{ km}$ east of Guadeloupe on 14 September. Later that day, the NHC designated the system Tropical Storm Fiona, and on 18 September an eye formed, with Fiona reaching hurricane status as it approached southwestern Puerto Rico, where it caused heavy flooding and severe power outages. The storm reached major hurricane status on 20 September while traversing the eastern Bahamas. Fiona reached its peak intensity as a Category 4 storm (120 kt ; 62 m s^{-1}) with a minimum pressure as a tropical system of 931 hPa 42 hours later as it tracked just northwest of Bermuda. The pressure rose to 940 hPa after Fiona passed Bermuda, and then the system underwent a volatile extratropical transition process late on 23 September and early on 24 September while still maintaining winds of Category 3 intensity (100 kt ; 51 m s^{-1}). During the early hours of 24 September, Fiona made landfall in

eastern Nova Scotia as a Category 2-force severe post-tropical cyclone with a minimum sea-level pressure of 931 hPa—the lowest ever recorded sea-level pressure of any cyclone over land in Canada. The storm rapidly accelerated as it approached Nova Scotia, then slowed significantly near Cape Breton. Fiona weakened as it moved slowly northward through the Gulf of St. Lawrence on 25 September and into the Labrador Sea. Fiona dissipated by 28 September.

Fiona was the most intense and most destructive tropical or post-tropical cyclone in Atlantic Canada's history. The extratropical transition (ET) was truly remarkable since an approaching upper-level potential vorticity anomaly interacted with the storm while it was still a major hurricane. The cloud and wind field expanded exceptionally quickly, with most of the ET process occurring over a 12-hour period from 1200 UTC on 23 September to 0000 UTC on 24 September. The damage swath of the storm was immense and occurred not just over the eastern (right-of-track) sector, but also over a large region west of the track where, in fact, the highest winds were observed (Fig. SB4.1). These winds were actually from the baroclinic energetics portion of the storm and were more persistent and produced greater storm surge than on the east side. The slow forward motion of Fiona worsened the impacts overall. Trapped-fetch wave growth (Bowyer and MacAfee 2005) east of the track over parts of northern Cape Breton and southwestern Newfoundland caused extensive damage and was responsible for the complete destruction of numerous homes

in the town of Port Aux Basques where an all-time record water level was recorded.

Many have described Fiona as Canada’s version of Superstorm Sandy, which devastated the northeastern United States in 2012. The event was like no other in the modern era

for Atlantic Canada. The closest analog is the 1873 Great Nova Scotia Cyclone, which had a similar track and similar impacts anecdotally. The financial toll was only second to post-tropical storm Hazel in 1954, which brought severe flooding over the populated Toronto region. Total estimated insured costs

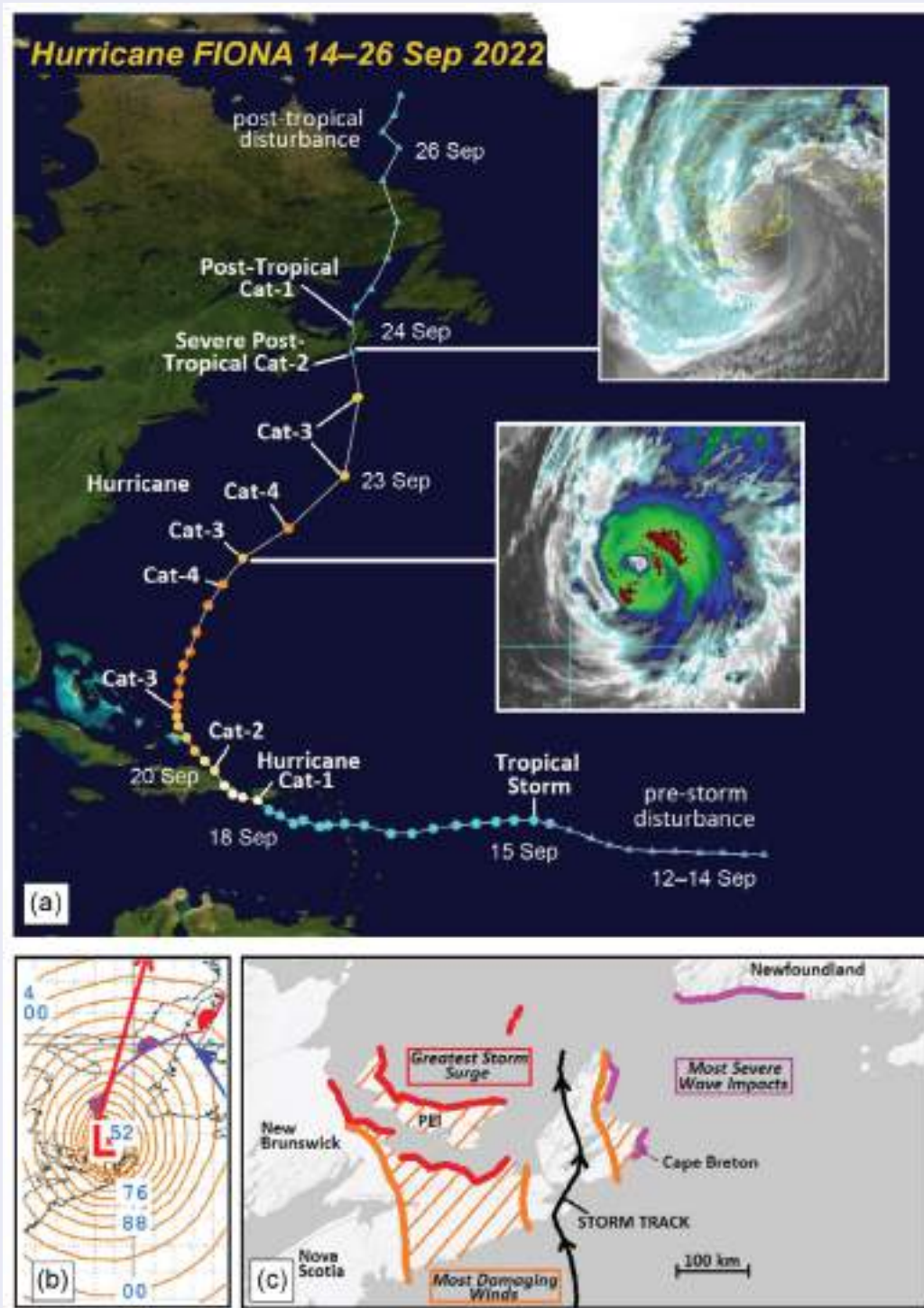


Fig. SB4.1. (a) Track of Hurricane Fiona at 6-hr intervals with select milestones labeled along the track. Triangles denote pre- and post-tropical phases. Two enhanced infrared GOES-16 satellite insets 24 hours apart show the rapid transformation of Fiona from tropical to post-tropical. (b) Sea-level pressure analysis (every 4 hPa, select contour labels marked, e.g., 52 = 952 hPa) from NOAA’s Ocean Prediction Center five hours after landfall. Minimum central pressure was ~940 hPa. Direction of travel shown by red arrow. (c) Highlighted regions in Atlantic Canada where the most significant storm impacts were observed.

from Fiona were \$800 million (Canadian dollars) as of early 2023, while Hazel’s insured losses were estimated to be near \$1.4 billion (Canadian dollars, adjusted to 2022).

While Fiona was moving northward towards Nova Scotia early on 23 September, Ian became a tropical depression in the eastern Caribbean Sea and grew to a minimal tropical storm by 0000 UTC on 24 September. Ian moved west-northwestward with little change in strength for the next two days. Upon entering a favorable thermodynamic and outflow environment in the western Caribbean late on 25 August, Ian’s maximum sustained winds rapidly intensified from 40 kt (21 m s^{-1}) to 110 kt (57 m s^{-1}) in the ~40 hours prior to initial landfall in western Cuba at 0830 UTC on 27 September. An eyewall replacement cycle occurred during that afternoon and evening as Ian turned north across the southeastern Gulf of Mexico, with a second period of rapid intensification from 105 kt (54 m s^{-1}) to Ian’s peak intensity as a Category 5 hurricane with 140 kt (72 m s^{-1}) sustained winds occurring between 0000 and 1200 UTC on the 28th. Maximum winds weakened slightly due to increasing vertical wind shear prior to landfall as a 130 kt (67 m s^{-1}) Category 4 hurricane at 1900 UTC near Cayo Costa in southwest Florida. Ian weakened to a tropical storm over central Florida early on 29 September, then moved offshore and re-strengthened to a Category 1 hurricane later that day as it turned north. The hurricane made a second U.S. landfall near Georgetown, South Carolina, with 75-kt (39-m s^{-1}) sustained winds around 1800 UTC on 30 September. Shortly thereafter, Ian underwent extratropical transition.

Ian stands in the upper echelon of Florida’s worst historical hurricanes. Its maximum sustained winds at initial landfall were Florida’s fourth strongest on record and equaled those of Hurricane Charley, which struck nearly the same location in 2004. However, Ian exceeded Charley in scope of sensible impacts, as surge, winds, and rain each caused widespread destruction across southwest and central Florida. Peak storm surge of 4 m to 5 m occurred in coastal Lee County (Fig. SB4.2, left panel), leveling portions of Fort Myers Beach and causing significant coastal flooding across parts of Charlotte, Collier, and Monroe Counties. Catastrophic wind gusts exceeding 120 kt (62 m s^{-1}) were observed in Lee and Charlotte Counties as the inner eyewall moved inland, with damaging gusts of 55 kt–70 kt (28 m s^{-1} to 36 m s^{-1}) affecting central Florida and coastal northeast Florida.

Ian’s forward speed of 7 kt (4 m s^{-1}) as it crossed the Florida peninsula led to extensive flash and river flooding. As shown in Fig. SB4.2 (right panel), storm-total precipitation along and east of the Interstate 4 corridor totaled 300 mm–500 mm, breaking numerous all-time one- and three-day rainfall records in southwest and central Florida and inundating the low-lying St. Johns and Peace River basins for several months. The severity of coastal and inland flooding resulted in 156 confirmed U.S. fatalities, making Ian Florida’s deadliest hurricane since 1935. Total economic losses from Ian are estimated by NOAA’s National Centers for Environmental Information to be \$114 billion (U.S. dollars), making it the third-costliest Consumer Price Index-adjusted U.S. hurricane on record and the most expensive in Florida’s history.

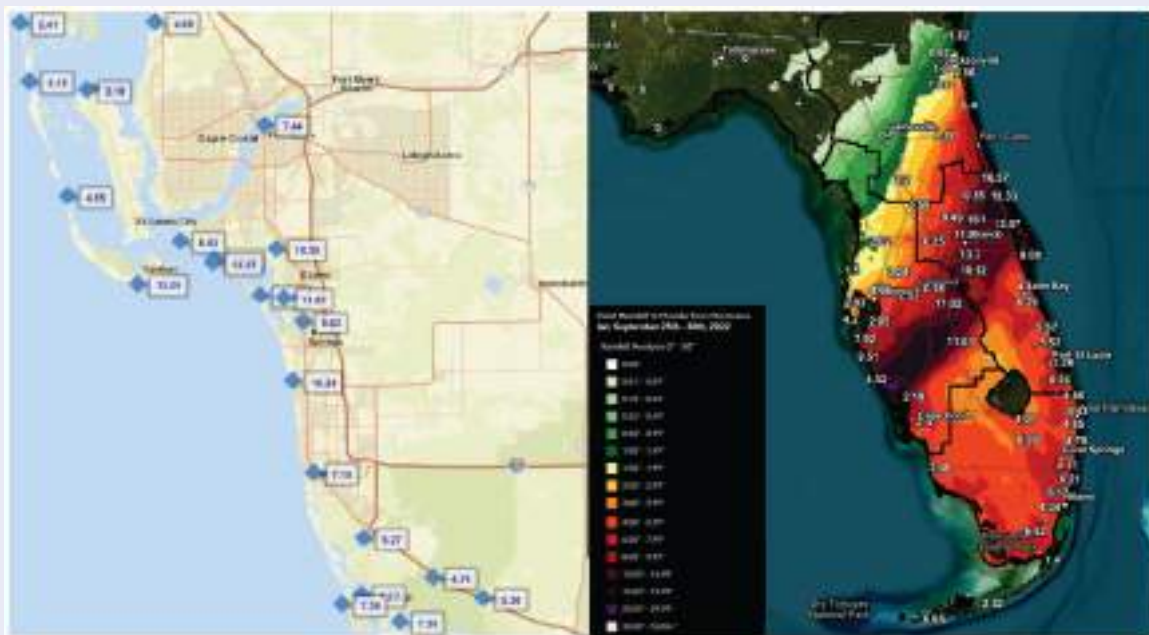


Fig. SB4.2. Hurricane Ian (left) peak inundation levels relative to North American Vertical Datum of 1988 from the United States Geological Survey Flood Event Viewer (Bowyer and MacAfee 2005) for southwest Florida and (right) storm total rainfall estimates (inches). Right panel courtesy of NWS Melbourne, Florida.

Sidebar 4.2: Tropical cyclone contributions during the 2022 North American monsoon

—K. M. WOOD

Overall, the 2022 North American monsoon (NAM) season, which is defined as the period 15 June–30 September, produced less rainfall than the near-record setting 2021 season (<https://www.weather.gov/psr/2021MonsoonReview>). However, many locations received rainfall above the 75th percentile from 1991 to 2020 according to the Parameter-elevation Relationships on Independent Slopes Model (PRISM; Daly et al. 2008) precipitation data. Eastern locations saw rainfall earlier than western locations, and an active period of rain occurred in Arizona during late July into August (Fig. SB4.3b). Tropical cyclone (TC) activity near northern Mexico and the southwestern United States may have influenced some of this rainfall, such as Hurricane Kay which brought rain and wind to California in a rather unusual event for the state (Fig. SB4.3a).

To examine TC activity that may have impacted rainfall during the NAM, we focus on the region north of 20°N and

between 120°W and the western North American coastline. Compared with the 1991–2020 average, 2022 had nearly 112% of the typical accumulated cyclone energy (ACE) for this region during 15 June–30 September and about 129% of the typical named storm days in a season that overall produced 88% of the average ACE (see section 4g3). It was the highest ACE for this region since 2016. Of the five TCs that spent at least 24 hours within this region, Kay showed the strongest apparent influence on subsequent rainfall across much of the southwestern United States following a dry period (Fig. SB4.3), corroborated by geostationary satellite imagery (not shown). Though Tropical Storm Madeline remained relatively far south, its passage near the southern end of Baja California was accompanied by a northward surge of moisture that may have supported subsequent rainfall. In summary, the TC season likely had a strong influence on the NAM season.

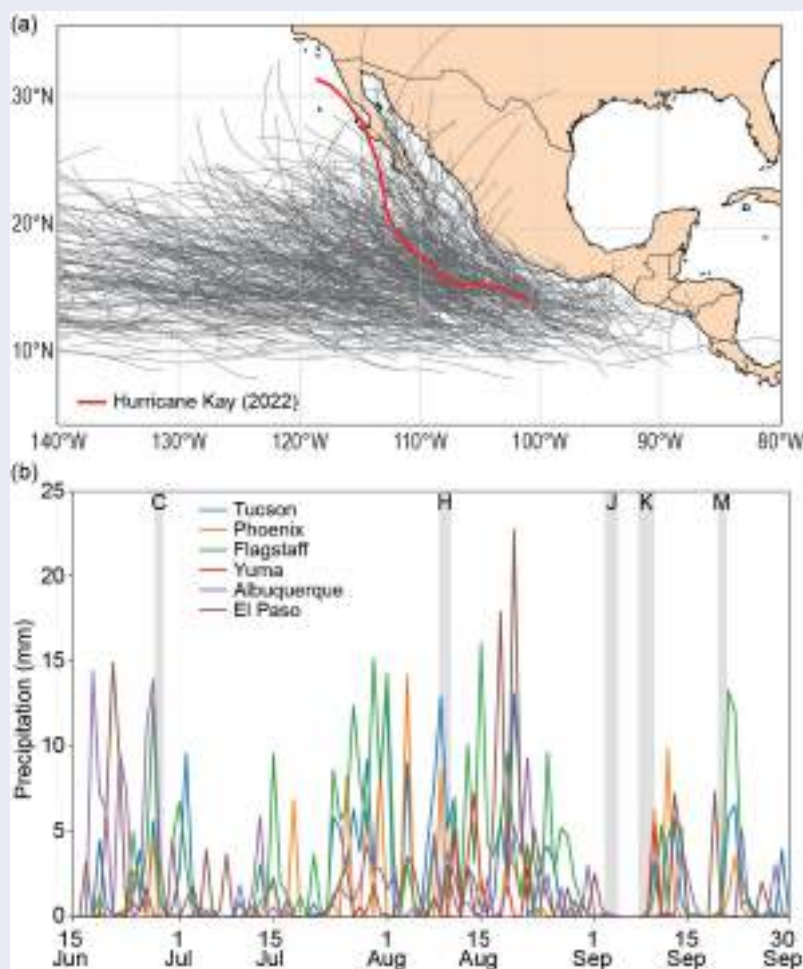


Fig. SB4.3. (a) Track of all eastern North Pacific tropical cyclones from 1991 to 2020 with Hurricane Kay's track highlighted in red. (b) Daily PRISM precipitation averaged within 25 km of Tucson (blue), Phoenix (orange), Flagstaff (green), Yuma (red), Albuquerque (violet), and El Paso (brown). Gray shading indicates times during which a tropical cyclone existed for at least 24 hours within the region north of 20°N and between 120°W and the North American coastline labeled by the first letter of each storm: Celia, Howard, Javier, Kay, and Madeline.

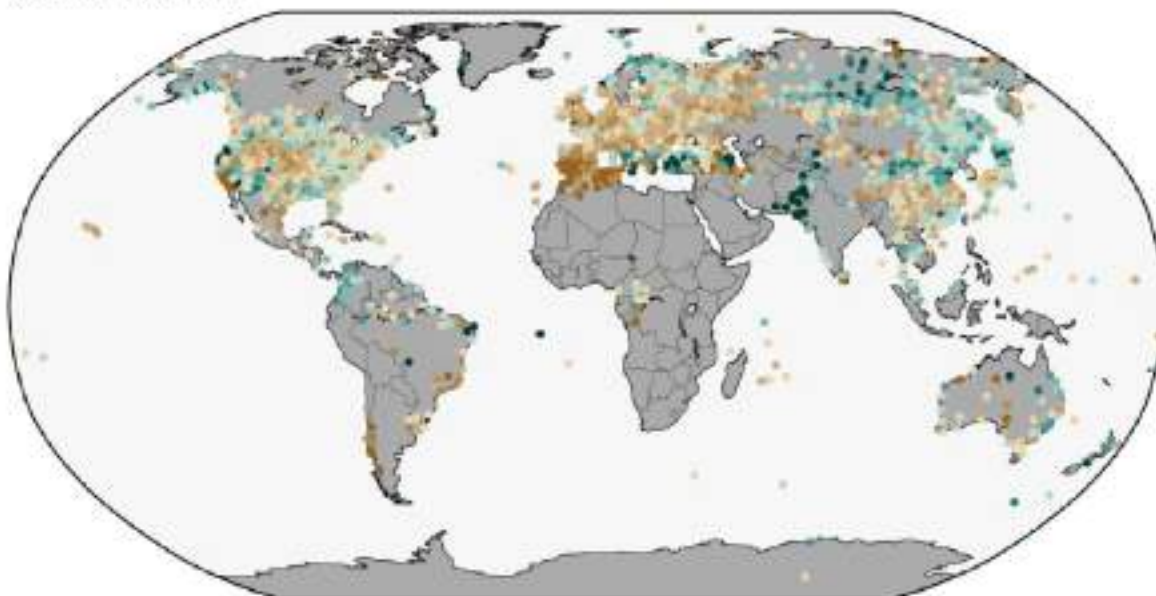
Appendix 1: Chapter 4 – Acronyms

ACE	accumulated cyclone energy
AMO	Atlantic Multi-decadal Oscillation
ASO	August–October
CNP	central North Pacific
CPC	Climate Prediction Center
D26	26°C isotherm
DJF	December–February
ENP	eastern North Pacific
ENSO	El Niño–Southern Oscillation
ERSST	Extended Reconstructed Sea Surface Temperature version 5
ET	extratropical transition
GPI	genesis potential index
HTC	hurricane/typhoon/cyclone
HTHH	Hunga Tonga-Hunga Ha’apai
HURDAT2	Hurricane Database
IBTrACS	International Best Track Archive for Climate Stewardship
IO	Indian Ocean
IOB	Indian Ocean basin
IOD	Indian Ocean dipole
IODE	eastern Indian Ocean dipole
IODW	western Indian Ocean dipole
ITCZ	Intertropical Convergence Zone
JAS	July–September
JASO	July–October
JJA	June–August
JJAS	June–September
JMA	Japan Meteorological Agency
JTWC	Joint Typhoon Warning Center
LMI	lifetime maximum intensity
LMR	land monsoon rainfall
MAM	March–May
MDR	Main Development Region
MJO	Madden-Julian Oscillation
MSLP	mean sea-level pressure
MSWEP	Multi-Source Weighted-Ensemble Precipitation
MTY	major typhoon
NAM	North American monsoon
NH	Northern Hemisphere
NHC	National Hurricane Center
NIO	North Indian Ocean
NOAA GlobalTemp	NOAA Global Surface Temperature Analysis
OISST	Optimum Interpolation Sea Surface Temperature
OLR	outgoing longwave radiation
ONI	Oceanic Niño Index
PAGASA	Philippine Atmospheric, Geophysical and Astronomical Services Administration
PRISM	Parameter-elevation Relationships on Independent Slopes Model
RMM	Real-time Multivariate Madden-Julian Oscillation
RSMC	Regional Specialized Meteorological Center
SAM	Southern Annular Mode

SH	Southern Hemisphere
SIO	South Indian Ocean
SON	September–November
SPCZ	South Pacific Convergence Zone
SPEARrTC	Southwest Pacific Enhanced Archive for Tropical Cyclones
SSHWS	Saffir-Simpson Hurricane Wind Scale
SST	sea-surface temperature
STS	Severe Tropical Storm
TC	tropical cyclone
TCHP	tropical cyclone heat potential
TS	tropical storm
TY	typhoon
WMO	World Meteorological Organization
WNP	western North Pacific

Appendix 2: Chapter 4 – Supplemental Materials

(a) Jun–Aug 2022



(b) Sep–Nov 2022

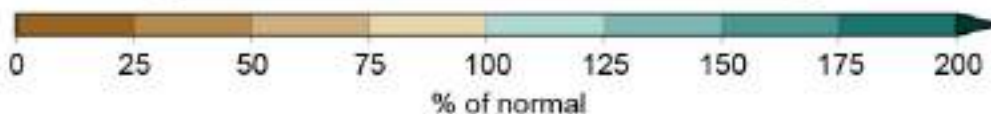
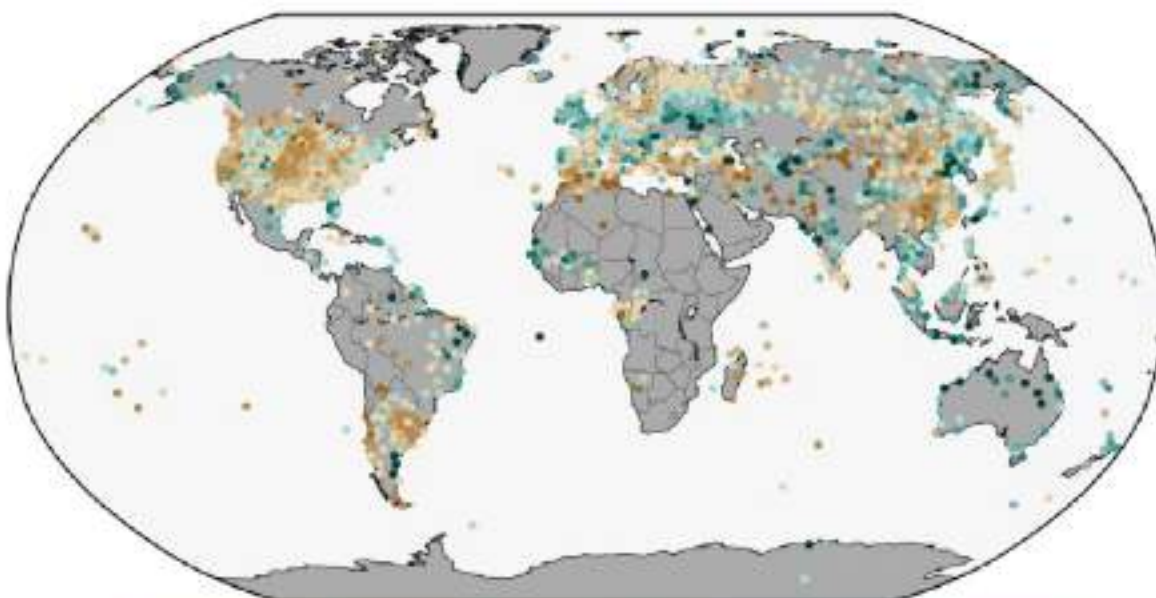


Fig. A4.1. Land-only percent of normal precipitation during (a) JJA 2022 and (b) SON 2022 (relative to a 1961–1990 base period). The figure is provided by NOAA NCEI and the data are from GHCN-M version 4beta (Menne et al. 2018).

References

- Aiyyer, A., and J. Molinari, 2008: MJO and tropical cyclogenesis in the Gulf of Mexico and eastern Pacific: Case study and idealized numerical modeling. *J. Atmos. Sci.*, **65**, 2691–2704, <https://doi.org/10.1175/2007JAS2348.1>.
- Aon, 2023: 2023 weather, climate, and catastrophe insight. Accessed 9 March 2023, 115 pp., www.aon.com/getmedia/f34ec133-3175-406c-9e0b-25cea768c5cf/20230125-weather-climate-catastrophe-insight.pdf.
- Balaguru, K., P. Chang, R. Saravanan, L. R. Leung, Z. Xu, M. Li, and J. S. Hsieh, 2012: Ocean barrier layers' effect on tropical cyclone intensification. *Proc. Natl. Acad. Sci. USA*, **109**, 14 343–14 347, <https://doi.org/10.1073/pnas.1201364109>.
- Banzon, V. F., and R. W. Reynolds, 2013: Use of WindSat to extend a microwave-based daily optimum interpolation sea surface temperature time series. *J. Climate*, **26**, 2557–2562, <https://doi.org/10.1175/JCLI-D-12-00628.1>.
- Beck, H. E., E. F. Wood, M. Pan, C. K. Fisher, D. G. Miralles, A. I. J. M. van Dijk, T. R. McVicar, and R. F. Adler, 2019: MSWEP V2 global 3-hourly 0.1° precipitation: Methodology and quantitative assessment. *Bull. Amer. Meteor. Soc.*, **100**, 473–500, <https://doi.org/10.1175/BAMS-D-17-0138.1>.
- Behringer, D. W., M. Ji, and A. Leetmaa, 1998: An improved coupled model for ENSO prediction and implications for ocean initialization. Part I: The ocean data assimilation system. *Mon. Wea. Rev.*, **126**, 1013–1021, [https://doi.org/10.1175/1520-0493\(1998\)126<0.CO;2](https://doi.org/10.1175/1520-0493(1998)126<0.CO;2).
- Bell, G. D., and Coauthors, 2000: The 1999 North Atlantic Hurricane season [in “Climate Assessment for 1999”]. *Bull. Amer. Meteor. Soc.*, **81** (6), S19–S22, [https://doi.org/10.1175/1520-0477\(2000\)81\[s1:CAF\]2.0.CO;2](https://doi.org/10.1175/1520-0477(2000)81[s1:CAF]2.0.CO;2).
- , —, —, S. B. Goldenberg, and R. J. Pasch, 2018: Atlantic basin [in “State of the Climate in 2017”]. *Bull. Amer. Meteor. Soc.*, **99** (8), S114–S118, <https://doi.org/10.1175/2018BAMS-StateoftheClimate.1>.
- , —, —, H. Wang, S. B. Goldenberg, and R. J. Pasch, 2019: Atlantic basin [in “State of the Climate in 2018”]. *Bull. Amer. Meteor. Soc.*, **100** (9), S113–S119, <https://doi.org/10.1175/2019BAMSStateoftheClimate.1>.
- , E. S. Blake, C. W. Landsea, M. Rosencrans, H. Wang, S. B. Goldenberg, and R. J. Pasch, 2020: Atlantic basin [in “State of the Climate in 2019”]. *Bull. Amer. Meteor. Soc.*, **101** (7), S204–S212, <https://doi.org/10.1175/BAMS-D-20-0077.1>.
- Besl, J., 2023: Tonga eruption may temporarily push Earth closer to 1.5°C of warming. *Eos*, **104**, <https://doi.org/10.1029/2023E0230104>.
- Beven, J. L., 2022: National Hurricane Center tropical cyclone report: Hurricane Agatha (EP012022), 28–31 May 2022. NHC Tech. Rep., 22 pp., https://www.nhc.noaa.gov/data/tcr/EP012022_Agatha.pdf.
- Bjerknes, J., 1969: Atmospheric teleconnections from the equatorial Pacific. *Mon. Wea. Rev.*, **97**, 163–172, [https://doi.org/10.1175/1520-0493\(1969\)097<03.CO;2](https://doi.org/10.1175/1520-0493(1969)097<03.CO;2).
- Bowyer, P. J., and A. W. MacAfee, 2005: The theory of trapped-fetch waves within tropical cyclones—An operational perspective. *Wea. Forecasting*, **20**, 229–244, <https://doi.org/10.1175/WAF849.1>.
- Bucci, L., L. Alaka, A. Hagen, S. Delgado, and J. Beven, 2023: National Hurricane Center tropical cyclone report: Hurricane Ian (AL092022), 23–30 September 2022. NHC Tech. Rep., 72 pp., https://www.nhc.noaa.gov/data/tcr/AL092022_Ian.pdf.
- Camargo, S. J., and A. H. Sobel, 2005: Western North Pacific tropical cyclone intensity and ENSO. *J. Climate*, **18**, 2996–3006, <https://doi.org/10.1175/JCLI3457.1>.
- , A. W. Robertson, S. J. Gaffney, P. Smyth, and M. Ghil, 2007a: Cluster analysis of typhoon tracks: Part II: Large-scale circulation and ENSO. *J. Climate*, **20**, 3654–3676, <https://doi.org/10.1175/JCLI4203.1>.
- , K. A. Emanuel, and A. H. Sobel, 2007b: Use of a genesis potential index to diagnose ENSO effects on tropical cyclone genesis. *J. Climate*, **20**, 4819–4834, <https://doi.org/10.1175/JCLI4282.1>.
- , M. C. Wheeler, and A. H. Sobel, 2009: Diagnosis of the MJO modulation of tropical cyclogenesis using an empirical index. *J. Atmos. Sci.*, **66**, 3061–3074, <https://doi.org/10.1175/2009JAS3101.1>.
- Cangialosi, J. P., 2023: National Hurricane Center tropical cyclone report: Hurricane Julia (AL132022, EP182022), 7–10 October 2022. NHC Tech. Rep., 23 pp., https://www.nhc.noaa.gov/data/tcr/AL132022_EP182022_Julia.pdf.
- Chen, L., and J.-J. Luo, 2021: Indian Ocean dipole and unique Indian Ocean basin warming in 2020 [in “State of the climate in 2020”]. *Bull. Amer. Meteor. Soc.*, **102** (8), S220–S222, <https://doi.org/10.1175/BAMS-D-21-0080.1>.
- , and —, 2022: Indian Ocean dipole [in “State of the Climate in 2021”]. *Bull. Amer. Meteor. Soc.*, **103** (8), S213–S217, <https://doi.org/10.1175/BAMS-D-22-0069.1>.
- Chia, H. H., and C. F. Ropelewski, 2002: The interannual variability in the genesis location of tropical cyclones in the northwest Pacific. *J. Climate*, **15**, 2934–2944, [https://doi.org/10.1175/1520-0442\(2002\)015<0.CO;2](https://doi.org/10.1175/1520-0442(2002)015<0.CO;2).
- Daly, C., M. Halbleib, J. I. Smith, W. P. Gibson, M. K. Doggett, G. H. Taylor, J. Curtis, and P. A. Pasteris, 2008: Physiographically-sensitive mapping of temperature and precipitation across the conterminous United States. *Int. J. Climatol.*, **28**, 2031–2064, <https://doi.org/10.1002/joc.1688>.
- Dare, R. A., and J. L. McBride, 2011: Sea surface temperature response to tropical cyclones. *Mon. Wea. Rev.*, **139**, 3798–3808, <https://doi.org/10.1175/MWR-D-10-05019.1>.
- DeMaria, M., M. Mainelli, L. K. Shay, J. A. Knaff, and J. Kaplan, 2005: Further improvements to the Statistical Hurricane Intensity Prediction Scheme (SHIPS). *Wea. Forecasting*, **20**, 531–543, <https://doi.org/10.1175/WAF862.1>.
- Diamond, H. J., and J. A. Renwick, 2015: The climatological relationship between tropical cyclones in the southwest Pacific and the Madden–Julian Oscillation. *Int. J. Climatol.*, **35**, 676–686, <https://doi.org/10.1002/joc.4012>.
- , and C. J. Schreck, 2022: The tropics [in “State of the Climate in 2021”]. *Bull. Amer. Meteor. Soc.*, **103** (8), S1–S59, <https://doi.org/10.1175/BAMS-D-22-0069.1>.
- , A. M. Lorrey, K. R. Knapp, and D. H. Levinson, 2012: Development of an enhanced tropical cyclone tracks database for the southwest Pacific from 1840 to 2011. *Int. J. Climatol.*, **32**, 2240–2250, <https://doi.org/10.1002/joc.2412>.
- Ding, Q., E. J. Steig, D. S. Battisti, and J. M. Wallace, 2012: Influence of the tropics on the Southern Annular Mode. *J. Climate*, **25**, 6330–6348, <https://doi.org/10.1175/JCLI-D-11-00523.1>.
- Domingues, R., and Coauthors, 2015: Upper ocean response to Hurricane Gonzalo (2014): Salinity effects revealed by targeted and sustained underwater glider observations. *Geophys. Res. Lett.*, **42**, 7131–7138, <https://doi.org/10.1002/2015GL065378>.

- Dube, S. K., D. Rao, P. C. Sinha, T. S. Murty, and N. Bahulayan, 1997: Storm surge in the Bay of Bengal and Arabian Sea: The problem and its prediction. *Mausam*, **48**, 288–304, <https://doi.org/10.54302/mausam.v48i2.4012>.
- Ebita, A., and Coauthors, 2011: The Japanese 55-year Reanalysis “JRA-55”: An interim report. *SOLA*, **7**, 149–152, <https://doi.org/10.2151/sola.2011-038>.
- Emanuel, K. A., 1988: The maximum intensity of hurricanes. *J. Atmos. Sci.*, **45**, 1143–1155, [https://doi.org/10.1175/1520-0469\(1988\)0452.0.CO;2](https://doi.org/10.1175/1520-0469(1988)0452.0.CO;2).
- , and D. S. Nolan, 2004: Tropical cyclone activity and the global climate system. *26th Conf. on Hurricanes and Tropical Meteorology*, Miami, FL, Amer. Meteor. Soc., 10A.2, https://ams.confex.com/ams/26HURR/techprogram/paper_75463.htm.
- Enfield, D. B., and A. M. Mestas-Nuñez, 1999: Multiscale variabilities in global sea surface temperatures and their relationships with tropospheric climate patterns. *J. Climate*, **12**, 2719–2733, [https://doi.org/10.1175/1520-0442\(1999\)0122.0.CO;2](https://doi.org/10.1175/1520-0442(1999)0122.0.CO;2).
- Fang, X., and Coauthors, 2023: Will the history-record southeasterly wind in March 2022 trigger a third-year La Niña event? *Adv. Atmos. Sci.*, **40**, 6–13, <https://doi.org/10.1007/s00376-022-2147-6>.
- Frank, W. M., and P. E. Roundy, 2006: The role of tropical waves in tropical cyclogenesis. *Mon. Wea. Rev.*, **134**, 2397–2417, <https://doi.org/10.1175/MWR3204.1>.
- Gallagher Re, 2023: Gallagher Re natural catastrophe report: 2022, 60 pp., <https://www.ajg.com/gallagherre/news-and-insights/2023/january/nat-cat-report-2022/>.
- Goldenberg, S. B., and L. J. Shapiro, 1996: Physical mechanisms for the association of El Niño and West African rainfall with Atlantic major hurricane activity. *J. Climate*, **9**, 1169–1187, [https://doi.org/10.1175/1520-0442\(1996\)0092.0.CO;2](https://doi.org/10.1175/1520-0442(1996)0092.0.CO;2).
- , C. W. Landsea, A. M. Mestas-Nuñez, and W. M. Gray, 2001: The recent increase in Atlantic hurricane activity: Causes and implications. *Science*, **293**, 474–479, <https://doi.org/10.1126/science.1060040>.
- Goni, G. J., and Coauthors, 2009: Applications of satellite-derived ocean measurements to tropical cyclone intensity forecasting. *Oceanography*, **22**, 176–183, <https://doi.org/10.5670/oceanog.2009.78>.
- , and Coauthors, 2017: Autonomous and Lagrangian ocean observations for Atlantic tropical cyclone studies and forecasts. *Oceanography*, **30**, 92–103, <https://doi.org/10.5670/oceanog.2017.227>.
- Gray, W. M., 1968: Global view of the origin of tropical disturbances and storms. *Mon. Wea. Rev.*, **96**, 669–700, [https://doi.org/10.1175/1520-0493\(1968\)0962.0.CO;2](https://doi.org/10.1175/1520-0493(1968)0962.0.CO;2).
- , 1990: Strong association between West African rainfall and U.S. landfall of intense hurricanes. *Science*, **249**, 1251–1256, <https://doi.org/10.1126/science.249.4974.1251>.
- Guo, Y., X. Jiang, and D. E. Waliser, 2014: Modulation of the convectively coupled Kelvin waves over South America and the tropical Atlantic Ocean in association with the Madden–Julian oscillation. *J. Atmos. Sci.*, **71**, 1371–1388, <https://doi.org/10.1175/JAS-D-13-0215.1>.
- Hastenrath, S., 1990: Decadal-scale changes of the circulation in the tropical Atlantic sector associated with Sahel drought. *Int. J. Climatol.*, **10**, 459–472, <https://doi.org/10.1002/joc.3370100504>.
- Hendon, H., C. Zhang, and J. Glick, 1999: Interannual variation of the Madden–Julian oscillation during austral summer. *J. Climate*, **12**, 2538–2550, [https://doi.org/10.1175/1520-0442\(1999\)0122.0.CO;2](https://doi.org/10.1175/1520-0442(1999)0122.0.CO;2).
- Hersbach, H., and Coauthors, 2020: The ERA5 global reanalysis. *Quart. J. Roy. Meteor. Soc.*, **146**, 1999–2049, <https://doi.org/10.1002/qj.3803>.
- Hong, C.-C., T. Li, and J.-J. Luo, 2008: Asymmetry of the Indian Ocean dipole. Part II: Model diagnosis. *J. Climate*, **21**, 4849–4858, <https://doi.org/10.1175/2008JCLI2223.1>.
- Huang, B., and Coauthors, 2017: Extended Reconstructed Sea Surface Temperature, version 5 (ERSSTv5): Upgrades, validations, and intercomparisons. *J. Climate*, **30**, 8179–8205, <https://doi.org/10.1175/JCLI-D-16-0836.1>.
- , C. Liu, V. Banzon, E. Freeman, G. Graham, B. Hankins, T. Smith, and H.-M. Zhang, 2020: Improvements of the Daily Optimum Interpolation Sea Surface Temperature (DOISST) version 2.1. *J. Climate*, **34**, 2923–2939, <https://doi.org/10.1175/JCLI-D-20-0166.1>.
- Huffman, G. J., R. F. Adler, D. T. Bolvin, and G. Gu, 2009: Improving the global precipitation record: GPCP version 2.1. *Geophys. Res. Lett.*, **36**, L17808, <https://doi.org/10.1029/2009GL040000>.
- , D. T. Bolvin, D. Braithwaite, K. Hsu, R. Joyce, and P. Xie, 2014: NASA Global Precipitation Measurement Integrated Multi-satellite Retrievals for GPM (IMERG). Algorithm Theoretical Basis Doc., version 4.4, 26 pp., https://pps.gsfc.nasa.gov/Documents/IMERG_ATBD_V4.pdf.
- Izumo, T., and Coauthors, 2010: Influence of the state of the Indian Ocean dipole on the following year’s El Niño. *Nat. Geosci.*, **3**, 168–172, <https://doi.org/10.1038/ngeo760>.
- Kalnay, E., and Coauthors, 1996: The NCEP/NCAR 40-Year Reanalysis Project. *Bull. Amer. Meteor. Soc.*, **77**, 437–471, [https://doi.org/10.1175/1520-0477\(1996\)0772.0.CO;2](https://doi.org/10.1175/1520-0477(1996)0772.0.CO;2).
- Kiladis, G. N., and K. M. Weickmann, 1992: Circulation anomalies associated with tropical convection during northern winter. *Mon. Wea. Rev.*, **120**, 1900–1923, [https://doi.org/10.1175/1520-0493\(1992\)1202.0.CO;2](https://doi.org/10.1175/1520-0493(1992)1202.0.CO;2).
- , M. C. Wheeler, P. T. Haertel, K. H. Straub, and P. E. Roundy, 2009: Convectively coupled equatorial waves. *Rev. Geophys.*, **47**, RG2003, <https://doi.org/10.1029/2008RG000266>.
- Klotzbach, P. J., K. M. Wood, C. J. Schreck III, S. G. Bowen, C. M. Patricola, and M. M. Bell, 2022: Trends in Global Tropical Cyclone Activity: 1990–2021. *Geophys. Res. Lett.*, **49**, e2021GL095774.
- Knaff, J. A., C. R. Sampson, and K. D. Musgrave, 2018: An operational rapid intensification prediction aid for the western North Pacific. *Wea. Forecasting*, **33**, 799–811, <https://doi.org/10.1175/WAF-D-18-0012.1>.
- , —, and B. R. Strahl, 2020: A tropical cyclone rapid intensification prediction aid for the Joint Typhoon Warning Center’s areas of responsibility. *Wea. Forecasting*, **35**, 1173–1185, <https://doi.org/10.1175/WAF-D-19-0228.1>.
- Knapp, K. R., M. C. Kruk, D. H. Levinson, H. J. Diamond, and C. J. Neumann, 2010: The International Best Track Archive for Climate Stewardship (IBTrACS): Unifying tropical cyclone data. *Bull. Amer. Meteor. Soc.*, **91**, 363–376, <https://doi.org/10.1175/2009BAMS2755.1>.
- , J. A. Knaff, C. R. Sampson, G. M. Riggio, and A. D. Schnapp, 2013: A pressure-based analysis of the historical western North Pacific tropical cyclone intensity record. *Mon. Wea. Rev.*, **141**, 2611–2631, <https://doi.org/10.1175/MWR-D-12-00323.1>.
- Krishnamurti, T. N., and D. Subrahmanyam, 1982: The 30–50 day mode at 850 mb during MONEX. *J. Atmos. Sci.*, **39**, 2088–2095, [https://doi.org/10.1175/1520-0469\(1982\)0392.0.CO;2](https://doi.org/10.1175/1520-0469(1982)0392.0.CO;2).

- Kumar, A., and Z.-Z. Hu, 2014: Interannual and interdecadal variability of ocean temperature along the equatorial Pacific in conjunction with ENSO. *Climate Dyn.*, **42**, 1243–1258, <https://doi.org/10.1007/s00382-013-1721-0>.
- Landsea, C. W., and J. L. Franklin, 2013: Atlantic Hurricane database uncertainty and presentation of a new database format. *Mon. Wea. Rev.*, **141**, 3576–3592, <https://doi.org/10.1175/MWR-D-12-00254.1>.
- , W. M. Gray, P. W. Mielke, and K. J. Berry, 1992: Long-term variations of western Sahelian monsoon rainfall and intense U.S. landfalling hurricanes. *J. Climate*, **5**, 1528–1534, [https://doi.org/10.1175/1520-0442\(1992\)0052.0.CO;2](https://doi.org/10.1175/1520-0442(1992)0052.0.CO;2).
- , G. A. Vecchi, L. Bengtsson, and T. R. Knutson, 2010: Impact of duration thresholds on Atlantic tropical cyclone counts. *J. Climate*, **23**, 2508–2519, <https://doi.org/10.1175/2009JCLI3034.1>.
- Lau, W. K.-M., and D. E. Waliser, 2012: *Intraseasonal Variability in the Atmosphere-Ocean Climate System*. Springer, 642 pp.
- Leipper, D. F., and D. Volgenau, 1972: Hurricane heat potential of the Gulf of Mexico. *J. Phys. Oceanogr.*, **2**, 218–224, [https://doi.org/10.1175/1520-0485\(1972\)0022.0.CO;2](https://doi.org/10.1175/1520-0485(1972)0022.0.CO;2).
- Liebmann, B., and C. A. Smith, 1996: Description of a complete (interpolated) outgoing longwave radiation dataset. *Bull. Amer. Meteor. Soc.*, **77**, 1275–1277, <https://doi.org/10.1175/1520-0477-77.6.1274>.
- Lin, I. I., and Coauthors, 2013: An ocean coupling potential intensity index for tropical cyclones. *Geophys. Res. Lett.*, **40**, 1878–1882, <https://doi.org/10.1002/grl.50091>.
- , I.-F. Pun, and C.-C. Lien, 2014: ‘Category-6’ Supertyphoon Haiyan in global warming hiatus: Contribution from subsurface ocean warming. *Geophys. Res. Lett.*, **41**, 8547–8553, <https://doi.org/10.1002/2014GL061281>.
- , and Coauthors, 2020: ENSO and tropical cyclones. *El Niño Southern Oscillation in a Changing Climate*, *Geophys. Monogr.*, Vol. 253, Amer. Geophys. Union, 377–408, <https://doi.org/10.1002/9781119548164.ch17>.
- Liu, T., J. Li, C. Sun, T. Lian, and Y. Zhang, 2021: Impact of the April–May SAM on central Pacific Ocean sea temperature over the following three seasons. *Climate Dyn.*, **57**, 775–786, <https://doi.org/10.1007/s00382-021-05738-4>.
- Luo, J.-J., S. Masson, S. Behera, and T. Yamagata, 2007: Experimental forecasts of the Indian Ocean dipole using a coupled OAGCM. *J. Climate*, **20**, 2178–2190, <https://doi.org/10.1175/JCLI4132.1>.
- , R. Zhang, S. K. Behera, Y. Masumoto, F.-F. Jin, R. Lukas, and T. Yamagata, 2010: Interaction between El Niño and extreme Indian Ocean dipole. *J. Climate*, **23**, 726–742, <https://doi.org/10.1175/2009JCLI3104.1>.
- , W. Sasaki, and Y. Masumoto, 2012: Indian Ocean warming modulates Pacific climate change. *Proc. Natl. Acad. Sci. USA*, **109**, 18 701–18 706, <https://doi.org/10.1073/pnas.1210239109>.
- Madden, R., and P. Julian, 1971: Detection of a 40–50 day oscillation in the zonal wind in the tropical Pacific. *J. Atmos. Sci.*, **28**, 702–708, [https://doi.org/10.1175/1520-0469\(1971\)0282.0.CO;2](https://doi.org/10.1175/1520-0469(1971)0282.0.CO;2).
- , and —, 1972: Description of global-scale circulation cells in the tropics with a 40–50 day period. *J. Atmos. Sci.*, **29**, 1109–1123, [https://doi.org/10.1175/1520-0469\(1972\)0292.0.CO;2](https://doi.org/10.1175/1520-0469(1972)0292.0.CO;2).
- , and —, 1994: Observations of the 40–50-day tropical oscillation: A review. *Mon. Wea. Rev.*, **122**, 814–837, [https://doi.org/10.1175/1520-0493\(1994\)1222.0.CO;2](https://doi.org/10.1175/1520-0493(1994)1222.0.CO;2).
- Mainelli, M., M. DeMaria, L. Shay, and G. Goni, 2008: Application of oceanic heat content estimation to operational forecasting of recent Atlantic category 5 hurricanes. *Wea. Forecasting*, **23**, 3–16, <https://doi.org/10.1175/2007WAF2006111.1>.
- Maloney, E. D., and D. L. Hartmann, 2001: The Madden–Julian oscillation, barotropic dynamics, and North Pacific tropical cyclone formation. Part I: Observations. *J. Atmos. Sci.*, **58**, 2545–2558, [https://doi.org/10.1175/1520-0469\(2001\)0582.0.CO;2](https://doi.org/10.1175/1520-0469(2001)0582.0.CO;2).
- Matthews, A. J., 2008: Primary and successive events in the Madden–Julian Oscillation. *Quart. J. Roy. Meteor. Soc.*, **134**, 439–453, <https://doi.org/10.1002/qj.224>.
- Menne, M. J., B. E. Gleason, J. Lawrimore, J. Rennie, and C. N. Williams, 2018: Global Historical Climatology Network – Monthly temperature, version 4 (BETA). NOAA National Centers for Environmental Information, <https://doi.org/10.7289/V5XW4GTH>.
- Millán, L., and Coauthors, 2022: The Hunga Tonga-Hunga Ha’apai Hydration of the stratosphere. *Geophys. Res. Lett.*, **49**, e2022GL099381, <https://doi.org/10.1029/2022GL099381>.
- Mo, K. C., 2000: The association between intraseasonal oscillations and tropical storms in the Atlantic Basin. *Mon. Wea. Rev.*, **128**, 4097–4107, [https://doi.org/10.1175/1520-0493\(2000\)1292.0.CO;2](https://doi.org/10.1175/1520-0493(2000)1292.0.CO;2).
- Moreno, P. I., and Coauthors, 2018: Onset and evolution of Southern Annular Mode-like changes at centennial timescale. *Sci. Rep.*, **8**, 3458, <https://doi.org/10.1038/s41598-018-21836-6>.
- Münnich, M., and J. D. Neelin, 2005: Seasonal influence of ENSO on the Atlantic ITCZ and equatorial South America. *Geophys. Res. Lett.*, **32**, L21709, <https://doi.org/10.1029/2005GL023900>.
- Nicholls, N., 1979: A possible method for predicting seasonal tropical cyclone activity in the Australian region. *Mon. Wea. Rev.*, **107**, 1221–1224, [https://doi.org/10.1175/1520-0493\(1979\)1072.0.CO;2](https://doi.org/10.1175/1520-0493(1979)1072.0.CO;2).
- Nobre, P., and J. Shukla, 1996: Variations of sea surface temperature, wind stress and rainfall over the tropical Atlantic and South America. *J. Climate*, **9**, 2464–2479, [https://doi.org/10.1175/1520-0442\(1996\)0092.0.CO;2](https://doi.org/10.1175/1520-0442(1996)0092.0.CO;2).
- Pasch, R. J., B. J. Reinhart, and L. Alaka, 2023: National Hurricane Center tropical cyclone report: Hurricane Ian (AL072022), 14–23 September 2022. NHC Tech. Rep., 60 pp., www.nhc.noaa.gov/data/tcr/AL072022_Fiona.pdf.
- Raga, G. B., B. Bracamontes-Ceballos, L. Farfán, and R. Romero-Centeno, 2013: Landfalling tropical cyclones on the Pacific coast of Mexico: 1850–2010. *Atmósfera*, **26**, 209–220, [https://doi.org/10.1016/S0187-6236\(13\)71072-5](https://doi.org/10.1016/S0187-6236(13)71072-5).
- Ramage, C. S., 1971: *Monsoon Meteorology*. Academic Press, 296 pp.
- Reinhart, B. J., 2022: Tropical Storm Lester. National Hurricane Center tropical cyclone report (EP132022), 15–17 September 2022. NHC Tech. Rep., 14 pp., www.nhc.noaa.gov/data/tcr/EP132022_Lester.pdf.
- Reynolds, R. W., N. A. Rayner, T. M. Smith, D. C. Stokes, and W. Wang, 2002: An improved in situ and satellite SST analysis for climate. *J. Climate*, **15**, 1609–1625, [https://doi.org/10.1175/1520-0442\(2002\)0152.0.CO;2](https://doi.org/10.1175/1520-0442(2002)0152.0.CO;2).
- Riddle, E., M. Stoner, N. Johnson, M. L’Heureux, D. Collins, and S. Feldstein, 2012: The impact of the MJO on clusters of wintertime circulation anomalies over the North American region. *Climate Dyn.*, **40**, 1749–1766, <https://doi.org/10.1007/s00382-012-1493-y>.

- Ropelewski, C. F., and M. S. Halpert, 1989: Precipitation patterns associated with the high index phase of the Southern Oscillation. *J. Climate*, **2**, 268–284, [https://doi.org/10.1175/1520-0442\(1989\)0022.0.CO;2](https://doi.org/10.1175/1520-0442(1989)0022.0.CO;2).
- Saha, S., and Coauthors, 2014: The NCEP Climate Forecast System version 2. *J. Climate*, **27**, 2185–2208, <https://doi.org/10.1175/JCLI-D-12-00823.1>.
- Saji, N. H., B. N. Goswami, P. N. Vinayachandran, and T. Yamagata, 1999: A dipole mode in the tropical Indian Ocean. *Nature*, **401**, 360–363, <https://doi.org/10.1038/43854>.
- Schneider, T., T. Bischoff, and G. H. Haug, 2014: Migrations and dynamics of the intertropical convergence zone. *Nature*, **513**, 45–53, <https://doi.org/10.1038/nature13636>.
- Schreck, C. J., 2015: Kelvin waves and tropical cyclogenesis: A global survey. *Mon. Wea. Rev.*, **143**, 3996–4011, <https://doi.org/10.1175/MWR-D-15-0111.1>.
- , 2016: Convectively coupled Kelvin waves and tropical cyclogenesis in a semi-Lagrangian framework. *Mon. Wea. Rev.*, **144**, 4131–4139, <https://doi.org/10.1175/MWR-D-16-0237.1>.
- , and J. Molinari, 2011: Tropical cyclogenesis associated with Kelvin waves and the Madden–Julian oscillation. *Mon. Wea. Rev.*, **139**, 2723–2734, <https://doi.org/10.1175/MWR-D-10-05060.1>.
- , J. Molinari, and A. Ayyer, 2012: A global view of equatorial waves and tropical cyclogenesis. *Mon. Wea. Rev.*, **140**, 774–788, <https://doi.org/10.1175/MWR-D-11-00110.1>.
- , K. R. Knapp, and J. P. Kossin, 2014: The impact of best track discrepancies on global tropical cyclone climatologies using IBTrACS. *Mon. Wea. Rev.*, **142**, 3881–3899, <https://doi.org/10.1175/MWR-D-14-00021.1>.
- , H.-T. Lee, and K. R. Knapp, 2018: HIRS outgoing longwave radiation—Daily climate data record: Application toward identifying tropical subseasonal variability. *Remote Sens.*, **10**, 1325, <https://doi.org/10.3390/rs10091325>.
- Shay, L. K., G. J. Goni, and P. G. Black, 2000: Effects of a warm oceanic feature on Hurricane Opal. *Mon. Wea. Rev.*, **128**, 1366–1383, [https://doi.org/10.1175/1520-0493\(2000\)1282.0.CO;2](https://doi.org/10.1175/1520-0493(2000)1282.0.CO;2).
- Tippett, M. K., S. J. Camargo, and A. H. Sobel, 2011: A Poisson regression index for tropical cyclone genesis and the role of large-scale vorticity in genesis. *J. Climate*, **24**, 2335–2357, <https://doi.org/10.1175/2010JCLI3811.1>.
- Trenberth, K. E., 1984: Signal versus noise in the Southern Oscillation. *Mon. Wea. Rev.*, **112**, 326–332, [https://doi.org/10.1175/1520-0493\(1984\)112.0.CO;2](https://doi.org/10.1175/1520-0493(1984)112.0.CO;2).
- Vecchi, G. A., and B. J. Soden, 2007: Effect of remote sea surface temperature change on tropical cyclone potential intensity. *Science*, **450**, 1066–1071, <https://doi.org/10.1038/nature06423>.
- Ventrone, M. J., C. D. Thorncroft, and M. A. Janiga, 2012a: Atlantic tropical cyclogenesis: A three-way interaction between an African easterly wave, diurnally varying convection, and a convectively coupled atmospheric Kelvin wave. *Mon. Wea. Rev.*, **140**, 1108–1124, <https://doi.org/10.1175/MWR-D-11-00122.1>.
- , —, and C. J. Schreck, 2012b: Impacts of convectively coupled Kelvin waves on environmental conditions for Atlantic tropical cyclogenesis. *Mon. Wea. Rev.*, **140**, 2198–2214, <https://doi.org/10.1175/MWR-D-11-00305.1>.
- Villarini, G., G. A. Vecchi, T. R. Knutson, and J. A. Smith, 2011: Is the recorded increase in short duration North Atlantic tropical storms spurious? *J. Geophys. Res.*, **116**, D10114, <https://doi.org/10.1029/2010JD015493>.
- Vincent, D. G., 1994: The South Pacific Convergence Zone (SPCZ): A review. *Mon. Wea. Rev.*, **122**, 1949–1970, [https://doi.org/10.1175/1520-0493\(1994\)122.0.CO;2](https://doi.org/10.1175/1520-0493(1994)122.0.CO;2).
- Vose, R. S., and Coauthors, 2021: Implementing full spatial coverage in NOAA’s Global Temperature Analysis. *Geophys. Res. Lett.*, **48**, e2020GL090873, <https://doi.org/10.1029/2020GL090873>.
- Waliser, D. E., and C. Gautier, 1993: A satellite-derived climatology of the ITCZ. *J. Climate*, **6**, 2162–2174, [https://doi.org/10.1175/1520-0442\(1993\)0062.0.CO;2](https://doi.org/10.1175/1520-0442(1993)0062.0.CO;2).
- Wang, B., 1994: Climatic regimes of tropical convection and rainfall. *J. Climate*, **7**, 1109–1118, [https://doi.org/10.1175/1520-0442\(1994\)0072.0.CO;2](https://doi.org/10.1175/1520-0442(1994)0072.0.CO;2).
- , and Q. Ding, 2008: Global monsoon: Dominant mode of annual variation in the tropics. *Dyn. Atmos. Ocean*, **44**, 165–183, <https://doi.org/10.1016/j.dynatmoce.2007.05.002>.
- , J. Liu, H. J. Kim, P. J. Webster, and S. Y. Yim, 2012: Recent change of the global monsoon precipitation (1979–2008). *Climate Dyn.*, **39**, 1123–1135, <https://doi.org/10.1007/s00382-011-1266-z>.
- Wheeler, M., and G. N. Kiladis, 1999: Convectively coupled equatorial waves: Analysis of clouds and temperature in the wavenumber–frequency domain. *J. Atmos. Sci.*, **56**, 374–399, [https://doi.org/10.1175/1520-0469\(1999\)0562.0.CO;2](https://doi.org/10.1175/1520-0469(1999)0562.0.CO;2).
- , and H. H. Hendon, 2004: An all-season real-time multivariate MJO index: Development of an index for monitoring and prediction. *Mon. Wea. Rev.*, **132**, 1917–1932, [https://doi.org/10.1175/1520-0493\(2004\)1322.0.CO;2](https://doi.org/10.1175/1520-0493(2004)1322.0.CO;2).
- Wood, K. M., and E. A. Ritchie, 2015: A definition for rapid weakening in the North Atlantic and eastern North Pacific. *Geophys. Res. Lett.*, **42**, 10091–10097, <https://doi.org/10.1002/2015GL066697>.
- , and C. J. Schreck, 2020: Eastern North Pacific and central North Pacific basins [in “State of the Climate in 2019”]. *Bull. Amer. Meteor. Soc.*, **101** (8), S212–S214, <https://doi.org/10.1175/BAMS-D-20-0077.1>.
- , and —, 2021: Eastern North Pacific and central North Pacific basins [in “State of the Climate in 2020”]. *Bull. Amer. Meteor. Soc.*, **102** (8), S233–S235, <https://doi.org/10.1175/BAMS-D-21-0080.1>.
- , and —, 2022: Eastern North Pacific and central North Pacific basins [in “State of the Climate in 2021”]. *Bull. Amer. Meteor. Soc.*, **103** (8), S229–S231, <https://doi.org/10.1175/BAMS-D-22-0069.1>.
- Yim, S. Y., B. Wang, J. Liu, and Z. W. Wu, 2014: A comparison of regional monsoon variability using monsoon indices. *Climate Dyn.*, **43**, 1423–1437, <https://doi.org/10.1007/s00382-013-1956-9>.
- Yin, J. F., H. Gu, X. Liang, M. Yu, J. Sun, Y. Xie, F. Li, and C. Wu, 2022: A possible dynamic mechanism for rapid production of the extreme hourly rainfall in Zhengzhou City on 20 July 2021. *J. Meteor. Res.*, **36**, 6–25, <https://doi.org/10.1007/s13351-022-1166-7>.
- Zhang, C., 2005: Madden–Julian oscillation. *Rev. Geophys.*, **43**, RG2003, <https://doi.org/10.1029/2004RG000158>.
- , and J. Gottschalck, 2002: SST anomalies of ENSO and the Madden–Julian oscillation in the equatorial Pacific. *J. Climate*, **15**, 2429–2445, [https://doi.org/10.1175/1520-0442\(2002\)0152.0.CO;2](https://doi.org/10.1175/1520-0442(2002)0152.0.CO;2).
- Zheng, Z.-W., I.-I. Lin, B. Wang, H.-C. Huang, and C.-H. Chen, 2015: A long neglected damper in the El Niño–typhoon relationship: A ‘Gaia-like’ process. *Sci. Rep.*, **5**, 11103, <https://doi.org/10.1038/srep11103>.
- Zuo, M., T. Zhou, W. Man, X. Chen, J. Liu, F. Liu, and C. Gao, 2022: Volcanoes and climate: Sizing up the impact of the recent Hunga Tonga–Hunga Ha’apai volcanic eruption from a historical perspective. *Adv. Atmos. Sci.*, **39**, 1986–1993, <https://doi.org/10.1007/s00376-022-2034-1>.

STATE OF THE CLIMATE IN 2022

THE ARCTIC

T. A. Moon, R. Thoman, and M. L. Druckenmiller, Eds.



Special Online Supplement to the *Bulletin of the American Meteorological Society* Vol. 104, No. 9, September, 2023

<https://doi.org/10.1175/10.1175/BAMS-D-23-0079.1>

Corresponding author: Twila Moon / Twila.Moon@colorado.edu

©2023 American Meteorological Society

For information regarding reuse of this content and general copyright information, consult the [AMS Copyright Policy](#).

STATE OF THE CLIMATE IN 2022

The Arctic

Editors

Ellen Bartow-Gillies
Jessica Blunden
Tim Boyer

Chapter Editors

Peter Bissolli
Kyle R. Clem
Howard J. Diamond
Matthew L. Druckenmiller
Robert J. H. Dunn
Catherine Ganter
Nadine Gobron
Gregory C. Johnson
Rick Lumpkin
Ademe Mekonnen
John B. Miller
Twila A. Moon
Marilyn N. Raphael
Ahira Sánchez-Lugo
Carl J. Schreck III
Richard L. Thoman
Kate M. Willett
Zhiwei Zhu

Technical Editor

Lukas Noguchi

BAMS Special Editor for Climate

Michael A. Alexander

American Meteorological Society

Cover Credit:

Patterned Ground in the Arctic by Ina Timling.

Ice wedge polygons are a common form of patterned ground in the Arctic. They occur in areas of continuous permafrost, such as the arctic coastal plain of Alaska, and are the result of freeze-thaw processes. These polygons create striking patterns on the landscape and provide habitats for many organisms. However, increased warming of the Arctic leads to the degradation/thawing of these ice wedges. As a result, not only the appearance of the patterned ground features changes but also their function as habitat.

How to cite this document:

The Arctic is one chapter from the *State of the Climate in 2022* annual report and is available from <https://doi.org/10.1175/10.1175/BAMS-D-23-0079.1>. Compiled by NOAA's National Centers for Environmental Information, *State of the Climate in 2022* is based on contributions from scientists from around the world. It provides a detailed update on global climate indicators, notable weather events, and other data collected by environmental monitoring stations and instruments located on land, water, ice, and in space. The full report is available from <https://doi.org/10.1175/2023BAMSStateoftheClimate.1>.

Citing the complete report:

Blunden, J., T. Boyer, and E. Bartow-Gillies, Eds., 2023: "State of the Climate in 2022". Bull. Amer. Meteor. Soc., 104 (9), S1–S501 <https://doi.org/10.1175/2023BAMSStateoftheClimate.1>.

Citing this chapter:

Moon, T. A., R. Thoman, and M. L. Druckenmiller, Eds., 2023: The Arctic [in "State of the Climate in 2022"]. Bull. Amer. Meteor. Soc., 104 (9), S271–S321, <https://doi.org/10.1175/10.1175/BAMS-D-23-0079.1>.

Citing a section (example):

Walsh, J. E., S. Bigalke, S. A. McAfee, R. Lader, M. C. Serreze, and T. J. Ballinger, 2023: Precipitation [in "State of the Climate in 2022"]. Bull. Amer. Meteor. Soc., 104 (9), S281–S284, <https://doi.org/10.1175/10.1175/BAMS-D-23-0079.1>.

Editor and Author Affiliations (alphabetical by name)

- Ahmasuk, Brandon**, Kawerak Inc., Nome, Alaska
- Backensto, Stacia A.**, National Park Service, Fairbanks, Alaska
- Ballinger, Thomas J.**, International Arctic Research Center, University of Alaska Fairbanks, Fairbanks, Alaska
- Benestad, Rasmus**, Norwegian Meteorological Institute, Oslo, Norway
- Berner, Logan T.**, Northern Arizona University, Flagstaff, Arizona
- Bernhard, Germar H.**, Biospherical Instruments Inc., San Diego, California
- Bhatt, Uma S.**, Geophysical Institute, University of Alaska Fairbanks, Fairbanks, Alaska
- Bigalke, Siiri**, Plant, Soils and Climate Department, Utah State University, Logan, Utah
- Bjerke Jarle, W.**, Department of Arctic Ecology, Norwegian Institute for Nature Research, Trondheim, Norway
- Brettschneider, Brian**, NOAA/NWS Alaska Region, Anchorage, Alaska
- Christiansen, Hanne H.**, Geology Department, University Centre in Svalbard, Svalbard, Norway
- Cohen, Judah L.**, Atmospheric and Environmental Research, Lexington, Massachusetts
- Decharme, Bertrand**, Centre National de Recherches Météorologiques, Météo-France/CNRS, Toulouse, France
- Derksen, Chris**, Climate Research Division, Environment and Climate Change Canada, Toronto, Canada
- Divine, Dmitry**, Norwegian Polar Institute, Fram Centre, Tromsø, Norway
- Drost Jensen, Caroline**, Danish Meteorological Institute, Copenhagen, Denmark
- Druckenmiller, Matthew L.**, National Snow and Ice Data Center, Cooperative Institute for Research in Environmental Sciences, University of Colorado, Boulder, Colorado
- Elias Chereque, Alesksandra**, Department of Physics, University of Toronto, Toronto, Canada
- Epstein, Howard E.**, University of Virginia, Charlottesville, Virginia
- Fausto, Robert S.**, Geological Survey of Denmark and Greenland (GEUS), Copenhagen, Denmark
- Fettweis, Xavier**, University of Liège, Belgium
- Fioletov, Vitali E.**, Environment and Climate Change Canada, Toronto, Canada
- Forbes, Bruce C.**, Arctic Centre, University of Lapland, Rovaniemi, Finland
- Frost, Gerald V. (JJ)**, ABR Inc., Fairbanks, Alaska
- Gerland, Sebastian**, Norwegian Polar Institute, Fram Centre, Tromsø, Norway
- Goetz, Scott J.**, Northern Arizona University, Flagstaff, Arizona
- Grooß, Jens-Uwe**, Forschungszentrum Jülich, Jülich, Germany
- Hanna, Edward**, Department of Geography and Lincoln Climate Research Group, Lincoln, United Kingdom
- Hanssen-Bauer, Inger**, Norwegian Meteorological Institute, Oslo, Norway
- Hendricks, Stefan**, Alfred Wegener Institute, Helmholtz Centre for Polar and Marine Research, Bremerhaven, Germany
- Holmes, Robert M.**, Woodwell Climate Research Center, Falmouth, Massachusetts
- Ialongo, Iolanda**, Finnish Meteorological Institute, Helsinki, Finland
- Isaksen, Ketil**, Norwegian Meteorological Institute, Oslo, Norway
- Johnsen, Bjørn**, Norwegian Radiation and Nuclear Safety, Østerås, Norway
- Jones, Timothy**, Coastal Observation and Seabird Survey Team, University of Washington, Seattle, Washington
- Kaler, Robb S.A.**, U.S. Fish and Wildlife Service, Alaska Region, Anchorage, Alaska
- Kaleschke, Lars**, Alfred Wegener Institute, Helmholtz Centre for Polar and Marine Research, Bremerhaven, Germany
- Kim, Seong-Joong**, Korea Polar Research Institute, Incheon, South Korea
- Labe, Zachary M.**, Princeton University, Princeton, New Jersey
- Lader, Rick**, International Arctic Research Center, University of Alaska Fairbanks, Fairbanks, Alaska
- Lakkala, Kaisa**, Finnish Meteorological Institute, Sodankylä, Finland
- Lara, Mark J.**, University of Illinois at Urbana-Champaign, Urbana, Illinois
- Lindsey, Jackie**, Coastal Observation and Seabird Survey Team, University of Washington, Seattle, Washington
- Loomis, Bryant D.**, NASA Goddard Space Flight Center, Greenbelt, Maryland
- Luojus, Kari**, Arctic Research Centre, Finnish Meteorological Institute, Helsinki, Finland
- Macander, Matthew J.**, ABR Inc., Fairbanks, Alaska
- Mamen, Jostein**, Norwegian Meteorological Institute, Oslo, Norway
- Mankoff, Ken D.**, Business Integra, New York, New York; NASA Goddard Institute for Space Studies, New York, New York
- Manney, Gloria L.**, NorthWest Research Associates, Socorro, New Mexico
- McAfee, Stephanie A.**, Department of Geography, University of Nevada Reno, Reno, Nevada
- McClelland, James W.**, Marine Biological Laboratory, Woods Hole, Massachusetts
- Meier, Walter N.**, National Snow and Ice Data Center, Cooperative Institute for Research in Environmental Sciences, University of Colorado, Boulder, Colorado
- Moon, Twila A.**, National Snow and Ice Data Center, Cooperative Institute for Research in Environmental Sciences, University of Colorado, Boulder, Colorado
- Moore, G. W. K.**, University of Toronto Mississauga, Mississauga, Canada
- Mote, Thomas L.**, University of Georgia, Athens, Georgia
- Mudryk, Lawrence**, Climate Research Division, Environment and Climate Change Canada, Toronto, Canada
- Müller, Rolf**, Forschungszentrum Jülich, Jülich, Germany
- Nyland, Kelsey E.**, Department of Geography, George Washington University, Washington, DC
- Overland, James E.**, NOAA Pacific Marine Environmental Laboratory, Seattle, Washington
- Parrish, Julia K.**, Coastal Observation and Seabird Survey Team, University of Washington, Seattle, Washington
- Perovich, Donald K.**, University of Dartmouth, Hanover, New Hampshire
- Petersen, Guðrún Nína**, Icelandic Meteorological Office, Reykjavik, Iceland
- Petty, Alek**, NASA Goddard Space Flight Center, Greenbelt, Maryland
- Phoenix, Gareth, K.**, University of Sheffield, Sheffield, United Kingdom
- Poinar, Kristin**, University at Buffalo, Buffalo, New York
- Rantanen, Mika**, Finnish Meteorological Institute, Helsinki, Finland
- Ricker, Robert**, NORCE Norwegian Research Centre, Tromsø, Norway
- Romanovsky, Vladimir E.**, Geophysical Institute, University of Alaska Fairbanks, Fairbanks, Alaska; Earth Cryosphere Institute, Tyumen Science Center, Tyumen, Russia
- Serbin, Shawn P.**, Brookhaven National Laboratory, Upton, New York
- Serreze, Mark C.**, National Snow and Ice Data Center, University of Colorado, Boulder, Colorado
- Sheffield, Gay**, Alaska Sea Grant, Marine Advisory Program, University of Alaska Fairbanks, Nome, Alaska
- Shiklomanov, Alexander I.**, University of New Hampshire, Durham, New Hampshire; Arctic and Antarctic Research Institute, St. Petersburg, Russia
- Shiklomanov, Nikolay I.**, Department of Geography, George Washington University, Washington, DC
- Smith, Sharon L.**, Geological Survey of Canada, Natural Resources Canada, Ottawa, Canada

Editor and Author Affiliations (continued)

Spencer, Robert G. M., Florida State University, Tallahassee, Florida
Streletskiy, Dmitry A., Department of Geography, George Washington University, Washington, DC
Suslova, Anya, Woodwell Climate Research Center, Falmouth, Massachusetts
Svendby, Tove, Norwegian Institute for Air Research, Kjeller, Norway
Tank, Suzanne E., University of Alberta, Edmonton, Canada
Tedesco, Marco, Lamont-Doherty Earth Observatory, Columbia University, Palisades, New York; NASA Goddard Institute of Space Studies, New York, New York
Thoman, Richard L., International Arctic Research Center, University of Alaska Fairbanks, Fairbanks, Alaska
Tian-Kunze, Xiangshan, Alfred Wegener Institute, Helmholtz Centre for Polar and Marine Research, Bremerhaven, Germany
Timmermans, Mary-Louise, Yale University, New Haven, Connecticut

Tømmervik, Hans, Arctic Department, Norwegian Institute for Nature Research, Tromsø, Norway
Tretiakov, Mikhail, Arctic and Antarctic Research Institute, St. Petersburg, Russia
Walker, Donald (Skip) A., Institute of Arctic Biology, University of Alaska Fairbanks, Fairbanks, Alaska
Walsh, John E., International Arctic Research Center, University of Alaska Fairbanks, Fairbanks, Alaska
Wang, Muyin, NOAA Pacific Marine Environmental Laboratory, Seattle, Washington; Cooperative Institute for Climate, Ocean, and Ecosystem Studies, University of Washington, Seattle, Washington
Webster, Melinda, University of Washington, Seattle, Washington
Wehrlé, Adrian, University of Zürich, Zürich, Switzerland
Yang, Daqing, National Hydrology Research Centre, Environment Canada, Saskatoon, Canada
Zolkos, Scott, Woodwell Climate Research Center, Falmouth, Massachusetts

Editorial and Production Team

Allen, Jessica, Graphics Support, Cooperative Institute for Satellite Earth System Studies, North Carolina State University, Asheville, North Carolina
Camper, Amy V., Graphics Support, Innovative Consulting and Management Services, LLC, NOAA/NESDIS National Centers for Environmental Information, Asheville, North Carolina
Haley, Bridgette O., Graphics Support, NOAA/NESDIS National Centers for Environmental Information, Asheville, North Carolina
Hammer, Gregory, Content Team Lead, Communications and Outreach, NOAA/NESDIS National Centers for Environmental Information, Asheville, North Carolina
Love-Brotak, S. Elizabeth, Lead Graphics Production, NOAA/NESDIS National Centers for Environmental Information, Asheville, North Carolina

Ohlmann, Laura, Technical Editor, Innovative Consulting and Management Services, LLC, NOAA/NESDIS National Centers for Environmental Information, Asheville, North Carolina
Noguchi, Lukas, Technical Editor, Innovative Consulting and Management Services, LLC, NOAA/NESDIS National Centers for Environmental Information, Asheville, North Carolina
Riddle, Deborah B., Graphics Support, NOAA/NESDIS National Centers for Environmental Information, Asheville, North Carolina
Veasey, Sara W., Visual Communications Team Lead, Communications and Outreach, NOAA/NESDIS National Centers for Environmental Information, Asheville, North Carolina

5. Table of Contents

List of authors and affiliations	S274
a. Overview	S277
b. Surface air temperature	S279
1. Overview.....	S279
2. Arctic annual temperatures during 2022.....	S279
3. Seasonal perspectives on Arctic temperatures in 2022.....	S280
c. Precipitation	S281
1. Overview.....	S281
2. Arctic precipitation in 2022.....	S282
3. Historical trends.....	S283
4. Indicators of precipitation extremes.....	S284
Sidebar 5.1: Extreme weather and climate events in 2022.....	S285
d. Sea-surface temperature	S287
e. Sea ice	S290
1. Sea-ice extent.....	S290
2. Sea-ice age, thickness, and volume.....	S291
f. Greenland Ice Sheet	S293
g. Terrestrial snow cover	S296
h. Arctic river discharge	S299
i. Permafrost	S301
1. Permafrost temperatures.....	S302
2. Active layer thickness.....	S304
j. Tundra greenness	S305
k. Ozone and UV radiation	S308
1. Ozone.....	S308
2. Ultraviolet radiation.....	S309
Sidebar 5.2: Alaska seabird die-offs and the changing Arctic marine ecosystem.....	S311
Acknowledgments	S314
Appendix 1: Chapter 5 – Acronyms	S315
References	S317

Please refer to Chapter 8 (Relevant Datasets and Sources) for a list of all climate variables and datasets used in this chapter for analyses, along with their websites for more information and access to the data.

5. THE ARCTIC

T. A. Moon, R. Thoman, and M. L. Druckenmiller, Eds.

a. Overview

—T. A. Moon, R. Thoman, and M. L. Druckenmiller

Rapid warming due to human-caused climate change is reshaping the Arctic, enhanced by physical processes that cause the Arctic to warm more quickly than the global average, collectively called Arctic amplification. Observations over the past 40+ years show a transition to a wetter Arctic, with seasonal shifts and widespread disturbances influencing the flora, fauna, physical systems, and peoples of the Arctic.

For the Arctic (poleward of 60°N), 2022 surface air temperatures were the fifth highest since records began in 1900, reaching 0.76°C above the 1991–2020 mean. Evidence of Arctic amplification is becoming more consistent, with 2022 being the ninth consecutive year with Arctic temperature anomalies exceeding global mean anomalies. Higher up in the atmosphere, 2022 saw a greater loss of stratospheric ozone compared to the 2004–21 mean, but not approaching the record losses of 2011 and 2020.

Aligning with climate change projections (IPCC 2021), near-surface air over land had higher temperature anomalies in 2022 than air over the ocean, yet oceanic impacts of global warming are also evident. August mean sea-surface temperatures reveal that most ice-free regions of the Arctic Ocean show warming trends since 1982. Regional exceptions fail to counter a narrative of recent, rapid warming; the 1982–2022 cooling trend for the Barents Sea is notably influenced by anomalously high sea-surface temperatures in the 1980s and 1990s. One ecosystem impact of increasing sea-surface temperatures is an increase in ocean primary productivity, which has been observed since 2003 and was especially strong in the Eurasian Arctic and Barents Sea (Frey et al. 2022).

Continued low sea-ice extent is a contributor to warming ocean surface waters. Arctic sea-ice extent in 2022 was similar to 2021 and remains well below the long-term average. Moving beyond sea-ice extent to sea-ice age, which is related to sea-ice thickness (older sea ice is thicker), reveals more sobering observations. The Arctic has transitioned from a region dominated by multiyear ice to one dominated by first-year (seasonal) sea ice. While sea ice greater than four years old covered over 1 million km² in September 2006, it covered only 127,000 km² in September 2022. One impact likely connected to increased high-latitude ocean temperatures and reduced sea ice is the repeated recent instances of observed seabird die-offs along coastal Alaska (see Sidebar 5.2). This and other ecosystem impacts, including climate-related changes in fish, marine mammals, and land-based food sources, are a grave concern to Arctic Indigenous Peoples and residents as a matter of food security and ecosystem health (e.g., SEARCH et al. 2022; Crozier et al. 2021; Mallory and Boyce 2018).

Arctic warming has been accompanied by an increase in precipitation. This *State of the Climate* report represents the first time that the Arctic chapter includes a full section on precipitation (section 5c), supported by reanalysis data that allow a pan-Arctic assessment despite sparse in situ gauge measurements. Since 1950, every season has shown an average increase in Arctic precipitation, in line with climate model projections (IPCC 2021). In some regions, the increase in precipitation is experienced through heavier precipitation events (e.g., Arctic Atlantic sector), while for others there has been an increase in the number of consecutive wet days (e.g., Svalbard eastward to the Chukchi Sea).

Increases in precipitation, combined with warming, are linked to altered seasonal patterns. Although April 2022 snow accumulation was higher than the 1991–2020 average for both the Eurasian and North American Arctic, snow-cover extent by June 2022 dipped to the second lowest for the North American Arctic and third lowest for the Eurasian Arctic in the 56-year record. Seasonal shifts also complicate the story of Arctic river discharge. Overall, Arctic river discharge is increasing, consistent with the observations of increasing precipitation and intensification of the Arctic hydrologic cycle. When examining eight major Arctic river basins, 2021 discharge and 2022 discharge exceeded the 1991–2020 mean by 7% and 5%, respectively. Yet, 2021 and 2022 discharges in June (the month of peak discharge) were remarkably low for the Arctic’s Eurasian river basins. In another example, despite 2022 glacial ice loss (totaling 165 ± 18 Gt) that was slightly below the 2002–22 average, the Greenland Ice Sheet experienced unprecedented September melt events, bringing melt conditions to 36% of the ice sheet surface during a month that is usually marked by a return to cold conditions and snow accumulation.

Warming air and longer snow-free periods both contribute to continued overall increases in Arctic permafrost temperatures. Continuous and discontinuous permafrost (frozen ground) underlies almost all of the Arctic, and effects of thawing permafrost include infrastructure damage, river discharge changes, ecosystem composition alterations, and releases of greenhouse gases to the atmosphere. Permafrost temperatures in 2022 were the highest on record at 11 of 25 long-term measurement sites. Thirteen sites, however, showed cooling for 2022 compared to 2021 due to short-term reductions in regional air temperatures, demonstrating the importance of long-term monitoring.

As the Arctic subsurface changes, so too does the surface landscape itself. Arctic tundra greenness declined in 2022 from record-high 2020 and 2021 values, yet was still fourth highest across a 23-year record. But, as with other measurements of environmental change, regional variation remains an important part of the story. In this case, low productivity in northeastern Siberia was observed alongside high productivity in most of the North American Arctic.

One of the elements contributing to regional variability and the differing local experiences of Arctic residents is an increase in extreme events, which can include record-setting rainfall or snowfall, heatwaves, wildfire, and cyclones (see Sidebar 5.1). In 2022, 56 separate extreme events were recorded by Arctic-connected meteorological services, with impacts felt by communities throughout the Arctic. Of course, the Arctic is also undergoing changes beyond those discussed in this chapter. For example, coastal erosion (Brady and Leichenko 2020; Irrgang et al. 2022; Nielsen et al. 2022) and biological changes across fauna (Davidson et al. 2020) are impacting Arctic residents (SEARCH et al. 2022) and the connected physical-biological-human systems. There is no doubt that the Arctic is a region of rapid change with serious consequences across systems.

Special Note: This chapter includes a focus on Arctic river discharge, section 5h, which alternates yearly with a section on glaciers and ice caps outside of Greenland, as the scales of regular observation for both of these climate components are better suited for reporting every two years. Note that most Arctic chapter observations now use a 1991–2020 climate baseline (exceptions are noted) updated from 1981–2010, meaning the long-term average now includes more years with stronger climate change influence. Due to different disciplinary norms and physical processes, seasonal definitions also vary and are defined within each chapter section.

b. Surface air temperature

—T. J. Ballinger, J. E. Overland, M. Wang, J. E. Walsh, B. Brettschneider, R. L. Thoman, U. S. Bhatt, E. Hanna, I. Hanssen-Bauer, and S.-J. Kim

1. OVERVIEW

Relative to global mean temperatures, Arctic temperatures have warmed more rapidly since the start of the record in 1900 (Fig. 5.1). The amplified warming of Earth's northernmost latitudes, known as Arctic amplification (AA), is associated with various localized land–ocean–sea-ice interactions and large-scale atmospheric and oceanic energy transport processes (Previdi et al. 2021) that drive impactful Arctic atmospheric extremes (Walsh et al. 2020). Recent research has emphasized that the magnitude of AA is sensitive to multiple constraints, including how the southern limit of the Arctic region is defined, which datasets (i.e., observational versus modeled) are analyzed, and what time periods are considered (England et al. 2021; Chylek et al. 2022; Rantanen et al. 2022). As examples, Chylek et al. (2022) and Rantanen et al. (2022) showed that land and ocean areas poleward of 60°N have warmed ~2–4 times faster than the global mean during the past several decades.

This section examines Arctic annual temperatures for northern land (60°N–90°N), ocean, and total area (land and ocean) temperatures. A summary of seasonal air temperature anomalies is also discussed with an emphasis on the large-scale patterns observed during 2022 (see Sidebar 5.1 for some temperature highlights).

2. ARCTIC ANNUAL TEMPERATURES DURING 2022

The year 2022 was the fifth-warmest for land and ocean areas poleward of 60°N since 1900 (Fig. 5.1a), according to analysis of the NASA Goddard Institute for Space Studies Surface Temperature analysis version 4 (GISTEMPv4). As described in Lenssen et al. (2019), GISTEMPv4 is comprised of weather station data over land from the NOAA Global Historical Climatology Network version 4 and Extended Reconstructed Sea Surface Temperature version 5 over ocean areas without sea ice and that are not adjacent to land-based stations (see more detailed sea-surface temperature discussion in section 5d). The annual average surface air temperature for 2022 was 0.76°C higher than the 1991–2020 mean. This marks the 13th consecutive year when Arctic air temperatures were above average and the ninth consecutive year when Arctic temperature anomalies have exceeded global mean anomalies. Including 2022, the 15 warmest years observed in the Arctic have all occurred since 2005 (Fig. 5.1a).

Considered independently, Arctic lands (Fig. 5.1b) and the Arctic Ocean (Fig. 5.1c) each experienced notable annual warm anomalies during 2022. Land temperatures were 0.92°C above the 1991–2020 mean, the fifth highest on record, while the Arctic Ocean 2022 mean temperature anomaly (0.17°C) was the 11th highest, both since 1900. Over the last half century, increased temperatures are apparent in both environments, with greater year-to-year variability observed over land compared to the ocean due to water's greater thermal inertia and heat capacity.

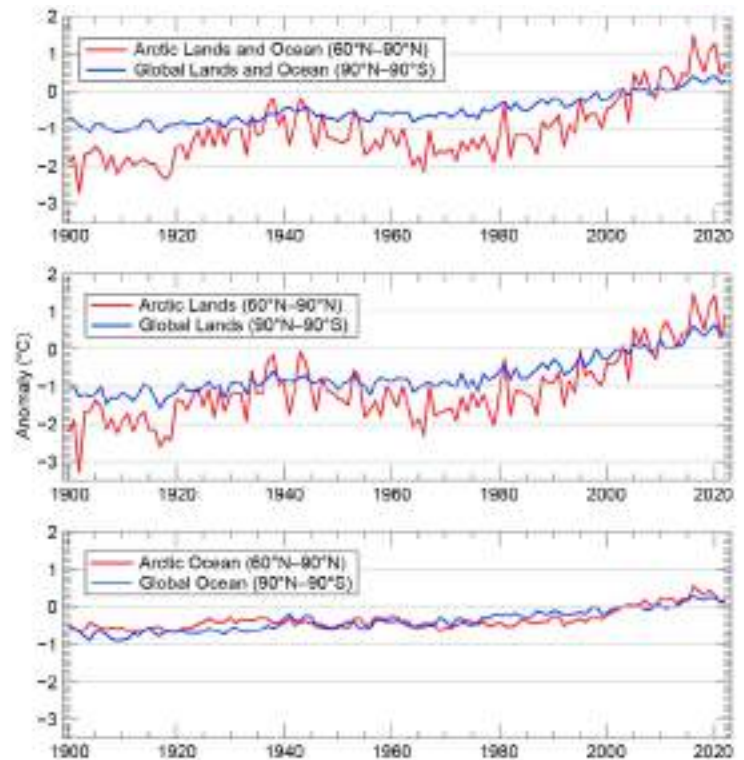


Fig. 5.1. Annual mean (Jan–Dec) Arctic (red lines) and global (blue lines) surface air temperature anomalies (°C) for (a) land and ocean areas, (b) land-only, and (c) ocean-only for 1900–2022. Spatial domains are listed in each panel. (Source: NASA GISTEMP v4.)

3. SEASONAL PERSPECTIVES ON ARCTIC TEMPERATURES IN 2022

Arctic air temperature anomalies for 2022, compared to the 1991–2020 mean, are presented in Fig. 5.2 for each season defined as: winter (January–March, JFM), spring (April–June, AMJ), summer (July–September, JAS), and autumn (October–December, OND). These seasonal definitions are selected to coincide with annual cycles discussed in the other sections of this chapter, including the spring onset of snow and sea-ice melt on the Arctic Ocean and the Greenland Ice Sheet’s period of peak ablation during summer. Data presented here are from the European Centre for Medium-Range Weather Forecasts Reanalysis version 5 (ERA5) reanalysis (Hersbach et al. 2020).

A Eurasian–North American temperature dipole was present during winter (Fig. 5.2a). This was characterized by above-normal air temperatures in the Eurasian Arctic and cold departures over the North American high latitudes, associated with prevailing positive Arctic Oscillation/North Atlantic Oscillation conditions during much of winter. A large region of $\geq 3^{\circ}\text{C}$ positive anomalies was concentrated over the central Arctic extending south to western Siberia and stretching across northern Eurasia. This region of above-average temperatures was associated with southerly flow off the Eurasian continent from a large, below-normal sea-level pressure (SLP) pattern (≤ -5 hPa) over the Barents and Kara Seas combined with broad, above-normal SLP spanning central Siberia into the North American Arctic (Fig. 5.3a). Contrasting winter cold temperature anomalies ($\leq -2^{\circ}\text{C}$) were noted across high-latitude North America, extending from northeastern Alaska southeastward over Hudson Bay and Labrador Sea to the east (Fig. 5.2a). These below-normal air temperatures were driven by a low-pressure anomaly north of Hudson Bay (≤ -5 hPa) and the aforementioned upstream high-pressure anomaly pattern (Fig. 5.3a).

Spring air temperatures over the Arctic Ocean were near average, with relatively small air temperature anomalies over Arctic lands (Fig. 5.2b). This seasonal pattern was characterized by positive anomalies ($\geq +1^{\circ}\text{C}$) in central and eastern Siberia and atop Hudson Bay. A small area of the highest Arctic air temperature anomalies ($+4^{\circ}\text{C}$ to $+5^{\circ}\text{C}$) was found just east of the Ural Mountains associated with low pressure anomalies (≤ -3 hPa) that transported warm air into the area (Fig. 5.3b). Record-high June-averaged air temperatures were found over Svalbard (5°C – 6°C ; Mamen et al. 2022), though seasonal temperatures over the island were 2°C – 3°C above normal. Meanwhile, near-normal air temperatures were found over the Arctic Ocean. Negative temperature anomalies ($\leq -1^{\circ}\text{C}$) were dispersed over northwestern North America, northwestern Greenland and adjacent Ellesmere Island, and westernmost Eurasia.

Summer air temperatures were above normal across much of the Arctic. Eastern Europe and eastern Siberia, and the Beaufort Sea and Canadian Archipelago saw positive anomalies $\geq +1^{\circ}\text{C}$ (Fig. 5.2c). Low pressure anomalies, suggestive of an active storm track, across Arctic Alaska and

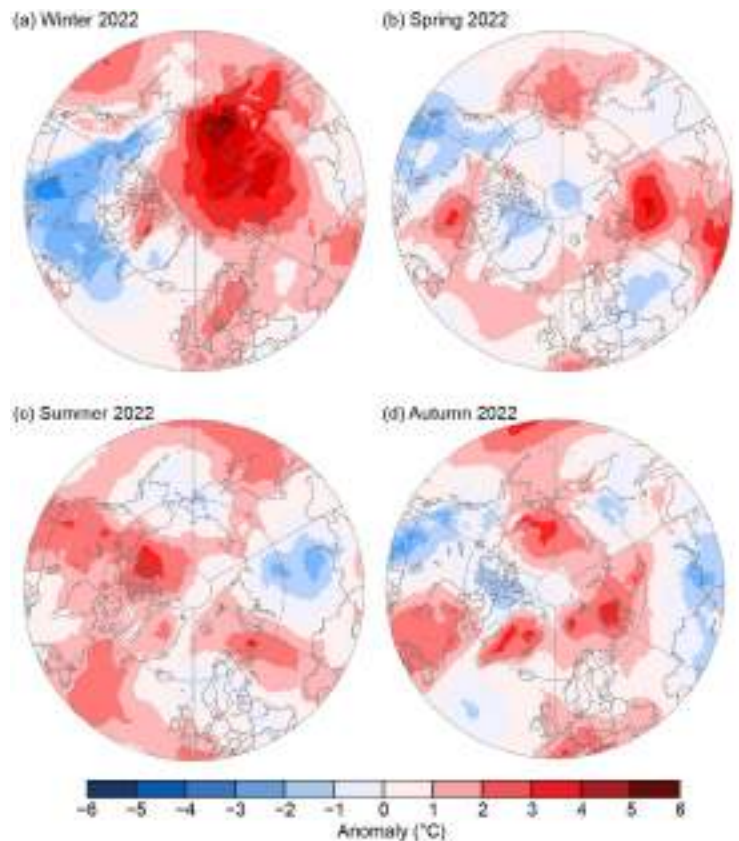


Fig. 5.2. Near-surface (925-hPa) air temperature anomaly maps ($^{\circ}\text{C}$) for each season during 2022: (a) winter (Jan–Mar), (b) spring (Apr–Jun), (c) summer (Jul–Sep), and (d) autumn (Oct–Dec). Temperature anomalies are shown relative to the 1991–2020 means. (Source: ERA5 reanalysis.)

northern Canada, supported the above-normal air temperatures in the latter areas (Fig. 5.3c). Below-normal temperatures were observed in central Eurasia and were associated with low pressure anomalies to the east that caused cold, northerly winds (Fig. 5.3c).

Autumn temperatures were characterized by above-normal temperatures in the Arctic marginal seas, with the largest temperature departures ($\geq +3^{\circ}\text{C}$) over Novaya Zemlya, Svalbard, the interior of the Greenland Ice Sheet, and the northern Chukchi Sea (Fig. 5.2d). Central Arctic Ocean air temperatures were near normal, but below-normal temperatures ($\leq -1^{\circ}\text{C}$) were found over the Canadian Archipelago. Higher-than-normal SLP and southerly flow were linked with the warm air temperature patterns (Fig. 5.3d). Notably, the southerly winds associated with the northern Chukchi Sea warm anomaly were a product of two strong pressure centers, with a positive pressure anomaly centered over mainland Alaska and the Gulf of Alaska ($\geq +5$ hPa) coupled with a negative pressure anomaly over the East Siberian Sea (≤ -5 hPa).

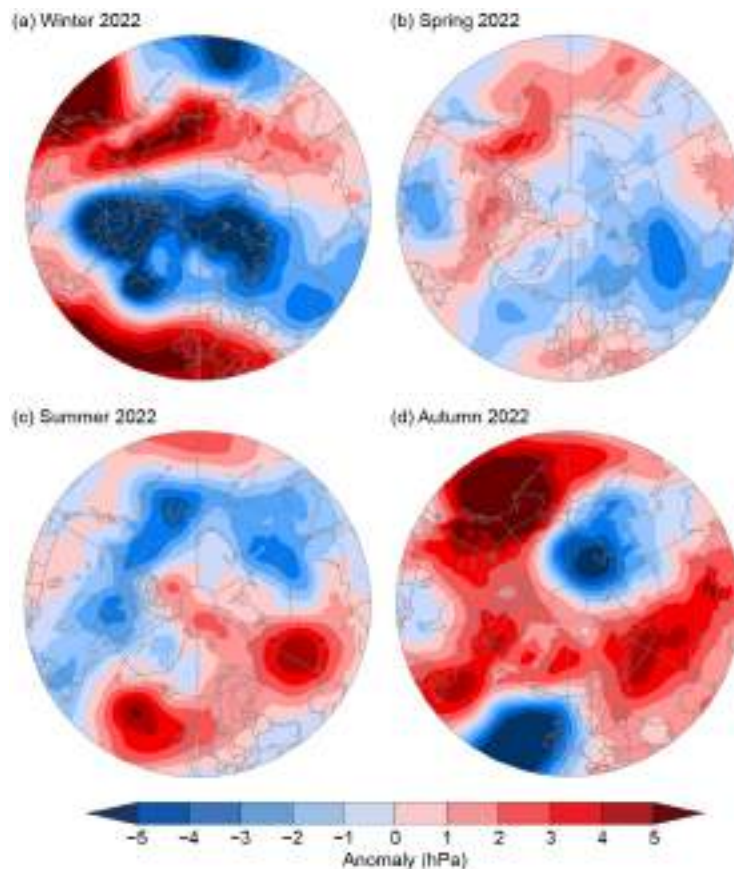


Fig. 5.3. Sea-level pressure (hPa) anomaly maps for each season during 2022: (a) winter (Jan–Mar), (b) spring (Apr–Jun), (c) summer (Jul–Sep), and (d) autumn (Oct–Dec). Anomalies are shown relative to the 1991–2020 means. (Source: ERA5 reanalysis.)

c. Precipitation

—J. E. Walsh, S. Bigalke, S. A. McAfee, R. Lader, M. C. Serreze, and T. J. Ballinger

1. OVERVIEW

Globally, precipitation over land has likely increased since 1950, consistent with increases in total atmospheric moisture (IPCC 2021). However, previous assessments of observed Arctic precipitation have not shown coherent trends (Walsh et al. 2020); results depend on the time period, region, and data product. Climate models project increased Arctic precipitation and more frequent heavy precipitation (e.g., Sillmann et al. 2013; Kusunoki et al. 2015; McCrystall et al. 2021).

Gauge measurements of precipitation are especially problematic in the Arctic, because the sparse gauge network does not provide representative measurements in many northern regions. Moreover, precipitation gauges suffer from undercatch in cold, windy conditions (Ye et al. 2021). For this reason, gridded reanalyses are increasingly used to assess Arctic precipitation. For example, Yu and Zhong (2021) and White et al. (2021) used the European Centre for Medium-Range Weather Forecasts Reanalysis-Interim (ERA-Interim) and ERA version 5 (ERA5) reanalyses, respectively, to show that Arctic precipitation trends vary regionally and seasonally over the past few decades. In this section, we use the newer and highly regarded ERA5 reanalysis (Hersbach et al. 2020) to provide an overview of 2022 Arctic precipitation anomalies in the context of recent and ongoing changes. Reanalyses have weaknesses related to changes in input data, notably the inclusion of satellite data beginning in 1979, thus we also use gridded station data from the Global Precipitation Climatology Centre’s GPCP V.2022 (Becker et al. 2013; Schneider et al. 2022).

2. ARCTIC PRECIPITATION IN 2022

Arctic precipitation in 2022 was characterized by wetter-than-normal conditions in many areas, with record-breaking heavy precipitation events at various locations. Overall, 2022 pan-Arctic (north of 60°N) precipitation was the third highest since 1950, trailing only 2020 and 2017, according to ERA5 reanalysis. Winter (January–March), summer (July–September), and autumn (October–December) were all among the 10 wettest for their respective seasons.

In winter 2022, there were positive precipitation anomalies in the North Atlantic subarctic, the Gulf of Alaska, and much of southern Alaska (Fig. 5.4). The wet anomalies over Alaska link to anomalously high pressure over western Canada and low-pressure anomalies offshore (see Fig. 5.3a). The positive precipitation departures from Greenland to Norway are typical of those during La Niña conditions (NOAA 2022), which prevailed during 2022. Sea-level pressures were more than 5 hPa below average from northeastern Canada to northern Europe (Fig. 5.3a), indicative of an active cyclone pattern in the Atlantic. A mid-January storm set 32 local heavy-precipitation records in Norway and contributed to the positive seasonal departures there.

Spring is normally dry in the Arctic, and April–June (AMJ) 2022 was characterized by generally small departures from relatively low seasonal means. The atmospheric circulation anomalies were relatively weak (see Fig. 5.3b). For the 60°N–90°N region as a whole, AMJ precipitation was close to the 1950–2022 median. Negative precipitation anomalies across the North American subarctic (Fig. 5.4b) coincided with positive sea-level pressure anomalies (see Fig. 5.2b). In central and southern Alaska, where all three months had well-below-normal precipitation, drought developed during May over southwestern Alaska and northern Cook Inlet and expanded into Interior Alaska in June, setting the stage for severe wildfires in early summer (Alaska Division of Forestry 2022).

Overall, summer 2022 was the Arctic's third-wettest summer since 1950, but some areas were dry (Fig. 5.4c). Southeastern and southern Alaska were exceptionally wet, with some locations reporting their wettest summer on record. Western Alaska experienced heavy rain and coastal flooding from ex-Typhoon Merbok in September. New monthly records for July rainfall were set at various locations in northern Norway. However, dry conditions prevailed over parts of northern Canada and northeastern Europe, which contributed to low water levels in eastern European rivers (section 5h).

Autumn in the Arctic was the ninth wettest since 1950. Precipitation departures were generally positive in the Pacific subarctic, but mixed in the North Atlantic. In contrast to winter and summer, negative anomalies extended from the Labrador Sea northeastward across Iceland and into the Nordic seas, consistent with positive sea-level pressure anomalies in the region (see Fig. 5.3d). However, parts of northern Greenland were wetter than normal,

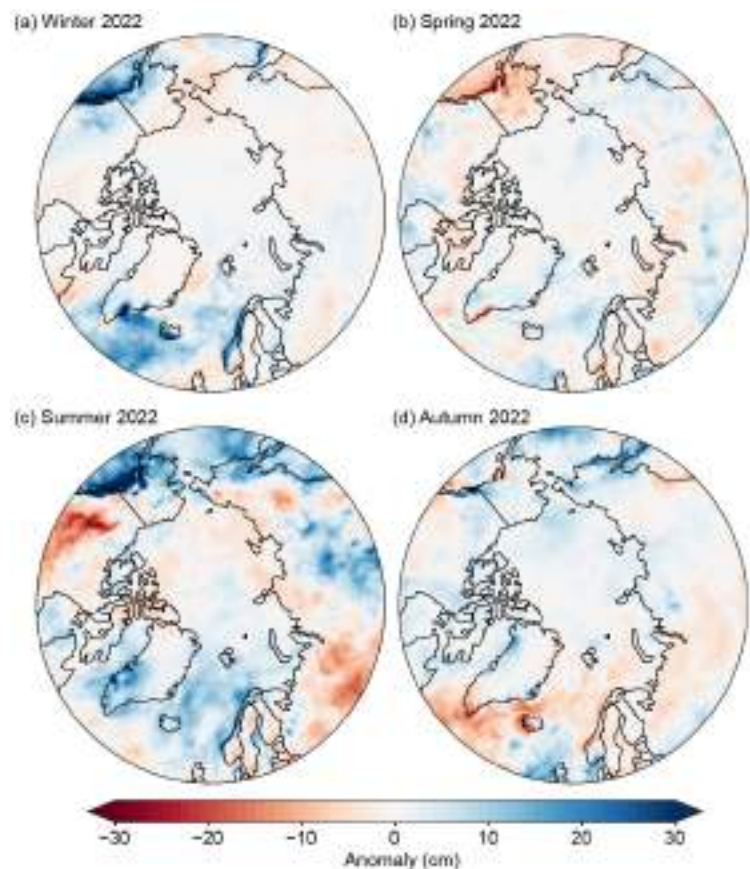


Fig. 5.4. Seasonal departures of 2022 precipitation (cm) from the 1991–2020 climatological means for the Arctic seasons: (a) winter (Jan–Mar), (b) spring (Apr–Jun), (c) summer (Jul–Sep), and (d) autumn (Oct–Dec). Blue shades denote above-normal precipitation; red shades denote below-normal precipitation. (Source: ERA5 reanalysis.)

especially in December. The southeastern Alaska Panhandle was also anomalously wet in autumn. Although south-central Alaska was seasonally dry (Fig. 5.4d), December was anomalously wet. These kinds of spatial and intraseasonal variability are not always well represented in seasonal average, relatively coarse data, such as ERA5.

3. HISTORICAL TRENDS

While there is considerable interannual variability in Arctic-wide average precipitation from 1950 to 2022, it is generally consistent across ERA5 and Global Precipitation Climatology Center (GPCC; Fig. 5.5). Both the reanalysis and gridded data show increases of about 10% in yearly total precipitation over this period, with more substantial increases in winter than summer. The consistency across seasons and datasets indicates that Arctic-wide precipitation is increasing, as expected from climate model simulations. For the more recent period 1979–2022, when ERA5 satellite data assimilation increased, trends in ERA5 (and also GPCC) precipitation are larger and remain statistically significant ($p < 0.05$) for the full year and for all seasons except AMJ. Spring trends for 1979–2022 are weaker than for 1950–2022 and insignificant in both datasets.

While the ERA5 product indicates scattered areas of decreasing precipitation in every season, areas of increase dominate (Fig. 5.6). Consistent with the area-averaged trends in Fig. 5.5, nearly

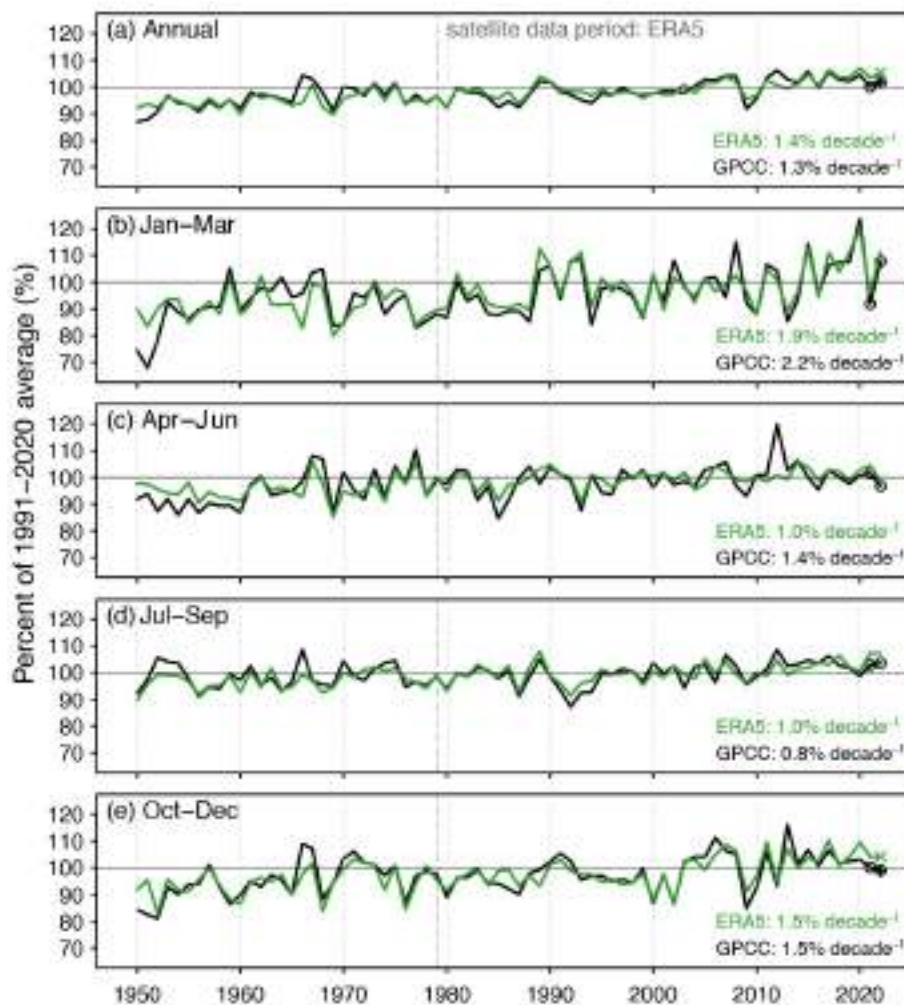


Fig. 5.5. Time series of Arctic (60°N–90°N) precipitation, expressed as percent departures from the corresponding 1991–2020 averages (%), for (a) the calendar years 1950–2022 and for each three-month Arctic season: (b) winter (Jan–Mar), (c) spring (Apr–Jun), (d) summer (Jul–Sep), and (e) autumn (Oct–Dec). Results are from ERA5 (green lines; “x” denotes value based in part on the ERA5 preliminary product for December 2022) and GPCC 1.0° data (black lines; “o” and “+” denote values based on GPCC monitoring and first-guess products, respectively). GPCC values are for land only, and ERA5 values are for land and ocean. Linear trends and are shown in lower right of each panel. All trends are significant at $p < 0.001$.

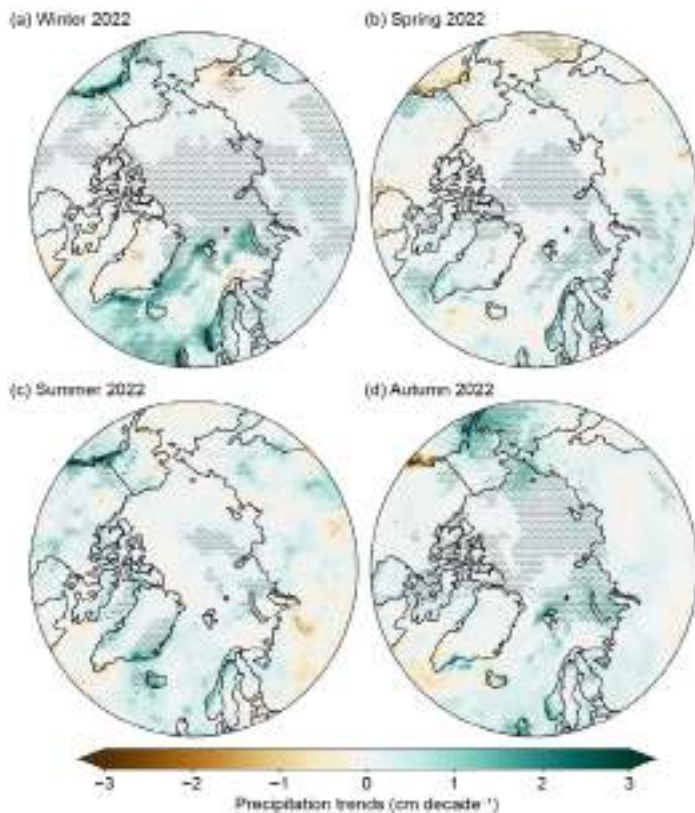


Fig. 5.6. Precipitation trends (cm decade^{-1}) over the period 1950–2022 for the Arctic seasons: (a) winter (Jan–Mar), (b) spring (Apr–Jun), (c) summer (Jul–Sep), and (d) autumn (Oct–Dec). Green shades denote trend increases and brown shades denote trend decreases. Stippling denotes trend significance at the 0.05 level. (Source: ERA5.)

all areas of statistically significant change are increases. Increased precipitation is especially pronounced in the subpolar Pacific south of Alaska during autumn, winter, and summer, and the subpolar North Atlantic during winter. The southwestern coast of Norway is dominated by increases in all seasons. Negative precipitation trends are most prominent in the subarctic during spring and summer.

4. INDICATORS OF PRECIPITATION EXTREMES

According to ERA5, heavy precipitation—defined here as yearly maximum one-day (Rx1) and five-day (Rx5) precipitation—shows no coherent trends over most of the Arctic. Large and significant increases in Rx1 and Rx5 as well as the annual maximum number of consecutive wet days (CWD) are apparent in the Atlantic sector, including northeastern Greenland (Fig. 5.7), indicating that heavy precipitation events contribute to the overall precipitation increase in these areas (Fig. 5.6). The CWD trend is positive from Svalbard eastward to the Chukchi Sea. Areas with increases in CWD generally coincide with areas of reduced sea-ice coverage. The annual maximum number of consecutive dry days (CDD) has decreased, especially in the European sector of the Arctic Ocean, the Canadian Archipelago, and north-central Asia. In moisture-limited areas such as the boreal forest during summer, these changes imply reduced vulnerability to drought stress and an increased potential for plant growth, although evapotranspiration also increases in a warming climate.

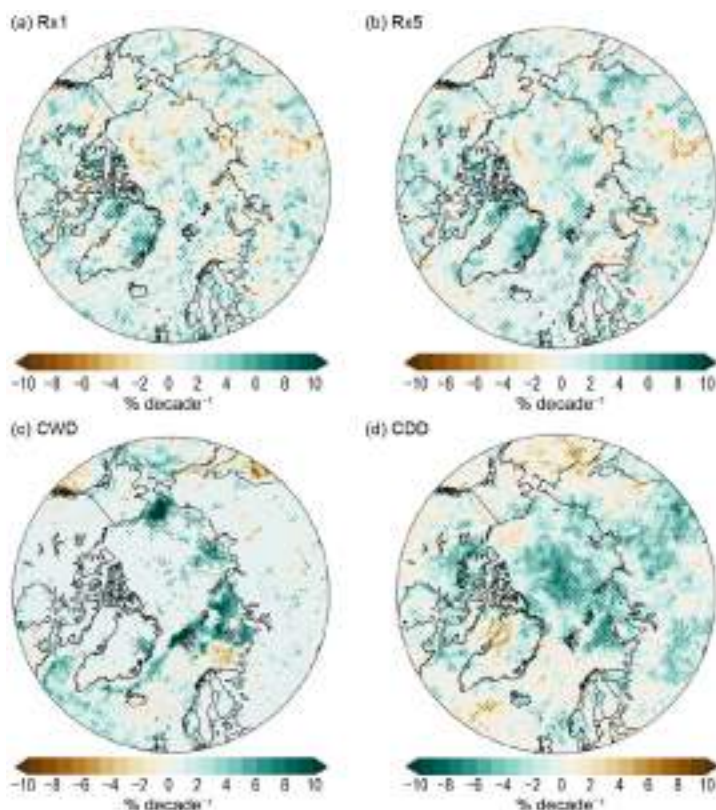


Fig. 5.7. Trends of daily extreme precipitation indices ($\% \text{ decade}^{-1}$) over the period 1950–2021. Plots are shown for yearly maximum one-day total precipitation (Rx1; upper left), yearly maximum five-day amount (Rx5; upper right), yearly maximum number of consecutive wet days (CWD; lower left), and yearly maximum number of consecutive dry days (CDD; lower right). Green shades denote trends toward wetter extremes; brown shades denote trends towards drier extremes. Stippling denotes trend significance at the 0.05 level. (Source: ERA5.)

Sidebar 5.1: Extreme weather and climate events in 2022

—R. BENESTAD, R. L. THOMAN, JR., J. L. COHEN, J. OVERLAND, E. HANNA, G. W. K. MOORE, M. RANTANEN, G. N. PETERSEN, AND M. WEBSTER

Arctic extreme events occur when natural weather variability interacts with the long-term climatic state, and vary by type, location, and season. They are also affected by long-term human-caused warming trends and arise from interactions between multiple anomalies in the atmosphere, ocean, and land, and can affect ecosystems and communities. These fluctuations, beyond typical variability, often have detrimental impacts. Global warming provides an ongoing thermodynamic response through Arctic amplification, which leads to temperature increases (see section 5b), permafrost thaw (see section 5i), and sea-ice loss/open water (see section 5e). These factors combine with the natural range of atmospheric and oceanic dynamics, e.g., jet-stream meanders, atmospheric blocking, weather patterns, storms, and upper ocean heat content (Overland 2022), to create extreme events. Thermodynamic responses to amplified Arctic warming provide precursors to major impacts. New extremes do not require much deviation from past ranges of atmospheric circulation patterns; hence, extreme events can occur in many locations with many different impacts. Weather and climate extremes influence ecosystems based on species-specific life histories (see section 5j), such as the timing of reproduction and migration (see Sidebar 5.2). Societal impacts on livelihoods follow from, for example, changes in sea ice, land cover, and ecosystems.

In a statistical sense, extremes are conditions that are infrequent and approach or exceed the limits of observed states. Record-breaking events are clear examples; however, previously unobserved events may also be extreme events (in 2022 for example, rain on Greenland and tongues of open water to the north of Novaya Zemlya and Franz Josef Land). We may consider extremes by their character in an objective scientific context, and through their effect on nature and society. Some events that may be characterized as “far out in the tail” may not necessarily have a strong impact on the environment, whereas others that are less spectacular in terms of statistical aspects may have catastrophic consequences for people, plants, or animals. The occurrence and nature of extreme weather and climate events reflect the state of Earth’s climate. Hence, the number, type, and intensity of extreme events in the Arctic are expected to change with the ongoing global warming, and be exacerbated by Arctic amplification.

Extreme weather and climate events vary in time scales, ranging from short-lived storms to long-lasting droughts. In the Arctic, such rare and forceful meteorological phenomena include cyclones, avalanches, droughts, heatwaves, wildfires, and floods. Cyclones are associated with strong winds, heavy precipitation, and waves over open sea, but extreme winds are also caused by weather fronts, atmospheric convection,

polar lows, and atmospheric rivers. Extreme precipitation involves both brief, intense rainfall and high accumulation over long wet spells. Droughts are also extreme events, caused by a lack of precipitation over longer periods. There are also compound extremes, such as rain-on-snow and freezing rain. Rain-on-snow may result in extreme transformations in the snow cover such as formations of ice layers. Extreme temperatures can be very cold or very hot, and both are typically due to long-lasting atmospheric blocking high pressure anomalies. Hot, dry conditions increase the risk of wildfires. Abrupt and extreme shifts or variations in conditions also create extreme events, such as the extreme warmth exceeding +8°C over central Greenland during 1–6 September 2022, which brought late-season melting over vast areas: the most on record in September (see section 5f). Other examples of abrupt changes include wildfires, which result in lasting transformation of the landscape and ecosystems.

Figure SB5.1 shows that 2022 was an extremely warm year over extensive regions of the Arctic. Much of the Eurasian Arctic was the second warmest since 1950 (see section 5b). The 2022 summer also brought the most extensive wildfire season on record to southwest Alaska, where wildfire is historically

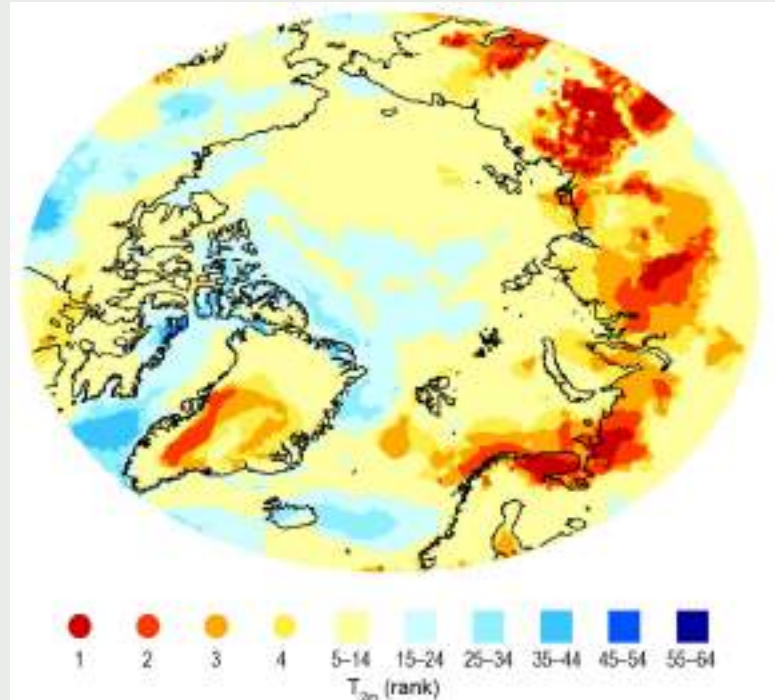


Fig. SB5.1. The historical temperature ranking (T_{2m}) of the 2022 mean air temperature compared to the 1950–2022 period. Note how many regions experienced air temperature rankings among the five highest temperatures on record, with extremely warm regions in the Barents Sea, central Greenland, and parts of Siberia.

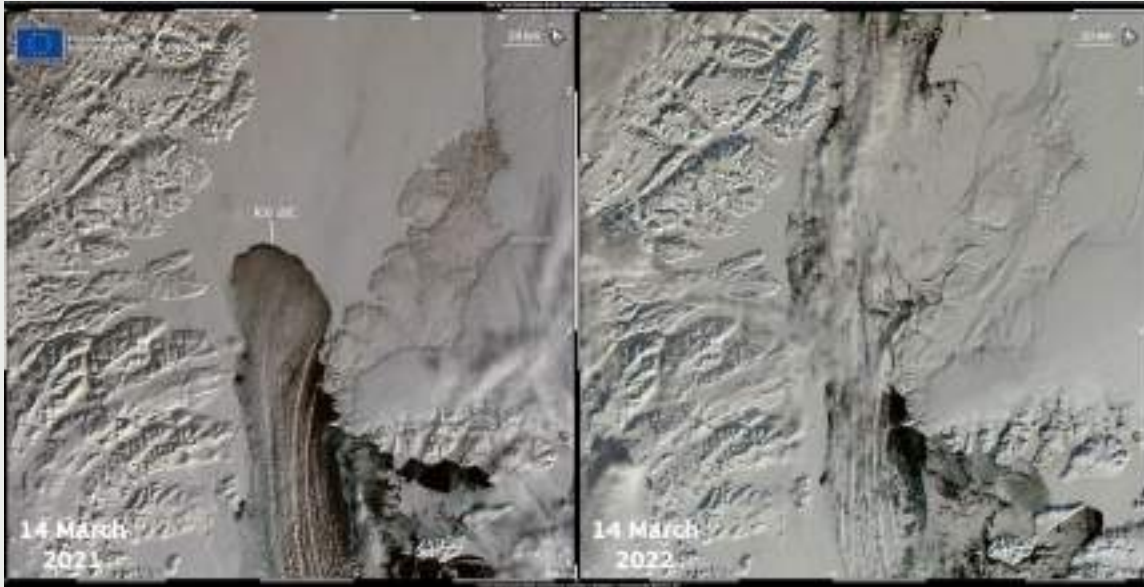


Fig. SB5.2. An ice arch in the Nares Strait between Canada and Greenland which typically appears in the winter such as in 2021 (left) but was absent in 2022 (right). Credit: European Union, Copernicus Sentinel-3 imagery. (Source: <https://www.copernicus.eu/en/media/image-day-gallery/absence-ice-arch-nares-strait-2022-winter>.)

rare. This was due to a warm, dry spring and an early snowpack melt-out. Heatwaves were observed in both the Barents and Beaufort Seas in 2022. Svalbard had a record-warm June, and November was the warmest on record for Iceland and the third warmest in Reykjavík, followed by the coldest December in Iceland since 1973. Early December brought extreme warmth to northwest Alaska, and some Bering Strait communities experienced a complete loss of snowpack due to rain and sustained above-freezing temperatures. On 5 December, the temperature at Utqiaġvik rose to 4.4°C, which was the highest winter temperature on record. No curve-shaped sea-ice edge spanning across the Nares Strait (known as “sea ice arches”; Fig. SB5.2) formed during 2022, only the third time since the early 1980s that such an arch has not formed. Thinning Arctic sea ice is a likely reason for the absent sea-ice arch (Moore et al. 2021).

Figure SB5.3 presents a summary of different categories of Arctic extremes reported for 2022. Of these, extremely high rainfall and temperatures accounted for most of the extreme Arctic events. Trends in extreme daily precipitation amounts (see section 5c) may be explained by increases in the number of days with precipitation (a dynamic effect) or increases in the mean precipitation intensity (a thermodynamic effect). It is also possible that daily precipitation has become more concentrated into smaller and more intense wet spots over Earth’s surface over the recent decades (Benestad et al. 2022).

Extreme storms can cause extensive societal impact. One of the most impactful Arctic extreme events in 2022 was a historically powerful storm that struck western Alaska in September. The storm originated as Typhoon Merbok in the subtropical North Pacific and transitioned to a very strong extratropical cyclone just prior to reaching the Bering Sea,

where the storm had the lowest pressure (932 hPa) of any storm to form that early in the autumn since at least 1950. Ex-Typhoon Merbok caused severe coastal flooding across western Alaska, with extensive infrastructure damage along a 1600-km stretch of coast from Kuskokwim Bay to the Bering Strait. Some communities experienced their highest water levels in at least the last 100 years. Another Arctic cyclone east of Svalbard, with record-low mean sea-level pressure (932 hPa) on 24 January, caused an unprecedented reduction in sea ice (Blanchard-Wrigglesworth et al. 2022). An extreme wind storm hit Iceland at the end of September with recorded wind speeds of up to 64 m s⁻¹. Due to the active North Atlantic storm track in February, extreme snowfall occurred in Reykjavik, Iceland,

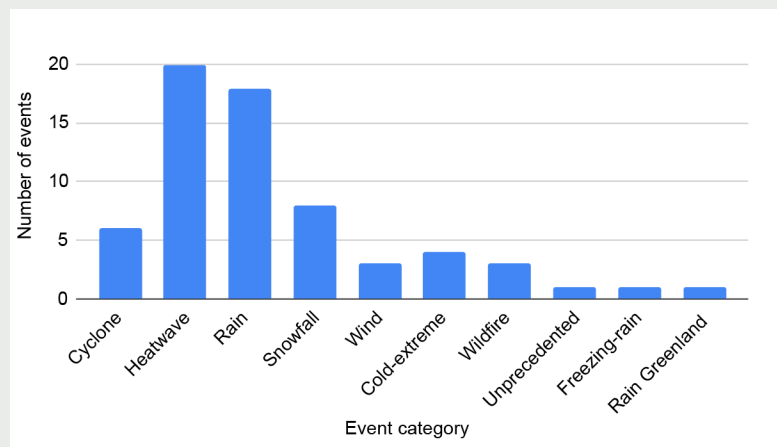


Fig. SB5.3. A summary of reported extreme event categories in the arctic in 2022. Cyclones and wind events may overlap. The total number of recorded events for 2022 was 56, and the summary is based on collected events from meteorological services connected to the Arctic, except from Russia. (Sources: National meteorological services associated with the Arctic.)

and a new national monthly rainfall record (142.7 mm) was set in Finland and Norway (see section 5c). In contrast, March was record dry in many places in Fennoscandia.

Changes in the Arctic may also contribute to extreme weather at lower latitudes, although there is not a scientific consensus on this issue (Cohen et al. 2020). North Pacific Arctic warming is a precursor to a polar vortex that stretches,

resulting in Arctic cold surface air outbreaks across North America (Cohen et al. 2021). Following the record Alaskan warmth in early December 2022, the stretched polar vortex unleashed extreme cold and blizzards across Canada and the U.S. lower 48 states during 21–26 December, making it one of the costliest and deadliest U.S. weather disasters in 2022 (<https://www.ncei.noaa.gov/access/billions/>).

d. Sea-surface temperature

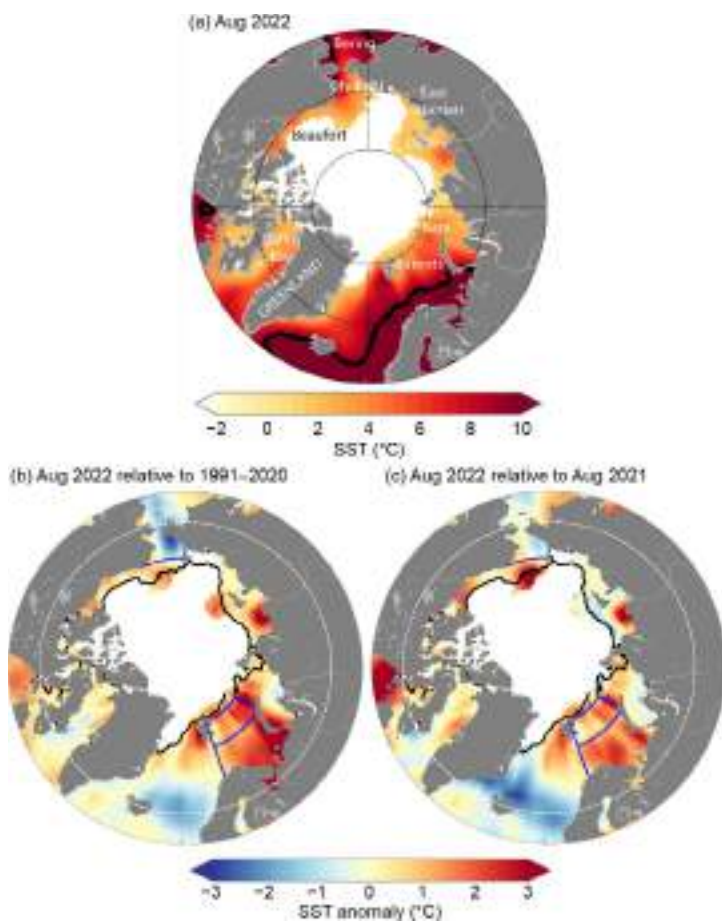
—M.-L. Timmermans and Z. Labe

Arctic Ocean sea-surface temperatures (SSTs) in the summer are driven by the amount of incoming solar radiation absorbed by the sea surface and by the flow of warm waters into the Arctic from the North Atlantic and North Pacific Oceans. Solar warming of the Arctic Ocean surface is influenced by the distribution of sea ice (with greater warming occurring in ice-free regions), cloud cover, and upper-ocean stratification. Discharge of relatively warm Arctic river waters can provide an additional source of heat in the coastal regions.

Arctic SST is an essential indicator of the role of the ice–albedo feedback cycle in any given summer sea-ice melt season. As the area of sea-ice cover decreases, more incoming solar radiation is absorbed by the darker ocean surface and, in turn, the warmer ocean melts more sea ice. Marine ecosystems are also influenced by SSTs, which affect the timing and development of production cycles, as well as available habitat. In addition, higher SSTs are associated with delayed autumn freeze-up and increased ocean heat storage throughout the year. An essential point for consideration, however, is that the total heat content contained in the ocean surface layer (i.e., the mixed layer) depends on its depth; a shallower mixed layer with higher SSTs could contain the same amount of heat as a deeper mixed layer with lower SSTs. We focus only on SSTs here and do not quantify ocean heat content due to a lack of in situ observations.

The SST data presented here are from the NOAA Optimum Interpolation (OI) SST version 2 product (OISSTv2; Reynolds et al. 2002, 2007) from 1982 to 2022, with comparisons made to the 1991–2020 baseline period. In the Arctic Ocean overall, the OISSTv2 product exhibits a cold bias (i.e., underestimates SST) of up to 0.5°C compared to ship-based measurements (Stroh et al. 2015). The OISSTv2 product uses a simplified linear relationship with sea-ice concentration to infer SST under sea ice (Reynolds et al. 2007), which means SSTs may be too cool by up to 0.2°C where there is sea-ice cover. There is an updated product (version 2.1) that employs a different method than OISSTv2 for setting a proxy SST in sea-ice-covered regions, applied only after January 2016 (in addition to some other differences that are not specific to the polar regions). See Huang et al. (2021) for a description. In our examination of trends in the Arctic Ocean, we require a product that estimates SST in the presence of sea ice using a consistent method for the duration of the data record. Otherwise, estimated trends might be artifacts of the change in methodology part way through the record. For this reason, we continue to use OISSTv2.

We focus primarily on August mean SSTs, which provide the most appropriate representation of Arctic Ocean summer SSTs. It is not appropriate to evaluate long-term SST trends in early summer (June and July) when most of the Arctic marginal seas still have significant sea-ice cover. SSTs generally plateau in the month of August, while surface cooling takes place in the latter half of September. This is evident, for example, in the fact that the mean of each year's standard deviation of weekly SST time series over 1991–2020 for the Arctic Ocean (north of 65°N) gives 0.1°C in August and 0.3°C in September (with even higher variance in September when individual marginal seas of the Arctic basin are considered separately).



August 2022 mean SSTs were as high as $\sim 12^{\circ}\text{C}$ in the southern Barents Sea and as high as $\sim 6^{\circ}\text{C}$ in other marginal regions of the Arctic basin (northern Barents, Chukchi, Beaufort, East Siberian, Kara, and Laptev Seas; Fig. 5.8a). August 2022 mean SSTs were notably warm ($\sim 2^{\circ}\text{C}$ – 3°C higher than the 1991–2020 August mean) in the Barents and Laptev Seas and cool in the Chukchi Sea ($\sim 3^{\circ}\text{C}$ lower than the 1991–2020 mean; Fig. 5.8b). In assessing these regional differences, it is important to note that SSTs exhibit significant variability from year to year. For example, there were considerably higher SSTs in the Barents Sea and lower SSTs in the waters off eastern Greenland in August 2022 compared to August 2021, with differences of up to 3°C in each case (Fig. 5.8c; see also Timmermans and Labe 2022). The August 2022 anomalously high SSTs in the Barents Sea, which were also observed in June and July (Fig. 5.9), aligned with anomalously high June–August 2022 surface air temperatures over northern Eurasia (section 5b).

Fig. 5.8. (a) Mean sea-surface temperature (SST; $^{\circ}\text{C}$) in Aug 2022. Black contours indicate the 10°C SST isotherm. (b) SST anomalies ($^{\circ}\text{C}$) in Aug 2022 relative to the Aug 1991–2020 mean. (c) Difference between Aug 2022 SSTs and Aug 2021 SSTs (negative values indicate where 2022 SSTs were lower). White shading in all panels is the Aug 2022 mean sea-ice extent. Black lines in (b) and (c) indicate the median ice edge for Aug 1991–2020. The regions marked by blue boundaries and the white dashed lines indicating 65°N in (b) and (c) relate to data presented in Fig. 5.10. Sea-ice concentration data are the NOAA/NSIDC Climate Data Record of Passive Microwave Sea Ice Concentration, version 4 (<https://nsidc.org/data/g02202>) and Near-Real-Time NOAA/NSIDC Climate Data Record of Passive Microwave Sea Ice Concentration, version 2 (<https://nsidc.org/data/g10016>; Peng et al. 2013; Meier et al. 2021a,b), where a threshold of 15% concentration is used to calculate sea-ice extent.

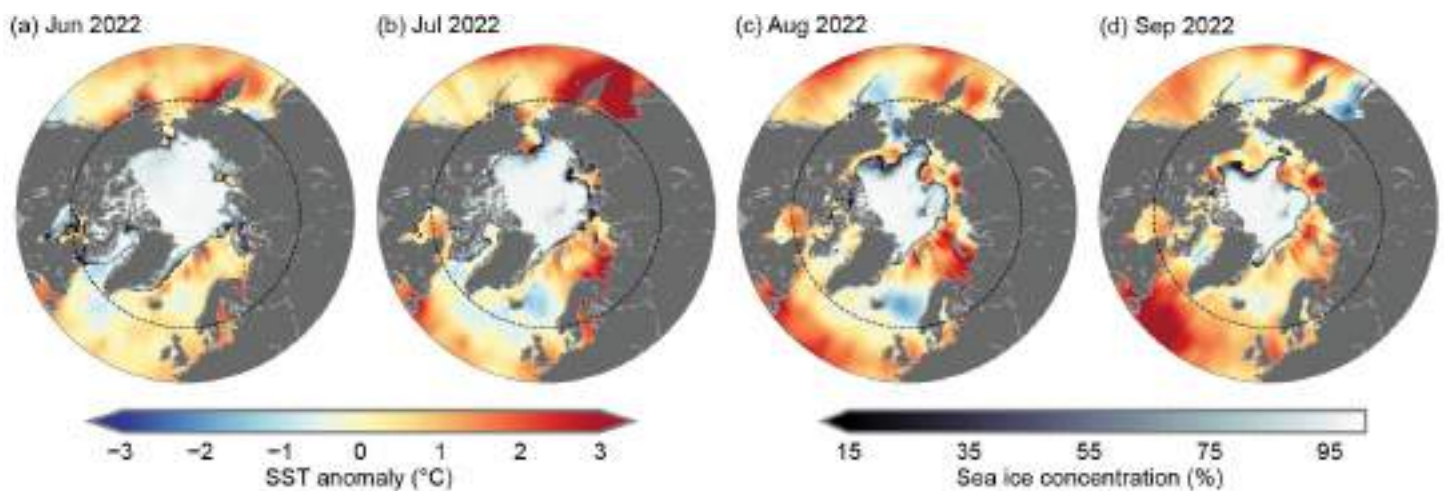


Fig. 5.9. Sea-surface temperature (SST) anomalies ($^{\circ}\text{C}$) for (a) Jun 2022, (b) Jul 2022, (c) Aug 2022, and (d) Sep 2022 relative to the 1991–2020 mean for the respective month. The sea-ice concentration for the corresponding month is also shown. The evolution of sea-ice concentration over the months of Jun to Aug illustrates why it is not appropriate to evaluate long-term SST trends in Jun and Jul over most of the Arctic marginal seas, which still have significant sea-ice cover in those months. While sea-ice extent is lowest in Sep, SSTs cool in the latter part of the month (see text). The black dashed circle indicates the latitudinal bound of the map images shown in Figs. 5.8 and 5.10. See Fig. 5.8 caption for sea-ice dataset information.

The August 2022 anomalously cool SSTs in the Chukchi Sea are commensurate with below-normal surface air temperatures in the region in June–August 2022 (section 5b). The persistence of a tongue of late-season sea ice near the coast where the East Siberian Sea meets the Chukchi Sea is further consistent with these anomalously low SSTs (Fig. 5.8b; section 5e). Conversely, to the north of this region of cool SSTs, sea-ice area was below normal and SSTs were anomalously high (Fig. 5.8b).

Mean August SST warming trends from 1982 to 2022 persist over much of the Arctic Ocean, with statistically significant (at the 95% confidence interval) linear warming trends in most regions, except the Laptev, East Siberian, and northern Barents Seas (Fig. 5.10a). Mean August SSTs for the entire Arctic (the Arctic Ocean and marginal seas north of 65°N) exhibit a linear warming trend of $+0.03 \pm 0.01^\circ\text{C yr}^{-1}$ (Fig. 5.10b). Even while anomalously low SSTs in the Chukchi Sea were prominent in the August 2022 SST field (Fig. 5.8b), SSTs show a linear warming trend over 1982–2022 of $+0.05 \pm 0.03^\circ\text{C yr}^{-1}$ (Fig. 5.10c) for this region. The cooling trend in mean August SSTs in the northern Barents Sea (Fig. 5.10d) remains an exception. This cooling trend has been notably influenced by anomalously high SSTs in that sector of the Barents Sea in the 1980s and 90s (Fig. 5.10d), although anomalously high SSTs in recent years in the region continue to have an influence on reversing the overall trend.

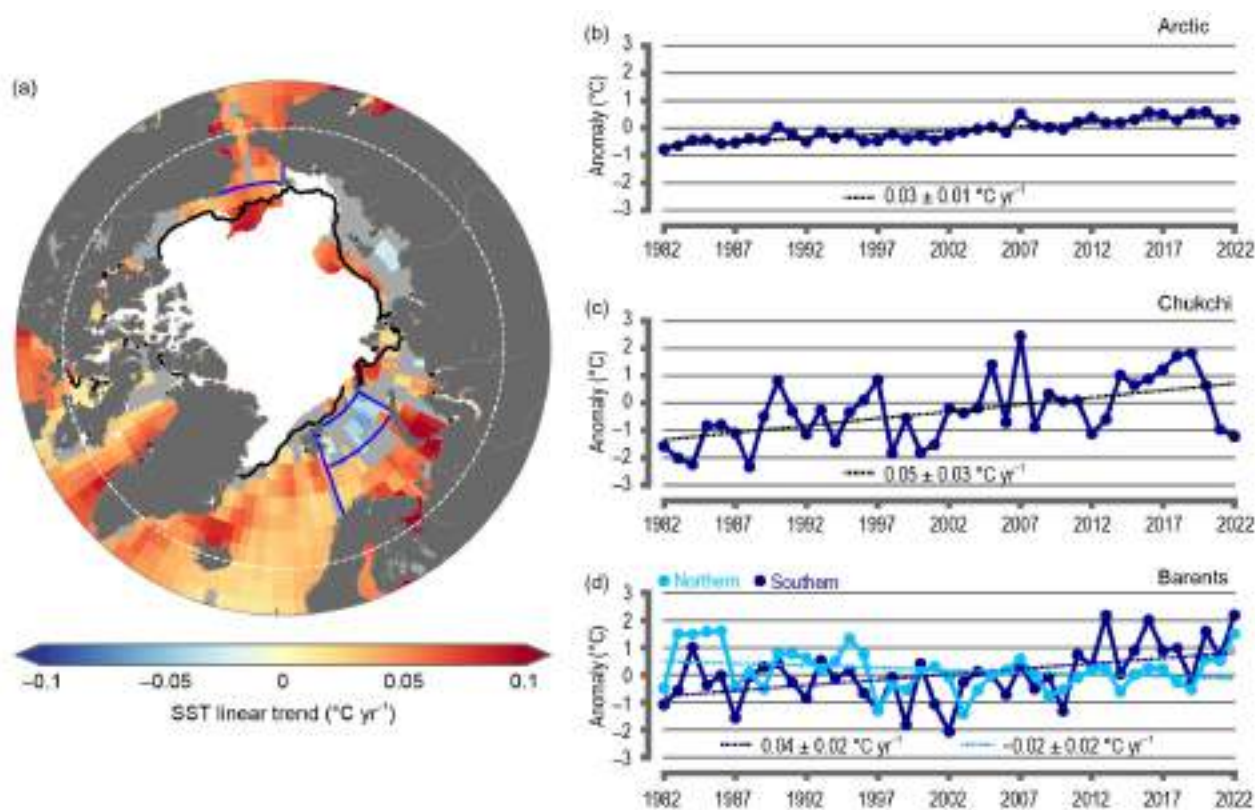


Fig. 5.10. (a) Linear sea-surface temperature (SST) trend ($^\circ\text{C yr}^{-1}$) for Aug of each year from 1982 to 2022. The trend is only shown for values that are statistically significant at the 95% confidence interval; the region is shaded gray otherwise. White shading is the Aug 2022 mean sea-ice extent, and the black line indicates the median ice edge for Aug 1991–2020. (b),(c),(d) Area-averaged SST anomalies ($^\circ\text{C}$) for Aug of each year (1982–2022) relative to the 1991–2020 Aug mean for (b) the entire Arctic Ocean north of 65°N, indicated by the dashed white circle in (a), (c) the Chukchi Sea, and (d) the northern and southern Barents Sea indicated by smaller blue boxes (intersecting with land boundaries) in (a). The dotted lines show the linear SST anomaly trends over the period shown and trends in $^\circ\text{C yr}^{-1}$ (with 95% confidence intervals) are indicated on the plots. See Fig. 5.8 caption for sea ice dataset information.

e. Sea ice

—W. N. Meier, A. Petty, S. Hendricks, D. Perovich, S. Farrell, M. Webster, D. Divine, S. Gerland, L. Kaleschke, R. Ricker, and X. Tian-Kunze

As the frozen interface between the ocean and atmosphere in the North, Arctic sea ice limits ocean–atmosphere exchanges of energy and moisture and plays a critical role in Arctic ecosystems and Earth’s climate. The presence of sea ice affects human activities in the Arctic, including Indigenous hunting and transportation, marine navigation, and national security responsibilities. The profound changes underway in the region continued to be illuminated by Arctic sea-ice conditions during 2022.

1. SEA-ICE EXTENT

Arctic sea ice began 2022 with higher coverage than in January 2021. In January 2022, sea-ice extent (defined as the total area covered by at least 15% ice concentration) was within the inter-decile range of the 1991–2020 median extent, which has been rare in recent years. Extent values are from the National Snow and Ice Data Center’s Sea Ice Index (Fetterer et al. 2017), one of several extent products (Lavergne et al. 2019; Ivanova et al. 2014) derived from satellite-borne passive microwave sensors operating since 1979. Persistently high sea-level pressure in the Siberian Arctic sector during January–February resulted in the divergence of ice from the Siberian coast as well as strong advection of thicker, multiyear ice into the Beaufort and Chukchi Seas from the north.

By March, the month with the greatest ice cover annually, the total sea-ice extent of $14.59 \times 10^6 \text{ km}^2$ was $0.44 \times 10^6 \text{ km}^2$ (5.1%) lower than the 1991–2020 average and the ninth-lowest March extent in the 44-year record. The March 2022 extent continued the statistically significant downward trend of $-2.6\% \text{ decade}^{-1}$ over the 1979–2022 record (Fig. 5.11a). On a regional basis, March 2022 was characterized by below-average extent in the Barents Sea and the Sea of Okhotsk, above-average extent in the Baffin Bay and Davis Strait, and near-average extent elsewhere (Fig. 5.11b).

After March, the seasonal retreat of sea ice began. In contrast to recent years, ice lingered along the Siberian coast until late summer, particularly in the East Siberian and Chukchi Seas. Weak pressure gradients and somewhat lower temperatures (relative to recent years) slowed sea-ice melt. In contrast, open water regions developed in late July north of the Kara Sea, near 88°N latitude, and persisted for several weeks. The openings resulted from a thinner, less compact ice cover, which may have been subjected to melt from warm ocean water.

September, the month of the annual minimum extent, was characterized in 2022 by below-average coverage in the Pacific sector, with the exception of a tongue

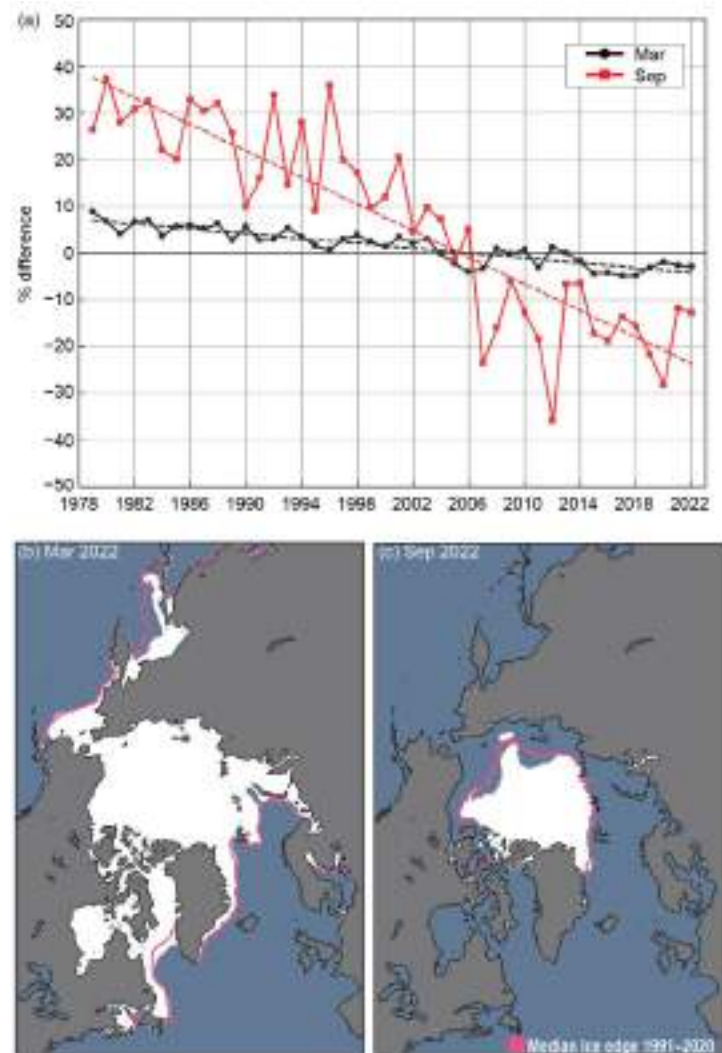


Fig. 5.11. (a) Monthly sea-ice extent anomalies (%; solid lines) and linear trend lines (dashed lines) for Mar (black) and Sep (red) from 1979 to 2022. The anomalies are relative to the 1991–2020 average for each month. (b) Mar 2022 and (c) Sep 2022 monthly average sea-ice extent; the median extent for 1991–2020 is shown by the magenta contour.

of ice in the East Siberian Sea that reached beyond the 1991–2020 median extent (Fig. 5.11c). The September 2022 Arctic sea-ice extent of $4.87 \times 10^6 \text{ km}^2$ was $0.71 \times 10^6 \text{ km}^2$ (12.7%) lower than the 1991–2020 average and the 11th-lowest September extent on record. The September trend from 1979 through 2022 is $-14.2\% \text{ decade}^{-1}$, and like all other months, is statistically significant. The 16 lowest September extents in the satellite record have all occurred in the last 16 years (2007–22), though the trend over that period has been near-zero.

2. SEA-ICE AGE, THICKNESS, AND VOLUME

Sea-ice age is a proxy for thickness as multiyear ice (ice that survives at least one summer melt season) grows thicker over successive winters. Sea-ice age is presented here (Fig. 5.12) for the period 1985–2022, based on Lagrangian tracking of ice parcels (Tschudi et al. 2019a,b). One week before the 2022 annual minimum extent, when the age values of the remaining sea ice are incremented by one year, the amount of multiyear ice remaining in the Arctic continued to be far lower than in the 1990s (Fig. 5.12). Since 2012, the Arctic has been nearly devoid of the oldest ice (>4 years old); this continued in 2022, with an end-of-summer oldest ice extent of 127,000 km^2 . In the 38 years since ice-age records began, the Arctic has changed from a region dominated by multiyear sea ice to one where first-year sea ice prevails. A younger ice cover implies a thinner, less voluminous ice pack—one that is more sensitive to atmospheric and oceanic conditions.

Sea ice drifts with winds and ocean currents, while growing and melting thermodynamically. Ice divergence creates leads and, in freezing conditions, new ice, while ice convergence leads to dynamic thickening. Sea-ice thickness provides a record of the cumulative effect of dynamic and thermodynamic processes and thus is an important indicator of overall ice conditions. European Space Agency satellites carrying the CryoSat-2 radar altimeter and the Soil Moisture and Ocean

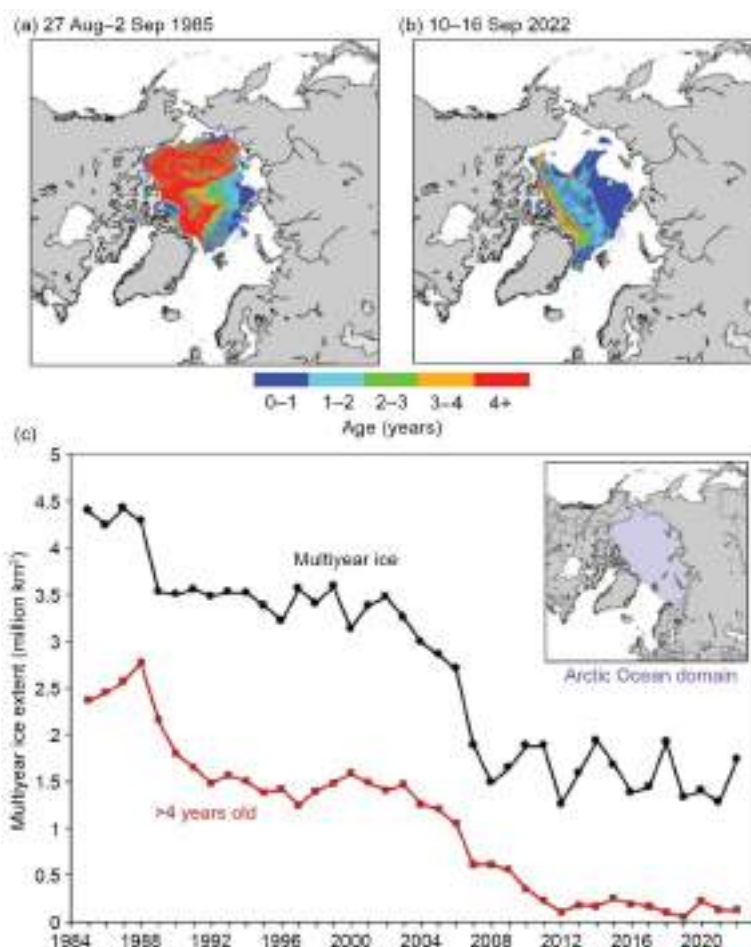


Fig. 5.12. Sea-ice age coverage map for the week before minimum total extent (when age values are incremented to one year older) in (a) 1985 and (b) 2022; (c) extent of multiyear ice (black) and ice >4 years old (red) within the Arctic Ocean (inset) for the week of the minimum total extent.

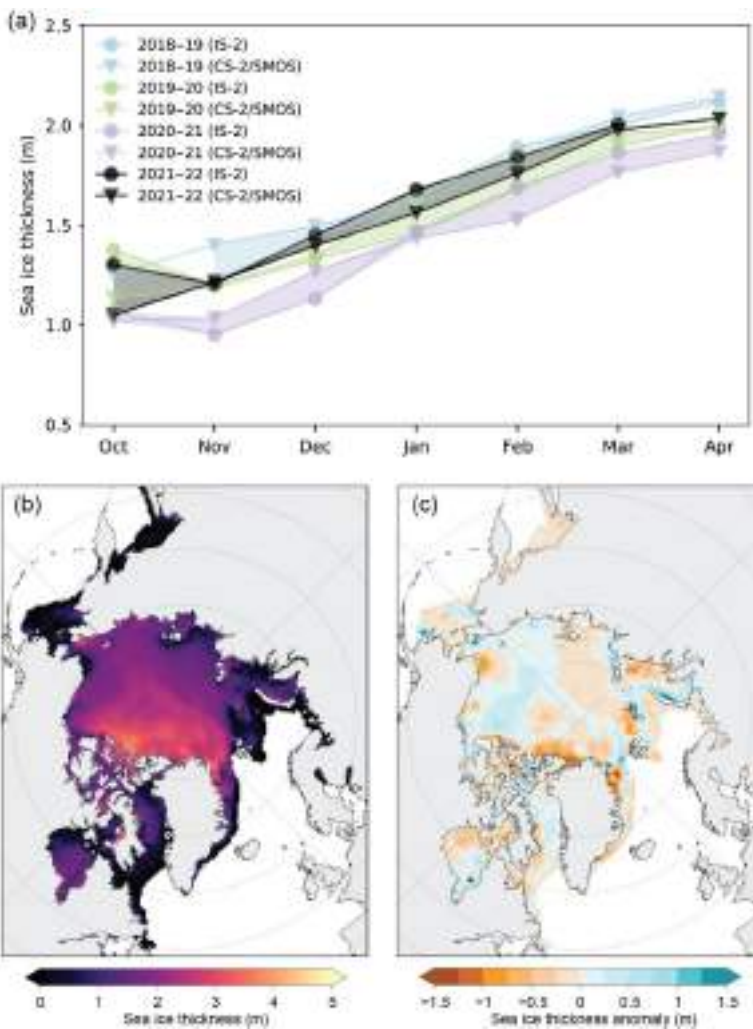


Fig. 5.13. (a) Oct–Apr monthly average sea-ice thickness, calculated over an inner-Arctic Ocean domain (inset of Fig. 5.12c), from ICESat-2 (circles) and CryoSat-2/SMOS (triangles) for 2018/19 (blue), 2019/20 (green), 2020/21 (lilac), and 2021/22 (black); (b) average Apr 2022 sea-ice thickness map from CryoSat-2/SMOS; (c) CryoSat-2/SMOS thickness anomaly map (relative to the 2010–21 average).



Fig. 5.14. Annual sea-ice volume loss (orange) and gain (blue) between annual maximum and minimum from the CryoSat-2/SMOS Sea Ice Thickness Version 205 product (<https://earth.esa.int/eogateway/catalog/smos-cryosat-l4-sea-ice-thickness>, accessed 5 Mar 2023). Volume is not estimated during summer, May–Sep. The volume gain represents the change in volume from the first autumn observation in Oct to the annual maximum observed volume, Apr of the following year. The volume loss is the difference between the maximum and Oct values.

Salinity (SMOS) microwave radiometer have provided a record of seasonal (October to April) ice thickness and volume (Ricker et al. 2017) since the 2010/11 winter; a summer record has also been developed (Landy et al. 2022). Since 2018, the laser altimeter on the NASA Ice, Cloud and land Elevation Satellite-2 (ICESat-2) satellite has also provided thickness estimates (Petty et al. 2020, 2021, 2023). Some differences between these two products are seen in the monthly winter average thickness, but both show 2022 thickness on the high end of the short time series (Fig. 5.13a); ICESat-2 did not compute an April 2022 average due to some missing data during the month. Spatially, the CryoSat-2/SMOS April thickness map (Fig. 5.13b) shows the typical pattern of thicker ice along the Canadian Archipelago. However, the anomaly map indicates thinner ice than the 2010–22 average in that region (Fig. 5.13c). Elsewhere, April 2022 ice was thicker in the Beaufort Sea and the East Siberian Sea (contributing to delayed ice loss there), but thinner in the Laptev and Kara Seas, and particularly along the north coast of Greenland.

Sea-ice thickness is integrated with ice concentration to provide winter volume estimates for 2010–22. The change from winter maximum volume to summer minimum and back to winter over the years illustrates the strong seasonal cycle and interannual variability (Fig. 5.14). There is little indication of a trend through the relatively short 11-year time series. After a record-low maximum volume in April 2021, there was a relatively small summer loss, which was then followed by a strong increase in sea ice through the October 2021 to April 2022 winter. This resulted in a notable increase in April 2022 volume compared to April 2021, as was also indicated by the average thickness (Fig. 5.13a).

f. Greenland Ice Sheet

—K. Poinar, K. D. Mankoff, T. A. Moon, B. D. Loomis, X. Fettweis, R. S. Fausto, T. L. Mote, C. D. Jensen, A. Wehrlé, and M. Tedesco

The Greenland Ice Sheet (GrIS) contributes directly to global sea levels when ice melts or breaks off into the ocean, increasing coastal erosion and flooding. Currently, the equivalent of ~7.4 m of eustatic sea level is contained in the GrIS (Morlighem et al. 2017). The GrIS has lost ice mass every mass balance year (1 September of the preceding year through 31 August) since 1998 (Mouginot et al. 2019). In 2022 (September 2021–August 2022), the Gravity Recovery and Climate Experiment Follow-on (GRACE-FO) satellite mission measured a GrIS mass loss of -165 ± 18 Gt, the equivalent of ~0.5 mm eustatic sea level rise (Fig. 5.15). This loss was 95 Gt (37%) less than the 2002–22 average of -260 ± 11 Gt.

The overall mass balance comprises surface mass balance (SMB, the accumulated snowfall minus the meltwater runoff) and solid ice discharge (break-off/calving of glacial ice directly into the ocean). In 2022, the SMB was above average, but within the 1991–2020 interannual variability. The highest cumulative snowfall since 1996 drove the relatively large SMB. However, melt in September 2022, just preceding the standard mass balance year, was unprecedented, with a record-breaking number of melting days at multiple sites. This included melt at Summit Station (3216 m a.s.l.), which has been observed only four other times in its 34-year observation history, and never in September.

The 2-meter air temperature observations at 16 Danish Meteorological Institute predominantly coastal, land-based weather stations from September 2021 through August 2022 showed temperature anomalies between -0.3°C and $+1.0^\circ\text{C}$, close to or slightly above the 1991–2020 average. While autumn (September–November 2021) temperatures were variable, winter (December 2021–February 2022) temperatures were predominantly close to or above average. Spring (March–May 2022) temperatures were also variable, but summer (June–August 2022) temperatures were slightly below average. On-ice weather stations operated by the Programme for Monitoring of the Greenland Ice Sheet (PROMICE) at the Geological Survey of Greenland and Denmark showed June air temperatures ~1 std. dev. below average and several snowfall events that month. By July and August, PROMICE temperatures were all within 1 std. dev. of the 2008–22 average. September was unusually warm (>1 std. dev. above average), due in part to a persistent high-pressure weather system over the southeast coast and a low-pressure system over the Canadian Arctic Archipelago that, together, imported warm, moist southerly air over Greenland in early September. This system brought thick clouds and heavy rain to western Greenland.

Ablation (ice loss via melt or other processes) measured by PROMICE (Fig. 5.16a) was also close to the 1991–2020 average. Regional exceptions were a +70% ablation anomaly at Thule in northwest Greenland and -42% at Kronprins Christians Land in northeast Greenland. Surface melting determined daily from the Special Sensor Microwave Imager/Sounder (SSMIS; Fig. 5.16b) also indicated an overall typical melt season. The southwest and northeast experienced more melt days than average, although the overall lower total melt, shown in Fig. 5.16a, suggests that

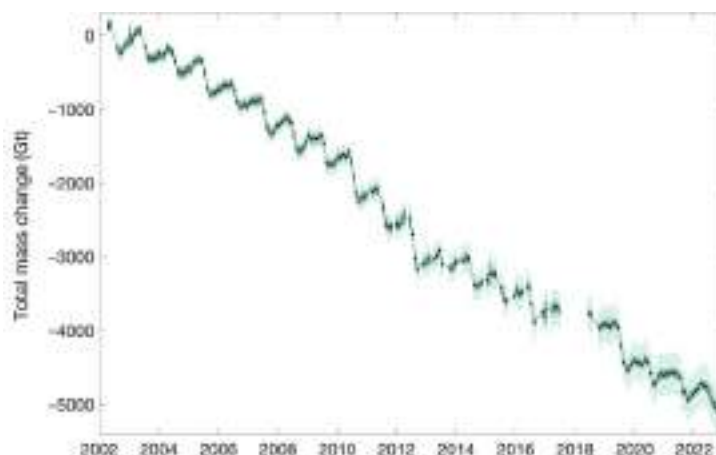


Fig. 5.15. Total mass change (Gt) of the GrIS from 2002 through mid-Nov 2022 determined from GRACE (2002–17) and GRACE-FO (2018–present; Tapley et al. 2019). Monthly estimates are shown as black circles, and 2-sigma uncertainties are provided with (light green) and without (dark green) errors due to leakage of external signals to the trend (i.e., mass changes near Greenland but not associated with the GrIS).

on average, the melt on these days was of lower volume. The southeast experienced fewer melt days than average; however, on 4–5 September, the warm air mass mentioned above descended from the ice sheet summit and initiated substantial melt there.

Only twice in 2022 did SSMIS observe melt conditions on >30% of the ice sheet surface (Fig. 5.16c): a July melt episode that peaked at 688,000 km² (42%) of the surface experiencing melt and the early September melt episode when 592,000 km² (36%) of the surface melted. Another series of unprecedented melt events occurred in late September, when warm air associated with the remains of Hurricane Fiona reached Greenland and melt occurred on 245,000 km² (15%) of the surface.

Ablation changes the reflective character of the ice sheet surface through the surface broadband albedo, or the fraction of incident light energy it reflects at all wavelengths. Ablation can expose bare glacial ice, which has a lower albedo (i.e., absorbs more energy) than snow cover. The annual transition from a snow-covered surface to a bare glacial ice surface creates a step change in surface broadband albedo (Ryan et al. 2019; Wehrlé et al. 2021).

The annually averaged summer albedo measured from Sentinel-3 and the Moderate Resolution Imaging Spectroradiometer (MODIS) was above (more reflective than) average (Figs. 5.17a,b),

especially in the western ablation zone and coastal areas in the east and northeast (Wehrlé et al. 2021). Seasonally, the high albedo paired with average or below-average bare-ice area through the summer (Fig. 5.17c). The bare-ice area reached ~130,000 km² (8%) of the ice-sheet surface on 1 August before dropping below 100,000 km², then peaked at ~140,000 km² during the abnormally warm September. A September bare-ice area maximum is unique in the six-year observational record.

The Modèle Atmosphérique Régional (MARv3.13) polar regional climate model, forced by the fifth European Centre for Medium-Range Weather Forecasts (ECMWF) Reanalysis (ERA5; Hersbach et al. 2020) fully coupled with a snow energy balance model, provides SMB figures at a horizontal resolution of 15 km. We present ice sheet-wide totals here. The total SMB was 436 Gt yr⁻¹, within the 1991–2020 average of 339±123 Gt yr⁻¹. This occurred from a combination of 12% larger snowfall accumulation than average (784 Gt yr⁻¹, the highest accumulation since 1996), average meltwater runoff (350 Gt yr⁻¹), average sublimation and

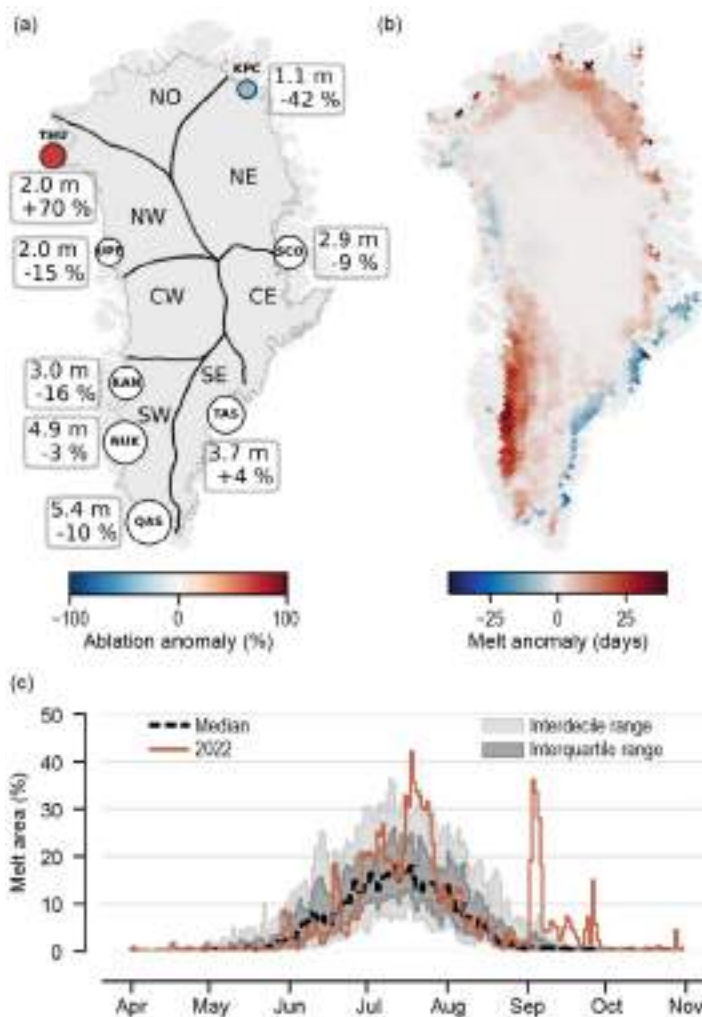


Fig. 5.16. (a) Net ablation for 2022 (m, top number) measured by PROMICE weather transects and referenced to the 1991–2020 period (% , bottom number). Circles are scaled in size to net ablation and scaled in color to the anomaly. White circles indicate anomaly values within methodological and measurement uncertainty. Stations are: Thule (THU), Upernavik (UPE), Kangerlussuaq (KAN), Nuuk (NUK), Qassimuit (QAS), Tasiliq (TAS), Scoresby Sund (SCO), and Kronprins Christians Land (KPC). The regions North (NO), Northeast (NE), Northwest (NW), Central East (CE), Central West (CW), Southeast (SE), and Southwest (SW) are referenced in Fig. 5.18. (b) Number of melt days expressed as an anomaly with respect to the 1991–2020 reference period, from daily SSMIS 37 GHz, horizontally polarized passive microwave radiometer satellite data (Mote 2007). (c) Surface melt extent as a percentage of the ice sheet area during 2022 (solid orange) derived from SSMIS.

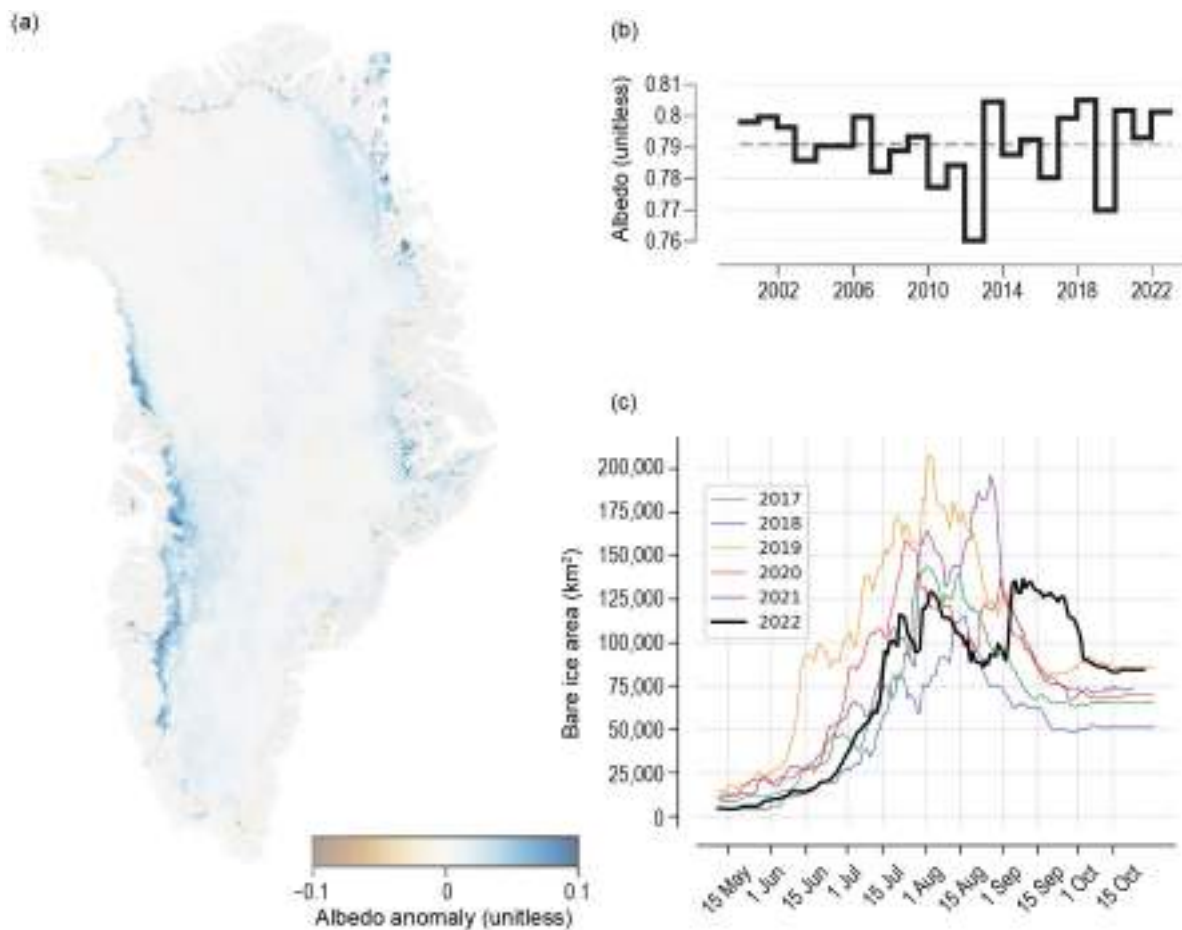


Fig. 5.17. (a) Albedo anomaly for Jun–Aug 2022 measured from Sentinel-3 data, relative to a 2017–2021 reference period (Wehrlé et al. 2021). (b) Time series for average Greenland Ice Sheet Jun–Aug albedo from MODIS. (c) Bare ice area (km²) measured from Sentinel-3 observations, with 2022 in black (Wehrlé et al. 2021).

evaporation (50 Gt yr⁻¹), and substantially greater annual rainfall than average (54 Gt yr⁻¹, an anomaly of +65% and >2 std. dev. above the mean), roughly half of which refroze in the snowpack. Much of the rainfall occurred in September, when fresh snow covered the ice sheet. That month, meltwater production was seven times larger than the 1991–2020 September average; snowfall quantities were also high, which allowed a large portion of this melt and rainwater to refreeze. This has the potential to affect local SMB in future melt seasons by forming ice lenses, which inhibit downward percolation of meltwater, allowing it to run off instead of being retained in the snowpack.

The second factor in the overall mass balance of the GrIS is solid ice discharge, which occurs around the perimeter of the ice sheet at hundreds of ice–ocean boundaries. Discharge is far less variable year-to-year than SMB, as continental ice flow responds to environmental changes relatively slowly (Mankoff et al. 2021). The 2022 discharge was 506 ± 47 Gt yr⁻¹ (Fig. 5.18), which is within the 1991–2020 average of 488 ± 44 Gt yr⁻¹. In 2022, the sectors with the highest discharge continued to be the southeast (144 Gt yr⁻¹) and the northwest (115 Gt yr⁻¹), with a modest increasing trend in the northwest over the past ~20 years.

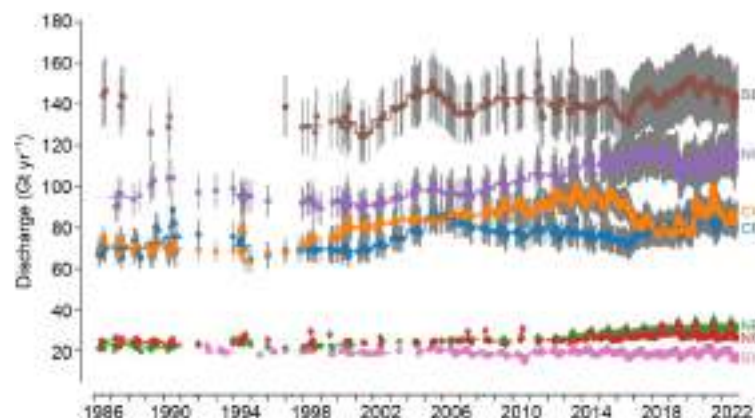


Fig. 5.18. Solid ice discharge (Gt yr⁻¹) based on ice velocity and thickness (Mankoff et al. 2020) by region of the Greenland Ice Sheet, as shown in Fig. 5.16a. Gray bars show uncertainty of ±10%.

g. Terrestrial snow cover

—L. Mudryk, A. Elias Chereque, C. Derksen, K. Luoju, and B. Decharme

Many components of the Arctic land surface are directly influenced by snow cover from autumn through spring, including the surface energy budget and ground thermal regime, with implications for the carbon cycle, permafrost, and terrestrial and freshwater ecosystems (Brown et al. 2017; Meredith et al. 2019, and references therein). Even following the snow-cover season, the influence of spring snow melt persists through impacts on river discharge timing and magnitude, surface water, soil moisture, vegetation phenology, and fire risk (Meredith et al. 2019).

Snow-cover extent anomalies (relative to the 1991–2020 climatology) in spring (May and June) 2022 are shown separately for the North American and Eurasian terrestrial sectors of the Arctic in Fig. 5.19 (data from the NOAA snow chart climate data record; Robinson et al. 2012). May anomalies were near average in the North American sector (29th lowest in the 56-year record available since 1967) but below average over the Eurasian sector (ninth lowest). Rapid snow loss after May resulted in low snow-cover extent across both sectors in June (second and third lowest, respectively).

Snow-cover duration (SCD) anomalies (relative to a 1998/99–2017/18 climatology) across the Arctic region for the 2021/22 snow season are shown in Figs. 5.20a,b as percent differences relative to the climatological number of snow-free days (data from the NOAA daily Interactive Multisensor Snow and Ice Mapping System [IMS] snow-cover product; U.S. National Ice Center 2008). Anomalies in the total number of days with snow cover were computed separately for each half of the snow season: August 2021–January 2022, referred to as "onset period," and February–July 2022, referred to as "melt period." Onset anomalies indicate that snow cover during 2021 began earlier than normal over Alaska, eastern Siberia, and Scandinavia, and began later than normal over central Arctic Canada and parts of central Siberia (Fig. 5.20a), a pattern consistent with below-average autumn temperatures (Thoman et al. 2022). Melt anomalies during spring 2022 show anomalously low SCD (indicating early melt) across much of the Arctic, with three areas as especially anomalous: east of the Ural Mountains, across eastern Siberia, and over the Canadian Arctic Archipelago (Fig. 5.20b), consistent with high spring and summer

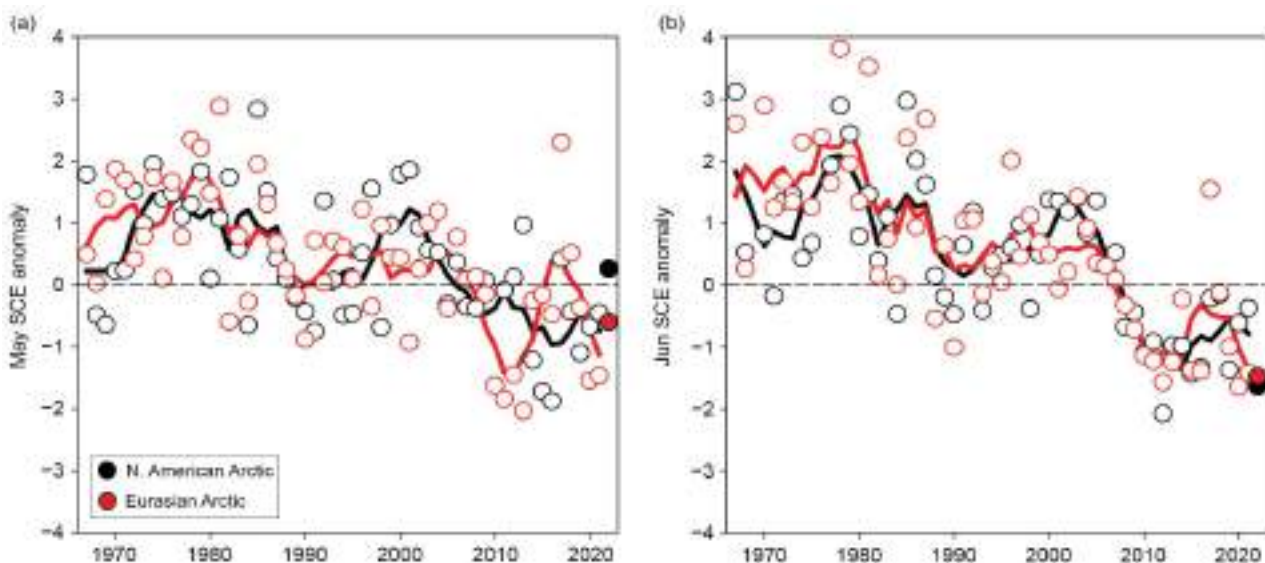


Fig. 5.19. Monthly snow-cover extent (SCE) anomalies for Arctic terrestrial land areas (>60°N) for (a) May and (b) Jun from 1967 to 2022. Anomalies are relative to the 1991–2020 average and standardized (each observation differenced from the mean and divided by the standard deviation, and thus unitless). Solid black and red lines depict 5-yr running means for North America and Eurasia, respectively. Filled circles highlight 2022 anomalies. (Source: Robinson et al. 2012).

2022 temperature anomalies (see Fig. 5.2). Similar to spring 2021, the duration of the spring 2022 snow-free period across broad expanses of Eurasia was 30%–50% longer than normal.

Snow water equivalent (SWE) characterizes the amount of water stored as snow, which enters the hydrologic cycle once it melts. SWE data during April–June were obtained from four daily-frequency gridded products over the 1981–2022 period: 1) the European Space Agency Snow Climate Change Initiative (CCI) SWE version 2 product derived through a combination of satellite passive microwave brightness temperatures and climate-station snow-depth observations (Luoju et al. 2022); 2) the Modern-Era Retrospective Analysis for Research and Applications version 2 (MERRA-2; GMAO 2015) daily SWE fields; 3) SWE output from the European Centre for Medium-Range Weather Forecasts (ECMWF) Reanalysis version 5-Land (ERA5-Land) analysis (Muñoz Sabater 2019); and 4) the physical snowpack model Crocus (Brun et al. 2013) driven by near-surface meteorological variables from ERA5. Reduced availability of climate-station

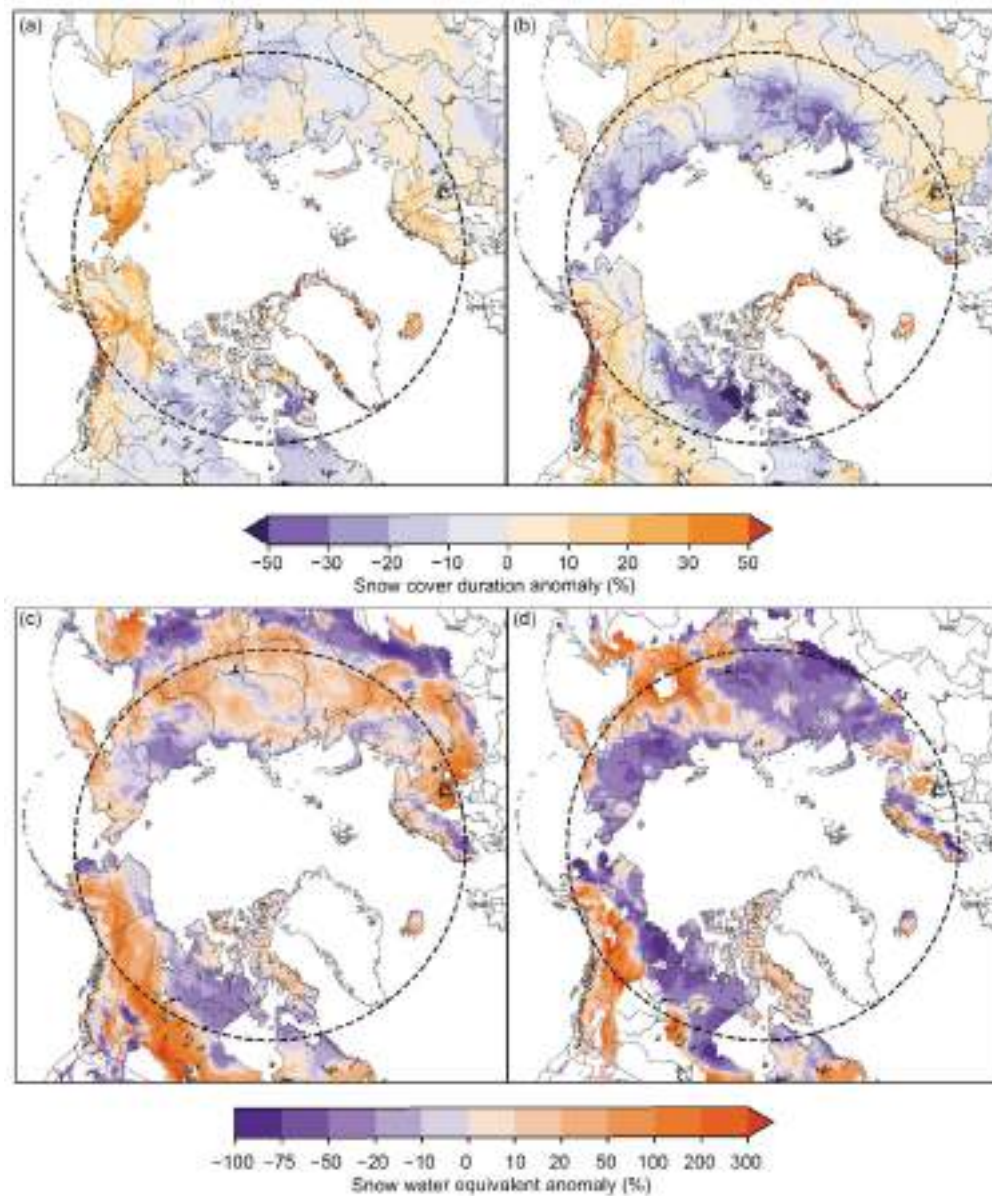


Fig. 5.20. Snow-cover duration (SCD) anomalies (% difference relative to climatological number of snow-free days for the 1998/99–2017/18 baseline) for the 2021/22 snow year: (a) snow onset period (Aug 2021–Jan 2022); and (b) snow melt period (Feb–Jul 2022). Purple (orange) indicates fewer (more) days than average. Snow water equivalent (SWE) anomalies (% difference from the 1991–2020 baseline) in 2022 for (c) Apr and (d) May. Purple (orange) indicates less (more) snow than average. Latitude 60°N marked by black dashed circle; land north of this defines the Arctic terrestrial area considered in this study. (Source: (a),(b) U.S. National Ice Center [2008]; (c),(d) four SWE products from Snow CCI [Luoju et al. 2022], MERRA2 [GMAO 2015], ERA5-Land [Muñoz Sabater 2019], and Crocus [Brun et al. 2013].)

snow-depth measurements limits the accuracy of the Snow CCI SWE product during May and June, hence it is omitted for those months. An approach using gridded products is required because in situ observations alone are too sparse to be representative of hemispheric snow conditions, especially in the Arctic.

For April, the spatially variable SWE data from each product are aggregated across Arctic land regions (>60°N) for both North American and Eurasian sectors and standardized relative to the 1991–2020 baseline to produce April snow-mass anomalies. The ensemble mean anomalies and the range of estimates among the products are presented in Fig. 5.21. April is chosen because it is the month in which total snow mass across the terrestrial pan-Arctic region typically peaks, reflecting total snowfall accumulations since the preceding autumn before increasing temperatures during May and June lead to melt. The 2022 anomalies highlighted in Fig. 5.21 indicate that snow accumulation was moderately above the 1991–2020 average across both the Eurasian and North American Arctic. Figures 5.20c,d illustrate how the SWE data varied spatially during both April and May, presented as percent differences of the ensemble-mean field relative to the 1991–2020 baseline. In April, both continents had mixed distributions of SWE: the northern regions of Arctic Eurasia had lower SWE than normal with higher-than-normal SWE located farther south. In North America, the central Canadian Arctic and northern Alaska had lower-than-normal SWE while higher-than-normal accumulations were present south of the Brooks Range and across the Yukon Territory. Melt during May caused widespread reductions in SWE across the Eurasian Arctic and further reduced the snowpack where it was already lower than average in the North American Arctic, consistent with the pattern of snow-cover duration anomalies shown in Fig. 5.20b. By June (not shown), SWE had melted across almost the entire Arctic except for the northern portion of the Canadian Arctic Archipelago, the Scandinavian mountains, and northernmost Taymyr Peninsula, consistent with the near-record lows in June snow extent across both continents (Fig. 5.19).

Similar to the previous year, the 2021/22 Arctic snow season saw a combination of increased snow accumulation (expressed as higher-than-average April snow mass in Fig. 5.21) and early snow melt (expressed in Fig. 5.20b as shorter snow-cover duration during the melt period). There is no significant trend in pan-Arctic snow mass since 1980, but there are significant reductions in spring snow extent, which has been persistently below normal for the last 15 years (Fig. 5.19). These attributes are consistent with the expected changes to Arctic snow cover in a warmer Arctic: regionally-dependent changes in snow accumulation but Arctic-wide reductions in spring snow extent and snow-cover duration (Meredith et al. 2019).

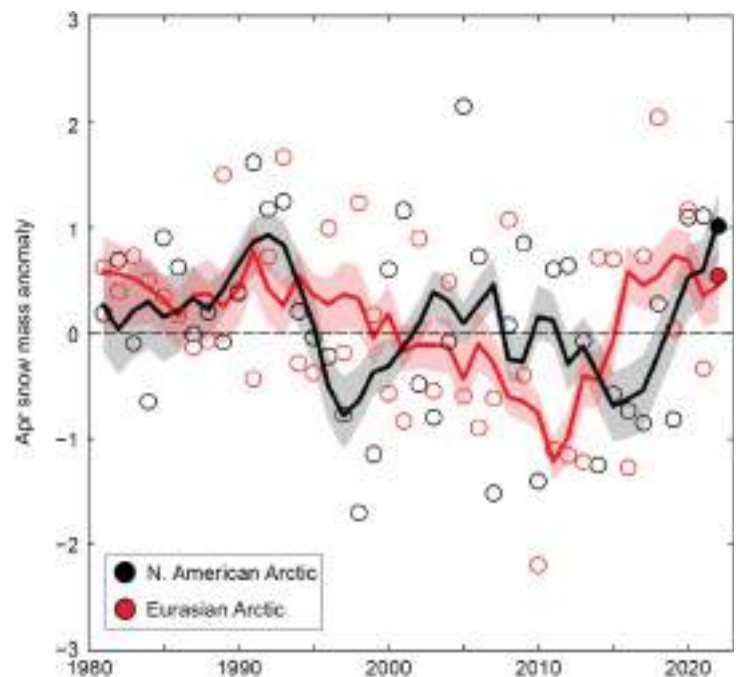


Fig. 5.21. Mean Apr snow mass anomalies for Arctic terrestrial areas calculated for North American (black) and Eurasian (red) sectors of the Arctic over 1981–2022. Anomalies are relative to the average for 1991–2020 and standardized (each observation differenced from the mean and divided by the standard deviation, and thus unitless). Filled circles highlight 2022 anomalies. Solid black and red lines depict 5-yr running means for North America and Eurasia, respectively, and the spread among the running means for individual datasets is shown in shading. (Source: four SWE products from Snow CCI [Luoju et al. 2022], MERRA2 [GMAO 2015], ERA5-Land [Muñoz Sabater 2019], and Crocus [Brun et al. 2013].)

h. Arctic river discharge

—J. W. McClelland, A. I. Shiklomanov, A. Suslova, M. Tretiakov, R. M. Holmes, R. G. M. Spencer, S. E. Tank, and S. Zolkos

The Arctic Ocean accounts for approximately 1% of the global ocean's volume but receives more than 10% of global river discharge (McClelland et al. 2012). Consequently, effects of river inputs on ocean processes are more pronounced in the Arctic and changes in river inputs have greater potential to impact ocean physics, chemistry, and biology than in other ocean basins. Because rivers naturally integrate the processes that are occurring throughout their watersheds, trends in the discharge and chemistry of Arctic rivers can also be indicative of widespread terrestrial change including permafrost thaw and the amount or seasonality of precipitation (Rawlins et al. 2010; Holmes et al. 2013).

Multiple studies over the past 20 years have demonstrated that discharge from Arctic rivers is increasing. Evidence first emerged from long-term Russian datasets (Peterson et al. 2002) and more recently from shorter U.S. and Canadian datasets (Durocher et al. 2019). While uncertainty remains around drivers of this trend, it is consistent with intensification of the Arctic hydrologic cycle (Rawlins et al. 2010). Warming is driving increased atmospheric moisture transport into the Arctic, resulting in greater precipitation (Box et al. 2019; section 5c). This is particularly evident during colder months of the year. For example, snowfall has increased during autumn and early winter in western Siberia (Wegmann et al. 2015) and in the Canadian Arctic (Kopec et al. 2016; Yu and Zhong 2021).

River discharge was last included in the *State of the Climate in 2020* report; therefore, discharge data for 2021 and 2022 are presented here. Data presentation and analysis focus on eight rivers that collectively drain much of the pan-Arctic watershed (Fig. 5.22). Six of these rivers are in Eurasia and two are in North America. Discharge measurements for the six Eurasian rivers began in 1936, whereas discharge measurements did not begin until 1973 for the Mackenzie River and 1976 for the Yukon River in North America. Years are presented as “water years”, 1 October–30 September, a common practice in hydrology to align runoff and associated precipitation within the same year. Thus, water year 2022 covers the period 1 October 2021– 30 September 2022. The data used in this analysis are freely available through the Arctic Great Rivers Observatory (<https://arcticgreatrivers.org/>).

Discharge data for 2021 and 2022 are compared to a 1991–2020 reference period in this report, a change from the 1981–2010 reference period used for the previous report. Both the old and new reference periods are included in Table 5.1 to allow for continuity between reports. Combined annual discharge averaged 2397 km³ during the new reference period and 2348 km³ during the old reference period. While this only represents a modest 2.1% increase between the two periods, it reflects increases observed in seven out of eight individual rivers and is consistent with long-term trends of increasing Arctic river discharge.



Fig. 5.22. Watersheds of the eight largest Arctic rivers featured in this analysis. Collectively, these rivers drain approximately 70% of the 16.8 million km² pan-Arctic watershed (indicated by the red boundary line). The red dots show the location of the discharge monitoring stations.

Combined annual discharge for the eight rivers was 2555 km³ for 2021 and 2516 km³ for 2022 (Table 5.1). These values exceeded the 1991–2020 reference average by approximately 7% and 5%, respectively. Differences relative to the reference period were largely driven by elevated discharge in the Yukon, Mackenzie, and Yenisey Rivers, which exceeded their associated reference averages in both years. Annual discharge reached a record high in 2021 for the Yenisey. Although data accuracy for this river has declined significantly since 2003 due to a lack of rating curve updates (Tretiyakov et al. 2022), elevated values were reported across multiple gauges on the Yenisey during the summer and autumn of 2021. Annual discharge values in the Severnaya Dvina, Pechora, Ob, and Kolyma were lower than the 1991–2020 reference average in both 2021 and 2022.

Monthly data for the Eurasian rivers show that June discharge during 2021 and 2022 was well below the reference average, whereas discharge during most other months was above the reference average (Fig. 5.23a). In contrast, discharge in the North American rivers during 2021 and 2022 was above the reference average during all months (Fig. 5.23b). These results are still provisional, but patterns represented in aggregate were also evident in individual rivers. The observed increases during winter months on both sides of the Arctic are consistent with findings of other

Table 5.1. Annual discharge (km³) for the eight largest Arctic rivers. Results are shown for 2021 and 2022 as well as mean values for old (1981–2010) and new (1991–2020) reference periods. *Italicized* values indicate provisional data and are subject to modification until official data are published.

Year ¹	Yukon (N. America)	Mackenzie (N. America)	S. Dvina (Eurasia)	Pechora (Eurasia)	Ob' (Eurasia)	Yenisey (Eurasia)	Lena (Eurasia)	Kolyma (Eurasia)	Total
2022	240	349	85	96	381	663	630	72	2516
2021	233	382	82	89	415	745	541	68	2555
1981–2010	205	288	104	114	398	612	557	70	2348
1991–2020	211	291	106	116	416	606	573	78	2397

¹Year refers to Water Year (1 October of the previous year to 30 September of the noted year)

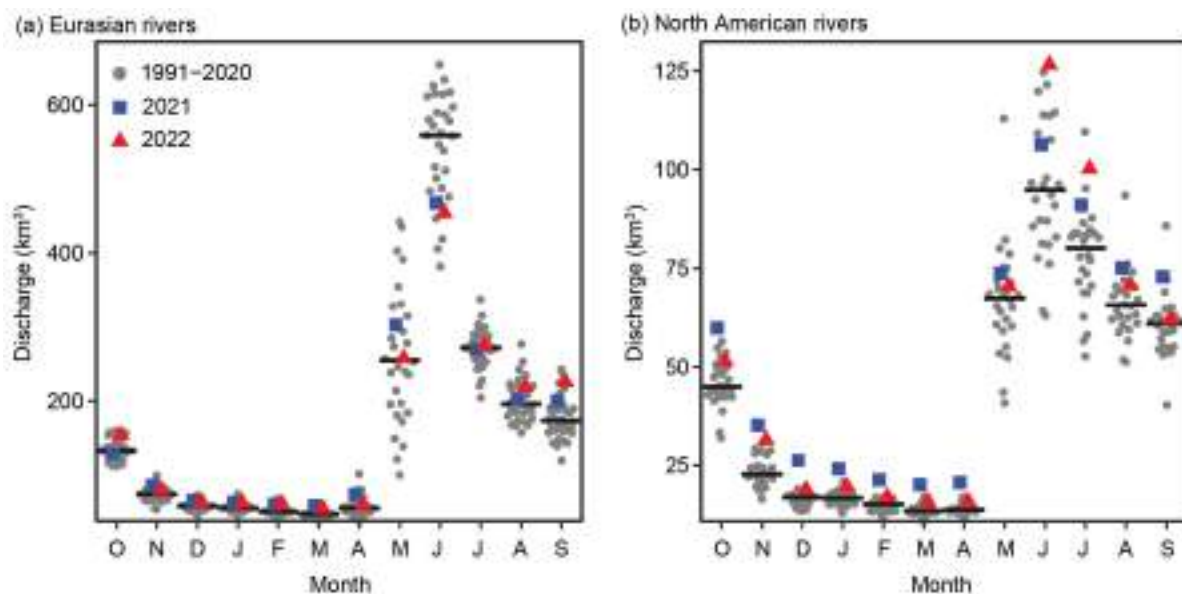


Fig. 5.23. Monthly discharge (km³) in (a) Eurasian and (b) North American rivers for 2021 (blue squares) and 2022 (red triangles) compared to monthly discharge throughout the 1991–2020 reference period (gray circles). The black bars indicate average monthly discharge during the reference period. Note the different magnitudes of discharge between the Eurasian and North American rivers (see y-axes).

recent studies of northern rivers (Gohari et al. 2022; Whitfield et al. 2021; Hiyama et al. 2023). Widespread changes in winter discharge have been attributed to increasing baseflow as a consequence of general warming and associated permafrost degradation that supports greater groundwater contributions as well as changes in the timing and magnitude of snowmelt events (Shrestha et al. 2021; Liu et al. 2022).

The 87-year time series available for the Eurasian Arctic rivers demonstrates a continuing, and perhaps accelerating, increase in their combined discharge (Fig. 5.24a). The positive linear trend across this entire time series indicates that the average annual discharge of Eurasian Arctic rivers is increasing by $2.5 \text{ km}^3 \text{ yr}^{-1}$. When data are considered from 1976 through 2022 (the period of record for North American rivers), the average annual increase in discharge for Eurasian Arctic rivers is $4.2 \text{ km}^3 \text{ yr}^{-1}$. For the North American Arctic rivers, the average discharge increase over the period of record is $1.5 \text{ km}^3 \text{ yr}^{-1}$. These observations show that, although river discharge varies widely over interannual-to-decadal timeframes, longer-term increases in river discharge are a pan-Arctic phenomenon. Evidence of increasing Arctic river discharge is strongest for Eurasian rivers where datasets are longest, but the signal of change in North American rivers is becoming increasingly robust as discharge datasets lengthen. This serves as a reminder that maintaining long-term datasets is crucial for tracking and understanding change.

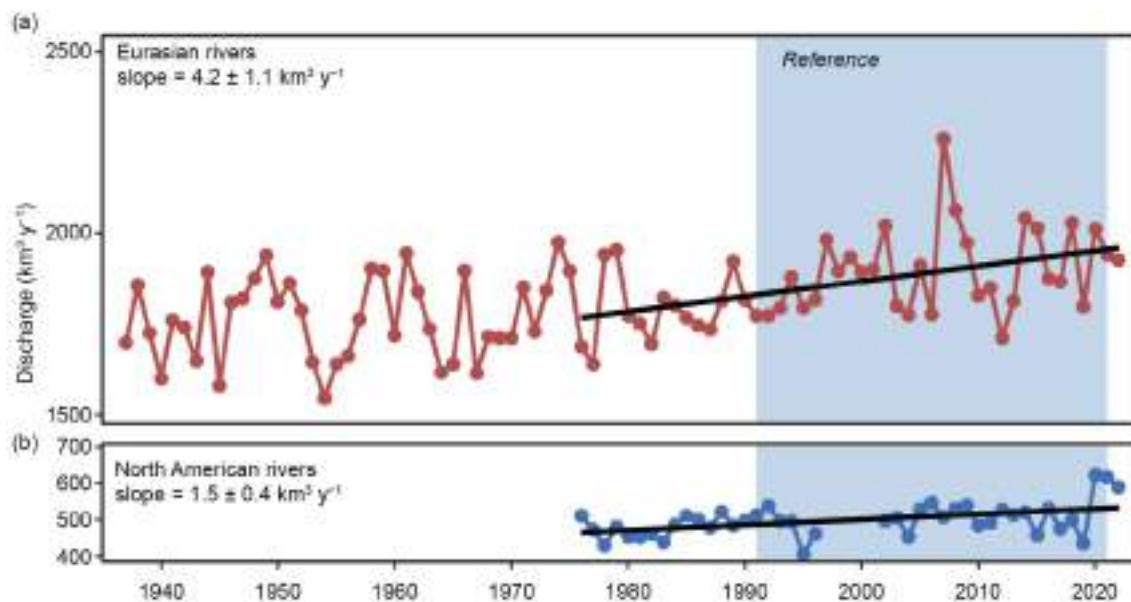


Fig. 5.24. Long-term trends in annual discharge (km^3) for (a) Eurasian and (b) North American Arctic rivers. The North American time series gap from 1996 to 2001 is due to insufficient data availability during those years. Reported slopes ($p < 0.001$ for both) are for 1976–2022.

i. Permafrost

—S. L. Smith, V. E. Romanovsky, K. Isaksen, K. E. Nyland, N. I. Shiklomanov, D. A. Streletskiy, and H. H. Christiansen

Permafrost refers to earth materials (e.g., bedrock, mineral soil, organic matter) that remain at or below 0°C for at least two consecutive years, although most permafrost has existed for much longer (centuries to several millennia). Overlying the permafrost is the active layer, which thaws and refreezes annually. Permafrost underlies extensive regions of the high-latitude landscape (Brown et al. 1997) and, especially if ice-rich, can play a critical role in the stability of Arctic landscapes. Warming of permafrost, active layer thickening, and ground-ice melt cause changes in surface topography, hydrology, and landscape stability, with implications for Arctic infrastructure and ecosystem integrity, as well as human livelihoods (Romanovsky et al. 2017; Hjort et al. 2022; Wolken et al. 2021). Changes in permafrost conditions can also affect the rate of greenhouse gas release to the atmosphere, with the potential to accelerate global warming (Schuur 2020).

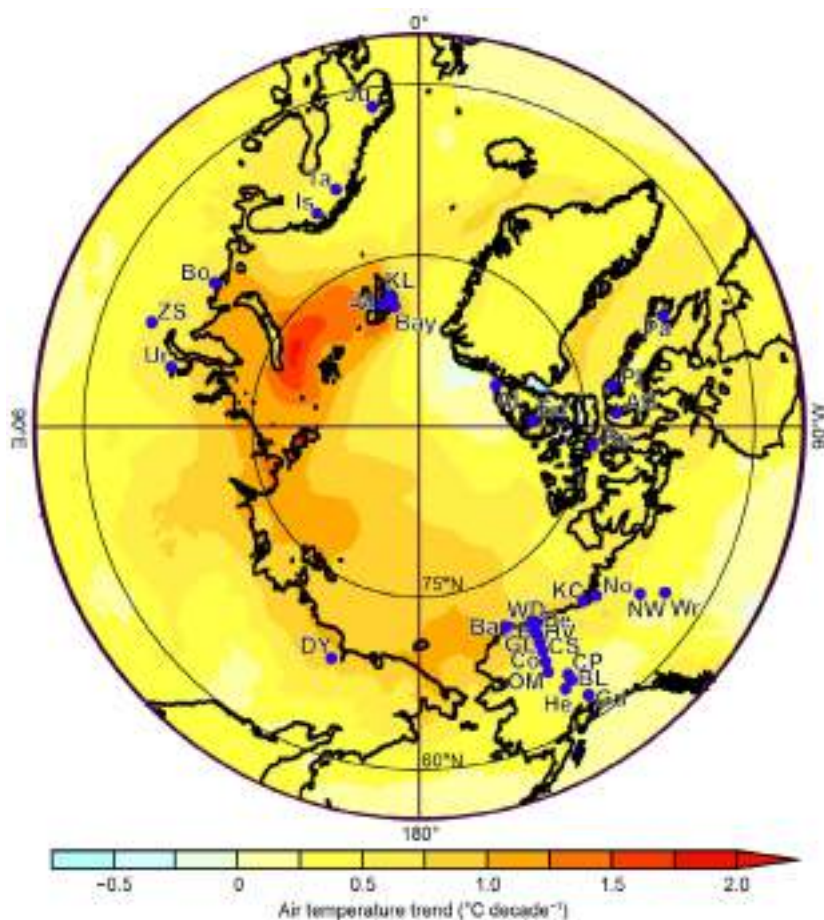


Fig. 5.25. Locations of the permafrost temperature monitoring sites (for which data are shown in Fig. 5.26), superimposed on average surface air temperature trends ($^{\circ}\text{C decade}^{-1}$) during 1981–2020 from ERA5 reanalysis (Hersbach et al. 2020; data available at <https://cds.climate.copernicus.eu>). See Table 5.2 for site names. Information about these sites is available at <http://gtnpdata.org/>, http://permafrost.gi.alaska.edu/sites_map, and <https://www2.gwu.edu/~calm/>.

Permafrost conditions respond to shifts in the surface energy balance through a combination of interrelated changes in ground temperature and active layer thickness (ALT). Near the surface, ground temperatures fluctuate seasonally, while below the depth of seasonal temperature variation, ground temperatures reflect longer-term changes in climate. Long-term changes in permafrost temperatures are driven by changes in air temperature (Romanovsky et al. 2017); however, permafrost temperature trends also show local variability due to other important influences such as snow cover, vegetation characteristics, and soil moisture. Monitoring sites across the Arctic (Fig. 5.25) have been recording ground temperature in the upper 30 m for up to five decades, providing critical data on changes in permafrost stability. Observed changes in ALT are more reflective of shorter-term (year-to-year) fluctuations in climate and are especially sensitive to changes in summer air temperature and precipitation.

1. PERMAFROST TEMPERATURES

Permafrost temperatures continue to increase on a decadal time scale across the Arctic. Greater increases in permafrost temperature are generally

observed in colder permafrost (temperature $< -2^{\circ}\text{C}$) at higher latitudes (Smith et al. 2022a,b), partly due to greater increases in air temperature (Figs. 5.25, 5.26). Permafrost temperatures in 2022 were the highest on record at 11 of the 25 sites reporting. However, cooling that began in 2020 has continued at other sites and temperatures were lower in 2022 compared to 2021 at 13 sites (Fig. 5.26; Table 5.2). In the Beaufort-Chukchi region, permafrost temperatures in 2022 were up to 0.3°C lower than in 2021 at all sites except Utqiagvik (Barrow; Fig 5.26a). The observed permafrost cooling in this region was a result of lower mean annual air temperatures after 2019. At Deadhorse (Prudhoe Bay, Alaska) for example, the average air temperature was almost 4°C lower in 2022 compared to 2018 and 2019. For discontinuous permafrost in Alaska and northwestern Canada, the 2022 permafrost temperatures were the highest on record at all sites except for three (Fig. 5.26b). Although the high-Arctic cold permafrost of Svalbard (Janssonhaugen) had been warmer each year from 2005 until 2019/20 (Isaksen et al. 2022), permafrost was colder in 2021 and 2022 but still among the five warmest years on record (Fig. 5.26d). In warmer permafrost at other Nordic sites, permafrost temperatures in 2022 were the highest on record. Permafrost was colder in 2022 at the one Russian site reporting.

Throughout the Arctic, the warming of permafrost with temperatures close to 0°C (i.e., at temperatures $> -2^{\circ}\text{C}$) is slower (generally $< 0.3^{\circ}\text{C decade}^{-1}$) than colder permafrost sites due to latent heat effects related to melting ground ice. At cold continuous permafrost sites in the

Beaufort-Chukchi region, permafrost temperatures have increased by 0.3°C–0.7°C decade⁻¹ (Fig. 5.26a; Table 5.2). In the eastern and high Canadian Arctic, similar increases (0.4°C–1.1°C decade⁻¹) have been observed (Fig. 5.26c; Table 5.2). Permafrost on Svalbard at the Janssonhaugen and Kapp Linne sites (Table 5.2), has warmed by about 0.7°C decade⁻¹. Significant permafrost warming has been detected to 100-m depth at Janssonhaugen (Isaksen et al. 2022).

Table 5.2. Rate of change in mean annual ground temperature (°C decade⁻¹) for permafrost monitoring sites shown in Fig. 5.25. For sites where measurements began prior to 2000, the rate of change for the entire available record and the period after 2000 are provided. The periods of record are shown in parenthesis below the rates of change. Stations with record-high temperatures in 2022 are shown underlined in red. Asterisks denote sites not reporting in 2022.

Region	Site	Entire Record	Since 2000
North of East Siberia (Beaufort-Chukchi Region)	Duvany Yar (DY)*	NA	+0.4 (2009–20)
Alaskan Arctic plain (Beaufort-Chukchi Region)	West Dock (WD), Deadhorse (De), Franklin Bluffs (FB), <u>Barrow (Ba)</u>	+0.4 to +0.7 (1978–2022)	+0.4 to +0.6 (2000–22)
Northern foothills of the Brooks Range, Alaska (Beaufort-Chukchi Region)	Happy Valley (HV), Galbraith Lake (GL)	+0.3 (1983–2022)	+0.3 (2000–22)
Northern Mackenzie Valley (Beaufort-Chukchi Region)	Norris Ck (No), KC-07 (KC)	NA	+0.6 to +0.7 (2008–22)
Southern foothills of the Brooks Range, Alaska (Discontinuous Permafrost, Alaska and NW Canada)	<u>Coldfoot (Co)</u> , Chandalar Shelf (CS), Old Man (OM)	+0.1 to +0.3 (1983–2022)	+0.2 to +0.3 (2000–22)
Interior Alaska (Discontinuous Permafrost, Alaska and NW Canada)	<u>College Peat (CP)</u> , Birch Lake (BL), <u>Gulkana (Gu)</u> , <u>Healy (He)</u>	+0.1 to +0.3 (1983–2022)	<+0.1 to +0.3 (2000–22)
Central Mackenzie Valley (Discontinuous Permafrost, Alaska and NW Canada)	Norman Wells (NW), <u>Wrigley (Wr)</u>	Up to +0.1 (1984–2022)	<+0.1 to +0.2 (2000–22)
Baffin Island (Baffin Davis Strait Region)	Pangnirtung (Pa)*, Pond Inlet (PI)*	NA	+0.4 (2009–21)
High Canadian Arctic (Baffin Davis Strait Region)	<u>Resolute (Re)</u>	NA	+1.1 (2009–22)
High Canadian Arctic (Baffin Davis Strait Region)	Alert (Al) @ 15 m*, Alert (Al) @ 24 m	+0.6, +0.4 (1979–2022)	+0.9, +0.6 (2000–22)
North of West Siberia (Barents Region)	Urengoy 15-06* and 15-08* (Ur)	+0.2 to +0.5 (1974–2021)	+0.1 to +0.8 (2005–21)
Russian European North (Barents Region)	Bolvansky 56 and 65* (Bo)	+0.1 to +0.3 (1984–2022)	0 to +0.5 (2001–22)
Svalbard (Barents Region)	Janssonhaugen (Ja), Bayelva (Bay)*, Kapp Linne 1 (KL)	+0.7 (1998–2022)	+0.2 to +0.7 (2000–22)
Northern Scandinavia (Barents Region)	Tarfalarggen (Ta)*, <u>Iskoras Is-B-2 (Is)</u>	NA	+0.1 to +0.5 (2000–22)
Southern Norway (Barents Region)	<u>Juvvasshøe (Ju)</u>	+0.2 (1999–2022)	+0.2 (2000–22)

In the discontinuous permafrost regions of Scandinavia (Juvvasshøe and Iskoras), warming is continuing at rates of about $0.2^{\circ}\text{C decade}^{-1}$, with thawing occurring at Iskoras (Fig. 5.26d; Isaksen et al. 2022). Similar rates of warming were found for warm permafrost in Russia (e.g., Bolvansky #56; Malkova et al. 2022) and northwestern North America (Figs. 5.26b,d).

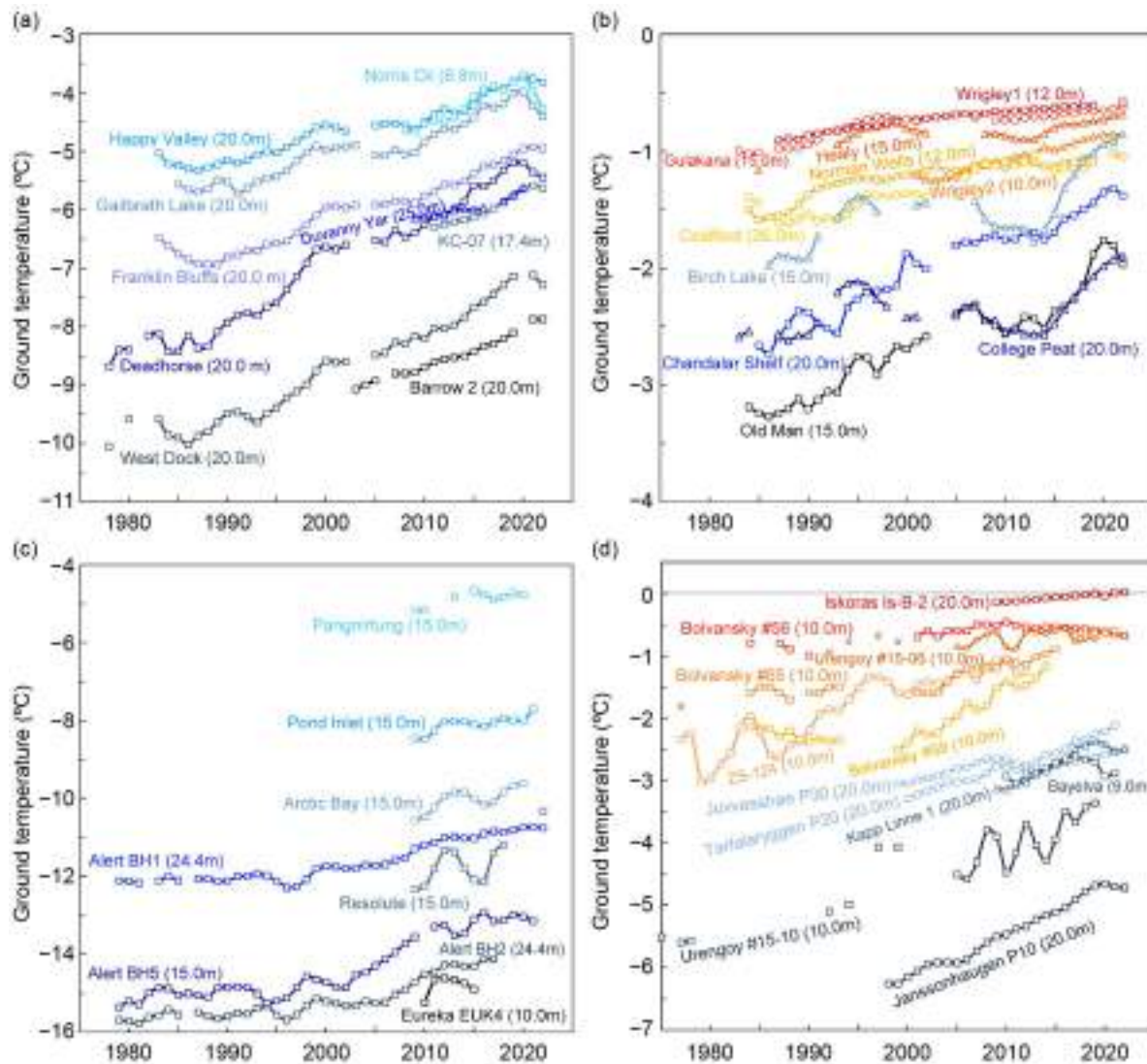


Fig. 5.26. Time series of mean annual ground temperature ($^{\circ}\text{C}$) at depths of 9 m–26 m below the surface at selected measurement sites that fall roughly into Adaptation Actions for a Changing Arctic Project priority regions (see Romanovsky et al. 2017): (a) cold continuous permafrost of northwestern North America and northeastern East Siberia (Beaufort-Chukchi region); (b) discontinuous permafrost in Alaska and northwestern Canada; (c) cold continuous permafrost of eastern and High Arctic Canada (Baffin Davis Strait); and (d) continuous to discontinuous permafrost in Scandinavia, Svalbard, and Russia/Siberia (Barents region). Temperatures are measured at or near the depth of zero annual amplitude where the seasonal variations of ground temperature are less than 0.1°C . Note differences in y-axis value ranges. Borehole locations are shown in Fig. 5.25 (data are updated from Smith et al. 2022b).

2. ACTIVE LAYER THICKNESS

Active layer thickness is determined using direct measurements, such as mechanical probing and thaw tubes, and also indirectly by interpolation of the maximum seasonal depth of the 0°C isotherm from borehole temperature records. Long-term ALT trends shown in Fig. 5.27 are primarily generated from spatially distributed mechanical probing across representative landscapes to determine the top of permafrost (Shiklomanov et al. 2012).

Over the last 28 years, positive ALT trends are evident for all regions reported, but trends are less apparent for the Alaskan North Slope, northwest Canada, and East Siberia (Smith et al. 2022a). West Siberia, the Russian European North, and Interior Alaska all experienced ALT in 2022 well above the 2009–18 mean, continuing a several-year increase in ALT (e.g., Kaverin et al.

2021). The Russian European North, Interior Alaska, and West Siberia are experiencing the greatest rates of ALT increase over the observation period at 0.013, 0.015, and 0.016 m yr⁻¹, respectively.

Active layer thickness regional anomalies for summer 2022 were within 0.05 m of the 2009–18 mean for the North Slope of Alaska, Greenland, Svalbard, northwest Canada, and East Siberia. The negligible ALT trend for the Alaska North Slope and northwest Canada for example, may be the result of consolidation (subsidence) resulting from the thaw of ice-rich material, which is not accounted for by manual probing (Nyland et al. 2021; Smith et al. 2022a). Reduced ALT reported for 2022 for the Alaska North Slope, Greenland, Svalbard, and East Siberia may be due to a cooler summer (e.g., Nyland et al. 2021; Strand et al. 2021; Abramov et al. 2021).

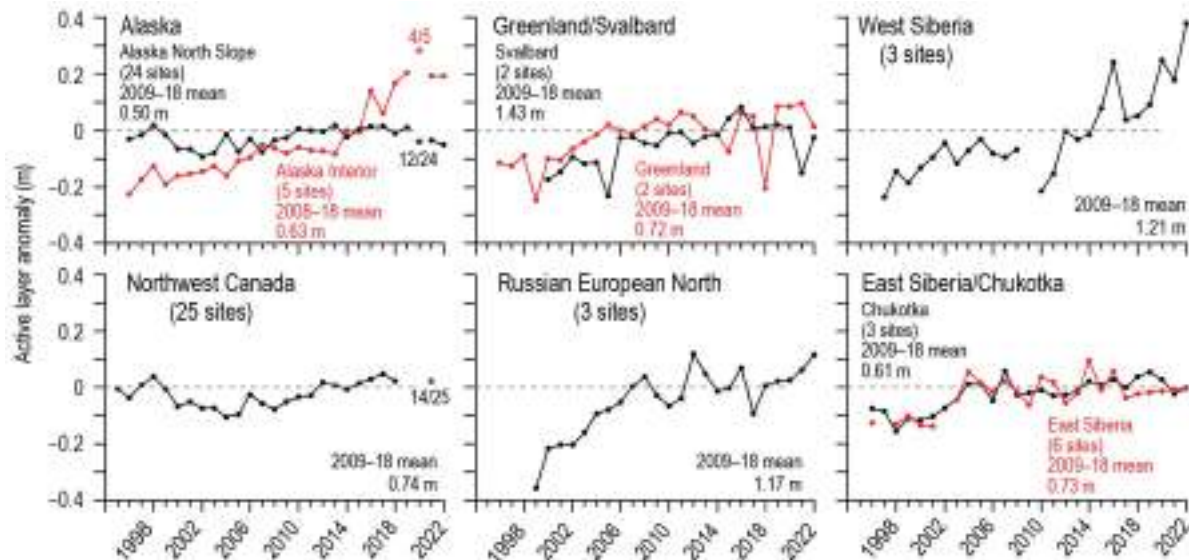


Fig. 5.27. Average annual active layer thickness (ALT) anomalies (m) relative to the 2009–18 mean for six Arctic regions as observed by the Circumpolar Active Layer Monitoring program. Positive and negative anomaly values indicate thicker or thinner ALT, respectively, than the 10-yr reference mean. Only sites with >20 years of continuous thaw depth observations are included. The number of sites and reference period mean ALT are provided on each figure panel. Asterisks indicate a lower number of observations due to pandemic-related restrictions, with the number of sites reporting provided on graph. Canadian ALT is derived from thaw tubes that record the maximum thaw depth over the previous year. Since Canadian sites were not visited in 2020 and 2021, the maximum thaw depth recorded during the 2022 visit could have occurred any summer from 2019 through 2021, although the data point is plotted in 2021. Site-specific data and metadata are available at www2.gwu.edu/~calm/.

j. Tundra greenness

—G. V. Frost, M. J. Macander, U. S. Bhatt, L. T. Berner, J. W. Bjerke, H. E. Epstein, B. C. Forbes, S. J. Goetz, M. J. Lara, R. Í. Magnússon, G. K. Phoenix, S. P. Serbin, H. Tømmervik, O. Tutubalina, D. A. Walker, and D. Yang

Earth’s northernmost continental landmasses and island archipelagos are home to the Arctic tundra biome, a 5.1 million km² region characterized by low-growing, treeless vegetation (Raynolds et al. 2019). The tundra biome forms a belt of cold-adapted vegetation atop the globe, bordered by the Arctic Ocean to the north and the boreal forest “treeline” to the south. Arctic tundra ecosystems are experiencing profound changes as the vegetation, soils, and underlying permafrost respond to rapidly warming air temperatures and the precipitous decline of sea ice on the neighboring Arctic Ocean (Bhatt et al. 2021; sections 5b,e,h). In the late 1990s, Earth-observing satellites began to detect a sharp increase in the productivity of tundra vegetation, a phenomenon known today as “the greening of the Arctic.” Arctic greening is dynamically linked with Earth’s changing climate, permafrost, seasonal snow, and sea-ice cover.

Global vegetation has been consistently monitored from space since 1982 by the Advanced Very High Resolution Radiometer (AVHRR), a series of sensors that has entered its fifth decade of operation onboard a succession of polar-orbiting satellites. In 2000, the Moderate Resolution Imaging Spectroradiometer (MODIS) sensor became operational and provides observations with higher spatial resolution and improved calibration. AVHRR and MODIS data are used to monitor

vegetation greenness via the Normalized Difference Vegetation Index (NDVI), a spectral metric that exploits the unique way in which green vegetation absorbs and reflects visible and infrared light. The long-term AVHRR NDVI dataset analyzed here is the Global Inventory Modeling and Mapping Studies 3g V1.2 dataset (GIMMS-3g+) with a spatial resolution of about 8 km (Pinzon and Tucker 2014); at the time of writing, processed data were not available for the 2022 growing season, so the GIMMS-3g+ time series covers the period 1982–2021. For MODIS, we computed trends for the period 2000–22 at a higher spatial resolution of 500 m, combining 16-day NDVI products from the *Terra* (Didan 2021a) and *Aqua* (Didan 2021b) satellites, referred to as MCD13A1. All data were masked to include only ice-free land within the extent of the Circumpolar Arctic Vegetation Map (Raynolds et al. 2019). MODIS data were further masked to exclude permanent waterbodies based on the 2015 MODIS *Terra* Land Water Mask (MOD44W, version 6). We summarize the GIMMS-3g+ and MODIS records for the annual maximum NDVI (MaxNDVI), the peak greenness value which is typically observed during July or August.

Both AVHRR and MODIS records indicate that MaxNDVI has increased across most of the Arctic tundra biome since 1982 and 2000, respectively (Figs. 5.28a,b), and show virtually identical trends for the period of overlap (2000–21; Fig. 5.29). In North America, both records indicate strong greening on Alaska’s North Slope and across continental Canada. In Eurasia, strong greening has occurred in Chukotka and the Laptev Sea region, but greenness has declined in parts of the Taymyr Peninsula and East Siberian Sea regions. Regional contrasts in greenness trends highlight the complexity of Arctic change and the interactions that connect tundra ecosystems with climate, sea ice, permafrost, seasonal snow, soil composition and moisture, disturbance processes, wildlife, and human activities (Heijmans et al. 2022; Zona et al. 2023). The neighboring boreal forest biome (Figs. 5.28a,b), which occupies extensive portions of northern Eurasia and North America, has also emerged as a “hotspot” of global environmental change and exhibits interspersed greening and “browning” (i.e., productivity decreases) that are also linked to interactions among climate change, wildfire, human land-use, and other factors (Berner and Goetz 2022; Jorgenson et al. 2022).

In 2021—the most recent year with observations from both AVHRR and MODIS—circumpolar mean MaxNDVI for tundra regions declined from the record-high values set in 2020 for both satellite records. AVHRR-observed MaxNDVI declined 8.3% from 2020; nonetheless, the

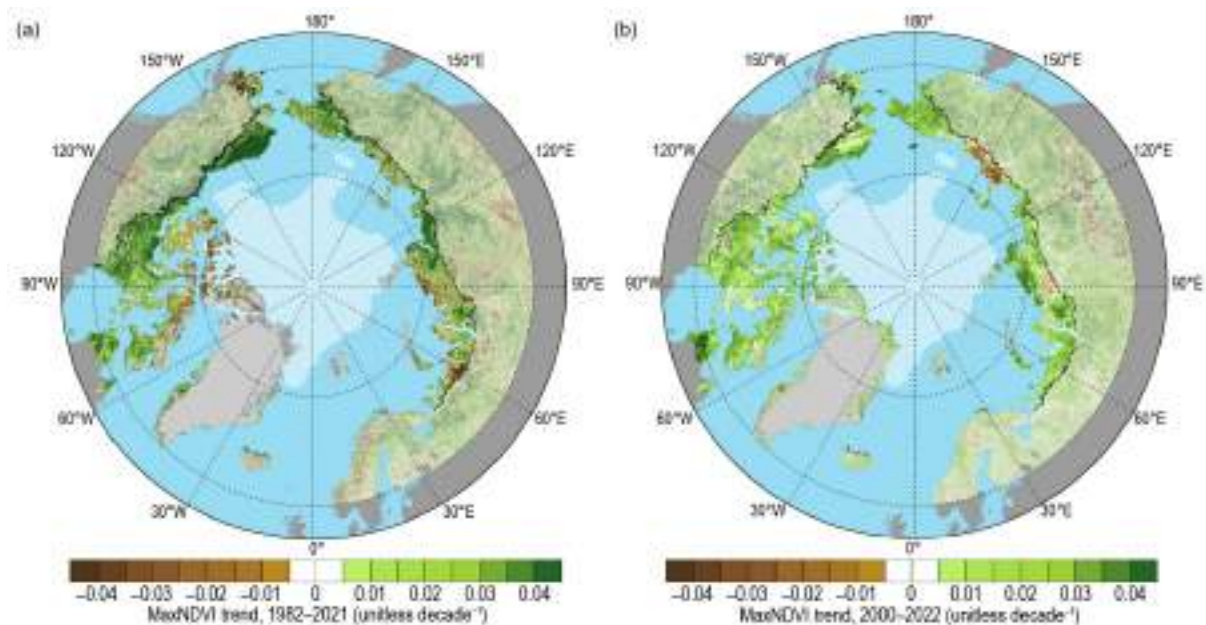


Fig. 5.28. Magnitude of Maximum Normalized Difference Vegetation Index (MaxNDVI) increases (“greening”) and decreases (“browning”) calculated as the change decade⁻¹ via ordinary least squares regression for Arctic tundra (solid colors) and boreal forest north of 60° latitude (muted colors) during (a) 1982–2021 based on the AVHRR GIMMS 3-g+ dataset, and (b) 2000–22 based on the MODIS MCD13A1 dataset. The circumpolar treeline is indicated by a black line, and the 2022 minimum sea-ice extent is indicated by light shading in each panel.

2021 value still exceeded the 1991–2020 mean and was the 15th-highest value recorded in the full record (Fig. 5.29). Notably, the six highest circumpolar average MaxNDVI values in the long-term AVHRR record (1982–2021) have all been recorded in the last 10 years. The 2020 to 2021 decline in MaxNDVI was less pronounced for MODIS (2.7%), and the 2021 value was the second-highest value in the 22-year record for that sensor.

In 2022, the circumpolar MODIS-observed MaxNDVI value declined 0.9% from the previous year, but nonetheless represented the fourth-highest value in the 23-year MODIS record and continued a sequence of exceptionally high values that began in 2020 (Fig. 5.30). Tundra greenness was relatively high in the Canadian Arctic Archipelago, northern Quebec, and northwestern Siberia, but was strikingly low in northeastern Siberia, which experienced unusually persistent summer sea ice and northerly winds in summer 2022 (Fig. 5.30). The overall trend in MODIS-observed circumpolar MaxNDVI is strongly positive, and circumpolar values have exceeded the 23-year mean in 11 of the last 13 growing seasons (Fig. 5.29).

What are the drivers that underlie tundra greening and browning trends, and what types of change might an observer see on the ground? Increases in the abundance, distribution, and height of Arctic shrubs are a major driver of Arctic greening and have important impacts on biodiversity, surface energy balance, permafrost temperatures, and biogeochemical cycling (Mekonnen et al. 2021; Macander et al. 2022), with the potential to serve as a positive feedback to climatic warming (Pearson et al. 2013). Although satellite records provide unequivocal evidence of widespread Arctic greening, there is substantial regional variability in trends. For example, tundra near the East Siberian Sea exhibits widespread browning, which is likely due in part to increased surface water triggered by permafrost thaw, flooding, and recent climate extremes (Magnússon 2021). In 2022, several regions experienced widespread disturbance and extreme weather which can trigger abrupt declines in greenness (see Sidebar 5.1). For example, western Alaska’s Yukon-Kuskokwim Delta

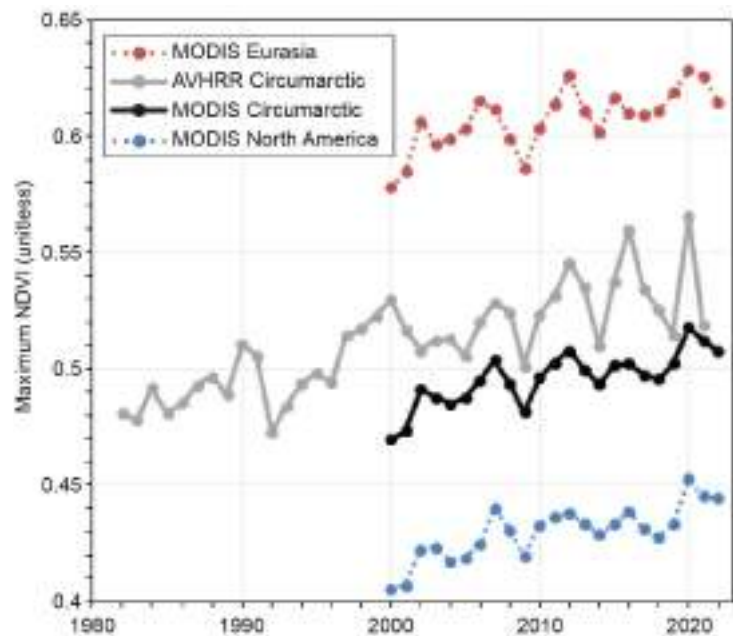


Fig. 5.29. Time series of Maximum Normalized Difference Vegetation Index (MaxNDVI) from the MODIS MCD13A1 (2000–22) dataset for the Eurasian Arctic (dark red), North American Arctic (blue), and the circumpolar Arctic (black), and from the long-term AVHRR GIMMS-3g+ dataset (1982–2021) for the circumpolar Arctic (gray).

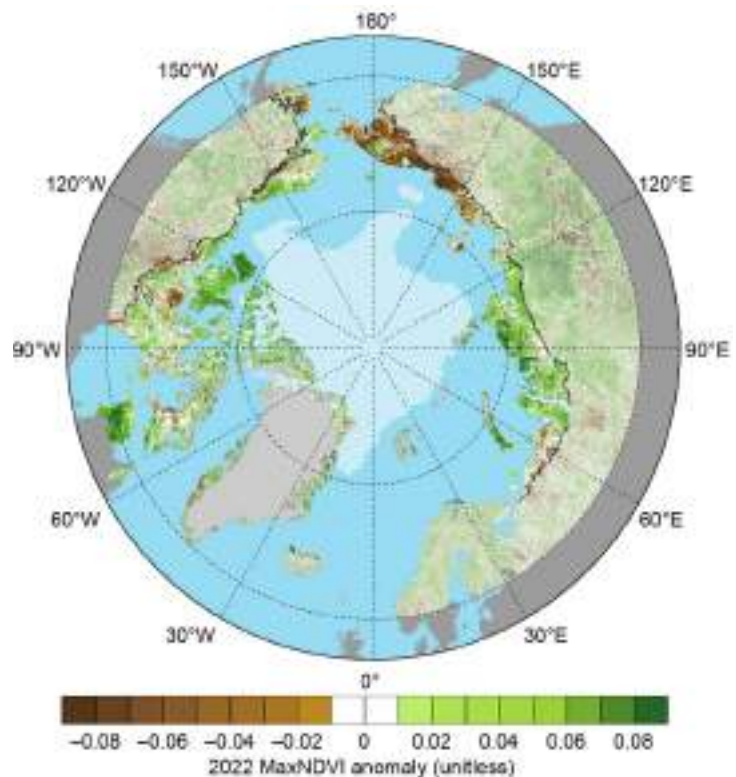


Fig. 5.30. Circumpolar Maximum Normalized Difference Vegetation Index (MaxNDVI) anomalies for the 2022 growing season relative to mean values (2000–22) for Arctic tundra (bright colors) and boreal forest north of 60° latitude (muted colors) from the MODIS MCD13A1 dataset. The circumpolar tree line is indicated by a black line, and the 2022 minimum sea-ice extent is indicated by light shading.

experienced extensive wildfires, continuing a series of years with burned areas far exceeding normal historical conditions. While warming is likely to continue to drive Arctic greening, increased disturbance, extreme events, and other causes of browning are also increasing in frequency (Christensen et al. 2021). Understanding the drivers and regional variability of complex Arctic greening trends continues to be a subject of multi-disciplinary scientific research (Myers-Smith et al. 2020; Rogers et al. 2022; Yang et al. 2022).

k. Ozone and UV radiation

—G. H. Bernhard, V. E. Fioletov, J.-U. Grooß, I. Ialongo, B. Johnsen, K. Lakkala, G. L. Manney, R. Müller, and T. Svendby

Past emissions of manufactured chlorine-containing substances such as chlorofluorocarbons (CFCs) have caused substantial chemical depletion of stratospheric ozone (WMO 2022). The resulting ozone loss led to increases of ultraviolet (UV) radiation at Earth’s surface with adverse effects on human health and the environment (Barnes et al. 2019; EEAP 2023). The chemical destruction of polar ozone occurs within a cold stratospheric cyclone known as the polar vortex, which forms over the North Pole every year during winter (WMO 2022). The 2022 polar vortex was somewhat colder than usual; between late January and March 2022, minimum temperatures in the vortex near 16 km–20 km altitude were about 1 st. dev. below the 2005–21 average.

1. OZONE

Chemical processes that drive ozone depletion in the polar stratosphere are initiated at temperatures below about 195 K (–78°C) at altitudes of approximately 15 km–25 km. These low temperatures allow polar stratospheric clouds (PSCs) to occur. These clouds act as a catalyst to transform inactive forms of chlorine-containing substances into active, ozone-destroying chlorine species such as chlorine monoxide (ClO).

According to *Aura* Microwave Limb Sounder (MLS; 2005–present) observations (Waters et al. 2006), temperatures dropped low enough for PSC occurrence in late November 2021.

Activation of chlorine started in early December 2021. ClO concentrations near ~16-km altitude (Fig. 5.31a) were near average (2004/05–2020/21) until early February 2022, were about 1 std. dev. above average from then until mid-March 2022, and returned to near-average values thereafter.

In 2021/22, the change of ozone concentrations inside the vortex near 16-km altitude (Fig. 5.31b) was consistent with the evolution of ClO (Fig. 5.31a). Ozone concentrations were near the mean of MLS measurements until mid-February 2022 and started to decrease after chemical depletion commenced. From late February through March 2022, ozone dropped more rapidly than the mean, indicating greater ozone destruction than typical, consistent with above-average ClO concentrations during that period. While there was more chemical destruction of ozone in late February and March 2022 compared to the mean (Fig. 5.31b), the ozone loss in 2022 was much less than in 2011 (e.g., Manney et al. 2011) or 2020 (e.g., Lawrence et al. 2020; Manney et al. 2020),

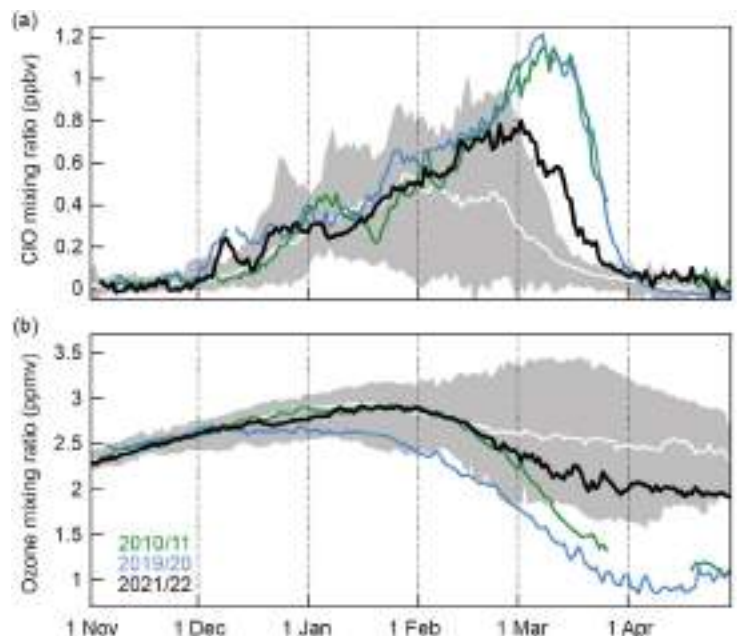


Fig. 5.31. Average (a) chlorine monoxide (ClO) and (b) ozone concentrations (expressed as mixing ratio in ppbv and ppmv, respectively) measured by MLS at an altitude of ~16 km for the area bounded by the Arctic stratospheric polar vortex. Data from 2010/11 (green), 2019/20 (blue), and 2021/22 (black) are compared with the average (solid white) and minimum/maximum range (gray shading) from 2004/05 to 2020/21, excluding the highlighted years. There is a gap in spring 2011 data due to an MLS instrument anomaly.

the years with the lowest ozone values in the MLS record (Fig. 5.31b) and the strongest and most persistent stratospheric polar vortices on record. These large year-to-year variations in Arctic ozone concentrations are mostly driven by differences in meteorological conditions and are expected to continue for as long as concentrations of human-made chlorine-containing substances remain elevated in the stratosphere (WMO 2022). In 2022, ozone concentrations in the lower stratosphere were less than 1 std. dev. below the mean for 2004/05–2020/21, but were near the lowest values of past observations at the end of April when the two extreme years of 2010/11 and 2019/20 are excluded. Compared to ozone concentrations at 16 km, ozone loss was near-average above 18 km but somewhat greater than average near 14 km–15 km.

Below-average ozone concentrations observed in the lower stratosphere after mid-February 2022 (Fig. 5.31b) contributed to below-average total ozone columns (TOC; i.e., ozone amounts integrated from Earth’s surface to the top of the atmosphere) in February and March 2022. Figure 5.32 illustrates the variation in TOC between 1979 and 2022 for March by showing the minimum of the daily mean TOC within an area that encloses the polar vortex and is surrounded by the 63°N contour of “equivalent latitude” (Butchart and Remsburg 1986). March was selected because it has historically been the month with the largest potential for chemical ozone depletion in the Arctic (WMO 2022). In March 2022, the minimum Arctic daily TOC was 9.5% (36 Dobson units; DU) below the average TOC since the start of satellite observations in 1979 and 7.4% (27 DU) below the average of 366 DU for the period of measurements (2005–present) by MLS and the Ozone Monitoring Instrument (OMI). TOC values in April 2022 (and later months) were near-average despite the continuation of below-average ozone concentrations in the lower

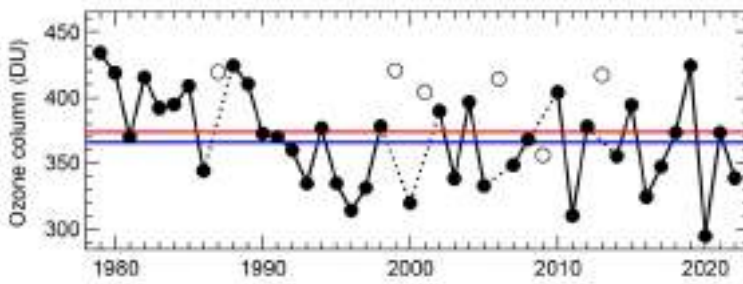


Fig. 5.32. Minimum of the daily average total ozone column (Dobson units, DU) for Mar poleward of 63°N equivalent latitude (Butchart and Remsburg 1986). Open circles represent years in which the polar vortex was not well-defined in Mar, resulting in relatively high values owing to mixing with lower-latitude air masses and a lack of significant chemical ozone depletion. Red and blue lines indicate the average total ozone column for 1979–2021 and 2005–21, respectively. Ozone data for 1979–2019 are based on the combined NIWA-BS total column ozone database version 3.5.1 (Bodeker and Kremser 2021). Ozone data for 2020–22 are from OMI. Adapted from Müller et al. (2008) and WMO (2022), and updated using ERA5 reanalysis data (Hersbach et al. 2020) to determine equivalent latitude.

stratosphere of the polar vortex (Fig. 5.31b). This apparent discrepancy is due to the smaller contribution of the vortex to the area enclosed by the 63°N contour in April compared to March. Decreases in TOC observed between 1979 and ~1996 (Fig. 5.32) did not continue because of the phase-out of ozone-depleting substances prompted by the implementation of the Montreal Protocol and its amendments (WMO 2022).

Spatial deviations of monthly average TOCs from past (2005–21) averages were estimated from OMI measurements. In March 2022 (Fig. 5.33a), Arctic TOC anomalies varied between –20% and +10% but stayed within 2 std. dev. of past observations, with the exception of a small area in northern Siberia. In April 2022 (Fig. 5.33b), TOC anomalies varied to within ±10% and remained within 2 std. dev. Ozone anomalies between May and October 2022 were unremarkable.

2. ULTRAVIOLET RADIATION

Ultraviolet radiation is quantified with the UV Index (UVI), which measures the intensity of UV radiation in terms of causing erythema (sunburn) in human skin. The UVI depends mostly on the sun angle, TOC, clouds, aerosols, and surface albedo (EEAP 2023). In the Arctic, the UVI scale ranges from 0 to about 7, with UVI values <3 north of 80°N. (For comparison, the summertime UVI at midlatitudes may reach 12 [Bernhard et al. 2022]).

Figures 5.33c,d quantify spatial differences in monthly average noontime UVIs from past (2005–21) averages based on measurements by OMI. UVI anomalies in March 2022 (Fig. 5.33c) varied between –35% and +48% and exceeded 2 std. dev. of past observations over Poland, the

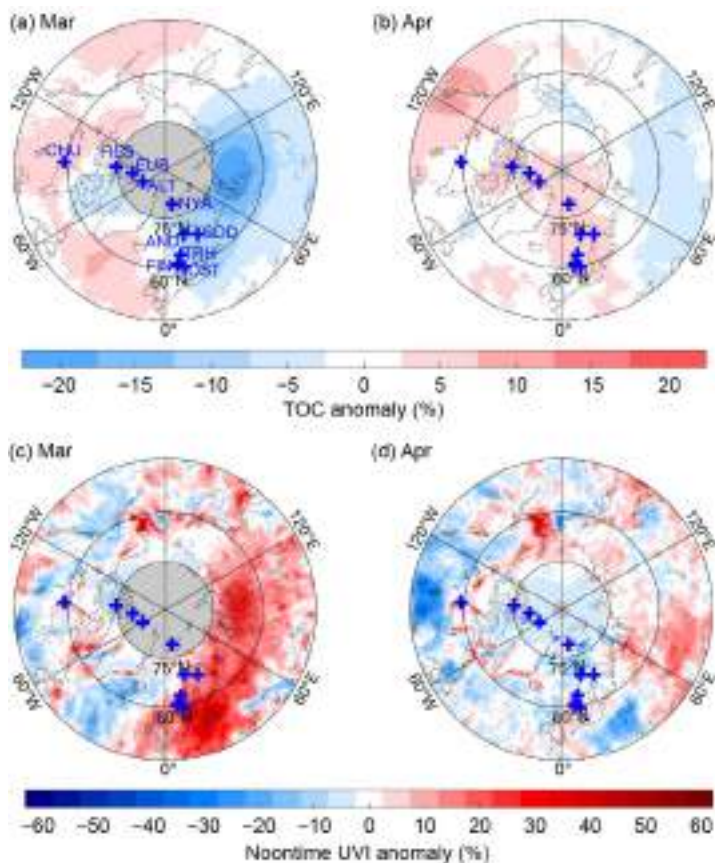


Fig. 5.33. Monthly mean anomaly maps of (a),(b) total ozone column (TOC; %) and (c),(d) noontime UV Index (UVI; %) for Mar and Apr 2022 relative to 2005–21 means. Stippling indicates pixels where anomalies exceed 2 st. dev. Gray-shaded areas centered at the North Pole indicate latitudes where no OMI data are available because of polar darkness. Locations of ground stations are indicated by blue crosses in every map, with labels added to the first map. Maps are based on the OMT03 Level 3 total ozone product (Bhartia and Wellemeyer 2002). Site acronyms are provided in Table 5.3.

Baltic Sea, Lithuania, and northern Siberia. The larger variability compared to TOC (Fig. 5.33a) can be explained by the added effect from clouds. UVIs in April 2022 (Fig. 5.33d) remained within 2 std. dev. While UVI anomalies assessed with OMI data provide complete spatial coverage, they can sometimes indicate spurious anomalies of up to 60% (Bernhard et al. 2015) when the surface reflectivity (albedo) assumed in the retrieval algorithm (Tanskanen et al. 2003) deviates from the actual albedo. Anomalies for 2022 derived from OMI data agree with

most ground-based measurements at 10 Arctic and sub-Arctic sites within $\pm 14\%$ (Table 5.3). Exceptions are Andøya in March (OMI anomaly +9%; ground-based anomaly -10%) and Trondheim in April (OMI anomaly +1%; ground-based anomaly +16%). The differences are caused by local cloud effects at these coastal sites not captured by OMI.

Table 5.3. Monthly mean anomalies (%) of the noontime UV Index (UVI) for Mar and Apr 2022 relative to 2005–21 means calculated from OMI and ground-based data. Site locations are shown in Fig. 5.33.

Site name (acronym)	Latitude	OMI UVI anomaly (March)	ground-based UVI anomaly (March)	OMI UVI anomaly (April)	ground-based UVI anomaly (April)
Alert (ALT)	83°	NA	-1%	-5%	-6%
Eureka (EUR)	80°	NA	5%	-3%	11%
Ny-Ålesund (NYA)	79°	NA	-1%	8%	1%
Resolute (RES)	75°	NA	2%	-2%	8%
Andøya (AND)	69°	9%	-10%	-7%	-4%
Sodankylä (SOD)	67°	16%	10%	1%	-2%
Trondheim (TRH)	63°	11%	6%	1%	16%
Finse (FIN)	61°	21%	8%	13%	9%
Østerås (OST)	60°	24%	13%	7%	6%
Churchill (CHU)	59°	2%	NA	-12%	NA

Sidebar 5.2: Alaska seabird die-offs and the changing Arctic marine ecosystem

—R. KALER, G. SHEFFIELD, S. BACKENSTO, J. LINDSEY, T. JONES, J. K. PARRISH, B. AHMASUK, B. BODENSTEIN, R. DUSEK, C. VAN HEMERT, AND M. SMITH

Prior to 2015, seabird die-offs in Alaska were infrequent, typically occurred in mid-winter, and were associated with epizootic disease events or elevated ocean temperatures due to large-scale climate variability, such as El Niño (Bodenstein et al. 2015; Jones et al. 2019). From 2017 through 2022 (Fig. SB5.3), seabird die-offs occurred annually, and observations suggest that die-offs stem from multiple ecosystem changes associated with abnormally high ocean temperatures, including zooplankton and forage fish quantity and quality, increased foraging competition, or exposure to harmful algal bloom biotoxins. The specific cause of recent seabird die-offs in Alaska remains largely unknown but are likely linked to warmer ocean conditions and reductions to sea-ice extent and duration as Arctic marine food webs are supported by ice-associated algae in spring and phytoplankton in summer and energy contributions vary with community composition and nutritional quality (Stabeno et al. 2019; Koch et al. 2023). In addition to die-off events, observations at northern seabird breeding colonies indicate lack of breeding attempts or late and unsuccessful breeding in 2017 through 2019 and may be a result of a lack of food or unfavorable foraging conditions brought on by elevated ocean water temperatures (Romano et al. 2020; Will et al. 2020).

Seabirds are often considered marine ecosystem sentinels, as changes to seabird populations and diets reflect changes in the marine resources they depend upon (Cairns 1988). Planktivorous auklets (*Aethia* spp.) consume Euphausiids (krill), which are high-value prey but only locally and seasonally available, and copepods—a group of small crustaceans that vary in size and energy value depending on ocean temperatures. Piscivorous murrelets (*Uria* spp.), puffins (*Puffinus* spp.), and kittiwakes (*Rissa* spp.) prey on forage fish such as sand lance (*Ammodytes hexapterus*) and capelin (*Mallotus villosus*). In recent years, the numbers of sand lance and capelin have declined while the numbers of lower-quality, prey-like juvenile walleye pollock (*Gadus chalcogrammus*) and Pacific cod (*Gadus macrocephalus*) have increased in the northern Bering and southern Chukchi Seas (Duffy-Anderson et al. 2019).

During 2017–21, apparent emaciation was the most significant factor contributing to death, based on a combination of field reports, laboratory assessments, and necropsies (Table SB5.1; Bodenstein et al. 2022; US Geological Survey 2022). Researchers continue to evaluate possible contributing factors, including highly pathogenic avian influenza (HPAI). Seabird carcass collection was limited in 2022 due to potential human health concerns of HPAI transmission.

Table SB5.1. Summary of Bering and Chukchi Seas seabird necropsies, 2017–21. More than 14,000 dead seabirds were reported and a total of 117 carcasses were examined. Ninety-two cases had emaciation identified as the cause of death (COD), 7 cases where COD was undetermined, and 17 cases where COD was determined as “other”, which included predation, trauma, encephalitis, peritonitis, and bacterial infection. Low pathogenic avian influenza (n=4; different from H5 or H7 highly pathogenic avian influenza strains which are highly infectious to poultry farms) and saxitoxin (n=15) were also detected; however, the virus and biotoxin were not determined to be the COD, except for one case in 2020 where saxitoxin toxicosis was suspected. Data are summarized from Bodenstein et al. (2022).

Necropsy data point	2017	2018	2019	2020	2021	Total
Total reported	>1600	>1200	>9000	>330	>2200	>14,330
Total examined	19	25	39	20	14	117
Reported cause of death — Emaciation	17	19	31	13	12	92
Reported cause of death — Undetermined	0	3	2	1	1	7
Reported cause of death — Other	2	3	6	6	1	18
Avian influenza detected	0	2	0	1	1	4
Saxitoxin detected	11	BDL ¹	3	1 ²	BDL ¹	15

¹ BDL - below detection limits for the laboratory test used.

² Saxitoxin toxicosis was also suspected to be the cause of death.

Fortunately, seabirds nesting in dense colonies (e.g., murres, kittiwakes) appeared to be unaffected in 2017–22.

Harmful algal bloom biotoxins have been detected in seabird tissues in the region. Most notably, saxitoxin, which is associated with paralytic shellfish poisoning, was detected in the majority of northern fulmar (*Fulmarus glacialis*) carcasses collected in 2017. While direct neurotoxic effects from saxitoxin could not be confirmed and starvation appeared to be the proximate cause of death, exposure to saxitoxin could have

been a contributing factor (Van Hemert et al. 2021). Little is known about the occurrence of these biotoxins or their impacts on wild seabirds; USGS Alaska Science Center researchers continue investigations (M. Smith, US Geological Survey 2022, pers. comm.).

Beached seabird carcasses continue to be reported over a wide geographic range throughout summer and autumn on an annual basis (Fig. SB5.4). Reported counts have been considerably lower in some recent years (e.g., 2020 and 2022).

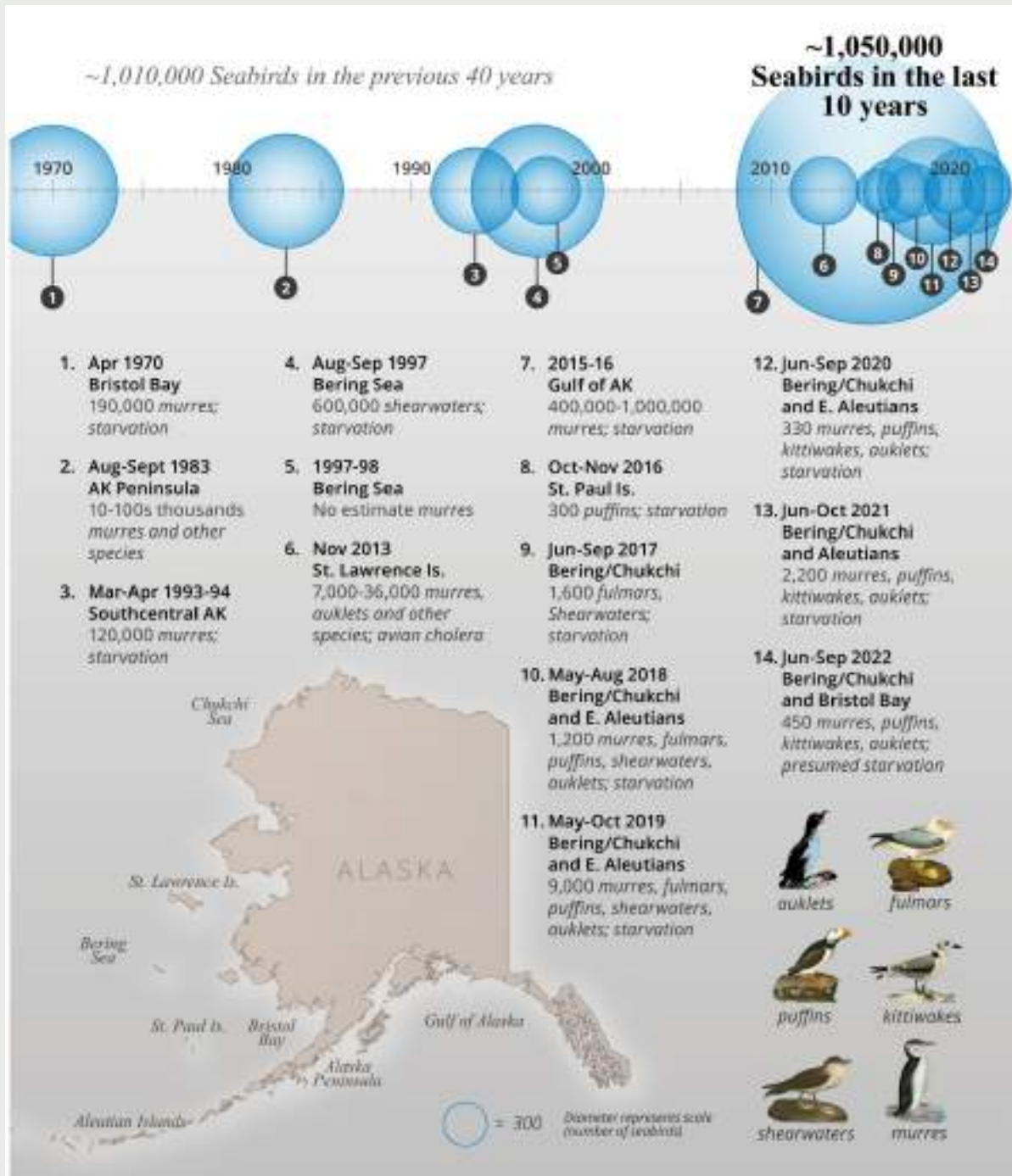


Fig. SB5.4 Alaska seabird die-offs, 1970 to present. Since 2015, mass die-offs have annually occurred in the northern Bering and southern Chukchi sea region. Species primarily affected include murres, puffins, auklets, shearwaters, fulmars, and kittiwakes.

However, due to the expansive and remote nature of Alaska's coastline, much bird mortality goes unreported. Even when bird carcasses are found, reported counts represent a small fraction of the total as many more are lost either due to sinking or scavenging before they can be documented.

The period of seabird die-offs and reduced reproductive success co-occurred with the northward expansion of gadid fishes, such as walleye pollock and Pacific cod (Duffy-Anderson et al. 2019). This may have caused increased competition for forage resources (Piatt et al. 2020) as gadids and piscivorous seabirds feed on much of the same prey. This shift was also layered onto a reduction in the availability of high-quality forage fish (sand lance, capelin) and an increase in lower-quality prey, such as juvenile gadids, in the northern Bering and southern Chukchi Seas in recent years (Duffy-Anderson et al. 2019). Additional work is needed to better understand the links between prey availability and the health and productivity of local seabird populations.

Wildlife mortality events are a public health concern for coastal communities that rely on ocean resources for their nutritional, cultural, and economic well-being. Seabirds and their eggs are important subsistence foods for remote Indigenous communities in rural Alaska. Members of subsistence-focused communities in the northern Bering and southern Chukchi Sea region are frustrated by the lack of timely answers regarding the cause of seabird die-off events and whether birds and eggs are safe to consume. Some communities have requested assistance to document these die-offs and collect samples for testing. The past three years have been especially challenging due to the COVID-19 pandemic, which limited abilities to conduct necropsies on carcasses to determine causes of death, as well as due to increased concerns regarding HPAI in 2022.

With increasing ocean temperatures and decreasing sea ice, the next decade will be critical for determining how marine mammals, marine birds, and human communities adapt to a fast-changing environment in northern Alaska.

Acknowledgments

The editors wish to thank several anonymous reviewers for their efforts. Their careful read and thoughtful input improved each of the sections and, importantly, led to better coherency across the chapter.

a. Overview

Matthew Druckenmiller and Twila Moon appreciate support from NOAA's Arctic Research Office. Rick Thoman appreciates support from NOAA's Climate Program Office.

c. Precipitation

Rune Graversen, Brian Brettschneider, and Rick Thoman contributed information used in this essay.

d. Sea surface temperature

Mary Louise Timmermans acknowledges support from the National Science Foundation Office of Polar Programs, and the Office of Naval Research. Zachary Labe acknowledges support under award NA18OAR4320123 from the National Oceanic and Atmospheric Administration, U.S. Department of Commerce.

h. Rivers

James McClelland and coauthors acknowledge NSF support for the Arctic Great Rivers Observatory (NSF 1913888, 1914081, 1914215, 1913962, 2230812). Shiklomanov and Tretiakov also acknowledge support from the Russian Foundation for Basic Research (grants 18-05-60192 and 18-05-60240). Discharge data for the Mackenzie River are courtesy of Environment Canada.

k. Ozone and UV radiation

Germar Bernhard and coauthors acknowledge the support of Biospherical Instruments, San Diego; the Research Council of Norway through its Centres of Excellence funding scheme, project number 223268/F50; the Academy of Finland for supporting UV measurements through the FARPOCC, SAARA, and CHAMPS (grant no. 329225) projects; the European Space Agency for supporting the DACES project; the Norwegian Environment Agency for funding UV measurements at Andøya and Ny-Ålesund; and the European Union for supporting e-shape. The authors also would like to thank Bodeker Scientific, funded by the New Zealand Deep South National Science Challenge, for providing the combined NIWA-BS total column ozone database; the Microwave Limb Sounder team at NASA's Jet Propulsion Laboratory for data-processing and analysis support; the European Centre for medium-range weather forecasts for providing reanalysis data; and Juha M. Karhu, Tomi Karppinen, and Markku Ahponen from the Finnish Meteorological Institute for operating the Brewer UV spectroradiometer at Sodankylä.

Appendix 1: Chapter 5 – Acronyms

AA	Arctic amplification
ALT	active layer thickness
AMJ	April–May
AVHRR	Advanced Very High Resolution Radiometer
BDL	below detection limits
CCI	Climate Change Initiative
CDD	consecutive dry days
CIO	chlorine monoxide
COD	cause of death
CWD	consecutive wet days
DU	Dobson Units
ERA5	European Centre for Medium-Range Weather Forecasts Reanalysis version 5
ERA-Interim	European Centre for Medium-Range Weather Forecasts Reanalysis Interim
ESA	European Space Agency
GEUS	Geological Survey of Denmark and Greenland
GIMMS-3g+	Global Inventory Modeling and Mapping Studies 3g V1.2 dataset
GISTEMP v4	Goddard Institute for Space Studies Surface Temperature analysis version 4
GPCC	Global Precipitation Climatology Centre
GRACE-FO	Gravity Recovery and Climate Experiment Follow-on
GrIS	Greenland Ice Sheet
HPAI	highly pathogenic avian influenza
ICESat-2	Ice, Cloud and land Elevation Satellite-2
IMS	Ice Mapping System
IPCC	Intergovernmental Panel on Climate Change
JAS	July–September
JFM	January–March
KC	KC-07
KL	Kapp Linne 1
KPC	Kronprins Christians Land
MaxNDVI	Maximum Normalized Difference Vegetation Index
MERRA-2	Modern-Era Retrospective Analysis for Research and Applications version 2
MLS	Microwave Limb Sounder
MOD44W	MODIS <i>Terra</i> Land Water Mask
MODIS	Moderate Resolution Imaging Spectroradiometer
NDVI	Normalized Difference Vegetation Index
NOAA	National Oceanic and Atmospheric Administration
OISST	Optimum Interpolation SST
OMI	Ozone Monitoring Instrument
OND	October–December
PROMICE	Programme for Monitoring of the Greenland Ice Sheet
PSC	polar stratospheric clouds
QAS	Qassimuit
Rx1	one-day precipitation
Rx5	five-day precipitation
SCD	snow-cover duration
SCE	snow-cover extent
SLP	sea-level pressure
SMB	surface mass balance
SMOS	Soil Moisture and Ocean Salinity

SSMIS	Special Sensor Microwave Imager/Sounder
SST	sea-surface temperature
SWE	snow water equivalent
TOC	total ozone column
UV	ultraviolet
UVI	UV Index

References

- Abramov, A., and Coauthors, 2021: Two decades of active layer thickness monitoring in northeastern Asia. *Polar Geogr.*, **44**, 186–202, <https://doi.org/10.1080/1088937X.2019.1648581>.
- Alaska Division of Forestry, 2022: Wildfires burn more than 3 million acres in Alaska. <https://akfireinfo.com/2022/07/21/wildfires-burn-more-than-3-million-acres-in-alaska/>.
- Barnes, P. W., and Coauthors, 2019: Ozone depletion, ultraviolet radiation, climate change and prospects for a sustainable future. *Nat. Sustainability*, **2**, 569–579, <https://doi.org/10.1038/s41893-019-0314-2>.
- Becker, A., P. Finger, A. Meyer-Christoffer, B. Rudolf, K. Schamm, U. Schneider, and M. Ziese, 2013: A description of the global land-surface precipitation data products of the Global Precipitation Climatology Centre with sample applications including centennial (trend) analysis from 1901–present. *Earth Syst. Sci. Data*, **5**, 71–99, <https://doi.org/10.5194/essd-5-71-2013>.
- Benestad, R. E., and Coauthors, 2022: Global hydro-climatological indicators and changes in the global hydrological cycle and rainfall patterns. *PLOS Climate*, **1**, e0000045, <https://doi.org/10.1371/journal.pclm.0000045>.
- Berner, L. T., and S. J. Goetz, 2022: Satellite observations document trends consistent with a boreal forest biome shift. *Global Change Biol.*, **28**, 3275–3292, <https://doi.org/10.1111/gcb.16121>.
- Bernhard, G., and Coauthors, 2015: Comparison of OMI UV observations with ground-based measurements at high northern latitudes. *Atmos. Chem. Phys.*, **15**, 7391–7412, <https://doi.org/10.5194/acp-15-7391-2015>.
- , R. L. McKenzie, K. Lantz, and S. Stierle, 2022: Updated analysis of data from Palmer Station, Antarctica (64°S), and San Diego, California (32°N), confirms large effect of the Antarctic ozone hole on UV radiation. *Photochem. Photobiol. Sci.*, **21**, 373–384, <https://doi.org/10.1007/s43630-022-00178-3>.
- Bhartia, P. K., and C. W. Wellemeyer, 2002: TOMS-V8 total O3 algorithm. OMI Algorithm Theoretical Basis Doc. Volume II, NASA Goddard Space Flight Center Tech. Doc. ATBD-OMI-02, 15–31, <https://eosps.gsf.nasa.gov/sites/default/files/atbd/ATBD-OMI-02.pdf>.
- Bhatt, U. S., and Coauthors, 2021: Climate drivers of Arctic tundra variability and change using an indicators framework. *Environ. Res. Lett.*, **16**, 055019, <https://doi.org/10.1088/1748-9326/abe676>.
- Blanchard-Wrigglesworth, E., M. Webster, L. Boisvert, C. Parker, and C. Horvat, 2022: Record Arctic cyclone of January 2022: Characteristics, impacts, and predictability. *J. Geophys. Res. Atmos.*, **127**, e2022JD037161, <https://doi.org/10.1029/2022JD037161>.
- Bodeker, G. E., and S. Kremser, 2021: Indicators of Antarctic ozone depletion: 1979 to 2019. *Atmos. Chem. Phys.*, **21**, 5289–5300, <https://doi.org/10.5194/acp-21-5289-2021>.
- Bodenstein, B., K. Beckman, G. Sheffield, K. Kuletz, C. Van Hemert, B. Berlowski, and V. Shearn-Bochsler, 2015: Avian cholera causes marine bird mortality in the Bering Sea of Alaska. *J. Wildl. Dis.*, **51**, 934–937, <https://doi.org/10.7589/2014-12-273>.
- , R. J. Dusek, M. M. Smith, C. R. Van Hemert, and R. S. A. Kaler, 2022: USGS National Wildlife Health Center necropsy results to determine cause of illness/death for seabirds collected in Alaska from January 1, 2017 through December 31, 2021. U.S. Geological Survey, accessed 11 July 2023, <https://doi.org/10.5066/P9XHBX75>.
- Box, J. E., and Coauthors, 2019: Key indicators of Arctic climate change: 1971–2017. *Environ. Res. Lett.*, **14**, 045010, <https://doi.org/10.1088/1748-9326/aafc1b>.
- Brady, M. B., and R. Leichenko, 2020: The impacts of coastal erosion on Alaska’s North Slope communities: A co-production assessment of land use damages and risks. *Polar Geogr.*, **43**, 259–279, <https://doi.org/10.1080/1088937X.2020.1755907>.
- Brown, J., O. J. Ferrans Jr., J. A. Heginbottom, and E. S. Melnikov, 1997: Circum-Arctic map of permafrost and ground-ice conditions: Map CP-45. U.S. Geological Survey, 1 pp., <https://pubs.er.usgs.gov/publication/cp45>.
- Brown, R., D. Vikhamar Schuler, O. Bulygina, C. Derksen, K. Luojus, L. Mudryk, L. Wang, and D. Yang, 2017: Arctic terrestrial snow cover. *ow, Water, Ice and Permafrost in the Arctic (SWIPA) 2017, Arctic, Monitoring and Assessment Programme*, 25–64, www.amap.no/documents/doc/snow-water-ice-and-permafrost-in-the-arctic-swipa-2017/1610.
- Brun, E., V. Vionnet, A. Boone, B. Decharme, Y. Peings, R. Valette, F. Karbou, and S. Morin, 2013: Simulation of northern Eurasian local snow depth, mass, and density using a detailed snow-pack model and meteorological reanalyses. *J. Hydrometeorol.*, **14**, 203–219, <https://doi.org/10.1175/JHM-D-12-012.1>.
- Butchart, N., and E. E. Remsberg, 1986: The area of the stratospheric polar vortex as a diagnostic for tracer transport on an isentropic surface. *J. Atmos. Sci.*, **43**, 1319–1339, [https://doi.org/10.1175/1520-0469\(1986\)0432.0.CO;2](https://doi.org/10.1175/1520-0469(1986)0432.0.CO;2).
- Cairns, D. K., 1988: Seabirds as indicators of marine food supplies. *Biol. Oceanogr.*, **5**, 261–271.
- Christensen, T. R., and Coauthors, 2021: Multiple ecosystem effects of extreme weather events in the Arctic. *Ecosystems*, **24**, 122–136, <https://doi.org/10.1007/s10021-020-00507-6>.
- Chylek, P., C. Folland, J. D. Klett, M. Wang, N. Hengartner, G. Lesins, and M. K. Dubey, 2022: Annual mean Arctic amplification 1970–2020: Observed and simulated by CMIP6 climate models. *Geophys. Res. Lett.*, **49**, e2022GL099371, <https://doi.org/10.1029/2022GL099371>.
- Cohen, J., and Coauthors, 2020: Divergent consensus on Arctic amplification influence on mid-latitude severe winter weather. *Nat. Climate Change*, **10**, 20–29, <https://doi.org/10.1038/s41558-019-0662-y>.
- , L. Agel, M. Barlow, C. I. Garfinkel, and I. White, 2021: Arctic change reduces risk of cold extremes—Response. *Science*, **375**, 729–730, <https://doi.org/10.1126/science.abn8954>.
- Crozier, L. G., B. J. Burke, B. E. Chasco, D. L. Widener, and R. W. Zabel, 2021: Climate change threatens Chinook salmon throughout their life cycle. *Commun. Biol.*, **4**, 222, <https://doi.org/10.1038/s42003-021-01734-w>.
- Davidson, S. C., and Coauthors, 2020: Ecological insights from three decades of animal movement tracking across a changing Arctic. *Science*, **370**, 712–715, <https://doi.org/10.1126/science.abb7080>.
- Didan, K., 2021a: MODIS/terra vegetation indices 16-day L3 global 500m SIN grid V061 [Data set]. NASA EOSDIS Land Processes DAAC, accessed 27 February 2023, <https://doi.org/10.5067/MODIS/MOD13A1.061>.
- , 2021b: MODIS/aqua vegetation indices 16-day L3 global 500m SIN Grid V061 [Data set]. NASA EOSDIS Land Processes DAAC, accessed 27 February 2023, <https://doi.org/10.5067/MODIS/MYD13A1.061>.

- Duffy-Anderson, J. T., and Coauthors, 2019: Responses of the northern Bering Sea and southeastern Bering Sea pelagic ecosystems following record-breaking low winter sea ice. *Geophys. Res. Lett.*, **46**, 9833–9842, <https://doi.org/10.1029/2019GL083396>.
- Durocher, M., A. I. Requena, D. H. Burn, and J. Pellerin, 2019: Analysis of trends in annual streamflow to the Arctic Ocean. *Hydrol. Processes*, **33**, 1143–1151, <https://doi.org/10.1002/hyp.13392>.
- EEAP, 2023: Environmental effects of stratospheric ozone depletion, UV radiation, and interactions with climate change. 2022 Assessment Rep., Environmental Effects Assessment Panel, United Nations Environment Programme, 372 pp., <https://ozone.unep.org/system/files/documents/EEAP-2022-Assessment-Report-May2023.pdf>.
- England, M. R., I. Eisenman, N. J. Lutsko, and T. J. W. Wagner, 2021: The recent emergence of Arctic amplification. *Geophys. Res. Lett.*, **48**, e2021GL094086, <https://doi.org/10.1029/2021GL094086>.
- Fetterer, F., K. Knowles, W. N. Meier, M. Savoie, and A. K. Windnagel, 2017: Sea ice index, version 3. National Snow and Ice Data Center, accessed 27 August 2021, <https://doi.org/10.7265/N5K072F8>.
- Frey, K. E., J. C. Comiso, L. W. Cooper, C. Garcia-Eidell, J. M. Grebmeier, and L. V. Stock, 2022: Arctic Ocean primary productivity: The response of marine algae to climate warming and sea ice decline. *Arctic Report Card 2022*, M. L. Druckenmiller, R. L. Thoman, and T. A. Moon, Eds., NOAA Tech. Rep. OAR ARC-22-08, 55–65, <https://doi.org/10.25923/0je1-te61>.
- GMAO, 2015: MERRA-2tavg1_2d_Ind_Nx:2d, 1-hourly, time-averaged, single-level, assimilation, land surface diagnostics V5.12.4. Goddard Earth Sciences Data and Information Services Center (GESDISC), accessed 13 February 2023, <https://doi.org/10.5067/RKPHT8KC1Y1T>.
- Gohari, A., A. J. Shahrood, S. Ghadimi, M. Alborz, E. R. Patro, B. Klöve, and A. T. Haghighi, 2022: A century of variations in extreme flow across Finnish rivers. *Environ. Res. Lett.*, **17**, 124027, <https://doi.org/10.1088/1748-9326/aca554>.
- Heijmans, M. M. P. D., and Coauthors, 2022: Tundra vegetation change and impacts on permafrost. *Nat. Rev. Earth Environ.*, **3**, 68–84, <https://doi.org/10.1038/s43017-021-00233-0>.
- Hersbach, H. B., and Coauthors, 2020: The ERA5 global reanalysis. *Quart. J. Roy. Meteor. Soc.*, **146**, 1999–2049, <https://doi.org/10.1002/qj.3803>.
- Hiyama, T., H. Park, K. Kobayashi, L. Lebedeva, and D. Gustafsson, 2023: Contribution of summer net precipitation to winter river discharge in permafrost zone of the Lena River basin. *J. Hydrol.*, **616**, 128797, <https://doi.org/10.1016/j.jhydrol.2022.128797>.
- Hjort, J., D. Streletskiy, G. Doré, Q. Wu, K. Bjella, and M. Luoto, 2022: Impacts of permafrost degradation on infrastructure. *Nat. Rev. Earth Environ.*, **3**, 24–38, <https://doi.org/10.1038/s43017-021-00247-8>.
- Holmes, R. M., and Coauthors, 2013: Climate change impacts on the hydrology and biogeochemistry of Arctic Rivers. *Climatic Change and Global Warming of Inland Waters: Impacts and Mitigation for Ecosystems and Societies*, C. R. Goldman, M. Kumagai, and R. D. Robarts, Eds., Wiley, 3–26.
- Huang, B., C. Liu, V. Banzon, E. Freeman, G. Graham, B. Hankins, T. Smith, and H. Zhang, 2021: Improvements of the Daily Optimum Interpolation Sea Surface Temperature (DOISST) version 2.1. *J. Climate*, **34**, 2923–2939, <https://doi.org/10.1175/JCLI-D-20-0166.1>.
- IPCC, 2021: *Climate Change 2021: The Physical Science Basis*. V. Masson-Delmotte et al., Eds., Cambridge University Press, 2391 pp.
- Irrgang, A. M., and Coauthors, 2022: Drivers, dynamics and impacts of changing Arctic coasts. *Nat. Rev. Earth Environ.*, **3**, 39–54, <https://doi.org/10.1038/s43017-021-00232-1>.
- Isaksen, K., J. Lutz, A. M. Sorensen, O. Godoy, L. Ferrighi, S. Eastwood, and S. Aaboe, 2022: Advances in operational permafrost monitoring on Svalbard and in Norway. *Environ. Res. Lett.*, **17**, 095012, <https://doi.org/10.1088/1748-9326/ac8e1c>.
- Ivanova, N., O. M. Johannessen, L. T. Pedersen, and R. T. Tonboe, 2014: Retrieval of Arctic sea ice parameters by satellite passive microwave sensors: A comparison of eleven sea ice concentration algorithms. *IEEE Trans. Geosci. Remote Sens.*, **52**, 7233–7246, <https://doi.org/10.1109/TGRS.2014.2310136>.
- Jones, T., L. Divine, H. Renner, S. Knowles, K. A. Lefebvre, H. K. Burgess, C. Wright, and J. Parrish, 2019: Unusual mortality of Tufted puffins (*Fratercula cirrhata*) in the eastern Bering Sea. *PLOS ONE*, **14**, e0216532, <https://doi.org/10.1371/journal.pone.0216532>.
- Jorgenson, M. T., D. R. N. Brown, C. A. Hiemstra, H. Genet, B. G. Marcot, R. J. Murphy, and T. A. Douglas, 2022: Drivers of historical and projected changes in diverse boreal ecosystems: Fires, thermokarst, riverine dynamics, and humans. *Environ. Res. Lett.*, **17**, 045016, <https://doi.org/10.1088/1748-9326/ac5c0d>.
- Kaverin, D., and Coauthors, 2021: Long-term active layer monitoring at CALM sites in the Russian European North. *Polar Geogr.*, **44**, 203–216, <https://doi.org/10.1080/1088937X.2021.1981476>.
- Koch, C. W., and Coauthors, 2023: Year-round utilization of sea ice-associated carbon in Arctic ecosystems. *Nat. Commun.*, **14**, 1964, <https://doi.org/10.1038/s41467-023-37612-8>.
- Kopec, B., X. Feng, F. A. Michel, and E. Posmentier, 2016: Influence of sea ice on Arctic precipitation. *Proc. Natl. Acad. Sci. USA*, **113**, 46–51, <https://doi.org/10.1073/pnas.1504633113>.
- Kusunoki, S., R. Mizuta, and M. Hosaka, 2015: Future changes in precipitation intensity over the Arctic projected by a global atmospheric model with a 60-km grid size. *Polar Sci.*, **9**, 277–292, <https://doi.org/10.1016/j.polar.2015.08.001>.
- Landy, J. C., and Coauthors, 2022: A year-round satellite sea-ice thickness record from CryoSat-2. *Nature*, **609**, 517–522, <https://doi.org/10.1038/s41586-022-05058-5>.
- Lavergne, T., and Coauthors, 2019: Version 2 of the EUMETSAT OSI SAF and ESA CCI sea-ice concentration climate data records. *Cryosphere*, **13**, 49–78, <https://doi.org/10.5194/tc-13-49-2019>.
- Lawrence, Z. D., J. Perlwitz, A. H. Butler, G. L. Manney, P. A. Newman, S. H. Lee, and E. R. Nash, 2020: The remarkably strong Arctic stratospheric polar vortex of winter 2020: Links to record-breaking Arctic oscillation and ozone loss. *J. Geophys. Res. Atmos.*, **125**, e2020JD033271, <https://doi.org/10.1029/2020JD033271>.
- Lenssen, N. J., G. A. Schmidt, J. E. Hansen, M. J. Menne, A. Persin, R. Ruedy, and D. Zyss, 2019: Improvements in the GISTEMP uncertainty model. *J. Geophys. Res. Atmos.*, **124**, 6307–6326, <https://doi.org/10.1029/2018JD029522>.
- Liu, S., and Coauthors, 2022: Mechanisms behind the uneven increases in early, mid- and late winter streamflow across four Arctic river basins. *J. Hydrol.*, **606**, 127425, <https://doi.org/10.1016/j.jhydrol.2021.127425>.

- Luoju, K., and Coauthors, 2022: ESA Snow Climate Change Initiative (Snow_cci): Snow Water Equivalent (SWE) level 3C daily global climate research data package (CRDP) (1979–2020), version 2.0. NERC EDS Centre for Environmental Data Analysis, accessed 8 September 2022, <https://doi.org/10.5285/4647c-c9ad3c044439d6c643208d3c494>.
- Macander, M. J., P. R. Nelson, T. W. Nawrocki, G. V. Frost, K. M. Orndahl, E. C. Palm, A. F. Wells, and S. J. Goetz, 2022: Time-series maps reveal widespread change in plant functional type cover across Arctic and boreal Alaska and Yukon. *Environ. Res. Lett.*, **17**, 054042, <https://doi.org/10.1088/1748-9326/ac6965>.
- Magnússon, R. Í., 2021: Shrub decline and expansion of wetland vegetation revealed by very high resolution land cover change detection in the Siberian lowland tundra. *Sci. Total Environ.*, **782**, 146877, <https://doi.org/10.1016/j.scitotenv.2021.146877>.
- Malkova, G., and Coauthors, 2022: Spatial and temporal variability of permafrost in the western part of the Russian Arctic. *Energies*, **15**, 2311, <https://doi.org/10.3390/en15072311>.
- Mallory, C. D., and M. S. Boyce, 2018: Observed and predicted effects of climate change on Arctic caribou and reindeer. *Environ. Rev.*, **26**, 13–25, <https://doi.org/10.1139/er-2017-0032>.
- Mamen, J., H. T. T. Tajet, and K. Tunheim, 2022: Klimatologisk månedsoversikt, June 2022. MET Info 6/2022 (in Norwegian). Meteorologisk Institutt, 23 pp., www.met.no/publikasjoner/met-info/met-info-2022.
- Mankoff, K. D., A. Solgaard, W. Colgan, A. P. Ahlstrøm, S. A. Khan, and R. S. Fausto, 2020: Greenland Ice Sheet solid ice discharge from 1986 through March 2020. *Earth Syst. Sci. Data*, **12**, 1367–1383, <https://doi.org/10.5194/essd-12-1367-2020>.
- , and Coauthors, 2021: Greenland ice sheet mass balance from 1840 through next week. *Earth Syst. Sci. Data*, **13**, 5001–5025, <https://doi.org/10.5194/essd-13-5001-2021>.
- Manney, G. L., and Coauthors, 2011: Unprecedented Arctic ozone loss in 2011. *Nature*, **478**, 469–475, <https://doi.org/10.1038/nature10556>.
- , and Coauthors, 2020: Record-low Arctic stratospheric ozone in 2020: MLS observations of chemical processes and comparisons with previous extreme winters. *Geophys. Res. Lett.*, **47**, e2020GL089063, <https://doi.org/10.1029/2020GL089063>.
- McClelland, J. W., R. M. Holmes, K. H. Dunton, and R. Macdonald, 2012: The Arctic Ocean estuary. *Estuaries Coasts*, **35**, 353–368, <https://doi.org/10.1007/s12237-010-9357-3>.
- McCrystall, M., J. Stroeve, M. C. Serreze, B. C. Forbes, and J. Screen, 2021: New climate models reveal faster and larger increases in Arctic precipitation than previously projected. *Nat. Commun.*, **12**, 6765, <https://doi.org/10.1038/s41467-021-27031-y>.
- Meier, W. N., F. Fetterer, A. K. Windnagel, and J. S. Stewart, 2021a: NOAA/NSIDC climate data record of passive microwave sea ice concentration, version 4. National Snow and Ice Data Center, accessed 10 September 2022, <https://doi.org/10.7265/efmz-2t65>.
- , —, —, and —, 2021b: Near-real-time NOAA/NSIDC climate data record of passive microwave sea ice concentration, version 2. National Snow and Ice Data Center, accessed 10 September 2022, <https://doi.org/10.7265/tgam-yv28>.
- Mekonnen, Z. A., and Coauthors, 2021: Arctic tundra shrubification: A review of mechanisms and impacts on ecosystem carbon balance. *Environ. Res. Lett.*, **16**, 053001, <https://doi.org/10.1088/1748-9326/abf28b>.
- Meredith, M., and Coauthors, 2019: Polar regions. *IPCC Special Report on the Ocean and Cryosphere in a Changing Climate*, H.-O. Pörtner et al., Eds., Cambridge University Press, 203–320.
- Moore, G. W. K., S. E. L. Howell, M. Brady, X. Xu, and K. McNeil, 2021: Anomalous collapses of Nares Strait ice arches leads to enhanced export of Arctic sea ice. *Nat. Commun.*, **12**, 1, <https://doi.org/10.1038/s41467-020-20314-w>.
- Morlighem, M., and Coauthors, 2017: BedMachine v3: Complete bed topography and ocean bathymetry mapping of Greenland from multi-beam radar sounding combined with mass conservation. *Geophys. Res. Lett.*, **44**, 11 051–11 061, <https://doi.org/10.1002/2017GL074954>.
- Mote, T., 2007: Greenland surface melt trends 1973–2007: Evidence of a large increase in 2007. *Geophys. Res. Lett.*, **34**, L22507, <https://doi.org/10.1029/2007GL031976>.
- Mouginot, J., and Coauthors, 2019: Forty-six years of Greenland Ice Sheet mass balance from 1972 to 2018. *Proc. Natl. Acad. Sci. USA*, **116**, 9239–9244, <https://doi.org/10.1073/pnas.1904242116>.
- Müller, R., J.-U. Grooß, C. Lemmen, D. Heinze, M. Dameris, and G. Bodeker, 2008: Simple measures of ozone depletion in the polar stratosphere. *Atmos. Chem. Phys.*, **8**, 251–264, <https://doi.org/10.5194/acp-8-251-2008>.
- Muñoz Sabater, J., 2019: ERA5-land hourly data from 1981 to present. Copernicus Climate Change Service (C3S) Climate Data Store (CDS), accessed 8 September 2022, <https://doi.org/10.24381/cds.e2161bac>.
- Myers-Smith, I. H., and Coauthors, 2020: Complexity revealed in the greening of the Arctic. *Nat. Climate Change*, **10**, 106–117, <https://doi.org/10.1038/s41558-019-0688-1>.
- Nielsen, D. M., P. Pieper, A. Barkhordarian, P. Overduin, T. Ilyina, V. Brovkin, J. Baehr, and M. Dobrynin, 2022: Increase in Arctic coastal erosion and its sensitivity to warming in the twenty-first century. *Nat. Climate Change*, **12**, 263–270, <https://doi.org/10.1038/s41558-022-01281-0>.
- NOAA, 2022: The Global Climate during El Niño and La Niña. Accessed 21 May 2023, <https://psl.noaa.gov/enso/compare/>.
- Nyland, K. E., N. I. Shiklomanov, D. A. Streletskiy, F. E. Nelson, A. E. Klene, and A. L. Kholodov, 2021: Long-term Circumpolar Active Layer Monitoring (CALM) program observations in Northern Alaskan tundra. *Polar Geogr.*, **44**, 176–185, <https://doi.org/10.1080/1088937X.2021.1988000>.
- Overland, J. E., 2022: Arctic climate extremes. *Atmosphere*, **13**, 1670, <https://doi.org/10.3390/atmos13101670>.
- Pearson, R. G., S. J. Phillips, M. M. Lorant, P. S. A. Beck, T. Damoulas, S. J. Knight, and S. J. Goetz, 2013: Shifts in Arctic vegetation and associated feedbacks under climate change. *Nat. Climate Change*, **3**, 673–677, <https://doi.org/10.1038/nclimate1858>.
- Peng, G., W. N. Meier, D. J. Scott, and M. H. Savoie, 2013: A long-term and reproducible passive microwave sea ice concentration data record for climate studies and monitoring. *Earth Syst. Sci. Data*, **5**, 311–318, <https://doi.org/10.5194/essd-5-311-2013>.
- Peterson, B. J., R. M. Holmes, J. W. McClelland, C. J. Vorosmarty, R. B. Lammers, A. I. Shiklomanov, I. A. Shiklomanov, and S. Rahmstorf, 2002: Increasing river discharge to the Arctic Ocean. *Science*, **298**, 2171–2173, <https://doi.org/10.1126/science.1077445>.
- Petty, A. A., N. T. Kurtz, R. Kwok, T. Markus, and T. A. Neumann, 2020: Winter Arctic sea ice thickness from ICESat 2 freeboards. *J. Geophys. Res. Oceans*, **125**, e2019JC015764, <https://doi.org/10.1029/2019JC015764>.
- , —, —, —, and —, 2021: ICESat-2 L4 monthly gridded sea ice thickness, version 1. NASA National Snow and Ice Data Center Distributed Active Archive Center, accessed 9 September, <https://doi.org/10.5067/CV6JEXEE31HF>.

- , N. Keeney, A. Cabaj, P. Kushner, and M. Bagnardi, 2023: Winter Arctic sea ice thickness from ICESat-2: Upgrades to freeboard and snow loading estimates and an assessment of the first three winters of data collection. *Cryosphere*, **17**, 127–156, <https://doi.org/10.5194/tc-17-127-2023>.
- Piatt, J. P., and Coauthors, 2020: Extreme mortality and reproductive failure of common murrelets resulting from the northeast Pacific marine heatwave of 2014–2016. *PLOS ONE*, **15**, e0226087, <https://doi.org/10.1371/journal.pone.0226087>.
- Pinzon, J., and C. Tucker, 2014: A non-stationary 1981–2012 AVHRR NDVI3g time series. *Remote Sens.*, **6**, 6929–6960, <https://doi.org/10.3390/rs6086929>.
- Previdi, M., K. L. Smith, and L. M. Polvani, 2021: Arctic amplification of climate change: A review of underlying mechanisms. *Environ. Res. Lett.*, **16**, 093003, <https://doi.org/10.1088/1748-9326/ac1c29>.
- Rantanen, M., A. Y. Karpechko, A. Lipponen, K. Nordling, O. Hyvärinen, K. Ruosteenoja, T. Vihma, and A. Laaksonen, 2022: The Arctic has warmed nearly four times faster than the globe since 1979. *Commun. Earth Environ.*, **3**, 168, <https://doi.org/10.1038/s43247-022-00498-3>.
- Rawlins, M. A., and Coauthors, 2010: Analysis of the Arctic system freshwater cycle intensification: Observations and expectations. *J. Climate*, **23**, 5715–5737, <https://doi.org/10.1175/2010JCLI3421.1>.
- Raynolds, M. K., and Coauthors, 2019: A raster version of the Circumpolar Arctic Vegetation Map (CAVM). *Remote Sens. Environ.*, **232**, 111297, <https://doi.org/10.1016/j.rse.2019.111297>.
- Reynolds, R. W., N. A. Rayner, T. M. Smith, D. C. Stokes, and W. Wang, 2002: An improved in situ and satellite SST analysis for climate. *J. Climate*, **15**, 1609–1625, [https://doi.org/10.1175/1520-0442\(2002\)015<1609:CO;2](https://doi.org/10.1175/1520-0442(2002)015<1609:CO;2).
- , T. M. Smith, C. Liu, D. B. Chelton, K. S. Casey, and M. G. Schlax, 2007: Daily high-resolution-blended analyses for sea surface temperature. *J. Climate*, **20**, 5473–5496, <https://doi.org/10.1175/2007JCLI1824.1>.
- Ricker, R., S. Hendricks, L. Kaleschke, X. Tian-Kunze, J. King, and C. Haas, 2017: A weekly Arctic sea-ice thickness data record from merged CryoSat-2 and SMOS satellite data. *Cryosphere*, **11**, 1607–1623, <https://doi.org/10.5194/tc-11-1607-2017>.
- Robinson, D. A., T. W. Estilow, and NOAA CDR Program, 2012: NOAA Climate Data Record (CDR) of Northern Hemisphere (NH) Snow Cover Extent (SCE), version 1 [r01]. NOAA National Centers for Environmental Information, accessed 15 August 2022, <https://doi.org/10.7289/V5N014G9>.
- Rogers, A., S. P. Serbin, and D. A. Way, 2022: Reducing model uncertainty of climate change impacts on high latitude carbon assimilation. *Global Change Biol.*, **28**, 1222–1247, <https://doi.org/10.1111/gcb.15958>.
- Romano, M., H. M. Renner, K. J. Kuletz, J. K. Parrish, T. Jones, H. K. Burgess, D. A. Cushing, and D. Causey, 2020: Die-offs and reproductive failure of murrelets in the Bering and Chukchi Seas in 2018. *Deep-Sea Res. II*, **181–182**, 104877, <https://doi.org/10.1016/j.dsr2.2020.104877>.
- Romanovsky, V., and Coauthors, 2017: Changing permafrost and its impacts. Snow, Water, Ice and Permafrost in the Arctic (SWIPA) 2017, Arctic, Monitoring and Assessment Programme, 65–102, www.amap.no/documents/doc/snow-water-ice-and-permafrost-in-the-arctic-swipa-2017/1610.
- Ryan, J. C., L. C. Smith, D. van As, S. W. Cooley, M. G. Cooper, L. H. Pitcher, and A. Hubbard, 2019: Greenland ice sheet surface melt amplified by snowline migration and bare ice exposure. *Sci. Adv.*, **5**, eaav3738, <https://doi.org/10.1126/sciadv.aav3738>.
- Schneider, U., P. Finger, E. Rustemeier, M. Ziese, and S. Hänsel, 2022: Global precipitation analysis products of the GPCC. DWD, 17 pp., https://opendata.dwd.de/climate_environment/GPCC/PDF/GPCC_intro_products_v2022.pdf.
- Schuur, E. A. G., 2020: Permafrost carbon [in “State of the Climate in 2019”]. *Bull. Amer. Meteor. Soc.*, **101** (8), S270–S271, <https://doi.org/10.1175/BAMS-D-20-0086.1>.
- SEARCH, and Coauthors, 2022: Consequences of rapid environmental Arctic change for people. *Arctic Report Card 2022*, M. L. Druckenmiller, R. L. Thoman, and T. A. Moon, Eds., NOAA Tech. Rep. OAR ARC-22-16, 123–129, <https://doi.org/10.25923/kgm2-9k50>.
- Shiklomanov, N. I., D. A. Streletskiy, and F. E. Nelson, 2012: Northern Hemisphere component of the global Circumpolar Active Layer Monitoring (CALM) Program. *Proc. 10th Int. Conf. on Permafrost*, Vol. 1, Salekhard, Russia, Tyumen Oil and Gas University, 377–382.
- Shrestha, R. R., K. E. Bennett, D. L. Peters, and D. Yang, 2021: Hydrologic extremes in Arctic rivers and regions: Historical variability and future perspectives. *Arctic Hydrology, Permafrost and Ecosystems*, D. Yang and D. L. Kane, Eds., Springer, 187–218, https://doi.org/10.1007/978-3-030-50930-9_7.
- Sillmann, J., V. V. Kharin, F. W. Zwiers, X. Zhang, and D. Bronaugh, 2013: Climate extremes indices in the CMIP5 multimodel ensemble: Part 2. Future climate projections. *J. Geophys. Res. Atmos.*, **118**, 2473–2493, <https://doi.org/10.1002/jgrd.50188>.
- Smith, S. L., and Coauthors, 2022a: Permafrost [in “State of the Climate in 2021”]. *Bull. Amer. Meteor. Soc.*, **103** (8), S286–S290, <https://doi.org/10.1175/BAMS-D-22-0082.1>.
- , H. B. O’Neill, K. Isaksen, J. Noetzli, and V. E. Romanovsky, 2022b: The changing thermal state of permafrost. *Nat. Rev. Earth Environ.*, **3**, 10–23, <https://doi.org/10.1038/s43017-021-00240-1>.
- Stabeno, P. J., R. L. Thoman, and K. Wood, 2019: Recent warming in the Bering Sea and its impacts on the ecosystem. *Arctic Report Card 2019*, J. Richter-Menge, M. L. Druckenmiller, and M. Jeffries, Eds., NOAA Tech. Rep., 81–87, https://arctic.noaa.gov/Portals/7/ArcticReportCard/Documents/ArcticReportCard_full_report2019.pdf.
- Strand, S. M., H. H. Christiansen, M. Johansson, J. Akerman, and O. Humlum, 2021: Active layer thickening and controls on interannual variability in the Nordic Arctic compared to the circum-Arctic. *Permafrost Periglacial. Processes*, **32**, 47–58, <https://doi.org/10.1002/ppp.2088>.
- Stroh, J. N., G. Panteleev, S. Kirillov, M. Makhotin, and N. Shakhova, 2015: Sea-surface temperature and salinity product comparison against external in situ data in the Arctic Ocean. *J. Geophys. Res. Oceans*, **120**, 7223–7236, <https://doi.org/10.1002/2015JC011005>.
- Tanskanen, A., A. Arola, and J. Kujanpää, 2003: Use of the moving time-window technique to determine surface albedo from the TOMS reflectivity data. *Proc. SPIE*, **4896**, 239–250, <https://doi.org/10.1117/12.483407>.
- Tapley, B. D., and Coauthors, 2019: Contributions of GRACE to understanding climate change. *Nat. Climate Change*, **9**, 358–369, <https://doi.org/10.1038/s41558-019-0456-2>.

- Thoman, R., M. L. Druckenmiller, and T. A. Moon, Eds., 2022: The Arctic [in "State of the Climate in 2021"]. *Bull. Amer. Meteor. Soc.*, **103** (8), S257–S306, <https://doi.org/10.1175/BAMS-D-22-0082.1>.
- Timmermans, M.-L., and Z. Labe, 2022: Sea surface temperature [in "State of the Climate in 2021"]. *Bull. Amer. Meteor. Soc.*, **103** (8), S268–S270, <https://doi.org/10.1175/BAMS-D-22-0082.1>.
- Tretiyakov, M. V., O. V. Muzhdaba, A. A. Piskun, and R. A. Terekhova, 2022: The state of the Roshydromet Hydrological Observation Network in the mouth areas of RFAZ. *Water Resour.*, **49**, 796–807, <https://doi.org/10.1134/S0097807822050153>.
- Tschudi, M., W. N. Meier, and J. S. Stewart, 2019a: Quicklook Arctic weekly EASE-grid sea ice age, version 1 [March, 2021]. NASA National Snow and Ice Data Center Distributed Active Archive Center, accessed 1 September 2021, <https://doi.org/10.5067/2XXGZY3DUGNQ>.
- , —, —, C. Fowler, and J. Maslanik, 2019b: EASE-grid sea ice age, version 4 [March, 1984–2020]. NASA National Snow and Ice Data Center Distributed Active Archive Center, accessed 1 September 2021, <https://doi.org/10.5067/UTAV7490FEPB>.
- U.S. Geological Survey, 2022: Wildlife Health Information Sharing Partnership–Event Reporting System (WHISPers) on-line database. Accessed October 2022, <https://whispers.usgs.gov/home>.
- U.S. National Ice Center, 2008: IMS daily Northern Hemisphere snow and ice analysis at 1 km, 4 km, and 24 km resolutions, version 1. National Snow and Ice Data Center, accessed 13 August 2022, <https://doi.org/10.7265/N52R3PMC>.
- Van Hemert, C., and Coauthors, 2021: Investigation of algal toxins in a multispecies seabird die-off in the Bering and Chukchi seas. *J. Wildl. Dis.*, **57**, 399–407, <https://doi.org/10.7589/JWD-D-20-00057>.
- Walsh, J. E., T. J. Ballinger, E. S. Euskirchen, E. Hanna, J. Mård, J. E. Overland, H. Tangen, and T. Vihma, 2020: Extreme weather and climate events in northern areas: A review. *Earth-Sci. Rev.*, **209**, 103324, <https://doi.org/10.1016/j.earscirev.2020.103324>.
- Waters, J. W., and Coauthors, 2006: The Earth Observing System Microwave Limb Sounder (EOS MLS) on the Aura satellite. *IEEE Trans. Geosci. Remote Sens.*, **44**, 1075–1092, <https://doi.org/10.1109/TGRS.2006.873771>.
- Wegmann, M., and Coauthors, 2015: Arctic moisture source for Eurasian snow cover variations in autumn. *Environ. Res. Lett.*, **10**, 054015, <https://doi.org/10.1088/1748-9326/10/5/054015>.
- Wehrlé, A., J. E. Box, A. M. Anesio, and R. S. Fausto, 2021: Greenland bare-ice albedo from PROMICE automatic weather station measurements and Sentinel-3 satellite observations. *Geol. Surv. Denmark Greenl. Bull.*, **47**, <https://doi.org/10.34194/geusb.v47.5284>.
- White, J., J. E. Walsh, and R. L. Thoman Jr., 2021: Using Bayesian statistics to detect trends in Alaskan precipitation. *Int. J. Climatol.*, **41**, 2045–2059, <https://doi.org/10.1002/joc.6946>.
- Whitfield, P. H., P. D. A. Kraaijenbrink, K. R. Shook, and J. W. Pomeroy, 2021: The spatial extent of hydrological and landscape changes across the mountains and prairies of Canada in the Mackenzie and Nelson River basins based on data from a warm-season time window. *Hydrol. Earth Syst. Sci.*, **25**, 2513–2541, <https://doi.org/10.5194/hess-25-2513-2021>.
- Will, A., and Coauthors, 2020: The breeding seabird community reveals that recent sea ice loss in the Pacific Arctic does not benefit piscivores and is detrimental to planktivores. *Deep-Sea Res.*, **181–182**, 104902, <https://doi.org/10.1016/j.dsr2.2020.104902>.
- WMO, 2022: Scientific assessment of ozone depletion: 2022. WMO GAW Rep. 278, 509 pp., <https://csl.noaa.gov/assessments/ozone/2022/>.
- Wolken, G. J., and Coauthors, 2021: Glacier and permafrost hazards. *Arctic Report Card 2021*, T. A. Moon, M. L. Druckenmiller, and R. L. Thoman, Eds., NOAA Tech. Rep. OAR ARC-21-13, NOAA, 93–101, <https://doi.org/10.25923/v40r-0956>.
- Yang, D., and Coauthors, 2022: Remote sensing from unoccupied aerial systems: Opportunities to enhance Arctic plant ecology in a changing climate. *J. Ecol.*, **110**, 2812–2835, <https://doi.org/10.1111/1365-2745.13976>.
- Ye, H., D. Yang, A. Behrangi, S. L. Stuefer, X. Pan, E. Mekis, Y. Dibike, and J. E. Walsh, 2021: Precipitation characteristics and changes. *Arctic Hydrology, Permafrost and Ecosystems*, D. Yang and D. L. Kane, Eds., Springer, 25–59, https://doi.org/10.1007/978-3-030-50930-9_2.
- Yu, L., and S. Zhong, 2021: Trends in Arctic seasonal and extreme precipitation in recent decades. *Theor. Appl. Climatol.*, **145**, 1541–1559, <https://doi.org/10.1007/s00704-021-03717-7>.
- Zona, D., and Coauthors, 2023: Pan-Arctic soil moisture control on tundra carbon sequestration and plant productivity. *Global Change Biol.*, **29**, 1267–1281, <https://doi.org/10.1111/gcb.16487>.

STATE OF THE CLIMATE IN 2022

ANTARCTICA AND THE SOUTHERN OCEAN

Kyle R. Clem and Marilyn N. Raphael, Eds.



Special Online Supplement to the *Bulletin of the American Meteorological Society* Vol. 104, No. 9, September, 2023

<https://doi.org/10.1175/BAMS-D-23-0077.1>

Corresponding author: Kyle R. Clem / kyle.clem@vuw.ac.nz

©2023 American Meteorological Society

For information regarding reuse of this content and general copyright information, consult the [AMS Copyright Policy](#).

STATE OF THE CLIMATE IN 2022

Antarctica and the Southern Ocean

Editors

Ellen Bartow-Gillies
Jessica Blunden
Tim Boyer

Chapter Editors

Peter Bissolli
Kyle R. Clem
Howard J. Diamond
Matthew L. Druckenmiller
Robert J. H. Dunn
Catherine Ganter
Nadine Gobron
Gregory C. Johnson
Rick Lumpkin
Ademe Mekonnen
John B. Miller
Twila A. Moon
Marilyn N. Raphael
Ahira Sánchez-Lugo
Carl J. Schreck III
Richard L. Thoman
Kate M. Willett
Zhiwei Zhu

Technical Editor

Lukas Noguchi

BAMS Special Editor for Climate

Michael A. Alexander

American Meteorological Society

Cover Credit:

Photograph taken near the Dry Valleys, Antarctica in January 2022 by David Mikolajczyk, Antarctic Meteorological Research and Data Center, SSEC, UW-Madison, Madison, WI.

How to cite this document:

Antarctica and the Southern Ocean is one chapter from the *State of the Climate in 2022* annual report and is available from <https://doi.org/10.1175/BAMS-D-23-0077.1>. Compiled by NOAA's National Centers for Environmental Information, *State of the Climate in 2022* is based on contributions from scientists from around the world. It provides a detailed update on global climate indicators, notable weather events, and other data collected by environmental monitoring stations and instruments located on land, water, ice, and in space. The full report is available from <https://doi.org/10.1175/2023BAMSStateoftheClimate.1>.

Citing the complete report:

Blunden, J., T. Boyer, and E. Bartow-Gillies, Eds., 2023: "State of the Climate in 2022". Bull. Amer. Meteor. Soc., 104 (9), Si–S501 <https://doi.org/10.1175/2023BAMSStateoftheClimate.1>.

Citing this chapter:

Clem, K. R. and M. N. Raphael, Eds., 2023: Antarctica and the Southern Ocean [in "State of the Climate in 2022"]. Bull. Amer. Meteor. Soc., 104 (9), S322–S365, <https://doi.org/10.1175/BAMS-D-23-0077.1>.

Citing a section (example):

MacFerrin, M., T. Mote, A. Banwell, and T. Scambos, 2023: Ice-sheet seasonal melt extent and duration [in "State of the Climate in 2022"]. Bull. Amer. Meteor. Soc., 104 (9), S339–S341, <https://doi.org/10.1175/BAMS-D-23-0077.1>.

Editor and Author Affiliations (alphabetical by name)

- Adusumilli, Susheel**, Scripps Institution of Oceanography, University of California, San Diego, La Jolla, California
- Baiman, Rebecca**, Department of Atmospheric and Oceanic Sciences, University of Colorado Boulder, Boulder, Colorado
- Banwell, Alison F.**, Earth Science Observation Center, Cooperative Institute for Research in Environmental Sciences (ESOC/CIRES), University of Colorado Boulder, Boulder, Colorado
- Barreira, Sandra**, Argentine Naval Hydrographic Service, Buenos Aires, Argentina
- Beadling, Rebecca L.**, Department of Earth and Environmental Science, Temple University, Philadelphia, Pennsylvania
- Bozkurt, Deniz**, Department of Meteorology, University of Valparaíso, Valparaíso, Chile; Center for Climate and Resilience Research (CR)2, Santiago, Chile
- Clem, Kyle R.**, School of Geography, Environment and Earth Sciences, Victoria University of Wellington, Wellington, New Zealand
- Colwell, Steve**, British Antarctic Survey, Cambridge, United Kingdom
- Coy, Lawrence**, Science Systems and Applications, Inc., Lanham, Maryland; NASA Goddard Space Flight Center, Greenbelt, Maryland
- Datta, Rajashree T.**, Department of Atmospheric and Oceanic Sciences, University of Colorado Boulder, Boulder, Colorado
- De Laat, Jos**, Royal Netherlands Meteorological Institute (KNMI), DeBilt, The Netherlands
- du Plessis, Marcel**, Department of Marine Sciences, University of Gothenburg, Gothenburg, Sweden
- Dunmire, Devon**, Department of Atmospheric and Oceanic Sciences, University of Colorado Boulder, Boulder, Colorado
- Fogt, Ryan L.**, Department of Geography, Ohio University, Athens, Ohio
- Freeman, Natalie M.**, Department of Atmospheric and Oceanic Sciences, University of Colorado Boulder, Boulder, Colorado
- Fricker, Helen A.**, Scripps Institution of Oceanography, University of California, San Diego, La Jolla, California
- Gardner, Alex S.**, NASA Jet Propulsion Laboratory, Pasadena, California
- Gille, Sarah T.**, Scripps Institution of Oceanography, University of California, San Diego, La Jolla, California
- Johnson, Bryan**, NOAA/OAR Earth System Research Laboratory, Global Monitoring Division, Boulder, Colorado; University of Colorado Boulder, Boulder, Colorado
- Josey, Simon A.**, National Oceanography Centre, Southampton, United Kingdom.
- Keller, Linda M.**, Antarctic Meteorological Research and Data Center, Space Science and Engineering Center, University of Wisconsin-Madison, Madison, Wisconsin
- Kramarova, Natalya A.**, NASA Goddard Space Flight Center, Greenbelt, Maryland
- Lazzara, Matthew A.**, Department of Physical Sciences, School of Arts and Sciences, Madison Area Technical College, Madison, Wisconsin; Antarctic Meteorological Research and Data Center, Space Science and Engineering Center, University of Wisconsin-Madison, Madison, Wisconsin
- Lieser, Jan L.**, Australian Bureau of Meteorology and Institute for Marine and Antarctic Studies (IMAS), University of Tasmania, Hobart, Australia
- MacFerrin, Michael**, Earth Science and Observation Center, CIRES, University of Colorado, Boulder, Colorado
- MacGilchrist, Graeme A.**, University of St. Andrews, St Andrews, United Kingdom; Princeton University, Princeton, New Jersey
- MacLennan, Michelle L.**, Department of Atmospheric and Oceanic Sciences, University of Colorado Boulder, Boulder, Colorado
- Massom, Robert A.**, Australian Antarctic Division, Australian Antarctic Program Partnership (AAPP) and Australian Centre for Excellence in Antarctic Science (ACEAS), Tasmania, Australia
- Mazloff, Matthew R.**, Scripps Institution of Oceanography, University of California, San Diego, La Jolla, California
- Mikolajczyk, David E.**, Antarctic Meteorological Research and Data Center, Space Science and Engineering Center, University of Wisconsin-Madison, Madison, Wisconsin
- Mote, Thomas L.**, Department of Geography, University of Georgia, Athens, Georgia
- Nash, Eric R.**, Science Systems and Applications, Inc., Lanham, Maryland; NASA Goddard Space Flight Center, Greenbelt, Maryland
- Newman, Paul A.**, NASA Goddard Space Flight Center, Greenbelt, Maryland
- Norton, Taylor**, Antarctic Meteorological Research and Data Center, Space Science and Engineering Center, University of Wisconsin-Madison, Madison, Wisconsin
- Ochwat, Naomi**, Earth Science Observation Center, Cooperative Institute for Research in Environmental Sciences (ESOC/CIRES), University of Colorado Boulder, Boulder, Colorado
- Petropavlovskikh, Irina**, NOAA/OAR Earth System Research Laboratory, Global Monitoring Division, Boulder, Colorado; University of Colorado Boulder, Boulder, Colorado
- Pezzi, Luciano P.**, Laboratory of Ocean and Atmosphere Studies (LOA), Earth Observation and Geoinformatics Division (DIOTG), National Institute for Space Research (INPE), São José dos Campos, Brazil
- Pitts, Michael**, NASA Langley Research Center, Hampton, Virginia
- Raphael, Marilyn N.**, Department of Geography, University of California, Los Angeles, Los Angeles, California
- Reid, Phillip**, Australian Bureau of Meteorology and Australian Antarctic Program Partnership (AAPP), Hobart, Australia
- Santee, Michelle L.**, NASA Jet Propulsion Laboratory, Pasadena, California
- Santini, Marcelo**, Laboratory of Ocean and Atmosphere Studies (LOA), Earth Observation and Geoinformatics Division (DIOTG), National Institute for Space Research (INPE), São José dos Campos, Brazil
- Scambos, Theodore**, Earth Science Observation Center, Cooperative Institute for Research in Environmental Sciences (ESOC/CIRES), University of Colorado Boulder, Boulder, Colorado
- Schultz, Cristina**, Northeastern University, Boston, Massachusetts
- Shi, Jia-Rui**, Woods Hole Oceanographic Institution, Woods Hole, Massachusetts
- Souza, Everaldo**, Federal University of Pará (UFPA), Belém, Brazil
- Stammerjohn, Sharon**, Institute of Arctic and Alpine Research, University of Colorado Boulder, Boulder, Colorado
- Strahan, Susan E.**, University of Maryland, Baltimore County, Baltimore, Maryland; NASA Goddard Space Flight Center, Greenbelt, Maryland
- Thompson, Andrew F.**, California Institute of Technology, Pasadena, California
- Trusel, Luke D.**, Pennsylvania State University, University Park, Pennsylvania
- Wille, Jonathan D.**, Institute for Atmospheric and Climate Science, ETH Zürich, Zürich, Switzerland; Institut des Géosciences de l'Environnement, CNRS/UGA/IRD/G-INP, Saint Martin d'Hères, France
- Yin, Ziqi**, Department of Atmospheric and Oceanic Sciences, University of Colorado Boulder, Boulder, Colorado

Editorial and Production Team

Allen, Jessica, Graphics Support, Cooperative Institute for Satellite Earth System Studies, North Carolina State University, Asheville, North Carolina

Camper, Amy V., Graphics Support, Innovative Consulting and Management Services, LLC, NOAA/NESDIS National Centers for Environmental Information, Asheville, North Carolina

Haley, Bridgette O., Graphics Support, NOAA/NESDIS National Centers for Environmental Information, Asheville, North Carolina

Hammer, Gregory, Content Team Lead, Communications and Outreach, NOAA/NESDIS National Centers for Environmental Information, Asheville, North Carolina

Love-Brotak, S. Elizabeth, Lead Graphics Production, NOAA/NESDIS National Centers for Environmental Information, Asheville, North Carolina

Ohlmann, Laura, Technical Editor, Innovative Consulting and Management Services, LLC, NOAA/NESDIS National Centers for Environmental Information, Asheville, North Carolina

Noguchi, Lukas, Technical Editor, Innovative Consulting and Management Services, LLC, NOAA/NESDIS National Centers for Environmental Information, Asheville, North Carolina

Riddle, Deborah B., Graphics Support, NOAA/NESDIS National Centers for Environmental Information, Asheville, North Carolina

Veasey, Sara W., Visual Communications Team Lead, Communications and Outreach, NOAA/NESDIS National Centers for Environmental Information, Asheville, North Carolina

6. Table of Contents

List of authors and affiliations	S325
a. Overview	S328
b. Atmospheric circulation and surface observations	S329
Sidebar 6.1: The Antarctic heatwave of March 2022.....	S333
c. Ice-sheet surface mass balance	S336
d. Ice-sheet seasonal melt extent and duration	S339
e. Ice-sheet mass balance	S341
f. Sea-ice extent, concentration, and seasonality	S344
Sidebar 6.2: Larsen B fast-ice breakout and initial glacier response.....	S349
g. Southern Ocean	S351
1. Sea-surface and mixed-layer properties.....	S351
2. Upper-ocean heat content.....	S354
3. Air–sea heat fluxes.....	S354
4. Ocean biogeochemistry.....	S355
h. 2022 Antarctic ozone hole	S355
Acknowledgments	S360
Appendix 1: Chapter 6 – Acronyms	S361
References	S362

Please refer to Chapter 8 (Relevant Datasets and Sources) for a list of all climate variables and datasets used in this chapter for analyses, along with their websites for more information and access to the data.

6. ANTARCTICA AND THE SOUTHERN OCEAN

Kyle R. Clem and Marilyn N. Raphael, Eds.

a. Overview

—K. R. Clem and M. N. Raphael

It was an extraordinary year in Antarctica and the surrounding Southern Ocean in 2022, marked by new records in temperature, surface mass balance, ice-sheet mass balance, surface melt, and sea ice. Many of these records can be linked to two strong and persistent atmospheric circulation anomalies: a deep Amundsen Sea Low that occupied the Bellingshausen, Amundsen, and Ross Seas for most of the year and a strong blocking high in the far southwest Pacific north-east of Wilkes Land, East Antarctica. These features directed warm, moist northerly flow to the Antarctic Peninsula/West Antarctica and East Antarctica, respectively, which was accompanied by an anomalously high number of landfalling atmospheric rivers (long and narrow regions of extreme poleward moisture transport), heavy snowfall, and well above-average surface mass balance in these two regions. This resulted in new record highs in net annual Antarctic surface mass balance and ice-sheet mass balance in 2022; this was the first time since 1993, the start of satellite-derived ice-sheet mass balance measurements, in which a positive net mass balance was observed in Antarctica, highlighting the extraordinary contribution of surface processes (i.e., snow accumulation) in 2022.

Offshore, these regions of persistent warm northerly flow, particularly across the Bellingshausen/Weddell Seas and the southeast Indian Ocean, enhanced sea-ice melt during the 2021/22 retreat season, prevented sea-ice growth during the autumn and winter advance phase, and led to early and rapid sea-ice retreat to start the 2022/23 retreat phase from late September onward; over 100 days of record-low sea-ice extent and sea-ice area were observed throughout 2022, including new all-time annual record lows in net sea-ice extent and area on the 25th and 21st of February 2022, respectively. Furthermore, on the eastern Peninsula, the warmth produced anomalously high surface melt across the Larsen Ice Shelf during the 2021/22 summer, punctuated by a record-breaking heatwave and surface melt event on the Peninsula in early February 2022. Combined with the large deficit of protective offshore sea ice in the Weddell Sea, which exposed the fast ice to open ocean swells, this contributed to the disintegration of a large area of decade-old fast ice in the remnant Larsen B embayment, as discussed in Sidebar 6.2. The breakup of fast ice was followed by rapid retreat and even collapse of upstream glaciers to which the fast ice had been attached. In East Antarctica, there was an unprecedented heatwave and coastal surface melt event in March due to a strong atmospheric river, which is detailed in Sidebar 6.1. Across a large portion of the high-elevation East Antarctic plateau, temperatures exceeded the previous March record maxima for several consecutive days, and a new all-time record-high temperature of -9.4°C (44°C above the March average) was set at Dome C II automated weather station on 18 March. Such high temperatures were especially remarkable to occur during March, which is the winter transition period characterized by rapid cooling on the plateau. Despite multiple historic warm events across Antarctica during the year, much of Antarctica closed the year with record to near-record-low temperatures and pressures associated with a strongly positive Southern Annular Mode pattern during November–December.

In the Southern Ocean, there were well-below-average annual-mean sea-surface temperatures (SSTs; 0.5 to 1.0°C below average) and above-average mixed layer depth in the South Pacific sector, which coincided with the enhanced storminess (more and/or deeper cyclones)

across the Amundsen Sea Low region through most of the year. In the South Atlantic, SSTs were well above average through the year, especially from September to December, likely due in part to the expansive open water across the northern Weddell Sea that is normally occupied by reflective sea ice. Finally, the Antarctic ozone hole re-emerged in early September and was the 18th largest (near average) in the 43-year satellite observational record. Following a similar seasonal development seen in 2020 and 2021, the 2022 ozone hole had a slower-than-average growth rate that is consistent with ozone recovery; however,

also like the previous two years, the ozone hole was very long-lived due to weaker-than-average planetary wave activity from September through early November, and it did not break up until 16 December.

More details on Antarctica’s climate and cryosphere, the Southern Ocean, and the ozone hole for 2022 are presented in this chapter. In most cases, where data are available, 2022 anomalies and standard deviations are based on the 1991–2020 climatological average. Otherwise, the climatological period is provided within each section. The geographical locations of place names mentioned throughout the chapter are provided in Fig. 6.1.

b. Atmospheric circulation and surface observations

—K. R. Clem, S. Barreira, S. Colwell, R. L. Fogt, L. M. Keller, M. A. Lazzara, D. E. Mikolajczyk, and T. Norton

Many of the major climate themes over Antarctica and the surrounding Southern Ocean in 2022 were a continuation of those seen during 2021. Most notable was the persistence of a deep Amundsen Sea Low (Clem et al. 2022) over the South Pacific, which produced another warm year on the Antarctic Peninsula; it was the second-warmest year on record for all five of the long-term staffed weather stations located on the Peninsula. Coupled with above-normal pressure over much of the southern middle latitudes and generally weak- to below-average pressure elsewhere over Antarctica, the Southern Annular Mode (SAM; Marshall 2003), the difference in pressure anomalies between the southern middle latitudes and Antarctica, remained in a strongly positive state through most of the year (except June), and 2022 saw the third-highest annual-mean SAM index on record (since 1957). This reflects a remarkably persistent positive SAM pattern over the Southern Hemisphere that dates back to October 2020: 24 of the past 27 months have recorded a positive monthly-mean SAM index. Furthermore, the persistence of La Niña through all of 2022 (see section 4b for details), combined with positive SAM conditions, enhanced the deepening and expansion of the Amundsen Sea Low (Fogt et al. 2011), especially from July onward when La Niña strengthened. This contributed to three of the five Peninsula stations recording their warmest July–December period on record. Lastly, there were two exceptional warming events in 2022 due to strong atmospheric rivers: one in early February on the Antarctic Peninsula (not shown; Gorodetskaya et al. 2023) and one in March on the East Antarctic plateau (see Sidebar 6.1 for details). A detailed overview of other noteworthy climate and circulation anomalies across Antarctica in 2022 is provided below.

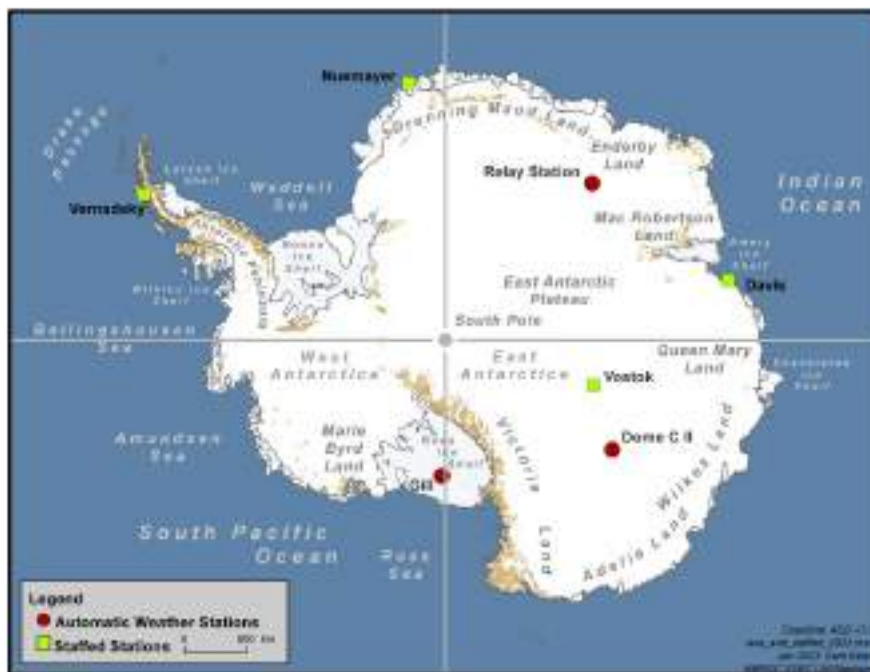


Fig. 6.1. Map of stations and geographic regions discussed in this chapter.

Atmospheric circulation anomalies were examined using the European Centre for Medium-Range Weather Forecasts Reanalysis version 5 (ERA5; Hersbach et al. 2020). Figure 6.2 shows the monthly geopotential height (Fig. 6.2a) and temperature (Fig. 6.2b) anomalies averaged over the polar cap (60°S–90°S) and the monthly circumpolar zonal wind anomalies (Fig. 6.2c) averaged over 50°S–70°S. Surface climate anomalies were grouped into three periods of relatively persistent features: January–March, April–October, and November–December (Fig. 6.3). Monthly temperature and pressure anomalies are also shown for select Antarctic staffed and automated weather stations (AWS; Fig. 6.4; see Fig. 6.1 for station locations).

Pressure/geopotential height over the southern polar cap was near the long-term average for most of 2022 (Fig. 6.2a) before decreasing significantly in November–December. The only noteworthy exceptions were lingering negative geopotential height anomalies in the stratosphere (above 200 hPa) in January, tied to one of the longest-lived ozone holes on record in 2021 (Kramarova et al. 2022), and the redevelopment of negative geopotential height anomalies and the ozone hole in the stratosphere around September 2022 (see section 6h for discussion of the 2022 Antarctic ozone hole). These anomalies propagated downward into the lower troposphere during November and December, likely contributing to the strong negative surface pressure anomalies (–8 to –10 hPa) over the continent in these months. Stratospheric temperature anomalies generally followed the geopotential height anomalies (Fig. 6.2b), with strong negative temperature anomalies in January 2022 that redeveloped in August and thereafter peaked in October and November at around 6°C–8°C (0.5–1 std. dev.) below the 1991–2020 average; there was also a modest stratospheric cooling event from April to June that peaked in May (1.5°C [1.5 std. dev.] below average). In the troposphere, temperatures averaged over the polar cap were generally about 1°C warmer (1–1.5 std. dev.) than average from February onward. The most noteworthy polar cap-wide warming event occurred in June, coinciding with positive surface pressure anomalies observed everywhere across the continent except on the Peninsula (Fig. 6.4) and the only month in which the SAM index was negative during 2022 (Fig. 6.2). There were no months with below-average tropospheric temperatures when averaged over the polar cap; however, there were several significant regional cold events throughout the year (Fig. 6.4).

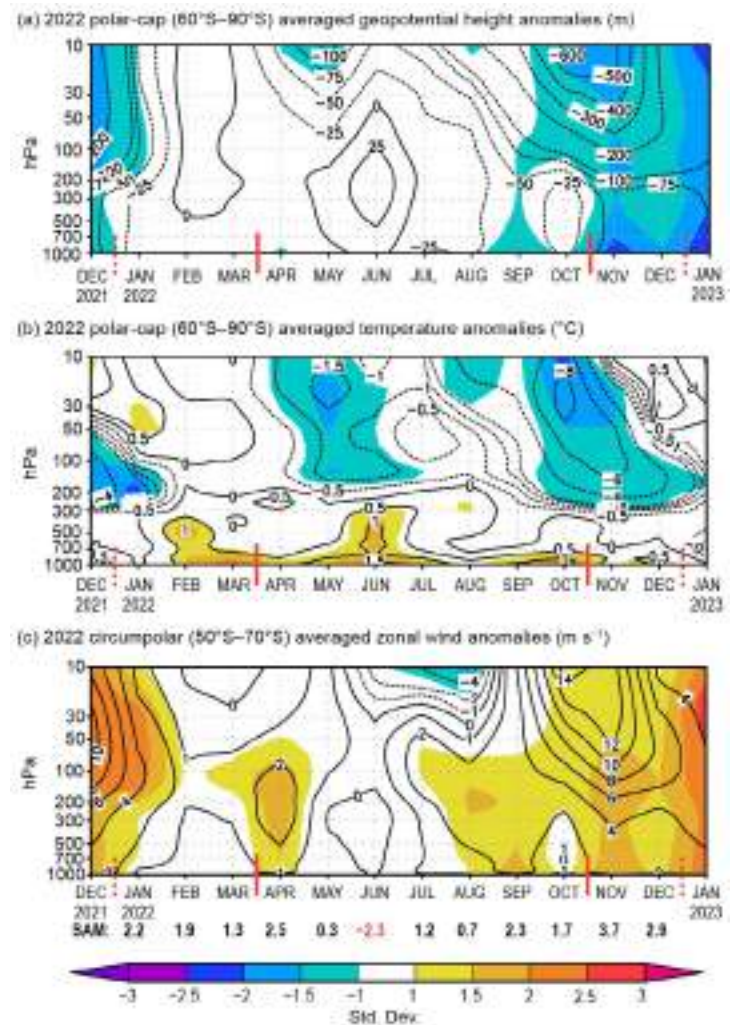


Fig. 6.2. Area-averaged (weighted by cosine of latitude) monthly anomalies over the southern polar region in 2022 relative to 1991–2020: (a) polar cap (60°S–90°S) averaged geopotential height anomalies (m; contour interval is 25 m up to ± 100 m and 100 m after ± 100 m); (b) polar cap averaged temperature anomalies ($^{\circ}\text{C}$; contour interval is 0.5°C up to $\pm 2^{\circ}\text{C}$ and 2°C after $\pm 2^{\circ}\text{C}$); (c) circumpolar (50°S–70°S) averaged zonal wind anomalies (m s^{-1} ; contour interval is 2 m s^{-1} with an additional contour at $\pm 1 \text{ m s}^{-1}$). Shading depicts standard deviation of monthly anomalies as indicated by color bar at bottom. Red vertical bars indicate the three climate periods used for compositing in Fig. 6.3; the dashed lines near Dec 2021 and Dec 2022 indicate circulation anomalies wrapping around the calendar year. Values from the Marshall (2003) Southern Annular Mode (SAM) index are shown below (c) in black (positive values) and red (negative values). (Source: ERA5.)

Consistent with the positive SAM pattern, circumpolar westerly winds were near or above their long-term average strength throughout the troposphere and stratosphere during the year (Fig. 6.2c). A few significant intensifications of the tropospheric westerlies in April, August–September, and November–December coincided with the highest monthly SAM index values of the year. Meanwhile, the strength of the stratospheric westerlies followed the same pattern as the stratospheric pressure and temperature anomalies, including a continued stronger-than-average polar vortex in January and the redevelopment of a stronger-than-average polar vortex in September, with westerly wind speeds 10 m s^{-1} to 15 m s^{-1} (1–1.5 std. dev.) above the long-term mean in November.

The surface pressure and temperature anomalies in Fig. 6.3 illustrate the impressive persistence and extent of the deep Amundsen Sea Low and associated warm conditions across the Peninsula region during the year. From January to March, below-average surface pressures of more than -6 hPa (2 std. dev.) were located in the Amundsen and Ross Seas extending onto adjacent areas of West Antarctica and the Ross Ice Shelf (Fig. 6.3a) along with above-normal temperatures in the Amundsen Sea Embayment and northeast Peninsula (Fig. 6.3b). South of New Zealand and Tasmania, an exceptionally strong positive pressure anomaly of $>6 \text{ hPa}$ (3 std. dev.) was present, coupled with below-average pressure off the coast of East Antarctica near 90°E . These features reflect the circulation pattern that produced the exceptional warming event on the East Antarctic plateau in March (see Sidebar 6.1), where Dome C II AWS (Fig. 6.4e) recorded its second-warmest March on record (5.4°C above the March average), and contributed to positive temperature anomalies of $+1$ to $+2^\circ\text{C}$ (1–2 std. dev.) on the plateau and Ross Ice Shelf. Lastly, a short-lived but strong zonal wave 3 pattern (three positive-negative pressure anomaly pairs over the Southern Ocean; Raphael 2007) occurred in January (not shown), which produced warm northerly flow onto Dronning Maud Land where Relay Station AWS recorded its warmest January on record at -25.8°C (3.1°C above average).

From April onward, the Amundsen Sea Low deepened and gradually grew in size (Fig. 6.3c), albeit with a sudden and short-lived eastward shift from the Ross Sea to the Bellingshausen Sea in June (not shown), illustrated by the rapid reversal of pressure anomalies between Gill AWS on the Ross Ice Shelf (Fig. 6.4f) and Vernadsky on the western Peninsula (Fig. 6.4a). Throughout April–October, seven-month average temperature anomalies of $+1^\circ\text{C}$ to $+3^\circ\text{C}$ (1.5–2.5 std. dev.) encompassed a vast region of the southeast Pacific and South Atlantic, including the Antarctic Peninsula. The evolution and significance of these positive temperature anomalies were captured

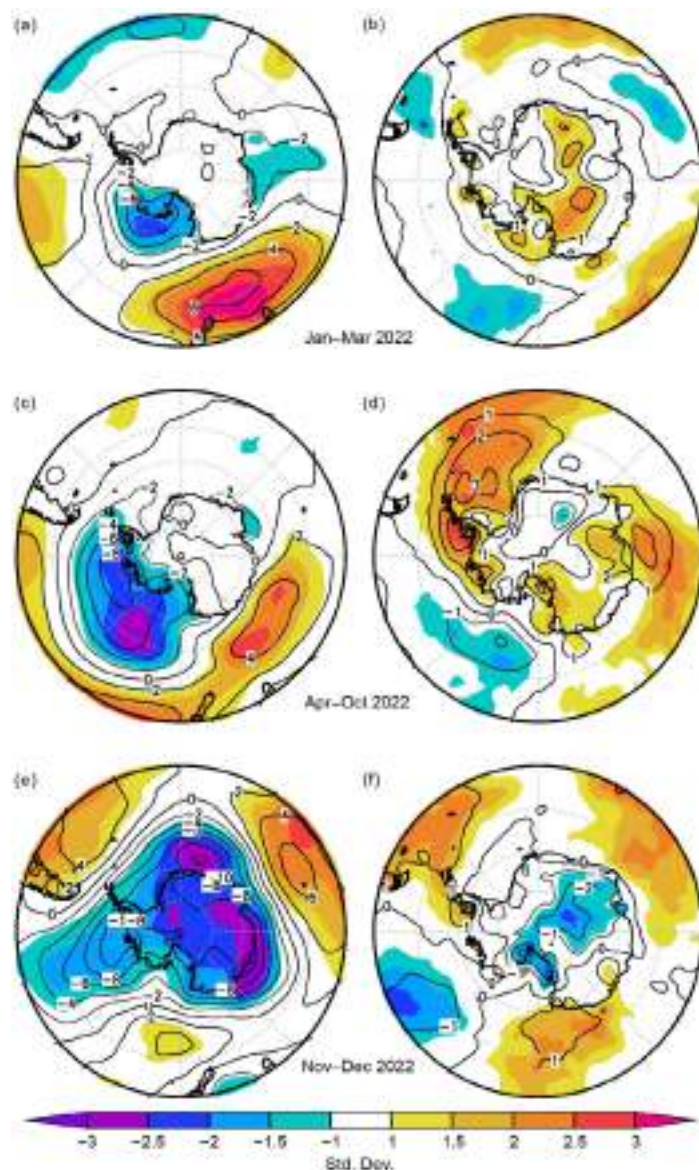


Fig. 6.3. (left) Surface pressure (hPa) and (right) 2-m temperature anomalies ($^\circ\text{C}$) relative to 1991–2020 for (a),(b) Jan–Mar 2022; (c),(d) Apr–Oct 2022; and (e),(f) Nov–Dec 2022. Contour interval is 2 hPa for surface pressure anomalies and 1°C for 2-m temperature anomalies. Shading shows the standard deviation of the anomalies. (Source: ERA5.)

at Vernadsky, including two new record-high monthly temperatures recorded in August (4.8°C above average) and September (4.7°C above average). Other notable temperature records on the Antarctic Peninsula (not shown) include the warmest spring for Vernadsky and Bellingshausen, the warmest August at Rothera, and the warmest November at Bellingshausen.

Elsewhere around Antarctica, surface pressure and temperature anomalies were highly variable from April to October. Dome C II AWS experienced a dramatic flip from its second-warmest March on record to its coldest April on record (4.1°C below average) as cold offshore flow developed in this region on the southwest side of the Amundsen Sea Low. Neumayer (Fig. 6.4b) experienced anomalously warm conditions from April to June followed by an anomalously cold August. Farther east at Davis (Fig. 6.4c), anomalously warm conditions developed from June to October (Fig. 6.3d) with the development of a deep cyclone west of Davis that produced warm northerly flow to this region.

In the final two months of the year, strong negative surface pressure anomalies of -8 hPa to -10 hPa (2–3 std. dev.) developed over much of the continent, and the circumpolar pattern transitioned to a prominent zonal wave 3 structure (Fig. 6.3e). This produced three distinct regions of warm northerly flow in the South Atlantic, Indian, and southwest Pacific Oceans, while below-average temperature anomalies of -1°C to -2°C (0.5–1.5 std. dev.) developed over the interior (Fig. 6.3f). All six stations experienced well-below-average pressure anomalies ranging from -5 hPa to -12 hPa during November and December. Numerous new record-low monthly pressures were recorded: Neumayer, Relay Station AWS, and Dome C II AWS all recorded their lowest November pressure on record, while Davis recorded its lowest pressure on record for both November and December. Some of the coldest temperatures occurred on the Ross Ice Shelf, where Gill AWS recorded its coldest November on record.

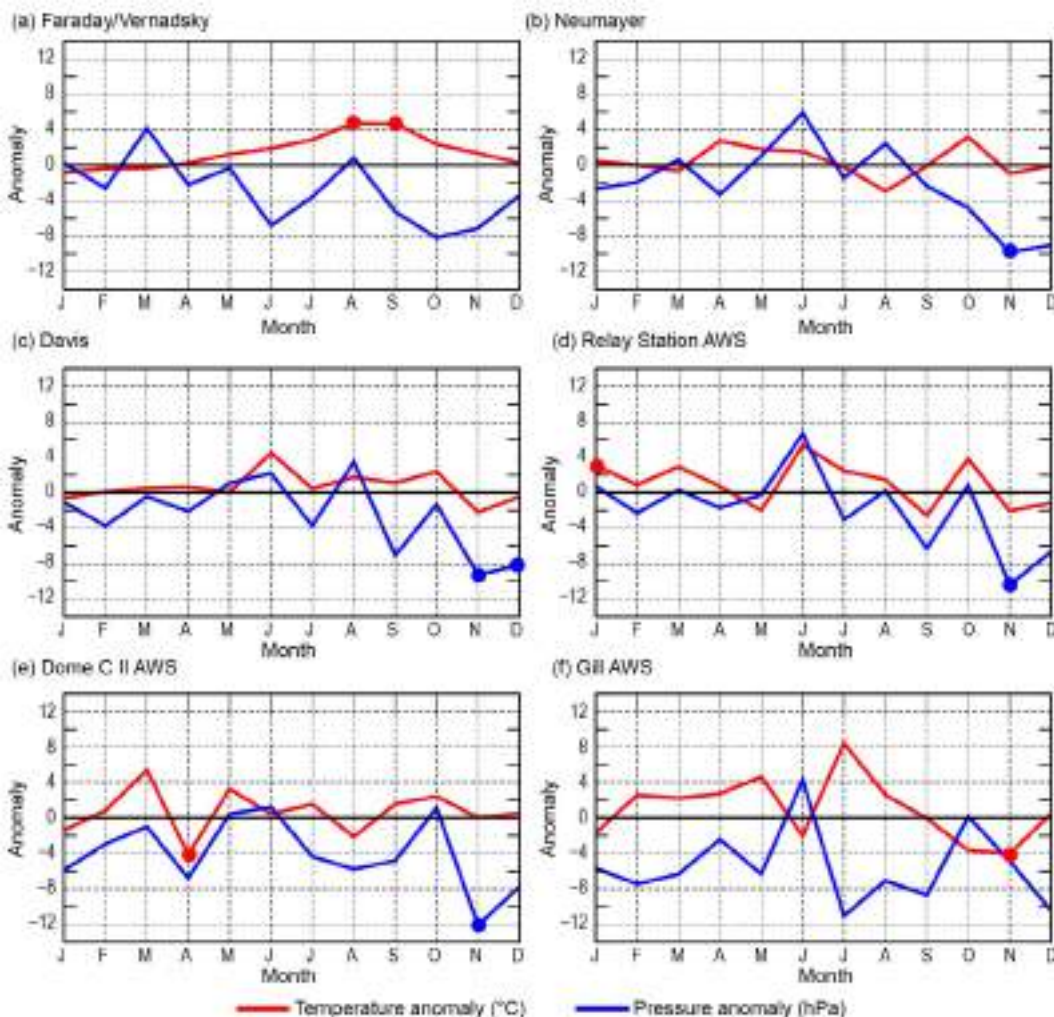


Fig. 6.4. Observed monthly Antarctic climate anomalies during 2022 from six representative stations (three staffed [a]–[c] and three automatic [d]–[f]). Anomalies for temperature (°C) are shown in red and mean sea-level pressure/surface pressure (hPa) are shown in blue, with filled circles denoting monthly-mean records set for each station in 2022. All anomalies are based on the monthly 1991–2020 averages where possible. The station observation records start in 1950 for Vernadsky, 1981 for Neumayer, 1957 for Davis, 1995 for Relay Station automated weather station (AWS), 1980 for Dome C II AWS, and 1985 for Gill AWS. See Fig. 6.1 for station locations.

Sidebar 6.1: The Antarctic heatwave of March 2022

—R. T. DATTA, J. D. WILLE, D. BOZKURT, D. E. MIKOLAJCZYK, K. R. CLEM, Z. YIN, AND M. MACFERRIN

In the middle of March 2022, East Antarctica experienced an unprecedented, large-scale heatwave, despite March historically marking the transition to Antarctic winter. This event was associated with an intense atmospheric river, which reached deep into the Antarctic interior, and was shortly followed by the collapse of the critically-unstable Conger Ice Shelf. While short-lived and unprecedented, these intense phenomena are more probable in future climate scenarios, with impacts including both enhanced precipitation and surface melt (Wille et al. 2023).

Temperatures

Between 14 and 20 March, temperatures over a large region of East Antarctica exceeded 10°C above the March climatological mean (Fig. SB6.1a), both at the coast and inland over the cold interior. The Dome C II automatic weather station (AWS) located high on the plateau at 3250 m a.s.l. (shown in green), captured the evolution of the heatwave at a high temporal resolution. For the first half of March, temperatures were near the Dome C II AWS March climatological mean of -53.4°C and ranged from around -45°C to -60°C (Fig. SB6.1b).

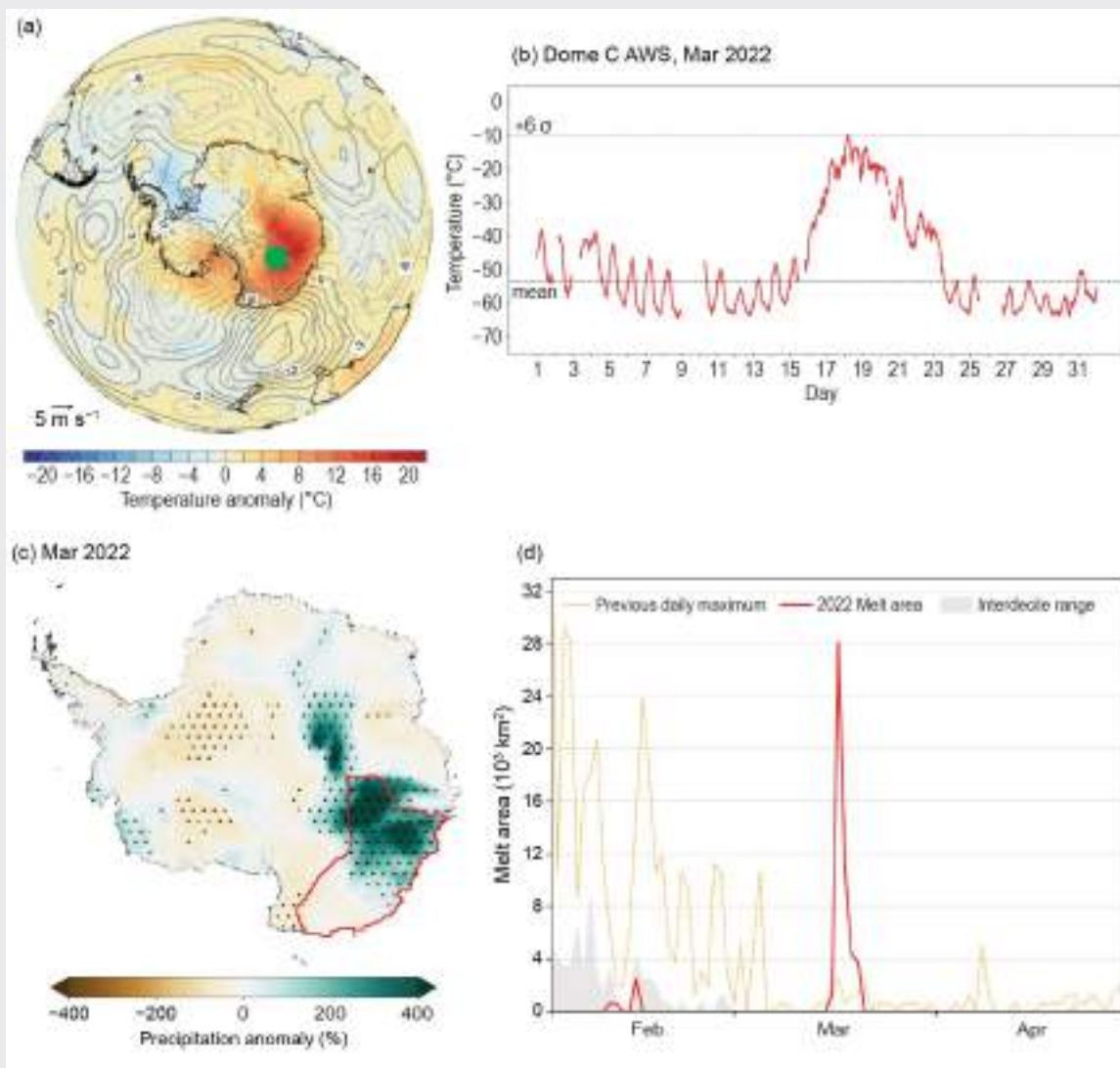


Fig. SB6.1. (a) Mean 2-m temperature anomaly ($^{\circ}\text{C}$) for 14–20 Mar 2022 as compared to the 1991–2020 Mar mean (Source: ERA5) and (b) UW-Madison Dome C II automated weather station (AWS; 75.106°S , 123.347°E) 10-min quality-controlled temperature observations for Mar 2022 ($^{\circ}\text{C}$; red line). The black horizontal dashed line denotes the Dome C II March climatological mean temperature (-53.4°C). The gray dashed line denotes the temperature (-9.6°C) 6 std. dev. above the mean, where 1 std. dev. is $\pm 7.3^{\circ}\text{C}$. (c) ERA5-Total precipitation anomaly (%) for Mar 2022 as compared to the 1991–2020 reference period with Wilkes and Adélie Land region outlined in red. (d) Surface melt area ($\times 10^3 \text{ km}^2$) over the Wilkes and Adélie Land region outlined in (d) as retrieved from passive microwave.

Temperatures followed a general cooling pattern with the onset of winter and exhibited diurnal cycles typical of March at this site. Beginning midday on 15 March, temperatures began a rapid and steady increase that overwhelmed the diurnal cycle signature, as the pressure and wind speeds also increased (not shown). The temperature reached a maximum of -9.4°C on 18 March at 04:40 UTC, establishing a new all-time high temperature record at the Dome C II AWS and breaking the previous all-time high temperature of -10.0°C set in the peak of summer on 2 January 2002. The occurrence of this record during the transition to winter is especially remarkable as the high-elevation interior ice sheet is marked by extreme radiational cooling during this time. Thereafter, temperatures only gradually decreased and did not return to normal until 23 March. For the remainder of the month, temperatures resumed the typical diurnal cycle pattern about the climatological average of around -60°C .

Impacts

The impacts on the surface of the ice sheet included an increase in both rain and snowfall as well as a short period of intense surface melt. Within the larger Wilkes and Adélie region, total precipitation in March from European Centre for Medium-Range Weather Forecasts Reanalysis version 5 (ERA5) exceeded 300% of the 1991–2020 climatological mean for the month of March (Fig. SB6.1c), contributing to 2022 having the highest annual surface mass balance in at least four decades (see section 6c). Throughout East Antarctica, large increases

in firn air content from snowfall gains were observed. Surface melt was limited to the coasts, geographically centered on the Holmes, Totten, and Moscow ice shelves. On 17 March, the region experienced a record-high maximum melt area of $28,100\text{ km}^2$ (Fig. SB6.1d), more than doubling the previous record March melt area of $10,600\text{ km}^2$ from 2002. It was the most extensive melt event recorded of any late-summer date beyond 4 February in the Wilkes and Adélie region of Antarctica since the beginning of the observational record in 1979. Additionally, the lack of sea ice and large swells associated with storms impacted the Conger ice shelf at the margins of this region (Wille et al. a,b submitted), which had been increasing in fragility in recent years and finally collapsed following this event (Baumhoer et al. 2021).

Large-scale drivers

The intruding burst of heat and moisture over East Antarctica was facilitated by the development of multiple moist tropical air masses over the Atlantic and Indian Oceans over several days that eventually merged and were directed toward the continent by a mid-level blocking ridge within a quasi-stationary zonal wave 3 pattern over the Southern Ocean (Fig. SB6.2). The evolution of this moisture can be seen in snapshots of integrated vapor transport from 10 March (Fig. SB6.2a in the Atlantic), strengthening over the Indian Ocean (Figs. SB6.2b,c) and finally reaching the continent on 16 March (Fig. SB6.2d). The intensified quasi-stationary mid-level ridge extending from New Zealand and southeast Australia toward

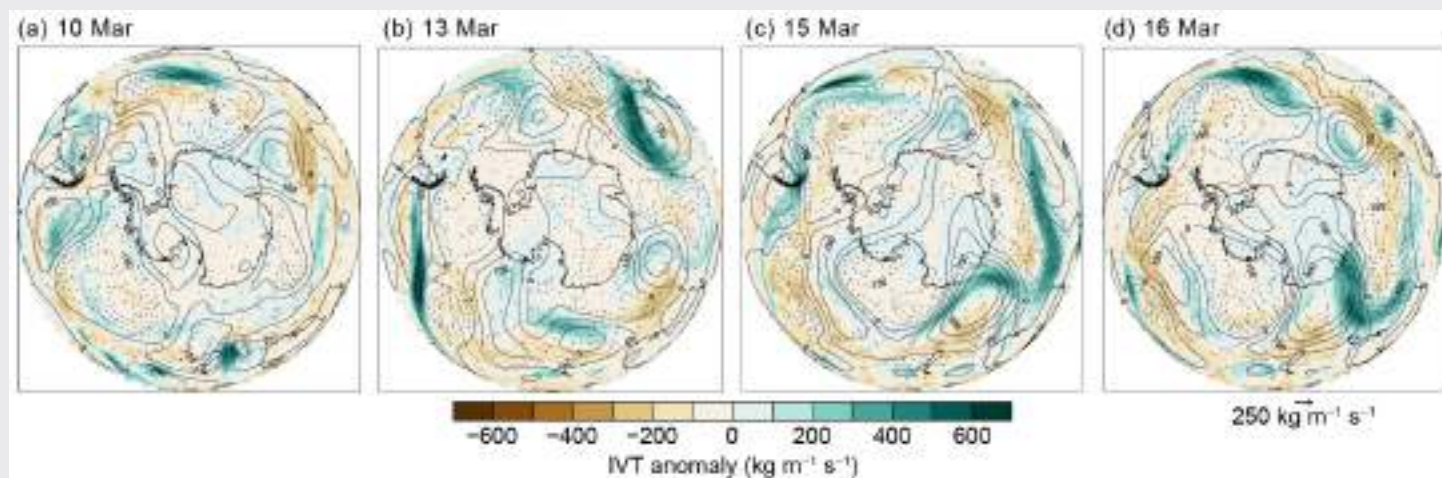


Fig. SB6.2. Snapshots of integrated water vapor transport (IVT) anomaly ($\text{kg m}^{-1} \text{s}^{-1}$) compared to the 1991–2020 reference period. Shown for (a) 10 Mar, (b) 13 Mar, (c) 15 Mar, and (d) 16 Mar. Vectors correspond to IVT vector deviations (zonal and meridional components) from the reference period. Also shown are 500-hPa geopotential height deviations (solid and dashed contours for positive and negative anomalies, respectively, every 75 m) from the 1991–2020 climatology. (Source: ERA5.)

East Antarctica and a mid-level trough on the western flank of the ridge during 15–16 March (Figs. SB6.2c,d) appeared crucial for the strong poleward meridional moisture transport within an intense atmospheric river (Fig. SB6.2d).

Atmospheric rivers are rare events that represent the transport of subtropical/midlatitude heat and moisture toward the polar regions. According to the polar-specific atmospheric river detection algorithm from Wille et al. (2021), a prolonged and intense atmospheric river was detected over East Antarctica during 14–18 March (Fig. SB6.3). The low-level moisture associated with the atmospheric river was transported by a warm conveyor belt into the upper troposphere leading to strong

upper-level latent heat release from cloud formation. This ultimately led to strong diabatic modification of potential vorticity which further reinforced and entrenched the downstream atmospheric ridge creating blocking conditions (Wernli and Davies 1997).

The net impact of this intense atmospheric river primarily increased surface mass balance with enhanced snowfall. However, in future climate scenarios, higher temperatures may enhance the relative mass loss during atmospheric river events, as surface melt contributes to both runoff (reducing surface mass balance directly) and to the increased fragility of buttressing ice shelves.

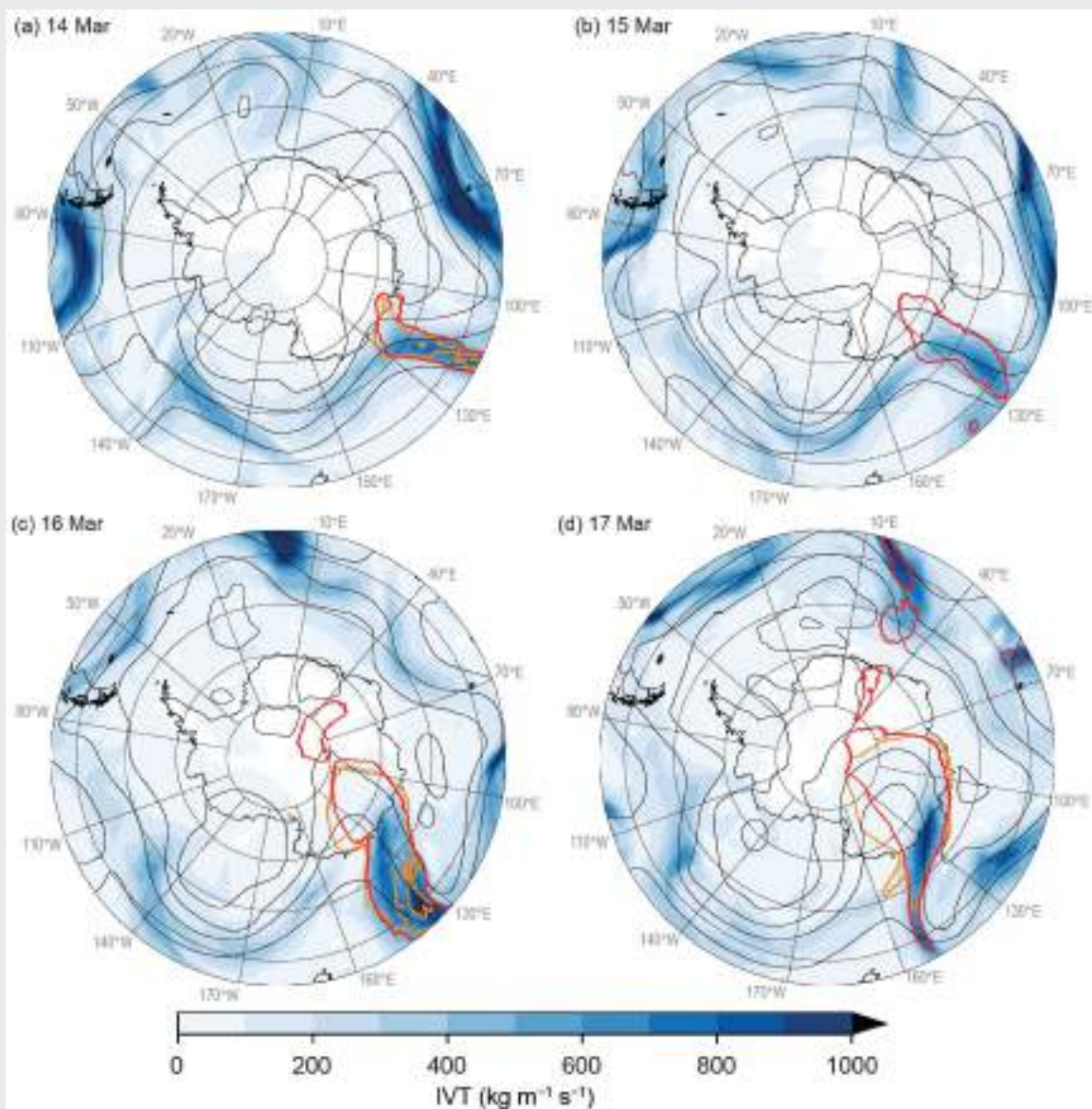


Fig. SB6.3. Atmospheric river shape. Integrated vapor transport (IVT; $\text{kg m}^{-1} \text{s}^{-1}$) in blue shading with the atmospheric river outline as detected by the meridional IVT (red outline) and integrated water vapor (IWV, orange outline) schemes in the detection algorithm described in Wille et al. (2021) along with 500-hPa geopotential height (contours). Shown for (a) 14 Mar, (b) 15 Mar, (c) 16 Mar, and (d) 17 Mar at 1200 UTC. (Source: MERRA2.)

c. Ice-sheet surface mass balance

—R. T. Datta, R. Baiman, Z. Yin, J. D. Wille, D. Dunmire, M. L. Maclennan, L. D. Trusel, and D. Bozkurt

Surface mass balance (SMB) represents the net effect of all processes that add or remove mass from the surface of an ice sheet. For the grounded Antarctic Ice Sheet (AIS), snowfall is the dominant SMB term, with approximately 2300 Gt accumulating each year (Agosta et al. 2019; Lenaerts and van den Broeke 2012; Mottram et al. 2021). Strong coast-to-plateau gradients in SMB exist across the AIS (Fig. 6.5b), with mass gains in coastal areas exceeding 500 mm water equivalent (w.e.) yr^{-1} compared to $<50 \text{ mm w.e. yr}^{-1}$ in the high-elevation interior of the East Antarctic Ice Sheet. At ice sheet wide and regional scales, as much as 40%–60% of annual snowfall results from “extreme precipitation events”, defined as delivering snowfall in the top 10% of the long-term daily mean snowfall, often in the form of atmospheric rivers (ARs; Turner et al. 2019; Maclennan and Lenaerts 2021; Wille et al. 2021). These mass gains are countered by losses from sublimation, the leading negative SMB term for the AIS (Mottram et al. 2021). While surface melt and hydrology are extensive across AIS ice shelves (Bell et al. 2018; Bevan et al. 2020; Banwell et al. 2021; Arthur et al. 2022), and observations of lake drainages suggest some meltwater runoff exists (Dunmire et al. 2020; Trusel et al. 2022), nearly all AIS surface melt is thought to refreeze within the firn layer (the layer of partially compacted snow from previous years located beneath the new surface snow accumulation), making it a negligible term in the

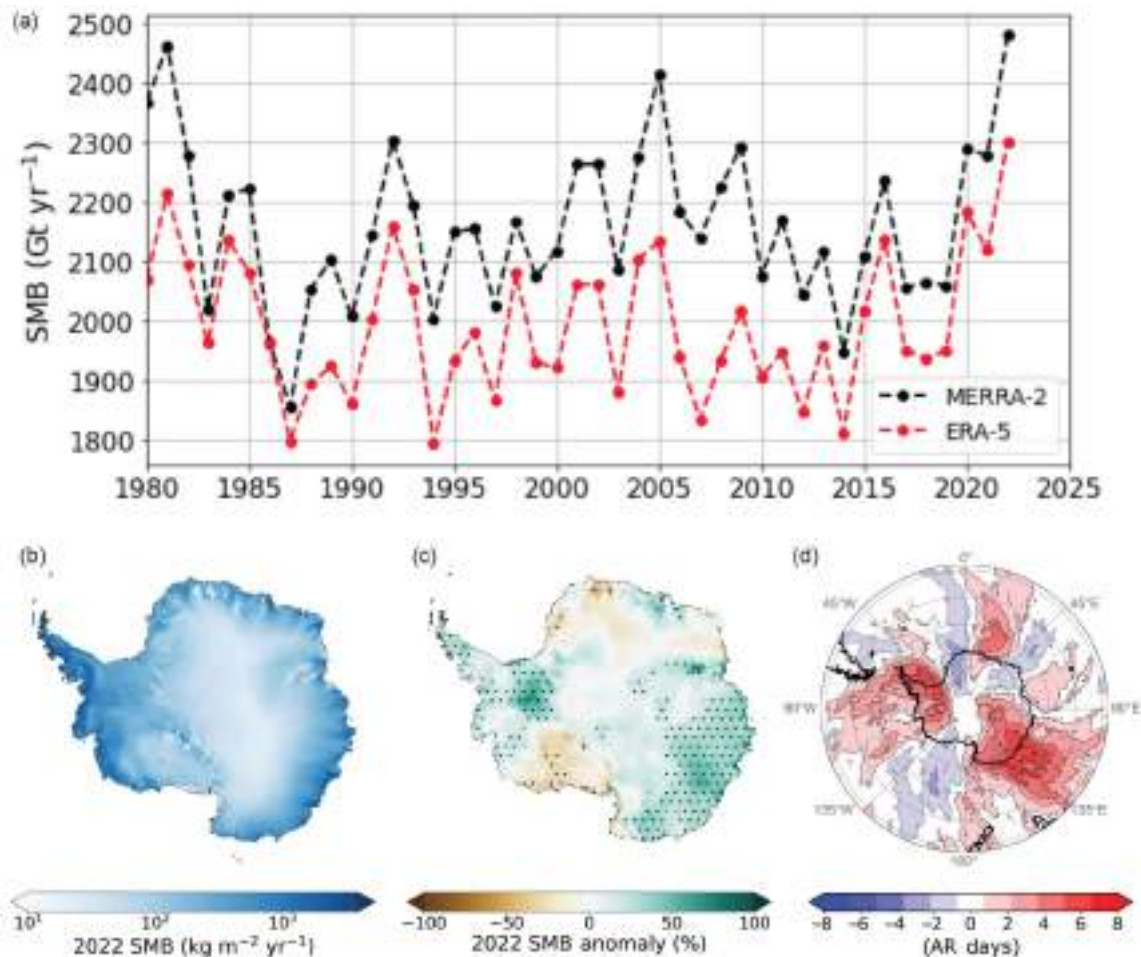


Fig. 6.5. (a) Time series of annual surface mass balance (SMB) in Gt (10^{12} kg) yr^{-1} . (b) MERRA-2 2022 SMB ($\text{kg m}^{-2} \text{yr}^{-1}$). (c) MERRA-2 2022 SMB anomaly relative to the 1991–2020 mean (%). The 2022 SMB anomaly is higher than the 1991–2020 standard deviation in the stippled areas. (d) 2022 atmospheric river occurrence anomaly (days) relative to the 1991–2020 mean from MERRA-2.

contemporary AIS SMB (van Wessem et al. 2018). It should be noted that despite its relatively small role in the total mass balance of the AIS, surface melt is an important indicator of processes and anomalies in the coastal regions with important consequences such as ice-shelf destabilization (discussed in section 6d). In future warming scenarios, surface melt is expected to intensify and play a more direct role in the AIS mass balance and ice shelf stability (Trusel et al. 2015; Kittel et al. 2021; Gilbert and Kittel 2021), while enhanced snowfall and SMB gains over the grounded ice sheet are also projected (Seroussi et al. 2020; Dunmire et al. 2022).

Global reanalysis products are useful tools to quantify AIS SMB in near-real time. Given negligible surface meltwater runoff in Antarctica today, AIS SMB can be reliably approximated as total precipitation minus surface evaporation and sublimation (i.e., $P-E$; e.g., Medley and Thomas 2019; Lenaerts et al. 2019; Mottram et al. 2021). Here, we use two reanalyses, Modern-Era Retrospective Analysis for Research and Applications version 2 (MERRA-2; at $0.5^\circ \times 0.625^\circ$ horizontal resolution, Gelaro et al. 2017) and European Centre for Medium-Range Weather Forecasts Reanalysis version 5 (ERA5; at 0.25° horizontal resolution, Hersbach et al. 2020), to analyze the 2022 AIS SMB, its spatial and seasonal characteristics, and compare it to the 1991–2020 climatological period. Though important biases remain associated with, for example, ice sheet–cloud–radiation feedbacks and precipitation, evaluations of various reanalysis products over Antarctica indicate that MERRA-2 and ERA5 represent recent Antarctic climate and SMB well (Gossart et al. 2019; Medley and Thomas 2019; Wang et al. 2016).

In 2022, SMB (driven by snowfall) was the highest on record (since 1980), at 2480 Gt (MERRA-2) or 2302 Gt (ERA5), over the grounded ice sheet, as compared to the climatological mean of 2155 ± 128 Gt yr^{-1} (MERRA-2) and 1977 ± 105 Gt yr^{-1} (ERA5; Figs. 6.5a,b). Though the AIS SMB from ERA5 is significantly ($p < 0.05$) drier than from MERRA-2 during the climatological period, both reanalyses have comparable interannual variations during the climatological period, and neither suggest a significant long-term trend in SMB (Fig. 6.5a). The 2022 AIS SMB was 2.5 std. dev. higher than the MERRA-2 climatological mean and 3.1 std. dev. higher than the ERA5 climatological mean. We note that the SMB estimates still need to be further validated to consider model uncertainties. Since both reanalysis datasets produce similar spatial results, we use MERRA-2 hereafter to focus on spatial characteristics of the 2022 SMB.

The historic high 2022 SMB is reflected spatially in Fig. 6.5c, indicating positive anomalies over much of West Antarctica with relative maxima around the northern Antarctic Peninsula and Palmer Land and Ellsworth Land in West Antarctica ($>150\%$ above the climatological mean), and over a broad swath (75°E – 165°E) of East Antarctica including Victoria Land and Wilkes Land ($>80\%$ above the climatological mean). These regions of high SMB in 2022 coincide with regions of below-average sea ice in the surrounding ocean (section 6f) and anomalously high ice-sheet mass balance (section 6e). They also coincide with the deep and persistent Amundsen Sea Low (ASL) that was present for nearly all of 2022 and a strong blocking high pressure south of New Zealand and Tasmania from January through October (section 6b). The ASL produced warm northerly flow across the Peninsula and West Antarctic (section 6f), while the blocking high in the far southwest Pacific/southeast Indian Oceans, reflecting the pattern seen during the East Antarctic heatwave in March (see Sidebar 6.1), delivered warm northerly flow to large portions of East Antarctica for much of the year. Despite the magnitude of the 2022 SMB, portions of Dronning Maud Land and the Ross Sea region feature anomalously low SMB ($<50\%$ of the climatological mean). Regions with high SMB are coincident with regions experiencing anomalously high numbers of ARs (Fig. 6.5d), favored by the aforementioned blocking high/low pressure anomaly couplets shown in Fig. 6.3, triggering poleward heat and moisture transport.

The climatological AIS SMB varies considerably throughout the year (Fig. 6.6a), with a minimum in summer (124 Gt–172 Gt month⁻¹) and a maximum in austral fall and winter (195 Gt–220 Gt month⁻¹). In 2022, the SMB diverged substantially from the climatological mean in both MERRA-2 and ERA5 reanalyses in January (2.9 std. dev. above the mean in MERRA-2), March (2.5 std. dev.), July (2.9 std. dev.), September (1.6 std. dev.), and November (1.4 std. dev.; Fig. 6.6a). The positive SMB anomaly in January is attributed to high snowfall over Dronning Maud Land in East Antarctica and the Amundsen Sea sector in West Antarctica. In March, the positive SMB

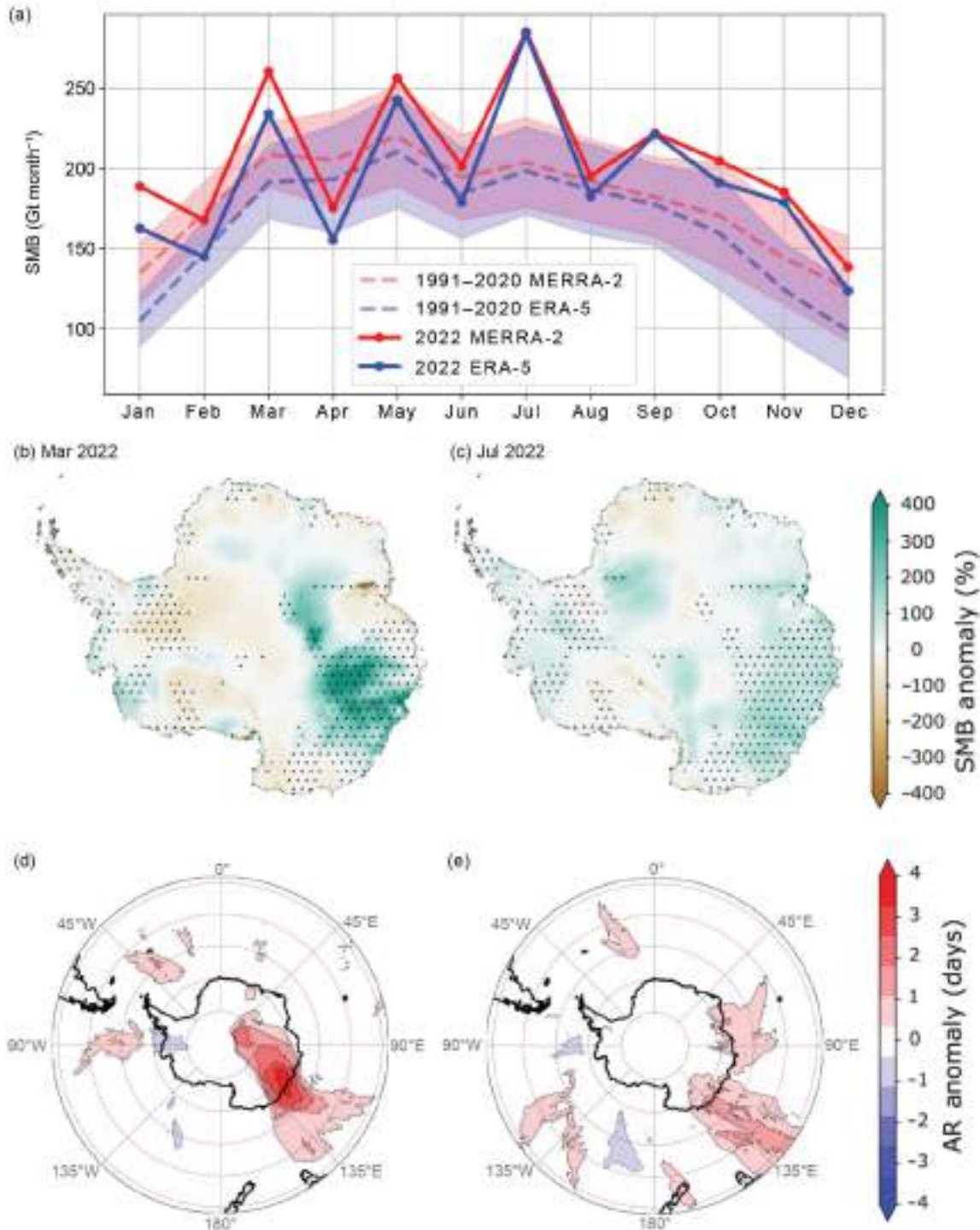


Fig. 6.6. (a) Seasonal cycle of (grounded) Antarctic Ice Sheet integrated surface mass balance (SMB) in Gt (10^{12} kg) month⁻¹, according to MERRA-2 (red) and ERA5 (blue), with 2022 value shown in solid line, 1991–2020 mean shown in a dashed line with shading showing 1 std. dev. MERRA-2 SMB anomaly for the month relative to the month’s 1991–2020 mean for (b) Mar 2022 and (c) Jul 2022, with stippled areas indicating regions where the SMB anomaly is higher than the 1991–2020 1 std. dev. MERRA-2 anomaly (days) when an atmospheric river (AR) was detected for the month compared to the 1991–2020 mean for (d) Mar 2022 and (e) Jul 2022.

anomaly (up to 400%) was primarily driven by a powerful AR that made landfall in East Antarctica from 15 to 19 March, which is discussed in Sidebar 6.1. July saw near ice sheet-wide anomalously high SMB (contributing 12% of the total SMB in 2022), with the strongest anomalies across Wilkes Land driven by ARs as well as poleward heat and moisture advection enhanced by the atmospheric blocking south of Tasmania (Figs. 6.6c,e). This blocking is accompanied by positive SMB anomalies across Marie Byrd Land, the Antarctic Peninsula, and Ellsworth Land. Deep cyclones over the Ross Sea in September (Fig. 6.3c) and over the Antarctic Peninsula and most of East Antarctica in November (Fig. 6.3e) led to anomalously high SMB over the AIS in these months as well.

d. Ice-sheet seasonal melt extent and duration

—M. MacFerrin, T. Mote, A. Banwell, and T. Scambos

Surface melt on the Antarctic Ice Sheet (AIS) occurs primarily on the coastal margins, especially on the Antarctic Peninsula and on the ice shelves surrounding the continent. Surface melt runoff plays a relatively small role in the total mass balance of the AIS compared to far larger contributions from snow accumulation, iceberg calving, and basal melting of ice shelves and the ice sheet. However, surface melting can be seen as a vital measure of ice-sheet health as it has a large effect on increasing the density of underlying firn in areas of significant melting. If melt volume is a large fraction of the annual accumulation, surface melt can contribute to ice-shelf break up and upstream grounded glacier acceleration through hydrofracture (Scambos et al. 2014; Banwell et al. 2013). Since the austral melt season spans two calendar years, we focus here on melt season spanning October 2021 through April 2022. The 2022/23 Antarctic melt season will be discussed in next year's report.

Daily surface melt is mapped using satellite-derived passive-microwave brightness temperatures. The source data are distributed as daily composited polar stereographic brightness temperatures by the National Snow and Ice Data Center (Meier et al. 2019; Gloersen 2006) spanning 1979 through present day. Daily passive microwave brightness temperatures using the 37-GHz horizontal polarization as well as the 37- and 19-GHz 363 vertical polarization channels are acquired by the Scanning Multi-channel Microwave Radiometer (SMMR), Special Sensor Microwave Imager (SSM/I), and Special Sensor Microwave Imager/Sounder (SSMIS) sensors. The austral melt season is defined here as 1 October through 30 April. Although small, brief melt events can be measured along Antarctica's northern coastal margins during the austral winter, the vast majority of melt happens during these seven months, with the most typically in December and January. An ice-extent mask of 25-km grid cells for the AIS was developed from the Quantarctica v3.0 Detailed Basemap dataset (Norwegian Polar Institute 2018). The AIS is divided into seven melt extent and climate regions by clustering glaciological drainage basins (based on Shepherd et al. 2012; Fig. 6.8a). The methods used here were first developed to track Greenland's ice-sheet surface melting on a daily basis (Mote and Anderson 1995; Mote 2007, 2014), modified slightly to accommodate Antarctic surface conditions, as outlined in previous reports (MacFerrin et al. 2021, 2022).

According to the passive-microwave satellite observations, the 2021/22 melt season recorded slightly higher-than-average cumulative melt index (days \times area) of 7.92 million km² days (Figs. 6.7a,c), about 5.1% greater than the median melt index of 7.54 million km² days during the 1990/91–2019/20 baseline period. However, this near-typical melt season averaged across the continent was punctuated by substantial spatial and temporal anomalies in individual regions. The Antarctic Peninsula (Fig. 6.8b) saw an annual melt index more than 31% above the baseline median value. Peninsula melt was affected by four consecutive extensive melt events in December and early January. Melting extended to an area of decade-old landfast ice in the embayment of the former Larsen B Ice Shelf, pre-conditioning it for a breakup that began on 18 January 2022

(see Sidebar 6.2). Late in the season on the Peninsula, a season-high melt event on 8 February covered a maximum area of 240,000 km² and broke the observational historical record for melt extent for the month of February, previously set at 233,000 km² on 1 February 1988. A majority of the area of the southern Larsen C and Larsen B-remnant ice shelves observed 30 more melt days than average (Fig. 6.7b). Indeed, Antarctica’s cumulative melt index is dominated by melting in the Peninsula, and greater-than-average melting in the 2022 season was driven by events where low pressure in the southern Bellingshausen Sea combined with high pressure in the Scotia Sea or Falklands delivered warm high-moisture air over the Peninsula, inducing foehn events along the northeastern Peninsula. The pattern was responsible for the 8 February spike in melt (Gorodetskaya et al. 2023) and the earlier December events as well. Considering the rest of the Peninsula, including the George VI and Wilkins ice shelves on the western Peninsula, melt days were on average also 10 to 20 days higher than the reference period (Figs. 6.7a,b). However, melt days on the George VI and Wilkins ice shelves were still less than the exceptional melt season of 2019/20 (Banwell et al. 2021).

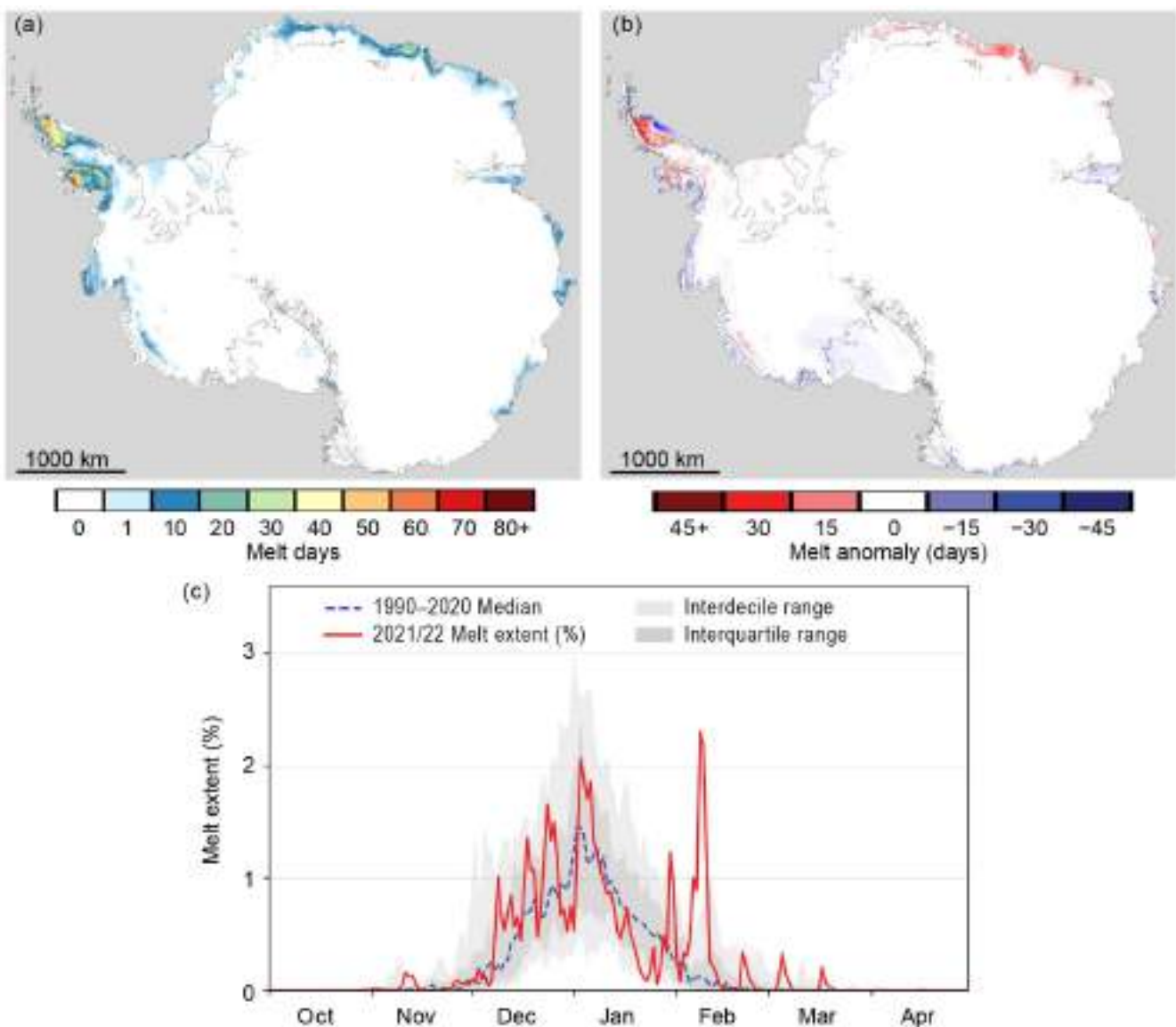


Fig. 6.7. Surface melt across the Antarctic Ice Sheet as detected from passive-microwave satellites. (a) Map of the sum of melt days from 1 Oct 2021–30 Apr 2022. (b) Map of the sum of melt days relative to the 1990–2020 baseline average. (c) Daily melt extent (%; solid red line) compared to median values (dashed blue line), interquartile ranges (dark gray), and inter-decile ranges (light gray) from the 1990–2020 reference period.

The Maud and Enderby regions of Antarctica also displayed a higher-than-average melt season in terms of days, with relatively extensive melt in late December and an extensive melt event in early January that briefly covered nearly 10% of the region’s area (Fig. 6.8c). Melt on the Wilkes and Adélie coast of Antarctica typically occurs only on a limited amount of its total land area because of the relatively small area of coastal ice shelves there. Most of the 2021/22 melt season was muted in the Wilkes and Adélie region

(Fig. 6.8d), registering nearly no melt with the exception of two extensive melt events in mid-December and mid-March, each of which briefly broke daily melt-extent records in the satellite observational history. The mid-March event was associated with an atmospheric river that caused record-breaking high-temperature anomalies high onto the East Antarctic plateau (see Sidebar 6.1). This event, with a peak extent of 28,100 km² on 17 March 2022, broke the observational record during the month of March in Wilkes and Adélie land by 164% (17,100 km²), and is thus far the most significant late-season melt event recorded in this region later than 4 February in any recorded melt year of the satellite observational record. Most of the remainder of the Antarctic continent saw near-to-below-average melt compared to the reference period, with the Ross Embayment registering nearly no melt for the second consecutive year.

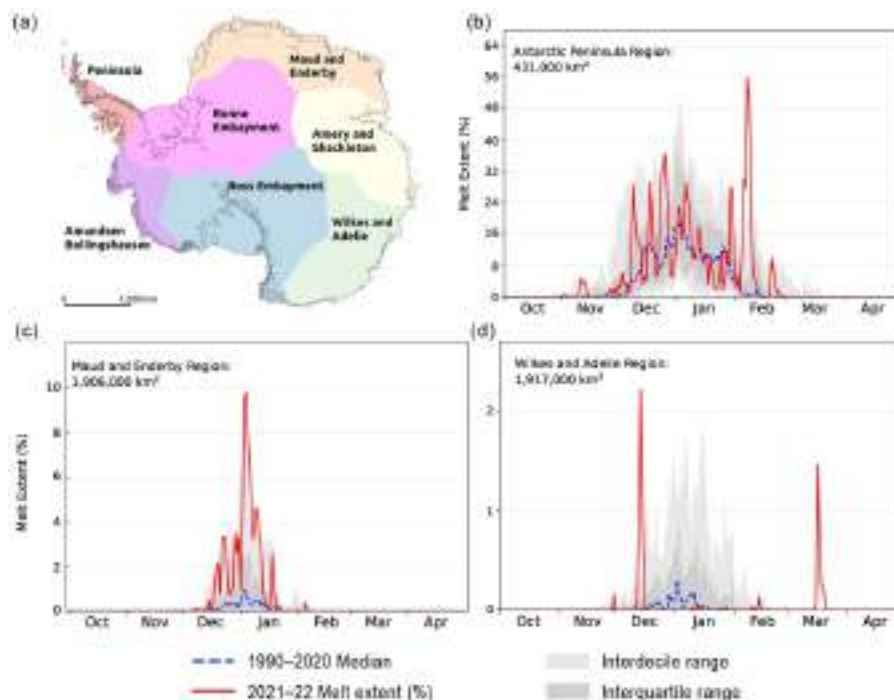


Fig. 6.8. (a) Map of major regions of Antarctica used in regional analyses. (b)–(d) Regional daily melt extents (%) from (b) the Antarctic Peninsula, (c) Maud and Enderby, and (d) Wilkes and Adélie regions.

e. Ice-sheet mass balance

—S. Adusumilli, H. A. Fricker, and A. S. Gardner

The Antarctic Ice Sheet gains mass from accumulation (snowfall minus sublimation) at the surface and primarily loses mass at the margins through its floating extensions, most of which are called ice shelves. Mass loss can occur due to the calving of icebergs at ice shelf fronts, which occurs episodically on multi-annual to multi-decadal time scales, or through continuous ocean-driven basal melting (Rignot et al. 2013; Depoorter et al. 2013; Adusumilli et al. 2020). For any given time period, the net mass balance between competing mass gains and losses depends on the cumulative effects of interactions between the ice, ocean, and atmosphere (e.g., Smith et al. 2020a). Over the past two decades, the ice sheet has experienced net mass loss of grounded ice (e.g., The IMBIE Team 2018), which is in part due to net mass loss of its floating ice shelves (e.g., Paolo et al. 2015) and a corresponding reduction in their “buttressing” effect that otherwise slows the flow of grounded ice into the ocean (e.g., Gudmundsson et al. 2019). Mass loss over the ice sheet has sometimes occurred rapidly in the past (e.g., during the collapse of Larsen B Ice Shelf; Scambos et al. 2004), stressing the need for continuous monitoring through satellite observations.

At the time of writing, there were no published estimates of total Antarctic mass or height change for 2022; however, recent studies (e.g., Smith et al. 2020a) have shown changes in height and mass over the previous decade. The conversion of height changes to mass changes requires a firn density model (e.g., Ligtenberg et al. 2011), which is not yet available for this period. We derived estimates of height changes over the grounded ice sheet from NASA’s Ice, Cloud and land Elevation Satellite-2 (ICESat-2) laser altimeter using data for 2022 until the latest available date (12 October 2022). We used the Advanced Topographic Laser Altimeter System (ATLAS)/ICESat-2 ATL06 L3A Land Ice Height data product version 5 (Smith et al. 2020b), which provides precise estimates of height along repeated ground tracks at 20-m along-track resolution. We derived along-track height changes between Cycle 13 (October–December 2021) and Cycle 16/17 (August–October 2022; Fig. 6.9a). To analyze seasonal variability, we also derived height changes over three-month intervals between successive ICESat-2 data acquisition cycles during the October 2021 to October 2022 period (Fig. 6.10). We smoothed the final height change map using a Gaussian filter with a 25-km diameter. We only consider changes in mass over the grounded portion of the ice sheet for the remainder of this study.

For further context, we provide an annual mass change estimate derived from NASA’s satellite gravimeter Gravity Recovery and Climate Experiment Follow-on (GRACE-FO; Fig. 6.9b) for 2022. We used data from the Jet Propulsion Laboratory Gravity Recovery and Climate Experiment (GRACE) and GRACE-FO Ocean, Ice, and Hydrology Equivalent Water Height Coastal Resolution Improvement (CRI) Filtered Release 06 Version 03 “mascon data” (Wiese et al. 2023a). Mascons (or mass concentration blocks) are $3^\circ \times 3^\circ$ spherical caps placed on an elliptical approximation of Earth’s surface over which these data are provided (Wiese et al. 2023a). We calculated the gravity-derived mass change for November 2021 to November 2022, approximately the same period as used for ICESat-2. To determine ice sheet mass change, we identified all mascons containing more than 10,000 km² of land, according to the provided Coastline Resolution Improvement (CRI) land mask. We interpolated the area-averaged rates of change using bilinear interpolation according to the location of the geometric center of the land area contained within the mascon. We then masked all non-land areas using the Bedmachine ice mask (Morlighem et al. 2020). We also show a time series of mass changes integrated over the ice sheet (Fig. 6.10a) from the Level 4 Antarctica Mass Anomaly Time Series data product (Wiese et al. 2023b).

The maps of annual changes in ice-sheet height from ICESat-2 (Fig. 6.9a) and mass from GRACE-FO (Fig. 6.9b) show ongoing losses of ice in the Amundsen Sea sector of West Antarctica,

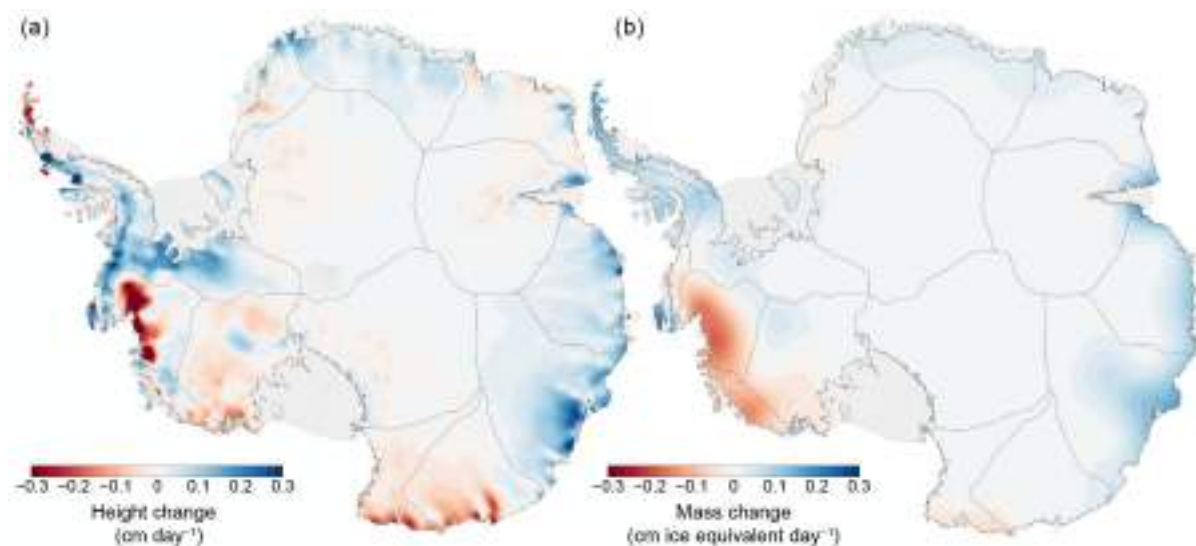


Fig. 6.9. Maps of (a) height change (cm day⁻¹) from ICESat-2 for the Oct 2021–Oct 2022 period and (b) ice equivalent mass change (cm ice equivalent day⁻¹) from GRACE-FO for the Nov 2021–Nov 2022 period.

the same region where losses have been observed over the previous two decades (e.g., Smith et al. 2020a; Clem and Raphael 2022). However, time series of mass changes (Fig. 6.10a) suggest a net mass gain of 290 Gt over the grounded portion of the ice sheet between January 2022 and November 2022, which was unprecedented in the past two decades and substantially different from the average annual mass loss of 120 Gt yr⁻¹ between December 2003 and December 2021.

The 2022 surface mass balance anomaly over grounded ice was estimated with reanalysis data to be +325 Gt (see section 6c), which is in line with the GRACE estimate of +290 Gt of mass gain during 2022, combined with the annual average mass loss 120 Gt yr⁻¹. Many of the spatial patterns of increases in height across Antarctica correspond well with patterns of record-high positive surface mass balance anomalies reported in 2022 (see section 6c). For example, large increases in height over Wilkes Land, East Antarctica, during February–May (Fig. 6.10c) coincided with increased frequency of landfalling atmospheric rivers during this period (Fig. 6.6d). This further suggests a major contribution of surface processes in driving seasonal and interannual height and mass changes. Although these increases led to a high positive mass balance signal in 2022, given the exceptional nature of the surface mass gains in 2022 that is unlikely to occur every year, we expect the Antarctic Ice Sheet to revert to its previous state of mass loss in coming years.

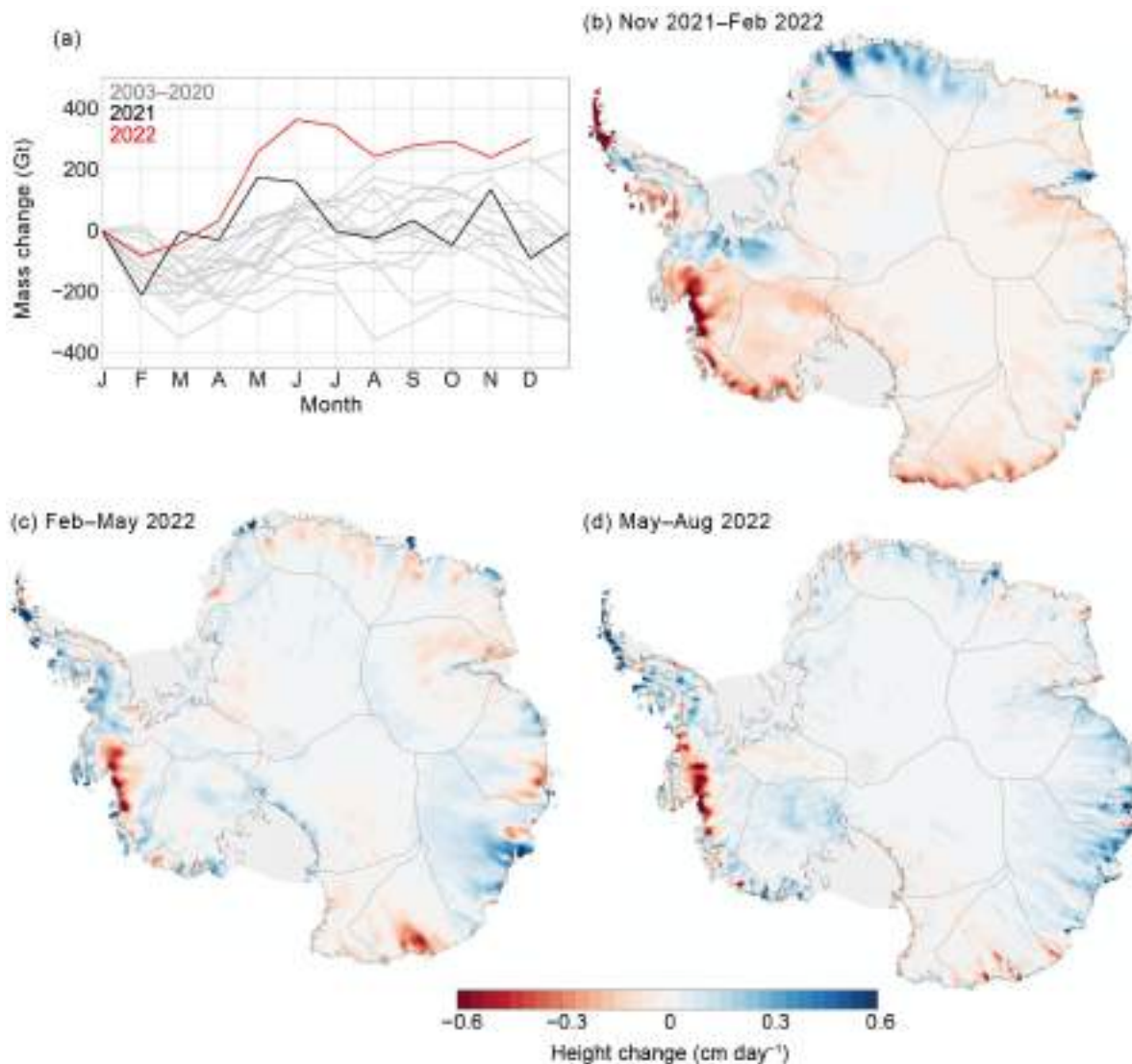


Fig. 6.10. (a) Time series of monthly mass changes from GRACE and GRACE-FO, with 2021 and 2022 highlighted in black and red, respectively. (b)–(d) Maps of height change (cm day⁻¹) from ICESat-2 shown at three-month intervals between Nov 2021 and Aug 2022. Dates represent the central month of each three-month ICESat-2 data acquisition cycle.

f. Sea-ice extent, concentration, and seasonality

—P. Reid, S. Stammerjohn, R. A. Massom, S. Barreira, T. Scambos, and J. L. Lieser

Net sea-ice extent (SIE) and sea-ice area (SIA) were well below or at record-low levels for all of 2022 (based on satellite passive-microwave ice concentration data since 1979 when the near-homogenous satellite record began; Cavalieri et al. 1996). Indeed, there were more than 80 record low daily values of SIE and SIA (Fig. 6.11a, with most occurring during the late 2021/22 retreat and early 2022/23 advance phase (January–March), the wintertime phase (June–September), and the mid 2022/23 retreat phase (December). A new record-low SIE annual

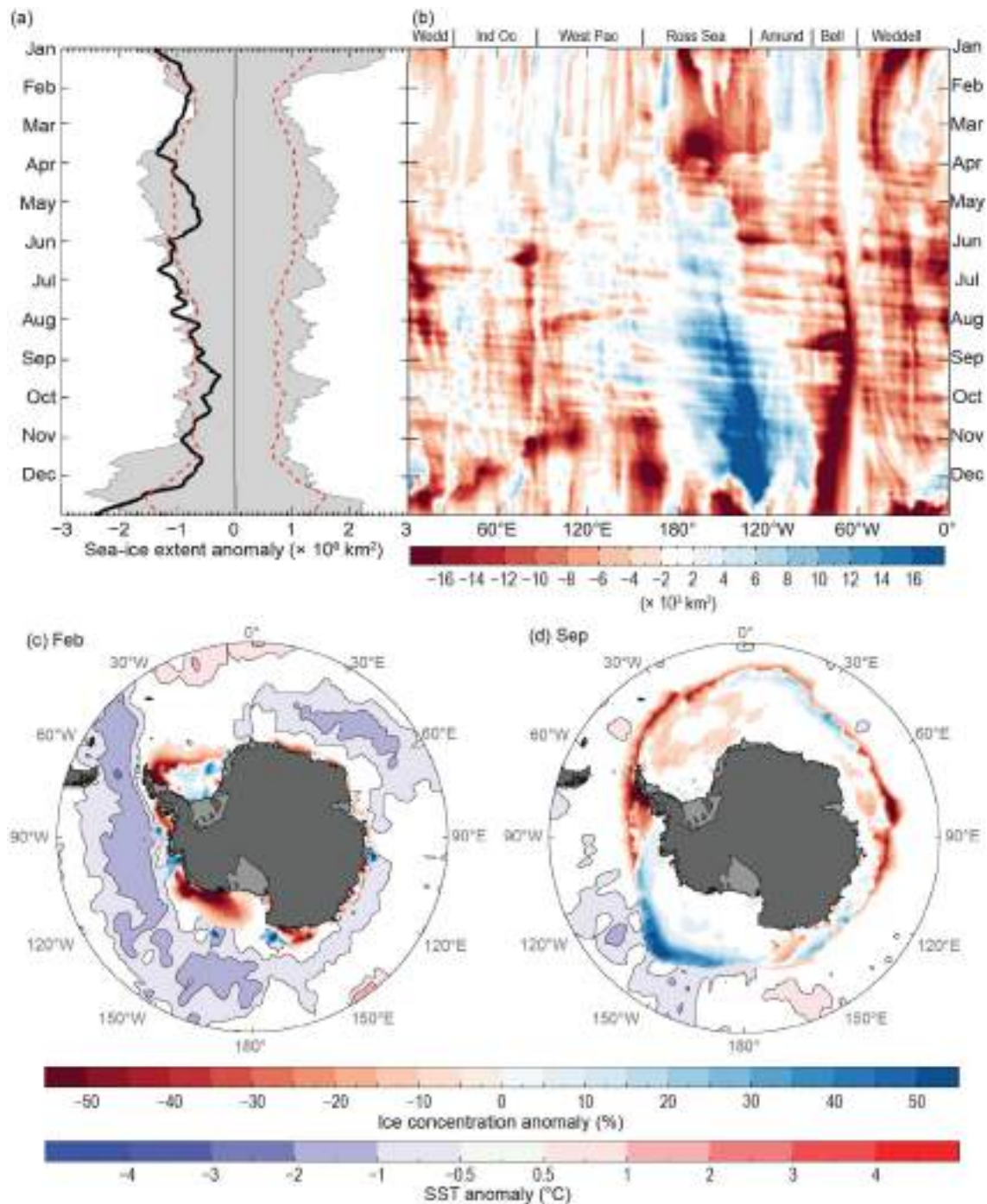


Fig. 6.11. (a) Time series of net daily sea-ice extent (SIE) anomaly for 2022 (solid black line; based on a 1991–2020 climatology). Gray shading represents historical (1979–2020) daily SIE anomaly, red dashed line represents ± 2 std. dev., and (b) Hovmöller (time-longitude) representation of daily SIE anomaly ($\times 10^3 \text{ km}^2$ per degree of longitude) for 2022. Maps of Sea-ice concentration anomaly (%) and sea-surface temperature (SST) anomaly ($^{\circ}\text{C}$; Reynolds et al. 2002; Smith et al. 2008) for (c) Feb 2022 and (d) Sep 2022. Sea-ice concentration is based on satellite passive-microwave ice concentration data (Cavalieri et al. 1996, updated yearly, for climatology; Maslanik and Stroeve 1999, for the 2022 sea-ice concentration). See Fig. 6.1 for relevant place names.

daily minimum of $\sim 1.96 \times 10^6$ km² was recorded on 25 February (Turner et al. 2022; Wang et al. 2022; NSIDC 2022), breaking the previous record of $\sim 2.08 \times 10^6$ km² on 1 March 2017 (Turner and Comiso 2017; Reid et al. 2018) using the same sea-ice concentration dataset. The annual daily minimum of SIA ($\sim 1.25 \times 10^6$ km² on 20 February) was also a record low value, while the 2022 annual daily maximum SIE of $\sim 18.28 \times 10^6$ km² (recorded on 13 September) was the fifth lowest on record. Three months (February, June, and July) observed record-low monthly-mean values of SIE, while there were five months of record-low monthly values of SIA throughout the year. The record-low monthly SIEs continue a recent trend since January 2016, whereby over 85% (72 out of 84) of monthly net SIE values have been below the long-term (1991–2020) average. This reduction in SIE has been most prominent in the late retreat phases (January and February) where net SIE has been below average or at record-low values for every year (2016–22). Fraser et al. (2023) observed record-low values of coastal fast ice area in 2022, along with record-high values of coastal exposure (which refers to the length of coastline without offshore sea ice cover; Reid and Massom 2022). Regionally and after May, the Ross Sea, then Amundsen Sea, experienced generally much greater-than-average SIE, while most other sectors recorded average or lower-than-average SIE throughout the year (Figs. 6.11b,d). Regional and temporal variations are discussed more fully below and closely reflect the three atmospheric phases shown in Figs. 6.2 and 6.3 (see section 6b).

Regional patterns of sea-ice coverage in January–March 2022 largely continued those observed in the latter part of 2021 (Reid et al. 2022), with strong negative SIE anomalies being 1–2 std. dev. below average in the Ross, Bellingshausen, and Weddell Seas (Fig. 6.11b). The negative net SIE anomaly (Fig. 6.11a) at this time was dominated by sea-ice loss in the Ross Sea which saw SIE anomalies of >2 std. dev. below average from late January onward (Fig. 6.11b). This major loss event was driven by wind anomalies associated with an intense and persistent Amundsen Sea Low (ASL; see section 6b, Fig. 6.3a) that had strengthened during September–December 2021 (Fig. 6.3g in Clem et al. 2022), resulting in strong northward ice advection from the Ross Sea into the Amundsen Sea. In the Ross Sea, this contributed to a rapid 2021/22 seasonal retreat (Fig. 6.12b in Reid et al. 2022) followed by persistently low summer sea-ice coverage (Figs. 6.11b,c) with extensive melting of sea ice in the lower latitudes of the northern Ross Sea. The onshore winds associated with the ASL influenced, possibly through melt and/or compaction, the low sea-ice coverage across eastern Bellingshausen and western Weddell Seas during the spring of 2021 and summer of 2022 (Figs. 6.11b,c). During this time, however, greater-than-average sea-ice extent occurred across several less-extensive regions (Figs. 6.11b,c): in the Amundsen and western Bellingshausen Seas (from $\sim 80^\circ$ W to 120° W) and off Oates Bank ($\sim 170^\circ$ E– 180° E), Bunger Hills ($\sim 100^\circ$ E– 110° E), and the Amery Ice Shelf ($\sim 70^\circ$ E– 80° E). Most of these positive ice anomalies were associated with below-normal sea-surface temperatures to the north of the ice edge (Fig. 6.11c).

In March, initial autumn sea-ice advance was particularly late around most of the continent except for a few coastal areas with small pockets of persistent summer sea ice (centered on 20° W, 90° E, 170° E, 105° W, 80° W; Fig. 6.12a). Seasonal advance was particularly slow in the Ross, western Amundsen, and Bellingshausen Seas where persistent and strong cyclonic activity occurred from January to March (see Fig. 6.3a) and in most of the Weddell Sea with relatively warm northerly flow on the eastern side of the ASL. In addition, as elsewhere, the reduced/delayed sea-ice formation was coincident with the presence of slightly above-average surface water temperatures (see section 6g) possibly as a result of a combination of enhanced solar heating and upwelling.

The unprecedented East Antarctic “heatwave” event on 17–18 March (see Sidebar 6.1) did not initially impact on the large-scale sea-ice pattern off Wilkes Land (the heatwave epicenter). Rather, on 21 March a distinct SIE anomaly was observed farther to the west, off the Amery Ice Shelf, possibly as the abnormal heat became entrained in a subsequent low-pressure system, reducing SIE in that region (Fig. 6.11b) and delaying sea-ice advance (Fig. 6.12a).

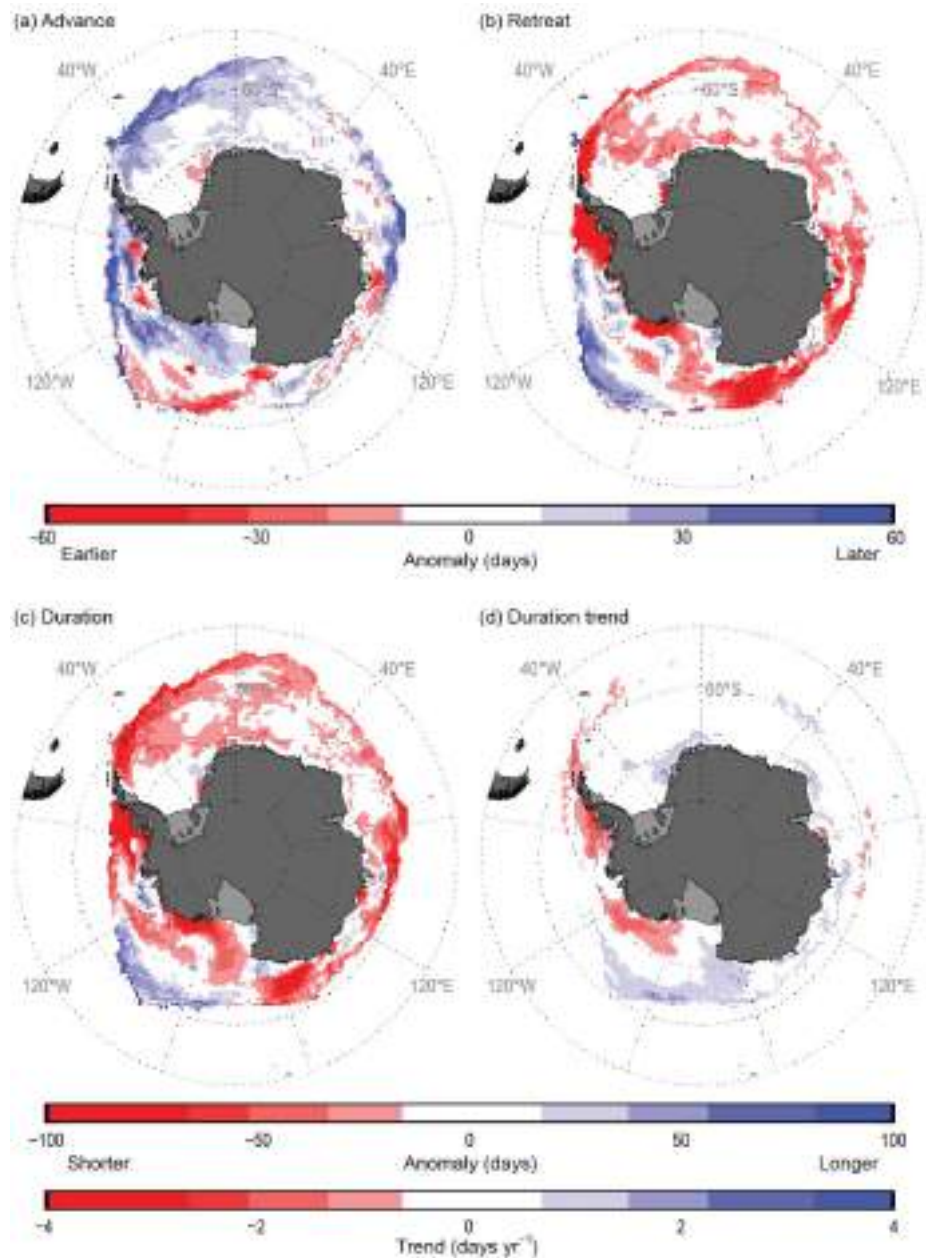


Fig. 6.12. Maps of seasonal sea-ice anomaly (days) in 2022 during (a) autumn ice-edge advance, (b) spring ice-edge retreat, and (c) winter ice season duration; together with (d) winter ice season duration trend (days yr⁻¹; Stammerjohn et al. 2008). The seasonal anomalies (a)–(c) are computed against the 1991/92 to 2020/21 climatology; the trend (d) is computed over 1979/80–2022/23. The climatology (for computing the anomalies) is based on data from Comiso (2017; updated yearly), while the 2022/23 ice-edge retreat duration-year data are from the NASA Team NRTSI dataset (Maslanik and Stroeve 1999); the trend is based on the merged dataset containing 1979–2021 data from Comiso (2017) and 2022/23 data from the NASA Team NRTSI dataset (Maslanik & Stroeve, 1999).

During April–October, the ASL both persisted and deepened (see Fig. 6.3c; especially in April–May and August–September, not shown), with relatively benign atmospheric conditions around the rest of the continent. Hence, annual sea-ice advance continued to be later than usual around most of the continent (Fig. 6.11b), the exception being around ~100°E–110°E (Bunger Hills) where the sea ice had not fully retreated in the previous year and subsequently advanced earlier than usual (shown in blue, Fig. 6.11b and in red, Fig. 6.12a). This region then had greater-than-average SIE through the end of May. Of some prominence is a pattern from May onward of an ice advance recovery in the outer Ross Sea (Fig. 6.11b), with a substantially higher-than-average SIE from mid-May onward that intensified at the beginning of August

(through early December). This was again consistent with the unusual persistence of a strong ASL (see Figs. 6.3c,e), which drew colder air seaward off the continent to enhance both northward sea-ice advection and freezing conditions over the Ross Sea. During this time, SIE within the Ross Sea was generally 1–2 std. dev., but as much as 2–4 std. dev., above average.

Elsewhere and from April through October, SIE was considerably lower than normal, with two regions being exceptionally low. The first is the Amery region (~60°E–100°E), an area across which transient cyclones are preferentially steered and then stalled by a strong blocking high to the east during this period (see Fig. 6.3c). One particularly deep cyclone on about 9 June caused a relatively rapid sea-ice retreat within the Amery region (leading to a SIE of >4 std. dev. below average for a few days), and localized SIE remained substantially lower than average through the end of 2022 (Fig. 6.11b). The second region that saw below-average SIE from April through October was the Bellingshausen-western Weddell Seas sector (~80°W–10°E). There, the persistence and eastward migration of the intense ASL maintained warm northerly winds, which substantially delayed or minimized ice advance and/or formation, leading to below-average SIE. For the region ~80°W–40°W, sea ice retreated early (Fig. 6.11b), exposing much of the far southwestern Peninsula and Eights Coast to open-ocean (sea ice-free) conditions. Hence during September when net SIE reached its annual maximum, only the Ross and Amundsen Seas had positive SIE anomalies (Figs. 6.11b,d). The September sea-ice concentration anomalies (Fig. 6.11d) further reflect the synoptic-scale effects of the repeat passage of transient cyclones across the Amundsen Sea (facilitating ice-edge expansion through divergence) and their subsequent stalling and weakening in the Bellingshausen Sea, causing warmer conditions and ice-edge compaction.

During November–December, the ASL remained stronger than average, combined with an overall intensification and southward contraction of the circumpolar low-pressure trough that was especially deep across much of East Antarctica (see Fig. 6.3e)—a pattern reflecting a strong positive Southern Annular Mode (SAM). Resultant increased cyclonic activity around maritime East Antarctica led to a rapid seasonal (late spring-early summer) sea-ice retreat and strongly negative SIE anomalies in this sector (of up to 2–4 std. dev. below average in some regions) i.e., the Amery region (~70°E–90°E) in early November and Adélie Land (~140°E–170°E) during most of December (Fig. 6.11b). In November, sea ice continued to retreat rapidly in many sectors, notably east of 80°E and particularly from 130°E to 170°E, as well as in the southeastern Ross Sea from 120°W to 180°W (Fig. 6.12b). In stark contrast, and as was the case in the early austral summer of 2021, strong northward sea-ice advection to warmer low latitudes maintained substantially higher-than-average SIE in the eastern Ross Sea to western Bellingshausen Sea (90°W–160°W) that persisted well into mid- to late-December (early summer), after which an abrupt switch to rapid recession/melting occurred (Fig. 6.11b). These rapid sea-ice retreat anomalies (Fig. 6.12b), coupled with the preceding slow sea-ice advance anomalies (Fig. 6.12a), resulted in anomalously short sea-ice seasons (duration) for most Antarctic sectors, with the exception of 120°W–170°W (Fig. 6.12c). The substantially short ice-season duration in the eastern Bellingshausen Sea (60°W–80°W) and western Amundsen/eastern Ross Seas (120°W–160°W) reinforce the strong negative ice-season duration trends observed over 1979/80–2022/23 (Fig. 6.12d). Similarly, the longer ice-season duration anomalies in the outer western Amundsen/eastern Ross Seas sector reinforce the positive ice-season duration trends observed there. Elsewhere, the 2022 ice-season anomalies stand in contrast to the 1979/80–2022/23 ice-season trend pattern.

Placing 2022 into longer-term context, the continuation in 2022 (and 2023 as of this writing, which will be discussed in next year's report) of a major negative net SIE trend that began in September 2016—and that abruptly followed on from successive record-high Antarctic SIE maxima in 2013 and 2014 (Reid and Massom 2015)—raises an important issue as to whether a major shift has occurred in Antarctica's tightly coupled sea ice–ocean–atmosphere–ice sheet system. Turner et al. (2017) attributed the sudden initial transition from near-record-high SIE to consistently below-average extents to a period of weak circumpolar winds and several strong cyclones that ushered in both warm air and warmer surface waters. However, the circumpolar

westerlies were stronger than average for most of 2021 and 2022 when new record-low SIE values have occurred (see section 6b). The persistently low net SIE since 2017 has since been attributed to a combination of long-term ocean and springtime atmospheric warming (Eayrs et al. 2021). Zhang et al. (2022) show that since 2016 the subsurface of the Southern Ocean has had a more dominant influence in driving the negative Antarctic SIE anomaly in comparison to atmospheric forcing. Similarly, Hobbs et al. (2023, manuscript submitted to *J. Climate*) show that recent summertime sea-ice variability has been largely influenced by the notable lack of ice coverage in the Amundsen and Bellingshausen Seas, such that net summer SIE in recent years has been determined by sea-ice variability in the Weddell Sea and hence has a weaker relationship to major large-scale climate modes such as the SAM. To some degree, apart from the very high SIE in the outer Ross and eastern Amundsen Seas due to a persistently deep ASL, the pan-Antarctic SIE (Figs. 6.11b–d) and ice season (Figs. 6.12a–c) anomalies observed in 2022 were unusually widespread and circumpolar as highlighted in Liu et al. (2023) and Hobbs et al. (2023, manuscript submitted to *J. Climate*).

There are major potential implications for a persistently low sea-ice cover. These include changes in continental snow accumulation (Wang et al. 2020), including: the potential that the low sea-ice cover in 2022 may have contributed to the record-high surface mass balance and ice-sheet mass balance in 2022; increased coastal air temperature; exposure of fast ice and ice-shelf fronts to longer periods of open water and wave action (see Sidebar 6.2; Massom et al. 2018; Teder et al. 2022); changes in deep water and bottom water formation (and hence ocean circulation and temperature); and the potential for greater bioactivity due to increased open-water fraction during warmer months.

Sidebar 6.2: Larsen B fast-ice breakout and initial glacier response

—N. OCHWAT, A. BANWELL, AND T. SCAMBOS

Since the disintegrations of the Larsen A and Larsen B ice shelves in 1995 and 2002, respectively, landfast sea ice (stationary and consolidated sea ice that is attached to the coastline, hereafter 'fast ice') has formed in the areas previously occupied by these ice shelves. For the Larsen A, this fast ice has broken out nearly every summer since the ice shelf's collapse. For several years following the collapse of the Larsen B, fast ice in the embayment was also generally absent by February. However, in late March 2011, fast ice formed in the Larsen B embayment and remained continuously for the next 11 years. The tributary glaciers along the Larsen B coast advanced several kilometers into this fast ice during the 11-year

occupation, forming extensive glacial ice tongues that compressed and rifted the adjacent fast ice. On 20 January 2022, the fast ice abruptly fractured throughout its extent, following small calving events during 17–19 January (Figs. SB6.4a–c). By 8 February, the embayment was almost completely clear of broken sea-ice floes. Concurrent with the break-out of the ice, the Larsen B glaciers in the embayment began a rapid retreat as the ice tongues calved rapidly into large tabular blocks and smaller calved ice debris, as shown in a series of aerial photos of the ice front areas and the *mélange* acquired by the British Antarctic Survey on 31 January 2022 (Fig. SB6.4d).

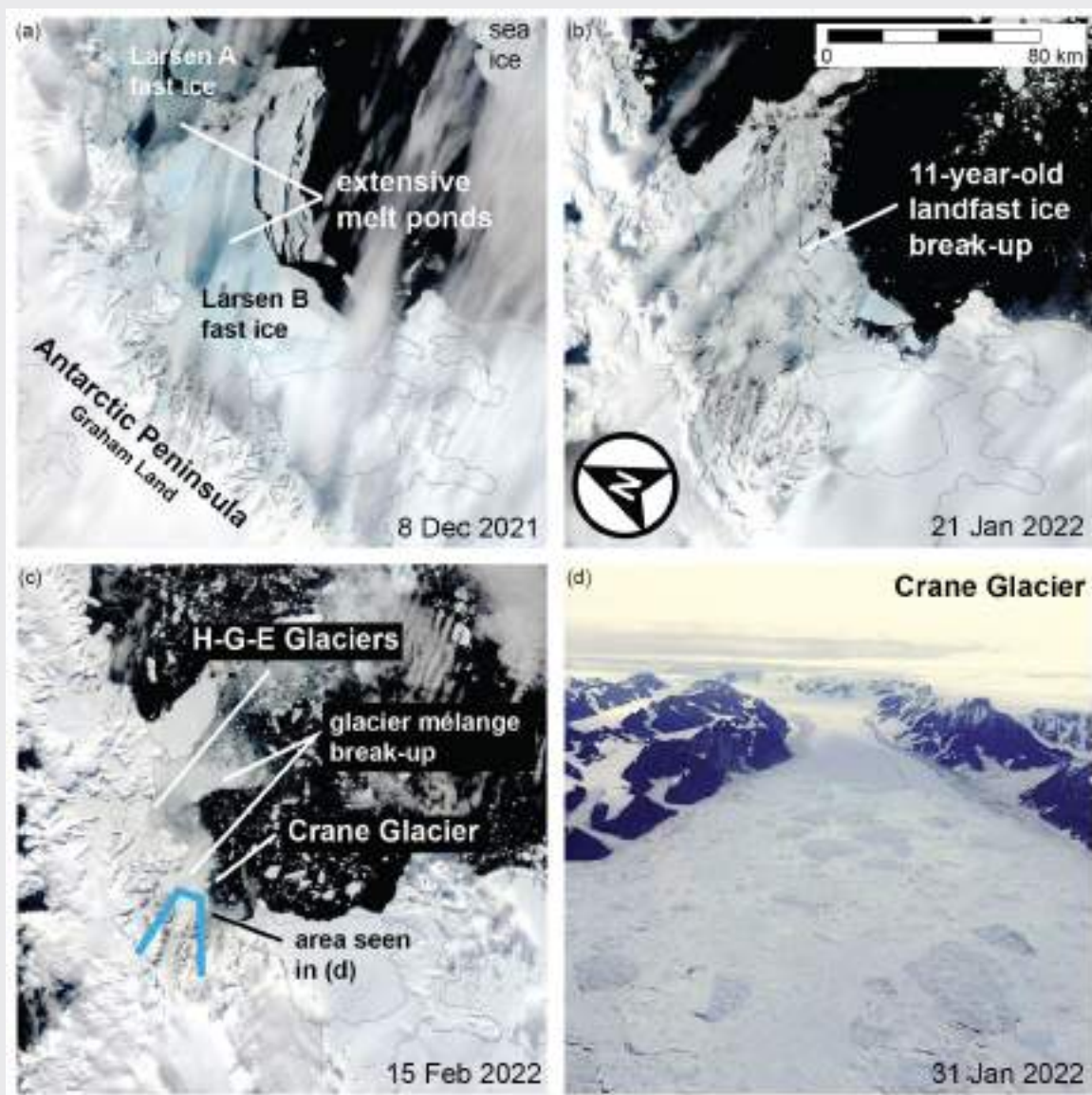


Fig. SB6.4. (a)–(c) Landsat 8 true-color images of the Larsen A and Larsen B embayments spanning the period of the breakup of the 11-year-old Larsen B fast ice. (d) Enhanced-color hand-held aerial photograph of the Crane Glacier fjord looking southwestward, acquired by British Antarctic Survey.

The cause of the fast-ice breakout appears to be a combination of warm summer air temperatures and wave action. Intense surface melting occurred in the region in the 2021/22 summer (<https://nsidc.org/greenland-today/2022/02/>) that likely pre-conditioned the fast ice cover for breakup, but intense surface melting and flooding of the fast ice by meltwater had happened before, particularly in 2015/16 and 2019/20 (e.g., Banwell et al. 2021, see their Fig. 2; Bevan et al. 2020; by inference of extensive melting in the northern Larsen C). However, unlike previous summers, sea ice in the adjacent northwestern Weddell Sea was greatly reduced in 2021/22 (Figs. SB6.5a,b). Sea-ice pack, even at relatively low concentrations, sharply dampens surface ocean waves within a few kilometers of the sea-ice front (Squire et al. 1995; Zhao et al. 2015). In early January 2022, for the first time in the 2011–22 fast ice period, a ~50 km-wide ice-free corridor (concentration below 15%) opened in the northwestern Weddell Sea, facilitating ocean swell penetration to the Larsen B fast-ice front. Examining both WAVEWATCH III (Tolman 2009) and European Centre for Medium-Range Weather Forecasts Reanalysis version 5 (ERA5) wave data (Hersbach et al. 2020; not shown), the first large swell able to reach the Larsen B fast ice edge occurred on 18–19 January (Fig. SB6.5c), with an estimated peak amplitude of 1.75 m and a peak wave period of 5 s (equal to a wavelength of ~40 m). Wave propagation direction was bearing ~250°±25°

through this period, similar to the orientation of the open corridor in the sea ice. Our analysis looked at wave data grid cells adjacent to the Larsen B fast ice front as well as cells ~150 km to the northeast near James Ross Island (Fig. SB6.5c). Subsequent foehn events, triggered by atmospheric rivers impacting the western flank of the Peninsula (e.g., 20 January, 29–30 January, and 7–9 February), cleared the broken ice and much of the mélange of ice blocks and rafted thick sea ice from the embayment as a rapid up-fjord retreat of the ice tongues progressed.

Fast ice has been shown to have a stabilizing effect on ice shelves and glaciers, and its loss is frequently associated with ice-shelf breakup or glacier retreat (Massom et al. 2010, 2018; Gomez-Fell et al. 2022; Fraser et al. 2023). After the Larsen B Ice Shelf collapsed in 2002, glaciers that formerly flowed into the ice shelf calved and retreated rapidly. However, over the 11-year period of fast-ice presence, the Larsen B glaciers partially re-advanced, protected from wave action and supported by backstress from the fast ice in the bay (notably Crane and Jorum glaciers, and the Hektor-Green-Evans glacier system).

With the break-out of the fast ice in early 2022, these glacier tongues, mélange areas, and in some cases previously grounded ice retreated and collapsed. Unlike previous winter seasons, fast ice did not form in the embayment in the 2022 winter. The pack ice in the embayment remained

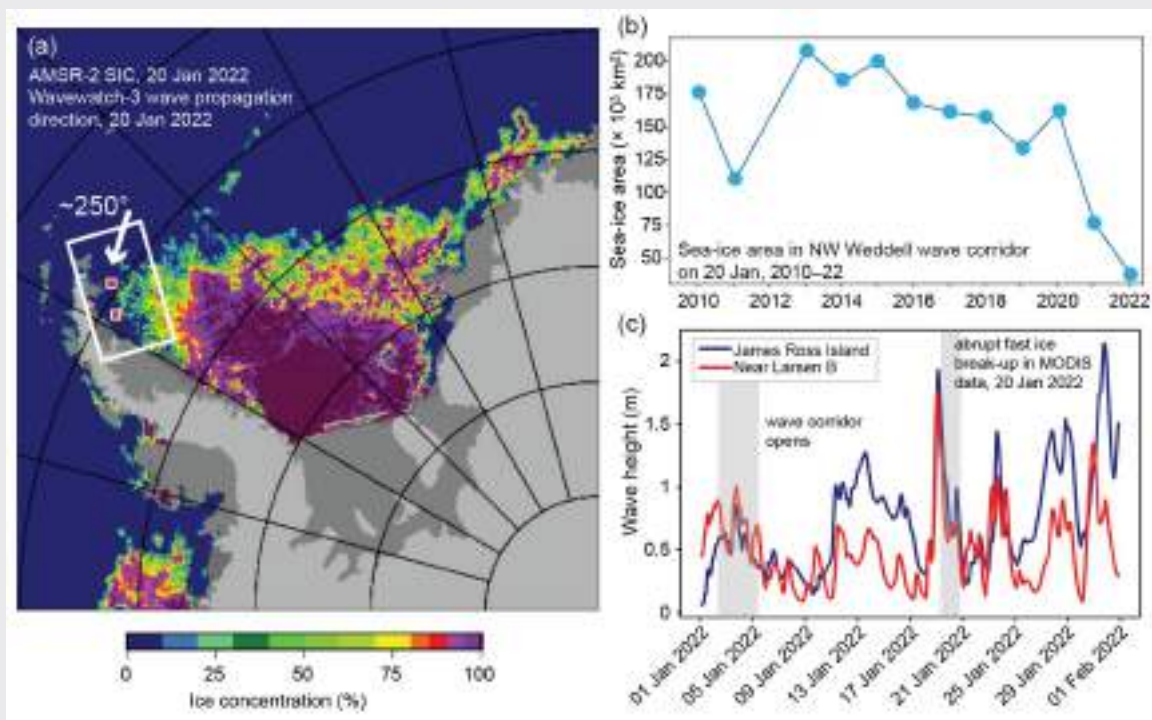


Fig. SB6.5. (a) Sea-ice conditions on 20 Jan 2022, showing ice concentration (%) and distribution from AMSR-2 data (Spren et al. 2008; <https://seaice.uni-bremen.de/sea-ice-concentration/amsre-amsr2>). Wave propagation direction on 20 Jan from Wavewatch-3 data is shown by the white arrow (~250° true); white outline shows the region assessed for sea-ice area in (b); red squares show the location of the Wavewatch-3 wave height grid cells shown in (c); (b) sea ice area (10³ km²) from AMSR and AMSR-2 data in the corridor region of the northwest (NW) Weddell Sea for 2010–22; (c) wave height data (m) for Jan (starting at 0000 UTC on 1 January 2022) from ERA5 Wavewatch-3 gridded wave timeseries for the grid cell areas in (a).

mobile and strong foehn wind events (e.g., 20–23 September) repeatedly cleared the ice from the glacier fronts. By the end of 2022, Crane Glacier had lost ~10 km of floating ice, and the ice front was at or slightly above the most upstream location ever observed (see Shuman et al. 2011). The Hektoria-Green-Evans system collapsed upstream a total of ~26 km, and the merged trunk for the three glaciers disintegrated. The collapse event is similar to the rapid evolution of the Röhss Glacier on James Ross Island in the years following the Prince Gustav Ice Shelf disintegration (Glasser et al. 2011).

The stark change in fast-ice stability as the fringing sea-ice pack dispersed timed closely to the arrival of a significant ocean wave train, and the rapid evolution of the former tributary glaciers in response to fast-ice loss, point to the potential impacts on ice-sheet stability and mass balance change that arise if the current downward trend in summer Antarctic sea-ice extent continues. The events point to a clear connection between late-summer wave flexure of warm, melt-laden fast ice, and significant glacier destabilization in areas where long-term fast ice is removed by wave action.

g. Southern Ocean

—L. Pezzi, R. Beadling, M. du Plessis, S. Gille, S. A. Josey, J.-R. Shi, M. Santini, E. Souza, G. MacGilchrist, and C. Schultz

The Southern Ocean (SO) has an important role in Earth's global climate. It is a significant sink for anthropogenic CO₂ and heat (Gille 2002; Frölicher et al. 2015; Shi et al. 2018) and is the world's most biologically productive ocean (Liu and Curry 2010). The SO is changing rapidly, exhibiting significant warming to the north of the Antarctic Circumpolar Current (ACC; Armour et al. 2016; Sallée 2018; Shi et al. 2021), as well as freshening (Swart et al. 2018) and decreasing oxygen (Shepherd et al. 2017). Here we analyze 2022 anomalies of SO sea-surface temperature (SST), surface salinity, mixed layer properties, air–sea heat fluxes, ocean heat content (OHC), surface chlorophyll, and oxygen concentrations. For surface chlorophyll and oxygen, we focus on austral spring 2021 and summer 2021/22 to highlight the phytoplankton growth season.

1. SEA-SURFACE AND MIXED-LAYER PROPERTIES

We present 2022 SO SST anomalies relative to the 1991–2020 climatology computed from the NOAA Optimum Interpolation SST version 2 product (Reynolds et al. 2002). The 2022 SO surface salinity and mixed layer depth (MLD) anomalies are relative to 2005–20 climatology and also presented (Figs. 6.13b,c), with data from the Argo-based dataset from Roemmich and Gilson (2009; RG09). The depth at which potential density referenced to the surface changes by 0.03 kg m⁻³ relative to potential density at 10 m (de Boyer Montégut et al. 2004) is used to define MLD. MLD anomalies are computed relative to a 2004–21 climatology. Following Beadling et al. (2022), we focus on 40°S–65°S since this region encapsulates SO climatic variability and the ACC.

Annually averaged SSTs in 2022 (Fig. 6.13a) were mostly below average, between –0.5°C and –1.5°C across much of the west and east Pacific, between –0.15°C and –0.5°C in the western Indian, and between –0.15°C and –0.5°C in the western Atlantic at the Drake Passage. With the exception of the Atlantic, the greatest negative SST anomalies were generally found south of the subantarctic front (SAF), while positive SST anomalies characterized regions farther north of the SAF, with particularly strong positive SST anomalies north of 40°S in the South Pacific. Most of the Atlantic sector of the SO was warmer than usual.

The anomalously high SSTs in the Atlantic and Indian sectors resulted in a net positive SST anomaly for the SO in 2022 (Fig. 6.13d), following the warming tendency shown in Beadling et al. (2022). Regions with the highest SST coincided with positive sea-surface salinity anomalies (Fig. 6.13b). Between the SAF and Southern Boundary Front in the South Pacific, positive surface salinity anomalies co-occurred with anomalous cooling. Positive surface salinity anomalies were observed in all oceans starting in April 2022 (Fig. 6.13e). The SO MLD reveals anomalously

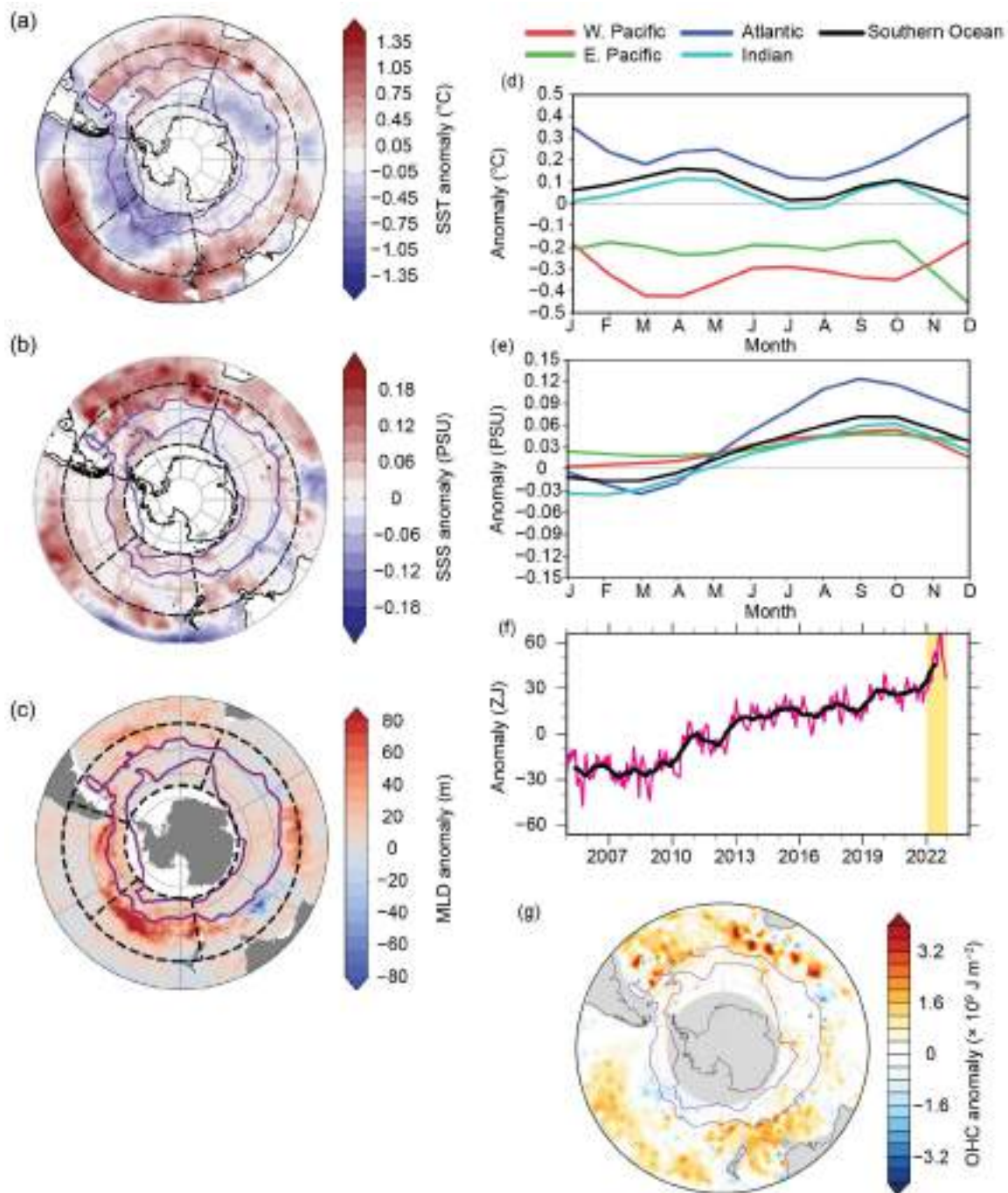


Fig. 6.13. 2022 annual average (a) sea-surface temperature (SST; °C), (b) surface salinity (SSS) (PSU), and (c) mixed layer depth (MLD; m) anomalies. Time series of monthly average (d) SST and (e) surface salinity anomalies. (f) Time series of monthly average of upper-2000-m ocean heat content (OHC) anomaly (ZJ or 10^{21} J) relative to 2005–20 Argo climatology south of 30°S (pink curve) with 12-month running mean on top (black curve) and 2022 highlighted in yellow shading. (g) Map of 2022 OHC anomalies ($\times 10^9$ J m^{-2}). SST anomalies are computed relative to a 1991–2020 climatology, while surface salinity, OHC, and MLD use a 2004–21 climatology given the limited extent of the RG09 product. Purple contours in the maps indicate the location of the subantarctic and southern boundary Antarctic Circumpolar Current fronts as defined by Orsi et al. (1995). Four distinct regions between 40°S and 65° are delineated by black dashed contours in Figs. 6.13a–c, corresponding to the western Pacific (170°W–120°W), eastern Pacific (120°W–70°W), Atlantic (70°W–20°E), and Indian (20°E–170°E) sectors discussed in the text.

deep mixing in the South Pacific just north of the SAF (Fig. 6.14c), similar to 2021 (Beadling et al. 2022). However, the deepest mixing was centered in the east Pacific sector in 2021 and migrated to the west Pacific in 2022. Deeper MLDs were found north of the SAF in the Atlantic and Indian sectors in 2022 relative to 2021.

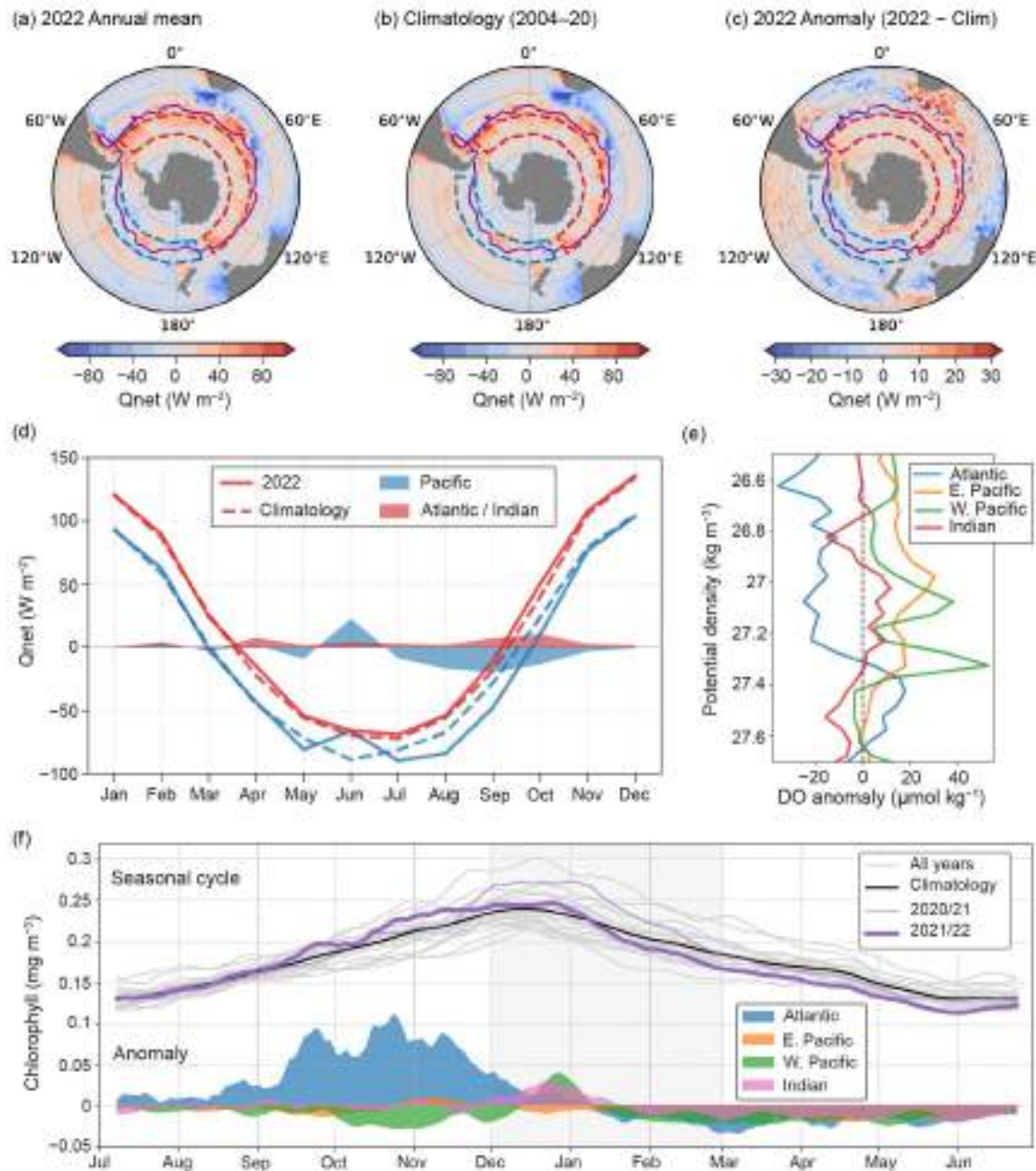


Fig. 6.14. ERA5 net heat flux, Q_{net} ($W m^{-2}$): (a) 2022 annual mean, (b) 2004–20 climatology, and (c) 2022 anomaly. The purple line denotes the location of the Subantarctic Front as in Fig. 6.13. The blue and red boxes indicate the Pacific ($50^{\circ}S-60^{\circ}S$, $160^{\circ}E-80^{\circ}W$) and Atlantic/Indian ($50^{\circ}S-60^{\circ}S$, $50^{\circ}W-150^{\circ}E$) sectors, respectively, chosen for further analysis. Positive values indicate the ocean heat gain. (d) Monthly mean net surface heat flux ($W m^{-2}$) for the Pacific (blue line) and Atlantic/Indian (red line) sectors of the Southern Ocean during 2022 (dashed) and the 2004–20 climatology (solid). Shading shows the 2022 anomaly from the climatology. (e) Jul 2021–Jun 2022 dissolved oxygen anomalies ($kg m^{-3}$) relative to the 2005–20 Argo climatology. Potential density was calculated from pressure, temperature, and salinity data, and binned into $0.05 kg m^{-3}$ intervals. (f) Seasonal cycle of the area-weighted ($40^{\circ}S-65^{\circ}S$), daily mean chlorophyll concentration ($mg m^{-3}$): all historical years (gray lines); the climatological mean for 1997–2022 (black line); the most recent two growing seasons (purple lines); anomalies relative to climatological mean for each basin (colored shading). A 14-day rolling average was applied to all time series. The x-axis is centered on the austral summer months. (Source: data are derived from the multi-satellite merged, cloud-free product; <https://doi.org/10.48670/moi-00281>.)

2. UPPER-OCEAN HEAT CONTENT

Monthly gridded temperature data from RG09 were used to evaluate 0-m–2000-m SO OHC anomalies relative to the 2005–20 climatological seasonal cycle. We focus on 30°S–65°S since a substantial OHC increase occurred in this region (Shi et al. 2021). In 2022, the SO annual mean upper-2000-m OHC anomaly increased by 16.2 ZJ (10^{21} J) to +45.2 ZJ (Fig. 6.13f). This increase in OHC is much larger than the increase between 2020 and 2021 (2.5 ZJ; Clem et al. 2022) and much larger than the interannual variability (5.2 ZJ south of 30°S) estimated from 1 std. dev. of the detrended annual OHC during 2005–20. The long-term positive trend in SO OHC is more apparent and larger in 2022 (+3.97 ZJ yr^{-1} during 2005–22 versus +3.68 ZJ yr^{-1} during 2005–21). This continuous heat gain is consistent with the 2022 OHC increase (Cheng et al. 2023). However, for the SO, a tremendous austral winter warming occurred in 2022 that was not clearly shown in Cheng et al. (2023).

Consistent with previous studies, most of the enhanced OHC occurred north of the ACC, with pronounced positive anomalies in the South Atlantic, Agulhas Return Current, South Pacific to the north of 50°S, and southwest Pacific around western boundary currents (Fig. 6.13g). The OHC anomalies are smaller within and south of the ACC associated with upwelling of deep water. Although they are smaller in magnitude compared with the lower-latitude anomalies, these positive anomalies can be found around the Antarctic, except for the negative anomalies in the vicinity of the Pacific Antarctic Ridge.

3. AIR–SEA HEAT FLUXES

The European Centre for Medium-Range Weather Forecasts Reanalysis version 5 (ERA5) is used to evaluate the 2022 and 2004–20 climatological state of the surface net heat flux for the Southern Ocean (Hersbach et al. 2020). Air–sea heat fluxes in 2022 showed asymmetrical patterns of anomalies relative to the 2004–20 climatology (Figs. 6.14a,b). This is consistent with previous work (Song 2020; Tamsitt et al. 2020; Josey et al. 2023). In both 2022 and the climatology, the Atlantic and Indian sectors showed a large spread in positive heat flux (ocean heat gain) of 20 W m^{-2} to 80 W m^{-2} . In comparison, the Pacific sector along the ACC experienced large regions of negative heat flux (ocean heat loss) down to -40 W m^{-2} , largely within and surrounding the SAF. Further heat loss was observed within the continental shelf regions surrounding Antarctica.

This zonal asymmetry was further amplified in 2022, with heat fluxes in the Atlantic and Indian sectors consistently higher than the climatology by up to 20 W m^{-2} and the Pacific regions around and south of the SAF experiencing negative heat fluxes as low as -15 W m^{-2} (Fig. 6.14c).

To elucidate potential mechanisms defining the seasonal cycle of heat-flux variability, we investigate the monthly average heat flux in regional boxes in the Atlantic and Indian sectors (50°S–60°S, 50°W–150°E) and the Pacific sector (50°S–60°S, 160°E–80°W) as defined in the zonal asymmetry analysis of Josey et al. (2023). The monthly mean heat flux revealed that the largest zonal asymmetry was observed in summer (December–February) at $\sim 25 \text{ W m}^{-2}$ and the lowest in winter (June–August) at $\sim 10 \text{ W m}^{-2}$ (Fig. 6.14d). Compared to the 2004–20 climatology, the 2022 annually averaged heat flux anomaly of the Atlantic/Indian sector was $+3.5 \pm 3.3 \text{ W m}^{-2}$ (Fig. 6.14d). This contrasted with the Pacific sector, where large monthly mean heat loss anomalies in winter/spring (reaching a most negative value of -19.5 W m^{-2} in September) led to an overall 2022 heat flux anomaly of $-3.9 \pm 10.7 \text{ W m}^{-2}$. The large monthly variability in the 2022 heat flux in the Pacific (most notably in June, which had heat gain rather than loss) may be due to variations in the number of episodic heat loss events as previously observed south of Australia (Ogle et al. 2018; Tamsitt et al. 2020). Additionally, Pacific heat loss in 2022 coincided with lower SSTs, deeper MLDs, and a decrease in the OHC (Fig. 6.13), suggesting a potential seasonal response time between heat flux, surface temperature, and mixing. However, further investigation is required to establish whether this was the case.

4. OCEAN BIOGEOCHEMISTRY

We present anomalies of dissolved oxygen (DO) relative to the 2005–20 Argo climatology and satellite-observed chlorophyll concentrations relative to the 1997–2022 climatological mean (Figs. 6.14e,f). For the DO anomalies, data from Argo floats that sampled each region were averaged for the period considered (July 2021–June 2022) and compared to the average DO from all Argo floats available in previous years, starting in 2005. Anomalous conditions were observed in satellite-observed chlorophyll and float-observed oxygen levels during 2021/22, particularly in the Atlantic sector. Mean chlorophyll concentrations were anomalously high during the spring and early summer growing season (Fig. 6.14f, thick purple line) before dropping below climatological levels by mid-January and reaching some of their lowest recorded levels by the onset of autumn. A basin breakdown of anomalies reveals that this pattern arose almost entirely from the Atlantic sector. Mean concentrations between $+0.05$ and $+0.10$ mg m^{-3} above climatological levels were seen throughout spring, reaching a maximum in mid-October, before a precipitous decline. By mid-summer, concentrations were anomalously low, indicating an early phytoplankton bloom cycle. In the Pacific and Indian Oceans, chlorophyll concentrations were anomalously low through 2021/22, with the exception of a spike during December and early January in the Pacific.

As with chlorophyll, there were distinct patterns in DO concentrations in the Atlantic relative to other sectors of the SO, with lighter water masses ($\rho_0 < 27.4$ kg m^{-3}) exhibiting anomalously low concentrations (Fig. 6.14e). A distinct pattern between the Atlantic and other ocean basins is somewhat consistent with the other metrics shown here. In particular, there is evidence that the positive MLD, surface temperature, and heat flux anomalies are weaker in the Atlantic compared to the Pacific basin. The different observational periods between metrics—where it is more intuitive for biogeochemical metrics to center the annual cycle around the growing season—make it challenging to ascertain what drove the anomalous Atlantic basin conditions in late 2021.

h. 2022 Antarctic ozone hole

—N. A. Kramarova, P. A. Newman, E. R. Nash, S. E. Strahan, B. Johnson, M. Pitts, M. L. Santee, I. Petropavlovskikh, L. Coy, and J. D. Laatz

The 2022 Antarctic ozone hole was the 18th largest in 43 years of satellite observations since 1979, with an average area of 21.6×10^6 km^2 (averaged for 7 September–13 October) and a minimum daily total ozone column of 97 DU on 1 and 2 October. The meteorological conditions and seasonal development of the Antarctic ozone hole in 2022 were similar to those observed in 2020 and 2021. Following the August–September depletion phase, the 2022 ozone hole persisted, breaking up on 16 December (the 1990–2022 average breakup date is 10 December).

Antarctic lower stratospheric temperatures were near average in July–September 2022. In October–December 2022, lower stratospheric temperatures were consistently below average (orange line in Fig. 6.15a). The volume of polar stratospheric clouds (PSCs) in 2022 stayed below or near the long-term average during July–October (Fig. 6.15b) and fell to zero as lower stratospheric temperatures rose above the threshold for PSC formation in late September (Figs. 6.15a,b). Heterogeneous chemical reactions occur on polar clouds particle surfaces, releasing chlorine into active forms (e.g., chlorine monoxide, ClO) that deplete ozone at about 1%–2% per day as sunlight returns to the Antarctic in August–September. Aura Microwave Limb Sounder (MLS) observations show that vortex-averaged ClO in 2022 was near or below average until

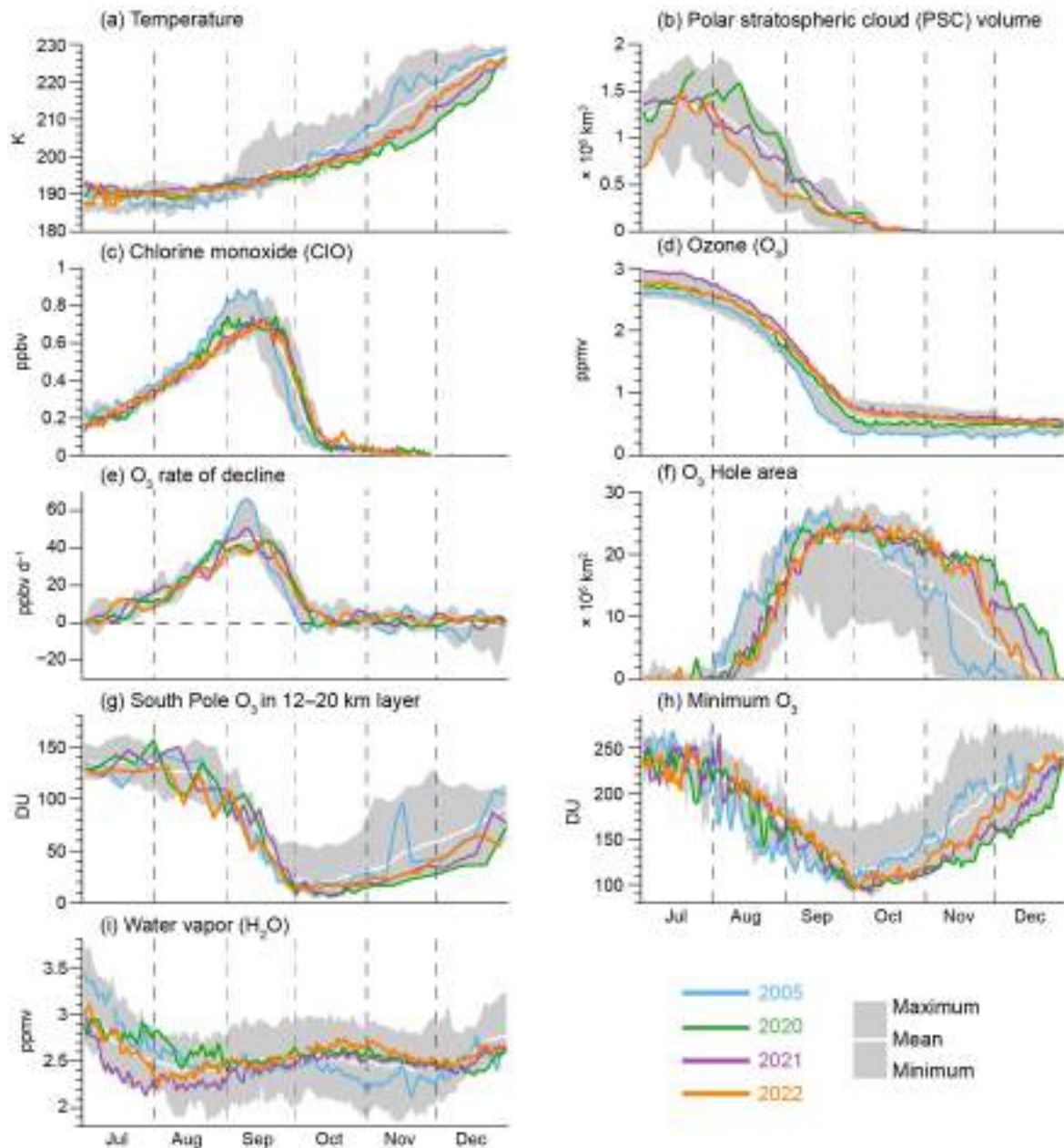


Fig. 6.15. Antarctic values of (a) vortex-averaged MERRA-2 temperature on the 440-K potential temperature surface (~ 19 km or 60 hPa), (b) CALIPSO polar stratospheric cloud (PSC) volume (updated from Pitts et al. 2018), (c),(d),(e),(i) vortex-averaged chlorine monoxide (ClO), ozone (O_3), O_3 rate of decline (calculated as time derivatives of vortex-averaged ozone), and water vapor (H_2O) on the 440-K potential temperature surface from Aura MLS (updated from Manney et al. 2011), (f) OMI/OMPS Antarctic ozone hole area (area with ozone total column less than 220, DU), (g) lower stratospheric ozone columns (12 km–20 km) based on sonde measurements at South Pole, and (h) minimum total ozone columns over $60^\circ S$ – $90^\circ S$ from OMI/OMPS. Gray shading shows the range of daily Antarctic values for 2005 (for all but (h), which starts in 2006) through 2021. The white curve indicates the 2005–21 long-term mean. DU is a unit of measurement of the amount of a trace gas in a vertical column. One DU represents the number of trace gas molecules in the 0.01-mm-thick layer at standard atmospheric surface conditions.

mid-September and above average in late September through October (Fig. 6.15c), similar to 2020 and 2021. The seasonal ClO peak was delayed by about a week in 2022. Vortex-averaged ozone on the 440-K isentropic surface (~60 hPa) was above or near average in July–December 2022 (Fig. 6.15d). The seasonal ozone reduction in 2022, estimated by the ozone changes between the first week of July and the first week of October, was about 2.05 ppmv, which is smaller than those in 2020 (2.18 ppmv) and 2021 (2.22 ppmv). The ozone rate of decline (Fig. 6.15e), calculated as time derivatives of vortex-averaged ozone (Fig. 6.15d), is mostly driven by reactive chlorine and bromine from ozone-depleting substances (ODS), with a smaller contribution from transport. The ozone depletion rate is highly correlated with available chlorine (Fig. 6.15c) and typically increases in July–August, reaching its peak between 1 and 20 September with a maximum around 10 September (Strahan et al. 2019). The maximum values of the depletion rate and ClO in the last 18 years were observed in 2005 when the levels of ODS were substantially larger than today. The 2022 ozone rate of decline was close to average.

The Antarctic ozone hole area, defined by the region with total ozone columns below 220 DU, reached its peak of 26.45×10^6 km² on 5 October (Fig. 6.15f). Weaker-than-average planetary wave activity in September through early November 2022 prolonged the ozone hole through the October–December period (NASA 2023a). Starting in mid-November, the ozone hole rapidly eroded, disappearing on 16 December. Overall, the ozone hole area in August through early September 2022 was below or near average, consistent with recovery trends of the onset of the ozone hole (Stone et al. 2021) due to ODS decreases.

The lower stratospheric ozone column between 12 km and 20 km derived from sonde measurements at South Pole (SP) station was near or below average in July–September 2022 (Fig. 6.15g), reaching a minimum of 12.4 DU on 5 October. The 2022 minimum total ozone column over the Antarctic (60°S–90°S), measured on 1 and 2 October at 97 DU, was close to the long-term average (Fig. 6.15h). Similar to the situation in 2020 and 2021, both the 12 km–20 km SP column and the minimum Antarctic polar ozone remained below average in October–December 2022 because of the weaker planetary wave activity and below-average lower stratospheric temperatures (Figs. 6.15g,h).

The eruption of the Hunga Tonga-Hunga Ha'apai underwater volcano in January 2022 injected aerosols and a record amount of water vapor directly into the stratosphere. The volcanic material reached altitudes as high as ~55 km–58 km (Carr et al. 2022), and the stratospheric optical depth was the highest since the 1991 Mt. Pinatubo eruption (Taha et al. 2022). While it injected a relatively small amount of sulfur dioxide (~0.4 Tg), Hunga Tonga injected an unprecedented amount of water vapor (146 ± 5 Tg or ~10% of the stratospheric total) into the stratosphere (Millan et al. 2022; Schoeberl et al. 2022). That excess water vapor induced changes in stratospheric temperatures and circulation (Coy et al. 2022). However, MLS observations inside the Antarctic vortex showed near-average water vapor (Fig. 6.15i), indicating that the volcanic plume did not directly affect the 2022 ozone hole's chemical composition.

Antarctic stratospheric ODS levels are slowly declining as a result of the Montreal Protocol (NASA 2023b). Abundances of reactive halogens in the Antarctic stratosphere from the ODSs are estimated using effective equivalent stratospheric chlorine (EESC; Newman et al. 2007). EESC levels in 2022 were 14% lower than the maximum levels observed in the early 2000s. While the reduction in ozone hole severity due to declining ODS concentrations is observable on decadal timescales (Fig. 6.16a), year-to-year ozone hole variations are modulated by Antarctic lower stratospheric temperatures. Temperature effects are estimated by a quadratic fit of EESC with a 5.2-year mean age of air to the observed ozone hole areas (gray line in Fig. 6.16a). Figure 6.16b shows the relationship between September lower stratospheric temperatures and area deviations from the fitted curve. Ozone holes are more severe in colder years (Newman et al. 2004). Below-average September 2022 50-hPa temperatures (green triangle in Fig. 6.16b) increased the area of the ozone hole by $2\text{--}3 \times 10^6 \text{ km}^2$ with respect to the EESC-fit projection (gray line in Fig. 6.16a). The November hole area also depends on lower stratospheric temperatures (Fig. 6.16d). The 2022 late-spring ozone hole was much larger than average (Fig. 6.15f) because of the late seasonal transition from winter to summer circulation and the associated low temperatures in late spring (Fig. 6.15a), similar to 2020/21.

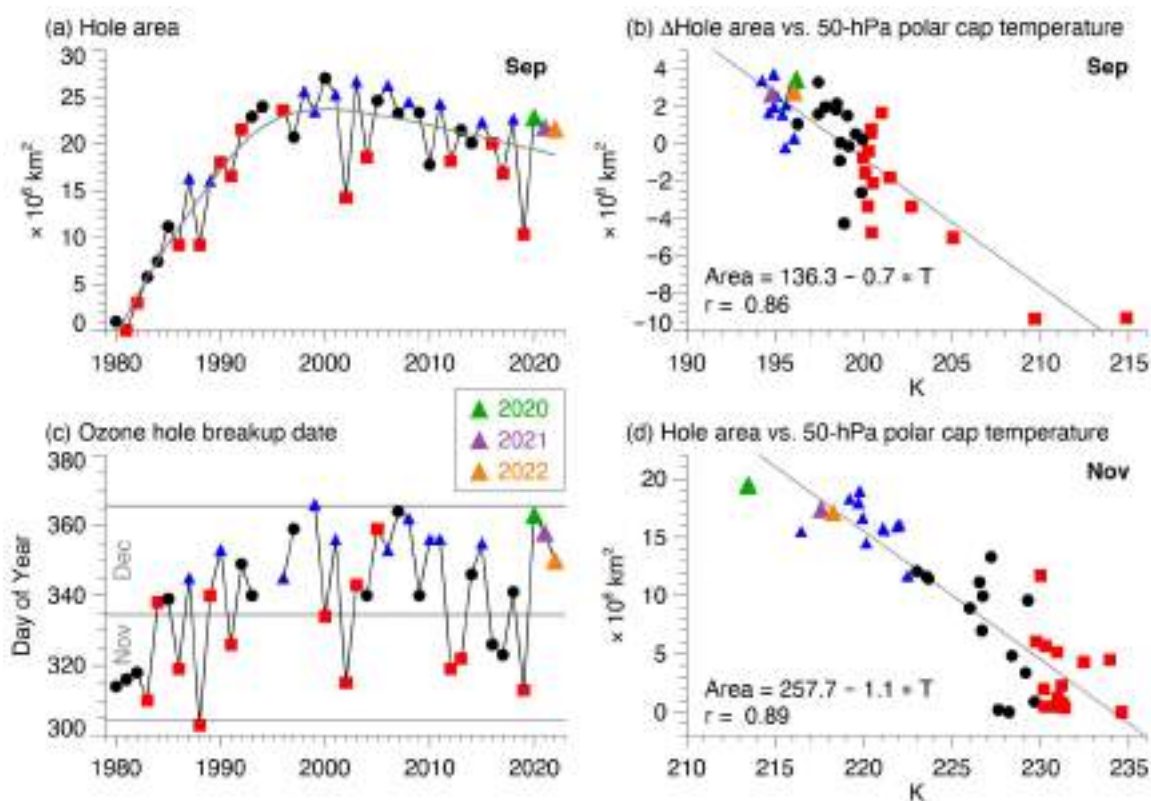


Fig. 6.16. (a) Sep average Antarctic ozone hole area ($\times 10^6 \text{ km}^2$). (b) Sep anomalies of the ozone hole area ($\times 10^6 \text{ km}^2$; see text) versus MERRA-2 Sep 50-hPa temperatures (K) averaged over the polar cap ($60^\circ\text{S}\text{--}90^\circ\text{S}$). (c) Ozone hole disappearance dates (day of yr). (d) Nov ozone hole areas ($\times 10^6 \text{ km}^2$) versus MERRA-2 Nov 50-hPa temperatures (K). In (a), the gray curve shows a quadratic fit of effective equivalent stratospheric chlorine (EESC) with a 5.2 year mean age of air (Newman et al. 2007) to the Sep hole areas. Years with temperatures in the lowest (highest) third are shown as blue triangles (red squares), and the three years 2020, 2021, and 2022 are highlighted in green, purple, and orange, respectively. Ozone data for 1979–92 are from Total Ozone Mapping Spectrometer (TOMS) Nimbus-7; 1993–94 are from TOMS Meteor-3; 1996–2004 are from EPTOMS, 2005–15 are from Aura Ozone Monitoring Instrument (OMI); and 2015–22 are from Suomi National Polar-orbiting Partnership (SNPP) Ozone Mapping and Profiler Suite (OMPS). There were no satellite total ozone observations for 1995.

The last three austral springs were characterized by very late ozone hole breakups (Fig. 6.16c). These late breakups were caused by anomalously weak planetary wave activity during spring. Planetary waves propagating upward from the troposphere decelerate the polar vortex and force downward motion, warming the vortex. Weak wave activity in 2020, 2021, and 2022 allowed the Antarctic vortex to persist into late spring, keeping stratospheric temperatures below average (Figs. 6.15a,f,g,h). The delay in the vortex breakup in 2022 in turn delayed the ozone hole breakup (Fig. 6.16c). The ozone hole breakup dates are strongly correlated with the vortex breakup dates from 1990 to the present, and in the last three years (2020–22) occurred later than average, producing a statistically significant trend of about 5 days decade⁻¹ delay in the ozone hole disappearance. The causes for this trend are not known at this time but potentially can be associated with the strong positive Southern Annular Mode observed in the last three years (see section 6b), which is associated with reduced planetary wave activity. The long-lasting stratospheric vortices in the last three years kept ozone columns below average for October–December and prevented meridional mixing of ozone-rich air from midlatitudes into polar latitudes.

In summary, the 2022 Antarctic ozone hole was slightly larger than average. The large areas of the Antarctic ozone hole in the last three years are consistent with our understanding of ozone depletion and are primarily driven by meteorological conditions. The Hunga Tonga-Hunga Ha'apai eruption did not have a direct effect on the chemical composition of the 2022 ozone hole. The delayed onset in ozone hole area in August–September observed in the last three years is consistent with ozone recovery due to the Montreal Protocol.

Acknowledgments

Work at the Jet Propulsion Laboratory, California Institute of Technology, was done under contract with the National Aeronautics and Space Administration (NASA). Support was also provided by the NASA Modeling and Analysis Program. We are indebted to the many NOAA Corps Officers and GML technical personnel who spend the winters at South Pole Station to obtain the ongoing balloon and ground-based data sets. We also acknowledge the logistics support in Antarctica provided by the National Science Foundation Office of Polar Programs. © 2023. All rights reserved.

- K. R. Clem acknowledges support from the Royal Society of New Zealand Marsden Fund grant MFP-VUW2010.
- J. D. Wille acknowledges support from the Agence Nationale de la Recherche project, ANR-20-CE01-0013 (ARCA).
- R. T. Datta would like to acknowledge NSF award OPP 1952199.
- L. Trusel and R. T. Datta would like to acknowledge NASA award S000885-NASA.
- P. Reid and J. Lieser were supported through the Australian Bureau of Meteorology, and R. Massom by the Australian Antarctic Division. The work of P. Reid and R. Massom also contributes to the Australian Government's Australian Antarctic Partnership Program (AAPP). For R. Massom, this work was also supported by the Australian Research Council Special Research Initiative the Australian Centre for Excellence in Antarctic Science (Project Number SR200100008).
- S. T. Gille acknowledges support from NSF's Southern Ocean Carbon and Climate Observations and Modeling (SOCCOM) Project under the NSF award OPP-1936222.
- L. P. Pezzi acknowledges support from PROANTAR's Antarctic Modeling and Observation System (ATMOS) Project under the CNPq/PROANTAR award 443013/2018-7.
- S. Stammerjohn was supported under NSF PLR-1552226; she also thanks the Institute of Arctic and Alpine Research and the National Snow and Ice Data Center, both at the University of Colorado Boulder, for institutional and data support.
- A. Banwell was supported by NSF award #1841607 to the University of Colorado Boulder.
- N. Ochwat and T. Scambos were supported by NASA award 80NSSC22K0386 on Larsen B evolution and NASA award 80NSSC21K0750 for sea ice monitoring.
- L. M. Keller, M. A. Lazzara, D. E. Mikolajczyk, and T. Norton appreciate support from NSF grant number 1924730, 1951720, and 1951603.

Appendix 1: Chapter 6 – Acronyms

ACC	Antarctic Circumpolar Current
AIS	Antarctic Ice Sheet
AR	atmospheric river
ASL	Amundsen Sea Low
ATLAS	Advanced Topographic Laser Altimeter System
AWS	automated weather station
CIO	chlorine monoxide
CRI	coastal resolution improvement
DO	dissolved oxygen
EESC	effective equivalent stratospheric chlorine
ERA5	European Centre for Medium-Range Weather Forecasts Reanalysis version 5
GRACE	Gravity Recovery and Climate Experiment
GRACE-FO	Gravity Recovery and Climate Experiment Follow-on
H ₂ O	water
IceSat-2	Ice, Cloud and land Elevation Satellite-2
IVT	integrated water vapor transport
IWV	integrated water vapor
MERRA-2	Modern-Era Retrospective Analysis for Research and Applications version 2
MLD	mixed layer depth
MLS	Microwave Limb Sounder
O ₃	ozone
ODS	ozone-depleting substances
OHC	ocean heat content
OMI	Ozone Monitoring Instrument
OMPS	Ozone Mapping and Profiler Suite
PSC	polar stratospheric cloud
PSU	surface salinity
Qnet	net heat flux
SAF	subantarctic front
SAM	Southern Annular Mode
SIA	sea-ice area
SIE	sea-ice extent
SMB	surface mass balance
SMMR	Scanning Multi-Channel Microwave Radiometer
SO	Southern Ocean
SP	South Pole
SSM/I	Special Sensor Microwave Imager
SSMIS	Special Sensor Microwave Imager/Sounder
SST	sea-surface temperature
TOMS	Total Ozone Mapping Spectrometer

References

- Adusumilli, S., H. A. Fricker, B. Medley, L. Padman, and M. R. Siegfried, 2020: Interannual variations in meltwater input to the Southern Ocean from Antarctic ice shelves. *Nat. Geosci.*, **13**, 616–620, <https://doi.org/10.1038/s41561-020-0616-z>.
- Agosta, C., and Coauthors, 2019: Estimation of the Antarctic surface mass balance using the regional climate model MAR (1979–2015) and identification of dominant processes. *Cryosphere*, **13**, 281–296, <https://doi.org/10.5194/tc-13-281-2019>.
- Armour, K. C., J. Marshall, J. R. Scott, A. Donohoe, and E. R. Newsum, 2016: Southern Ocean warming delayed by circumpolar upwelling and equatorward transport. *Nat. Geosci.*, **9**, 549–554, <https://doi.org/10.1038/ngeo2731>.
- Arthur, J. F., C. R. Stokes, S. S. R. Jamieson, J. Rachel Carr, A. A. Leeson, and V. Verjans, 2022: Large interannual variability in supraglacial lakes around East Antarctica. *Nat. Commun.*, **13**, 1711, <https://doi.org/10.1038/s41467-022-29385-3>.
- Banwell, A. F., D. R. MacAyeal, and O. V. Sergienko, 2013: Breakup of the Larsen B Ice Shelf triggered by chain reaction drainage of supraglacial lakes. *Geophys. Res. Lett.*, **40**, 5872–5876, <https://doi.org/10.1002/2013GL057694>.
- , R. T. Datta, R. L. Dell, M. Moussavi, L. Brucker, G. Picard, C. A. Shuman, and L. A. Stevens, 2021: The 32-year record-high surface melt in 2019/2020 on the northern George VI Ice Shelf, Antarctic Peninsula. *Cryosphere*, **15**, 909–925, <https://doi.org/10.5194/tc-15-909-2021>.
- Baumhoer, C. A., A. J. Dietz, C. Kneisel, H. Paeth, and C. Kuenzer, 2021: Environmental drivers of circum-Antarctic glacier and ice shelf front retreat over the last two decades. *Cryosphere*, **15**, 2357–2381, <https://doi.org/10.5194/tc-15-2357-2021>.
- Beadling, R. L., N. M. Freeman, G. A. MacGilchrist, M. Mazloff, J.-R. Shi, A. F. Thompson, and E. Wilson, 2022: Southern Ocean [in “State of the Climate in 2021”]. *Bull. Amer. Meteor. Soc.*, **103** (8), S329–S332, <https://doi.org/10.1175/BAMS-D-22-0078.1>.
- Bell, R. E., A. F. Banwell, L. D. Trusel, and J. Kingslake, 2018: Antarctic surface hydrology and impacts on ice-sheet mass balance. *Nat. Climate Change*, **8**, 1044–1052, <https://doi.org/10.1038/s41558-018-0326-3>.
- Bevan, S., A. Luckman, H. Hendon, and G. Wang, 2020: The 2020 Larsen C Ice Shelf surface melt is a 40-year record high. *Cryosphere*, **14**, 3551–3564, <https://doi.org/10.5194/tc-14-3551-2020>.
- Carr, J. L., Á. Horváth, D. L. Wu, and M. D. Friberg, 2022: Stereo plume height and motion retrievals for the record-setting Hunga Tonga-Hunga Ha’apai eruption of 15 January 2022. *Geophys. Res. Lett.*, **49**, e2022GL098131, <https://doi.org/10.1029/2022GL098131>.
- Cavalieri, D. J., C. L. Parkinson, P. Gloersen, and H. J. Zwally, 1996: Sea ice concentrations from Nimbus-7 SMMR and DMSP SSM/I-SSMIS passive microwave data, version 1. NASA National Snow and Ice Data Center Distributed Active Archive Center, accessed 3 January 2023, <https://doi.org/10.5067/8GQ8LZQVL0VL>.
- Cheng, L., and Coauthors, 2023: Another year of record heat for the oceans. *Adv. Atmos. Sci.*, **40**, 963–974, <https://doi.org/10.1007/s00376-023-2385-2>.
- Clem, K. R., and M. N. Raphael, Eds., 2022: Antarctica and the Southern Ocean [in “State of the Climate in 2021”]. *Bull. Amer. Meteor. Soc.*, **103** (8), S307–S340, <https://doi.org/10.1175/BAMS-D-22-0078.1>.
- , S. Barreira, R. L. Fogt, S. Colwell, L. M. Keller, M. A. Lazzara, and T. Norton, 2022: Atmospheric circulation and surface observations [in “State of the Climate in 2021”]. *Bull. Amer. Meteor. Soc.*, **103**, S313–S316, <https://doi.org/10.1175/BAMS-D-22-0078.1>.
- Comiso, J. C., 2017: Bootstrap sea ice concentrations from Nimbus-7 SMMR and DMSP SSM/I-SSMIS, version 3. NASA National Snow and Ice Data Center Distributed Active Archive Center, accessed 2 February 2023, <https://doi.org/10.5067/7Q8HC-CWS4I0R>.
- Coy, L., P. A. Newman, K. Wargan, G. Partyka, S. E. Strahan, and S. Pawson, 2022: Stratospheric circulation changes associated with the Hunga Tonga-Hunga Ha’apai eruption. *Geophys. Res. Lett.*, **49**, e2022GL100982, <https://doi.org/10.1029/2022GL100982>.
- de Boyer Montégut, C., G. Madec, A. S. Fischer, A. Lazar, and D. Iudicone, 2004: Mixed layer depth over the global ocean: An examination of profile data and a profile-based climatology. *J. Geophys. Res.*, **109**, C12003, <https://doi.org/10.1029/2004JC002378>.
- Depoorter, M. A., J. L. Bamber, J. A. Griggs, J. T. M. Lenaerts, S. R. M. Ligtenberg, M. R. van den Broeke, and G. Moholdt, 2013: Calving fluxes and basal melt rates of Antarctic ice shelves. *Nature*, **502**, 89–92, <https://doi.org/10.1038/nature12567>.
- Dunmire, D., and Coauthors, 2020: Observations of buried lake drainage on the Antarctic Ice Sheet. *Geophys. Res. Lett.*, **47**, e2020GL087970, <https://doi.org/10.1029/2020GL087970>.
- , J. T. M. Lenaerts, R. T. Datta, and T. Gorte, 2022: Antarctic surface climate and surface mass balance in the Community Earth System Model version 2 during the satellite era and into the future (1979–2100). *Cryosphere*, **16**, 4163–4184, <https://doi.org/10.5194/tc-16-4163-2022>.
- Eayrs, C., X. Li, M. N. Raphael, and D. M. Holland, 2021: Rapid decline in Antarctic sea ice in recent years hints at future change. *Nat. Geosci.*, **14**, 460–464, <https://doi.org/10.1038/s41561-021-00768-3>.
- Fogt, R. L., D. H. Bromwich, and K. M. Hines, 2011: Understanding the SAM influence on the South Pacific ENSO teleconnection. *Climate Dyn.*, **36**, 1555–1576, <https://doi.org/10.1007/s00382-010-0905-0>.
- , A. M. Sleinkofer, M. N. Raphael, and M. S. Handcock, 2022: A regime shift in seasonal total Antarctic sea ice extent in the twentieth century. *Nat. Climate Change*, **12**, 54–62, <https://doi.org/10.1038/s41558-021-01254-9>.
- Fraser, A. D., and Coauthors, 2023: Antarctic landfast sea ice: A review of its physics, biogeochemistry and ecology. *Rev. Geophys.*, **61**, e2022RG000770, <https://doi.org/10.1029/2022RG000770>.
- Frölicher, T. L., J. L. Sarmiento, D. J. Paynter, J. P. Dunne, J. P. Krasting, and M. Winton, 2015: Dominance of the Southern Ocean in anthropogenic carbon and heat uptake in CMIP5 models. *J. Climate*, **28**, 862–886, <https://doi.org/10.1175/JCLI-D-14-00117.1>.
- Gelaro, R., and Coauthors, 2017: The Modern-Era Retrospective Analysis for Research and Applications, version 2 (MERRA-2). *J. Climate*, **30**, 5419–5454, <https://doi.org/10.1175/JCLI-D-16-0758.1>.
- Gilbert, E., and C. Kittel, 2021: Surface melt and runoff on Antarctic ice shelves at 1.5°C, 2°C, and 4°C of future warming. *Geophys. Res. Lett.*, **48**, e2020GL091733, <https://doi.org/10.1029/2020GL091733>.

- Gille, S. T., 2002: Warming of the Southern Ocean since the 1950s. *Science*, **295**, 1275–1277, <https://doi.org/10.1126/science.1065863>.
- Glasser, N. F., T. A. Scambos, J. Bohlander, M. Truffer, E. Pettit, and B. J. Davies, 2011: From ice-shelf tributary to tidewater glacier: Continued rapid recession, acceleration and thinning of Röhss Glacier following the 1995 collapse of the Prince Gustav Ice Shelf, Antarctic Peninsula. *J. Glaciol.*, **57**, 397–406, <https://doi.org/10.3189/002214311796905578>.
- Gloersen, P., 2006: Nimbus-7 SMMR polar gridded radiances and sea ice concentrations, version 1. Subset: 37 & 19 GHz, h-polarization, 25 km grid, October 1979–April 1987. NASA National Snow and Ice Data Center Distributed Active Archive Center, accessed 5 May 2020, <https://doi.org/10.5067/QOZIVYV3V9JP>.
- Gomez-Fell, R., W. Rack, H. Purdie, and O. Marsh, 2022: Parker Ice Tongue collapse, Antarctica, triggered by loss of stabilizing land-fast sea ice. *Geophys. Res. Lett.*, **49**, e2021GL096156, <https://doi.org/10.1029/2021GL096156>.
- Gossart, A., S. Helsen, J. T. M. Lenaerts, S. V. Broucke, N. P. M. van Lipzig, and N. Souverijns, 2019: An evaluation of surface climatology in state-of-the-art reanalyses over the Antarctic ice sheet. *J. Climate*, **32**, 6899–6915, <https://doi.org/10.1175/JCLI-D-19-0030.1>.
- Gudmundsson, G. H., F. S. Paolo, S. Adusumilli, and H. A. Fricker, 2019: Instantaneous Antarctic ice sheet mass loss driven by thinning ice shelves. *Geophys. Res. Lett.*, **46**, 13903–13909, <https://doi.org/10.1029/2019GL085027>.
- Hersbach, H., and Coauthors, 2020: The ERA5 global reanalysis. *Quart. J. Roy. Meteor. Soc.*, **146**, 1999–2049, <https://doi.org/10.1002/qj.3803>.
- Josey, S. A., J. P. Grist, J. V. Mecking, B. I. Moat, and E. Schulz, 2023: A clearer view of Southern Ocean air-sea interaction using surface heat flux asymmetry. *Philos. Trans. Roy. Soc.*, **A381**, 20220067, <https://doi.org/10.1098/rsta.2022.0067>.
- Kittel, C., and Coauthors, 2021: Diverging future surface mass balance between the Antarctic ice shelves and grounded ice sheet. *Cryosphere*, **15**, 1215–1236, <https://doi.org/10.5194/tc-15-1215-2021>.
- Kramarova, N. A., and Coauthors, 2022: 2021 Antarctic ozone hole [in “State of the Climate in 2021”]. *Bull. Amer. Meteor. Soc.*, **103** (8), S332–S335, <https://doi.org/10.1175/BAMS-D-22-0078.1>.
- Lenaerts, J. T. M., and M. R. van den Broeke, 2012: Modeling drifting snow in Antarctica with a regional climate model: 2. Results. *J. Geophys. Res.*, **117**, D05109, <https://doi.org/10.1029/2010JD015419>.
- , B. Medley, M. R. Broeke, and B. Wouters, 2019: Observing and modeling ice sheet surface mass balance. *Rev. Geophys.*, **57**, 376–420, <https://doi.org/10.1029/2018RG000622>.
- Ligtenberg, S. R. M., M. M. Helsen, and M. R. van den Broeke, 2011: An improved semi-empirical model for the densification of Antarctic firn. *Cryosphere*, **5**, 809–819, <https://doi.org/10.5194/tc-5-809-2011>.
- Liu, J., and J. A. Curry, 2010: Accelerated warming of the Southern Ocean and its impacts on the hydrological cycle and sea ice. *Proc. Natl. Acad. Sci. USA*, **107**, 14987–14992, <https://doi.org/10.1073/pnas.1003336107>.
- , Z. Zhu, and C. Dake, 2023: Lowest Antarctic sea ice record broken for the second year in a row. *Ocean Land Atmos. Res.*, **2**, 0007, <https://doi.org/10.34133/olar.0007>.
- MacFerrin, M., T. Mote, H. Wang, L. Liu, L. Montgomery, and T. Scambos, 2021: Ice sheet seasonal melt extent and duration [in “State of the Climate in 2020”]. *Bull. Amer. Meteor. Soc.*, **102** (8), S331–S334, <https://doi.org/10.1175/BAMS-D-21-0081.1>.
- , —, A. Banwell, and T. Scambos, 2022: Ice sheet seasonal melt extent and duration [in “State of the Climate in 2021”]. *Bull. Amer. Meteor. Soc.*, **103** (8), S321–S323, <https://doi.org/10.1175/BAMS-D-22-0078.1>.
- MacLennan, M. L., and J. T. M. Lenaerts, 2021: Large-scale atmospheric drivers of snowfall over Thwaites Glacier, Antarctica. *Geophys. Res. Lett.*, **48**, e2021GL093644, <https://doi.org/10.1029/2021GL093644>.
- Manney, G. L., and Coauthors, 2011: Unprecedented Arctic ozone loss in 2011. *Nature*, **478**, 469–475, <https://doi.org/10.1038/nature10556>.
- Marshall, G. J., 2003: Trends in the Southern Annular Mode from observations and reanalyses. *J. Climate*, **16**, 4134–4143, [https://doi.org/10.1175/1520-0442\(2003\)0162.0.CO;2](https://doi.org/10.1175/1520-0442(2003)0162.0.CO;2).
- Maslanik, J., and J. Stroeve, 1999: Near-real-time DMSP SSM/I-SSMIS daily polar gridded sea ice concentrations. National Snow and Ice Data Center, accessed 9 March 2023, <https://doi.org/10.5067/U8C09DWVX9LM>.
- Massom, R. A., A. B. Giles, H. A. Fricker, R. C. Warner, B. Legrésy, G. Hyland, N. Young, and A. D. Fraser, 2010: Examining the interaction between multi-year landfast sea ice and the Mertz Glacier Tongue, East Antarctica: Another factor in ice sheet stability? *J. Geophys. Res.*, **115**, C12027, <https://doi.org/10.1029/2009JC006083>.
- , T. A. Scambos, L. G. Bennetts, P. Reid, V. A. Squire, and S. E. Stammerjohn, 2018: Antarctic ice shelf disintegration triggered by sea ice loss and ocean swell. *Nature*, **558**, 383–389, <https://doi.org/10.1038/s41586-018-0212-1>.
- Medley, B., and E. R. Thomas, 2019: Increased snowfall over the Antarctic ice sheet mitigated twentieth-century sea-level rise. *Nat. Climate Change*, **9**, 34–39, <https://doi.org/10.1038/s41558-018-0356-x>.
- Meier, W. N., H. Wilcox, M. A. Hardman, and J. S. Stewart, 2019: DMSP SSM/I-SSMIS daily polar gridded brightness temperatures, version 5. Subset: 37 & 19 GHz, h-polarization, 25 km grid, October 1987–April 2020. NASA National Snow and Ice Data Center Distributed Active Archive Center, accessed 11 February 2021, <https://doi.org/10.5067/QU2UYQ6T0B3P>.
- Millan, L., and Coauthors, 2022: Hunga Tonga-Hunga Ha’apai hydration of the stratosphere. *Geophys. Res. Lett.*, **49**, e2022GL099381, <https://doi.org/10.1029/2022GL099381>.
- Morlighem, M., and Coauthors, 2020: Deep glacial troughs and stabilizing ridges unveiled beneath the margins of the Antarctic ice sheet. *Nat. Geosci.*, **13**, 132–137, <https://doi.org/10.1038/s41561-019-0510-8>.
- Mote, T. L., 2007: Greenland surface melt trends 1973–2007: Evidence of a large increase in 2007. *Geophys. Res. Lett.*, **34**, L22507, <https://doi.org/10.1029/2007GL031976>.
- , 2014: MEASUREs Greenland surface melt daily 25km EASE-Grid 2.0, version 1. NASA National Snow and Ice Data Center Distributed Active Archive Center, accessed 30 August 2021, <https://doi.org/10.5067/MEASURES/CRYOSPHERE/nsidc-0533.001>.
- , and M. R. Anderson, 1995: Variations in snowpack melt on the Greenland ice sheet based on passive microwave measurements. *J. Glaciol.*, **41**, 51–60, <https://doi.org/10.3189/S0022143000017755>.
- Mottram, R., and Coauthors, 2021: What is the surface mass balance of Antarctica? An intercomparison of regional climate model estimates. *Cryosphere*, **15**, 3751–3784, <https://doi.org/10.5194/tc-15-3751-2021>.

- NASA, 2023a: OzoneWatch, 45°–75°S 45-day wave 1–3 total eddy heat flux, November monthly mean at 100 hPa. Accessed 10 February 2023, https://ozonewatch.gsfc.nasa.gov/meteorology/figures/merra2/heat_flux/vt1-3w45_75-45s_100_10_merra2.pdf.
- , 2023b: OzoneWatch, what is EESC? Accessed 10 February 2023, https://ozonewatch.gsfc.nasa.gov/facts/eesc_SH.html.
- Newman, P. A., S. R. Kawa, and E. R. Nash, 2004: On the size of the Antarctic ozone hole. *Geophys. Res. Lett.*, **31**, L21104, <https://doi.org/10.1029/2004GL020596>.
- , J. S. Daniel, D. W. Waugh, and E. R. Nash, 2007: A new formulation of equivalent effective stratospheric chlorine (EESC). *Atmos. Chem. Phys.*, **7**, 4537–4552, <https://doi.org/10.5194/acp-7-4537-2007>.
- Norwegian Polar Institute, 2018: Quantarctica v3.0, detailed base-map. www.npolar.no/quantarctica/.
- NSIDC, 2022: Antarctic sea ice minimum sets a record. 8 March, <http://nsidc.org/arcticseaicenews/2022/03/arctic-sea-ice-approaches-maximum-record-low-minimum-in-the-south/>.
- Ogle, S. E., V. Tamsitt, S. A. Josey, S. T. Gille, I. Cerovečki, L. D. Talley, and R. A. Weller, 2018: Episodic Southern Ocean heat loss and its mixed layer impacts revealed by the farthest south multi-year surface flux mooring. *Geophys. Res. Lett.*, **45**, 5002–5010, <https://doi.org/10.1029/2017GL076909>.
- Orsi, A. H., T. Whitworth, and W. D. Nowlin, 1995: On the meridional extent and fronts of the Antarctic Circumpolar Current. *Deep-Sea Res. I*, **42**, 641–673, [https://doi.org/10.1016/0967-0637\(95\)00021-W](https://doi.org/10.1016/0967-0637(95)00021-W).
- Paolo, F. S., H. A. Fricker, and L. Padman, 2015: Volume loss from Antarctic ice shelves is accelerating. *Science*, **348**, 327–331, <https://doi.org/10.1126/science.aaa0940>.
- Pitts, M. C., L. R. Poole, and R. Gonzalez, 2018: Polar stratospheric cloud climatology based on CALIPSO spaceborne lidar measurements from 2006 to 2017. *Atmos. Chem. Phys.*, **18**, 10881–10913, <https://doi.org/10.5194/acp-18-10881-2018>.
- Raphael, M. N., 2007: The influence of atmospheric zonal wave three on Antarctic sea ice variability. *J. Geophys. Res.*, **112**, D12112, <https://doi.org/10.1029/2006JD007852>.
- Reid, P. A., and R. A. Massom, 2015: Successive Antarctic sea ice extent records during 2012, 2013 and 2014 [in “State of the Climate in 2014”]. *Bull. Amer. Meteor. Soc.*, **96** (7), S163–S164, <https://doi.org/10.1175/2015BAMSStateoftheClimate.1>.
- , and R. A. Massom, 2022: Change and variability in Antarctic coastal exposure, 1979–2020. *Nat. Commun.*, **13**, 1164, <https://doi.org/10.1038/s41467-022-28676-z>.
- , S. Stammerjohn, R. A. Massom, J. Lieser, S. Barreira, and T. Scambos, 2018: Sea ice extent, concentration, and seasonality [in “State of the Climate in 2017”]. *Bull. Amer. Meteor. Soc.*, **99** (8), S183–S185, <https://doi.org/10.1175/2018BAMSStateoftheClimate.1>.
- , —, —, S. Barreira, T. Scambos, and J. L. Lieser, 2022: Sea ice extent, concentration, and seasonality [in “State of the Climate in 2021”]. *Bull. Amer. Meteor. Soc.*, **103** (8), S325–S329, <https://doi.org/10.1175/BAMS-D-22-0078.1>.
- Reynolds, R. W., N. A. Rayner, T. M. Smith, D. C. Stokes, and W. Wang, 2002: An improved in situ and satellite SST analysis for climate. *J. Climate*, **15**, 1609–1625, [https://doi.org/10.1175/1520-0442\(2002\)0152.0.CO;2](https://doi.org/10.1175/1520-0442(2002)0152.0.CO;2).
- Rignot, E., S. Jacobs, J. Mouginot, and B. Scheuchl, 2013: Ice-shelf melting around Antarctica. *Science*, **341**, 266–270, <https://doi.org/10.1126/science.1235798>.
- Roemmich, D., and J. Gilson, 2009: The 2004–2008 mean and annual cycle of temperature, salinity, and steric height in the global ocean from the Argo Program. *Prog. Oceanogr.*, **82**, 81–100, <https://doi.org/10.1016/j.pocean.2009.03.004>.
- Sallée, J.-B., 2018: Southern Ocean warming. *Oceanography*, **31**, 52–62, <https://doi.org/10.5670/oceanog.2018.215>.
- Scambos, T. A., J. A. Bohlander, C. A. Shuman, and P. Skvarca, 2004: Glacier acceleration and thinning after ice shelf collapse in the Larsen B embayment, Antarctica. *Geophys. Res. Lett.*, **31**, L18402, <https://doi.org/10.1029/2004GL020670>.
- , E. Berthier, T. Haran, C. A. Shuman, A. J. Cook, S. R. M. Ligtenberg, and J. Bohlander, 2014: Detailed ice loss pattern in the northern Antarctic Peninsula: Widespread decline driven by ice front retreats. *Cryosphere*, **8**, 2135–2145, <https://doi.org/10.5194/tc-8-2135-2014>.
- Schoeberl, M., Y. Wang, R. Ueyama, G. Taha, E. Jensen, and W. Yu, 2022: Analysis and impact of the Hunga Tonga-Hunga Ha’apai stratospheric water vapor plume. *Geophys. Res. Lett.*, **49**, e2022GL100248, <https://doi.org/10.1029/2022GL100248>.
- Seroussi, H., and Coauthors, 2020: ISMIP6 Antarctica: A multi-model ensemble of the Antarctic ice sheet evolution over the 21st century. *Cryosphere*, **14**, 3033–3070, <https://doi.org/10.5194/tc-14-3033-2020>.
- Shepherd, A., and Coauthors, 2012: A reconciled estimate of ice-sheet mass balance. *Science*, **338**, 1183–1189, <https://doi.org/10.1126/science.1228102>.
- Shepherd, J. G., P. G. Brewer, A. Oschlies, and A. J. Watson, 2017: Ocean ventilation and deoxygenation in a warming world: Introduction and overview. *Philos. Trans. Roy. Soc.*, **A375**, 20170240, <https://doi.org/10.1098/rsta.2017.0240>.
- Shi, J.-R., S.-P. Xie, and L. D. Talley, 2018: Evolving relative importance of the Southern Ocean and North Atlantic in anthropogenic ocean heat uptake. *J. Climate*, **31**, 7459–7479, <https://doi.org/10.1175/JCLI-D-18-0170.1>.
- , L. D. Talley, S.-P. Xie, Q. Peng, and W. Liu, 2021: Ocean warming and accelerating Southern Ocean zonal flow. *Nat. Climate Change*, **11**, 1090–1097, <https://doi.org/10.1038/s41558-021-01212-5>.
- Shuman, C. A., E. Berthier, and T. A. Scambos, 2011: 2001–2009 elevation and mass losses in the Larsen A and B embayments, Antarctic Peninsula. *J. Glaciol.*, **57**, 737–754, <https://doi.org/10.3189/002214311797409811>.
- Smith, B., and Coauthors, 2020a: Pervasive ice sheet mass loss reflects competing ocean and atmosphere processes. *Science*, **368**, 1239–1242, <https://doi.org/10.1126/science.aaz5845>.
- , and Coauthors, 2020b: ATLAS/ICESat-2 L3A land ice height, version 5. NASA National Snow and Ice Data Center Distributed Active Archive Center, accessed 25 January 2022, <https://doi.org/10.5067/ATLAS/ATL06.005>.
- Smith, T. M., R. W. Reynolds, T. C. Peterson, and J. Lawrimore, 2008: Improvements to NOAA’s historical merged land–ocean surface temperature analysis (1880–2006). *J. Climate*, **21**, 2283–2296, <https://doi.org/10.1175/2007JCLI2100.1>.
- Song, X., 2020: Explaining the zonal asymmetry in the air–sea net heat flux climatology over the Antarctic Circumpolar Current. *J. Geophys. Res. Oceans*, **125**, e2020JC016215, <https://doi.org/10.1029/2020JC016215>.
- Spreen, G., L. Kaleschke, and G. Heygster, 2008: Sea ice remote sensing using AMSR-E 89-GHz channels. *J. Geophys. Res.*, **113**, C02S03, <https://doi.org/10.1029/2005JC003384>.

- Squire, V. A., J. P. Dugan, P. Wadhams, P. J. Rottier, and A. K. Liu, 1995: Of ocean waves and sea ice. *Annu. Rev. Fluid Mech.*, **27**, 115–168, <https://doi.org/10.1146/annurev.fl.27.010195.000555>.
- Stammerjohn, S. E., D. G. Martinson, R. C. Smith, X. Yuan, and D. Rind, 2008: Trends in Antarctic annual sea ice retreat and advance and their relation to El Niño–Southern Oscillation and Southern Annular Mode variability. *J. Geophys. Res.*, **113**, C03S90, <https://doi.org/10.1029/2007JC004269>.
- Stone, K. A., S. Solomon, D. E. Kinnison, and M. J. Mills, 2021: On recent large Antarctic ozone holes and ozone recovery metrics. *Geophys. Res. Lett.*, **48**, e2021GL095232, <https://doi.org/10.1029/2021GL095232>.
- Strahan, S. E., A. R. Douglass, and M. R. Damon, 2019: Why do Antarctic ozone recovery trends vary? *J. Geophys. Res. Atmos.*, **124**, 8837–8850, <https://doi.org/10.1029/2019JD030996>.
- Swart, N. C., S. T. Gille, J. C. Fyfe, and N. P. Gillett, 2018: Recent Southern Ocean warming and freshening driven by greenhouse gas emissions and ozone depletion. *Nat. Geosci.*, **11**, 836–841, <https://doi.org/10.1038/s41561-018-0226-1>.
- Taha, G., R. Loughman, P. Colarco, T. Zhu, L. Thomason, and G. Jaross, 2022: Tracking the 2022 Hunga Tonga-Hunga Ha’apai aerosol cloud in the upper and middle stratosphere using space-based observations. *Geophys. Res. Lett.*, **49**, e2022GL100091, <https://doi.org/10.1029/2022GL100091>.
- Tamsitt, V., I. Cerovečki, S. A. Josey, S. T. Gille, and E. Schulz, 2020: Mooring observations of air–sea heat fluxes in two subantarctic mode water formation regions. *J. Climate*, **33**, 2757–2777, <https://doi.org/10.1175/JCLI-D-19-0653.1>.
- Teder, N. J., L. G. Bennetts, P. A. Reid, and R. A. Massom, 2022: Sea ice-free corridors for large swell to reach Antarctic ice shelves. *Environ. Res. Lett.*, **17**, 045026, <https://doi.org/10.1088/1748-9326/ac5edd>.
- The IMBIE Team, 2018: Mass balance of the Antarctic Ice Sheet from 1992 to 2017. *Nature*, **558**, 219–222, <https://doi.org/10.1038/s41586-018-0179-y>.
- Tolman, H. L., 2009: User manual and system documentation of WAVEWATCH III version 3.14. MMAB Rep. 276, NOAA/NCEP, 220 pp., https://polar.ncep.noaa.gov/mmab/papers/tm276/MMAB_276.pdf.
- Trusel, L. D., K. E. Frey, S. B. Das, K. B. Karnauskas, P. Kuipers Munneke, E. van Meijgaard, and M. R. van den Broeke, 2015: Divergent trajectories of Antarctic surface melt under two twenty-first-century climate scenarios. *Nat. Geosci.*, **8**, 927–932, <https://doi.org/10.1038/ngeo2563>.
- Trusel, L. D., Z. Pan, and M. Moussavi, 2022: Repeated tidally induced hydrofracture of a supraglacial lake at the Amery ice shelf grounding zone. *Geophys. Res. Lett.*, **49**, e2021GL095661, <https://doi.org/10.1029/2021GL095661>.
- Turner, J., and J. Comiso, 2017: Solve Antarctica’s sea-ice puzzle. *Nature*, **547**, 275–277, <https://doi.org/10.1038/547275a>.
- , T. Phillips, G. J. Marshall, J. S. Hosking, J. O. Pope, T. J. Bracegirdle, and P. Deb, 2017: Unprecedented springtime retreat of Antarctic sea ice in 2016: The 2016 Antarctic Sea Ice Retreat. *Geophys. Res. Lett.*, **44**, 6868–6875, <https://doi.org/10.1002/2017GL073656>.
- , and Coauthors, 2019: The dominant role of extreme precipitation events in Antarctic snowfall variability. *Geophys. Res. Lett.*, **46**, 3502–3511, <https://doi.org/10.1029/2018GL081517>.
- , and Coauthors, 2022: Record low Antarctic sea ice cover in February 2022. *Geophys. Res. Lett.*, **49**, e2022GL098904, <https://doi.org/10.1029/2022GL098904>.
- van Wessem, J. M., and Coauthors, 2018: Modelling the climate and surface mass balance of polar ice sheets using RACMO2 – Part 2: Antarctica (1979–2016). *Cryosphere*, **12**, 1479–1498, <https://doi.org/10.5194/tc-12-1479-2018>.
- Wang, H., J. G. Fyke, J. T. M. Lenaerts, J. M. Nusbaumer, H. Singh, D. Noone, P. J. Rasch, and R. Zhang, 2020: Influence of sea-ice anomalies on Antarctic precipitation using source attribution in the Community Earth System Model. *Cryosphere*, **14**, 429–444, <https://doi.org/10.5194/tc-14-429-2020>.
- Wang, J., H. Luo, Q. Yang, J. Liu, L. Yu, Q. Shi, and B. Han, 2022: An unprecedented record low Antarctic sea-ice extent during austral summer 2022. *Adv. Atmos. Sci.*, **39**, 1591–1597, <https://doi.org/10.1007/s00376-022-2087-1>.
- Wang, Y., and Coauthors, 2016: A comparison of Antarctic ice sheet surface mass balance from atmospheric climate models and in situ observations. *J. Climate*, **29**, 5317–5337, <https://doi.org/10.1175/JCLI-D-15-0642.1>.
- Wernli, H., and H. C. Davies, 1997: A Lagrangian-based analysis of extratropical cyclones. I: The method and some applications. *Quart. J. Roy. Meteor. Soc.*, **123**, 467–489, <https://doi.org/10.1002/qj.49712353811>.
- Wiese, D. N., D.-N. Yuan, C. Boening, F. W. Landerer, and M. M. Watkins, 2023a: JPL GRACE mascon ocean, ice, and hydrology equivalent water height RL06.1 CRI filtered version 3. Ver. RL06.1Mv03. PO.DAAC, accessed 10 February 2023, <https://doi.org/10.5067/TEMSC-3JC63>.
- , —, —, —, and —, 2023b: Tellus Level-4 ocean mass anomaly time series from JPL GRACE/GRACE-FO mascon CRI filtered release 6.1 version 3. Ver. RL06.1Mv03. PO.DAAC, accessed 10 February 2023, <https://doi.org/10.5067/TEMSC-AT613>.
- Wille, J. D., and Coauthors, 2021: Antarctic atmospheric river climatology and precipitation impacts. *J. Geophys. Res. Atmos.*, **126**, e2020JD033788, <https://doi.org/10.1029/2020JD033788>.
- Zhang, L., T. L. Delworth, X. Yang, F. Zeng, F. Lu, Y. Morioka, and M. Bushuk, 2022: The relative role of the subsurface Southern Ocean in driving negative Antarctic sea ice extent anomalies in 2016–2021. *Commun. Earth Environ.*, **3**, 302, <https://doi.org/10.1038/s43247-022-00624-1>.
- Zhao, X., H. H. Shen, and S. Cheng, 2015: Modeling ocean wave propagation under sea ice covers. *Acta Mech. Sin.*, **31** (1), 1–15, <https://doi.org/10.1007/s10409-015-0017-5>.

STATE OF THE CLIMATE IN 2022

REGIONAL CLIMATES

P. Bissolli, C. Ganter, A. Mekonnen, A. Sánchez-Lugo, and Z. Zhu, Eds.



Special Online Supplement to the *Bulletin of the American Meteorological Society* Vol. 104, No. 9, September, 2023

https://doi.org/10.1175/2023BAMSSStateoftheClimate_Chapter7.1

Corresponding authors:

North America: Ahira Sánchez-Lugo / Ahira.Sanchez-Lugo@noaa.gov.

Central America and the Caribbean: Ahira Sánchez-Lugo / Ahira.Sanchez-Lugo@noaa.gov

South America: Ahira Sánchez-Lugo / Ahira.Sanchez-Lugo@noaa.gov

Africa: Ademe Mekonnen / amekonne@ncat.edu

Europe: Peter Bissolli / Peter.Bissolli@dwd.de

Asia: Zhiwei Zhu / zwz@nuist.edu.cn

Oceania: Catherine Ganter / Catherine.Ganter@bom.gov.au

©2023 American Meteorological Society

For information regarding reuse of this content and general copyright information, consult the [AMS Copyright Policy](#).

STATE OF THE CLIMATE IN 2022

Regional Climates

Editors

Ellen Bartow-Gillies
Jessica Blunden
Tim Boyer

Chapter Editors

Peter Bissolli
Kyle R. Clem
Howard J. Diamond
Matthew L. Druckenmiller
Robert J. H. Dunn
Catherine Ganter
Nadine Gobron
Gregory C. Johnson
Rick Lumpkin
Ademe Mekonnen
John B. Miller
Twila A. Moon
Marilyn N. Raphael
Ahira Sánchez-Lugo
Carl J. Schreck III
Richard L. Thoman
Kate M. Willett
Zhiwei Zhu

Technical Editor

Lukas Noguchi

BAMS Special Editor for Climate

Michael A. Alexander

American Meteorological Society

Cover Credit:

Photo by Jiangxi Meteorological Bureau

Poyang Lake, China's largest freshwater lake in the Yangtze River basin, is dry on 2 September 2022 after the strongest recorded heatwave and drought on record in the region.

How to cite this document:

Regional Climates is one chapter from the *State of the Climate in 2022* annual report and is available from https://doi.org/10.1175/2023BAMSSateoftheClimate_Chapter7.1. Compiled by NOAA's National Centers for Environmental Information, *State of the Climate in 2022* is based on contributions from scientists from around the world. It provides a detailed update on global climate indicators, notable weather events, and other data collected by environmental monitoring stations and instruments located on land, water, ice, and in space. The full report is available from <https://doi.org/10.1175/2023BAMSSateoftheClimate.1>.

Citing the complete report:

Blunden, J., T. Boyer, and E. Bartow-Gillies, Eds., 2023: "State of the Climate in 2022". Bull. Amer. Meteor. Soc., 104 (9), Si–S501 <https://doi.org/10.1175/2023BAMSSateoftheClimate.1>.

Citing this chapter:

Bissolli, P., C. Ganter, A. Mekonnen, A. Sánchez-Lugo, and Z. Zhu, Eds., 2023: Regional Climates [in "State of the Climate in 2022"]. Bull. Amer. Meteor. Soc., 104 (9), S366–S473, https://doi.org/10.1175/2023BAMSSateoftheClimate_Chapter7.1.

Citing a section (example):

Aldeco, L. S., J. S. Stella, A. J. Reyes Kohler, N. Misevicius, and G. Jadra, 2023: Southern South America [in "State of the Climate in 2022"]. Bull. Amer. Meteor. Soc., 104 (9), S393–S396, https://doi.org/10.1175/2023BAMSSateoftheClimate_Chapter7.1.

Editor and Author Affiliations (alphabetical by name)

- Abida, A.**, Agence Nationale de l'Aviation Civile et de la Météorologie, Moroni, Union of the Comoros
- Agyakwah, W.**, NOAA/NWS National Centers for Environmental Prediction Climate Prediction Center, College Park, Maryland
- Aldeco, Laura S.**, Servicio Meteorológico Nacional, Buenos Aires, Argentina
- Alfaro, Eric J.**, Center for Geophysical Research and School of Physics, University of Costa Rica, San José, Costa Rica
- Alves, Lincoln M.**, Centro Nacional de Monitoramento e Alertas de Desastres Naturais CEMADEN, São Paulo, Brazil
- Amador, Jorge A.**, Center for Geophysical Research and School of Physics, University of Costa Rica, San José, Costa Rica
- Andrade, B.**, Seychelles Meteorological Authority, Mahe, Seychelles
- Avalos, Grinia**, Servicio Nacional de Meteorología e Hidrología del Perú, Lima, Perú
- Bader, Stephan**, Federal Office of Meteorology and Climatology MeteoSwiss, Switzerland
- Baez, Julian**, Universidad Católica Nuestra Señora de la Asunción, Asunción, Paraguay
- Bardin, M. Yu.**, Yu. A. Izrael Institute of Global Climate and Ecology, Institute of Geography, Russian Academy of Sciences, Moscow, Russia
- Bekele, E.**, NOAA/NWS National Centers for Environmental Prediction Climate Prediction Center, College Park, Maryland
- Bellido, Guillem Martín**, Govern d'Andorra, Andorra la Vella, Andorra
- Berne, Christine**, Météo France, Toulouse, France
- Bhuiyan, MD A. E.**, NOAA/NWS Climate Prediction Center, Silver Spring, Maryland
- Bissolli, Peter**, Deutscher Wetterdienst, WMO RA VI Regional Climate Centre Network, Offenbach, Germany
- Bochníček, Oliver**, Slovak Hydrometeorological Institute, Bratislava, Slovakia
- Bukunt, Brandon**, NOAA/NWS Weather Forecast Office, Tiyan, Guam
- Calderón, Blanca**, Center for Geophysical Research, University of Costa Rica, San José, Costa Rica
- Campbell, Jayaka**, Department of Physics, The University of the West Indies, Kingston, Jamaica
- Chandler, Elise**, Bureau of Meteorology, Melbourne, Australia
- Chen, Hua**, Nanjing University of Information Science and Technology, Nanjing, China
- Cheng, Vincent Y. S.**, Environment and Climate Change Canada, Toronto, Ontario, Canada
- Clarke, Leonardo**, Department of Physics, The University of the West Indies, Kingston, Jamaica
- Correa, Kris**, Servicio Nacional de Meteorología e Hidrología del Perú, Lima, Perú
- Costa, Felipe**, Centro Internacional para la Investigación del Fenómeno de El Niño (CIIFEN), Guayaquil, Ecuador
- Crhova, Lenka**, Czech Hydrometeorological Institute, Prague, Czech Republic
- Cunha, Ana P.**, Centro Nacional de Monitoramento e Alertas de Desastres Naturais CEMADEN, São Paulo, Brazil
- De Bock, Veerle**, Royal Meteorological Institute of Belgium (KMI), Brussels, Belgium
- Demircan, Mesut**, Turkish State Meteorological Service, Iğdir, Türkiye
- Deus, Ricardo**, Portuguese Sea and Atmosphere Institute, Lisbon, Portugal
- Dhurmea, K. R.**, Mauritius Meteorological Service, Vacoas, Mauritius
- Dirkse, S.**, Namibia Meteorological Service, Windhoek, Namibia
- Drumond, Paula**, Portuguese Sea and Atmosphere Institute, Lisbon, Portugal
- Dulamsuren, Dashkhuu**, Institute of Meteorology, Hydrology and Environment, National Agency for Meteorology, Ulaanbaatar, Mongolia
- Ekici, Mithat**, Turkish State Meteorological Service, Ankara, Türkiye
- ElKharrim, M.**, Direction de la Météorologie Nationale Maroc, Rabat, Morocco
- Espinoza, Jhan-Carlo**, Université Grenoble Alpes, Institut des Géosciences de l'Environnement, IRD, CNRS, Grenoble INP, Grenoble, France
- Fenimore, Chris**, NOAA/NESDIS National Centers for Environmental Information, Asheville, North Carolina
- Fogarty, Chris**, Environment and Climate Change Canada, Dartmouth, Nova Scotia, Canada
- Fuhrman, Steven**, NOAA/NWS NOAA/NWS National Centers for Environmental Prediction Climate Prediction Center, College Park, Maryland
- Ganter, Catherine**, Bureau of Meteorology, Melbourne, Australia
- Gleason, Karin**, NOAA/NESDIS National Centers for Environmental Information, Asheville, North Carolina
- Guard, Charles "Chip" P.**, Tropical Weather Sciences, Sinajana, Guam
- Hagos, S.**, Pacific Northwest National Lab, Department of Energy, Richland, Washington
- Heim, Richard R. Jr.**, NOAA/NESDIS National Centers for Environmental Information, Asheville, North Carolina
- Hellström, Sverker**, Swedish Meteorological and Hydrological Institute, Norrköping, Sweden
- Hicks, J.**, NOAA/NWS National Centers for Environmental Prediction Climate Prediction Center, College Park, Maryland
- Hidalgo, Hugo G.**, Center for Geophysical Research and School of Physics, University of Costa Rica, San José, Costa Rica
- Huang, Hongjie**, Nanjing University of Information Science and Technology, Nanjing, China
- Jadra, Gerardo**, Instituto Uruguayo de Meteorología, Montevideo, Uruguay
- Jumaux, G.**, Météo France, Direction Interregionale Pour L'Océan Indien, Reunion
- Kabidi, K.**, Direction de la Météorologie Nationale Maroc, Rabat, Morocco
- Kazemi, Amin Fazl**, Iran National Climate and Drought Crisis Management, National Meteorology Organization, Tehran, Iran
- Kendon, Mike**, Met Office National Climate Information Centre, Exeter, United Kingdom
- Kerr, Kenneth**, Trinidad and Tobago Meteorological Service, Piarco, Trinidad
- Khan, Valentina**, Hydrometcenter of Russia, WMO North EurAsia Climate Center, Moscow, Russia
- Khiem, Mai Van**, Vietnam National Center for Hydro-Meteorological Forecasting, Vietnam Meteorological and Hydrological Administration, Hanoi, Vietnam
- Kim, Mi Ju**, Climate Change Monitoring Division, Korea Meteorological Administration, Seoul, South Korea
- Korshunova, Natalia N.**, All-Russian Research Institute of Hydrometeorological Information, World Data Center, Obninsk, Russia
- Kruger, A. C.**, Climate Service, South African Weather Service, Pretoria, South Africa
- Lakatos, Mónika**, Climatology Unit, Hungarian Meteorological Service, Budapest, Hungary
- Lam, Hoang Phuc**, Vietnam National Center for Hydro-Meteorological Forecasting, Vietnam Meteorological and Hydrological Administration, Hanoi, Vietnam
- Lavado-Casimiro, Waldo**, Servicio Nacional de Meteorología e Hidrología del Perú, Lima, Perú
- Lee, Tsz-Cheung**, Hong Kong Observatory, Hong Kong, China
- Leung, Kinson H. Y.**, Environment and Climate Change Canada, Toronto, Ontario, Canada
- Likso, Tanja**, Croatian Meteorological and Hydrological Service, Zagreb, Croatia
- Lu, Rui**, Nanjing University of Information Science and Technology, Nanjing, China
- Mamen, Jostein**, Climate Division, Norwegian Meteorological Institute, Oslo, Norway
- Marcinonienė, Izolda**, Lithuanian Hydrometeorological Service, Vilnius, Lithuania
- Marengo, Jose A.**, Centro Nacional de Monitoramento e Alertas de Desastres Naturais CEMADEN, São Paulo, Brazil
- Marjan, Mohammadi**, Iran National Climate and Drought Crisis Management, National Meteorology Organization, Tehran, Iran

Editor and Author Affiliations (continued)

- Martínez, Ana E.**, National Meteorological Service of Mexico, Mexico City, Mexico
- McBride, C.**, Climate Service, South African Weather Service, Pretoria, South Africa
- Mekonnen, A.**, North Carolina A&T University, Greensboro, North Carolina
- Meyers, Tristan**, National Institute of Water and Atmospheric Research, Ltd. (NIWA), Auckland, New Zealand
- Misevicius, Noelia**, Instituto Uruguayo de Meteorología, Montevideo, Uruguay
- Moise, Aurel**, Centre for Climate Research Singapore, Meteorological Service Singapore, Singapore
- Molina-Carpio, Jorge**, Universidad Mayor de San Andrés, La Paz, Bolivia
- Mora, Natali**, Center for Geophysical Research, University of Costa Rica, San José, Costa Rica
- Morán, Johnny**, Centro Internacional para la Investigación del Fenómeno de El Niño (CIIFEN), Guayaquil, Ecuador
- Morehen, Claire**, Environment and Climate Change Canada, Vancouver, British Columbia, Canada
- Mostafa, A. E.**, Department of Seasonal Forecast and Climate Research, Cairo Numerical Weather Prediction, Egyptian Meteorological Authority, Cairo, Egypt
- Nieto, Juan J.**, Centro Internacional para la Investigación del Fenómeno de El Niño (CIIFEN), Guayaquil, Ecuador
- Oikawa, Yoshinori**, Tokyo Climate Center, Japan Meteorological Agency, Tokyo, Japan
- Okunaka, Yuka**, Tokyo Climate Center, Japan Meteorological Agency, Tokyo, Japan
- Pascual Ramírez, Reynaldo**, National Meteorological Service of Mexico, Mexico City, Mexico
- Perčec Tadić, Melita**, Croatian Meteorological and Hydrological Service, Zagreb, Croatia
- Pires, Vanda**, Portuguese Sea and Atmosphere Institute, Lisbon, Portugal
- Quisbert, Kenny**, Servicio Nacional de Meteorología e Hidrología de Bolivia, La Paz, Bolivia
- Quispe, Willy R.**, Servicio Nacional de Meteorología e Hidrología de Bolivia, La Paz, Bolivia
- Rajeevan, M.**, Ministry of Earth Sciences, New Delhi, India
- Ramos, Andrea M.**, Instituto Nacional de Meteorología, Brasilia, Brazil
- Recalde, Cristina**, NOAA/NWS National Centers for Environmental Prediction, Climate Prediction Center, College Park, Maryland
- Reyes Kohler, Alejandra J.**, Dirección de Meteorológica de Chile, Santiago de Chile, Chile
- Robjhon, M.**, NOAA/NWS National Centers for Environmental Prediction Climate Prediction Center, College Park, Maryland
- Rodriguez Guisado, Esteban**, Agencia Estatal de Meteorología, Madrid, Spain
- Ronchail, Josyane**, Laboratoire LOCEAN-IPSL, Paris, France
- Rösner, Benjamin**, Laboratory for Climatology and Remote Sensing, Faculty of Geography, University of Marburg, Marburg, Germany
- Rösner, Henrieke**, Humboldt University, Berlin, Germany
- Rubek, Frans**, Danish Meteorological Institute, Copenhagen, Denmark
- Salinas, Roberto**, Dirección de Meteorología e Hidrología / Dirección Nacional de Aeronáutica Civil, Asunción, Paraguay
- Sánchez-Lugo, Ahira**, NOAA/NESDIS National Centers for Environmental Information, Asheville, North Carolina
- Sayouri, A.**, Direction de la Météorologie Nationale Maroc, Rabat, Morocco
- Schimanke, Semjon**, Swedish Meteorological and Hydrological Institute, Norrköping, Sweden
- Segele, Z. T.**, NOAA/NWS National Centers for Environmental Prediction Climate Prediction Center, College Park, Maryland
- Sensoy, Serhat**, Turkish State Meteorological Service, Ankara, Türkiye
- Setiawan, Amsari Mudzakir**, Division for Climate Variability Analysis, BMKG, Jakarta, Indonesia
- Shukla, R.**, NOAA/NWS National Centers for Environmental Prediction Climate Prediction Center, College Park, Maryland
- Sima, F.**, Division of Meteorology, Department of Water Resources, Banjul, The Gambia
- Smith, Adam**, NOAA/NESDIS National Centers for Environmental Information, Asheville, North Carolina
- Spence-Hemmings, Jacqueline**, Meteorological Service, Jamaica, Kingston, Jamaica
- Spillane, Sandra**, Climate Services Division, Met Éireann, The Irish Meteorological Service, Dublin, Ireland
- Spillane, Sandra**, Met Éireann, Dublin, Ireland
- Sreejith, O. P.**, India Meteorological Department, Pune, India
- Srivastava, A. K.**, India Meteorological Department, Pune, India
- Stella, Jose L.**, Servicio Meteorológico Nacional, Buenos Aires, Argentina
- Stephenson, Tannecia S.**, Department of Physics, The University of the West Indies, Kingston, Jamaica
- Takahashi, Kiyotoshi**, Tokyo Climate Center, Japan Meteorological Agency, Tokyo, Japan
- Takemura, Kazuto**, Tokyo Climate Center, Japan Meteorological Agency, Tokyo, Japan
- Taylor, Michael A.**, Department of Physics, The University of the West Indies, Kingston, Jamaica
- Thiaw, W. M.**, NOAA/NWS National Centers for Environmental Prediction Climate Prediction Center, College Park, Maryland
- Tobin, Skie**, Bureau of Meteorology, Melbourne, Australia
- Trescilo, Lidia**, State Hydrometeorological Service, Chisinau, Republic of Moldova
- Trotman, Adrian**, Caribbean Institute for Meteorology and Hydrology, Bridgetown, Barbados
- van der Schrier, Gerard**, Royal Netherlands Meteorological Institute (KNMI), De Bilt, The Netherlands
- Van Meerbeeck, Cedric J.**, Caribbean Institute for Meteorology and Hydrology, Bridgetown, Barbados
- Vazife, Ahad**, Iran National Climate and Drought Crisis Management, National Meteorology Organization, Tehran, Iran
- Willems, An**, Royal Meteorological Institute of Belgium (KMI), Brussels, Belgium
- Zhang, Peiqun**, Beijing Climate Center, Beijing, China
- Zhu, Zhiwei**, Nanjing University of Information Science and Technology, Nanjing, China

Editorial and Production Team

Allen, Jessica, Graphics Support, Cooperative Institute for Satellite Earth System Studies, North Carolina State University, Asheville, North Carolina

Camper, Amy V., Graphics Support, Innovative Consulting and Management Services, LLC, NOAA/NESDIS National Centers for Environmental Information, Asheville, North Carolina

Haley, Bridgette O., Graphics Support, NOAA/NESDIS National Centers for Environmental Information, Asheville, North Carolina

Hammer, Gregory, Content Team Lead, Communications and Outreach, NOAA/NESDIS National Centers for Environmental Information, Asheville, North Carolina

Love-Brotak, S. Elizabeth, Lead Graphics Production, NOAA/NESDIS National Centers for Environmental Information, Asheville, North Carolina

Ohlmann, Laura, Technical Editor, Innovative Consulting and Management Services, LLC, NOAA/NESDIS National Centers for Environmental Information, Asheville, North Carolina

Noguchi, Lukas, Technical Editor, Innovative Consulting and Management Services, LLC, NOAA/NESDIS National Centers for Environmental Information, Asheville, North Carolina

Riddle, Deborah B., Graphics Support, NOAA/NESDIS National Centers for Environmental Information, Asheville, North Carolina

Veasey, Sara W., Visual Communications Team Lead, Communications and Outreach, NOAA/NESDIS National Centers for Environmental Information, Asheville, North Carolina

7. Table of Contents

List of authors and affiliations	S369
a. Overview	S374
b. North America	S374
1. Canada.....	S374
2. United States.....	S377
3. Mexico.....	S380
c. Central America and the Caribbean	S382
1. Central America.....	S382
2. Caribbean.....	S384
Sidebar 7.1: Notable events across Central America.....	S386
d. South America	S388
1. Northern South America.....	S388
2. Central South America.....	S390
3. Southern South America.....	S393
e. Africa	S397
1. North Africa.....	S398
2. West Africa.....	S401
3. Central Africa.....	S404
4. East Africa.....	S407
5. Southern Africa.....	S409
6. Western Indian Ocean island countries.....	S413
f. Europe and the Middle East	S416
1. Overview.....	S417
2. Western Europe.....	S420
3. Central Europe.....	S422
4. Iberian Peninsula.....	S424
5. The Nordic and Baltic countries.....	S426
6. Central Mediterranean region.....	S427
7. Eastern Europe.....	S430
8. Middle East.....	S431
9. Türkiye and South Caucasus.....	S433
g. Asia	S435
1. Overview.....	S435
2. Russia.....	S438
3. East and Southeast Asia.....	S441
Sidebar 7.2: The record-breaking hot summer of 2022 in the Yangtze River basin.....	S443
4. South Asia.....	S445
5. Southwest Asia.....	S447
6. Central Asia.....	S449

7. Table of Contents

h. Oceania	S452
1. Overview.....	S452
2. Northwest Pacific and Micronesia.....	S452
3. Southwest Pacific.....	S456
4. Australia.....	S460
5. New Zealand.....	S463
Acknowledgments	S466
Appendix 1: Chapter 7 – Acronyms	S467
Appendix 2: Chapter 7 – Supplemental Materials	S469
References	S472

Please refer to Chapter 8 (Relevant Datasets and Sources) for a list of all climate variables and datasets used in this chapter for analyses, along with their websites for more information and access to the data.

7. REGIONAL CLIMATES

P. Bissolli, C. Ganter, A. Mekonnen, A. Sánchez-Lugo, and Z. Zhu, Eds.

a. Overview

This chapter provides summaries of the 2022 temperature and precipitation conditions across seven broad regions: North America, Central America and the Caribbean, South America, Africa, Europe and the Middle East, Asia, and Oceania. In most cases, summaries of notable weather events are also included. Local scientists provided the annual summary for their respective regions and, unless otherwise noted, the source of the data used is typically the agency affiliated with the authors. The base period used for these analyses is 1991–2020, unless otherwise stated. Please note that on occasion different nations, even within the same section, may use unique periods to define their normal. Section introductions typically define the prevailing practices for that section, and exceptions will be noted within the text. In a similar way, many contributing authors use languages other than English as their primary professional language. To minimize additional loss of fidelity through re-interpretation after translation, editors have been conservative and careful to preserve the voice of the author. In some cases, this may result in abrupt transitions in style from section to section.

b. North America

—A. Sánchez-Lugo, Ed.

Below-average annual temperatures were observed across central Canada, the northern contiguous United States, and parts of northern and western Mexico during 2022, while the rest of the region experienced near- to above-average annual temperatures. Averaged as a whole, North America's annual temperature was 1.00°C above the 1991–2020 base period and the 16th-warmest year in the 113-year continental record (extends back to 1910).

Precipitation varied across the region, with significant annual deficits across parts of western and central contiguous United States and northeastern and central Mexico. Several significant events occurred during the year, including Hurricanes Fiona and Ian, among others.

Anomalies in this section are all based on the 1991–2020 base period, unless otherwise noted.

1. CANADA

—K. H. Y. Leung, V. Y. S. Cheng, C. Fogarty, and C. Morehen

In Canada, the national 2022 average temperatures for summer and autumn ranked among the six warmest such periods in the nation's 75-year record (1948–2022). The national winter and spring temperatures were below the 1991–2020 average and ranked seasonally as the 27th lowest and 30th highest, respectively. Overall, Canada had its 16th-warmest year on record. The temperature records presented in this section are based on adjusted and homogenized Canadian climate data.

(i) Temperature

The annual 2022 average temperature for Canada was 0.1°C above the 1991–2020 average and ranked as the 16th-warmest year on record (Fig. 7.1). Over the past 75 years (1948–2022), the national annual average temperature exhibited a warming of 1.9°C and 3 of the 10 warmest years have occurred since 2012. Spatially, annual anomalies of more than +1.0°C were recorded in easternmost Canada, and anomalies of more than +0.5°C were recorded mainly in northeastern and small regions of western Canada. In 2022, 4 of the 13 provinces and territories (Nova Scotia, Prince Edward Island, New Brunswick, and Newfoundland and Labrador) experienced annual average temperatures that were among their 10 highest in the 75-year record. Annual anomalies of more than –0.5°C were observed in areas from central Saskatchewan to northern Ontario, along with small areas in southern British Columbia. Temperatures of more than 1.5°C below average were recorded in the regions between the provincial border of southern Manitoba and northern Ontario (Fig. 7.2).

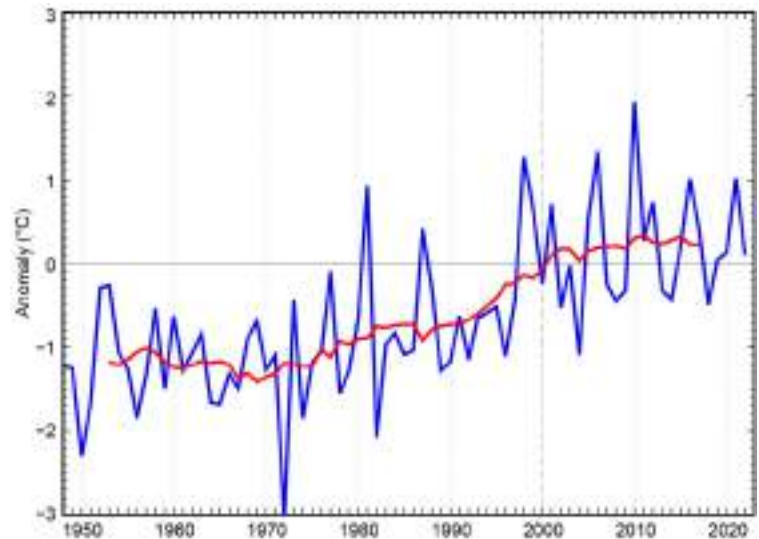


Fig. 7.1. Annual average temperature anomalies (°C; 1991–2020 base period) in Canada for the period 1948–2022. Red line is the 11-year running mean. (Source: Environment and Climate Change Canada.)

Seasonally, the national average temperature for winter (December 2021–February 2022) was 1.6°C below average, making it the 27th-coolest winter on record. Winter anomalies of –4.5°C were recorded over the southeastern portion of Northwest Territories as well as northern Saskatchewan. Most of Canada experienced winter temperatures at least 0.5°C below average. However, above-average temperatures were recorded in most of Labrador, Prince Edward Island, Nova Scotia, and northeastern Nunavut. The national average temperature for winter has increased by 3.4°C over the past 75 years.

During spring (March–May), temperature departures of at least –0.5°C were observed mainly in British Columbia and from central Yukon southeastward to northern Ontario. Above-average temperatures were recorded in northern Nunavut, northern and southern Quebec, southern Ontario, and most of the Atlantic provinces. The rest of the country experienced near-average temperatures. Although the national average temperature for spring 2022 was 0.2°C below the 1991–2020 average, it was still the 30th-warmest spring on record. The most anomalously warm spring was observed in the northernmost region of Nunavut, with temperature departures of more than +2.0°C. The national average spring temperature has increased by 1.6°C over the past 75 years.



Fig. 7.2. Annual average temperature anomalies (°C; 1991–2020 base period) in Canada for 2022. (Source: Environment and Climate Change Canada.)

Labrador. Nine of the 13 provinces and territories had temperatures among their 10 highest on record for summer. The national average summer temperature has increased by 1.6°C over the past 75 years.

The national average temperature for autumn (September–November) was 1.0°C above average and the sixth highest on record. Most of Canada experienced temperatures at least 0.5°C above average, with the Northwest Territories, New Brunswick and some areas in Yukon, northern British Columbia, Alberta, Saskatchewan, Manitoba, Ontario, Quebec, and Nova Scotia experiencing temperatures 1.5°C to 3.0°C above average. Only a small region in northern and eastern Nunavut experienced below-average temperatures. Prince Edward Island had its highest autumn temperature on record, Nova Scotia had its second highest, and New Brunswick and Northwest Territories had their third highest. The national average autumn temperature has increased by 1.8°C over the past 75 years.

(ii) Precipitation

Over the past decade, precipitation monitoring technology has evolved and Environment and Climate Change Canada (ECCC) and its partners have implemented a transition from manual observations to the use of automatic precipitation gauges. Extensive data integration is required to link the current precipitation observations to the long-term historical manual observations. The updating and reporting of historical adjusted precipitation trends and variations will be on temporary hiatus pending an extensive data reconciliation, and will be resumed thereafter. ECCC remains committed to providing credible climate data to inform adaptation decision-making while also ensuring that necessary data reconciliation occurs as monitoring technology evolves.

(iii) Notable events and impacts

On 21 May, a line of widespread and fast-moving thunderstorms traversed 1000 km from southwestern Ontario to Quebec City. These storms featured torrential rains, hail, and a cluster of straight-line downburst winds (i.e., a derecho). Four tornadoes were also associated with this event, with two Enhanced Fujita (EF)-1s occurring in the London area (with maximum winds between 160 km h⁻¹ and 175 km h⁻¹) along with two EF-2s near Toronto and Oshawa (with maximum winds between 180 km h⁻¹ and 195 km h⁻¹). Most of the weather stations along the derecho's path recorded wind gusts near or above 100 km h⁻¹. The derecho lasted approximately 11 hours and caused 11 fatalities and widespread damage in a swath over 100 km wide. Winds devastated farm properties in rural areas, while more than a million customers across Ontario and Quebec were left without power. The event caused more than \$1 billion Canadian dollars (\$750 million U.S. dollars) in damage—the sixth-costliest natural disaster in Canadian history in terms of insured losses. The last time Canada experienced a derecho of this ferocity was in July 1999, when a long line of storms swept into Ontario from Minnesota.

Hurricane Fiona, another devastating storm, made landfall in eastern Nova Scotia on 24 September as a Category 2-strength post-tropical cyclone with a minimum extrapolated sea-level pressure of 931 hPa. Fiona was the most intense and destructive tropical or post-tropical cyclone ever recorded for Canada's Atlantic coast. Fiona's maximum sustained winds at the time of landfall in Nova Scotia were around 165 km h⁻¹. It was the strongest storm in Canadian history (as gauged by barometric pressure), with a pressure of 932.7 hPa measured on Hart Island, Nova Scotia, which was used to determine the extrapolated central pressure of 931 hPa at the moment of landfall. A record-high water height (before waves) of 2.73 meters was also recorded in Channel-Port aux Basques, Newfoundland. Numerous homes were damaged or destroyed in Newfoundland, with almost 200 people displaced and more than 500,000 left without power. Fiona became the costliest weather event in Atlantic Canada's history with insured losses estimated to be at least \$800 million Canadian dollars (\$600 million U.S. dollars). Please refer to section 4g2 and Sidebar 4.1 for more information about Hurricane Fiona.

2. UNITED STATES

—K. Gleason, C. Fenimore, R. R. Heim Jr., and A. Smith

The annual average temperature for the contiguous United States (CONUS) in 2022 was 11.9°C, which was 0.1°C above the 1991–2020 average and equal with 1953 as the 18th-warmest year in the 128-year record (Fig. 7.3a). Below-average temperatures were concentrated across the Upper Midwest while above-average temperatures were scattered across parts of California, Texas, Florida, and New England (Fig. 7.4a). Based on a linear regression of data from 1895 to 2022, the annual CONUS temperature is increasing at an average rate of 0.09°C decade⁻¹ (0.27°C decade⁻¹ since 1970). Average precipitation for the nation totaled 722 mm, which is 91% of the 1991–2020 average (Fig. 7.3). However, the annual precipitation total has been increasing at an average rate of 5 mm decade⁻¹ since 1895 (2 mm decade⁻¹ since 1970). The average annual temperature across Alaska in 2022 was 0.4°C above average and was 16th highest on record. The annual temperature for Alaska over its 98-year record is increasing at an average rate of 0.17°C decade⁻¹ since 1925 (0.44°C decade⁻¹ since 1970).

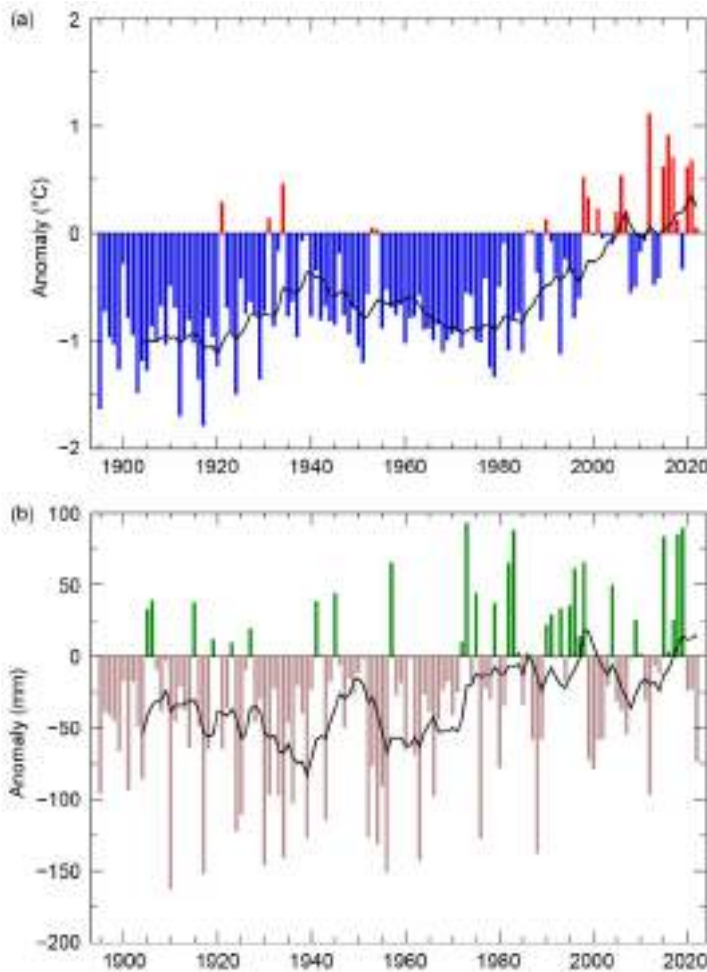


Fig. 7.3. Annual (a) mean temperature anomalies (°C) and (b) precipitation anomalies (mm; 1991–2020 base period) for the contiguous United States during 1895–2022. The black line is the lagged 10-year running mean. (Source: NOAA/NCEI.)

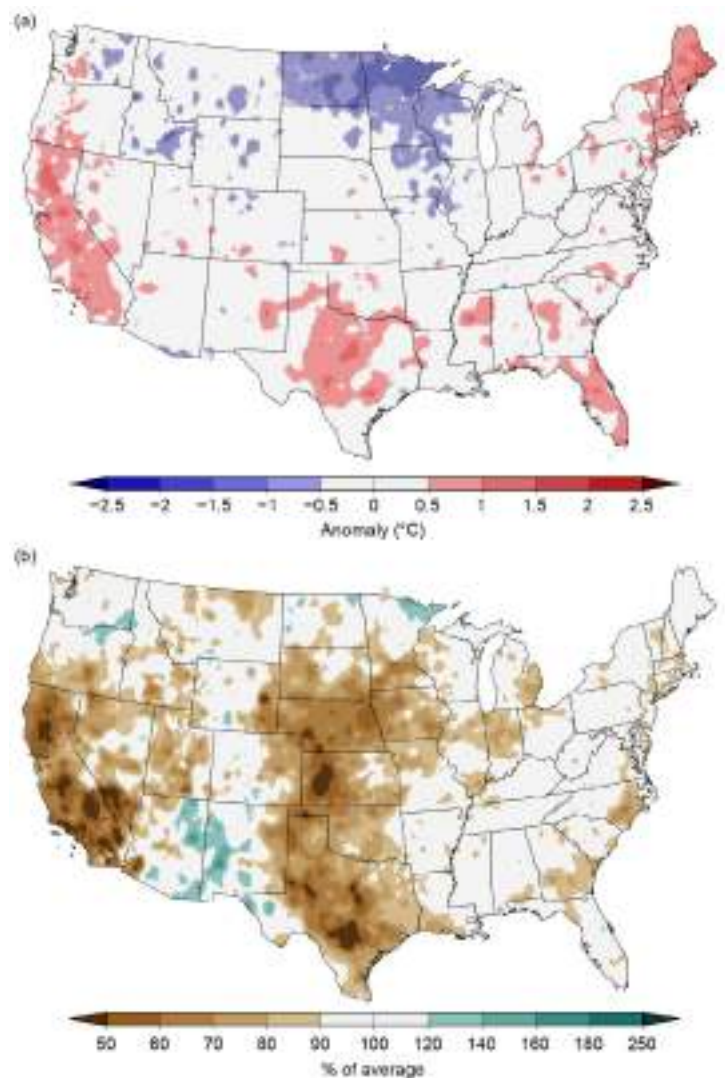


Fig. 7.4. Annual (a) average temperature anomalies (°C) and (b) total precipitation (% of average) in the contiguous United States for 2022 (1991–2020 base period). (Source: NOAA/NCEI.)

(i) Temperature

The winter (December–February) 2021/22 CONUS temperature was 0.4°C above average, with most of the anomalous warmth in the Southeast. The CONUS spring (March–May) temperature was near average, with above-average temperatures spanning from California to the Mississippi River and from the Gulf Coast to New England and below-average temperatures extending from Washington State to the Great Lakes. The summer (June–August) CONUS temperature was 0.9°C above average, the third highest on record. Above-average temperatures dominated the western half of the CONUS as well as the southern Plains and parts of the Northeast. Massachusetts, Rhode Island, and Texas each had their second-warmest summer while California observed its third warmest. The autumn (September–November) CONUS temperature was 0.1°C above average, with the highest anomalies occurring across portions of the West, Great Lakes, and Northeast. Maine had its fifth-warmest autumn on record.

(ii) Precipitation

The climate of the CONUS in 2022 was driven by ridges of high pressure along both the East and West coasts, which exacerbated the multi-year drought by suppressing precipitation across much of the West. Nebraska had its fourth-driest year on record while California ranked ninth driest (Fig. 7.4b).

Winter precipitation across the CONUS was 83% of average and ranked in the driest third of the historical record. Precipitation was above average across portions of the Upper Midwest and from the middle of the Mississippi River Valley to the eastern Great Lakes. Dry conditions prevailed across much of the Plains and Gulf Coast as well as parts of the West and East coasts. Precipitation totals for Louisiana, Nebraska, and Kansas were third, fourth, and fifth lowest on record, respectively. Spring precipitation was 97% of average, but was above average from the Northwest to the Great Lakes as well as in portions of the central Plains, Southeast, and the Northeast. North Dakota had its third-wettest spring on record. Below-average precipitation occurred from California to the western Plains and Texas. Summer precipitation was 95% of average, with above-average wetness occurring across parts of the Northwest, Southwest, Gulf Coast, and Ohio Valley. West Virginia experienced its seventh-wettest summer on record while monsoon rains across Arizona and New Mexico resulted in a ranking of eighth wettest for each state. It was drier than average across much of the Plains and in parts of the Northeast where Nebraska and New Jersey each had their fourth-driest summer on record. The autumn CONUS precipitation total was 81% of average, ranking in the driest third of the record. Precipitation was above average across portions of the Northeast and Florida while drier-than-average conditions were present across parts of the Northwest and from the Plains to the Ohio Valley. Nebraska had its seventh-driest autumn on record.

Drought coverage across the CONUS remained significant for the third consecutive year, with a minimum spatial extent of 44% occurring on 6 September and a maximum coverage of 63% on 25 October—the largest CONUS footprint since the drought of 2012. The rapid intensification and expansion of drought at times during 2022 resulted from the low precipitation occurring with record and near-record high temperatures that, in combination with sunny skies, low humidity, and windy conditions, led to a “flash drought” which rapidly reduced soil moisture, especially in parts of the Plains to the lower and middle parts of the Mississippi Valley during the summer and early autumn. Drought impacted much of the western half of the United States for a majority of the year with some improvement resulting from the summer monsoon across the Southwest. Nonetheless, the multi-year western U.S. drought resulted in water stress/shortages across many locations as some major reservoirs dropped to their lowest levels on record.

(iii) Notable events and impacts

There were 18 weather and climate events across the United States during 2022 with losses each exceeding \$1 billion (U.S. dollars): six severe storms, three tropical cyclones, three hail events, two tornado events and one each for drought, flood, winter storm, and wildfire events (Fig. 7.5). Total disaster costs for these events in 2022 exceeded \$175 billion (U.S. dollars; adjusted to the Consumer Price Index)—the third-highest cost on record. The costliest event of the year was Hurricane Ian (\$114 billion U.S. dollars) which ranks as the third-costliest hurricane on record (1980–2022; see section 4g2 and Sidebar 4.1 for more details about Hurricane Ian). Over the last seven years (2016–2022), 122 separate billion-dollar disasters have killed at least 5000 people and incurred costs greater than \$1 trillion (U.S. dollars) in damage.

The tornado count for 2022 was slightly below average with 1143 tornadoes reported across the CONUS. March had triple its average number of verified tornadoes (234) and the most tornadoes for any March in the 1950–2022 record. One of the most significant severe weather days occurred on 5 April when approximately 68 tornadoes were reported from Mississippi to South Carolina, including an EF-4 tornado that struck the town of Pembroke, Georgia, causing damage, injuries, and one fatality.

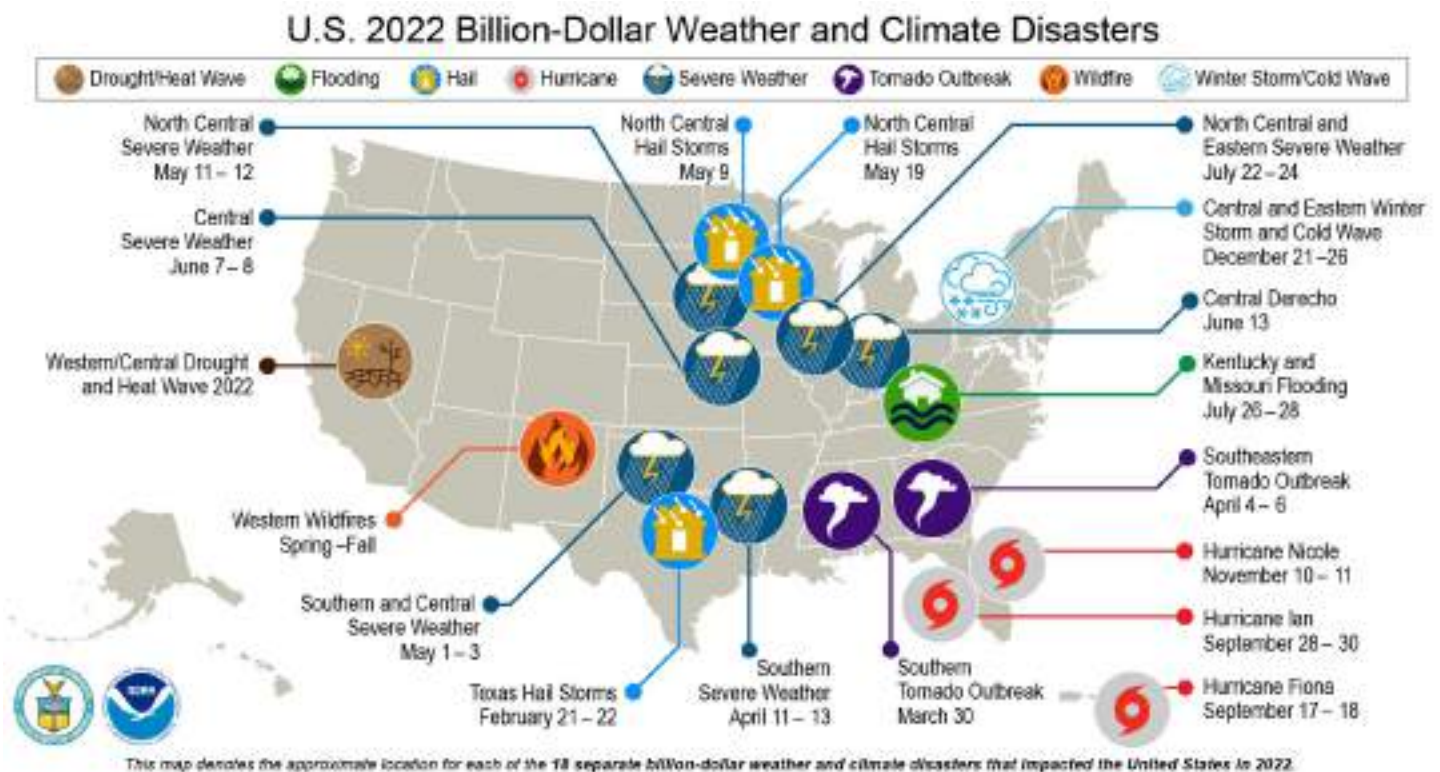


Fig. 7.5. Map depicting date, approximate location, and type of the 18 weather and climate disasters in the United States in 2022 whose losses each exceeded \$1 billion (U.S. dollars). (Source: NOAA/NCEI.)

3. MEXICO

—R. Pascual Ramírez and A. E. Martínez

Mexico's mean annual temperature for 2022 was the eighth highest since national records began in 1950 (Fig. 7.6a). The national precipitation total for 2022 was 743.6 mm, which is slightly below the 1991–2020 average and ranked in the middle of the 73-year record (Fig. 7.6b). Precipitation was below average across the northeast, central region, and the northern coast of the Gulf of Mexico. Conversely, the northwest, southern Baja California Peninsula, and the Yucatan Peninsula had above-average annual rainfall through the year (Fig. 7.7b).

(i) Temperature

The 2022 national average annual temperature was 22.0°C, which was 0.6°C above the 1991–2020 average (Fig. 7.6a), marking the eighth-warmest year in the 73-year record. Although 2022 did not rank among Mexico's five warmest years, the nation continued its warming trend, and 2022 marked the 13th consecutive year with an above-average national temperature. The year was characterized by above-average temperatures across much of the nation, although parts of the northwest and areas along the Gulf of Mexico coast experienced near- to below-average annual temperatures (Fig. 7.7a). February, March, October, and November each had monthly temperatures slightly below average, while the remaining months had above-average temperatures, with the month of May setting a record high.

During January–March, below-average temperatures were observed in the northwest and along the states in the Gulf of Mexico. The rest of the country had slightly above-average temperatures. From April through June, temperatures were near average from the central to southern regions of the country as the rainy season began;

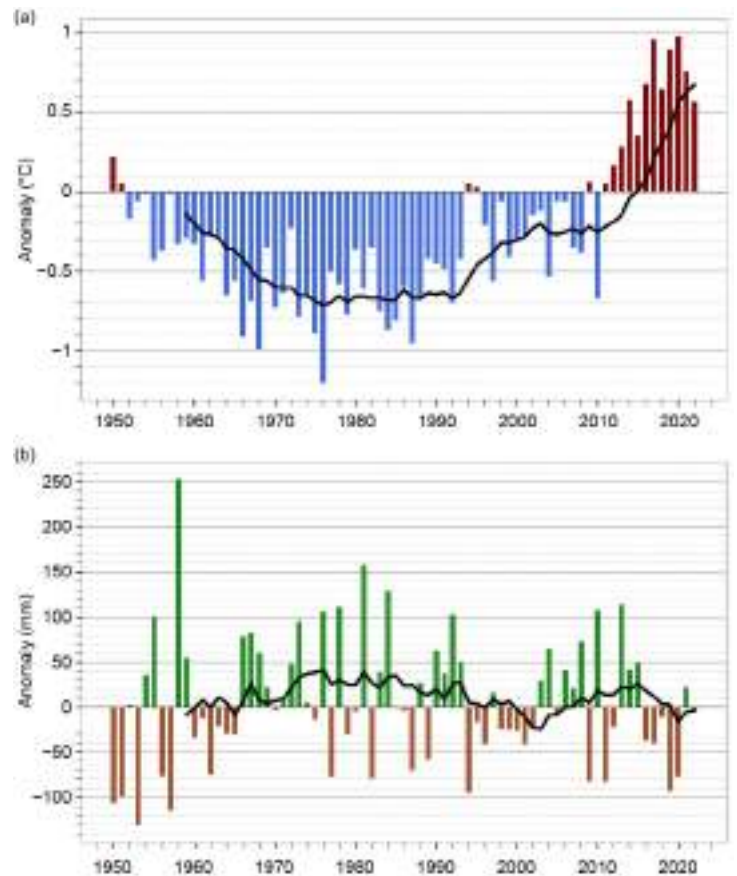


Fig. 7.6. Annual anomalies of (a) temperature (°C) and (b) precipitation (mm) for Mexico for the period 1950–2022 (1991–2020 base period). Black solid lines represent a 10-year running mean. (Source: National Meteorological Service of Mexico.)

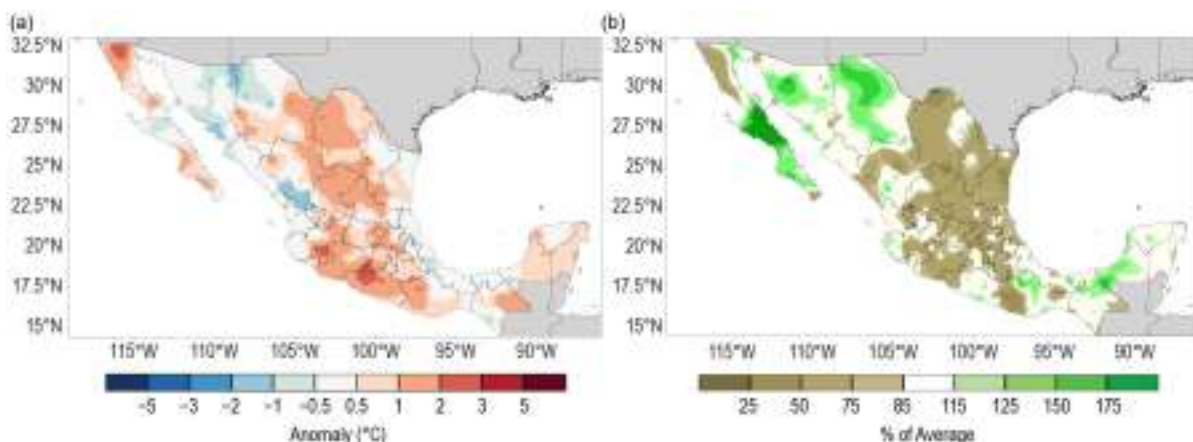


Fig 7.7. Annual anomalies of (a) mean temperature (°C) and (b) precipitation (% of average) over Mexico in 2022 (1991–2020 base period). (Source: National Meteorological Service of Mexico.)

above-average temperatures were present across northern Mexico. When the rains reached the northwest region and the Sierra Madre Occidental, temperatures in the region dropped to below average between July and September. During October–December, above-average temperatures were present across central and southern Mexico, while slightly below- to near-normal temperatures prevailed in the northwest and along the states of the Gulf of Mexico.

(ii) Precipitation

The national precipitation total for 2022 was 743.4 mm (99.4% of average). Climatologically, September tends to be the nation’s rainiest month. However, similar to 2021, August 2022 contributed more than any other month to the annual precipitation total. Meanwhile, March was the driest month for the year and contributed the least to the annual total among all months, coinciding with the driest month climatologically.

During January–March, below-average rainfall was observed across most of the country, especially along the Sierra Madre Occidental and in Baja California, exacerbating drought conditions in the region. The Yucatan Peninsula and the Isthmus of Tehuantepec in southern Mexico received above-average rainfall in January.

The onset of the rainy season from central to southern Mexico occurred in late May and early June. Tropical Storm Alex in the Gulf of Mexico and Hurricane Agatha in the Pacific were the main precursors of rainfall in early June. Monsoon rain began in the northwest at the end of June and continued through September. During the summer (June–August), rains associated with tropical cyclones were less than typical in the foothills of the Gulf of Mexico and the northeast. On the Pacific side, Hurricane Kay and Tropical Storm Lester brought considerable amounts of precipitation on the Pacific coast and in Baja California Sur. See sections 4g2 and 4g3 for more details about these hurricanes.

The last quarter of the year marks the transition between the end of the rainy season and the beginning of the dry season in Mexico. During this transition period, it is common to see a combination of tropical and winter systems. From September through December, three tropical cyclones (Orlene and Roslyn from the Pacific and Lisa from the Gulf of Mexico) and several cold fronts were the main sources of rainfall in Mexico. Mexico’s drought footprint was at its lowest for the year (7.48%) by 31 October, according to the North American Drought Monitor. The dry season began in late November, and the dry conditions led to an increase in drought, with close to 19% of the nation experiencing moderate to exceptional drought by the end of the year.

(iii) Notable events and impacts

Northeastern Mexico was severely affected by the lack of precipitation during most of the year. Rainfall deficits combined with high temperatures during March and April resulted in a wildfire in the state of Nuevo León that lasted more than 20 days. The fire spread rapidly due to strong winds, burning at least 5000 hectares. According to Mexico’s Drought Monitor, during the first half of the year, severe to exceptional drought prevailed in most of the northern portion of the country. During this time, there were 6305 forest fires and over 400,000 hectares burned. At the end of the year, a total of 6755 forest fires were recorded that burned 739,626 hectares (National Forestry Commission), the second-largest area burned by fires, behind only 2011 (956,404 hectares), according to fire data that began in 1998.

Only three tropical cyclones (Tropical Storms Alex and Karl and Hurricane Lisa) from the Atlantic basin (see section 4g2 for details) affected Mexico’s eastern coast during 2022. On the Pacific side, Hurricanes Agatha, Blas, Kay, Orlene, and Roslyn, as well as Tropical Storm Lester, made landfall or tracked near the country and brought significant rainfall to the western region (see section 4g3 for details). Precipitation from these Pacific systems caused floods and landslides, mainly around the Isthmus of Tehuantepec in the Pacific coast, as well as the Baja California Peninsula.

c. Central America and the Caribbean

—A. Sánchez-Lugo, Ed.

1. CENTRAL AMERICA

—H. G. Hidalgo, J. A. Amador, E. J. Alfaro, B. Calderón, and N. Mora

For this region, nine stations from five countries were analyzed (see Fig. 7.8 for data and station list). The station distribution is representative of the relevant seasonal and intraseasonal regimes of precipitation (Amador 1998; Magaña et al. 1999; Amador et al. 2016a,b), wind (Amador 2008), and temperature (Hidalgo et al. 2019) on the Caribbean and Pacific slopes of Central America (CA). Precipitation and temperature records for the stations analyzed and regional winds were provided either by CA National Weather Services (CA-NWS), NOAA, or the University of Costa Rica. Anomalies are reported using a 1991–2020 base period and were calculated from CA-NWS data. The methodologies used for all variables can be found in Amador et al. (2011).

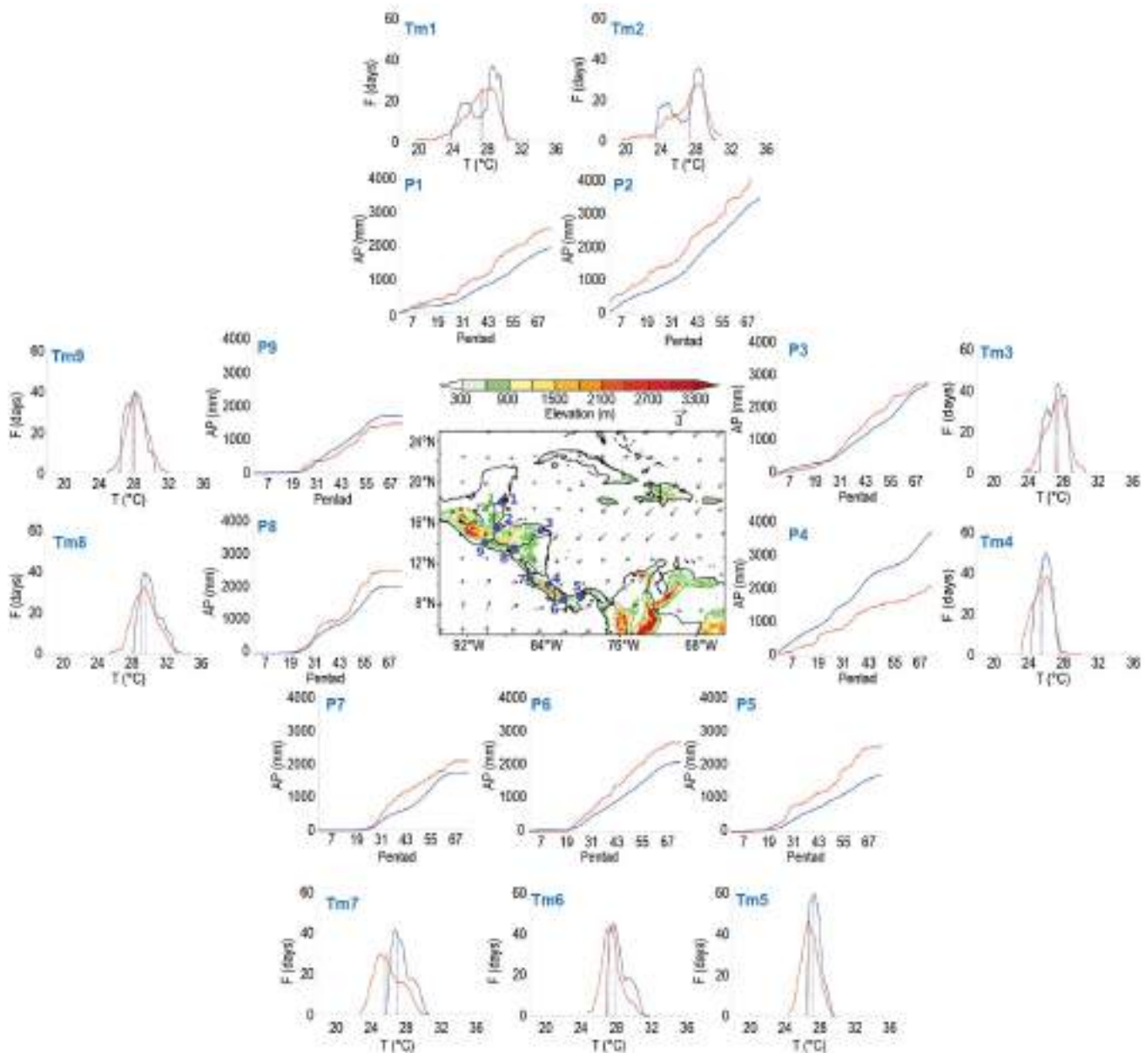


Fig. 7.8. Mean surface temperature (T_m ; °C) frequency (F ; days) and accumulated pentad precipitation (P ; mm) time series are presented for nine stations (blue dots) in Central America: (1) Philip Goldson International Airport, Belize; (2) Puerto Barrios, Guatemala; (3) Puerto Lempira, Honduras; (4) Puerto Limón, Costa Rica; (5) Tocumen International Airport, Panamá; (6) David, Panamá; (7) Liberia, Costa Rica; (8) Choluteca, Honduras; (9) Puerto San José, Guatemala. The blue solid line represents the 1991–2020 average values and the red solid line shows 2022 values. Vertical dashed lines show the mean temperature for 2022 (red) and the 1991–2020 period (blue). Vectors indicate July wind anomalies at 925 hPa (1991–2020 base period). Shading depicts regional elevation (m). (Sources: NOAA/NCEI and CA-NWS.)

(i) Temperature

The mean temperature (T_m , °C) pentad frequency distributions in 2022 as well as the climatology for all stations analyzed are shown in Fig. 7.8. Most stations across Central America had near-average annual temperatures. Only the stations of David, Panamá (T_{m6}), and Liberia, Costa Rica (T_{m7}) had significant (in the tails of the 95% confidence distributions using a t-test) below-average annual temperature anomalies of -0.8°C and -1.3°C , respectively. The two northernmost stations in the Caribbean coast, Philip Goldson International Airport, Belize (T_{m1}), and Puerto Barrios, Guatemala (T_{m2}), had a bimodal temperature distribution over the course of the seasonal cycle during 1991–2020. This was also reported in the last two yearly climate reports. However, contrary to what was found for the 2021 data, the two-peak distribution in mean temperature is not clearly visible in both stations in 2022, a feature observed in the temperature records of this location in the period 2017–21 (Amador et al. 2018). In terms of seasonal changes, only Liberia, Costa Rica (T_{m7}) had significant (in the tails of the 95% confidence distributions) below-average temperatures in all seasons.

(ii) Precipitation

The accumulated pentad precipitation (P , mm) time series for the nine stations in Central America is presented in Fig. 7.8. Most stations had near-average annual rainfall totals, with the exceptions of Puerto Barrios, Guatemala ($P2$), which had an above-average total accumulation of 751 mm (119% of normal) and Puerto Limon, Costa Rica ($P4$), which had an exceptionally dry year with a deficit of 1618 mm (56% of normal). Most of the stations in the Pacific coast had above-average annual accumulations, consistent with the cold phase of the El Niño–Southern Oscillation (La Niña) teleconnection response in the area. The prevailing wind patterns (Fig. 7.8) increased flow from the Pacific Ocean to the coast in the southernmost regions and resulted in larger accumulations in those stations (David, Panamá [$P6$]; Liberia, Costa Rica [$P7$]; and Choluteca, Honduras [$P8$]). However, farther north near the El Salvador and Guatemala border, the anomalies were much weaker, and the annual precipitation totals were below average (San Jose, Guatemala [$P9$]). Another contributor to the anomalously wet Pacific coast in the southern countries is that 2022 was the third consecutive year with an anomalously active hurricane season in both basins. At seasonal scales, extreme precipitation (in the tail of the distribution of the annual values from 1991 to 2020) occurred during winter in Puerto Barrios, Guatemala ($P2$), and in spring and autumn in Tocumen, Panamá ($P5$).

(iii) Notable events and impacts

Tropical cyclone activity in the Caribbean in 2022 consisted of five named storms in the basin: Tropical Storm Bonnie (1–2 July) and Hurricanes Fiona (17–19 September), Ian (23–27 September), Julia (7–9 October), and Lisa (31 October–3 November). Three of the five storms affected the Central American isthmus. Bonnie made landfall and crossed Central America near the Costa Rican-Nicaraguan border. Strong winds and heavy rains from Bonnie affected the region, and two fatalities in El Salvador were associated with the storm. Bonnie exited into the eastern Pacific basin, moving westward, away from the Central American coast by 4 July.

Julia was a Category 1 hurricane that made landfall on the Caribbean coast of Nicaragua on 9 October. Direct and indirect effects were observed across Central America, as Julia became the deadliest cyclone of the season with over 30 fatalities in the region. Julia also managed to survive its passage through the isthmus and continued its path into the eastern Pacific basin. The system moved to the west and then to the west-northwest, parallel to and near the coasts of Nicaragua and El Salvador. On 10 October, the center of the storm crossed the coast of El Salvador and later affected Guatemala. (see Sidebar 7.1 for additional details)

Hurricane Lisa made landfall as a Category 1 hurricane on the coast of Belize on 2 November. There were no systems from the eastern tropical Pacific that impacted Central America.

Other rain-producing systems caused landslides and flooding that killed 110 people: 2 in Panamá, 10 in Costa Rica, 7 in Nicaragua, 27 in El Salvador, 12 in Honduras, and 52 in Guatemala. Lightning strikes caused 13 fatalities in the region during the season (three in Costa Rica, three in Nicaragua, one in El Salvador, four in Honduras, and two in Guatemala).

Please refer to sections 4g2 and 4g3 for more information on these tropical cyclones.

2. CARIBBEAN

—T. S. Stephenson, M. A. Taylor, A. Trotman, C. J. Van Meerbeek, J. Spence-Hemmings, L. Clarke, J. Campbell, and K. Kerr

(i) Temperature

The Caribbean had relatively small positive temperature anomalies in 2022 compared to the previous four years (2018–21, as analyzed from European Centre for Medium-Range Weather Forecasts Reanalysis version 5 [ERA5] reanalysis data). The annual temperature anomaly for the region was 0.42°C above average, marking the eighth-warmest year since records began in 1950 (Fig 7.9a). Annual temperatures have increased at a rate of 0.11°C decade⁻¹ since 1950 (0.17°C decade⁻¹ since 1970). Much of the region had above-average annual temperatures for 2022 (Fig. 7.10a). Freeport, Bahamas, had its warmest year on record since 1973, with an annual average maximum temperature of 29.7°C (1.0°C above average) and Canefield, Dominica, equaled its highest annual average maximum temperature at 31.8°C (0.7°C above average) since 1985. The Sancti Spiritus Airport and the National Airport at Camagüey in Cuba each recorded their third-warmest year in the 52-year record with annual average maximum temperatures of 31.5°C (0.9°C above average) and 31.3°C (0.7°C above average), respectively. Conversely, Grantley Adams, Barbados, had its ninth-lowest annual average maximum temperature since 1979 at 29.7°C, which was 0.5°C below average.

Seasonally, December–February and March–May temperatures were above average for most of the region. The temperature anomaly averaged regionally for March–May was +0.46°C and the eighth-warmest such period on record. June–August temperatures were near average across much of the Caribbean, but parts of Barbados, northern Belize, Curaçao, Jamaica, and Trinidad had below-average temperatures. There were fewer heatwaves (defined by the Caribbean Climate Outlook Forum as periods of at least two consecutive days with daily maximum temperatures exceeding the 90th percentile) in 2022 than in recent years (May–October). St. Kitts recorded its highest daytime maximum temperature of 33°C on 5 July and again on 8 July. The September–November temperature anomaly for the region was 0.50°C above the 1991–2020 average and the seventh warmest on record since 1950.

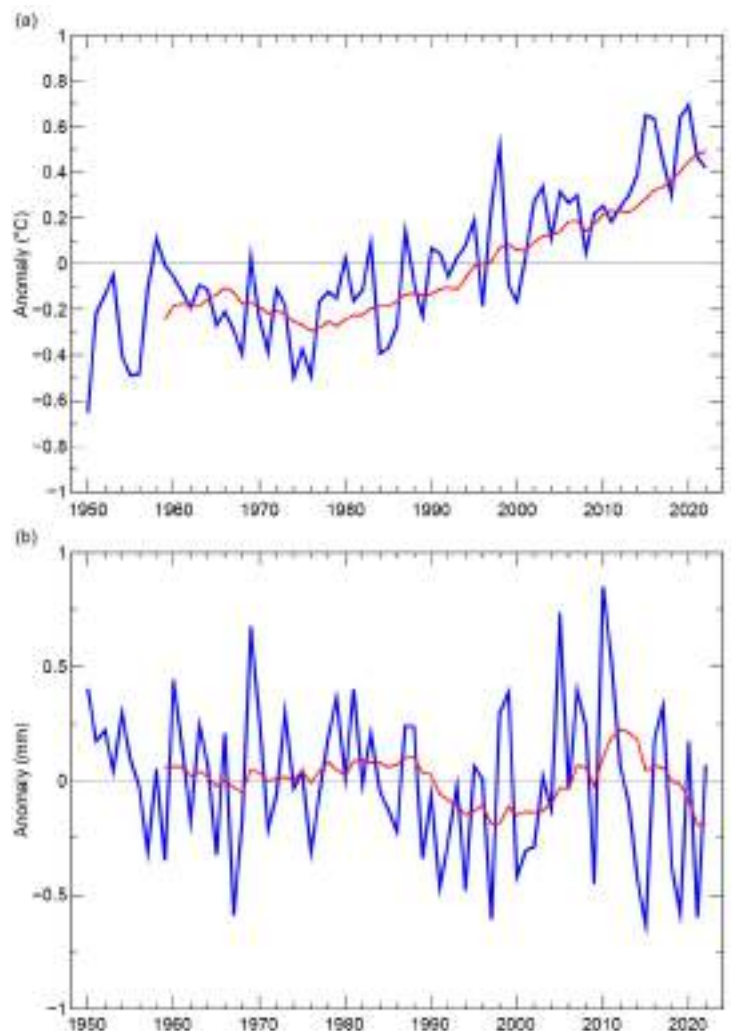


Fig. 7.9. Annual average (a) 2-m temperature anomalies (°C) and (b) rainfall anomalies (mm day⁻¹) for the Caribbean (9°N–27°N, 58°W–90°W) for 1950–2022 relative to the 1991–2020 average. The red line is the 10-yr running mean. (Sources: ERA5 from the KNMI Climate Explorer.)

(ii) Precipitation

Most of the Caribbean islands had near-average rainfall during 2022 (Fig. 10b). The average rainfall anomaly for the region was $-0.22 \text{ mm day}^{-1}$ (Fig. 7.9b). Moderately-to-exceptionally wet conditions were observed across the northern Bahamas (in the far north Caribbean) and Trinidad (eastern Caribbean). Three locations in Trinidad reported their highest rainfall totals: Caroni (3422.9 mm, 158% of average; since 1985), Hillsborough (3264.9 mm, 147% of average; since 1971), and Hollis (4281.5 mm, 144% of average; since 1971). Two other locations in Trinidad had their second-highest amounts since 1971: Navet (3141.9 mm, 143% of average) and Piarco (2378.9 mm, 132% of average). Rancho Coloso, Aguada, Puerto Rico, had its second-highest annual rainfall total (2403.1 mm, 132% of average) since 1971. It was also dry in places. With records dating from 1979, E.T. Joshua, St. Vincent, recorded its lowest annual rainfall total (1511.1 mm, 70% of average). Since 1971, El Valle, Hato Mayor, Dominican Republic, experienced its second-driest year (717.9 mm, 50% of average), Rivière, Martinique, had its fourth-driest year (1797.6 mm, 70% of average), and La Trinité, Martinique, recorded its fifth-driest year (1522.3 mm, 72% of average).

December–February was characterized by a lingering seasonal dryness throughout most of the eastern Caribbean, with many islands experiencing moderate-to-severely dry conditions. During spring (March–May), the region transitioned to near- to above-average rainfall, with the exception of the Cayman Islands and the Leeward Islands where below-average conditions prevailed. Summer (June–August) rainfall anomalies were mixed over the region with most islands recording above-average precipitation, consistent with the ongoing La Niña event in the eastern tropical Pacific Ocean. The La Niña signature continued into September–November, with Cuba and southwest Haiti receiving below-average rainfall while other locations (generally in the south and east) had above-average precipitation.

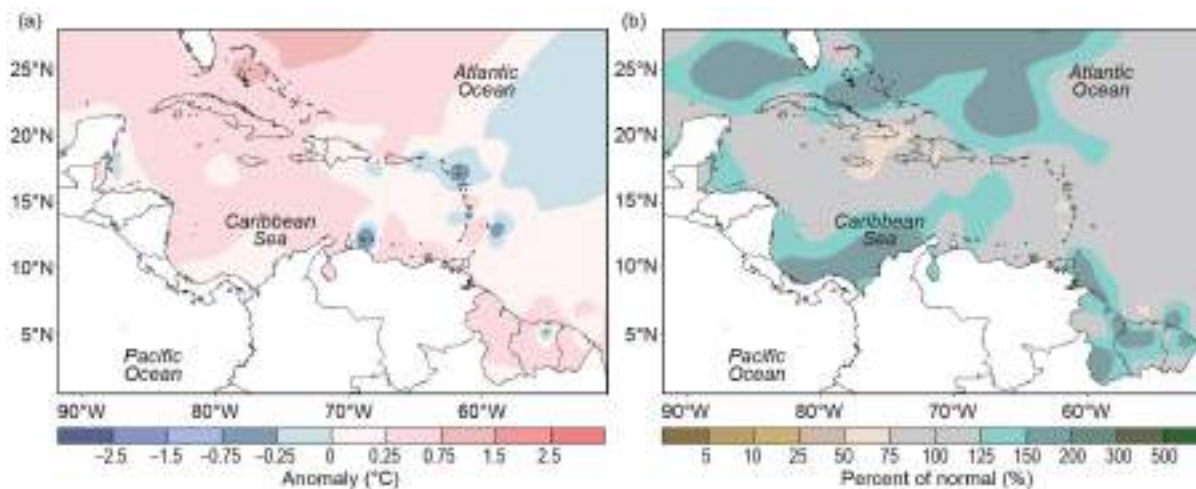


Fig. 7.10. Annual (a) mean temperature anomalies ($^{\circ}\text{C}$) and (b) total precipitation anomalies (% of normal) relative to 1991–2020. (Source: Caribbean Climate Outlook Forum [CariCOF] and the Caribbean Institute for Meteorology and Hydrology.)

(iii) Notable events and impacts

Hurricane Fiona crossed the eastern Caribbean as a tropical storm on 16–20 September, causing minor damage for most locations. However, Fiona left considerable damage to infrastructure in Guadeloupe and caused one fatality. Hurricane Fiona made landfall in Puerto Rico on 18 September and resulted in widespread flooding and loss of power across the entire island, impacting over one million people. The storm intensified and severely impacted the Dominican Republic on 19 September and the Turks and Caicos Islands on 20 September. Fiona was associated with two fatalities each in Puerto Rico and the Dominican Republic.

Hurricane Ian impacted Jamaica as a tropical storm on 26 September and resulted in landslides, mudslides, fallen trees, and floods, and left some communities inaccessible. Damage to the road network was estimated to be \$2.3 million (U.S. dollars). Ian impacted the Cayman Islands

as a Category 1 hurricane on 26 September. Debris generated from flooding made some areas inaccessible. Hurricane Ian made direct landfall in Pinar del Rio, western Cuba, with maximum sustained winds of 185 km h⁻¹. The storm reportedly caused three deaths and, in Pinar del Rio province, damaged 63,000 homes.

Nicole made landfall on Grand Bahama Island on 9 November as a Category 1 hurricane. Coastal flooding from storm surge was reported around the Abaco Islands. Flooding in coastal areas near Nassau, New Providence, reportedly caused two road closures.

Please refer to section 4g2 for more details on these storms and to Sidebar 4.1 for more information about Hurricanes Fiona and Ian.

Sidebar 7.1: **Notable events across Central America**

—S. FUHRMAN, C. RECALDE, AND W. M. THIAW

Heavy rains plagued Central America for large portions of the year. In February, Honduras's national disaster agency Permanent Contingency Commission of Honduras (COPECO) reported high river levels, flooding, damaged houses, and infrastructure over the Atlántida, Yoro, the Bay Islands, and Cortés Departments of Honduras. Notably, the Leán River overflowed its banks in Atlántida department, where around 500 homes were affected and at least 300 families were evacuated.

During the end of May, dangerous rains were widespread across Guatemala where the National Coordination for Disaster Reduction agency (CONRED) reported that over 38,900 people were affected in the municipalities of Villa Nueva, Aguacatán, Nebaj, Chiquimulilla, Solola, Estanzuela, Gualán, and Zacapa.

Continued heavy rains, 150%–200% of normal September totals (Fig. SB7.1), caused deadly and destructive impacts in several countries. In El Salvador, the General Directorate of Civil Protection reported that homes were damaged and one person died after rivers overflowed in La Paz and San Salvador departments. The agency also reported five fatalities from a landslide in the La Libertad department. In Costa Rica, the National Emergency Commission (CNE) said personnel responded to floods in 191 locations. According to the Red Cross, about 80 homes were damaged and 50 people evacuated in San Jose province after the Cañas River overflowed.

Landslides and floods affected Panama during November. According to the National Civil Protection System (SINAPROC), more than 300 families in three south-central provinces were affected by flooding on 10 November. SINAPROC also reported two fatalities in a landslide in Cativá, Colón Province, on 21 November.

Conversely, two periods of insufficient rain during the first and second rainy seasons impacted Central America, which resulted in abnormal dryness and degraded vegetation health. In Guatemala and western Honduras, rainfall was less than 50% of normal during April, according to Climate Prediction Center morphing technique (CMORPH) analysis, which led to a period of abnormal dryness in May. While May rainfall

improved in central Guatemala and Honduras, continued suppression (less than 50% of normal rainfall) during May and June kept abnormal dryness in place over northern Guatemala until the third week of June. A second period of insufficient rains led to a short period of abnormal dryness in northern Guatemala, eastern Honduras, and Nicaragua during the third dekad (10-day period) of September and the first dekad of October. Rainfall deficits in these regions exceeded 100 mm and September's rainfall was 25%–80% of average, according to CMORPH (Fig. SB7.1).

Two tropical cyclones made landfall in Central America during the 2022 Atlantic hurricane season: Tropical Storm

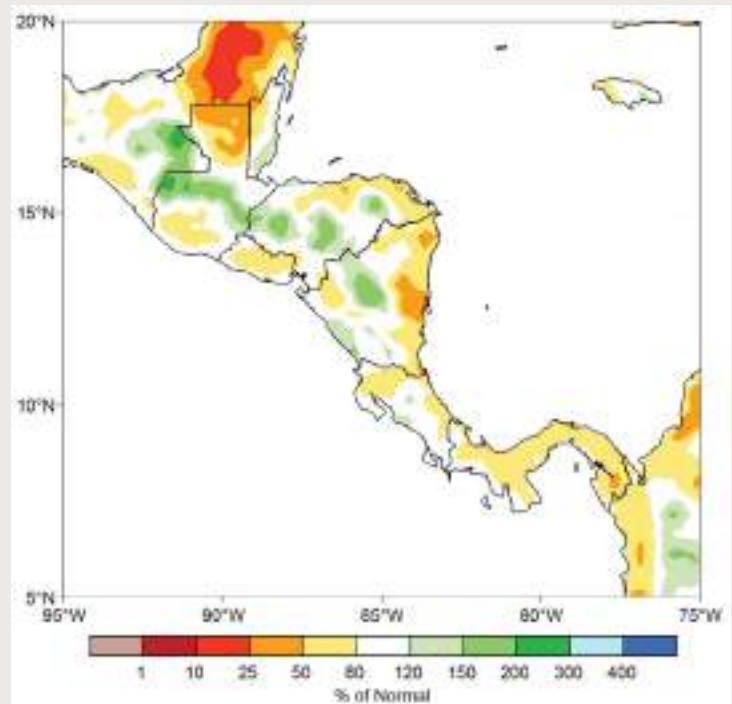


Fig. SB7.1. Satellite-estimated rainfall (% of normal) during Sep 2022. Anomalies are computed with respect to the 1998–2020 base period. (Source: NOAA Climate Prediction Center's CMORPH.)

Bonnie and Hurricane Julia (Fig. SB7.2). Tropical Storm Bonnie made landfall on 2 July near the Caribbean coast in southern Costa Rica with sustained winds of 85 km hr^{-1} and traversed southern Nicaragua, moving northwest across the country to the Pacific Ocean coast near El Salvador. In Nicaragua, heavy rains flooded 21 municipalities, resulting in four casualties, over 400 houses damaged, and more than 3000 people displaced, according to the country's National System for the Prevention, Mitigation and Attention of Disasters.

Although no deaths were reported in Costa Rica, heavy rainfall caused floods and landslides, and about 1600 people were evacuated to storm shelters; damage to highway bridges and agriculture was also reported. Heavy rain in El Salvador caused floods and damaged infrastructure, which led to three casualties and the evacuation of about 243 people to shelters, according to Civil Protection.

Julia made landfall in Nicaragua on 9 October as a Category 1 hurricane, weakening into a tropical storm before affecting several Central America countries. Hurricane Julia's impacts in Nicaragua affected approximately 7500 people, flooded 3000 houses, displaced 2000 roofs from winds, overflowed 78 rivers, and collapsed walls; however, no casualties were reported. Meanwhile, the storm's passage in Guatemala affected about 66,350 people, led to 15 casualties, and damaged roads and bridges. Impacts to El Salvador included floods, landslides, over 10 casualties, and the overflow of at least 78 rivers. Damage in Panama was less severe; there, the storm caused landslides, the collapse of some infrastructures, and the evacuation of people in the province of Chiriquí.

Forest fire activity was high in Central America, especially in Guatemala, Honduras, and Costa Rica. In Guatemala, the

National Coordination for Disaster Reduction organization reported that during the fire season, there were 950 incidents, which affected 21,877 hectares, and local news reported that there were at least 10 fatalities. The report also added that much of the wildfire activity was due to human activities such as agriculture or pasture burning. Meanwhile, the Honduran Forest Conservation Institute reported more than 98,000 hectares were affected by 1202 forest fires. One of the most intense wildfire incidents occurred during March in the Biological Reserve Lomas de Barbudal in the province of Guanacaste, Costa Rica, where 1715 hectares burned, affecting diverse flora and fauna.



Fig. SB7.2. Plot of the tracks of the two tropical cyclones (Bonnie and Julia) that made landfall in Central America during the 2022 hurricane season. Size of the circle indicates the relative strength of the storm. (Source: National Hurricane Center best track archive.)

d. South America

—A. Sanchez-Lugo, Ed.

Much of South America had near- to above-average annual temperatures in 2022, with several locations across the north experiencing below-average annual temperatures. As a whole, South America had an annual temperature that was 0.11°C above average, tying with 2018 as the 11th highest since continental records began in 1910. Nine of South America's 10 warmest years have occurred since 2010.

Precipitation varied greatly across the continent, with much of the north and northwest receiving above-average annual rainfall, while much of the western and southern regions had below-average annual rainfall.

Anomalies in this section are all based on the 1991–2020 base period, unless otherwise noted.

1. NORTHERN SOUTH AMERICA

—J.J. Nieto, F. Costa, and J. Morán

The northern South America region includes Colombia, Ecuador, French Guiana, Guyana, Suriname, and Venezuela.

(i) Temperature

Mean annual temperature anomalies for most of the region were near to below average (Fig. 7.11). The most notable cool temperature anomaly was along the Caribbean coast of Colombia. Parts of southern Colombia, on the other hand, had near- to above-average mean annual temperatures. In northern Ecuador, temperature anomalies were between 0.5°C and 1.0°C below average.

While temperatures were near to below average for much of the region (where data were available) during March–May, June–July, and September–October, there were some locations, specifically in the southern half of Colombia, that had above-average temperatures during March–May and June–July. An analysis was not available for December–February for the region due to lack of data at the time of this writing.

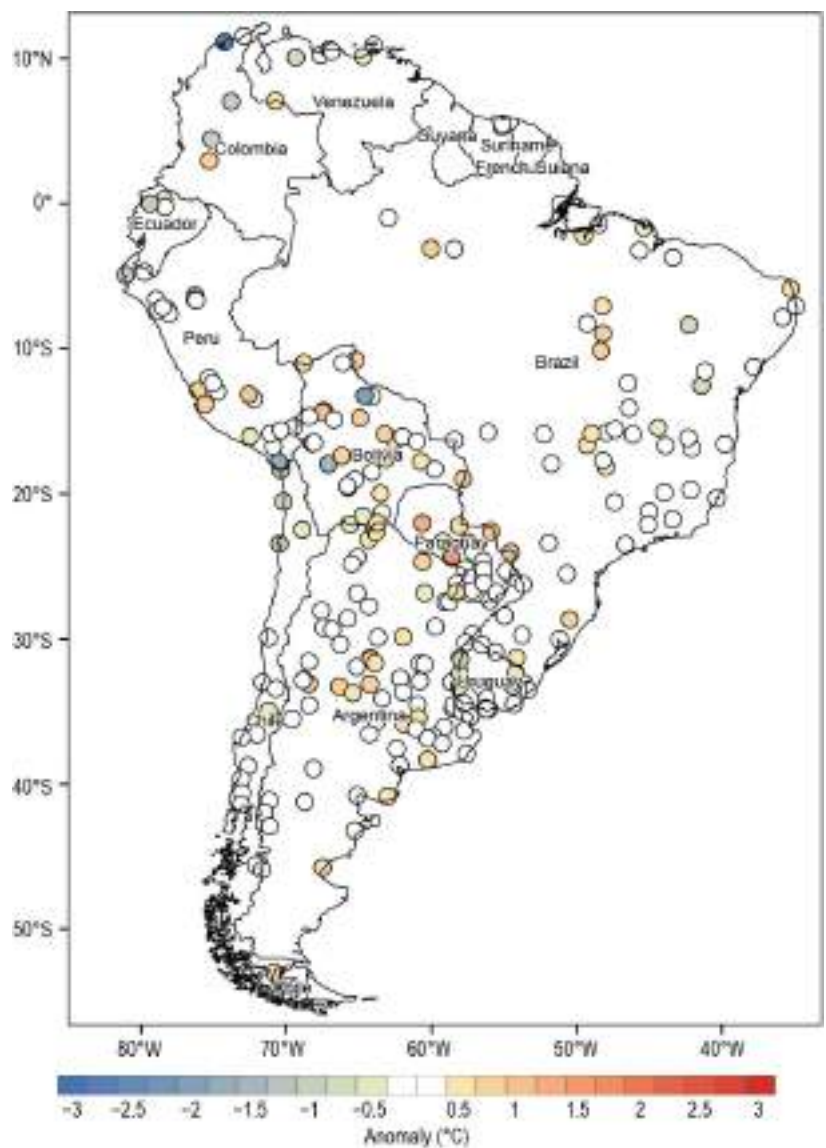


Fig. 7.11. 2022 mean annual temperature anomalies (°C; 1991–2020 base period). (Source: data from NMHSs of Argentina, Bolivia, Brazil, Chile, Colombia, Ecuador, Paraguay, Peru, Suriname, Uruguay, and Venezuela. Processed by CIIFEN.)

(ii) Precipitation

Precipitation across northern South America was generally above average during 2022 (Fig. 7.12). This could be associated with the warm sea-surface temperatures (SSTs) across the Caribbean region throughout much of the year, as well as the La Niña that was present across the central and eastern tropical Pacific Ocean during 2022.

Suriname had on average 30% above-normal precipitation for the year, with most of the rain falling during winter (December–February 2021/22) and autumn (September–November). Precipitation varied throughout the year for Venezuela. Most locations along the northern coast of Venezuela had near- to below-average precipitation during spring and summer (June–August); however, above-average conditions predominated during autumn, with some locations receiving twice their normal precipitation. The annual precipitation totals across most locations in Venezuela were near average. Much of the Caribbean and the Andean region of Colombia had above-average precipitation throughout the year, with annual totals 20%–30% above average. The highest seasonal precipitation totals fell during June–August, with some stations recording precipitation anomalies as high as +150%. In Ecuador, most locations also had near- to above-average annual precipitation, while the coastal region had anomalies close to 20% below average.

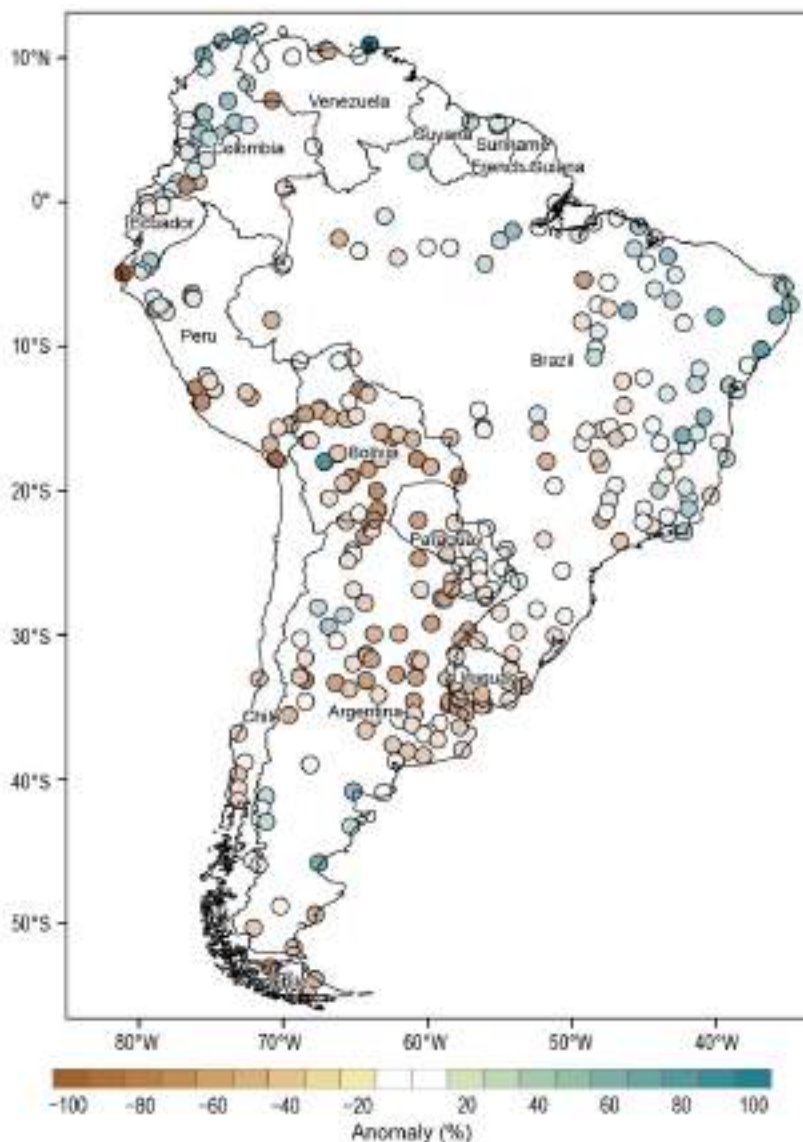


Fig. 7.12. Annual precipitation anomalies (%; 1991–2020 base period) for 2022. (Source: data from NMHSs of Argentina, Bolivia, Brazil, Chile, Colombia, Ecuador, Paraguay, Peru, Suriname, Uruguay, and Venezuela. Processed by CIIFEN.)

(iii) Notable events and impacts

An intense rainfall event occurred on 8 October in the city of Las Tejerías, Aragua, Venezuela, when 108 mm fell in six hours, equivalent to the average monthly rainfall for this region. The main cause of this event was the passage of Hurricane Julia in the Caribbean. The heavy rain fell over an area that was already saturated after receiving 180% of its normal precipitation in September. As a result of the October storm, a torrential flow of mud and debris inundated the city, resulting in 56 fatalities, forcing 10,000 residents to relocate, and damaging or destroying almost 800 homes. Economic losses were estimated at \$500 million (U.S. dollars). Hurricane Julia also affected parts of Colombia. La Guajira received 120 mm of rain in 12 hours. The storm affected over 48,000 people and 174 homes were destroyed. On the islands of San Andrés and Providencia, more than 490 people were affected, roads were damaged, and more than 120 homes were damaged or destroyed.

Rainfall totals were atypical during 2022 in Barranquilla, a city in northern Colombia, with some places receiving as much as twice their normal precipitation. This event could be associated with La Niña since it increases the probability of tropical wave occurrences in the Caribbean. Notably, on 4 November, rainfall totals exceeding 70 mm in a 40-minute period were reported in the city.

In the city of Babahoyo, Province of Los Ríos, Ecuador, 140 mm of rain fell in the early hours of 12 March, prompting floods that inundated roads, damaged homes, affected over 100 families, and caused the San Pablo River to rise by 6.5 meters. The heavy rain was associated with increased convection due to sea-surface warming on the Ecuadorian coast.

2. CENTRAL SOUTH AMERICA

—J. A. Marengo, J. C. Espinoza, L. M. Alves, J. Ronchail, A. P. Cunha, A. M. Ramos, J. Molina-Carpio, K. Correa, G. Avalos, W. Lavado-Casimiro, J. Baez, R. Salinas, W. R. Quispe, and K. Quisbert

The central South America region includes Brazil, Peru, Paraguay, and Bolivia.

(i) Temperature

The 2022 mean temperature for central South America was 0.23°C above the 1991–2020 average (Fig. 7.13). Much of the region had near- to above-average mean annual temperatures (Fig. 7.11). Seasonally, during December–February, much of the northern half of Brazil and some areas in northwestern Peru and southwestern Bolivia had near- to below-average temperatures. Meanwhile, the rest of region had near- to above-average conditions. During boreal autumn (March–May), most of the region experienced near- to above-average temperatures, with southern Peru and southwestern Bolivia observing below-average temperatures. Above-average temperatures also encompassed much of the region during boreal winter (June–August), with some locations experiencing mean temperature anomalies that were +2°C or higher. Parts of southern Peru continued to experience near- to below-average conditions during their winter. Below-average temperatures were observed in southern Brazil, Bolivia, and Paraguay during September–November, while the rest of the region experienced near- to above-average temperatures.

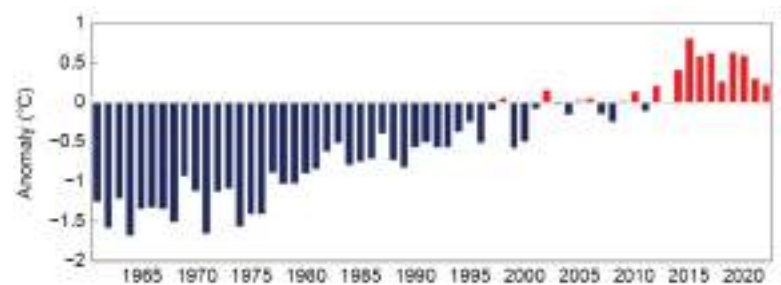


Fig. 7.13. Time series of mean annual regional air-temperature anomalies (°C; 1991–2020 base period) for the period 1961–2022 for central South America (Brazil, Bolivia, Paraguay, and Peru). (Source: NOAA /NCEP GHCN CAMS data.)

(ii) Precipitation

Above-average annual precipitation was observed across parts of northern and eastern Brazil, while the rest of central South America had below-average annual precipitation (Fig. 7.12). Abundant rainfall in the central and northern Amazon and drought in the southern Amazon and Parana-La Plata basin (LPB) were associated with La Niña in 2022.

Below-average rainfall was dominant during the austral summer in southern Peru, eastern Bolivia, southeastern Brazil, and parts of Paraguay, suggesting an early ending to the South American Monsoon. Above-average rainfall was observed across much of eastern Brazil and southwestern Bolivia during the austral summer. During boreal autumn, below-average rainfall extended across southern Peru, Bolivia, and southern parts of Brazil. Southern Paraguay and the northern region and southern tip of Brazil had above-average autumn rainfall. Much of southern Peru, the western half of Bolivia, and parts of southern Brazil reported little to no rain during the boreal winter. Meanwhile, northern Peru, eastern Bolivia, and northeastern and southeastern Brazil had above-average rainfall during winter. Boreal spring was characterized by below-average conditions across much of the region, with central Paraguay and northeastern Brazil experiencing above-average rainfall.

(iii) Notable events and impacts

Several significant weather extremes occurred across central South America in 2022, as shown in Fig. 7.14. Some of these events are discussed in more detail below.

The La Plata Basin had drought-induced damage to agriculture and reduced crop production, including soybeans and maize, which affected global crop markets. The 2022 drought conditions across the Basin were the worst since 1944 (Fig. 7.15). Several locations across Bolivia had record-dry conditions since the 1950s throughout the year when rainfall totals were between 4% and 45% of normal. The dry conditions affected over 160 Bolivian municipalities, including more than 3100 communities, 171,000 families, and 247,000 hectares (SENAMHI-Bolivia). In the southern Andes of Peru, drought conditions were the worst they had been since 1965, with rainfall ranging from none to 40% of normal. The rainfall deficits in the region were associated with the persistence of the continuous La Niña event in the tropical Pacific Ocean.

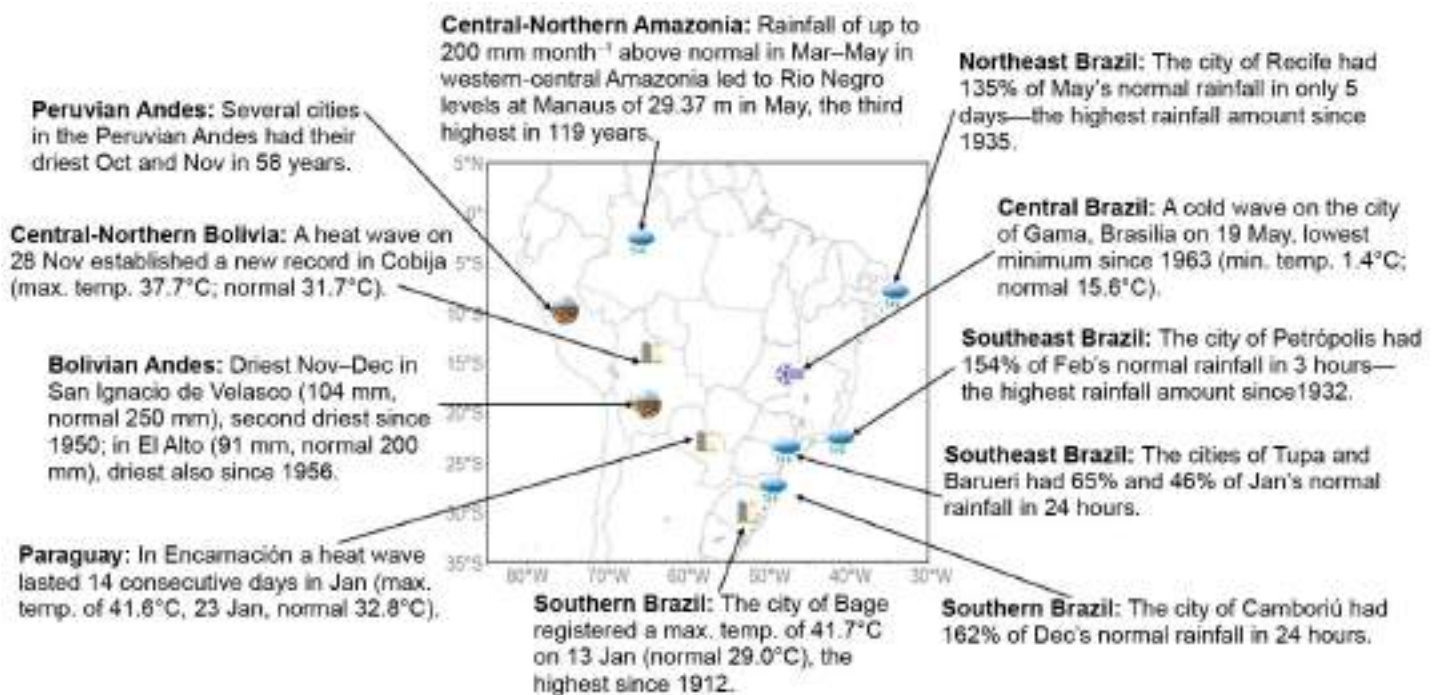


Fig. 7.14. Extreme and notable events across central South America in 2022. (Sources: Peru: SENAMHI; Bolivia: SENAMHI, Paraguay: DMH; Brazil: INMET, CEMADEN, CLIMATEMPO, INPE; International: UN OCHA, Flood list, UNDRR.)

An intensely invigorated mesoscale convective system on 15 February brought heavy rain to parts of Brazil. Of note, Petrópolis (Rio de Janeiro) received 258 mm of rain in just three hours and a total of 530 mm in 24 hours (the monthly February average is 210 mm). This caused the worst disaster in Petrópolis since 1931 with over 230 fatalities (Alcantara et al. 2023). During 2–4 April, Petrópolis and the city of Angra dos Reis (coastal region in the state of Rio de Janeiro) were affected by record rainfall when over 800 mm fell in 48 hours in each location. The torrential rain prompted floods and landslides that caused widespread damage to the area. Paraty was one of the worst-affected areas. A landslide destroyed seven houses, burying at least eight residents.

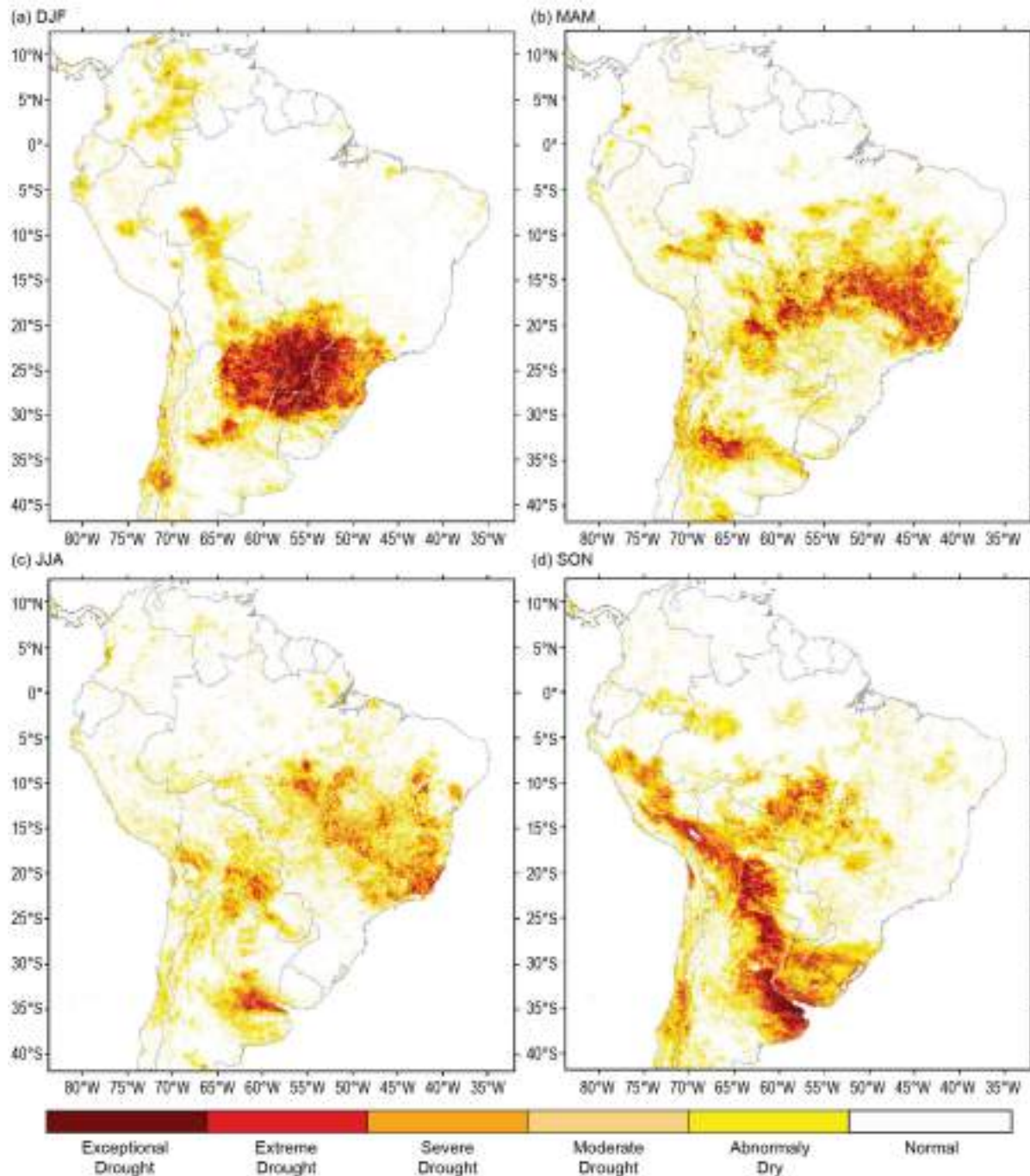


Fig. 7.15. Integrated Drought Index (IDI) maps for central South America during (a) DJF 2021/22, (b) MAM 2022, (c) JJA 2022, and (d) SON 2022. (Source: CEMADEN.)

Heavy rain on 20 February in the Bolivian Tarija department caused a 2 m-high torrent of water, mud, and debris to slide down a narrow ravine, destroying homes, crops, and livestock in various Guarani communities. The precipitation was mainly due to intense convective activity in the region associated with a cold front that crossed the southern Bolivia-northern Argentina region. In Rondônia in western Brazilian Amazonia, heavy rain from early February increased river levels, causing flooding in the municipality of Cacoal and the evacuation of 19,400 families. Damaged roads and bridges left many communities isolated.

The Rio Negro at Manaus reached the severe flood stage of 29 m in early May and 29.37 m by 23 May, the fourth-highest level since 1903. The three highest levels occurred in 2021, 2012, and 2009 (Espinoza et al. 2022). The Civil Defense reported that flooding affected over 306,000 people across the Amazonas state, and 35 municipalities declared a state of emergency.

Exceptional heavy rain fell in northeastern Brazil at the end of May. The city of Recife received 551 mm during 25–30 May, which is 140 mm more than its average total for May. The torrential rains affected 130,000 people and caused over 90 fatalities, and the city declared a state of emergency (Marengo et al. 2023). In Alagoas, 97.6 mm of rain fell in 24 hours in Porto de Pedras Largo on 2 July, resulting in more than 39,000 people evacuating their homes due to flooding.

In southern Brazil, parts of the state of Santa Catarina received over 300 mm of rain in a 72-hour period during 3–5 May. By 6 May, at least three people died, and thousands of people were displaced due to floods and landslides. On 20 December, in Camboriu (in Brazil's state of Santa Catarina), a total of 256 mm of rain fell in 24 hours, which is more than the monthly normal of 158 mm. The heavy rain triggered intense flash floods in the affected region.

On 16 May, Subtropical Storm Yakecan favored the intensification of a cold air surge that reached most of subtropical South America east of the Andes. In Brazil, a cold wave from 16 to 23 May, the country's longest cold event in 2022, affected most of the country, along with western Amazonia and Bolivia. On 18 May, the city of São Paulo recorded its third-lowest May minimum temperature in 32 years when temperatures dropped to 6.6°C, which is 6.5°C below average. In Gama (Brasília), the minimum temperature was 1.4°C on 19 May (normal is 15.6°C), the lowest there since 1963. In the Bolivian Altiplano, the El Alto station reported its lowest May temperature on record when temperatures dropped to -9.8°C on 23 May, which is 9.2°C below average.

The central coastal region of Peru recorded its lowest minimum temperature in 15 years when temperatures dropped to 12.7°C on 13 August, which is 2.3°C below average. During 18–23 August, a cold spell impacted Santa Catarina (southern Brazil), bringing snow to the region's mountains and below-freezing temperatures (-6.4°C, or 16.4°C below average) on 19 August in Bom Jardim da Serra. This was the second-coldest event in southern Brazil in 15 years.

During 13–26 January, a heatwave event was recorded at 90% of the meteorological stations in Paraguay. The warmest day was 24 January; Concepción recorded a maximum temperature of 43.0°C, which was 8.8°C above average. The longest heatwave, which lasted for 14 consecutive days, was detected in Encarnación.

3. SOUTHERN SOUTH AMERICA

—L. S. Aldeco, J. S. Stella, A. J. Reyes Kohler, N. Misevicius, and G. Jadra

The southern South America region includes Argentina, Chile, and Uruguay.

(i) Temperature

Near- to below-average temperatures were observed across most parts of southern South America (SSA) during 2022. The most notable below-average temperatures were recorded across Uruguay and northern Chile. The national mean temperature anomaly for Argentina was +0.2°C, marking its 20th-warmest year since national records began in 1961; Chile had its 10th-coldest year since 1961 at 0.24°C below normal; Uruguay had its second-coldest year since 1991 at 0.5°C below normal (Figs. 7.16a,b,c).

During austral summer (December–February) 2021/22, above-average mean temperatures were recorded across much of the region, with the exception of the northern half of Chile, which had below-average temperatures. The highest positive anomalies, up to +3°C, were in north-eastern Argentina. Heatwaves affected the region, leading to new multiple historical maximum temperature records. The city of Florida in Uruguay recorded a maximum temperature of 44.0°C on 14 January, the highest value for this location since 1991; Rivadavia, Argentina, recorded 46.5°C on 1 January, which was the highest value for this location since 1961 and the highest value for the region and nation during 2022. Overall, Argentina observed its second-warmest summer since 1961, while Uruguay’s department of Artigas had its warmest summer since 1991.

During autumn (March–May), temperatures were below average across much of the region, while above-average temperatures were recorded across parts of northern, central, and southern Argentina and Chile. Cold irruptions on 31 May led to new historical minimum temperatures records in the region. Among the most notable were: –12.6°C in Chapelco, Argentina, the lowest minimum temperature record for May for this location since 1961; –4.3°C in Mercedes, Uruguay, the lowest minimum temperature for May for this location since 1991; and –5.9°C in Chillán, Chile, also a monthly record for this location.

Winter (June–August) was characterized by near- to above-average temperatures across Argentina, while below-average temperatures were present across Uruguay and most of Chile. Cold irruptions affected central Argentina and southern Patagonia, while a warm air mass affected northern Argentina, leading to both new minimum and maximum temperature records for July. Several cities across Uruguay, including Treinta y Tres, Colonia, and Rocha, set new low minimum monthly temperatures records (since the start of the record in 1991) during June and August.

Spring (September–November) temperatures were below average across much of Uruguay, Chile, and northern Argentina. Above-average temperatures were observed south of 33°S. An early heatwave in November affected the southern half of Argentina, with the highest temperatures (>30.0°C) in southern Argentina. Several locations set new daily and monthly maximum temperature records. Of note, temperatures of 31.2°C

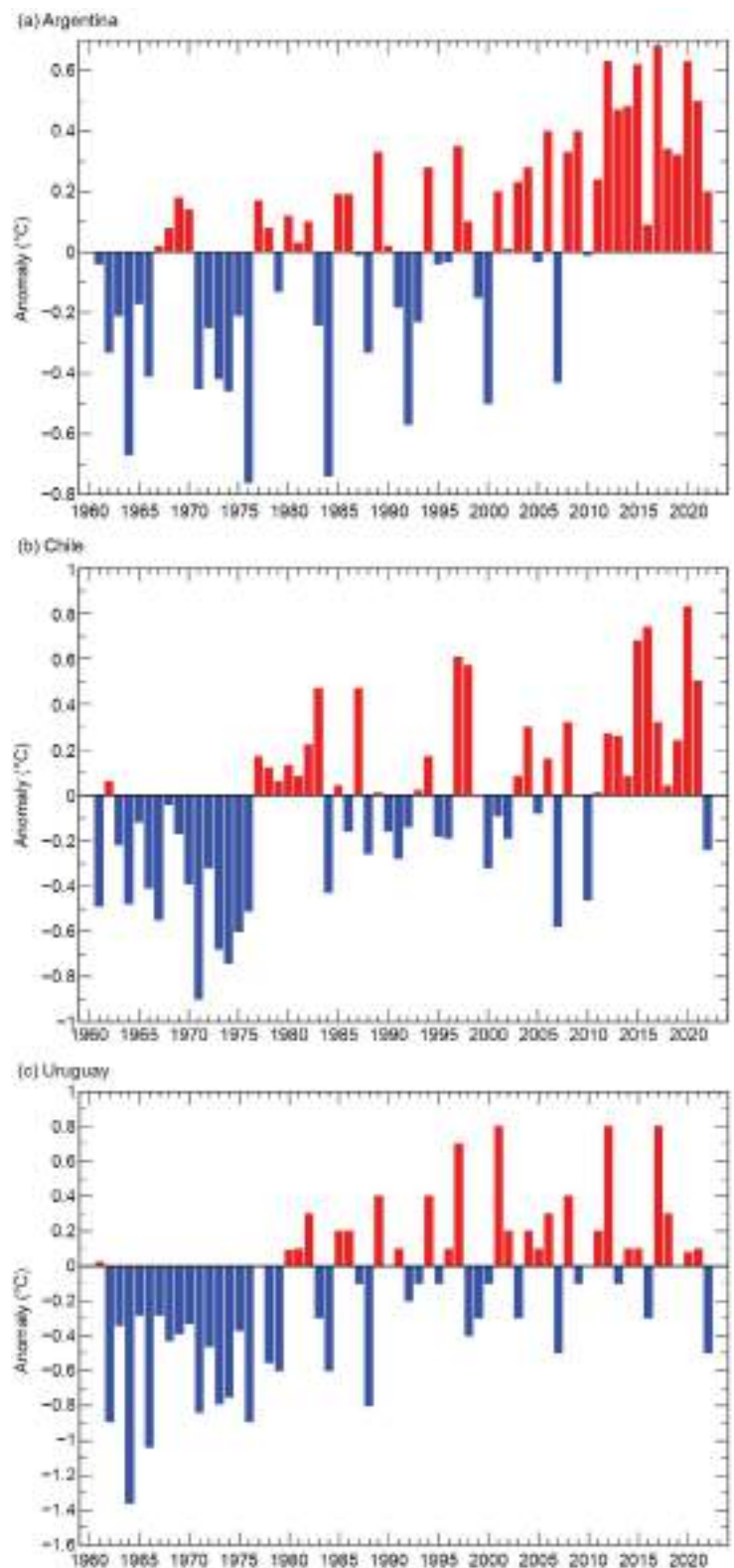


Fig. 7.16. National annual temperature anomalies (°C; 1991–2020 base period) for (a) Argentina, (b) Chile, and (c) Uruguay for the period 1961–2022.

in Esquel on 3 November and 38.6°C in Ezeiza on 5 November were recorded. This was the highest maximum temperature for November since 1961 for each location. Meanwhile, the city of Treinta y Tres in Uruguay recorded its lowest monthly minimum temperature for September (6.8°C) since 1991.

(ii) Precipitation

Similar to previous years, most of SSA had below-average annual rainfall during 2022. The most-affected regions were Uruguay, Chile, northwestern Patagonia, and north-central Argentina (Fig. 7.12). The year 2022 adds to a long period of rainfall deficit in south-central Chile, which has been called “Mega Drought” and also marks the third consecutive year of rainfall deficit in most of the region due to La Niña (Fig. 7.17). Punta Arenas in southern Chile had its second-driest year since 1966. Eastern Patagonia and northwestern Argentina had above-average annual rainfall, as much as 20%–60% above average.

During austral summer 2021/22, drier-than-average conditions were observed across northern Argentina and northern Uruguay, mostly due to the effects of La Niña. In Argentina, rainfall was 60%–87% below average in the northern region and, in Uruguay, the greatest deficits were 40%–50% below average in Rivera and Artigas. However, sub-seasonal variability favored some precipitation events that led to above-average rainfall in southern Uruguay, northern Patagonia of Chile and Argentina, and central and northwestern Argentina. In Argentina, the highest anomalies were recorded in Patagonia, with several stations receiving 100%-above-average precipitation, and in some cases, more than 150% above average. In Uruguay, Cerro Chato recorded 477 mm in January, setting its highest January rainfall total since 1991. In northwestern Argentina, Tartagal recorded 163 mm on 4 February—the highest daily rainfall for February for this location since 1961.

During autumn, drier-than-average conditions were present across most of the region;

nevertheless, frontal activity favored above-average rainfall in northeastern Argentina and northern Uruguay, ranging from +72% to +89%. In central and northwestern Argentina, most stations recorded little to no rain. In Uruguay, the stations in Colonia Rivera and Javier de Viana recorded 210 mm on 25 April, which was the highest daily April rainfall since 1991 for both locations.

During winter, below-average precipitation was recorded across most of the region, with several stations having their driest June on record (since 1961 in Argentina and 1991 in Uruguay). Northern Patagonia had above-average precipitation of +45% to +88%, mainly due to snow events during the season. Local precipitation events led to new records. Quebracho, Uruguay, received 205 mm on 25 August—its highest daily precipitation total for August since 1991; Freirina Nicolasa in Chile recorded its most intense precipitation event since 1991, with 33.1 mm in six hours on 11 July.

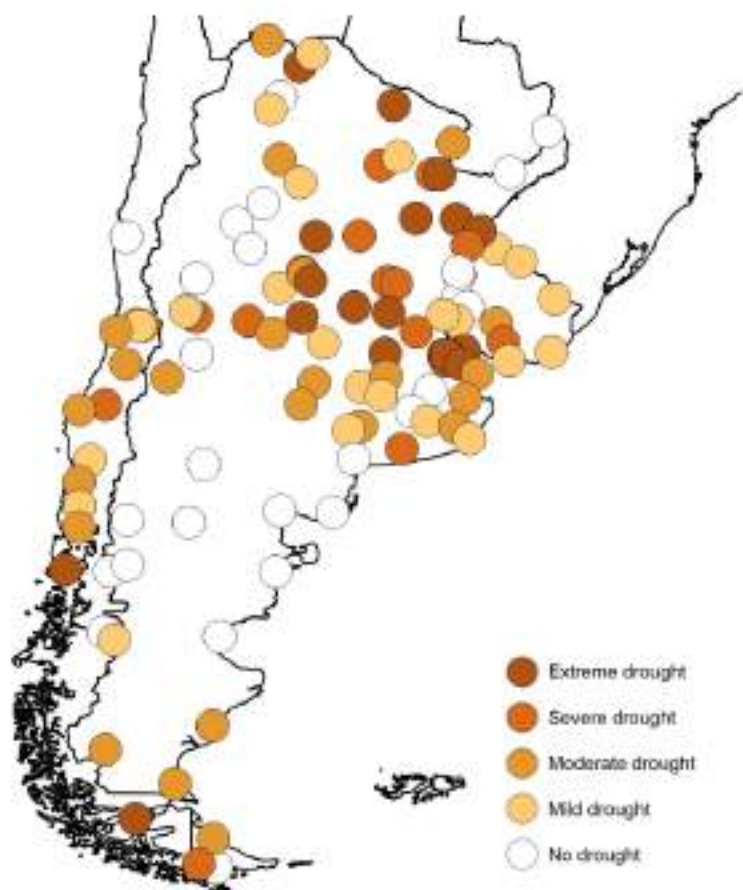


Fig. 7.17. Standardized precipitation index (SPI) for January–December 2022. SPI values can be referenced here: <https://droughtmonitor.unl.edu/About/AbouttheData/DroughtClassification.aspx>.

During spring, drought intensified with the peak of La Niña. The driest regions were recorded in Uruguay and central and northeastern Argentina, with some areas receiving little to no rainfall. Above-average rainfall was recorded in eastern Patagonia, with the highest daily rainfall for September since 1961 recorded in Comodoro Rivadavia (82.1 mm on 20 September, 228% of normal).

(iii) Notable events and impacts

Figure 7.18 shows numerous notable events that occurred across the region during 2022. Several are discussed in more detail below.

Argentina, parts of Uruguay, and Chile experienced severe drought conditions throughout much of 2022 (Fig. 7.17), which affected the region’s hydrology. Extreme drought conditions prevailed across central Argentina and southern Uruguay from May onward, mostly due to the prolonged La Niña event. Between October and December, severe drought conditions spread to northeastern Argentina. Several locations in Argentina observed their driest year on record, ranging between 50% and 60% of normal precipitation: Corrientes (818.8 mm); Paso de los Libres (773.3 mm); Rosario (561.1 mm); Junín (591.7 mm); Ezeiza (507.0 mm); Río Cuarto (457.0 mm); La Plata (567.1 mm). Due to the impacts across most of the region, this drought is considered one of the worst on record.

During January, a blocking event led to persistent heatwaves in central and northern Argentina and Uruguay, with several locations recording maximum temperatures above 40.0°C. In Argentina, the heatwave lasted for most of the month and was considered one of the most intense and prolonged heatwaves. In Uruguay, two heatwaves occurred: 12–16 January and 20–23 January. Summer 2022 was the driest summer for Corrientes, northern Argentina, which received only 83.1 mm (21% of normal) of precipitation. Drought conditions combined with high temperatures enabled the development of fires and bushfires during summer, burning close to 800,000 hectares.

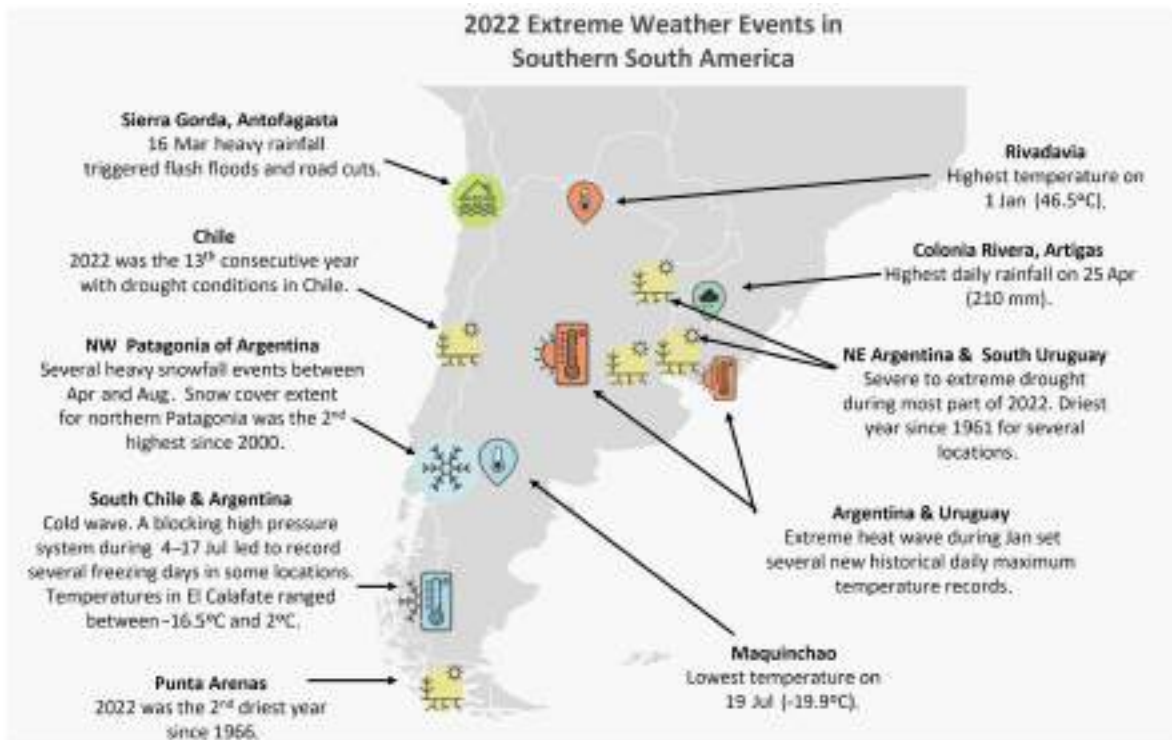


Fig. 7.18. Extreme and notable events in southern South America (Argentina, Chile, and Uruguay) during 2022.

e. Africa

—A. Mekonnen, Ed.

This analysis for Africa is based on observational records from meteorological and hydrological services across the region, rainfall from the Global Precipitation Climatology Project (GPCP), and reanalysis products from the National Centers for Environmental Prediction/National Center for Atmospheric Research (NCEP/NCAR). Notable events in 2022 were compiled based on reports from government agencies, regional and international organizations, and research/Early Warning organizations. The climatological base period is 1991–2020, and the terms “normal” and “average” are interchangeably used to refer to this climatology.

Figure 7.19 presents the 2022 mean temperature anomalies for Africa. Annual temperatures greater than 1°C above normal were observed over most of northwest Africa (Algeria, Mauritania, Morocco, and Tunisia), while Mali, Niger, Chad, and northern Nigeria had annual mean temperatures as much as 2°C below normal. Most of eastern and equatorial Africa experienced above-normal temperatures (Fig. 7.19). Except for some areas across the western half of Angola, most of Africa south of the equator remained within their annual normal temperature ranges.

West Africa north of 10°N received above-average annual rainfall, while rains over the Guinea Highlands and Nigeria were below normal. Rainfall over Ethiopia, Kenya, northern Uganda, and northern Tanzania in eastern Africa were below normal. Rainfall over the adjoining areas of the Democratic Republic of the Congo, Zambia, and Angola were more than 1 mm day⁻¹ below normal (Fig. 7.20a).

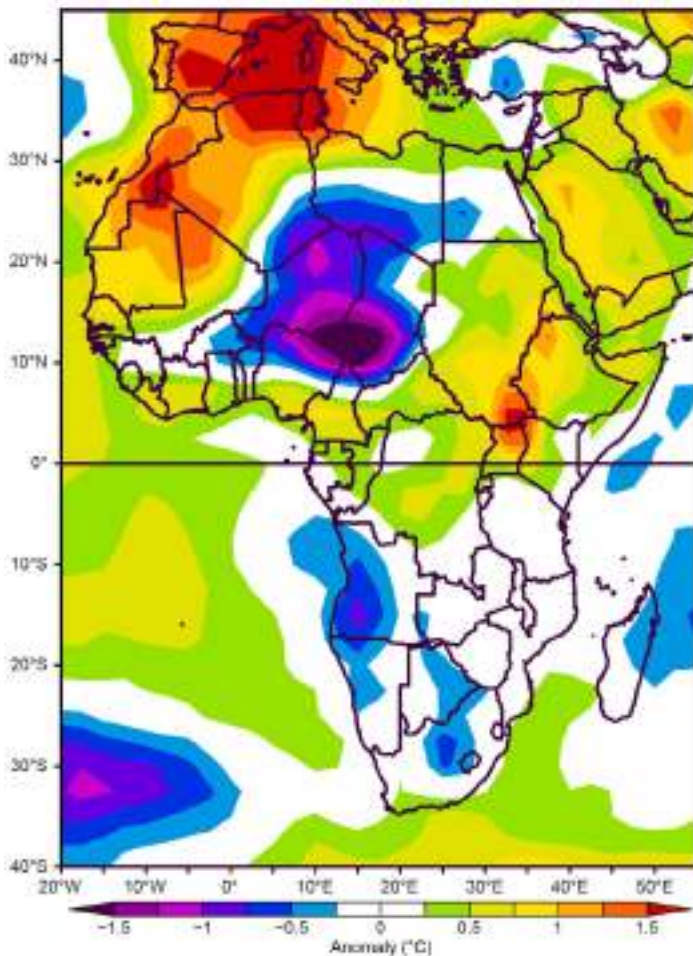


Fig. 7.19. 2022 annual mean temperature anomalies for Africa (°C; base period 1991–2020). (Source: NCEP/NCAR.)

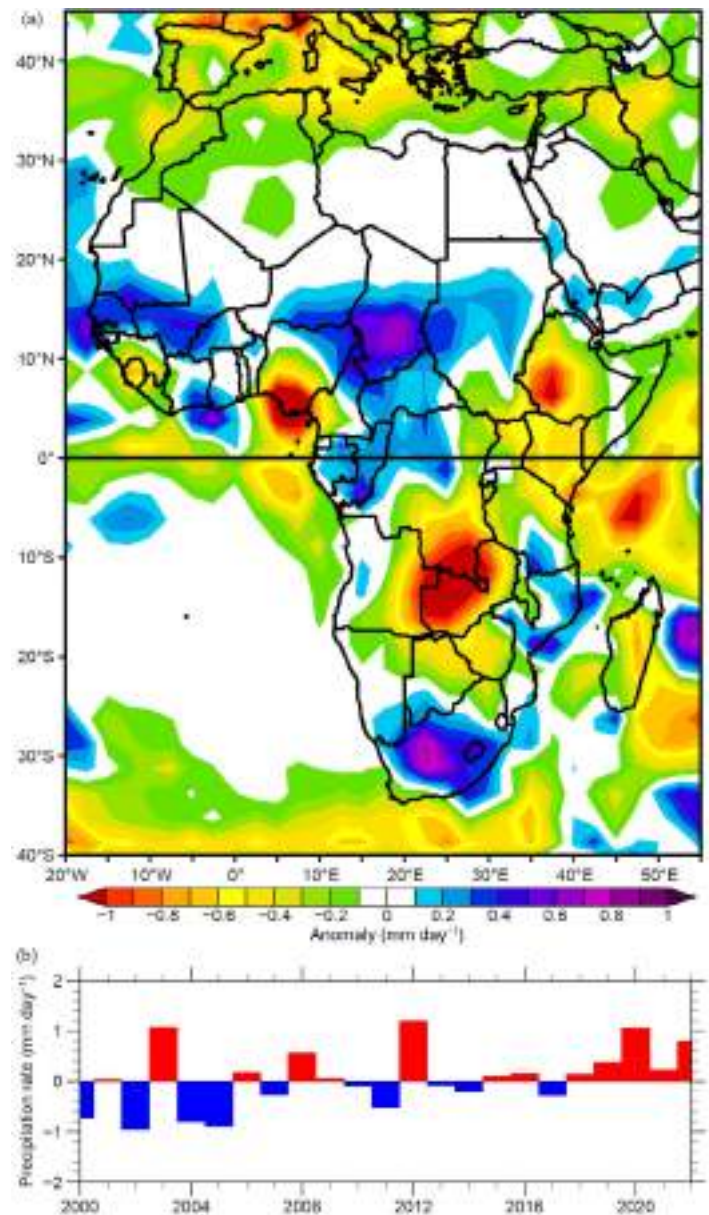


Fig. 7.20 (a) 2022 annual rainfall anomalies for Africa (mm day⁻¹; base period 1991–2020). (Source: NCEP/NCAR.) (b) Rainfall anomalies (mm day⁻¹) for West Africa (10°N–15°N, 15°W–10°E; base period 1991–2020) for the period Jul–Sep from 2000 to 2022. (Source: GPCP v2.3.)

After the devastating droughts in the 1970s through the 1990s, a rainfall “recovery” has been reported in the literature (e.g., Giannini 2015; Biasutti 2019). Although there is no consensus on the recovery, a significant increase in seasonal rainfall has been reported (c.f. Nicholson et al. 2018). To provide context, the West African (10°N–15°N, 15°W–10°E) rainfall trend for the July–September period, the peak rainfall season over West Africa north of 5°N, for 2000–22 is presented in Fig. 7.20b. Rainfall has been above normal since 2018, with July–September 2022 being the fourth-wettest such period in this record (~ 0.8 mm day⁻¹ above normal)

Extreme weather events and high climate variabilities were also reported from regions, the details of which are compiled below.

1. NORTH AFRICA

—K. Kabidi, A. Sayouri, M. ElKharrim, and A. E. Mostafa

North Africa comprises Mauritania, Morocco, Algeria, Tunisia, Libya, and Egypt. Much of this region is characterized by arid and semi-arid climate, while northern parts exhibit Mediterranean climates. Precipitation over the region was highly variable, but in general, below-normal precipitation was observed in winter (December 2021–February 2022) and heatwaves were observed during summer (June–August).

(i) Temperature

During winter, most of the region experienced temperatures greater than 0.5°C above normal (Fig. 7.21a). Moroccan records show above-average minimum temperatures over its southern and coastal Atlantic regions. Mean minimum temperatures over Tunisia, Libya, Algeria, and Egypt remained near normal (not shown). Mean temperature anomalies ranging from -1°C over Tunisia to more than -3°C over southeastern Algeria, southern Libya, and most of Egypt were observed in January. A minimum temperature of about -2°C was recorded on 5 February at Saint Catherine in Egypt.

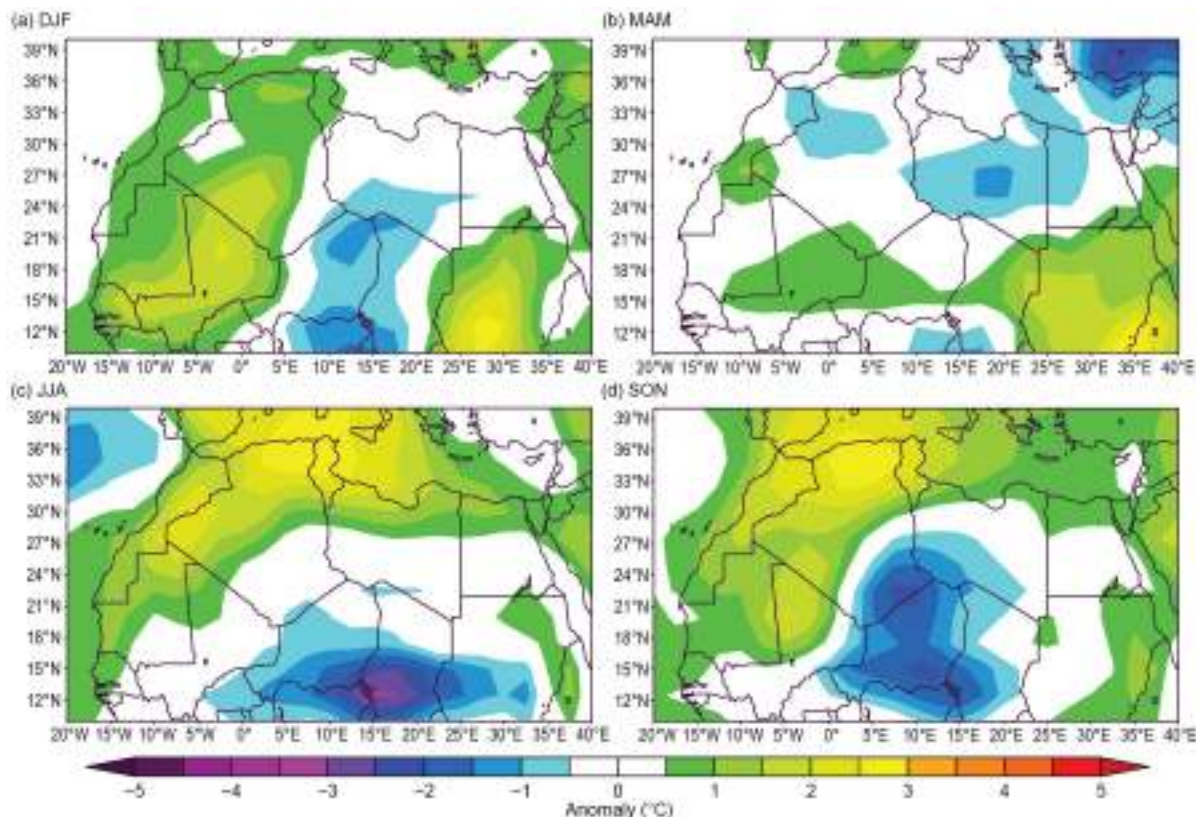


Fig. 7.21. North Africa seasonally averaged temperature anomalies ($^{\circ}\text{C}$; 1991–2020 base period) for (a) Dec–Feb 2021/22, (b) Mar–May 2022, (c) Jun–Aug 2022, and (d) Sep–Nov 2022. (Source: NOAA /NCEP.)

In general, spring (March–May; Fig. 7.21b) temperatures were near normal across North Africa, with a slight positive anomaly over southern Morocco and slight negative anomaly over Libya (Fig. 7eb). However, a new record of 47.3°C on 20 May broke the previous May maximum temperature of 45.8°C on 23 May 2015 at Sidi Slimane in Morocco. A maximum temperature of 47°C was reported at Aswan, Egypt, on 14 May 2022.

Summer (June–August; Fig. 7.21c) temperatures were more than 2°C above normal over north-northwest Mauritania, Morocco, and adjoining Algeria, Tunisia, and the northern half of Libya and Egypt. A high maximum temperature of 49.1°C was observed during summer at Smara, Morocco. The overall average maximum temperature in June in Tunisia exceeded the normal by 4.2°C, marking the highest average June maximum temperature on record for the country. Record maximum temperatures ranging from 46°C to 47°C were recorded at Monastir, Jerba, and Gafsa in Tunisia during July and August.

Above-average mean temperatures dominated the region during autumn (September–November, Fig. 7.21d), except for extreme southeastern Algeria where below-average mean temperatures were observed. In December, temperatures of 1°C to 5°C above normal dominated central and southern Algeria and extended into the southern half of Tunisia, the northern half of Egypt, and western Libya (not shown). Records show that mean temperatures in December 2022 over Tunisia were about 3.4°C above normal, the highest since 1950.

(ii) Precipitation

Below-normal precipitation dominated much of the region during winter (Fig. 7.22a). The lack of winter precipitation over Morocco and adjacent countries was associated with expansive dominance of Azores high pressure. The precipitation deficit over Morocco in January and February ranged from 62% to 74% of normal. However, above-normal winter precipitation was reported from meteorological stations at Errachidia and Ouarzazate in southeast Morocco. Reports from various observatories show that winter precipitation was generally below normal over Egypt. However, extremely heavy rainfall was reported from stations in January.

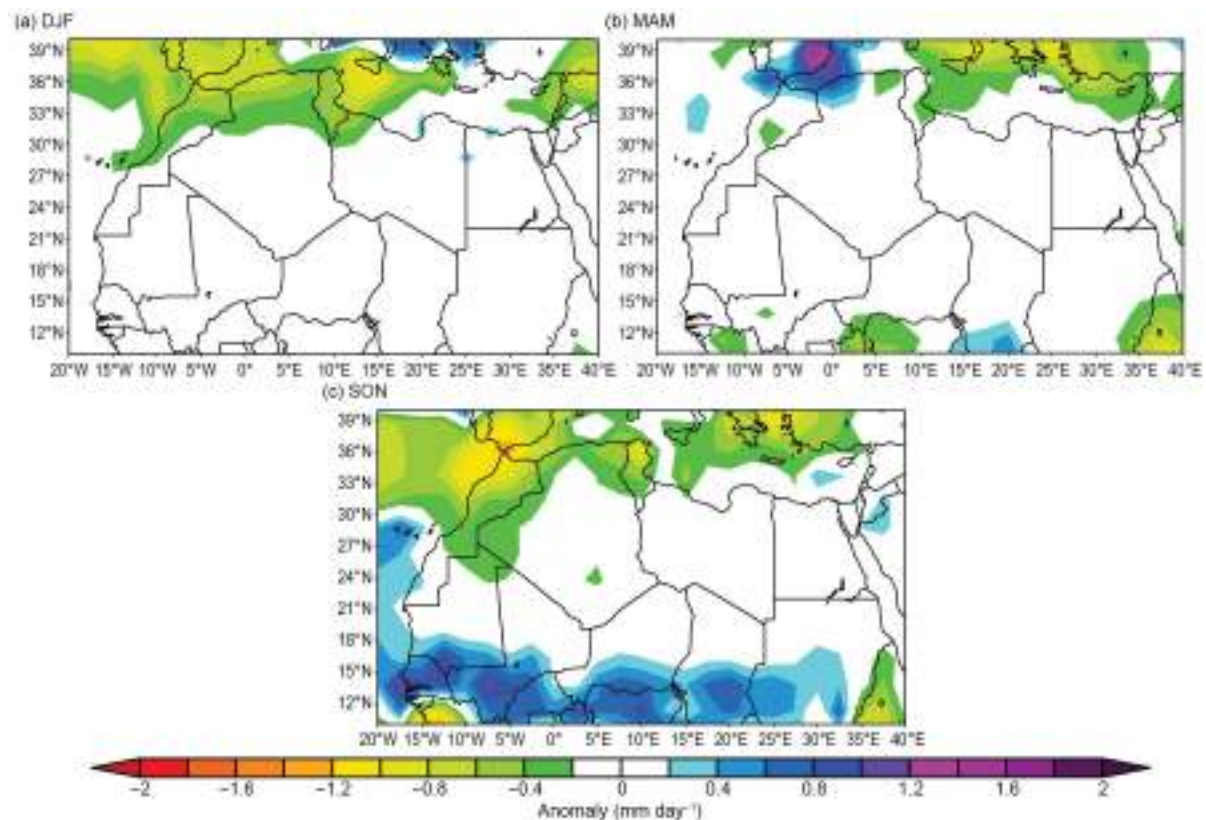


Fig. 7.22. North Africa seasonally averaged rainfall anomalies (mm day⁻¹; 1991–2020 base period) for (a) Dec–Feb 2021/22, (b) Mar–May 2022, and (c) Sep–Nov 2022. (Source: GPCP NOAA/NCEP.)

For example, Alexandria received 60 mm on 8 January and Elkolliya-ElBaharia received 75.4 mm on 9 January. Precipitation in January and February was near normal in Algeria.

Spring mean precipitation did not ameliorate winter deficits, although precipitation was near normal (Fig. 7.22b). Above-normal precipitation was reported in March over northern Morocco, but drought conditions prevailed in April and May over most of the country. In Algeria, March and April precipitation was above normal. In Tunisia, record precipitation fell in some areas, including 92 mm at Kairouan on 19 March (previous record 76.6 mm on 15 March 1991) and 79 mm at Tozeur on 19 March (previous record 25.7 mm on 26 March 1993).

Rainfall during June–August is not discussed in this analysis because the season is normally dry over North Africa, north of 20°N–25°N. Autumn precipitation (Fig. 7.22c) was below normal for the region, but some stations in Morocco reported above-average precipitation during the last 10 days of September (Smara ~194% of normal, Dakhla 280%, Agadir ~120%). Rainfall deficits during October and November were associated with the extension of the Azores high into the region. October was the driest on record since 1960 in Tunisia. Wet conditions were observed in northern Tunisia during November (above normal in some stations), while drier-than-normal conditions were reported in central and southern parts of the country (deficits were approximately 30% of normal). December 2022 was the driest December on record for Tunisia since 1950 (e.g., Enfidha 100%, Jerba 97%, Gafsa 37% below normal). On the other hand, in Egypt, Ras Elitine received 84.2 mm on 25 December 2022, marking the highest one-day rainfall in the country in 2022.

(iii) Notable events and impacts

In late January, heavy snowfall (10 cm–20 cm) affected northern regions of Libya (Sidi AlHamri, Shahat, Al-Bayda, Qandula, and Belqes), including some road closures. The snow was associated with a cold air mass centered on the northeastern regions.

During summer 2022, a series of forest fires broke out in Morocco, Algeria, and Tunisia. Heatwaves due to exceptional drought and water stress especially affected Morocco in July and August. Forest fires destroyed about 11,000 hectares of forest and 1156 families had to be relocated in the Moroccan provinces of Larache, Ouezzane, Tetouan, Chefchaouen, Taza, and Al Hoceima. In Tunisia, 219 forest fires were reported between June and September, which destroyed 5900 hectares. Nabeul, Tunis, Bizerte, Siliana, Béja, and Jendouba were the main regions affected. In addition, several forest fires broke out in northern and eastern Algeria during August and September, causing 43 deaths and the destruction of 800 hectares of forest and 1800 hectares of coppice. The areas of Bejaia, Jijel, Setif, Khenchela, El Tarf, Tebessa, Souk Ahras, and Skikda et Tipaza were all affected.

In October, violent floods due to heavy rains hit northeastern regions of Algeria, especially in the region of Bordj Bou Arreridj, killing four people. Flash floods in late November affected Tripoli and western areas of Libya as 128 mm of precipitation fell within a 24-hour period. The main roads were flooded and schools were disrupted.

2. WEST AFRICA

—W. Agyakwa, J. Hicks, W. M. Thiaw, S. Hagos, and F. Sima

West Africa extends from the Guinea coast to about 20°N and from the eastern Atlantic coast to Niger. West Africa consists of two sub-regions: 1) The Sahel (12°N to 17°N; Senegal and The Gambia in the west to Niger in the east) and 2) the Gulf of Guinea region to the south (from about 4°N to 10°N; the Guineas to the west along the east Atlantic coast and Nigeria and Cameroon to the east).

(i) Temperature

The highest mean annual temperatures ranged between 28°C and 30°C, mainly across the western and central Sahel (Senegal, Mauritania, and Mali; Fig. 7.23a). Most countries in the Gulf of Guinea region had lower mean annual temperatures ranging from 22°C to 24°C. Areas in the central Sahel region (northern Nigeria and southern Niger) had mean annual temperatures between 22°C and 26°C, which were 1°C to 2°C below normal (Fig. 7.23b).

Mean annual maximum temperatures were normal to below normal over the Sahel region, with anomalies as much as -3°C in southern Niger. Conversely, above-normal annual maximum temperatures were recorded in the Gulf of Guinea countries, including Liberia, Cote d'Ivoire, Ghana, Togo, Benin, and southern Nigeria. The highest positive anomalies of +1.5°C to +3°C were recorded in southern Nigeria. Mean annual minimum temperatures were 0.5°C to 1.5°C below normal in northeastern Nigeria and southeastern Niger and 0.5°C to 2.5°C above average across western parts of West Africa.

The warmest months in the Sahel were April, May, June, and July, with mean daily temperatures ranging from 34°C to more than 36°C, with the highest temperatures over Mauritania and Mali during June. However, compared with climatology, April had the highest above-average temperature, with anomalies from +0.5°C to +2°C over the western and central Sahel regions.

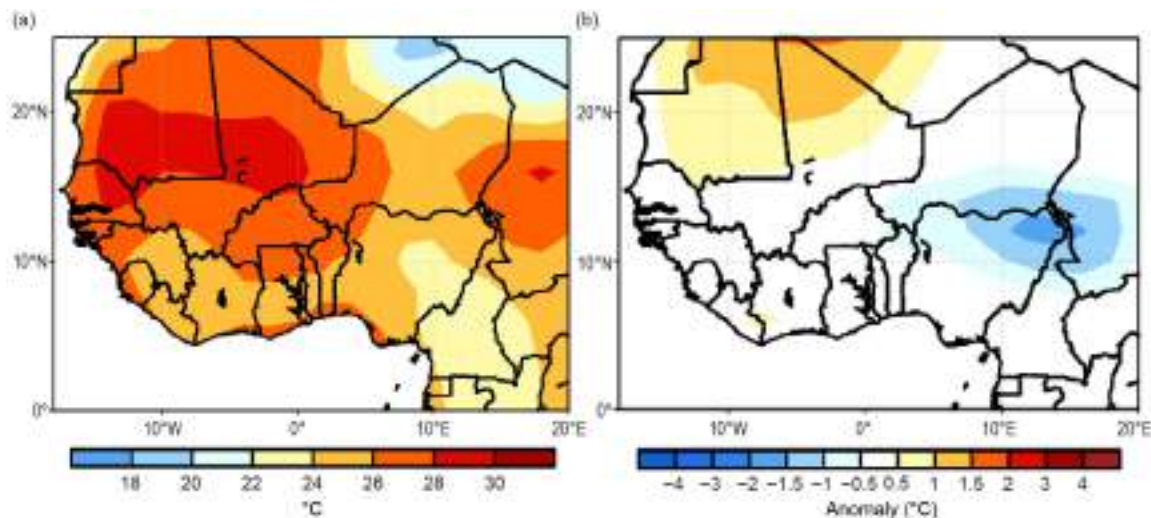


Fig. 7.23. Annual (a) mean temperatures and (b) mean temperature anomalies in 2022 for West Africa (°C; 1991–2020 base period). (Source: NOAA/NCEP.)

(ii) Precipitation

In the Sahel, annual rainfall ranges from 200 mm to 1500 mm, and increases to the south. The highest rainfall amounts, between 1000 mm and 1500 mm, occurred in southern Senegal, The Gambia, and southern Mali (Fig. 7.24a). Average rainfall anomalies of +50 mm to +150 mm were observed over Mauritania, Senegal, The Gambia, southern Mali, Burkina Faso, central and eastern Niger, and northeastern Nigeria. Over Mauritania, Senegal, central Mali, and eastern Niger, recorded rainfall was about 120%–200% of normal rainfall.

Annual rainfall totals over the Gulf of Guinea region ranged from 1000 mm to over 2000 mm, with the highest totals over Sierra Leone. Even with these high totals, Sierra Leone still registered

below-average rainfall (50 mm to 150 mm below normal; Fig. 7.24b). The most significant anomalies of -50 mm to more than -300 mm occurred in Nigeria. The greatest deficits (more than -300 mm) occurred in southeastern Nigeria (10th percentile). Above-average rainfall ($+50$ mm to $+200$ mm) was recorded over eastern Cote d'Ivoire and Ghana. The highest departures from the mean ($+150$ mm to $+200$ mm) were observed in southwestern Ghana (90th percentile).

Significant rainfall totals were observed in the southern Sahel and the Gulf of Guinea from April to October, with the highest occurring from June to September, resulting in much of the annual cumulative rainfall. In August and September, almost the entire Gulf of Guinea region received more than 200 mm of rain, which was reflected in the July–September (JAS) and August–October (ASO) seasonal rainfall, with surpluses of $+50$ mm to $+150$ mm. During JAS and ASO, rainfall totals were above average ($+20$ mm to $+150$ mm) over western Guinea, southwestern Sierra Leone, Liberia, Cote d'Ivoire, Ghana, Togo, Benin, and Nigeria. The highest departures from average ($+100$ mm to $+150$ mm) were recorded over Cote d'Ivoire and Ghana, which received 120%–200% of their average rainfall (90th percentile). Throughout the seasons, as mentioned above, rainfall deficits (-20 mm to more than -150 mm) were registered over Guinea, Sierra Leone, Liberia, and Nigeria. In addition, over the Gulf of Guinea, the highest rainfall anomalies (more than $+150$ mm) occurred in southern Ghana during April–June, the peak rain season over the region. Surpluses between $+50$ mm and $+100$ mm (120%–200% of normal) were observed during April and June.

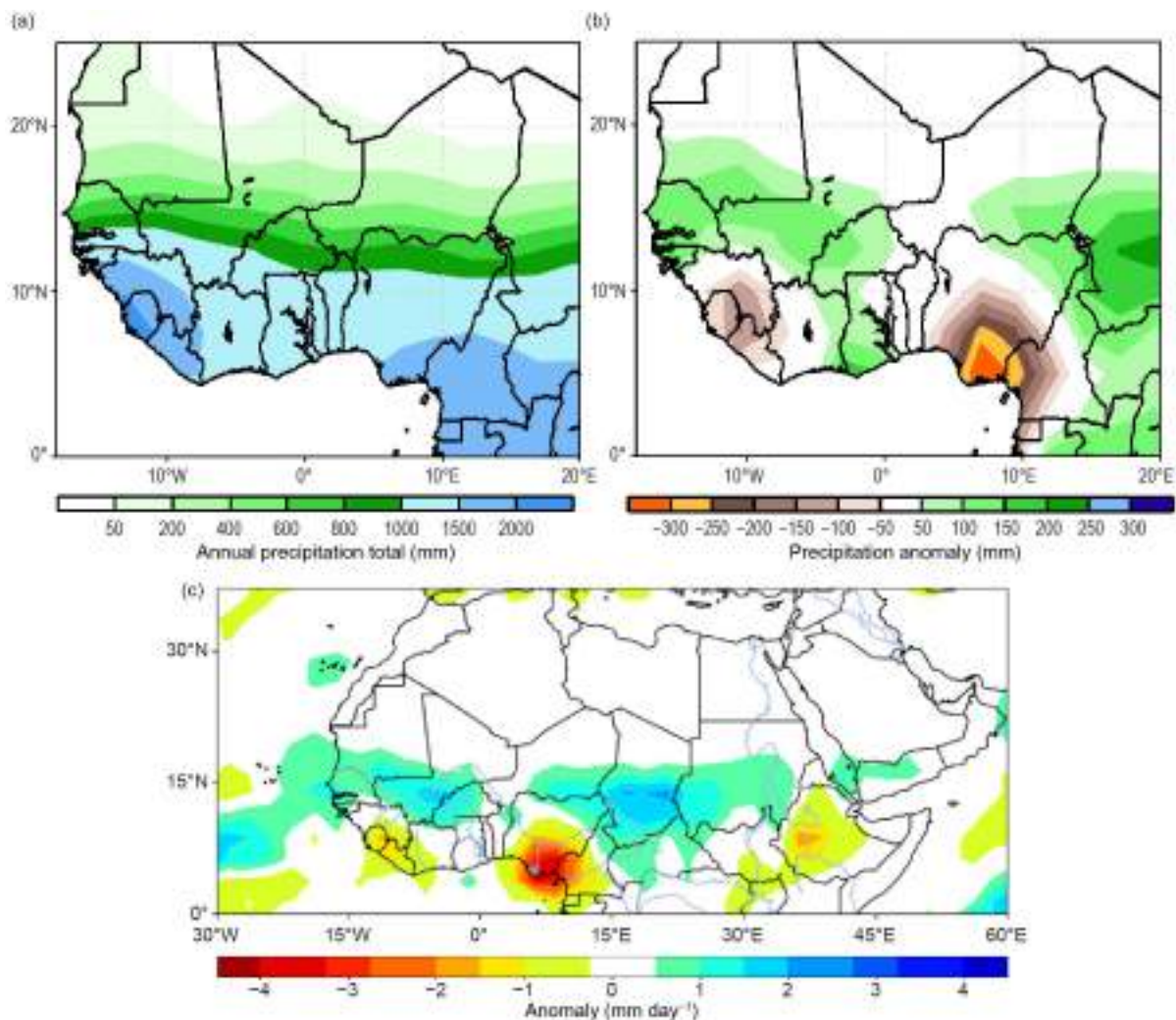


Fig. 7.24. Cumulative (a) annual total precipitation (mm), (b) annual total precipitation anomalies (mm), and (c) Jun–Sep precipitation anomalies (mm day⁻¹) in 2022 for West Africa (1991–2020 base period). (Source: NOAA/NCEP.)

Substantial rainfall occurred in the Sahel region during June–August (JJA), JAS, and ASO, with more than 500 mm recorded over the southern Sahel region, 20 mm–150 mm above normal, with the highest anomalies (+100 mm to +150 mm, 120%–200% of normal) over southern Mauritania, southern Mali, and western Burkina Faso. Among the three seasons (JJA, JAS, and ASO), southern Mali, western Burkina Faso, southeastern Niger, and northeastern Nigeria registered substantial rainfall surpluses ranging from +100 mm to more than +150 mm during JAS. At the northeastern tip of Nigeria, surpluses exceeding +150 mm were recorded. Over the Sahel, rainfall surpluses of about +20 mm to +30 mm occurred in July and August, and surpluses reached their peak of about +50 mm to +100 mm in September over southern Mali, Burkina Faso, northern Nigeria, and southern Nigeria.

Overall, widespread above-normal precipitation throughout the West African Sahel region from the western coast to the eastern border of Chad during June–September was observed (Fig. 7.24c). The seasonal mean precipitation was particularly high over southern Mali and southern Chad, which led to several extreme precipitation events.

(iii) Notable events and impacts

Above-average rainfall and heavy rain events led to widespread flooding across the region during the boreal summer. The Civil Protection Directorate of Niger indicated that eight people lost their lives due to heavy rain and flooding between June and July. Heavy rain on 15 July damaged roads and homes in the Diffa, Zinder, Maradi, and Tahoua regions, causing one additional fatality. In Senegal, short-duration heavy rainfall totaling 127 mm in Dakar was reported on 5 August, leaving city streets inundated. Flood waters ~1 m deep caused widespread traffic disruption. In Mali, the government of the Mopti Region reported rivers overflowing in several places in September. Several places in Mauritania and The Gambia were also affected by floods during June–September. The flash floods that impacted The Gambia were among the worst there in nearly half a century. Torrential rain and thunderstorms caused widespread damage that affected large parts of the country, particularly the densely populated Banjul area. According to the Department of Water Resources of The Gambia, 276 mm of rain fell during 30–31 July at Banjul International Airport. The National Disaster Management Agency of The Gambia reported that four people were killed by lightning in the North Bank region.

In the Gulf of Guinea region, the United Nations reported flood conditions in Cote d'Ivoire (16 July), Sierra Leone (29 August), Benin (throughout September), and Guinea (17 September). The flooding affected thousands of people and houses. Significant livestock losses were recorded, and several hectares of crops and farmlands were also affected. The United Nations Children's Fund (UNICEF) reported that since September 2022, the worst floods in a decade affected 3.2 million people across Nigeria. It is estimated that 60% of the people affected were children, and the highest number of displaced persons occurred in Anambra, Bayelsa, Cross River, and Jigawa States. Heavy rainfall and river overflow damaged public health facilities, water systems, and sanitation facilities, which increased the risk of waterborne diseases, such as cholera, diarrhea, and malaria, and heightened the chances of an epidemic as well as childhood illnesses. The children living in makeshift displacement sites lacked basic facilities and were exposed to additional risks, such as separation from their families and gender-based violence.

3. CENTRAL AFRICA

—W. Agyakwa, J. Hicks, and W. M. Thiaw

Central Africa features a unique climate system marked by a strong annual cycle as it spans a wide area of Africa across both the Northern and Southern Hemispheres. The region extends from the southern tip of the Democratic Republic of Congo (DRC) northward into the central areas of Chad. Longitudinally, the region extends from about 5°E to ~35°E. Given the overlap with areas in West Africa and East Africa, this analysis focuses strictly on the sub-region encompassing Cameroon, Chad, Central Africa Republic (CAR), DRC, Congo, Gabon, Equatorial Guinea, and Sao Tome and Principe.

(i) Temperature

Mean annual temperatures ranged from 21°C to 25°C throughout Central Africa and approached 27°C in central Chad and 19°C in east-central DRC. These temperatures correspond to anomalies that were about 0.75°C above the mean in northeastern DRC and 1°C–1.5°C below the mean in northern Cameroon and central and southern Chad. In central portions of DRC and east-central portions of CAR, annual mean temperatures were above the 85th percentile (Fig. 7.25a). Southwestern portions of Chad experienced their lowest annual mean temperatures. Annual maximum temperatures were mostly between 24°C and 32°C, but up to 37°C in central Chad. This translated to maximum temperatures that were 1°C–2°C above the mean from southern Cameroon to central and southern CAR and 1°C–2.25°C above the mean in southern and eastern DRC (Fig. 7.25b). Conversely, maximum temperatures were about 1°C–3°C below the mean in southern and central Chad, where much of the region experienced its lowest maximum temperatures.

The northern sector of Central Africa experiences its highest mean temperatures from March–June, from around 28°C in northern CAR to more than 32°C in northern Cameroon and central Chad. Central CAR observed mean temperatures in March that were 1°C–2.25°C above normal, placing this region above the 90th percentile for that month. However, mean temperatures north of the Mbang Mountains in Cameroon were more than 2°C below the mean for May, ranking as the coldest or second-coldest May on record. This region—including southern and central Chad—had an additional six consecutive months (June–November) where mean temperatures ranked as the coldest or second coldest on record relative to the climatological mean. Conversely, the southern sector of Central Africa (southern Cameroon to DRC) had nine months where a majority of this region experienced mean temperatures ranking above the 70th percentile, including central DRC, which experienced three months (May, July, and August) with

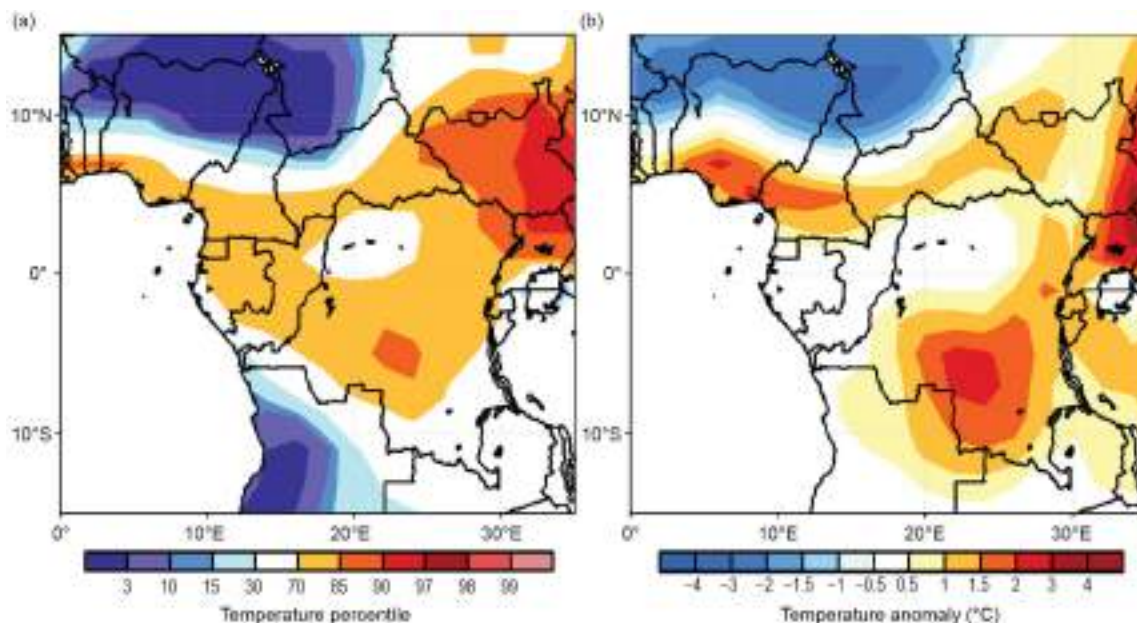


Fig. 7.25. Annual (a) mean temperature percentile rank and (b) maximum temperature anomalies (°C) in 2022 for Central Africa (1991–2020 base period). (Source: NOAA/NCEP.)

mean temperatures above the 90th percentile (up to 3°C above normal). Maximum temperatures ranged from 32°C in central Cameroon/southern CAR to about 43°C in central Chad in March before transitioning to below-normal maximum temperatures by May—more than 5°C below the mean—especially throughout northern Cameroon and central/southern Chad. This cold pattern extended from May until the end of the year, resulting in some regions experiencing their lowest maximum temperatures on record, particularly during May–August. As maximum temperatures plummeted in this region around May, maximum temperatures throughout central and southern DRC soared to 30°C to 31°C. This corresponded to anomalies that were 4°C to nearly 7°C above the mean from July to October, with two months (July and August) ranking above the 90th percentile. Annual minimum temperature anomalies were less pronounced than the maximum temperature anomalies. Northern Cameroon and western Chad observed annual minimum temperatures up to about 1°C below the mean. Southern Cameroon, Equatorial Guinea, Gabon, western Congo, eastern CAR, and northeastern DRC observed annual minimum temperatures up to 1°C above normal.

The monthly evolution of the minimum temperatures was highly variable throughout the year. Most of DRC, Gabon, and Congo observed near- to above-normal minimum temperatures during January–May. From Gabon to central and southern DRC, minimum temperatures ranked above the 90th percentile—particularly in April and May—before observing near- to below-normal minimum temperatures in June that ranked below the 10th percentile in central DRC and most of Congo. June also saw the greatest below-average minimum temperatures for portions of east-central Congo and west-central DRC. In addition, a large swath of below-normal minimum temperatures covered northern Cameroon and southern and western Chad in February, June, and November, with much of the region experiencing its coldest or second-coldest minimum temperatures on record. Southern Cameroon observed minimum temperatures above the 90th percentile, particularly in April, May, July, and October. Eastern CAR also experienced minimum temperatures above the 90th percentile in April.

(ii) Precipitation

Most of the rainfall in Central Africa is tied to the summer season across both sides of the equator. In the northern part of the region, greater rainfall totals typically begin after April and extend until October, giving way to heavier rainfall in the southern part of the region from October to April. Closer to the equator, rainfall is persistent throughout the year and changes in intensity due to the north–south movement of the Intertropical Convergence Zone. On average, rainfall totals are highest in coastal Cameroon, which receives just over 2000 mm of rainfall. This region received below-average rainfall in 2022, with deficits exceeding –250 mm, yielding rainfall totals below the 10th percentile. Annual rainfall deficits extended from coastal Cameroon to coastal Gabon, ranking below the 30th percentile from Equatorial Guinea to coastal Gabon. Farther inland, central Chad to southeastern DRC experienced annual rainfall surpluses. From central to southern Chad, a tight north–south gradient in annual precipitation existed, from around 200 mm in central Chad to over 1000 mm in southern Chad (Fig. 7.26a). Central Chad observed annual rainfall surpluses upwards of +200 mm (Fig. 7.26b), ranking above the 90th percentile. Eastern Gabon to western DRC—an area that typically receives up to 1800 mm of rainfall each year—experienced rainfall surpluses of over +150 mm, yielding a rainfall ranking of greater than the 90th percentile in a small area of central Congo (in the higher elevations near Djambala). Southeastern DRC typically receives around 1300 mm of rainfall each year. This region was drier than normal in 2022, as much as 300 mm below average, placing it below the 10th percentile.

Coastal Cameroon experienced nine months of near- to below-normal rainfall, especially in March, June, and August, which saw deficits of up to –100 mm. Rainfall deficits up to –50 mm in August extended into northern Congo, resulting in monthly rainfall below the 10th percentile from southwestern Cameroon to northern Congo and below the 30th percentile around coastal Cameroon. Farther north, the beginning of the rainy season lasting from April to June resulted in seasonal rainfall surpluses of +20 mm to +60 mm, particularly over CAR and southern Chad.

These surpluses increased, as up to 275 mm of precipitation fell in northern Cameroon, southern Chad, and throughout most of CAR in July and September. This resulted in seasonal (July–September) and monthly (July and September) rainfall above the 90th percentile for much of the region. In southeastern DRC, significant deficits were observed in January (–50 mm to > –100 mm) and February/March (–50 mm to –70 mm), resulting in the driest month (January) and three-month (January–March) period on record.

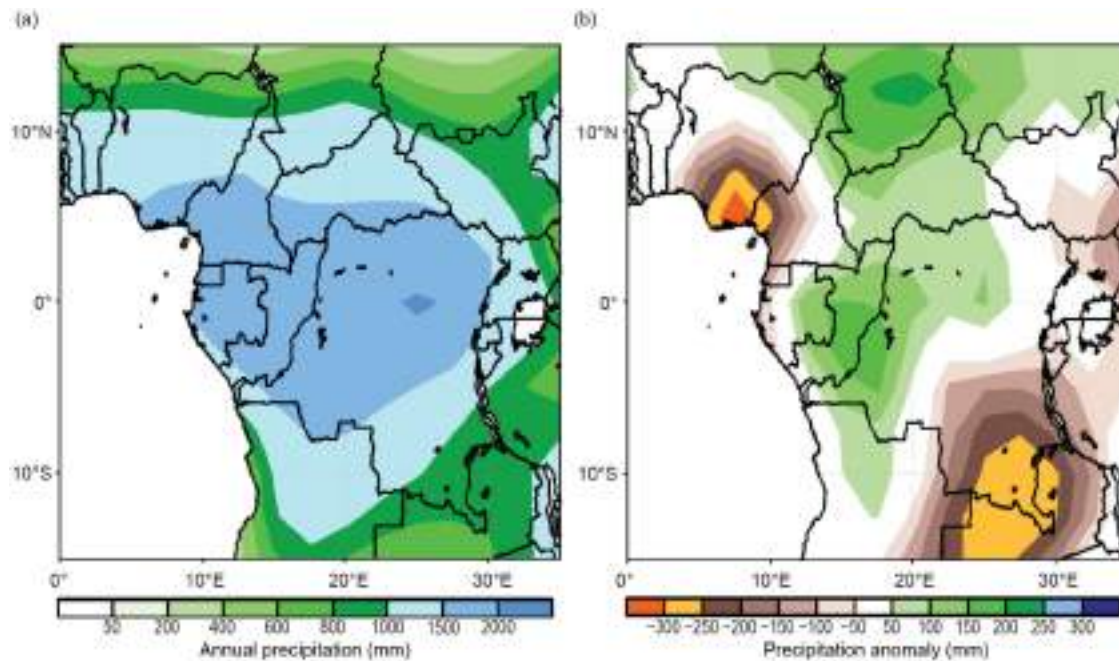


Fig. 7.26. Cumulative annual (a) precipitation totals and (b) precipitation anomalies in 2022 for Central Africa (mm; 1991–2020 base period). (Source: GPCP data, NOAA/NCEP.)

(iii) Notable events and impacts

According to the U.S. Agency for International Development, heavy rainfall from June to October triggered extensive flooding in 19 of Chad’s 23 provinces and affected more than a million people. Following months of persistent heavy rainfall, over 190,000 people were displaced in and around the capital city of N’Djamena after up to 160 mm of rain fell in 24 hours beginning on 2 August. According to the United Nations, 22 people were killed and approximately 55,000 houses were damaged or destroyed due to flooding in July and August. The U.S. ambassador declared the need for humanitarian assistance in September, resulting in the distribution of cash funds, shelter, water, sanitation, hygiene, and food. Flooding occurred during the season of heightened malnutrition risks, resulting in more than 2.1 million people across Chad requiring emergency food assistance.

The aforementioned flooding was part of a widespread pattern that also led to heavy rains and flooding in the far north region of Cameroon. Flooding began in mid-August, and by September had affected more than 150,000 people, damaged over 18,000 houses, destroyed over 27,000 hectares of farmland, and killed over 5800 livestock in the departments of Mayo-Danay, Logone-et-Chari, and Mayo-Tsanaga. In addition, a reported 200 mm of rain fell in 48 hours ending on 11 August in the coastal city of Douala in southwest Cameroon. On the same day, heavy rainfall exceeding 100 mm according to the NOAA’s Climate Prediction Center satellite rainfall estimates version 2 (RFE2) triggered landslides that killed five people in the northwest town of Widikum.

DRC also experienced a destructive landslide during 12–13 December that killed 169 people and displaced over 5000 households in the capital city of Kinshasa after heavy rainfall exceeding 80 mm, according to the RFE2.

4. EAST AFRICA

—E. Bekele, Z. T. Segele, and W. M. Thiaw

The Greater Horn of Africa (GHA), or East Africa, encompasses 11 countries and extends 12°S–24°N and 21°E–52°E. Its northern sector comprises Sudan, South Sudan, the northern two-thirds of Ethiopia, Eritrea, Djibouti, and the northern two-thirds of Somalia. Southern Somalia, southern and southeastern Ethiopia, Kenya, northern Tanzania, Uganda, Rwanda, and Burundi are in its equatorial sector, while the southern sector encompasses central and southern Tanzania. The region has a complex terrain, with elevation ranging from about 160 m below sea level at Ethiopia’s northern exit of the Rift Valley to more than 5000 m above sea level at glaciated Mount Kilimanjaro. This complex topography is further typified by the presence of large lakes and is reflective of multi-faceted climate zones modulated by local and large-scale forcing such as the deep convective and moisture convergence zone, the El Niño–Southern Oscillation, the Indian Ocean dipole, the Madden-Julian Oscillation, and tropical–extratropical interactions. Rainfall is bimodal in the equatorial sub-region, with two distinct rainfall seasons in March–May (MAM) and October–December (OND). Seasonal rainfall is unimodal in the northern and southern sectors, spanning November–April in the south and June–September (JJAS) in the north.

(i) Temperature

Annual mean temperatures exceeded 26°C over most of Sudan, Somalia, Djibouti, Eritrea, eastern Ethiopia, and Kenya (Fig. 7.27a). Although it was anomalously warm over Ethiopia (1.5°C–2°C above normal), annual mean temperatures were less than 20°C across most of central

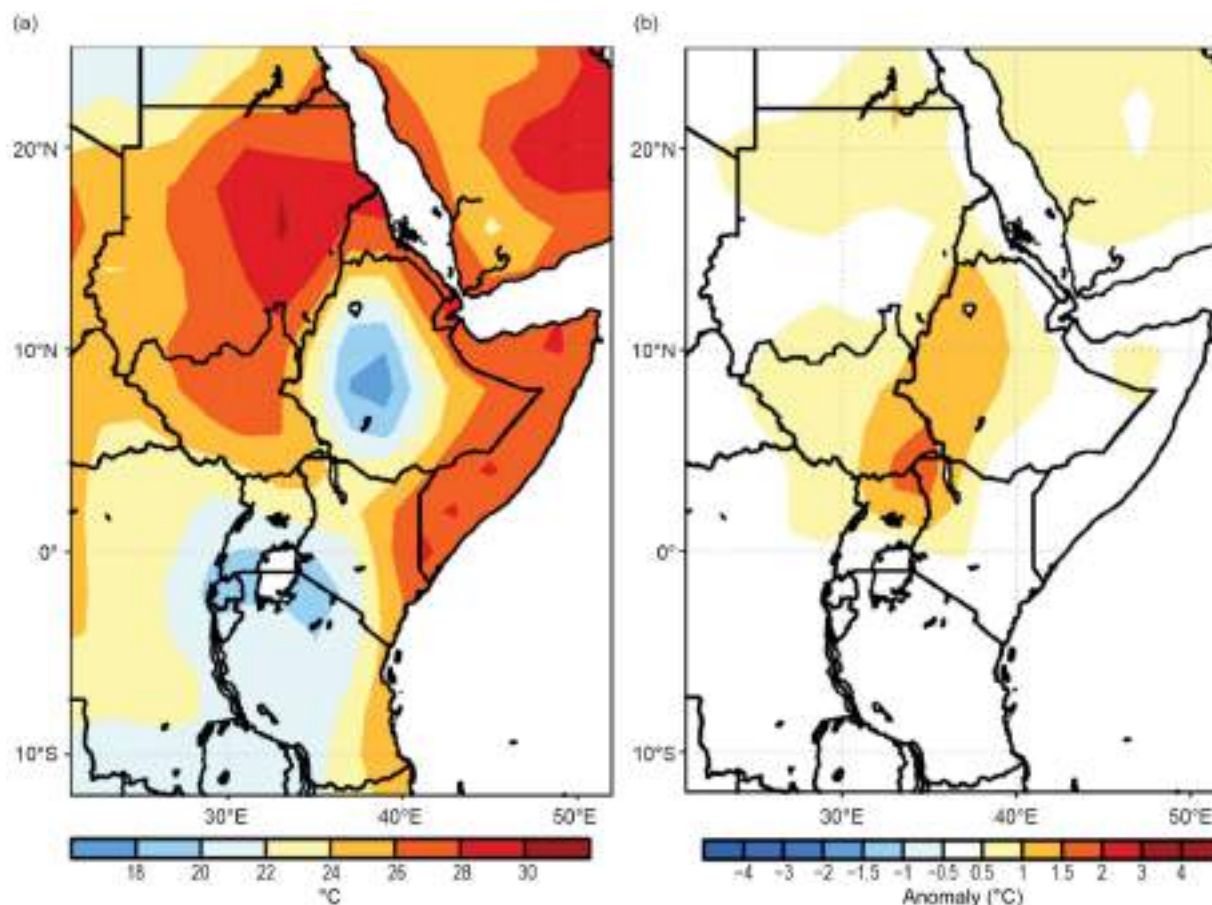


Fig. 7.27. Annual (a) mean temperature and (b) mean temperature anomalies (°C; 1991–2020 base period) in 2022 for East Africa. (Source: NOAA/NCEP.)

Ethiopia and in the Lake Victoria regions of equatorial East Africa (Fig. 7.27b). Anomalous warm mean temperatures were most pronounced during March–May over Ethiopia, South Sudan, Sudan, and northern Uganda due to higher-than-average minimum and maximum temperatures. On the other hand, seasonal mean temperatures were 0.5°C–1.5°C below average over eastern Tanzania, southeastern Ethiopia, and parts of Sudan during June–September.

Annual maximum temperatures exceeded 36°C in central and eastern Sudan but were 24°C–26°C across central Ethiopia and the Great Lake regions of East Africa. However, annual maximum temperatures were 2°C–3°C above normal across the Karamoja cross-border regions of Uganda, South Sudan, Kenya, and Ethiopia. Annual minimum temperatures exceeding 24°C were recorded in the coastal regions of Sudan, Eritrea, Djibouti, Kenya, Somalia, and Tanzania, while central Ethiopia and parts of Tanzania had annual minimum temperatures below 16°C. The greatest negative annual minimum temperature anomalies of >–3°C were observed over Tanzania during June–September.

(ii) Precipitation

Annual rainfall surpassed 1000 mm across western Ethiopia, parts of South Sudan, Uganda, Rwanda, Burundi, and northwestern and southern Tanzania (Fig. 7.28a). Western Kenya, central Ethiopia, eastern South Sudan, northeastern Uganda, and much of Tanzania received rainfall between 600 mm and 1000 mm. Totals were less over northern Sudan, Eritrea, Djibouti, southeastern Ethiopia, northeastern Kenya, and Somalia, with amounts between 50 mm and 600 mm. Overall, rainfall was below normal over much of equatorial East Africa (Fig. 7.28b).

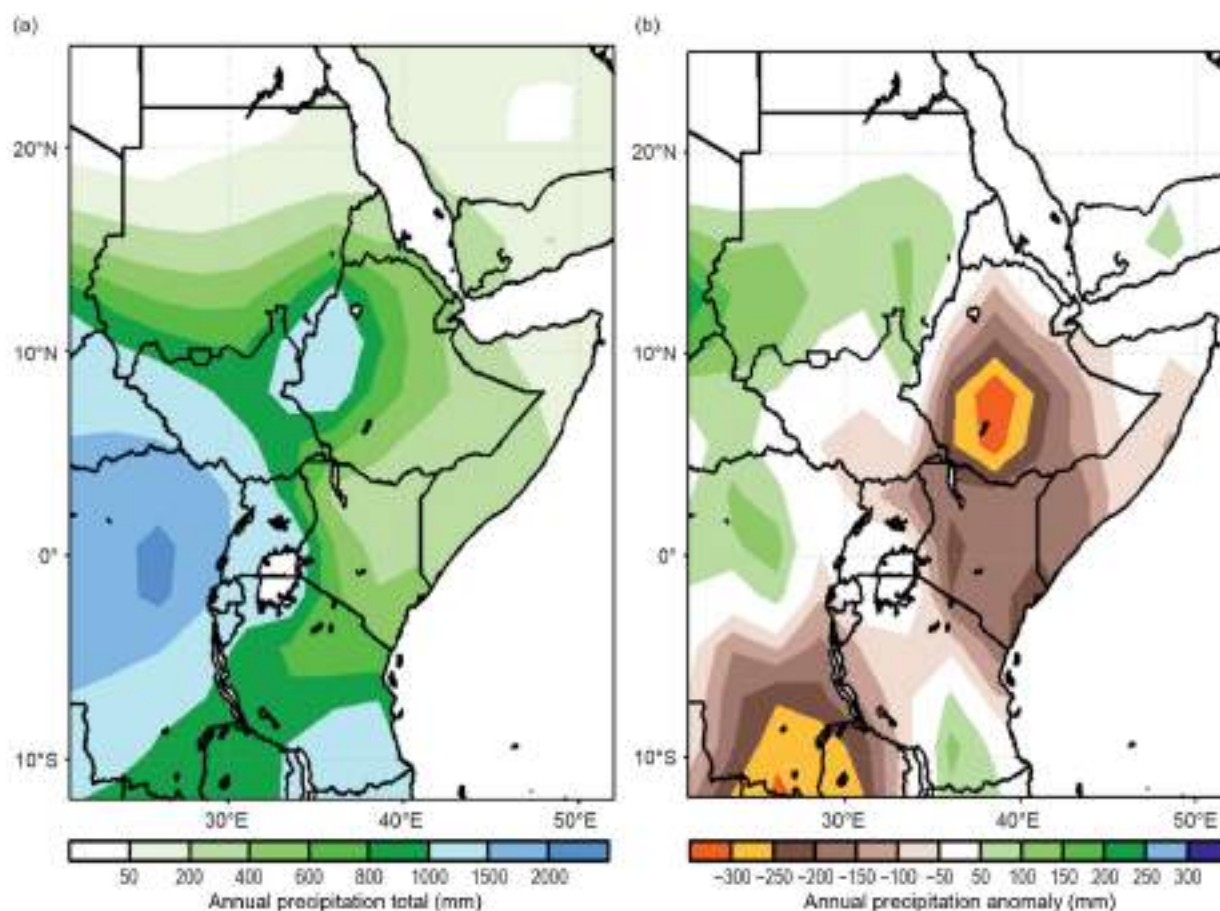


Fig. 7.28. Cumulative annual (a) rainfall totals and (b) rainfall anomalies (mm; 1991–2020 base period) in 2022 for East Africa. (Source: GPCP, NOAA/NCEP.)

Negative rainfall anomalies of -100 mm month⁻¹ began in March over Tanzania and extended into Kenya, Somalia, and southern Ethiopia in April and May. Annual rainfall deficits exceeded -250 mm (-150 mm) over parts of southern Ethiopia (Kenya).

Annual rainfall was below the third percentile over southern Ethiopia and below the 10th percentile over much of Kenya and central Ethiopia. The dryness over southern and equatorial regions was pronounced during April, May, and October, and contributed to the excessively deficient MAM and OND rainfall seasons. In particular, during MAM, many locations in the equatorial regions received rainfall below the 10th percentile of their respective records.

(iii) Notable events and impacts

Over 100 mm of rainfall per day on average was observed over local areas in Sudan and upstream areas of northwestern Ethiopia during the June–September season, according to RFE. The annual and JJAS rainfall over central and western Sudan was above the 90th percentile. These persistent heavy rains led to widespread flooding in many places in Sudan.

According to the United Nations and Sudan’s Humanitarian Aid Commission, around 226,200 people were affected by flooding and heavy rains across 15 states as of 28 August 2022. The most affected states were Gedaref, Central Darfur, South Darfur, White Nile, Kassala, River Nile, and West Darfur. Nine other states were also affected: West Kordofan, South Kordofan, North Kordofan, East Darfur, Sennar, Al Jazirah, Khartoum, and North Darfur. The rains and floods destroyed at least 13,200 houses and damaged another 34,200 since the beginning of the rainy season in June. Government authorities reported that 89 people died and more than 30 people were injured.

A large part of equatorial Eastern Africa (especially in Kenya, Somalia, and Ethiopia) experienced consecutive failed rainy seasons during OND 2020 through 2022. The annual total rainfall for 2022 was the lowest on record since 1991 in portions of equatorial East Africa. The March–May season was exceptionally dry over Tanzania, Kenya, central Somalia, and southern Ethiopia. Northeastern Tanzania and southern Ethiopia recorded deficient rainfall totals below the third percentiles of their historical records. Similarly, most of Kenya, south-central Somalia, and southern Ethiopia received 50 mm–150 mm below their average seasonal rain during OND 2022.

According to the U.S. Agency for International Development Famine Early Warning Systems Network (FEWS NET), the five-season drought (ongoing for 2.5 years) is the most extensive and persistent drought event in decades, leading to crop failure, millions of livestock deaths, water scarcity, and soaring staple food prices.

5. SOUTHERN AFRICA

—A. C. Kruger, C. McBride, M. Robjhon, W. M. Thiaw, and S. Dirkse

Southern Africa extends from about 5°S to 35°S and comprises Angola, Namibia, Zambia, Botswana, Zimbabwe, Malawi, South Africa, Lesotho, Eswatini, and Mozambique. The region is characterized by two main seasons: the wet and warm season from November of the previous year to April, and the dry and cold season from May to October.

(i) Temperature

Annual mean temperatures below 22°C dominated the central and southern sectors of southern Africa, whereas temperatures up to 26°C were observed in northwestern Angola and Mozambique (Fig. 7.29a). Annual mean temperatures were near normal across most areas, except southwestern Angola and northwestern Namibia, where abnormally low temperatures, with negative anomalies of up to -1.5°C , were observed (Fig. 7.29b). South Africa experienced a warm

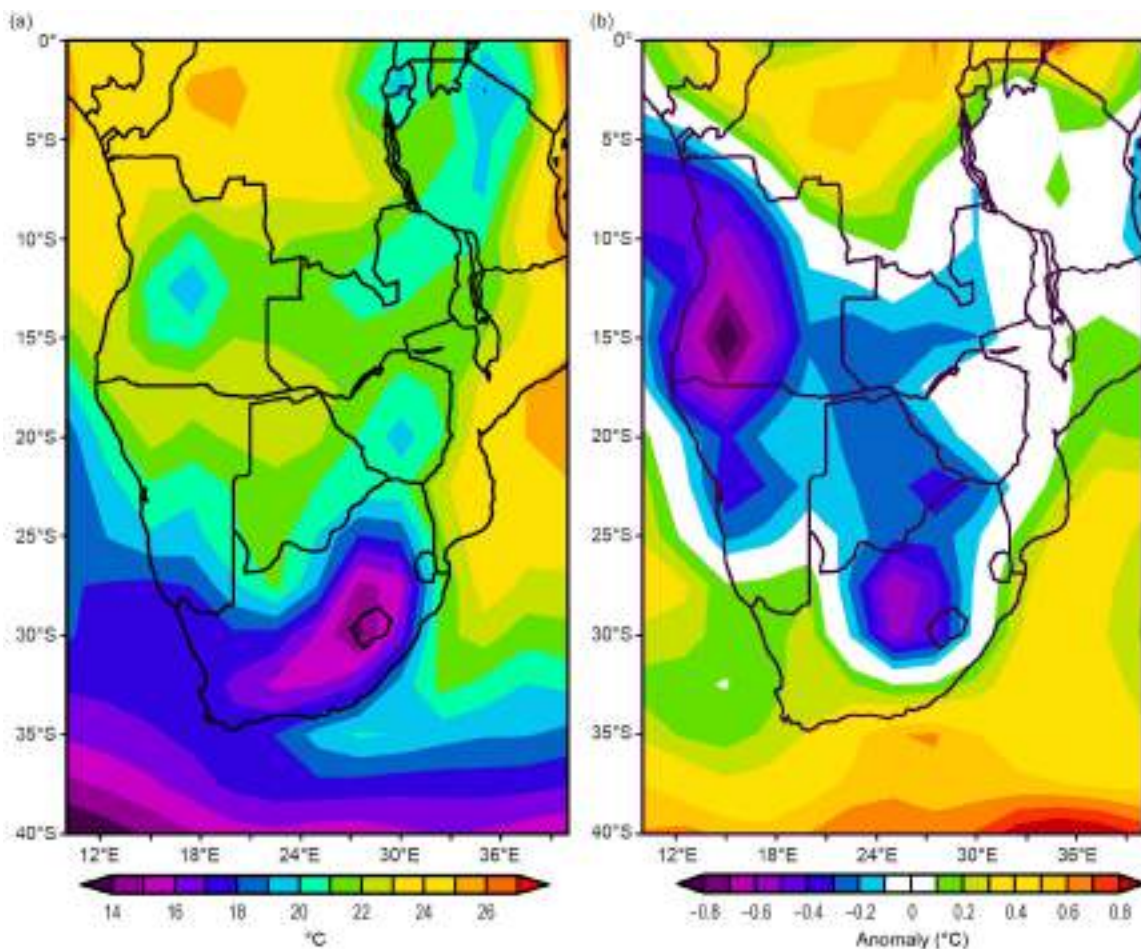


Fig. 7.29. Annual (a) mean temperatures and (b) mean temperature anomalies (°C; 1991–2020 base period) for southern Africa. (Source: NCEP/NCAR.)

year, especially in the western interior and southern and eastern coastal regions. The annual mean temperature anomaly for 2022, based on the data of 26 climate stations, was about 0.4°C above average, the fourth highest on record since 1951 (Fig. 7.30). A warming trend of +0.16°C per decade is indicated for the country, statistically significant at the 5% level.

Seasonally, the warmest period was austral spring (September–November), when abnormally high mean temperatures (anomalies of up to +2°C) were observed over most areas of South Africa, parts of Namibia, and portions of Botswana (not shown). October was the warmest month, with maximum temperatures above 36°C across the central sector, including southern Angola, western Zambia, much of Botswana, western Zimbabwe, and western Mozambique, which corresponded to anomalies as high as +5°C in eastern Angola, northwestern Zambia, western South Africa, southeastern Namibia, and southern Botswana, placing this October among the three warmest Octobers on record.

The coldest season occurred during austral winter (June–August), when minimum temperature dropped below 10°C across the southern two-thirds of southern Africa, with negative anomalies as low as –3.5°C in Angola and northern Namibia (not shown). August was the coldest month of 2022 and the coldest August on record, when minimum temperatures reached as low as 5°C below normal over Angola, western Zambia, and northern Namibia.

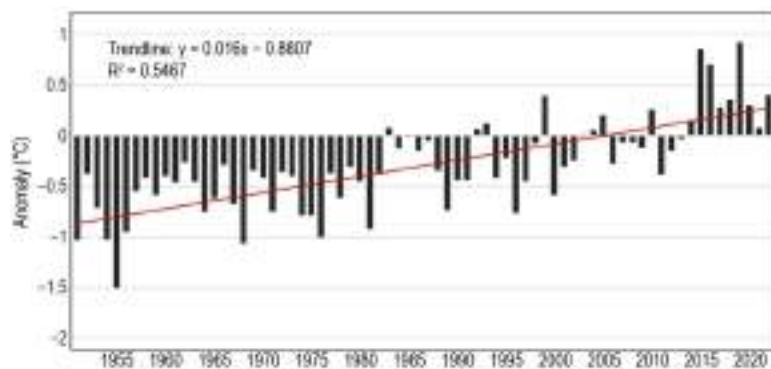


Fig. 7.30. Time series of annual average surface temperature anomalies (°C; 1991–2020 base period) over South Africa based on 26 climate stations for the period 1951–2022. The dark red line shows the linear trend. (Source: South African Weather Service.)

(ii) Precipitation

Annual rainfall exceeded 1000 mm over northern Angola, Malawi, northern Mozambique, eastern Lesotho, and eastern South Africa, varied between 600 mm and 1000 mm across Zambia, and totaled less than 600 mm across the central and western sectors of the region (Fig. 7.31a). Annual rainfall was well above normal in central South Africa and Lesotho, with surpluses of up to 300 mm, placing the year above the 90th percentile in their historical records.

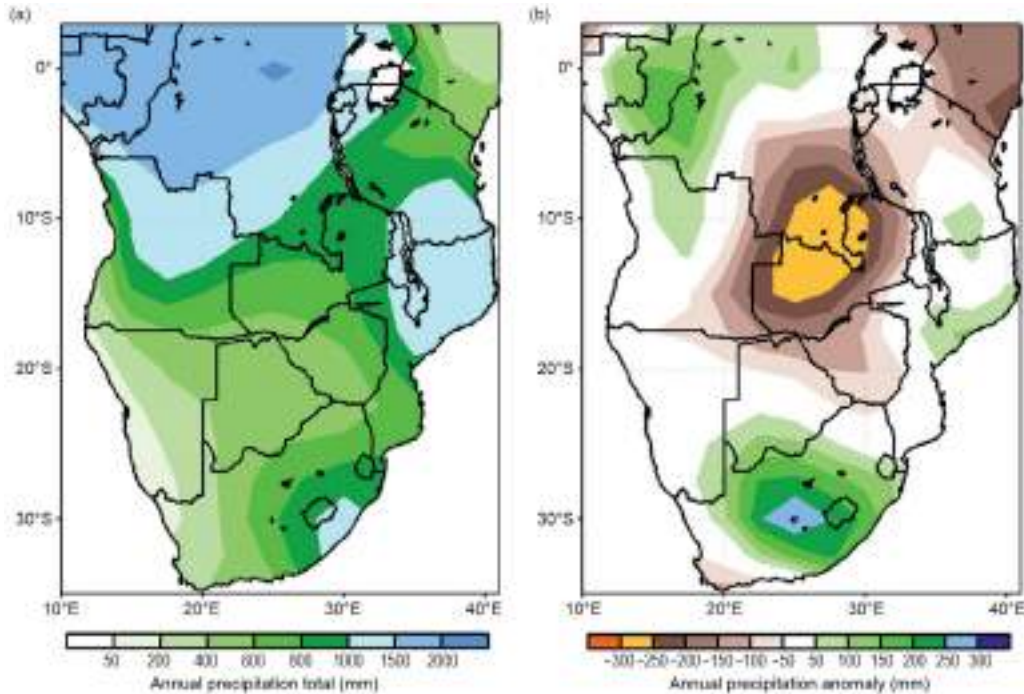


Fig. 7.31. Annual (a) rainfall totals and (b) rainfall anomalies (mm; 1991–2020 base period) in 2022 for southern Africa. (Source: GPCP, NOAA/NCEP.)

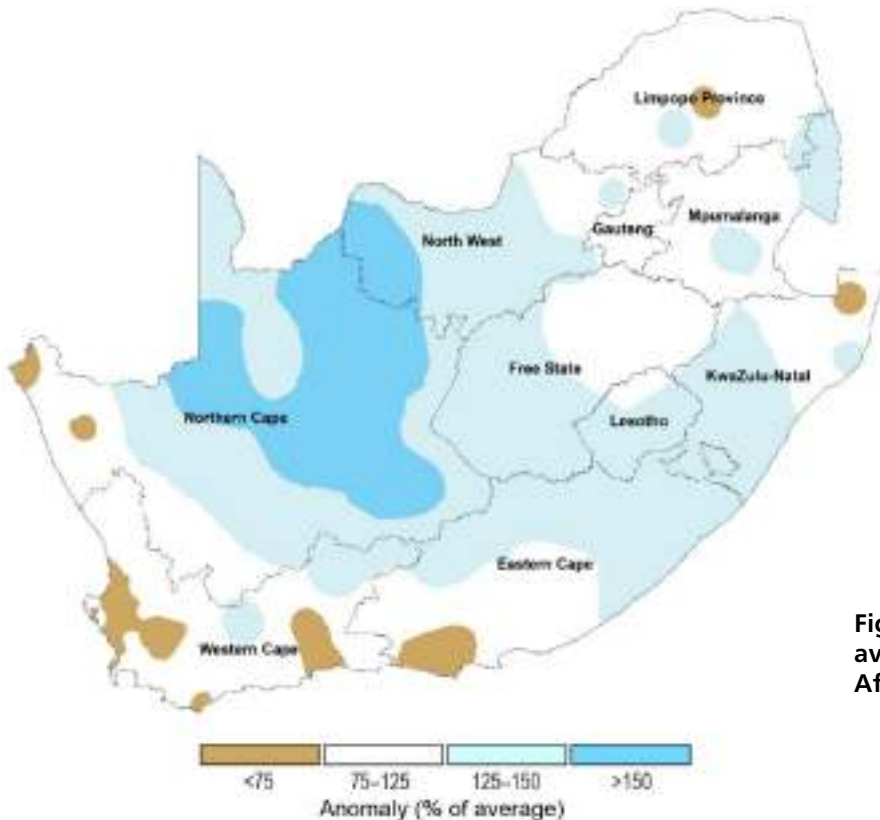


Fig. 7.32. Annual rainfall anomalies (% of 1991–2020 average) in 2022 for South Africa. (Source: South African Weather Service.)

However, annual rainfall amounts were well below normal in Zambia, where deficits reached -300 mm (Fig. 7.31b; 3rd to 10th percentiles). Additionally, extensive areas in central South Africa received well-above-normal rainfall, but there were clear signals of drying in the western parts of the Northern Cape and Western Cape Provinces. Dry conditions persisted in parts of the Eastern Cape Province (Fig. 7.32).

Seasonally, rainfall was above normal in the southern tier of southern Africa during December–February (DJF) 2021/22, March–May, and September–November, with the largest surpluses of over 100 mm recorded across eastern South Africa, Lesotho, Eswatini, and coastal Mozambique during March–May. November was the wettest month, where anomalies of up to +100 mm were observed in central South Africa, Lesotho, eastern Zimbabwe, central Mozambique, and parts of northern Angola (90th to 97th percentile, not shown).

Rainfall was more than 100 mm below normal over the northern sector extending from eastern Angola, Zambia, and Malawi, to northern Mozambique during DJF. February was the driest month, with rainfall deficits surpassing –50 mm across eastern Angola, Zambia, north-eastern Botswana, Zimbabwe, and southern Mozambique (not shown).

(iii) Notable events and impacts

Tropical Storm Ana caused severe flooding and infrastructure damage in Nsanje in the Chikwawa District of Malawi, with local rainfall totaling up to 200 mm during 22–25 January. This resulted in 64 deaths, 206 injuries, and more than 940,000 people affected, according to the Emergency Events Database (EM-DAT), an international disaster database. The government in Malawi declared a state of disaster on 26 January due to the substantial impacts of the storm.

During 11–14 March, Category 3 Cyclone Gombe, with sustained winds of 185 km h⁻¹ and a 24-hour rainfall total over 200 mm, triggered flooding in the Nampula, Zambezia, Sofala, Beira, Tete, and Niassa Provinces in Mozambique. The impacts from the storm left 63 people dead, 108 injured, and over 736,000 affected.

Heavy rain with a 24-hour accumulation of over 300 mm during 8–18 April led to flooding and landslides in Umlazi Town in Durban in the KwaZulu-Natal Province of South Africa, leading to 544 deaths, 50 injuries, and affecting more than 140,000 people. The government in South Africa considered this storm event among the worst in history and declared a nation-wide state of disaster. Infrastructure was badly damaged, more than 4000 homes were destroyed, and more than 40,000 people were displaced from their homes. The event was caused by a cut-off low that moved from the interior eastward over the ocean before strengthening. The wet conditions continued in May, with more damaging floods in the eastern KwaZulu-Natal Province.

Although August had some heavy rainfall episodes over parts of the southwestern, southern, and eastern coastal regions, some parts of the Eastern Cape Province remained dry; the Nelson Mandela Bay Metropole in the Eastern Cape was the hardest hit by water shortages due to drought after seven years of below-normal rainfall. However, rainfall brought some relief to some places in September and October. In November, normal to above-normal rainfall occurred mainly over the eastern half of the country, as well as isolated areas of the Northern and Western Cape. Some urban areas experienced severe flooding; more than 300 families at the Nancefield Hostel in Soweto, Gauteng Province, were left destitute as water from heavy floods entered their homes from 11 to 13 November.

A cold front with its associated cut-off low-pressure system along with a reported 24-hour rainfall of more than 100 mm on 21 June brought sub-zero temperatures, snowfall, strong winds, and freezing rain to Helmeringhausen in the southern parts of the western escarpment and central regions in Namibia. This led to road and infrastructure damage and livestock deaths.

A convective hailstorm with strong winds on 5 November destroyed infrastructure in the Nsingizini and Nsubane communities under the Hosea and Somntongo in the Shiselweni region of Eswatini, which affected over 1000 people.

On 14 December, a thunderstorm with strong winds, hail, lightning, and heavy rain totaling 85 mm in less than an hour impacted Windhoek (capital of Namibia), killing two people and causing costly infrastructure damage.

6. WESTERN INDIAN OCEAN ISLAND COUNTRIES

—G. Jumaux, K. R. Dhurmea, A. Abdallah, B. Andrade, M. Robjhon, and W. M. Thiaw

The Western Indian Ocean island countries consist of Madagascar, Seychelles, Comoros, Mayotte (France), Réunion (France), Mauritius, and Rodrigues (Mauritius). There are two distinct main seasons: a warm and wet period spanning from November of the antecedent year to April and a cold and dry season lasting from May to October.

Overall, temperatures in 2022 were near normal, but lower than those of the last decade (Fig. 7.33). Near-normal temperatures were associated with large-scale prevailing environmental conditions of La Niña and a negative Indian Ocean dipole. Annual rainfall was below normal over Comoros and near normal across the rest of the Western Indian Ocean island countries (Fig. 7.33).

(i) Temperature

In Madagascar, annual mean temperatures were 20°C–22°C across the central highlands and up to 26°C along the west coast (Fig. 7.34). Although annual mean temperatures were near normal over the island, their seasonal evolutions showed above-normal mean temperatures of up to +1°C. Maximum temperatures ranked between the 85th and 97th percentile across central Madagascar during December–February 2021/22, and below-normal mean temperatures up to –1°C (below the 10th percentile) and minimum temperatures that ranked between the 3rd and 10th percentile in the northern parts during June–August.

The annual mean temperature over Réunion (based on three stations) was 0.03°C above normal, the 16th highest since records began in 1968 (Fig. 7.33). March, at 0.8°C above normal, was among the three warmest on record. Most months observed near- or slightly below-normal temperatures, especially during austral winter, which was related to a strong negative Indian Ocean dipole and below-normal sea-surface temperatures around the island.

In Mauritius, the annual mean temperature (based on two stations at Vacoas and Plaisance) was near normal. The maximum temperature was 0.18°C below average, and the minimum was 0.18°C above average. May 2022 was the warmest May on record with a mean temperature anomaly of +0.94°C. With a well-established La Niña, below-normal temperatures prevailed during October–December, notably at night.

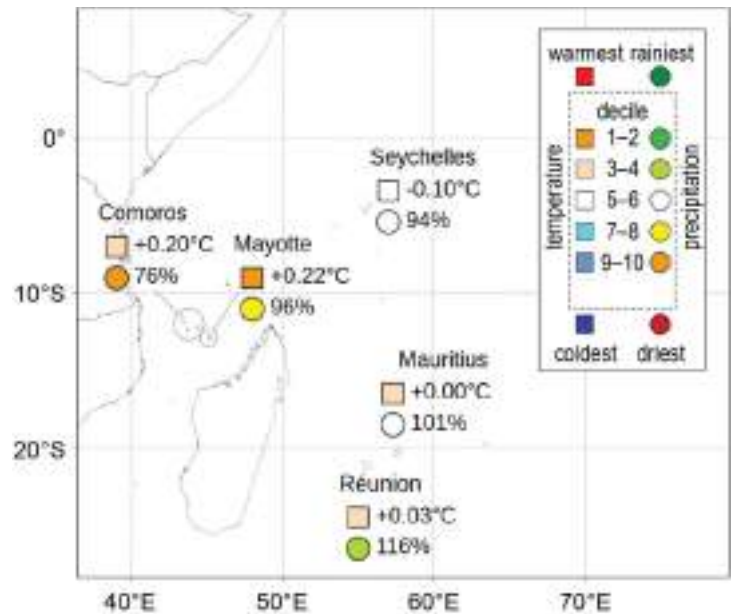


Fig. 7.33. Mean annual temperature anomalies (°C, squares), annual rainfall ratio to normal (%), and their respective deciles for the western Indian Ocean islands countries in 2022 (top right inset box). Base period is 1991–2020. (Sources: Météo France and Meteorological Services of Mauritius, Seychelles, and Comoros.)

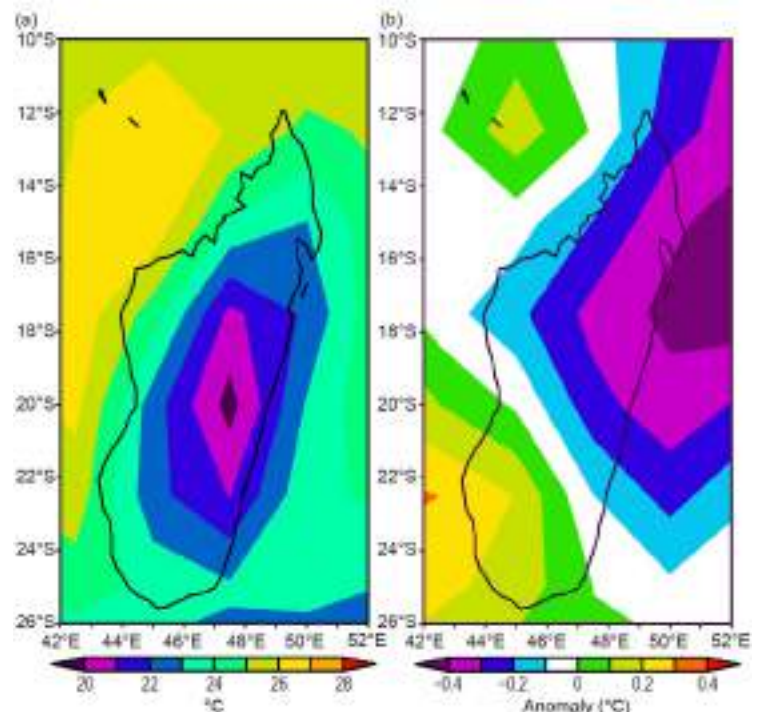


Fig. 7.34. Annual (a) mean temperatures and (b) mean temperature anomalies (°C; 1991–2020 base period) in 2022 for Madagascar. (Source: NOAA/NCEP.)

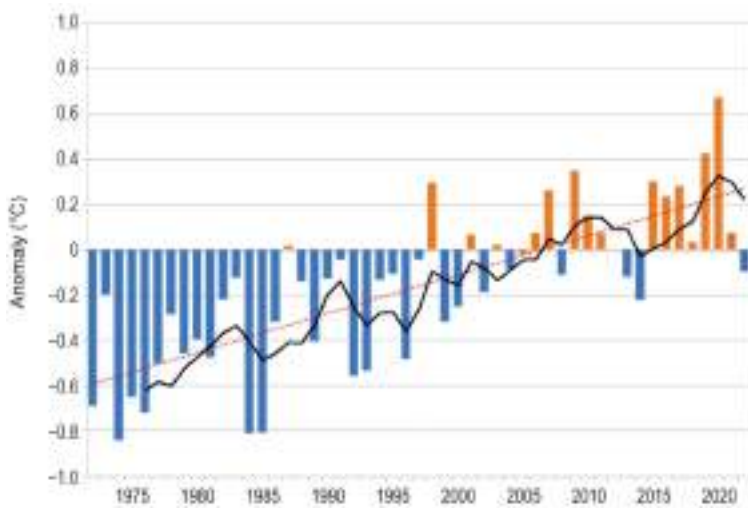


Fig. 7.35. Time series of Seychelles annual mean temperature anomalies (°C; 1991–2020 base period) for the period 1972–2022. The black line is the five-yr running mean and the dotted red line represents the linear trend. (Source: Seychelles Meteorological Authority.)

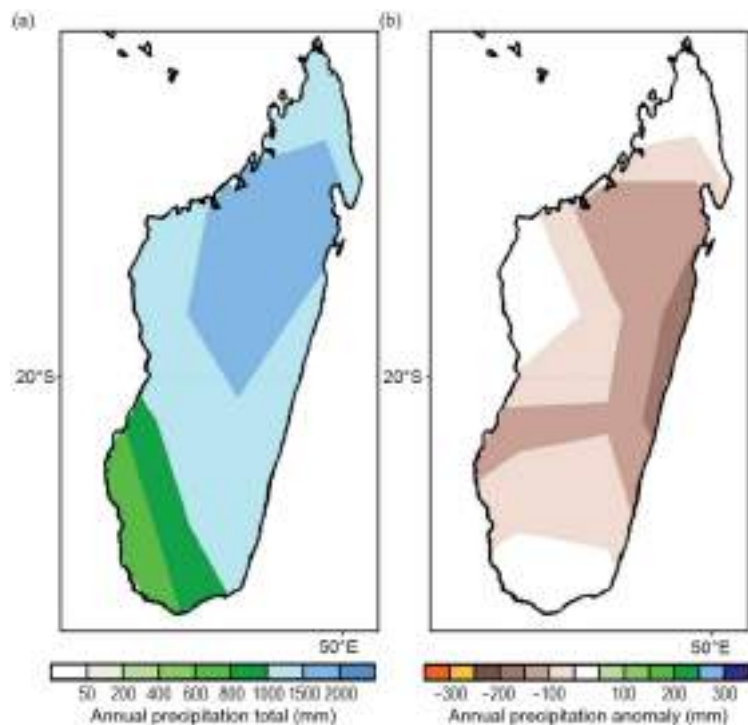
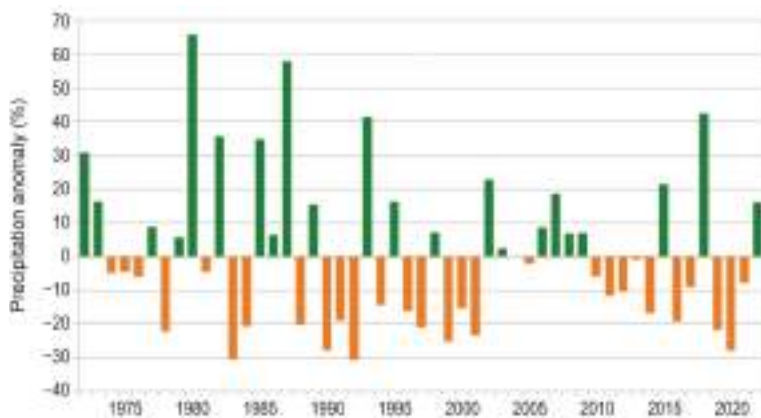


Fig. 7.36. Annual (a) total rainfall and (b) total rainfall anomalies (mm; 1991–2020 base period) in 2022 for Madagascar. (Source: NOAA/NCEP.)



In Comoros, the annual mean temperature was the ninth highest since 1981 (0.2°C above normal). December–April was warmer than normal, with the exception of February. During August–October, temperatures were below normal.

In Mayotte (Pamandzi Airport), the annual mean temperature was the 11th highest in the 62-year record, at 27.26°C. The first half of the year was 0.41°C above normal, and the second half was near normal (+0.02°C). The annual maximum and minimum temperatures were above normal by 0.32°C and 0.12°C, respectively.

At Seychelles, the annual mean temperature was 0.1°C below normal (Fig. 7.35). Nearly all months were near normal except March and April, which were above normal, and July and August, which were significantly below normal. July 2022 was the second-coldest July on record (anomaly of -1.1°C).

(ii) Precipitation

Annual rainfall was below normal across most of Madagascar, particularly in the eastern portions of the island, where the annual total was as much as 200 mm below normal (Fig. 7.36b). Seasonally, December–February 2021/22 rainfall was predominantly below normal, with the largest deficits exceeding -150 mm and ranking below the third percentile in the southwest.

The annual rainfall total over Réunion was 116% of normal (Fig. 7.37). The rainy season (December–April) produced 144% of normal precipitation, the fifth-wettest such period on record. Two tropical cyclones (Batsirai and Emnati) influenced the weather in February, the first one generating heavy rains. The dry season (May–November) was the third driest on record (68% of normal), which is often the case during a negative phase of the Indian Ocean dipole (see section 4f for details). October was the driest on record, while April was the wettest.

In Mauritius, normal mean annual rainfall of about 2040 mm was observed (average is 2019 mm). However, there was a marked

Fig. 7.37. Annual rainfall anomaly time series (%; 1991–2020 base period) in Réunion for the period 1972–2022. (Source: Météo-France.)

seasonal variability (Fig. 7.38). During February–April, above-normal rainfall was observed, with April being the second wettest in the last 20 years. During winter (July–October), rainfall was deficient, and this persisted into November and December.

In Comoros, total annual rainfall was 76% of normal and the fourth-lowest total since 1979. The start of the rainy season was delayed until February. The month of April and the late winter (August–September) were also wetter than normal. Most other months had rainfall deficits.

In Mayotte, total annual rainfall was 96% of normal. April and July were wet but five consecutive months from August to December, during the dry season and the early rainy season, were each drier than normal, leading to a 41% rainfall deficit in this period; this was the sixth-driest such period in the 62-year record.

In Seychelles, the total annual rainfall was 94% of normal, making 2022 the 26th-driest year since the start of the record in 1972. The rainfall was below normal in most months, but January and December were the wettest in 2022. October (18% of normal) was the third driest on record, while December (183% of normal) was the sixth wettest on record.



Fig. 7.38. Monthly rainfall totals for 2022 (blue bars), 1991–2020 mean (black bars), and 2022 anomalies (dark red line; 1991–2020 base period). Units are mm. (Source: Meteorological Services of Mauritius.)

(iii) Notable events and impacts

The 2021/22 rainfall season included 12 named tropical storms, including five tropical cyclones, which ranked the season as the fifth most active since 1998/99. Tropical storm Ana brought a total rainfall of 150 mm during 22–25 January, which resulted in floods, landslides, collapsed houses, and damaged infrastructures in the Analamanga Region, including Antananarivo in Madagascar, leading to 55 fatalities and more than 130,000 people affected.

Tropical Cyclone Batsirai, with sustained winds of 165 km h⁻¹ and gusts up to 235 km h⁻¹, hit the eastern coast of Madagascar in the evening of 5 February. Its center made landfall just north of the city of Mananjary. Batsirai’s impacts were the most violent in this sector of Madagascar for more than 25 years, as the region was exposed to the storm surge and to the strongest winds, with maximum gusts estimated up to 230 km h⁻¹. It brought 48-hour rainfall totals of up to 150 mm during 5–7 February, impacting Mananjary, Nosy Varika, Ikongo District, Manakara Atsimo, Fianarantsoa, and Ambositra in Madagascar and leading to 121 deaths and over 140,000 total people affected.

Prior to landfall on Madagascar, Batsirai affected weather conditions in Mauritius and Réunion from 1 to 5 February. The center of the cyclone passed 170 km north of Mauritius and 190 km north of Réunion. Réunion remained under the influence of the cyclone for a longer period, as Batsirai remained less than 220 km north of the island for 26 hours on 3 February. The storm influence was remarkable in the highlands (Fig. 7.39). Over the five-day period, the highest cumulative rainfall was 2044 mm at the Commerson Crater. Maximum hourly gusts exceeded 100 km h^{-1} at Gillot Airport for 32 consecutive hours, a new record at this station. The following maximum gusts were recorded: 135 km h^{-1} on the coast at the Port and 208 km h^{-1} in the highlands at Piton Maïdo.

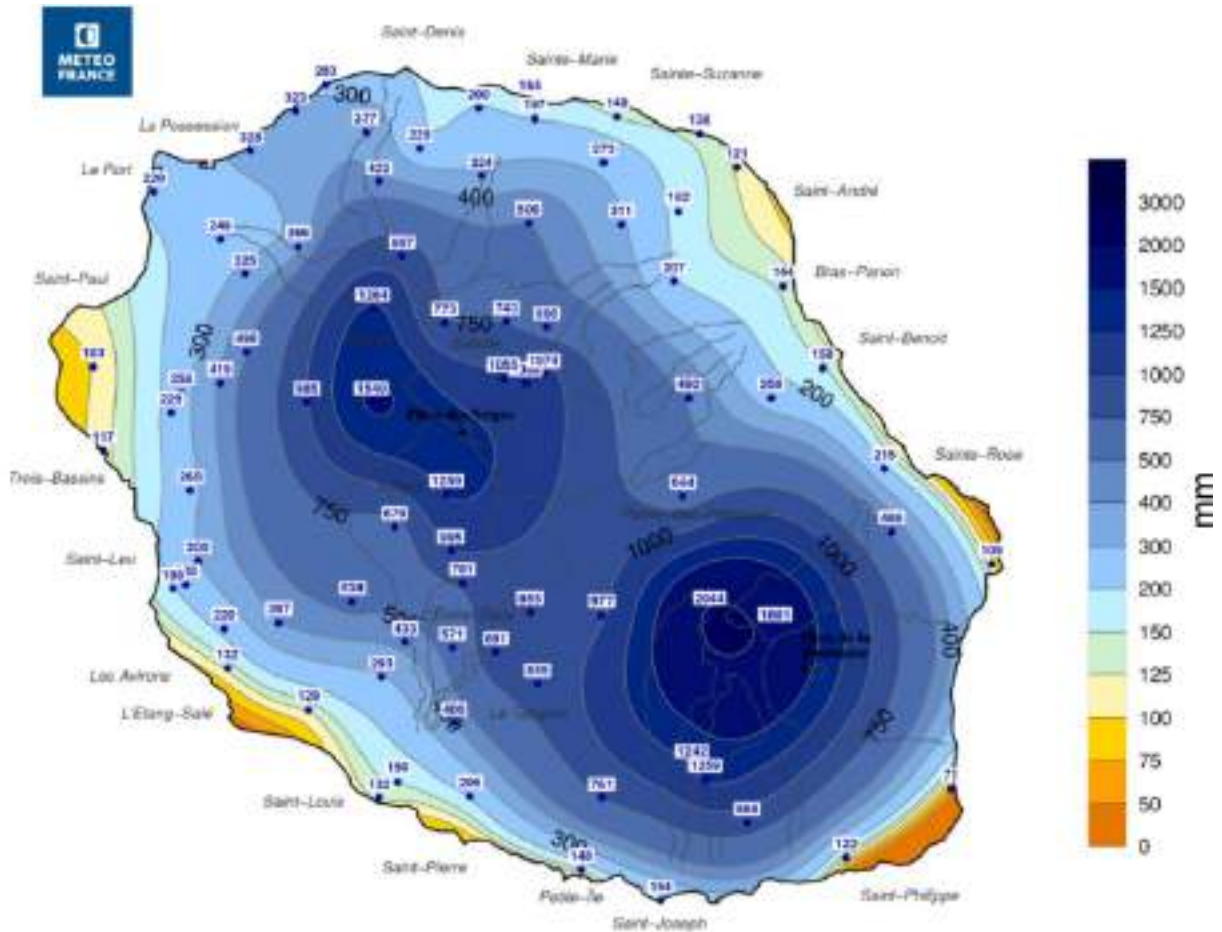


Fig. 7.39. Cumulative five-day rainfall (mm) in Réunion during tropical cyclone Batsirai (1–5 Feb 2022). (Source: Météo-France.)

f. Europe and the Middle East

—P. Bissolli (Ed.), H. Rösner, S. Bader, G. M. Bellido, C. Berne, O. Bochníček, L. Crhova, V. De Bock, M. Demircan, R. Deus, P. Drumond, M. Ekici, S. Hellström, M. Kendon, V. Khan, M. Lakatos, T. Likso, J. Mamen, I. Marcioniené, M. Perčec Tadić, V. Pires, E. Rodriguez Guisado, B. Rösner, F. Rubek, S. Schimanke, S. Sensoy, S. Spillane, L. Trescilo, G. van der Schrier, and A. Willems

Throughout this section, 1991–2020 is the base period used for both temperature and precipitation, unless otherwise specified. European countries conform to different standards applied by their individual national weather services. All seasons mentioned in this section refer to the Northern Hemisphere. More detailed information can be found in the *Monthly and Annual Bulletin on the Climate* in Regional Association VI (RA VI) – European and the Middle East, provided by the World Meteorological Organization (WMO) RA VI Regional Climate Centre on Climate Monitoring (RCC-CM; <http://www.dwd.de/rcc-cm>). Anomaly information has been taken from Figs. 7.41–7.44 and aggregations of CLIMAT station data when national reports are not available. The length of national temperature and precipitation records for each country are provided in Supp. Table A7.1.

1. OVERVIEW

Based on the Global Historical Climate Network (GHCN) v4.0.1 dataset (Menne et al. 2018), Europe (36°N–72°N, 23°W–60°E) experienced its second-warmest year in its record with an anomaly of +1.0°C (1991–2020 base period; Fig. 7.40). An evaluation of several other datasets (WMO 2023) has shown that the 2022 annual average temperature for Europe (defined by the area of the WMO RA VI region) was likely between the second and fourth highest on record, with an anomaly between +0.7°C and +0.9°C compared to the 1991–2020 average. All countries reported above-normal annual temperatures (Fig. 7.41). Nationally, it was the warmest year on record for Spain (+1.7°C), Portugal (+1.4°C), Belgium (+1.2°C), France (+1.6°C), Luxembourg (+1.1°C), the United Kingdom (+0.9°C), Ireland (+0.7°C), Switzerland (+1.6°C), Hungary (+1.1°C), Germany (+2.3°C), Italy (+1.1°C), Croatia (+1.2°C), Bosnia and Herzegovina (+1.1°C), Monaco (+1.4°C), Montenegro (+1.2°C), and Slovenia (+1.2°C).

Many other countries reported an annual temperature among their four highest: Serbia (second warmest, +1.0°C), the Netherlands (third warmest, +1.1°C), Denmark (third warmest, +0.8°C), Finland (third warmest, +0.9°C), Romania (third warmest, +1.0°C), and Bulgaria (fourth warmest, +0.8°C). See Supp. Table A7.1 for a complete list of national temperature anomalies and rankings. Winter 2021/22 was warmer than normal across most of Europe due to a positive phase of the North Atlantic Oscillation (NAO; see further explanation in Lindsey and Dahlman 2009), which persisted throughout the season, with positive temperature anomalies in the Northern Hemisphere midlatitudes ranging from +1.0°C in France and Türkiye to above +3.0°C in southern European Russia and Kazakhstan (Fig. 7.42a). The most intense warmth in Eastern Europe was additionally caused by subtropical air from the south, which flowed to the north at the west flank of the Russian high. The season ended with an exceptionally warm February for all of Europe when the positive NAO phase was strongest, with anomalies above +2.0°C almost everywhere and even above +6.0°C in eastern parts of Europe.

Spring was slightly warmer than normal (anomalies around +1.0°C) in western and northern Europe while it was colder than normal (anomalies around -1.0°C) in much of Eastern Europe (Fig. 7.42b). This reflects an outstanding meridional circulation pattern with anticyclonic conditions in Western Europe and cyclonic conditions in Eastern Europe. France reported its warmest May on record, Italy and Slovenia their second warmest, and Luxembourg and Croatia their third warmest.

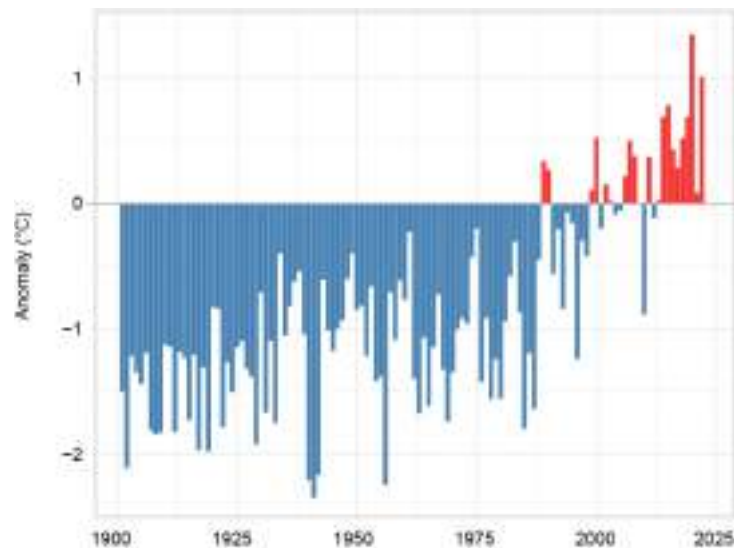


Fig. 7.40. Annual average land-surface temperature anomalies over the period 1900–2022 for Europe (36°N–72°N, 10°W–60°E) relative to the 1991–2020 base period. (Source: GHCN version 4.0.1 [Menne et al. 2018].)

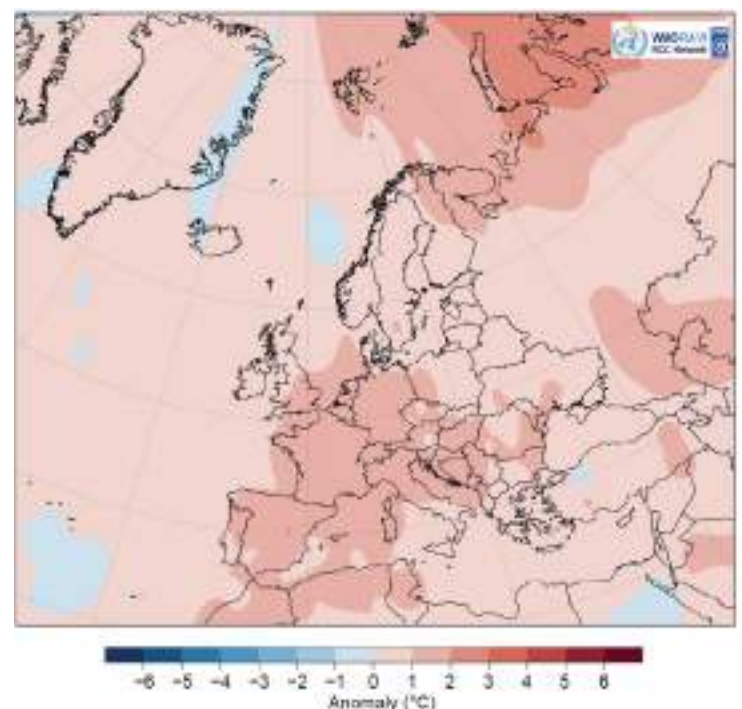


Fig. 7.41. Annual mean temperature anomalies (°C; 1991–2020 base period) for 2022. (Source: interpolated climate station and ship data, Deutscher Wetterdienst [DWD].)

Summer was exceptionally warm across all of Europe with large areas observing anomalies between +2.0°C and +3.0°C (Fig. 7.42c) as warm subtropical air from the southwest spread over much of the region up to the northeast and prevailed under the influence of high pressure. Portugal, Spain, and Hungary reported their warmest summer on record, Switzerland, Romania, Croatia, France, and Italy their second warmest, and Poland, the Russian Federation, the Netherlands, and Serbia their third warmest.

During autumn, anomalies were above +1.0°C across the western half of Europe (Fig. 7.42d), which was continuously influenced by subtropical air from the southwest. Only regions east of Germany and north of the Black Sea reported anomalies around or slightly below normal, since they were occasionally affected by cold air from the northeast. Spain had its warmest autumn on record, Italy and France their second warmest, Switzerland, the United Kingdom, the Netherlands, Luxembourg, Belgium, and Croatia their third warmest, and Denmark and Ireland their fourth warmest. It was the warmest October on record for France, Germany, Austria, Croatia, and Slovenia. December 2022 was colder than normal in northwestern Europe (below -4°C in Iceland) and warmer than normal in the southeast (up to +5°C in eastern Türkiye).

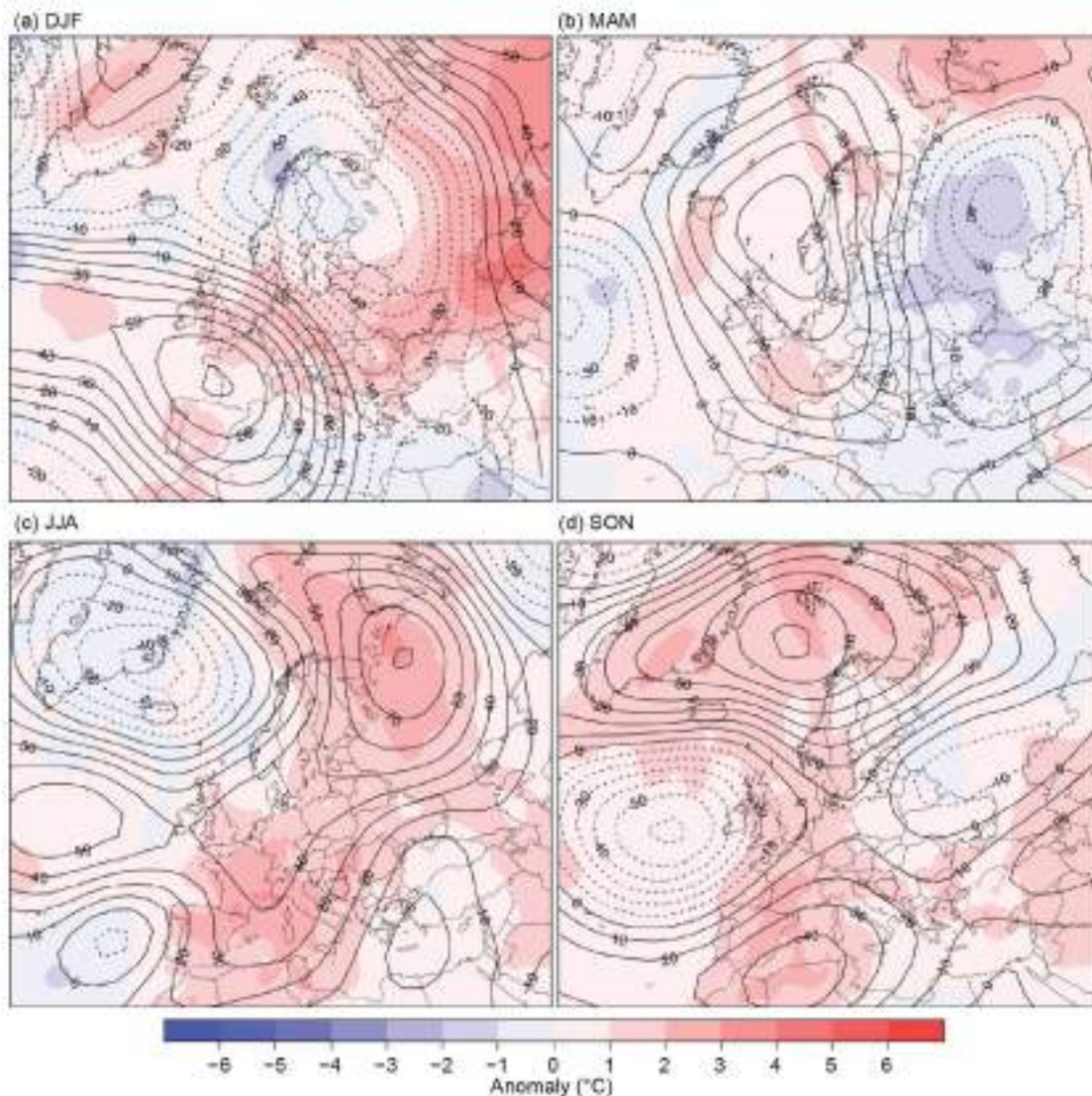


Fig. 7.42. Seasonal anomalies (1991–2020 base period) of 500-hPa geopotential height (contour; m) and surface temperature (shading; °C) using data from the NCEP/NCAR reanalysis and DWD, respectively, for (a) DJF 2021/22, (b) MAM 2022, (c) JJA 2022, and (d) SON 2022.

Annual precipitation was mostly near normal or drier than normal and mainly ranged between below 80% and 125% of normal (Fig. 7.43). Locally, precipitation below 60% of normal was observed in south-eastern France, northern Spain, northwestern Italy, Estonia, the Middle East, and on the west coast of the Black Sea.

Winter 2021/22 was drier than normal, particularly on the Iberian Peninsula and in the Middle East with large parts receiving less than 60% of normal precipitation and less than 20% locally, revealing a severe winter drought in regions that normally receive most of their precipitation during the cold season (Fig. 7.44a). The dryness in southwestern Europe was caused by a relatively intense Azores high in combination with dry air advection from northwest Africa, while the Middle East was affected by dry air from the Arabian Peninsula. The winter months were drier than normal for almost all of the Iberian Peninsula and the Middle East (large areas below 40% of normal).

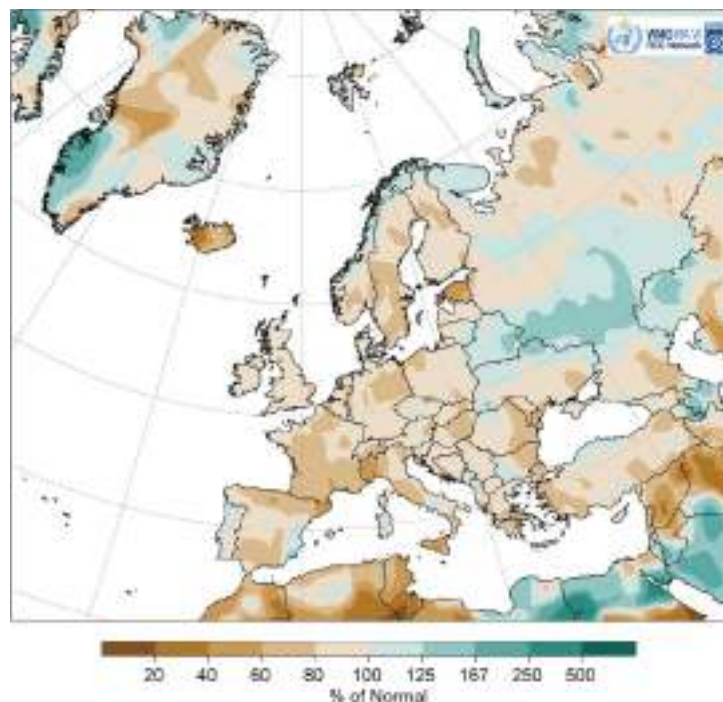


Fig. 7.43. European precipitation totals (% of 1991–2020 average) for 2022. (Source: GPCP, created by DWD.)

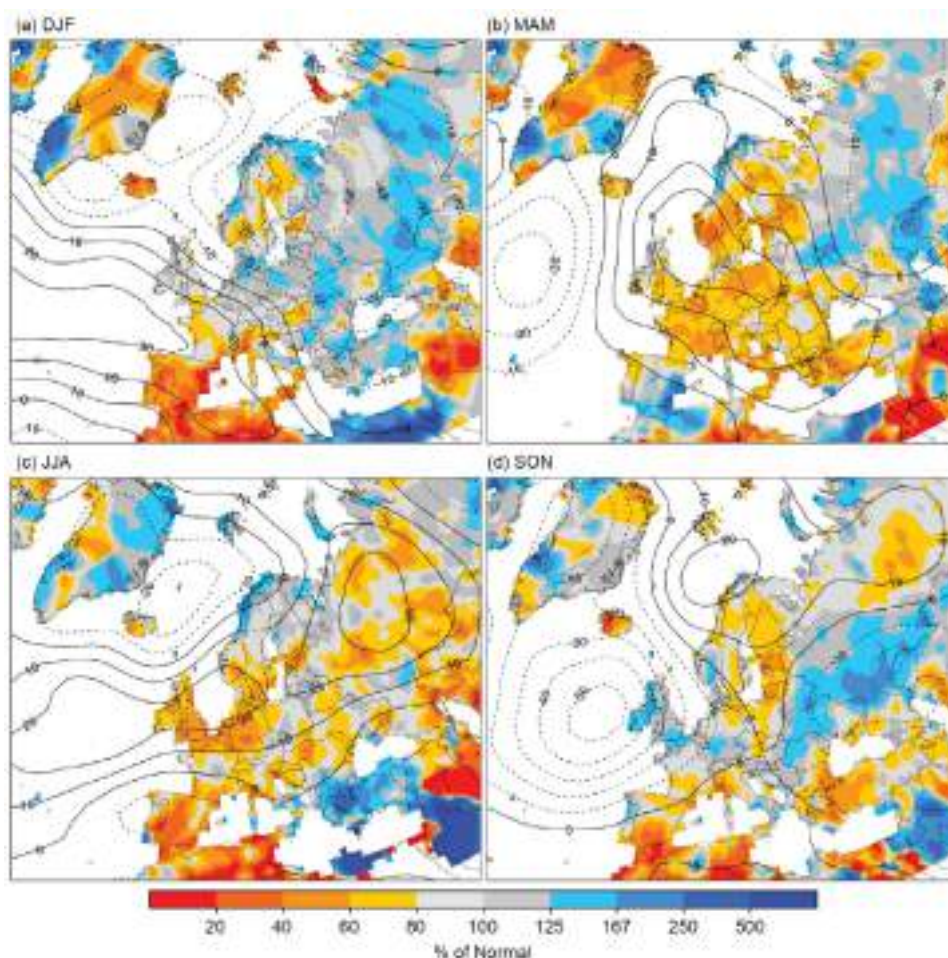


Fig. 7.44. Seasonal anomalies for 2022 (1991–2020 base period) of sea-level pressure (hPa) from NCEP/NCAR reanalysis (contours) for (a) DJF 2021/22, (b) MAM 2022, (c) JJA 2022, and (d) SON 2022. Colored shading represents the percentage of seasonal mean precipitation for 2022 compared with the 1991–2020 mean from GPCP (Schneider et al. 2018).

Spring was drier than normal across most of Europe, with large areas receiving only 60% to 80% of normal precipitation as high-pressure patterns over the continent prevailed (Fig. 7.44b). Above-normal precipitation was observed across most of Belarus, European Russia, and the Caspian Sea as well as most of the Iberian Peninsula, ending its winter drought. Iberia was affected by low-pressure developments over the North Atlantic, which expanded quite far to the south. Cyclonic conditions also occurred over Eastern Europe, expanding southward to the Caspian Sea region. However, not all eastern countries saw cyclonic conditions throughout spring. Poland and Belarus reported their driest March on record, and the Czech Republic had its third driest.

Summer was again a dry season, with most of Europe receiving between 50% and 90% of normal precipitation (Fig. 7.44c). Anticyclonic conditions dominated over much of the continent; however, eastern Mediterranean cyclones contributed to above-normal precipitation across the southern Balkans, Greece, western Türkiye, and large areas of the Middle East.

Autumn was wetter than normal for Eastern Europe with around 130% of normal precipitation where cyclonic conditions prevailed (Fig. 7.44d). Poland, Finland, and the Baltic countries as well as Greece, western Türkiye, and southern Spain received 60% to 80% of their normal precipitation and even lower in some localized areas. High-pressure conditions continued from summer into autumn over Scandinavia and over the western Mediterranean, but no longer dominated over the European midlatitudes. Autumn 2022 was the second wettest autumn in Ireland. During October, it was drier than normal almost everywhere in continental Europe (except for some areas in southern Germany and eastern France) with precipitation locally below 20%. Only Belarus and some areas of central European Russia received above-normal precipitation. Ireland had its wettest October on record (from 1941). November was wetter than normal for the Mediterranean, Balkans, and central parts of Eastern Europe, while Central Europe and the Nordic and Baltic countries received 50% to 80% of normal precipitation in many areas, a result of Scandinavian blocking. In December 2022 (not shown), above-normal precipitation fell over Iberia, southern France, northern Italy, and the northern Balkans up to central parts of eastern European Russia, while the southeast from Kazakhstan to the eastern Mediterranean region was notably dry, often with less than 20% of the normal precipitation.

2. WESTERN EUROPE

This region includes Ireland, the United Kingdom, the Netherlands, Belgium, Luxembourg, and France.

(i) Temperature

The year was the warmest or tied with or close to the warmest year on record for many countries in this region. It was the warmest for France (+1.6°C), Luxembourg (+1.1°C), Belgium (+1.2°C), the United Kingdom (+0.9°C), and Ireland (+0.7°C), and third warmest for the Netherlands (+1.1°C). All seasons were warmer than normal for the region.

During winter 2021/22, anomalies were +0.8°C for France while the other countries of the region reported higher anomalies of +1.1°C in the United Kingdom and Ireland, +1.4°C in Belgium and Luxembourg, and +1.9°C in the Netherlands. In January, anomalies were below +0.8°C in the region, except for the Netherlands (+1.6°C) and Ireland (0.9°C). February saw even higher anomalies, with the highest ranging from +2.3°C in Luxembourg to +2.7°C in the Netherlands.

Spring anomalies were also positive, ranging from +0.3°C in the Netherlands to +1.1°C in France. In March, most of the region except for Ireland (+0.5°C) had anomalies ranging from +1.0°C to +1.5°C. April temperatures were near or slightly below normal. May was exceptionally warm for most of the region. France observed its warmest May on record with an anomaly of +2.4°C. Anomalies in the rest of the region during May ranged from +1.3°C in Ireland (its third warmest) and the United Kingdom to +1.9°C in Luxembourg.

June, July, and August were all warmer than normal. For many countries, summer 2022 was among their five warmest. Anomalies ranged from +0.7°C in Ireland to +2.3°C in France.

Temperatures at the start of summer were near normal for Ireland (+0.3°C) and slightly higher for the United Kingdom. France had its third-warmest June on record (2.3°C above normal) and also its third-warmest July (+2.1°C). In Luxembourg, the July anomaly was close to +2.0°C. August was among the three warmest on record for most countries in the region, with monthly anomalies ranging from +2.3°C in the Netherlands to +3.1°C in Luxembourg. For France, it was the second-warmest August on record (+2.6°C). Only Ireland and the United Kingdom experienced anomalies below +2.0°C.

Autumn was also warmer than normal. Anomalies ranged from +1.1°C in Ireland to +1.6°C in Belgium. For all countries except Ireland, it was either the second- or third-warmest autumn on record. In Ireland, it was the fourth warmest. In September, only France reported an anomaly of +0.7°C while the other countries had temperatures near or slightly below normal. October was very warm across the entire region. France reported its warmest October on record at 3.5°C above normal. In November, temperature anomalies were close to +2.0°C in the region except for Ireland (+1.4°C). It was the third- and fifth-warmest November on record for the United Kingdom and France, respectively. December was colder than normal in the west and warmer than normal in the southeast, with anomalies ranging from -1.4°C in Ireland to +2.0°C in southern France.

(ii) Precipitation

Most of Western Europe received near-normal precipitation over the year. During winter 2021/22, precipitation was mostly near normal; only parts of southern France and the north-west had below-normal precipitation. January was drier than normal in all countries except Luxembourg where precipitation was near normal. France, Ireland, and the United Kingdom received only around 50% of their normal precipitation. February was wetter than normal (120% to 145%) for all countries except France, where most areas only received 40% to 80% of normal precipitation.

Spring was drier than normal across the region. Precipitation ranged from 60% of normal in Luxembourg to 80% in Ireland. All countries saw below-normal precipitation during March. Belgium experienced its driest March on record having received just 5% of its normal precipitation, and the Netherlands had its third driest having received only around 20% of normal. In April, the rest of the region received 70% to 85% of normal precipitation, and parts of England and France were even drier. France reported its driest May in history, receiving only 35% of normal. Luxembourg received around 40% of its normal precipitation.

Summer 2022 was the driest summer since at least 1991 for Belgium and Luxembourg (47% and 34% of normal precipitation, respectively). Ireland, the United Kingdom, and the Netherlands each received around 60% of their normal precipitation. June was wetter than normal (114% to 130%) for all countries except Luxembourg (65% of normal) and the United Kingdom (80%). July was exceptionally dry across the entire region. The Netherlands and France reported only 25% of normal precipitation, making it the second-driest July in history for France and Belgium. Luxembourg had its driest July on record (less than 20% of normal). Ireland and the United Kingdom received around 50% to 60% of normal precipitation in both July and August. All countries also reported below-normal precipitation for August. Some areas in France received well below 50% of normal. Many areas of the Netherlands, Belgium, and Luxembourg received only around 30% of their normal precipitation.

Autumn precipitation was near or slightly wetter than normal across most of the region. All three months of the season were wetter than normal for Ireland and the United Kingdom. During September, most countries received about 120% to 140% of their normal precipitation, while Belgium and northeastern France observed about 150% to 175%. October was drier than normal in the Netherlands, Belgium, and France (45% to 65% of normal). Mesoscale rain events contributed to above-normal precipitation in Luxembourg and some areas in eastern France. November precipitation in the region was near to slightly above normal. December precipitation was also near normal in most areas.

(iii) Notable events and impacts

On 27 June, a tornado hit the city of Zierikzee (Zeeland Province, Netherlands), causing one fatality, 10 injuries, and extensive damage that included torn off roofs and uprooted trees. This was the first tornado in the region since 1992.

On 12 November, North Atlantic low-pressure systems brought mild air to northern and western Europe. This influx of warm air led to new high minimum temperature records in Scotland (14.6°C) and Northern Ireland (14.5°C).

During 16–18 November, heavy rain in Scotland and England caused flooding, damage, and casualties due to flash floods. In Charr, Aberdeenshire, 140 mm of rain was recorded in 48 hours (close to the monthly normal). Aboyne, Aberdeenshire, recorded 71.4 mm in 24 hours. Rail services were suspended and left hundreds of travelers stranded in Newcastle. Several roads were flooded and cars submerged in the region of Angus and Edinburgh. Some residents had to be evacuated. Earlier that week, heavy rain led to flooded roads and submerged cars in West Sussex, England.

During 2–7 June, France was affected by severe thunderstorms that brought hail and heavy rain that led to flooding. Hail diameters measuring up to 7 cm damaged cars, infrastructure, and vineyards. Multiple stations measured 24-hour precipitation totals above 50 mm (some above 70 mm), which are amounts comparable to normal monthly June totals. The station Saint-Yan in Saône-et-Loire, central eastern France, received 108 mm in 48 hours. Thousands of households experienced power outages, and flights at Paris airports were either suspended or delayed.

A 14-day heatwave in France peaked on 18–19 July when 104 stations broke their all-time records (e.g., Brest, 39.3°C; Nantes, 42.0°C; Dieppe, 40.4°C; Calais, 39.9°C). This was the fifth-longest and third-most intense heatwave in France since 1947, after those of July 2019 and August 2003. On the same day, Ireland achieved its highest maximum air temperature since 1887 with 33.0°C. On 19 July, a temperature of 40.0°C was measured in the United Kingdom for the first time on record (Coningsby in Lincolnshire recorded the highest temperature of 40.3°C), and temperature records at several long-running stations were broken by margins of 3°C to 4°C. Additionally, a new high daily minimum record of 25.8°C was set in Kenley (Greater London). In the Netherlands, station De Kooy set a new local all-time high temperature record of 36.1°C on the same day. Overall, monthly temperatures reached 39.5°C in the Netherlands (Beek), 40.0°C in Belgium (Kapelle-op-den-Bos), and 36.3°C in Luxembourg.

3. CENTRAL EUROPE

This region includes Germany, Switzerland, Austria, Poland, the Czech Republic, Slovakia, and Hungary.

(i) Temperature

Overall, 2022 was very warm in the region. Switzerland reported its warmest year on record at 1.6°C above normal, and many other countries observed one of their five warmest years. Except for the Czech Republic, Slovakia, and Poland, which each reported anomalies slightly below +1.0°C, all countries experienced temperatures 1.2°C to 1.6°C above normal.

Winter was warmer than normal, with anomalies ranging from +1.1°C in Switzerland to +2.0°C in Germany and the Czech Republic. February was exceptionally warm. Much of the region reported monthly anomalies between +3.0°C and +3.4°C, while Switzerland and Austria reported slightly lower anomalies of +1.8°C and +2.1°C, respectively.

During spring, only Germany and Switzerland had above-normal temperatures (+1.0°C and +1.4°C, respectively), while the rest of the region reported near- to slightly-below-normal temperatures. April was colder than normal for all countries except Switzerland, which reported near-normal temperatures. May was warmer than normal in Poland, Slovakia, Czechia, Germany, and Hungary (1.0°C to 1.3°C above normal). Austria reported a higher anomaly of +1.8°C and Switzerland reported its second-warmest May on record at 2.6°C above normal.

Summer was exceptional in Central Europe, with many countries experiencing one of their warmest on record. Switzerland and Germany reported their second-warmest summer with anomalies of +2.3°C and +1.7°C, respectively, and Poland had its third warmest (+1.3°C). Slovakia reported +1.8°C, Austria +1.6°C, Poland +1.3°C, and the Czech Republic +1.2°C. June, July, and August were all warm with many countries reporting record or near-record monthly temperatures. Switzerland reported its second-warmest June on record at 2.7°C above normal and Slovakia its third warmest (2.3 °C). Hungary observed its third-warmest June (+2.3°C) and fifth-warmest July on record (+1.6°C) and Switzerland its fourth warmest July (+2.4°C). Germany reported its warmest August on record (+2.3°C), Hungary its second warmest (+2.6°C), Poland and Switzerland their third warmest (+2.1°C and +1.8°C, respectively), Slovakia its fourth warmest (+2.0°C), and Austria and Czechia their fifth warmest (+1.1°C and +1.2°C, respectively).

The year continued with a warmer-than-usual autumn. Switzerland reported its third-warmest autumn on record at 1.7°C above normal. Poland, Slovakia, and Czechia reported anomalies between +0.4°C and +0.7°C, and Germany and Austria reported +1.4°C and +1.3°C, respectively. September was colder than normal for all countries in the region, while October was exceptionally warm. Germany, Austria, and Switzerland each reported their warmest October on record, with anomalies of +3.1°C, +3.4°C, and +3.8°C, respectively. Poland and Czechia reported their fourth warmest October on record (+2.5°C). December was colder than normal in the north, but warm in the south, with anomalies ranging from -1.0°C in northern Poland to +3.0°C in southern Hungary.

(ii) Precipitation

The year was slightly drier than normal across Central Europe, with most areas receiving 80% to 92% of their typical annual totals. Some parts received even less. During winter, precipitation was near normal for Germany, Poland, Austria, and Czechia. Hungary and Slovakia reported only around 70% and 80% of normal, respectively. Switzerland reported 90% of normal precipitation, but only up to 40% of normal on the Alpine Southside. In January, only Poland reported above-normal precipitation, while Hungary, Slovakia, and Switzerland received just 30% to 46% of their normal amounts. February was wetter than normal for Germany and Poland (155% of normal), while Hungary continued to be dry (36%).

Spring was drier than normal, with precipitation 60% to 80% of normal for most of the region. Czechia and Poland each reported their third-driest spring on record (70% and 62% of normal). In March, almost the entire region received less than 35% of normal precipitation. It was the second-driest March for Poland and Austria, third driest for Czechia, fourth driest for Germany, and fifth driest for Switzerland. April precipitation was near normal, but May was dry in Germany, Czechia, and Poland (63% to 71% of normal) and even drier in Switzerland (48%), Hungary (47%), and Slovakia (46%).

Summer was near normal for Czechia but drier than normal elsewhere. Poland and Austria reported 89% of normal, and Slovakia, Switzerland, Germany, and Hungary 78%, 72%, 61%, and 54% of normal, respectively. June was the fourth driest on record for Hungary (59% of normal), and July was drier than normal across the entire region. August was drier than normal for Austria (81% of normal), Switzerland (70%), Hungary (66%), and Germany (64%).

Autumn precipitation was near normal for Germany, Hungary, Switzerland, Czechia, and Slovakia. Austria and Poland reported 88% and 79% of normal precipitation, respectively. The season started with a wetter-than-normal September almost everywhere in the region. Hungary reported its ninth-wettest September on record but also its eighth-driest October. October was drier than normal everywhere in the region except for southwestern Germany and Switzerland, where precipitation was near normal. In November, Slovakia and Poland received only 46% and 48% of normal precipitation, respectively, making it the third-driest November for Poland. December was wetter than normal in eastern Poland, Slovakia, and Hungary, and drier than normal in southwestern Germany, Austria, and parts of Switzerland.

(iii) Notable events and impacts

During 2–4 April, an unusual cold spell accompanied by frost occurred in parts of Europe. Following warmer temperatures in the previous weeks that saw the greening of flora, there was widespread damage to agriculture in Germany, Austria, and France. In Germany, minimum temperatures dropped from -5°C to -10°C , and some stations broke their April minimum temperature records.

On 19–20 May, following the first heatwave of the year over central Europe, two consecutive upper-level troughs led to severe thunderstorms. On 20 May, a strong cell developed over the Eifel Mountain range in western Germany and produced hailstones as large as 5 cm that were accompanied by precipitation rates of 30 mm h^{-1} to 40 mm h^{-1} , which caused local flooding. Wind gusts of up to 113 km h^{-1} were measured. In North Rhine-Westphalia, multiple tornados were spawned by a supercell, one of which struck Paderborn. Trees were uprooted, roofs were damaged, and windows burst. The supercells reached Czechia, causing further damage. At least 3 people were killed during these storms and more than 50 were injured.

Warm air from Spain advanced into Central Europe on 18–19 June, setting new temperature records. In Germany, Cottbus and Dresden-Strehlen stations recorded 39.2°C , which is a new monthly record in time series dating to 1887 (Cottbus) and 1936 (Dresden). Temperatures did not drop below 24°C during the night at some German stations. In Switzerland, Beznau (Aargau Canton) set a new national June record of 36.9°C (previously held by Basel since 1947) on 19 June. That same day, Feldkirch (Austria) set a new regional record for Vorarlberg (northwestern Austria) at 36.5°C . In Slubice (Poland), the temperature of 38.3°C was on par with the previous June record set in 2019. A new June maximum temperature of 39.0°C was recorded in Czechia on 19 June. On 30 June, a new June national maximum temperature record of 39.6°C was set in Berettyóújfalu, Hungary. The temperature did not fall below 24.7°C at the station Budapest Lágymányos, setting a new national high daily minimum temperature record (the previous June record of 24.4°C had been held by Budapest Istvánmező since 1946).

A heatwave in July also led to many new temperature records across Central Europe. In Germany, daily maxima reached over 40°C on 19 July. That same day, 38.1°C was reached in Genève-Cointrin (Switzerland). On 21 July, a new national temperature record of 38.6°C was set in Slovakia.

During yet another heatwave in the region, many new local monthly and all-time records were set during 4–5 August. On 4 August, Bad Kreuznach (Germany) recorded a new maximum temperature of 39.6°C as did the station Weinbiet (553 m a.s.l.) with 38.0°C . The same day, a new record temperature of 38.3°C was measured in Geneva (Switzerland). On 5 August, Stuttgart (Germany) measured a new highest daily minimum temperature of 21.2°C , and Zurich Airport (Switzerland) set a new record with 18.9°C .

4. IBERIAN PENINSULA

This region includes Spain, Portugal (1971–2000), and Andorra.

(i) Temperature

The year was the warmest on record for Andorra, Spain, and Portugal, with anomalies of $+2.6^{\circ}\text{C}$, $+1.7^{\circ}\text{C}$ and $+1.4^{\circ}\text{C}$, respectively. All seasons, especially summer and autumn, were warmer than normal for the Iberian Peninsula. In Andorra, May, June, July and October were the warmest on record with anomalies above $+4^{\circ}\text{C}$. Portugal had its fourth-warmest winter on record with an anomaly of $+1.4^{\circ}\text{C}$, while Spain was 0.8°C warmer than normal. In February, monthly anomalies reached almost $+1.5^{\circ}\text{C}$.

Spring temperatures were near normal on the Iberian Peninsula. While the first two months of the season were colder than normal, (anomalies of -0.2°C to -0.6°C), May temperatures were more than 2.0°C above normal in Portugal and Spain, marking the warmest May on record.

Summer was the warmest on record for both Portugal and Spain (anomalies of $+1.7^{\circ}\text{C}$ and $+2.2^{\circ}\text{C}$, respectively). June, July, and August were all among the four warmest on record for their

respective months for Spain (+1.7°C, +2.3°C, and +1.7°C, respectively). June and August were near normal for Portugal, while July was among the three warmest on record, with an anomaly of +2.0°C.

All three months of autumn were warmer than normal for the Iberian Peninsula. With an anomaly of +2.0°C, it was the warmest autumn on record for Spain and the fifth warmest for Portugal (+1.1°C). October was the warmest month of the season, with temperatures 2.0°C above normal for Portugal (fifth warmest on record) and 2.9°C above normal for Spain (warmest on record). Spain had its fifth-warmest November at 1.8°C above normal. December was record warm for both Spain and Portugal, with temperatures more than 2.0°C above normal over the entire peninsula.

(ii) Precipitation

Total precipitation for the year was around 90% of normal on the Iberian Peninsula. Locally, precipitation was slightly less than 60% of normal in certain places. Winter was dry, seeing only 30% to 60% of normal precipitation. For Portugal, it was the fifth-driest winter on record, with January and February receiving only 20% to 40% of normal precipitation.

Spring was drier than normal in Portugal (80% of normal), while it was near to wetter than normal in Spain, particularly in the southeast (more than 250%). March was wet across the Peninsula (around 180% of normal). During April, most of Portugal received below-normal precipitation while most of Spain was near normal. May was dry, with Portugal reporting only 20% of normal precipitation (fourth-driest May on record). Most of Spain received only 20% to 40% of normal precipitation.

The summer was also drier than normal for both Portugal (47% of normal) and Spain (65%). During June, only the northwestern tip of the Iberian Peninsula received above-normal precipitation. Portugal had 60% of normal precipitation while most of the stations in Spain reported below 20%. In July, most areas on the Iberian Peninsula received less than 20% of normal precipitation or none at all; only a few stations in eastern Spain reported above-normal precipitation. During August, Portugal received only 25% of normal precipitation. Some areas in Spain recorded less than 20% of normal precipitation, while others received 140% to 250% of their normal amounts.

Autumn precipitation was near normal for most areas in Portugal, but less than normal for Spain, particularly in the southeast which saw only 10% to 50% of normal precipitation. September was wet in Portugal (up to 160% of normal precipitation), but in Spain, precipitation was mostly below normal, especially in the south (20% to 40% of normal). October was near normal for Portugal while Spain was again drier than normal. November was drier than normal for the southern Iberian Peninsula with precipitation less than 50% of normal. The northern Peninsula mostly received near to slightly above-normal precipitation. December 2022 was a wet month for much of Iberia, with local reports above 250% of normal precipitation.

(iii) Notable events and impacts

On 20 April, the mountain observatory of Navacerrada in Spain (northwest of Madrid, located at 1894 m a.s.l.) recorded a fresh snow cover of 36 cm, an unusual accumulation of snow for a single day in April.

A notable heatwave (the longest and largest area affected since 2003) occurred during 9–17 June on the Iberian Peninsula. Temperatures surpassed 40°C on several days and broke some June records (Pinhão in Portugal: 42.3°C on 13 June; Andujar in Spain: 44.5°C on 17 June).

More exceptional heat in July on the Peninsula led to multiple temperature records. In Portugal, average daily temperatures were above 25°C beginning on 7 July, and multiple stations reported daily maximum temperatures above 40°C. In Alvega and Mora, the temperature surpassed 40°C for 10 consecutive days. On 14 July, Pinhão recorded a new July record with a maximum temperature of 47°C. In Spain, Madrid reported a new maximum temperature record of 40.7°C and a new high minimum temperature record of 26.2°C. New all-time records with temperatures above

40°C were recorded in Ponferrada, Valladolid, and Ourense (northern Spain). The extreme heat contributed to more than 1000 fatalities in Portugal and Spain. Along with the heat, it was very dry in both countries, and severe and extreme drought developed across large areas. In central Portugal and central western Spain, multiple large wild fires broke out and damaged large areas. Portugal declared a state of emergency during 11–15 July, and efforts to extinguish the fires led to some casualties. In the region of Galicia in Spain, 8000 people had to be evacuated.

On 30 August, hailstones as large as 10 cm caused significant damage to houses, vehicles, and infrastructure in parts of Catalonia (Spain). At least 50 people were injured, and some casualties were reported.

Severe storms during 10–14 November brought heavy rain, hail, and strong winds that caused extensive damage in central and eastern Spain. Flooding was reported in the regions of Valencia, Castile, and León. Valencia airport was closed due to the flooding. Wind caused damage to power infrastructure, leading to power outages for around 7000 homes in Catalonia. Multiple places recorded 48-hour totals of 150 mm to 300 mm of rain during 10–12 November, breaking November precipitation records for the most intense 1-hour total (66.1 mm) and the highest 24-hour total (148.4 mm).

5. THE NORDIC AND BALTIC COUNTRIES

This section includes Iceland, Norway, Denmark, Sweden, Finland, Estonia, Latvia, and Lithuania.

(i) Temperature

Annual temperatures in the Nordic and Baltic countries were normal to above normal, with anomalies from 0.0°C in Iceland to +0.9°C in Finland. Some stations in Sweden reported their second-warmest year (the warmest was 2020). Winter 2021/22 was colder than normal in northern Scandinavia, but warmer than normal in southern Scandinavia and the Baltic countries. Anomalies ranged from –1.0°C in northern Norway to +1.4°C in Lithuania and Denmark. January was mild in the southern parts of the region, up to 3.0°C above normal in Lithuania; February was even more mild (locally +4.0°C). Conversely, Iceland saw a cold February (–2.0°C anomaly) due to a cold air outbreak from Greenland.

Spring was relatively mild in Scandinavia, especially in the north and in Iceland (+1.0°C anomaly), but colder than normal in the Baltic countries, which were influenced by cold troughs over Eastern Europe. The largest negative seasonal anomalies were recorded in Lithuania (–1.0°C). The warmth over Scandinavia reached the Arctic regions in March, resulting in Svalbard being 4.0°C warmer than normal. A cold spell followed in April, resulting in below-normal temperatures in most of the region, with the largest anomalies (–1.5°C) in Lithuania. Similar anomalies occurred in May in the Baltics, having been affected by cold air from northern Russia.

Summer brought near-normal temperatures to western parts of the region, while Finland and the Baltics were 1°C to 2°C above normal. During June and once in August, warm air from the subtropics reached northern Europe. July 2022 had the highest (station-level) daily maximum temperature of all July months in Denmark. August was record warm in parts of Finland; records were broken or equaled at 18 observation stations. Lithuania saw its warmest August on record (anomaly of +2.8°C). Summer was relatively cold in Iceland.

During autumn, Iceland and western Scandinavia (Norway, Denmark, and southern Sweden) were at least 1.0°C warmer than normal, while temperatures were closer to normal farther east. Widespread warmth dominated the whole region during October and to a lesser extent in November. Iceland reported its warmest November on record as warm easterly winds prevailed. The country was almost completely without snow, which is unusual in November. On 12 November, three stations in Sweden reached 16.7°C, the highest temperature ever reported in Sweden so late in the month. December brought a large Arctic cold air outbreak to almost the whole region, with the largest anomalies in western Iceland (–4.0°C). It was the coldest December for the country since 1973 and the coldest December for the capital city of Reykjavík in more than

100 years (equal to December 1916). Some warmth was seen in late December, however. A new daily maximum temperature record (10.7°C) was set on 31 December in Lithuania.

(ii) Precipitation

Precipitation totals for 2022 were below normal across much of the region. Southeastern Sweden was very dry. The lowest annual precipitation amount for the country in 2022 was 281 mm at station Ölands norra udde; this was also the lowest total for that station since 1921. Conversely, Reykjavik, Iceland, reported its eighth-wettest year on record. In Latvia, it was the first year since 2017 that was wetter than normal, although only by 0.2 mm.

Winter 2021/22 precipitation was below 80% of normal across much of southern Norway, Sweden, and Finland, mainly due to dry weather in January, as February was generally wetter. In southern Sweden, Lund recorded 97 mm of precipitation, a new February record for a series dating to 1753. Heavy snow fell over all of Iceland in February.

Spring was also dry in much of the region, with less than 40% of normal precipitation in southern Norway. Only Svalbard and the northern Norwegian coasts had above-normal precipitation. March was particularly wet in Iceland; many weather stations in the south, west, and northwest of the country recorded their highest March precipitation totals on record. Conversely, March was record dry in Denmark, and in southern Sweden 50 stations had no measurable precipitation for the month. Estonia recorded only 4 mm (13% of normal), its lowest March total since 1961. Lithuania was also record dry for the month.

Summer was notably dry in southern Scandinavia. Southern Norway and southern Sweden reported totals that were 60% or less of normal for the season. Helsinki-Vantaa airport (Finland) received its lowest August precipitation total (5.9 mm) on record for its observation station. Other parts of the region were less affected by dryness, as seasonal totals were closer to normal.

Autumn was also dry in much of the region with precipitation less than 80% of normal over large areas, notably in Sweden, Finland, and the Baltics, where some local totals in those places were below 60%. November was particularly dry, with several areas throughout the region receiving 40% or less of their normal precipitation; however, it was very wet in eastern Iceland. Generally dry weather continued in December. It was the driest December in decades for many places in Iceland.

(iii) Notable events and impacts

Strong winds impacted western Lithuania on 30 January with gusts of up to 34.5 m s⁻¹ (124 km h⁻¹) along the coast. Klaipėda seaport was closed, and power lines were downed from fallen trees. Flooding was even observed close to the sea at Šventoji resort due to the strong winds.

A heatwave occurred in the last decade of June in Estonia. Temperatures reached 30°C or higher in many places for two to five consecutive days. Five stations set new June high-temperature records.

The highest temperature in the Norwegian Arctic in 2022 (20.1°C) was recorded at Bjørnøya on 29 June, marking only the second time Bjørnøya has surpassed 20°C in that month. The first occurrence was on 22 June 1953, with 23.6°C.

The highest maximum temperature in 2022 in Norway was 33.6°C, recorded on 20 July at Lysebotn (Sandnes, Rogaland). Since 1957, Rogaland has had the highest temperature of the year only once before in 1978, when Sola reached 30.7°C on 31 July. On 21 July, Målilla (Sweden) reported a daily maximum of 37.2°C, marking the highest temperature in the country since 29 June 1947.

On 12 December, snow reached a depth of 55 cm in Kuldīga (western Latvia). This was the thickest snow cover in Latvia since April 2013.

6. CENTRAL MEDITERRANEAN REGION

This section includes Italy, Monaco, Malta, Slovenia, Croatia, Serbia, Montenegro, Bosnia and Herzegovina, Albania, North Macedonia, Greece, and Bulgaria.

(i) Temperature

The year 2022 was the warmest on record for Monaco, Italy, Slovenia, Croatia, and Bosnia and Herzegovina and second warmest for Serbia, behind 2019. Annual mean temperatures in the central Mediterranean region were around 1.0°C above normal.

Winter 2021/22 temperatures were near to above normal. Anomalies ranged from slightly below normal in southernmost Italy, especially Sicily Island, Malta, and southern Greece, to +2.0°C in northern Bulgaria and northern Serbia. January was colder than normal over the Mediterranean (−1.0°C anomaly), while the northern Balkans in particular were affected by a warm westerly flow due to the positive phase of the North Atlantic Oscillation. February anomalies up to around +3.0°C were observed in northern Serbia and northeastern Croatia.

Spring had near- to below-normal temperatures across almost the entire region, except for northwestern Italy (+1.0°C anomaly). March temperatures were below normal, as cold air from Russia advanced to the eastern and central Mediterranean. Greece reported a monthly anomaly of −3.0°C (third-coldest March on record), mainly due to a cold wave during 9–16 March. This wave brought rare snowfall to the northern suburbs of the Attica region and Viotia (East Sterea Periphery) in Greece. In April, the northern Balkans were impacted by cold air from eastern central Europe that advanced southward, resulting in anomalies close to −2.0°C in northern Serbia. The eastern Mediterranean experienced a warming due to subtropical air, which warmed southern Greece (1.0°C above normal). In May, the entire region experienced a flow of warm air from southwestern Europe, leading to temperatures 1°C to 2°C above normal.

Summer was generally warmer than normal, as influxes of warm air from the southwest continued. The highest anomalies (above +3.0°C) were observed in northwestern Italy and eastern Bulgaria. June, July, and August were each warmer than normal across the entire region. Some stations in Slovenia recorded their highest July maximum temperature on record (e.g., Doblice: 39.4°C). The highest temperature of 2022 in Bosnia and Herzegovina (41.5°C) was recorded at Mostar and in Greece (42.0°C) at Ruse, both in July. The highest temperature in Serbia of 2022 (40.6°C) was measured at Smederevska Palanka on 23 July. Greece experienced an early heatwave in June, when temperatures above 38°C were recorded in the central and eastern mainland.

Above-normal temperatures continued in autumn, though with lower anomalies compared to summer (up to +2.0°C in northwestern Italy). September temperatures were mostly near normal, except for the western Mediterranean islands (Sardinia, Sicily, Malta), which were 1°C to 2°C above normal. Anomalies up to +3.0°C were observed in northern Italy in October and in eastern Bulgaria in November. December was mild, with several new local monthly mean records set in Serbia. Greece experienced its warmest December on record.

(ii) Precipitation

It was mainly a dry year for the central Mediterranean region. Italy reported its driest year on record, as the country experienced a critical drought situation in some areas, notably the northwest and the south (Sicily) where both regions received less than 60% of normal precipitation for the year. Other parts of Italy and parts of southern Greece and eastern Bulgaria registered 60% to 80% of normal. Precipitation was closer to normal elsewhere, though it was locally very dry in some areas. Slovenia, for example, experienced a dry spell (defined here as a long period with well-below-normal precipitation) from 28 April to 7 September with agricultural losses estimated at 100 million Euro (\$108 million U.S. dollars).

During winter 2021/22, some areas in northwest Italy and Sicily received less than 40% of their normal precipitation, while other parts of the region were occasionally affected by troughs expanding from the northeast. However, due to a frequent expansion of the Azores high into the central Mediterranean region, there were also several drier-than-normal periods throughout the region in January and February.

Spring was generally dry. Seasonal totals were mainly 60% to 80% of normal, although some areas in Italy, including the northwest, again received less than 40%. North Macedonia in the southern Balkans had its driest spring on record. March was dry throughout most of the region.

In April, much of Italy, Greece, and North Macedonia received around 60% of normal precipitation, and much less in localized areas. The rest of the region had normal precipitation. May was drier than normal except in the western Mediterranean (Sardinia and Sicily). Monaco had its second-driest May on record.

Summer precipitation presented a contrasting pattern between north and south. The northern half of Italy and the northwestern half of the Balkans received less than 80% of normal precipitation, while the south had 150% of normal around the Aegean Sea in Greece. This pattern persisted through the season, with a larger dry area in July and a larger wetter-than-normal area in August. Croatia experienced its second-driest summer on record. Drought occurred in northern Serbia from mid-June to mid-August during its critical crop period, as well as in parts of Bulgaria.

Autumn was drier than normal in parts the region. Italy, Greece, and eastern Bulgaria received less than 80% of normal precipitation, with northwestern Italy receiving less than 40%. The remainder of the region had normal to above-normal precipitation. September was rainy in central Italy and much of the Balkans (local totals over 150% to 200% of normal), while October was extremely dry throughout most of the region with less than 20% of normal precipitation in Italy and the Balkans. Bosnia and Herzegovina observed its third-driest October on record. November was generally wetter than normal (local totals over 150%). December was wet in the north, while Greece, North Macedonia, and Bulgaria received less than 80% of normal and Sicily less than 40%.

(iii) Notable events and impacts

Heavy rainfall on 2–3 September in the upper watershed of the Stryama River (around the village of Klisura, Plovdiv District, Bulgaria) led to high wave formation in the mountainous part of the tributaries that swept debris from the slopes, affecting the villages Bogdan, Karavelovo, Stoletovo, Rozino, and Slatina. Most of the infrastructure and many houses were either destroyed or inundated by water and mud. At least 150 people were displaced. An emergency was declared in the municipality of Karlovo. The return period of the high wave formed along the Stryama River is estimated to be around 600 years. The 24-hour rainfall amounts measured on 2 September in Rozino (164 mm) and Klisura (156.5 mm) were the highest on record for this area (return periods are estimated to be about 440 and 600 years, respectively). Damage was estimated to be more than 30 million Euro (\$32.5 million U.S. dollars).

Heavy rain fell during 15–17 September in Slovenia. Osilnica station in the Kolpa River region received 423 mm in 56 hours and Šebreljski in the Littoral region received 372 mm in 51 hours, far exceeding their 100-year return levels. Additionally, strong wind affected several counties in Croatia on 15 September, causing damage estimated at more than 6 million Euro (\$6.5 million U.S. dollars).

On 14–15 October, a barometric low reached Greece from southern Italy and was intensified by the warm Ionian Sea. The station in Siteia (east Crete) recorded 293 mm of daily precipitation (281.8 mm in 12 hours), which was the third-highest 24-hour rainfall on record for the country. Torrential rain on 15 October triggered flash floods in the Heraklion and Lasithi Regional Units on the island of Crete, causing two fatalities and significant damage to buildings and infrastructure, particularly in coastal areas.

Heavy precipitation in Montenegro and southwestern Serbia during 19–22 November led to high water levels on the Ibar River and its tributaries as well as the Lim River, causing local flooding. On 20 November, an emergency situation was declared in three municipalities in southwestern Serbia.

On 11 December, heavy rain caused the river water levels throughout Croatia to rise. A state of emergency was declared on the Sunja and Una Rivers near Sunja, Dvor, and Hrvatska Kostajnica.

7. EASTERN EUROPE

This section includes the European part of Russia, Belarus, Ukraine, Moldova, Romania, and West Kazakhstan.

(i) Temperature

The year was warmer than normal in Eastern Europe, with anomalies ranging from +0.7°C in Ukraine to +1.0°C in Romania and higher in certain localities. It was the third-warmest year on record for Romania, behind 2019 and 2020.

Winter 2021/22 temperatures were near normal in northern European Russia, but above normal toward the southeast (highest in West Kazakhstan at +4.0°C). This was due to a mild westerly flow from the North Atlantic that advanced far into Eastern Europe while the Russian Blocking High retreated to areas farther east. February was particularly warm, when the westerly flow changed its direction toward the north just over European Russia due to the blocking. The result was a warming, which was most intense just along the 50°E meridian (eastern European Russia to West Kazakhstan) where monthly anomalies exceeded +6.0°C.

A relatively cold spring followed. Belarus, northern and eastern Ukraine, and central European Russia had anomalies of –1.0°C or more. Only northernmost parts of European Russia were warmer than normal (+1.0°C). Southern areas of the region were affected in March when cold continental air from Siberia reached Kazakhstan and the Caucasus region (–3.0°C anomalies). Elsewhere, mild Atlantic air warmed northern parts of European Russia (close to 3.0°C above normal). In April, cold Arctic air reached Europe from the north, with western areas of the region most affected. Belarus, western Ukraine, and westernmost Romania reported anomalies around –2.0°C. In May, another cold spell originating from the north affected European Russia and West Kazakhstan, with temperatures 4.0°C below normal. Other parts of the region were also colder than normal, but less so, while western parts of Romania were 1.0°C warmer than normal.

Following these cold spells, summer was warm. Seasonal anomalies were mostly between +1.0°C and +2.0°C and as high as +3.0°C in northeastern European Russia. Warm airflow from southwestern Europe reached western parts of Eastern Europe in June, leading to monthly anomalies of around +2.0°C in western Romania, western Ukraine, and Belarus. In July, cooler air flowed in from Scandinavia over part of the region, but another strong warming took place in August as warm air arrived from both southwestern Europe and the Middle East. August temperatures were more than 4.0°C above normal in eastern European Russia.

Temperatures in autumn were mainly near normal. Only northernmost parts (northern coastal regions of European Russia) and southernmost parts (Romania, Moldova, southern European Russia, and West Kazakhstan) were around 1.0°C warmer than normal. In September, a cold spell affected western European Russia, Belarus, and northern Ukraine (–2.0°C anomaly), then warm air from the southwest spread over the entire region in October (+1°C to +2°C). In November, warm air flowed into both the northernmost and southernmost parts of the region, and cold continental air reached north-central European Russia. In December, cold air from Scandinavia affected Belarus and northern European Russia (–1.0°C anomaly), while southern parts experienced a warming from the southwest (+2.7°C anomaly in Romania).

(ii) Precipitation

The year was mostly drier than normal in Eastern Europe. Eastern Romania, parts of Moldova, southern and eastern Ukraine, and southern European Russia received less than 80% of their normal precipitation. Moldova reported a drought period during May–July, when only 30 mm to 90 mm (15% to 45% of normal) fell; this occurred for the first time in measurement history in Moldova. The year was wetter than normal across Belarus, northern Ukraine, central European Russia, and West Kazakhstan, with some areas receiving over 125% of normal. European Russia as a whole received 103% of its normal precipitation.

Precipitation in winter 2021/22 was mostly normal to above normal, mainly due to the positive North Atlantic Oscillation pattern (see overview of recent studies in McKenna and Maycock 2022). Locally, 150% to 200% of normal precipitation amounts fell, particularly in the mountains (Caucasus, Carpathians) and along the coasts of the Black Sea. In January, central parts of the region (Belarus, northern Ukraine, central European Russia, West Kazakhstan) received above-normal precipitation. In February, northwestern Russia was wetter than normal while southern areas (Romania, Moldova, Ukraine) were much drier than normal under the influence of high pressure.

Spring was wetter than normal (mostly above 125% of normal precipitation and 150% in certain places) in eastern Belarus, northern Ukraine, central European Russia, and West Kazakhstan. Other areas received less than 80% of their typical totals and less than 60% locally. March was dry in the west. Much of Belarus received less than 20% of its normal and large parts of Ukraine and western European Russia received below 40%; however, in April, some of these areas received 150% to 200% of their normal. May was again dry, with Romania, Moldova, and Ukraine receiving less than 60% of normal, while eastern parts of European Russia and West Kazakhstan were wetter than normal (125% to 200% of normal over large areas).

Summer was mainly drier than normal. July was the only summer month that was mostly wetter than normal, except for in Romania, Moldova, and Ukraine. In August, European Russia received only 44% of its monthly average total.

Autumn was wetter than normal in Belarus, Ukraine, central European Russia, West Kazakhstan, and western Romania. Conversely, it was drier than normal in northern European Russia and around the Black Sea, with the latter being an area where heavy precipitation frequently occurs. In autumn 2022, some northern Black Sea coastal areas received less than 80% of normal amounts. October was dry, with less than 20% of normal precipitation received in eastern parts of Romania and southern parts of Ukraine. In December, above-normal precipitation fell over Belarus, Ukraine, and central European Russia, while other areas were drier than normal.

(iii) Notable events and impacts

Heavy rain fell over European Russia in late June. On 24 June, 85 mm to 103 mm of rain led to a sharp rise in small river water levels in the Greater Sochi region close to the Black Sea. Two cars were swept into the sea due to flooding. On 26–27 June, heavy rains of 115 mm to 145 mm affected the Crimea Peninsula as water flooded streets, infrastructure, residential homes, and greenhouses.

8. MIDDLE EAST

This section includes Israel, Cyprus, Jordan, Lebanon, and Syria.

(i) Temperature

The Middle East saw near- to above-average annual temperatures in 2022. Anomalies were highest in northeastern Syria and eastern Jordan at +1.0°C. The year was in the top third of warmest years in Israel, but it was the coolest year since 2011.

Winter 2021/22 temperatures were normal to above normal, with anomalies increasing from the southwest (0°C in Israel) to the northeast (+1.0°C in northeastern Syria). A cold spell occurred in January, with the largest negative anomalies in the south (–1.0°C in southern Israel). Warming followed in February, expanding to the northern Middle East (up to +3.0°C anomaly in northern Syria).

Spring was slightly colder than normal in Cyprus, at the Mediterranean coast, and in northern Syria, while temperatures were above normal in southwestern Jordan (+1.0°C anomaly). In March, cold air from Russia flowed southward, resulting in below-normal temperatures throughout the region. Anomalies were largest in northwest Syria (–4.0°C) and decreased toward the southeast (–1.5°C in southeastern Jordan). During 10–26 March, temperatures were 7°C to 9°C below

normal in Israel. The duration of this cold wave was unusual and even unprecedented for March in many places. Israel and Cyprus each reported their coldest March on record. In April however, warming spread over the region, with temperatures 2°C to 3°C above normal across most of the region and as much as 4°C in southeastern Jordan. Israel recorded its third-warmest April, behind 2016 and 1989. In May, temperatures were below normal in northeastern Syria (-1.0°C anomaly), while the rest of the region had temperatures near or slightly above normal.

In summer, heat from the Arabic Peninsula affected eastern Syria and eastern Jordan (+1.0°C anomaly) and less so farther west. This mostly moderate warming persisted throughout the season.

Autumn was also warmer than normal across the region, with anomalies of +1.0°C or higher. In terms of anomalies, September, October, and November were similar. December was particularly mild, as a large-scale warming expanded over the Mediterranean region. Monthly anomalies ranged from +1.5°C in southeastern Jordan to +3.0°C in northern Syria. Cyprus observed its second-warmest December on record, behind 2010.

(ii) Precipitation

The year was mostly drier than normal across the Middle East. Syria, Lebanon, and northern parts of Israel and Jordan received less than 80% of their normal precipitation, while Syria received less than 40%. Southern Israel and southern Jordan were slightly wetter than normal. The 2021/22 rainy season (October–April) was wetter than the 1991–2020 average in Israel; the last four rainfall seasons have been wetter than average, which is unprecedented in the last 100 years.

Winter 2021/22 was dry in Syria and northeastern Jordan, with large areas receiving less than 30 mm total (less than 20% of normal in some areas). Lebanon also received below-normal precipitation, while the rest of the region was slightly wetter than normal. Notably, Israel experienced an unusually wet January (120% to 160% of normal). It was the third-rainiest January in the central-southern coastal plain in Israel since the 1940s (exact year depends on the stations), behind 2013 and 1974.

Spring was generally drier than normal throughout the region. Eastern parts of Syria and Jordan received less than 20% of their normal precipitation. In March, above-normal precipitation fell locally along the coasts, while eastern parts of the region remained mainly dry. In April, the entire region received little to no rain, which is unusual so early in the year, at least for the northern areas. This extreme dryness in the northern mountains of Israel last occurred in 2012. Cyprus had its driest April on record. May was also mostly dry, except for some rain in parts of Cyprus, western and northern Syria, and northern Lebanon.

Summer is the dry season in the Middle East. Monthly totals above 10 mm were only registered in Cyprus and western Syria in June, which were above normal. In northeastern Israel, a few millimeters of rain were measured. Locally, more than 5 mm were measured.

Autumn brought above-normal precipitation to Cyprus and parts of the continental region, at the coasts in localized places, and in the interior. Up to 250% of the seasonal normal fell in eastern Jordan, but in absolute terms this was only around 10 mm. September and October were mainly dry, except for Cyprus, which saw above-normal rainfall in October. November was wetter than normal, with heavy rain observed at Syria and Lebanon's coasts. December was unusually dry in much of the region. Large parts of Syria and northeastern Jordan saw no rain at all, whereas precipitation was above normal in southern Jordan. The first half of the rainy season 2022/23 in Israel was deficient at the end of 2022, despite significant rains at the end of December.

(iii) Notable events and impacts

Heavy precipitation (that included snow in the mountains) fell during 25–28 January in Israel. The first part of the system was named "Elpis" (as part of the windstorm naming in Europe) and brought snow to the mountains. In the northern and central Golan Heights, the snow depth

reached 20 cm to 40 cm. In Jerusalem, snow depth reached 15 cm to 25 cm, its largest snowfall since 2015. Precipitation totals during the event reached 100 mm to 150 mm in the northern and central mountains and the southern coastal plain.

Due to cold weather in March, significant and unusual snow fell in the northern mountains of Israel. For example, more than 30 cm fell on Mt. Hermon during a heavy precipitation event on 23–26 March.

During 24–26 April, severe haze prevailed for three consecutive days. The source of the haze was from the east (as opposed to the southwest, from which it typically originates). The haze caused sandstorms in the Jordanian and southern Syrian deserts due to strong winds and developed clouds in the area. The dust that rose into the air was transported to Israel by easterly to northeasterly winds in upper layers, so that elevated areas were most affected by it.

In Israel, temperatures reached 43°C to 45°C in the Jordan Valley and the Arava during a heatwave from 27 to 31 August.

9. TÜRKIYE AND SOUTH CAUCASUS

This section includes Türkiye, Armenia, Georgia, and Azerbaijan.

(i) Temperature

The year was warmer than normal for almost all of Türkiye and the South Caucasus region, with anomalies up to +1.0°C and slightly higher in eastern Türkiye. A few places in western Türkiye were slightly colder than normal. The average temperature in Türkiye was 0.6°C above normal.

Winter 2021/22 was mostly mild, especially in northeastern Türkiye and the South Caucasus with anomalies of +1°C to +2°C. Temperatures in the rest of Türkiye were generally near normal, with some places in western Türkiye slightly below normal. A cold spell in January affected mainly Türkiye (monthly anomaly of around –1.0°C), but February was warmer than normal everywhere in the region, most notably in the east.

Cold air from Russia resulted in a colder-than-normal spring in the region with seasonal anomalies around –1.0°C in places. In March, anomalies ranged from –1.0°C in eastern Azerbaijan to –5.0°C in parts of western Türkiye. A warmer-than-normal April followed, with anomalies between +1.0°C and +3.0°C. May again brought an influx of cold air, albeit less intense than that of March, with eastern parts of the region being most affected (anomalies ranged from –1.8°C in northern Georgia to +1.0°C in southwestern Türkiye).

Summer was mainly warmer than normal across the region, particularly in the South Caucasus and eastern Türkiye at 1.0°C above normal; only places in northwestern Türkiye were slightly colder than normal, which was mainly due to a cooler period in July. It was the fifth-warmest summer on record for Armenia.

Autumn was also warmer than normal, specifically 1.0°C or more above normal across much of the region. It was the second-warmest autumn on record in Armenia behind 2010. The greatest departures from average occurred in November in Türkiye and Georgia with anomalies of around +2.0°C in most parts, whereas September and October were particularly warm in Armenia. It was also warmer than average in December (up to +3.0°C in Türkiye).

(ii) Precipitation

The year was drier than normal in Türkiye, Georgia, and western Armenia. Some areas, particularly in Türkiye, received as little as 60% to 80% of their normal precipitation. Most of Azerbaijan and eastern Armenia by contrast received above-normal precipitation (mostly more than 125%). Armenia received 75% of its normal total on average, making 2022 its fourth-driest year since 1935.

Winter 2021/22 was wetter than normal in the western half of Türkiye, with some areas receiving more than 125% of normal. The eastern half of Türkiye and the South Caucasus were mainly drier than normal. Some of these areas received less than 80% of normal precipitation and some less than 60%. In Armenia, precipitation was only 36% of its normal in February.

In spring, the pattern was reversed compared to winter. Western Türkiye was considerably drier than normal with less than 80% in most areas and below 40% in westernmost Türkiye. Eastern Türkiye and the South Caucasus saw above-normal precipitation, with the highest anomalies in Azerbaijan (more than 250% of normal in certain places). Precipitation in March accounted for much of this excess. It was the second-wettest March in Armenia since 1935. April, however, was drier than normal in almost the entire region. Large parts of Türkiye, Armenia, and Azerbaijan received less than 60% of their typical rainfall, with less than 20% being received in southern Türkiye.

In summer, there was again a reversal of patterns. Western Türkiye was wetter than normal with locally heavy precipitation, including hail. Seasonal totals were more than 150% of normal in many places. In contrast, eastern Türkiye had a dry summer with widespread precipitation below 80% of normal. Summer precipitation was also below normal in most of the South Caucasus. Seasonal precipitation in Armenia was only 58% of normal, making this its second-driest summer on record.

Autumn was generally drier than normal across most of the region. Several areas received less than 80% of their normal precipitation, and western Türkiye and Armenia received less than 60%. December was also a dry month, with many places receiving less than 20% of normal, especially in Türkiye. Only Azerbaijan had above-normal precipitation that month, with some locations seeing more than 250% of normal.

(iii) Notable events and impacts

The year 2022 had the highest number of extreme weather- and climate-related events in Türkiye on record, with 1030 reported through the database of the Turkish Meteorological Service. Most of the reported events were heavy rain and floods (34%), severe storms (21%), and hail (19%). As an example, 336 landslides occurred in 11 districts of the Ordu Municipality (located at the eastern Black Sea coast of Türkiye) due to heavy rain on 18 July. There is an increasing trend in the number of extreme events, especially in the last two decades.

In Yerevan (Armenia), the daily maximum temperature reached 39.5°C on 17 August, setting a new record for that day of the year. The highest temperature overall during 2022 in Armenia was 41.2°C at Ararat station (southwest Armenia) during the same heatwave on 15–19 August. The highest temperature in Türkiye was 47.9°C in Silopi/Şırnak on 15 July.

g. Asia

—Z. Zhu, Ed.

Throughout this section, the base period for the climatological normal and anomalies is 1991–2020. All seasons refer to the Northern Hemisphere, with winter referring to December–February 2021/22, unless otherwise noted.

1. OVERVIEW

—P. Zhang, T.-C. Lee, A.-M. Setiawan, Y. Oikawa, K. Takemura, Y. Okunaka, K. Takahashi, M.-J. Kim, D. Dulamsuren, M.-V. Khiem, H.-P. Lam, H. Chen, and R. Lu

Annual mean surface air temperatures for 2022 were above normal across most of Asia and Siberia, except for Southeast and South Asia, with anomalies of more than +1.0°C in eastern China, from northwestern China to Central Asia, and in northern central and western Siberia (Fig. 7.45). Annual precipitation totals were more than 120% of normal across most of central Siberia, northeastern China, parts of Southeast Asia, from India to Pakistan, and western Central Asia. Annual precipitation totals were less than 80% of normal from western Mongolia to western China (Fig. 7.46).

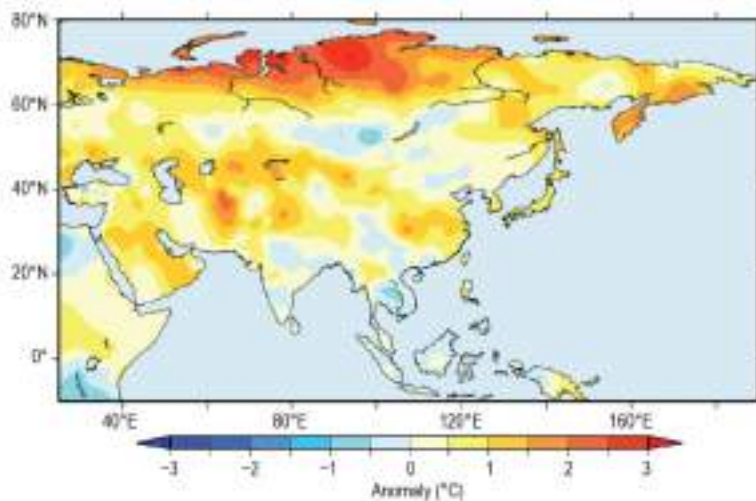


Fig. 7.45. Annual mean surface temperature anomalies (°C; 1991–2020 base period) over Asia in 2022. (Source: Japan Meteorological Agency, JMA.)

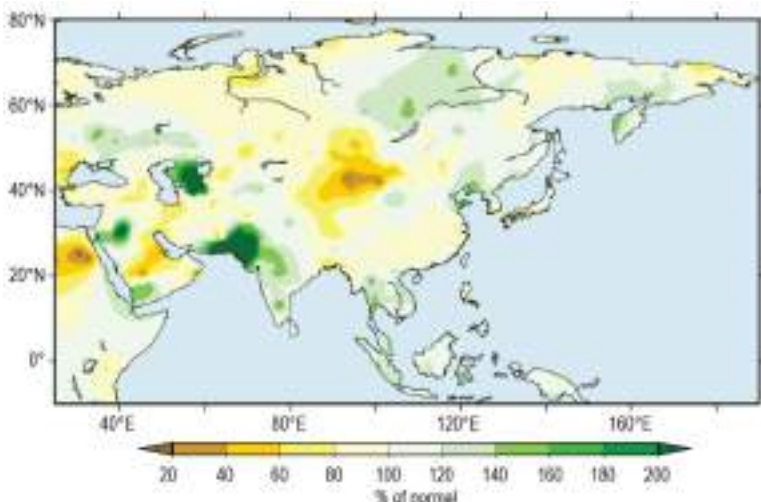


Fig. 7.46. Annual precipitation totals (% of normal; 1991–2020 base period) over Asia in 2022. (Source: JMA.)

In winter, above-normal temperatures dominated from northern central Siberia to northern India (Fig. 7.47a). Seasonal precipitation was much above normal from the Indochina Peninsula to India and below normal from western Japan to eastern China and from Mongolia to northwestern China (Fig. 7.47b). In spring, temperatures were above normal across most of Asia and Siberia, except for parts of eastern Siberia, Southeast Asia, and Central Asia (Fig. 7.47c). Seasonal precipitation was above normal from southern China to the Philippines and in western China, and below normal from Mongolia to northern China and from northwestern India to southwestern Asia (Fig. 7.47d). In summer, Pakistan experienced much-below-normal temperatures and much-above-normal precipitation (Figs. 7.47e,f). Positive temperature anomalies were observed in most of China, while temperatures were below normal from northern Mongolia to southern central Siberia (Fig. 7.47e). Seasonal precipitation was above normal in and around central Siberia, from northeastern China to northern Japan, and in Indonesia and southwestern Asia. Summer precipitation was below normal from western Mongolia to western China, and in southern Central Asia (Fig. 7.47f). In autumn, temperatures were above normal in northern central and western Siberia, southeastern China, and western Asia and below normal in far eastern

Siberia (Fig. 7.47g). Seasonal precipitation was much above normal from southwestern China to northern India as well as in Indonesia and western Central Asia and below normal in southwestern Asia and from southern Mongolia to northern China (Fig. 7.47h).

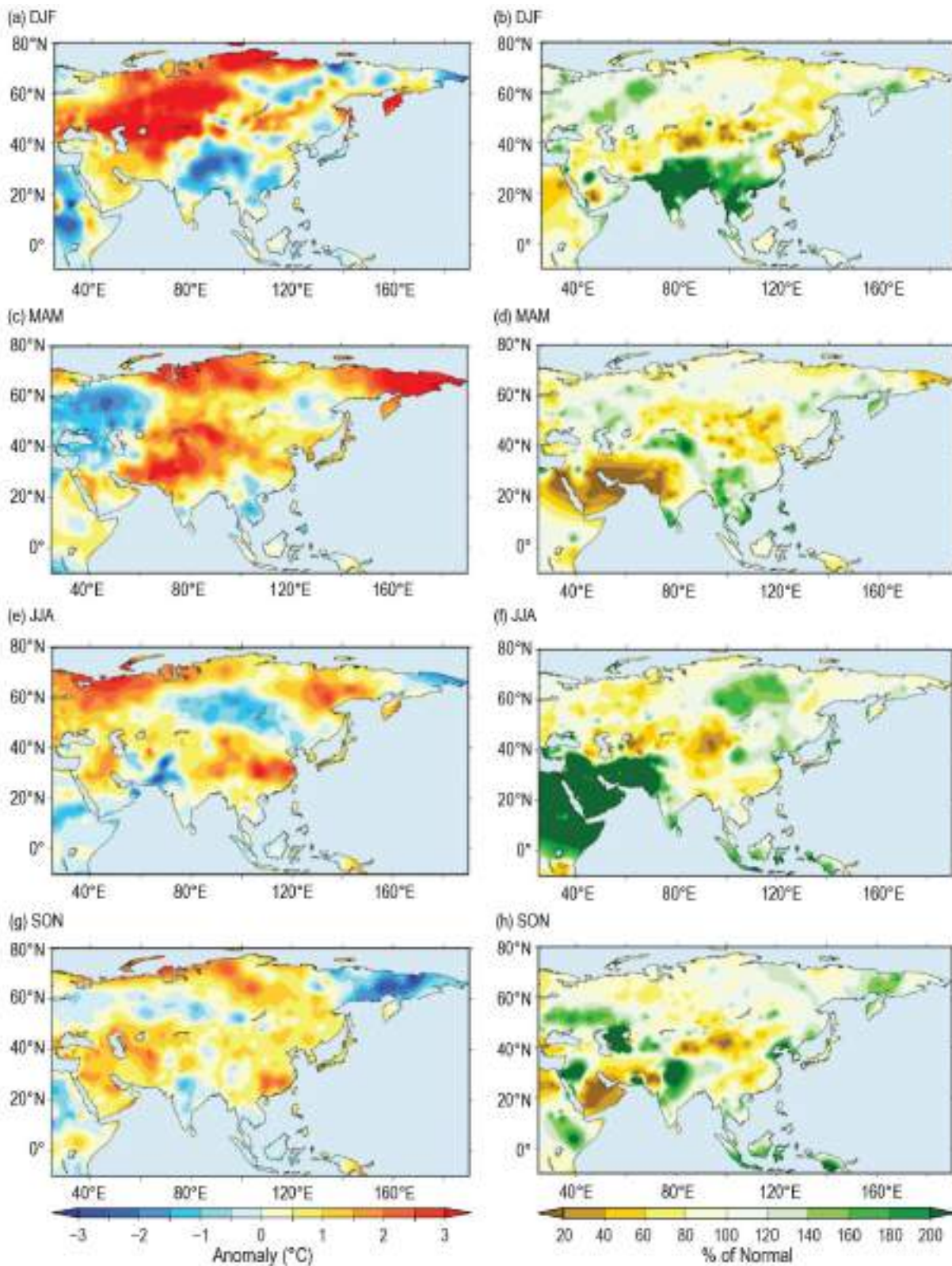


Fig. 7.47. Seasonal mean surface temperature anomalies (°C, left column) and precipitation ratios (% of normal, right column) over Asia in 2022 for (a),(b) winter, DJF; (c),(d) spring, MAM; (e),(f) summer, JJA; and (g),(h) autumn, SON. Anomalies and ratios are relative to 1991–2020. (Source: JMA.)

In winter, positive 500-hPa geopotential height anomalies were dominant from Central Asia to Siberia, while negative 500-hPa geopotential height anomalies accompanying negative 850-hPa temperature anomalies were observed from South Asia to East Asia (Fig. 7.48a). In spring, positive anomalies of geopotential height and temperature were seen over Central and East Asia (Fig. 7.48c). The enhanced convection from southwestern India to the seas east of the Philippines (Fig. 7.48d) was observed. In summer, above-normal geopotential heights and temperatures were observed over China (Fig. 7.48e). Convective activity was enhanced from the Arabian Sea to near Indonesia (Fig. 7.48f). In autumn, above-normal geopotential heights and temperatures were clearly seen in the midlatitudes from Eurasia to the North Pacific (Fig. 7.48g). Convective activity was enhanced near Indonesia, accompanied by 850-hPa cyclonic circulation anomalies straddling the equator over the eastern tropical Indian Ocean (Fig. 7.48h).

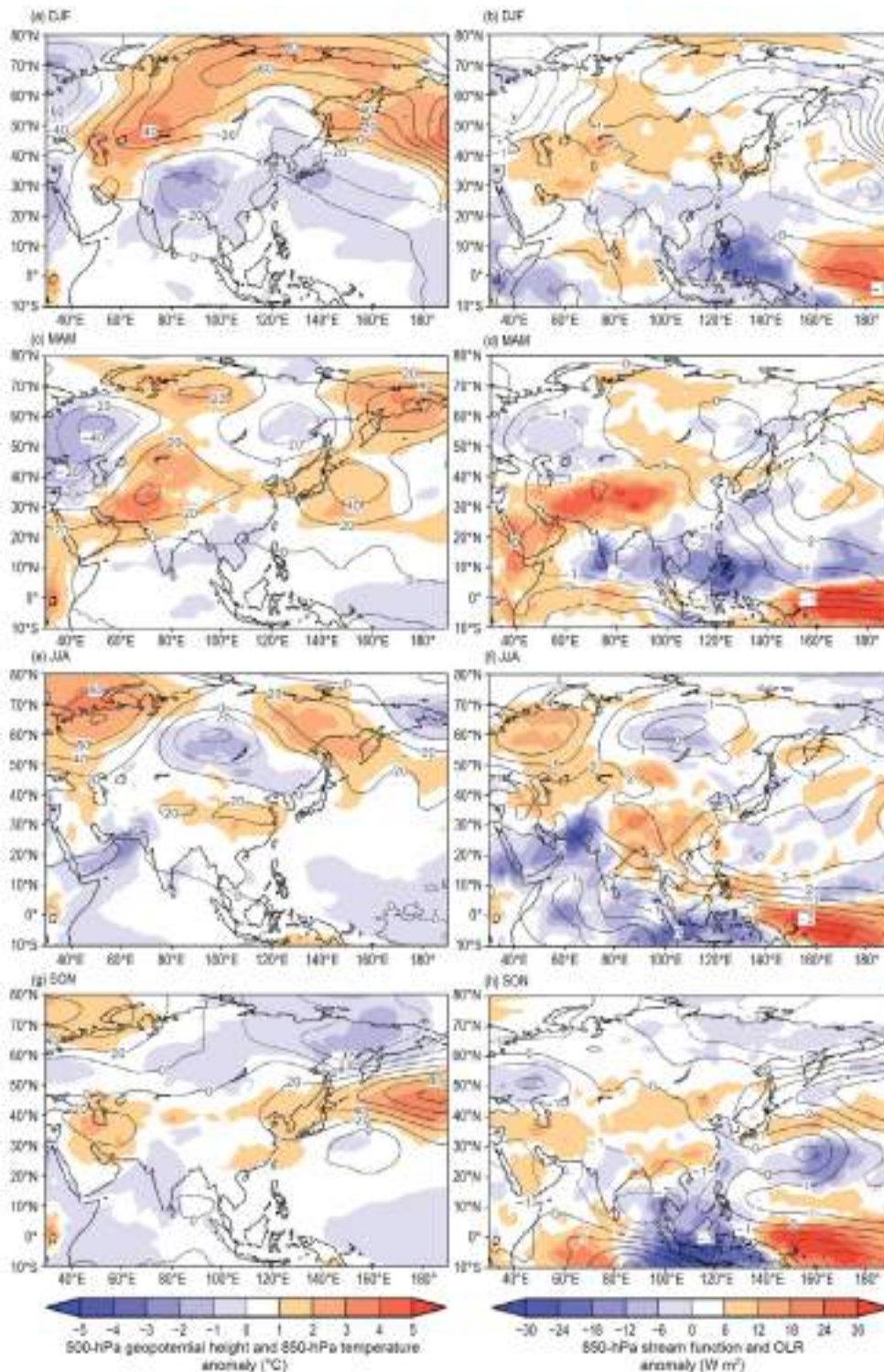


Fig. 7.48. Seasonal mean anomalies of atmospheric circulation variables in 2022 for (a),(b) winter, DJF; (c),(d) spring, MAM; (e),(f) summer, JJA; and (g),(h) autumn, SON. Left column: 500-hPa geopotential height (contour, gpm) and 850-hPa temperature (shading, °C). Right column: 850-hPa stream function (contour, $1 \times 10^6 \text{ m}^2 \text{ s}^{-1}$) using data from the JRA-55 reanalysis and outgoing longwave radiation (OLR; shading, W m^{-2}) using data originally provided by NOAA. Anomalies are relative to 1991–2020. (Source: JMA.)

2. RUSSIA

—M. Yu. Bardin and N. N. Korshunova

Estimates of climate features for Russia are obtained from hydrometeorological observations of the Roshydromet Observation Network. Anomalies are relative to the 1991–2020 base period, and national rankings and percentiles reflect the 1936–2022 period of record. Note that the temperature database was extended significantly, which in some cases changed previous rankings. The boundary between Asian Russia and European Russia is considered to be 60°E.

(i) Temperature

The year 2022 in Russia was the fifth warmest on record with an annual mean temperature 0.87°C above normal (Fig. 7.49), significantly higher than that of the previous year (0.15°C above normal) but below that of 2020 (2.02°C above normal), the record-warmest year.

The warmest areas, with respect to their climatology (anomalies above the 95th percentile), were the Arctic zone from the Kola peninsula to the Yenisei River, the southern Far East (Khabarovsk region, Kamchatka, Sakhalin), and the eastern North Caucasus.

Winter was the 10th warmest on record for Russia as a whole, with February in European Russia ranking among its five warmest on record (5.2°C above normal).

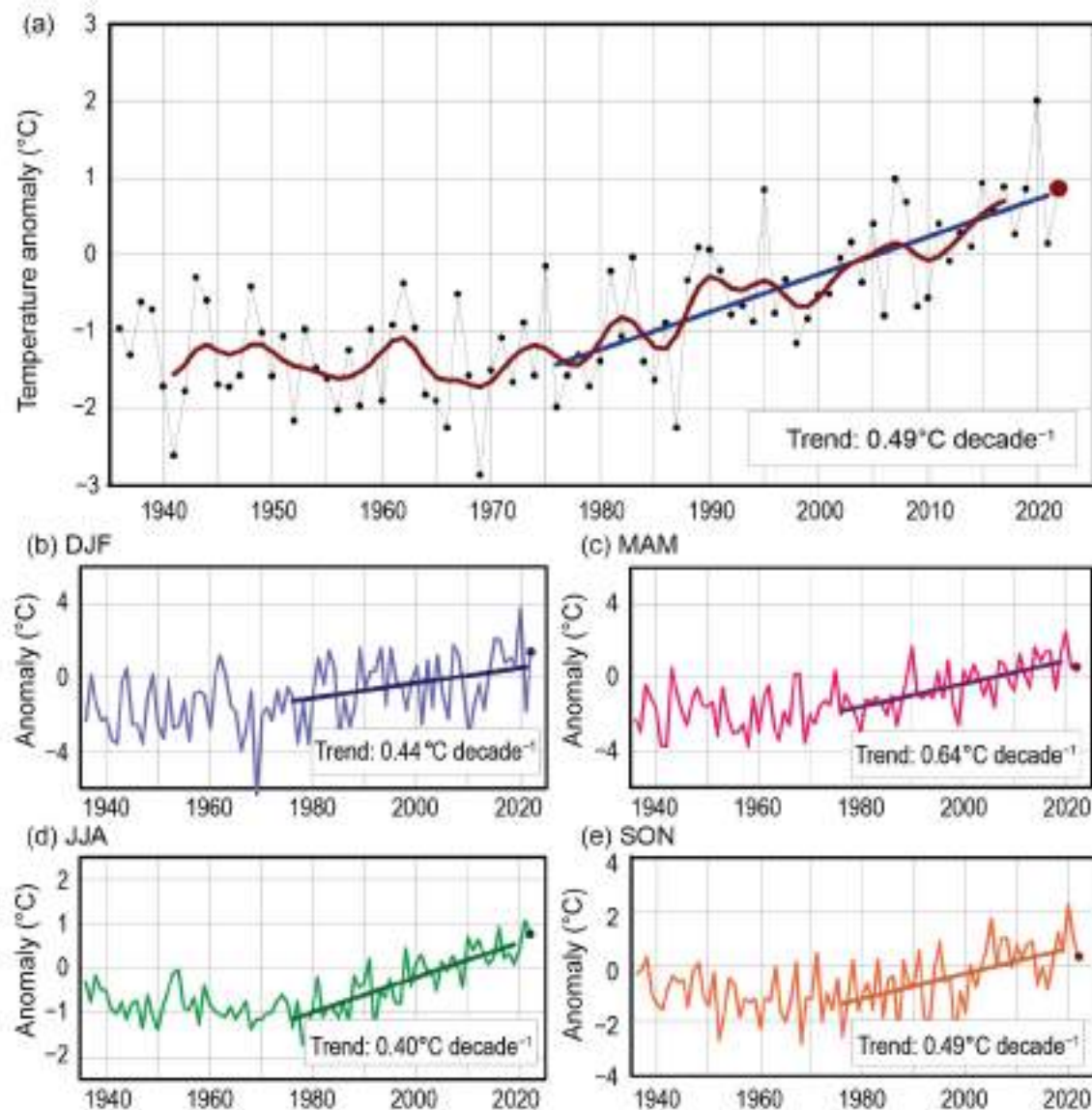


Fig. 7.49. Annual and seasonal mean temperature anomalies (°C; 1991–2020 base period) averaged over the territory of Russia for the period 1936–2022: (a) annual, (b) winter, (c) spring, (d) summer, and (e) autumn. The bold red line in (a) is an 11-point binomial filter. Linear trend (°C decade⁻¹) is calculated for the period 1976–2022.

Spring was colder than normal in European Russia (0.84°C below normal), but warmer than normal in its Asian counterpart (1.2°C above normal; 10th warmest). May in Asian Russia was the second warmest on record (1.6°C above normal), while in European Russia the May temperature was in the bottom quartile (2.1°C below normal). The largest positive anomalies in May were observed in the Yamalo-Nenets Autonomous Okrug. At the meteorological stations Nadym and Tarko-Sale, May 2022 was the second warmest after 2020 (Fig. 7.50). Conversely, abnormally cold

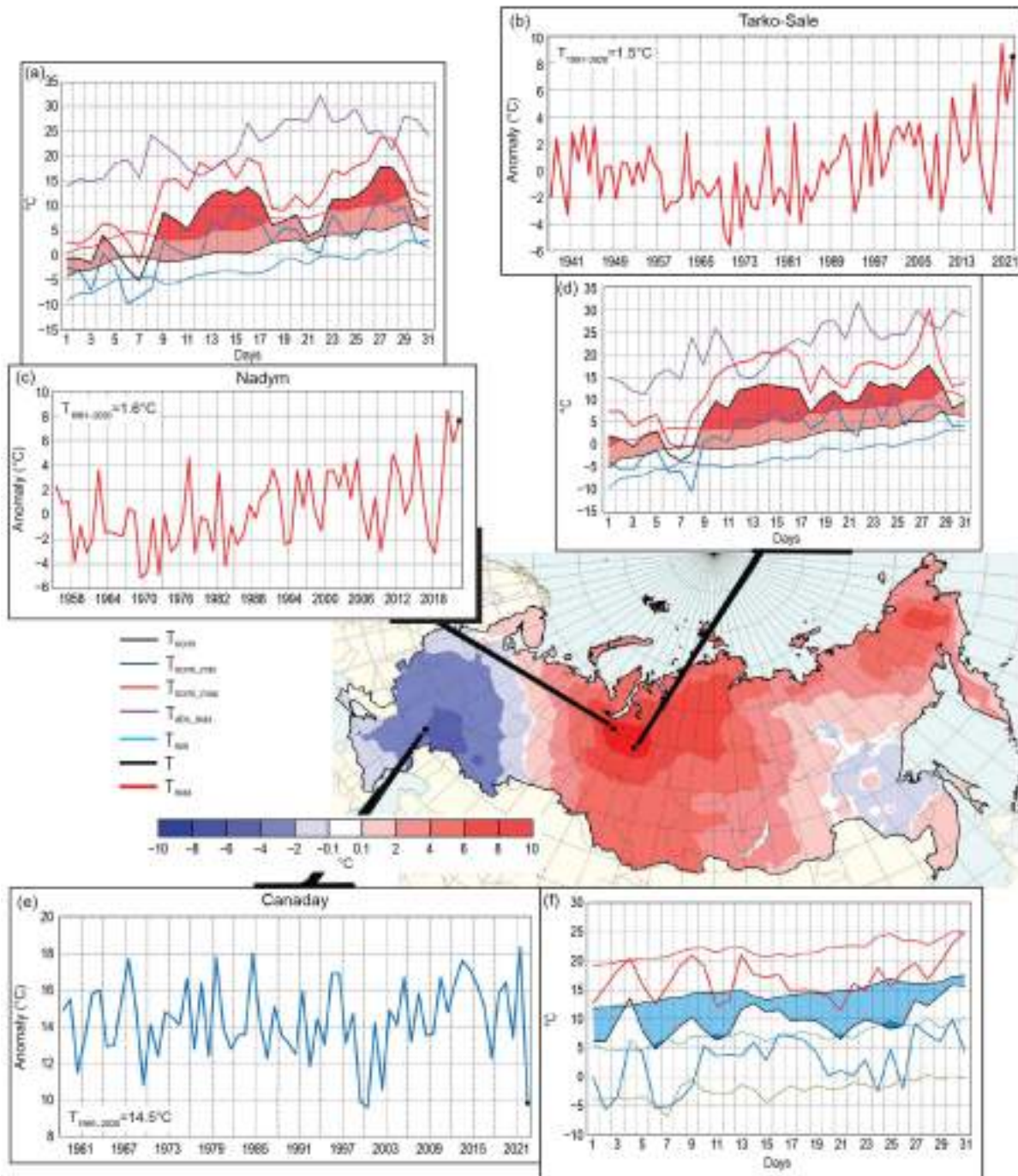


Fig. 7.50. Map: temperature anomalies across Russia (shading, contour interval is 2°C) for May 2022. Insets: Monthly mean temperature (°C) in (b) Tarko-Sale (1937–2022), (c) Nadym (1955–2022), and (e) Canaday (1958–2022), and mean, minimum, and maximum daily temperatures (°C) in May 2022 in (d) Tarko-Sale, (a) Nadym, and (f) Canaday. T_{91-20} on plots of monthly mean temperatures is 1991–2020 mean. Plots of daily temperature show observed daily mean (T_{91-20} , black line), daily minimum (T_{min} , blue line), and daily maximum (T_{max} , red line) temperatures along with their climatological values (three lowermost curves: T_{norm} , black; $T_{norm,min}$, blue; $T_{norm,max}$, red) and absolute maximum temperature ($T_{abs,max}$, dark red). For (a) Nadym and (d) Tarko-Sale, the area between the normal daily mean curve T_{norm} and the observed daily mean curve is shaded pink where $T > T_{norm}$, and is shaded red if T was above normal daily maximum $T_{norm,max}$. For (f) Canaday, the area where $T < T_{norm}$ is shaded blue.

weather was observed in European Russia for almost the entire month. New daily temperature minima were recorded from the Vologda Oblast to the Lower Volga. At the Canaday meteorological station, the daily average temperature was below normal for 30 days in May. Daily minimum temperature records were broken six times at the same station. This contrasting temperature regime was associated with a pattern of tropospheric circulation, in which a deep trough located over European Russia provided an influx of arctic air while a large ridge over western Siberia provided an influx of warm air from the subtropics; this pattern persisted with some variations for almost the entire month.

Summer was the third warmest on record both for Russia as a whole (0.77°C above normal) and European Russia (1.69°C above normal). Summer for Asian Russia was the sixth warmest (0.43°C above normal). July was especially warm (0.73°C above normal; second warmest on record) there, and August was record warmest in European Russia (3.5°C above normal). Monthly temperatures above the 95th percentile were recorded in August at all European stations of Russia.

Autumn was moderately warm (0.35°C above normal), due primarily to a warm October (1.44°C above normal; sixth warmest on record). Temperatures in September and November were below normal, especially in the northern Far East Russia.

All seasons in Russia have warmed since the mid-1970s. Annual and seasonal trends are statistically significant at 1%, except winter. Due to long-term changes in atmospheric circulation in the Atlantic-European sector, winter temperatures showed no discernable trend from the mid-1990s to around 2010, then began to increase thereafter (Fig. 7.49), but the trend remained insignificant. After the abnormally warm winter of 2020, the trend became significant at least at the 5% level.

(ii) Precipitation

Across Russia as a whole, the total precipitation in 2022 was 105% of normal, the fourth wettest on record (equal with 1961, 1966, and 1990; Fig. 7.51). Asian Russia received 105% of its normal precipitation (fourth wettest), while European Russia had 104% (14th wettest). The seasons that ranked among their 10 wettest were: winter (120% of normal; third wettest) and autumn (118% of normal; seventh) in European Russia and summer in Asian Russia (112% of normal; sixth). In contrast, summer in European Russia was dry with only 83% of normal precipitation. In particular, August in European Russia was the second driest on record (50% of its normal precipitation).

Precipitation in Russia has increased during the period of warming since the mid-1970s by about 1.8% per decade. Increases are most notable in spring, with a rate of about +6% decade⁻¹. However, a vast area in southern European Russia is seeing decreasing precipitation; combined with the high rate of warming, this has led to an increasing risk of drought in this principal agricultural region.

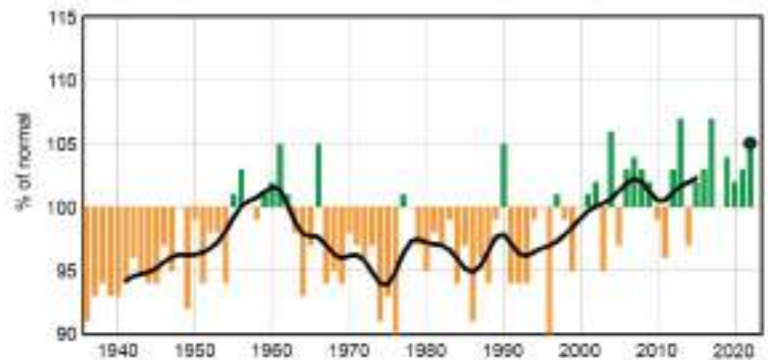


Fig. 7.51. Annual precipitation (% of normal; 1991–2020 base period) averaged over the Russian territory for 1936–2022. Bold black line denotes the smoothed time series (11-point binomial filter). The black dot indicates 2022 precipitation percentage.

(iii) Notable events and impacts

On 12 May, in the Bryansk region, heavy thunderstorms were accompanied by strong winds up to 27 m s⁻¹. Emergency power outages were recorded, 435 trees were felled, 272 houses were damaged, and three people were injured.

During 19–20 June, heavy rains (48 mm–74 mm) caused a sharp rise in water levels for the rivers of the Trans-Baikal Territory. Roads were washed out and bridges were destroyed. On one section of the Trans-Siberian Railway, the railway track was washed out, which led to a halt in the movement of trains.

On 24 June, heavy rain (85 mm–103 mm) caused a sharp water rise in small rivers in the Lazarevsky district of Greater Sochi. Twenty-eight adjacent territories were flooded and six people were swept out to sea. A landslide occurred at the railway station Chemitokvadzhe. Several trains were delayed, and the automobile bridge was washed away.

On 14–17 July, heavy rains (138 mm–311 mm) occurred in the Primorsky Territory and caused rivers to rise by 2.5 m–4 m. Roads and low-water bridges were destroyed, agricultural lands were flooded, and power lines were washed out. In the village of Timofeevka, mudslides descended on two houses, with one fatality recorded.

On 6 August, for two hours, inclement weather was observed in St. Petersburg; heavy rain (44 mm) was accompanied by winds up to 22 m s⁻¹ and hail with a diameter of 5 mm. Several sections of roads as well as the lobby of a metro station were flooded, and the contact network of trolleybuses was broken. One person was injured.

On 19 September, in Moscow, wind speeds reached 19 m s⁻¹ to 21 m s⁻¹, causing a power outage, 81 downed trees, damage to 65 cars, and one injury.

On 21–23 December, heavy snowfall (6 cm–13 cm) and blizzard conditions (27 m s⁻¹ to 32 m s⁻¹) were recorded in the Primorsky Territory. The storm disrupted the power supply in 22 settlements, hindered traffic in 10 road sections, and canceled 128 bus trips.

3. EAST AND SOUTHEAST ASIA

—P. Zhang, T. C. Lee, A. M. Setiawan, A. Moise, Y. Oikawa, K. Takemura, K. Takahashi, M.-J. Kim,,
D. Dulamsuren, M.-V. Khiem, and H.-P. Lam

Countries and places considered in this section include China, Hong Kong (China), Indonesia, Japan, Korea, Mongolia, Singapore, and Vietnam. Unless otherwise noted, anomalies refer to the 1991–2020 base period.

(i) Temperature

Annual mean temperature anomalies for 2022 across East and Southeast Asia are shown in Fig. 7.45. The annual mean temperature for China was 0.62°C above normal and the second highest since the start of the record in 1951. It was the sixth-warmest year in Hong Kong since its records began in 1884, at 0.4°C above normal.

In Japan, annual mean temperatures were above normal nationwide and significantly above normal in northern Japan. In western Japan, summer temperatures in 2022 were the highest on record since 1946, equal with 2013 and 2018. The annual mean temperature anomaly in South Korea was 0.4°C above normal, which was the ninth highest since its records began in 1973. Notably, it was significantly warmer than normal from spring to early summer. The annual mean temperature anomaly over Mongolia was 2.3°C above average (16th highest since 1940); the country recorded its fifth-warmest January and sixth-warmest May, 2.4°C and 1.7°C above normal, respectively.

Based on observation of 91 stations in Indonesia, the country recorded an annual average temperature that was 0.2°C above normal, making 2022 the 13th-warmest year since 1981. The maximum anomaly (+0.8°C) was recorded at Sentani–Jayapura meteorological station, while

the minimum anomaly (-0.7°C) was recorded at Karel Sadsuitubun–Maluku Tenggara meteorological station.

The annual mean temperature for Singapore in 2022 was 0.1°C above average. This was equal with 2021 as the 10th-warmest year since records began in 1929.

The monthly mean temperature was near-normal across Vietnam for most months in 2022. While the annual mean temperature was 0.4°C above normal, it was the coolest year since 2015.

(ii) Precipitation

Annual precipitation for 2022 as a percent of normal over East and Southeast Asia is shown in Fig. 7.46. The annual precipitation total for China was 95% of normal and the lowest total in the past 10 years. Total precipitation was significantly above normal in northeast China (124% of normal) and the Liaohe River Basin (135%; second wettest since 1961) and below normal in the Yangtze River Basin (86%). Total rainfall for Hong Kong in 2022 was about 91% of normal.

In Japan, annual precipitation totals were above normal in Okinawa/Amami and below normal on the Sea of Japan side of western Japan. The annual precipitation total for South Korea was 86.7% of its normal. Precipitation from winter 2021/22 to spring was below normal, mainly due to the influence of high-pressure systems. The annual precipitation in Mongolia was about 50% of normal.

Based on observed precipitation data from 115 BMKG official stations over the Indonesian region, 2022 was the second-wettest year since 1985 after 2010, with annual rainfall being 122% of normal. The highest rainfall anomaly (219% of normal) was recorded at Tampa Padang–Majene meteorological stations.

In Singapore, above-average annual total rainfall was recorded at most of the island stations in 2022. The annual total rainfall averaged across these stations (3012.0 mm) was 119% of the 1991–2020 average of 2534.3 mm, making 2022 the sixth-wettest year since 1980.

Total annual rainfall in 2022 in Vietnam varied from 80% to 120% of average across the country, except for the Red River Delta region to the Nghe An province, where annual rainfall was 140%–170% of average.

(iii) Notable events and impacts

In China, the Meiyu (also named Baiu in Japan and Changma in Korea) season, which started and ended earlier than usual, was eight days shorter than normal with 258.3 mm rainfall (81% of normal). The rainy season in North China, which was 23 days longer than normal (with a length of 53 days; third longest since 1961), had an average total rainfall of 214.7 mm (257% of normal).

In 2022, regional and periodic droughts occurred in China, especially in southern China which suffered from severe summer and autumn drought that had wide range, long duration, and heavy intensity. From July to the first half of November, the middle and lower reaches of the Yangtze River as well as Sichuan and Chongqing suffered from a series of summer and autumn droughts, impacting a maximum area of 1.63 million km^2 . Seventy-seven days of drought accompanied high temperatures and little rainfall; the drought duration was the longest on record during this period since 1961. The persistent drought had a great impact on agriculture, water supply, energy, ecosystem balance, and human health in the Yangtze River basin.

From 13 June to 30 August, east-central China was affected by a widespread and enduring heatwave that lasted up to 79 days, the longest heatwave since 1961. Sichuan basin, Jianghuai, Jiangnan, and Jiangnan all reported high temperatures above 35°C for 30 to 65 days, depending on the location. There were 361 stations (about 15% of the total number of stations in the country) in which the daily maximum temperature reached or exceeded its historical extreme. Beibei in Chongqing reached a daily maximum temperature of 45°C for two consecutive days.

In Hong Kong, total rainfall in April 2022 was only 3.5 mm, the lowest on record for the month. July 2022 was the hottest month on record with the monthly mean temperature reaching 30.3°C .

Contributing to this record were 25 hot nights (daily minimum temperature $\geq 28.0^{\circ}\text{C}$) and 21 very hot days (daily maximum temperature $\geq 33.0^{\circ}\text{C}$), both of which were the highest number in a month on record. Moreover, the consecutive 21 hot nights from 9 to 29 July were the hottest nights on record.

An extreme heavy rainfall event during 13–16 October in central Vietnam, from Quang Binh to Quang Ngai provinces, was the consequence of the combination of Tropical Storm Sonca (TS. No 5), the northeast monsoon, and easterly waves. Da Nang recorded record rainfall of 600 mm (Da Nang station) and 642 mm (Suoi Da station) in seven hours on 14 October, and level 3 floods (highest level in Vietnam's flood warning system) occurred in Kien Giang, Thach Han, Phu Oc, and Ai Nghia. These high floods, combined with high tide, caused prolonged inundation for central Vietnam that day.

South Korea observed its highest mean temperature from late June to early July (26.4°C ; 3.5°C above normal) since 1973. From 8 to 11 August, South Korea experienced downpours (exceeding 140 mm h^{-1}) as a stationary front anchored over the central region. A few weeks later, on 6 September, Typhoon Hinnamnor made landfall in South Korea, bringing heavy rain and significant flooding.

In Semarang, Central Java of Indonesia, more than 200 mm of rainfall during 30–31 December caused massive flooding that inundated most of Semarang City and forced the government to stop operating the trans-Java train services.

Please refer to section 4g4 for details about the 2022 western Pacific tropical cyclone season.

Sidebar 7.2: **The record-breaking hot summer of 2022 in the Yangtze River basin**

—Z. ZHU, H. HUANG, H. CHEN, K. TAKEMURA, AND K. TAKAHASHI

The record-breaking hot summer of 2022 in Central and East Asia, especially in the Yangtze River basin (YRB), was long-lasting and extremely intense. Unusually high temperatures led to serious hydrological drought, agricultural failure, and ecological damage causing a direct economic loss of 32.8 billion yuan (\$4.75 billion U.S. dollars) and affecting more than 38 million people.

The highest above-average temperatures were mainly located in the YRB in July and August (Figs. SB7.3a,b). Relative to the 90th percentile of temperature records in the period of 1991–2020, there were 30% more extreme high-temperature days (EHDs) during July and August across the YRB (slashed region in Fig. SB7.3a). The above-normal temperatures, averaged over the YRB, lasted about 80 days, with a maximum anomaly of $+5.3^{\circ}\text{C}$ on 22 August (Fig. SB7.3b). There were 35 EHDs from June to August, with 31 of those in July and August.

The detrended normalized July–August mean temperature averaged over the YRB (referred to as YT afterwards) in 2022 was more than two standard deviations, which was the largest since 1979 (Fig. SB7.3c).

The descending motion over the YRB was related to a local anomalous barotropic anticyclone (Figs. SB7.3d–f), which was

one of the centers of anomalous anticyclones and cyclones. Based on regressions of the anomalous atmospheric fields onto the YT, the extreme high-temperature event was thought to be caused by: 1) the positive phase of North Atlantic Oscillation (NAO; Figs. SB7.3d–f), 2) the positive convection anomalies over the tropical Atlantic (Fig. SB7.3e), and 3) below-normal sea-surface temperatures (SSTs) due to La Niña in the tropical Pacific (Fig. SB7.3f).

The rare “triple-dip” La Niña event (see section 4b and Sidebar 3.1 for details), with negative SST anomalies in the central and eastern Pacific and positive SST anomalies in the western Pacific (Fig. SB7.3f), led to enhanced convection over the Maritime Continent (Fig. SB7.3e), which resulted in an anomalous local meridional cell favorable for the anomalous anticyclone (and descending motion) over the YRB. Furthermore, the anomalous convection over the tropical Atlantic, as well as the positive phase of NAO, could have also contributed to the anomalous anticyclone (and descending motion) over the YRB by stimulating the Rossby wave train propagating from the Atlantic to the North Pacific (Yang et al. 2023; Fu et al. 2023).

The three contributors noted above could be applied to reconstructing the YT index through a multiple linear

regression model (Fig. SB7.3c). Using the tropical Pacific SST (TPS) index (defined as the difference between the western and eastern tropical Pacific SSTs) as the only independent variable, the model was not able to reproduce the observed YT index or the extreme high-temperature event in 2022. When the NAO index was added as another independent variable, the simulated YT index was much closer to the observed one. It was found that the TPS index could be replaced by the

precipitation over the tropical Atlantic (TAP) in the model. The observed YT index was reproduced to a large extent by the multiple regression model using the TAP and NAO indices, with a correlation coefficient of 0.67 ($p < 0.01$) and root mean square error of 0.81. The record-breaking hot summer in 2022 over the YRB was also captured by this model, which suggests the irrelevance to the La Niña.

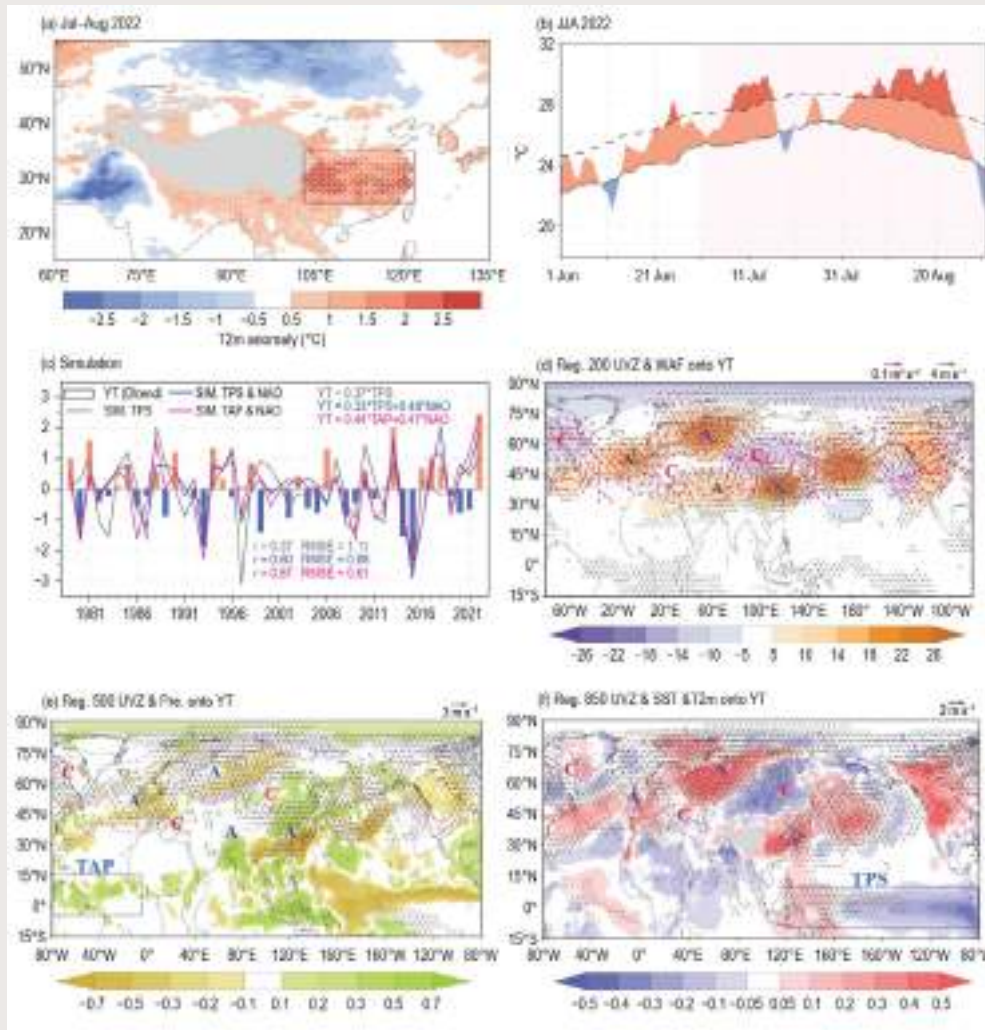


Fig. SB7.3. (a) 2-m air-temperature anomalies (T2m, shading, °C) for Jul–Aug 2022. Areas with extreme high-temperature days (EHDs) 30% more than normal (1991–2020) are slashed. (b) Daily evolution of temperatures averaged in the Yangtze River basin (YRB) from Jun to Aug 2022. The dashed (solid) curve represents the 90th percentile (climatological mean) of the temperature records, and the EHDs in Jul–Aug are marked. (c) Time series of the detrended normalized Jul–Aug mean temperature averaged over the YRB (i.e., $YT = 0.37 \cdot TPS$, $YT = 0.33 \cdot TPS + 0.48 \cdot NAO$, $YT = 0.44 \cdot TAP + 0.47 \cdot NAO$) during 1979–2022 from observations (bar) and reconstruction by the multiple linear regression model (curves), with tropical Pacific sea-surface temperature (TPS) as the only independent variable (gray curve), with TPS and the North Atlantic Oscillation (NAO) indices as independent variables (blue curve), and with TAP and NAO as independent variables (red curve). (d) Regressions of the geopotential height (shading, gpm), wind (black vectors, $m s^{-1}$), and wave activity flux (red vectors, $m^2 s^{-2}$) at 200 hPa onto the YT index. (e) Regressions of the geopotential height (contours, gpm) and wind (vectors, $m s^{-1}$) at 500 hPa and precipitation (shading, $mm day^{-1}$) onto the YT index. (f) Regressions of the geopotential height (contours, gpm) and wind (vectors, $m s^{-1}$) at 850 hPa and SST/T2m (shading, °C) onto the YT index. In (d)–(f), the letters “A” and “C” represent the centers of anomalous anticyclones and cyclones, respectively, and regressions exceeding the 90% significance level are marked by white slashes. In (a) and (f), the Tibetan Plateau is denoted by gray shading. In (a), (e), and (f), the red and blue boxes are the domains for calculating the YT, TAP, and TPS indices.

4. SOUTH ASIA

—O. P. Sreejith, A. K. Srivastava, and M. Rajeevan

Countries in this section include Bangladesh, India, Pakistan, and Sri Lanka.

(i) Temperature

In 2022, South Asia generally experienced above-normal temperatures. The annual mean temperature in India was 0.51°C above the 1981–2010 average, making 2022 the fifth-warmest year on record since national records commenced in 1901 (Fig. 7.52). The seasonal mean temperatures in India were above normal for all seasons, except winter. The seasonal mean temperatures in India during the pre-monsoon season (March–May, anomaly of $+1.06^{\circ}\text{C}$), monsoon season (June–September, $+0.36^{\circ}\text{C}$), and post-monsoon season (October–December, $+0.52^{\circ}\text{C}$) accounted for most of the warmth. The 10 warmest years on record have all occurred since 2009.

(ii) Precipitation

The summer monsoon season (June–September) contributes about 75% of the annual precipitation over South Asia. The 2022 summer monsoon set in over Kerala (southwestern parts of peninsular India) on 29 May (normal is 1 June). The monsoon covered all of India by 2 July (normal is 8 July).

For India, the long-term average (LTA; 1971–2020) total of the summer monsoon rainfall is 869 mm with a standard deviation of about 10%; however, over smaller regions the standard deviation can be much larger. During 2022, the Indian summer monsoon rainfall (ISMR) averaged over the country as a whole was 106% of its LTA. Rainfall was fairly well distributed over the country except over the eastern and northeastern regions (Fig. 7.53). Seasonal rainfall over the homogeneous regions of Northwest India, Central India, South Peninsula, and East and Northeast India was 101%, 119%, 122%, and 82% of their respective LTA. On a monthly scale, rainfall for the country as a whole was above normal during July and September (117% and 108% of LTA, respectively), below normal during June (92%), and near normal during August (104%; Fig. 7.54).

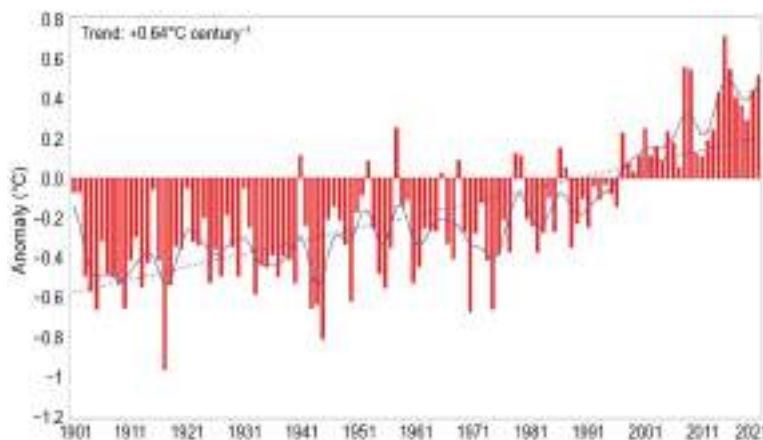


Fig. 7.52. Annual mean temperature anomalies ($^{\circ}\text{C}$; with respect to 1981–2010 normal) averaged over India for the period 1901–2022. Continuous blue line indicates the smoothed time series (nine-point binomial filter). Dotted blue line indicates the trend over the period.

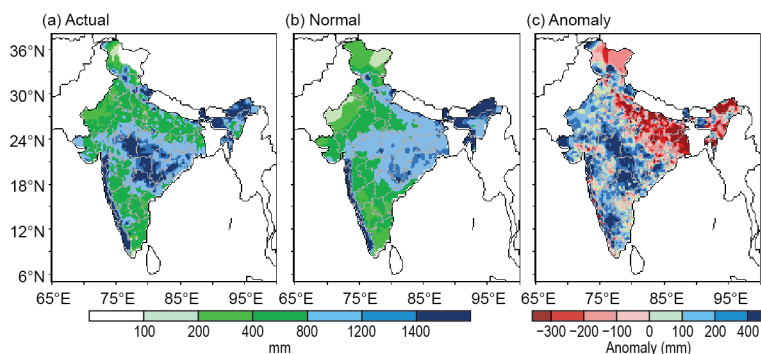


Fig. 7.53. Spatial distribution of actual, normal, and anomalous monsoon seasonal (Jun–Sep) rainfall (mm) over India in 2022.

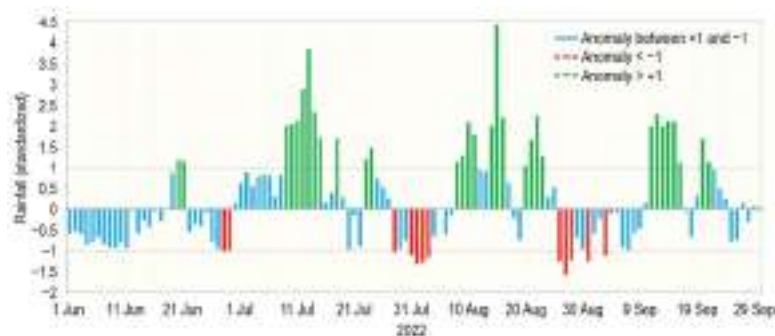


Fig. 7.54. Daily standardized rainfall time series averaged over the core monsoon zone of India (1 Jun–30 Sep 2022).

During the winter season (January–February), rainfall over India was above normal (147% of its LTA). It was near normal (99%) during the pre-monsoon season (March–May), and above normal (119%) during the post-monsoon season (October–December).

Pakistan, which is at the western edge of the pluvial region of the South Asian monsoon, typically receives 60%–70% of its annual rainfall during the summer monsoon season (July–September). The summer monsoon usually sets over eastern parts of Pakistan around 1 July with a standard deviation of five days. In 2022, the monsoon set over Pakistan on 30 June and withdrew during the third week of September. Summer monsoon rainfall was significantly above normal (175% of LTA). Pakistan experienced above-normal rains during July (183%) and August (241%), and below-normal rains during September (81%). Torrential rains during the season caused massive devastating floods in eastern and southern Balochistan, Sindh, Southwest Punjab, and Khyber Pakhtunkhwa. The seasonal rainfall (October–December) 2022 was 67% of the LTA value.

Bangladesh received normal (104% of LTA) rainfall during its summer 2022 monsoon season, while Sri Lanka received above-normal rainfall during its summer monsoon season (May–September).

Later in the year, the northeast monsoon (NEM) sets in over southern peninsular India during October and over Sri Lanka in late November. The NEM contributes 30%–50% of the annual rainfall over southern peninsular India and Sri Lanka as a whole. The NEM, which set in over southern peninsular India on 29 October, contributed to above-normal seasonal rainfall (110% of LTA).

(iii) Notable events and impacts

Fifteen cyclonic disturbances (three cyclonic storms and 12 depressions) formed over the North Indian Ocean in 2022, four more than the normal of 11 based on data from 1965–2021. The three tropical cyclones were: Severe Cyclonic Storms Asani and Mandous and Cyclonic Storm Sitrang. All three formed over the Bay of Bengal. The tracks of these cyclonic storms are shown in Fig. 7.55. Please refer to section 4g5 for details of the North Indian Ocean basin cyclone season.

In 2022, thunderstorms and lightning claimed around 1285 lives in India. On 25 July at least 26 people were killed in lightning strikes in Bihar and Uttar Pradesh.

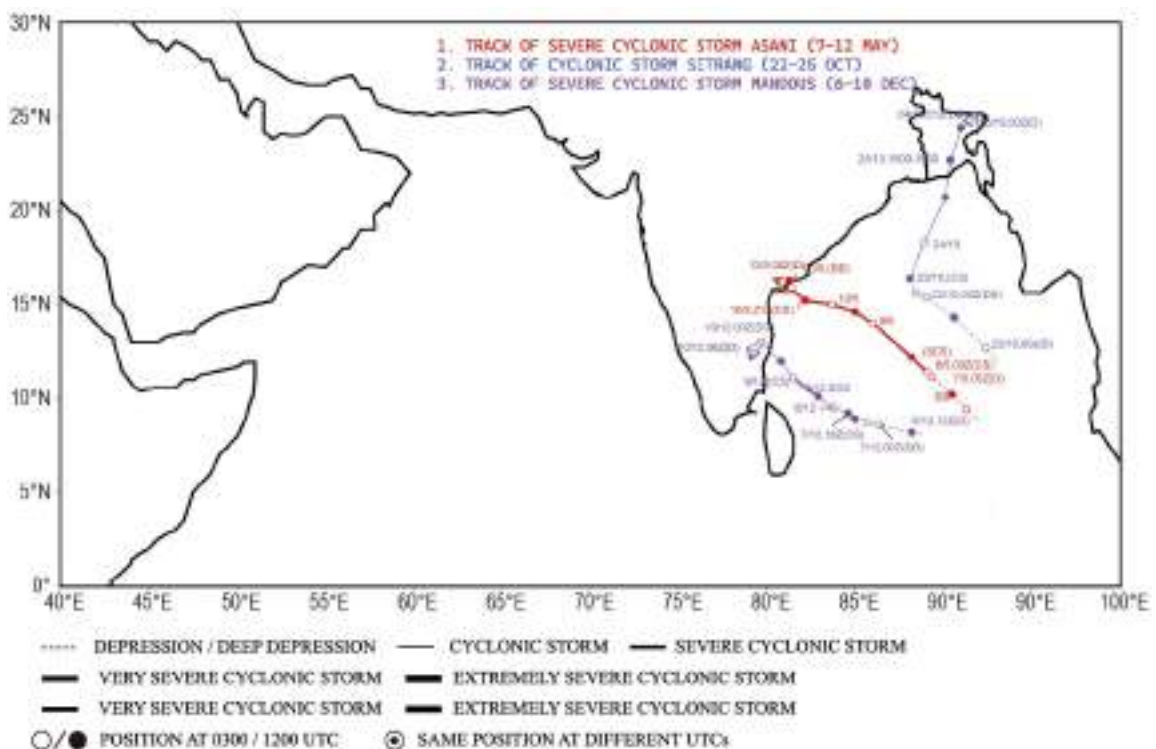


Fig. 7.55. Tracks of 2022 cyclonic storms over the North Indian Ocean.

During March and April, large parts of northwest India and Pakistan experienced prolonged heatwaves, prompting an early onset of the hot weather season. March 2022 was the hottest March in India since 1901. Mean temperatures in March and April were consistently 3°C to 8°C above normal, breaking many all-time records. In Pakistan, many stations recorded monthly all-time highs during the month. The city of Nawabshah recorded a high temperature of 49.5°C while the cities of Jacobabad and Sibi each recorded 47°C. This heatwave led to at least 90 deaths and reduced wheat crop yields across India and Pakistan. It also triggered forest fires in India.

Heavy rainfall and flood-related incidents claimed over 835 lives in different parts of India during 2022. Of these, 198 were from Assam, 116 from Maharashtra, 98 from Uttar Pradesh, 75 from Himachal Pradesh, and 56 from Manipur.

In Bangladesh, continuous heavy rains during the third week of June caused severe floods in several districts, claiming more than 60 lives. More than 4.3 million people were affected and there was a widespread loss of crops and houses. The Sylhet district was most affected, as almost two-thirds of the district was submerged.

Floods in Pakistan during June, July, and August caused over 1700 fatalities and led to major crop and property losses. Billions of dollars of damage and economic losses were reported. The flood in summer 2022 was also recorded as one of the world's costliest natural disasters of all time. The favorable monsoon circulation features enhanced monsoon lows and depressions that formed over the Bay of Bengal, moved up to Sindh-Balochistan, and caused heavy precipitation. In Bangladesh, 32 people died in June due to severe floods.

5. SOUTHWEST ASIA

—A. Vazife, A. F. Kazemi, and M. Mohammadi

This section covers Iran. Anomalies refer to the 1991–2020 base period.

(i) Temperature

The year 2022 was generally dry and warm in Iran, with anomalies of +0.5°C to +2.5°C; the eastern regions were exceptionally warm (Fig. 7.56a). Figure 7.56b shows that 2022 ranked in the top 20th percentile of all years since 1971.

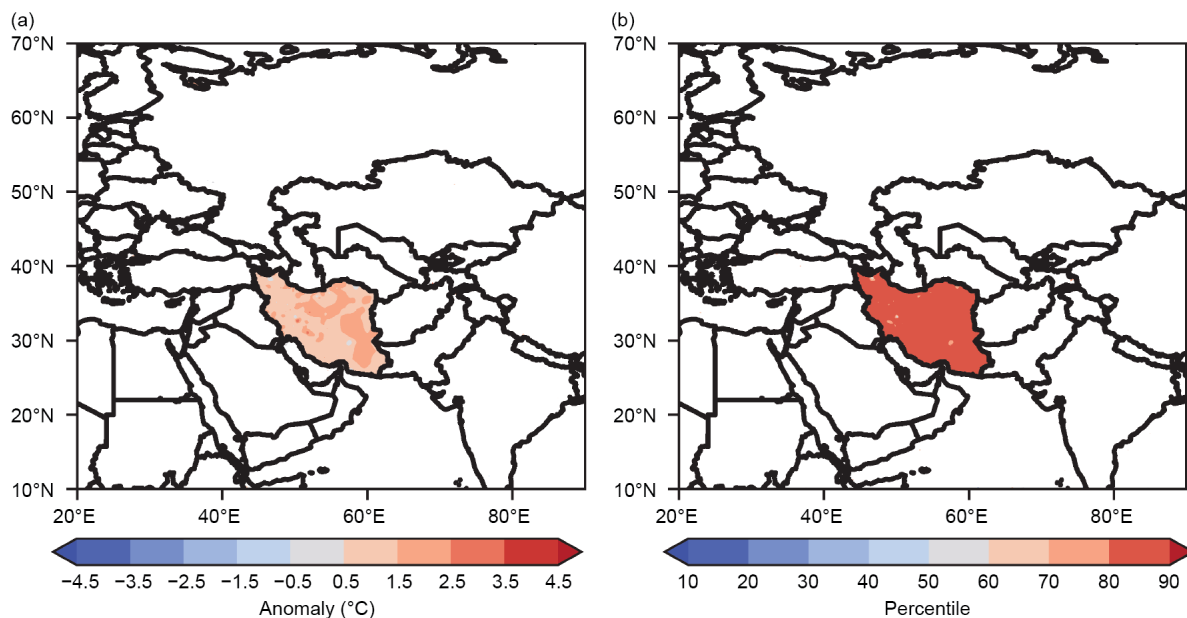


Fig. 7.56. (a) Mean annual temperature anomalies (°C; base period 1991–2020) and (b) percentile of the surface temperature for 2022 (period 1971–2020).

(ii) Precipitation

The annual precipitation total in 2022 averaged over Iran was 177.0 mm, which was more than that of 2021 (114.8 mm), but less than normal (236.9 mm). This marked the second-driest year (behind 2021) on record for the country.

Figure 7.57 shows precipitation anomalies in Iran for every season. Precipitation in the main rainy seasons of the year (winter, spring, and autumn) was below normal, and rain deficits were severe across parts of western, northwestern, and northeastern Iran.

Summer precipitation was above normal due to the northward track of the low-level Somali jet north of the Indian Ocean and the Oman Sea. Humid air currents in summer were pushed northward by the jet, and Iran received above-normal precipitation in the south and southeast via local thunderstorms. The normal range of summer precipitation typically provides less than 10% of annual precipitation in the country, but in summer 2022, Iran received more than 15% of its annual total. This was mainly attributed to the low-level humidity track of the Indian Ocean region surface and low-level winds.

Despite above-average summer precipitation, the annual 2022 precipitation was much less than normal since the main precipitation periods of the country (winter, spring, and autumn) were much drier than normal. Due to the dryness, Iran experienced severe and exceptional drought in many provinces of the country, especially in western mountainous provinces across the Zagross chain.

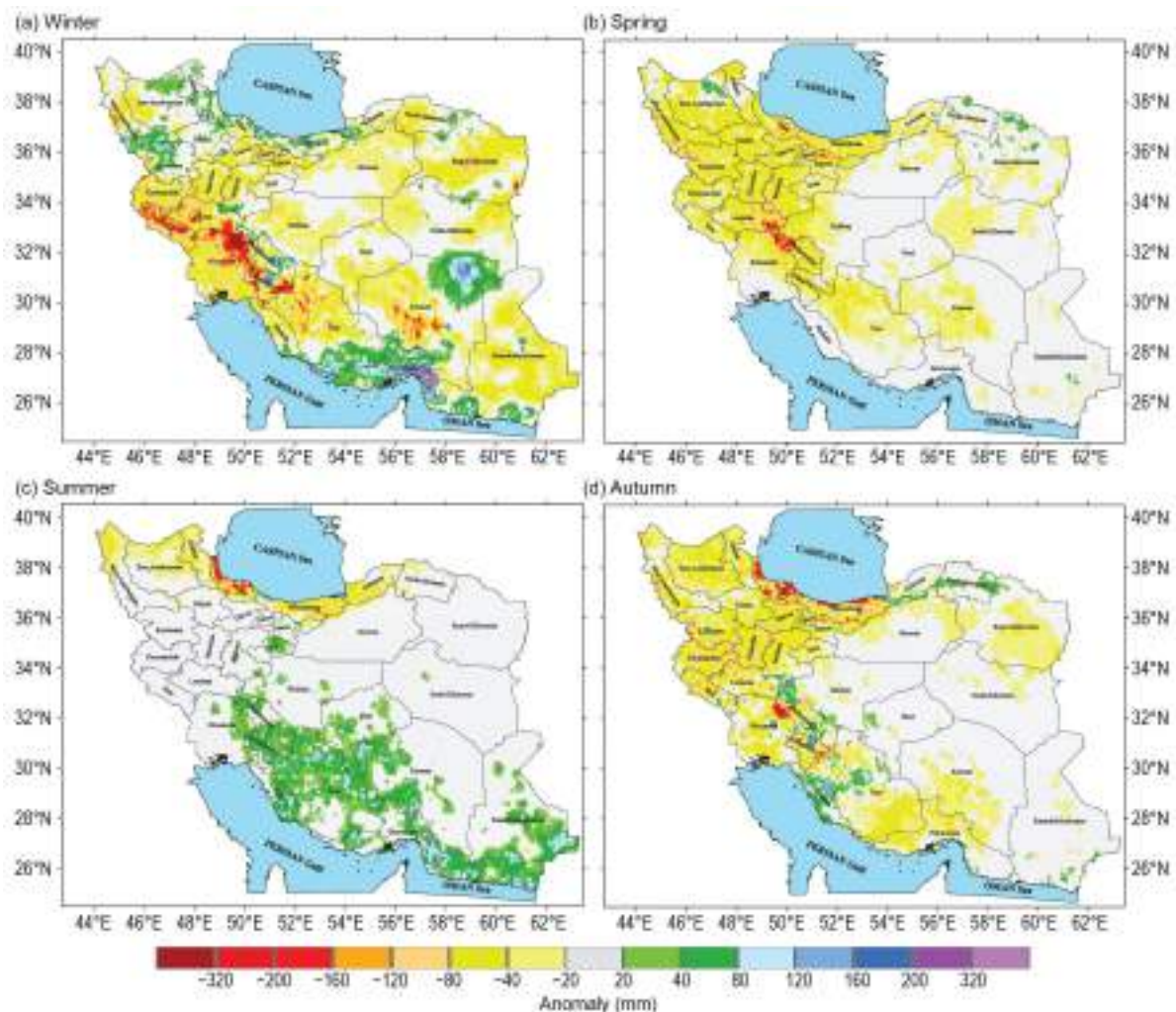


Fig. 7.57. Precipitation anomalies (mm) across Iran in 2022 for (a) winter (Jan–Mar, JFM), (b) spring (Apr–Jun, AMJ), (c) summer (Jul–Sep, JAS), and (d) autumn (Oct–Dec, OND).

(iii) Notable events and impacts

Droughts and summer flash floods in Iran caused enormous damage to crop yields and rural areas. The water shortages were more visible and severe in the central plateau of the country. Flash floods in Tehran and southern provinces in the north of the Persian Gulf during June and July caused dozens of deaths. Together, the drought and floods caused nearly \$7 billion (U.S. dollars) in damage to the agriculture sector, with two-thirds of the damage due to drought and one-third due to floods.

6. CENTRAL ASIA

—R. Shukla, MD A. E. Bhuiyan, and W. M. Thiaw

Central Asia (CA) is a landlocked semi-arid region spanning a wide latitudinal area extending from the northern temperate zone with Russia at its northern border to the southern subtropics. It exhibits a complex topography ranging from vast plains to high mountains, and the Caspian Sea at its western edge. Its climate is diverse and influenced by terrain inhomogeneity. For the purpose of this analysis, we define CA as the region encompassing the countries of Afghanistan to the south, Turkmenistan, Uzbekistan, Tajikistan, Kyrgyzstan (from west to east) in the central part of the region, and Kazakhstan to the north. The climatological base period for both temperature and precipitation is 1991–2020.

(i) Temperature

During 2022, annual mean temperatures were lowest (-10°C – 0°C) in central and eastern Tajikistan, southeast regions of Kyrgyzstan, and in northern high-elevation regions of Afghanistan (Fig. 7.58a). The northwest, central, northern, and eastern regions of Kazakhstan, western and northern Kyrgyzstan, western Tajikistan, and northern and northeast regions of Afghanistan registered 0°C – 10°C . Annual mean temperatures were higher (10°C – 20°C) across southwest and southern Kazakhstan, Uzbekistan, Turkmenistan, and western, southern, and southeast Afghanistan, with 20°C – 25°C for the southern region of Afghanistan. The annual mean temperature anomalies were $+0.5^{\circ}\text{C}$ to $+1.5^{\circ}\text{C}$ in western and southern Karaganda, southeast Kazakhstan, western and central Uzbekistan, southwest Kyrgyzstan, and southern Afghanistan (Fig. 7.58b). 2022 ranked in the 90th–97th percentiles of warmest years on record in southwest Kazakhstan and southern Afghanistan. In contrast, the annual mean temperature anomalies were below normal (-1°C to -0.5°C) in the northern Kostanay regions of Kazakhstan and near the Kyrgyzstan/Tajikistan border, ranking 2022 in the 3rd–15th percentiles of coldest years on record for the latter area.

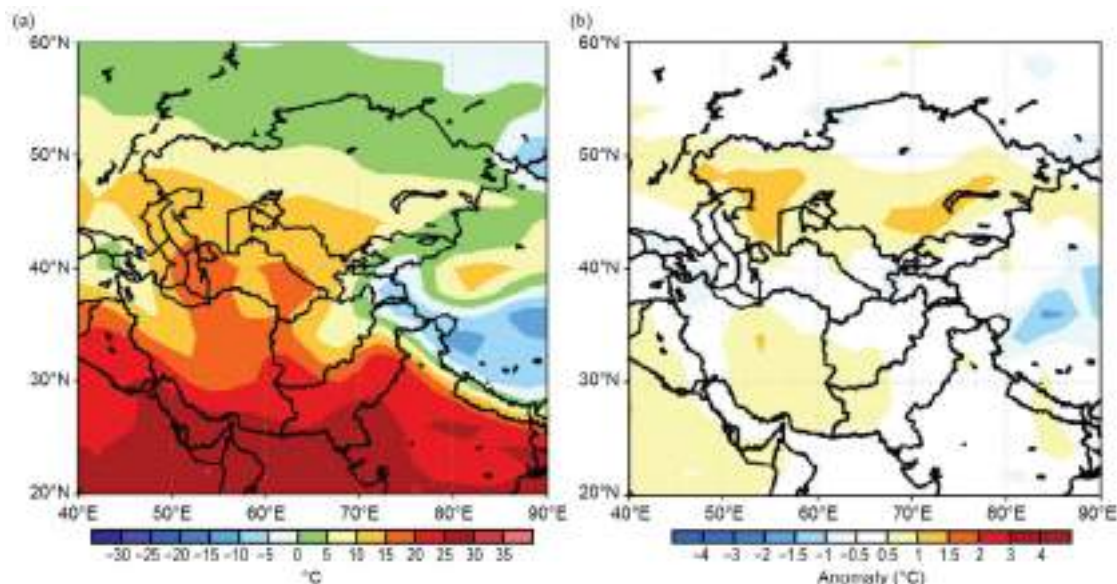


Fig. 7.58. Annual (a) mean temperature ($^{\circ}\text{C}$) and (b) mean temperature anomalies ($^{\circ}\text{C}$; 1991–2020 base period) for Central Asia. (Source: NOAA/NCEP.)

(ii) Precipitation

Annual precipitation totals for 2022 varied across Central Asia (Fig. 7.59a). About 100 mm–200 mm were received in southern Afghanistan, central and northern Turkmenistan, and central and southwest Uzbekistan during the year. Kazakhstan, Kyrgyzstan, Tajikistan, northwest and eastern Uzbekistan, western and eastern Turkmenistan, and the central, eastern, and northern regions of Afghanistan received 200 mm–500 mm. Larger precipitation totals (500 mm–600 mm) were observed in the high-elevation region of northern Afghanistan and in the northern and northeast regions of Kazakhstan.

Most regions in Central Asia received their maximum precipitation (rain and snowfall) during winter and spring seasons. Northern and eastern regions of Kazakhstan received precipitation during all months, while southern Kazakhstan, Uzbekistan, Turkmenistan, and western and southern Afghanistan received little to no rain during May–August. The annual precipitation totals were 10 mm–100 mm below average in the western, central, northern, and northeast regions of Afghanistan, western, southern, and eastern Turkmenistan, southeast Uzbekistan, and northern, northeast, and southwest Kazakhstan (Fig. 7.59b). In contrast, the annual precipitation totals were 10 mm–100 mm above normal in northwest, southern, and southeast Kazakhstan, western and northeast Uzbekistan, northern, central, and eastern Tajikistan and southeast Afghanistan, and were 100 mm–150 mm above average in northwest Kazakhstan and near the southeast border of Afghanistan and Pakistan.

Large precipitation deficits (–10 mm to –50 mm; lowest 10th percentile) were observed across Afghanistan during February–April. Most regions in Afghanistan received 25%–50% below-normal rainfall amounts during this period, according to data from the Global Precipitation Climatology Project (GPCP). The precipitation was 10 mm–30 mm below average across the northern, eastern, and southeast regions of Kazakhstan during April–September.

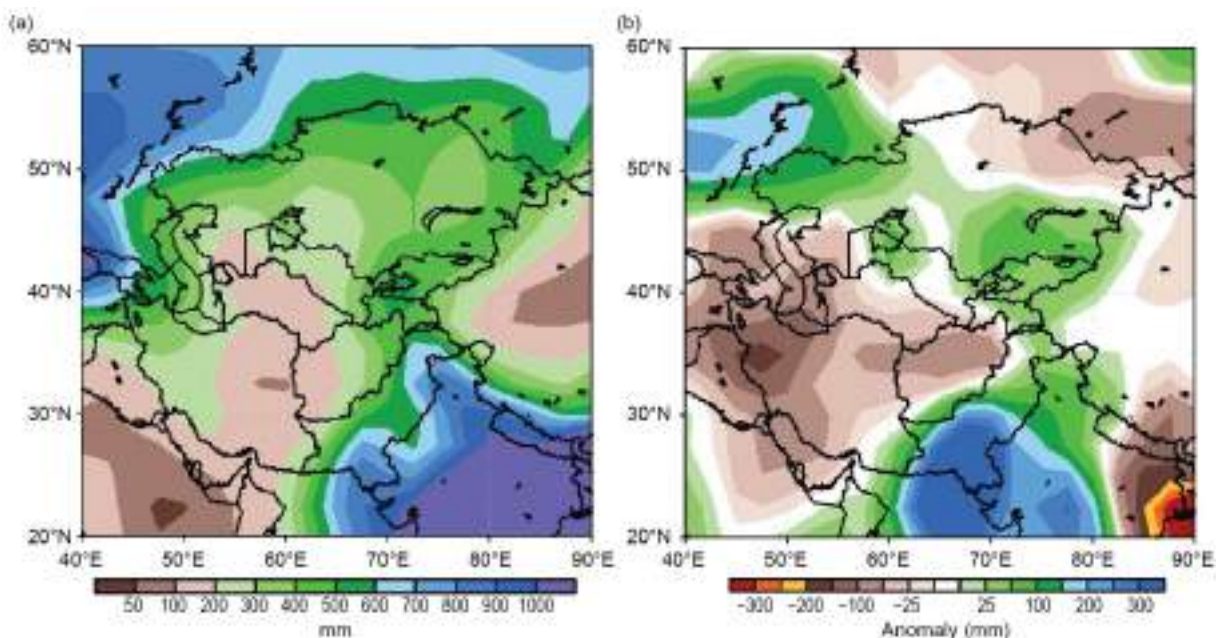


Fig. 7.59. Cumulative annual (a) precipitation (mm) and (b) precipitation anomalies (mm; 1991–2020 base period) for Central Asia. (Source: NOAA/NCEP GPCP data.)

(iii) Notable events and impacts

According to the Uzbekistan Hydrometeorological Service and analysis from NOAA's Climate Prediction Center (CPC) Unified Gauge, areas in the Samarkand and Jizzakh regions recorded 25 mm–50 mm of rainfall in two hours on 20 April, more than that normally received during the entire month. This rainfall damaged crops, homes, schools, and other buildings in the Bakhmal, Farish, Gallaaral, and Sharof Rashidov districts. Four fatalities were also reported.

According to the United Nations Office for the Coordination of Humanitarian Affairs (UN-OCHA), heavy and unseasonal rainfall (25 mm–75mm), based on analysis from the CPC Morphing Technique (CMORPH), fell in the Badakhshan, Herat, Badghis, Helmand, Takhar, Parwan, Kandahar, Wardag, Kunduz, Baghlan, Logar, and Juzjan regions of Afghanistan on 2–3 May, which caused flash flooding and affected nearly 3400 people. The flooding caused 22 fatalities and infrastructure damage.

According to UN-OCHA, eastern Afghanistan experienced flash flooding due to heavy rainfall (25 mm–75 mm) on 22 June that affected 1288 people. There were 19 fatalities and 131 injuries, and 356 houses were damaged or destroyed. Throughout July, heavy rains also caused floods and flash floods across several provinces in eastern, central, southern, and western Afghanistan, according to Afghan Red Crescent Society (ARCS) branches and the Ministry for Disaster Management. Also during the month, 25 mm–200 mm rainfall was observed across eastern regions of Afghanistan, based on analysis from CPC Unified Gauge rainfall. According to UN-OCHA, 39 people lost their lives and more than 1200 houses were damaged or destroyed, affecting at least 3000 families. Critical infrastructure, such as wheat mills and bridges, was also destroyed. Throughout August, heavy rains and flash floods were reported in several provinces across eastern, central, southeastern, southern, and northern Afghanistan, according to the United Nations International Children's Emergency Fund (UNICEF) and the International Federation of Red Cross and Red Crescent Societies (IFRC). Total rainfall across these regions ranged from 25 mm to 300 mm, according to analysis from the CPC Unified Gauge rainfall. From rainfall events in August, 141 fatalities were reported and 124 people were injured, with 44 others reported missing. Based on the Afghanistan National Disaster Management Authority (ANDMA) report, more than 16,000 houses were destroyed and 19,700 were damaged, and 249,900 people were affected. Thousands of hectares of crops were destroyed. From 11 to 15 August, most of eastern and southeastern Afghanistan received heavy rainfall (10 mm–50 mm) that caused flash flooding, resulting in 41 fatalities and significant infrastructure damage, according to UN-OCHA. In the following six days (16–21 August), the same regions received more heavy rainfall (25 mm–100 mm based on analysis from the CPC Unified Gauge). These rains also caused flash flooding, resulting in 63 fatalities and significant infrastructure damage.

h. Oceania

—C. Ganter, Ed.

1. OVERVIEW

—C. Ganter

The region of Oceania was dominated by La Niña conditions in 2022. This follows on from the past two years, which were also under its influence. As is typical for a La Niña year, most parts of Oceania were affected. Drier conditions were seen in some Southwest Pacific islands near the equator, while rainfall was higher than usual to the southwest of the South Pacific Convergence Zone. Broad areas of Australia had wetter conditions and persistent flooding. Micronesia had a quiet year for typhoon activity along with dryness near the equator, which is also typical of La Niña. In New Zealand, air and sea-surface temperatures were generally higher than average, as is typical of La Nina conditions.

In addition to La Niña, a negative Indian Ocean dipole (IOD) during the austral winter and spring, as well as persistently positive Southern Annular Mode (SAM) conditions for much of the year, influenced Australia during 2022. Both the negative IOD and the positive SAM contributed alongside the La Niña to Australia's second-wettest spring in 123 years. The positive SAM was associated with higher-than-normal pressure over New Zealand and, in combination with La Niña, it contributed to the country's warmest year, marking the second consecutive year to break the record.

2. NORTHWEST PACIFIC AND MICRONESIA

—B. Bukunt and C. P. Guard

This assessment covers the area from the date line west to 130°E, between the equator and 20°N. It includes the U.S.-Affiliated Islands of Micronesia, but excludes the western islands of Kiribati and nearby northeastern islands of Indonesia (see Fig. 7.61). Temperature and rainfall station data anomalies are reported with respect to the 1991–2020 base period.

For much of Micronesia, the weather and climate of 2022 was similar to that of 2021—quiet, with few extremes of rainfall, wind, or ocean waves. Of note were the wet conditions in eastern (Kwajalein, Majuro, Kosrae) and western (Yap, Palau) non-equatorial regions of Micronesia during the first six months of 2022. Only the central Micronesian island of Chuuk and the Marianas (Saipan, Guam) exhibited rainfall totals near or slightly below average. There was a low number of typhoons in the western North Pacific basin (see section 4g4 for details). With the third consecutive year of La Niña, three climate characteristics typical of La Niña were of note and similar to 2021: extreme dryness confined to locations along the equator, higher-than-normal sea levels across all of Micronesia, and a dearth of tropical cyclone activity in Micronesia.

(i) Temperature

While temperatures across most of Micronesia during 2022 were a mix of above and below average, most locations were near average. Wet locations had below-normal daytime temperatures due to persistent cloudy conditions, especially during the first half of the year. Nighttime temperatures were less attributable, but Yap and Pohnpei had large nighttime (minimum) temperature anomalies for the entire year, likely due to nighttime cloudiness.

The average six-month maximum and minimum temperature anomalies and the six-month and annual rainfall values for selected locations across Micronesia are summarized in Table 7.1.

Table 7.1. Average six-month temperature anomalies (first half and second half), and six-month and annual rainfall totals as well as percent of average values for selected Micronesia locations during 2022. The average values are for the 1991–2020 base period. Latitudes and longitudes are approximate. “Kapinga” stands for Kapingamarangi Atoll in Pohnpei State, Federated States of Micronesia. The color coding indicates: red highlights for above-average temperature (up arrow) and blue highlights for below-average temperature (down arrow); green fill for above-average rainfall (up arrow) and yellow fill for below-average rainfall (down arrow). The excessive coolness at Palau is likely an effect of the relocation of the weather station from the municipality of Koror to the international airport in Airai. Official stations inspections have been spotty since COVID started in early 2020. This lack of maintenance may have introduced some unknown issues to the station data.

Location	Jan-Jun Max, Min Temp (°C)	Jul-Dec Max, Min Temp (°C)	Jan-Jun AVG Rainfall (mm)	Jan-Jun 2022 Rainfall (mm)	Jan-Jun % Rainfall (mm)	Jul-Dec AVG Rainfall (mm)	Jul-Dec 2022 Rainfall (mm)	Jul-Dec % Rainfall (mm)	Jan-Dec 2022 Rainfall (mm)	Jan-Dec % Rainfall (mm)
Saipan 15°N, 146°E	+0.56 ↑, +0.22 ↑	+0.77 ↑, +0.73 ↑	462.8	527.3 ↑	113.9 ↑	1306.1	1412.5 ↑	108.1 ↑	1939.8 ↑	109.7 ↑
Guam 13°N, 145°E	-0.37 ↓, +0.03 ↑	-0.55 ↓, -0.22 ↓	678.7	542.8 ↓	80.0 ↓	1813.6	1745.0 ↓	96.2 ↓	2287.8 ↓	91.8 ↓
Yap 9°N, 138°E	-1.26 ↓, +1.37 ↑	-0.64 ↓, +1.37 ↑	1191.5	1511.8 ↑	126.9 ↑	1943.4	1968.8 ↑	101.3 ↑	3480.6 ↑	110.0 ↑
Palau 7°N, 134°E	-1.19 ↓, -1.02 ↓	-0.48 ↓, -1.45 ↓	1798.1	2391.7 ↑	133.0 ↑	2279.4	2154.4 ↓	94.5 ↓	4546.1 ↑	111.5 ↑
Chuuk 7°N, 152°E	-0.44 ↓, +0.58 ↑	-0.11 ↓, +1.03 ↑	1678.2	1666.5 ↓	99.3 ↓	1917.7	1856.5 ↓	96.8 ↓	3523.0 ↓	98.0 ↓
Pohnpei 7°N, 158°E	-0.29 ↓, +1.30 ↑	-0.29 ↓, +1.45 ↑	2361.2	3160.3 ↑	133.8 ↑	2308.4	2827.0 ↑	122.5 ↑	5987.3 ↑	128.2 ↑
Kapinga 1°N, 155°E	n/a	n/a	1880.6	1040.1 ↓	55.3 ↓	1485.1	768.4 ↓	51.7 ↓	1808.5 ↓	53.7 ↓
Kosrae 5°N, 163°E	-0.35 ↓, -0.19 ↓	-0.90 ↓, +0.14 ↑	2635.8	3451.6 ↑	131.0 ↑	2354.8	3111.8 ↑	132.1 ↑	6563.4 ↑	131.5 ↑
Majuro 7°N, 171°E	-0.51 ↓, +0.33 ↑	-0.31 ↓, +0.25 ↑	1459.0	1819.9 ↑	124.7 ↑	1875.0	1989.8 ↑	106.1 ↑	3809.8 ↑	114.3 ↑

(ii) Precipitation

Two particular characteristics of Micronesian regional precipitation during 2022 stood out: 1) extreme dryness at Kapingamarangi, which was considerably more extreme than in 2021 and 2) very wet conditions in eastern (Kwajalein, Majuro, Kosrae) and western (Yap, Palau) non-equatorial regions of Micronesia during the first six months of the year.

A sharp north-to-south gradient was observed across Pohnpei State. While Kapingamarangi (1°N latitude) had its second-driest January–June on record, the main island of Pohnpei reported its second-wettest January–June. Kapingamarangi ended the year as second driest on record

while Pohnpei ended the year as the third-wettest year. This unusual meridional gradient in rainfall is likely due to the strengthening La Niña during the April–July timeframe, which led to a compressed Intertropical Convergence Zone (ITCZ) constantly meandering over Pohnpei at 7°N latitude while the cold tongue sea-surface temperature signal along the equator limited convection around Kapingamarangi.

Typical rainfall distribution during a La Niña event includes moderate-to-extreme dryness at western Pacific locations near and along the equator, especially from May to November, while wet conditions are typical across the latitudes of the ITCZ (4°N–8°N; He et al. 1998). During a prolonged La Niña event, dryness is often experienced in eastern Micronesia, including Majuro and Kwajalein; however, this was not the case in 2022. An early and active tropical upper tropospheric trough (Sadler 1976) contributed to the wetness of the Marshall Islands in eastern Micronesia.

Table 7.2 illustrates the rainfall variability, comparing the percent of average between the 2021 and 2022 rainfall totals for selected islands. Negative values indicate greater rainfall in 2021 than in 2022. Despite both 2021 and 2022 being in an extended La Niña status, there was

Table 7.2. Difference ($\Delta\%$) of 2021 and 2022 percent of average six-month rainfall (first half and second half) and annual rainfall values for selected Micronesia locations. Negative values indicate greater rainfall in 2021 than in 2022. The average values are for the 1991–2020 base period. Latitudes and longitudes are approximate. The fill color of the boxes indicates green for values of $\pm 0\%$ – 10% difference between 2021 and 2022 (right arrow), blue for values of $\pm 11\%$ – 25% difference (northeast arrow), and purple for greater than $\pm 25\%$ difference (up arrow).

Location	2021 % Jan-Jun Rainfall (mm)	2022 % Jan-Jun Rainfall (mm)	$\Delta\%$ Jan-Jun Rainfall (mm)	2021 % Jul-Dec Rainfall (mm)	2022 % Jul-Dec Rainfall (mm)	$\Delta\%$ Jul-Dec Rainfall (mm)	2021 % Jan-Dec Rainfall (mm)	2022 % Jan-Dec Rainfall (mm)	$\Delta\%$ Jan-Dec Rainfall (mm)
Saipan 15°N, 146°E	92.7	113.9	21.2 ↗	105.6	108.1	2.5 →	102.2	109.7	7.5 →
Guam 13°N, 145°E	86.3	80.0	-6.3 →	107.6	96.2	-11.4 ↗	101.8	91.8	10.0 →
Yap 9°N, 138°E	139.5	126.9	-12.6 ↗	86.9	101.3	14.4 ↗	106.9	110.0	3.1 →
Palau 7°N, 134°E	120.7	133.1	12.40 ↗	110.8	94.5	-16.3 ↗	115.2	111.5	-3.7 →
Chuuk 7°N, 152°E	125.3	99.3	-26.0 ↑	110.7	96.8	-13.9 ↗	117.5	98.0	-19.5 ↗
Pohnpei 7°N, 158°E	128.6	133.8	5.2 →	102.0	122.5	20.5 ↗	115.5	128.2	12.7 ↗
Kapinga 1°N, 155°E	90.0	55.3	-34.7 ↑	71.7	51.7	-20.0 ↗	81.9	53.7	-28.2 ↑
Kosrae 5°N, 163°E	149.5	131.0	-18.5 ↗	114.1	132.1	18.0 ↗	132.8	131.5	-1.3 →
Majuro 7°N, 171°E	141.5	124.7	-16.8 ↗	99.9	106.1	6.2 →	118.1	114.3	-3.8 →
Kwajalein 9°N, 168°E	92.6	141.2	48.6 ↑	84.9	102.0	17.1 ↗	87.7	116.3	28.6 ↑

substantial variability in rainfall amounts. Some differences were large, especially at Kwajalein where it was much wetter and at Kapingamarangi and Chuuk where it was much drier in the first half of 2022. Differences at all locations were within 25% in the second half of the year. Six of the 10 locations had differences of 10% or less by the end of the year.

(iii) Notable events and impacts

In keeping with a typical response to La Niña, conditions were very dry at Kapingamarangi (1.1°N, 154.8°E). Prolonged dry conditions there led to severe drought that impacted potable water supplies, local vegetation, and food crops. Abundant rainfall needed at Kapingamarangi to help the island recover from the effects of the long-term 2022 drought did not appear by year's end. Overall, impacts to the residents were minimized by the early import of water and food resources by the Federated States of Micronesia government and the U.S. Agency of International Development through the International Office for Migration.

Within Micronesia, Ulithi (10.0°N, 139.7°E) and Fais (9.8°N, 140.5°E) in Yap State were affected when Tropical Storm Malakas passed nearby in early April. Several tropical disturbances made significant contributions to seasonal rainfall at islands across western Micronesia.

Much-higher-than-average sea level across the tropics of the western Pacific is typical during La Niña. Sea-level heights by boreal summer 2022 were near their historical peaks throughout Micronesia. Time series of the sea level from two widely separated stations (Guam and Kwajalein) illustrate the strength of the coherence of the regional sea level and the historical perspective of the high stands during 2022 (Fig. 7.60). There were no reports of significant coastal inundation from any of the selected islands.

Since 1998, the tropics of the western North Pacific has experienced the largest magnitude of sea-level rise across the globe. The character of this rise was not gradual, but instead is best described as a step-function jump during 1998. The sea level increased by 30 cm from its low stand at the end of 1997 to a historically high stand at the end of 1998 (Merrifield et al. 2012). Elevated sea levels then persisted to the present, with three major short-term dips during the 2002, 2015, and 2018 El Niño events. Absolute historical high stands during 2010–12 and 2020–22 occur with periods of prolonged La Niña. At Guam, the high stands reached during 2021 and 2022 were the second and fourth highest in the historical record, respectively. The high sea level in the tropics of the western North Pacific is not primarily a signal of climate change, but rather an artifact of a substantial increase in the strength of the Pacific trade-wind system (Merrifield et al. 2012). An abrupt increase in the strength of the trade winds in 1998 separates the recent historical climate of the western Pacific into two regimes: 1) weak trades, low sea level (1975–98); and 2) strong trades, high sea level (1998–present).

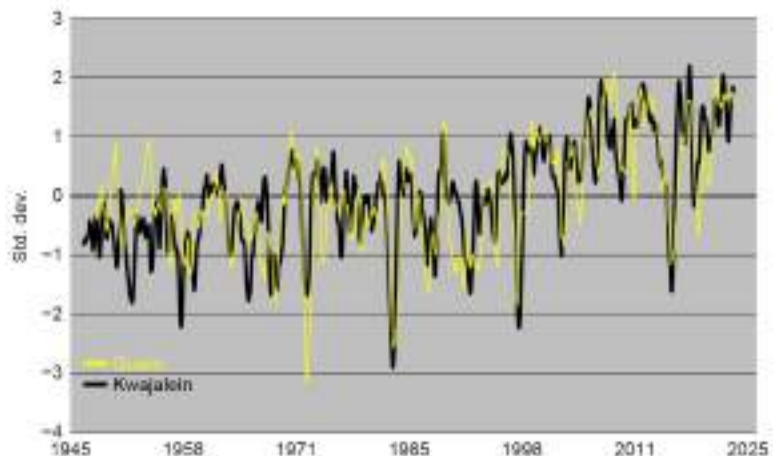


Fig. 7.60. A six-month moving average of the sea level at Guam (yellow) and at Kwajalein (black) from 1948 to 2022. Plotted values are normalized: (average)/(std. dev). Strong El Niño events stand out as sharp dips. (Data source: NOAA’s Center for Operational Oceanographic Products and Services (CO-OPS).)

3. SOUTHWEST PACIFIC

—E. Chandler

Countries considered in this section include American Samoa, the Cook Islands, Fiji, French Polynesia, Kiribati, New Caledonia, Niue, Papua New Guinea (PNG), Samoa, the Solomon Islands, Tonga, Tuvalu, Vanuatu, and Wallis and Futuna (Fig. 7.61). The temperature analysis is based on the Climate Anomaly Monitoring System (CAMS) Monthly Surface Air Temperature Anomalies (https://iridl.ldeo.columbia.edu/maproom/Global/Atm_Temp/Anomaly.html). Anomalies are calculated with respect to the 1991–2020 base period. The precipitation analysis is based on the Multi-Source Weighted-Ensemble Precipitation (MSWEP) monthly analyses as presented for the South Pacific (<http://www.bom.gov.au/climate/pacific/outlooks/>) and the COSPPac Online Climate Outlook Forum (<https://www.pacificmet.net/products-and-services/online-climate-outlook-forum>). The base period for precipitation is 1980–2021.

The year began with a mature La Niña event that persisted into the second quarter of the year, before atmospheric and oceanic indicators in the Pacific briefly eased. La Niña strengthened again towards the end of 2022. Below-normal sea-surface temperatures (SSTs) were present across the central and western equatorial Pacific during the first half of 2022 before the cool regions contracted, although rainfall patterns remained persistently La Niña-like. Signs that La Niña would strengthen later in the year were present in the cloud and pressure patterns as early as June, with trade winds re-strengthening during August. The ocean lagged the atmospheric indicators but began to cool during the third quarter of the year.

Air temperatures and rainfall patterns were both typical of a La Niña event throughout 2022. Air temperatures at the start of the year were below normal along the central to eastern equatorial region. In the second quarter, the below-normal air temperatures expanded westward across the date line, in line with expanding negative sea-surface temperature anomalies. These cooler air temperatures persisted along the central and western equator during the third quarter while



Fig. 7.61. Islands (highlighted in blue) in the Oceania region. (Source: SPREP.)

easing slightly in the far eastern Pacific during the middle months of the year. During the second and third quarter, above-normal air temperatures emerged in a band between Papua New Guinea and the south of Fiji, extending southeast across the Solomon Islands and New Caledonia and persisting through to the end of the year.

Rainfall was suppressed along the equator throughout the year, as is typical with La Niña. The negative rainfall anomalies eased slightly in the third quarter of the year in the central and eastern equatorial Pacific before re-strengthening again towards the end of the year. In the off-equatorial South Pacific, positive rainfall anomalies were strongest in a band from southern PNG to New Caledonia and Vanuatu during the second half of the year. Generally, rainfall was higher than usual throughout the year in the region to the southwest of the South Pacific Convergence Zone (SPCZ), as is usual during La Niña.

(i) Temperature

Along the equator, air temperatures were 1°C to 2°C below normal to the east of the date line during January and February, extending as far west as Kiribati during March. These temperatures were associated with the underlying region of below-normal SSTs. A large region with air temperatures 1°C to 2°C above normal was present in the far South Pacific (south of 20°S) during January. However, this region had cooled and returned to near-normal levels by the end of the first quarter (Fig. 7.62a).

The broad area of below-normal air temperatures along the equator contracted in spatial extent through April to June (AMJ; Fig. 7.62b), associated with increasing SSTs, although cool air-temperature anomalies persisted across Nauru and Kiribati during these months. A region with air temperatures 1°C to 2°C above normal developed over southern French Polynesia during April, spreading west to cover the southern Cook Islands during May before becoming patchy in June. A small region of above-average air temperatures was also present over south-east PNG

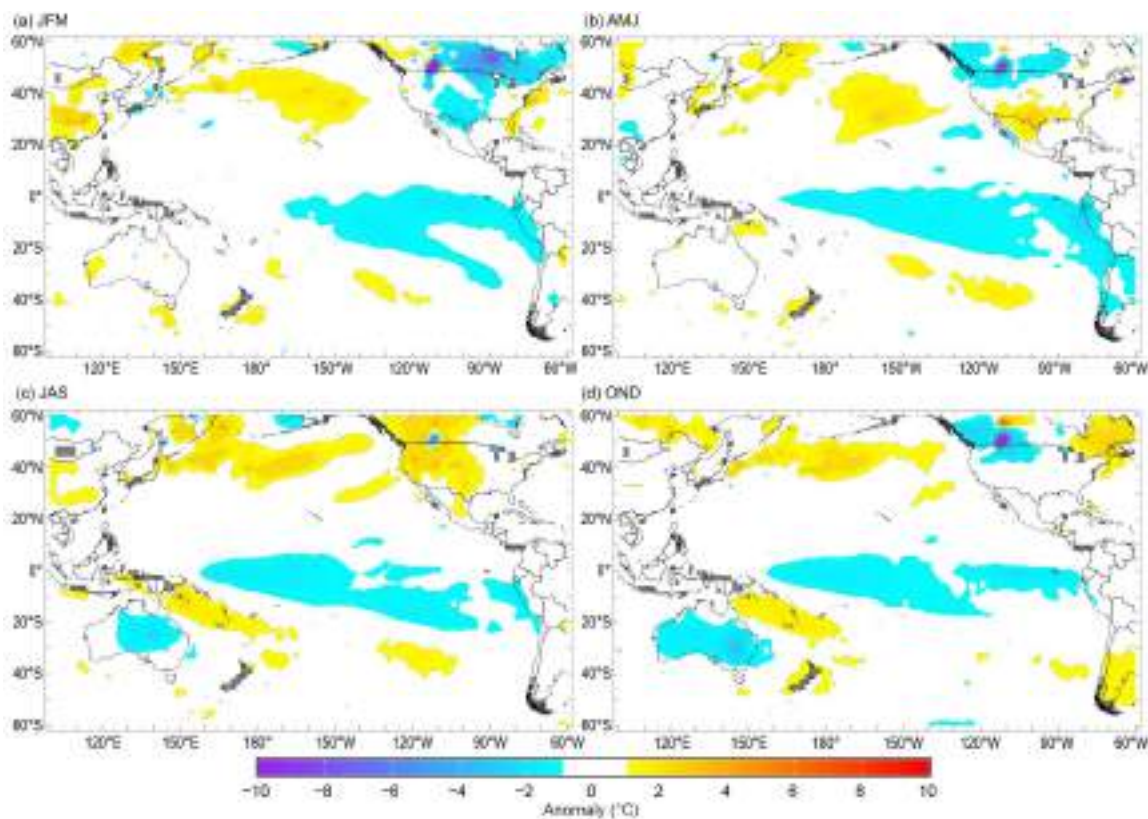


Fig. 7.62. Seasonal air-temperature surface anomalies (°C) across the Pacific for (a) Jan–Mar, (b) Apr–Jun, (c) Jul–Sep, and (d) Oct–Dec. (Source: CAMS.)

during May. This region grew in extent and continued to warm in parts with anomalies of up to +2°C as it expanded southeast to cover the southern Solomon Islands, Vanuatu, and New Caledonia during June.

During July–September (JAS), the area of -1°C to -2°C anomalies expanded westward along the equator in the South Pacific (Fig. 7.62c), matching the expanding region of below-average SSTs as La Niña re-emerged. The band of warmer air temperatures between PNG and New Caledonia continued to increase in strength with anomalies of greater than +2°C covering southeastern PNG by September. This region of air temperatures 1°C to 2°C above normal also expanded to the southeast covering Fiji and southern Tonga.

During October–December (OND), the region of negative air-temperature anomalies along the central equatorial region persisted, although the anomalies became patchy in the far east as the waters in the coastal area of South America warmed. The region of positive anomalies in the off-equatorial western South Pacific persisted through October and November before reducing in spatial extent during December (Fig. 7.62d). The peak positive anomaly area of +2°C located west of Vanuatu in November shifted eastward during December to the south of Fiji, matching the peak positive anomaly locations of SSTs at the time.

(ii) Precipitation

Rainfall patterns at the start of the year reflected typical La Niña patterns across the tropical Pacific. Rainfall deficits were observed along the equator east of 160°E during January–March (JFM), with the strongest negative rainfall anomalies occurring over Kiribati. Patchy positive rainfall anomalies occurred over most off-equatorial South Pacific Islands between the Solomon Islands and Niue (Fig. 7.63a), with some islands in Vanuatu receiving twice their usual JFM rainfall totals. The SPCZ was located to the south of its climatologically normal position during JFM, bringing it closer to Vanuatu and Fiji. As a result, rainfall totals above the 90th percentile were recorded at stations in Fiji, Vanuatu, Niue, and Tonga. In Vanuatu, Bauerfield and Port Vila recorded their wettest JFM on record with 1670 mm (50-year climatology) and 1667 mm (70-year

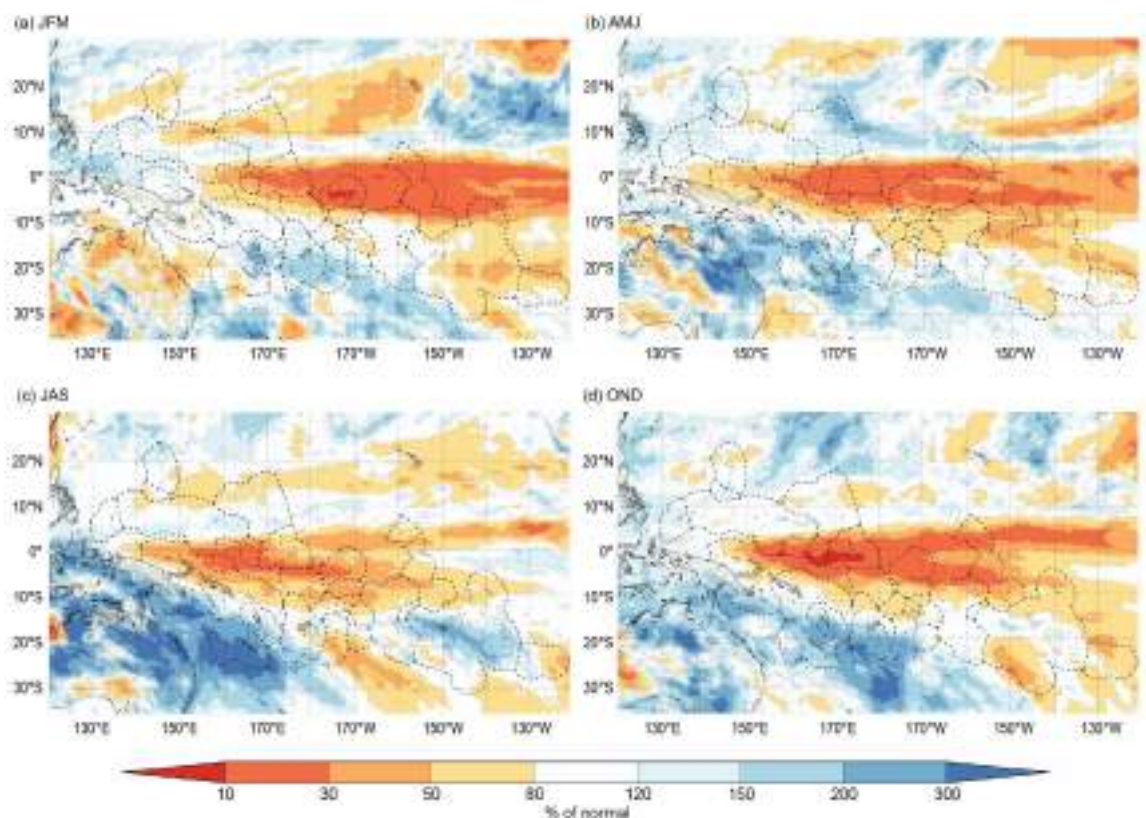


Fig. 7.63. Seasonal percentage of normal rainfall (%) across the Southwest Pacific for (a) Jan–Mar, (b) Apr–Jun, (c) Jul–Sep, and (d) Oct–Dec. (Source: MSWEP.)

climatology), respectively. In stark contrast, parts of Kiribati, Tuvalu, and Samoa recorded rainfall in the lowest 10th percentile on record.

The rainfall deficiencies along the equator persisted into the second quarter of the year (Fig. 7.63b), expanding south to cover Tuvalu, Wallis and Futuna, Tokelau, Samoa, American Samoa, northern Tonga, the northern Cook Islands, and large parts of French Polynesia. Conversely, the positive off-equatorial rainfall anomalies remained in a band from southeastern PNG, extending southeast to Vanuatu, New Caledonia, and southern Fiji. Rainfall was largely close to normal in the Solomon Islands, central and northern Fiji, central Tonga, Niue, and the southern Cook Islands, coinciding with the start of the dry season and the SPCZ becoming less active (as is usual for the time of year). Kiribati, northeastern PNG, the Solomon Islands, northern Fiji, and Tuvalu all recorded rainfall in their bottom 10th percentiles for AMJ. Arorae (Gilbert Islands, Kiribati) recorded its lowest AMJ total in its 55-year record with 66 mm. Conversely, in Vanuatu, Whitegrass recorded its third-wettest AMJ in 48 years (600 mm) and Aneityum recorded its second-wettest AMJ on record (1045 mm) in its 68-year record.

During JAS, the largest positive rainfall anomalies shifted to the southwest over New Caledonia and Australia, with parts of southern PNG, patches of Vanuatu and Fiji as well as New Caledonia receiving above-average rainfall (Fig. 7.63c). The region of reduced rainfall along the equator persisted eastward past the Line Islands of Kiribati from northern PNG. The spatial extent of the dry anomalies over Wallis and Futuna, Samoa, and American Samoa shrank, and rainfall became closer to normal in this region. Fiji, Tonga, the Solomon Islands, Tuvalu, and Kiribati recorded rainfall below the 10th percentile for JAS, with Arorae in Kiribati recording 52 mm, the lowest in its 54-year record, and Kavieng in northeast PNG recording 189 mm, its driest JAS in 90 years.

Rainfall patterns during the last quarter of 2022 reflected the re-emergence of La Niña, although the SPCZ remained less active than usual during this time. Rainfall during October–December continued to be suppressed along the equator. The off-equatorial region of reduced rainfall observed south of 20°S in the area during JAS contracted eastward during OND, which impacted the southern Cook Islands and French Polynesia (Fig 7.63d). Enhanced rainfall anomalies covered a broad region from southern PNG southeast over Vanuatu, New Caledonia, Fiji, Tonga, and Niue, coinciding with a region of above-normal SSTs. Rainfall totals below the 10th percentile for OND were recorded at several locations across the Gilbert Islands (Kiribati), Rotuma (northern Fiji), and over northern Papua New Guinea. Arorae in Kiribati recorded its second-driest OND in its 56-year history (10 mm). Conversely, Fiji and Tonga recorded rainfall above the 90th percentile. Ono-i-Lau (Fiji) recorded 807 mm, its second-wettest OND in 75 years, and Ha'apai in Tonga recorded 863 mm, its third-wettest OND on record (76 years).

(iii) Notable events and impacts

The most powerful tropical cyclone to impact the South Pacific for 2022 was Tropical Cyclone Dovi, which formed early in February 2022 as the third named storm of the western North Pacific season. Dovi formed to the west of New Caledonia before tracking eastward toward southern Vanuatu and then turned in a southerly direction past southern New Caledonia towards New Zealand. At its peak, Dovi had one-minute sustained winds of 175 km h⁻¹ (94 kt) and a lowest central pressure of 940 hPa.

Tropical Cyclone Dovi caused heavy rainfall and flash flooding across Vanuatu. Several rivers overflowed, causing damage to housing and crops in nearby areas, and mudslides destroyed several bridges in Port Vila, Vanuatu's capital. In southern New Caledonia, Dovi caused all flights from the country to be cancelled for two days and businesses and schools to be closed. The heavy rainfall led to landslides and mudslides and resulted in some evacuations in the capital Nouméa. As Dovi weakened and tracked west of Norfolk Island and across northern New Zealand, the storm brought strong winds and heavy rainfall to both regions. In total, there was approximately \$80 million (U.S. dollars) of damage across the four regions according to AON's Global Catastrophe Recap, with one fatality recorded in New Caledonia.

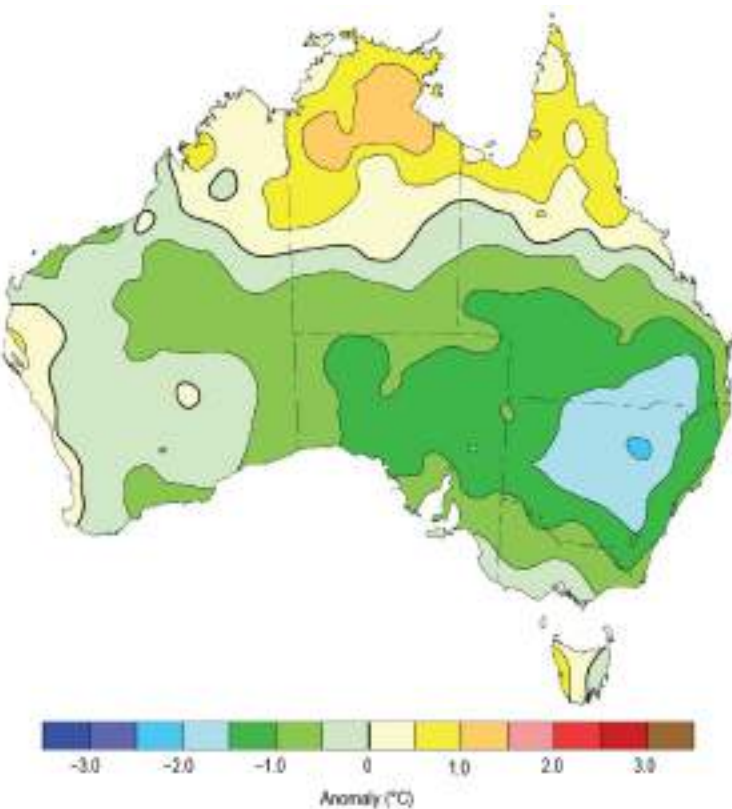
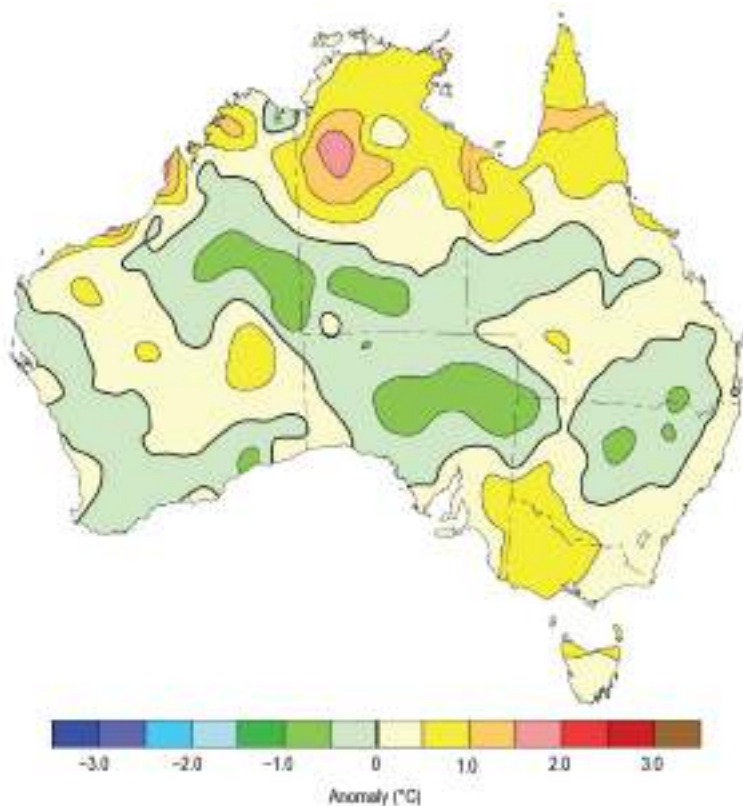


Fig. 7.64. Maximum temperature anomalies (°C) for Australia, averaged over 2022, relative to a 1991–2020 base period. Australian States/Territories are as follows, starting clockwise from the west: Western Australia, the Northern Territory, Queensland, New South Wales, Victoria, and South Australia, with the island of Tasmania in the southeast. (Source: Australian Bureau of Meteorology.)



4. AUSTRALIA

—S. Tobin

In this section, monthly area-averaged temperatures are based on the Australian Climate Observations Reference Network–Surface Air Temperature (ACORN-SAT) dataset (Trewin 2018), while mapped temperature analyses are based on the Australian Water Availability Project (AWAP) dataset (Jones et al. 2009), both of which begin in 1910. Area-averaged rainfall values and mapped analyses use the Australian Gridded Climate Data (AGCD) dataset (Evans et al. 2020), which begins in 1900. Anomalies are based on the 1991–2020 average.

(i) Temperature

The area-averaged annual mean temperature for 2022 was slightly below the 1991–2020 average (0.13°C below average), but overall was the 22nd warmest in Australia's 113-year record. The decade 2013–22 was the warmest 10-year period on record for Australia, 0.38°C above the 1991–2020 average, despite recurrent La Niña and high rainfall bringing relatively cool years during 2021 and 2022. Only six years prior to 2000 were warmer than 2022.

The annual nationwide mean maximum temperature (Fig. 7.64) was 0.40°C below average, and the mean minimum temperature (Fig. 7.65) was 0.13°C above average.

In terms of annual anomalies, both mean annual maximum and minimum temperatures were above average for most of tropical northern Australia. Compared to the distribution across all 113 years of observations (1910–2022), maximum temperatures were in the highest 10% of observations for most of the Top End in the Northern Territory and Queensland's Cape York Peninsula, and also in western Tasmania. New South Wales, much of southern Queensland, and large parts of South Australia were in the bottom 30% of observations. The mean annual minimum

Fig. 7.65. Minimum temperature anomalies (°C) for Australia, averaged over 2022, relative to a 1991–2020 base period. (Source: Australian Bureau of Meteorology.)

temperature was in the top 30% of observations compared to all years 1910–2022 across the majority of Australia.

In the first half of the year, most months were warmer than average for large parts of Australia. In the second half of the year, temperatures generally remained warmer than average for the tropics, but were cooler than average across large areas, particularly the central and southern mainland during spring.

Warm sea-surface temperature anomalies to the west and northwest of Western Australia as well as a ridge of high pressure south of the Great Australian Bight played an important role early in the year, with extreme heatwave conditions affecting the north and west throughout the first quarter of 2022.

July was unusually cool for large parts of the tropics due to unusual dry-season rainfall, although farther south much of southwest Australia and parts of the southeast continued to experience warmer-than-average days and nights.

During August, September, October, and December, far-northern Australia experienced above-average temperatures, with heatwave conditions in some parts of the tropics.

Spring (September–November; SON) brought a shift to cooler-than-average days for most of the mainland south of the tropics. In November, both mean maximum and mean minimum temperatures were below average for most areas except the very far north. Nationally, November was Australia's coolest since 1999 and the eighth-coolest November on record.

December was also cooler than average for much of eastern Australia, with cold outbreaks during the month leading to a large number of stations across the region observing a record-low daily minimum temperature during the first half of the month.

(ii) Precipitation

Averaged across Australia, rainfall for 2022 was 587.8 mm, the ninth-wettest year on record for Australia and 20.9% above the 1991–2020 average of 486.0 mm. Compared to the distribution across all 123 years of observations (1900–2022), annual rainfall was above average for most of mainland Australia and in the top 10 percent for most of the southeastern quarter of the mainland (Fig. 7.66). Rainfall was below average for western Tasmania, much of the north of the Northern Territory, and for parts of the south-west of Western Australia.

La Niña was a dominant influence on Australia's climate during 2022, persisting through summer 2021/22, weakening during autumn, and returning to neutral before a third successive La Niña re-emerged in early September. A negative Indian Ocean dipole (IOD) during winter and spring as well as a persistently positive phase of the Southern Annular Mode (SAM) from mid-autumn also influenced Australia's climate and weather patterns during 2022 (Ashok et al. 2003; Hendon et al. 2007; Risbey et al. 2009).

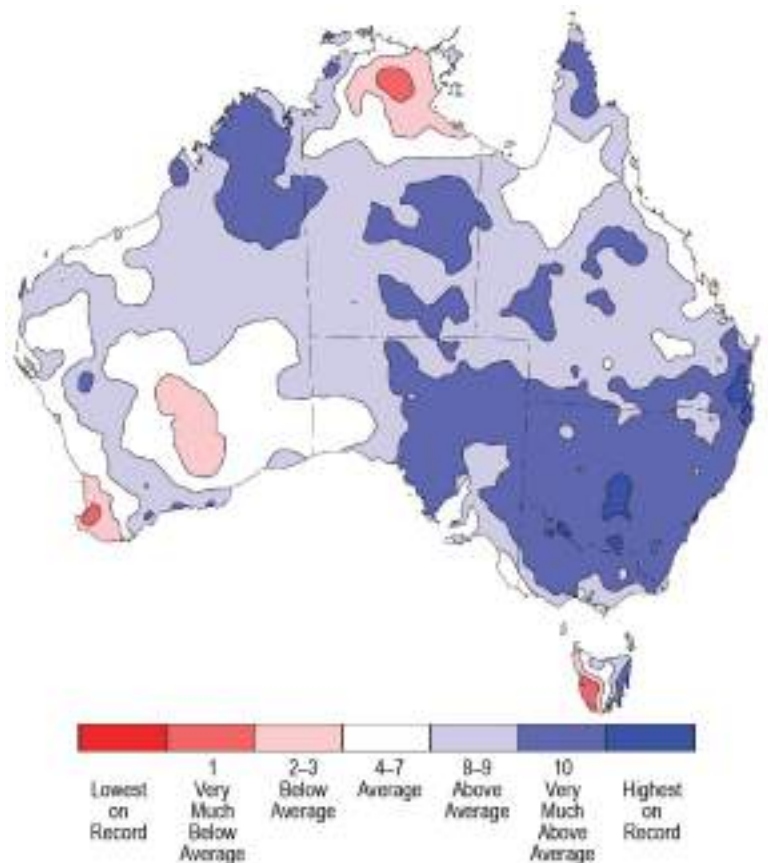


Fig. 7.66. Rainfall deciles for Australia for 2022, based on the 1900–2022 distribution. (Source: Australian Bureau of Meteorology.)

La Niña typically brings wetter conditions to much of northern and eastern Australia, and when La Niña and negative IOD conditions combine, the likelihood of above-average rainfall over Australia is further increased. Together, they also increase the chances of warmer nights for northern Australia and cooler days for much of the eastern mainland. SAM is often positive during La Niña, and during 2022 the persistently positive SAM was also boosted by a strong polar vortex over Antarctica. The positive SAM likely contributed both to above-average rainfall across parts of eastern Australia and below-average rainfall in parts of southern Australia, particularly in areas with west-facing coastlines (Fig. 7.66).

In northern Australia, the latter part of the 2021/22 northern wet season (October–April) was particularly dry, with rainfall for February–April 2022 being in the lowest 10% of observations for much of the northern half of the Northern Territory. A lack of days with the Madden-Julian Oscillation (MJO) in phases 5–7, typically associated with wetter conditions for northern Australia (see Wheeler et al. 2009) in the second half of the northern wet season meant that there was a reduction in the number of rainy monsoon bursts. This MJO behavior, with a persistent pattern of MJO events stalling in the Indian Ocean and/or weakening rapidly as they approached Australia, may have been influenced by above-average sea-surface temperatures in the Indian Ocean (Marshall et al. 2023).

In eastern Australia, persistent rain caused significant flooding that affected large areas multiple times during the year, with some areas in the east seeing a third wet year in a row. Flooding affected southeastern Queensland and eastern New South Wales from late February into March, inland central and northern Queensland and inland northern New South Wales during May, around Sydney and the New South Wales coast in early July, and across large parts of the eastern states from August. Flooding affected many parts of the Murray–Darling Basin over prolonged periods or on multiple occasions throughout spring.

Austral spring was the second wettest on record for Australia as a whole, and the wettest on record for the Murray–Darling Basin, New South Wales, and Victoria. Numerous locations near the coast of New South Wales and in southern Queensland broke their annual rainfall record by the end of October, and for Victoria, October was the state's wettest month on record for any time of the year. In the north of Western Australia, the Kimberley region was affected by flooding near both the start and the end of the year.

High rainfall, wet soils, and high streamflows meant that water storage levels were high across much of Australia during 2022. In parts of northern Australia and southeast Queensland, water storages started the year well below capacity and experienced significant increases during February. Surface water storage levels remained at near-full capacity for many parts of the country across the year, including most of those in the Murray–Darling Basin. However, storage levels remained low in parts of central coastal Queensland, western Tasmania, southeast New South Wales, and western Victoria.

Predominantly easterly winds over much of Australia influenced by La Niña, a generally positive SAM, and persistent blocking highs were associated with below-average rainfall in parts of southern Australia, particularly in areas with west-facing coastlines. Summer 2021/22 was the fifth driest on record for Tasmania as a whole, and the driest since 1980/81.

Serious rainfall deficiencies (defined as totals in the lowest 10% of historical observations since 1900) emerged across western Tasmania and parts of coastal southern Australia from early in the year. Despite heavy rain and periods of flooding in eastern Australia, these rainfall deficiencies persisted into spring 2022 for much of the west-facing coasts of southeastern Australia, with deficiencies still in place in western Tasmania at the end of the year.

(iii) Notable events and impacts

Ex-tropical Cyclone Tiffany brought heavy rain and damaged transport infrastructure across northwest Australia through to southern South Australia during the second half of January. Tiffany also contributed to extreme high temperatures over the Pilbara during mid-January. Onslow Airport reached 50.7°C on 13 January, equaling Australia's highest temperature on record. Heatwave conditions continued along the west coast on and off into February, contributing to high fire danger in early February, with multiple fires breaking out across Western Australia's South West Land Division.

The remnants of Tropical Cyclone Seth caused significant flooding in Queensland in early January in the Wide Bay and Burnett districts in the southeast of the state. The Mary River catchment received rainfall totals in excess of 600 mm.

Extreme multi-day rainfall in late February to early March produced record-breaking floods in southeast Queensland and eastern New South Wales. Record flooding resulted in multiple catchments extending from Maryborough in Queensland to Grafton in New South Wales. Parts of southeast Queensland observed their highest flood peaks since 1893, including the Mary River at Gympie. In parts of northeast New South Wales, peak flood levels surpassed previous observations by considerable margins, and in the Hawkesbury–Nepean they were comparable to levels that occurred in 1978.

From late winter and into spring, persistent rain falling onto already wet catchments led to renewed river-level rises and flooding along many rivers in southern Queensland, inland New South Wales, and northern and central inland Victoria. In many parts of the Murray–Darling Basin, flooding occurred over prolonged periods or on multiple occasions, and continued to affect a number of communities throughout October and into November. Flooding continued during December as flood waters progressed through inland rivers in southern Queensland and the southeastern mainland. Multiple flood peaks were observed at some locations in the generally flat downstream catchments of the Murray–Darling Basin.

December was the seventh wettest on record for the Northern Territory, partly due to the passage of ex-Tropical Cyclone Ellie over northern and central parts of the region during the last week of the year. Significant flooding occurred on the Fitzroy River in Western Australia's Kimberley region, with heavy rain continuing into the start of 2023.

5. NEW ZEALAND

—T. Meyers

In the following discussion, the base period is 1981–2010. The nationwide average temperature is based upon New Zealand's National Institute of Water and Atmospheric Research (NIWA) seven-station temperature series that began in 1909. All statistics are based on data available as of 11 January 2023.

(i) Temperature

According to NIWA's seven-station temperature series, 2022 was New Zealand's warmest year since records began in 1909, surpassing the record set just the previous year. The nationwide average temperature for 2022 was 13.76°C, which was 1.15°C above the annual average. Annual temperatures were above average (+0.51°C to +1.20°C) or well above average (>1.20°C) for almost all of New Zealand, although near-normal ($\pm 0.50^\circ\text{C}$ of average) temperatures occurred in pockets around the eastern South Island and also parts of Marlborough and Nelson (Fig. 7.67a).

Various climate drivers contributed to the exceptional warmth, with La Niña being the primary driver. In New Zealand, La Niña is typically linked with higher-than-normal air pressure near and to the east of the country with lower pressures to the north. These circulation anomalies were observed in 2022, which led to more northeasterly winds than usual and were likely a major cause of the above-average air temperatures. Throughout 2022, coastal sea-surface temperatures (SSTs) were either above or well above average every month, with January, November, and December having the most anomalously warm SSTs. This resulted in a protracted marine heatwave (MHW), where SSTs are above the 90th percentile as derived from a 30-year climatology, with ocean temperatures staying unseasonably warm over thousands of kilometers for much of the year. The MHWs of 2022 also likely contributed to the observed above-average air temperatures over New Zealand. Additionally, the Southern Annular Mode was positive for the vast majority of 2022, which is associated with higher-than-normal pressures over the New Zealand region. Climate change also continues to affect New Zealand's long-term temperature trend, which is increasing at a rate of around 1.17°C (±0.2°C) per century, according to NIWA's seven-station series.

It was the warmest year on record for 47 locations while an additional 33 locations experienced annual average temperatures among their four warmest on record. No locations experienced a record or near-record cold year, and no locations experienced below-average annual mean daily temperatures. The last year New Zealand observed any locations where annual temperatures were record or near-record cold was 2015.

Unlike 2021, which featured high temperatures in the high 30s during summer, no station recorded a temperature over 35°C in 2022. The last time New Zealand failed to reach a temperature higher than 35°C during a calendar year was 2007.

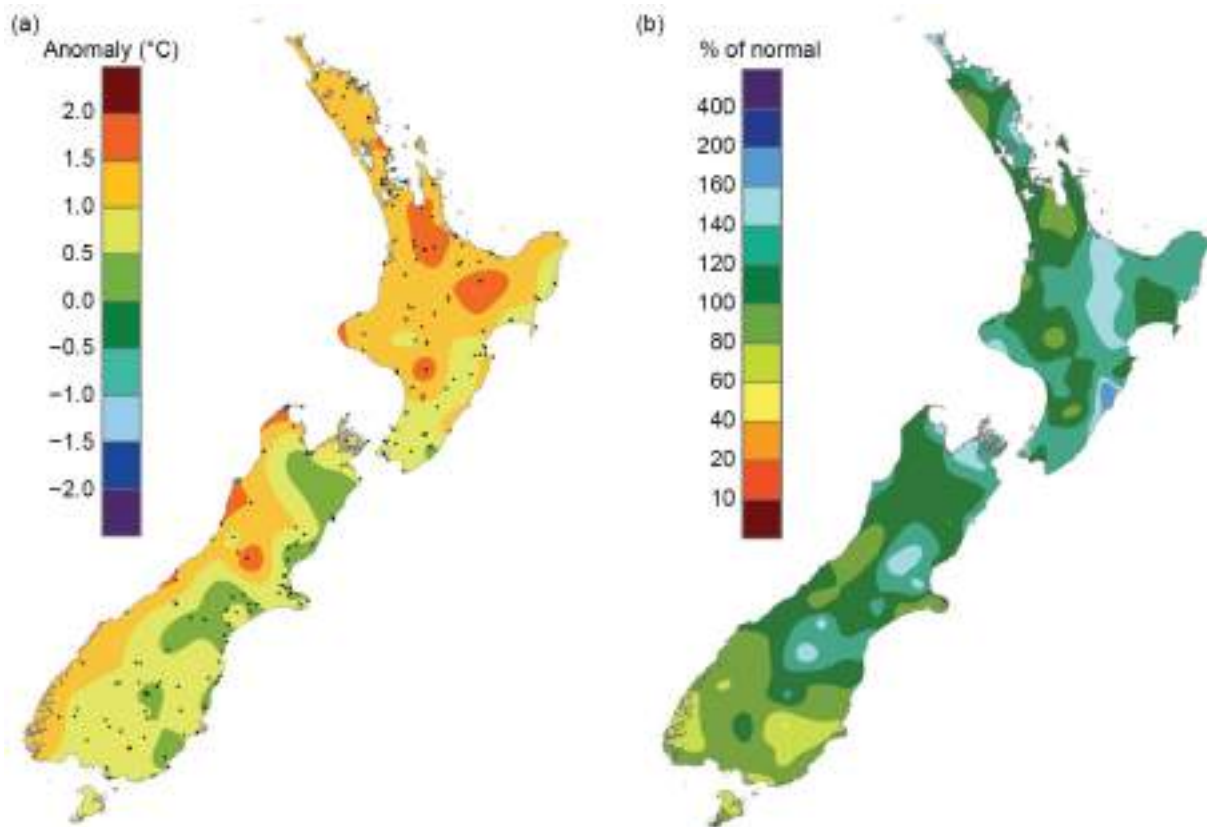


Fig. 7.67. 2022 annual (a) average temperature anomaly (°C) and (b) total rainfall (% of normal), relative to the 1981–2010 base period. The black dots on (a) represent the locations of climate stations used to create both the temperature and rainfall maps. Note: some data used to create these plots have been identified as not homogenized. As NIWA switches to the 1991–2020 normal period, these data will be homogenized (Source: NIWA.)

(ii) Precipitation

The majority of the country experienced near-normal annual rainfall (80%–119%) in 2022, although rainfall totals were above normal (120%–149% of normal) or well above normal (>150%) for parts of Northland, Tauranga, Gisborne, the Central Plateau, southern Taranaki, parts of Manawatū-Whanganui, much of Wellington, Nelson, northern Marlborough, parts of Tasman, the West Coast near Westport, and pockets of Canterbury and below normal (50%–79%) for pockets of Southland and Dunedin (Fig. 7.67b). Overall, 2022 was New Zealand’s eighth-wettest year on record, based on an analysis of NIWA’s Virtual Climate Station Network (<https://niwa.co.nz/climate/our-services/virtual-climate-stations>) dating to 1960. Of all the regularly reporting gauges, the wettest location in 2022 was Cropp River (West Coast), 975 meters a.s.l. with 11,034 mm for the year. The driest of the regularly reporting rainfall sites in 2022 were Roxburgh and Middlemarch in the Otago region of the South Island, both reporting just 368 mm.

(iii) Notable Events

Widespread meteorological drought and dryness (based on the NZ Drought Index; <https://niwa.co.nz/climate/information-and-resources/drought-monitor>) developed by the end of January. The city of Auckland experienced a 37-day dry spell (defined as less than 1 mm of rain observed in the 24 hours to 9am local time) from 17 December 2021 to 22 January 2022, which was its second-longest dry spell since records began in 1943. Many areas around New Zealand introduced water restrictions during January due to the dry conditions. While these conditions eased for the North Island during February, parts of the South Island continued to experience dryness or meteorological drought well into autumn.

On 13 February, the landfall of ex-Tropical Cyclone Dovi brought heavy rainfall and strong wind gusts to the North Island and upper South Island. This was the first cyclone to make landfall in New Zealand since Fehi and Gita in February 2018. Widespread power outages occurred, numerous roads were temporarily closed due to surface flooding or landslides, and homes in Wellington were evacuated due to landslides.

From 16 to 20 August, an atmospheric river (AR) that extended from the tropics led to a long-duration heavy rain and flooding event. ARs are long, narrow, and transient corridors of strong horizontal water vapor transport that are typically associated with a low-level jet stream ahead of a cold front or an extratropical cyclone. Although ARs are responsible for the majority of annual normal precipitation for sections of the country, they also disproportionately account for the amount of extreme precipitation in some parts of New Zealand; over 90% of extreme (6-hourly) precipitation occurs due to AR activity for parts of the West Coast on the South Island and over 70% for Nelson (Prince 2019). An analysis from the [European Centre for Medium-Range Weather Forecasts Reanalysis version 5 \(ERA5\)](#) dataset revealed that the August AR was the strongest landfalling August AR for New Zealand since at least 1950, with the total amount of water vapor flowing through an atmospheric column (known as integrated water vapor transport) reaching a maximum value of 1749 kg m⁻¹ s⁻¹. The AR resulted in a 1-in-120-year rain event in Nelson, severe flooding, and numerous landslides, as two to four times the normal August rainfall was recorded in just a few days across parts of the upper South Island and North Island.

Acknowledgments

Europe

Much of the information in this section is based on national climate reports kindly provided by the National Meteorological and Hydrological Services (NMHSs) of the WMO RA VI Region. The information has been compiled at the WMO RA VI Regional Climate Centre (RCC) Node on Climate Monitoring, located at Deutscher Wetterdienst (DWD) in Germany. The national contributions have been provided as part of the cooperation between NMHSs and the RCC.

Specifically, we acknowledge the Instytut Meteorologii i Gospodarki Wodnej PIB in Poland for its kind cooperation with RCC in this subject.

Oceania

The editors acknowledge and thank the numerous national meteorological and hydrological services for collecting and providing data for this report. Data centers like NCEP/NCAR, ECMWF-ERA, and CHIRPS are also acknowledged for making their data freely available.

Appendix 1: Chapter 7 – Acronyms

ACORN-SAT	Australian Climate Observations Reference Network–Surface Air Temperature
AGCD	Australian Gridded Climate Data
AMJ	April–June
ANDMA	Afghanistan National Disaster Management Authority
AR	atmospheric river
ARCS	Afghan Red Crescent Society
ASO	August–October
AWAP	Australian Water Availability Project
CA	Central America
CA	Central Asia
CAMS	Climate Anomaly Monitoring System
CA-NWS	CA-NWS
CAR	Central African Republic
CMORPH	Climate Prediction Center Morphing Technique
CNE	National Emergency Commission
CONRED	National Coordination for Disaster Reduction
CONUS	contiguous United States
COPECO	Permanent Contingency Commission of Honduras
CPC	Climate Prediction Center
DJF	December–February
DRC	Democratic Republic of the Congo
DWD	Deutscher Wetterdienst
ECCC	Environment and Climate Change Canada
EF	Enhanced Fujita
EHD	extreme high-temperature days
EM-DAT	Emergency Events Database
ERA 5	European Centre for Medium-Range Weather Forecasts Reanalysis version 5
FEWS NET	Famine Early Warning Systems Network
GHA	Greater Horn of Africa
GHCN	Global Historical Climate Network
GPCC	Global Precipitation Climatology Centre
GPCP	Global Precipitation Climatology Project
HAC	Humanitarian Aid Commission
IDI	Integrated Drought Index
IFRC	International Federation of Red Cross and Red Crescent Societies
IOD	Indian Ocean dipole
ISMR	Indian summer monsoon rainfall
ITCZ	Intertropical Convergence Zone
JAS	July–September
JFM	January–March
JJA	June–August
JJAS	June–September
JMA	Japan Meteorological Agency
LTA	long-term average
MAM	March–May
MHW	marine heatwave
MJO	Madden-Julian Oscillation
MSWEP	Multi-Source Weighted-Ensemble Precipitation
NAO	North Atlantic Oscillation

NCAR	National Center for Atmospheric Research
NCEP/NCAR	National Centers for Environmental Prediction/National Center for Atmospheric Research
NEM	northeast monsoon
NIWA	National Institute of Water and Atmospheric Research
NMHS	National Meteorological and Hydrological Services
OLR	outgoing longwave radiation
OND	October–December
P	accumulated pentad precipitation
PNG	Papua New Guinea
RA VI	(WMO) Regional Association VI
RCC-CM	Regional Climate Centre on Climate Monitoring
RFE2	RainFall Estimate version 2
SAM	Southern Annular Mode
SINAPROC	National Civil Protection System
SON	September–November
SPCZ	South Pacific Convergence Zone
SPI	standardized precipitation index
SSA	southern South America
SST	sea-surface temperature
TAP	tropical Atlantic precipitation
Tm	mean temperature
Tmax	maximum temperature
Tmin	minimum temperature
TPS	tropical Pacific SST
UNICEF	United Nations Children’s Fund
UN-OCHA	United Nations Office for the Coordination of Humanitarian Affairs
WMO	World Meteorological Association
YRB	Yangtze River Basin
YT	mean temperature averaged over the YRB

Appendix 2: Chapter 7 – Supplemental Materials

Table A7.1. Temporal coverage of nationally averaged temperature and precipitation in situ observations for Europe / WMO RA VI Region. For some countries, only one station (preferably with long time series) has been used (name of the location in brackets). All records extend to the present. Anomalies refer to the 1991–2020 reference unless otherwise specified. Data are checked for consistency with the text. Inconsistencies with maps shown in the figures might occur because not all national data have been available for generation of maps.

Nation	Temperature start of record	Precipitation start of record	Source	Temperature anomaly (°C)	Rank (ordered from warmest to coldest)	Precipitation anomaly (annual total in % of normal)	Rank (ordered from wettest to driest)
European average	1950	1881	GHCN ¹ data (temperature), GPCP (precipitation)	+1.0	2	95%	91
Albania (Korce)	1963	1963	CLIMAT ²	-	-	-	-
Andorra	1931	1927	NMHS ³	+2.6	1	78%	76
Armenia	1935	1935	NMHS	+1.7	5	75%	85
Austria	1767	1858	NMHS	+1.1	3	85%	155
Azerbaijan (Astara)	1991	1991	CLIMAT	-	-	-	-
Belarus	1881	1945	NMHS	-	-	-	-
Belgium	1833	1833	NMHS	+1.2	1	84%	29
Bosnia & Herzegovina (Banja Luka)	1950	1950	NMHS	+1.1	1	82%	66
Bulgaria	1930	1930	NMHS	+0.8	4	80%	-
Croatia	1961	1961	NMHS	+1.2	1	84%	56
Cyprus (Nicosia)	1899	1899	NMHS	+0.6	14	-	-
Czechia	1961	1961	NMHS	+0.9	5	93%	-
Denmark	1873	1874	NMHS	+0.8	3	91%	66
Estonia	1961	1961	NMHS	+0.7	8	80%	56

¹ GHCN = Global Historical Climatology Network (Menne et al. 2018), GPCP = Global Precipitation Climatology Centre (Schneider et al. 2018), averaged over RA VI land areas without Greenland

² CLIMAT station data as reported worldwide via the WMO Global Telecommunication System

³ NMHS = National Meteorological and Hydrological Service; for individual names of NMHSs see <https://public.wmo.int/en/about-us/members>

⁴ reference period 1971–2000

⁵ reference period 1981–2010

Nation	Temperature start of record	Precipitation start of record	Source	Temperature anomaly (°C)	Rank (ordered from warmest to coldest)	Precipitation anomaly (annual total in % of normal)	Rank (ordered from wettest to driest)
Finland (Helsinki)	1900	1961	NMHS	+0.9	-	-	-
France	1900	1959	NMHS	+1.6	1	76%	63
Georgia	1956	1881 (Tbilisi)	NMHS	-	-	-	-
Germany	1881	1881	NMHS	+2.3	1	85%	119
Greece	1960	1960	NMHS	+0.7 ⁵	5	80% ⁵	59
Hungary	1901	1901	NMHS	+1.1	3	81%	106
Iceland (Stykkishólmur for temperature, Reykjavik for precipitation)	1900	1921	NMHS	+0.0	-	-	8
Ireland	1900	1941	NMHS	+0.7	1	97%	37
Israel	1951	1935 (Deganya)	NMHS	+0.1	19	102%	30
Italy	1961	1961	NMHS	+1.1	1	77%	62
Jordan (Amman)	1981	1981	NMHS	-	-	-	-
Kazakhstan	1941	1941	NMHS	-	-	-	-
Latvia	1924	1924	NMHS	+0.5	12	100%	39
Lebanon (Beirut)	1949	1949	CLIMAT	-	-	-	-
Lithuania	1961	1887 (Vilnius)	NMHS	+0.5	11	97%	31
Luxembourg (Findel)	1838	1854	NMHS	+1.1	1	85%	110
Malta (Luqa)	1923	1949	NMHS/CLIMAT	-	-	-	-
Moldova (Chisinau)	1886	1891	NMHS	+0.9	4	80%	30

¹ GHCN = Global Historical Climatology Network (Menne et al. 2018), GPCC = Global Precipitation Climatology Centre (Schneider et al. 2018), averaged over RA VI land areas without Greenland

² CLIMAT station data as reported worldwide via the WMO Global Telecommunication System

³ NMHS = National Meteorological and Hydrological Service; for individual names of NMHSs see <https://public.wmo.int/en/about-us/members>

⁴ reference period 1971–2000

⁵ reference period 1981–2010

Nation	Temperature start of record	Precipitation start of record	Source	Temperature anomaly (°C)	Rank (ordered from warmest to coldest)	Precipitation anomaly (annual total in % of normal)	Rank (ordered from wettest to driest)
Monaco	1969	1969	NMHS	+1.4	1	60%	51
Montenegro (Podgorica)	1949	1949	NMHS	+1.2	1	-	-
Netherlands	1901	1901	NMHS	+1.1	3	66%	53
North Macedonia	1981	1981	NMHS	+0.7 ⁵	12	91%	31
Norway	1900	1900	NMHS	+0.7	9	104%	17
Poland	1951	1951	NMHS	+0.8	7	87%	59
Portugal	1931	1931	NMHS	+1.4 ⁴	1	90% ⁴	-
Romania	1961	1961	NMHS	+1.0	3	82%	53
Russia, European part	1936	1936	NMHS	+0.8	-	103%	-
Serbia	1951	1951	NMHS	+1.0	2	93%	46
Slovakia	1951	1961	NMHS	+1.0	4	81%	57
Slovenia	1961	1961	NMHS	+1.2	1	84%	56
Spain	1961	1961	NMHS	+1.7 ⁵	1	84% ⁵	57
Sweden	1860	1880	NMHS	+0.8	4	88%	79
Switzerland	1864	1864	NMHS	+1.6	1	82%	137
Syrian Arab Republic (Aleppo)	1960	1960	-	-	-	-	-
Türkiye	1971	1991	NMHS	+0.6	7	88%	
Ukraine	1891	1891	NMHS	+0.7	19	99%	43
United Kingdom	1884	1836	NMHS	+0.9	1	94%	76

¹ GHCN = Global Historical Climatology Network (Menne et al. 2018), GPCP = Global Precipitation Climatology Centre (Schneider et al. 2018), averaged over RA VI land areas without Greenland

² CLIMAT station data as reported worldwide via the WMO Global Telecommunication System

³ NMHS = National Meteorological and Hydrological Service; for individual names of NMHSs see <https://public.wmo.int/en/about-us/members>

⁴ reference period 1971–2000

⁵ reference period 1981–2010

References

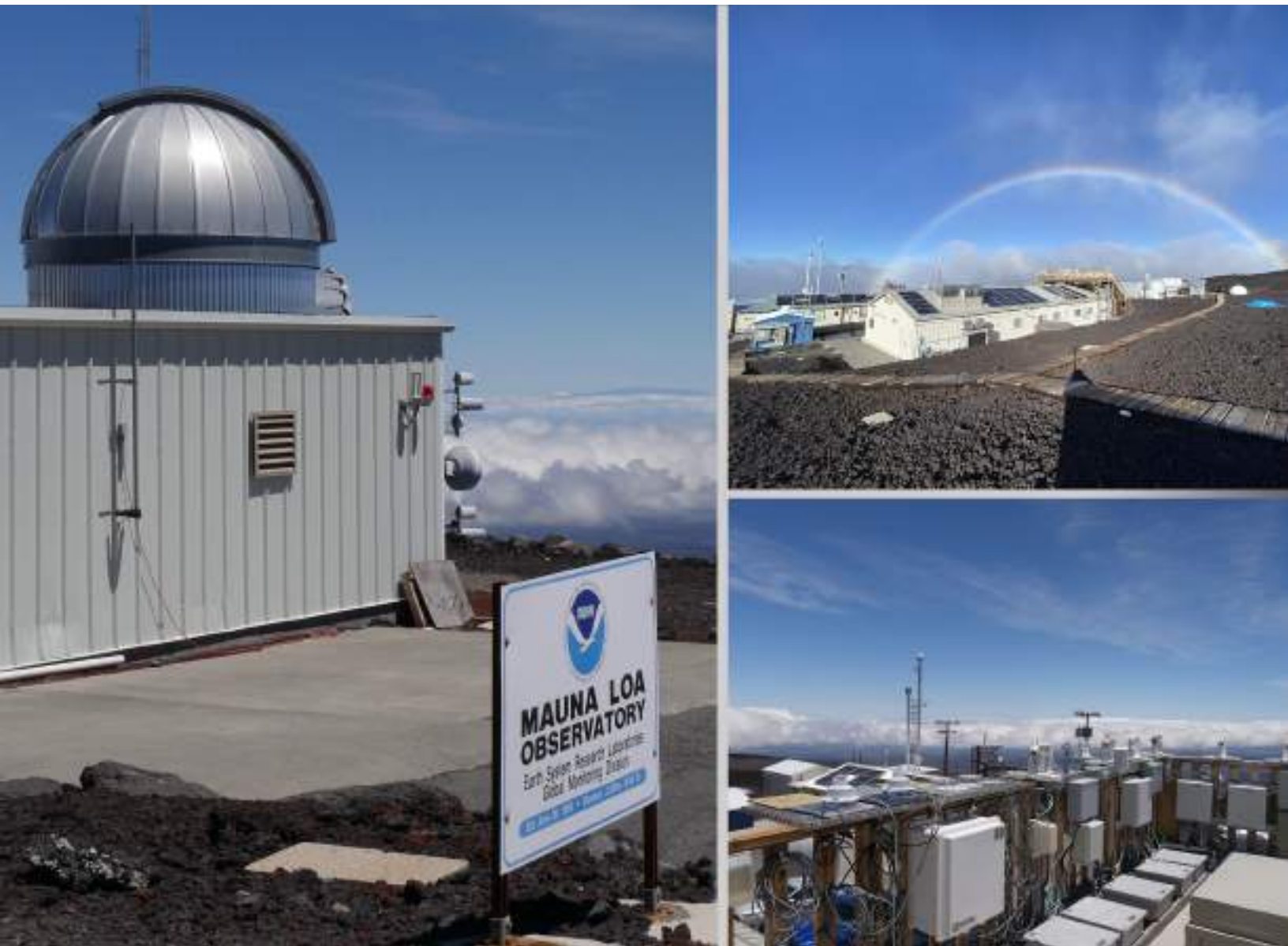
- Alcántara, E., and Coauthors, 2023: Deadly disasters in the southeastern South America: Flash floods and landslides of February 2022 in Petrópolis, Rio de Janeiro. *Nat. Hazards Earth Syst. Sci.*, **23**, 1157–1175, <https://doi.org/10.5194/nhess-23-1157-2023>.
- Amador, J. A., 1998: A climatic feature of the tropical Americas: The trade wind easterly jet. *Top. Meteor. Oceanogr.*, **5**, 91–102.
- , 2008: The Intra-Americas Seas Low-Level Jet (IALLJ): Overview and future research. *Ann. N. Y. Acad. Sci.*, **1146**, 153–188, <https://doi.org/10.1196/annals.1446.012>.
- , E. J. Alfaro, H. Hidalgo, and B. Calderon, 2011: Central America and the Caribbean [in “State of the Climate in 2010”]. *Bull. Amer. Meteor. Soc.*, **92** (6), S182–S183, <https://doi.org/10.1175/1520-0477-92.6.S1>.
- , E. R. Rivera, A. M. Durán-Quesada, G. Mora, F. Sáenz, B. Calderón, and N. Mora, 2016a: The easternmost tropical Pacific. Part I: A climate review. *Rev. Biol. Trop.*, **64** (S1), S1–S22, <https://doi.org/10.15517/rbt.v64i1.23407>.
- , A. M. Durán-Quesada, E. R. Rivera, G. Mora, F. Sáenz, B. Calderón, and N. Mora, 2016b: The easternmost tropical Pacific. Part II: Seasonal and intraseasonal modes of atmospheric variability. *Rev. Biol. Trop.*, **64** (S1), S23–S57, <https://doi.org/10.15517/rbt.v64i1.23409>.
- , H. G. Hidalgo, E. J. Alfaro, B. Calderón, and N. Mora, 2018: Central America and the Caribbean [in “State of the Climate 2017”]. *Bull. Amer. Meteor. Soc.*, **99** (8), S199–S200, <https://doi.org/10.1175/2018BAMSStateoftheClimate.1>.
- Ashok, K., Z. Guan, and T. Yamagata, 2003: Influence of the Indian Ocean dipole on the Australian winter rainfall. *Geophys. Res. Lett.*, **30**, 1821, <https://doi.org/10.1029/2003GL017926>.
- Biasutti, M., 2019: Rainfall trends in the African Sahel: Characteristics, processes, and causes. *Wiley Interdiscip. Rev.: Climate Change*, **10**, e591, <https://doi.org/10.1002/wcc.591>.
- Espinoza, J. C., J. A. Marengo, J. Schongart, and J. C. Jimenez, 2022: The new historical flood of 2021 in the Amazon River compared to major floods of the 21st century: Atmospheric features in the context of the intensification of floods. *Wea. Climate Extremes*, **35**, 100406, <https://doi.org/10.1016/j.wace.2021.100406>.
- Evans, A., D. Jones, R. Smalley, and S. Lellyett, 2020: An enhanced gridded rainfall analysis scheme for Australia. Bureau of Meteorology Research Rep. 41, 45 pp., <http://www.bom.gov.au/research/publications/researchreports/BRR-041.pdf>.
- Fu, S., Z. Zhu, and R. Lu, 2023: Changes in the factors controlling Northeast Asian spring surface air temperature in the past 60 years. *Climate Dyn.*, **61**, 169–183, <https://doi.org/10.1007/s00382-022-06569-7>.
- Giannini, A., 2015: Climate change comes to the Sahel. *Nat. Climate Change*, **5**, 720–721, <https://doi.org/10.1038/nclimate2739>.
- He, Y., A. G. Barnston, and A. C. Hilton, 1998: A precipitation climatology for stations in the tropical Pacific Basin: Effects of ENSO. NCEP/Climate Prediction Center Atlas 5, NOAA, 280 pp.
- Hendon, H. H., D. W. Thompson, and M. C. Wheeler, 2007: Australian rainfall and surface temperature variations associated with the Southern Hemisphere annular mode. *J. Climate*, **20**, 2452–2467, <https://doi.org/10.1175/JCLI4134.1>.
- Hidalgo, H., E. Alfaro, J. Amador, and A. Bastidas, 2019: Precursors of quasi-decadal dry-spells in the Central America Dry Corridor. *Climate Dyn.*, **53**, 1307–1322, <https://doi.org/10.1007/s00382-019-04638-y>.
- Jones, D. A., W. Wang, and R. Fawcett, 2009: High-quality spatial climate data-sets for Australia. *Aust. Meteor. Oceanogr. J.*, **58**, 233–248, <https://doi.org/10.22499/2.5804.003>.
- Magaña, V., J. A. Amador, and S. Medina, 1999: The mid-summer drought over México and Central America. *J. Climate*, **12**, 1577–1588, [https://doi.org/10.1175/1520-0442\(1999\)0122.0.CO;2](https://doi.org/10.1175/1520-0442(1999)0122.0.CO;2).
- Lindsey, R., and L. Dahlman, 2009: Climate variability: North Atlantic Oscillation. Climate.gov, 30 August, www.climate.gov/news-features/understanding-climate/climate-variability-north-atlantic-oscillation.
- Marengo, J. A., and Coauthors, 2023: Flash floods and landslides in the city of Recife, Northeast Brazil after heavy rain on May 25–28, 2022: Causes, impacts, and disaster preparedness. *Wea. Climate Extremes*, **39**, 100545, <https://doi.org/10.1016/j.wace.2022.100545>.
- McKenna, C. M., and A. C. Maycock, 2022: The role of the North Atlantic Oscillation for projections of winter mean precipitation in Europe. *Geophys. Res. Lett.*, **49**, e2022GL099083, <https://doi.org/10.1029/2022GL099083>.
- Menne, M. J., C. N. Williams, and B. E. Gleason, 2018: The Global Historical Climatology Network monthly temperature dataset, version 4. *J. Climate*, **31**, 9835–9854, <https://doi.org/10.1175/JCLI-D-18-0094.1>.
- Merrifield, M. A., P. R. Thompson, and M. A. Lander, 2012: Multidecadal sea level anomalies and trends in the western tropical Pacific. *Geophys. Res. Lett.*, **39**, L13602, <https://doi.org/10.1029/2012GL052032>.
- Naumann, G., and Coauthors, 2022: Extreme and long-term drought in the La Plata Basin: Event evolution and impact assessment until September 2022. JRC Tech Rep. 132245, 53 pp., <https://doi.org/10.2760/62557>.
- Nicholson, S. E., A. H. Fink, and C. Funk, 2018: Assessing recovery and change in West Africa’s rainfall regime from a 161-year record. *Int. J. Climatol.*, **38**, 3770–3786, <https://doi.org/10.1002/joc.5530>.
- Prince, H. D., N. J. Cullen, P. B. Gibson, J. Conway, and D. G. Kingston, 2021: A climatology of atmospheric rivers in New Zealand. *J. Climate*, **34**, 4383–4402, <https://doi.org/10.1175/JCLI-D-20-0664.1>.
- Risbey, J. S., M. J. Pook, P. C. McIntosh, M. C. Wheeler, and H. H. Hendon, 2009: On the remote drivers of rainfall variability in Australia. *Mon. Wea. Rev.*, **137**, 3233–3253, <https://doi.org/10.1175/2009MWR2861.1>.
- Sadler, J. C., 1976: A role of the tropical upper tropospheric trough in early season typhoon development. *Mon. Wea. Rev.*, **104**, 1266–1278, [https://doi.org/10.1175/1520-0493\(1976\)1042.0.CO;2](https://doi.org/10.1175/1520-0493(1976)1042.0.CO;2).
- Schneider, U., P. Finger, A. Meyer-Christoffer, M. Ziese, and A. Becker, 2018: Global precipitation analysis products of the GPCC. Deutscher Wetterdienst (DWD), 15 pp., https://opendata.dwd.de/climate_environment/GPCC/PDF/GPCC_intro_products_v2018.pdf.
- Trewin, B., 2018: The Australian Climate Observations Reference Network–Surface Air Temperature (ACORN-SAT) version 2. Bureau of Meteorology Research Rep. 032, 67 pp., <http://www.bom.gov.au/research/publications/researchreports/BRR-032.pdf>.
- Wheeler, M. C., H. H. Hendon, S. Cleland, H. Meinke, and A. Donald, 2009: Impacts of the Madden–Julian Oscillation on Australian Rainfall and Circulation. *J. Climate*, **22**, 1482–1498, <https://doi.org/10.1175/2008JCLI2595.1>.

WMO, 2023: *State of the Climate in Europe 2022*. WMO-No. 1320, 40 pp., https://library.wmo.int/index.php?lvl=notice_display&id=22285

Yang, Y., Z. Zhu, X. Shen, L. Jiang, and T. Li, 2023: The influences of Atlantic sea surface temperature anomalies on the ENSO-independent interannual variability of East Asian summer monsoon rainfall. *J. Climate*, **36**, 677–692, <https://doi.org/10.1175/JCLI-D-22-0061.1>.

STATE OF THE CLIMATE IN 2022

RELEVANT DATASETS AND SOURCES



Special Online Supplement to the *Bulletin of the American Meteorological Society* Vol. 104, No. 9, September, 2023

https://doi.org/10.1175/2023BAMSSStateoftheClimate_Chapter8.1

Corresponding author: Jessica Blunden / jessica.blunden@noaa.gov

©2023 American Meteorological Society

For information regarding reuse of this content and general copyright information, consult the [AMS Copyright Policy](#).

Cover Credit:

Mauna Loa observatory, island of Hawai'i, site of atmospheric carbon dioxide measurements since March, 1958.

(Image credits: Left image: Susan Cobb, Global Systems Laboratory; Right upper image: Brian Vassel, Global Monitoring Laboratory; Right lower image: Susan Cobb, Global Systems Laboratory).

8. RELEVANT DATASETS AND SOURCES

Chapter 2: Global Climate – Datasets and Sources

Section 2b Temperature			
Sub-section	General Variable or Phenomenon	Specific dataset or variable	Source
2b1	Temperature, [Near] Surface	Berkeley Earth	http://berkeleyearth.org/data/
2b1, 2b3	Temperature, [Near] Surface	ERA5	https://www.ecmwf.int/en/forecasts/datasets/reanalysis-datasets/era5
2b1	Temperature, [Near] Surface	HadCRUT5 Global Temperature	https://www.metoffice.gov.uk/hadobs/hadcrut5/
2b1	Temperature, [Near] Surface	CRUTEM5	https://www.metoffice.gov.uk/hadobs/crutem5/
2b1, 2b3	Temperature, [Near] Surface	HadSST4	https://www.metoffice.gov.uk/hadobs/hadsst4/
2b1, 2b4	Temperature, [Near] Surface	JRA-55 Atmospheric Reanalysis	https://search.diasjp.net/en/dataset/JRA55
2b1, 2b2	Temperature, [Near] Surface	NASA/GISS Global Temperature V4	https://data.giss.nasa.gov/gistemp/
2b1	Temperature, [Near] Surface	NOAA/NCEI NOAA GlobalTemp	https://www.ncei.noaa.gov/products/land-based-station/noaa-global-temp
2b2	Lake Temperature	ERA5	https://doi.org/10.24381/cds.adbb2d47
2b2	Lake Temperature	National Buoy Data Center Great Lakes Buoys	https://www.ndbc.noaa.gov/mobile/region.php?reg=great_lakes
2b2	Lake Temperature	Balaton Lakes	https://odp.met.hu/climate/observations_hungary/hourly/historical/
2b2	Lake Temperature	Canadian Lakes	https://www.meds-sdmm.dfo-mpo.gc.ca/isdm-gdsi/waves-vagues/data-donnees/index-eng.asp
2b2	Lake Temperature	Douglas Lake	https://uglos.mtu.edu/station_page.php?station=UMBIO
2b2	Lake Temperature	Trout Lake	https://portal.edirepository.org/nis/mapbrowse?scope=knb-lter-ntl&identifier=116&revision=27
2b2	Lake Temperature	ESA CCI LAKES LSWT v2.0.2	https://catalogue.ceda.ac.uk/uuid/a07deacaffb8453e93d57ee214676304

Sub-section	General Variable or Phenomenon	Specific dataset or variable	Source
2b2	Lake Temperature	Sentinel 3 Sea and Land Surface Temperature Radiometer (SLSTR)	https://sentinel.esa.int/web/sentinel/user-guides/sentinel-3-slstr/overview
2b3	Nighttime marine Air Temperature	CLASSmat	https://catalogue.ceda.ac.uk/uuid/5bbf48b128bd488dbb10a56111feb36a
2b3	Nighttime marine Air Temperature	UAHNMATv1	https://www.nsstc.uah.edu/climate/ , https://doi.org/10.1002/joc.6354
2b4	Sea Surface Temperature	NOAA Optimum Interpolation Sea Surface Temperature (OISST) v2.1	https://www.ncei.noaa.gov/products/optimum-interpolation-sst
2b4	Temperature, [Near] Surface	GHCNDEX	www.climdex.org/
2b4	Temperature, [Near] Surface	MERRA-2	http://gmao.gsfc.nasa.gov/reanalysis/MERRA-2/
2b4	Temperature, Upper Atmosphere	ERA5	https://www.ecmwf.int/en/forecasts/datasets/reanalysis-datasets/era5
2b4	Temperature, Upper Atmosphere	JRA-55 Atmospheric Reanalysis	http://jra.kishou.go.jp/JRA-55/index_en.html
2b5	Temperature, Upper Atmosphere	ERA5	https://www.ecmwf.int/en/forecasts/datasets/reanalysis-datasets/era5
2b5	Temperature, Upper Atmosphere	JRA-55 Atmospheric Reanalysis	http://jra.kishou.go.jp/JRA-55/index_en.html
2b5	Temperature, Upper Atmosphere	MERRA-2	http://gmao.gsfc.nasa.gov/reanalysis/MERRA-2/
2b5	Temperature, Upper Atmosphere	NOAA/NESDIS/STAR MSU v5	https://www.star.nesdis.noaa.gov/pub/smcd/emb/mscat/data/MSU_AMSU_v5.0/Monthly_Atmospheric_Layer_Mean_Temperature/
2b5	Temperature, Upper Atmosphere	RAOBCORE, RICH	https://imgw.univie.ac.at/forschung/klimadiagnose/raobcore/
2b5	Temperature, Upper Atmosphere	RATPAC A2	https://www.ncei.noaa.gov/products/weather-balloon/radiosonde-atmospheric-temperature-products
2b5	Temperature, Upper Atmosphere	RSS v4.0	https://www.remss.com/measurements/upper-air-temperature/
2b5	Temperature, Upper Atmosphere	UAH MSU v6.0	https://www.nsstc.uah.edu/data/msu/v6.0/
2b5	Temperature, Upper Atmosphere	UW MSU v1.0	https://pochedls.github.io/#!/data.md
2b5	Sea Surface Temperature	Niño 3.4 Index	https://psl.noaa.gov/gcos_wgsp/Timeseries/Nino34/
2b6	Temperature, Upper Atmosphere	Aura MLS	https://mls.jpl.nasa.gov/eos-aura-mls/data-products/temperature

Section 2c Cryosphere			
Sub-section	General Variable or Phenomenon	Specific dataset or variable	Source
2c1	Permafrost	Global Terrestrial Network for Permafrost (GTN-P)	http://gtnpdatabase.org/
2c1	Permafrost	GTN-P global mean annual ground temperature data for permafrost	https://doi.org/10.1594/PANGAEA.884711
2c1	Permafrost	Permafrost Temperature at Chinese (QTP) sites	https://nsidc.org/data/GGD700/versions/1
2c1	Permafrost	Permafrost Temperature at French sites	permafrance.osug.fr
2c1	Permafrost	Permafrost Temperature at Norwegian sites	https://cryo.met.no/
2c1, 2c2	Permafrost	Permafrost Temperature at Swiss sites (PERMOS)	www.permos.ch , https://www.permos.ch/doi/permos-dataset-2022-1
2c2	Rock Glacier Velocity	Regional Rock Glacier Velocity	Available from authors upon request. Austria: V. Kaufmann and A. Kellner-Pirklbauer, Central Asia: A. Kääh, Dry Andes: S. Vivero, France: X. Bodin, D. Cusicanqui and E. Thibert, Switzerland: R. Delaloye, J. Noetzli and C. Pellet
2c3	Glacier Mass, Area or Volume	World Glacier Monitoring Service	http://dx.doi.org/10.5904/wgms-fog-2022-09
2c3	Glacier Area	Copernicus Sentinel-2 MSI image	https://sentinels.copernicus.eu/web/sentinel/user-guides/sentinel-2-msi/overview
2c4	Lake Ice	ERA5	https://doi.org/10.24381/cds.adbb2d47
2c4	Lake Ice	Lake ice clearance and formation data for Green Lakes Valley, 1968 - ongoing. ver 5. Environmental Data Initiative	https://portal.edirepository.org/nis/mapbrowse?packageid=knb-lter-nwt.106.5
2c4	Lake Ice	Global Lake and River Ice Phenology Database, Version 1	https://doi.org/10.7265/N5W66HP8
2c4	Lake Ice	Mountain Lake Biology, Chemistry, Physics, and Climate Data since 1959 at Castle Lake ver 1. Environmental Data Initiative	https://doi.org/10.6073/pasta/a8e3b81cfe5864731b29ad42506c65d7
2c4	Lake Ice	Great Lakes Annual Maximum Ice Cover (%)	https://www.glerl.noaa.gov/data/ice/
2c4	Lake Ice	Great Lakes Ice	www.glerl.noaa.gov/data/ice

Sub-section	General Variable or Phenomenon	Specific dataset or variable	Source
2c4	Lake Ice	Geographic variation and temporal trends in ice phenology in Norwegian lakes during a century, Dryad	https://datadryad.org/stash/dataset/doi:10.5061/dryad.bk3j9kd9x
2c4	Temperature, [Near] Surface	NASA/GISS Global Temperature	https://data.giss.nasa.gov/gistemp/
2c5	Snow Properties	Northern Hemisphere (NH) Snow Cover Extent (SCE), Version 1	doi:10.7289/V5N014G9, www.snowcover.org

Section 2d Hydrological Cycle			
Sub-section	General Variable or Phenomenon	Specific dataset or variable	Source
2d1, 2d2	Humidity, [Near] Surface	ERA5	https://www.ecmwf.int/en/forecasts/datasets/reanalysis-datasets/era5
2d1, 2d2	Humidity, [Near] Surface	HadISDH	www.metoffice.gov.uk/hadobs/hadisdh , https://catalogue.ceda.ac.uk/uuid/251474c7b09449d8b9e7aeaf1461858f
2d1	Humidity, [Near] Surface	JRA-55 Atmospheric Reanalysis	http://jra.kishou.go.jp/JRA-55/index_en.html
2d1, 2d2	Humidity, [Near] Surface	MERRA-2	https://gmao.gsfc.nasa.gov/reanalysis/MERRA-2/
2d2	Water Vapor, Total Column	COSMIC	https://cdaac-www.cosmic.ucar.edu/
2d2	Water Vapor, Total Column	ERA5	https://www.ecmwf.int/en/forecasts/datasets/reanalysis-datasets/era5
2d2	Water Vapor, Total Column	GNSS Ground-Based Total Column Water Vapor	https://doi.org/10.25326/68
2d2	Water Vapor, Total Column	JRA-55 Atmospheric Reanalysis	http://jra.kishou.go.jp/JRA-55/index_en.html
2d2	Water Vapor, Total Column	MERRA-2	https://gmao.gsfc.nasa.gov/reanalysis/MERRA-2/
2d2	Water Vapor, Total Column	SSM/I -AMSR-E Ocean Total Column Water Vapor	http://www.remss.com
2d3	Humidity, Upper Atmosphere	Upper Troposphere Humidity (UTH)	Available on request to Brian Soden
2d3	Humidity, Upper Atmosphere	ERA5	https://www.ecmwf.int/en/forecasts/datasets/reanalysis-datasets/era5
2d3	Humidity, Upper Atmosphere	High Resolution Infrared Sounder (HIRS)	https://www.ncei.noaa.gov/products/climate-data-records/hirs-ch12-brightness-temperature

Sub-section	General Variable or Phenomenon	Specific dataset or variable	Source
2d3	Temperature, Upper Atmosphere	NOAA/NESDIS/STAR MSU v5	https://www.star.nesdis.noaa.gov/pub/smcd/emb/mscat/data/MSU_AMSU_v5.0/Monthly_Atmospheric_Layer_Mean_Temperature/
2d4, 2d5	Precipitation	GPCP	www.dwd.de/EN/ourservices/gpcc/gpcc.html
2d4	Precipitation	Global Precipitation Climatology Project (GPCP) v2.3	https://www.ncei.noaa.gov/products/global-precipitation-climatology-project
2d5	Precipitation	Global Historical Climatology Network daily (GHCNd)	https://www.ncei.noaa.gov/products/land-based-station/global-historical-climatology-network-daily
2d5	Precipitation	Climate Hazards Group InfraRed Precipitation with Station data (CHIRPS)	https://www.chc.ucsb.edu/data/chirps
2d5	Precipitation	Climate Extremes Index Component 4	https://www.ncdc.noaa.gov/extremes/cei/
2d5	Precipitation	ERA5	https://www.ecmwf.int/en/forecasts/datasets/reanalysis-datasets/era5
2d5	Precipitation	GHCN v4	www.ncdc.noaa.gov/temp-and-precip/ghcn-gridded-products/precipitation
2d5	Precipitation	GHCINDEX	www.climdex.org/
2d5	Precipitation	GPCP	www.dwd.de/EN/ourservices/gpcc/gpcc.html
2d5	Precipitation	MERRA-2	https://gmao.gsfc.nasa.gov/reanalysis/MERRA-2/
2d6	Cloud properties	PATMOS-x v6.0	https://www.ncei.noaa.gov/products/climate-data-records/avhrr-hirs-cloud-properties-patmos
2d6	Cloud Properties	Aqua MODIS C6.1 MYD08_M3	https://ladsweb.modaps.eosdis.nasa.gov/missions-and-measurements/products/MYD08_M3
2d6	Cloud Properties	Clouds and the Earth's Radiant Energy System Energy Balance and Filled (CERES EBAF) v4.2	https://ceres.larc.nasa.gov/data/
2d7	Lake Water Levels	NASA/CNES Topex/Poseidon and Jason satellite missions through the Global Reservoir and Lake Monitoring (G-REALM) project v2.5	https://ipad.fas.usda.gov/cropexplorer/global_reservoir/
2d7	Lake Water Levels	Theia's Hydroweb database	https://hydroweb.theia-land.fr
2d7	Lake Surface Area	HydroLAKES database	https://www.hydrosheds.org/products/hydrolakes
2d7	Lake Water Levels	Kraemer (2023) Lake Water Levels	https://zenodo.org/record/7635482

Sub-section	General Variable or Phenomenon	Specific dataset or variable	Source
2d8	Groundwater and terrestrial water storage	GRACE / GRACE-FO	https://podaac.jpl.nasa.gov/dataset/TELLUS_GRAC-GRFO_MASCON_CRI_GRID_RL06.1_V3
2d8	Lake Water Level	Database for Hydrological Time Series of Inland Waters (DAHITI) - Lake Kariba	https://dahiti.dgfi.tum.de/en/31/time_series/
2d9	Soil Moisture	Copernicus Climate Change Service (C3S) v202012 product based on the ESA Climate Change Initiative for Soil Moisture (ESA CCI SM) v05.2 merging algorithm	https://cds.climate.copernicus.eu/cdsapp#!/dataset/satellite-soil-moisture?tab=form
2d10	Drought	Climatic Research Unit gridded Time Series (CRU TS) 4.07	https://crudata.uea.ac.uk/cru/data/hrg/cru_ts_4.07/
2d11	Land Evaporation	Climatic Research Unit gridded Time Series (CRU TS) 4.07	www.gleam.eu/
2d11	Modes of Variability	Southern Oscillation Index	https://crudata.uea.ac.uk/cru/data/soi/

Section 2e Atmospheric Circulation

Sub-section	General Variable or Phenomenon	Specific dataset or variable	Source
2e1	Modes of Variability	Antarctic Oscillation (AAO)/Southern Annular Mode (SAM)	https://ftp.cpc.ncep.noaa.gov/cwlinks/norm.daily.aao.index.b790101.current.ascii
2e1	Pressure, Sea Level or Near-Surface	ERA5	https://www.ecmwf.int/en/forecasts/datasets/reanalysis-datasets/era5
2e1	Pressure, Sea Level or Near-Surface	NCEP/NCAR Reanalysis	www.esrl.noaa.gov/psd/data/gridded/data.ncep.reanalysis.html
2e2	Modes of Variability	Antarctic Oscillation (AAO)/Southern Annular Mode (SAM)	https://ftp.cpc.ncep.noaa.gov/cwlinks/norm.daily.aao.index.b790101.current.ascii
2e2	Wind, [Near] Surface	ERA5	https://www.ecmwf.int/en/forecasts/datasets/reanalysis-datasets/era5
2e2	Wind, [Near] Surface	HadISD v3.3.0.2022f	https://hadleyserver.metoffice.gov.uk/hadisd/v330_2022f/index.html
2e2	Wind, [Near] Surface	Modern-Era Retrospective Analysis for Research and Applications version 2 (MERRA-2)	http://gmao.gsfc.nasa.gov/reanalysis/MERRA-2/
2e2	Wind [Near Surface]	Remote Sensing System (RSS) Merged 1-deg monthly radiometer winds	https://www.remss.com/measurements/wind/

Sub-section	General Variable or Phenomenon	Specific dataset or variable	Source
2e2	Wind [Near Surface]	Remote Sensing System (RSS) Advanced Scatterometer (ASCAT)	https://www.remss.com/missions/ascats/
2e2	Wind [Near Surface]	Remote Sensing System (RSS) QuickScat4	https://www.remss.com/missions/qscats/
2e3	Wind [Upper Atmosphere]	Integrated Global Radiosonde Archive (for Quasi biennial Oscillation, QBO)	https://www.ncei.noaa.gov/products/weather-balloon/integrated-global-radiosonde-archive
2e3	Modes of Variability	Antarctic Oscillation (AAO), Southern Annular Mode (SAM)	https://www.cpc.ncep.noaa.gov/products/precip/CWlink/daily_ao_index/ao/ao.shtml , http://www.nerc-bas.ac.uk/icd/gjma/sam.html
2e3	Wind [Upper Atmosphere]	ERA5 hourly data on pressure levels from 1940 to present. Copernicus Climate Change Service (C3S) Climate Data Store (CDS)	https://cds.climate.copernicus.eu/cdsapp#!/dataset/reanalysis-era5-pressure-levels?tab=overview
2e3	Wind [Upper Atmosphere]	ERA-Interim	www.ecmwf.int/en/research/climate-reanalysis/era-interim
2e3	Wind [Upper Atmosphere]	MERRA-2	http://gmao.gsfc.nasa.gov/reanalysis/MERRA-2/
2e3	Wind [Upper Atmosphere]	JRA-55 Atmospheric Reanalysis	http://jra.kishou.go.jp/JRA-55/index_en.html
2e4	Lightning	Lightning Imaging Sensor (LIS) on International Space Station (ISS) Science Data Version 1	http://dx.doi.org/10.5067/LIS/ISSLIS/DATA108
2e4	Lightning	Lightning Imaging Sensor (LIS) on TRMM Science Data V4	http://dx.doi.org/10.5067/LIS/LIS/DATA201
2e4	Lightning	Optical Transient Detector (OTD) Lightning v1	http://dx.doi.org/10.5067/LIS/OTD/DATA101
2e4	Lightning	GOES-R Geostationary Lightning Mapper (GLM) Gridded Data Products V1	http://dx.doi.org/10.5067/GLM/GRID/DATA101

Section 2f Earth's Radiation Budget			
Sub-section	General Variable or Phenomenon	Specific dataset or variable	Source
2f1	TOA Earth Radiation Budget	CERES Energy Balanced and Filled version 4.2	https://ceres-tool.larc.nasa.gov/ord-tool/jsp/EBAFTOA42Selection.jsp
2f1	TOA Earth Radiation Budget	CERES FLASHflux version 4A	https://ceres-tool.larc.nasa.gov/ord-tool/jsp/FLASH_TISASelection.jsp
2f1	TOA Earth Radiation Budget	TSIS TIM Level 3 Total Solar Irradiance 24-hour Means	doi:10.5067/TSIS/TIM/DATA306
2f2	Solar Transmission, Apparent	HYSPLIT	https://www.ready.noaa.gov/HYSPLIT.php
2f2	Solar Transmission, Apparent	Mauna Loa Observatory	https://www.esrl.noaa.gov/gmd/webdata/grad/mloapt/mauna_loa_transmission.dat
2f2	Cloud Aerosol	Cloud-Aerosol LIDAR and Infrared Pathfinder Satellite Observations (CALIPSO)	http://www-calipso.larc.nasa.gov
2f2	Ozone, Stratospheric	Ozone Mapping and Profiler Suite (OMPS)	https://ozoneaq.gsfc.nasa.gov/data/ozone/
2f2	Ozone, Stratospheric	Stratospheric Aerosol and Gas Experiment (SAGE) limb sounder	https://asdc.larc.nasa.gov/project/SAGE%20III-ISS

Section 2g Atmospheric Composition			
Sub-section	General Variable or Phenomenon	Specific dataset or variable	Source
2g1	Trace Gases	Atmospheric Gas trends	www.esrl.noaa.gov/gmd/ccgg/trends
2g1	Trace Gases	Global Greenhouse Gas Reference Network	https://gml.noaa.gov/ccgg/about.html
2g1	Trace Gases	Atmospheric Greenhouse Gas Index (AGGI)	www.esrl.noaa.gov/gmd/aggi
2g2	Trace Gases	Halocarbons and other Atmospheric Trace Species	https://gml.noaa.gov/aftp/data/hats/
2g2	Trace Gases	Advanced Global Atmospheric Gases Experiment	https://agage2.eas.gatech.edu/data_archive/global_mean/global_mean_ms.txt
2g2	Trace Gases	Ozone-Depleting Gas Index (ODGI)	www.esrl.noaa.gov/gmd/odgi
2g3	Aerosols	Advanced Along Track Scanning Radiometer (AATSr)	https://earth.esa.int/eogateway/instruments/aatsr

Sub-section	General Variable or Phenomenon	Specific dataset or variable	Source
2g3	Aerosols	Copernicus Atmosphere Monitoring Service Reanalysis (CAMSRA)	https://ads.atmosphere.copernicus.eu/cdsapp#!/dataset/cams-global-radiative-forcing-auxilliary-variables?tab=overview
2g4	Ozone, Total Column and Stratospheric	GOME/SCIAMACHY/GOME2 (GSG) Merged Total Ozone	http://www.iup.uni-bremen.de/UVSAT/datasets/merged-wfdoas-total-ozone
2g4	Ozone, Total Column and Stratospheric	GOME/SCIAMACHY/GOME2 (GTO) Merged Total Ozone	https://atmos.eoc.dlr.de/gto-ecv
2g4	Ozone, Total Column and Stratospheric	GOZCARDS ozone profiles	https://www.earthdata.nasa.gov/esds/competitive-programs/measures/gozcards
2g4	Ozone, Total Column and Stratospheric	Multi Sensor Reanalysis (MSR-2) of total ozone	http://www.temis.nl/protocols/O3global.html
2g4	Ozone, Total Column and Stratospheric	NASA BUV/SBUV/OMPS v8.7 (MOD) Merged Ozone	https://acd-ext.gsfc.nasa.gov/Data_services/merged/
2g4	Ozone, Total Column and Stratospheric	NOAA SBUV V8.6 OMPS V4r1 cohesive data set (COH)	ftp://ftp.cpc.ncep.noaa.gov/SBUV_CDR/
2g4	Ozone, Total Column and Stratospheric	Network for the Detection of Atmospheric Composition Change (NDACC) lidar, microwave and FTIR	https://www-air.larc.nasa.gov/missions/ndacc
2g4	Ozone, Total Column and Stratospheric	SAGE/OSIRIS	Bourassa et al. (2018) doi:10.5194/amt-11-489-2018
2g4	Ozone, Total Column and Stratospheric	SAGE-SCIA-OMPS	Arosio et al., (2018) doi:10.5194/amt-2018-275
2g4	Ozone, Total Column and Stratospheric	SWOOSH	www.esrl.noaa.gov/csd/groups/csd8/swoosh/
2g4	Ozone, Total Column and Stratospheric	WOUDC Ground-based Ozone	ftp://tor.ec.gc.ca/cd/pub/woudc/Projects_Campaigns/ZonalMeans
2g5	Stratospheric Water Vapor	the Aura Microwave Limb Sounder version 5.0 data, as merged into SWOOSH	www.esrl.noaa.gov/csd/groups/csd8/swoosh/
2g5	Tropopause Temperature	MERRA-2	http://gmao.gsfc.nasa.gov/reanalysis/MERRA-2/
2g5	Stratospheric Water Vapor	NOAA Frostpoint Hygrometer (FPH)	https://gml.noaa.gov/aftp/data/ozwv/WaterVapor/
2g5	Stratospheric Water Vapor	Cryogenic Frostpoint Hygrometer (CFH)	https://ndacc.org
2g6	Ozone, Tropospheric	NOAA Global Monitoring Laboratory	https://gml.noaa.gov/aftp/data/ozwv/SurfaceOzone/
2g7	Trace Gases	Copernicus Atmosphere Monitoring Service Reanalysis (CAMSRA) for Carbon Monoxide	https://ads.atmosphere.copernicus.eu/cdsapp#!/dataset/cams-global-radiative-forcing-auxilliary-variables?tab=overview

Section 2h Land Surface Properties			
Sub-section	General Variable or Phenomenon	Specific dataset or variable	Source
2h1	Albedo	MODIS/Terra+Aqua BRDF/Albedo Albedo Daily L3 Global 0.05Deg CMG V061	https://lpdaac.usgs.gov/products/mcd43c3v061/
2h2	fraction of absorbed photosynthetically active radiation (FAPAR)	JRC TIP MODIS	https://fapar.jrc.ec.europa.eu
2h2	FAPAR	MERIS	https://fapar.jrc.ec.europa.eu
2h2	FAPAR	SeaWiFS FAPAR	http://fapar.jrc.ec.europa.eu/
2h3	Biomass, Greenness or Burning	GFAS v1.4	ftp://ftp.mpic.de/GFAS/sc17 (special reprocessing)
2h3	Biomass, Greenness or Burning	Modis Fire Power Radiative Product	https://lpdaac.usgs.gov/products/mod14v061/ , https://lpdaac.usgs.gov/products/myd14v061/
2h3	Biomass, Greenness or Burning	Global Fire Emissions Database	https://www.globalfiredata.org/data.html
2h3	Deforestation	PRODES Amazonia	http://www.obt.inpe.br/OBT/assuntos/programas/amazonia/prodes
2h4	Phenology	MODIS Normalized Difference Vegetative Index	https://modis.gsfc.nasa.gov/data/dataproduct/mod13.php
2h4	Temperature [Near] Surface	MERRIS-2 monthly temperature	https://goldsmr4.gesdisc.eosdis.nasa.gov/data/MERRA2_MONTHLY/M2TMNXLND.5.12.4/
2h4	Phenology	USA-National Phenology Network (NPN)	https://www.usanpn.org/data/observational
2h4	Phenology	German oak phenology data	https://opendata.dwd.de/
2h4	Phenology	Harvard Forest	https://harvardforest1.fas.harvard.edu/exist/apps/datasets/showData.html?id=hf003
2h4	Phenology	Natures Calendar	https://naturescalendar.woodlandtrust.org.uk/
2h4	Phenology	PhenoCam	http://phenocam.sr.unh.edu
2h4	Phenology	UK Cumbrian lakes data	https://catalogue.ceh.ac.uk/documents/bf30d6aa-345a-4771-8417-ffbfc8c08c28/
2h5	Vegetation Optical Depth	Global Long-term Microwave Vegetation Optical Depth Climate Archive (VODCA_	https://zenodo.org/record/2575599
2h5	Modes of Variability	Southern Oscillation Index	http://www.bom.gov.au/climate/enso/soi/

Sidebar 2.1 Assessing Humid heat extremes over land

Sub-section	General Variable or Phenomenon	Specific dataset or variable	Source
SB2.1	Temperature [Near] Surface	WMO Climpact indices	https://climpact-sci.org/
SB2.1	Temperature [Near] Surface	HadISDH.extremes v1.0.0.2022f	https://catalogue.ceda.ac.uk/uuid/2d1613955e1b4cd1b156e5f3edbd7e66 , https://www.metoffice.gov.uk/hadobs/hadisdh/

Sidebar 2.2 Hunga Tonga–Hunga Ha‘apai eruption

Sub-section	General Variable or Phenomenon	Specific dataset or variable	Source
SB2.2	Stratospheric Aerosol	Suomi National Polar-Orbiting Partnership OMPS Limb Profiler data.	https://www.earthdata.nasa.gov/sensors/omps
SB2.2	Ozone, Total Column and Stratospheric	Aura MLS	https://disc.gsfc.nasa.gov/datasets?page=1&source=AURA%20MLS
SB2.2	Stratospheric Water Vapor	Aura MLS	https://disc.gsfc.nasa.gov/datasets?page=1&source=AURA%20MLS
SB2.2	Temperature upper atmosphere	Aura MLS	https://disc.gsfc.nasa.gov/datasets?page=1&source=AURA%20MLS

Section 3b Sea Surface Temperature			
Sub-section	General Variable or Phenomenon	Specific dataset or variable	Source
3b	Sea Surface Temperature	ERSSTv5	https://doi.org/10.7289/V5T72FNM
3b	Sea Surface Temperature	HadSST4	https://www.metoffice.gov.uk/hadobs/hadsst4/
3b	Sea Surface Temperature	NOAA Daily Optimum Interpolated Temperature (DOISST)	https://doi.org/10.25921/RE9P-PT57

Section 3c Ocean Heat Content			
Sub-section	General Variable or Phenomenon	Specific dataset or variable	Source
3c	Ocean Heat Content	Argo	http://doi.org/10.17882/42182#98916
3c	Ocean Heat Content	Argo monthly climatology	https://sio-argo.ucsd.edu/RG_Climatology.html
3c	Ocean Heat Content	CLIVAR and Carbon Hydrographic Data Office	https://cchdo.ucsd.edu/
3c	Ocean Heat Content	IAP/CAS	http://www.ocean.iap.ac.cn/pages/dataService/dataService.html
3c	Ocean Heat Content	MRI/JMA	www.data.jma.go.jp/gmd/kaiyou/english/ohc/ohc_global_en.html
3c	Ocean Heat Content	NCEI	https://www.ncei.noaa.gov/access/global-ocean-heat-content/
3c	Ocean Heat Content	PMEL/JPL/JIMAR	http://oceans.pmel.noaa.gov
3c	Ocean Heat Content	UK Met Office EN4.2.2	https://www.metoffice.gov.uk/hadobs/en4/download-en4-2-2.html
3c	Ocean Salinity	Argo	https://usgodae.org/argo/argo.html

Section 3d Salinity			
Sub-section	General Variable or Phenomenon	Specific dataset or variable	Source
3d2	Ocean Salinity	Aquarius V3.0	http://podaac.jpl.nasa.gov/aquarius
3d2	Ocean Salinity	Argo	https://usgodae.org/argo/argo.html
3d2	Ocean Salinity	Blended Analysis for Surface Salinity	ftp://ftp.cpc.ncep.noaa.gov/precip/BASS
3d2	Ocean Salinity	SMAP	https://podaac.jpl.nasa.gov/SMAP
3d2	Ocean Salinity	SMOS	https://earth.esa.int/eogateway/missions/smos

Sub-section	General Variable or Phenomenon	Specific dataset or variable	Source
3d2	Ocean Salinity	World Ocean Atlas 2013	www.nodc.noaa.gov/OC5/woa13/
3d3	Ocean Salinity	NCEI salinity anomaly	https://www.ncei.noaa.gov/access/global-ocean-heat-content/
3d3	Ocean Salinity	World Ocean Atlas 2018	www.nodc.noaa.gov/OC5/woa18/

Section 3e Global ocean heat, freshwater, and momentum flux			
Sub-section	General Variable or Phenomenon	Specific dataset or variable	Source
3e1	Air-sea fluxes (shortwave/longwave radiation)	CERES Energy Balanced and Filled version 4.2	https://asdc.larc.nasa.gov/project/CERES/CERES_EBAF_Edition4.2
3e1	Air-sea fluxes (shortwave/longwave radiation)	CERES FLASHflux 4A product	https://cmr.earthdata.nasa.gov/search/concepts/C1719147151-LARC_ASDC.html
3e1	Air-sea fluxes (latent heat/sensible heat)	ERA5	https://www.ecmwf.int/en/forecasts/datasets/reanalysis-datasets/era5
3e2	Precipitation	Global Precipitation Climatology Project (GPCP) v2.3	https://psl.noaa.gov/data/gridded/data.gpcp.html
3e2	Evaporation	ERA5	https://www.ecmwf.int/en/forecasts/datasets/reanalysis-datasets/era5
3e3	Wind stress	ERA5	https://www.ecmwf.int/en/forecasts/datasets/reanalysis-datasets/era5

Section 3f Sea Level variability and change			
Sub-section	General Variable or Phenomenon	Specific dataset or variable	Source
3f	Ocean Heat Content	Argo monthly climatology	https://sio-argo.ucsd.edu/RG_Climatology.html
3f	Ocean Mass	GRACE/GRACE FO	https://grace.jpl.nasa.gov/data/get-data
3f	Sea Level / Sea Surface Height	Argo	https://usgodae.org/argo/argo.html
3f	Sea Level / Sea Surface Height	NASA MEaSURES	https://podaac.jpl.nasa.gov/dataset/SEA_SURFACE_HEIGHT_ALT_GRIDS_L4_2SATS_5DAY_6THDEG_V_JPL2205
3f	Sea Level/Sea Surface Height	NASA Sea Level Change Program	https://podaac.jpl.nasa.gov/dataset/MERGED_TP_J1_OSTM_OST_ALL_V51
3f	Sea Level / Sea Surface Height	NCEI steric sea level	https://www.ncei.noaa.gov/access/global-ocean-heat-content/
3f	Sea Level / Sea Surface Height	NOAA Laboratory for Sea Level Altimetry	www.star.nesdis.noaa.gov/sod/lssa/SeaLevelRise/LSA_SLR_timeseries.php

Sub-section	General Variable or Phenomenon	Specific dataset or variable	Source
3f	Sea Level / Sea Surface Height	Tide Gauge	http://uhslc.soest.hawaii.edu/
3f	Sea Level / Sea Surface Height	University of Texas Center for Space Research Gravity field	https://podaac.jpl.nasa.gov/dataset/TELLUS_GRAC_L3_CSR_RL06_OCN_v04

Section 3g Surface Currents			
Sub-section	General Variable or Phenomenon	Specific dataset or variable	Source
3g	ocean currents	Global Drifter Program	https://www.aoml.noaa.gov/phod/gdp/
3g	ocean currents	Ocean Surface Current Analysis - Real time (OSCAR)	https://www.esr.org/research/oscar/oscar-surface-currents/
3g3	ocean currents	Atlantic ocean monitoring	https://www.aoml.noaa.gov/phod/altimetry/cvar/

Section 3h Meridional Overturning Circulation and Heat Transport in the Atlantic Ocean			
Sub-section	General Variable or Phenomenon	Specific dataset or variable	Source
3h	ocean currents	Atlantic Ship of Opportunity XBT	https://www.aoml.noaa.gov/phod/goos/xbt_network/
3h	ocean currents	Argo	https://usgodae.org/argo/argo.html
3h	ocean currents	Florida Current transport	https://www.aoml.noaa.gov/phod/floridacurrent/data_access.php
3h	ocean currents	Global Temperature and Salinity Profile Program (GTSPP)	https://www.ncei.noaa.gov/products/global-temperature-and-salinity-profile-programme
3h	ocean currents	MOVE array	http://www.oceansites.org/tma/move.html
3h	ocean currents	OSNAP	https://www.o-snap.org/
3h	ocean currents	RAPID array	https://rapid.ac.uk/rapidmoc/
3h	ocean currents	SAMBA	http://www.oceansites.org/tma/samba.html

Section 3i Global Ocean Phytoplankton			
Sub-section	General Variable or Phenomenon	Specific dataset or variable	Source
3i	Phytoplankton, Ocean Color	MODIS-Aqua	https://oceancolor.gsfc.nasa.gov/reprocessing/

Section 3j Global Ocean Carbon Cycle			
Sub-section	General Variable or Phenomenon	Specific dataset or variable	Source
3j2	Ocean Carbon	SOCAT version 2022	https://doi.org/10.25921/r7xa-bt92
3j2	Sea Surface Temperature	NOAA Optimum Interpolation SST (OISST) v2.1	https://www.ncei.noaa.gov/products/optimum-interpolation-sst
3j2	Chlorophyll	GlobColour	https://www.globcolour.info/
3j2	Atmospheric Carbon Dioxide	NOAA Greenhouse Gas Marine Boundary Layer Reference	https://gml.noaa.gov/ccgg/mbl/mbl.html
3j2	Winds [Near] Surface	ERA5	https://www.ecmwf.int/en/forecasts/datasets/reanalysis-datasets/era5
3j2	Ocean Salinity	Hadley Center EN4	https://www.metoffice.gov.uk/hadobs/en4/
3j3	Ocean Temperature	Argo monthly climatology	https://sio-argo.ucsd.edu/RG_Climatology.html
3j3	Ocean Salinity	Argo monthly climatology	https://sio-argo.ucsd.edu/RG_Climatology.html

Sidebar 3.1 The 2020–22 triple-dip La Niña			
Sub-section	General Variable or Phenomenon	Specific dataset or variable	Source
SB3.1	Sea Surface Temperature	ERSSTv5	https://doi.org/10.7289/V5T72FNM
SB3.1	Winds [Upper Atmosphere]	NCEP/DOE Reanalysis 2	https://www.cpc.ncep.noaa.gov/products/wesley/reanalysis2/
SB3.1	Precipitation	NCEP/DOE Reanalysis 2	https://www.cpc.ncep.noaa.gov/products/wesley/reanalysis2/
SB3.1	Precipitation	Global Precipitation Climatology Project (GPCP)	https://www.ncei.noaa.gov/products/climate-data-records/precipitation-gpcp-monthly
SB3.1	Sea Surface Temperature	HadISST	https://www.metoffice.gov.uk/hadobs/hadisst/
SB3.1	Temperature [Near] Surface	Global Temperature Anomalies	https://www.ncei.noaa.gov/access/monitoring/global-temperature-anomalies/anomalies

Sidebar 3.2 Tracking global ocean oxygen content			
Sub-section	General Variable or Phenomenon	Specific dataset or variable	Source
SB3.2	Ocean dissolved oxygen content	GLODAP v2	https://www.ncei.noaa.gov/access/ocean-carbon-acidification-data-system/oceans/GLODAPv2_2022/
SB3.2	Ocean dissolved oxygen content	GOBAI-O ₂	https://www.pmel.noaa.gov/gobai/

Section 4b ENSO and the tropical Pacific			
Sub-section	General Variable or Phenomenon	Specific dataset or variable	Source
4b	Sea Surface Temperature	ERSSTv5	https://doi.org/10.7289/V5T72FNM
4b1	Sea Surface Temperature	NOAA Optimum Interpolation SST (OISST)v2.1	https://www.ncei.noaa.gov/products/optimum-interpolation-sst
4b1	Subsurface ocean temperature	Global Ocean Data Assimilation System (GODAS, Behringer, 2007)	https://www.cpc.ncep.noaa.gov/products/GODAS/
4b2	Outgoing longwave radiation	NCEP CPC OLR (Liebmann and Smith, 1996)	https://www.cpc.ncep.noaa.gov/products/global_precip/html/wpage_olr.html
4b3	wind vectors/wind speed	NCEP NCAR reanalysis 1	https://psl.noaa.gov/data/gridded/data.ncep.reanalysis.html

Section 4c Tropical Intraseasonal Activity			
Sub-section	General Variable or Phenomenon	Specific dataset or variable	Source
4c	Outgoing longwave radiation	HIRS OLR (Schreck et al. 2018)	https://www.ncei.noaa.gov/access/metadata/landing-page/bin/iso?id=gov.noaa.ncdc:C00875
4c	wind velocity potential anomalies	Climate Forecast System Reanalysis (CFSR)	https://climatedataguide.ucar.edu/climate-data/climate-forecast-system-reanalysis-cfsr
4c	Subsurface ocean heat content	Global Ocean Data Assimilation System (GODAS, Behringer et al. 1998)	https://www.cpc.ncep.noaa.gov/products/GODAS/

Section 4d Intertropical Convergence Zone			
Sub-section	General Variable or Phenomenon	Specific dataset or variable	Source
4d1	Precipitation	Multisource weighted ensemble precipitation (MSWEP v2.8)	https://www.gloh2o.org/mswep/
4d2	Sea level pressure	NCEP NCAR reanalysis 1	https://psl.noaa.gov/data/gridded/data.ncep.reanalysis.html
4d2	Precipitation	Integrated Multi-satellitE Retrievals for GPM (IMERG)	https://gpm.nasa.gov/data/imerg
4d2	Outgoing Longwave Radiation	NCEP CPC OLR (Liebmann and Smith, 1996)	https://www.cpc.ncep.noaa.gov/products/global_precip/html/wpage_olr.html
4d2	Sea Surface Temperature	NOAA Optimum Interpolation SST (OISST)v2.1	https://www.ncei.noaa.gov/products/optimum-interpolation-sst

Section 4e Global Monsoon Summary			
Sub-section	General Variable or Phenomenon	Specific dataset or variable	Source
4e	Precipitation	Global Precipitation Climatology Project (GPCP)	https://www.ncei.noaa.gov/products/climate-data-records/precipitation-gpcp-monthly
4e	Sea Surface Temperature	ERSSTv5	https://doi.org/10.7289/V5T72FNM
4e	Sea Surface Temperature	HadISST	https://www.metoffice.gov.uk/hadobs/hadisst/
4e	Wind, [Near] Surface	ERA5	https://www.ecmwf.int/en/forecasts/datasets/reanalysis-datasets/era5
4e	Wind, Upper Atmosphere	ERA5	https://www.ecmwf.int/en/forecasts/datasets/reanalysis-datasets/era5

Section 4f Indian Ocean Dipole			
Sub-section	General Variable or Phenomenon	Specific dataset or variable	Source
4f	Precipitation	Climate Prediction Center (CPC) Merged Analysis of Precipitation (CMAP)	https://www.cpc.ncep.noaa.gov/products/global_precip/html/wpage.cmap.html
4f	Sea Surface Temperature	NOAA Optimum Interpolation SST (OISST)v2	https://www.ncei.noaa.gov/products/optimum-interpolation-sst
4f	Wind, [Near] Surface	JRA-55 Atmospheric Reanalysis	http://jra.kishou.go.jp/JRA-55/index_en.html

Section 4g Tropical Cyclones			
Sub-section	General Variable or Phenomenon	Specific dataset or variable	Source
4g1, 4g5, 4g6, 4g7	Tropical Cyclone Data	International Best Track Archive for Climate Stewardship (IBTrACS)	https://www.ncei.noaa.gov/products/international-best-track-archive
4g2	Tropical Cyclone Data	Hurdat2	www.aoml.noaa.gov/hrd/hurdat/Data_Storm.html
4g2, 4g4	Sea Surface Temperature	ERSSTv5	https://doi.org/10.7289/V5T72FNM
4g2	Outgoing Longwave Radiation	NCEP CPC OLR (Liebmann and Smith, 1996)	https://www.cpc.ncep.noaa.gov/products/global_precip/html/wpage.olr.html
4g2, 4g4	Wind, [Near] Surface	ERA5	https://www.ecmwf.int/en/forecasts/datasets/reanalysis-datasets/era5
4g3, 4g5, 4g6	Sea Surface Temperature	NOAA Optimum Interpolation SST (OISST)v2	https://www.ncei.noaa.gov/products/optimum-interpolation-sst

Sub-section	General Variable or Phenomenon	Specific dataset or variable	Source
4g3	Wind, [Near] Surface	Climate Forecast System Reanalysis (CFSR)	https://climatedataguide.ucar.edu/climate-data/climate-forecast-system-reanalysis-cfsr
4g3, 4g5	Outgoing longwave radiation	HIRS OLR (Schreck et al. 2018)	https://www.ncei.noaa.gov/access/metadata/landing-page/bin/iso?id=gov.noaa.ncdc:C00875
4g4	Tropical Cyclone Data	RSMC-Tokyo, JMA best-track data	www.jma.go.jp/jma/jma-eng/jma-center/rsmc-hp-pub-eg/besttrack.html
4g5	Wind, [Near] Surface	Climate Forecast System Reanalysis (CFSR)	https://climatedataguide.ucar.edu/climate-data/climate-forecast-system-reanalysis-cfsr
4g6	Temperature, [Near] Surface	GHCNDEX	www.climdex.org/
4g6	Wind, [Near] Surface	Climate Forecast System Reanalysis (CFSR)	https://climatedataguide.ucar.edu/climate-data/climate-forecast-system-reanalysis-cfsr
4g8	Tropical Cyclone Data	Southwest Pacific Enhanced Archive of Tropical Cyclones (SPEARTC)	http://apdrc.soest.hawaii.edu/projects/speartc

Sidebar 4.1 Hurricanes Fiona and Ian: A pair of impactful North Atlantic major hurricanes

Sub-section	General Variable or Phenomenon	Specific dataset or variable	Source
SB4.1	Floods	United States Geological Survey Flood Event Viewer	https://stn.wim.usgs.gov/FEV/

Sidebar 4.2 Tropical cyclone contributions during the 2022 North American Monsoon

Sub-section	General Variable or Phenomenon	Specific dataset or variable	Source
SB4.2	Precipitation	Parameter-elevation Relationships on Independent Slopes Model (PRISM)	https://prism.oregonstate.edu/

Section 5b Surface Air Temperature			
Sub-section	General Variable or Phenomenon	Specific dataset or variable	Source
5b2	Temperature, [Near] Surface	NASA GISTEMP v4	https://data.giss.nasa.gov/gistemp/
5b3	Temperature, [Near] Surface	NCEP/NCAR Reanalysis 1	https://psl.noaa.gov/data/gridded/data.ncep.reanalysis.html
5b3	Pressure, Sea Level or Near-Surface	ERA5	https://www.ecmwf.int/en/forecasts/datasets/reanalysis-datasets/era5
5b3	Precipitation	ERA5	https://www.ecmwf.int/en/forecasts/datasets/reanalysis-datasets/era5

Section 5c Precipitation			
Sub-section	General Variable or Phenomenon	Specific dataset or variable	Source
5c2, 5c3, 5c4	Precipitation	ERA5	https://www.ecmwf.int/en/forecasts/datasets/reanalysis-datasets/era5
5c3	Precipitation	GPCC	https://opendata.dwd.de/climate_environment/GPCC/html/download_gate.html

Section 5d Sea Surface Temperature			
Sub-section	General Variable or Phenomenon	Specific dataset or variable	Source
5d	Sea Surface Temperature	NOAA Optimum Interpolation SST (OISST) v2	https://www.ncei.noaa.gov/products/optimum-interpolation-sst
5d	Sea Ice Concentration	NOAA NSIDC Climate Data Record of Passive Microwave Sea Ice Concentration, Version 4	https://nsidc.org/data/g02202
5d	Sea Ice Concentration	NOAA/NSIDC Climate Data Record of Passive Microwave Sea Ice Concentration, Version 2	https://nsidc.org/data/g10016

Section 5e Sea Ice			
Sub-section	General Variable or Phenomenon	Specific dataset or variable	Source
5e1	Sea Ice Extent	NSIDC Sea Ice Extent	https://nsidc.org/data/g02135
5e2	Sea Ice Thickness	Cryosat-2/SMOS	https://earth.esa.int/eogateway/catalog/smos-cryosat-l4-sea-ice-thickness
5e2	Sea Ice Thickness	ICESat-2	https://icesat-2.gsfc.nasa.gov/icesat-2-data

Section 5f Greenland Ice Sheet			
Sub-section	General Variable or Phenomenon	Specific dataset or variable	Source
5f	Albedo	MODIS (Greenland)	https://nsidc.org/data/MODGRNLD/versions/1
5f	Glacier Ablation	PROMICE Glacier Front Line (Greenland)	https://doi.org/10.22008/promice/data/calving_front_lines
5f	Glacier Mass, Area or Volume	Gravity Recovery and Climate Experiment Follow-on (GRACE-FO)	https://grace.jpl.nasa.gov/data/get-data/
5f	Air temperature	DMI/PROMICE Weather Stations	http://polarportal.dk/en/weather/historisk-vejr/#:~:text=DMI%20has%20a%20number%20of,go%20back%20almost%20250%20years.&text=One%20cannot%20expect%20that%20temperature%20observations%20spanning%20centuries%20are%20homogeneous.
5f	Ice Sheet Melt	Special Sensor Microwave Imager/Sounder (SSMIS)	https://nsidc.org/data/nsidc-0001
5f	Ice Sheet Albedo	Moderate Resolution Imaging Spectroradiometer (MODIS)	https://nsidc.org/data/MODGRNLD/versions/1
5f	Ice Sheet Albedo	Sentinel-3	https://cds.climate.copernicus.eu/cdsapp#!/dataset/satellite-albedo?tab=overview
5f	Ice Sheet Discharge	Ice Discharge (Greenland)	https://doi.org/10.22008/promice/data/ice_discharge/d/v02
5f	Ice Sheet Surface Mass Balance	Modèle Atmosphérique Régionale surface mass	https://mar.cnrs.fr/

Section 5g Terrestrial Snow Cover			
Sub-section	General Variable or Phenomenon	Specific dataset or variable	Source
5g	Snow Mass	GRACE / GRACE-FO	https://grace.jpl.nasa.gov/data/get-data/
5g	Snow Properties	Crocus Snowpack Model	http://www.umr-cnrm.fr/spip.php?article265
5g	Snow Properties	ERA5	https://www.ecmwf.int/en/forecasts/datasets/reanalysis-datasets/era5
5g	Snow Properties	MERRA-2	http://gmao.gsfc.nasa.gov/reanalysis/MERRA-2/
5g	Snow Properties	NOAA Interactive Multi-sensor Snow and Ice Mapping System (Snow Cover Duration)	https://usicecenter.gov/Products/lmsHome
5g	Snow Properties	Northern Hemisphere (NH) Snow Cover Extent (SCE), Version 1	http://doi.org/10.7289/V5N014G9
5g	Snow Properties	Snow CCI	http://snow-cci.enveo.at/

Section 5h Arctic river discharge			
Sub-section	General Variable or Phenomenon	Specific dataset or variable	Source
5h	River Discharge	ArcticGRO Discharge	https://arcticgreativers.org/

Section 5i Permafrost			
Sub-section	General Variable or Phenomenon	Specific dataset or variable	Source
5i1	Permafrost	Global Terrestrial Network for Permafrost (GTN-P)	http://gtnpdatabase.org/
5i1	Permafrost	Permafrost Temperature	http://permafrost.gi.alaska.edu/sites_map
5i1	Temperature, [Near] Surface	ERA5 Copernicus Climate Store	https://cds.climate.copernicus.eu
5i2	Permafrost	CALM Active Layer Thickness	www2.gwu.edu/~calm/

Section 5j Tundra Greenness			
Sub-section	General Variable or Phenomenon	Specific dataset or variable	Source
5j	Vegetative Index	Global Inventory Modeling and Mapping Studies (GIMMS) 3gv1	https://iridl.ldeo.columbia.edu/SOURCES/.NASA/.ARC/.ECOCAST/.GIMMS/.NDVI3g/.v1p0/index.html?Set-Language=en
5j	Vegetative Index	MODIS Normalized Difference Vegetative Index (NDVI)	https://modis.gsfc.nasa.gov/data/dataproduct/mod13.php

Section 5k Ozone and UV Radiation			
Sub-section	General Variable or Phenomenon	Specific dataset or variable	Source
5k1	Ozone, Total Column and Stratospheric	Aura OMI/MLS	https://disc.gsfc.nasa.gov/datasets/ML2O3_004/summary
5k1	Ozone, Total Column and Stratospheric	Bodeker Scientific	http://www.bodekerscientific.com/data/total-column-ozone
5k2	Ozone, Total Column and Stratospheric	OMTO3	https://disc.gsfc.nasa.gov/datasets/OMTO3_003/summary

Section 6b Atmospheric circulation and surface observations			
Sub-section	General Variable or Phenomenon	Specific dataset or variable	Source
6b	Modes of Variability	Marshall Southern Annular Mode Index	http://www.nerc-bas.ac.uk/icd/gjma/sam.html
6b	Temperature, [Near] Surface	ERA5	https://www.ecmwf.int/en/forecasts/datasets/reanalysis-datasets/era5
6b	Geopotential Height	ERA5	https://www.ecmwf.int/en/forecasts/datasets/reanalysis-datasets/era5
6b	Pressure, Sea Level or Near-Surface	ERA5	https://www.ecmwf.int/en/forecasts/datasets/reanalysis-datasets/era5
6b	Pressure, Sea Level or Near-Surface	University of Wisconsin Madison automated weather stations - Antarctic Meteorological Research and Data Center	https://amrdcdata.ssec.wisc.edu
6b	Temperature, [Near] Surface	University of Wisconsin Madison automated weather stations - Antarctic Meteorological Research and Data Center	https://amrdcdata.ssec.wisc.edu
6b	Temperature, Upper Atmosphere	ERA5	https://www.ecmwf.int/en/forecasts/datasets/reanalysis-datasets/era5
6b	Wind, Upper Atmosphere	ERA5	https://www.ecmwf.int/en/forecasts/datasets/reanalysis-datasets/era5

Section 6c ice-sheet surface mass balance			
Sub-section	General Variable or Phenomenon	Specific dataset or variable	Source
6c	Ice-sheet surface mass balance	ERA5	https://www.ecmwf.int/en/forecasts/datasets/reanalysis-datasets/era5
6c	Ice-sheet surface mass balance	MERRA-2	http://gmao.gsfc.nasa.gov/reanalysis/MERRA-2/

Section 6d ice-sheet melt extent and duration			
Sub-section	General Variable or Phenomenon	Specific dataset or variable	Source
6d	Ice-Sheet Surface Melt	DMSP-SSMIS	https://nsidc.org/data/nsidc-0001/versions/6
6d	Sea Ice Extent / Area / Concentration	Nimbus-7 SMMR Sea Ice Concentration	https://nsidc.org/data/nsidc-0007

Section 6e Ice-sheet Mass Balance			
Sub-section	General Variable or Phenomenon	Specific dataset or variable	Source
6e	Ice-Sheet Surface Height	ATLAS/ICESat-2 Land Height	https://nsidc.org/data/atl06/versions/5
6e	Ice-Sheet Mass	GRACE - GRACE FO CRI	https://podaac.jpl.nasa.gov/dataset/TELLUS_GRAC-GRFO_MASCON_CRI_GRID_RL06_V2
6e	Ice-Sheet Surface Height	ICESat-2	https://icesat-2.gsfc.nasa.gov/

Section 6f Sea Ice Extent, Concentration, and Seasonality			
Sub-section	General Variable or Phenomenon	Specific dataset or variable	Source
6f	Sea Ice Duration	Near-Real-Time DMSP SSM/I-SSMIS Daily Polar Gridded	https://nsidc.org/data/nsidc-0081/versions/2
6f	Sea Ice Duration	Nimbus-7 SMMR and DMSP SSM/I (Bootstrap)	https://nsidc.org/data/nsidc-0079/versions/3
6f	Sea Surface Temperature	NOAA Optimum Interpolation SST (OISST) v2.1	https://www.ncei.noaa.gov/products/optimum-interpolation-sst

Section 6g Southern Ocean			
Sub-section	General Variable or Phenomenon	Specific dataset or variable	Source
6g1	Sea Surface Temperature	NOAA Optimum Interpolation SST (OISST) v2	https://www.ncei.noaa.gov/products/optimum-interpolation-sst
6g1, 6g2, 6g3	Ocean Heat Content	Argo monthly climatology	https://sio-argo.ucsd.edu/RG_Climatology.html
6g1	Sea Surface Salinity	Argo monthly climatology	https://sio-argo.ucsd.edu/RG_Climatology.html
6g1	Mixed Layer Depth	Argo monthly climatology	https://sio-argo.ucsd.edu/RG_Climatology.html
6g3	Surface Heat flux	ERA5	https://www.ecmwf.int/en/forecasts/datasets/reanalysis-datasets/era5
6g3	Dissolved Oxygen	Argo profiling floats	https://argo.ucsd.edu/data/
6g3	Ocean Chlorophyll	GlobColour	https://doi.org/10.48670/moi-00281

Section 6h 2022 Antarctic Ozone Hole			
Sub-section	General Variable or Phenomenon	Specific dataset or variable	Source
6h	Cloud Volume	CALIPSO	http://www-calipso.larc.nasa.gov
6h	Temperature, upper atmosphere	MERRA-2	https://gmao.gsfc.nasa.gov/reanalysis/MERRA-2/
6h	Ozone, Total Column and Stratospheric	Aura MLS	https://disc.gsfc.nasa.gov/datasets?page=1&source=AURA%20MLS
6h	Ozone, Total Column and Stratospheric	Ozone Mapping Instrument (OMI) Ozone Mapping & Profiler Suite (OMPS), Total Ozone Mapping Spectrum (TOMS), Earth Probe TOMS (EPTOMS)	https://ozoneaq.gsfc.nasa.gov/data/ozone/ , http://ozonewatch.gsfc.nasa.gov
6h	Ozone, Lower Stratosphere	Ozonesonde	https://gml.noaa.gov/dv/spo_oz/
6h	Temperature, [Near] Surface	MERRA-2	http://gmao.gsfc.nasa.gov/reanalysis/MERRA-2/

Section SB6.1 The Antarctic Heat Wave of March 2022			
Sub-section	General Variable or Phenomenon	Specific dataset or variable	Source
SB6.1	Ice-Sheet Surface Melt	DMSPP-SSMIS	https://nsidc.org/data/nsidc-0001/versions/6
SB6.1	Temperature, [Near] Surface	University of Wisconsin Madison automated weather stations - Antarctic Meteorological Research and Data Center	https://amrdcdata.ssec.wisc.edu
SB6.1	Water Vapor Transport	ERA5	https://www.ecmwf.int/en/forecasts/datasets/reanalysis-datasets/era5
SB6.1	Water Vapor Transport	MERRA-2	http://gmao.gsfc.nasa.gov/reanalysis/MERRA-2/
SB6.1	Geopotential Height	MERRA-2	http://gmao.gsfc.nasa.gov/reanalysis/MERRA-2/
SB6.2	Ice Extent (photographic)	LANDSAT-8	https://www.usgs.gov/landsat-missions/landsat-data-access
SB6.2	Sea Ice Concentration	AMSR-2	https://seaice.uni-bremen.de/sea-ice-concentration/amsre-amsr2/
SB6.2	Wave propagation direction	WaveWatch III	https://polar.ncep.noaa.gov/waves/ensemble/download.shtml
SB6.2	Wave height	ERA5	https://www.ecmwf.int/en/forecasts/datasets/reanalysis-datasets/era5
	Ice-sheet surface mass balance	ERA5	https://www.ecmwf.int/en/forecasts/datasets/reanalysis-datasets/era5

SB6.2 Larsen B Fast Ice Breakout and Initial Glacial Response

Sub-section	General Variable or Phenomenon	Specific dataset or variable	Source
SB6.2	Ice Extent (photographic)	LANDSAT-8	https://www.usgs.gov/landsat-missions/landsat-data-access
SB6.2	Sea Ice Concentration	AMSR-2	https://seaice.uni-bremen.de/sea-ice-concentration/amsre-amsr2/
SB6.2	Wave propagation direction	WaveWatch III	https://polar.ncep.noaa.gov/waves/ensemble/download.shtml
SB6.2	Wave height	ERA5	https://www.ecmwf.int/en/forecasts/datasets/reanalysis-datasets/era5
	Ice-sheet surface mass balance	ERA5	https://www.ecmwf.int/en/forecasts/datasets/reanalysis-datasets/era5

